Radiogenic Isotope Geology

Second edition

ALAN P. DICKIN

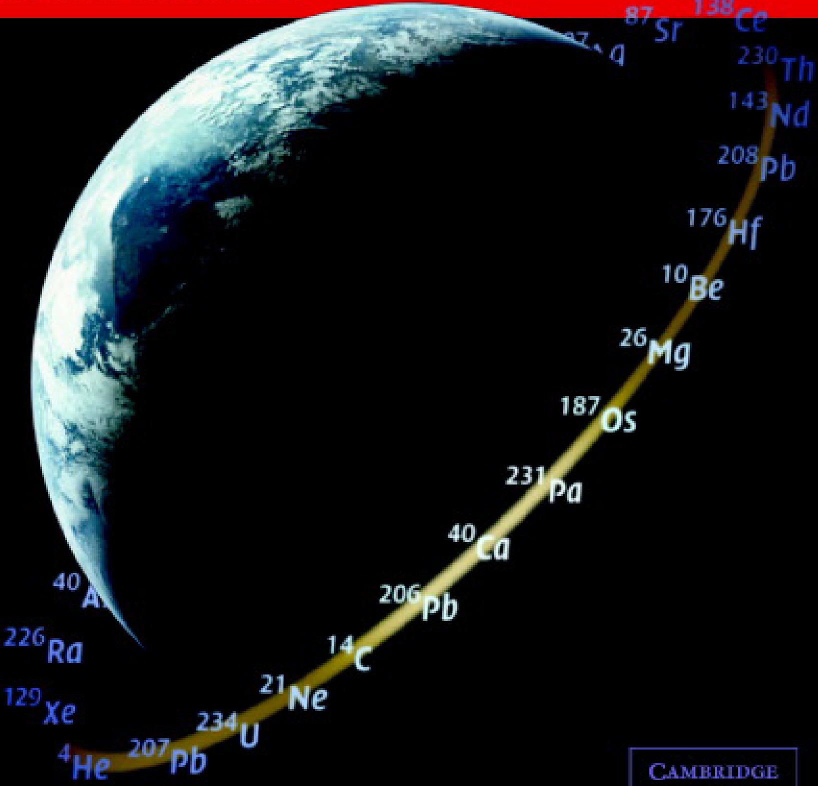

CAMBRIDGE

CAMBRIDGE

more information - www.cambridge.org/9780521823166

Radiogenic Isotope Geology

Modern isotope geochemistry is a rapidly expanding field that has a part to play in a broad range of Earth and planetary sciences – from extra-solar-system processes to environmental geoscience. This new edition of a popular textbook is completely updated and places more emphasis on the uses of radiogenic isotopes in environmental Earth science.

The author reviews the field of radiogenic isotope geology in a concise and visual manner to provide a comprehensive introduction to the subject and its wide variety of applications. For each technique, current ideas are presented in their historical context to allow the reader to understand the development of the theory. The latest ideas and methods, classic papers and case studies all come under scrutiny within this book.

An accessible introduction for scientists from other disciplines and an important reference for students and researchers working in isotope geology.

ALAN DICKIN has held a teaching position at McMaster University for 18 years. The first edition of this textbook was published in 1995, and has become widely established as the standard reference in the field.

Radiogenic Isotope Geology

Second Edition

Alan P. Dickin

School of Geography and Earth Sciences
McMaster University, Hamilton, Ontario

CAMBRIDGE
UNIVERSITY PRESS

CAMBRIDGE UNIVERSITY PRESS
Cambridge, New York, Melbourne, Madrid, Cape Town, Singapore, São Paulo

Cambridge University Press
The Edinburgh Building, Cambridge CB2 2RU, UK

Published in the United States of America by Cambridge University Press, New York

www.cambridge.org
Information on this title: www.cambridge.org/9780521823166

First published in print format 2005

ISBN-13 978-0-511-11544-8 eBook (MyiLibrary)
ISBN-10 0-511-11544-X eBook (MyiLibrary)

ISBN-13 978-0-521-82316-6 hardback
ISBN-10 0-521-82316-1 hardback

ISBN-13 978-0-521-53017-0 paperback
ISBN-10 0-521-53017-2 paperback

to Margaret

CONTENTS

8 Osmium isotopes 203

PREFACE

The objective of this book is to review the field of radiogenic isotope geology in a concise manner, in order to give readers an overview of the subject and to allow them to critically assess the past and future literature.

The approach is historical for three reasons: firstly, to give an impression of the development of thought in the field so that the reader can understand the origin of present ideas; secondly, to explain why past theories have had to be modified; and thirdly, to present 'fall back' positions lest current models be refuted at some future date. The need for this type of approach has been illustrated by several recent papers that have attempted to 'resurrect' old theories that had been discarded in the face of apparently strong evidence against them. Hence, we see that a knowledge of the 'classic work' in the field is an important starting point for current research.

The text is focussed on three types of literature. Firstly, it attempts to give accurate attribution of new ideas or methods; secondly, it reviews classic papers, although these may not have historical precedence; and thirdly, it presents case studies that have evoked controversy in the literature, as examples of alternative interpretations of data.

The radiogenic isotopic systems described in this book offer an analytical 'tool-box' of methods. The varied physical and chemical properties of different parent–daughter pairs suit them to a range of different dating and tracing tasks. Together, they allow constraints to be placed on the behaviour of complex natural systems in the solid and environmental Earth sciences.

The book is organised so that each chapter is a nearly free-standing entity covering one segment of the field of radiogenic isotope geology. However, the reader may benefit from an understanding of the thread, which, in the author's mind, links these chapters together.

Chapter 1 introduces radiogenic isotopes by discussing the synthesis and decay of nuclides within the context of nuclear stability. Decay constants and the radioactive decay law are introduced. Chapter 2 then provides an experimental background to many of the chapters that follow by discussing the details of mass spectrometric analysis (TIMS and ICP-MS) together with isochron regression fitting.

The next three chapters introduce the three pillars of lithophile isotope geology, comprising the Sr, Nd and Pb isotope methods. The emphasis is on their applications to geochronology and their evolution in terrestrial systems. Chapter 3 covers the Rb–Sr system, since this is one of the simplest and most basic dating methods. Chapter 4 covers the Sm–Nd system, including the use of Nd model ages to date crustal formation. Chapter 5 examines U–Pb geochronology and introduces the complexities of terrestrial Pb isotope evolution in a straightforward fashion. Each chapter ends with an examination of these isotopes as environmental tracers, focussing particularly on the oceans.

Chapters 6 and 7 apply Sr, Nd and Pb, as geochemical tracers, to the study of oceanic and continental igneous rocks. This is appropriate, because these isotopes are some of the basic tools of the isotope geochemist, which together may allow an understanding of the complexities of mantle processes and magmatic evolution. These methods are supplemented in Chapters 8 and 9 by insights from the Re–Os, Lu–Hf and other lithophile isotope systems, arising from their distinct chemistry.

Chapter 10 completes the panoply of long-lived isotopic dating systems by introducing the K–Ar and Ar–Ar methods, including their applications to magnetic and thermal histories. This leads us naturally in Chapter 11 to the consideration of rare gases as isotopic tracers, which give unique insights into the degassing history of the Earth.

Chapter 12 introduces the short-lived isotopes of the uranium decay series, covering classical and recent developments in the dating of Quaternary-age sedimentary rocks. This prepares us for the complexities of Chapter 13, which examines U-series isotopes as tracers in igneous systems. Short-lived processes in

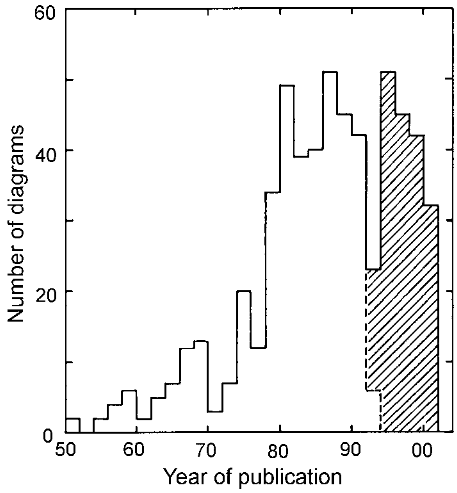

Histogram of the numbers of figures used in the second edition of *Radiogenic Isotope Geology* according to their publication dates (in biennial samples). The hatched area represents new material added since the publication of the first edition.

mantle melting and magma evolution are the focus of attention.

Chapter 14 examines the most important of the cosmogenic isotopes. These are not 'radiogenic' in the strictest sense, but represent a vast and growing field of chronology and isotope chemistry that is especially pertinent to environmental geoscience.

Finally, in Chapters 15 and 16, we examine two specialised fields that are on the fringes of radiogenic isotope analysis, but which provide powerful geological tools. The 'extinct' nuclides discussed in Chapter 15 are used to throw light on the early evolution of the solar system. Lastly, Chapter 16 examines the use of (radiogenic) fission-track analysis as a specialised dating tool for low-temperature thermal histories.

The text is gathered around a large number of diagrams, many of which are classic figures from the literature. Because of the centrality of these figures in the text, they give an indication of the historical coverage of the field in this book. The adjacent figure shows a 'snap-shot' of this data set, in the form of a histogram of the numbers of diagrams used from a series of two-yearly periods over the past fifty years. This analysis shows a 'period of emergence' of isotope geology in the first thirty years, followed by a 'mature period' with essentially uniform coverage over the last twenty years. The period of coverage ends in December 2002. Material from 2003 and subsequent years will be reviewed on the web site that supports this book (radiogenic.com).

I am very grateful to Conrad Guettler for his encouragement to begin this work, and to subsequent CUP editors Matt Lloyd and Sally Thomas for their ongoing assistance with the updating of the text. I also thank the many members of the geological community who gave helpful comments on the text during its evolution, and acknowledge the many authors and publishers for permission to reproduce their classic figures. Finally, and especially, I thank my family for their support and encouragement over the years, without which this book would not have been completed.

Acknowledgements

I am very grateful to the publishers listed below for permission to redraw figures from journals and books for which they hold the copyright. Author acknowledgement for all figures is given within individual figure captions, and corresponding titles, journal names, volumes and pages are contained in the list of cited references at the end of each chapter.

Elsevier Science Publishers B.V.	
Earth and Planetary Science Letters:	150 figures
Geochimica et Cosmochimica Acta:	87 figures
Chemical Geology:	35 figures
Nuclear Instruments and Methods:	6 figures
Nuclear Tracks:	6 figures
Lithos:	2 figures
Quaternary International:	1 figure
Macmillan Magazines Ltd	
Nature:	64 figures
American Geophysical Union	
Journal of Geophysical Research:	21 figures
Geophysical Research Letters:	8 figures
Water Resources Research:	4 figures
G cubed:	1 figure
American Association for the Advancement of Science	
Science:	32 figures
Geological Society of America	
Geology:	17 figures
Geological Society of America Bulletin:	2 figures
Springer-Verlag GmbH & Co.	
Contributions to Mineralogy and Petrology:	20 figures
Neodymium Isotopes in Geology (DePaolo, 1988):	1 figure
The Royal Society of London	
Philosophical Transactions, Royal Society of London	8 figures
Annual Reviews Inc.	
Annual Review of Earth & Planetary Sciences:	5 figures
Blackwell Scientific Publishers	
Australian Journal of Earth Sciences:	3 figures

Oxford University Press	
Journal of Petrology:	3 figures
The American Physical Society	
Reviews of Modern Physics:	2 figures
Blackie Ltd	
Handbook of Silicate Rock Analysis (Potts, 1987):	2 figures
Society for Sedimentary Geology (SEPM)	
Journal of Sedimentary Petrology:	2 figures
The University of Chicago Press	
Astrophysical Journal:	2 figures
Journal of Geology:	1 figure
Radiocarbon Dating (Libby, 1955):	1 figure
Academic Press, Inc.	
Icarus:	1 figure
American Chemical Society	
Environmental Science and Technology:	1 figure
American Geological Institute	
Geotimes:	1 figure
McGraw-Hill, Inc.	
Ages of Rocks, Planets and Stars (Faul, 1966):	1 figure
National Research Council of Canada	
Canadian Journal of Earth Science:	1 figure
University of California Press	
Nuclear Tracks in Solids (Fleischer *et al.*, 1975):	1 figure
Geological Association of Canada:	1 figure
Geoarchaeology:	1 figure
Journal of the Geological Society of London:	1 figure
Memoirs of the Institute of the University of Padova:	2 figures
Meteoritics and Planetary Science:	2 figures
Paleoceanography	1 figure
Quaternary Research	1 figure
Quaternary Science Review	1 figure
Radiocarbon:	2 figures
Reviews of Scientific Instruments:	1 figure
Scottish Journal of Geology:	1 figure
Tectonics:	1 figure
Tectonometrics:	1 figure
Zeitschrift für Physik:	1 figure
Total books	64 figures
Own	42 figures

1 Nucleosynthesis and nuclear decay

1.1 The chart of the nuclides

In the field of isotope geology, neutrons, protons and electrons can be regarded as the fundamental building blocks of the atom. The composition of a given type of atom, called a nuclide, is described by specifying the number of protons (atomic number, Z) and the number of neutrons (N) in the nucleus. The sum of these is the mass number (A). By plotting Z against N for all of the nuclides that have been known to exist (at least momentarily), the chart of the nuclides is obtained (Fig. 1.1). In this chart, horizontal rows of nuclides represent the same element (constant Z) with a variable number of neutrons (N). These are isotopes.

There are 264 known stable nuclides, which have not been observed to decay (with available detection equipment). These define a central 'path of stability', coloured black in Fig. 1.1. On either side of this path, the zig-zag outline defines the limits of experimentally known unstable nuclides (Hansen, 1987). These tend to undergo increasingly rapid decay as one moves out on either side of the path of stability. The smooth outer envelopes are the theoretical limits of nuclide stability, beyond which 'prompt' decay occurs. In that case the

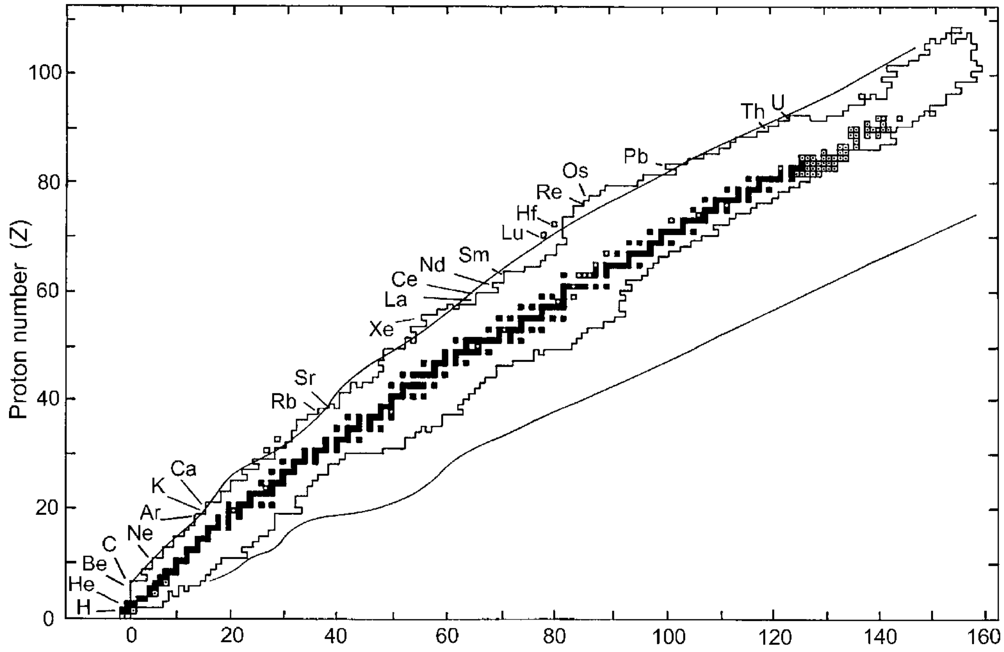

Fig. 1.1. Chart of the nuclides in coordinates of proton number, Z, against neutron number, N. (■) = stable nuclides; (◘) = naturally occurring long-lived unstable nuclides; (□) = naturally occurring short-lived unstable nuclides. Some geologically useful radionuclides are marked. Smooth envelope = theoretical nuclide stability limits. For links to more detailed nuclide charts on the web, see radiogenic.com.

synthesis and decay of an unstable nuclide occurs in a single particle interaction, giving it a zero effective lifetime. As work progresses, the domain of experimentally known nuclides should approach the theoretical envelope, as has already occurred for nuclides with $Z < 22$ (Hansen, 1987).

Recent experiments on the Darmstadt heavy-ion accelerator, reviewed by Normile (1996), have helped to expand the field of experimentally known unstable nuclides on the neutron-rich side of the path of stability (Fig. 1.1). These new isotopes were manufactured by bombarding target material with ^{238}U, triggering fission reactions that produce a few very-neutron-rich nuclei. The products were separated by mass spectrometry and their properties examined using high-energy detectors (e.g. Fig. 14.41). Knowledge about these unstable nuclei will improve our understanding of the nucleosynthetic r-process, which operates within this part of the nuclide chart (Fig. 1.7).

A few unstable nuclides have sufficiently long half-lives that they have not entirely decayed to extinction since the formation of the solar system. A few other short-lived nuclides are either continuously generated in the decay series of uranium and thorium, or produced by cosmic-ray bombardment of stable nuclides. These nuclides, and one or two extinct short-lived isotopes, plus their daughter products, are the realm of radiogenic isotope geology. Most of those with half-lives over 0.5 Myr are marked in Fig. 1.2. Nuclides with half-lives over 10^{12} yr decay too slowly to be geologically useful. Observation shows that all of the other long-lived isotopes either have been or are being applied in geology.

1.2 Nucleosynthesis

A realistic model for the nucleosynthesis of the elements must be based on empirical data for their 'cosmic abundances'. True cosmic abundances can be derived from stellar spectroscopy or by chemical analysis of galactic cosmic rays. However, such data are difficult to measure at high precision, so cosmic abundances are normally approximated by solar-system abundances. These can be determined by solar spectroscopy or by direct analysis of the most 'primitive' meteorites, carbonaceous chondrites. A comparison of the latter two sources of data (Ross and Aller, 1976) demonstrates that there is good agreement for most elements (Fig. 1.3). Exceptions are the volatile elements, which have been lost from meteorites, and elements of the Li–Be–B group, which are unstable in stars.

It is widely believed (e.g. Weinberg, 1977) that, about 30 minutes after the 'hot big bang', the matter of the universe (in the form of protons and neutrons) consisted mostly of ^{1}H and 22%–28% by mass of ^{4}He, along with traces of ^{2}H (deuterium) and ^{3}He. Hydrogen is still by far the most abundant element in the universe (88.6% of all nuclei) and, with helium,

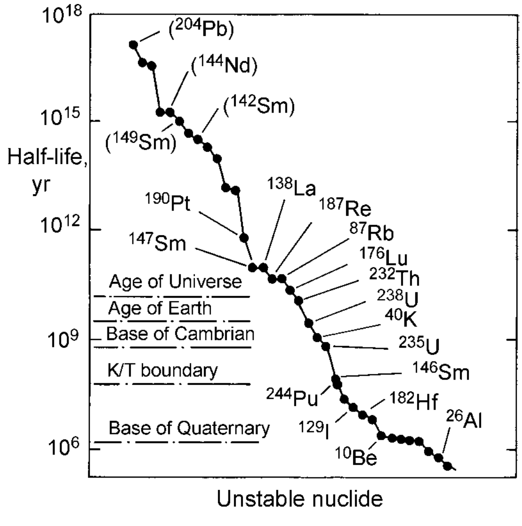

Fig. 1.2. Unstable nuclides with half-lives ($t_{1/2}$) over 0.5 Myr, in order of decreasing stability. Geologically useful parent nuclides are marked. Some very-long-lived radionuclides with no geological application are also marked, in brackets.

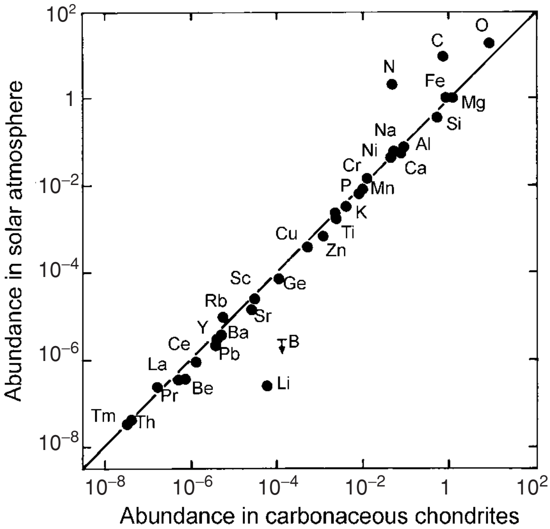

Fig. 1.3. Comparison of solar-system abundances (relative to silicon) determined by solar spectroscopy and by analysis of carbonaceous chondrites. After Ringwood (1979).

makes up 99% of its mass, but naturally occurring heavy nuclides now exist up to atomic weight 254 or beyond (Fig. 1.1). These heavier nuclei must have been produced by nucleosynthetic processes in stars, rather than in the big bang, because stars of different ages have different compositions that can be detected spectroscopically. Furthermore, stars at particular evolutionary stages may have compositional abnormalities, such as the presence of ^{254}Cf in supernovae. If nucleosynthesis of the heavy elements had occurred in the big bang, their distribution would be uniform throughout the universe.

1.2.1 Stellar evolution

Present-day models of stellar nucleosynthesis are based heavily on a classic review paper by Burbidge *et al.* (1957), in which eight element-building processes were identified (hydrogen burning, helium burning, α, e, s, r, x and p). Different processes were invoked to explain the abundance patterns of different groups of elements. These processes are, in turn, linked to different stages of stellar evolution. It is therefore appropriate at this point to summarise the life-history of some typical stars (e.g. Iben, 1967). The length of this life-history depends directly on the stellar mass, and can be traced on a plot of absolute magnitude (brightness) against spectral class (colour), referred to as the Hertzsprung–Russell or H–R diagram (Fig. 1.4).

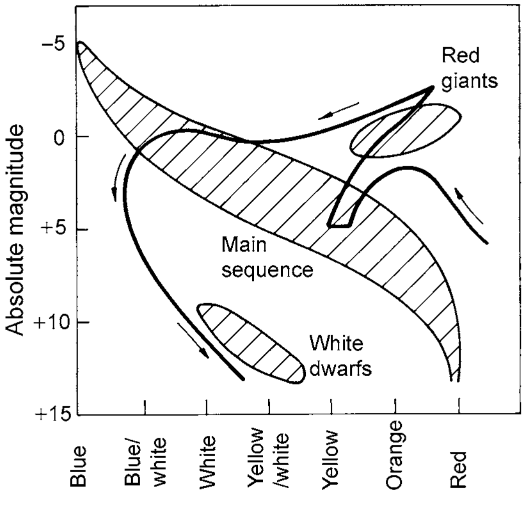

Fig. 1.4. Plot of absolute magnitude against spectral class of stars. Hatched areas show distributions of the three main star groups. The postulated evolutionary path of a star of solar mass is shown.

Gravitational accretion of a star of solar mass from cold primordial hydrogen and helium would probably take about 10^6 yr to raise the core temperature to about 10^7 K, when nuclear fusion of hydrogen to helium can begin (Atkinson and Houtermans, 1929). This process is also called 'hydrogen burning'. The star spends most of its life at this stage, as a 'main-sequence' star, where equilibrium is set up between energy supply by fusion and energy loss in the form of radiation. For the Sun, this stage will probably last about 10^{10} yr, but a very large star with fifteen times the Sun's mass may remain in the main sequence for only 10^7 yr.

When the bulk of hydrogen in a small star has been converted into ^{4}He, inward density-driven forces exceed outward radiation pressure, causing gravitational contraction. However, the resulting rise in core temperature causes expansion of the outer hydrogen-rich layer of the star. This forms a huge low-density envelope whose surface temperature may fall to about 4000 K, observed as a 'red giant'. This stage lasts only one tenth as long as the main-sequence stage. When core temperatures reach 1.5×10^7 K, a more efficient hydrogen-burning reaction becomes possible if the star contains traces of carbon, nitrogen and oxygen inherited from older generations of stars. This form of hydrogen burning is called the C–N–O cycle (Bethe, 1939).

At some point during the red-giant stage, core temperatures may reach 10^8 K, when fusion of He to carbon is ignited (the 'helium flash'). Further core contraction, yielding a temperature of about 10^9 K, follows as the helium supply becomes exhausted. At these temperatures an endothermic process of α-particle emission can occur, allowing the building of heavier nuclides up to mass 40. However, this quickly expends the remaining burnable fuel of the star, which then cools to a white dwarf.

More massive stars (of several solar masses) have a different life-history. In these stars, the greater gravitationally induced pressure–temperature conditions allow the fusion of helium to begin early in the red-giant stage. This is followed by further contraction and heating, allowing the fusion of carbon and successively heavier elements. However, as supplies of lighter elements become exhausted, gravitationally induced contraction and heating occur at an ever increasing pace (Fig. 1.5), until the implosion is stopped by the attainment of neutron-star density. The resulting shock wave causes a supernova explosion, which ends the star's life (e.g. Burrows, 2000).

In the minutes before explosion, when temperatures exceed 3×10^9 K, very rapid nuclear interactions occur. Energetic equilibrium is established between nuclei and free protons and neutrons, synthesising

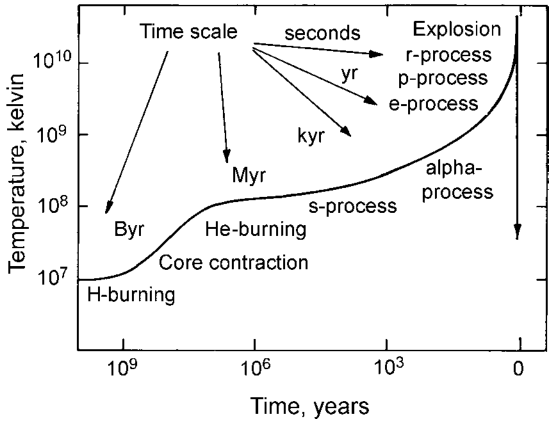

Fig. 1.5. Schematic diagram of the evolution of a large star, showing the nucleosynthetic processes that occur along its accelerating life-history in response to increasing temperature. Note that time is measured backwards from the end of the star's life on the right. After Burbidge *et al.* (1957).

elements like Fe by the so-called e-process. The supernova explosion itself lasts only a few seconds, but is characterised by colossal neutron fluxes. These very rapidly synthesise heavier elements, terminating at ^{254}Cf, which undergoes spontaneous fission. Products of the supernova explosion are distributed through space and later incorporated in a new generation of stars.

1.2.2 Stages in the nucleosynthesis of heavy elements

A schematic diagram of the cosmic abundance chart is given in Fig. 1.6. We will now see how various nucleosynthetic processes are invoked to account for its form.

The element-building process begins with the fusion of four protons to one ^{4}He nucleus, which occurs in three stages:

$$
\begin{aligned}
&{}^1\mathrm{H} + {}^1\mathrm{H} \rightarrow {}^2\mathrm{D} + \mathrm{e}^+ + \nu \\
&\qquad (Q = +1.44\ \mathrm{MeV},\ t_{1/2} = 1.4 \times 10^{10}\ \mathrm{yr}) \\
&{}^2\mathrm{D} + {}^1\mathrm{H} \rightarrow {}^3\mathrm{He} + \gamma \\
&\qquad (Q = +5.49\ \mathrm{MeV},\ t_{1/2} = 0.6\ \mathrm{s}) \\
&{}^3\mathrm{He} + {}^3\mathrm{He} \rightarrow {}^4\mathrm{He} + 2\,{}^1\mathrm{H} + \gamma \\
&\qquad (Q = +12.86\ \mathrm{MeV},\ t_{1/2} = 10^6\ \mathrm{yr})
\end{aligned}
$$

where Q is the energy output and $t_{1/2}$ is the reaction time of each stage (the time necessary to consume one-half of the reactants) for the centre of the Sun. The long reaction time for the first step explains the long duration of the hydrogen-burning (main-sequence) stage for small stars like the Sun. The overall reaction converts four protons into one helium nucleus, two positrons and two neutrinos, plus a large output of energy in the form of high-frequency photons. Hence the reaction is very strongly exothermic. Although deuterium and ^{3}He are generated in the first two reactions above, their consumption in the third accounts for their much lower cosmic abundances than that of ^{4}He.

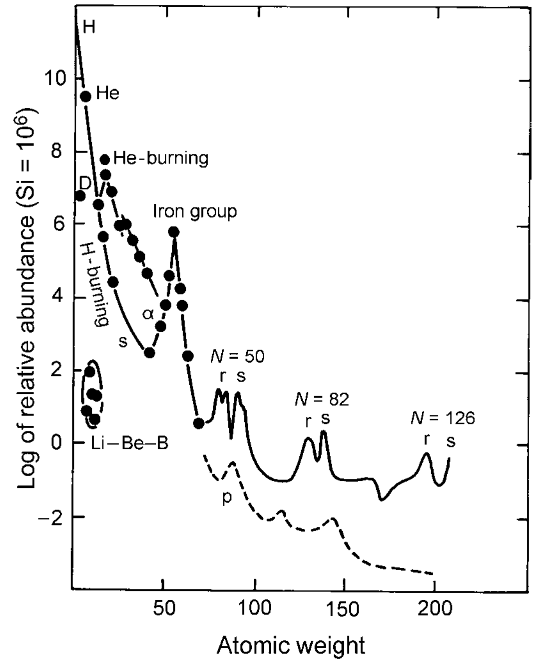

Fig. 1.6. Schematic diagram of the cosmic abundances of the elements, highlighting the nucleosynthetic processes responsible for forming various groups of nuclides. After Burbidge *et al.* (1957).

If heavier elements are present in a star (e.g. carbon and nitrogen) then the catalytic C–N–O sequence of reactions can occur, which also combines four protons to make one helium nucleus:

$$
\begin{aligned}
{}^{12}\mathrm{C} + {}^1\mathrm{H} &\rightarrow {}^{13}\mathrm{N} + \gamma \\
&\qquad (Q = +1.95\ \mathrm{MeV},\ t_{1/2} = 1.3 \times 10^7\ \mathrm{yr}) \\
{}^{13}\mathrm{N} &\rightarrow {}^{13}\mathrm{C} + \mathrm{e}^+ + \nu \\
&\qquad (Q = +2.22\ \mathrm{MeV},\ t_{1/2} = 7\ \mathrm{min}) \\
{}^{13}\mathrm{C} + {}^1\mathrm{H} &\rightarrow {}^{14}\mathrm{N} + \gamma \\
&\qquad (Q = +7.54\ \mathrm{MeV},\ t_{1/2} = 3 \times 10^6\ \mathrm{yr}) \\
{}^{14}\mathrm{N} + {}^1\mathrm{H} &\rightarrow {}^{15}\mathrm{O} + \gamma \\
&\qquad (Q = +7.35\ \mathrm{MeV},\ t_{1/2} = 3 \times 10^5\ \mathrm{yr}) \\
{}^{15}\mathrm{O} &\rightarrow {}^{15}\mathrm{N} + \mathrm{e}^+ + \nu \\
&\qquad (Q = +2.70\ \mathrm{MeV},\ t_{1/2} = 82\ \mathrm{s}) \\
{}^{15}\mathrm{N} + {}^1\mathrm{H} &\rightarrow {}^{12}\mathrm{C} + {}^4\mathrm{He} \\
&\qquad (Q = +4.96\ \mathrm{MeV},\ t_{1/2} = 10^5\ \mathrm{yr})
\end{aligned}
$$

The C–N–O elements have greater potential energy barriers to fusion than hydrogen, so these reactions require higher temperatures to operate than the simple proton–proton (p–p) reaction. However, the reaction times are much shorter than for the p–p reaction. Therefore the C–N–O reaction contributes less than 10% of hydrogen-burning reactions in a small star like the Sun, but is overwhelmingly dominant in large stars. This explains their much shorter lifespan in the main sequence.

Helium burning also occurs in stages:

$$\begin{aligned} {}^{4}\mathrm{He} + {}^{4}\mathrm{He} &\rightarrow {}^{8}\mathrm{Be} && (Q = +0.09\ \mathrm{MeV}) \\ {}^{8}\mathrm{Be} + {}^{4}\mathrm{He} &\rightarrow {}^{12}\mathrm{C}^{*} && (Q = -0.37\ \mathrm{MeV}) \\ {}^{12}\mathrm{C}^{*} &\rightarrow {}^{12}\mathrm{C} + \gamma && (Q = +7.65\ \mathrm{MeV}) \end{aligned}$$

The ^{8}Be nucleus is very unstable ($t_{1/2} < 10^{-15}$ s) and the Be/He equilibrium ratio in the core of a red giant is estimated at 10^{-9}. However, its life is just long enough to allow the possibility of collision with another helium nucleus. (Instantaneous three-particle collisions are very rare.) The energy yield of the first stage is small, and the second is actually endothermic, but the decay of excited ^{12}C* to the ground state is strongly exothermic, driving the equilibria to the right.

The elements Li, Be and B have low nuclear binding energies, so they are unstable at the temperatures of 10^{7} K and above found at the centres of stars. They are therefore bypassed by stellar nucleosynthetic reactions, leading to low cosmic abundances (Fig. 1.6). The fact that the five stable isotopes ^{6}Li, ^{7}Li, ^{9}Be, ^{10}B and ^{11}B exist at all has been attributed to fragmentation effects (spallation) of heavy cosmic rays (atomic nuclei travelling through the galaxy at relativistic speeds) as they hit interstellar gas atoms (Reeves, 1974). This is termed the x-process.

Problems have been recognised in the x-process model for generating the light elements Li, Be and B, since cosmic-ray spallation cannot explain the observed isotope ratios of these elements in solar-system materials. However, Casse *et al.* (1995) proposed that carbon and oxygen nuclei ejected from supernovae can generate these nuclides by collision with hydrogen and helium in the surrounding gas cloud. This process is believed to occur in regions such as the Orion nebula. The combination of supernova production with spallation of galactic cosmic rays can explain observed solar-system abundances of Li, Be and B.

Following the synthesis of carbon, further helium-burning reactions are possible, to produce heavier nuclei:

$$\begin{aligned} {}^{12}\mathrm{C} + {}^{4}\mathrm{He} &\rightarrow {}^{16}\mathrm{O} + \gamma && (Q = +7.15\ \mathrm{MeV}) \\ {}^{16}\mathrm{O} + {}^{4}\mathrm{He} &\rightarrow {}^{20}\mathrm{Ne} + \gamma && (Q = +4.75\ \mathrm{MeV}) \\ {}^{20}\mathrm{Ne} + {}^{4}\mathrm{He} &\rightarrow {}^{24}\mathrm{Mg} + \gamma && (Q = +9.31\ \mathrm{MeV}) \end{aligned}$$

Intervening nuclei such as ^{13}N can be produced by adding protons to these species, but are themselves consumed in the process of catalytic hydrogen burning mentioned above.

In old red-giant stars, carbon-burning reactions can occur:

$$\begin{aligned} {}^{12}\mathrm{C} + {}^{12}\mathrm{C} &\rightarrow {}^{24}\mathrm{Mg} + \gamma && (Q = +13.85\ \mathrm{MeV}) \\ &\rightarrow {}^{23}\mathrm{Na} + {}^{1}\mathrm{H} && (Q = +2.23\ \mathrm{MeV}) \\ &\rightarrow {}^{20}\mathrm{Ne} + {}^{4}\mathrm{He} && (Q = +4.62\ \mathrm{MeV}) \end{aligned}$$

The hydrogen and helium nuclei regenerated in these processes allow further reactions, which help to fill in gaps between masses 12 and 24.

When a small star reaches its maximum core temperature of 10^{9} K, the endothermic α-process can occur:

$$^{20}\mathrm{Ne} + \gamma \rightarrow {}^{16}\mathrm{O} + {}^{4}\mathrm{He} \qquad (Q = -4.75\ \mathrm{MeV})$$

The energy consumption of this process is compensated by strongly exothermic reactions such as

$$^{20}\mathrm{Ne} + {}^{4}\mathrm{He} \rightarrow {}^{24}\mathrm{Mg} + \gamma \qquad (Q = +9.31\ \mathrm{MeV})$$

so that the overall reaction generates a positive energy budget. The process resembles helium burning, but is distinguished by the different source of ^{4}He. The α-process can build up from ^{24}Mg through the sequence ^{28}Si, ^{32}S, ^{36}Ar and ^{40}Ca, where it terminates, owing to the instability of ^{44}Ti.

The maximum temperatures reached in the core of a small star do not allow substantial heavy-element production. However, in the final stages of the evolution of larger stars, before a supernova explosion, the core temperature exceeds 3×10^{9} K. This allows energetic equilibrium to be established by very rapid nuclear reactions between the various nuclei and free protons and neutrons (the e-process). Because ^{56}Fe is at the peak of the nuclear binding-energy curve, this element is most favoured by the e-process (Fig. 1.6). However, the other first-series transition elements V, Cr, Mn, Co and Ni in the mass range 50–62 are also attributed to this process.

During the last few million years of a red giant's life, a slow process of neutron addition with emission of γ rays (the s-process) can synthesise many additional nuclides up to mass 209 (see Fig. 1.7). Two possible neutron sources are

$$\begin{aligned} {}^{13}\mathrm{C} + {}^{4}\mathrm{He} &\rightarrow {}^{16}\mathrm{O} + \mathrm{n} + \gamma \\ {}^{21}\mathrm{Ne} + {}^{4}\mathrm{He} &\rightarrow {}^{24}\mathrm{Mg} + \mathrm{n} + \gamma \end{aligned}$$

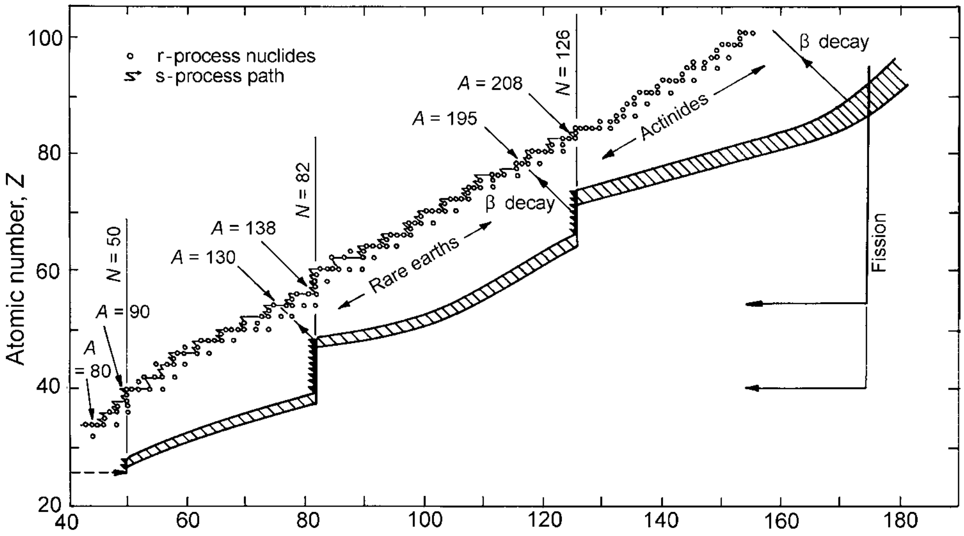

Fig. 1.7. Neutron-capture paths of the s-process and r-process shown on the chart of the nuclides. The hatched zone indicates the r-process nucleosynthetic pathway for a plausible neutron flux. Neutron 'magic numbers' are indicated by vertical lines, and mass numbers of nuclide-abundance peaks are marked. After Seeger *et al.* (1965).

The ^{13}C and ^{21}Ne parents can be produced by proton bombardment of the common ^{12}C and ^{20}Ne nuclides.

Because neutron capture in the s-process is relatively slow, unstable neutron-rich nuclides generated in this process have time to decay by β emission before further neutron addition. Hence the nucleosynthetic path of the s-process climbs in many small steps up the path of greatest stability of proton/neutron ratio (Fig. 1.7) and is finally terminated by the α decay of ^{210}Po back to ^{206}Pb and ^{209}Bi back to ^{205}Tl.

The 'neutron-capture cross-section' of a nuclide expresses how readily it can absorb incoming thermal neutrons, and therefore determines how likely it is to be converted to a species of higher atomic mass by neutron bombardment. Nuclides with certain neutron numbers (e.g. 50, 82 and 126) have unusually small neutron-capture cross-sections, making them particularly resistant to further reaction, and giving rise to local peaks in abundance at masses 90, 138 and 208. Hence, $N = 50$, 82 and 126 are empirically referred to as neutron 'magic numbers'.

In contrast to the s-process, which may occur over periods of millions of years in red giants, r-process neutrons are added in very rapid succession to a nucleus before β decay is possible. The nuclei are therefore rapidly driven to the neutron-rich side of the stability line, until they reach a new equilibrium between neutron addition and β decay, represented by the hatched zone in Fig. 1.7. Nuclides move along this r-process pathway until they reach a configuration with low neutron-capture cross-section (a neutron magic number). At these points a 'cascade' of alternating β decays and single neutron additions occurs, indicated by the notched ladders in Fig. 1.7. Nuclides climb these ladders until they reach the next segment of the r-process pathway.

Nuclides with neutron magic numbers build to excess abundances, as with the s-process, but they occur at proton-deficient compositions relative to the s-process stability path. Therefore, when the neutron flux falls off and nuclides on the ladders undergo β decay back to the stability line, the r-process local abundance peaks are displaced about 6–12 mass units below the s-process peaks (Fig. 1.6).

The r-process is terminated by neutron-induced fission at mass 254, and nuclear matter is fed back into the element-building processes at masses of about 108 and 146. Thus, cycling of nuclear reactions occurs above mass 108. Because of the extreme neutron flux postulated for the r-process, its occurrence is probably limited to supernovae.

The effects of r- and s-process synthesis of typical heavy elements may be demonstrated by an examination of the chart of the nuclides in the region of the light rare earths (Fig. 1.8). The step-by-step building of the s-process contrasts with the 'rain of nuclides' produced by β decay of r-process products. Some nuclides, such as those from ^{143}Nd to ^{146}Nd, are produced

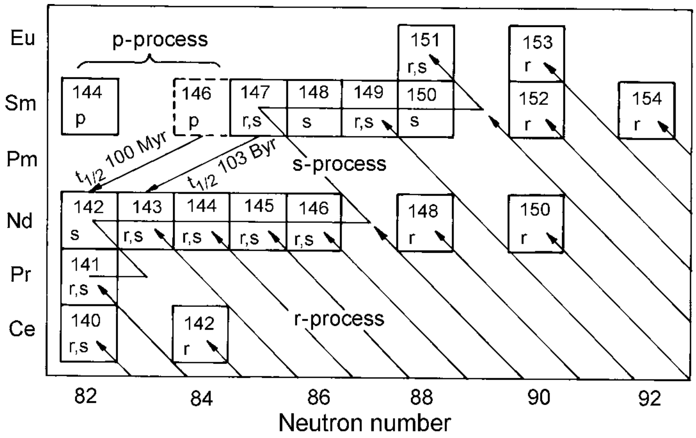

Fig. 1.8. Part of the chart of the nuclides in the area of the light rare earths to show p-, r- and s-process product nuclides. After O'Nions *et al.* (1979).

by both r- and s-processes. Some, such as ^{142}Nd, are s-only nuclides 'shielded' from the decay products of the r-process by intervening nuclides. Others, such as ^{148}Nd and ^{150}Nd, are r-only nuclides that lie off the s-process production pathway.

Several heavy nuclides from ^{74}Se to ^{196}Hg lie isolated on the proton-rich side of the s-process growth path (e.g. ^{144}Sm in Fig. 1.8), and are also shielded from r-process production. In order to explain the existence of these nuclides, it is necessary to postulate a p-process by which normal r- and s-process nuclei are bombarded by protons at very high temperature ($>2 \times 10^9$ K), probably in the outer envelope of a supernova.

1.3 Radioactive decay

Nuclear stability and decay are best understood in the context of the chart of nuclides. It has already been noted that naturally occurring nuclides define a path in the chart of the nuclides, corresponding to the greatest stability of proton/neutron ratio. For nuclides of low atomic mass, the greatest stability is achieved when the numbers of neutrons and protons are approximately equal ($N = Z$) but as atomic mass increases, the stable neutron/proton ratio increases until $N/Z = 1.5$. Theoretical stability limits are illustrated on a plot of N/Z against mass number (A) in Fig. 1.9 (Hanna, 1959).

The path of stability is in fact an energy 'valley' into which the surrounding unstable nuclides tend to fall, emitting particles and energy. This constitutes the process of radioactive decay. The nature of particles emitted depends on the location of the unstable nuclide relative to the energy valley. Unstable nuclides on either side of the valley usually decay by 'isobaric' processes. That is, a nuclear proton is converted to a neutron, or vice-versa, but the mass of the nuclide does not change significantly (except for the 'mass defect' consumed as nuclear binding energy). In contrast, unstable nuclides at the high end of the energy valley often decay by emission of a heavy particle (e.g. an α particle), thus reducing the overall mass of the nuclide.

1.3.1 Isobaric decay

The various decay processes indicated in Fig. 1.9 can best be understood by looking at example sections of the chart of nuclides. Figure 1.10 shows a part of the chart around the element potassium. The diagonal lines indicate isobars (nuclides of equal mass), which are displayed on energy sections in Figs. 1.11 and 1.12.

Nuclides deficient in protons decay by transformation of a neutron into a proton and an electron. The latter is then expelled from the nucleus as a negative 'β' particle (β^-), together with an anti-neutrino ($\bar{\nu}$). The energy released by the transformation is divided between the β particle and the anti-neutrino as kinetic energy (Fermi, 1934). The observed consequence is that the β particles emitted have a continuous energy distribution from nearly zero to the maximum decay energy. Low-energy β particles are very difficult to separate from background noise in a detector, making the β-decay constant of nuclides such as ^{87}Rb very difficult to determine accurately by direct counting (section 3.1).

In many cases the nuclide produced by β decay is left in an excited state, which subsequently decays to the

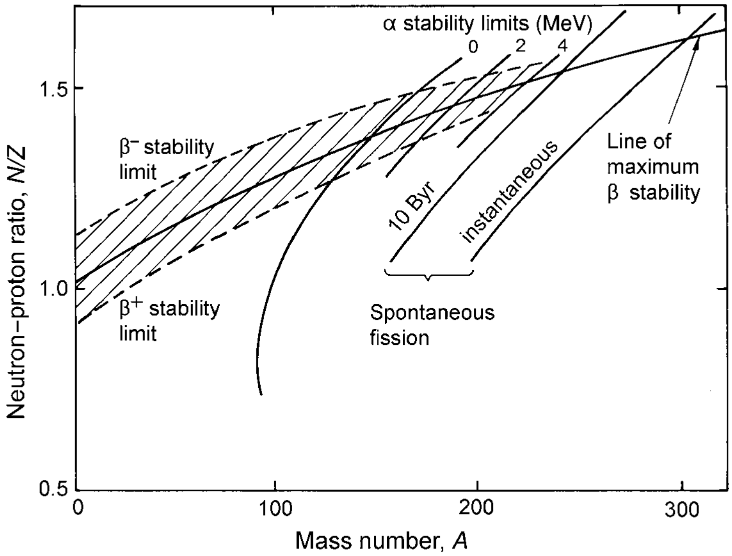

Fig. 1.9. Theoretical stability limits of nuclides illustrated on a plot of *N/Z* against mass number (*A*). Lower limits for α emission are shown for α energies of 0, 2 and 4 MeV. Stability limits against spontaneous fission are shown for half-lives of 10^{10} yr and zero (instantaneous fission). After Hanna (1959).

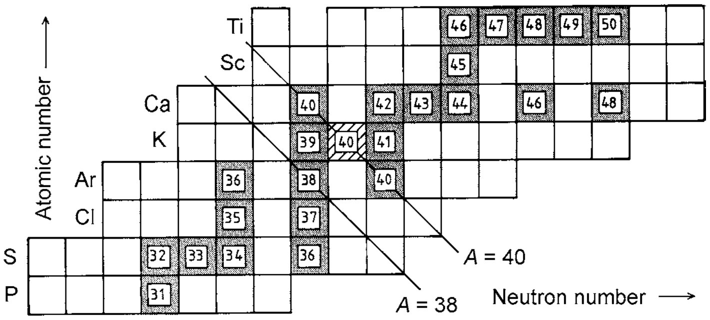

Fig. 1.10. Part of the chart of the nuclides, in coordinates of atomic number (*Z*) against neutron number (*N*) in the region of potassium. Stable nuclides are shaded; the long-lived unstable nuclide ^{40}K is hatched. Diagonal lines are isobars (lines of constant mass number, *A*).

ground-state nuclide by a release of energy. This may be lost as a γ ray of discrete energy, or may be transferred from the nucleus to an orbital electron, which is then expelled from the atom. In the latter case, nuclear energy emitted in excess of the binding energy of the electron is transferred to the electron as kinetic energy, which is superimposed as a line spectrum on the continuous spectrum of the β particles. The metastable states, or 'isomers', of the product nuclide are denoted by the superfix 'm', and have half-lives from less than a picosecond up to 241 years (in the case of ^{192m}Ir). Many β emitters have complex energy spectra involving a ground-state product and more than one short-lived isomer, as shown in Fig. 1.11. The decay of ^{40}Cl can yield 35 different isomers of ^{40}Ar (Lederer and Shirley, 1978), but these are omitted from Fig. 1.12 for the sake of clarity.

Nuclides deficient in neutrons, e.g. ^{38}K (Fig. 1.11), may decay by two different processes: positron emission and electron capture. Both processes yield a product nuclide that is an isobar of the parent, by transformation of a proton into a neutron. In positron emission a positively charged electron (β^+) is emitted from the nucleus together with a neutrino. As with β^- emission, the decay energy is shared between the kinetic energies of the two particles. After having been slowed down

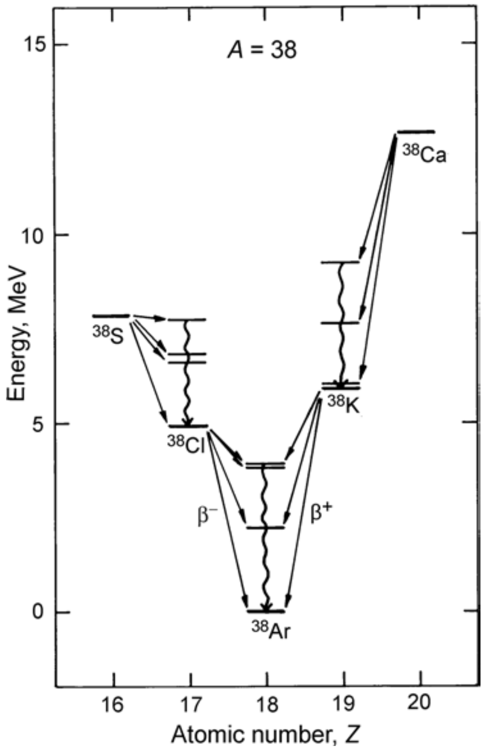

Fig. 1.11. A simple energy section through the chart of nuclides along the isobar $A = 38$ showing nuclides and isomers. Data from Lederer and Shirley (1978).

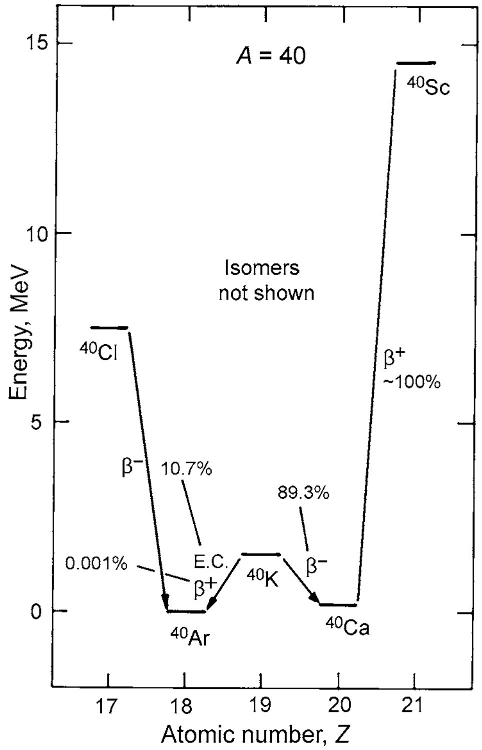

Fig. 1.12. Energy section through the chart of nuclides along isobar $A = 40$. Isomers are omitted for simplicity. For nuclides with more than one decay mechanism the percentages of transitions by different decay routes are indicated. Data from Lederer and Shirley (1978).

by collision with atoms, the positron interacts with an orbital electron, whereby both are annihilated, yielding two 0.511-MeV γ rays. (This forms part of the decay energy of the nuclear transformation.)

In electron-capture decay (EC) a nuclear proton is transformed into a neutron by capture of an orbital electron, usually from one of the inner shells, but possibly from an outer shell. A neutrino is emitted from the nucleus, and an outer orbital electron falls into the vacancy produced by electron capture, emitting a characteristic X-ray. The product nucleus may be left in an excited state, in which case it decays to the ground state by γ emission.

When the transition energy of a decay route is less than the energy equivalent of the positron mass ($2m_ec^2 = 1.022$ MeV), decay is entirely by electron capture. Thereafter, the ratio β^+/EC increases rapidly with increasing transition energy (Fig. 1.12), but a small amount of electron capture always accompanies positron emission even at high transition energies.

It is empirically observed (Mattauch, 1934) that adjacent isobars cannot be stable. Since ^{40}Ar and ^{40}Ca are both stable species (Fig. 1.10), ^{40}K must be unstable, and exhibits a branched decay to the isobars on either side (Fig. 1.12).

1.3.2 Alpha- and heavy-particle decay

Heavy atoms above bismuth in the chart of nuclides often decay by emission of an α particle, consisting of two protons and two neutrons (He^{2+}). The daughter product is not an isobar of the parent, and has an atomic mass reduced by four. The product nuclide may be in the ground state, or remain in an excited state and subsequently decay by γ emission. The decay energy is shared between kinetic energy of the α particle and recoil energy of the product nuclide.

The U and Th decay series are shown in Fig. 12.2. Because the energy valley of stable proton/neutron ratios in this part of the chart of the nuclides has a slope of less than unity, α decays tend to drive the products off to the neutron-rich side of the energy valley, where they undergo β decay. In fact, β decay may occur before the corresponding α decay.

At intermediate masses in the chart of the nuclides, α decay may occasionally be an alternative to positron or electron-capture decay for proton-rich species such as ^{147}Sm. However, α decays do not occur at low atomic numbers because the path of nuclear stability has a Z/N slope close to unity in this region (Fig. 1.1). Any such decays would simply drive unstable species along (parallel to) the energy valley.

An exotic kind of radioactive decay was discovered in the ^{235}U to ^{207}Pb decay series (Rose and Jones, 1984), whereby ^{223}Ra decays by emission of ^{14}C directly to ^{209}Pb with a decay energy of 13.8 MeV. However, this mode of decay occurs with a frequency of less than 10^{-9} that of the α decay of ^{223}Ra.

1.3.3 Nuclear fission and the Oklo natural reactor

The nuclide ^{238}U (atomic number 92) undergoes spontaneous fission into two product nuclei of different atomic numbers, typically about 40 and 53 (Sr and I), together with various other particles and a large amount of energy. Because the heavy parent nuclide has a high neutron/proton ratio, the daughter products have an excess of neutrons and undergo isobaric decay by β emission. Although the frequency of spontaneous fission of ^{238}U is less than 2×10^{-6} that of α decay, for heavier transuranium elements spontaneous fission is the principal mode of decay. Other nuclides, such as ^{235}U, may undergo fission if they are struck by a neutron. Furthermore, since fission releases neutrons, which promote further fission reactions, a chain reaction may be established. If the concentration of fissile nuclides is high enough, this leads to a thermonuclear explosion, as in a supernova or atomic bomb.

In special cases where an intermediate heavy-element concentration is maintained, a self-sustaining but non-explosive chain reaction may be possible. This depends largely on the presence of a 'moderator'. Energetic 'fast' neutrons produced by fission undergo multiple elastic collisions with atoms of the moderator. They are decelerated into 'thermal' neutrons, having velocities characteristic of the thermal vibration of the medium, the optimum velocity for promoting fission reactions in the surrounding heavy atoms. One natural case of such an occurrence is known, termed the Oklo natural reactor (Cowan, 1976; Naudet, 1976).

In May 1972, ^{235}U depletions were found in uranium ore entering a French processing plant and traced to an ore deposit at Oklo in the Gabon republic of central Africa. Despite its apparent improbability, there is overwhelming geological evidence that the ^{235}U depletions were caused by the operation of a natural fission reactor about 1.8 Byr ago. It appears that, during the Early Proterozoic, conditions were such that the series of coincidences needed to create a natural fission reactor were achieved more easily than at the present day.

This probably began when uranium dispersed in granitic basement was eroded and concentrated in stream-bed placer deposits. It was immobilised in this environment as the insoluble reduced form due to the nature of prevailing atmospheric conditions. With the appearance of blue–green algae, the first organisms capable of photosynthesis, the oxygen content of the atmosphere, and hence of river water, probably rose, converting some reduced uranium into more-soluble oxidised forms. These were carried down-stream in solution. When the soluble uranium reached a river delta, it must have encountered sediments rich in organic ooze, creating an oxygen deficiency that again reduced and immobilised uranium, but now at a much higher concentration (up to 0.5% uranium by weight).

After burial and compaction of the deposit, it was subsequently uplifted, folded and fractured, allowing oxygenated ground-waters to re-mobilise and concentrate the ores into veins over 1 m wide of almost pure uranium oxide. Hence the special oxygen-fugacity conditions obtaining in the Proterozoic helped to produce a particularly concentrated deposit. However, its operation as a reactor depended on the greater ^{235}U abundance (3%) at that time, compared with the present-day level of 0.72%, which has been reduced by α decay in the intervening time (half-life 700 Myr).

In the case of Oklo, light water (H_2O) must have acted as a moderator, and the nuclear reaction was controlled by a balance between loss of hot water (by convective heating or boiling) and its replacement by an influx of cold ground-water. In this way the estimated total energy output (15 000 megawatt years, representing the consumption of six tons of ^{235}U) was probably maintained at an average of only 20 kilowatts for about 0.8 Myr.

Geochemical evidence for the occurrence of fission is derived firstly from the characteristic elemental abundances of fission products. For example, excess concentrations of rare earths and other immobile elements such as Zr are observed. Concentrations of alkali metals and alkaline earths were probably also enriched, but these elements have subsequently been removed by leaching. Secondly, the characteristic isotope abundances of some elements can be explained only by invoking fission (Raffenach *et al.*, 1976).

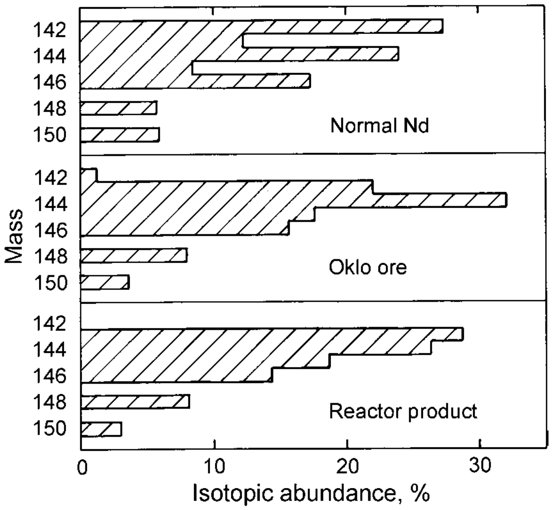

Fig. 1.13. Bar charts to compare the isotope compositions in normal Nd, Oklo ore, and reactor fission-product waste. Data from Cowan (1976).

The Nd isotope composition of the Oklo ore is very distinctive (Fig. 1.13). ^{142}Nd is shielded from isobaric decay of the neutron-rich fission products (Fig. 1.8), so its abundance indicates the level of normal Nd. After correction for enhanced abundances of ^{144}Nd and ^{146}Nd due to neutron capture by the large-cross-section nuclides ^{143}Nd and ^{145}Nd, Oklo Nd has an isotopic composition closely resembling that of normal reactor fission-product waste (Fig. 1.13).

Evidence for a significant neutron flux is also demonstrated by the isotope signatures of actinide elements. For example, the abundant isotope of uranium (^{238}U) readily captures fast neutrons to yield an appreciable amount of ^{239}U, which decays by β emission to ^{239}Np and then ^{239}Pu (Fig. 1.14). The latter decays by α emission with a half-life of 24 400 yr to yield more ^{235}U, contributing an extra 50% to the 'burnable' fuel, as in a 'fast' breeder reactor ('fast' refers to the speed of the neutrons involved). Because the fission products of ^{239}Pu and ^{235}U have distinct isotopic signatures, it is determined that very little ^{239}Pu underwent neutron-induced fission before decaying to ^{235}U. Hence, the low flux and prolonged lifetime of the natural reactor are deduced.

1.4 The law of radioactive decay

The rate of decay of a radioactive parent nuclide to a stable daughter product is proportional to the number of atoms, n, present at any time t (Rutherford and Soddy, 1902):

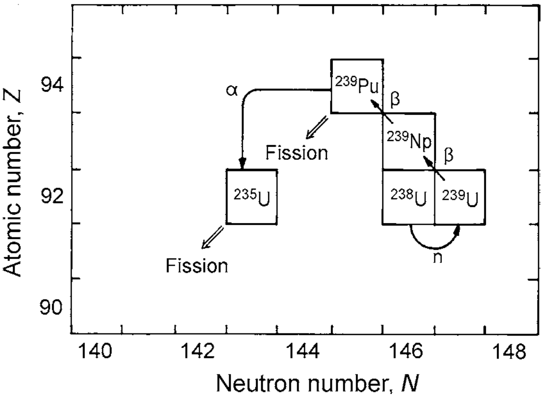

Fig. 1.14. Nuclear reactions leading to 'breeding' of transuranium element fuel in the Oklo natural reactor.

$$-\frac{dn}{dt} = \lambda n \qquad [1.1]$$

where λ is the constant of proportionality, which is characteristic of the radionuclide in question and is called the decay constant (expressed in units of reciprocal time). The decay constant states the probability that a given atom of the radionuclide will decay within a stated time. The term dn/dt is the rate of change of the number of parent atoms, and is negative because this rate decreases with time. On rearranging equation [1.1], we obtain

$$\frac{dn}{dt} = -\lambda n \qquad [1.2]$$

This expression is integrated from $t = 0$ to t, given that the number of atoms present at time $t = 0$ is n_0:

$$\int_{n_0}^{n} \frac{dn}{n} = -\lambda \int_{t=0}^{t} dt \qquad [1.3]$$

Hence

$$\ln\left(\frac{n}{n_0}\right) = -\lambda t \qquad [1.4]$$

which can also be written as

$$n = n_0 e^{-\lambda t} \qquad [1.5]$$

A useful way of referring to the rate of decay of a radionuclide is the 'half-life', $t_{1/2}$, which is the time required for half of the parent atoms to decay. On substituting $n = n_0/2$ and $t = t_{1/2}$ into [1.5], and taking the natural logarithm of both sides, we obtain

$$t_{1/2} = \frac{\ln 2}{\lambda} = \frac{0.693}{\lambda} \qquad [1.6]$$

The number of radiogenic daughter atoms formed, D^*, is equal to the number of parent atoms consumed:

$$D^* = n_0 - n \qquad [1.7]$$

but $n_0 = ne^{\lambda t}$ (from [1.5]); so substituting for n_0 in [1.7] yields

$$D^* = ne^{\lambda t} - n \qquad [1.8]$$

i.e.

$$D^* = n(e^{\lambda t} - 1) \qquad [1.9]$$

If the number of daughter atoms at time $t = 0$ is D_0, then the total number of daughter atoms after time t is given as

$$D = D_0 + n(e^{\lambda t} - 1) \qquad [1.10]$$

This equation is the fundamental basis of most geochronological dating tools.

In the uranium-series decay chains, the daughter products of radioactive decay (other than three Pb isotopes) are themselves radioactive. Hence the rate of decay of such a daughter product is given by the difference between its rate of production from the parent and its own decay rate:

$$dn_2/dt = n_1\lambda_1 - n_2\lambda_2 \qquad [1.11]$$

where n_1 and λ_1 are the abundance and decay constant of the parent, and n_2 and λ_2 correspond to the daughter.

However, [1.5] can be substituted for n_1 in [1.11] to yield

$$dn_2/dt = n_{1,\text{initial}}e^{-\lambda_1 t}\lambda_1 - n_2\lambda_2 \qquad [1.12]$$

This equation is integrated for a chosen set of initial conditions, the simplest of which sets $n_2 = 0$ at $t = 0$. Then

$$n_2\lambda_2 = \frac{\lambda_1}{\lambda_2 - \lambda_1} n_{1,\text{initial}}(e^{-\lambda_1 t} - e^{-\lambda_2 t}) \qquad [1.13]$$

This type of solution was first demonstrated by Bateman (1910) and is named after him. Catchen (1984) examined more general initial conditions for these equations, leading to more complex solutions.

1.4.1 Uniformitarianism

When using radioactive decay to measure the ages of rocks, we must apply the classic principle of uniformitarianism (Hutton, 1788), by assuming that the decay constant of the parent radionuclide has not changed during the history of the Earth. It is therefore important to outline some evidence that this assumption is justified.

The decay constant of a radionuclide depends on nuclear constants, such as a (which equals the square of the elementary charge, divided by Planck's constant and the velocity of light). Shlyakhter (1976) argued that the neutron-capture cross-section of a nuclide is very sensitively dependent on nuclear constants. Because neutron absorbers (such as ^{143}Nd and ^{145}Nd) in the 1.8-Byr-old Oklo natural reactor give rise to the expected increases in abundance of product isotopes (Fig. 1.13), this constrains nuclear constants to have remained more or less invariant over the last 2 Byr.

The possibility that physical conditions (e.g. pressure and temperature) could affect radionuclide decay constants must also be examined. Because radioactive decay is a property of the nucleus, which is shielded from outside influence by orbital electrons, it is very unlikely that physical conditions influence α or β decay, but electron-capture decay could be affected. Hensley *et al.* (1973) demonstrated that the electron-capture decay of ^{7}Be to ^{7}Li is increased by 0.59% when BeO is subjected to 270 ± 10 kbar pressure in a diamond anvil. This raises the question of whether the electron-capture decay of ^{40}K to ^{40}Ar could be pressure-dependent, affecting K–Ar dates. In fact, this is very unlikely, because under high-pressure–temperature conditions at depth in the Earth, K–Ar systems will be chemically open and unable to yield dates at all, while at crustal depths the pressure dependence of λ will be negligible compared with experimental errors.

There are a few ways in which the invariance of decay constants has been verified experimentally. Uranium-series dates have been calibrated against coral growth bands back to one thousand years (section 12.4.2), the radiocarbon method has been calibrated against tree rings (dendrochronology) back to 10 kyr (section 14.1.4), and K–Ar ages have been calibrated against rates of sea-floor spreading over periods of several million years (section 10.4). In addition, age agreements between systems with very different decay constants also provide supporting evidence.

There have been many attempts to test the consistency of various decay constants by comparing ages for geologically 'well-behaved' systems using different dating methods (e.g. Begemann *et al.*, 2001). As well as verifying the uniformitarian assumption, such geological decay-constant comparisons allow the values for poorly known decay schemes to be optimised by comparison with better-known decay schemes. At present, the uranium decay constants are the most well established, and therefore the basis for most comparisons. However, a promising new calibration is the 'astronomical timescale', which is based on the tuning of

Table 1.1. *Summary of decay constants and half-lives of long-lived nuclides*

	Decay constant			
Nuclide	Steiger and Jäger (1977)	'Best value'	Half-life	Reference
^{40}K(^{40}Ar)	5.81×10^{-11}		11.93 Byr	Beckinsale and Gale (1969)
^{40}K(^{40}Ca)	4.962×10^{-10}		1.397 Byr	
^{40}K(total)	5.543×10^{-10}		1.25 Byr	
^{87}Sr	1.42×10^{-11}	1.402×10^{-11}	49.44 Byr	Minster *et al.* (1982)
^{147}Sm		6.54×10^{-12}	106.0 Byr	Lugmair and Marti (1978)
^{176}Lu		1.867×10^{-11}	37.1 Byr	Scherer *et al.* (2001)
^{186}Re		1.666×10^{-11}	41.6 Byr	Smoliar *et al.* (1996)
^{190}Pt		1.477×10^{-12}	469.3 Byr	Brandon *et al.* (1999)
^{230}Th		9.1577×10^{-6}	75.69 kyr	Cheng *et al.* (2000)
^{232}Th		4.9475×10^{-11}	14.01 Byr	Jaffey *et al.* (1971)
^{231}Pa		2.116×10^{-5}	32.76 kyr	Robert *et al.* (1969)
^{234}U		2.826×10^{-6}	245.25 kyr	Cheng *et al.* (2000)
^{235}U	9.8485×10^{-10}	Unchanged	703.8 Myr	Jaffey *et al.* (1971)
^{238}U	1.55125×10^{-10}	Unchanged	4 468.0 Myr	Jaffey *et al.* (1971)

glacial cycles to the Earth's orbital motions (section 10.4).

The best approach to the improvement of decay constants is new and better measurement. Where this is not possible, a useful alternative is acceptance by the geological community of a 'recommended value'. The most successful application of this procedure was the IUGS Subcommission on Geochronology (Steiger and Jäger, 1977). The recommendations served as a useful standard for 20 years but are now in need of revision. Therefore, Table 1.1 presents these values where applicable, together with a compilation of the best values of decay constants obtained since that time, by various methods. Full references and further details are given in the appropriate chapters.

References

Atkinson, R. and Houtermans, F. G. (1929). Zur Frage der Aufbaumöglichkeit der Elemente in Sternen. *Z. Physik* **54**, 656–65.

Bateman, H. (1910). Solution of a system of differential equations occurring in the theory of radio-active transformations. *Proc. Cambridge Phil. Soc.* **15**, 423–7.

Begemann, F., Ludwig, K. R., Lugmair, G. W. *et al.* (2001). Call for an improved set of decay constants for geochronological use. *Geochim. Cosmochim. Acta* **65**, 111–21.

Bethe, H. A. (1939). Energy production in stars. *Phys. Rev.* **55**, 434–56.

Burbidge, E. M., Burbidge, G. R., Fowler, W. A. and Hoyle, F. (1957). Synthesis of the elements in stars. *Rev. Mod. Phys.* **29**, 547–647.

Burrows, A. (2000). Supernova explosions in the Universe. *Nature* **403**, 727–33.

Casse, M., Lehoucq, R. and Vangioni-Flam, E. (1995). Production and evolution of light elements in active star-forming regions. *Nature* **373**, 318–19.

Catchen, G. L. (1984). Application of the equations of radioactive growth and decay to geochronological models and explicit solution of the equations by Laplace transformation. *Isot. Geosci.* **2**, 181–95.

Cowan, G. A. (1976). A natural fission reactor. *Sci. Amer.* **235** (1), 36–47.

Fermi, E. (1934). Versuch einer Theorie der β-Strahlen. *Z. Physik* **88**, 161–77.

Hanna, G. C. (1959). Alpha-radioactivity. In Segre, E. (Ed.), *Experimental Nuclear Physics, Vol. 3*. Wiley, pp. 54–257.

Hansen, P. G. (1987). Beyond the neutron drip line. *Nature* **328**, 476–7.

Hensley, W. K., Basset, W. A. and Huizenga, J. R. (1973). Pressure dependence of the radioactive decay constant of beryllium-7. *Science* **181**, 1164–5.

Hutton, J. (1788). Theory of the Earth; or an investigation of the laws observable in the composition, dissolution, and restoration of land upon the globe. *Trans. Roy. Soc. Edinburgh* **1**, 209–304.

Iben, I. (1967). Stellar evolution within and off the Main Sequence. *Ann. Rev. Astron. Astrophys.* **5**, 571–626.

Lederer, C. M. and Shirley, V. S. (1978). *Table of Isotopes*, 7th edn. Wiley.

Mattauch, J. (1934). Zur Systematik der Isotopen. *Z. Physik* **91**, 361–71.

Naudet, R. (1976). The Oklo nuclear reactors: 1800 million years ago. *Interdisc. Sci. Rev.* **1**, 72–84.

Normile, D. (1996). Nuclear physics – flood of new isotopes offers keys to stellar evolution. *Science* **273**, 433.

O'Nions, R. K., Carter, S. R., Evensen, N. M. and Hamilton P. J. (1979). Geochemical and cosmochemical applications of Nd isotope analysis. *Ann. Rev. Earth Planet. Sci.* **7**, 11–38.

Raffenach, J. C., Menes, J., Devillers, C., Lucas, M. and Hagemann, R. (1976). Etudes chimiques et isotopiques de l'uranium, du plomb et de plusieurs produits de fission dans un échantillon de minéral du réacteur naturel d'Oklo. *Earth Planet. Sci. Lett.* **30**, 94–108.

Reeves, H. (1974). Origin of the light elements. *Ann. Rev. Astron. Astrophys.* **12**, 437–69.

Ringwood, A. E. (1979). Composition and origin of the Earth. In: McElhinny, M. W. (Ed.) *The Earth: Its Origin, Structure and Evolution*. Academic Press, pp. 1–58.

Rose, H. J. and Jones, G. A. (1984). A new kind of radioactivity. *Nature* **307**, 245–7.

Ross, J. E. and Aller, L. H. (1976). The chemical composition of the Sun. *Science* **191**, 1223–9.

Rutherford, E. and Soddy, F. (1902). The radioactivity of thorium compounds II. The cause and nature of radioactivity. *J. Chem. Soc. Lond.* **81**, 837–60.

Seeger, P. A., Fowler, W. A. and Clayton, D. D. (1965). Nucleosynthesis of heavy elements by neutron capture. *Astrophys. J. Suppl.* **11**, 121–66.

Shlyakhter, A. I. (1976). Direct test of the constancy of fundamental nuclear constants. *Nature* **264**, 340.

Steiger, R. H. and Jäger, E. (1977). Subcommission on geochronology: convention on the use of decay constants in geo- and cosmo-chronology. *Earth Planet. Sci. Lett.* **36**, 359–62.

Weinberg, S. (1977). *The First Three Minutes*. André Deutsch, 190 pp.

2 Mass spectrometry

In order to use radiogenic isotopes as dating tools or tracers, they must be separated from non-radiogenic isotopes in a 'mass spectrometer'. The concept of separating positive ions according to their mass was conceived by Thompson, who proposed the use of this technique in chemical analysis (Thompson, 1913). The first type of mass spectrometer to be invented was a 'magnetic-sector' instrument, and one of the earliest such instruments was described by Dempster (1918). A cloud of positive ions was accelerated and collimated, then passed through a sector-shaped magnetic field, which separated the ions by mass. Aston (1927) used such an instrument to make the first isotope-ratio measurements on lead.

Other methods of mass separation are also possible, such as the 'quadrupole' instrument (section 2.2.2). A fore-runner of this design was actually the first instrument to be named a mass spectrometer (Smyth and Mattauch, 1932). However, the first high-precision mass spectrometer (Nier, 1940), was based on the magnetic-sector approach. Nier's design pioneered so many of the features of modern mass spectrometers (Fig. 2.1) that these have often been called 'Nier-type' instruments.

The normal method of ionising a sample in a mass spectrometer is simply to heat it under vacuum, either from a gaseous source, as in the case of the rare gases He, Ne, Ar and Xe, or from a purified solid sample loaded on a metal filament. Hence the method is termed thermal-ionisation mass spectrometry (TIMS). However, thermal ionisation is only effective if the sample is first purified by extraction from the matrix that makes up most of the rock sample. Therefore, the normal starting point of precise isotopic measurements by TIMS is chemical separation of the element to be analysed.

More recently, the use of an inductively coupled plasma (ICP) source has relaxed some of the requirements for chemical purification before mass spectrometry (section 2.5). In particular, minerals with relatively high concentrations of radiogenic elements may be analysed by *in situ* laser ablation. However, in matrices such as whole-rocks, where the concentration of radiogenic isotopes is often low, it is still necessary to pre-concentrate most samples, after which they are introduced into the plasma in aqueous solution. Therefore, methods of dissolution and chemical extraction will now be examined.

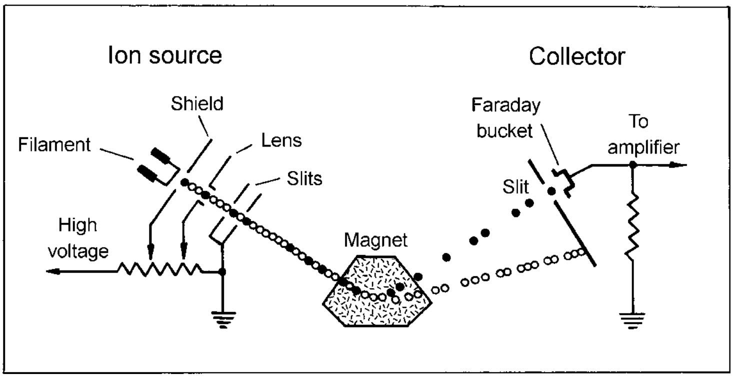

Fig. 2.1. Schematic illustration of the basic features of a 'Nier-type' magnetic-sector mass spectrometer. Solid and open circles represent the light and heavy isotopes of an element. After Faul (1966).

2.1 Chemical separation

Geological samples, which are commonly silicates, are routinely dissolved in concentrated hydrofluoric acid (HF), although some laboratories use perchloric acid ($HClO_4$) as well. Most rock-forming minerals will dissolve in hot concentrated HF at atmospheric pressure. However, certain resistant minerals such as zircon must be dissolved under pressure in a bomb, in order to achieve the temperatures of up to 220 °C necessary for decomposition. The bomb liners and beakers used for dissolution are almost universally made of polyfluorinated ethylene (PFE).

The conventional bomb-dissolution technique for zircons is described by Krogh (1973). A more recent technique, pioneered by Krogh and described by Parrish (1987), is to place several 'micro-capsules' carrying different samples into one larger bomb. The micro-capsules are open to vapour transfer of HF, but Pb blanks are very low (less than 50 pg), showing that volatile transfer of Pb between samples does not occur.

A major problem that may be encountered after dissolution in HF is the formation of fluorides that are insoluble in other 'mineral' acids (e.g. hydrochloric acid, HCl). Refluxing with nitric acid (HNO_3) helps to convert these into soluble forms. Experiments by Croudace (1980) suggested that this process was promoted if additional nitric acid was added before complete evaporation of the HF stage.

If at some stage complete dissolution is not achieved, it may be necessary to decant off the solution and return the undissolved fraction to the previous stage of the process for a second acid attack (Patchett and Tatsumoto, 1980). When complete dissolution has been achieved, the solution may need to be split into weighed aliquots, so that one fraction can be 'spiked' with an enriched isotope for isotope-dilution analysis (section 2.4) while another is left 'unspiked' for accurate isotope-ratio analysis (section 2.3). Following dissolution, the sample is often converted into a chloride for elemental separation, which is normally performed by ion exchange between a dilute acid (eluent) and a resin (stationary phase) contained in quartz or PFE columns.

2.1.1 Rb–Sr

The separation of Rb and Sr, and the preliminary separation of Sm–Nd, is often performed on a cation-exchange column eluted with dilute (e.g. 2.5 M) HCl. Columns are normally calibrated in advance of use by means of test solutions. Finally, before separation of the sample, the column resin is cleaned by passing sequential volumes of 50% acid and water.

A small volume of the rock solution is loaded into the column, washed into the resin bed carefully with eluent, and then washed through with more eluent until a fraction is collected when the desired element is released from the resin. For TIMS analysis, the sample is evaporated to dryness, ready to load onto a metal filament. Elements are eluted from the cation column by HCl in roughly the following order: Fe, Na, Mg, K, Rb, Ca, Sr, Ba, rare-earth elements (Crock *et al.*, 1984). This series is defined by increasing partition coefficient onto the solid phase (resin), requiring increasing volumes of eluent to release successive elements.

It is very important to remove the 'major elements' of the rock, e.g. Na, K and Ca, from the Sr cut. Nitric acid is not effective for this purpose because it does not separate Sr from Ca (Fig. 2.2). Rb must also be

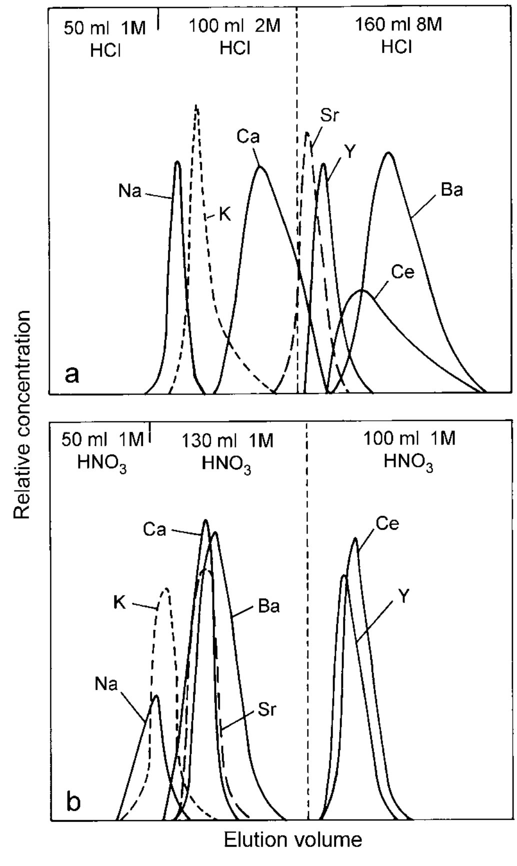

Fig. 2.2. Elution curves for various elements from cation exchange columns: (a) with hydrochloric acid and (b) with nitric acid. Modified after Crock *et al.* (1984).

eliminated from Sr because ^{87}Rb causes a direct isobaric interference onto ^{87}Sr. Small levels of Rb are not a problem in an otherwise clean sample because the Rb burns off before collection of Sr data begins. However, the presence of significant amounts of Ca in the Sr cut prevents burn-off of Rb, causing major interference problems.

2.1.2 Sm–Nd

Rare-earth elements (REE) may be separated as a group on a cation-exchange column eluted with dilute mineral acid, but because the chemical properties of individual rare earths are so similar, more refined techniques must be used for separations within the REE group. This is necessary for TIMS analysis because there are several isobaric interferences (e.g. ^{144}Sm interferes onto ^{144}Nd). Ba must also be kept to a minimum in the REE cut because it suppresses the ionisation of trivalent REE ions. This can be done by switching to a dilute (e.g. 2 M) nitric acid medium after collection of the Sr cut, whereupon Ba is rapidly washed off the column ahead of the rare earths (Crock *et al.*, 1984). The REE can be stripped most quickly as a group in about 50% HNO_3 (Fig. 2.2).

Several methods of separation between the rare earths have been used:

(1) Hexyl di-ethyl hydrogen phosphate (HDEHP)-coated Teflon powder (stationary phase) with dilute mineral-acid eluent (Richard *et al.*, 1976). In this technique, which may be called the 'reverse-phase' method, light REE are eluted first, whereas in the other techniques, heavy REE are eluted first. The reverse-phase method yields sharp elution fronts but long tails (Fig. 2.3). It is very effective for removing the Sm interference from ^{144}Nd, and at present most popular. However, substantial Ce is usually present in the Nd cut, so ^{142}Nd cannot be measured accurately (section 2.2.3). Similarly, the separation between light REE is not good enough for Ce isotope analysis.

(2) Cation-exchange resin with hydroxy-isobutyric acid (HIBA) eluent (Eugster *et al.*, 1970; Dosso and Murthy, 1980). This method requires more work in preparation of eluent, whose pH must be carefully controlled. It is therefore less popular than (1) for Nd, but very effective for Ce (Tanaka and Masuda, 1982; Dickin *et al.*, 1987).

(3) Anion-exchange resin with methanol–dilute acetic acid–dilute nitric acid eluent (Hooker *et al.*, 1975, O'Nions *et al.*, 1977). This method is least popular at present, but may be better than (1) if an analysis of ^{142}Nd is required.

(4) An alternative approach described by Cassidy and Chauvel (1989) is to use high-pressure liquid chromatography (HPLC).

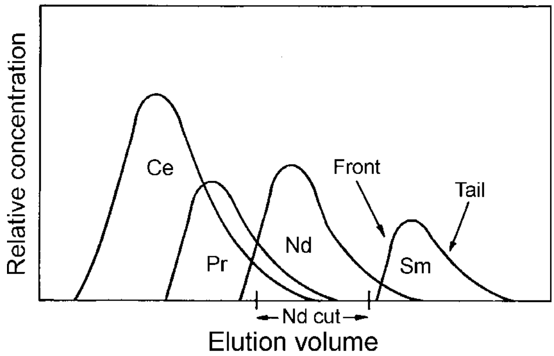

Fig. 2.3. Elution profiles of light REE from a reverse-phase HDEHP column, showing sharp peak fronts and long tails.

2.1.3 Lu–Hf

Precise Hf isotope analysis requires a high-quality separation from Zr, because the presence of Zr strongly suppresses ionisation of Hf. However, separating Hf and Zr is difficult because of the similar chemistries of these elements. In addition, Ti also has similar chemistry to Hf, and, because of its high abundance in mafic rocks, this must be efficiently removed. Hence, the method developed by Patchett and Tatsumoto (1980) involved three stages of ion-exchange column separation. It was also necessary to carry out much of the procedure in HF, due to the risk of deposition of insoluble fluorides.

Although Hf isotope analysis is now performed by MC-ICP-MS, it is still necessary to purify Hf before analysis in order to obtain good data. A revised method developed by Barovich *et al.* (1995) has been used quite widely. This also involves three stages of (anion) column chemistry, but only the first is eluted with HF. The second and third columns are eluted principally with H_2SO_4. A modification of this process by David *et al.* (1999) was able to use only two columns by having a multi-step elution process with several changes in type of acid (e.g. H_2SO_4–H_2O–HF–HCl).

2.1.4 Lead

Lead (Pb) and uranium (U) have normally been separated from zircons by elution with HCl on

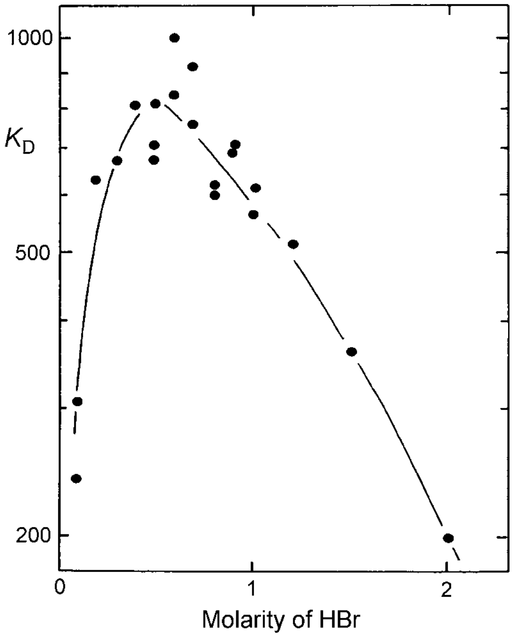

Fig. 2.4. Plot showing the distribution coefficient (K_D) of Pb from dilute HBr onto anion-exchange resin as a function of molarity. The curve represents a best fit to the data points. After Manton (1988).

anion-exchange columns (Catanzaro and Kulp, 1964). However, this method is not able to separate Pb from the large quantities of Fe in whole-rock samples, which then causes unstable Pb emission during mass spectrometry. A widely used alternative is to elute all elements except Pb from a miniature anion column with dilute hydrobromic acid (Chen and Wasserburg, 1981). The distribution coefficient for Pb onto the resin has a maximum value at just under 1 M HBr, and falls off sharply on either side (Fig. 2.4). Elution with HBr effectively strips most elements, including Fe, from the column. However, an alternative is to elute with a mixture of 0.5 M HBr and 0.5 M HNO_3, which removes Zn more efficiently than does HBr alone (e.g. Kuritani and Nakamura, 2002). Finally, Pb is collected with 6 M HCl or water. (Pb also has a maximum distribution coefficient onto the solid phase at 2–3 M HCl, which falls off in more dilute and more concentrated acid.)

The purity of Pb samples is improved by a second pass through an ion-exchange column. This could involve a second pass through the same column (after cleaning). However, a smaller clean-up column gives better results. For example, Kuritani and Nakamura (2002) used a clean-up column with only 10 μl of anion resin. Alternatively, Manton (1988) showed that the distribution coefficient for Pb onto anion resin in dilute HBr is large enough for the absorption of small Pb samples onto a single large resin bead. The Pb is subsequently back-extracted into water. Yields from zircon samples were about 50%, after an equilibration period (with stirring) of about 8 h. Alternatively, the process can be accelerated by agitation in an ultrasonic bath. The somewhat low efficiency may be outweighed by the high purity of the product.

An alternative method for separation of Pb from rocks is to use a two-stage electro-deposition method by which Pb is first deposited onto the cathode at an accurately regulated potential, then redissolved and redeposited in a miniature cell on the anode (Arden and Gale, 1974). This method yields a high quality of separation, but is cumbersome to operate. Nevertheless, the anion stage may be useful alone for purifying galena Pb.

Levels of environmental contamination introduced during laboratory procedures are determined by the analysis of ‘blanks’. These are measured by taking an imaginary sample through the whole chemical separation procedure, after which the amount of extraneous contamination introduced is measured by isotope dilution (section 2.4). Blank levels must be minimised in all of the chemical procedures described above, but particularly strenuous efforts are necessary to limit Pb contamination due to its relatively high concentration in the environment compared with its concentration in normal rocks.

The minimum laboratory requirements to maintain low blanks would be an overpressure air system, sub-boiling distillation of all reagents in quartz or PFE stills and evaporation of all samples under filtered air. For typical terrestrial whole-rock samples, acceptable total-chemistry blanks would normally be less than a nanogram ($1 \text{ ng} = 10^{-9}$ g) for Pb, Sr and Nd. This is necessary because the samples to be analysed often contain less than a microgram ($1 \ \mu\text{g} = 10^{-6}$ g) of the element of interest. However, in the analysis of very small samples (e.g. single zircons) blanks of a few picograms ($1 \text{ pg} = 10^{-12}$ g) are necessary (e.g. Roddick *et al.*, 1987), since the Pb sample itself may weigh less than 1 ng.

2.2 Ion sources

As noted above, the traditional start of mass-spectrometric analysis is to heat the sample under vacuum, leading to thermal ionisation. With the exception of the rare gases, thermal ionisation is normally achieved by loading a solid deposit of the sample onto a

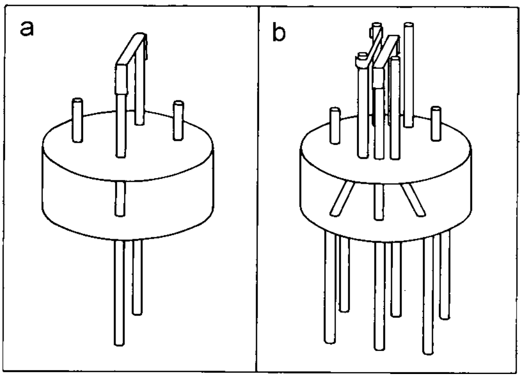

Fig. 2.5. The arrangement of filament ribbons on commonly used single- and triple-filament bead assemblies. Note that only one side filament is shown attached to the 'triple' bead.

metal filament, which can then be subjected to resistive heating. However, the manner by which the sample is deposited and then heated has a major effect on the efficiency of the analysis. Therefore these procedures will be discussed in some detail.

2.2.1 Thermal ionisation

For some elements such as Sr, stable emission of metal ions is achieved from a salt deposited directly onto a single metal filament (Fig 2.5a), usually tantalum (Ta). The loading procedure involves evaporating the salt solution onto the filament before insertion into the vacuum system. The sample is often loaded in phosphoric acid, which seems to (a) displace all other anion species to yield a uniform salt composition, (b) destroy organic residues (such as ion-exchange resin) mixed with the sample and (c) glue the sample to the filament. During mass-spectrometric analysis, the filament current is raised by means of a stabilised power supply to yield a temperature at which simultaneous volatilisation and ionisation of the sample occurs.

However, for many elements, stable volatilisation and ionisation of metal species do not occur at the same temperature. This problem was noted by Ingram and Chupka (1953), who first proposed the use of multiple source filaments (Fig. 2.5b). In this configuration, one or more filaments bearing the sample load can be heated to the optimum temperature for stable volatilisation, while another, hotter filament can be used to ionise the atomic cloud by bombarding it with electrons.

This method is particularly effective for REE analysis, where the sample is usually loaded onto one or both of the Ta side filaments of a triple-filament bead. These are held at a moderate temperature (about 1400 °C) at which REE volatilisation is most stable. The centre filament (usually Re) is held at a much higher temperature (about 2000 °C), which promotes ionisation of the metal vapour. To some extent the ratio of metal to oxide species can be controlled by the centre-filament temperature, which may help to suppress REE isobaric interferences. The properties of the REE under such conditions vary from light to heavy rare earths. La and Ce tend to form oxides unless extremely high centre-filament temperatures are used, whereas heavier REE tend to form the metal species (Hooker *et al.*, 1975; Thirlwall, 1982).

Uranium and thorium may also be analysed by the triple-filament technique. Again, the temperature of the centre filament controls the metal/oxide ratio of the emitted ions (Li *et al.*, 1989). The triple-filament method was also used in the first successful analysis of Hf (Patchett and Tatsumoto, 1980). However, Hf analysis is now exclusively performed by ICP-MS (section 2.5.2).

An alternative to TIMS analysis with multiple filaments is to use special conditions to control the evaporation–ionisation behaviour from a single filament. For example, in the case of Pb, the sample is usually loaded on a rhenium filament in a suspension of silica gel (Cameron *et al.*, 1969). This is thought to form a blanket over the sample, which effectively retards volatilisation of Pb so that the filament can be raised to a higher temperature (at which fractionation of Pb is more reproducible) without burning off the sample uncontrollably.

Early Nd isotope determinations (Lugmair *et al.*, 1975; DePaolo and Wasserburg, 1976) were performed using NdO^+ ions, whose emission from a single-filament source was promoted by relatively high oxygen pressures in the mass spectrometer source housing. Some workers have continued to use this method, rather than the more popular multiple-filament method, since it can yield higher efficiency. Oxygen may be bled into the source in minute amounts to increase oxide emission. Alternatively, loading with silica gel may achieve the same objective without degrading source vacuum (Thirlwall, 1991a). Uranium may also be analysed as the oxide by mixing it with TaO_2 powder on a tungsten filament.

A different approach to single-filament U and Th analysis is to use graphite to promote the formation of metal ions (Edwards *et al.*, 1987). In this procedure it is critical to prevent oxidation during sample loading by avoiding the use of oxidising acids and by maintaining temperatures below the point of visible glowing. Noble *et al.* (1989) applied a similar technique to Nd isotope analysis. The use of platinised graphite was argued to give greater thermal stability to the reducing agent.

2.2.2 Plasma-source mass spectrometry

Technically, plasma-source mass spectrometry is a kind of thermal-ionisation mass spectrometry, because it relies on heating in a gas plasma to achieve ionisation of the sample. However, for practical purposes, the term 'TIMS' is usually restricted to the case of thermal ionisation achieved by a heated filament under vacuum. Therefore, plasma-source mass spectrometry is regarded as a distinct technique.

Plasma-source mass spectrometry was invented in the late 1970s when the inductively coupled plasma (ICP) was first attached to a mass spectrometer (MS) to produce the ICP-MS (Houk *et al.*, 1980). The ICP source consists of a plasma torch made by using a radio-frequency (RF) generator to induce intense eddy currents in a stream of ionised argon gas. The RF generator transmits about a kilowatt of power into the plasma, raising its temperature to about 5000 °C and causing very efficient ionisation of most elements (Houk, 1986). Furthermore, the extreme temperature of the plasma ensures that nearly all of these ions are monatomic ions, which are ideal for mass-spectrometric analysis.

When the ICP-MS was first conceived, it was found most convenient to use a quadrupole mass spectrometer (Dawson, 1976) as the analyser (Fig. 2.6). This analyser has four rods, which are arranged parallel to the path of the ion beam. When alternating voltages with variable frequencies are applied to these rods, the analyser can be tuned to allow ions of a certain mass to pass through to the collector, while all other masses are de-focussed. By rapidly changing the electrical frequencies on the rods, the quadrupole analyser can be made to 'scan' the mass spectrum from mass zero to 250, allowing the detector (usually an ion multiplier) to measure the relative abundance of every mass in the 'spectrum'. A detailed review is given by Potts (1987).

The main technical breakthrough in the development of the ICP-MS was the physical feat of actually feeding a plasma at 5000 °C and atmospheric pressure into a mass spectrometer whose analyser pressure is about 10^8 times lower (10^{-5} mbar). This was achieved by firing the plasma at a two-stage water-cooled orifice, with continuous pumping of the intermediate space by a mechanical pump (Fig. 2.6). Subsequent technical developments in ICP-MS over the next twenty years have mainly involved greatly increasing the efficiency of sampling the plasma by the mass spectrometer. This has allowed ICP-MS to reach remarkable sensitivity, with detection limits as low as parts per trillion (picograms per gram). However, the precision of isotope-ratio measurements by conventional ICP-MS is limited by instabilities in the plasma. By rapidly scanning the 'mass spectrum', the quadrupole analyser can achieve precision of around 1%, but this is a practical limit for single-collector analysis. This level of precision was found to be useful in early development of the Re–Os method (section 8.1), but is not useful for most radiogenic isotopic systems. Hence, to apply ICP-MS to these systems it was necessary to introduce multiple-collection techniques to cancel out the instability of the source.

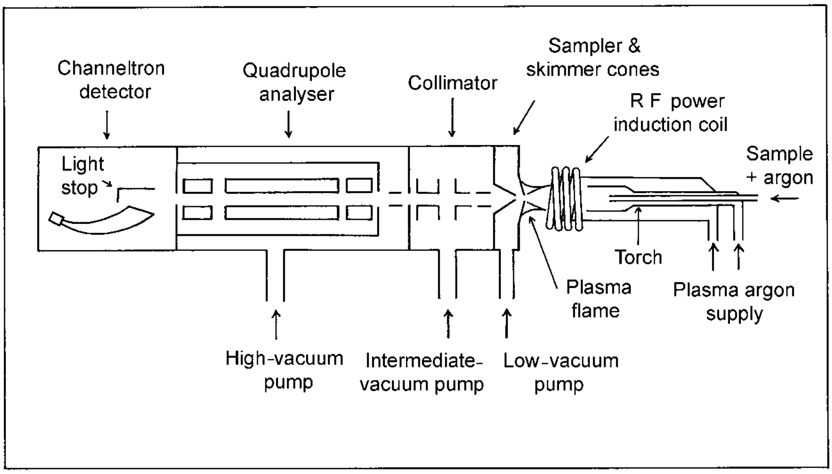

Fig. 2.6. Schematic illustration of an ICP-MS instrument with quadrupole analyser.

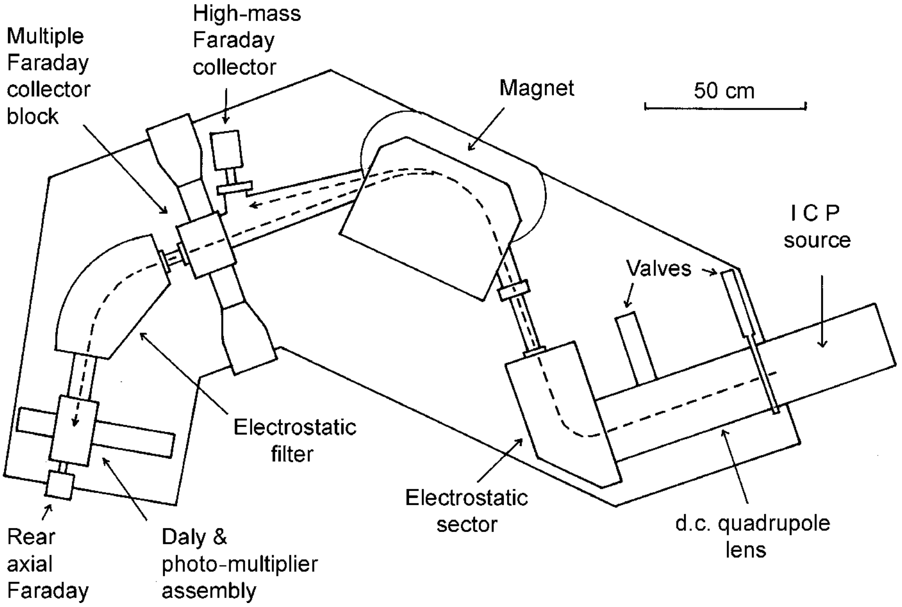

Fig. 2.7. Simplified plan view of the VG Elemental Plasma 54 instrument. After Halliday *et al.* (1998).

To perform multiple-collection mass spectrometry (MC-MS) with a plasma ion source it was necessary to link the ICP source with a magnetic-sector mass spectrometer of the type normally used in TIMS instruments (section 2.3). This involved two main technical challenges. The first problem is that magnetic-sector mass spectrometry requires a large accelerating voltage to raise ions to the high velocities at which magnetic separation is efficient. However, in order to keep the whole analyser assembly at electrical ground, the ion source must be at up to 8000 V positive. For MC-ICP-MS, this means isolating the plasma at up to 8000 V positive, with all of the attendant engineering problems. The second problem is that magnetic-sector mass spectrometry requires an ion beam with a very small range of ion energy, whereas the ICP source generates ions with a relatively large energy range. This was overcome in the first MC-ICP-MS instruments by using both quadrupole and electrostatic pre-filters to smooth the energy distribution in the ion beam before it entered the magnetic sector (Fig. 2.7). Subsequent instruments have used a variety of other filtering devices to achieve similar objectives.

2.2.3 Mass fractionation

The process of volatilisation and ionisation during mass spectrometry requires the breaking of chemical bonds, but the strength of these bonds is mass-dependent. Therefore, excitation of the sample leads to mass-dependent fractionation, which can be understood by approximating the chemical bond between two atoms as a harmonic oscillator.

The energy of a molecule (or part of an ionic lattice) decreases with decreasing temperature, but at absolute zero it has a certain finite value called the zero-point energy, equal to $0.5h\nu$ (where h is Planck's constant and ν is the vibrational frequency). A bond involving the light isotope of an element has a higher vibration frequency and hence a higher zero-point energy than one involving a heavier isotope, as illustrated in Fig. 2.8. The difference in bond energies diminishes as temperature rises, but still persists. Because the potential-energy well of the bond involving the lighter isotope is always shallower than that for the heavier, the bond with the lighter isotope is more readily broken. Hence it is preferentially released from the hot filament, causing isotopic fractionation.

In a plasma-source mass spectrometer (section 2.2.2), fresh sample is continually fed into the plasma torch. Hence, mass fractionation produces a fairly constant (but large) discrepancy between the isotopic composition of the solid sample and the ion cloud. In contrast, solid-source TIMS analysis produces smaller fractionation effects, but the continual process of fractionation starts to 'use up' the lighter isotope on the filament so that the isotopic composition of the sample becomes progressively heavier (the 'reservoir effect').

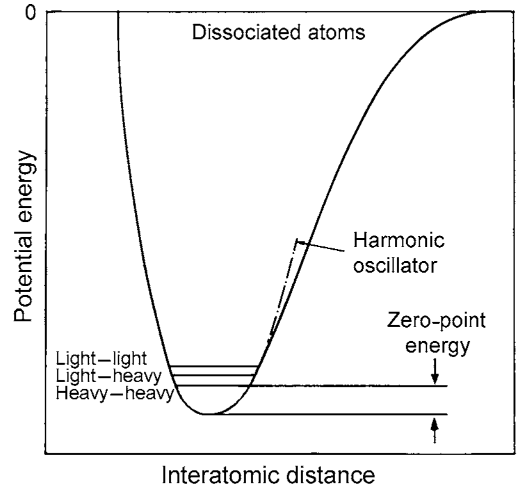

Fig. 2.8. Schematic diagram of potential energy against bond length for a hypothetical molecule made of two isotopes, based on the 'harmonic-oscillator' model.

Eberhardt *et al.* (1964) showed that this process follows a Rayleigh fractionation law (Fig. 2.9). The magnitude of this effect could yield totally unacceptable errors of up to 1% in measured isotope ratio. However, for elements with two or more non-radiogenic isotopes, an internal normalisation for such mass-dependent fractionation can be performed.

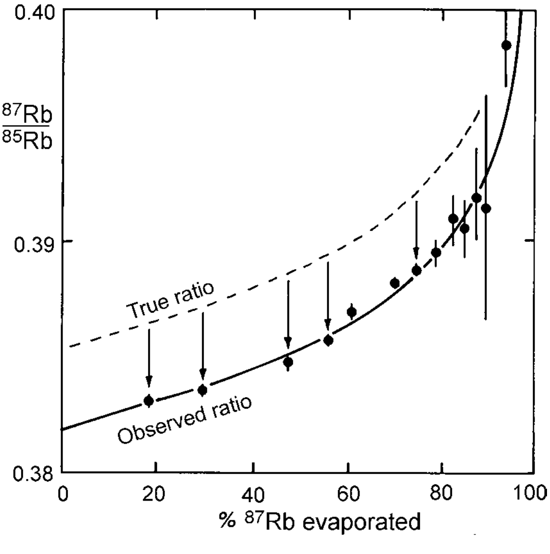

Fig. 2.9. Effect of within-run fractionation, over time, on a sample of natural rubidium undergoing isotopic analysis. Points are observed ratios; the dashed line schematically indicates the actual composition of Rb on the filament. Data from Eberhardt *et al.* (1964).

In the case of strontium, the fractionation of $^{87}\mathrm{Sr}/^{86}\mathrm{Sr}$ can be monitored using the $^{88}\mathrm{Sr}/^{86}\mathrm{Sr}$ ratio, since $^{88}\mathrm{Sr}$ and $^{86}\mathrm{Sr}$ are both non-radiogenic (i.e. produced only by nucleosynthetic processes in stars). The ratio $^{86}\mathrm{Sr}/^{88}\mathrm{Sr}$ is constant throughout the Earth and is taken to be 0.1194 by international convention. This value cannot be measured absolutely, but was originally estimated from the average beam composition half-way through very many TIMS runs. The deviation of the observed $^{86}\mathrm{Sr}/^{88}\mathrm{Sr}$ ratio from 0.1194 at each point through the run is divided by the difference between the two masses ($\Delta_{\mathrm{mass}} = 2.003$) in order to calculate a fractionation factor per mass unit:

$$F = \frac{\dfrac{(^{86}\mathrm{Sr}/^{88}\mathrm{Sr})_{\mathrm{obs}}}{0.1194} - 1}{\Delta_{\mathrm{mass}}} \qquad [2.1]$$

This fractionation factor can then be used to correct the observed (raw) $^{87}\mathrm{Sr}/^{86}\mathrm{Sr}$ ratio, for which $\Delta_{\mathrm{mass}} = 1.003$:

$$\left(\frac{^{87}\mathrm{Sr}}{^{86}\mathrm{Sr}}\right)_{\mathrm{true}} = \left(\frac{^{87}\mathrm{Sr}}{^{86}\mathrm{Sr}}\right)_{\mathrm{obs}} (1 + F\Delta_{\mathrm{mass}}) \qquad [2.2]$$

This has the effect of improving the within-run precision of the $^{87}\mathrm{Sr}/^{86}\mathrm{Sr}$ ratio from about 1% to better than 0.01%. Neodymium metal analyses are similarly normalised for fractionation (Fig. 2.10) using an internationally agreed value of $^{146}\mathrm{Nd}/^{144}\mathrm{Nd} = 0.7219$ (O'Nions *et al.*, 1979). However, Nd oxide analyses are normalised with respect to different values (Wasserburg *et al.*, 1981), which are incompatible with the Nd metal normalising value.

The fractionation correction described above is usually called the linear law, but the power law (Wasserburg *et al.*, 1981; Thirlwall, 1991b) is effectively identical. Both of these laws assume that fractionation is proportional to mass difference only, and is independent of the absolute masses of the fractionating species. In other words, fractionation per mass unit is constant. However, this is an approximation to the real evaporation process, in which fractionation per mass unit must vary inversely with the absolute masses of the evaporating species. Russell *et al.* (1978) first observed a breakdown of the linear law in isotopic analysis of the 'light' element Ca. To remedy this, they introduced an 'exponential' law, whereby the fractionation factor depends also on the mass of the evaporating species. This gave a better fit to Ca isotope data than did the linear law (Fig. 2.11).

These problems are much less severe for Sr and Nd isotope analysis because of their heavier masses. However, Thirlwall (1991b) found small deviations from linear-law behaviour in a large data set of Sr standard

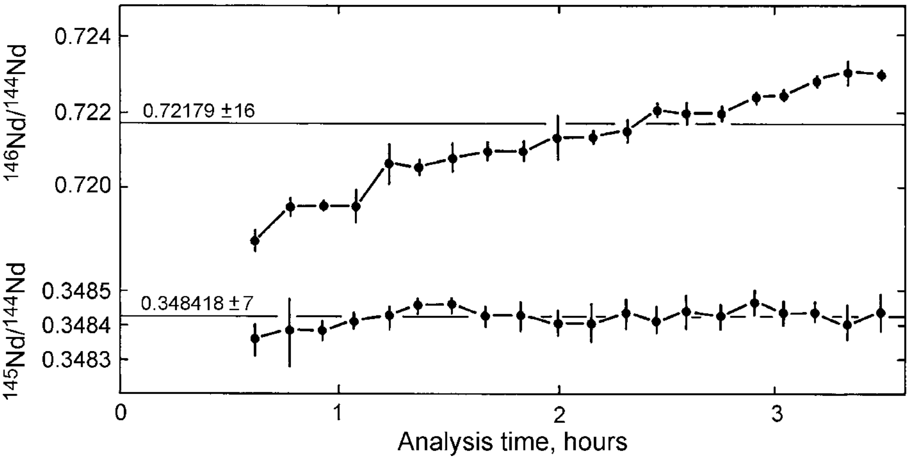

Fig. 2.10. Plot of raw ^{146}Nd/^{144}Nd ratios and fractionation-corrected ^{145}Nd/^{144}Nd ratios (normalised with respect to ^{146}Nd/^{144}Nd = 0.7219) for a single mass-spectrometer run. Each point is a mean of ten scans of the mass spectrum, while horizontal lines are grand means. After Noble (personal communication).

analyses. This is revealed by a correlation between normalised ^{87}Sr/^{86}Sr and average observed ^{86}Sr/^{88}Sr ratios for complete runs (Fig. 2.12). Thirlwall found that he could eliminate the correlation by retrospectively applying an exponential-law correction to the data. This is described as follows:

$$\left[\frac{(^{87}\mathrm{Sr}/^{86}\mathrm{Sr})_{\mathrm{norm}}}{(^{87}\mathrm{Sr}/^{86}\mathrm{Sr})_{\mathrm{corr}}}\right]^{\ln(86/88)} = \left[\frac{(^{86}\mathrm{Sr}/^{88}\mathrm{Sr})_{\mathrm{obs}}}{0.1194}\right]^{\ln(87/86)} \qquad [2.3]$$

where ‘norm’ and ‘corr’ refer to products of linear normalisation and exponential correction, and where 86, 87 and 88 are the actual masses of evaporating ions.

This model assumes that strontium evaporates from the filament as the species ‘Sr’. On the other hand, Habfast (1983) suggested that a strontium sample on a rhenium filament might evaporate as a species such as $SrReO_4$ rather than atomic Sr. Hence the ‘apparent mass’ of ^{88}Sr which should be used in the exponential correction would be about 330 rather than 88. Under

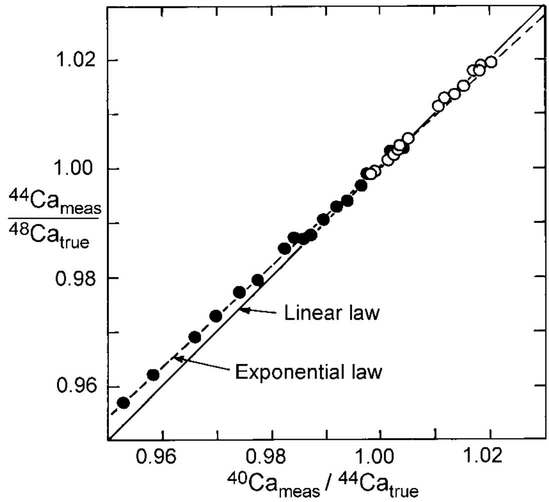

Fig. 2.11. Plot of measured/true ^{44}Ca/^{48}Ca *versus* ^{40}Ca/^{44}Ca ratios, showing fit of linear and exponential fractionation laws to typical data from two runs. After Russell *et al.* (1978).

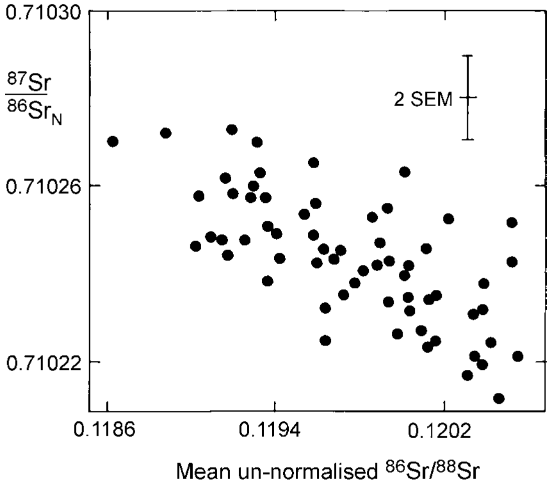

Fig. 2.12. Plot of fractionation-corrected ^{87}Sr/^{86}Sr ratios against mean un-corrected ^{86}Sr/^{88}Sr ratios for measurements of the SRM987 standard over a period of several months. The error bar indicates average within-run precision. After Thirlwall (1991b).

such conditions the exponential law might actually produce a worse fit to the true fractionation behaviour of the sample than the linear law. However, Thirlwall's data suggest that evaporation from a tantalum filament does occur as the metal species, so the exponential model is an improvement over the linear model.

Thirlwall (1991b) argued that between-bead precision of Nd isotope analyses could also be improved to a level comparable to within-run precision by using a secondary normalisation against ^{142}Nd/^{144}Nd. This is based on an observed correlation between fractionation-corrected ^{143}Nd/^{144}Nd and ^{142}Nd/^{144}Nd ratios from standard runs over a period of months (Fig. 2.13). Subsequent work on Nd fractionation during MC (multi-collector)-ICP-MS analysis of Nd revealed similar behaviour (Vance and Thirlwall, 2002). However, because mass fractionation in the plasma source is an order of magnitude larger, the effect is much bigger (Fig. 2.13).

Vance and Thirlwall showed that this problem could be solved using two alternative approaches. One is to apply a post-analysis correction to ^{143}Nd/^{144}Nd ratios using the information from the ^{142}Nd/^{144}Nd ratio, as in Fig. 2.13. An alternative approach is to choose masses for the fractionation monitor that bracket the masses to be corrected. For example, the mean mass of ^{143}Nd and ^{144}Nd is 143.5, which is the same as the mean mass of ^{142}Nd and ^{145}Nd. Therefore, ^{142}Nd/^{145}Nd represents the ideal monitor ratio for fractionation correction of ^{143}Nd/^{144}Nd ratios. This approach is only possible if interferences of Ce on ^{142}Nd are low, and is therefore not feasible for TIMS analysis using the popular 'reverse-phase' Nd separation (section 2.1.2). However, for most TIMS analysis the fractionation problem can be avoided by collecting data near a ^{146}Nd/^{144}Nd ratio of 0.7219. For Nd analysis by MC-ICP-MS it is necessary to take account of this problem in order to achieve reproducibilities comparable to those obtained with TIMS. However, Ce isobaric interferences can be accurately corrected in MC-ICP-MS analysis, so ^{142}Nd can be used as one of the fractionation monitors.

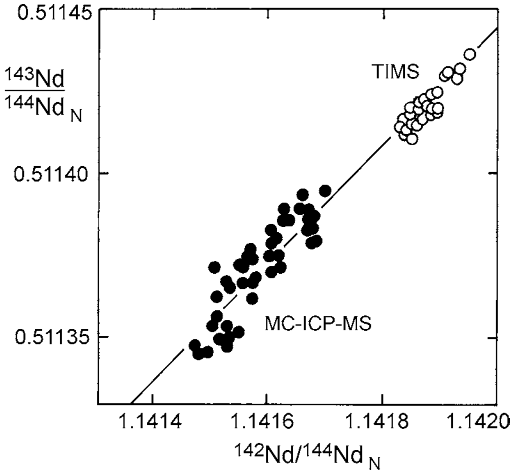

Fig. 2.13. Plot of fractionation-corrected ^{143}Nd/^{144}Nd ratio against ^{142}Nd/^{144}Nd ratio for analyses of a laboratory standard over a period of several months using normalisation with respect to ^{146}Nd/^{144}Nd = 0.7219. (○) = TIMS data; (●) = MC-ICP-MS data. After Vance and Thirlwall (2002).

Internal fractionation correction is only possible when there are two or more isotopes present in a constant ratio. This is not the case for Pb isotope analysis by TIMS, or in the isotope-dilution analysis of Rb, so an external correction must be used. This depends on achieving uniform fractionation behaviour between standards and different samples, so that an across-the-board correction can be made to all runs. In the case of Pb, the use of a silica-gel blanket on the filament achieves this objective by reducing the magnitude of fractionation processes drastically, from a previous between-lab variation of about 3% to a present-day variation of about 0.3%. This improvement is partly due to the higher filament temperatures possible using silica gel. Because bond energy levels become closer with increasing temperature, the magnitude of isotope fractionation falls with increasing temperature. However, for this technique to work well, the Pb sample has to be well purified during the chemical separation (section 2.1.4). In the analysis of uranium, fractionation effects may similarly be reduced by running at high temperature as the oxide. Alternatively, analysis as the metal ion produces larger but relatively consistent degrees of fractionation, which can be corrected by comparison with standard runs.

When the relevant nuclides exist, double spiking with two artificial isotopes may be used to apply an internal fractionation correction to elements such as Pb with only one natural non-radiogenic isotope (section 2.4.2). In MC-ICP-MS analysis the two isotopes that form this double spike do not even have to be the same element as the isotope ratios being corrected. For example, the two isotopes of thallium can be used to correct Pb isotope data (section 2.5.4).

2.3 Magnetic-sector mass spectrometry

In a typical 'magnetic-sector' instrument (Fig. 2.1) the nuclides to be separated are ionised under vacuum and accelerated through a high potential (V) before passing between the poles of a magnet. A uniform magnetic field (H) acting on particles in the ion beam bends them into curves of different radii (r) according to the following equation:

$$r^2 = \frac{m}{e}\frac{2V}{H^2} \qquad [2.4]$$

where m/e is the mass/charge ratio for the ion in question. Since most of the ions produced by TIMS or ICP sources are singly charged, the different isotopes in the sample will be separated into a simple spectrum of masses. The relative abundance of each mass is then determined by measuring its corresponding ion current, captured by a Faraday bucket or a multiplier detector.

2.3.1 Ion optics

The ion-optic properties of an instrument determine how the cloud of ions generated in the source is accelerated, focussed into a beam, separated by the magnetic field, and collected for measurement. Correct ion-optic alignment is essential to obtain reliable results, because, if part of the ion beam hits an obstruction, different masses may be affected to different degrees, leading to a bias in the results.

Most older mass spectrometers follow Nier's (1940) design (Fig. 2.1). From the filament (several kilovolts positive), the beam traverses a series of focussing source plates (the 'collimator stack'). These plates are at progressively lower potential and bring the beam to a principal focus at the source slit (zero volts). Thereafter, the beam slowly diverges (Fig. 2.14). In the y direction, the magnet brings each nuclide (isotope) beam back into focus at the primary collector slit, which is wide enough to let the whole of one nuclide beam through into the collector. This focussing effect of a sector-shaped magnet was already understood by Aston (1919).

To bring a heavier nuclide into the collector, the magnetic field may be increased, or the momentum of the ions may be reduced by lowering the high-voltage (HV) potential across the collimator stack. If the whole of one nuclide beam is focussed into the collector slit in the y direction, an apparently flat-topped peak is produced when the magnetic field or HV is varied to sweep the mass spectrum across the collector slit (e.g. Fig. 2.15). In practice, the magnetic field rather than the HV is normally switched to bring different nuclide beams into the collector, because the field can

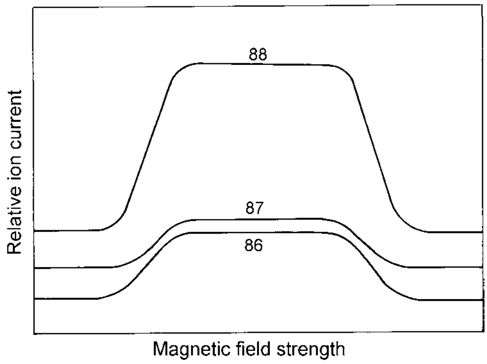

Fig. 2.15. The appearance of flat-topped 'peaks' when strontium 88, 87 and 86 nuclide beams are swept across a triple (Faraday)-collector system by varying the magnetic field strength.

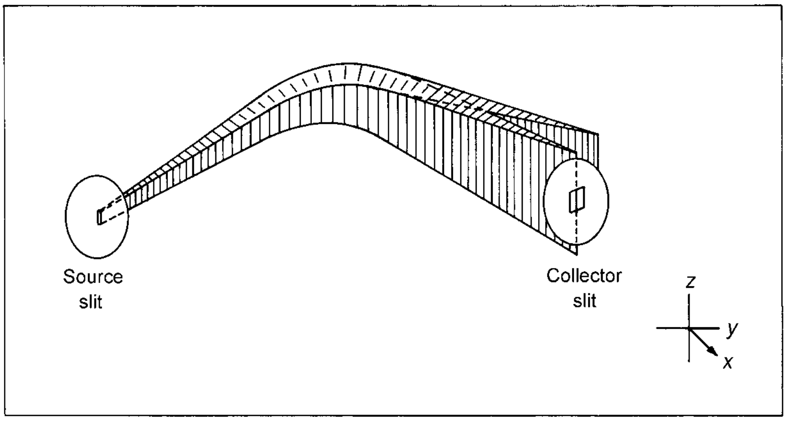

Fig. 2.14. Schematic diagram of the envelope of a double-nuclide beam from the source slit to the collector slit in a Nier-type mass spectrometer.

be more precisely monitored and controlled, using a 'Hall probe'. This is used to sense the field strength and adjust the magnet power supply in a feed-back loop ('field control'). The magnet (whose pole pieces are perpendicular to the beam) does not focus in the *z* direction, and in this direction the beam is 'clipped' by baffle plates.

This type of magnet design has a disadvantage, because the process of switching from one mass to another changes 'fringing fields' which are generated by the ends of the magnet poles. The change in these fringing fields may cause slight convergence or divergence of the beam, so that different amounts of different nuclide beams are clipped by the collector slit. Hence, a slight bias is introduced into the beam current reaching the collector, according to whether the magnet is switching 'up-mass' or 'down-mass'.

Instruments built since 1980 feature refinements in the design of the magnet pole pieces, based on theoretical work by Cotte (1938). If the pole pieces are set at a slightly oblique angle to the beam, the fringing fields generated by the magnet have the effect of focussing the beam in the *z* direction (Fig. 2.16). However, the focussing effect in the *y* direction is weakened, so the distance from the magnet exit pole to the principal focus in the *y* plane is increased. Therefore this design is referred to as 'extended geometry'. The ion optics in this type of machine are shown in Fig. 2.17. This configuration has three advantages:

(1) Because the whole of the *z*-focussed beam can pass through the collector slit, the transmission of the machine (defined as the number of ions in the source required to yield each ion at the collector) is improved.

(2) Small variations in fringing field do not cause signal bias, so accuracy is improved.

(3) Extended geometry increases the distance between nuclide beams at the collector, so multiple Faraday buckets can be more easily accommodated. Hence a magnet of 30 cm radius yields a beam separation equivalent to that formerly obtained with a magnet of 54 cm radius.

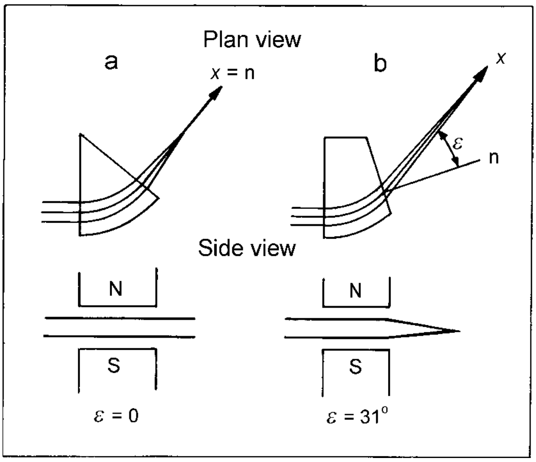

Fig. 2.16. The effect of differently shaped pole faces in generating fringing fields that cause focussing of the ion beam in the *y* and *z* planes: (a) exit pole piece perpendicular to beam yields short focal length in the *x* direction but no focussing in *z*; and (b) the normal to the exit pole face (n) is at an angle ε to the beam direction, yielding a longer focal length in *x* and also *z* focussing.

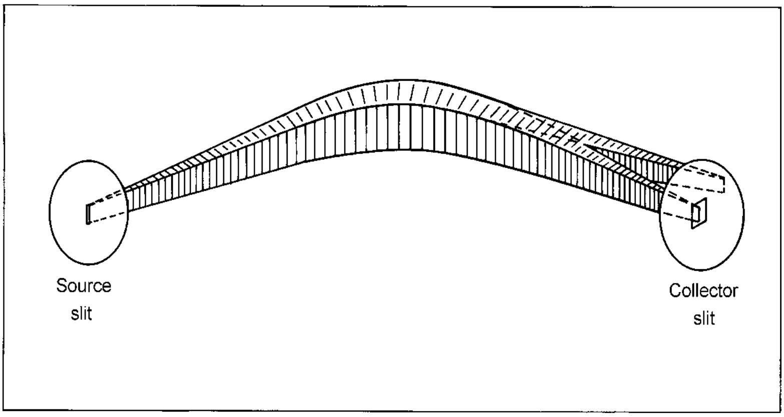

Fig. 2.17. Schematic diagram of the ion optics of an extended-geometry machine between the source and collector slits (compare with Fig. 2.14).

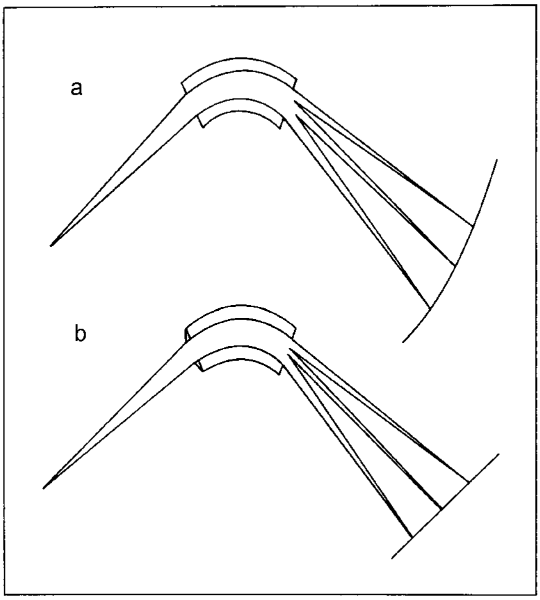

Fig. 2.18. Effect of magnet entry pole face shape: (a) a flat pole face yields an oblique curved focal plane at collector; and (b) a convex pole face yields a flat focal plane perpendicular to the flight path.

If one of the magnet pole faces (e.g. the entry pole) is made slightly convex, this changes the normally oblique focal plane of nuclide beams in the *y* direction into a flat plane perpendicular to the beams (Fig. 2.18). This facilitates the installation of multiple collectors, whose spacing can then be adjusted to fit ion beams one atomic mass unit (a.m.u.) apart in any part of the spectrum. However, a more complex adjustable multiple-collector configuration can be constructed on the oblique focal plane. At higher mass numbers the spacing of the collectors becomes closer and closer until their outer grounded screens are actually touching during uranium analysis.

A very high vacuum throughout the ion path is essential, otherwise the ion beam becomes scattered, particularly to the low-mass side, by inelastic collisions with air molecules. Such beam scattering becomes serious at analyser pressures $> 10^{-8}$ mbar. This causes the formation of a tail from one peak that may interfere with the adjacent nuclide. The problem is particularly severe in the case of a small peak down-mass from a very large peak. For example, interference by ^{232}Th onto ^{230}Th may be severe for silicate rocks with ^{232}Th/^{230}Th ratios approaching 10^6. The magnitude of interference by a peak on a position one a.m.u. lower is called the 'abundance sensitivity' of the instrument (measured in ppm of the peak size). A typical specification for a single-focussing TIMS machine with analyser vacuum $<5 \times 10^{-9}$ mbar is 2 ppm at 1 a.m.u. from ^{238}U.

If a very high abundance sensitivity is essential, it can be obtained by adding a type of ion-energy filter between the magnet and collector, thereby creating a double-focussing machine. The ion-energy filter has the effect of removing ions with unusually high or low energy (i.e. velocity). Thus, ions that have suffered a collision, and therefore lost energy, should be weeded out. Three types of filter that have been applied to this task are 'electrostatic', quadrupole, and ion-retardation types. They typically result in a 10–100-fold improvement in abundance sensitivity.

2.3.2 Detectors

Ion beams in mass spectrometry normally range up to about 10^{-10} A. For beams as small as 10^{-13} A, the most suitable detector is the Faraday bucket. This is connected to electrical ground (Fig. 2.1) via a large resistance (e.g. 10^{11} Ω). Electrons travel from ground through this output resistor to neutralise the ion beam, and the potential across the resistor is then amplified and converted into a digital signal. A typical ion beam of 10^{-11} A then generates a potential of 1 V, converted to, say, 100 000 digital counts. Traditionally, an indefinite lifetime has been assumed for Faraday buckets. However, the very narrow buckets in modern multicollector arrays quickly become coated inside with sample debris when large beams are analysed. This degrades ion-beam measurements by allowing stray beams to escape from the Faraday bucket. This problem is now solved by putting absorbent charcoal blocks in the buckets.

For ion beams smaller than about 10^{-13} A, the electrical noise of the Faraday amplifier becomes significant relative to the signal size, so that some form of signal multiplication is necessary. One of the most useful approaches was pioneered by Daly (1960). In the Daly detector, ions passing into the collector are attracted by a large negative potential (e.g. 20 kV). Collision of each ion with the polished electrode surface (Fig. 2.19) yields a secondary electron shower. When this impinges on a phosphor, the resulting light pulse is amplified by a photo-multiplier (situated behind a glass window, outside the vacuum system). In the analogue mode this system can have a gain (i.e. amplification) about 100 times that of the Faraday cup. Because ions do not strike the multiplier directly, the detector has a long lifetime.

The Daly detector can only be used with positive ion beams. On the other hand, channel electron multipliers (CEM) can be used to amplify either positive

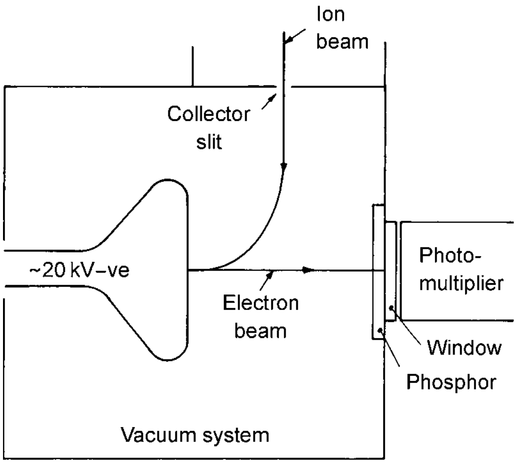

Fig. 2.19. Schematic diagram of a Daly detector, showing the means of amplification of an incoming positive-ion beam. After Daly (1960).

or negative ion beams. These devices are therefore used for Re and Os analysis by negative-molecular-ion TIMS (section 8.1). The negative ion enters the orifice of the CEM at a potential near zero, releasing electrons when it strikes the semi-conducting channel wall. These electrons are multiplied during further collisions, as they are attracted to a positive HV collector. Because the collector is at high voltage, the signal cannot be amplified directly, but a pulsed ion-counting signal can be transmitted through an isolating capacitor to low-voltage pulse-counting electronics (e.g. Kurz, 1979). The drawback of CEM detectors is their tendency to suffer damage when struck by heavy ions. Therefore signal sizes should be minimised to prolong their life.

2.3.3 Data collection

Depending on the size of the ion beam, it is necessary to measure each nuclide signal for up to an hour to achieve high-precision data. To achieve this in a single-collector TIMS machine the magnetic field is 'switched' to cycle round a sequence of peak positions. On switching to a new peak there is a waiting period of 1–2 s to allow the output resistor and amplifier to reach a steady state in response to the new ion current. Then data are collected for a few seconds. In practice, each peak must normally be corrected for incomplete decay of the signal from previous peaks (termed 'dynamic-zero', 'tau' or 'resistor-memory' correction). The computer then cycles round and round a series of peaks, baseline/background(s) and interference monitor position(s), interpolating between successive measurements of the same peak to correct for growth or decay of the beam size. A simple linear time interpolation may be used (Fig. 2.20), but Dodson (1978) developed a more sophisticated 'double-interpolation' algorithm, which can make better allowance for non-linear beam growth or decay.

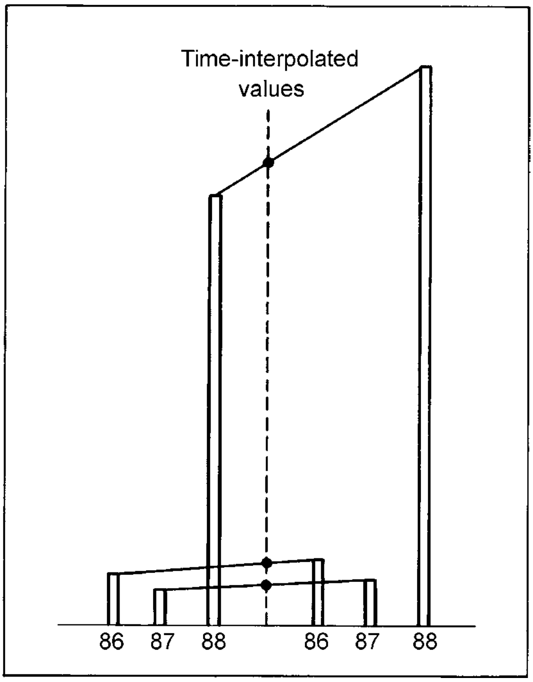

Fig. 2.20. Schematic illustration of the principle of linear time interpolation for a strontium ion beam growing at an (immense) rate of 30% per scan.

Before isotope ratios can be determined from the different signals, background electronic noise must be subtracted in order to determine net peak heights. In TIMS analysis this is done by measuring a baseline position in each collector channel at approximately 0.4 a.m.u. above a whole-mass position, usually a few a.m.u. away from the masses of interest. In plasma-source analysis, backgrounds are often measured under each peak ('on peak zeros') before the analysis starts in order to remove the memory effects of previous samples from the nebuliser.

From a single cycle of time-interpolated net peak heights, a set of net peak ratios is extracted. These are often collected in blocks of ten scans. The cycle time round a set of peaks may be shortened by the measurement of backgrounds and interferences 'between blocks' rather than 'within-scan'. For a single-collector TIMS instrument, collecting 200 scans in about 3 h might give a statistical within-run precision of 0.004%

(2σ = two standard errors on the mean). That is, the scatter of data around the mean suggests that one can be 95% confident that the 'correct' answer lies within 0.004% (40 ppm) of either side of the mean. For ^{87}Sr/^{86}Sr this is equivalent to 0.71000 ± 0.00003 (2σ).

Occasional signal 'spikes' and other perturbations outside normal random error are inevitable in a long mass-spectrometer run. It is generally regarded as acceptable to run through the data a few times and test for outliers which are more than a certain number of population standard deviations (SD) from the mean (Pierce and Chauvenet, 1868; in Crumpler and Yoe, 1940). The cut-off level should depend on the size of data set, so that only a minimal number of outliers resulting from normal random variation will be rejected. In practice the cut-off would normally be between two and three SD.

Ideally, a multiple-collector machine can analyse isotope ratios in a 'static' mode without peak-jumping. However, this may be limited, firstly by the extent to which all of the Faraday buckets are identical in terms of beam-transmission characteristics; and secondly by the extent to which the gain of each bucket's amplifier system can be calibrated. Until the 1990s, these problems did not allow static analysis to achieve the highest levels of analytical precision, necessary for Sr or Nd isotope analysis.

The alternative approach for high-precision analysis is double- or triple-collector peak-jumping (multidynamic analysis). The simplest (double-collector) method is given below:

High collector:	87	88	91.4	–
Low collector:	86	87	90.4	85
Place in sequence:	1	2	3	4

After background subtraction, the ^{85}Rb monitor is used to correct both ^{87}Sr peaks. The following algorithm represents an approximation, assuming unit mass differences between the isotopes:

$$\left(\frac{87}{86}\right)_{\text{true}} = \left[\left(\frac{87}{86}\right)_1 \left(\frac{87}{86}\right)_2 \frac{1}{0.1194}\right]^{0.5} \qquad [2.5]$$

where suffices denote places in the scan sequence. This equation cancels out beam growth or decay and amplifier bias, as well as performing a power-law mass-fractionation correction, all in a single calculation. To use the exponential law for evaporation of Sr as the metal, the function above is raised to the power of 0.5036 (Thirlwall, 1991b). Using multi-dynamic analysis, within-run precision should reach 0.002% (2σ) after 3 h. Triple-collection analysis allows a further improvement in efficiency. In this method, two double-collector determinations on adjacent collectors are averaged to yield a more precise result.

Unfortunately, while within-run precision can be taken to lower and lower levels by more efficient sample ionisation and data collection, between-run reproducibility often reaches a limiting 2σ value of about 0.004% (40 ppm), which is difficult to break through. Thirlwall (1991b) attributed this phenomenon to imperfect centring of some peaks during dynamic multiple collection. This occurs because mass separations decrease as absolute masses increase, so the collectors are actually set slightly different distances apart. Using the above example, if the three collectors are set up with masses 86–87 perfectly centred (position 1 in the sequence) then at position 2 the peaks will be slightly off-centre. This slight mis-centring may amplify any non-idealities in the optical path of the beam, so that slightly different source configurations (for different bead numbers) yield small systematic variations in isotope ratio.

A more recent development in multi-collector analysis obtains the best compromise between static and multi-dynamic analysis, by allowing the signal from each Faraday bucket to be switched in turn to each amplifier channel. This cancels out the electrical gains of the different amplifiers, without the problem of peak switching. Reproducibilities of better than 10 ppm (2σ) can then be achieved in isotope-ratio measurements (Finnigan MAT technical report, 2001). Provided that the ion-optical bias of each collector can be accurately calibrated, this system offers a new level of precision and accuracy in isotope-ratio mass spectrometry. It should be particularly useful for applications such as seawater Sr, ^{186}Os and ^{142}Nd, for which isotopic variations are at the limits of analytical precision.

2.4 Isotope dilution

Isotope dilution is generally agreed to be the supreme analytical method for very accurate concentration determinations. In this technique, a sample containing an element of natural isotopic composition is mixed with a 'spike' solution, which contains a known concentration of the element, artificially enriched in one of its isotopes. When known quantities of the two solutions are mixed, the resulting isotopic composition (measured by mass spectrometry) can be used to calculate the concentration of the element in the sample solution. The element in question must normally have two or more naturally occurring isotopes, one of which can be enriched on a mass separator. However, in some cases a long-lived artificial isotope is used.

2.4.1 Analysis technique

Before use, the isotopic composition of a 'spike' must be accurately determined by mass spectrometry. This measurement cannot be normalised for fractionation, because there is no 'known' ratio to use as a fractionation monitor. Therefore, several long runs are generally made, from which the average midpoint of the run is taken to be the actual spike composition. The concentration of the spike is generally determined by isotope dilution against standard solutions (of natural isotopic composition) whose concentrations are themselves calculated gravimetrically. Metal oxides are generally weighed out, but if these are hygroscopic (e.g. Nd_2O_3) then accurate weighing requires part of a metal ingot.

A simple example of isotope-dilution analysis is the determination of Rb concentration for the Rb–Sr dating method. Typical mass spectra of natural, spike and mixed solutions are shown in Fig. 2.21.

In the mixture, each isotope peak is the sum of spike (S) and natural (N) material. Hence,

$$\frac{^{87}\text{Rb}}{^{85}\text{Rb}} = R = \frac{\text{moles } 87_N + \text{moles } 87_S}{\text{moles } 85_N + \text{moles } 85_S} \qquad [2.6]$$

However, the number of moles of an isotope is equal to the number of moles of the element as a whole, multiplied by the isotopic abundance. If the total numbers of moles of natural and spike Rb are represented by M_N and M_S, then

$$R = \frac{M_N \cdot \%87_N + M_S \cdot \%87_S}{M_N \cdot \%85_N + M_S \cdot \%85_S} \qquad [2.7]$$

where percentages indicate the isotopic abundances in the spike and natural solutions. This equation is rearranged in the following steps:

$$R(M_N \cdot \%85_N + M_S \cdot \%85_S) = M_N \cdot \%87_N + M_S \cdot \%87_S$$

$$RM_N \cdot \%85_N + RM_S \cdot \%85_S = M_N \cdot \%87_N + M_S \cdot \%87_S$$

$$RM_N \cdot \%85_N - M_N \cdot \%87_N = M_S \cdot \%87_S - RM_S \cdot \%85_S$$

$$M_N(R \cdot \%85_N - \%87_N) = M_S(\%87_S - R \cdot \%85_S)$$

$$M_N = M_S \frac{\%87_S - R \cdot \%85_S}{R \cdot \%85_N - \%87_N} \qquad [2.8]$$

If we insert figures for the isotopic abundance of natural Rb and the isotopic abundance of a typical spike, such that 27.83/72.17 is the natural ^{87}Rb/^{85}Rb ratio and 99.4/0.6 is the spike ^{87}Rb/^{85}Rb ratio, then the number of moles of natural Rb is given by

$$M_N = \frac{99.4 - R \cdot 0.6}{R \cdot 72.17 - 27.83} M_S \qquad [2.9]$$

where R is the measured isotope ratio. Since number of moles = molarity × mass, the molarity of the natural sample is given by

$$\text{Molarity}_N = \frac{99.4 - R \cdot 0.6}{R \cdot 72.17 - 27.83} \frac{\text{wt}_S}{\text{wt}_N} \text{Molarity}_S \qquad [2.10]$$

Molarity is then multiplied by atomic weight to yield concentration:

$$\text{Conc}_N = \text{At. wt}_N \frac{99.40 - R \cdot 0.6}{R \cdot 72.17 - 27.83} \frac{\text{wt}_S}{\text{wt}_N} \frac{\text{Conc}_S}{\text{At.wt}_S} \qquad [2.11]$$

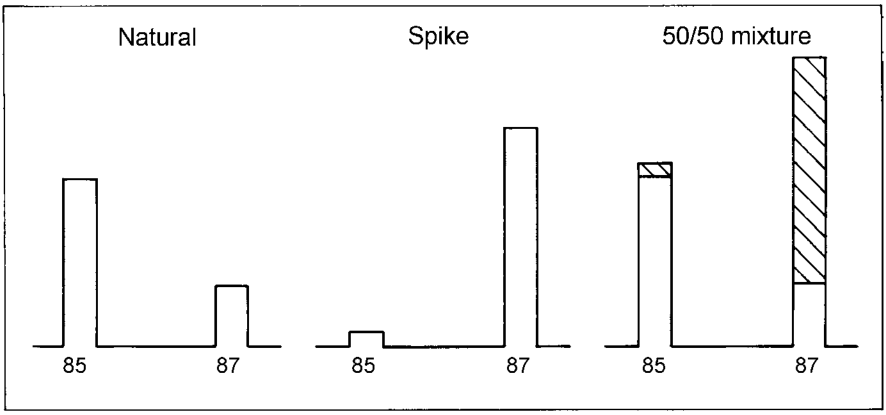

Fig. 2.21. Summation of spike (hatched) and natural ion beams to generate aggregate mixed peaks, as illustrated by rubidium isotope dilution.

Because there are only two isotopes of Rb, no internal correction for fractionation is possible in the measurement of ^{87}Rb/^{85}Rb. However, in the isotope-dilution analysis of Sr, fractionation correction based on measurement of the ^{88}Sr/^{86}Sr ratio is possible, which allows a much more accurate measurement of the ^{84}Sr/^{86}Sr ratio (spike Sr/natural Sr) to be made.

Isotope dilution is potentially a very-high-precision method. However, error magnification may occur if the proportions of sample to spike which are mixed are far from unity (Fig. 2.22). Consequently, it is generally believed that the analysed peaks in an isotope-dilution mixture should have an abundance ratio of close to unity. In actual fact, the ideal composition of the mixture is half-way between those of the natural and spike compositions. However, the best precision normally required in an isotope-dilution analysis is about 1 per mil (0.1%), which is two orders of magnitude worse than the precision normally achieved in Sr or Nd isotope-ratio measurements. Hence, significantly non-ideal spike–natural mixtures can be tolerated under normal circumstances.

The only other sources of error in isotope-dilution analysis are incomplete homogenisation between sample and spike solution, and weighing errors. The first of these can be overcome by centrifuging the sample solution to check for any undissolved material and repeating the dissolution steps as necessary until complete solution is achieved. Given sufficient care, including the use of non-hygroscopic standard material and correct balance calibration, spike solutions can be calibrated to 0.1% accuracy (Wasserburg *et al.*, 1981). The use of mixed spikes (e.g. Sm–Nd, Rb–Sr) then eliminates further weighing errors in the analysis of these ratios in sample material. The result is that isotope-dilution accuracy can exceed 1% with ease, and 0.1% if necessary. This compares very favourably with all other methods of concentration determination.

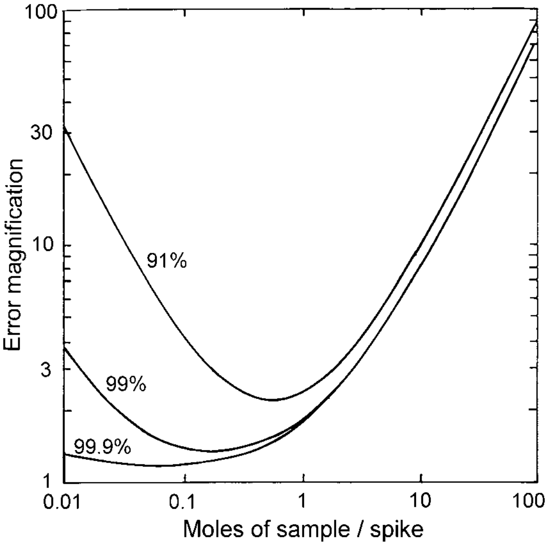

Fig. 2.22. Estimates of error magnification in isotope-dilution analysis as a function of the total number of moles of sample/spike. Cases are shown for three different percentages of spike isotope enrichment, mixed with a natural sample with a 50–50 isotopic abundance ratio. After De Bièvre and Debus (1965).

2.4.2 Double spiking

The selection of an arbitrary non-radiogenic ratio for fractionation normalisation (e.g. ^{88}Sr/^{86}Sr = 8.37521) results in no loss of information for terrestrial samples. However, for meteorites, use of such a procedure means that the true isotopes responsible for certain anomalous isotope ratios cannot be uniquely identified. An example is provided by inclusions EK 1-4-1 and C1 of the Allende chondritic meteorite (Papanastassiou *et al.*, 1978), for which several mixing models of nucleosynthetic components are possible (e.g. Clayton, 1978).

The double-spike isotope-dilution technique can be used to overcome this problem by correcting for fractionation in the mass-spectrometer source, thus allowing comparison of all of the isotope ratios in a suite of samples, including those used for fractionation normalisation. The theory of double spiking was first investigated in detail by Dodson (1963). The calculations may be made iteratively (e.g. Compston and Oversby, 1969) or algebraically (e.g. Gale, 1970). However, it is not usually possible to calculate 'absolute' values of isotopic abundance because there is not normally any absolute standard to calibrate the double spike.

Double spiking has been used to study processes of Sr isotope fractionation in the solar nebula, as sampled by inclusions and chondrules in the Allende meteorite, relative to the composition of all terrestrial samples (Patchett, 1980). Variations in ^{88}Sr/^{86}Sr ratio *versus* ^{84}Sr/^{86}Sr ratio were found to fit a mass-fractionation line very well (Fig. 2.23). Ca–Al inclusions were enriched in the lighter isotopes of Sr, which is surprising, since these inclusions are thought to be relatively early condensates from the nebula, which should therefore be enriched in heavy isotopes. The simplest explanation for the effect is that the inclusions condensed from an isotopically light region of the nebula.

Several workers have investigated the use of double Pb spikes to allow within-run mass-fractionation correction of Pb isotope ratios. Most of these studies utilised double stable-isotope spikes such as ^{207}Pb–^{204}Pb (Compston and Oversby, 1969; Hamelin *et al.*, 1985), which necessitate two separate mass-spectrometer runs, one with spike and one without. This is because the spike interferes with the determination of natural ^{207}Pb and ^{204}Pb. In contrast, the use of a ^{202}Pb/^{205}Pb double spike allows both concentration determination and a correction for analytical mass fractionation to be made on a single Pb mass-spectrometer run (Todt *et al.*, 1996). These isotopes are difficult to manufacture, but the procedure for ^{205}Pb was described by Parrish and Krogh (1987). The double-spiking technique has not been used widely for Pb, because between-run fractionation has been controlled successfully by the silica-gel loading technique. In addition, the double-spike method may cause error magnification if the spike/sample ratio is not close to optimal, or if the mass-spectrometer run is not of high precision (Fig. 2.24).

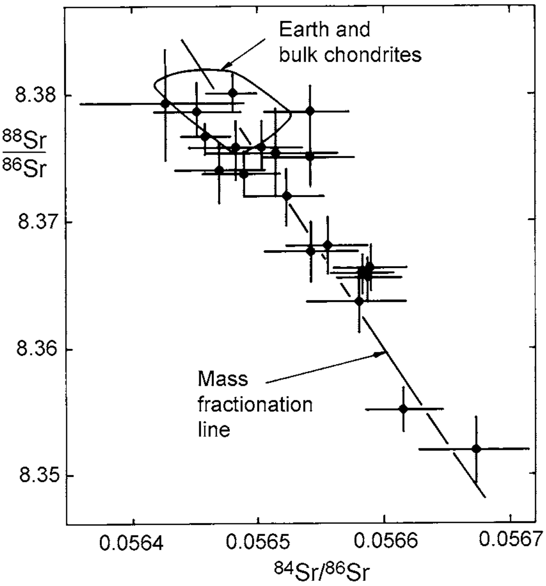

Fig. 2.23. Plot of ^{88}Sr/^{86}Sr ratio against ^{84}Sr/^{86}Sr ratio for samples from Allende chondrules. Instrumental mass fractionation has been corrected using a double-spike algorithm. After Patchett (1980).

More recent work on double-spike TIMS Pb analysis has been done by Powell *et al.* (1998), Galer (1999) and Thirlwall (2000). However, the advent of plasma-source mass spectrometry has offered an alternative approach for fractionation correction in the analysis of common Pb (see below).

2.5 Applications of MC-ICP-MS to radiogenic isotopes

MC-ICP-MS is a more expensive technology than conventional TIMS, both to build and to operate. This is because the instruments have several complex engineering systems, involving the RF generator, the torch assembly with its argon supply, and the ion-extraction system with its pumps, in addition to the magnetic-sector analyser. Hence, MC-ICP-MS is most effectively applied to isotope systems where TIMS has

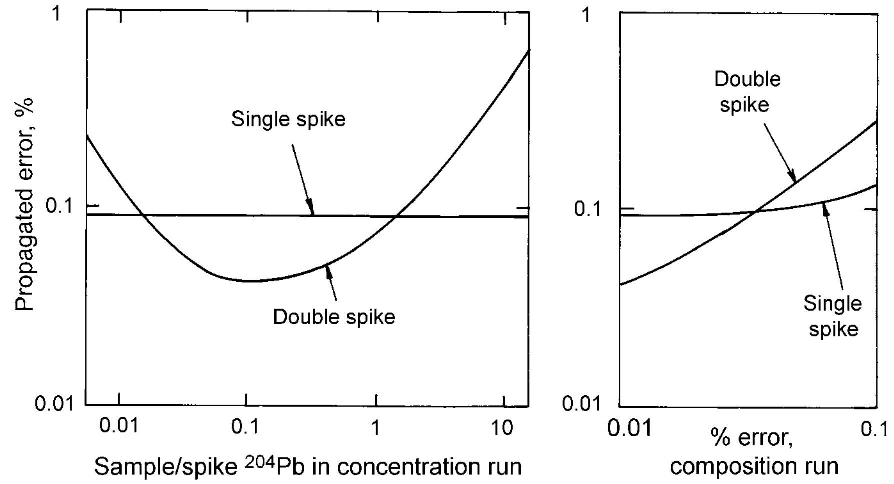

Fig. 2.24. Error propagation in Pb double-spike analysis: (a) the effect of differing proportions of spike to natural Pb; and (b) the effect of within-run precision. After Hamelin *et al.* (1985).

encountered technical difficulties. A few of these systems will be described.

2.5.1 Hf–W

^{182}W is the decay product of the short-lived nuclide ^{182}Hf ($t_{1/2} = 9$ Myr). As an extinct nuclide ^{182}Hf can place important constraints on the origin and early history of the solar system, but the very high ionisation potential of tungsten (7.98 eV, similar to that of osmium) precludes its analysis as a positive ion by TIMS. The first high-precision W isotope measurements were made by negative-ion TIMS, but MC-ICP-MS proved ideally suited to the analysis of this element. Following the establishment of the method (Lee and Halliday, 1995), these authors made numerous W isotope analyses of meteoritic and planetary samples, throwing new light on the timing of terrestrial core formation and the formation of the solar nebula (section 15.5.4).

2.5.2 Lu–Hf

The Lu–Hf isotope system was first exploited using positive-ion TIMS analysis (section 9.1), but the high ionisation potential of hafnium (6.65 eV) has always rendered TIMS Hf analysis difficult, requiring large sample size and high-purity ion-exchange separation in order to achieve good results. The ability of MC-ICP-MS to achieve excellent ionisation on impure sample solutions makes the method ideal for Hf isotope analysis. Whole-rock samples containing as little as 100 ng Hf can be analysed after pre-concentration only (Blichert-Toft *et al.*, 1997), and zircons can be analysed *in situ* by laser-probe MC-ICP-MS (Thirlwall and Walder, 1995). Previously, TIMS analysis of Hf also required a very demanding chemical separation method (Patchett and Tatsumoto, 1980), Hence, for all of these reasons, MC-ICP-MS has effectively rendered TIMS analysis of hafnium obsolete.

2.5.3 U–Th

Thorium is another element with a high ionisation potential (6.97 eV). It is routinely analysed by TIMS, but the poor ionisation efficiency is a significant problem, particularly for samples with large common-thorium (^{232}Th) contents (section 13.1). Such samples are well suited to simultaneous analysis on a Faraday and Daly collector. In this approach the small ^{230}Th beam is analysed on a Daly or multiplier collector, while the large ^{232}Th beam is analysed simultaneously on a Faraday collector (e.g. Luo *et al.*, 1997). In order to calibrate the relative gain of the Daly and Faraday collectors, Luo *et al.* added uranium of known isotopic composition directly to the Th sample. The ^{235}U/^{238}U ratio measured on two Faraday collectors is used for mass fractionation correction of both U and Th, while the ^{234}U/^{235}U ratio is used to calibrate the Daly/Faraday collector gain. Results for the Table Mountain Latite standard gave excellent external (between-run) precision, as well as internal (within-run) precision. In more recent work, the method was used successfully to duplicate TIMS analyses of carbonate samples (Shen *et al.*, 2002) and igneous rock analysis (Pietruszka *et al.*, 2002).

2.5.4 Pb–Pb

Pb isotope analysis has long been performed by TIMS, but the existence of only one stable non-radiogenic isotope has always made mass fractionation the principal source of analytical error. Mass fractionation occurs in the plasma source, but it is almost completely independent of the chemistry of the species involved. Therefore, the two stable isotopes of thallium (202 and 205) can be used to make accurate fractionation corrections for Pb (Walder and Furuta, 1993).

More detailed experiments (White *et al.*, 2000) appeared to reveal small differences between the mass-fractionation behaviours of Pb and Tl, although these could be corrected for. Some minor problems were also found by Thirlwall (2002) and attributed to subtle solution-chemistry effects in the nebuliser. However, Collerson *et al.* (2002) observed coherent fractionation behaviour between Pb and Tl, demonstrated by plotting interference-corrected raw ratios for both elements on a log–log plot. Hence, they were able to obtain accurate fractionation-corrected Pb isotope data on several different types of sample, with an average reproducibility of about 300 ppm.

It is concluded that MC-ICP-MS can achieve accuracies of Pb isotope analysis approaching those produced by the much more experimentally demanding double-spiking methods using TIMS (section 2.4.2). Therefore it can be expected that MC-ICP-MS will take over from TIMS as the preferred method for Pb isotope analysis where large suites of samples must be analysed to high precision. This would apply to studies of igneous petrogenesis and especially to Pb isotope analysis as an environmental tracer, such as in the study of seawater evolution from the analysis of ferromanganese crusts (Christensen *et al.*, 1997).

2.5.5 U–Pb

Another area where MC-ICP-MS has been successfully applied is the *in situ* U–Pb analysis of zircons by

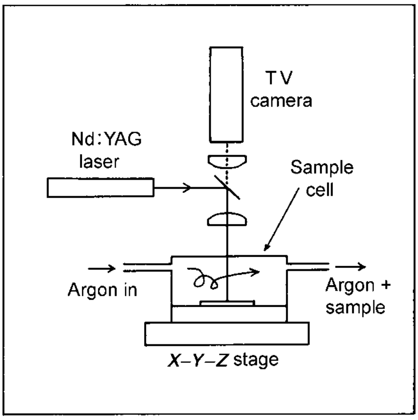

Fig. 2.25. Schematic illustration of the equipment set-up for feeding laser-ablated material into the ICP source. After Halliday *et al.* (1998).

laser ablation, for applications in geochronology. An infra-red or (more usually) an ultra-violet laser is used to ablate the sample inside a small chamber, which is at atmospheric pressure. The atomic sample cloud in the chamber is carried to the plasma by the argon 'sampler' gas flow, and is then ionised in the plasma in the usual way (Fig. 2.25).

Walder *et al.* (1993a) used a glass standard to calculate the efficiency of laser-ablation MC-ICP-MS for ion production. They found that the efficiency was comparable to that of ion-microprobe analysis using the SHRIMP (section 5.2.3). However, because the volume of sample excavated by laser ablation can be larger than that with the SHRIMP, laser-ablation MC-ICP-MS can generate ion beams large enough for analysis by multiple Faraday collectors (Halliday *et al.*, 1998). Hence the instrument is potentially capable of generating ages with higher precision than the SHRIMP. The instrument used by Halliday *et al.* (1998) was fitted with a wide flight tube to permit simultaneous analysis of U and Pb.

Some problems remain in the accurate calibration of U/Pb ratios measured during the laser-ablation process. However, Horn *et al.* (2000) proposed that ^{202}Tl, ^{205}Tl and ^{235}U spikes could be added by solution nebulisation to the gas stream from laser ablation of the sample. Use of a zircon standard showed that elemental U/Pb fractionation during ablation could be quantified for a given laser power, spot size and depth of excavation. This calibration procedure then allowed U/Pb fractionation during sample ablation to be calibrated. Pb mass fractionation during beam extraction from the plasma was also corrected. Horn *et al.* applied this procedure on a quadrupole ICP-MS, whose ultimate precision is limited to about $\pm 1\%$ (2σ) by the instability of the plasma. However, the use of this spiking technique in combination with MC-ICP-MS offers the possibility of matching the dating precision of ion microprobes such as the SHRIMP (section 5.2.3).

2.5.6 Sm–Nd

Experiments to test the effectiveness of MC-ICP-MS for Nd isotope analysis were reported by Walder *et al.* (1993b) and Luais *et al.* (1997). Most analyses were made in static multi-collection mode, but a few multi-dynamic analyses gave similar results to static analysis. It was shown that Sm interference corrections could be made very accurately, so that Nd isotope ratio determinations could be made on bulk REE separates from a cation column, without secondary clean-up to remove Sm. In addition, the typical analysis time was only 20 min per sample.

Disadvantages of the ICP method were the longer instrument-setup times, the need to analyse more standards and the slightly lower external (between-run) reproducibility. This was found to be about 30 ppm over short periods, but 60 ppm over a period of a year. However, results of a more recent study (Vance and Thirlwall, 2002) suggest that this lower reproducibility was due to the inadequacy of the exponential law to correct for the large fractionation factors encountered with ICP, which are more consistent than TIMS fractionation effects, but usually more than an order of magnitude larger. Vance and Thirlwall showed that these problems could be solved using information from the fractionation of additional non-radiogenic ratios, therefore allowing MC-ICP-MS to generate reproducibilities comparable to those with TIMS. However, TIMS Nd analysis is simpler and cheaper, making it accessible to a wider range of users. Therefore, it appears that Nd isotope analysis will be a niche where TIMS will be applied for some time to come.

2.6 Isochron regression-line fitting

When radiogenic isotope ratios for a co-genetic sample suite (e.g. ^{87}Sr/^{86}Sr) are plotted against the parent/daughter ratio in those samples (e.g. ^{87}Rb/^{86}Sr), the points should ideally define a perfect straight line or 'isochron' (section 3.2.2). Typically, the slope of this isochron line can then be used to determine the age of the system. However, since both quantities involved are measured experimentally, experimental errors are inevitable. Hence, these errors must be considered when calculating the slope of a best-fit line though the data.

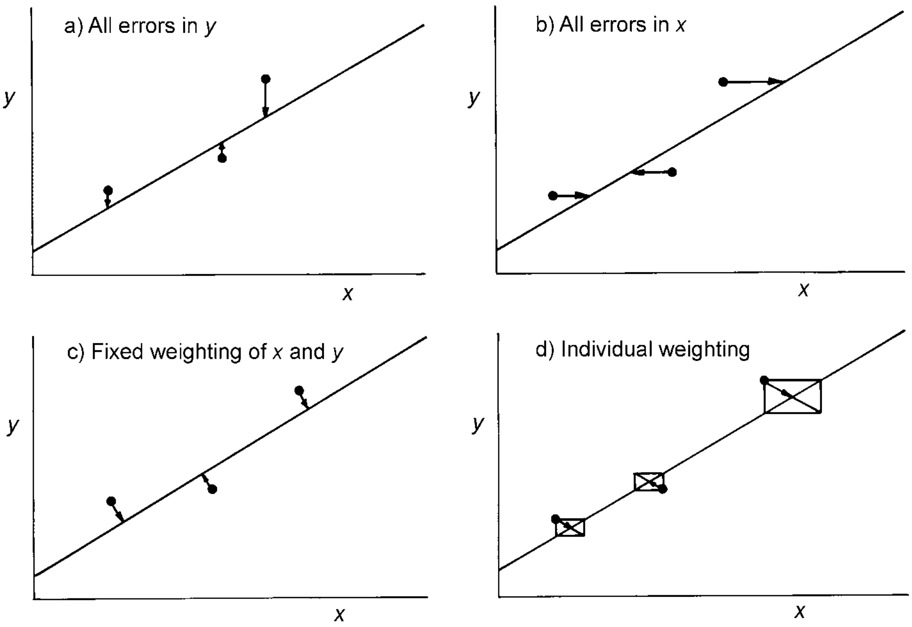

Fig. 2.26. Schematic illustration of least-squares regression analysis with different conditions of weighting; (a) infinite weighting of *x* (all errors in *y*); (b) infinite weighting of *y*; (c) fixed weighting of *x versus y*; and (d) individual weighting of each point, inversely proportional to squares of standard deviations. After York (1967).

A straight line fitted to an array of points is termed a 'linear regression'. One of the best approaches involves minimising the sum of the squares of the distances that data points lie away from a line drawn through the points, and hence is called a least-squares fit. This involves iteration, and is therefore done by calculator or computer.

2.6.1 Types of regression fit

In simple linear-regression programs, one ordinate is defined as 'free of error' and the regression line is calculated to minimise the mis-fit of points in the other ordinate (Figs. 2.26a, b). If the data define a very gentle slope and are somewhat scattered, disastrous fits can be produced by regressing onto the wrong ordinate. Where errors are present in both ordinates, as in the case of the isochron fit, a two-error regression treatment must be used (Figs. 2.26c, d). Several methods of this type have been presented in the literature (e.g. McIntyre *et al.*, 1966; York, 1966; York, 1967; Brooks *et al.*, 1972; Ludwig, 1997), sometimes including a ready-to-run computer program.

In cases where the actual deviations of the data points from the regression line are equal to or less than those expected from experimental error, all regression treatments effectively give the same isochron age and initial ratio. In such cases, the only matter of debate is the manner in which experimental errors are assigned.

Ideally, the analysed error in $^{87}Sr/^{86}Sr$ and $^{87}Rb/^{86}Sr$ ratios (for example) would be determined by measuring the reproducibility of an almost infinite number of duplicates (Brooks *et al.*, 1972). Since this is very time-consuming, the best empirical estimate is probably the long-term reproducibility of standard analyses. Within-run precision of sample analyses is almost certainly an under-estimate of error, since it is typically about 50% of the reproducibility error. For $^{87}Rb/^{86}Sr$ ratios, quoted accuracies must include an estimate for sample-weighing errors, spike-calibration errors etc., as well as mass-spectrometry errors (in the case of isotope dilution).

While some of the regression programs in use provide the facility for weighting each data point according to its precision of measurement, this may sometimes be detrimental, as it tends to 'destabilise' the fit. In practice, $^{87}Rb/^{86}Sr$ and $^{87}Sr/^{86}Sr$ errors are probably best assigned as a blanket percentage (e.g. 0.5% and 0.002% 1σ, respectively). If one point has a particularly bad precision, it is better to re-analyse it than give it less weight in the regression.

2.6.2 Regression fitting with correlated errors

In conventional isochron analysis (e.g. Rb–Sr), analytical errors in the two ordinates (isotope ratio and elemental abundance ratio) are effectively uncorrelated. However, in the lead isotope dating methods, this is far from the case. In common Pb–Pb dating, correlated errors are found between $^{207}Pb/^{204}Pb$ and $^{206}Pb/^{204}Pb$, due to the greater analytical uncertainties on the small ^{204}Pb peak (which is common to both ratios) and due to the uncertainty of mass fractionation. These two correlation lines have different slopes, and while the former may be important for very small Pb beam sizes, the latter is normally dominant. Data for the NBS 981 standard shown in Fig. 2.27 yield a correlation coefficient of 0.94 (Ludwig, 1980).

In U–Pb zircon dating, errors may exhibit a much stronger correlation. This is because errors in $^{206}Pb/^{238}U$ and $^{207}Pb/^{235}U$ are mainly attributable to the elemental U/Pb ratio, which may be five or more times less reproducible than the $^{206}Pb/^{207}Pb$ ratio (Davis, 1982). This difference arises from the analytical errors inherent in isotope dilution and from uncertainties in common-Pb correction (section 5.2). Regression treatments for correlated errors using the least-squares technique were given by York (1969) and Ludwig (1980). Davis (1982) used the alternative 'maximum-likelihood' method, and showed that the two approaches yielded similar estimates of error using test data (see also Titterington and Halliday, 1979).

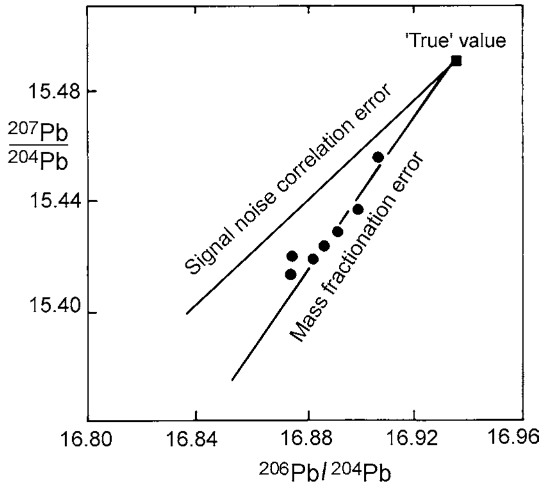

Fig. 2.27. Results of seven analytical runs on the NBS 981 Pb standard performed with large beam sizes at varying filament temperatures. Data cluster near the mass-fractionation line. Solid square = 'true value'. After Ludwig (1980).

2.6.3 Errorchrons

Brooks *et al.* (1972) argued that 'a line fitted to a set of data that display a scatter about this line in excess of the experimental error is simply not an isochron'. They proposed that Rb–Sr regression fits with excess or 'geological' scatter (McIntyre *et al.*, 1966) should be called 'errorchrons' and treated with a high degree of suspicion. This raises the problem of how to detect the presence of geological scatter, bearing in mind the fact that analytical errors are only probabilities.

The sum of the squares of the mis-fits of each point to the regression line (i.e. squared residuals; York, 1969) or sum of χ^2 (Brooks *et al.*, 1968; 1972), may be divided by the degrees of freedom (number of data points minus two) to yield mean-squared weighted deviates (MSWD), which represents the most convenient expression of scatter. If the scatter of data points is, on average, exactly equivalent to that predicted from the analytical errors, then the calculation will yield MSWD $= 1$. Excess scatter of data points yields MSWD > 1, whereas less scatter than predicted from experimental errors yields MSWD < 1.

Problems may arise with the interpretation of these MSWD values, since the analytical errors input into the program are only estimates of error. To address this problem, Brooks *et al.* (1972) constructed a table of probabilities (Table 2.1) to distinguish between errorchrons and isochrons from their MSWD values. They established a 'rule of thumb' that, on average, if MSWD < 2.5, then the data define an isochron, whereas if MSWD > 2.5, they define an errorchron. Unfortunately this rule of thumb has been much abused over subsequent years, because the original objectives of Brooks *et al.* (1972) have been misunderstood. They set up the MSWD $= 2.5$ cut-off in order to reject errorchrons with a 95% certainty of excess scatter over analytical error. This corresponds to only 5% confidence that a fit with MSWD $= 2.5$ is an isochron (e.g. Wendt and Carl, 1991). However, many workers have wrongly assumed that if MSWD is less than 2.5 then there is a high degree of confidence that the suite is a true isochron (where analytical errors express most or all of the error on the age). In actual fact, MSWD must be near unity for one to have a high degree of confidence that the data represent a true isochron.

2.6.4 Dealing with errorchrons

Because the number of errorchrons will continually increase as analytical errors decrease, the suggestion that

Table 2.1. *MSWD values indicating 95% confidence of an errorchron*

	Number of samples regressed								
Number of duplicates	3	4	5	6	8	10	12	14	26
10	4.96	4.10	3.71	3.48	3.22	3.07	2.98	2.91	$\underline{2.74}$
20	4.35	3.49	3.10	2.87	$\underline{2.60}$	2.45	2.35	2.28	2.08
30	4.17	3.32	2.92	$\underline{2.69}$	2.42	2.27	2.16	2.09	1.89
40	4.08	3.23	2.84	$\underline{2.61}$	2.34	2.18	2.08	2.00	1.79
60	4.00	3.15	2.76	$\underline{2.53}$	2.25	2.10	1.99	1.92	1.70
120	3.92	3.07	$\underline{2.68}$	2.45	2.18	2.02	1.91	1.83	1.61

Numbers underlined just exceed the MSWD = 2.5 cut-off.

errorchrons be rejected outright is unhelpful. Therefore, other workers have looked for ways of quantifying geological scatter in terms of an error on the age result. McIntyre *et al.* (1966) emphasised that statistical error estimation of errorchrons cannot be properly meaningful unless the geological reasons for the mis-fit are understood. Therefore, they suggested four alternative approaches for error handling. These are as follows:

(1) No excess scatter above predicted analytical errors (i.e. a true isochron).
(2) All excess scatter is attributed to Rb/Sr, equivalent to assuming that there are small differences between the initial ages of the samples.
(3) All excess scatter is attributed to ^{87}Sr/^{86}Sr, equivalent to assuming that there is variation in the initial isotopic ratio of samples.
(4) Excess scatter is attributed to some combination of models (2) and (3).

The program of York (1966) allows the analytical errors on X and Y ordinates (e.g. ^{87}Rb/^{86}Sr and ^{87}Sr/^{86}Sr) to be multiplied in equal and uniform proportion by an error factor ($\sqrt{\text{MSWD}}$) until the expanded errors equal geological scatter (MSWD = 1). The error on the calculated age will be magnified by this process to give a reasonable estimate of uncertainty, which includes both geological and analytical scatter.

Some form of error expansion must *always* be performed if a meaningful geological error estimate is to be given for a data set with MSWD $>$ 1, because this is a definite indicator that excess scatter of some form is present. The only uncertainty is whether the excess scatter is geological or analytical. The York (1966) procedure is the most common method of dealing with excess scatter, but it is an arbitrary procedure that takes no account of geological processes and their resulting contribution to errors. Where initial ratio variability is suspected, option (3) of McIntyre (above) is preferable (amplification of isotope ratios only). However, this can lead to misinterpretation of a data set if all points are not identical in age.

A new DOS/Windows-based computer program incorporating these concepts was provided by Ludwig (1997). Amongst several types of isochron fit, this program (Isoplot version 2.95) provides York-type fits under three categories which are similar to those above:

(1) Fits based on individually assigned analytical errors. Errors on the age are calculated (a) based on analytical errors only (applicable if MSWD $\leq$ 1); and (b) by equal expansion of assigned analytical errors. A warning was given that the latter approach can give rise to serious errors if the assigned analytical errors are significantly variable.
(2) A fit based on expansion of assigned errors to encompass the scatter, but all points have equal weights. If the assigned errors are uniform, fit (1b) is the same as fit (2).
(3) A fit based on model (3) of McIntyre, with excess scatter absorbed by expanding initial ratios only. Sketches to show categories (1) and (3) are presented in Fig. 2.28.

Misinterpretation of errorchrons is usually due to a failure to visualise the distribution of data and attendant errors adequately. This can be avoided by using a graphical presentation. Various types of graphical assessment using isochron diagrams will be discussed for the Rb–Sr method (section 3.2.2). However, an alternative approach is the so-called ‘bootstrap method’ (Kalsbeek and Hansen, 1989). In this method a set of errorchron data is analysed by computer to see how stable the regression line is to the application of a greater weighting to various points. This test is performed by successive random selection of a sample of points from the data set, such that this sample is equal in size to the data set. (This is not as strange as it sounds.) What

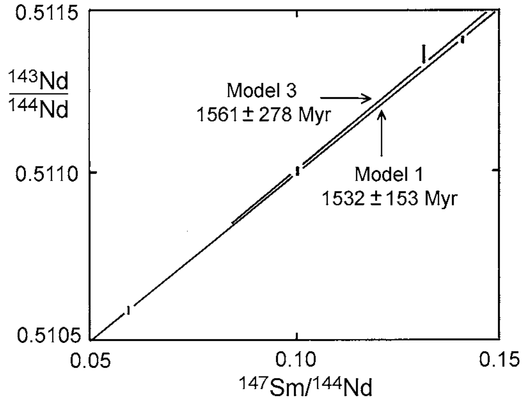

Fig. 2.28. Sketches to show the effects of Ludwig's Model 1 and Model 3 on a four-point errorchron (MSWD = 6.9) with one aberrant point with larger error. (Input data: 0.06, 0.1, 0.5106, 0.002; 0.10, 0.1, 0.511, 0.002; 0.14, 0.1, 0.5114, 0.002; and 0.13, 0.1, 0.511 35, 0.005.)

will normally happen is that a few points are selected more than once, while others are omitted. By repeating this process a few thousand times, a probability distribution is set up, portraying the stability of the best-fit line against the influence of certain sub-sets of the data suite (Fig. 2.29).

If geological errors are randomly distributed, the frequency histogram derived from the data set will have a symmetrical (Poisson) distribution. In this case the result is identical to expanding analytical errors by $\sqrt{\text{MSWD}}$. (Of course, a true isochron should always yield a Poisson distribution, because analytical errors are assumed to be random.) However, if geological scatter is uneven, the probability histogram of an errorchron may be skewed or even bimodal (Fig. 2.29) and hence highly suspect in terms of age assignment. This diagram therefore constitutes an excellent visual test for isochron data quality, and could help to avoid the misinterpretation of problematical data sets.

A more recent form of the bootstrap approach was described by Powell *et al.* (2002). The objective of their method was to downplay the significance of extreme data points that lie outside a Poisson distribution, by amplifying the errors on these data points more than the main data set (similar to Fig. 2.28). This approach was intended to generate more 'robust' ages and error estimates by avoiding the distortion of an isochron age that could occur with full weighing of 'aberrant' points, while also reducing the 'temptation' to exclude such points from the calculation, as many workers do. The ideal approach would be to collect more data in order to resolve the non-Gaussian data more clearly, but in the real world this might not be possible.

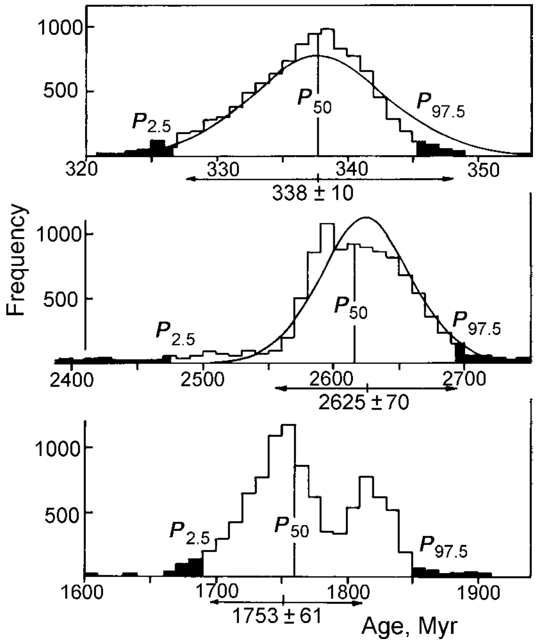

Fig. 2.29. Frequency distribution of 10 000 selection permutations from three sets of errorchron data. 95% (2σ) confidence limits of the 'bootstrap' age determination are indicated ($P_{2.5}$ and $P_{97.5}$). Arrows represent symmetrical 2σ confidence limits resulting from expansion of analytical errors until MSWD = 1. After Kalsbeek and Hansen (1989).

References

Arden, J. W. and Gale N. H. (1974). New electrochemical technique for the separation of lead at trace levels from natural silicates. *Anal. Chem.* **46**, 2–9.

Aston, F. W. (1919). A positive ray spectrograph. *Phil. Mag.* (Series 6), **38**, 707–14.

Aston, F. W. (1927). The constitution of ordinary lead. *Nature* **120**, 224.

Barovich, K. M., Beard, B. L., Cappel, J. B., Johnson, C. M., Kyser, T. K. and Morgan, B. E. (1995). A chemical method for hafnium separation from high-Ti whole-rock and zircon samples. *Chem. Geol. (Isot. Geosci. Section)* **121**, 303–8.

Blichert-Toft, J., Chauvel, C. and Albarède, F. (1997). Separation of Hf and Lu for high-precision isotope analysis by magnetic sector–multiple collector ICP-MS.*Contrib. Mineral. Petrol.* **127**, 248–60.

Brooks, C., Hart, S. R. and Wendt, I. (1972). Realistic use of two-error regression treatments as applied to rubidium–strontium data. *Rev. Geophys. Space Phys.* **10**, 551–77.

Brooks, C., Wendt, I. and Harre, W. (1968). A two-error regression treatment and its application to Rb–Sr and initial Sr^{87}/Sr^{86} ratios of younger Variscan granitic rocks from the Schwarzwald massif, southwest Germany. *J. Geophys. Res.* **73**, 6071–84.

Cameron, A. E., Smith, D. H. and Walker, R. L. (1969). Mass spectrometry of nanogram-size samples of lead. *Anal. Chem.* **41**, 525–6.

Cassidy, R. M. and Chauvel, C. (1989). Modern liquid chromatographic techniques for the separation of Nd and Sr for isotopic analyses. *Chem. Geol.* **74**, 189–200.

Catanzaro, E. J. and Kulp, J. L. (1964). Discordant zircons from the Little Butte (Montana), Beartooth (Montana) and Santa Catalina (Arizona) Mountains. *Geochim. Cosmochim. Acta* **28**, 87–124.

Chen, J. H. and Wasserburg, G. J. (1981). Isotopic determination of uranium in picomole and sub-picomole quantities. *Anal. Chem.* **53**, 2060–7.

Christensen, J. N., Halliday, A. N., Godfrey, L. V., Hein, J. R. and Rea, D. K. (1997). Climate and ocean dynamics and the lead isotopic records in Pacific ferromanganese crusts. *Science* **277**, 913–8.

Clayton, D. D. (1978). On strontium isotopic anomalies and odd-*A* p-process abundances. *Astrophys. J.* **224**, L93–5.

Collerson, K. D., Kamber, B. S. and Schoenberg, R. (2002). Applications of accurate, high-precision Pb isotope ratio measurement by multi-collector ICP-MS. *Chem. Geol.* **188**, 65–83.

Compston, W. and Oversby, V. M. (1969). Lead isotopic analysis using a double spike. *J. Geophys. Res.* **74**, 4338–48.

Cotte, M. (1938). Recherches sur l'optique électronique. *Ann. Physique* **10**, 333–405.

Crock, J. G., Lichte, F. E. and Wildeman, T. R. (1984). The group separation of the rare-earth elements and yttrium from geologic materials by cation-exchange chromatography. *Chem. Geol.* **45**, 149–63.

Croudace, I. W. (1980). A possible error source in silicate wet-chemistry caused by insoluble fluorides. *Chem. Geol.* **31**, 153–5.

Crumpler, T. B. and Yoe, J. H. (1940). *Chemical Computations and Errors*. Wiley, pp. 189–90.

Daly, N. R. (1960). Scintillation type mass spectrometer ion detector. *Rev. Sci. Instrum.* **31**, 264–7.

David, K., Birch, J. L., Télouk, P. and Allègre, C. J. (1999). Application of isotope dilution for precise measurement of Zr/Hf and ^{176}Hf/^{177}Hf ratios by mass spectrometry (ID-TIMS/ID-MC-ICP-MS). *Chem. Geol.* 157, 1–12.

Davis, D. W. (1982). Optimum linear regression and error estimation applied to U–Pb data. *Can. J. Earth Sci.* **19**, 2141–9.

Dawson, P. H. (1976). (Ed.), *Quadrupole Mass Spectrometry and its Applications*. Elsevier, 349 pp.

De Bièvre, P. J. and Debus, G. H. (1965). Precision mass spectrometric isotope dilution analysis. *Nucl. Instr. Meth.* **32**, 224–8.

Dempster, A. J. (1918). A new method of positive ray analysis. *Phys. Rev.* **11**, 316–24.

DePaolo, D. J. and Wasserburg, G. J. (1976). Nd isotopic variations and petrogenetic models. *Geophys. Res. Lett.* **3**, 249–52.

Dickin, A. P., Jones, N. W., Thirlwall, M. and Thompson, R. N. (1987). A Ce/Nd isotope study of crustal contamination processes affecting Palaeocene magmas in Skye, NW Scotland. *Contrib. Mineral. Petrol.* **96**, 455–64.

Dodson, M. H. (1963). A theoretical study of the use of internal standards for precise isotopic analysis by the surface ionisation technique: Part I – general first-order algebraic solutions. *J. Sci. Instrum.* **40**, 289–95.

Dodson, M. H. (1978). A linear method for second-degree interpolation in cyclical data collection. *J. Phys. E (Sci. Instrum.)* **11**, 296.

Dosso, L. and Murthy, V. R. (1980). A Nd isotopic study of the Kerguelen islands: inferences on enriched oceanic mantle sources. *Earth Planet. Sci. Lett.* **48**, 268–76.

Eberhardt, A., Delwiche, R. and Geiss, J. (1964). Isotopic effects in single filament thermal ion sources. *Z. Naturf.* **19a**, 736–40.

Edwards, R. L., Chen, J. H. and Wasserburg, G. J. (1987). ^{238}U–^{234}U–^{230}Th–^{232}Th systematics and the precise measurement of time over the past 500,000 years. *Earth Planet. Sci. Lett.* **81**, 175–92.

Eugster, O., Tera, F., Burnett, D. S. and Wasserburg, G. J. (1970). The isotopic composition of gadolinium and neutron capture effects in some meteorites. *J. Geophys. Res.* **75**, 2753–68.

Faul, H. (1966). *Ages of Rocks, Planets, and Stars*. McGraw-Hill, 109 pp.

Gale, N. H. (1970). A solution in closed form for lead isotopic analysis using a double spike. *Chem. Geol.* **6**, 305–10.

Galer, S. J. G. (1999). Optimal double and triple spiking for high precision lead isotopic measurement. *Chem. Geol.* **157**, 255–74.

Habfast, K. (1983). Fractionation in the thermal ionization source. *Int. J. Mass Spectrom. Ion Phys.* **51**, 165–89.

Halliday, A. N., Lee, D.-C., Christensen, J. N. *et al.* (1998). Applications of multiple collector-ICPMS to cosmochemistry, geochemistry, and paleoclimatology. *Geochim. Cosmochim. Acta* **62**, 919–40.

Hamelin, B., Manhès, G., Albarède, F. and Allègre, C. J. (1985). Precise lead isotope measurements by the double spike technique: a reconsideration. *Geochim. Cosmochim. Acta* **49**, 173–82.

Hooker, P., O'Nions, R. K. and Pankhurst, R. J. (1975). Determination of rare-earth elements in U.S.G.S. standard rocks by mixed-solvent ion exchange and mass spectrometric isotope dilution. *Chem. Geol.* **16**, 189–96.

Horn, I., Rudnick, R. L. and McDonough, W. F. (2000). Precise elemental and isotope ratio determination by simultaneous solution nebulization and laser ablation-ICP-MS: application to U–Pb geochronology. *Chem. Geol.* **164**, 281–301. (Erratum *Chem. Geol.* **167**, 405–25.)

Houk, R. S. (1986). Mass spectrometry of inductively coupled plasmas. *Anal. Chem.* **58**, 97A–105A.

Houk, R. S., Fassel, V. A., Flesch, G. D., Svec, H. J., Gray, A. L. and Taylor, C. E. (1980). Inductively coupled argon plasma for mass spectrometric determination of trace elements. *Anal. Chem.* **52**, 2283–9.

Ingram, M. G. and Chupka, W. A. (1953). Surface ionisation source using multiple filaments. *Rev. Sci. Instrum.* **24**, 518–20.

Kalsbeek, F. and Hansen, M. (1989). Statistical analysis of Rb–Sr isotope data by the 'bootstrap' method. *Chem. Geol. (Isot. Geosci. Section)* **73**, 289–97.

Krogh, T. E. (1973). A low contamination method for hydrothermal decomposition of zircon and extraction of U and Pb for isotopic age determination. *Geochim. Cosmochim. Acta* **37**, 485–94.

Kuritani, T. and Nakamura, E. (2002). Precise isotope analysis of nanogram-level Pb for natural rock samples without use of double spikes. *Chem. Geol.* **186**, 31–43.

Kurz, E. A. (1979). Channel electron multipliers. *Amer. Lab.* **11** (3), 67–74.

Lee, D.-C. and Halliday, A. N. (1995). Precise determinations of the isotopic compositions and atomic weights of molybdenum, tellurium, tin and tungsten using ICP source magnetic sector multiple collector mass spectrometry. *Int. J. Mass Spectrom. Ion Process.* **146/147**, 35–46.

Li, W. X., Lundberg, J., Dickin, A. P. *et al.* (1989). High-precision mass spectrometric uranium-series dating of cave deposits and implications for paleoclimate studies. *Nature* **339**, 534–6.

Luais, B., Télouk, P. and Albarède, F. (1997). Precise and accurate neodymium isotopic measurements by plasma-source mass spectrometry. *Geochim. Cosmochim. Acta* **61**, 4847–54.

Ludwig, K. R. (1980). Calculation of uncertainties of U–Pb isotope data. *Earth Planet. Sci. Lett.* **46**, 212–20.

Ludwig, K. R. (1997). *Isoplot*. Program and documentation, version 2.95. Revised edition of U.S. Geological Survey Open-File report 91-445 (kludwig@bgc.org).

Lugmair, G. W., Scheinin, N. B. and Marti, K. (1975). Search for extinct ^{146}Sm, I. The isotopic abundance of ^{142}Nd in the Juvinas meteorite. *Earth Planet. Sci. Lett.* **27**, 9479–84.

Luo, X., Rehkämper, M., Lee, D.-C. and Halliday, A. N. (1997). High precision ^{230}Th/^{232}Th and ^{234}U/^{238}U measurements using energy-filtered ICP magnetic sector multiple collector mass spectrometry. *Int. J. Mass Spectrom Ion Process.* **171**, 105–17.

Manton, W. I. (1988). Separation of Pb from young zircons by single-bead ion exchange. *Chem. Geol. (Isot. Geosci. Section)* **73**, 147–52.

McIntyre, G. A., Brooks, A. C., Compston, W. and Turek, A. (1966). The statistical assessment of Rb–Sr isochrons. *J. Geophys. Res.* **71**, 5459–68.

Nier, A. O. (1940). A mass spectrometer for routine isotope abundance measurements. *Rev. Sci. Instrum.* **11**, 212–16.

Noble, S. R., Lightfoot, P. C. and Schärer, U. (1989). A new method for single-filament isotopic analysis of Nd using *in situ* reduction. *Chem. Geol. (Isot. Geosci. Section)* **79**, 15–19.

O'Nions, R. K., Carter, S. R., Evensen, N. M. and Hamilton P. J. (1979). Geochemical and cosmochemical applications of Nd isotope analysis. *Ann. Rev. Earth Planet. Sci.* **7**, 11–38.

O'Nions, R. K., Hamilton, P. J. and Evensen, N. M. (1977). Variations in ^{143}Nd/^{144}Nd and ^{87}Sr/^{86}Sr ratios in oceanic basalts. *Earth Planet. Sci. Lett.* **34**, 13–22.

Papanastassiou, D. A., Huneke, J. C., Esat, T. M. and Wasserburg, G. J. (1978). Pandora's box of the nuclides. *Lunar Planet. Sci.* **9**, 859–61 (abstract).

Parrish, R. R. (1987). An improved micro-capsule for zircon dissolution in U–Pb geochronology. *Chem. Geol. (Isot. Geosci. Section)* **66**, 99–102.

Parrish, R. R. and Krogh, T. E. (1987). Synthesis and purification of ^{205}Pb for U–Pb geochronology. *Chem. Geol. (Isot. Geosci. Section)* **66**, 103–10.

Patchett, P. J. (1980). Sr isotopic fractionation in Ca–Al inclusions from the Allende meteorite. *Nature* **283**, 438–41.

Patchett, P. J. and Tatsumoto, M. (1980). A routine high-precision method for Lu–Hf isotope geochemistry and chronology. *Contrib. Mineral. Petrol.* **75**, 263–7.

Pietruszka, A. J., Carlson, R. W. and Hauri, E. H. (2002). Precise and accurate measurement of ^{226}Ra–^{230}Th–^{238}U disequilibria in volcanic rocks using plasma ionization multicollector mass spectrometry. *Chem. Geol.* **188**, 171–91.

Potts, P. J. (1987). *Handbook of Silicate Rock Analysis*. Blackie, 622 p.

Powell, R., Hergt, J. and Woodhead, J. (2002). Improving isochron calculations with robust statistics and the bootstrap. *Chem. Geol.* **185**, 191–204.

Powell, R., Woodhead, J. and Hergt, J. (1998). Uncertainties on lead isotope analyses: deconvolution in the double-spike method. *Chem. Geol.* **148**, 95–104.

Richard, P., Shimizu, N. and Allègre, C. J. (1976). ^{143}Nd/^{146}Nd, a natural tracer: an application to oceanic basalts. *Earth Planet. Sci. Lett.* **31**, 269–78.

Roddick, J. C., Loveridge, W. D. and Parrish, R. R. (1987). Precise U/Pb dating of zircon at the sub-nanogram Pb level. *Chem. Geol. (Isot. Geosci. Section)* **66**, 111–21.

Russell, W. A., Papanastassiou, D. A. and Tombrello, T. A. (1978). Ca isotope fractionation on the Earth and other solar system materials. *Geochim. Cosmochim. Acta* **42**, 1075–90.

Shen, C.-C., Edwards, R. L., Cheng, H. *et al.* (2002). Uranium and thorium isotopic and concentration measurements by magnetic sector inductively coupled plasma mass spectrometry. *Chem. Geol.* **185**, 165–78.

Smythe, W. R. and Mattauch, J. (1932). A new mass spectrometer. *Phys. Rev.* **40**, 429–33.

Tanaka, T. and Masuda, A. (1982). The La–Ce geochronometer: a new dating method, *Nature* **300**, 515–18.

Thirlwall, M. F. (1982). A triple-filament method for rapid and precise analysis of rare-earth elements by isotope dilution. *Chem. Geol.* **35**, 155–66.

Thirlwall, M. F. (1991a). High-precision multicollector isotopic analysis of low levels of Nd as oxide. *Chem. Geol. (Isot. Geosci. Section)* **94**, 13–22.

Thirlwall, M. F. (1991b). Long-term reproducibility of multicollector Sr and Nd isotope ratio analysis. *Chem. Geol. (Isot. Geosci. Section)* **94**, 85–104.

Thirlwall, M. F. (2000). Inter-laboratory and other errors in Pb isotope analyses investigated using a ^{207}Pb–^{204}Pb double spike. *Chem. Geol.* **163**, 299–322.

Thirlwall, M. F. (2002). Multicollector ICP-MS analysis of Pb isotopes using a ^{207}Pb–^{204}Pb double spike demonstrates up to 400 ppm/amu systematic errors in Tl-normalization. *Chem. Geol.* **184**, 255–79.

Thirlwall, M. F. and Walder, A. J. (1995). *In situ* hafnium isotope ratio analysis of zircon by inductively coupled plasma multiple collector mass spectrometry. *Chem. Geol.* **122**, 241–7.

Thompson J. J. (1913). *Rays of Positive Electricity and Their Application to Chemical Analysis*. Longmans, Green and Co. Ltd.

Titterington, D. M. and Halliday, A. N. (1979). On the fitting of parallel isochrons and the method of maximum likelihood. *Chem. Geol.* **26**, 183–95.

Todt, W., Cliff, R. A., Hanser, A. and Hofmann, A. W. (1996). Evaluation of a ^{202}Pb–^{205}Pb double spike for high-precision lead isotopic analysis. In: Basu, A. and Hart, S. R. (Eds.), *Earth Processes: Reading the Isotopic Code. Geophysics Monograph* **95**. American Geophysical Union, pp. 429–37.

Vance, D. and Thirlwall, M. (2002). An assessment of mass discrimination in MC-ICPMS using Nd isotopes. *Chem. Geol.* **185**, 227–40.

Walder, A. J., Abell, I. D., Freedman, P. A. and Platzner, I. (1993a). Lead isotopic ratio measurement of NIST 610 glass by laser ablation-inductively coupled plasma-mass spectrometry. *Spectrochim. Acta* **48B**, 397–402.

Walder, A. J. and Furuta, N. (1993). High precision lead isotope ratio measurement by inductively coupled plasma multiple collector mass spectrometry. *Anal. Sci.* **9**, 675–80.

Walder, A. J., Platzner, I. and Freedman, P. A. (1993b). Isotope ratio measurement of lead, neodymium and neodymium–samarium mixtures, hafnium and hafnium–lutetium mixtures with a double focussing multiple collector inductively coupled plasma mass spectrometer. *J. Anal. Atomic Spectrom.* **8**, 19–23.

Wasserburg, G. J., Jacobsen, S. B., DePaolo, D. J. McCulloch, M. T. and Wen, T. (1981). Precise determination of Sm/Nd ratios, Sm and Nd isotopic abundances in standard solutions. *Geochim. Cosmochim. Acta* **45**, 2311–23.

Wendt, I. and Carl, C. (1991). The statistical distribution of the mean squared weighted deviation. *Chem. Geol. (Isot. Geosci. Section)* **86**, 275–85.

White, W. M., Albarède, F. and Télouk, P. (2000). High-precision analysis of Pb isotope ratios by multi-collector ICP-MS. *Chem. Geol.* **167**, 257–270.

York, D. (1966). Least-squares fitting of a straight line. *Can. J. Phys.* **44**, 1079–86.

York, D. (1967). The best isochron. *Earth Planet. Sci. Lett.* **2**, 479–82.

York, D. (1969). Least-squares fitting of a straight line with correlated errors. *Earth Planet. Sci. Lett.* **5**, 320–4.

3 The Rb–Sr method

Rubidium, a group-1 alkali metal, has two naturally occurring isotopes, ^{85}Rb and ^{87}Rb, whose abundances are 72.17% and 27.83%, respectively. These figures yield an atomic abundance ratio of $^{85}\mathrm{Rb}/^{87}\mathrm{Rb} = 2.593$ (Catanzaro *et al.*, 1969), which is a constant throughout the Earth, Moon and most meteorites due to isotopic homogenisation in the solar nebula. ^{87}Rb is radioactive, and decays to the stable isotope ^{87}Sr by emission of a β particle and anti-neutrino ($\bar{\nu}$). The decay energy (Q) is shared as kinetic energy by these two particles:

$$^{87}_{37}\mathrm{Rb} \rightarrow {}^{87}_{38}\mathrm{Sr} + \beta^- + \bar{\nu} + Q$$

3.1 The Rb decay constant

The low decay energy for this transformation (275 keV) has always caused problems in the accurate determination of the Rb decay constant. Because the decay energy is divided between the β particle and the anti-neutrino, the β particles have a smooth distribution of kinetic energy from the total energy down to zero. When attempting to determine the decay constant by direct counting, the low-energy β particles cause great problems because they may be absorbed by surrounding Rb atoms before they ever reach the detector. For example, in a thick (>1 μm) solid Rb sample, attenuation is so severe that a false frequency maximum is generated at about 10 keV (Fig. 3.1).

One way to avoid the attenuation problem is to use a photo-multiplier with a liquid scintillator solution doped with Rb. The β particles will be absorbed by molecules of the scintillator (emitting flashes of light) before they can be absorbed by other Rb atoms. The major problem with this method is that a low-energy cut-off at about 10 keV must be applied in order to avoid the high background noise associated with liquid scintillation. The consequent extrapolation of count-rate curves down to zero energy leads to a large uncertainty in the result (Fig. 3.1). Hence this method has given values for the ^{87}Rb half-life from 47.0 ± 1.0 Byr (Flynn and Glendenin, 1959) to 52.1 ± 1.5 Byr (Brinkman *et al.*, 1965).

Another approach to direct counting is to make measurements with progressively thinner solid Rb sources using a proportional counter. The results are then extrapolated to a theoretical source of zero thickness to remove the effect of self-absorption. The proportional counter has a much lower noise level, so the energy cut-off can be set as low as 0.185 keV. Rb films with thicknesses down to 1 μm were measured by Neumann and Huster (1974), and extrapolated to zero thickness by Neumann and Huster (1976) to derive an ^{87}Rb half-life of 48.8 ± 0.8 Byr (equivalent to a decay constant of $1.42 \times 10^{-11}\ \mathrm{yr}^{-1}$).

An alternative approach to determining the Rb decay constant is to measure the amount of ^{87}Sr produced by decay of a known quantity of ^{87}Rb in the laboratory over a known period of time. This method was first attempted by McMullen *et al.* (1966) on a rubidium sample they had purified in 1956, and was repeated on the same sample batch by Davis *et al.* (1977). Unfortunately, McMullen *et al.* omitted to measure the small but significant level of residual ^{87}Sr present in their rubidium before they put it away on the shelf. Hence, the accuracy of their determination was compromised. However, this problem contributes less than 1% uncertainty to the later determination of Davis *et al.* (1977). Their proposed value for the ^{87}Rb half-life (48.9 ± 0.4 Byr, equivalent to a decay constant of $1.42 \times 10^{-11}\ \mathrm{yr}^{-1}$) can therefore be taken to support the value of Neumann and Huster (1976).

A third approach to the determination of the Rb decay constant is to date geological samples whose ages have also been measured by other methods with more reliable decay constants. This method has the disadvantage that it involves geological uncertainties, such as whether all isotopic systems closed at the same time and remained closed. However, it provides a useful check on the direct laboratory determinations. In this respect it is worth noting that Pinson *et al.* (1963)

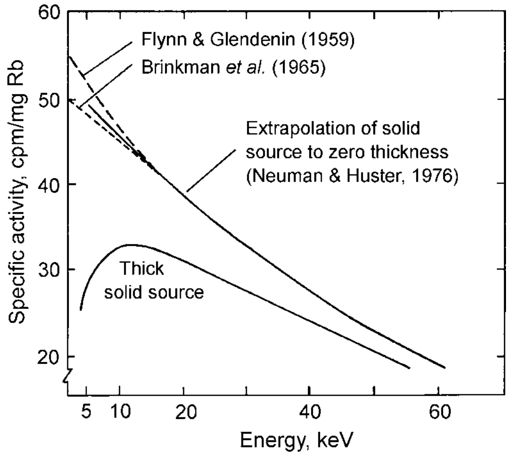

Fig. 3.1. Plot of activity against kinetic energy for β particles generated by ^{87}Rb decay. Solid lines = solid Rb sources; dashed lines = liquid scintillator measurements. After Neumann and Huster (1976).

proposed a rubidium half-life of 48.8 Byr on the basis of Rb–Sr dating of stony meteorites.

During the last thirty years, values of the decay constant used in geological age calculations have varied between 1.47×10^{-11} and $1.39 \times 10^{-11}\,\mathrm{yr}^{-1}$ ($t_{1/2} =$ 46.8–50.0 Byr). The most commonly used value of $1.42 \times 10^{-11}\,\mathrm{yr}^{-1}$ ($t_{1/2} = 48.8$ Byr) was adopted by international convention (Steiger and Jäger, 1977), but probably needs to be revised. For example, very precise U–Pb and Rb–Sr isochrons for chondritic meteorites can be made to agree only if the ^{87}Rb decay constant is reduced to $1.402\ (\pm 0.008) \times 10^{-11}\,\mathrm{yr}^{-1}$, equivalent to a half-life of 49.4 ± 0.3 Byr (Minster *et al.*, 1982).

3.2 Dating igneous rocks

The Rb–Sr method has largely been superseded as a means for dating igneous rocks. However, the method provides a good illustration of the principles of isotope dating, and will therefore be reviewed here to demonstrate those principles. This application begins from the general equations for radioactive decay (section 1.4). Hence, the number of ^{87}Sr daughter atoms produced by decay of ^{87}Rb in rock or mineral since its formation t years ago is given by substituting into decay equation [1.10]:

$$^{87}\mathrm{Sr} = {}^{87}\mathrm{Sr}_{\mathrm{I}} + {}^{87}\mathrm{Rb}(e^{\lambda t} - 1) \qquad [3.1]$$

where $^{87}\mathrm{Sr}_{\mathrm{I}}$ is the number of ^{87}Sr atoms present initially. However, it is difficult to measure precisely the absolute abundance of a given nuclide. Therefore it is more convenient to convert this number into an isotope ratio by dividing by the number of atoms of ^{86}Sr (which is not produced by radioactive decay and therefore remains constant with time). Hence we obtain:

$$\left(\frac{^{87}\mathrm{Sr}}{^{86}\mathrm{Sr}}\right)_{\mathrm{P}} = \left(\frac{^{87}\mathrm{Sr}}{^{86}\mathrm{Sr}}\right)_{\mathrm{I}} + \frac{^{87}\mathrm{Rb}}{^{86}\mathrm{Sr}}(e^{\lambda t} - 1) \qquad [3.2]$$

The present-day Sr isotope ratio (P) is measured by mass spectrometry, and the atomic ^{87}Rb/^{86}Sr ratio is calculated from the Rb/Sr weight ratio. If the initial ratio $(^{87}\mathrm{Sr}/^{86}\mathrm{Sr})_{\mathrm{I}}$ is known or can be estimated, then t can be determined, subject to the assumption that the system has been closed to Rb and Sr mobility from time t until the present:

$$t = \frac{1}{\lambda}\ln\left\{1 + \frac{^{86}\mathrm{Sr}}{^{87}\mathrm{Rb}}\left[\left(\frac{^{87}\mathrm{Sr}}{^{86}\mathrm{Sr}}\right)_{\mathrm{P}} - \left(\frac{^{86}\mathrm{Sr}}{^{87}\mathrm{Sr}}\right)_{\mathrm{I}}\right]\right\} \qquad [3.3]$$

3.2.1 Sr model ages

When the Rb–Sr method was first used in geochronology, the poor precision attainable in mass spectrometry limited the technique to the dating of Rb-rich minerals such as lepidolite. These minerals develop such high ^{87}Sr/^{86}Sr ratios over geological time that a uniform initial ^{87}Sr/^{86}Sr ratio of 0.712 could be assumed in all dating studies without introducing significant errors. Such determinations are called ‘model ages’ because the initial ratio is predicted by a model rather than measured directly.

Subsequently, the Rb–Sr method was extended to less exotic rock-forming minerals such as biotite, muscovite and K-feldspar, with lower Rb/Sr ratios. However, discordant dates were often generated by assuming an initial ratio of 0.712 when the real initial ratio was higher. This problem was first recognised by Compston and Jeffery (1959), and was overcome by the invention of the isochron diagram (Nicolaysen, 1961). Model ages subsequently re-appeared in more specialised aspects of Rb–Sr dating, such as meteorite chronology, and as an important approach in the Sm–Nd method (section 4.2).

3.2.2 The isochron diagram

An examination of equation [3.2] shows that it is equivalent to the equation for a straight line:

$$y = c + xm \qquad [3.4]$$

This led Nicolaysen (1961) to develop a new way of treating Rb–Sr data, by plotting ^{87}Sr/^{86}Sr (y) against

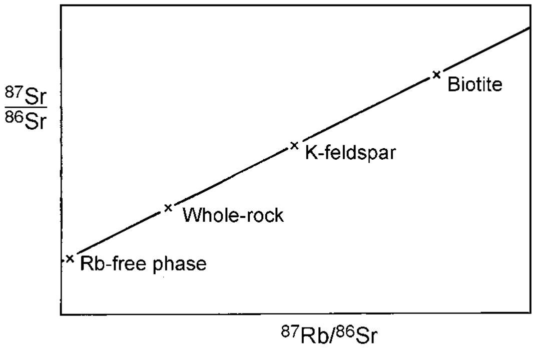

Fig. 3.2. Schematic Rb–Sr isochron diagram for a suite of co-magmatic igneous minerals.

^{87}Rb/^{86}Sr (x). The intercept (c) is then the initial ^{87}Sr/^{86}Sr ratio of the system. On this diagram, a suite of co-magmatic minerals having the same age and initial ^{87}Sr/^{86}Sr ratio, and which have since remained as closed systems, define a line termed an 'isochron'. The slope of this line, $m = e^{\lambda t} - 1$, yields the age of the minerals. If one of the minerals is very Rb-poor then this may yield the initial ratio directly. Otherwise, the initial ratio is determined by extrapolating back to the y axis a best-fit line through the available data points (Fig. 3.2). Because λ^{87}Rb is so small, for geologically young rocks the slope may be quite accurately approximated by λt. Such an approximation does not hold for nuclides with shorter half-lives such as K and U.

The isotopic evolution of a suite of hypothetical minerals in the isochron diagram is illustrated in Fig. 3.3. At the time of crystallisation of the rock, all three minerals have the same ^{87}Sr/^{86}Sr ratio, and plot as points on a horizontal line. After each mineral has become a closed system (effectively at the same instant for the minerals in a high-level, fast-cooling intrusion) isotopic evolution begins. On a diagram where the two axes have the same scale (Fig. 3.3), the points move up straight lines with a slope of -1 as each ^{87}Rb decay increases the ^{87}Sr/^{86}Sr ratio and reduces the ^{87}Rb/^{86}Sr ratio by the same amount. Each mineral composition remains on the isochron as its slope increases with time. In practice, the y axis is usually very much expanded to display rocks of geological age in a suitable format, and the growth lines are then nearly vertical.

Another development of the Rb–Sr method (Schreiner, 1958), was the analysis of co-genetic whole-rock sample suites, as an alternative to separate minerals. To be effective, a whole-rock suite must display variation in modal mineral content, such that samples display a range of Rb/Sr ratios, without introducing any variation in initial Sr isotope ratio. In actual fact, perfect initial ratio homogeneity may not be achieved, especially in rocks with a mixed magmatic parentage. However, if the spread in Rb/Sr ratios is sufficient, then any initial ratio variations are swamped, and an accurate age can be determined. Initial ratio heterogeneity is a greater problem in Sm–Nd isochrons, and is therefore discussed under that heading (section 4.1.2). Schreiner's proposal actually preceded the invention of the Rb–Sr isochron diagram, but some of his data are presented on an isochron diagram in Fig. 3.4 to demonstrate the method.

Graphical calculation of isochron ages was superseded in the 1960s by the application of least-squares regression techniques (section 2.6), but the isochron diagram remains a very useful means for assessing the distribution of data points about a regression. However, Papanastassiou and Wasserburg (1970) found that the vertical scale of the isochron diagram was too compressed to allow clear portrayal of the experimental error bars on their data points. To overcome this problem they developed the ε notation, which they defined as the relative deviation of a data point from the best-fit

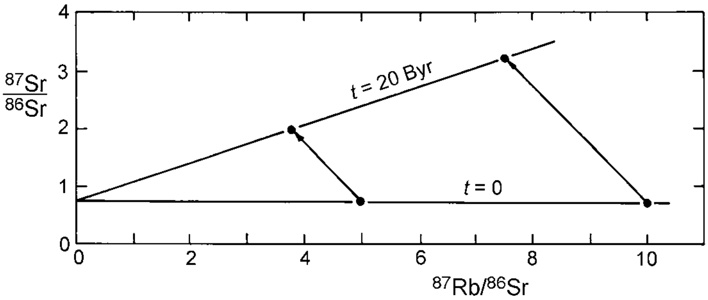

Fig. 3.3. Rb–Sr isochron diagram on axes of equal magnitude showing production of ^{87}Sr as ^{87}Rb is consumed in two hypothetical samples.

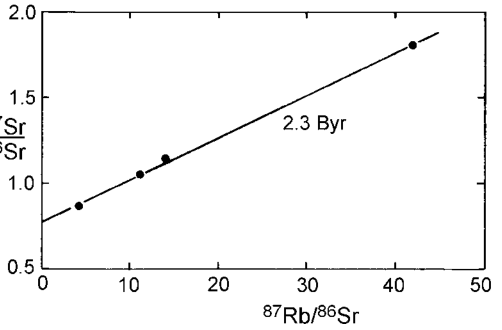

Fig. 3.4. Rb–Sr whole-rock isochron for the 'red granite' of the Bushveld complex, using the data of Schreiner (1958).

isochron in parts per 10^4. This is given by

$$\varepsilon = \left(\frac{(^{87}\mathrm{Sr}/^{86}\mathrm{Sr})_{\mathrm{measured}}}{(^{87}\mathrm{Sr}/^{86}\mathrm{Sr})_{\mathrm{best\text{-}fit}}} - 1 \right) \times 10^4 \quad [3.5]$$

Figure 3.5 shows a combined mineral isochron diagram and ε diagram for an Apollo 11 sample from the Sea of Tranquillity. A limitation of the ε diagram is that the vertical error bars only describe errors in $^{87}\mathrm{Sr}/^{86}\mathrm{Sr}$ ratio, whereas errors in Rb/Sr ratio can also cause points to deviate from the line. In practice, the samples dated by Papanastassiou and Wasserburg (1970) had small Rb/Sr ratios, so errors in this variable were normally subordinate to errors in the Sr isotope ratio.

Provost (1990) has pointed out that isochrons determined on granitic rocks are dominated by errors in Rb/Sr ratio rather than $^{87}\mathrm{Sr}/^{86}\mathrm{Sr}$ ratio (Fig. 3.6a). He developed a new version of the isochron plot (Fig. 3.6b), with non-linear axes, which attempts to portray both sources of error at once. Uncertainties in isotope ratio and Rb/Sr ratio both generate vertical or sub-vertical error bars, but their meaning changes progressively across the diagram from an error on the initial ratio (left-hand side) to an error on the age (right-hand side). Unfortunately this diagram is conceptually quite difficult to understand, so a more practical approach may be to improve the ε diagram of Papanastassiou and Wasserburg by adding error bars that represent the effect of Rb/Sr uncertainties on each data point, in the form of equivalent errors in ε value.

3.2.3 Erupted isochrons

A primary basic magma should inherit the isotopic composition of its mantle source, provided that melting occurs under equilibrium conditions. Tatsumoto (1966) first suggested, on the basis of U–Pb data, that primitive basic magmas could also inherit the parent/daughter ratio of their mantle source. If different magma batches were to sample the elemental and isotopic composition of different source domains, this might lead to the eruption of an 'isochron' suite whose slope would yield the time over which these sources were isolated. This concept was examined for the Rb–Sr system in alkalic ocean-island basalts by Sun and Hanson (1975).

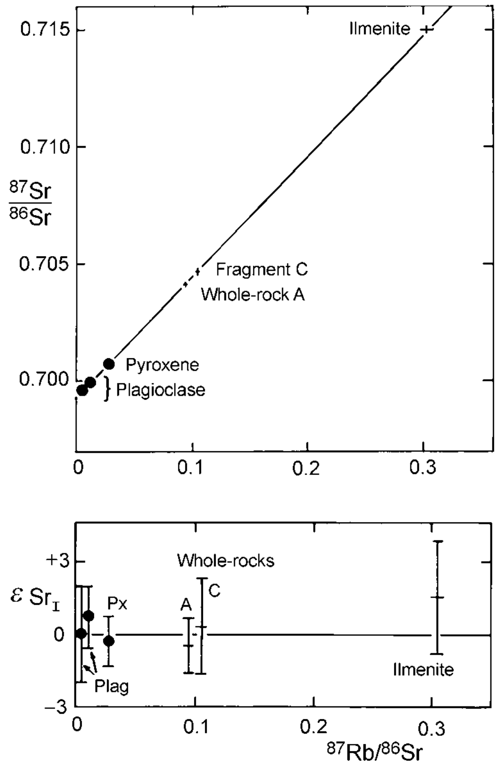

Fig. 3.5. Rb–Sr data for lunar mare sample 10017 plotted on a conventional isochron diagram and on a diagram of ε Sr against Rb/Sr. After Papanastassiou and Wasserburg (1970).

Average compositions for fourteen different ocean-island basalts were plotted on an isochron diagram (Fig. 3.7). The data are fairly scattered, but form a positive correlation with a slope age of about 2 Byr. Individual ocean islands may also define arrays with positive slope, but usually with more scatter. Sun and Hanson attributed the positive correlations between Rb/Sr ratio and isotopic composition to mantle heterogeneity, suggesting that the apparent ages represented the time since mantle domains were isolated from the convecting mantle. Brooks *et al.* (1976a) termed these ages 'mantle isochrons'.

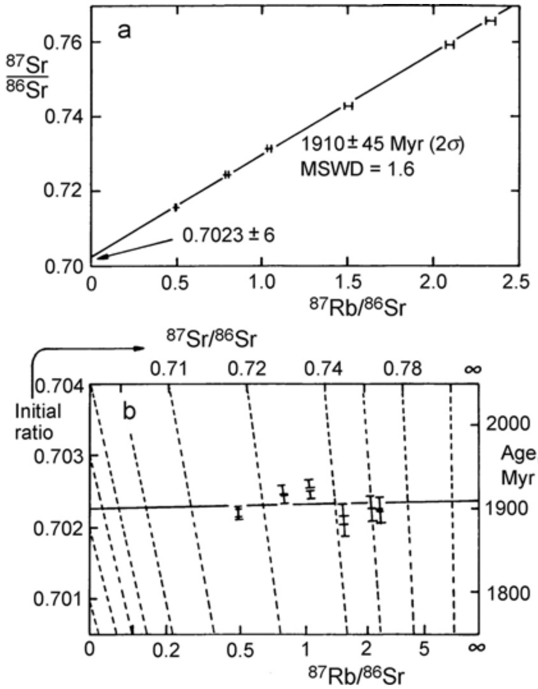

Fig. 3.6. Rb–Sr data for the Agua Branca adamellite, Brazil, plotted (a) on the conventional isochron diagram; and (b) on an 'improved' isochron diagram. After Provost (1990).

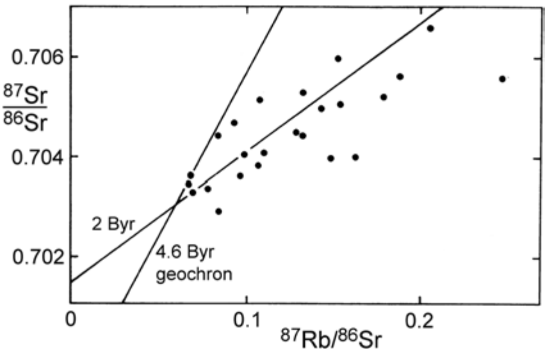

Fig. 3.7. Rb–Sr isochron diagram for young volcanic rocks (mostly alkali basalts) from ocean islands. After Sun and Hanson (1975).

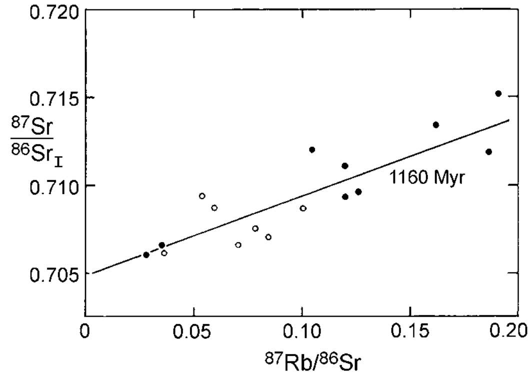

Fig. 3.8. Pseudo-isochron for quartz and olivine norites from Arnage (○) and Haddo House (●) in NE Scotland, yielding an apparent age of 1160 ± 420 Myr (2σ) prior to intrusion. After Brooks *et al.* (1976b).

The mantle-isochron concept was extended to continental igneous rocks by Brooks *et al.* (1976b). Because these are often ancient (unlike most ocean-island basalts), it was necessary to correct measured ^{87}Sr/^{86}Sr ratios back to their calculated initial ratios at the time of magmatism, before plotting them against Rb/Sr ratios (e.g. Fig. 3.8). Hence Brooks *et al.* termed these plots 'pseudo-isochron' diagrams. They listed thirty examples, from both volcanic and plutonic continental igneous rock suites, where the data formed a roughly linear array. The controversial aspect of this work was that Brooks *et al.* rejected the possibility that pseudo-isochrons were mixing lines produced by crustal contamination of mantle-derived basic magmas. Instead, they believed them to date mantle differentiation events that established domains of different Rb/Sr ratio in the sub-continental lithosphere.

It is a fundamental assumption of the mantle isochron model that neither isotope nor elemental ratios are perturbed during the ascent of magma through the crust. However, it is now generally accepted that this assumption is not upheld with sufficient reliability to attribute age significance to erupted isochrons. For example, the Haddo House norites of NE Scotland (Fig. 3.8) are known to contain pelitic xenoliths, so this array must document crustal assimilation. Another pseudo-isochron example from Lower Tertiary lavas of NW Scotland (Beckinsale *et al.*, 1978) can be attributed to Sr depletion in the melt by plagioclase fractionation, followed by crustal contamination (Fig. 3.9). Breakdown of the mantle-isochron model can also be caused by low degrees of melting in the mantle source, leading to fractionation between Rb, an ultra-incompatible element, and Sr, a moderately incompatible element. Hence it is concluded that only isotope–isotope mantle isochrons (such as those provided by the Pb–Pb system) can reliably be interpreted as dating the ages of mantle differentiation events.

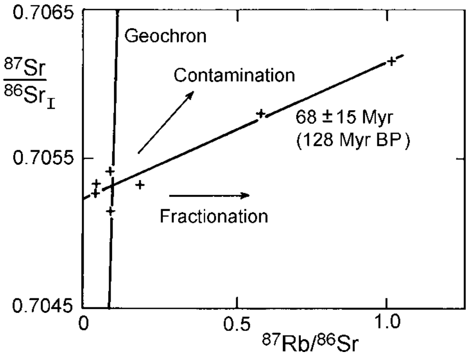

Fig. 3.9. Pseudo-isochron diagram for Tertiary lavas from the Isle of Mull, NW Scotland, showing an apparent age of 68 Myr prior to eruption. Vectors illustrate effects of crystal fractionation and crustal contamination. Modified after Beckinsale *et al.* (1978).

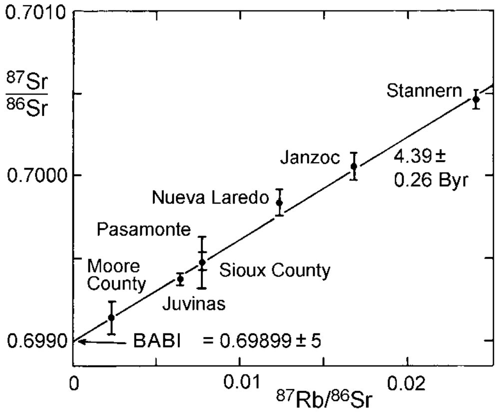

Fig. 3.10. Rb–Sr isochron diagram for whole-rock samples of basaltic achondrites, showing the determination of 'BABI'. After Papanastassiou and Wasserburg (1969).

3.2.4 Meteorite chronology

Meteorites have been the subject of numerous Rb–Sr dating studies, but some of the most important Rb–Sr results on meteorites are initial-ratio determinations. These have significance, both as a reference point for terrestrial Sr isotope evolution, and as a model age tool for estimating the relative condensation times of solar-system bodies.

The first accurate measurement of meteorite initial ratios was made by Papanastassiou *et al.* (1969) on basaltic achondrites. These differ from chondritic meteorites in showing evidence of differentiation after their accretion from the solar nebula. However, they might not have participated in the full planetary differentiation process which generated iron meteorites. Their low Rb/Sr ratios have resulted in only limited radiogenic Sr production since differentiation, so an accurate initial-ratio determination is possible.

In order to make this determination, Papanastassiou *et al.* analysed whole-rock samples from seven different basaltic achondrites, yielding an isochron (Fig. 3.10) without any excess scatter over analytical error. An age of 4.39 ± 0.26 Byr was calculated using the old decay constant ($\lambda = 1.39 \times 10^{-11}\ \text{yr}^{-1}$). The initial ratio of 0.69899 ± 5 was referred to by Papanastassiou *et al.* as the 'basaltic achondrite best initial' or BABI. This value represents a bench-mark against which other meteorite initial ratios may be compared. Birck and Allègre (1978) repeated this study with the addition of separated minerals from Juvinas and Ibitira, yielding an identical initial ratio, but an improved age determination of 4.57 ± 0.13 Byr (with the same decay constant). However, Rb–Sr mineral isochrons are not possible for other achondrites due to later disturbance of the Rb–Sr system.

The determination of precise initial ratios for chondritic meteorites is problematical because their Rb/Sr ratios are much higher than those of basaltic achondrites. However, by separating out low-Rb/Sr-ratio phosphate minerals, Wasserburg *et al.* (1969) and Gray *et al.* (1973) were able to determine good initial ratios for the chondrites Guarena and Peace River. Gray *et al.* also determined accurate initial ratios by analysis of bulk samples from the achondrite Angra dos Reis (ADOR) and Rb-poor inclusions from the carbonaceous chondrite Allende.

These initial ratios can be translated into a relative chronology for meteorite condensation (Fig. 3.11) by assuming a homogeneous Rb/Sr ratio in the solar nebula (Papanastassiou *et al.*, 1969). The results are only 'model' ages because they depend on an assumed composition for the source reservoir (solar nebula), and they would be rendered invalid if it did not evolve as a homogeneous reservoir. The estimate of the Rb/Sr ratio in the solar nebula was based on cited spectroscopic measurements from the Sun, yielding a value of 0.65 that is capable of generating an increase in $^{87}Sr/^{86}Sr$ ratio of about 0.0001 in 4 Myr.

If we assume a homogeneous Sr isotope distribution in the solar nebula, the Allende data suggest it to be the oldest known object in the solar system, pre-dating the condensation of basaltic achondrites by about 10 Myr (Fig. 3.11). Similarly, Angra dos Reis has a model age about 5 Myr older than the BABI. Application of the same model to the high initial ratios of Guarena and Peace River would imply unduly late condensation from the solar nebula. Therefore, Gray *et al.* interpreted

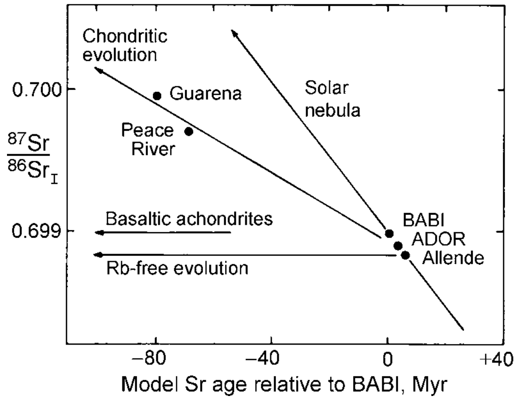

Fig. 3.11. Plot of initial Sr isotope compositions for selected meteorites against model ages for condensation or differentiation–metamorphism, based on assumed Rb/Sr ratios in major reservoirs. ADOR = Angra dos Reis. After Gray *et al.* (1973).

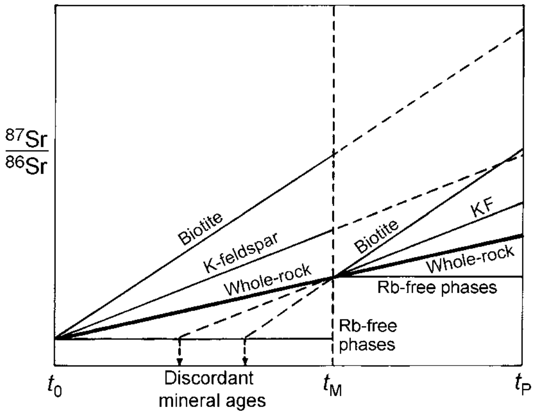

Fig. 3.12. Plot of Sr isotope ratio against time to model the effect of a metamorphic event that opens Rb–Sr mineral systems, but not the whole-rock system. t_0 = age of rock; t_M = age of metamorphism; t_P = present. After Fairbairn *et al.* (1961).

these as metamorphic ages produced by re-distribution of Rb and Sr between mineral phases within chondritic bodies. However, basaltic achondrites and ADOR are themselves products of planetary differentiation. Therefore, a better interpretation (Tilton, 1988) is that the entire model chronology really indicates times of differentiation and metamorphism, rather than condensation. Subsequent work has confirmed this interpretation (e.g. Halliday and Porcelli, 2001).

3.3 Dating metamorphic rocks

3.3.1 Open mineral systems

Mineral and whole-rock Rb–Sr systems may respond differently to metamorphic events. ^{87}Sr generated by decay of Rb occupies unstable lattice sites in Rb-rich minerals and tends to migrate out of the crystal if subjected to a thermal pulse, even of a magnitude well below the melting temperature. However, if fluids in the rock remain static, Sr released from Rb-rich minerals such as mica and K-feldspar will tend to be taken up by the nearest Sr sink such as plagioclase or apatite. Hence, the whole-rock system may remain closed, even though mineral systems are open.

The idea of using whole-rock analysis to see back through a metamorphic event that disturbed mineral systems was first conceived by Compston and Jeffery (1959). The model was illustrated graphically by Fairbairn *et al.* (1961) on a plot of isotope ratio against time (Fig. 3.12). After the formation of the rock at time t_0, different minerals move along different growth lines, whose steepnesses correspond to their Rb/Sr ratios. Isotopic evolution continues until the minerals are homogenised by a thermal event at time t_M. Thereafter, isotopic evolution continues, along different growth lines, to the present day (t_P). Individual minerals in this model are open systems during the metamorphism. Therefore, a mineral isochron yields the age of cooling from the thermal event, when each mineral again became a closed system. However, a whole-rock domain of a certain minimum size remains as an effectively closed system during the thermal event, and can be used to date the initial crystallisation of the rock.

The effects of metamorphism on mineral and whole-rock systems can also be demonstrated on the isochron diagram, Fig. 3.13 (Lanphere *et al.*, 1964). All systems start on a horizontal cord. Isotopic evolution then occurs along near-vertical parallel paths (due to the extreme amplification of the y axis). During the thermal event, isotope ratios are homogenised to the whole-rock value. If this involved only ^{87}Sr, then vertical vectors would be produced. However, a possible complication illustrated in Fig. 3.13 involves limited re-mobilisation of Rb. Rb-rich minerals tend to suffer some Rb loss, while Rb-poor phases may be contaminated by growth of Rb-rich alteration products, leading to somewhat unpredictable vectors (R). After the event, whole-rock evolution continues undeflected, while mineral systems define an isochron whose slope yields the age of metamorphism.

A practical example of dating plutonism and metamorphism by whole-rock and mineral analysis of the same body was provided by the work of Wetherill

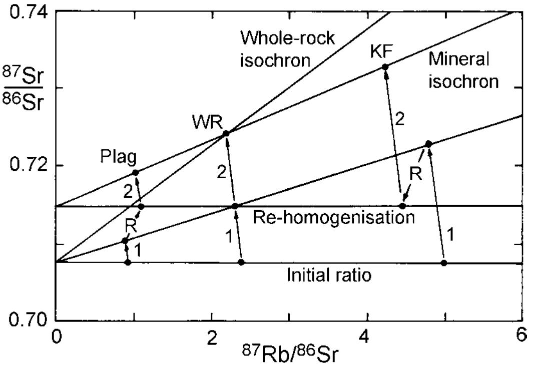

Fig. 3.13. Hypothetical behaviour of a partially disturbed mineral–whole-rock isochron. Evolution lines: 1 = period from igneous crystallisation to metamorphism; R = metamorphic re-homogenisation; 2 = period from metamorphism to present day.

et al. (1968) on the Baltimore gneiss (Fig. 3.14). Several mineral isochrons all yield ages of about 290 Myr, interpreted as the time of closure of mineral systems after isotopic homogenisation associated with the Appalachian orogeny. The good fit of points to the mineral isochrons is evidence that complete isotopic homogenisation on a mineralogical scale was achieved during the metamorphic event. In contrast, whole-rock samples define an isochron whose slope corresponds to an age of 1050 Myr. This was interpreted as the time of crystallisation of igneous precursors of the gneiss. However, more recent studies have shown that even whole-rock Rb–Sr systems may be open during metamorphism. Therefore the 1050 Myr age of the Baltimore gneiss could alternatively represent the time of closure of Rb–Sr whole-rock systems after high-grade Grenvillian metamorphism. More examples of open whole-rock systems will be discussed below.

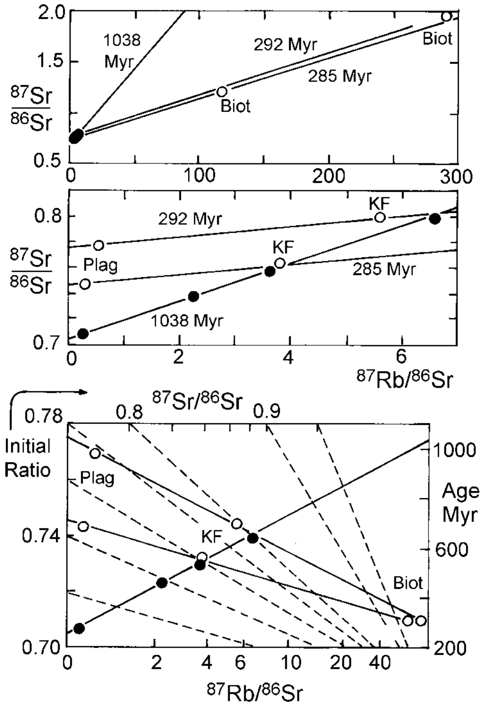

Fig. 3.14. Rb–Sr isochrons for the Baltimore gneiss, showing 1038 Myr 'plutonic' and 285–292 Myr metamorphic ages defined by whole-rocks (●) and minerals (○). The data are shown in the diagram of Provost (1990) for comparison. After Provost (1990).

3.3.2 Blocking temperatures

After Rb–Sr mineral systems have been opened in the thermal pulse of a regional metamorphic event, there must come a time when mineral systems are again closed to element mobility. By dating the closure or 'blocking' of various mineral systems, Rb–Sr ages give information about the cooling history of metamorphic terranes. This was first demonstrated by Jäger *et al.* (1967) and Jäger (1973), working on the central European Alps.

Jäger *et al.* found that, in rocks of low metamorphic grade round the exterior of the Central Alps, Hercynian Rb–Sr ages (>200 Myr) were preserved both in biotites and in muscovites. On moving to a higher metamorphic grade characterised by the appearance of stilpnomelane (which Jäger *et al.* believed equivalent to a temperature of 300 ± 50 °C), Rb–Sr biotite ages of 35–40 Myr were measured. Jäger *et al.* attributed these younger ages to Rb–Sr biotite systems opened at the peak of Lepontine metamorphism. They argued that the temperature of 300 °C at which biotites were just opened at the peak of metamorphism would correspond to the temperature at which biotites would re-close up to several million years after suffering a higher peak temperature (e.g. >500 °C within the central staurolite isograd). In other words, Jäger *et al.* concluded that biotite had a blocking temperature of 300 ± 50 °C for the Rb–Sr system.

The blocking temperature of white mica (muscovite and phengite) was similarly constrained to 500 ± 50 °C by the first re-setting of the white mica Rb–Sr ages 'somewhat outside the staurolite–chloritoid boundary' (Purdy and Jäger, 1976). However, unlike biotite, white micas can undergo primary crystallisation below the Rb–Sr blocking temperature, so that ages as low as 35–40 Myr have been obtained even from the outer zones of low-grade Alpine metamorphism. These ages are argued to date new mica growth at the peak of metamorphism (Hunziker, 1974). This makes the muscovite Rb–Sr system a more problematical tool than biotite for studying post-orogenic cooling processes.

Jäger *et al.* (1967) obtained biotite ages of about 12–16 Myr from the Simplon and Gotthard areas of the Central Alps, and results averaging about 8 Myr older in coexisting muscovites. Clark and Jäger (1969) used these data to make two different estimates of cooling rate for the Central Alps. Firstly, the age difference between muscovite and biotite closure (200 °C) leads to a cooling rate of about 25 °C/Myr between 500 and 300 °C. Secondly, the biotite ages yield cooling rates of about 20–25 °C/Myr between 300 and 0 °C (average surface temperature at the present day). Division of these results by an estimated geothermal gradient (25–40 °C/km) allows the calculation of uplift rates between 0.5 and 1.0 km/Myr for the Central Alps, which compare well with modern uplift rates of 0.4–0.8 mm/yr obtained from geodetic measurements. More recent calculations of past uplift rate make use of combined Rb–Sr, K–Ar and fission-track cooling ages (section 16.6).

Purdy and Jäger (1976) recognised that the blocking temperature of 300 ± 50 °C for biotite might need to be revised if new experimental data for the stability of stilpnomelane were obtained. Most workers continue to use a value of 300 °C; however, experimental work (e.g. Brown, 1971) points to an upper stability limit of 440–480 °C at about 4 kbar for stilpnomelane, implying a biotite Rb–Sr blocking temperature of over 400 °C. This would be consistent with evidence from SW Norway, where biotites subjected to temperatures of over 400 °C in the Caledonian orogeny nevertheless preserve (800 Myr) Sveco-Norwegian ages (Verschure *et al.*, 1980).

A more direct method of determining blocking temperatures is to measure mineral ages in deep boreholes. Del Moro *et al.* (1982) determined biotite–whole-rock Rb–Sr ages at depths of up to 3.8 km in the Sasso 22 well in the Larderello geothermal field, Italy. All of the biotites exhibited almost complete retention of ^{87}Sr at directly measured in-hole temperatures up to nearly 380 °C, supporting a biotite closure temperature of about 400 °C. However, Cliff (1985) has argued that, in active geothermal systems, convective heat transport could generate localised thermal pulses whose durations are too short to allow significant diffusional loss of Sr, thus yielding an anomalously high blocking temperature.

Blocking temperatures can also be determined theoretically, from calculations of the temperature dependence of volume-diffusion processes (Dodson, 1973; 1979). Ideally, closure of the Rb–Sr system represents an instantaneous transition from a time when Rb and Sr were completely mobile to when they were completely immobile. In a fast-cooling igneous body the moment of crystallisation is a good approximation to this ideal. However, in a slow-cooling regional metamorphic terrane there is a continuous transition from a high-temperature regime, when radiogenic ^{87}Sr escapes from crystal lattices by diffusion as fast as it is produced, to low-temperature conditions when there is negligible escape of ^{87}Sr (Fig. 3.15). In such a system, the apparent age of a mineral such as biotite corresponds to a linear extrapolation of the low-temperature ^{87}Sr growth line back into the x axis. The temperature prevailing in the system at the time of the apparent age of the mineral is then defined as the blocking temperature of the mineral in question (Dodson, 1973). This blocking temperature is dependent on cooling rate, since the slower the cooling, the longer the time during which partial loss of daughter product may occur, and the lower the apparent age will be (Fig. 3.15).

If a mineral is in contact with a fluid phase that can remove radiogenic Sr from its surface, then the rate of

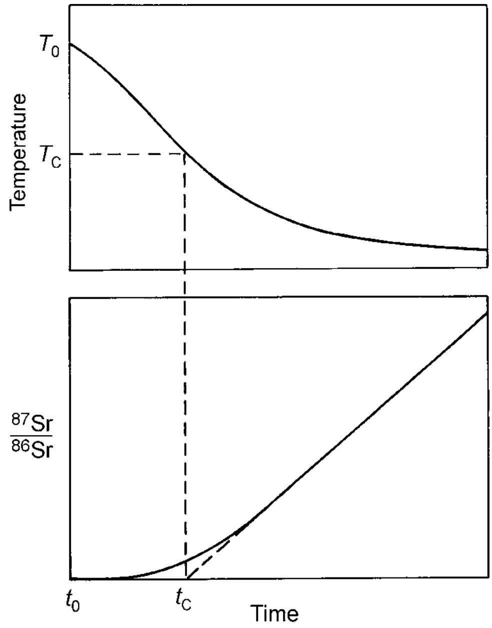

Fig. 3.15. Schematic diagram to show variation of temperature and Sr isotope ratio with time in a mineral cooling from a regional metamorphic event. T_0 = peak metamorphic temperature; T_C = closure or 'blocking' temperature; t_C = apparent closure age. After Dodson (1973).

loss of ^{87}Sr depends on the rate of volume diffusion across a certain size of lattice. In the case of biotite, this diffusion will be predominantly parallel to cleavage planes rather than across them. Assuming that the Arrhenius law is obeyed, Dodson (1979) calculated blocking temperatures (at a cooling rate of 30 °C/Myr) of 300 °C for the Rb–Sr system in biotites of 0.7 mm diameter. This was based on experimental work on argon diffusion in biotite (Hofmann and Giletti, 1970), because the two elements are thought to have similar diffusional behaviour in crystal lattices.

A problem with the volume-diffusional control of blocking temperature is that large (30 cm) fissure-filling biotites in the Central Alps have the same ages, and hence apparent blocking temperatures, as small (<1 mm) ground-mass biotites in adjacent gneisses. Dodson (1979) suggested three possible explanations:

(1) Diffusion geometry is independent of grain size. This could be due to the effects of stress on the crystal lattice.
(2) Sr loss is controlled by the rate at which radiogenic atoms leave the site where they were formed.
(3) Blocking temperature is not kinetically controlled, but depends on a change in the biotite lattice at the blocking temperature.

The susceptibility of Sr to mobilisation by fluids increases complexity in the interpretation of Sr blocking temperatures. Such problems do not arise for argon, because it is an inert gas. Therefore the latter element is a more reliable tool for studies of 'thermochronology'. This subject is discussed in detail in section 10.5.

3.3.3 Open whole-rock systems

The Rb–Sr whole-rock method was widely used as a dating tool for igneous crystallisation during the 1960s and 1970s, but lost credibility during the 1980s as evidence of whole-rock open-system behaviour mounted. For example, Rb–Sr isochrons in metamorphic terranes can yield good linear arrays whose slope is nevertheless a meaningless value between the protolith and metamorphic ages. This problem is probably caused by the need to sample over a relatively large geographical area in order to maximise the range of Rb/Sr ratios. A good example is provided by the Arendal charnockites of south Norway (Field and Raheim, 1979a; 1979b).

Eight whole-rock sample suites were collected from individual outcrops of Arendal charnockite over an area of several km^2. They yielded ages that were dominantly in two groups, of about 1540 and 1060 Myr. Field and Raheim (1979a) interpreted the older age as the time of formation of the high-grade charnockite mineralogy and the younger as dating a subsequent low-grade event. This was manifested as slight mineralogical alteration, probably associated with irregularly spaced narrow fractures which traverse the area. The younger re-setting event also fell within error of the 1063 ± 20 Myr age of undeformed granite sheets in the area.

In order to test the effect of making a regional sample collection from an area of slightly disturbed gneisses, Field and Raheim (1979b) collected a suite of eight samples over an area of 1 km^2. The data (Fig. 3.16) define a good linear array with an apparent age of 1259 ± 26 Myr. The MSWD value of 1.58 implies that the scatter of data about the line could probably be accounted for by analytical error, but there is no geological evidence for an event at this time. Therefore, Field and Raheim attributed the linear array to a series of closely spaced *en échelon* arrays with slopes corresponding to the age of re-setting, defined

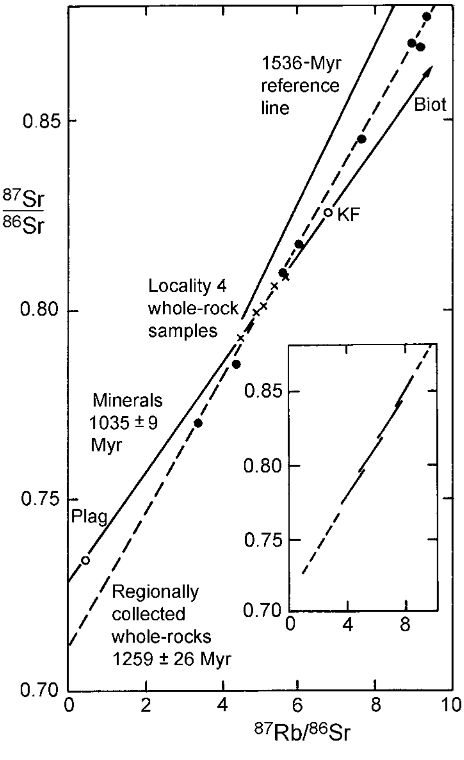

Fig. 3.16. Rb–Sr 'isochron' diagram for Arendal charnockites showing fictitious 1259-Myr regional isochron composed of a series of *en échelon* local isochrons with the same slope as separated minerals. After Field and Raheim (1979b).

by a 1035 Myr mineral isochron. Because the range in Rb/Sr ratio at each locality is small (e.g. 'locality 4', Fig. 3.16), samples lying on each sub-isochron do not deviate much from the fictitious composite 'isochron'. It is therefore concluded that, in areas where Rb–Sr systems may have been disturbed, detailed sampling is necessary to measure the mobility of the species before regional geochronological interpretations are made.

Whole-rock open-system behaviour can occur at even lower grades of metamorphism in fine-grained acid volcanic rocks. Such units are attractive for absolute calibration of the stratigraphic column because they are conformable with sedimentary strata. They tend to have large and variable Rb/Sr ratios, thus yielding good isochrons. However, experience has shown that they are particularly susceptible to loss of radiogenic Sr. A good example is provided by the Stockdale rhyolite of northern England.

The Stockdale rhyolite is a fine-grained, flow-banded lava, included in the uppermost Ordovician succession, and is argued to have a bio-stratigraphic uncertainty of less than 0.5 Myr. Gale *et al.* (1979) determined a sixteen-point whole-rock isochron, which yielded an age of 421 ± 3 Myr (2σ) with MSWD = 1.92. They argued that, because of the relatively small number of data points, this MSWD value could be attributed to experimental errors (section 2.6.3), and hence that the 421 Myr age probably represented the time of eruption of the lava. However, if this age were correct, it would require substantial revision of the Ordovician timescale determined by other methods.

McKerrow *et al.* (1980) argued that because a section of the Stockdale rhyolite that lay inside the Shap granite aureole gave the same age (424 ± 18 Myr) as the rest of the lava (421 Myr), the whole unit was probably disturbed by some kind of hydrothermal event after eruption and subsequent burial. Compston *et al.* (1982) sought to explain the excess scatter over analytical error by invoking a re-setting event post-dating the eruption of the lava (estimated at 440 Myr from McKerrow *et al.*, 1980). Consistently with this, re-examination of the probability table of Brooks *et al.* (section 2.6.3) indicates that for sixteen data points an MSWD value of 1.92 indicates up to a 95% probability that the result is not an isochron.

A perfect isochron would imply complete re-setting, but apparently this did not occur. Plotting isotope ratios at 395 Myr ago (the date of intrusion of the Shap granite) on a pseudo-isochron diagram (Fig. 3.17) allows an assessment of scatter introduced by an event after eruption. Compston *et al.* found that if the four samples with highest Rb/Sr ratios were removed, together with one sample (no. 5) with an anomalously high Sr content, then all of the other samples lie close to a 440-Myr reference line. In fact a regression through ten of these points yields a 'minimum' age of 430 ± 7 Myr. Compston *et al.* also noted that isochrons calculated individually for each of the four sampling localities yield lower MSWD values than the combined data set. This evidence warns us that the combined data set is unsuitable for constructing a single isochron, despite the attractively precise result. Compston *et al.* calculated a weighted mean of 412 ± 7 Myr for the four local isochrons and interpreted this as the time of hydrothermal alteration of the rhyolite. Insofar as the Rb–Sr evidence 'marks a real event', 412 Myr may be the date of this event.

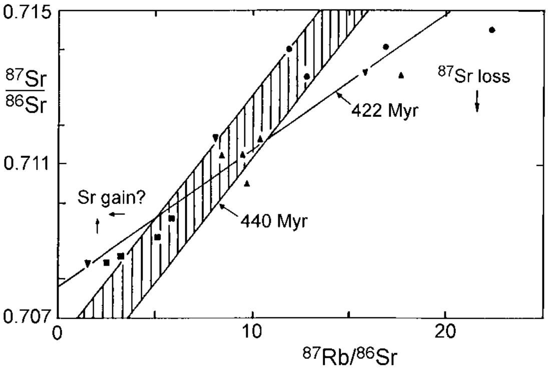

Fig. 3.17. Rb–Sr pseudo-isochron diagram for the Stockdale rhyolite at the time of Shap granite emplacement (395 Myr ago) to show possible open-system behaviour of Sr in samples outside the hatched zone. Four sampling sites are distinguished by different symbols. After Compston *et al.* (1982).

The evidence for open-system Rb–Sr systematics in numerous environments, coupled with the availability of high-precision U–Pb and Ar–Ar ages, means that these other methods have now superseded the Rb–Sr method for dating igneous crystallisation. However, Rb–Sr isochrons still find uses in certain specialised applications. One such application is the direct dating of metallic ore deposits, where phases suitable for U–Pb or Ar–Ar analysis are not always available. We will therefore examine some applications in this area.

3.4 Dating ore deposits

Metallic ore deposits have always been notoriously difficult to date reliably. The most common approach to dating such deposits is to analyse gangue mineralisation and hope that this material was deposited during the same episode as the associated metallic ores.

Another alternative has been to date fluid inclusions believed to form part of a hydrothermal ore-forming system. One or two successful attempts at this technique have been reported (e.g. Sheppard and Darbyshire, 1981), but fluid-inclusion populations may represent more than one stage in the evolution of a hydrothermal system, leading to complex mixtures that have no age significance.

Typically, the large-ion lithophile (LIL) elements which comprise most long-lived decay systems do not partition into metal sulphides, preventing direct dating of such ores. However, LIL elements may partition onto some sulphide ores in just sufficient abundances to allow analysis. One sulphide ore mineral that has successfully been dated by this means is sphalerite.

Nakai *et al.* (1990) made the first successful Rb–Sr isochron determination on sphalerite samples from a Mississippi Valley Type (MVT) lead–zinc deposit from Tennessee. The sphalerite grains were found to have low Sr contents, averaging only 1 ppm. As a result, fluid inclusions in the sphalerite grains, estimated to make up only 300 ppm by weight of the host mineral, actually contained more Sr than the host. Therefore, it was necessary to remove these inclusions by crushing the samples and leaching with de-ionised water before dissolving the sphalerite host for analysis.

This procedure gave a suitable range of Rb/Sr ratios and generated the errorchron shown in Fig. 3.18. One outlier, believed to have been disturbed during a deformation event, was excluded from the data set, after which the remaining seven points gave an age of 377 ± 29 Myr (2σ). This is a 'scatter error', determined by expanding the analytical errors to reduce the original MSWD of 62.6 to unity (section 2.6.3). The fluid inclusions leached during crushing were also analysed, and were found to lie on the isochron defined by the host phase (Fig. 3.18); however, these analyses were not included in the isochron calculation. The age of 377 ± 29 Myr suggested that MVT mineralisation occurred during the Acadian orogeny (380–350 Myr ago), which caused the expulsion of basin brines from strata within the deformation zone in the Appalachians. These fluids were then transported to the west, causing ore deposition when they mixed with other fluids during their return to the surface.

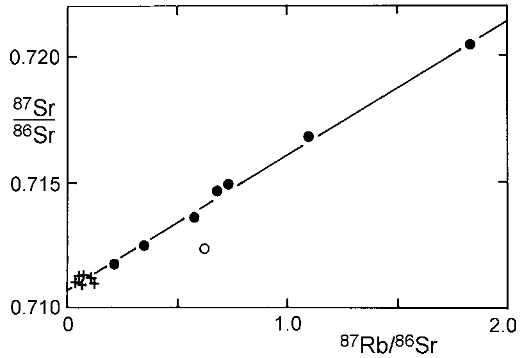

Fig. 3.18. Rb–Sr isochron diagram for sphalerite grains from the Coy mine, Tennessee. (●) = sphalerite host; (+) = fluid inclusions. The open symbol was excluded from the age calculation. After Nakai *et al.* (1990).

Brannon *et al.* (1992) applied this method to other MVT deposits. However, the range of Rb/Sr ratios in the ores themselves was not sufficient for the determination of a precise isochron. Therefore, it was necessary to combine analyses of the host sulphide with fluid inclusions (Fig. 3.19a). This procedure yielded a precise age (269 ± 6 Myr, 2σ), but was effectively a 'two-point' isochron, raising fears that,

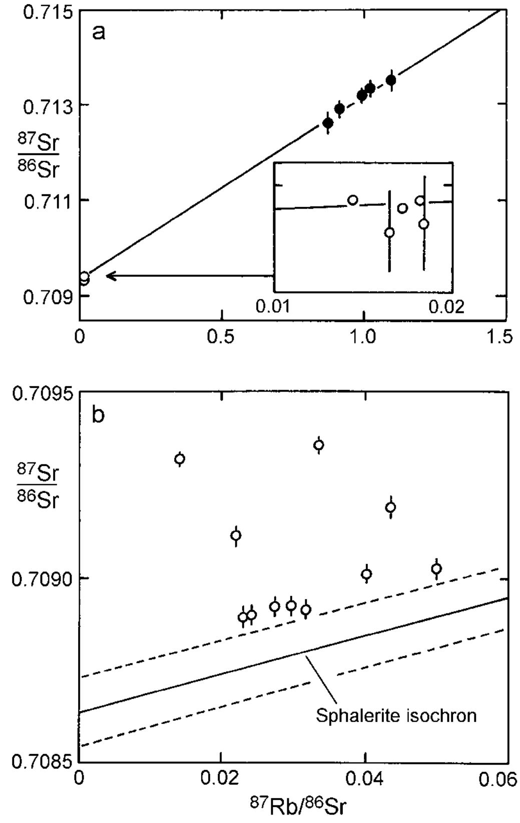

Fig. 3.19. Rb–Sr isochron analysis of sphalerite host (●) and extracted fluid inclusions (○) from MVT lead–zinc deposits: (a) West Hayden, Wisconsin; and (b) Polaris, arctic Canada. After Brannon *et al.* (1992) and Christensen *et al.* (1995a).

if the host sulphide and the inclusions were not co-genetic, the calculated age might be geologically meaningless.

Further studies by Nakai *et al.* (1993) revealed two more examples (from the Pine Point MVT deposit in Canada and the Immel mine in east Tennessee) where the inclusions lay on a well-defined host isochron. However, analysis of the Polaris MVT deposit in arctic Canada provided an example where the inclusions lay off a well-defined host isochron (Christensen *et al.*, 1995a). In this case the host (ore minerals) gave an age of 366 ± 15 Myr, in good agreement with the age of the wall-rocks from paleomagnetic evidence, whereas the inclusions defined a cloud of points above the isochron (Fig. 3.19b). Seven of these leachate samples lay just outside error of the sphalerite isochron, whereas four were more radiogenic, suggesting that the inclusion population included primary inclusions that were co-genetic with the ores, together with more radiogenic secondary inclusions.

To avoid possible complications arising from mixing between host ores and fluid inclusions, Christensen *et al.* (1995b) tested for mixing relationships when they dated sphalerites from the Canning Basin MVT deposit of western Australia. They found that Sr concentrations in the sphalerite host grains exhibited no correlation with the ^{87}Rb/^{86}Sr ratio, suggesting that the sphalerite residues after crushing and leaching were not significantly contaminated by Sr from unopened inclusions (Fig. 3.20a). On the other hand, Rb contents were found to be strongly correlated with the ^{87}Rb/^{86}Sr ratio. Since the fluid inclusions contain negligible Rb, these Rb contents must have originated from the host sulphide ore itself. Therefore the isochron must also date the sulphide ore itself.

Pettke and Diamond (1996) used a similar approach to test the possibility of mixing in the sphalerite-inclusion Rb–Sr isochron of Brannon *et al.* (1992). They plotted the data on a graph of Sr isotope ratio against the reciprocal of Sr concentration, on which mixing processes generate straight lines (Fig. 3.20b). On this graph, the fluid inclusions have Sr contents that are essentially infinite (relative to the low abundances in the host), so they are plotted on the *y* axis. The results of this analysis showed that one of the isochrons determined by Brannon *et al.* (1992) was probably a mixing line generated by sampling of sphalerite grains with a few un-released inclusions (sample 58-B). Therefore, this age determination is meaningful only if the host and the fluid were co-genetic. However, the other isochron (sample 10-C) does not exihibit the mixing effect, so this age is more reliable. Since both isochrons gave results within error (269 ± 6 and 270 ± 4 Myr), it was concluded that this is a reasonable estimate of the age of ore deposition.

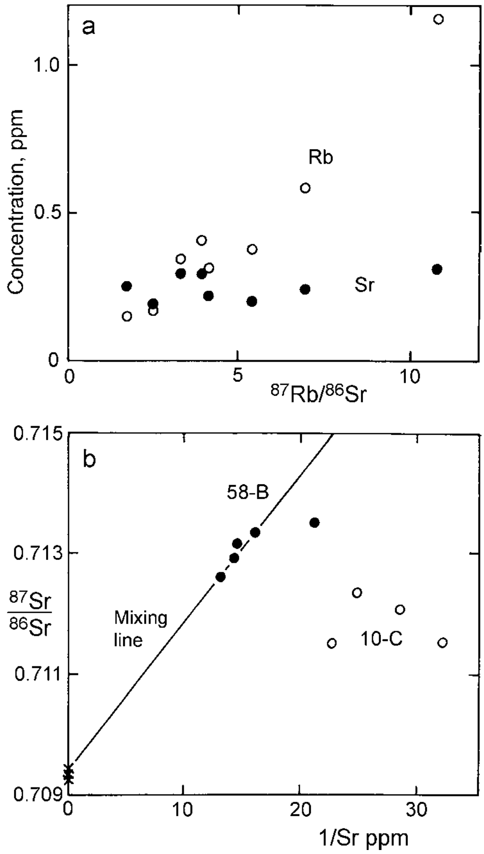

Fig. 3.20. Plots to test for mixing relationships between sphalerite hosts and inclusions: (a) ^{87}Rb/^{86}Sr ratio versus Rb and Sr concentrations in the Canning Basin MVT deposit, Australia; (b) Sr isotope ratio versus reciprocal of Sr concentration from the West Hayden MVT deposit, Wisconsin. After Pettke and Diamond (1996).

Another sulphide mineral successfully used to date ore deposition is the mercury sulphide galkhaite. This hydrothermal mineral was found associated with Carlin-type gold mineralisation in Nevada, and was used to estimate a date of 39 ± 2 Myr for gold mineralisation at the Getchell deposit in northern Nevada (Tretbar *et al.*, 2000).

3.5 Dating sedimentary rocks

Absolute dating of the time of deposition of sedimentary rocks is an important problem, but one that is very difficult to solve. Accurate dates depend on thorough re-setting of isotopic clocks. In the case of Rb–Sr dating of sediments, this rests on the assumption that Sr isotope systematics in the rock were homogenised during deposition or early diagenesis, and thereafter remained as a closed system until the present day. However, we will see that these two requirements may be mutually exclusive.

In principle, sedimentary rocks may be divided into two groups according to the nature of the Rb-bearing phase present. Allogenic (detrital) minerals are moderately resistant to open-system behaviour during burial metamorphism, but problems arise from inherited isotopic signatures. Authigenic minerals are deposited directly from seawater and hence display good initial Sr isotope homogeneity. However, they are highly susceptible to recrystallisation after burial and do not necessarily remain closed systems.

In practice, the two distinct dating approaches associated with these sediment types have tended to converge. Analysis of detrital sediments has moved towards the analysis of fine-grained, almost authigenic, minerals such as illite, in order to escape the effects of the detrital component. In contrast, analysis of authigenic minerals has been focussed on the sub-authigenic mineral glauconite, since the truly authigenic Rb-bearing evaporite minerals are too susceptible to burial metamorphism to be viable geochronometers.

3.5.1 Shales

Detrital Rb-bearing minerals (mica, K-feldspar, clay minerals etc.) can be expected to contain inherited old radiogenic Sr. Therefore, dating of such material should give an average of the provenance ages of the sedimentary constituents. However, if sufficiently fine-grained shales are sampled, it appears that the constituent minerals (mainly illite) often suffer substantial exchange of Sr during post-depositional diagenesis. In this case they may develop an almost homogeneous initial Sr isotope composition soon after deposition, thereafter remaining effectively closed systems until the present day.

Compston and Pidgeon (1962) pioneered whole-rock Rb–Sr dating of shales, and found that, in some circumstances (e.g. the State Circle shale from SE Australia), the above conditions were closely approached. However, in other cases (e.g. the Cardup shale of W Australia), gross inherited ^{87}Sr/^{86}Sr variations remained, preventing the calculation of a meaningful age. Compston and Pidgeon attributed this to undecomposed detrital micas, probably sericite. In contrast, the carbonaceous shales of the Cardup unit contained much less detrital mica and, taken alone, gave a tentative depositional age of 660 Myr.

Subsequent work on the dating of shales sought to avoid problems of contamination with detrital micas and feldspars by analysing separated clay-mineral fractions, whose purity is checked by X-ray diffraction (XRD). XRD analysis of illites can also yield information about the nature and origin of clay minerals in a shale that is to be dated.

The ‘illite crystallinity index’ (Kubler, 1966) is defined as the width of the (001) XRD peak at half its height. A well-crystallised illite, characteristic of a relatively high-temperature history, has sharp peaks and therefore a low index, whereas low-temperature illites are more disordered and have irregular peaks with large indices. In addition to this discriminant, illite has high-temperature (2M) and low-temperature (1M) polymorphs, which can also be distinguished by XRD (Dunoyer de Segonzac, 1969). ‘1M’ illites with a large crystallinity index are characteristic of low-temperature growth and recrystallisation in the sedimentary–diagenetic regime, whereas ‘2M’ illites with a small index are indicative of temperatures of zeolite-facies metamorphism or above. The latter reflect a detrital component, or post-diagenetic metamorphism.

A comparison of Rb–Sr whole-rock and clay mineral analysis of a Precambrian shale from Mauritania (W Africa) is shown in Fig. 3.21 (Clauer, 1979). Four clay fractions were analysed, containing smectite and the 1M illite polymorph with a crystallinity index over 6 (very-low-grade metamorphism is characterised by an index below 5.75). These define an array that is collinear with associated dolomites, yielding an age of 860 ± 35 Myr and an initial ratio of 0.7088, characteristic of Precambrian seawater. A whole-rock sample (4) shown by XRD to be free of detrital feldspar also

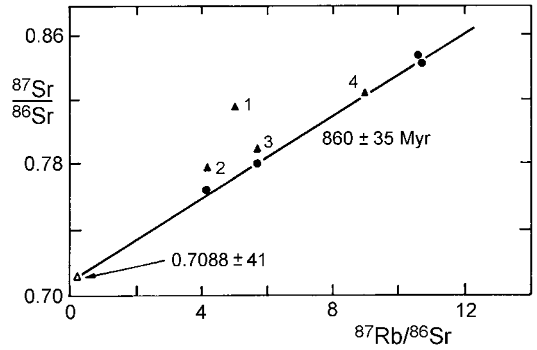

Fig. 3.21. Rb–Sr isochron diagram for whole-rock shales (▲); separated illites (●); and a carbonate sample (△) from Mauritania. Numbered whole-rock samples are discussed in the text. After Clauer (1979).

Table 3.1. *Age data (in Myr) for shales from the Yangtze gorge, based on whole-rock or coarse clay (left column) and fine clay separates (right)*

Coarse fraction or whole-rock		Fine fraction	
573 ± 7	(Rb–Sr > 1.5 μm)		
613 ± 23	(Rb–Sr)		
568 ± 12	(U–Pb whole-rock)		
572 ± 14	(Rb–Sr whole-rock)	435–415	(Rb–Sr < 1 μm)
570 ± 4	(Rb–Sr)		
574 ± 20	(Rb–Sr)	565–490	(Rb–Sr)
602 ± 15	(Rb–Sr ~ 1.5 μm)	460 ± 9	(Rb–Sr < 1 μm)
Stratigraphic Cambrian–Precambrian boundary			
614 ± 18	(Rb–Sr > 1.5 μm)		
700 ± 5	(Rb–Sr > 1.5 μm)	580 ± 25	(Rb–Sr < 1 μm)
691 ± 29	(Rb–Sr)		
580–420	(Rb–Sr > 1.5 μm)		
727 ± 9	(Rb–Sr > 1.5 μm)	460–340	(Rb–Sr < 1 μm)
728 ± 27	(Rb–Sr)	500–360	(Rb–Sr < 1 μm)
608 ± 15	(Rb–Sr > 1.5 μm)		

lay on the isochron. However, two whole-rocks with traces of microcline (2 and 3) lay slightly above it, whereas one with 15% microcline (1) was displaced well above the isochron. It appears from this example that whole-rock Rb–Sr dating of shales is an unreliable geochronometer, but that analysis of separated illite fractions may give meaningful ages of diagenesis or low-grade metamorphism. However, there is always a danger that the detrital component might not be completely eliminated from the illite fraction. An important example of this problem is provided by the dating of the Sinian–Cambrian boundary.

In China, the Sinian (youngest Precambrian)–Cambrian boundary is very well exposed, with an apparently continuous fossil-rich succession of black shales across the base of the Cambrian. Rb–Sr analysis of shales would be a very convenient method of dating this boundary if reliable ages for deposition or early diagenesis could be obtained. Some of these results, summarised by Cowie and Johnson (1985) and Odin *et al.* (1985), are shown on the left-hand side of Table 3.1. They appear to support an age of about 600 Myr for the base of the Cambrian. However, the analysis of fine-grained fractions (right-hand column in Table 3.1) almost invariably gave ages significantly lower than the whole-rock or coarse clay fractions. This suggests that a diagenetic event affected the rocks some time after deposition, so that the data in the left column of Table 3.1 are probably mixed ages of inherited and diagenetic components, rather than depositional ages.

This interpretation is supported by recent U–Pb zircon dates on tuff and bentonite from near the base of the Cambrian in Morocco, China and Siberia, which confirm a young boundary age near 540 Myr (Compston *et al.*, 1990; Bowring *et al.*, 1993). Therefore, Rb–Sr dating of shales cannot be considered a reliable technique for dating sedimentary deposition.

3.5.2 Glauconite

The mineral glauconite offers an attractive possibility for dating sedimentary rocks directly, due to its high Rb content, easy identification and widespread stratigraphic distribution. Glauconite is a micaceous mineral similar to illite which is best developed in macroscopic pellets (called 'glauconies' by Odin and Dodson, 1982). These are probably formed by the alteration of a very-fine-grained clay precursor intermixed with organic matter in a faecal pellet. Glauconies form near the sediment–water interface in the marine environment. However, by studying pellets on the present-day ocean floor, Odin and Dodson (1982) have shown that 'glauconitisation' is a slow process that may take hundreds of thousands of years to reach completion. During this process, the potassium content of the pellet increases, and this can therefore be used to monitor the maturation of the pellet.

Rb–Sr analysis of Holocene glauconies (Clauer *et al.*, 1992) shows that Sr isotope equilibrium with seawater is achieved only slowly as the potassium content increases. The Rb–Sr data can be used to calculate a model Sr age for the pellet by making the initial ratio equal to the isotopic composition of seawater Sr at the estimated time of sedimentation (see below).

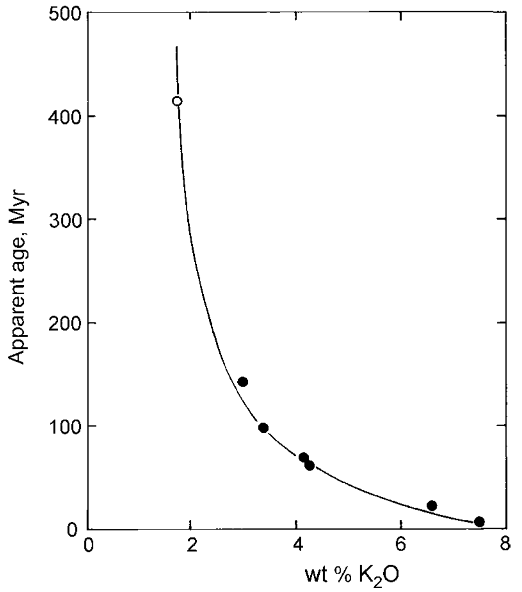

Fig. 3.22. Rb–Sr model ages of Holocene (zero-age) glauconies as a function of potassium content. The open symbol indicates the clay fraction. After Clauer *et al.* (1992).

A zero-age pellet starts with a high apparent model age due to a large content of Sr in detrital mineral phases. However, as it matures, the pellet homogenises with seawater so that the model age falls to zero in a fully equilibrated pellet (Fig. 3.22). Analysis of the potassium content of glauconies therefore provides an essential screening procedure, in order to select only fully mature material for dating.

Cretaceous and younger glauconies often yield ages concordant with those obtained from other dating methods (e.g. Harris, 1976), but Paleozoic glauconies commonly give ages that are 10%–20% younger than expected. Early workers (e.g. Hurley *et al.*, 1960) attributed this to post-depositional uptake of K and Rb during diagenesis. However, Morton and Long (1980) attributed the young ages to loss of ^{87}Sr from the expandable layers of the clay lattice, by some form of ion exchange with circulating brines.

Morton and Long calculated model ages for a series of glauconite separates, using initial ratios based on the ^{87}Sr/^{86}Sr ratio of seawater at the time of deposition (see section 3.6.1). They showed that, in some cases, erroneous glauconite model ages could be increased to near the stratigraphic age by leaching with ammonium acetate, which is thought to remove excess loosely bound Rb from the expandable layers of the lattice. In contrast, leaching with acetic acid or HCl had unpredictable effects on the glauconite age, probably due to removal of some tightly bound Sr.

Similar experiments were performed on glauconites from the 525-Myr-old Bonneterre Formation (Missouri) by Grant *et al.* (1984). Eight un-leached glauconite pellets gave model ages in the range 413–440 Myr. However, the most radiogenic sample (model age 426 Myr) converged only slightly towards the true age when subjected to ammonium acetate leaching (437 Myr). Therefore, more rigorous criteria are needed in order to determine whether old glauconites have suffered open-system behaviour, prior to a dating attempt. Until such criteria are developed, glauconite dating in the Paleozoic must be regarded as a monitor of diagenetic processes rather than a viable dating tool for stratigraphic correlation.

3.6 Seawater evolution

Biogenic carbonates fulfil two of the requirements of a sedimentary dating tool: they are fairly resistant to diagenetic alteration; and, since they are secreted directly from seawater by the organism, they contain no detrital fraction. Unfortunately, the negligible Rb content of carbonates precludes application of the conventional Rb–Sr dating method. However, calibration of the seawater Sr isotope evolution path would allow the 'initial' ^{87}Sr/^{86}Sr isotope ratios of carbonates to be used as an indirect dating tool. In the following section we will assess the realisation of this concept, as well as the application of Sr isotopes as an oceanographic tracer.

3.6.1 Measurement of the curve

Interest in the strontium isotope composition of seawater dates back to Wickman (1948). He argued that decay of ^{87}Rb to ^{87}Sr in crustal rocks over geological time, and its subsequent release into the hydrosphere by erosion, should have led to a 25% increase in seawater Sr isotope composition over the last 3 Byr. This model was tested by Gast (1955), who analysed carbonates of various ages as a means of characterising the evolution of seawater through geological time. However, he found that any natural variations were of the same order as the analytical errors of ^{87}Sr/^{86}Sr analysis pertaining at that time (about 0.004), thus refuting Wickman's model. Evidently the average crustal Rb/Sr ratio assumed by Wickman was an over-estimate.

Resolution of the actual extent of seawater Sr isotope variation through time had to wait fifteen years for the advent of more precise mass spectrometry.

Peterman *et al.* (1970) measured the ^{87}Sr/^{86}Sr composition of macro-fossil shell carbonates with an order-of-magnitude improvement in precision (± 0.0005, 2σ). They found a total isotopic range of 0.0022 ($4 \times$ analytical error), which would have been imperceptible using earlier equipment. Peterman *et al.* showed that, contrary to Wickman's prediction, the seawater Sr isotope ratio actually *decreased* during the Paleozoic, reaching a minimum during the Mesozoic, before rising quickly to a maximum at the present day.

In order to avoid the effects of post-depositional alteration, Peterman *et al.* rejected any recrystallised shell material, which they claimed to be able to recognise visually. The possibility of Sr exchange between matrix and un-recrystallised shells was rendered unlikely by the good compositional agreement between different shells in a bed. A mixture of different types of mollusc was used (belemnites, bivalves and brachiopods). Since no variation among such classes was seen at the present day, they were assumed to behave in the same way as fossils.

Additional data were collected by Dasch and Biscaye (1971) and Veizer and Compston (1974) from different types of sample material. Dasch and Biscaye used Cretaceous-to-Recent pelagic foraminifera, whereas Veizer and Compston analysed 'sedimentary carbonate' (in other words not macro-fossil carbonate) to test its reliability for the determination of seawater Sr isotope ratios. In both cases the authors found general agreement with the data of Peterman *et al.* (1970). This implies global homogenisation of seawater Sr, which can be attributed to the very long residence time of Sr in seawater (about 2.5 Myr; Hodell *et al.*, 1990) compared with the average mixing time of oceanic water (about 1.6 kyr; section 14.1.7). However, Veizer and Compston recognised that 'sedimentary carbonate' is more susceptible to post-depositional exchange with pore waters. They argued that since detrital grains would normally have radiogenic Sr isotope signatures, post-depositional exchange would normally be expected to raise ^{87}Sr/^{86}Sr ratios. Therefore the minimum Sr isotope ratio found at any given time should be the most reliable guide to contemporaneous seawater composition.

While the analysis of whole-rock carbonate provides fewer constraints on post-depositional processes, it provides more opportunity for sampling, and is essential for Precambrian carbonates. Using the principles outlined above, Veizer and Compston (1976) performed a reconnaissance study of the Sr isotope evolution of Precambrian seawater. They found uniformly unradiogenic Sr isotope ratios in Archean carbonates, with values only slightly elevated over those for contemporaneous upper mantle (Fig. 3.23). However, there was a substantial rise in Sr isotope ratio during the Proterozoic, reaching a maximum in the early Cambrian which was similar to the present-day composition.

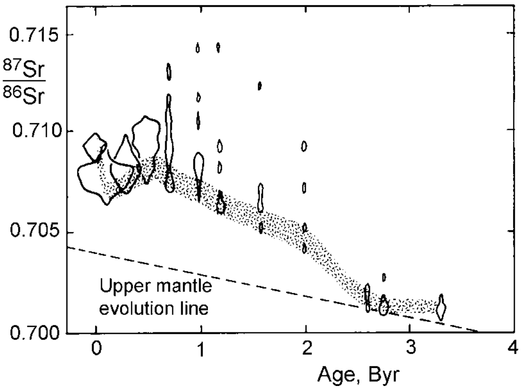

Fig. 3.23. Sr isotope composition of marine carbonates over the last 3.5 Byr, from which the isotopic evolution of seawater is deduced (shaded band). After Veizer and Compston (1976).

A major expansion of the seawater Sr data set was achieved by Burke *et al.* (1982), who presented 786 isotopic analyses of marine carbonates, phosphates and evaporites, with good coverage of all of Phanerozoic time except the Lower Cambrian (Fig. 3.24). In addition, work by Derry *et al.* (1989), Asmerom *et al.* (1991) and Kaufman *et al.* (1993) extended the curve back to the Late Proterozoic. In the absence of fossil material, the latter studies were performed principally on whole-rock carbonates, which are susceptible to contamination by fluid-borne Sr during post-depositional alteration. Therefore, Sr was extracted from bulk carbonates by leaching with dilute acetic acid to reduce the amount of contamination from detrital phases containing radiogenic Sr.

Following the wide-ranging study of Burke *et al.* (1982), subsequent work was generally devoted to improving precision on small segments of the curve. This requires material to be well-dated stratigraphically and carefully screened before analysis in order to exclude the possibility of post-depositional alteration. In Paleozoic rocks, this screening is best achieved chemically. Brand and Veizer (1980) showed that open-system diagenesis of carbonates is accompanied by a decrease in Sr/Ca ratio and an increase in Mn content (Fig. 3.25). However, Mn-enriched calcite can be detected by cathodoluminescence, so sections of shell can be screened for alteration before sample analysis. Popp *et al.* (1986) showed that samples of brachiopod

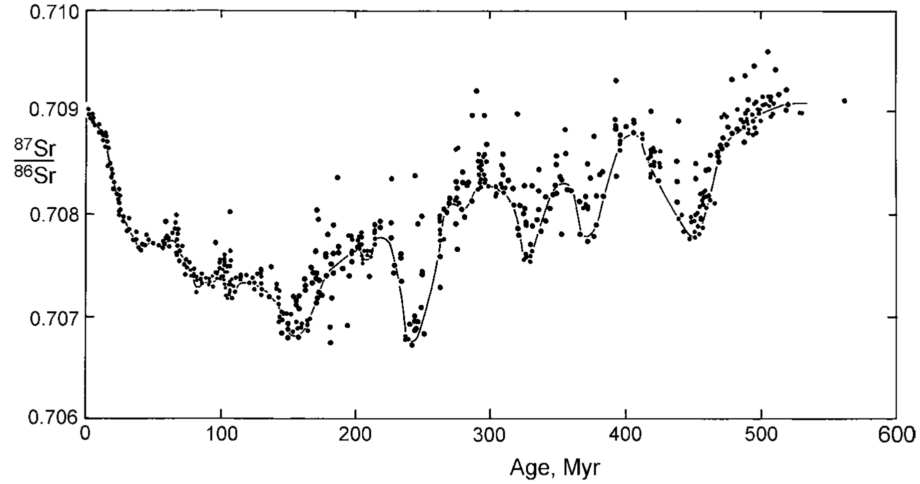

Fig. 3.24. Sr isotope data for Phanerozoic carbonates. The solid line indicates the lower bound of most of the data, which is the most probable seawater Sr composition. After Burke *et al.* (1982).

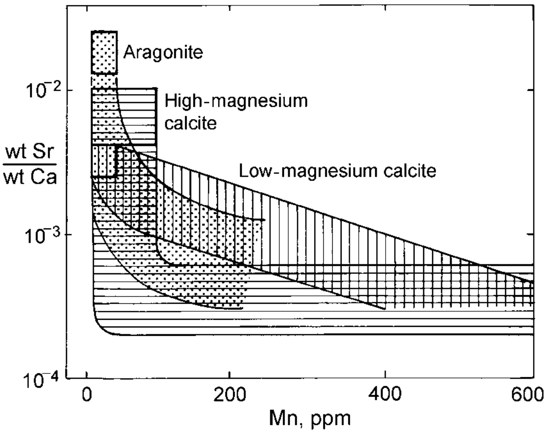

Fig. 3.25. Summary of diagnostic chemical changes that occur during the diagenetic alteration of carbonates. Boxes represent primary fields. After Brand and Veizer (1980).

shell prepared in this way gave more reliable results than whole brachiopod shells (which were sometimes contaminated by unradiogenic Sr) or whole-rock carbonates (which were usually contaminated by radiogenic Sr).

The use of high-quality brachiopod shells and belemnites from around the world allowed Veizer *et al.* (1999) to present a complete Sr evolution curve for the Mesozoic and Paleozoic, based on 1450 new analyses. They utilised the interior shell layers from brachiopods and single laminae of belemnites, and much of their material exhibited excellent preservation of textures on a sub-micrometre scale, as demonstrated by examination under the scanning electron microscope (SEM). This study therefore constitutes a successor to that of Burke *et al.* (1982) in giving an overview of seawater Sr evolution between 100 and 500 Myr ago.

Construction of a very precise seawater Sr isotope evolution curve for the last 100 Myr was made easier by the availability of numerous Deep Sea Drilling Project (DSDP) cores. These cores provide overlapping continuous sections with well-preserved microfossils such as foraminifera. Relatively constant sedimentation rates in these sections are used to interpolate between biostratigraphic and magnetostratigraphic calibration points. This avoids the age uncertainty involved in correlating short stratigraphic sections from different localities.

Two different sampling approaches have been adopted for DSDP core material. DePaolo (1986) performed a study on a single DSDP hole reaching back to the Early Miocene, but with duplicate analysis of all samples to improve analytical precision. In his approach, bulk samples of foram–nano-fossil ooze were analysed by direct acetic acid leaching of washed whole-rock samples. This necessitates a correction for post-depositional exchange in order to determine original seawater compositions. These corrections were based on the analysis of pore waters. However, pore waters displayed relatively small deviations in $^{87}Sr/^{86}Sr$ ratio from the carbonate fraction (<0.0001), and were also found to have Sr contents an order of magnitude lower (Richter and DePaolo, 1987). Hence

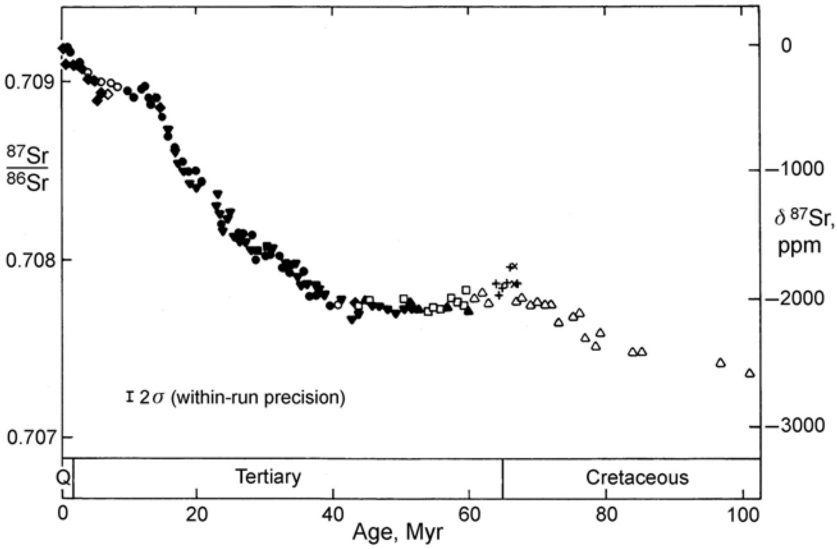

Fig. 3.26. Plot of Sr isotope ratio against age for forams from eight DSDP holes (distinguished by symbol shapes). Solid symbols and crosses indicate most reliable data; open symbols may be slightly disturbed. After Hess *et al.* (1986).

it was argued that corrections for Sr exchange were smaller than mass-spectrometric reproducibilities.

In the other approach (Hess *et al.*, 1986), hand-picked whole foram tests were analysed. These were screened for secondary alteration by SEM examination and chemical analysis (e.g. Mn and Sr content). Figure 3.26 shows data from eight partially overlapping DSDP sections. Slight scatter is seen, but much of this can be attributed to analytical error rather than diagenetic effects. In selected samples from two sites, pore waters had very similar isotope ratios to forams. At one other site, pore waters were somewhat more radiogenic, but there was no evidence that the foram data had been perturbed. Most subsequent studies have also employed hand-picked forams. Since less than 50 ng of Sr is now needed for a precise analysis, this may be possible on a few forams or even a single foram. As an additional precaution, Martin and Macdougall (1991) were able to break open large Cretaceous forams to examine them by SEM for internal calcite growth.

The high-precision seawater Sr isotope evolution curve can be used as a stratigraphic dating tool, with a (conservative) precision as good as 0.5 Myr for periods of rapid Sr isotope evolution, but as bad as 2 Myr during periods of slow isotopic evolution. This precision cannot compete with biostratigraphic dating in the Cretaceous and Tertiary periods, but it may be useful for calibration of un-fossiliferous borehole sections (e.g. Rundberg and Smalley, 1989; McArthur *et al.*, 2001).

An interesting observation by Hess *et al.* (1986) in their Cretaceous–Tertiary data set was a 'spike' in seawater Sr isotope ratio at the so-called 'K–T boundary' (Fig. 3.26). They speculated as to whether a meteorite impact could have released sufficient Sr, either from the bolide or in the terrestrial impact ejecta, to explain this peak. If the spike in ^{87}Sr is attributed to a meteorite, it is critical to demonstrate that it occurred at exactly the correct stratigraphic level. Martin and Macdougall (1991) collected data from four widely spaced localities around the world, which appeared to support the model. However, detailed analysis of sample suites close to the K–T boundary in Denmark and Antarctica failed to find such a spike (McArthur *et al.*, 1998). Instead, the data of McArthur *et al.* (1998) fitted the lower bound of the more-scattered older data (Fig. 3.27), suggesting that the elevated values in these older studies reflect diagenetic alteration, despite the precautions taken to exclude this effect.

To examine this problem further, MacLeod *et al.* (2001) studied Sr isotope variation in a section across the K–T boundary in a DSDP hole off Florida. Because this section is close to the impact site, the spherulitic K–T boundary horizon here is 10 cm thick, and can therefore be studied in more detail. Bulk carbonates from the spherulitic layer itself are radiogenic, due to exchange of Sr with silicate phases (Fig. 3.28).

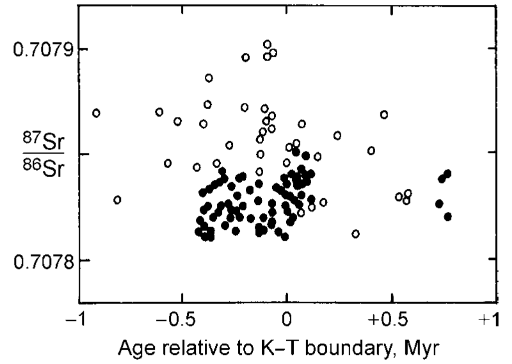

Fig. 3.27. Variation of Sr isotope ratio in the vicinity of the K–T boundary, showing data of McArthur *et al.* on macro-fossils and leached chalk (●) in comparison with data from Martin and Macdougall (1991) (○). After McArthur *et al.* (1998).

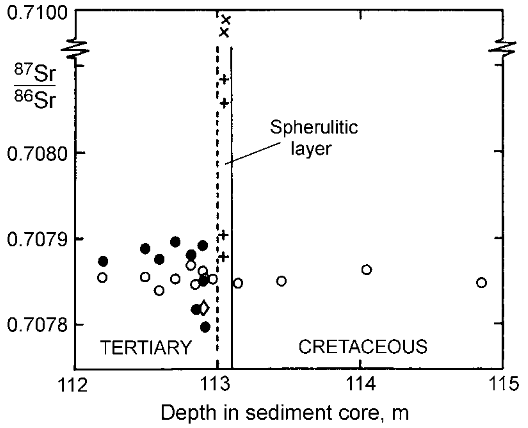

Fig. 3.28. Variation in Sr isotope ratio in various types of sample at the K–T boundary, from a DSDP site off Florida. (○) = Cretaceous foram taxon; (●) = Tertiary foram taxon; (◇) = dolomite rhomb overgrowths; (+) = bulk carbonate; (×) = silicate. After MacLeod *et al.* (2001).

However, to test for global seawater Sr variations, MacLeod *et al.* analysed the isotopic compositions of two different groups of foraminifera in the vicinity of the boundary. The results (Fig. 3.28) showed that forams found only above the boundary (Tertiary taxa) generally had more radiogenic Sr than those that straddled the boundary (Cretaceous taxa).

MacLeod *et al.* considered two alternative explanations for these observations. One is that the Tertiary taxa (solid symbols in Fig. 3.28) were more susceptible to contamination by overgrowths because they have thinner tests. However, an analysis of such overgrowths suggested that this might lower rather than increase the $^{87}Sr/^{86}Sr$ ratio (Fig. 3.28). The other explanation is that the Tertiary strata were contaminated by Cretaceous forams reworked elsewhere from below the boundary and then carried into the section as clastic sediment. The fact that the drill hole comes from part way down the continental slope makes this a significant possibility. This would imply that the Tertiary taxa best represent the composition of seawater Sr after the impact, and hence that a very small (0.00003) increase in seawater $^{87}Sr/^{86}Sr$ ratio occurred across the boundary. This suggests that the impact event at the boundary did have a small effect on seawater Sr. However, this evidence needs to be tested at a site less susceptible to sedimentary reworking.

Neogene seawater evolution has provided a challenge to geochemists to find the most short-term variations in Sr isotope evolution which can be documented. In early work on this question, Hodell *et al.* (1990) determined a smooth evolution curve. However, Dia *et al.* (1992) and Clemens *et al.* (1993) claimed to observe changes in $^{87}Sr/^{86}Sr$ ratio, correlated with $\delta\ ^{18}O$, with a periodicity of about 0.1 Myr (Figs. 3.29a–c). This was surprising, in view of the long seawater residence of Sr. However, subsequent work by Henderson *et al.*, (1994) and Clemens *et al.*, (1995) failed to reproduce these cycles in three drill cores (including two used in the original work). Instead, the new data fell on the evolution path defined by Hodell *et al.* (1990). Hence, the apparent periodicity in the earlier work is attributed to analytical artefacts and does not reflect seawater Sr isotope evolution.

For the data of Dia *et al.* (1992), the analytical artefact was apparently a breakdown in the accuracy of the fractional correction. Thus, Clemens *et al.* (1995) were able to reproduce the temporal periodicity using a linear-law fractionation correction, but this also generated a positive correlation between $^{88}Sr/^{86}Sr$ ratio and fractionation-corrected $^{87}Sr/^{86}Sr$ ratios, indicative of a fractionation bias (section 2.2.3). After correction of this bias, the periodicity disappeared (Fig. 3.29d). The data of Clemens *et al.* (1993) were not subject to this bias, since the more accurate exponential law was used. However, Henderson *et al.* (1994) showed that only eight of 75 samples analysed by Clemens *et al.* (1993) lay outside 2σ (95%) confidence limits from the linear evolution path of Hodell *et al.* (1990). Since four outliers would be expected at this confidence limit, the apparent periodicity in this data set is probably not statistically significant (Fig. 3.29b).

Farrell *et al.* (1995) carried out a study with similar sampling density and analytical precision to the above work, but using 455 samples extending over the

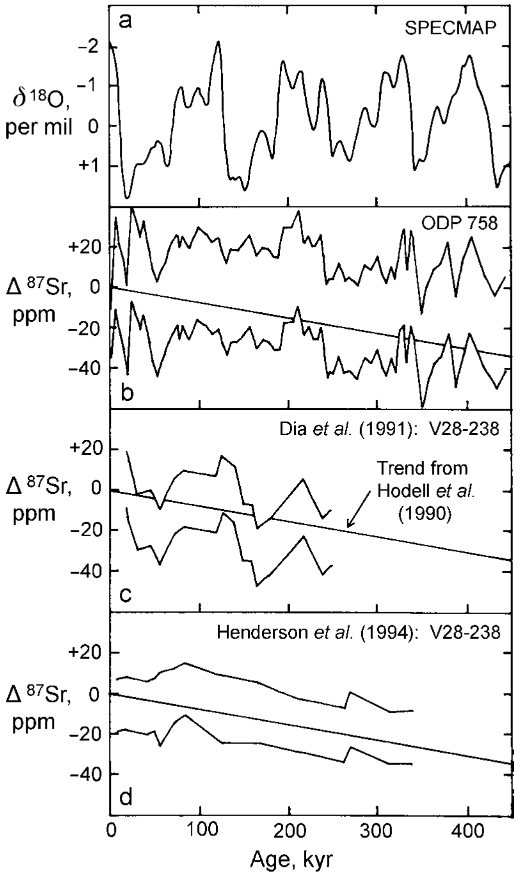

Fig. 3.29. Comparison between seawater Sr and oxygen isotope data for the past 400 kyr: (a) oxygen isotope record; (b) data of Clemens *et al.* (1993) expressed by 2σ error limits; (c) and (d) data of Dia *et al.* (1991) and Henderson *et al.* (1994), respectively, on the same drill core. Modified after Henderson *et al.* (1994).

past 6 Myr. These data constrain the seawater evolution curve to an average confidence limit of ± 0.00002 (2σ). The curve exhibits undulations with a periodicity of 1–2 Myr, which are realistic reflections of changing Sr fluxes, given a 2.5 Myr residence time of Sr in the ocean system.

3.6.2 Modelling the fluxes

The first model for the Sr isotopic composition of seawater was constructed by Faure *et al.* (1965) to explain the present-day Sr isotope ratio of the North Atlantic. They suggested that there was a balance between the supply of unradiogenic Sr by erosion of young volcanics, radiogenic Sr from old crustal rocks, and Sr of intermediate composition from the erosion of carbonates. This model was adopted by Peterman *et al.* (1970) to explain the rise and fall of seawater Sr isotope ratio during the Phanerozoic. Armstrong (1971) supplemented this model, suggesting that peaks in seawater Sr isotope ratio during the Carboniferous and Tertiary periods were due to enhanced glacial erosion of old shields with elevated ^{87}Sr contents (Fig. 3.30). However, in other ways the model remained largely unchallenged.

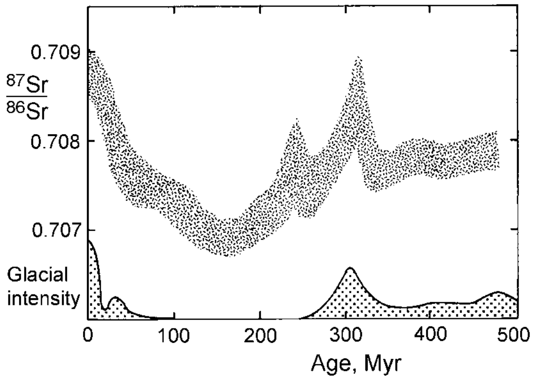

Fig. 3.30. Illustration of a glacial–erosional model to explain the seawater Sr evolution curve of Peterman *et al.* (shaded band). After Armstrong (1971).

A major advance in modelling seawater Sr evolution was the proposal of Spooner (1976) that the unradiogenic Sr flux was due to submarine hydrothermal exchange with basaltic crust, rather than sub-aerial erosion of basic rock. Spooner calculated that the hydrothermal flux must be six times the magnitude of the river-water Sr flux. However, this was based on high estimates of the isotopic compositions of run-off (0.716) and hydrothermally buffered water (0.708). Subsequent analysis of hydrothermal vent waters from the East Pacific Rise (Albarède *et al.*, 1981) indicated much less radiogenic compositions. Albarède *et al.* estimated the flux of hydrothermally recycled Sr as less than one-quarter of the flux due to continental run-off. This model predicted an average Sr isotope composition for run-off between 0.710 and 0.711, in good agreement with major rivers such as the Amazon (Brass, 1976). The magnitudes of present-day Sr fluxes were further refined by Palmer and Edmond (1989), who measured the Sr budgets and isotope compositions of hydrothermal vent fluids and of most of the world's major rivers. Taken together, the complete data set of Palmer and Edmond led to an estimated global river flux of 3.3×10^{10} mol Sr per year, with an $^{87}Sr/^{86}Sr$

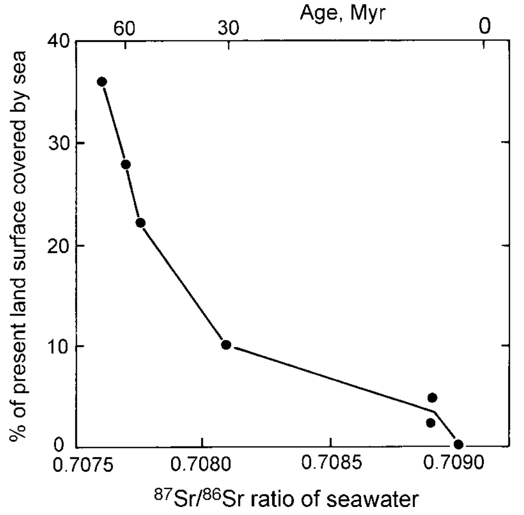

Fig. 3.31. Plot of seawater Sr isotope composition over the last 85 Myr against percentage continental flooding (relative to the present-day land area). After Spooner (1976).

ratio of 0.7119, and an ocean-ridge hydrothermal Sr flux of about one-half this magnitude, with an $^{87}Sr/^{86}Sr$ ratio of 0.7035.

The recognition of competing riverine and hydrothermal fluxes raises the question of how these fluxes interacted in the past to cause variations in seawater isotope ratio with time. Spooner (1976) assumed that the hydrothermal Sr flux was fairly constant over time. Therefore, he attributed the increase in $^{87}Sr/^{86}Sr$ ratio since the Cretaceous principally to an increase in continental exposure (and hence run-off of Sr) over the last 85 Myr (Fig. 3.31). In contrast, Albarède *et al.* (1981) argued that a drop in the ocean-ridge Sr-exchange flux from a Mesozoic value nearly four times higher was more important than a rise in the flux of continental run-off. However, these two effects are difficult to separate, since they are bound together as a system. A drop in spreading rate causes ridge collapse and a consequent fall in sea-level, so continental exposure should increase as hydrothermal buffering of seawater decreases.

In addition to run-off and hydrothermal exchange, two other fluxes have been proposed to control seawater Sr. One, which has been widely accepted, although small in size, is the Sr released from ocean-floor carbonates by diagenetic recrystallisation (Elderfield and Gieskes, 1982). This is estimated at about 10% of the run-off flux and tends to dampen isotopic fluctuations because it recycles old seawater Sr.

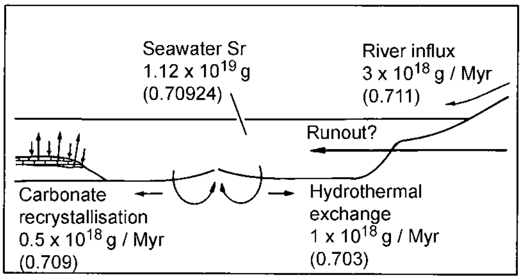

Fig. 3.32. Simplified circulation model for the present-day seawater Sr budget. Modified after DePaolo (1987).

Another proposed flux is the sub-surface outflow of continental groundwater, from below the water table, into the sea (Fig. 3.32). This flux was termed 'run-out' by Chaudhuri and Clauer (1986), who proposed that it could explain seawater Sr isotope fluctuations that are not in harmony with variations in sea-level. For example, run-out would be affected by the length of the continental perimeter as well as the extent of continental uplift, so plate-tectonic configurations that form super-continents would be characterised by low run-out, whereas fragmented continents (such as those existing at the present day) should be characterised by high run-out. This model attributes the rising Sr isotope ratio during the early Cretaceous (despite rising sea-level) to progressive continental break-up at that time.

Chaudhuri and Clauer suggested that the run-out (continental groundwater) Sr flux could be almost as large as the riverine run-off flux. This proposal has received very little attention over subsequent years, but a similar model based on studies of groundwater flow in the Bengal Fan was recently proposed by Basu *et al.* (2001). Basu *et al.* cited evidence that this groundwater flux could supply as much strontium to the sea as the riverine Sr flux of the Ganges–Brahmaputra system. If this flux were extrapolated world-wide, it might imply a doubling of the continental Sr flux, as proposed by Chaudhuri and Clauer (1986). This would have a fairly dramatic effect on calculations of global Sr fluxes, including a reduction of the estimated oceanic residence time of Sr to 2 Myr. However, our present knowledge of groundwater Sr fluxes is too poor to constrain the importance of this process.

3.6.3 The effects of Himalayan erosion

The best opportunity to study the interaction of competing fluxes in the buffering of seawater Sr is during periods of rapid change in isotope ratio with time. The Tertiary represents one such period, which is characterised by an overall trend of increasing Sr isotope ratio, on which several smaller steps are superimposed. These variations can be represented in terms of the rate of change of Sr isotope ratio with time (Fig. 3.33).

Raymo *et al.* (1988) attributed the general trend of seawater evolution over the last 40 Myr to increased rates of uplift of the Himalayas, Tibet and Andes. This could have caused a substantial increase in the supply of radiogenic Sr to the oceans, since the rivers which rise in these regions (Ganges–Brahmaputra, Yangtze and Amazon) together supply 20% of the total solid load to the oceans. On the other hand, changes in the hydrothermal Sr flux are not thought to have occurred during the Neogene, since ocean-spreading rates have been nearly uniform during this time.

Additional evidence for the control of seawater Sr by Himalayan erosion rates was provided by Richter *et al.* (1992). Ar–Ar thermochronology was used to date the sudden unroofing of the Quxu granite pluton, corresponding to a period of exceptionally rapid erosion of the Tibetan plateau. The timing of this event, which began 20 Myr ago, matches exactly with the peak rate of change in the seawater Sr isotope record (Fig. 3.33). However, Harris (1995) claimed that there was no evidence in the Bengal Fan for an increase in Himalayan erosion 20 Myr ago. Instead, he suggested that the inferred ^{87}Sr spike in river water at that time was due to the exposure and chemical weathering of meta-sedimentary rocks with a large budget of leachable ^{87}Sr.

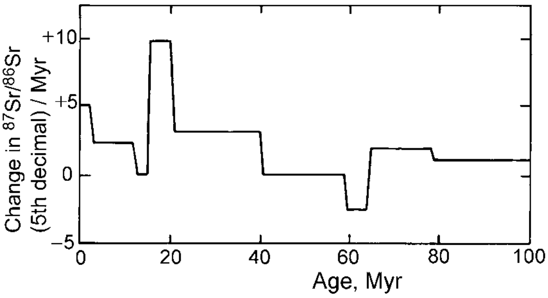

Fig. 3.33. Representation of seawater Sr isotope variation during the last 100 Myr in terms of the rate of change per million years. After Richter *et al.* (1992).

In order to reach a better understanding of how variations in riverine Sr influence seawater Sr, Palmer and Edmond (1989) performed the first comprehensive study of the Sr budget of the world's rivers. This revealed an inverse relationship between isotope ratio and concentration (Fig. 3.34a), which was attributed to mixing between radiogenic Sr from silicate weathering and less-radiogenic Sr from carbonate weathering. The Ganges and Brahmaputra, which drain the Himalayan uplift, lie off the general trend. However, within the drainage basin of the Ganges, its tributaries themselves display a mixing line, although with a steeper slope than those of other rivers (Fig. 3.34b).

Further examination of these data (Palmer and Edmond, 1992) showed that the mixing line for the Ganges system had a more elevated intercept (Sr isotope ratio) than other rivers of the world, as well as a steeper trend. Palmer and Edmond attributed this pattern to the presence of carbonate rocks in the Ganges watershed with abnormally radiogenic Sr isotope ratios. They speculated that these carbonates had become enriched in radiogenic Sr by exchange with the surrounding very-radiogenic silicate rocks.

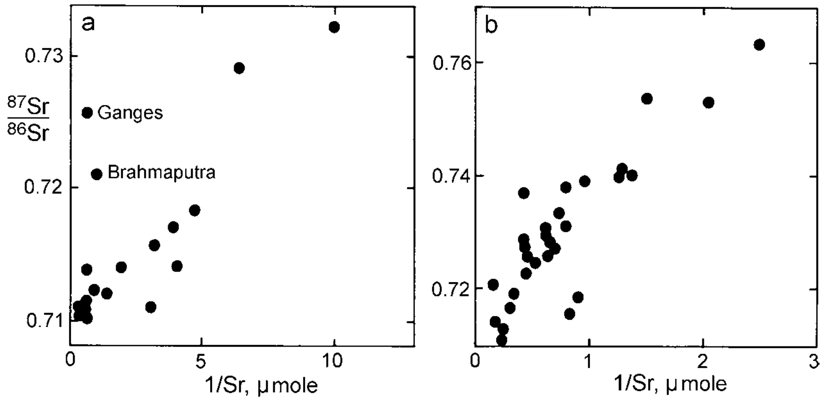

Fig. 3.34. Plot of Sr isotope ratio against reciprocal of Sr concentration: (a) for the world's major rivers; and (b) for tributaries of the Ganges. After Palmer and Edmond (1989).

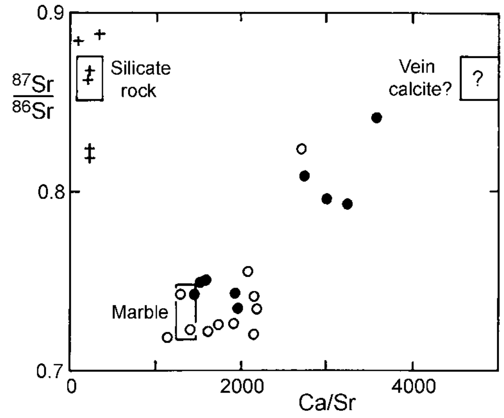

Fig. 3.35. Plot of Sr isotope ratio against Ca/Sr ratio for samples from the Raikot river watershed, northern Pakistan. (●) = waters; (+) = silicate rocks; (○) = carbonate rocks; boxes = proposed end-members. After Blum *et al.* (1998).

Subsequent to this work, more detailed studies have been made of the rivers draining the High Himalayas, which are tributaries to the Indus and Ganges–Brahmaputra river systems. For example, Blum *et al.* (1998) analysed river water, rock outcrops and river-bed sands from the Raikot watershed in northern Pakistan. They showed that river and stream waters define a positive trend on a plot of Sr isotope ratio against Ca/Sr ratio (Fig. 3.35). This trend runs from the composition of marbles and marble sands at the unradiogenic end, to a radiogenic end-member with a much higher Ca/Sr ratio than that of silicate rocks. Blum *et al.* speculated that this unknown end-member might be calcite that had inherited its radiogenic Sr during hydrothermal alteration of the surrounding silicate rocks.

Further study (Jacobson and Blum, 2000) identified disseminated calcite interstitially within silicates, at grain boundaries, and in fracture fillings. This calcite makes up less than 0.5% of the orthogneissic rocks in the Raikot watershed, but appears to dominate the Sr budget of streams draining this terrain. Similar conclusions about the role of carbonate dissolution were reached by English *et al.* (2000), from a study of the Seti watershed in western Nepal. In addition, carbonates in the Seti watershed have also been proposed as a source of radiogenic osmium in Himalayan rivers (Pierson-Wickmann *et al.*, 2002).

An alternative explanation for recent increases in the Sr isotope signature of seawater is the onset of Tertiary glaciation, as originally proposed by Armstrong (1971). Hodell *et al.* (1990) revived this model, attempting to link inflections in the Tertiary Sr isotope evolution path to glacial advances and retreats, and this type of argument has been examined in several subsequent papers. The basis of this model is that glaciation creates rock flour, which is then more susceptible to chemical weathering than are *in situ* crystalline rocks.

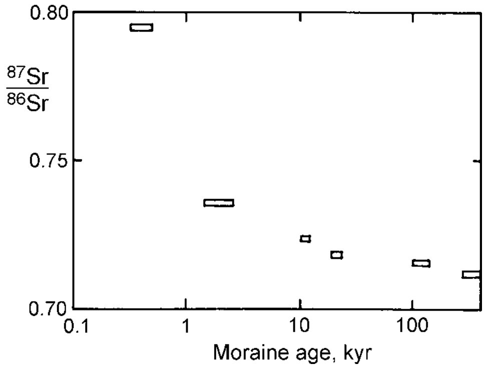

Fig. 3.36. Sr isotope ratio of ammonium acetate soil leachates plotted against the geological age of the moraines on which the soils were formed. After Blum and Erel (1995).

Blum and Erel (1995) attempted to quantify the amount of radiogenic Sr that could be released by glacial erosion. In order to do this, they used ammonium acetate leaching to analyse the isotopic composition of exchangeable Sr in glacial moraines. Weathered soils from six moraines in the Wind River Range, Wyoming, displayed a negative correlation between the isotopic composition of leachable Sr and the age of the soil (Fig. 3.36). Most notably, a very radiogenic $^{87}Sr/^{86}Sr$ ratio of 0.795 was obtained by leaching soil from the youngest (400-yr-old) moraine. Blum and Erel used these data to argue that a spike of radiogenic Sr is released by weathering of moraines immediately after glaciation. Modelling of this spike suggested that it could yield an incremental increase in $^{87}Sr/^{86}Sr$ of 0.00005 for each 100-kyr glacial cycle of the Quaternary period, thus reproducing (within error) the seawater evolution curve for this interval.

The glacial erosion model was further developed by Jacobson *et al.* (2002), who showed that this could also be a facet of Himalayan erosion. Analysis of exchangeable Sr from weathered moraines, together with the carbonate and silicate fractions, showed that a carbonate fraction as low as 1% by weight could nevertheless supply as much as 90% of soluble Sr to streams that are tributaries to the Indus River system. Although these observations might not be applicable to the whole Himalayan drainage system, they do show that the two competing explanations for Tertiary seawater Sr isotope evolution may be facets of a single model.

References

Albarède, F., Michard, A., Minster, J. F. and Michard, G. (1981). ^{87}Sr/^{86}Sr ratios in hydrothermal waters and deposits from the East Pacific Rise at 21 °N. *Earth Planet. Sci. Lett.* **55**, 229–36.

Armstrong, R. L. (1971). Glacial erosion and the variable isotopic composition of strontium in sea water. *Nature Phys. Sci.* **230**, 132–3.

Asmerom, Y., Jacobsen, S. B., Knoll, A. H., Butterfield, N. J. and Swett, K. (1991). Strontium isotopic variations of Neoproterozoic seawater: implications for crustal evolution. *Geochim. Cosmochim. Acta* **55**, 2883–94.

Basu, A. R., Jacobsen, S. B., Poreda, R. J., Dowling, C. B. and Aggarwal, P. K. (2001). Large groundwater strontium flux to the oceans from the Bengal Basin and the marine strontium isotope record. *Science* **293**, 1470–3.

Beckinsale, R. D., Pankhurst, R. J., Skelhorn, R. R. and Walsh, J. N. (1978). Geochemistry and petrogenesis of the early Tertiary lava pile of the Isle of Mull, Scotland. *Contrib. Mineral. Petrol.* **66**, 415–27.

Birck, J. L. and Allègre, C. J. (1978). Chronology and chemical history of the parent body of basaltic achondrites studied by the ^{87}Rb–^{87}Sr method. *Earth Planet. Sci. Lett.* **39**, 37–51.

Blum, J. D. and Erel, Y. (1995). A silicate weathering mechanism linking increases in marine ^{87}Sr/^{86}Sr with global glaciation. *Nature* **373**, 415–18.

Blum, J. D., Gazis, C. A., Jacobson, A. D. and Chamberlain, C. P. (1998). Carbonate versus silicate weathering in the Raikhot watershed within the High Himalayan Crystalline Series. *Geology* **26**, 411–14.

Bowring, S. A., Grotzinger, J. P., Isachsen, C. E., Knoll, A. H., Pelechaty, S. M. and Kolosov, P. (1993). Calibrating rates of Early Cambrian evolution. *Science* **261**, 1293–8.

Brand, U. and Veizer, J. (1980). Chemical diagenesis of a multicomponent carbonate system – 1: trace elements. *J. Sed. Petrol.* **50**, 1219–36.

Brannon, J. C., Podosek, F. A. and McLimans, R. K. (1992). Alleghenian age of the Upper Mississippi Valley zinc–lead deposit determined by Rb–Sr dating of sphalerite. *Nature* **356**, 509–11.

Brass, G. W. (1976). The variation of the marine ^{87}Sr/^{86}Sr ratio during Phanerozoic time: interpretation using a flux model. *Geochim. Cosmochim. Acta* **40**, 721–30.

Brinkman, G. A., Aten, A. H. W. and Veenboer, J. T. (1965). Natural radioactivity of K-40, Rb-87 and Lu-176. *Physica* **31**, 1305–19.

Brooks, C., Hart, S. R., Hofmann, A. and James, D. E. (1976a). Rb–Sr mantle isochrons from oceanic regions. *Earth Planet. Sci. Lett.* **32**, 51–61.

Brooks, C., James, D. E. and Hart, S. R. (1976b). Ancient lithosphere: its role in young continental volcanism. *Science* **193**, 1086–94.

Brown, E. H. (1971). Phase relations of biotite and stilpnomelane in the green-schist facies. *Contrib. Mineral. Petrol.* **31**, 275–99.

Burke, W. H., Denison, R. E., Hetherington, E. A., Koepnick, R. B., Nelson, H. F. and Otto, J. B. (1982). Variations of seawater ^{87}Sr/^{86}Sr throughout Phanerozoic time. *Geology* **10**, 516–19.

Catanzaro, E. J., Murphy, T. J., Garner, E. L. and Shields, W. R. (1969). Absolute isotopic abundance ratio and atomic weight of terrestrial rubidium. *J. Res. NBS* **73A**, 511–16.

Chaudhuri, S. and Clauer, N. (1986). Fluctuations of isotopic composition of strontium in seawater during the Phanerozoic eon. *Chem. Geol. (Isot. Geosci. Section)* **59**, 293–303.

Christensen, J. N., Halliday, A. N., Leigh, K. E., Randell, R. N. and Kesler, S. E. (1995a). Direct dating of sulfides by Rb–Sr: a critical test using the Polaris Mississippi Valley-type Zn–Pb deposit. *Geochim. Cosmochim. Acta* **59**, 5191–7.

Christensen, J. N., Halliday, A. N., Vearncombe, J. R. and Kesler, S. E. (1995b). Testing models of large-scale crustal fluid flow using direct dating of sulfides: Rb–Sr evidence for early dewatering and formation of Mississippi Valley-type deposits, Canning Basin, Australia. *Econ. Geol.* **90**, 877–84.

Clark, S. P. and Jäger, E. (1969). Denudation rate in the Alps from geochronologic and heat flow data. *Amer. J. Sci.* **267**, 1143–60.

Clauer, N. (1979). A new approach to Rb–Sr dating of sedimentary rocks. In: Jäger, E. and Hunziker, J. C. (Eds.), *Lectures in Isotope Geology.* Springer-Verlag, pp. 30–51.

Clauer, N., Keppens, E. and Stille, P. (1992). Sr isotopic constraints on the process of glauconitization. *Geology* **20**, 133–6.

Clemens, S. C., Farrell, J. W. and Gromet, L. P. (1993). Synchronous changes in seawater strontium isotope composition and global climate. *Nature* **363**, 607–10.

Clemens, S. C., Gromet, L. P. and Farrell, J. W. (1995). Artefacts in Sr isotope records. *Nature* **373**, 201.

Cliff, R. A. (1985). Isotope dating in metamorphic belts. *J. Geol. Soc. Lond.* **142**, 97–110.

Compston, W. and Jeffery, P. M. (1959). Anomalous common strontium in granite. *Nature* **184**, 1792–3.

Compston, W., McDougall, I. and Wyborn, D. (1982). Possible two-stage ^{87}Sr evolution in the Stockdale rhyolite. *Earth Planet. Sci. Lett.* **61**, 297–302.

Compston, W. and Pidgeon, R. T. (1962). Rubidium–strontium dating of shales by the total-rock method. *J. Geophys. Res.* **67**, 3493–502.

Compston, W., Williams, I. S., Kirschvink, J. and Zhang, Z. (1990). Zircon U–Pb ages relevant to the Cambrian numerical timescale. *Geol. Soc. Australia* **27**, 21 (abstract).

Cowie, J. W. and Johnson, M. R. W. (1985). Late Precambrian and Cambrian geological time-scale. In: Snelling, N. J. (Ed.), *The Chronology of the Geological Record. Mem. Geol. Soc. Lond.* **10**, 47–64.

Dasch, E. J. and Biscaye, P. E. (1971). Isotopic composition of strontium in Cretaceous-to-Recent, pelagic foraminifera. *Earth Planet. Sci. Lett.* **11**, 201–4.

Davis, D. W., Gray, J. and Cumming, G. L. (1977). Determination of the ^{87}Rb decay constant. *Geochim. Cosmochim. Acta* **41**, 1745–9.

Del Moro, A., Puxeddu, M., Radicati de Brozolo, F. and Villa, I. M. (1982). Rb–Sr and K–Ar ages on minerals at temperatures of 300–400 °C from deep wells in the Larderello geothermal field (Italy). *Contrib. Mineral. Petrol.* **81**, 340–9.

DePaolo, D. J. (1986). Detailed record of the Neogene Sr isotopic evolution of seawater from DSDP Site 590B. *Geology* **14**, 103–6.

DePaolo, D. J. (1987). Correlating rocks with strontium isotopes. *Geotimes* (December), 16–18.

Derry, L. A., Keto, L. S., Jacobsen, S. B., Knoll, A. H. and Swett, K. (1989). Sr isotopic variations in Upper Proterozoic carbonates from Svalbard and East Greenland. *Geochim. Cosmochim. Acta* **53**, 2331–9.

Dia, A. N., Cohen, A. S., O'Nions, R. K. and Shackleton, N. J. (1992). Seawater Sr isotope variation over the past 300 kyr and influence of global climate cycles. *Nature* **356**, 786–8.

Dodson, M. H. (1973). Closure temperature in cooling geochronological and petrological systems. *Contrib. Mineral. Petrol.* **40**, 259–74.

Dodson M. H. (1979). Theory of cooling ages. In: Jäger, E. and Hunziker, J. C. (Eds.), *Lectures in Isotope Geology.* Springer-Verlag, pp. 194–202.

Dunoyer de Segonzac, G. (1969). Les minéraux argileux dans la diagenèse. Passage au métamorphisme. *Mém. Serv. Carte Géol. Alsace Lorraine* **29**, 320 pp.

Elderfield, H. and Gieskes, J. M. (1982). Sr isotopes in interstitial waters of marine sediments from Deep Sea Drilling Project cores. *Nature* **300**, 493–7.

English, N. B., Quade, J., DeCelles, P. G. and Garzione, C. N. (2000). Geologic control of Sr and major element chemistry in Himalayan rivers, Nepal. *Geochim. Cosmochim. Acta* **64**, 2549–66.

Fairbairn, H. W., Hurley, P. M. and Pinson, W. H. (1961). The relation of discordant Rb–Sr mineral and rock ages in an igneous rock to its time of crystallization and subsequent Sr^{87}/Sr^{86} metamorphism. *Geochim. Cosmochim. Acta* **23**, 135–44.

Farrell, J. W., Clemens, S. C. and Gromet, L. P. (1995). Improved chronostratigraphic reference curve of late Neogene seawater $^{87}Sr/^{86}Sr$. *Geology* **23**, 403–6.

Faure, G., Hurley, P. M. and Powell, J. L. (1965). The isotopic composition of strontium in surface water from the North Atlantic Ocean. *Geochim. Cosmochim. Acta* **29**, 209–20.

Field D. and Raheim, A. (1979a). Rb–Sr total rock isotope studies on Precambrian charnockitic gneisses from South Norway: evidence for isochron resetting during a low-grade metamorphic-deformational event. *Earth Planet. Sci. Lett.* **45**, 32–44.

Field D. and Raheim, A. (1979b). A geologicaly meaningless Rb–Sr total rock isochron. *Nature* **282**, 497–9.

Flynn, K. F. and Glendenin, L. E. (1959). Half-life and β spectrum of Rb87. *Phys. Rev.* **116**, 744–8.

Gale, N. H., Beckinsale, R. D. and Wadge, A. J. (1979). A Rb–Sr whole rock isochron for the Stockdale rhyolite of the English Lake District and a revised mid-Paleozoic time-scale. *J. Geol. Soc. Lond.* **136**, 235–42.

Gast, P. W. (1955). Abundance of Sr^{87} during geologic time. *Bull. Geol. Soc. Amer.* **66**, 1449–64.

Grant, N. K., Laskowski, T. E. and Foland, K. A. (1984). Rb–Sr and K–Ar ages of Paleozoic glauconites from Ohio–Indiana and Missouri, USA. *Isot. Geosci.* **2**, 217–39.

Gray, C. M., Papanastassiou, D. A. and Wasserburg, G. J. (1973). The identification of early condensates from the solar nebula. *Icarus* **20**, 213–39.

Halliday, A. N. and Porcelli, D. (2001). In search of lost planets – the paleocosmochronology of the inner solar system. *Earth Planet. Sci. Lett.* **192**, 545–59.

Harris, N. (1995). Significance of weathering Himalayan metasedimentary rocks and leucogranites for the Sr isotope evolution of seawater during the early Miocene. *Geology* **23**, 795–8.

Harris, W. B. (1976). Rb–Sr glauconite isochron, Maestrichtian unit of Peedee Formation, North Carolina. *Geology* **4**, 761–2.

Henderson, G. M., Martel, D. J., O'Nions, R. K. and Shackleton, N. J. (1994). Evolution of seawater $^{87}Sr/^{86}Sr$ over the last 400 ka: the absence of glacial/interglacial cycles. *Earth Planet. Sci. Lett.* **128**, 643–51.

Hess, J., Bender, M. L. and Schilling, J. G. (1986). Evolution of the ratio of strontium-87 to strontium-86 in seawater from Cretaceous to present. *Science* **231**, 979–84.

Hodell, D. A., Mead, G. A. and Mueller, P. A. (1990). Variation in the strontium isotopic composition of seawater (8 Ma to present): implications for chemical weathering rates and dissolved fluxes to the oceans. *Chem. Geol. (Isot. Geosci. Section)* **80**, 291–307.

Hofmann, A. W. and Giletti, B. J. (1970). Diffusion of geochronologically important nuclides under hydrothermal conditions. *Eclogae Geol. Helv.* **63**, 141–50.

Hunziker, J. C. (1974). Rb–Sr and K–Ar age determination and the Alpine tectonic history of the Western Alps. *Mem. Ist. Geol. Min. Univ. Padova* **31**, 1–54.

Hurley, P. M., Cormier, R. F., Hower, J., Fairbairn, H. W. and Pinson, W. H. (1960). Reliability of glauconite for age measurement by K–Ar and Rb–Sr methods. *Amer. Assoc. Petrol. Geol. Bull.* **44**, 1793–808.

Jacobson, A. D. and Blum, J. D. (2000). Ca/Sr and $^{87}Sr/^{86}Sr$ geochemistry of disseminated calcite in Himalayan silicate rocks from Nanga Parbat: influence on river-water chemistry. *Geology* **28**, 463–6.

Jacobson, A. D., Blum, J. D., Chamberlain, C. P., Poage, M. A. and Sloan, V. F. (2002). Ca/Sr and Sr isotope systematics of a Himalayan glacial chronosequence: carbonate versus silicate weathering rates as a function of landscape surface age. *Geochim. Cosmochim. Acta* **66**, 13–27.

Jäger, E. (1973). Die alpine Orogenese im Lichte der radiometrischen Altersbestimmung. *Eclogae Geol. Helv.* **66**, 11–21.

Jäger, E., Niggli, E. and Wenk, E. (1967). Rb–Sr Altersbestimmungen an Glimmern der Zentralalpen. *Beitr. Geol. Karte Schweiz N.F.* **134**, 1–67.

Kaufman, A. J., Jacobsen, S. B. and Knoll, A. H. (1993). The Vendian record of Sr and C isotopic variations in seawater: implications for tectonics and paleoclimate. *Earth Planet. Sci. Lett.* **120**, 409–30.

Kubler, B. (1966). La cristallinité d'illite et les zones tout à fait supérieures du métamorphisme. *Colloque sur les étages tectoniques*. Université de Neuchâtel à la Baconnière Neuchâtel, pp. 105–22.

Lanphere, M. A., Wasserburg, G. J., Albee, A. L. and Tilton, G. R. (1964). Redistribution of strontium and rubidium isotopes during metamorphism, World Beater complex, Panamint Range, California. In: Craig, H., Miller, S. L. and Wasserburg, G. J. (Eds.), *Isotopic and Cosmic Chemistry*. North Holland Publishers, pp. 269–320.

MacLeod, K. G., Huber, B. T. and Fullagar, P. D. (2001). Evidence for a small (~0.000 030) but resolvable increase in seawater ^{87}Sr/^{86}Sr ratios across the Cretaceous–Tertiary boundary. *Geology* **29**, 303–6.

Martin, E. E. and Macdougall, J. D. (1991). Seawater Sr isotopes at the Cretaceous/Tertiary boundary. *Earth Planet. Sci. Lett.* **104**, 166–80.

McArthur, J. M., Howarth, R. J. and Bailey, T. R. (2001). Strontium isotope stratigraphy: LOWESS Version 3: best fit to the marine Sr-isotope curve for 0–509 Ma and accompanying look-up table for deriving numerical age. *J. Geol.* **109**, 155–7.

McArthur, J. M., Thirlwall, M. F., Engkilde, M., Zinsmeister, W. J. and Howarth, R. J. (1998). Strontium isotope profiles across K/T boundary sequences in Denmark and Antarctica. *Earth Planet. Sci. Lett.* **160**, 179–192.

McKerrow, W. S., Lambert, R. St J. and Chamberlain, V. E. (1980). The Ordovician, Silurian and Devonian time scales. *Earth Planet. Sci. Lett.* **51**, 1–8.

McMullen, C. C., Fritze, K. and Tomlinson, R. H. (1966). The half-life of rubidium-87. *Can. J. Phys.* **44**, 3033–8.

Minster, J.-F., Birck, J.-L. and Allègre, C. J. (1982). Absolute age of formation of chondrites studied by the ^{87}Rb–^{87}Sr method. *Nature* **300**, 414–19.

Morton, J. P. and Long, L. E. (1980). Rb–Sr dating of Palaeozoic glauconite from the Llano region, central Texas. *Geochim. Cosmochim. Acta* **44**, 663–72.

Nakai, S., Halliday, A. N., Kesler, S. E. and Jones, H. D. (1990). Rb–Sr dating of sphalerites from Tennessee and the genesis of Mississippi Valley type ore deposits. *Nature* **346**, 354–7.

Nakai, S., Halliday, A. N., Kesler, S. E., Jones, H. D., Kyle, J. R. and Lane, T. E. (1993). Rb–Sr dating of sphalerites from Mississippi Valley-type (MVT) ore deposits. *Geochim. Cosmochim. Acta* **57**, 417–27.

Neumann, W. and Huster, E. (1974). The half-life of ^{87}Rb measured as a difference between the isotopes of ^{87}Rb and ^{85}Rb. *Z. Physik* **270**, 121–7.

Neumann, W. and Huster, E. (1976). Discussion of the ^{87}Rb half-life determined by absolute counting. *Earth Planet. Sci. Lett.* **33**, 277–88.

Nicolaysen, L. O. (1961). Graphic interpretation of discordant age measurements on metamorphic rocks. *Ann. N.Y. Acad. Sci.* **91**, 198–206.

Odin, G. S. and Dodson, M. H. (1982). Zero isotopic age of glauconies. In: Odin, G. S. (Ed.), *Numerical Dating in Stratigraphy.* Wiley, pp. 277–305.

Odin, G. S., Gale, N. H. and Dore, F. (1985). Radiometric dating of Late Precambrian times. In: Snelling, N. J. (Ed.), *The Chronology of the Geological Record. Mem. Geol. Soc. Lond.* **10**, 65–72.

Palmer, M. R. and Edmond, J. M. (1989). The strontium isotope budget of the modern ocean. *Earth Planet. Sci. Lett.* **92**, 11–26.

Palmer, M. R. and Edmond, J. M. (1992). Controls over the strontium isotope composition of river water. *Geochim. Cosmochim. Acta* **56**, 2099–111.

Papanastassiou, D. A., Wasserburg, G. J. and Burnett, D. S. (1969). Initial strontium isotopic abundances and the resolution of small time differences in the formation of planetary objects. *Earth Planet. Sci. Lett.* **5**, 361–76.

Papanastassiou, D. A. and Wasserburg, G. J. (1970). Rb–Sr ages of lunar rocks from the Sea of Tranquillity. *Earth Planet. Sci. Lett.* **8**, 1–19.

Peterman, Z. E., Hedge, C. E. and Tourtelot, H. A. (1970). Isotopic composition of strontium in sea water throughout Phanerozoic time. *Geochim. Cosmochim. Acta* **34**, 105–20.

Pettke, T. and Diamond, L. W. (1996). Rb–Sr dating of sphalerite based on fluid inclusion–host mineral isochrons: a clarification of why it works. *Econ. Geol.* **91**, 951–6.

Pierson-Wickmann, A.-C., Reisberg, L. and France-Lanord, C. (2002). Impure marbles of the Lesser Himalaya: another source of continental radiogenic osmium. *Earth Planet. Sci. Lett.* **204**, 203–14.

Pinson, W. H., Schnetzler, C. C., Beiser, E., Fairbairn, H. W. and Hurley, P. M. (1963). Rb–Sr age of stony meteorites. *MIT Geochron. Lab. 11th Ann. Rep.* **NYO-10**, 517.

Popp, B. N., Podosek, F. A., Brannon, J. C., Anderson, T. F. and Pier, J. (1986). ^{87}Sr/^{86}Sr ratios in Permo-Carboniferous sea water from the analyses of well-preserved brachiopod shells. *Geochim. Cosmochim. Acta* **50**, 1321–8.

Provost, A. (1990). An improved diagram for isochron data. *Chem. Geol. (Isot. Geosci. Section)* **80**, 85–99.

Purdy, J. W. and Jäger, E. (1976). K–Ar ages on rock-forming minerals from the Central Alps. *Mem. Ist. Geol. Min. Univ. Padova* **30**, 3–31.

Raymo, M. E., Ruddiman, W. F. and Froelich, P. N. (1988). Influence of late Cenozoic mountain building on ocean geochemical cycles. *Geology* **16**, 649–53.

Richter, F. M. and DePaolo, D. J. (1987). Numerical models for diagenesis and the Neogene Sr isotope evolution of seawater from DSDP Site 590B. *Earth Planet. Sci. Lett.* **83**, 27–38.

Richter, F. M., Rowley, D. B. and DePaolo, D. J. (1992). Sr isotope evolution of seawater: the role of tectonics. *Earth Planet. Sci. Lett.* **109**, 11–23.

Rundberg, Y. and Smalley, P. C. (1989). High-resolution dating of Cenozoic sediments from northern North Sea using ^{87}Sr/^{86}Sr stratigraphy. *AAPG Bull.* **73**, 298–308.

Schreiner, G. D. L. (1958). Comparison of the Rb-87/Sr-87 ages of the red granite of the Bushveld complex from measurements on the total rock and separated mineral fractions. *Proc. Roy. Soc. Lond. A* **245**, 112–17.

Sheppard, T. J. and Darbyshire, D. P. F. (1981). Fluid inclusion Rb–Sr isochrons for dating mineral deposits. *Nature* **290**, 578–9.

Spooner, E. T. C. (1976). The strontium isotopic composition of seawater, and seawater–oceanic crust interaction. *Earth Planet. Sci. Lett.* **31**, 167–74.

Steiger, R. H. and Jäger, E. (1977). Subcommission on geochronology: convention on the use of decay constants in geo- and cosmo-chronology. *Earth Planet. Sci. Lett.* **36**, 359–62.

Sun, S. S. and Hanson, G. N. (1975). Evolution of the mantle: geochemical evidence from alkali basalt. *Geology* **3**, 297–302.

Tatsumoto, M. (1966). Genetic relations of oceanic basalts as indicated by lead isotopes. *Science* **153**, 1094–101.

Tilton, G. R. (1988). Age of the solar system. In: Kerridge, J. F. and Matthews, M. S. (Eds.), *Meteorites and the Early Solar System*, University of Arizona Press, pp. 259–75.

Tretbar, D. R., Arehart, G. B. and Christensen, J. N. (2000). Dating gold deposition in a Carlin-type gold deposit using Rb/Sr methods on the mineral galkhaite. *Geology* **28**, 947–50.

Veizer, J. and Compston, W. (1974). ^{87}Sr/^{86}Sr composition of seawater during the Phanerozoic. *Geochim. Cosmochim. Acta* **38**, 1461–84.

Veizer, J. and Compston, W. (1976). ^{87}Sr/^{86}Sr in Precambrian carbonates as an index of crustal evolution. *Geochim. Cosmochim. Acta* **40**, 905–14.

Veizer, J. Ala, D., Azmy, K. *et al.* (1999). ^{87}Sr/^{86}Sr, del ^{13}C and del 18O evolution of Phanerozoic seawater. *Chem. Geol.* **161**, 59–88.

Verschure, R. H., Andriessen, P. A. M., Boelrijk, N. A. I. M., Hebeda, E. H., Maijer, C., Prien, H. N. A. and Verdurmen, E. A. T. (1980). On the thermal stability of Rb–Sr and K–Ar biotite systems: evidence from co-existing Sveconorwegian (ca 870 Ma) and Caledonian (ca 400 Ma) biotites in S.W. Norway. *Contrib. Mineral. Petrol.* **74**, 245–52.

Wasserburg, G. J., Papanastassiou, D. A. and Sanz, H. G. (1969). Initial strontium for a chondrite and the determination of a metamorphism or formation interval. *Earth Planet. Sci. Lett.* **7**, 33–43.

Wetherill, G. W., Davis, G. L. and Lee-Hu, C. (1968). Rb–Sr measurements on whole rocks and separated minerals from the Baltimore Gneiss, Maryland. *Geol. Soc. Amer. Bull.* **79**, 757–62.

Wickman, F. E. (1948). Isotope ratios: a clue to the age of certain marine sediments. *J. Geol.* **56**, 61–6.

4 The Sm–Nd method

Sm is a rare-earth element with seven naturally occurring isotopes. Of these ^{147}Sm, ^{148}Sm and ^{149}Sm are all radioactive, but the latter two have such long half-lives (about 10^{16} yr) that they are not capable of producing measurable variations in the daughter isotopes of ^{144}Nd and ^{145}Nd, even over cosmological intervals (10^{10} yr). However the half-life of ^{147}Sm (106 Byr) is sufficiently short to produce small but measurable differences in the abundance of ^{143}Nd over periods of several million years, thus providing the basis for the Sm–Nd dating method. This half-life, equivalent to a decay constant of 6.54×10^{-12} yr^{-1}, is the weighted mean of several determinations, and yields ages consistent with U–Pb dating (Lugmair and Marti, 1978).

Another samarium isotope, ^{146}Sm, does not occur naturally, but has a relatively long half-life of 103 Myr. If Sm/Nd fractionation occurred within a few hundred million years of Sm nucleosynthesis then variations in the abundance of the daughter product, ^{142}Nd, might be observable in different terrestrial reservoirs. This subject will be discussed under the heading of 'extinct nuclides' (section 15.5.5).

4.1 Sm–Nd isochrons

Considering a given system, such as an igneous rock or mineral, we can write the following equation based on the decay of ^{147}Sm:

$$^{143}\mathrm{Nd} = {}^{143}\mathrm{Nd}_\mathrm{I} + {}^{147}\mathrm{Sm}(\mathrm{e}^{\lambda t} - 1) \qquad [4.1]$$

where I signifies initial abundance and t is the age of the system. In view of the possibility of variation in ^{142}Nd (due to ^{146}Sm), it is convenient to divide through by ^{144}Nd, the second most abundant isotope of Nd. Thus we obtain

$$\frac{^{143}\mathrm{Nd}}{^{144}\mathrm{Nd}} = \left(\frac{^{143}\mathrm{Nd}}{^{144}\mathrm{Nd}}\right)_\mathrm{I} + \frac{^{147}\mathrm{Sm}}{^{144}\mathrm{Nd}}(\mathrm{e}^{\lambda t} - 1) \qquad [4.2]$$

This equation has the same form as that for Rb–Sr (section 3.2) and can be plotted as an isochron diagram. However, because Sm and Nd have very similar chemical properties (unlike Rb and Sr), large ranges of Sm/Nd ratio in whole-rock systems are rare, and in particular, low Sm/Nd ratios near the y axis are very rare. Therefore, because of the difficulty of obtaining a wide range of Sm/Nd ratios from a single rock body, and because of the greater technical demands of Nd isotope analysis, the Sm–Nd isochron method was generally applied to problems for which Rb–Sr isochrons had proved unsatisfactory. Many of these applications were also made before the U–Pb zircon method had reached its present level of development (section 5.2.2). Therefore some of these units have subsequently been dated to greater accuracy and precision by the U–Pb method. However, it is important to review a few case studies to show the development of the method.

4.1.1 Meteorites

Chondritic meteorites have readily been dated by the Rb–Sr method, but achondrites are more problematical. Bulk samples usually have low Rb/Sr ratios, yielding ages of low precision, while separated minerals in many achondrites yield Rb–Sr ages below 4.5 Byr, indicative of disturbance. The Sm–Nd system in separated minerals from achondrites is more resistant to resetting, yielding better age estimates. The first Sm–Nd dating study was performed by Notsu *et al.* (1973) on the achondrite Juvinas, but with low analytical precision. Lugmair *et al.* (1975) obtained much more precise results on minerals from the same meteorite (Fig. 4.1) yielding an age of 4560 ± 80 Myr (2σ).

Numerous other basaltic achondrites have been dated by Sm–Nd measurements, and with the exception of Stannern (Lugmair and Scheinin, 1975), all yield ages in the range 4550–4600 Myr. These age determinations have since been superseded by Pb–Pb dating studies (section 5.3). However, the good agreement between the Sm–Nd and Pb–Pb dates has served the important function of confirming the ^{147}Sm half-life of 106 Byr.

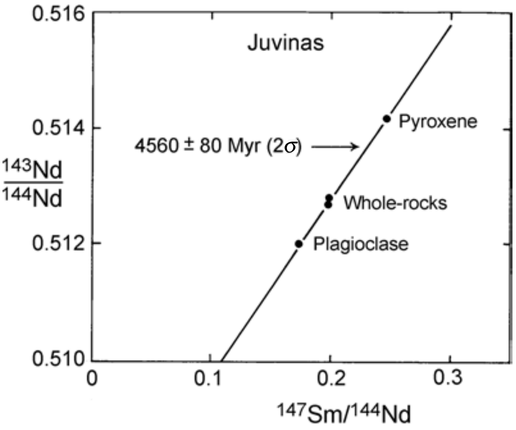

Fig. 4.1. Sm–Nd isochron for whole-rocks and minerals from the basaltic achondrite Juvinas. Nd isotope ratios are affected by the choice of normalising factor for mass fractionation. Data from Lugmair *et al.* (1975).

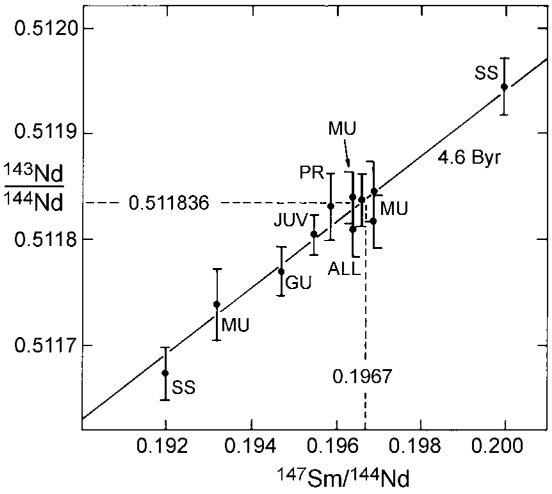

Fig. 4.2. Sm–Nd isochron diagram for whole-rock samples of six different chondrites. SS = St Severin; MU = Murchison; GU = Guarena; PR = Peace River; ALL = Allende; JUV = new analysis of the Juvinas achondrite. The large apparent errors are due to the very expanded axis scales. After Jacobsen and Wasserburg (1980).

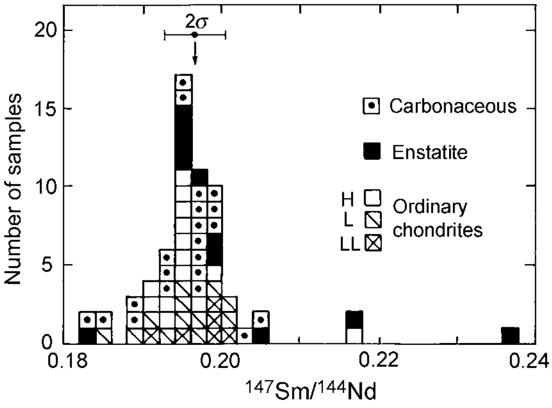

Fig. 4.3. Histogram of chondritic ^{147}Sm/^{144}Nd ratios determined from elemental analysis, compared with the value from Fig. 4.2 (arrow). Ordinary chondrites are subdivided into compositional classes (H, L and LL). After Jacobsen and Wasserburg (1980).

Sm–Nd dating of chondritic meteorites was not a high priority, due to the success of other methods. However, the isotopic composition of the chondrites is a critical benchmark for the evolution of solar-system bodies such as the Earth, because chondrites are believed to represent the nearest approach to the primordial solar nebula. DePaolo and Wasserburg (1976a) coined the acronym CHUR (chondritic uniform reservoir) for this benchmark, but in the absence of isotopic data for chondrites, had to use Lugmair *et al.*'s (1975) ^{143}Nd/^{144}Nd ratio of 0.511836 from the achondrite Juvinas as an indicator of the present-day CHUR value (using a fractionation normalisation to ^{146}Nd/^{142}Nd = 0.636151 for Nd analysis as the oxide).

This value was tested by direct Sm–Nd analysis of chondrites by Jacobsen and Wasserburg (1980). They obtained a whole-rock isochron with an age of about 4.6 Byr, but, more importantly, the measured ^{143}Nd/^{144}Nd ratios clustered closely around the original Juvinas measurment (dashed line in Fig. 4.2). The intersection of this value with the isochron regression led to a ^{147}Sm/^{144}Nd ratio of 0.1967 for CHUR. Jacobsen and Wasserburg compared this value with the average of 64 elemental Sm/Nd analyses of chondrites (Fig. 4.3), and demonstrated that there was good agreement between the two values.

In 1981, Wasserburg *et al.* revised the isotopic composition of their oxide correction and modified their recommended ^{143}Nd/^{144}Nd value for CHUR to 0.511847. However, most workers use the alternative normalisation convention (to ^{146}Nd/^{144}Nd = 0.7219) which was proposed by O'Nions *et al.* (1977) for Nd analysis as the metal (section 2.2.3). This leads to the corresponding present-day CHUR values: ^{143}Nd/^{144}Nd = **0.512638** and ^{147}Sm/^{144}Nd = **0.1966** (Hamilton *et al.*, 1983).

4.1.2 Low-grade meta-igneous rocks

The long half-life of ^{147}Sm makes it most useful for dating in the Precambrian. Therefore, most early Sm–Nd

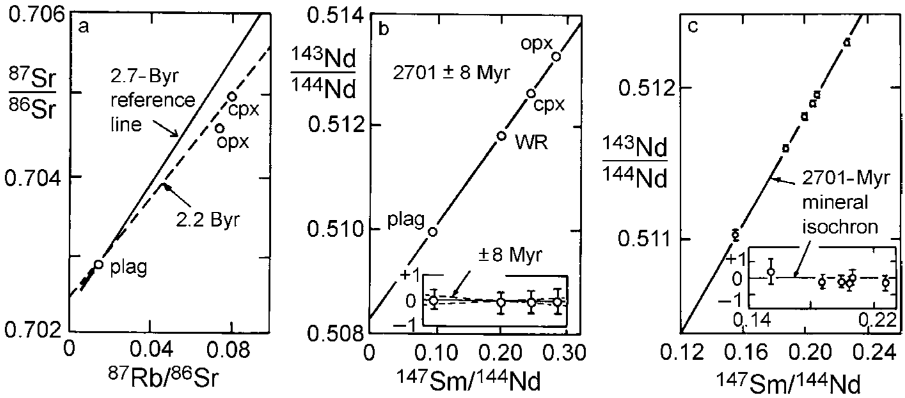

Fig. 4.4. Isochron diagrams for the Stillwater complex: (a) Rb–Sr diagram showing scatter of mineral data; (b) Sm–Nd mineral isochron; (c) whole-rock data with reference line from (b). After DePaolo and Wasserburg (1979).

work was focussed on the determination of crystallisation ages for Archean igneous rocks. In such suites the Rb–Sr and K–Ar methods had often revealed open-system behaviour, and precise U–Pb dates were not yet available. The Stillwater Complex (DePaolo and Wasserburg, 1979) provides a good example of such an application.

Rb–Sr data on three separated minerals from a single adcumulus unit of the Stillwater layered series form a scatter that does not define an isochron (Fig. 4.4a). This was attributed to open-system behaviour of Rb–Sr in minerals. However, Sm–Nd data on the same samples defined an excellent linear array (Fig. 4.4b), from which DePaolo and Wasserburg calculated an age of 2701 ± 8 Myr (2σ). The analysis of separated minerals provided a much greater range of Sm/Nd ratios than analysis of whole-rock samples, but raised the possibility that Sm–Nd mineral systems might have been opened by the event that disturbed Rb–Sr systems. To test for this, DePaolo and Wasserburg also analysed six whole-rock samples from different levels in the intrusion with a wide range of plagioclase/pyroxene abundances. Sm–Nd data from these samples fell within analytical uncertainty of the mineral isochron (Fig. 4.4c), suggesting that the mineral isochron yields a true crystallisation age for the intrusion, and that the magma had a homogeneous initial Nd isotope composition.

Subsequently, the Sm–Nd mineral age was corroborated by U–Pb dating of zircon from the chilled margin of the intrusion (Nunes, 1981), which gave an age of 2713 ± 3 Myr (2σ). However, Sm–Nd analysis of whole-rock samples from a wider stratigraphic range in the intrusion revealed larger variations of initial ratio (Lambert *et al.*, 1989). This is not surprising, since the initial ratio of DePaolo and Wasserburg falls well away from estimated mantle values at 2.7 Byr, and is best explained by contamination of the magma by old crustal Nd from the Wyoming craton.

The Stillwater data emphasise the importance of combined mineral and whole-rock isochrons to verify the accuracy of Sm/Nd ages. However, this approach is not possible for fine-grained rocks such as Archean basalts and komatiites. In these situations, whole-rock analysis has often been used alone, but subtle changes to the slopes of whole-rock isochrons can be caused by analysing samples with slight variations in crustal contamination. A good example is provided by the Kambalda volcanics of western Australia.

McCulloch and Compston (1981) determined a composite Sm–Nd isochron on a suite of rocks comprising the ore-bearing Kambalda ultramafic unit, the footwall and hanging-wall basalts, and an ‘associated’ sodic-granite and felsic porphyry. Although the whole suite yielded a good isochron age of 2790 ± 30 Myr (Fig. 4.5), the basic and ultra-basic samples alone gave an older best-fit age of 2910 ± 170 Myr.

The danger of constructing a ‘composite’ Sm–Nd isochron of acid, basic and ultra-basic rocks that might not be co-magmatic was pointed out by Claoué-Long *et al.* (1984). These workers attempted to date the Kambalda lavas by the Sm–Nd method without utilising acid rocks. However, they were forced to combine analyses from komatiites and basalts in order to achieve a good spread of Sm/Nd ratios (Fig. 4.6). After the exclusion of one komatiite point from Kambalda and a suite of basalt lavas from Bluebush (40 km south of the main Kambalda sequence), ten data points gave an age of 3262 ± 44 Myr (2σ). This was interpreted as the time of eruption.

Chauvel *et al.* (1985) challenged this interpretation on the basis that Pb–Pb dating of the Kambalda volcanics and associated igneous sulphide mineralisation gave an age of 2726 ± 34 Myr, which they argued to be resistant to re-setting by later events. They attributed the 3.2 Byr apparent Sm–Nd age to either variable crustal contamination of the magma suite by older basement, or possibly a heterogeneous mantle source. U–Pb dating of 3.4-Byr-old zircon xenocrysts in one of the hanging-wall basalts subsequently confirmed the contamination model (Compston *et al.*, 1985).

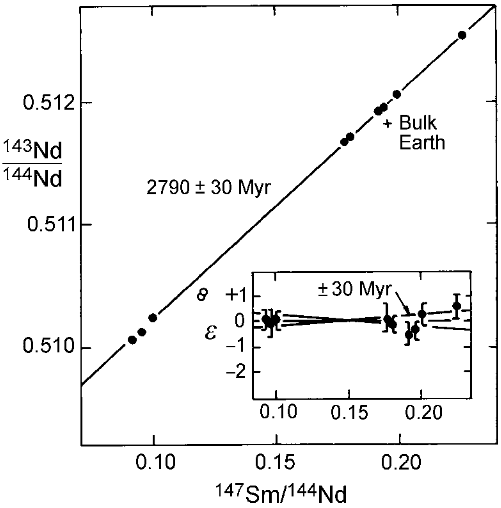

Fig. 4.5. Composite acid–basic Sm–Nd isochron diagram for a suite of Archean rocks from Kambalda, Western Australia. Open symbols were omitted from the regression. After McCulloch and Compston (1981).

In retrospect, danger signals can be seen in the whole-rock Sm–Nd data. Taken alone, the komatiites (including the sample rejected by Claoué-Long *et al.*) define a slope of less than 3.2 Byr, as do the Bluebush lavas (Fig. 4.6). Only the hanging-wall basalts define a slope of 3.2 Byr, but these are the samples which have probably suffered most contamination. Hence the data probably consist of a series of sub-parallel isochrons with about 2.7 Byr slope.

Similar effects have been demonstrated for komatiitic and basaltic lavas from Newton township in the Abitibi belt of Ontario. Cattell *et al.* (1984) obtained an apparent age of 2.83 Byr from a whole-rock Sm–Nd isochron of basic and ultra-basic lavas. However, a maximum eruption age of 2697 ± 1 Myr was conclusively demonstrated by U–Pb zircon analysis of an underlying dacitic volcaniclastic rock. Cattell *et al.* plotted initial ^{143}Nd/^{144}Nd ratios at 2697 Myr against the Sm/Nd ratio (Fig. 4.7), giving an erupted Sm–Nd isochron with an apparent age of 130 ± 64 Myr (MSWD = 2.52). No age significance was attached to this pseudo-isochron, which was attributed to sampling of a variably depleted mantle source. However, contamination by older crustal rock is a strong possibility.

4.1.3 High-grade metamorphic rocks

Most dating systems, including U–Pb zircon, can be re-set during high-grade metamorphic events. However, the Sm–Nd method provides an opportunity to

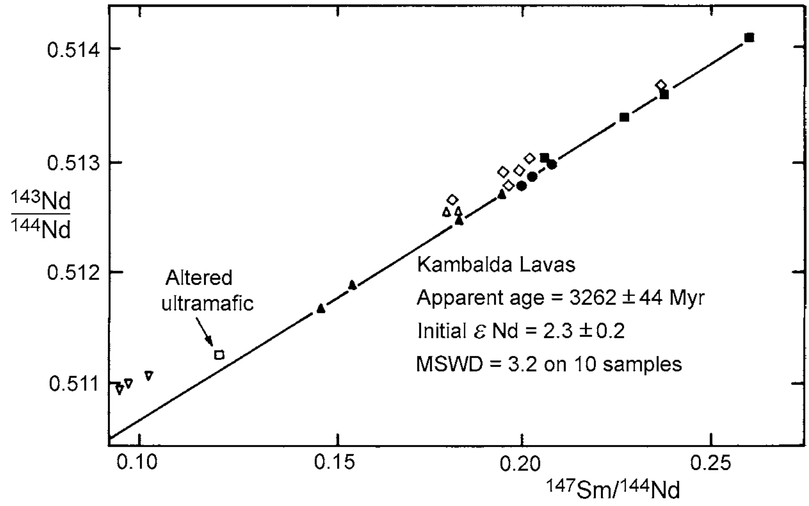

Fig. 4.6. Sm–Nd isochron diagram for whole-rock samples of Kambalda volcanics. (■) = komatiites; (▲) = hanging-wall basalts; (◇) = Bluebush lavas; (△) = 'ocelli' basalts; (▽) = granites. Modified after Claouè-Long *et al.* (1984).

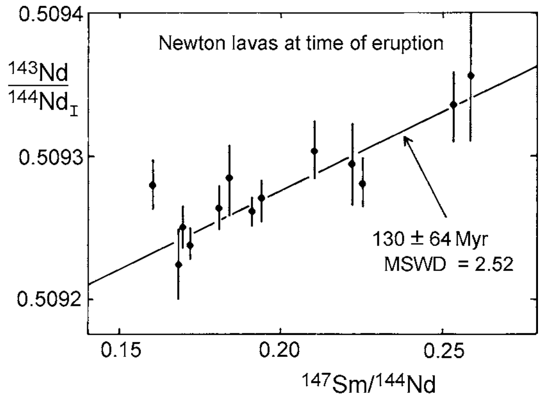

Fig. 4.7. Sm–Nd pseudo-isochron diagram for whole-rock samples of komatiite and basalt from Newton township, Ontario. The large apparent errors and scatter of data are due to the very expanded *y*-axis scale. After Cattell *et al.* (1984).

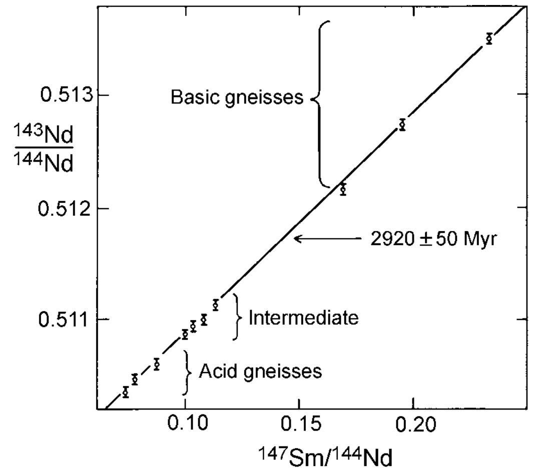

Fig. 4.8. Sm–Nd isochron for a mixed suite of granitic, tonalitic and layered basic gneisses from the Lewisian complex of NW Scotland, yielding an age of 2920 Myr. After Hamilton *et al.* (1979).

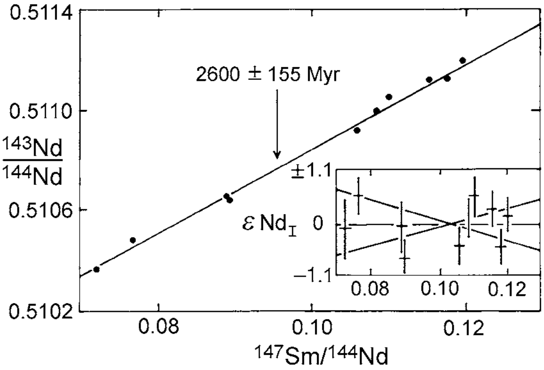

Fig. 4.9. Sm–Nd 'errorchron' for Lewisian tonalitic gneisses, defining an age of 2600 Myr, attributed to granulite-facies metamorphism. After Whitehouse (1988).

determine igneous protolith ages in high-grade metamorphic gneiss terranes where other systems are re-set. An example is provided by dating work on the Lewisian gneisses of NW Scotland. Whole-rock Rb–Sr, whole-rock Pb–Pb and U–Pb zircon ages on granulite-facies and amphibolite-facies gneisses are concordant at 2630 ± 140, 2680 ± 60 and 2660 ± 20 Myr (2σ), respectively (Moorbath *et al.*, 1975; Chapman and Moorbath, 1977; Pidgeon and Bowes, 1972). However, these gneisses are generally very Rb- and U-depleted, suggesting that even large whole-rock samples were probably open systems for these elements during the depletion event.

A suite of whole-rock samples was dated by the Sm–Nd method (Hamilton *et al.*, 1979) to see whether this system had remained undisturbed during the Badcallian metamorphic event which the other systems are presumed to date. An older age of 2920 ± 50 Myr (2σ) suggested that the gneisses had remained closed systems for Sm–Nd during granulite-facies metamorphism (Fig. 4.8). Hamilton *et al.* therefore interpreted the age as the time of protolith formation, which occurred 200–300 Myr before the closing of U–Pb zircon and whole-rock Rb–Sr and Pb–Pb systems following metamorphism.

Despite the good quality of the Sm–Nd isochron, there are two problems with the sample selection. Firstly, the sample suite combined amphibolite- and granulite-facies gneisses, and secondly it contained a bimodal petrological suite, including tonalitic gneisses and basic rocks from the Drumbeg layered complex. Nevertheless, because the slope ages of the tonalites and mafic gneisses are very similar, the samples as a whole display good linearity, with an MSWD value of only 1.3 (using 1σ errors of 0.1% for Sm/Nd, and the individual within-run isotopic errors).

More detailed investigation by Whitehouse (1988) showed that the Drumbeg layered basic rocks retain a 2.91 Byr isochron age, but Sm–Nd whole-rock systems in intermediate-to-acid rocks have been re-set to the same age as the U–Pb zircon and other whole-rock systems. Ten samples of the latter suite define an errorchron with MSWD = 5.7, yielding an age (with estimate of geological error) of 2600 ± 155 Myr (2σ), shown in Fig. 4.9. Therefore, the isochron of Hamilton *et al.* (1979) apparently does correctly date the time of protolith formation, but only the basic rocks remained closed systems during the Badcallian event. This work shows that even whole-rock Sm–Nd isochrons can be perturbed by granulite-facies metamorphism. However, it will be shown below that Sm–Nd *model ages* can preserve the approximate protolith ages of the intermediate gneisses, even though the isochron is disturbed (section 4.3.3). These model ages agree with the isochron age for the Drumbeg basic pluton.

4.1.4 High-grade metamorphic minerals

Another area where the Sm–Nd isochron method has been widely applied is the dating of high-grade metamorphic minerals. For example, garnet and clinopyroxene (cpx) have mirror-image distribution coefficients for rare-earth elements (REE), giving rise to a large range of Sm/Nd ratios and hence allowing precise age determinations. The classic example of a garnet–cpx rock is eclogite, so this has been a major focus of Sm–Nd mineral dating. However, the relative immobility of the REE, which is such an asset in dating igneous crystallisation, is a problem in using the Sm–Nd method to date metamorphism. Mineral systems may be opened sufficiently to disrupt the original igneous chemistry, but not enough to overprint the system completely. An example is provided by the dating of Caledonian eclogites by Mørk and Mearns (1986).

Some gabbros from western Norway were transformed to an eclogite mineralogy (garnet and omphacite), but retained a relict igneous texture. These samples did not reach isotopic equilibrium during Caledonian metamorphism. In contrast, nearby country-rocks that had been transformed into eclogite generated a mineral isochron with very low scatter (MSWD = 0.1) and a typical Caledonian metamorphic age of 400 ± 16 Myr. The contrasting behaviour of the two types of eclogite cannot be attributed to variable P, T conditions, since they are from within 1 km of each other. However, the country-rock eclogite had completely lost its pre-existing texture due to penetrative deformation and recrystallisation. Mørk and Mearns suggested that such physical disruption might be necessary to achieve complete Nd isotopic equilibrium between metamorphic mineral phases.

Examination of the metagabbro Sm–Nd data at 400 Myr (Fig. 4.10) suggests that the main obstacle to isotopic homogenisation in this rock was the cpx phase. Because the transformation of augite into omphacite requires relatively minor cation exchange, complete resetting of the Sm–Nd system in this mineral rarely occurs. In contrast, major chemical exchange and structural reorganisation are required to replace plagioclase with garnet, so complete re-setting is more likely. Hence, garnet–whole-rock isochrons are more reliable than the garnet–cpx pairs used in early dating work on eclogites (e.g. Griffin and Brueckner, 1980).

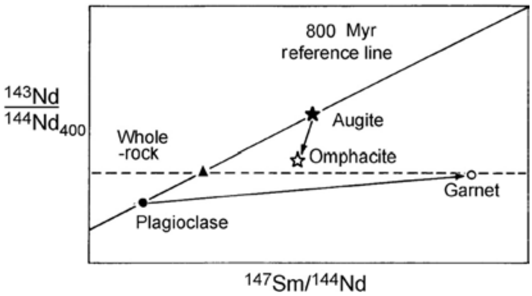

Fig. 4.10. Schematic illustration of the process of Sm–Nd re-mobilisation during the replacement of gabbro by an eclogite mineralogy. Modified after Mørk and Mearns (1986).

Vance and O'Nions (1990) argued that garnet chronology provides a powerful tool for dating prograde metamorphism, in contrast to other methods, such as Ar–Ar and Rb–Sr, which date metamorphic cooling (section 10.5). Garnets are widely distributed in meta-pelitic rocks and develop in response to the changing P, T conditions of prograde metamorphism. Their chemistry (including the Sm–Nd system) is usually preserved during cooling because cation-diffusion rates in garnet are very slow. The chemical composition of garnets can be used to calculate the P, T conditions of their growth, which, combined with age data, provide a method of determining progradational P, T – time paths for high-grade metamorphic terranes. An application of this technique was demonstrated by Burton and O'Nions (1991) in a study of Caledonian regional metamorphism of a Proterozoic supracrustal sequence at Sulitjilma, northern Norway.

Burton and O'Nions dated garnet growth in adjacent graphite-bearing and graphite-free bands using the Sm–Nd and U–Pb isochron methods. An example is shown in Fig. 4.11 for a case where garnet rims and cores are distinct. The rims yield a slightly younger age, as would be expected. Note that the core is regressed with the whole-rock composition, whereas the rim is regressed with the matrix of the rock only, since this is the only part of the rock with which the rims were in diffusional contact at the time of their growth.

Concordant results for the Sm–Nd and U–Pb techniques provide strong evidence that the ages for garnet–matrix pairs are dating prograde mineral growth. When these ages are coupled with temperature data (Fig. 4.12), they indicate that garnet growth occurred first in the graphite-bearing assemblage and

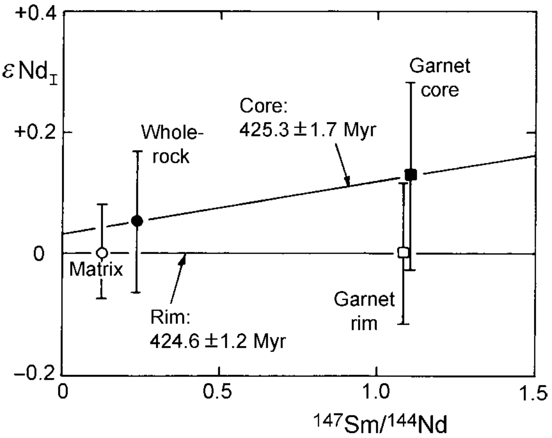

Fig. 4.11. Sm–Nd isochrons for whole-rock–garnet-core, and matrix–garnet-rim pairs from a graphite-free metapelite. Error bars indicate within-run precision. After Burton and O'Nions (1991).

subsequently, at higher temperatures, in the graphite-free assemblage. Peak metamorphic conditions were registered by the garnet rims of the latter assemblage. Hence, an average heating rate of 9 °C/Myr was calculated. On the other hand, Rb–Sr mineral ages on muscovite and biotite were used to deduce a cooling rate of 4 °C/Myr (Fig. 4.12).

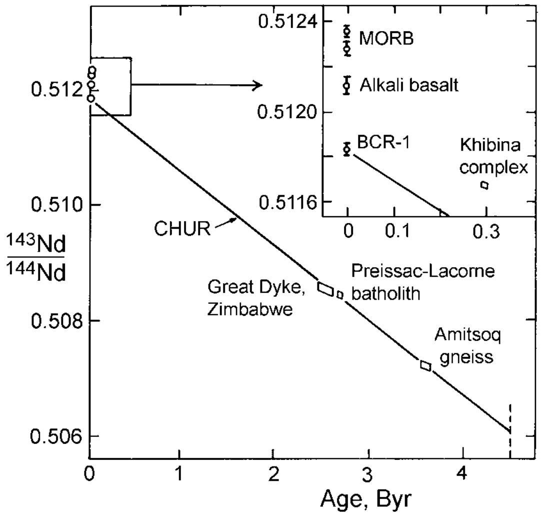

Fig. 4.13. Diagram of ^{143}Nd/^{144}Nd ratio against time, showing the close correspondence of early Nd isotope analyses of terrestrial igneous rocks to the chondritic growth line. BCR-1 = Columbia River basalt, USA. After DePaolo and Wasserburg (1976a).

4.2 Nd isotope evolution and model ages

DePaolo and Wasserburg (1976a) made the first Nd isotope determinations on terrestrial igneous rocks. When they plotted the ages and initial ^{143}Nd/^{144}Nd ratios of these units on a diagram of Nd isotope evolution against time, they found that Archean plutons had initial ratios that were remarkably consistent with the evolution of the chondritic uniform reservoir (CHUR) observed in meteorites (Fig. 4.13). The CHUR evolution path is normally drawn as a straight line, but in fact it is a very gentle curve, due to the finite half-life of ^{147}Sm (about 106 Byr).

Because Sm and Nd are REE with atomic numbers only two units apart, their chemical properties are very similar, and they undergo only slight relative fractionation during crystal–liquid processes. This means that in terrestrial rocks, departures of ^{143}Nd/^{144}Nd

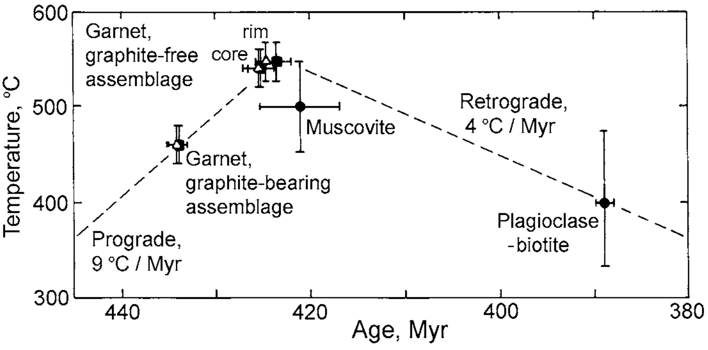

Fig. 4.12. Temperature–time diagram for Sulitjilma supracrustals, northern Norway. The progradational heating rate is from garnet Sm–Nd ages (△) and U–Pb ages (■). The retrogressive cooling rate is from Rb–Sr ages (●). After Burton and O'Nions (1991).

ratio from the CHUR evolution line are small relative to the steepness of the line (Fig. 4.13). DePaolo and Wasserburg therefore developed a notation whereby initial $^{143}\text{Nd}/^{144}\text{Nd}$ isotope ratios could be represented in parts per 10^4 deviation from the CHUR evolution line, termed epsilon units (ε Nd). Mathematically, this notation is defined as

$$\varepsilon\ \text{Nd}(t) = \left(\frac{(^{143}\text{Nd}/^{144}\text{Nd})_{\text{sample}}(t)}{(^{143}\text{Nd}/^{144}\text{Nd})_{\text{CHUR}}(t)} - 1\right) \times 10^4 \quad [4.3]$$

where t indicates the time at which ε Nd is calculated. The ε notation makes it much easier to compare the initial Nd isotope ratios of bodies of different ages. Also, by normalising all data with respect to CHUR, it removes the effects of the different fractionation corrections which have been applied for Nd analysis as the metal or as the oxide species.

Using the ε notation, DePaolo and Wasserburg (1976b) presented a larger data set of Nd isotope analyses on a diagram of ε Nd against time (Fig. 4.14). They noted that continental igneous rocks through time had ε Nd values very close to zero. Indeed, for Archean rocks the error bars overlapped with zero, suggesting that continental igneous rocks were 'derived from a reservoir with a chondritic REE pattern, which may represent primary material remaining since the formation of the Earth.'

4.2.1 Chondritic model ages

DePaolo and Wasserburg (1976b) argued that, if the CHUR evolution line defines the initial ratios of continental igneous rocks through time, measurement of $^{143}\text{Nd}/^{144}\text{Nd}$ and $^{147}\text{Sm}/^{144}\text{Nd}$ ratios in any crustal rock would yield a model age for the formation of that rock (or its precursor) from the chondritic reservoir. This is true, providing that there was sufficient Nd/Sm fractionation during the process of crustal extraction from the mantle to give a reasonable divergence of crustal and mantle evolution lines (Fig. 4.15) and hence a precise intersection. The model age is then given as

$$T_{\text{CHUR}} = \frac{1}{\lambda}\ln\left[1 + \frac{\left(\frac{^{143}\text{Nd}}{^{144}\text{Nd}}\right)^0_{\text{sample}} - \left(\frac{^{143}\text{Nd}}{^{144}\text{Nd}}\right)^0_{\text{CHUR}}}{\left(\frac{^{147}\text{Sm}}{^{144}\text{Nd}}\right)^0_{\text{sample}} - \left(\frac{^{147}\text{Sm}}{^{144}\text{Nd}}\right)^0_{\text{CHUR}}}\right] \quad [4.4]$$

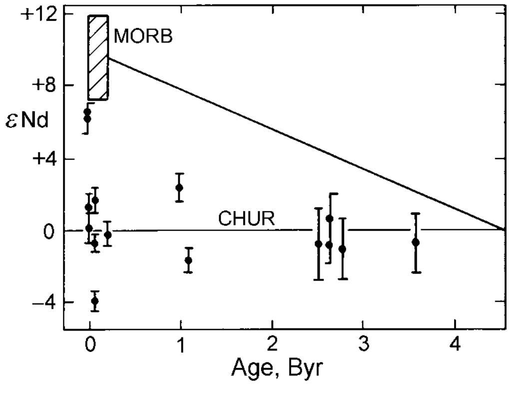

Fig. 4.14. Diagram of Nd isotope evolution against time in the form of deviations from the chondritic evolution line in ε units. MORB = mid-ocean-ridge basalts. After DePaolo and Wasserburg (1976b).

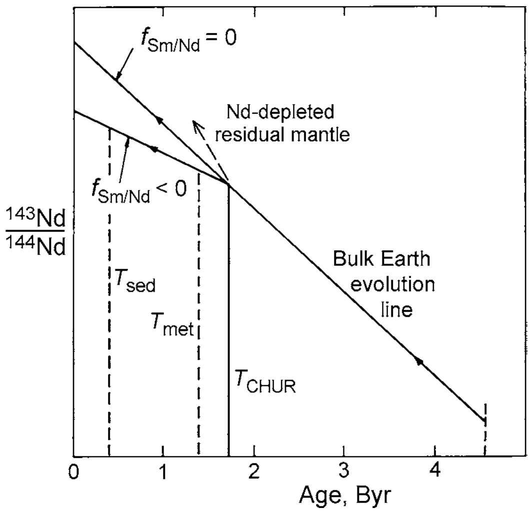

Fig. 4.15. Schematic Nd isotope evolution diagram, showing the theory of model ages. T_{met} = age of metamorphic event; T_{sed} = age of erosion–sedimentation event; f = fractionation of sample Sm/Nd relative to Bulk Earth. The dashed vector shows the development of the depleted mantle as a result of crustal extraction. After McCulloch and Wasserburg (1978).

DePaolo and Wasserburg argued that, if the Sm/Nd ratio of a rock sample had not been disturbed since its separation from the chondritic reservoir (taken to be the mantle source), then T_{CHUR} might provide a 'crustal-formation' age for a wide variety of rocks. Elemental investigations have indicated the general immobility of REE on a whole-rock scale during the processes of weathering and low-temperature metamorphism associated with sedimentary-rock formation (e.g. Haskin *et al.*, 1966), and even during high-grade metamorphism (Green *et al.*, 1969). This immobility is schematically illustrated by the lack of deflection in the evolution line of a crustal rock sample in Fig. 4.15 during metamorphic and sedimentary events. Hence, Nd model ages may be able to date crustal formation in rocks that have been subjected to high-grade metamorphism and even erosion–sedimentation.

These premises were applied by McCulloch and Wasserburg (1978) in a model age study aimed at measuring the crustal-formation ages of several cratonic rock bodies, mainly from the Canadian Shield. McCulloch and Wasserburg found Nd model ages within the range 2.5–2.7 Byr for composite samples of the Superior, Slave, and Churchill structural provinces. In the first two areas, previously determined K–Ar and Rb–Sr ages had given the same results, but the 2.7 Byr model age for the Churchill province was 0.8 Byr older than the previously determined K–Ar age, which presumably had been re-set by more recent metamorphism. These data supported a model of episodic continental growth by showing the period 2.5–2.7 Byr ago to be a time of remarkably widespread continental growth. In contrast, a Grenville province composite yielded a model age of 0.8 Byr, which did not reveal any Archean component, suggesting it to be an addition of more recent crust to the pre-existing shield. However, this sample was by no means representative of the Grenville Province as a whole, which also contains extensive areas of reworked Archean and Early Proterozoic crust (Dickin, 2000).

Although Nd model ages are generally applied to dating the time of crustal separation from the mantle, other, more specialised applications have been made. For example, Richardson *et al.* (1984) investigated the time of diamond formation in the South African mantle lithosphere by dating garnet inclusions in diamonds. Three samples were analysed, each consisting of a composite of several hundred sub-calcic garnet inclusions and yielding a total of 10–45 ng Nd. The unradiogenic Nd in these samples gave T_{CHUR} ages of 3.19–3.41 Byr (Fig. 4.16). When this evidence is combined with evidence of sub-solidus temperatures for diamond growth (based on equilibrium garnet–olivine inclusions in diamonds), it suggests that subcontinental lithosphere has existed under the African craton since the Early Archean. This material may represent the residue from 3.5-Byr-old komatiite extraction (section 7.1).

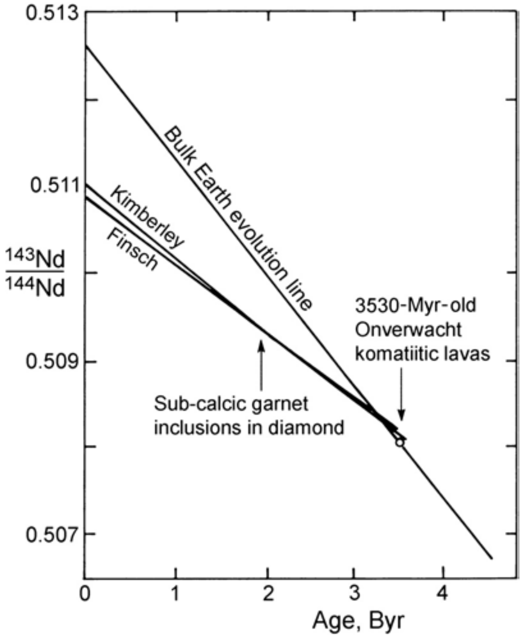

Fig. 4.16. ^{143}Nd isotope evolution diagram showing model age calculations for silicate inclusions in South African diamonds. The initial ratio of Onverwacht lavas is shown for comparison. After Richardson *et al.* (1984).

4.2.2 Depleted-mantle model ages

While observing the good fit of Archean plutons to the CHUR Nd isotope evolution line, DePaolo and Wasserburg (1976b) also noted that young mid-ocean-ridge basalts (MORB) lay $+7$ to $+12\ \varepsilon$ units above the CHUR evolution line (Fig. 4.14). They recognised that Archean continental igneous rocks that fall within error of the CHUR evolution line could conceivably lie on a depleted-mantle evolution line characterised by progressively increasing Sm/Nd and ^{143}Nd/^{144}Nd ratios. Such a source could be formed as a residue from magma extraction, as shown in Fig. 4.15. However, DePaolo and Wasserburg rejected this model in favour of a chondritic source for continental igneous rocks on the basis of a comparison with lunar Nd isotope evolution.

Lunar basalts and troctolites with ages of 3.3–4.3 Byr exhibit a wide range of initial ^{143}Nd/^{144}Nd ratios, equivalent to a variation from $+7$ to $-2\ \varepsilon$ units relative to CHUR (Fig. 4.17; Lugmair and Marti, 1978). This spread shows that very early Sm/Nd fractionation occurred in the Moon, and that there was no long-lived uniform magma source with a chondritic Sm/Nd ratio. In contrast, none of the Archean terrestrial rocks analysed by 1976 exhibited any dispersion outside error of CHUR, which led DePaolo and Wasserburg (1976b) to conclude that the Earth did not undergo early differentiation, or if it did, that this was re-mixed by convection.

The paucity of Nd isotope data for the Proterozoic was a serious weakness in this model, since it left

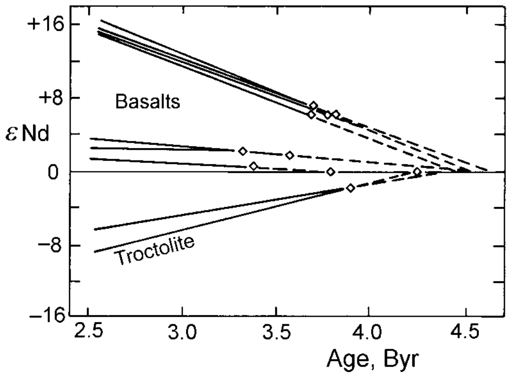

Fig. 4.17. ε Nd evolution diagram for lunar rocks, indicating very early Sm/Nd fractionation between lunar reservoirs. After Lugmair and Marti (1978).

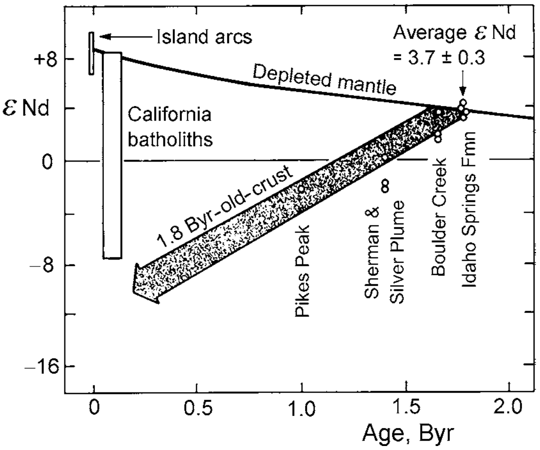

Fig. 4.18. Plot of ε Nd against time, showing Colorado data relative to a model depleted-mantle evolution curve. After DePaolo (1981).

a gap between the Archean CHUR data and the depleted MORB source (attributed to an elevated Sm/Nd ratio), with questions about the relationship between the two. An important stage in filling this gap was a study on Proterozoic metamorphic basement from the Colorado Front Range (DePaolo, 1981). Four metavolcanics and two charnockitic granulites from the Idaho Springs Formation were dated by the Sm–Nd isochron method. In addition, Nd isotope and Sm/Nd determinations were made on three plutons previously dated by the Rb–Sr whole-rock method (the Boulder Creek, Silver Plume and Pikes Peak granitoids). The initial ^{143}Nd/^{144}Nd ratios of all these samples are plotted on an ε Nd *versus* time diagram in Fig. 4.18.

The Idaho Springs meta-igneous rocks cluster at $\varepsilon\,\mathrm{Nd}(t) = +3.7 \pm 0.3$, showing them to be derived from a depleted mantle reservoir with respect to CHUR at 1.8 Byr. Boulder Creek samples also have positive ε Nd (+1.7 to +3.5), whereas the Silver Plume and Pikes Peak granites have progressively lower ε Nd values which lie on the ^{143}Nd/^{144}Nd evolution line of average Idaho Springs crust, suggesting that they contain a large fraction of re-melted 1.8-Byr-old basement.

DePaolo was able to fit a quadratic curve to Idaho Springs and modern island-arc data (Fig. 4.18), representing the Nd isotope evolution of a progressively depleted reservoir that was the source area for calc-alkaline (subduction-related) magmatism. This curve begins on the CHUR evolution line in the Early Archean, but diverges progressively to the present day. The composition of the depleted reservoir, relative to the CHUR, at time T, is given as

$$\varepsilon\,\mathrm{Nd}(T) = 0.25T^2 - 3T + 8.5 \qquad [4.5]$$

Sm–Nd model ages calculated using this depleted-mantle curve are denoted T_{DM}. DePaolo argued that T_{DM} model ages would be a more accurate indication of 'crustal formation ages' than T_{CHUR} ages for studies of continental evolution. For example, an anomalously low T_{CHUR} age of 0.8 Byr for McCulloch and Wasserburg's Grenville composite (section 4.2.1) was revised to a T_{DM} age of 1.3 Byr, within the range expected for juvenile crust formation during the Grenville orogeny.

Subsequent to the discovery of Proterozoic depleted mantle by DePaolo (1981), new analyses have prompted several re-interpretations of the evolution of the depleted-mantle reservoir. An important alternative to DePaolo's (1981) model was proposed by Goldstein *et al.* in 1984 (Fig. 4.19). This model assumes linear depletion of the mantle from $\varepsilon\,\mathrm{Nd} = 0$ at 4560 Myr to $\varepsilon\,\mathrm{Nd} = +10$ at 0 Myr (the MORB composition). It also provides a good fit to Early Proterozoic greenstones from the SW USA and Greenland (Nelson and DePaolo, 1984; Patchett and Arndt, 1986). The most depleted ε Nd values in these suites may represent flood basalts erupted in rifting environments that suffered little crustal contamination. Goldstein *et al.* denoted Nd model ages based on this mantle model as T_{CR} (crustal residence). However, this is not the most appropriate mantle model for calculating crustal-extraction ages of tonalitic crust-forming rocks generated in arc settings, which at the present day have less depleted Nd isotope signatures than spreading ridges.

More recently, Nägler and Kramers (1998) reverted to a model involving essentially chrondritic mantle evolution until 3 Byr ago, followed by more or less

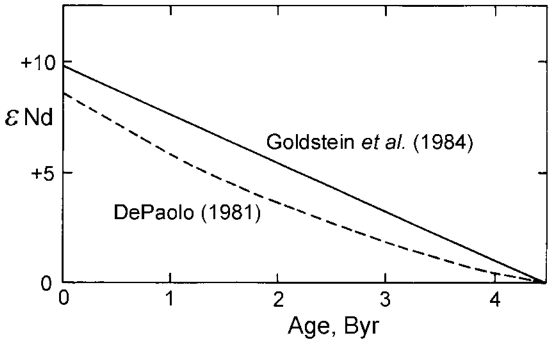

Fig. 4.19. Plot of ε Nd against time, showing two of the most widely used depleted-mantle evolution models. Dashed curve: DePaolo (1981); solid line: Goldstein *et al.* (1984).

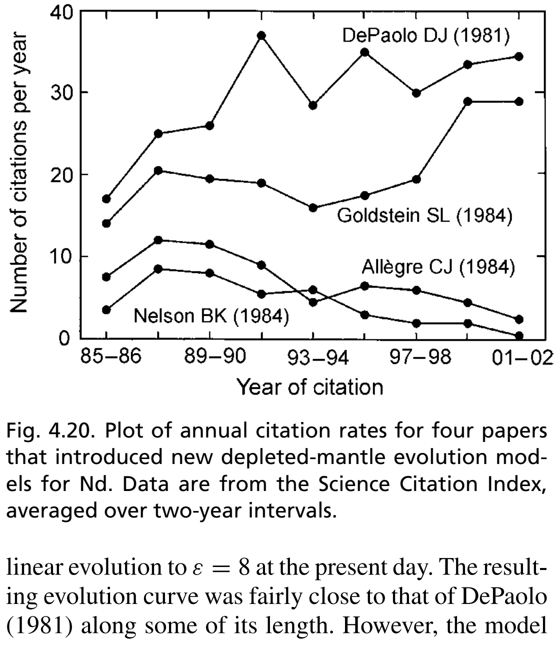

Fig. 4.20. Plot of annual citation rates for four papers that introduced new depleted-mantle evolution models for Nd. Data are from the Science Citation Index, averaged over two-year intervals.

linear evolution to $\varepsilon = 8$ at the present day. The resulting evolution curve was fairly close to that of DePaolo (1981) along some of its length. However, the model of Nägler and Kramers was constrained to fit the average ε Nd values of a wide variety of different rock types, some of which (e.g. the Stillwater Complex) have been shown to exhibit crustal contamination. The result is a model that does not seem to be in tune with recent thinking about depleted-mantle evolution in the Archean (section 4.4.3).

There has been a tendency towards a proliferation of depleted-mantle models as new data for various geographical areas become available. However, an examination of the literature suggests that the models of DePaolo (1981) and Goldstein *et al.* (1984) have had the widest application by other workers. This is illustrated in Fig. 4.20 by a comparison of citation rates for these two studies, compared with two control papers: Nelson and DePaolo (1984), discussed above, and Allègre and Rousseau (1984), who proposed a curved mantle-evolution line similar to that of DePaolo (1981). The durability of citations for DePaolo (1981) and Goldstein *et al.* (1984) indicates the wide usefulness of these mantle models, which therefore provide an important basis for the comparison of different magma suites, even if the absolute values of the model ages are slightly in error. Hence it is desirable that the T_{DM} and T_{CR} notations should be restricted to the models of DePaolo (1981) and Goldstein *et al.* (1984), while other acronyms can be used to denote different models.

4.3 Model ages and crustal processes

As outlined above, one of the principal uses of the Sm–Nd model age method is to determine what are often called 'crustal-formation' or 'crustal-extraction' ages. However, the model age method is most often applied when a long or complicated geological history precludes a more direct method of determining crustal age. One of the strengths of the Sm–Nd model age method, as applied to whole-rock systems, is that it provides the opportunity to see back through erosion, sedimentation, high-grade metamorphism and even crustal melting events, which usually re-set other dating methods. However, these processes may cause complications in the interpretation of model ages. Hence, it is important to examine Sm–Nd systematics in well-constrained examples in order to estimate the reliability of model ages in more complex environments.

4.3.1 Sedimentary systems

The behaviour of the Sm–Nd system during erosion can be examined by comparing the calculated model ages of river-borne particulates with the average geological age of sediment sources in the watershed. Goldstein and Jacobsen (1988) performed such a study on particulates in American rivers. They found that rivers draining primary igneous rocks carried sediment that accurately reflected the crustal-residence age of the source (Fig. 4.21). Rivers draining sedimentary watersheds were not properly testable, since the crustal-residence age of their sources had not been quantified adequately.

The behaviour of the Sm–Nd system during sedimentation can be further tested by comparing Nd model ages of different size-fractions of sediment. In an early study on bottom sediment from the Amazon River, Goldstein *et al.* (1984) found that different

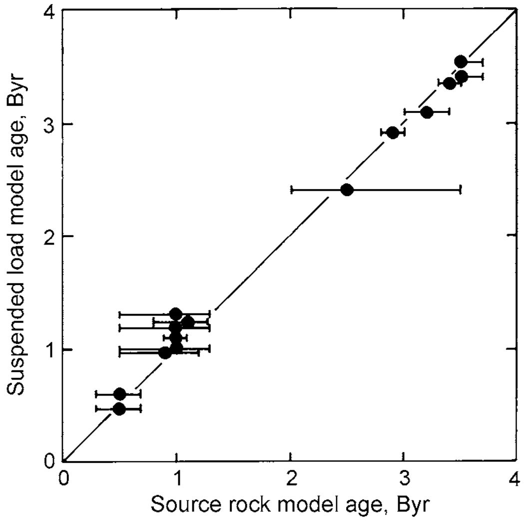

Fig. 4.21. Plot of Nd model ages for river particulates against the area-weighted average crustal residence age of rocks within the watershed. Data are shown for igneous–metamorphic drainage basins only. After Goldstein and Jacobsen (1988).

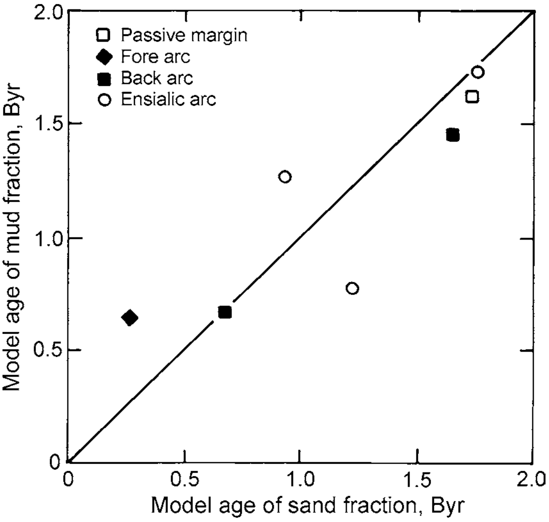

Fig. 4.22. Plot of depleted-mantle model ages in mud *versus* sand-grade fractions from deep-sea turbidites in different tectonic environments. After McLennan *et al.* (1989).

size-fractions yield only a small range of crustal-residence ages (1.54–1.64 Byr), despite having a large range of total Nd contents (17–47 ppm). Similar agreements in model age were found by Awwiller and Mack (1991) on mud- and sand-grade sediments from the Rio Grande and Mississippi rivers. However, the bottom sediments of large rivers may be atypical in displaying good chemical homogeneity.

In order to see whether a similar degree of homogeneity is displayed by deep-sea turbidites, McLennan *et al.* (1989) compared model ages on sand and mud pairs in turbidites from several different tectonic environments (Fig. 4.22). Their findings were rather variable; some pairs demonstrating good agreement in model age, whereas others gave poor agreement. These variations probably reflect the petrological make-up of the sediment. Both a mature passive margin sediment with less than 5% lithic volcanic fragments and a very immature back-arc sediment with about 90% lithic volcanic fragments displayed good agreement of model age between sand and mud fractions (square symbols). These uniform types of sediment may therefore yield useful constraints on model age. In contrast, sediments with intermediate fractions of volcaniclastic material gave inconsistent model ages (◆ and ○ in Fig. 4.22). The latter type was prevalent in continental arcs, and can be attributed to variable mixing between old continental detritus and young volcanic detritus with different grain sizes. Continental arcs therefore tend to generate widely scattered model age data.

Nelson and DePaolo (1988) tested the effects of mixed sediment provenance on Sm–Nd systematics in two small basinal systems. In both cases, the different sediment sources were petrographically and geochemically well characterised. In order to quantify the mixing process, Nelson and DePaolo plotted ε Nd against a petrographic index (percentage of lithic volcanic fragments). The good correlation observed between the end-members and various mixtures (Fig. 4.23) attests to the 'immobile' behaviour of Nd during erosion and sedimentation. This does not *avoid* the problem of mixed provenance, but it shows that coupled isotopic and petrological analysis of a suite of samples can be used to detect and quantify the mixing process.

It should not be inferred from these results that the Sm–Nd system is completely immune to disturbance during erosion and sedimentation. Any situation in which chemical weathering is involved can potentially mobilise the REE, and, if this mobilisation occurs a very long time after crustal formation, it can have a significant effect on model ages (e.g. Öhlander *et al.*, 2000). This means that Nd model ages should always be based on the sampling of fresh, unweathered material. However, the above results show that in the absence of chemical weathering, Sm–Nd analysis of sedimentary rocks can often give accurate provenance information.

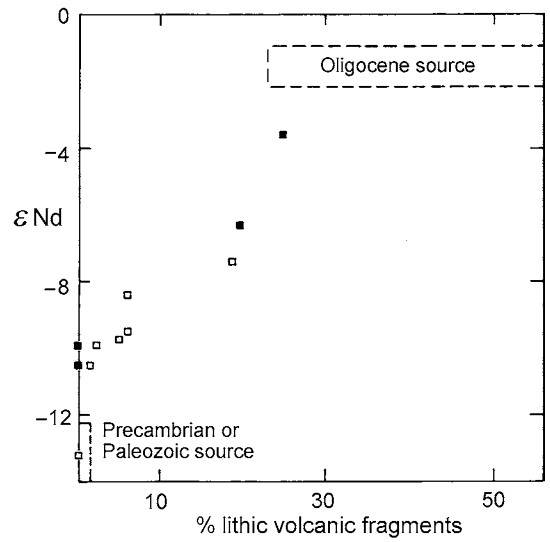

Fig. 4.23. Plot of ε Nd against modal percentage of lithic volcanic fragments, to show the petrographic dependence of the Sm–Nd system in sedimentary basins with mixed provenance. (■) = Hagar basin; (□) = Espanola basin. After Nelson and DePaolo (1988).

4.3.2 Meta-sedimentary systems

Many studies have been undertaken to assess the mobility of REE, and specifically Sm–Nd, under various diagenetic and metamorphic conditions. Paradoxically, the evidence suggests that the REE may be more mobile during diagenesis and low-grade metamorphism than during high-grade metamorphism and partial melting. This may be because of a paucity of mineral phases growing under low-grade metamorphic conditions into which REE are strongly partitioned. In contrast, there are several igneous and high-grade metamorphic minerals into which REE are strongly partitioned.

Stille and Clauer (1986) and Bros *et al.* (1992) demonstrated that, in carbonaceous (black) shales, Sm–Nd systematics in the microscopic clay-mineral fraction can be re-set by diagenesis. They showed that, in some cases, sub-micrometre-sized particles could yield Sm–Nd isochrons, which they interpreted as dating diagenesis. The accuracy of such ages remains to be proven, given the evidence that Rb–Sr dating of clay minerals can be upset by detrital inheritance (section 3.5.1).

Diagenetic mobilisation of REE on a mineralogical scale does not necessarily imply the existence of open Sm–Nd systems on a whole-rock scale. A suggestion that such a scenario *could* occur was made by Awwiller and Mack (1991) on the basis of Sm–Nd analysis of borehole samples from Texas. Weak positive correlations were observed between depth in the borehole and depleted-mantle model age, which these authors attributed to diagenetic loss of radiogenic Nd, as well as minor increases of Sm/Nd ratio with depth. However, the study was based on very small 'whole-rock' samples (weighing less than 10 g), and variations in sediment provenance could not be ruled out, so the evidence was equivocal.

Additional evidence for diagenetic disturbance of Sm–Nd systems was obtained by Bock *et al.* (1994), from sampling of turbiditic sandstones and shales from eastern New York State, which had been deposited during the Taconic orogeny (about 470 Myr ago). Nd isotope analysis was undertaken to determine sediment provenance, but the model age results displayed more scatter than could be explained by variations in provenance alone. This can be seen in Fig. 4.24, where two shales gave impossibly old ages, while two other samples gave ages somewhat older than the remainder of the suite. Furthermore, these four samples were found to be moderately or severely depleted in light REE relative to the other samples. Since Nd isotope evolution lines converged at around 500 Myr, it was suggested that the isotope system in some samples had been disturbed, probably during early diagenesis. Unfortunately, the size of samples analysed in this work was not reported.

The lack of sample information in the preceding study was rectified in later work by Cullers *et al.*

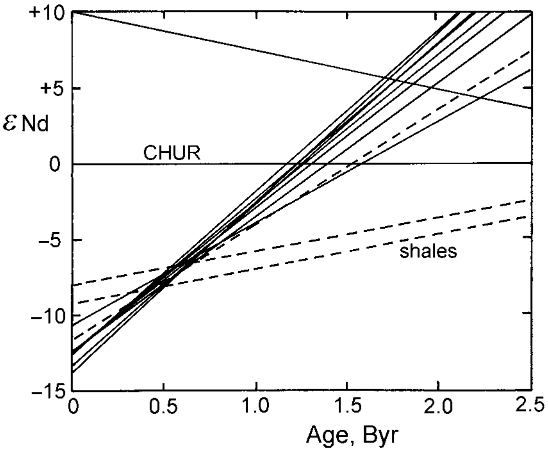

Fig. 4.24. Nd isotope evolution diagram for Middle Ordovician turbidites from eastern New York State, showing an average provenance age of 1.8 Byr, together with disturbed samples with anomalously old model ages: (——) = sandstone; (- - -) = shale. After Bock *et al.* (1994).

(1997) on Silurian pelitic schists from western Maine. Whole-rock samples averaging more than 1 kg in size were collected from pelitic units within lithologically variable formations consisting of finely interbedded quartzite and pelitic schist. Most samples gave very consistent depleted-mantle model ages of 1.8 ± 0.1 Byr, but a few samples from the Perry Mountain Formation were found to give abnormally old ages of 2.5–5.3 Byr. The samples which yielded these old ages were again found to be depleted in light REE, yielding abnormally large $^{147}\text{Sm}/^{144}\text{Nd}$ ratios in the range 0.15–0.19. These disturbances were attributed to leaching of light REE from shales during diagenesis, and the lack of suitable minerals locally to take up the released REE. Based on comparison with an earlier study of REE mobility in similar carbonaceous shales from central Wales (Mildowski and Zalasiewicz, 1991), it was suggested that the REE released from shale layers may have been incorporated into phosphates that grew in more arenaceous layers.

Collectively, these results show that caution must be exercised when using Nd isotope data to determine provenance ages for sediments, especially on carbonaceous shales. One way of dealing with this kind of material is to use a 'two-stage' model age calculation (e.g. Keto and Jacobsen, 1987). In this approach the measured Sm/Nd ratio of the sample is used to make an age correction to the estimated time of disturbance, beyond which an average crustal Sm/Nd ratio is used to estimate the provenance age. This approach may have some validity, but there is no substitute for the analysis of a large sample suite containing a variety of rock types. It is then possible to detect and screen out samples that have been subjected to diagenetic disturbance, allowing accurate provenance ages to be determined for the formation as a whole.

4.3.3 Meta-igneous systems

Mafic and ultramafic rocks cannot be used to determine accurate crustal-formation ages because they have Sm/Nd evolution lines sub-parallel to the chondritic evolution line. However, this property allows the determination of precise initial Nd isotope ratios, which have been widely used to determine the degree of mantle depletion early in the Earth's history (section 4.4.3). Results of a study by Lahaye *et al.* (1995) have important implications for this type of data, because they imply that the initial Nd isotope signatures of many komatiites may have been disturbed by subsequent alteration. Lahaye *et al.* compared calculated initial isotope compositions (ε Nd(t)) for whole-rock samples and separated pyroxenes in five komatiite flows from the Abitibi and Barberton belts. Many whole-rocks exhibited small (1–2 ε unit) deviations from the pyroxenes, but a few exhibited much larger deviations, up to +5 and −10 units (Fig. 4.25). In view of this evidence, Nd isotope data on komatiites should be based on a combination of whole-rock and mineral analyses in order to determine reliable initial Nd isotope ratios.

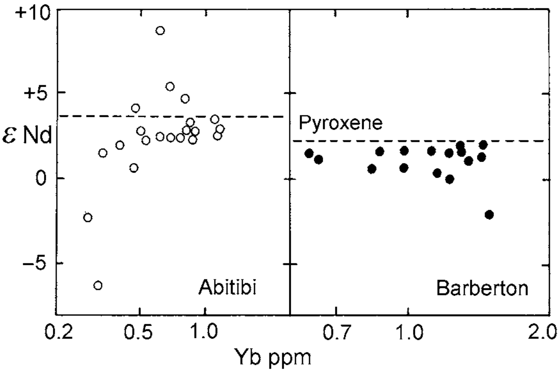

Fig. 4.25. Calculated initial Nd isotope ratios for whole-rock samples of komatiites compared with separated pyroxenes (dashed lines). Data are plotted against Yb concentration. After Lahaye *et al.* (1995).

In contrast to the evidence for disturbance of Sm–Nd systems in meta-basic rocks, most granitoid rocks offer much greater resistance to re-setting. For example, Barovich and Patchett (1992) demonstrated that whole-rock Sm–Nd systems in granitic rocks can remain undisturbed even during severe metamorphic deformation. They studied a 60-m-wide Mesozoic ductile shear zone cutting the Mid-Proterozoic Harquahala granite. Samples of increasingly deformed granite were found to yield a narrow range of T_{CHUR} model ages around 1.58 Byr in two different traverses to within 1 m of the thrust plane (Fig. 4.26). Closed-system behaviour was preserved even in samples exhibiting widespread sericitisation of plagioclase and significant epidote growth. Only in ultra-mylonites less than 1 m from the main thrust was a reduction in model age of up to 150 Myr observed, possibly due to a high fluid flux that caused calcite veining and intense alteration in the immediate vicinity of the thrust.

The resistance of whole-rock Sm–Nd model ages to significant re-setting, even during granulite-facies metamorphism, is demonstrated by the Lewisian granulites from NW Scotland (Whitehouse, 1988). A ten-point Sm–Nd isochron for tonalitic gneisses (section 4.1.3) yields an age of 2.60 Byr and an initial ratio ($\varepsilon(t)$) of −2.4 relative to CHUR (Fig. 4.27a). This

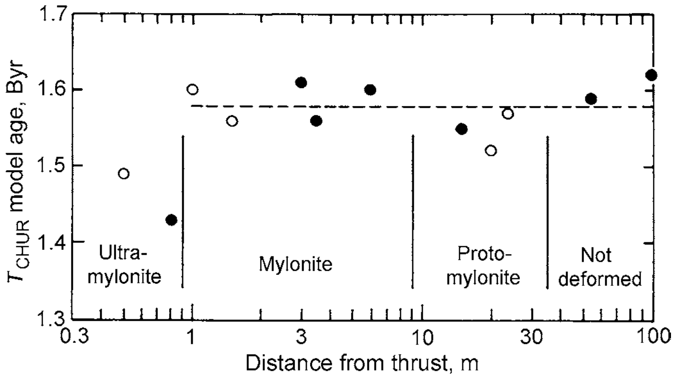

Fig. 4.26. Plot of T_{CHUR} model ages for samples of the Harquahala granite (Arizona) as a function of distance from the Harquahala thrust. Solid and open symbols indicate samples from two different traverses. Approximate boundaries between deformation zones are shown. Data from Barovich and Patchett (1992).

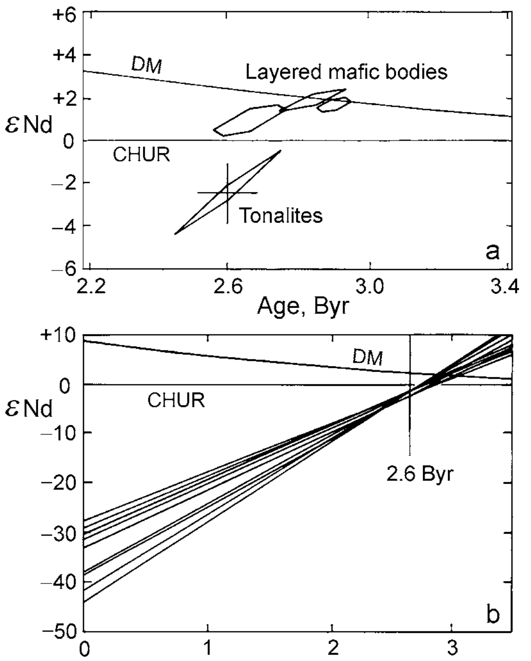

Fig. 4.27. Nd isotope evolution diagrams for the Lewisian complex of NW Scotland: (a) showing initial ratios for layered mafic bodies and a suite of granulite-facies tonalitic gneisses; and (b) showing Sm–Nd evolution lines for individual tonalitic gneisses. After Whitehouse (1988).

isochron is argued to date the metamorphic event. However, the T_{DM} model ages of these gneisses fall in the range 2.84–3.04 Byr, with an average value of 2.93 Byr (Fig. 4.27b). These ages have been scattered slightly by metamorphism, but still yield an average value very close to the undisturbed isochron age of the Drumbeg mafic complex (2.91 Byr). The effects of metamorphism on Sm–Nd systematics in granitoid rocks will be discussed further in section 4.4.4.

4.3.4 Partially melted systems

Nelson and DePaolo (1985) attempted to place upper limits on the disturbance of model ages under conditions of intra-crustal reworking by considering the limiting case of crustal anatexis. From crustal-melting models (Hanson, 1978), they estimated that the maximum amount of Sm/Nd fractionation likely to arise by intra-crustal melting processes (Δ) was 20% of the pre-existing fractionation between sample Sm/Nd and CHUR Sm/Nd. This fractionation factor f was defined by Nelson and DePaolo (1985):

$$f_{\mathrm{Sm/Nd}} = \frac{{}^{147}\mathrm{Sm}/{}^{144}\mathrm{Nd}_{\mathrm{sample}}}{0.1967} - 1 \qquad [4.6]$$

Using this notation, the error in depleted-mantle model age (T_{DM}) introduced by an intra-crustal fractionation event is given by

$$\mathrm{Err}\, T_{\mathrm{DM}} = \Delta f_{\mathrm{Sm/Nd}}(T_{\mathrm{CF}} - T_{\mathrm{m}}) \qquad [4.7]$$

where T_{CF} is the true crustal-formation age and T_{m} is the age of the partial-melting event. This error propagation is illustrated schematically in Fig. 4.28. The problem can be minimised by analysing samples with melting ages fairly close (<300 Myr away?) to their formation age.

Evidence that intra-crustal melting causes relatively minor perturbations in model age has encouraged the use of granitic plutons to determine crustal-formation

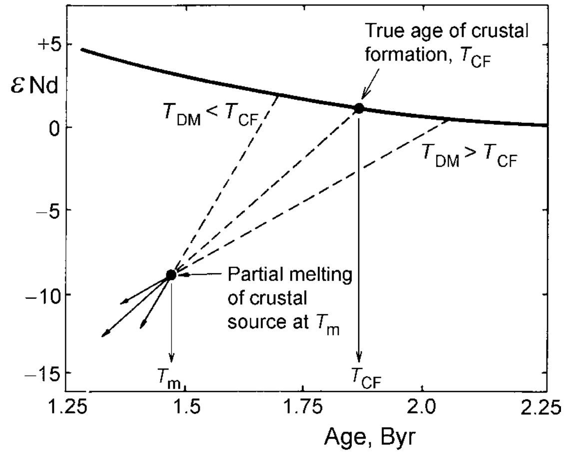

Fig. 4.28. Schematic diagram of Nd isotope systematics, to show possible errors in model age arising from Sm/Nd fractionation during intra-crustal melting. After Nelson and DePaolo, (1985).

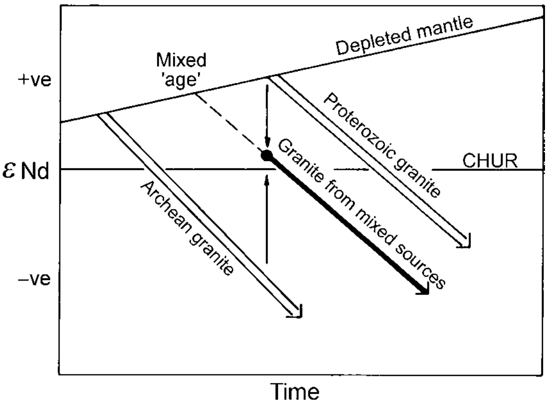

Fig. 4.29. Schematic illustration of magma mixing as a mechanism capable of generating mixed provenance ages, which do not date any real geological event. After Arndt and Goldstein (1987).

ages on associated country-rocks (assuming that the granites are the products of anatexis of those country-rocks). The approach has the advantage of allowing basement mapping of large areas with a minimal number of analyses, since each pluton can be expected to have averaged the composition of a large volume of crust. It was used to great effect by Nelson and DePaolo (1985) to map out the crustal-extraction ages of huge belts in the central USA. The method is appropriate for this application because Phanerozoic cover obscures most of the central US basement, which can be dated only from drill cores or drill chips.

Weaknesses in this approach are revealed, however, when model age results do not correspond to known events represented by igneous crystallisation ages. The model ages of 2.2–2.3 Byr in the 'Penokean' and 'Mojavia' terranes proposed by Bennett and De Paolo (1987), exemplify this problem. It is likely that they represent Proterozoic mantle-derived magmas that mixed with large quantities of re-melted Archean crust to generate mixed model ages (Fig. 4.29), which have no meaning as crustal-extraction ages (Arndt and Goldstein, 1987).

It is concluded that model age mapping of gneiss terranes is a powerful method to delimit the geographical extent of different crustal provinces, but that geochronological confirmation of the resulting model age provinces must be provided by other methods. Typically, Nd model ages define the oldest apparent age for a terrane, whereas a minimum age is defined by U–Pb dating of cross-cutting plutons. The smaller the difference between the average Nd model age and U–Pb igneous crystallisation ages, the tighter the constraints on the Nd model age as a true crustal-extraction age.

4.4 The crustal-growth problem

The question of whether the crust has grown progressively over geological time, or maintained an approximately constant volume, is one of the most fundamental in geology but has proved hard to answer conclusively. A review of the 'crustal-growth' model by its most persistent critic (Armstrong, 1991) shows that Nd isotope data provide critical tests for alternative models. Hence, three of the most important lines of Nd isotope evidence will be examined here.

4.4.1 Crustal-accretion ages

The ability of the Sm–Nd method to 'see back' through younger thermal events and measure the crustal-formation ages of continental rocks makes the method ideally suited to chart the present-day age distribution of crustal basement. This yields an apparent profile of continental growth through time which does not take into account crustal recycling into the mantle. Nevertheless, it is an appropriate starting point for this subject.

Attempts to map the age structure of the continents were begun using the Rb–Sr method (Hurley *et al.*, 1962), before the development of Sm–Nd analysis. Hurley *et al.* compared Rb–Sr isochron ages with Sr model ages calculated assuming a mantle ^{87}Sr/^{86}Sr ratio of 0.708. On average the two values were correlated, leading them to suppose that the isochron ages

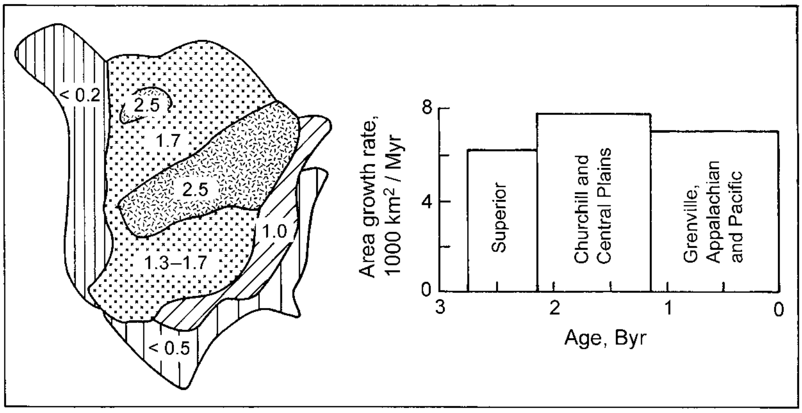

Fig. 4.30. Estimated areas of North American crustal basement attributable to different Rb–Sr age provinces: (a) map showing provinces of different ages (in Byr); and (b) histogram of growth rate against time. After Hurley *et al.* (1962).

dated the time of crustal extraction from a basic source. This was a good approach, although we now know that the Rb–Sr system is too easily re-set to yield reliable crustal-extraction ages for old terranes. (Also the mantle-growth curve is less radiogenic than 0.708.) Hurley *et al.* applied the method to the North American continent in order to calculate the approximate areas of crustal basement attributable to provinces of various ages (Fig. 4.30).

Hurley and Rand (1969) extended this approach to include two-thirds of the land area of the world (excluding the USSR and China, for which data were not available). K–Ar data were used to extrapolate geographically from the more limited set of Rb–Sr data, bearing in mind the tendency for the former to be re-set. Rb–Sr model ages were calculated using an improved mantle ^{87}Sr/^{86}Sr growth curve, yielding values now somewhat older than apparent crystallisation ages. Hurley and Rand's data are presented on a plot of cumulative crustal age distribution against time (Fig. 4.31). From these data it appeared that crustal growth was accelerating somewhat with time. However, more recent studies have yielded curves of different shapes.

A study of comparable sweep to that of Hurley *et al.* (1962) was performed by Nelson and DePaolo (1985), who used Nd model ages to map the age structure of the basement of the USA. Nelson and DePaolo found Nd model ages substantially older than igneous crystallisation ages, leading to a greatly increased estimate of the rate of Lower Proterozoic crustal growth in the mid-continent. These data, together with recently published ages on the Canadian Shield, led to a dramatic increase in the estimated average age of the North American craton, compared with that of Hurley *et al.* (1962). This picture was reinforced by Patchett and Arndt (1986), who further amplified the estimated area of newly accreted Lower Proterozoic (1.9-Byr-old) crustal basement in North America. This has generated a 'sigmoidal' curve of crustal formation against time (Fig. 4.31), which suggests that the greatest rates of new crustal accretion occurred during the middle of the Earth's history.

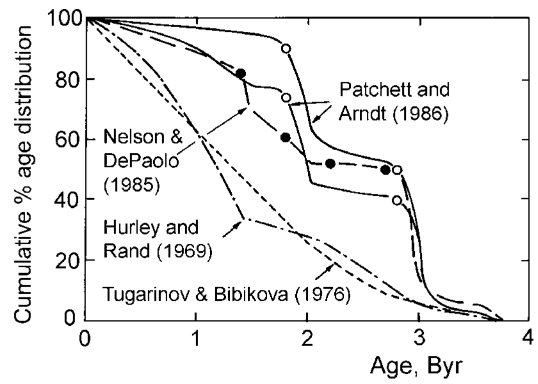

Fig. 4.31. Estimated continental growth rates on a cumulative basis. After Jacobsen (1988).

As more detailed model age mapping is performed in areas of old crustal basement, it is likely that further increases in average crustal-extraction age will be found. The Superior and Slave provinces of Canada provide good examples of this. Hurley *et al.* (1962) mapped the Superior craton as 2.7 Byr in age, a concept still widely held today. However, U–Pb geochronology has shown the presence of large areas of 3-Byr-old crust in the NW Superior province (reviewed by Thurston *et al.*, 1991). Similarly, the Slave province is largely a 2.7-Byr craton, but a small belt of tonalitic gneisses with Early Archean zircons yield T_{CHUR} model ages of up to 4.1 Byr (Bowring *et al.*, 1989). Therefore, continued mapping of old cratons will probably fill the dip in the Early–Mid-Archean segment of the sigmoid (Fig. 4.31), yielding a linear or concave-downwards curve of apparent crustal growth with time.

4.4.2 Sediment-provenance ages

In response to proponents of the 'continental-growth' model (e.g. Moorbath, 1976), Armstrong (1981) argued that the record of continental accretion documented by various methods (as above) did not prove that the continental area had actually grown over geological time. Armstrong argued that a model in which the continental area was approximately the same 4.5 Byr ago as it is today could also generate *apparent* continental growth with time, provided that the rate of recycling of crust into the mantle (by sediment subduction) was equal to the rate of new crustal formation above subduction zones.

Undoubtedly, recycling of crust back into the mantle does occur on a significant scale. Old crustal terranes may be shortened by orogeny, then flattened again by erosion and subduction of sediment. However, some sediment should be expected to escape the recycling process and provide a record of the old, recycled terrane. Therefore, the search for evidence of constancy or growth in the continental mass turned to the sedimentary record. The ability of the Nd model age method to 'see back' through erosion and sedimentation to an original crustal-extraction event made it ideal for these studies.

To study this problem, it is convenient to portray sediment data on a diagram of Nd model age (crustal-residence age) against the stratigraphic depositional age of the sediment in question (Fig. 4.32). Sediments eroded from juvenile mantle-derived sources will have $T_{\mathrm{CR}} = T_{\mathrm{STRAT}}$ and lie on a 'concordia' line (Allègre and Rousseau, 1984). In contrast, reworking of older sediments without any input of juvenile material will displace compositions to the right along horizontal vectors. A compilation of data from several sources is shown in Fig. 4.32, including clastic sediments (Hamilton *et al.*, 1983; O'Nions *et al.*, 1983; Taylor *et al.*, 1983; Allègre and Rousseau, 1984) and particulates from major river systems at the present day (Goldstein *et al.*, 1984).

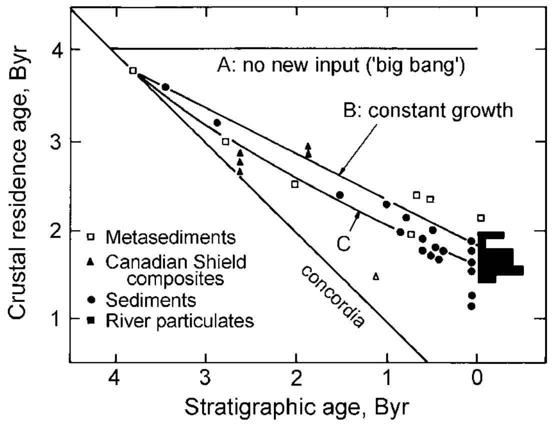

Fig. 4.32. Model age *versus* stratigraphic age diagram, showing a compilation of early-1980s data from several clastic sediment studies. Crustal growth models A, B and C are discussed in the text. After Goldstein *et al.* (1984).

Allègre and Rousseau (1984) compared the sediment data with various theoretical models for continental evolution involving different rates of continental growth through time (Fig. 4.32). A 'big-bang' model (A), whereby the whole continental mass was extracted about 4 Byr ago or before, was ruled out. Allègre and Rousseau argued that a model involving uniform growth of the continents from 3.8 Byr ago to the present (B) was a better fit to the data, but that the best fit was produced by a curved line (C), representing decreasing growth of the crust through time.

Unfortunately this diagram is not as conclusive as it may appear, due to the great difficulty of determining a global average sediment-provenance age at any given time from the very variable provenance ages in individual provinces. This makes the data very susceptible to sampling bias. One source of such bias is preferential recycling of old sediments relative to erosion of more juvenile cratonic material. This will exaggerate the slowing down of continental growth with time, appearing to favour models of type C over those of type B. Another source of bias is the neglect of young orogenic belts such as the accreted terranes of the Canadian Cordillera (Samson *et al.*, 1989). The inclusion of such data in Fig. 4.32 would favour linear evolution models (type B), suggesting that crustal growth has *not* slowed significantly in the Phanerozoic.

The interpretation of Fig. 4.32 is also heavily influenced by assumptions about the degree of recycling of sediment into the mantle. The so-called 'big-bang' model shown in Fig. 4.32 involves no recycling

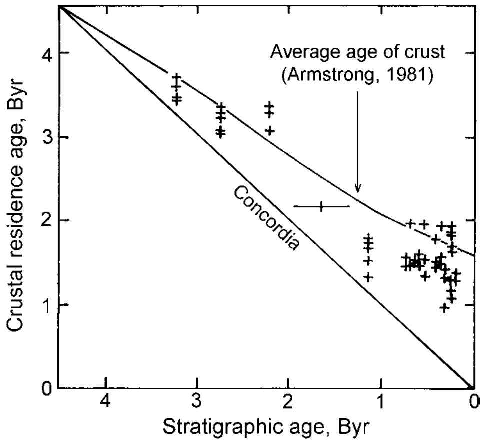

Fig. 4.33. Model age *versus* stratigraphic age diagram, showing data of Dia *et al.* (1990) for clastic sedimentary rocks from South Africa. The curve shows provenance ages predicted by the crustal model of Armstrong (1981). After Armstrong (1991).

of crustal material into the mantle. This does not correspond to Armstrong's model, which involves constant recycling of old crust into the mantle and its replacement by an equal volume of juvenile crust. Armstrong (1991) claimed that his model gave rise to a curve (shown in Fig. 4.33) that looks remarkably like the steady-growth model in Fig. 4.32. It is clear, then, that young sediments provide much too loose a constraint on crustal-growth models. Therefore, the argument must focus on the provenance ages of the oldest surviving sediments.

Isua supracrustals from western Greenland, which are the oldest clastic sediments analysed, yield identical stratigraphic and Nd model ages of 3750 Myr, indicating that they did not incorporate a significant amount of older reworked crust. However, the data of Dia *et al.* (1990) from South Africa reveal surprisingly old provenance ages for Mid-to-Late Archean sediments. On balance, the sediment data seem to favour a crustal-growth model, but ultimately the argument rests on a null hypothesis (no sediments with very old provenance have yet been seen, therefore none exist). This is an inherently weak argument upon which to base such an important conclusion. This weakness comes from the need for representative sampling of old crust using a sediment data set that is inherently very noisy.

4.4.3 Archean depleted mantle

An alternative route to assessing the volume of crust at a given time in the Earth's history is to measure the composition of the depleted reservoir which balances the enriched crustal reservoir, namely the upper mantle (section 6.2.1). Because the upper mantle is stirred by convection, we can expect to sample this reservoir (in ancient volcanism) in a much more representative fashion than the sampling of the enriched reservoir by ancient sediments. Hence, the problem of crustal growth may be soluble if we can determine the extent of mantle depletion during the Earth's early history. If there was a large volume of continental crust in the early Earth, there should be evidence for strong mantle depletion.

In the mid 1980s, several studies revealed initial Nd isotope data for Early and Mid-Archean rocks that lay well above the chondritic evolution line, and in some cases above the depleted-mantle evolution line of Goldstein *et al.* (1984). Smith and Ludden (1989) argued that some of the strongly positive ε Nd values calculated for early mafic rocks are in error due to incorrect age assignments. The Kambalda example has already been mentioned (section 4.1.2), and doubtless there are problems with some of the other data. However, they concluded that there are enough depleted-mantle compositions in the Early Archean for the phenomenon to be real.

Such evidence for very early depletion of the upper mantle presents a problem for the model in which continental crust grew progressively over Earth history. On the other hand, Armstrong (1991) argued that these data supported his model of no crustal growth. In order to examine this claim, the data compilation of Armstrong (1991) is shown in Fig. 4.34, together

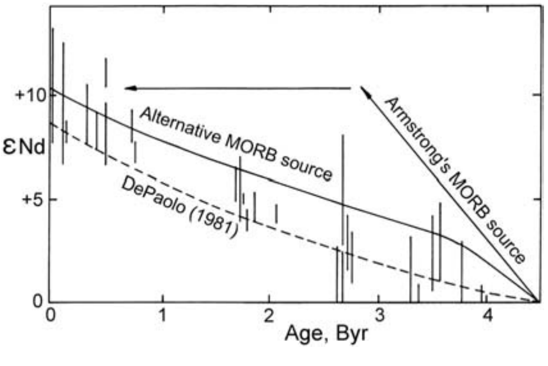

Fig. 4.34. Initial ε Nd for terrestrial rocks, compiled by Armstrong (1991), compared with his 'big-bang' MORB evolution line. The solid curve is an alternative MORB depletion line for a crustal growth model. Note that this is not expected to agree with the dashed arc-source model of DePaolo (1981).

with an evolution line for the MORB source which he claimed was a product of his 1981 model. However, most of the available Nd data can be satisfied by a less-extreme evolution line in Fig. 4.34 (solid line), which is sub-parallel to DePaolo's curve since 4 Byr ago. The solid evolution line represents the composition of the most depleted mantle sources, whereas DePaolo's line represents the source of arc magmatism, which is generally less depleted.

The gradual depletion of the upper mantle which is portrayed by the solid line in Fig. 4.34 can be reconciled with a constant-crustal-volume model only if the average *composition* of the crust changes over geological time. In principle this requirement is satisfied in a model whereby the Earth begins its evolution with a thick basaltic ('oceanic') crust, which is gradually replaced by continental crust over geological time. This involves a non-plate-tectonic model for Archean crustal evolution (e.g. West, 1980). A similar model was also supported by Galer and Goldstein (1991), who proposed that a thick, long-lived alkali basalt crust was built up in the Archean by small-degree melting of the deep mantle. However, as evidence mounts for earlier and earlier operation of plate-tectonic processes in the Earth's history (e.g. Williams *et al.*, 1992), there seems little reason to invoke a prolonged pre-plate-tectonic era.

Chase and Patchett (1988) proposed that accelerated early mantle depletion is in fact consistent with plate-tectonic processes. They postulated that the storage of subducted oceanic crust in the mantle, before re-homogenisation with the depleted mantle (by convection), would give rise to a hidden enriched reservoir in the deep mantle to balance early depleted mantle. According to this model, the amount of 'stored' subducted oceanic crust has grown over the Earth's history, although gradual cooling of the Earth prevents the system from reaching a steady state by increasing the lifetime of subducted crust over geological time. Taking the cooling process into account, a duration of several hundred million years to establish Early Archean mantle depletion is consistent with evidence for a 1–2 Byr present-day lifetime of subducted oceanic crust, as deduced from ocean-island basalts (section 6.3.1).

4.4.4 Early Archean crustal provinces

Evidence for open-system behaviour of Sm–Nd in komatiites (section 4.3.3) casts doubt on some of the evidence for strong mantle depletion during the Earth's early history. However, new evidence for early depletion of the mantle was provided by Bennett *et al.* (1993) and Bowring and Housh (1995). This was based on analysis of granitoid orthogneisses from western Greenland and the Slave province of northern Canada. Since these rock types are generally resistant to metamorphic Nd disturbance, the new evidence for Early Archean depleted mantle appeared much stronger. However, the new evidence was itself challenged by Moorbath and Whitehouse (1996) and Moorbath *et al.* (1997). Since this discussion has critical implications for crust–mantle evolution, it will be examined in some detail, beginning with the data from the Acasta gneisses of the Slave province.

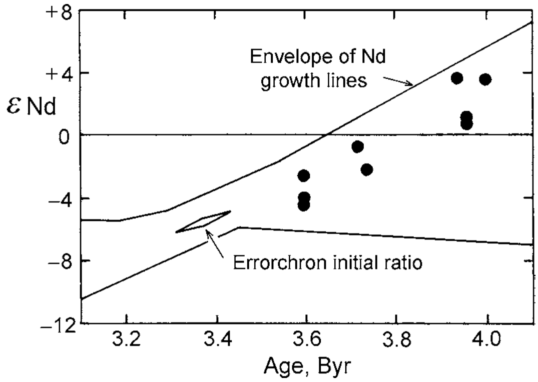

Fig. 4.35. Nd isotope evolution diagram showing initial ε Nd values calculated at the various U–Pb ages of the Acasta gneisses (●) compared with the initial ratio of a 3.3-Byr-old best-fit errorchron. The outer envelope of Nd isotope growth curves is shown for reference. After Moorbath *et al.* (1997).

Bowring and Housh (1995) used SHRIMP U–Pb ages to calculate Nd initial ratios for a variety of rock types from Early Archean Acasta gneisses, aged 3.6–4.0 Byr, yielding ε Nd values as high as +4 and as low as −5 (Fig. 4.35). However, Moorbath and Whitehouse (1996) observed that most of the suite analysed by Bowring and Housh lay on an 'errorchron' (section 2.6.3) with an age of about 3.3 Byr, which they attributed to an intense metamorphic event that partially homogenised whole-rock Sm–Nd systems at that time. This result was later confirmed (Moorbath *et al.*, 1997) by the analysis of twenty new samples, yielding a combined errorchron age of 3370 ± 60 Myr and an initial ratio (ε Nd) of −5.6 (Fig. 4.35). Hence, they argued that ε Nd values calculated at the U–Pb crystallisation ages of 3.6–4.0 Byr were not accurate measures of the magma source compositions at those times.

Bowring and Housh (1996) argued in reply that the 3.3 Byr errorchron age could itself be a mixing line with no age significance. However, Moorbath *et al.* (1997) showed that there was no correlation between

Nd isotope ratios and Nd concentrations in the Acasta gneisses, as would be expected from a mixing line. Such a mixing line was seen in Archean lavas from the Abitibi Belt of Ontario, which had been contaminated with crustal material (Fig. 4.7). Moorbath *et al.* also argued that the relatively low MSWD value for their own Acasta samples (8.8) could not be explained by a fortuitous combination of short segments of 3.8-Byr isochrons, since this would yield a much higher MSWD value of several hundred. From this evidence, it appears that the 3.3-Byr-old errorchron may date a real geological event (or series of events) which caused homogenisation of Sm–Nd systems in the Acasta gneisses. Since this event post-dates the oldest zircon ages by up to 600 Myr, it is concluded that reliable initial ε values for the mantle source cannot be calculated.

Early Archean rocks from western Greenland represent the other principal source of evidence about the composition of the Early Archean mantle. Evidence for strongly depleted mantle sources was first found in the Isua supracrustal sequence (e.g. Hamilton *et al.*, 1983), and was supported by analysis of Amitsoq gneisses, and mafic enclaves in these gneisses named the Akilia suite (Bennett *et al.*, 1993). The upper envelope of these three suites defines an evolution line for highly depleted mantle in the Early Archean (Fig. 4.36). This led Bennett *et al.* to propose a model of two-stage evolution in the early Earth, in which early intense mantle depletion was followed by a period of mixing with deeper less-depleted mantle, causing an inflection in the depleted-mantle evolution line.

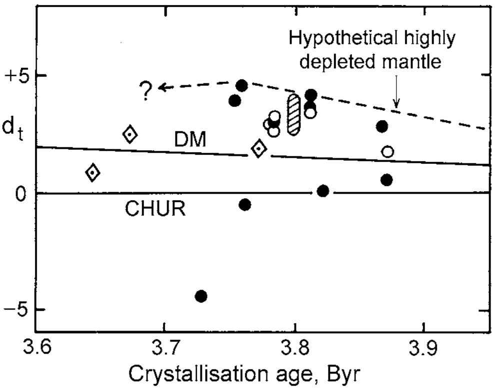

Fig. 4.36. Nd isotope evolution plot showing ε Nd values of Bennett *et al.* (1993) at the ages determined by U–Pb analysis: (●) = Amitsoq gneiss; (○) = Akilia enclaves in Amitsoq gneisses; shaded zone = Isua supracrustals. Diamonds indicate ages and initial ratios for three Sm–Nd errorchrons of Moorbath *et al.* (1997).

However, Moorbath *et al.* (1997) showed that Akilia, Amitsoq and Isua suites all yield Sm–Nd errorchrons with ages significantly younger than SHRIMP U–Pb zircon ages. This suggested to Moorbath *et al.* that the Sm–Nd systems in many of these rocks had been re-set in a manner similar to the Acasta gneisses. However, this critique was itself the subject of a scientific discussion (Bennett and Nutman, 1998; Kamber *et al.*, 1998), after which further debate was continued by Kamber and Moorbath (1998), Whitehouse *et al.* (1999) and Nutman *et al.* (2000). Since space here is limited, the present author will give only a brief overview of the debate.

The belt of Early Archean rocks in west Greenland runs in a northeasterly direction parallel to Godhabsfjord, from Amitsoq on the coast, to Isua at the edge of the inland ice field. On the basis of detailed SHRIMP U–Pb analysis (see section 5.2.3 for the method), it now appears that this belt (termed the Itsaq gneiss complex) was created in two main events. Near Isua in the north, most U–Pb ages cluster around 3.8 Byr, which appears to be the date of the earliest crust-forming event in the area (Nutman *et al.*, 2000). However, near Amitsoq in the south, most U–Pb ages cluster round 3.65 Byr, but zircons sometimes have cores up to 3.8 Byr in age. Furthermore, in the latter area, whole-rock Rb–Sr, Pb–Pb and Sm–Nd errorchrons all give ages around 3.65 Byr (Whitehouse *et al.* 1999). This suggests that most of the crust in the south is 3.65 Byr old, but contains inherited fragments of 3.8-Byr-old material. We can infer from this that any fragments of 3.8-Byr-old rocks in the south probably had their Nd isotope systems re-set 3.65 Byr ago, but the extent to which the rocks in the north preserve an accurate 3.8-Byr-old initial ratio is unclear.

The Amitsoq gneisses analysed by Bennett *et al.* (1993) came from both ends and the middle of the Itsaq gneiss complex. On the Sm–Nd isochron diagram (Moorbath *et al.*, 1997) these samples had much more scatter than did 26 Amitsoq gneisses from the southern end of the belt, which defined an errorchron age of 3640 ± 120 Myr (MSWD = 10) with an initial ε Nd value of +0.9 ± 1.4 (Fig. 4.37). Unfortunately there were not enough Nd isotope analyses from the northern area of the gneiss complex, where old U–Pb ages predominate, to see whether this part of the complex had consistently different Nd isotope signatures from the southern part. Therefore, Moorbath *et al.* suggested that the generally greater scatter in the suite analysed by Bennett *et al.* was more likely to be due to later partial metamorphic disturbance during Late Archean or Mid-Proterozoic events. They were not able to prove that re-setting had occurred, although Hf isotope analysis

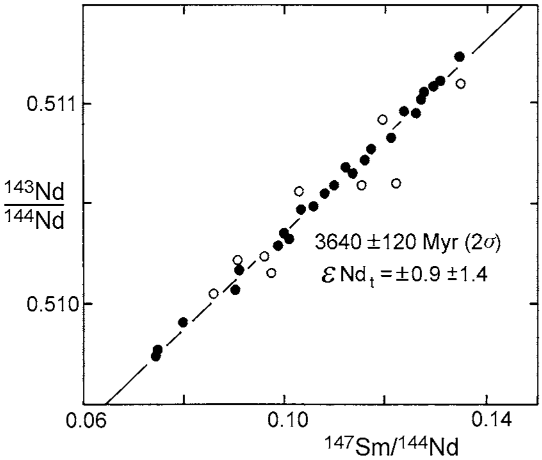

Fig. 4.37. Sm–Nd isochron diagram showing Amitsoq gneisses of the Itsaq gneiss complex: (●) = southern suite of gneisses, which define a 3640-Myr errorchron; (○) = more scattered data of Bennett *et al.* (1993). After Moorbath *et al.* (1997).

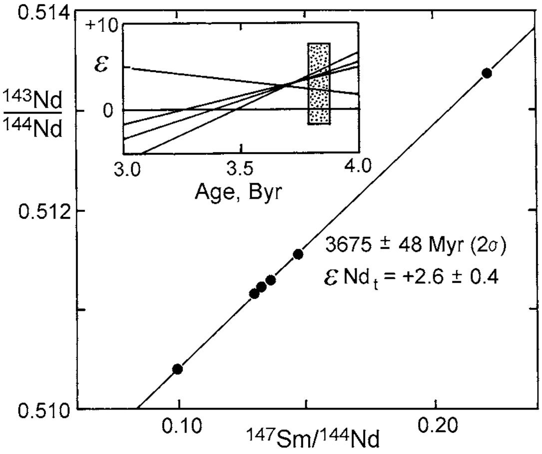

Fig. 4.38. Sm–Nd isochron for Akilia enclaves in the Amitsoq gneisses. The inset shows Nd isotope evolution lines for four samples. The shaded box shows the range of U–Pb ages. After Moorbath *et al.* (1997).

(section 9.2.3) suggested that this might be the case, because the extremely positive ε Nd values determined by Bennett *et al.* were not matched by similarly positive ε Hf values.

When Moorbath *et al.* (1997) examined Nd data for five samples of Akilia mafic enclaves analysed by Bennett *et al.* (1993), they discovered a very strong linear array with an age of 3675 ± 48 Myr and an initial ratio of +2.6 ± 0.4 ε units (Fig. 4.38). The low MSWD of 2.1 for this regression makes it statistically an isochron, but, since U–Pb ages for the gneissic host rocks range from 3784 to 3872 Myr, Moorbath *et al.* interpreted the age as an isotopic homogenisation event associated with the engulfing of the enclaves by the Amitsoq magmas. Bennett and Nutman (1998) countered that these samples came from too wide an area to be attributed to metamorphic homogenisation, and in response Kamber *et al.* (1998) re-interpreted the Sm–Nd age for the enclaves as intrusive, and attributed the older U–Pb ages in the host gneisses to inherited zircons.

Unfortunately, these interpretations are also equivocal, due to the small size of the sample suite. Four of the five samples analysed are from the southern area of the gneiss complex where the host gneisses are generally of 3.65 Byr age. Hence, in this area, both the isotope-homogenisation model of Moorbath *et al.* (1997) and the young intrusive age proposed by Kamber *et al.* (1998) can explain the 3675-Myr array. Only one enclave from the northern area was analysed, although three duplicates were determined. This sample appears to be more than 3.8 Byr old, but since it has the same Nd isotope signature as the host rocks, it cannot be proven that the sample has not been isotopically homogenised with the host rocks at some time. Hence, this sample might provide evidence for very depleted Early Archean mantle, but it is very risky to base such a model on a single sample.

It is concluded from the above discussion that the re-setting model of Moorbath *et al.* (1997) does not apply to most of the western Greenland rocks, but nevertheless, the extremely depleted ε Nd values proposed by Bennett *et al.* (1993) remain unproven in the face of the geologically complex evolution of these rocks and in the face of Hf isotope evidence (section 9.2.3). A more conclusive determination of Early Archean Nd isotope signatures must depend on the analysis of a larger number of samples from the northern part of the Itsaq gneiss complex, where 3.8-Byr-old rocks seem to dominate. This shows that geochemical deductions are only as good as the geological sampling, even in one of the world's most inaccessible field localities.

4.5 Nd in the oceans

The abundance of Nd in seawater is about a million times lower than that in rocks, at about three parts per trillion (Goldberg *et al.*, 1963; Piepgras *et al.*, 1979). This can be attributed to effective scavenging of rare earths from seawater by particulate matter. In contrast, ions such as sodium have similar abundances in rocks and seawater. This led Goldberg *et al.* to propose that

Nd has a very short residence time in seawater, possibly less than 300 yr, and less than the turnover rate of water in the oceans. As a result, we can expect Nd isotope systematics in seawater to be quite different from those of Sr (section 3.6.2), which has an ocean-residence time of more than 2 Myr.

4.5.1 Modern seawater Nd

The very low Nd concentrations in seawater present significant analytical difficulties. In contrast, manganese nodules, which are believed to precipitate directly from seawater, have Nd contents up to hundreds of ppm. Consequently the early studies of O'Nions *et al.* (1978) and Piepgras *et al.* (1979) focussed principally on this material. Significant Nd isotopic variations were found between Mn nodules from different ocean basins (Fig. 4.39b) and attributed by Piepgras *et al.* to real variations in the isotopic composition of seawater.

Piepgras *et al.* justified their interpretation on the grounds that Mn nodules from a wide geographical area within each ocean mass had distinct but reproducible Nd isotope compositions. This was confirmed by the direct analysis of filtered ocean water samples (Fig. 4.39a), which were shown to be consistent with the isotopic composition of sea-floor nodules from the same ocean basin. Direct Nd isotope analyses of four water samples from the Pacific (totalling 10–20 litres each) were presented by Piepgras *et al.* (1979), while analyses of Atlantic ocean water were presented by Piepgras and Wasserburg (1980).

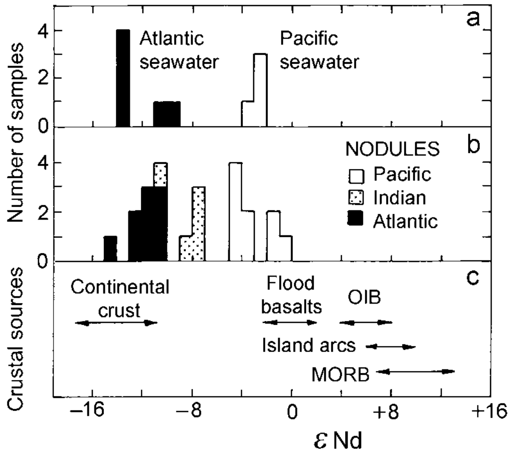

Fig. 4.39. Histograms showing the ranges of ε Nd displayed by (a) seawater and (b) manganese nodules from different ocean basins, relative to (c) major crustal reservoirs. After Piepgras and Wasserburg (1980).

Comparison of seawater isotope compositions with possible source reservoirs (Fig. 4.39c) suggested that Nd in Atlantic seawater is primarily continental in origin. This is consistent with a greater discharge of river water into the Atlantic. However, about 50% of Nd in Pacific seawater appears to be derived from basaltic crustal sources, either from erosion of mafic rocks or from some form of exchange with ocean-floor basalts. Second-order isotopic variations were also seen within Atlantic Ocean water. Samples from depths of at least 1 km in the Sargasso Sea have very consistent ε Nd compositions averaging −13.5, whereas shallower samples from depths of 300 and 50 m have more radiogenic ε Nd values of −10.9 and −9.6 respectively. This implies isotopic stratification of Atlantic water masses, a conclusion consistent with long-established oceanographic observations of the Atlantic (Wust, 1924).

A more detailed Nd isotope study of the North Atlantic Ocean was performed by Piepgras and Wasserburg (1987) using water samples from five vertical sections. Contoured ε Nd values (Fig. 4.40a) are consistent with water masses recognised on the basis of salinity and temperature (Fig. 4.40b). Surface water at mid-latitudes (SW) has ε Nd values consistent with the dissolved-Nd budgets of major rivers such as the Amazon and Mississippi (Piepgras and Wasserburg, 1987; Goldstein and Jacobsen, 1987). Outflow of water from the Mediterranean also has a similar composition (Piepgras and Wasserburg, 1983). In contrast, the major water body of the ocean, North Atlantic Deep Water (NADW), has very uniform unradiogenic Nd ($\varepsilon = -13.5$). It is well known that this water largely originates from Arctic Intermediate Water (AIW), which has been shown by Stordal and Wasserburg (1986) to have ε Nd as low as −25 in Baffin Bay. Therefore the ε Nd composition of NADW must result from mixing of AIW and mid-latitude surface water. Finally, as NADW flows southwards towards the equator, it becomes sandwiched between two tongues of water with intermediate ε Nd, Antarctic Intermediate Water (AAIW) and Antarctic Bottom Water (AABW) (Fig. 4.40b).

Although the continental origin of Atlantic seawater Nd is well established, the origin of the radiogenic Nd in Pacific seawater is more problematical. The most obvious source is hydrothermal alteration of ocean-floor basalts. However, the low REE contents of hydrothermal vent fluids (Michard *et al.*, 1983) rule out a simple hydrothermal origin, as proposed for Sr and Pb (sections 3.6.2 and 5.6.2). It is possible that a diffuse alteration flux from the whole ocean floor contributes some radiogenic Nd. However, a more important source may

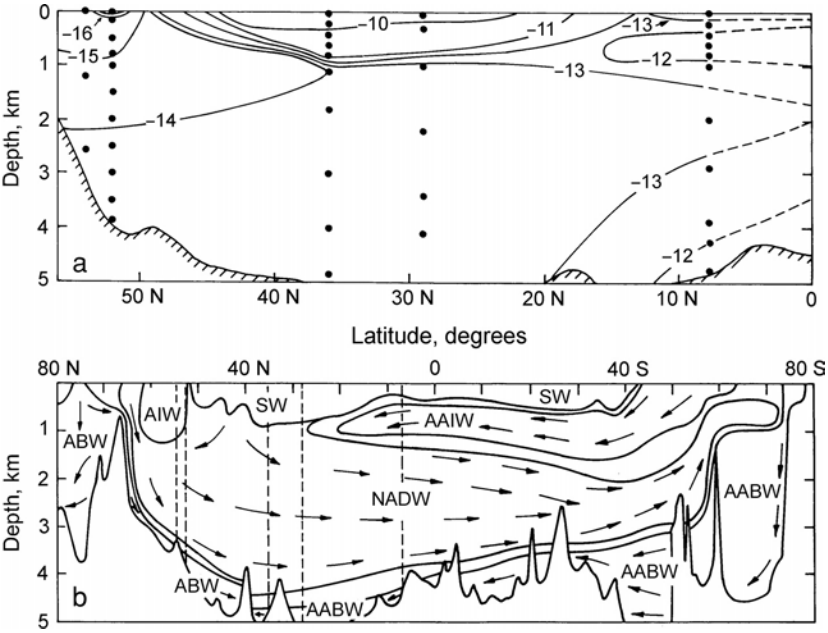

Fig. 4.40. Schematic longitudinal sections through the Atlantic Ocean to show (a) contoured Nd isotope variations in the North Atlantic and (b) oceanographically established water masses for the whole Atlantic (with sample locations in (a) shown by dashed lines). After Piepgras and Wasserburg (1987).

be volcanic dust from circum-Pacific volcanoes (Albarède and Goldstein, 1992).

Wind-blown sediment has also been proposed as a major source for the continental Nd signatures in Atlantic Ocean water. This is supported by the regionality of the seawater Nd signatures, which can be tied in with prevailing wind directions. For example, unradiogenic Nd in the eastern North Atlantic can be traced to wind-blown particulates from the Sahara desert (Chester *et al.*, 1979). Similar effects occur in the eastern North Pacific, which receives wind-blown particulates from the deserts of the American southeast (Albarède and Goldstein, 1992).

Dissolution of Nd from wind-blown dust can also solve a 'Nd paradox' arising from conflicting oceanic residence times of Nd based on elemental and isotopic data. This paradox arises from the fact that Nd concentrations of deep ocean water increase from Atlantic to Pacific, along a deep ocean current termed the 'ocean conveyor belt' (section 14.1.7). This implies a long residence time of Nd in seawater (possibly as high as 10 kyr). However, the isotopic variation between Atlantic and Pacific seawater Nd implies a short residence time, which must be less than the 1500 yr circulation time of the 'conveyor belt'. To resolve this paradox, Bertram and Elderfield (1993) proposed exchange of Nd between the suspended and dissolved Nd budgets in seawater.

This exchange process was revealed in more detail by measuring oceanic depth profiles of particulate and dissolved Nd off western Africa, within the range of Saharan wind-borne particles (Tachikawa *et al.*, 1999). This work revealed a large flux of Nd to surface ocean water, derived from dissolution of 'lithogenic' (i.e. clastic) particulates, largely of atmospheric origin. This input flux is balanced by an equally large output flux, comprising Nd which is adsorbed onto sinking biogenic and authigenic particulates.

4.5.2 Ancient seawater Nd

Following the successful characterisation of the Nd isotope budget of the modern oceans, Shaw and Wasserburg (1985) evaluated various types of material as indicators of the Nd isotope composition of paleo-oceans. They found that carbonate and phosphate in living organisms were very low in Nd (with concentrations in the part per billion range), but that fossil carbonates and phosphates had concentrations in the tens to hundreds of ppb and ppm respectively. Shaw and Wasserburg attributed the elevated Nd contents of fossil carbonates largely to diagenetic re-mobilisation of detrital Nd, but they attributed the high Nd contents of ancient phosphates (conodonts, fish debris, lingulid brachiopods and inorganic phosphorites) to scavenging directly from seawater (after death). Several studies on this kind of material were performed during the late 1980s, allowing a general understanding of the evolution of seawater Nd through time.

Keto and Jacobsen (1988) collated conodont and phosphorite data with analyses of fish teeth (Staudigel *et al.*, 1985), ferromanganese coatings on forams (Palmer and Elderfield, 1986) and conodonts and lingulids (Keto and Jacobsen, 1987; Keto and Jacobsen, 1988) to construct a paleo-seawater Nd curve for the Phanerozoic. Because the Pacific Ocean dominates the world ocean system (as did its predecessor, the Panthalassan Ocean) this was used to determine a global average evolution curve (Fig. 4.41a). This curve was then extended into the Precambrian (Fig. 4.41b) by the analysis of Archean and Proterozoic banded iron formations (BIF), which were argued to sample the Nd isotope composition of the Precambrian oceans (Jacobsen and Pimentel-Klose, 1988). Despite the lack of reliable paleogeographical information for this period of the Earth's history, it may be justifiable to assume world-wide homogenisation of Nd in seawater on the grounds that a smaller continental mass during the Precambrian presented less impediment to circulatory mixing of the oceans.

The Precambrian curve based on BIF data suggests that unlike the Phanerozoic, when continental run-off was the dominant influence, Archean seawater Nd was controlled by the weathering of matic mantle-derived rocks. This is consistent with the presumed smaller continental mass at this time. The Proterozoic is then a period of transition from the mantle-dominated regime of the Archean to the crust-dominated regime of the Phanerozoic.

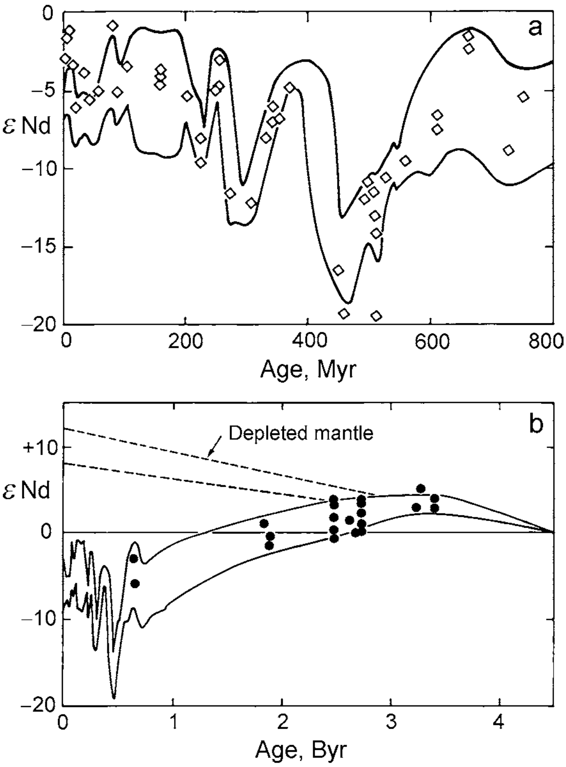

Fig. 4.41. Proposed global seawater evolution curves. (a) For the Phanerozoic, based on phosphate samples from the Pacific–Panthalassan Ocean. (b) For the Precambrian, based on banded iron formations. After Keto and Jacobsen (1988) and Jacobsen and Pimentel-Klose (1988).

4.5.3 Tertiary seawater Nd

Although these results were important in understanding the ancient oceans, the most powerful applications of Nd isotope analysis to oceanography have resulted from more detailed studies of seawater evolution during the Tertiary epoch, paralleling the detailed study of seawater Sr for this period (section 3.6.1). These studies have been revolutionised by the ability to measure continuous secular variations of Nd isotope composition from ferromanganese crusts.

Ferromanganese crusts grow on any exposed surface in the deep ocean at a rate of about 1–3 mm/Myr. Because of this very slow rate of growth they are easily swamped by sedimentation; but on elevated areas, such as seamounts and volcanic plateaux, ferromanganese crusts can grow unimpeded for more than 20 Myr (Ling *et al.*, 1997). Furthermore, crusts growing on these features can sample the isotopic composition at different water depths, from as shallow as 850 m to abyssal depths of 5000 m (Reynolds *et al.*, 1999). In order to use ferromangenese crusts as an inventory of past seawater Nd signatures, it is necessary to measure the growth rates of crusts accurately. Consequently, this has been the focus of considerable research.

The most precise measurements of the growth rates of ferromangenese crusts are obtained from U-series isotopes (section 12.3.2). Because internal checks can be made using different U-series methods, these are also the most accurate data. However, these methods cannot reach beyond 400 kyr, whereas many crusts have grown for more than 20 Myr. An alternative approach attempted in early work on crusts was to use Sr isotope stratigraphy (section 3.6.1). This method was investigated by Ingram *et al.* (1990) and VonderHaar *et al.* (1995), and appeared to give reasonable growth rates on one or two Atlantic samples (e.g. Burton *et al.*, 1997). However, more detailed studies (e.g. Ling *et al.*, 1997; O'Nions *et al.*, 1998) revealed inconsistencies with other dating techniques, so the method has now largely been abandoned.

An alternative dating technique with a range of 10 Myr involves the cosmogenic isotope ^{10}Be (section 14.3.4). This method has proved quite reliable, especially when ^{10}Be abundances are normalised with respect to ^{9}Be (e.g. Ling *et al.*, 1997). Beyond 10 Myr, the only method that has been proved reliable is cobalt dating. This is based on the assumption that ferromangenese crusts receive a constant input of cobalt with time, so that lower cobalt concentrations imply a faster growth rate, and vice-versa. Frank *et al.* (1999a) showed that growth rates of three long-lived crusts, based on cobalt abundances, were consistent with growth rates extrapolated from the ^{10}Be/^{9}Be chronometer.

One of the most interesting observations from these studies, which were based initially on the analysis of one crust from the North Atlantic (Burton *et al.*, 1997) and one from the Central Pacific (Ling *et al.*, 1997), was the existence of a sharp change in Nd isotope composition in both ocean masses about 4 Myr ago (Fig. 4.42). This period had previously been identified from oxygen isotope evidence as one of increased salinity in the Caribbean, due to closure of the 'Panama Gateway' that had once linked the Pacific Ocean to the Caribbean. Hence, Burton *et al.* (1997) attributed inflections in the Nd isotope profiles about 4 Myr ago to changes in the global ocean-circulation pattern (section 14.1.7) prompted by the closure of the Gateway.

Unfortunately, the Atlantic data in Fig. 4.42 were dated by the seawater Sr method, which was subsequently shown to give ages about double the true value. However, close examination of the data for the Atlantic ocean shows that there are actually two inflections in the curve, and that the 4-Myr timeline passes half-way between them. Therefore, after recalibration of the profile to cosmogenic Be ages, the inflections moved to about 4 and 8 Myr ago, respectively, consistent with more recent measurements by Burton *et al.* (1999) and Frank *et al.* (1999b).

The new data (Fig. 4.43) continue to support the idea that there was a change in Atlantic Oceanic Nd signatures about 4 Myr ago, possibly due to the closure of the Panama Gateway. However, Reynolds *et al.* suggested that this closure may have been progressive, reflecting a gradual shallowing of the Gateway starting 8 Myr ago, which was finally completed 4 Myr ago. In addition, some other Atlantic ferromanganese crusts analysed by Reynolds *et al.* (1999) exhibited inflections at different times. Therefore, closure of the Gateway was probably not the only factor which led to changes in ocean circulation patterns over the past 10 Myr (Frank, 2002). Pb isotope ratios were also analysed in the same samples, but since Pb was significantly decoupled from Nd, the data will be discussed separately (section 5.6.2).

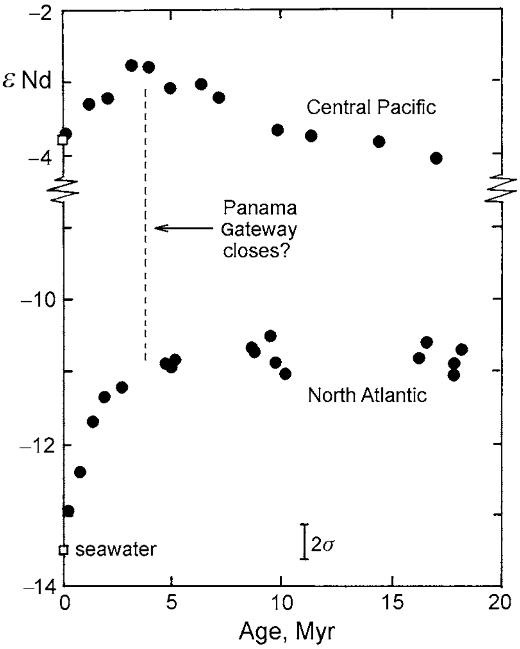

Fig. 4.42. Preliminary Nd isotope data for Fe–Mn crusts from the Pacific and Atlantic oceans, showing possible inflection points in seawater evolution, relative to the estimated time of closure of the Panama gateway. After Burton *et al.* (1997).

4.5.4 Quaternary seawater Nd

The slow growth rates of ferromanganese crusts preclude their use to study short-term changes in seawater Nd signatures, such as might be found during Quaternary glacial cycles. Therefore, other types of material, capable of reliably recording short-term variations, were sought. Forams present an attractive prospect because they are widely distributed, their rapid rates of sedimentation can yield high-resolution profiles, and they are already linked to glacial cycles by stable isotope measurements. A problem is that forams become coated after accumulation on the seafloor with

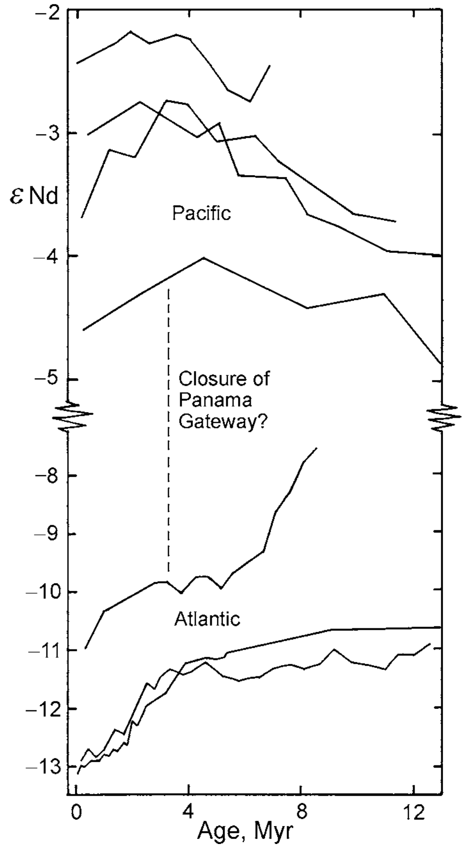

Fig. 4.43. Comparison of several Fe–Mn profiles for the Pacific and Atlantic oceans, relative to the time of closure of the Panama gateway. After Frank *et al.* (1999b).

ferromanganese deposits whose Nd concentrations are much higher than those in the forams themselves. However, Vance and Burton (1999) showed that, after removal of these coatings by leaching with a strong reducing agent, the original Nd isotope compositions of forams could successfully be recovered.

Burton and Vance (2000) applied this method to the analysis of forams in a 3-m-long core from the northern Indian Ocean, covering the past 150 kyr. Several tests were done to check that the measured Nd isotope ratios were original rather than secondary. These included analysis of Mn/Ca ratios as a monitor of the effectiveness of the cleaning procedure, comparisons between two different fossil foram species, and comparisons of Nd content and isotope ratio with modern Indian Ocean forams. All these tests gave confidence that the method was recovering original seawater Nd signatures. When the resulting down-hole record of Nd isotope composition was examined (Fig. 4.44), an almost perfect mirror image of the oxygen isotope record was seen for the last glacial cycle. This suggests strongly that the Nd isotope record reflects climatic processes associated with the glacial cycle. Burton and Vance attributed the isotopic fluctuations to a balance between the supply of radiogenic Nd from the main body of the Indian Ocean and the supply of unradiogenic Nd from Himalayan erosion. Hence, if the monsoon was attenuated during the last glacial maximum, the result would be the more radiogenic Indian Ocean Nd signatures seen in Fig. 4.44.

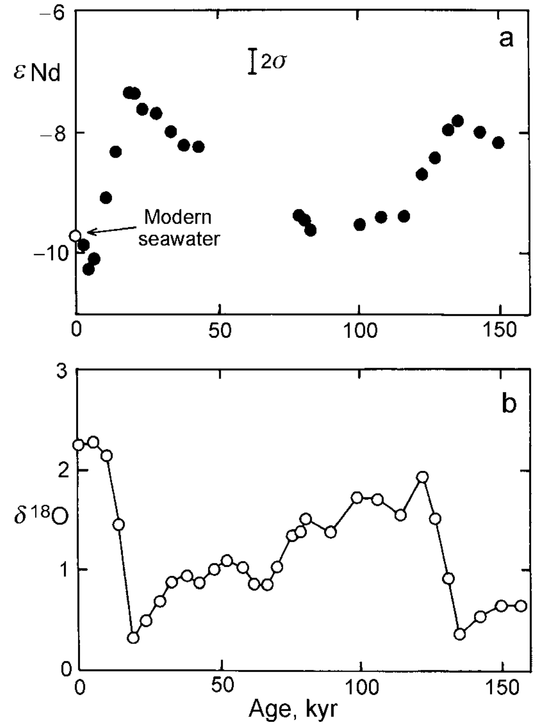

Fig. 4.44. Plots of (a) Nd isotope ratio and (b) oxygen isotope ratio (per mil relative to PDB) in planktonic forams from a drill core in the northern Indian Ocean. After Burton and Vance (2000).

A somewhat surprising observation made by Burton and Vance (2000) was that uncleaned forams with ferromanganese coatings had the same isotopic signatures as cleaned forams, and that even bulk sediment samples gave a profile that was parallel to that for the cleaned samples, but offset 1–2 ε units above it. This suggests that even dispersed ferromanganese oxides in sediment cores may be a viable record of past seawater Nd signatures. On the basis of this assumption, Rutberg *et al.* (2000) extracted Nd from bulk core sediments by leaching with a strong reducing agent. By

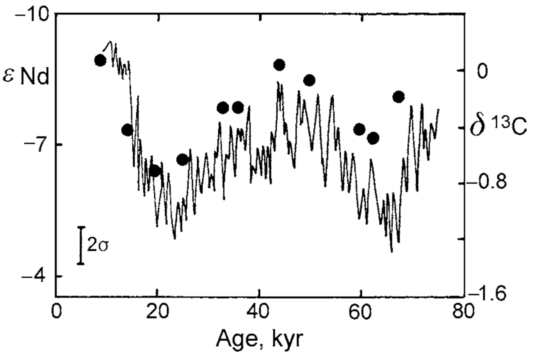

Fig. 4.45. Plot of Nd isotope data for leached ferromanganese phases from a drill core in the Southern Ocean (●), compared with carbon isotope variations in benthic forams from the same core (solid line). After Rutberg *et al.* (2000).

this means they examined an 80-kyr record of seawater Nd in a sediment core from the southeast Atlantic Ocean, in the Cape Basin off South Africa. This is a critical location for understanding the behaviour of the ocean system because many tracer studies have shown that North Atlantic Deep Water (NADW) is mixed with Antarctic Bottom Water in the southern ocean to form Circum-Polar Water, which is then exported to the Pacific. This forms the so-called 'ocean conveyor belt' (section 14.1.7).

From radiocarbon evidence (section 14.1.7) it is expected that the ocean conveyor belt was 'turned off' or reduced during the last glacial maximum (about 20 kyr ago). However, this model was challenged by evidence from U-series isotopes (section 12.3.6), which implied that the conveyor continued unabated during the glacial maximum. Nevertheless, U-series tracers are susceptible to disturbance by changes in biological production, whereas the Nd isotope system is less susceptible to this kind of disturbance. Therefore, Nd isotope data may help to resolve this conflict.

The study of Rutberg *et al.* (2000) provides preliminary data to address this problem, provided that the observed isotopic variations are original rather than diagenetic. Evidence in support of their validity as original seawater compositions came from the preservation of typical seawater Sr isotope signatures in the analysed leachates, despite the presence of radiogenic Sr in coexisting detrital phases. Given this assumption, variations in Nd isotope ratio can be attributed to variations in the supply of NADW to the southern ocean. The fact that these variations are in step with climatically controlled carbon isotope variations (Fig. 4.45) provides evidence to support the hypothesis that there have been changes in the strength of the conveyer belt between glacial and interglacial periods.

References

Albarède, F. and Goldstein, S. L. (1992). World map of Nd isotopes in sea-floor ferromanganese deposits. *Geology* **20**, 761–3.

Allègre, C. J. and Rousseau, D. (1984). The growth of the continents through geological time studied by Nd isotope analysis of shales. *Earth Planet. Sci. Lett.* **67**, 19–34.

Armstrong, R. L. (1981). Radiogenic isotopes: the case for crustal recycling on a near steady-state no-continental-growth Earth. *Phil. Trans. Roy. Soc. Lond. A* **301**, 443–72.

Armstrong, R. L. (1991). The persistent myth of crustal growth. *Australian J. Earth Sci.* **38**, 613–30.

Arndt, N. T. and Goldstein, S. L. (1987). Use and abuse of crust-formation ages. *Geology* **15**, 893–5.

Awwiller, D. N. and Mack, L. E. (1991). Diagenetic modification of Sm–Nd model ages in Tertiary sandstones and shales, Texas Gulf Coast. *Geology* **19**, 311–14.

Barovich, K. M. and Patchett, P. J. (1992). Behaviour of isotopic systematics during deformation and metamorphism: a Hf, Nd and Sr isotopic study of mylonitized granite. *Contrib. Mineral. Petrol.* **109**, 386–93.

Bennett, V. C. and De Paolo, D. J. (1987). Proterozoic crustal history of the western United States as determined by neodymium isotope mapping. *Geol. Soc. Amer. Bull.* **99**, 674–85.

Bennett, V. C. and Nutman, A. P. (1998). Extreme Nd-isotope heterogeneity in the early Archean – fact or fiction? Case histories from northern Canada and West Greenland – comment. *Chem. Geol.* **148**, 213–17.

Bennett, V. C., Nutman, A. P. and McCulloch, M. T. (1993). Nd isotopic evidence for transient, highly depleted mantle reservoirs in the early history of the Earth. *Earth Planet. Sci. Lett.* **119**, 299–317.

Bertram, C. J. and Elderfield, H. (1993). The geochemical balance of the rare earth elements and Nd isotopes in the oceans. *Geochim. Cosmochim. Acta* **57**, 1957–86.

Bock, B., McLennan, S. M. and Hanson, G. N. (1994). Rare earth element redistribution and its effects on the neodymium isotope system in the Austin Glen Member of the Normanskill Formation, New York, USA. *Geochim. Cosmochim. Acta* **58**, 5245–53.

Bowring, S. A. and Housh, T. (1995). The Earth's early evolution. *Science* **269**, 1535–40.

Bowring, S. A. and Housh, T. (1996). Sm–Nd isotope data and Earth's evolution: reply. *Science* **273**, 1878–9.

Bowring, S. A., King, J. E., Housh, T. B., Isachsen, C. E. and Podosek, F. A. (1989). Neodymium and lead isotope evidence for enriched early Archean crust in North America. *Nature* **340**, 222–5.

Bros, R., Stille, P., Gauthier-Lafaye, F., Weber, F. and Clauer, N. (1992). Sm–Nd isotopic dating of Proterozoic clay material: an example from the Francevillian sedimentary series, Gabon. *Earth Planet. Sci. Lett.* **113**, 207–18.

Burton, K. W., Lee, D.-C., Christensen, J. N., Halliday, A. N. and Hein, J. R. (1999). Actual timing of neodymium isotopic variations recorded by Fe–Mn crusts in the western North Atlantic. *Earth Planet. Sci. Lett.* **171**, 149–56.

Burton, K. W., Ling, H.-F. and O'Nions, R. K. (1997). Closure of the Central American Isthmus and its effect on deep-water formation in the North Atlantic. *Nature* **386**, 382–5.

Burton, K. W. and O'Nions, R. K. (1991). High-resolution garnet chronometry and the rates of metamorphic processes. *Earth Planet. Sci. Lett.* **107**, 649–71.

Burton, K. W. and Vance, D. (2000). Glacial–interglacial variations in the neodymium isotope composition of seawater in the Bay of Bengal recorded by planktonic foraminifera. *Earth Planet. Sci. Lett.* **176**, 425–41.

Cattell, A., Krogh, T. E. and Arndt, N. T. (1984). Conflicting Sm–Nd whole rock and U–Pb zircon ages for Archean lavas from Newton Township, Abitibi Belt, Ontario. *Earth Planet. Sci. Lett.* **70**, 280–90.

Chapman, H. J. and Moorbath, S. (1977). Lead isotope measurements from the oldest recognised Lewisian gneisses of northwest Scotland. *Nature* **268**, 41–2.

Chase, C. G. and Patchett, P. J. (1988). Stored mafic/ultramafic crust and early Archean mantle depletion. *Earth Planet. Sci. Lett.* **91**, 66–72.

Chauvel, C., Dupré, B. and Jenner, G. A. (1985). The Sm–Nd age of Kambalda volcanics is 500 Ma too old! *Earth Planet. Sci. Lett.* **74**, 315–24.

Chester, R., Griffiths, A. G. and Hirst, J. M. (1979). The influence of soil-sized atmospheric particulates on the elemental chemistry of deep sea sediments of the northeastern Atlantic. *Marine Geol.* **32**, 141–54.

Claoué-Long, J. C., Thirlwall, M. F. and Nesbitt, R. W. (1984). Revised Sm–Nd systematics of Kambalda greenstones, Western Australia. *Nature* **307**, 697–701.

Compston, W., Williams, I. S., Campbell, I. H. and Gresham, J. J. (1985). Zircon xenocrysts from the Kambalda volcanics: age constraints and direct evidence for older continental crust below the Kambalda–Norseman greenstones. *Earth Planet. Sci. Lett.* **76**, 299–311.

Cullers, R. L., Bock, B. and Guidotti, C. (1997). Elemental distributions and neodymium isotopic compositions of Silurian metasediments, western Maine, USA: redistribution of rare earth elements. *Geochim. Cosmochim. Acta* **61**, 1847–61.

DePaolo, D. J. (1981). Neodymium isotopes in the Colorado Front Range and crust – mantle evolution in the Proterozoic. *Nature* **291**, 193–7.

DePaolo, D. J. and Wasserburg, G. J. (1976a). Nd isotopic variations and petrogenetic models. *Geophys. Res. Lett.* **3**, 249–52.

DePaolo, D. J. and Wasserburg, G. J. (1976b). Inferences about magma sources and mantle structure from variations of ^{143}Nd/^{144}Nd. *Geophys. Res. Lett.* **3**, 743–6.

DePaolo, D. J. and Wasserburg, G. J. (1979). Sm–Nd age of the Stillwater complex and the mantle evolution curve for neodymium. *Geochim. Cosmochim. Acta* **43**, 999–1008.

Dia, A., Allègre, C. J. and Erlank, A. J. (1990). The development of continental crust through geological time: the South African case. *Earth Planet. Sci. Lett.* **98**, 74–89.

Dickin, A. P. (2000). Crustal formation in the Grenville Province: Nd-isotope evidence. *Can. J. Earth Sci.* **37**, 165–81.

Frank, M. (2002). Radiogenic isotopes: tracers of past ocean circulation and erosional input. *Rev. Geophys.* **40** (1), 1–38.

Frank, M., O'Nions, R. K., Hein, J. R. and Banakar, V. K. (1999a). 60 Myr records of major elements and Pb–Nd isotopes from hydrogenous ferromanganese crusts: reconstruction of seawater paleochemistry. *Geochim. Cosmochim. Acta* **63**, 1689–708.

Frank, M., Reynolds, B. C. and O'Nions, R. K. (1999b). Nd and Pb isotopes in Atlantic and Pacific water masses before and after closure of the Panama gateway. *Geology* **27**, 1147–50.

Galer, S. J. G. and Goldstein, S. L. (1991). Early mantle differentiation and its thermal consequences. *Geochim. Cosmochim. Acta* **55**, 227–39.

Goldberg, E. D., Koide, M., Schmidt, R. A. and Smith, R. H. (1963). Rare earth distributions in the marine environment. *J. Geophys. Res.* **68**, 4209–17.

Goldstein, S. J. and Jacobsen, S. B. (1987). The Nd and Sr isotopic systematics of river-water dissolved material: implications for the sources of Nd and Sr in seawater. *Chem. Geol. (Isot. Geosci. Section)* **66**, 245–72.

Goldstein, S. J. and Jacobsen, S. B. (1988). Nd and Sr isotopic systematics of river water suspended material: implications for crustal evolution. *Earth Planet. Sci. Lett.* **87**, 249–65.

Goldstein, S. L., O'Nions, R. K. and Hamilton, P. J. (1984). A Sm–Nd isotopic study of atmospheric dusts and particulates from major river systems. *Earth Planet. Sci. Lett.* **70**, 221–36.

Green, T. H., Brunfeldt, A. O. and Heier, K. S. (1969). Rare earth element distribution in anorthosites and associated high grade metamorphic rocks, Lofoten–Vesteraalen, Norway. *Earth Planet. Sci. Lett.* **7**, 93–8.

Griffin, W. L. and Brueckner, H. K. (1980). Caledonian Sm–Nd ages and a crustal origin for Norwegian eclogites. *Nature* **285**, 319–20.

Hamilton, P. J., O'Nions, R. K., Bridgwater, D. and Nutman, A. (1983). Sm–Nd studies of Archean metasediments and metavolcanics from West Greenland and their implications for the Earth's early history. *Earth Planet. Sci. Lett.* **62**, 263–72.

Hamilton, P. J., Evensen, N. M., O'Nions, R. K. and Tarney, J. (1979). Sm–Nd systematics of Lewisian gneisses: implications for the origin of granulites. *Nature* **277**, 25–8.

Hanson, G. N. (1978). The application of trace elements to the petrogenesis of igneous rocks of granitic composition. *Earth Planet. Sci. Lett.* **38**, 26–43.

Haskin, L. A., Frey, F. A., Schmidt, P. A. and Smith, R. H. (1966). Meteoritic, solar and terrestrial rare-earth distributions. *Phys. Chem. Earth* **7**, 167–321.

Hurley, P. M., Hughes, H., Faure, G., Fairbairn, H. W. and Pinson, W. H. (1962). Radiogenic strontium-87 model of continent formation. *J. Geophys. Res.* **67**, 5315–34.

Hurley, P. M. and Rand, J. R. (1969). Pre-drift continental nuclei. *Science* **164**, 1229–42.

Ingram, B. L., Hein, J. R. and Farmer, G. L. (1990). Age determinations and growth rates of Pacific ferromanganese deposits using strontium isotopes. *Geochim. Cosmochim. Acta* **54**, 1709–21.

Jacobsen, S. B. (1988). Isotopic constraints on crustal growth and recycling. *Earth Planet. Sci. Lett.* **90**, 315–29.

Jacobsen, S. B. and Pimentel-Klose, M. R. (1988). Nd isotopic variations in Precambrian banded iron formations. *Geophys. Res. Lett.* **15**, 393–6.

Jacobsen, S. B. and Wasserburg, G. J. (1980). Sm–Nd isotopic evolution of chondrites. *Earth Planet. Sci. Lett.* **50**, 139–55.

Kamber, B. S. and Moorbath, S. (1998). Initial Pb of the Amitsoq gneiss revisited: implication for the timing of early Archean crustal evolution in West Greenland. *Chem. Geol.* **150**, 19–41.

Kamber, B. S., Moorbath, S. and Whitehouse, M. J. (1998). Extreme Nd-isotope heterogeneity in the early Archean – fact or fiction? Case histories from northern Canada and West Greenland – reply. *Chem. Geol.* **148**, 219–24.

Keto, L. S. and Jacobsen, S. B. (1987). Nd and Sr isotopic variations of Early Paleozoic oceans. *Earth Planet. Sci. Lett.* **84**, 27–41.

Keto, L. S. and Jacobsen, S. B. (1988). Nd isotopic variations of Phanerozoic paleo-oceans. *Earth Planet. Sci. Lett.* **90**, 395–410.

Lahaye, Y., Arndt, N., Byerly, G., Chauvel, C., Fourcade, S. and Gruau, G. (1995). The influence of alteration on the trace-element and Nd isotopic composition of komatiites. *Chem. Geol.* **126**, 43–64.

Lambert, D. D., Morgan, J. W., Walker, R. J. *et al.* (1989). Rhenium–osmium and samarium–neodymium isotopic systematics of the Stillwater Complex. *Science* **244**, 1169–74.

Ling, H. F., Burton, K. W., O'Nions, R. K. *et al.* (1997). Evolution of Nd and Pb isotopes in Central Pacific seawater from ferromanganese crusts. *Earth Planet. Sci. Lett.* **146**, 1–12.

Lugmair, G. W. and Marti, K. (1978). Lunar initial ^{143}Nd/^{144}Nd: differential evolution of the lunar crust and mantle. *Earth Planet. Sci. Lett.* **39**, 349–57.

Lugmair, G. W. and Scheinin, N. B. (1975). Sm–Nd systematics of the Stannern meteorite. *Meteoritics* **10**, 447–8 (abstract).

Lugmair, G. W., Scheinin, N. B. and Marti, K. (1975). Search for extinct ^{146}Sm, I. The isotopic abundance of ^{142}Nd in the Juvinas meteorite. *Earth Planet. Sci. Lett.* **27**, 79–84.

McCulloch, M. T. and Compston, W. (1981). Sm–Nd age of Kambalda and Kanowna greenstones and heterogeneity in the Archean mantle. *Nature* **294**, 322–7.

McCulloch, M. T. and Wasserburg, G. J. (1978). Sm–Nd and Rb–Sr chronology of continental crust formation. *Science* **200**, 1003–11.

McLennan, S. M., McCulloch, M. T., Taylor, S. R. and Maynard, J. B. (1989). Effects of sedimentary sorting on neodymium isotopes in deep-sea turbidites. *Nature* **337**, 547–9.

Michard, A., Albarède, F., Michard, G., Minster, J. F. and Charlou, J. L. (1983). Rare-earth elements and uranium in high-temperature solutions from East Pacific Rise hydrothermal vent field (13 °N). *Nature* **303**, 795–7.

Mildowski, A. E. and Zalasiewicz, J. A. (1991). Redistribution of rare earth elements during diagenesis of turbidite/hemipelagite mudstone sequences of Llandovery age from central Wales. In: Morton, A. C. *et al.* (Eds.), *Developments in Sedimentary Provenance Studies*. *Geol. Soc. Spec. Pap.* **56**, pp. 789–95.

Moorbath, S. (1976). Age and isotope constraints for the evolution of Archaean crust. In: Windley, B. F. (Ed.), *The Early History of the Earth*. Wiley, pp. 351–60.

Moorbath, S., Powell, J. L. and Taylor, P. N. (1975). Isotopic evidence for the age and origin of the grey gneiss complex of the southern Outer Hebrides, Scotland. *J. Geol. Soc. Lond.* **131**, 213–22.

Moorbath, S. and Whitehouse, M. J. (1996). Sm–Nd isotope data and Earth's evolution: comment. *Science* **273**, 1878.

Moorbath, S., Whitehouse, M. J. and Kamber, B. S. (1997). Extreme Nd-isotope heterogeneity in the early Archean – fact or fiction? Case histories from northern Canada and West Greenland. *Chem. Geol.* **135**, 213–31.

Mørk, M. B. E. and Mearns, E. W. (1986). Sm–Nd isotopic systematics of a gabbro–eclogite transition. *Lithos* **19**, 255–67.

Nägler, Th. F. and Kramers, J. D. (1998). Nd isotopic evolution of the upper mantle during the Precambrian: models, data and the uncertainty of both. *Precamb. Res.* **91** 233–52.

Nelson, B. K. and DePaolo, D. J. (1984). 1,700-Myr greenstone volcanic successions in southwestern North America and isotopic evolution of Proterozoic mantle. *Nature* **312**, 143–6.

Nelson, B. K. and DePaolo, D. J. (1985). Rapid production of continental crust 1.7 to 1.9 b.y. ago: Nd isotopic evidence from the basement of the North American mid-continent. *Geol. Soc. Amer. Bull.* **96**, 746–54.

Nelson, B. K. and DePaolo, D. J. (1988). Application of Sm–Nd and Rb–Sr isotope systematics to studies of provenance and basin analysis. *J. Sed. Petrol.* **58**, 348–57.

Notsu, K., Mabuchi, H., Yoshioka, O., Matsuda, J. and Ozima, M. (1973). Evidence of the extinct nuclide ^{146}Sm in 'Juvinas' achondrite. *Earth Planet. Sci. Lett.* **19**, 29–36.

Nunes, P. D. (1981). The age of the Stillwater complex: a comparison of U–Pb zircon and Sm–Nd isochron systematics. *Geochim. Cosmochim. Acta* **45**, 1961–3.

Nutman, A. P., Bennett, V. C., Friend, C. R. L. and McGregor, V. R. (2000). The early Archean Itsaq Gneiss Complex of southern West Greenland: the importance of field observations in interpreting age and isotopic constraints for early terrestrial evolution. *Geochim. Cosmochim. Acta* **64**, 3035–60.

Öhlander, B., Ingri, J., Land, M. and Schöberg, H. (2000). Change of Sm–Nd isotope composition during weathering of till. *Geochim. Cosmochim. Acta* **64**, 813–20.

O'Nions, R. K. (1984). Isotopic abundances relevant to the identification of magma sources. *Phil. Trans. Roy. Soc. Lond. A* **310**, 591–603.

O'Nions, R. K., Carter, S. R., Cohen, R. S., Evensen, N. M. and Hamilton, P. J. (1978). Pb, Nd and Sr isotopes in oceanic ferromanganese deposits and ocean floor basalts. *Nature* **273**, 435–8.

O'Nions, R. K., Frank, M., von Blanckenburg, F. and Ling, H.-F. (1998). Secular variation of Nd and Pb isotopes in ferromanganese crusts from the Atlantic, Indian and Pacific Oceans. *Earth Planet. Sci. Lett.* **155**, 15–28.

O'Nions, R. K., Hamilton, P. J. and Evensen, N. M. (1977). Variations in ^{143}Nd/^{144}Nd and ^{87}Sr/^{86}Sr in oceanic basalts. *Earth Planet. Sci. Lett.* **34**, 13–22.

O'Nions, R. K., Hamilton, P. J. and Hooker, P. J. (1983). A Nd isotope investigation of sediments related to crustal development in the British Isles. *Earth Planet. Sci. Lett.* **63**, 229–40.

Palmer, M. R. and Elderfield, H. (1986). Rare earth elements and neodymium isotopes in ferromanganese oxide coatings of Cenozoic foraminifera from the Atlantic Ocean. *Geochim. Cosmochim. Acta* **50**, 409–17.

Patchett, P. J. and Arndt, N. T. (1986). Nd isotopes and tectonics of 1.9–1.7 Ga crustal genesis. *Earth Planet. Sci. Lett.* **78**, 329–38.

Pidgeon, R. T. and Bowes, D. R. (1972). Zircon U/Pb ages of granulites from the central region of the Lewisian, north western Scotland. *Geol. Mag.* **109**, 247–58.

Piepgras, D. J. and Wasserburg, G. J. (1980). Neodymium isotopic variations in seawater. *Earth Planet. Sci. Lett.* **50**, 128–38.

Piepgras, D. J. and Wasserburg, G. J. (1983). Influence of the Mediterranean Outflow on the isotopic composition of neodymium in waters of the North Atlantic. *J. Geophys. Res.* **88**, 5997–6006.

Piepgras, D. J. and Wasserburg, G. J. (1987). Rare earth element transport in the western North Atlantic inferred from Nd isotopic observations. *Geochim. Cosmochim. Acta* **51**, 1257–71.

Piepgras, D. J., Wasserburg, G. J. and Dasch, E. J. (1979). The isotopic composition of Nd in different ocean masses. *Earth Planet. Sci. Lett.* **45**, 223–36.

Reynolds, B. C., Frank, M. and O'Nions, R. K. (1999). Nd- and Pb-isotope time series from Atlantic ferromanganese crusts: implications for changes in provenance and paleocirculation over the last 8 Myr. *Earth Planet. Sci. Lett.* **173**, 381–96.

Richardson, S. H., Gurney, J. J., Erlank, A. J. and Harris, J. W. (1984). Origin of diamonds in old enriched mantle. *Nature* **310**, 198–202.

Rutberg, R. L., Hemming, S. R. and Goldstein, S. L. (2000). Reduced North Atlantic Deep Water flux to the glacial Southern Ocean inferred from neodymium isotope ratios. *Nature* **405**, 935–8.

Samson, S. D., McClelland, W. C., Patchett, P. J., Gehrels, G. E. and Anderson, R. G. (1989). Evidence from neodymium isotopes for mantle contributions to Phanerozoic crustal genesis in the Canadian Cordillera. *Nature* **337**, 705–9.

Shaw, H. F. and Wasserburg, G. J. (1985). Sm–Nd in marine carbonates and phosphates: implications for Nd isotopes in seawater and crustal ages. *Geochim. Cosmochim. Acta* **49**, 503–18.

Smith, A. D. and Ludden, J. N. (1989). Nd isotopic evolution of the Precambrian mantle. *Earth Planet. Sci. Lett.* **93**, 14–22.

Staudigel, H., Doyle, P. and Zindler, A. (1985). Sr and Nd isotope systematics in fish teeth. *Earth Planet. Sci. Lett.* **76**, 45–56.

Stille, P. and Clauer, N. (1986). Sm–Nd isochron-age and provenance of the argillites of the Gunflint Iron Formation in Ontario, Canada. *Geochim. Cosmochim. Acta* **50**, 1141–6.

Stordal, M. C. and Wasserburg, G. J. (1986). Neodymium isotopic study of Baffin Bay water: sources of REE from very old terranes. *Earth Planet. Sci. Lett.* **77**, 259–72.

Tachikawa, K., Jeandel, C. and Roy-Barman, M. (1999). A new approach to the Nd residence time in the ocean: the role of atmospheric inputs. *Earth Planet. Sci. Lett.* **170**, 433–46.

Taylor, S. R., McLennan, S. M. and McCulloch, M. T. (1983). Geochemistry of loess, continental crustal composition and crustal model ages. *Geochim. Cosmochim. Acta* **47**, 1897–905.

Thurston, P. C., Osmani, I. A. and Stone, D. (1991). Northwest Superior province: review and terrane analysis. In: Thurston, P. C., Williams, H. R., Sutcliffe, R. H. and Stott, G. M. (Eds.), *Geology of Ontario. Ontario Geol. Surv. Spec. Vol.* **4**, 81–139.

Tugarinov, A. I. and Bibikova, Y. V. (1976). Evolution of the chemical composition of the Earth's crust. *Geokhimiya* **8**, 1151–9.

Vance, D. and Burton, K. (1999). Neodymium isotopes in planktonic foraminifera: a record of the response of continental weathering and ocean circulation rates to climate change. *Earth Planet. Sci. Lett.* **173**, 365–79.

Vance, D. and O'Nions, R. K. (1990). Isotopic chronometry of zoned garnets: growth kinetics and metamorphic histories. *Earth Planet. Sci. Lett.* **97**, 227–40.

VonderHaar, D. L., Mahoney, J. J. and McMurtry, G. M. (1995). An evaluation of strontium isotopic dating of ferromanganese oxides in a marine hydrogeneous ferromanganese crust. *Geochim. Cosmochim. Acta* **59**, 4267–77.

Wasserburg, G. J., Jacobsen, S. B., DePaolo, D. J., McCulloch, M. T. and Wen, T. (1981). Precise determination of Sm/Nd ratios, Sm and Nd isotopic abundances in standard solutions. *Geochim. Cosmochim. Acta* **45**, 2311–23.

West, G. F. (1980). Formation of continental crust. In: Strangway, D. W. (Ed.), *The Continental Crust and Its Mineral Deposits. Geol. Assoc. Canada Spec. Pap.* **8**, 117–48.

Whitehouse, M. J. (1988). Granulite facies Nd-isotopic homogenisation in the Lewisian complex of northwest Scotland. *Nature* **331**, 705–7.

Whitehouse, M. J., Kamber, B. S. and Moorbath, S. M. (1999). Age significance of U–Th–Pb zircon data from early Archean rocks of west Greenland – a reassessment based on combined ion-microprobe and imaging studies. *Chem. Geol.* **160**, 201–24.

Williams, H. R., Stott, G. M., Thurston, P. C. *et al.* (1992). Tectonic evolution of Ontario: summary and synthesis. In: Thurston, P. C., Williams, H. R., Sutcliffe, R. H. and Stott, G. M. (Eds.), *Geology of Ontario. Ontario Geol. Surv. Spec. Vol.* **4**, 1255–1332.

Wust, G. (1924). Florida und Antillenstrom. *Veröffentl. Inst. Meeresh. Univ. Berlin* **12**, 1–48.

5 Lead isotopes

Of the four stable isotopes of lead, only ^{204}Pb is non-radiogenic. The other lead isotopes are the final decay products of three complex decay chains from uranium (U) and thorium (Th). However, the intermediate members of each series are relatively short-lived, so they can usually be ignored when geological timescales of millions of years are involved. Table 5.1 shows the ultimate parent–daughter pairs, of which the parent of highest atomic weight (^{238}U) decays to the daughter of lowest atomic weight (^{206}Pb) and vice-versa. It will be noted that the half-life of ^{238}U is comparable to the age of the Earth, whereas that for ^{235}U is much shorter, so that almost all primordial ^{235}U in the Earth has now decayed to ^{207}Pb. The half-life of ^{232}Th is comparable to the age of the universe.

If we consider a system of age t (e.g. a granite intrusion that crystallised from a magma), then, for the nuclides involved in each decay scheme, we can write an equation derived from the general equation [1.10]:

$$^{206}\mathrm{Pb_P} = {}^{206}\mathrm{Pb_I} + {}^{238}\mathrm{U}(e^{\lambda_{238}t} - 1) \qquad [5.1]$$

$$^{207}\mathrm{Pb_P} = {}^{207}\mathrm{Pb_I} + {}^{235}\mathrm{U}(e^{\lambda_{235}t} - 1) \qquad [5.2]$$

$$^{208}\mathrm{Pb_P} = {}^{208}\mathrm{Pb_I} + {}^{232}\mathrm{Th}(e^{\lambda_{232}t} - 1) \qquad [5.3]$$

where P indicates the abundance of a given nuclide at the present and I indicates the initial abundance of that nuclide. It is convenient to divide throughout by ^{204}Pb to obtain equations containing isotope ratios rather than absolute nuclide abundances. ^{204}Pb is chosen because it is the only non-radiogenic isotope. Hence, for the two uranium decay schemes, we obtain

Table 5.1. *Ultimate parent–daughter pairs of uranium and thorium*

Decay route	$t_{1/2}$, Byr	Decay constant λ, yr^{-1}
^{238}U → ^{206}Pb	4.47	1.55125×10^{-10}
^{235}U → ^{207}Pb	0.704	9.8485×10^{-10}
^{232}Th → ^{208}Pb	14.01	0.49475×10^{-10}

Data from Jaffey *et al.* (1971).

$$\left(\frac{^{206}\mathrm{Pb}}{^{204}\mathrm{Pb}}\right)_P = \left(\frac{^{206}\mathrm{Pb}}{^{204}\mathrm{Pb}}\right)_I + \frac{^{238}\mathrm{U}}{^{204}\mathrm{Pb}}(e^{\lambda_{238}t} - 1) \qquad [5.4]$$

$$\left(\frac{^{207}\mathrm{Pb}}{^{204}\mathrm{Pb}}\right)_P = \left(\frac{^{207}\mathrm{Pb}}{^{204}\mathrm{Pb}}\right)_I + \frac{^{235}\mathrm{U}}{^{204}\mathrm{Pb}}(e^{\lambda_{235}t} - 1) \qquad [5.5]$$

5.1 U–Pb isochrons

In principle, the decay equations [5.4] and [5.5] can be used to construct isochron diagrams and hence to date rocks in a manner analogous to the Rb–Sr system (section 3.2.2). U–Pb isochrons are subject to assumptions similar to those for Rb–Sr, the most critical of which is that the samples remained closed to U and Pb during the lifetime of the system being dated. Unfortunately, the U–Pb system rarely stays closed in silicate rocks, due to the mobility of Pb, and especially U, under conditions of low-grade metamorphism and superficial weathering. For example, in a case study on the Granite Mountains batholith, Wyoming (Fig. 5.1) whole-rock samples suffered disastrous uranium losses, displacing the data points far from a reference line defined by the intrusive age.

The mobility of uranium greatly limits the application of simple U–Pb isochron dating. However, the unique properties of the U–Pb system, involving two separate decay schemes with common parent and daughter nuclides, mean that age information can be obtained even from disturbed systems. Three dating techniques exploit this situation, namely the U–Pb 'zircon' method, the common Pb–Pb method, and the galena model age method. These methods will be discussed in the subsequent sections. Nevertheless, there are a few systems to which conventional U–Pb isochron dating has successfully been applied. These include dating sediment deposition by means of marine carbonate and dating prograde metamorphism by means

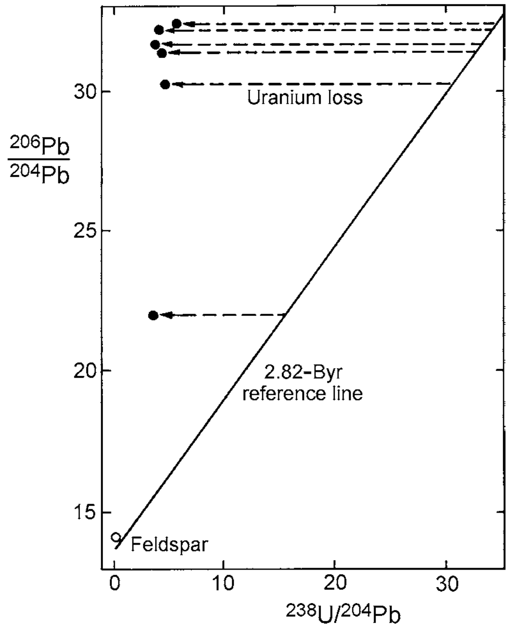

Fig. 5.1. U–Pb isochron diagram for the Granite Mountains batholith, showing displacement of whole-rock data points far to the left of the 2.82-Byr reference line, due to disastrous losses of uranium. After Rosholt and Bartel (1969).

of garnet porphyroblasts. The first of these examples will be examined here. U–Pb dating of garnets will be discussed in section 5.2.7.

5.1.1 U–Pb dating of carbonates

One area where U–Pb isochron dating has been applied with moderate success is the direct dating of marine carbonates, which have proven very difficult to date by other radiometric methods. Uranium has a seawater residence time four orders of magnitude longer than that for Pb, leading to a very high ^{238}U/^{204}Pb ratio (μ value) of about 75 000 (Jahn and Cuvellier, 1994). Because U is also thought to have a higher carbonate/seawater partition coefficient than Pb, the μ value of marine carbonates could be even higher. An upper limit of 230 000 was suggested by Jahn and Cuvellier, corresponding to a U content of 1–3 ppm and Pb content of about 1 ppb (part per billion). The highest μ value observed in an ancient biogenic calcite is 50 000 (Smith *et al.*, 1991). However, most ancient carbonates have values far lower than this, which are therefore attributed to open-system behaviour during post-depositional diagenesis and secondary alteration.

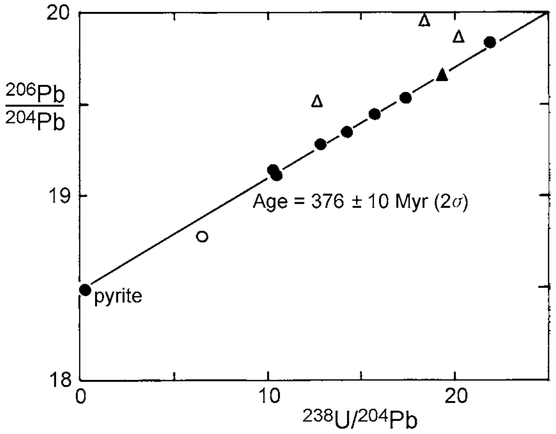

Fig. 5.2. U–Pb isochron diagram for Devonian corals from SW Ontario, Canada: (●, ○) = Heliophyllum; (▲, △) = Cystiphylloides. Open symbols were omitted from the regression. After Smith and Farquhar (1989).

An example of U–Pb dating of typical marine carbonates is the study of Smith and Farquhar (1989) on Devonian rugose (Heliophyllum) corals from Ontario. Several coral samples, together with authigenic pyrite from one specimen, formed a reasonably good linear array on a $^{238}\text{U}-^{206}\text{Pb}$ isochron diagram (Fig. 5.2). In this figure the solid points form an errorchron (MSWD = 4.7), but the age of $376 \pm 10\,\text{Myr}\,(2\sigma)$ compares well with a stratigraphic age of about 375–385 Myr. However, this result was only achieved by omitting data for one Heliophyllum coral and three out of four Cystiphylloides corals, which lie well off the regression line. This scatter was probably caused by open-system behaviour during recrystallisation, since the Cystiphylloides corals have a more porous structure which would facilitate movement of fluids. In subsequent work the diagenetic calcite overgrowths were studied, but reliable ages were difficult to determine, due to the effects of multiple growth stages (Smith *et al.*, 1991). Hence it is concluded that only primary depositional carbonates yield reliable age information.

Jones *et al.* (1995) showed that some samples from the Capitan Limestone of New Mexico had μ values over 3000, which appear to correspond to a primary depositional feature. The sample suite came from a Permian reef complex and consisted of massive abiotic botryoids (about 1 cm in size), made of acicular aragonite recrystallised to low-Mg calcite. However, micro-sampling for oxygen and carbon isotope analysis suggested that relatively pristine

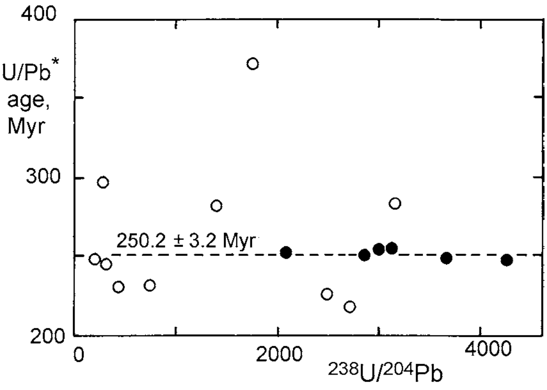

Fig. 5.3. Plot of radiogenic ^{206}Pb*/^{238}U ages against U/Pb ratio for the Capitan Limestone, New Mexico. Texturally well-preserved carbonates with high U/Pb ratios (●) yield ages consistent with the known age of deposition. However, other samples are badly scattered. After Jones *et al.* (1995).

and diagenetically disturbed domains were intimately interfingered. Samples preserving possibly primary μ values had high U (3 ppm), high Sr (3000 ppm) and low Mn contents (<10 ppm). The high μ values allowed the calculation of radiogenic ^{206}Pb*/^{238}U ages, as in equation [5.8], after correction for a small common-Pb component. Using this method, six samples gave an average age of 250 ± 3 Myr, which is consistent with the age of deposition (Fig. 5.3). However, many other samples gave scattered ages, including some with μ values above 2000, within the same range as the 'undisturbed' samples. Since there is no *a priori* way of recognising the disturbed samples, the method cannot be considered reliable.

Another kind of carbonate material that has been proposed for dating stratigraphic sections is paleosol calcite (Rasbury *et al.* 1997). This type of calcite grows on the sediment surface when marine sequences are subjected to sub-aerial exposure, forming a soil horizon. Under these conditions sparry calcite grows as a cement, and has a brown colour which is caused by organic material. This brown calcite can develop high U/Pb ratios (about 1000) that are suitable for U–Pb isochron dating. Rasbury *et al.* analysed seven calcite samples from a horizon of this type near the Carboniferous–Permian boundary in Texas. These samples define a U–Pb isochron with an age of 298 ± 1.5 Myr (2σ, MSWD = 1.5), which is in good agreement with the estimated stratigraphic age of 295 ± 5 Myr. Hence, this method has potential to be a useful stratigraphic calibration tool.

5.2 U–Pb (zircon) dating

If we had a mineral that strongly incorporated uranium at the time of formation but did not incorporate lead, equation [5.1] above could be simplified by removal of the initial ^{206}Pb term to yield

$$^{206}\text{Pb}^* = {}^{238}\text{U}(e^{\lambda_{238}t} - 1) \qquad [5.6]$$

where Pb* represents radiogenic lead only. Taking ^{238}U to the other side yields the equation

$$\frac{^{206}\text{Pb}^*}{^{238}\text{U}} = (e^{\lambda_{238}t} - 1) \qquad [5.7]$$

A similar equation can be derived from [5.2] above:

$$\frac{^{207}\text{Pb}^*}{^{235}\text{U}} = (e^{\lambda_{235}t} - 1) \qquad [5.8]$$

Minerals that have remained closed systems for U and Pb give concordant values of t when their isotopic compositions are inserted into the left-hand sides of [5.7] and [5.8]. When compositions yielding such concordant ages are plotted graphically (Fig. 5.4) they define a curve that was termed the concordia by Wetherill (1956a). The concordia curve can be drawn by substituting decay constants and successive values of t into the right-hand sides of [5.7] and [5.8], and plotting the results for each value of t.

Uraninite and monazite were the first minerals used in U–Pb geochronology, in view of their tendency to incorporate large concentrations of uranium but very little initial (non-radiogenic) lead. However, their limited distribution restricts their usefulness. On the other

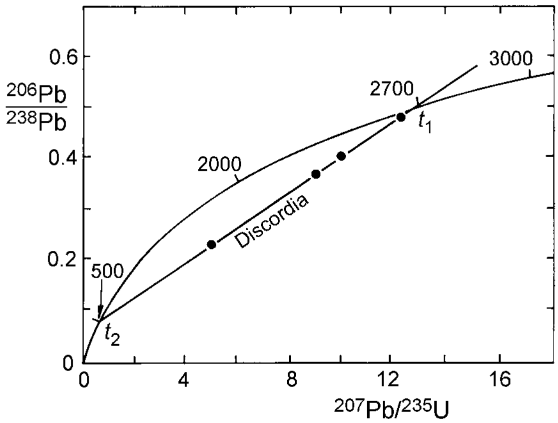

Fig. 5.4. U–Pb concordia diagram showing the concordia line calibrated in Myr, and a discordia line generated by variable Pb loss from 2700-Myr-old U-rich minerals of Zimbabwe (Rhodesia). After Wetherill (1956a).

hand, zircon is a U-rich mineral with a much wider distribution, being present in most intermediate-to-acid rocks. This has therefore become the principal material used in U–Pb dating. A short review of alternative dating materials is given in section 5.2.7.

Corrections for the small fractions of initial ('common') Pb which are incorporated by zircons are made by measuring the amount of (initial) ^{204}Pb in the mineral and then using the ^{206}Pb/^{204}Pb and ^{207}Pb/^{204}Pb ratios of the whole-rock to estimate the initial amounts of ^{206}Pb and ^{207}Pb incorporated into the zircon. These amounts are subtracted from the present-day ^{206}Pb and ^{207}Pb to yield the radiogenic fractions. For zircons with very low common-Pb contents, an adequate correction may be made by estimating common Pb from a general terrestrial Pb evolution model (e.g. Stacey and Kramers, 1975; section 5.4.3), rather then by direct analysis of the whole-rock sample.

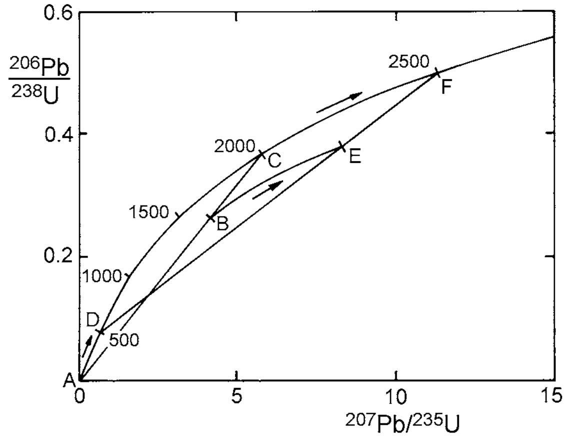

Fig. 5.5. Hypothetical effects of episodic lead loss from a 2500-Myr-old U-rich mineral, showing formation of a discordia 500 Myr ago (A–B–C) and its rotation (D–E–F) due to subsequent closed-system evolution (see the text for discussion).

5.2.1 Lead-loss models

Early dating work on U-rich minerals soon revealed that most samples yield discordant ^{206}Pb/^{238}U and ^{207}Pb/^{235}U ages. This discordance was attributed to loss of Pb by Holmes (1954). Since that time, much research on U–Pb dating has been devoted to studying the mechanism of lead loss, and to the determination of accurate dates on samples that have suffered lead loss.

Ahrens (1955) found that monazite and uraninite from Zimbabwe (then called Southern Rhodesia) yielded discordant U–Pb ages but nevertheless defined a linear array on the concordia diagram (Fig. 5.4). Such arrays were later termed discordia. Ahrens argued against loss of lead from monazites occurring by leaching, since he (erroneously?) claimed them not to be metamict due to radiation damage. Instead, he thought that lead loss occurred by some kind of continuous diffusional process. This model was elaborated by Russell and Ahrens (1957), who postulated that intermediate members of the uranium decay series were ejected into micro-fissures in the mineral lattice (pitchblende in this case) by the 'recoil energy from α-particle emission'. These nuclides or their decay products could subsequently be removed by diffusion or leaching.

Wetherill (1956a) advanced an alternative interpretation of the data, now called the episodic lead-loss model. He agreed that the upper intersection of the discordia with the concordia corresponds to the time of formation of the minerals (t_1). However, Wetherill argued that the lower intersection of the discordia and concordia (t_2) also had age significance, representing the time of a thermal event that caused lead loss from the minerals. For the 'Rhodesian' minerals these episodes are dated at 2700 and 500 Myr ago, respectively. He supported his model by citing Rb–Sr and K–Ar ages of 500 Myr on lepidolite as evidence for a thermal event at that time.

Wetherill (1956b) presented an algebraic proof that the episodic lead-loss model could generate the graphically observed results. This can be visualized (Fig. 5.5) by imagining that the data are plotted at the time of lead loss (500 Myr ago). When lead loss occurs, the data points move from the original composition (C) towards the origin (e.g. forming composition B). Subsequent Pb evolution simply rotates the lead-loss line in proportion: A → D; B → E; C → F.

Tilton (1960) showed that U-rich minerals with similar formation ages from Archean shield areas in five continents all lay near a discordia line with a lower intersection at about 600 Myr (Fig. 5.5). According to the episodic lead-loss model this would imply a worldwide metamorphic event at 600 Myr, but geological evidence for such an event is lacking. Instead, Tilton proposed that the minerals had undergone continuous diffusional lead loss over geological time, yielding a curve on Fig. 5.6 that for much of its length closely resembles a straight line, only curving downwards to an intersection at the origin for cases of strong recent lead loss.

Goldrich and Mudrey (1972) developed this diffusional lead-loss model by arguing that radiation damage of a U-rich mineral was responsible for the formation of a micro-capillary network in the crystal, which would become filled with fluid. Pb that diffused into

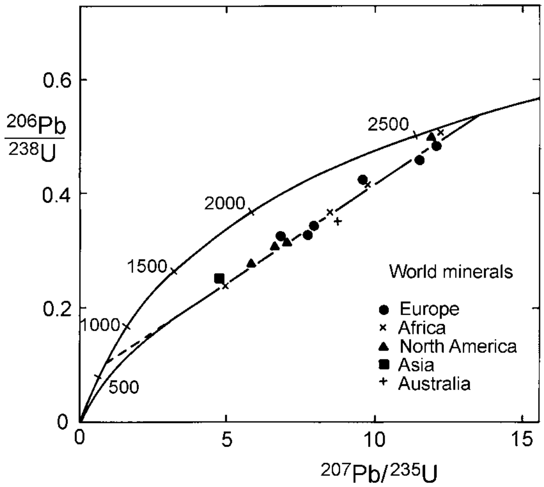

Fig. 5.6. Concordia diagram for Archean U-rich minerals from five continents, showing the common discordia lower intercept at about 500 Myr. The curved line shows the expected effect of extreme diffusional loss of lead. The dotted line shows extrapolation to an apparent episodic lead-loss event. After Tilton (1960).

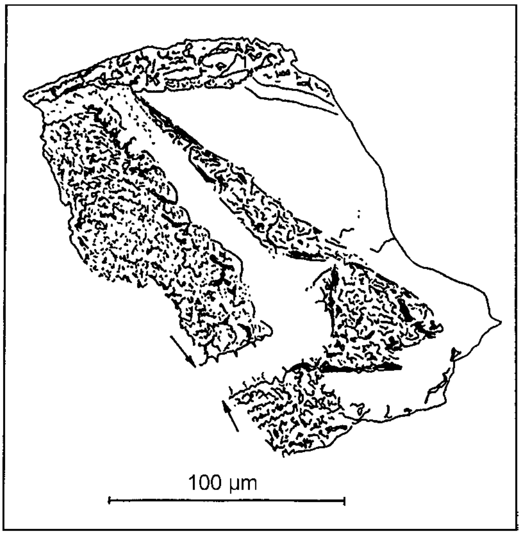

Fig. 5.7. Drawing of a metamict zircon, showing inward advance of alteration fronts (arrows). Unaltered material is white. From a photograph by van Breemen *et al.* (1986).

these fluids would be lost from the mineral when uplift of basement rock caused the mineral to dilate and expel the capillary-filling fluids. Evidence in support of this ‘dilatancy’ model was provided by the agreement of various lower intersection ages from North America with times of basement uplift derived from paleogeographical evidence.

Further understanding of lead-loss mechanisms comes from consideration of the nature of the zircon crystal lattice. For example, Kober (1986) has shown that when Pb is evaporated *in situ* from zircon grains in the mass spectrometer, discordant Pb can be driven off at low filament temperatures (less than 1350 °C), whereas the concordant-Pb fraction is usually emitted between about 1400 and 1500 °C (section 5.2.4 below). Given the high temperatures of concordant Pb emission, Kober (1987) argued that the concordant radiogenic Pb fraction is substituted into the zircon lattice itself, rather than filling defects and voids in the lattice. A stable lattice site would be difficult to envisage for the Pb^{2+} ion, which has an ionic radius (1.18–1.29 Å) much too large to allow substitution for Zr^{4+} (0.72–0.84 Å) or Hf^{4+} (0.71–0.83 Å). However, Pb^{4+} has an ionic radius of only 0.78–0.94 Å, making it a possible candidate for admission into the lattice. Kober (1987) suggested that the emission of β particles during radioactive decay and the transformation of emitted He^{2+} (α particles) into neutral He can effect this oxidation.

The microscopic examination of analysed zircon grains now suggests that lead loss from zircons is a fairly ‘black-and-white’ process. In other words, unaltered zircon lattices lose very little or no lead, whereas altered zircon (promoted by metamictisation) loses lead very readily. Any given zircon crystal may contain both kinds of material. For example, Fig. 5.7 shows alteration fronts advancing through the metamict U-rich parts of a zircon. In reality, the exact mechanism of lead loss from altered zircon may in fact be different in different circumstances. Hence it is concluded that the lower intersection of a U–Pb zircon discordia should only be attributed age significance if this is supported by other geological evidence. However, the interpretation of the upper intersection as the age of formation of the zircons is unaffected.

5.2.2 Upper intersection ages

Silver and Deutsch (1963) made a pioneering case study of lead loss from different zircon fractions in a single rock sample. They found that large zircons lost less lead than small ones (due to the larger surface area/volume ratio of the latter) and that zircons with low uranium contents lost less lead than high-U zircons. The latter effect was attributed to the greater radiation damage suffered by U-rich grains. In addition to losing lead, metamict zircons tend to incorporate impurities, including iron. Hence magnetic separation of zircons can yield fractions with variable discordance.

In order to obtain the best intersection of the discordia with the concordia, it is desirable to analyse several zircon fractions with variable discordance and perform a linear regression on the results. This regression cannot be solved algebraically to yield upper and lower intersection ages; hence these ages are usually calculated iteratively by computer. In order to calculate a regression fit to an array of data displaying some geological scatter, it is common practice to expand analytical error bars to encompass the scatter (section 2.6.3). However, if lead-loss processes have operated at different times during the history of a zircon, the resulting discordia array may fan out somewhat from the upper intercept as the points become more discordant. Therefore, Davis (1982) suggested that, rather than expanding all errors equally to encompass geological scatter, the error bars should instead be magnified in proportion to their discordance (Fig. 5.8).

Krogh (1982a; 1982b) argued that, instead of refining the mathematical treatment of lead-loss models to obtain an accurate upper intersection from discordant zircons, it would be better to remove discordant Pb from the sample before analysis. In early experiments, Krogh and Davis (1975) attempted to remove altered parts of the zircon by chemical leaching prior to analysis. However, they found that Pb was also leached from other parts of the grain. Therefore, it was concluded that physical rather than chemical methods must be used to remove discordant zones of the zircon crystal.

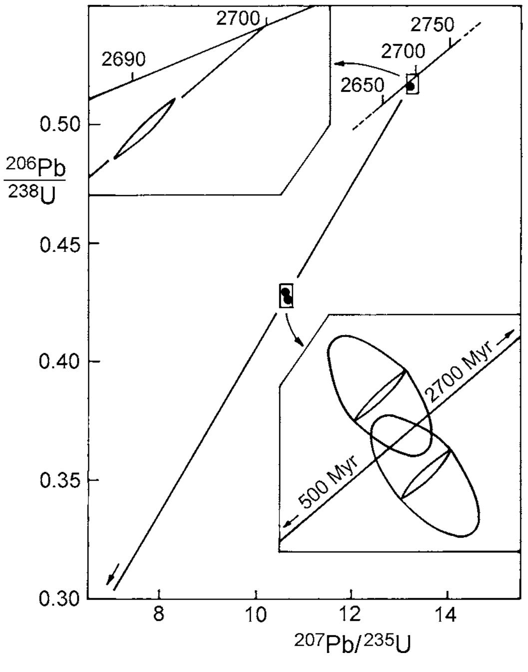

Fig. 5.8. Concordia diagram showing expansion of analytical errors in proportion to discordance to encompass geological scatter on a discordia line. Enlargements are shown for two parts of the discordia. After Davis (1982).

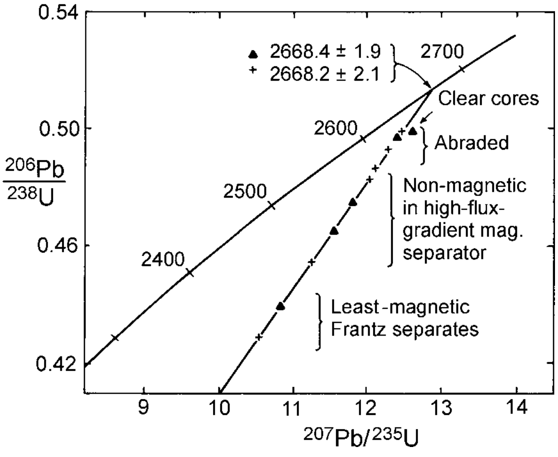

Fig. 5.9. The effect of selecting very non-magnetic zircons and of abrading off the outer rims, to increase concordance. Symbols (+, ▲) indicate two different rock samples. After Krogh (1982b).

A technique of physical separation tested by Krogh (1982a) was the use of a very-high-flux magnetic separator, which removes all but the least-metamict grains. This was found to be relatively successful (Fig. 5.9), but the most successful approach was to abrade the zircons in a pneumatic mill (Krogh, 1982b). This procedure removes the outer layers of the crystals, which are usually the most U-rich and hence metamict. Spectacular increases in concordance were obtained in this manner (Fig. 5.9), and the technique has become a standard procedure in zircon geochronology.

An alternative method of dating zircons with complex geological histories is to break single large zircon crystals into fragments and analyse the individual fragments after a very-low-blank chemical separation (e.g. Schärer and Allègre, 1982). Corfu (1988) developed this method by breaking the tips off large zircons to analyse the age of crystallisation of new zircon over older cores. Aleinikoff *et al.* (1990) achieved a similar effect by analysing the zircon dust produced by gentle air abrasion of prismatic grains with long terminations. The effect of air abrasion on such a grain is shown in Fig. 5.10. Cracked grains must be excluded to prevent their disintegration during abrasion, which would release core material into the dust.

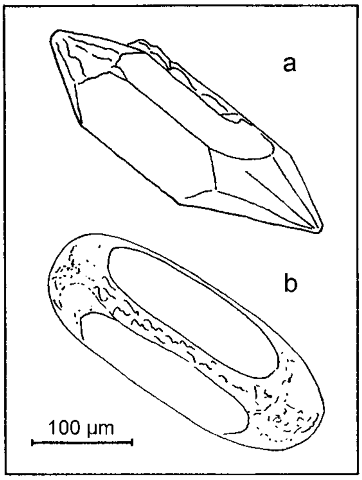

Fig. 5.10. Drawings of zircon grains before and after abrasion to remove tips and interfacial edges for analysis. From photographs by Aleinikoff *et al.* (1990).

Recently, there has been a renewed interest in stepwise dissolution experiments on zircon (e.g. Mattinson, 1994; Corfu, 2000; Davis and Krogh, 2000). However, the new work encountered the same complex fractionation effects that had been observed in early leaching studies. This is attributed to preferential release of radiogenic Pb from energetically unstable lattice sites in radiation-damaged parts of the zircon crystal (the 'hot-atom' effect). To solve this problem, Mattinson (2001) proposed that samples could be annealed before dissolution. This will neutralise the hot-atom effect, but still permit stepwise dissolution of different zones of the crystal, which may have suffered variable Pb loss over geological history. Hence, Mattinson suggested that a U–Pb 'spectrum' plot analogous to that used in Ar–Ar dating (section 10.2.3) could be constructed. It remains to be seen how widely useful the method will be.

With the greatly improved statistics that are now obtainable using the various methods described above, the analytical uncertainty on upper intercept ages is often lower than 0.1% (2σ). This now falls within the same range as the uncertainty on the ^{238}U and ^{235}U decay constants (0.11% and 0.14%, 2σ). Hence, Mattinson (1987) argued that these decay-constant errors should not be ignored, and that the uncertainty on a typical U/Pb upper intercept age might often double if these errors are taken into account.

Many workers have taken the contrary view, that provided U–Pb ages are compared only with other U–Pb ages, it is legitimate to ignore decay-constant errors.

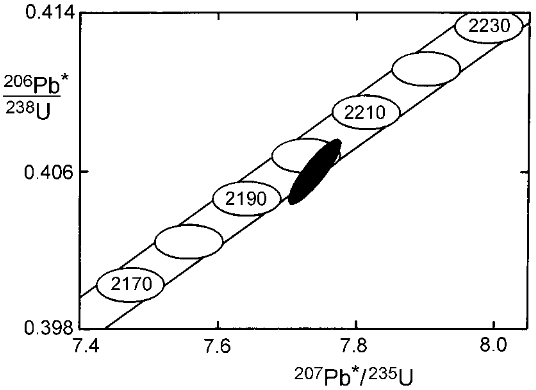

Fig. 5.11. Part of the concordia diagram, showing a nearly-concordant data point (solid ellipse) relative to a concordia band that takes uncertainties in decay constant into account. After Ludwig (1998).

Since U–Pb ages are usually more precise than those obtained with other absolute dating methods (with a few exceptions, such as Ar–Ar dating in the Tertiary period), this argument is usually reasonable. However, Ludwig (1998; 2000) argued that even different dating calculations within the U–Pb method could introduce small biases due to decay-constant errors. In other words, decay-constant uncertainties have slightly different effects on age errors using the ^{206}Pb/^{238}U, ^{207}Pb/^{235}U and ^{207}Pb/^{206}Pb systems.

In general, overall age uncertainties are minimised when both U–Pb decay routes are used together in the concordia diagram. However, even in this system, error magnification can occur. An example of these effects is shown in Fig. 5.11, where the concordia curve has a finite width when decay-constant uncertainties are taken into account (Ludwig, 1998). In principle there is a moderate chance (26%) that the error ellipse in this diagram is concordant, whereas the chance that the ellipse is concordant falls to only 4% if the concordia is drawn as a single line. Even if these effects are not included in reported age errors, it is important to be aware of them.

5.2.3 Ion-microprobe analysis

A completely different approach to achieving concordant U–Pb ages is the *in situ* analysis of Pb isotope composition (and U/Pb ratio) of zircon grains by ion microprobe. The general configuration of such an instrument is shown in Fig. 5.12. A beam of light ions (e.g. O^-) is used to bombard and sputter a polished section of the zircon grain to yield a secondary beam of Pb ions (hence the term secondary-ion mass spectrometry

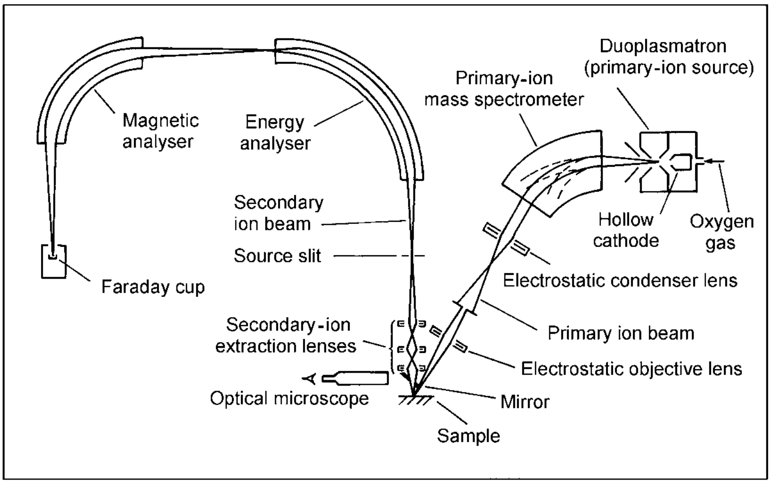

Fig. 5.12. Schematic illustration of a secondary-ion mass spectrometer (SIMS), showing the components of the negative-ion gun and double-focussing analyser. After Potts (1987).

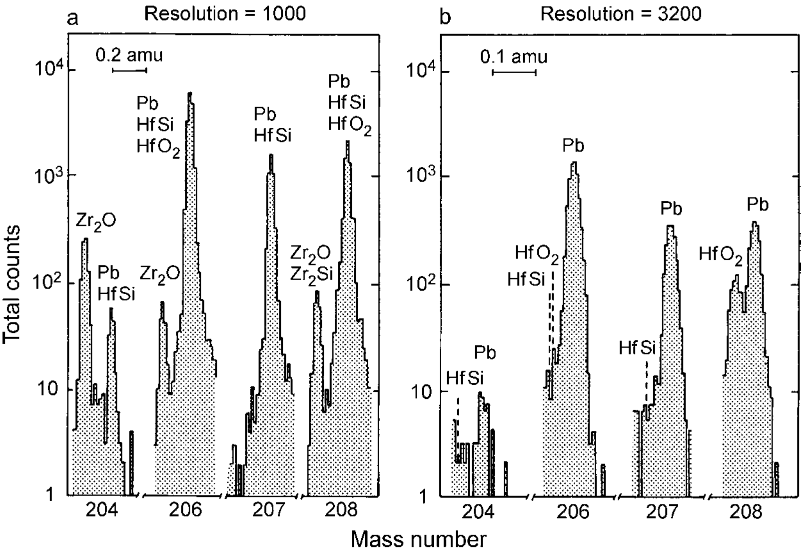

Fig. 5.13. Use of a high-resolution mass spectrometer to separate Pb from interfering molecular-ion signals: (a) low resolution, about 1000; and (b) high resolution, about 3200. After Hinton and Long (1979).

or 'SIMS'). Pb ions are analysed in a double (electrostatic and magnetic)-focussing mass spectrometer. The electrostatic analyser is necessary because emitted secondary ions have a range of energies that would yield bad peak tails in the mass spectrum if not filtered.

A major problem in SIMS analysis is the interference of sputtered molecular ions on the masses of atomic species. In the case of Pb isotope analysis of zircon, this is caused by species such as HfO_2^+, which have almost exactly the same mass as the Pb isotopes, causing isobaric interference (Hinton and Long, 1979). To overcome this problem, the instrument (including the magnet) must have a very large physical size, in order to generate a large spatial separation between different masses (equivalent to a resolution of one mass unit in several thousand). This allows the separation of Pb from molecular-ion interferences using the 'mass-defect' phenomenon (Fig. 5.13), by which small variations in atomic mass result from the varying nuclear binding energies of different atoms. The most successful example of a SIMS instrument used for U–Pb dating is the 'sensitive high-resolution ion microprobe' or 'SHRIMP' developed at the Australian National University (Compston *et al.*, 1984).

An important example of the use of the SHRIMP as a dating tool is provided by the reconnaissance search for very old rocks (Froude *et al.*, 1983). Zircons were selected from a formation of Archean quartzites surrounded by 3.6-Byr-old gneisses (at Mount Narryer, western Australia) to see whether these metasediments contained any component derived from a pre-3.6-Byr-old source. Different areas of single zircon crystals were analysed using the ion microprobe, yielding quite concordant results. Many ages were in the range 3–3.8 Byr, but a few grains gave ages of 4.1–4.2 Byr (Fig. 5.14).

Some of the Mount Narryer zircon spots fell above the concordia line, displaying what is termed 'reverse discordance'. This phenomenon is common if whole-rock compositions are plotted on a concordia diagram (which is sometimes done for uranium-ore deposits), and in that case is usually due to loss of uranium. Froude *et al.* considered whether a process such as U loss could have caused the data to migrate back up the concordia to yield a spuriously old age. In theory, loss of U from 3.7-Byr-old zircons during a Late Archean metamorphic episode could have caused points to move to the right and above concordia. This would have to be followed by recent of loss Pb (bringing them back down onto the concordia). However, Froude *et al.* argued that the scatter of data points was too small to be consistent with this model. In addition, Isua zircons were analysed to test the reliability of ion-microprobe analyses for complex metamorphic terranes. These gave the expected age of 3.8 Byr.

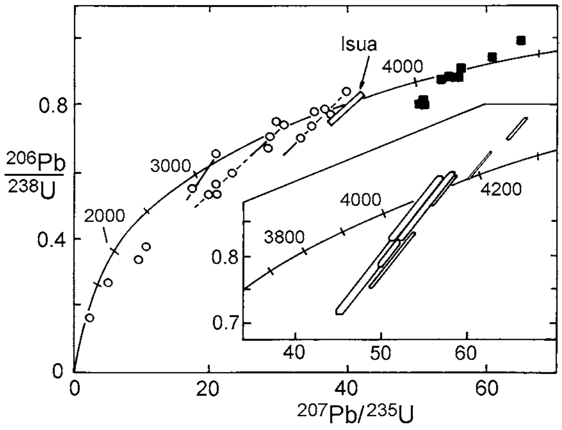

Fig. 5.14. Concordia plot showing ion-microprobe analyses of zircon from the Mount Narryer quartzite: (■) = very old zircons (the inset shows error ellipses). Isua zircons (box) were analysed as a calibration check. After Froude *et al.* (1983).

Results from a SHRIMP study on zircons from Mount Sones, Enderby Land, Antarctica, help to explain the phenomenon of reverse discordance in ion-microprobe analyses (Williams *et al.*, 1984). Uranium concentrations were found to vary quite smoothly as ion sputtering deepened the analysis spots, whereas lead concentrations varied erratically, giving rise to sudden variations in Pb/U ratio (Fig. 5.15). Hence Williams *et al.* suggested that reverse discordance is due to migration of radiogenic Pb between different regions within a zircon crystal, rather than loss of U. Subsequent to these studies, zircons with even older ages (4.40 Byr) have been found in the Jack Hills conglomerate of Western Australia, this time with a range from concordant to normally discordant compositions (Wilde *et al.*, 2001).

5.2.4 Lead 207/206 ages

In the dating of Phanerozoic rocks, monazites and zircons may both lie so close to the concordia, sometimes in a clump, that a good discordia line is not generated.

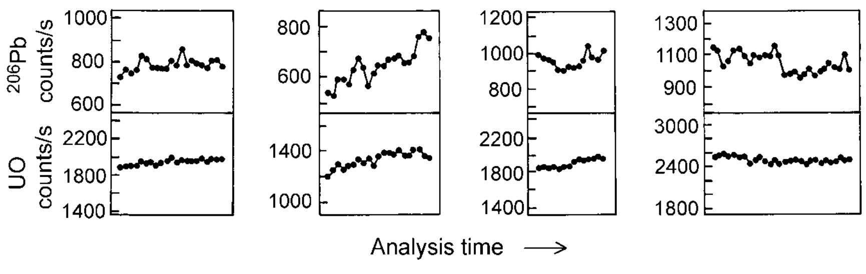

Fig. 5.15. U and Pb concentrations measured as a function of progressive pit deepening during the ion-microprobe analysis of four different zircon spots. Pb emission is seen to be less stable than U emission After Williams *et al.* (1984).

In such circumstances it may be necessary to force a discordia line through the origin, assuming that lead loss occurred at the present. The reciprocal of the gradient of this line yields a ^{207}Pb/^{206}Pb age, amounting to a simple division of equation [5.8] by [5.7] above. ^{207}Pb/^{206}Pb ages are normally minimum ages, since well-defined discordia usually have slopes too shallow to go through the origin. However, if the data display reverse discordance (e.g. Fig. 5.14) then ^{207}Pb/^{206}Pb ages are maximum ages.

Kober (1986; 1987) demonstrated a new method of zircon dating based on ^{207}Pb/^{206}Pb ages, in which lead is distilled directly from the zircon crystal in the mass spectrometer. Kober's method is a two-stage process, providing an improvement on techniques previously tried by other workers (e.g. Gentry *et al.*, 1982). A zircon is wrapped in the side filament of a multiple-filament bead, and the temperature of this filament is raised until Pb evaporates directly from the zircon. Some of this lead is redeposited on the centre filament of the bead assembly, which is mounted in front of the evaporation filament (Fig. 5.16). After a deposition period of 5–10 min, the side filament is turned off and the centre filament is heated to re-emit the deposited lead. It is thought that other species evaporated from the zircon (mainly SiO_2) may form a blanket that holds Pb on the centre filament in a manner similar to the silica-gel method for direct Pb analysis (Chapman and Roddick, 1994). When the deposited Pb is exhausted, a new deposition step is performed (if possible) at a higher side-filament temperature.

Kober's method is based on the premise that discordant lead is contained in less-stable lattice sites than those occupied by concordant lead. The discordant lead is driven off (one hopes) at comparatively low temperatures, so that above 1400 °C it can be assumed that all lead is concordant. Results of experiments by Chapman and Roddick (1994) suggested that the release of concordant Pb occurs as a reaction front migrates into the grain, converting zircon into zirconium oxide (baddeleyite). The results of each evaporation run are best plotted against filament temperature (Fig. 5.17). If the data define a plateau of ^{207}Pb/^{206}Pb ages while the evaporation temperature is gradually ramped up, this suggests that the emission of Pb from these steps represents a single phase of lead, rather than mixtures of concordant and discordant lead. The ^{207}Pb/^{206}Pb ratio will then yield the true crystallisation age of the zircon. Analysis of zircon from the population previously dated by Froude *et al.* (1983) gave similarly old ages (Kober *et al.*, 1989).

Another development in ^{207}Pb/^{206}Pb dating (Feng *et al.*, 1993) utilises a combination of laser ablation and ICP-MS. A finely focussed laser beam is used to ablate cylindrical pits from single zircon grains, in a manner analogous to the ion microprobe. However, laser ablation is performed at atmospheric pressure, yielding a molecular vapour that is carried by argon gas to the plasma torch. Temperatures of several thousand degrees Centigrade in the plasma cause effective atomisation of the sample, destroying potential

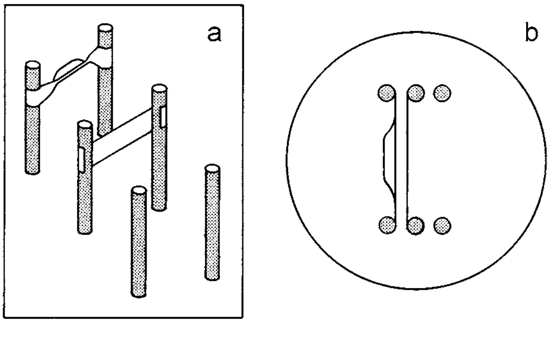

Fig. 5.16. Arrangement of a filament bead for Pb–Pb dating of zircon by the two-stage evaporation method: (a) exploded view; and (b) plan view.

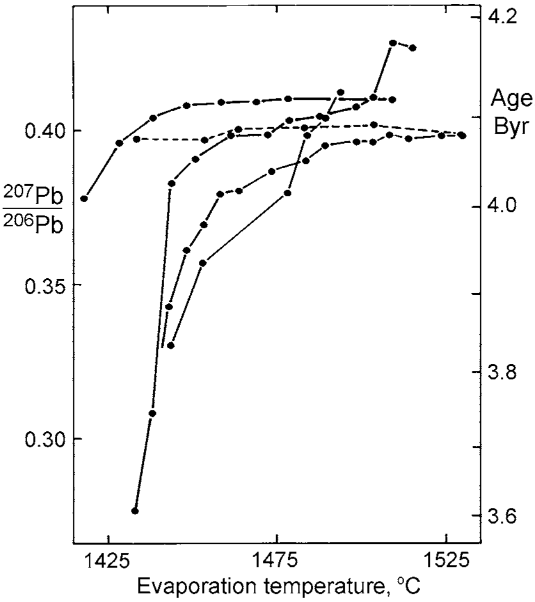

Fig. 5.17. Plot of measured ^{207}Pb/^{206}Pb ratios (corresponding to apparent age) against evaporation temperature for five Mount Narryer zircons. Low-temperature domains have suffered Pb loss but high-temperature plateaux are argued to be concordant. After Kober *et al.* (1989).

molecular-ion interferences of Pb. The sample then passes into a quadrupole mass spectrometer (section 2.2.2), where $^{207}Pb/^{206}Pb$ ratios are analysed. Feng *et al.* were able to obtain $^{207}Pb/^{206}Pb$ ages from twenty large zircons (>60 μm grain size) that fell within 1% of conventional U–Pb data. A further development of this method (section 2.5.5) involves nebulising a U–TL spike solution at the same time as laser ablation, allowing U/Pb ratios to be determined, and hence providing a full U–Pb age from laser-ablation analysis. Analysis by MC-ICP-MS also promises further advances in the field of U–Pb dating by laser ablation (section 2.5.5).

5.2.5 Inherited zircon

If a magma is derived by partial melting of the crust, or assimilates crustal material, old zircons may be entrained into the magma. These 'inherited' zircons usually dissolve in per-alkaline magmas, which have a high Zr saturation level. However, they may survive in per-aluminous melts, especially if these are cool and dry, due to the low Zr saturation levels of such magmas (Watson and Harrison, 1983). Inherited zircon xenocrysts tend to lose much of their old Pb, and may be overgrown by a new zircon crystal. However, they may still retain enough old lead to yield meaningful upper intersection ages, which yield the age of inheritance. In contrast, the lower intersection yields the age of melting. Figure 5.18 shows an example from the Ben Vuirich granite of Scotland (Pankhurst and Pidgeon, 1976). The lower intersection (514 ± 7 Myr) was interpreted as the age of intrusion and the upper intersection (1316 ± 26 Myr) as the approximate age of assimilated old crustal material.

This study was extended by Pidgeon and Aftalion (1978) to include U–Pb analysis of twenty-four Caledonian granites from Scotland and northern England. Of this suite, seventeen plutons with inherited zircon lie north of the Highland Boundary fault in Scotland and only one (Eskdale granite) lies to the south. In contrast, all six granites without inherited zircon lie south of the fault. Pidgeon and Aftalion discussed various possible explanations for these observations.

Because the granites north and south of the fault have similar chemistry, Pidgeon and Aftalion ruled out the dissolution of inherited zircons during magma evolution and their removal during emplacement. They also rejected contamination of granite magmas by sedimentary zircons north of the fault, since these granites do not have the S-type (per-aluminous) chemistry characteristic of assimilation. (In contrast, inherited zircon in the S-type Eskdale granite was probably derived by assimilation of sediments containing old zircon.) Hence, it was concluded that there is a fundamental difference in granite source rocks between the Scottish Highlands and crust to the south, a model later supported by whole-rock Nd isotope analysis (Halliday, 1984).

The early study by Pankhurst and Pidgeon (1976) made use of bulk zircon separates (the total quantity of zircon separated was 8 g!). In an attempt to refine and test the old determination, Rogers *et al.* (1989) redated the pluton using modern techniques of miniature-sample analysis and zircon abrasion. The results (Fig. 5.19) were startlingly different. The lower intercept was increased by 76 Myr to 590 ± 2 Myr, while the upper intercept was increased by 132 Myr to 1448 ± 7 Myr. The lower ages determined from the earlier study can be attributed to the effects of secondary lead loss after intrusion, from a system that already represented a two-component mixing line. This caused rotation of the apparent discordia, yielding erroneously young ages for both the upper and the lower intercept.

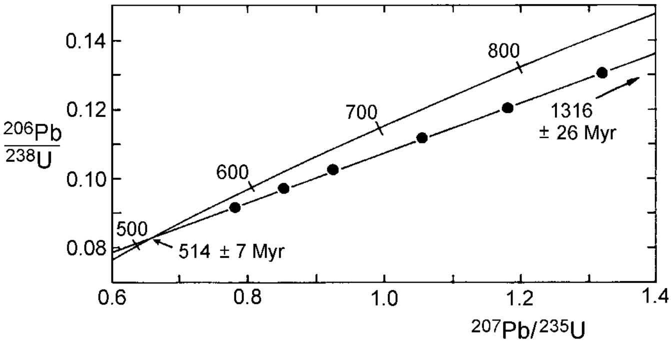

Fig. 5.18. Concordia diagram for Ben Vuirich granite (Scotland), showing mixing between new Caledonian Pb and inherited Mid-Proterozoic Pb. After Pankhurst and Pidgeon (1976).

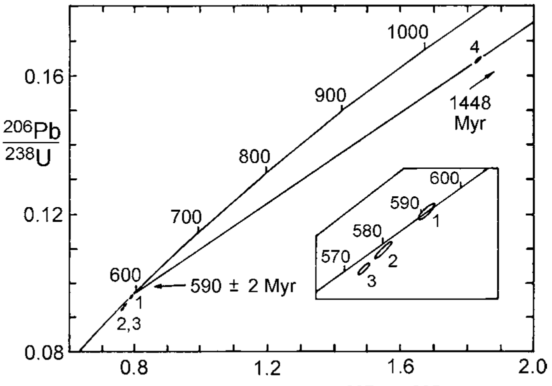

Fig. 5.19. Concordia diagram for Ben Vuirich granite, showing a discordia between needle-shaped magmatic zircon (1) and stubby inherited zircon (4). The inset shows a Pb-loss line that defines the intrusive age. 1 and 4 = strongly abraded; 2 = slightly abraded; 3 = unabraded, (to control Pb-loss line). After Rogers *et al.* (1989).

The occurrence of secondary lead loss from Ben Vuirich zircons is demonstrated by a comparison of abraded and unabraded needle-shaped grains (representing new 590-Myr-old magmatic zircons). In contrast, abraded stubby grains provided a closer approach to the inherited zircon composition than the bulk fractions of large non-magnetic grains analysed by Pankhurst and Pidgeon. The study of Rogers *et al.* is typical of much recent work showing the dangers of bulk zircon analysis in rocks with complex geological histories. Such samples can yield discordia of high statistical quality that nevertheless yield erroneous ages. Consequently the *painstaking* selection and abrasion of crack-free and inclusion-free grains is essential in order to ensure the reliability of U–Pb data.

5.2.6 Alternative U–Pb data presentations

In the classical concordia diagram the variables are strongly correlated, because of the manner in which the data are analysed. The $^{207}Pb/^{235}U$ ratio is calculated from the $^{206}Pb/^{238}U$ ratio on the basis of the constant value of $^{235}U/^{238}U$ and the measured $^{207}Pb/^{206}Pb$ ratio, which is known much more accurately than the U/Pb ratio. The correlation of errors is taken into account when fitting discordia regression lines (section 2.6.2), but it is largely avoided in an alternative presentation of U–Pb data pioneered by Tera and Wasserburg (1973; 1974), where the $^{238}U/^{206}Pb$ ratio is plotted directly against the $^{207}Pb/^{206}Pb$ ratio. This concordia has a different curvature from that of the conventional presentation, and is preferred by workers dating young rocks (e.g. Schärer *et al.*, 1984) because it displays these discordia lines more clearly than the conventional diagram (Fig. 5.20).

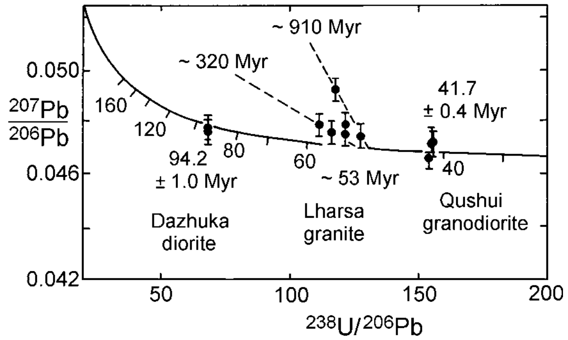

Fig. 5.20. 'Tera–Wasserburg' concordia diagram on axes of $^{207}Pb/^{206}Pb$ ratio against $^{238}U/^{206}Pb$ ratio, showing data for Himalayan granites. After Schärer *et al.* (1984).

Wendt (1984) further developed the Tera–Wasserburg plot into a three-dimensional U–Pb diagram by the addition of an axis in $^{204}Pb/^{206}Pb$ ratio, representing the level of common Pb present in the samples. In this construction the discordia is a plane, and ages can be calculated without independent knowledge of the isotopic composition of the common-Pb component, subject to the assumption that only one such component is present. An example of the application of this method is the dating of Mesozoic uranium minerals from Germany by Carl and Dill (1985). The three-dimensional diagram may also allow dating of partially open whole-rock U–Pb systems because it allows more accurate correction of large common-Pb fractions (e.g. Carl *et al.*, 1989).

Ludwig (1998) termed the three-dimensional U–Pb isochron the 'total-Pb/U isochron' and the 'Tera–Wasserburg' discordia the 'semi-total-Pb/U isochron'. He argued that the total-Pb/U isochron is useful because it allows a more explicit view of error sources. For example, a schematic three-dimensional view of a total-Pb/U isochron in Fig. 5.21 shows that it has two anchor points. The radiogenic end of the isochron plane intersects the Tera–Wasserburg concordia to define the age of the samples, while the other end of the isochron plane describes the non-radiogenic component of the samples, which should lie close to a reasonable crustal-growth curve.

When U–Pb ages are calculated on a concordia diagram with a correction for common Pb, this is

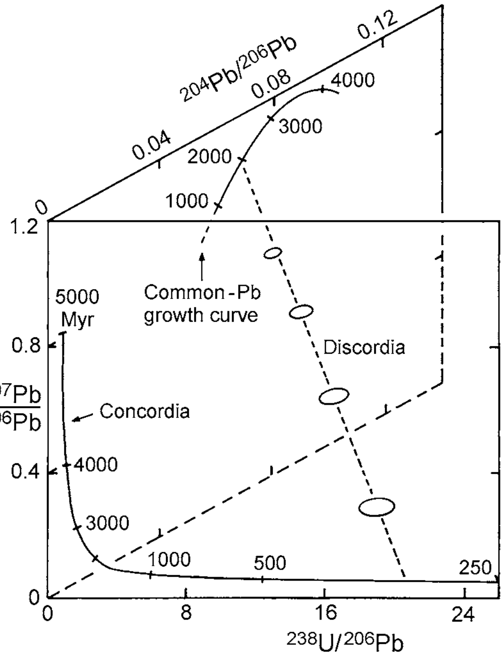

Fig. 5.21. Schematic illustration of a three-dimensional total-Pb/U isochron. The discordia intersects with the concordia curve at its radiogenic end and with the common-Pb growth curve at its non-radiogenic end. After Ludwig (1998).

equivalent to forcing the three-dimensional isochron through a point on the common-Pb growth curve. For samples with low common-Pb contents, such a forced fit may actually be more reliable than a 'free fit'. However, when common-Pb contents are large, forcing the isochron through an assumed common-Pb composition may introduce errors if an incorrect common-Pb point is used. A good example comes from the analysis of U–Pb data from whole-rock chondrule samples from chondritic meteorites (Tera and Carlson, 1999). In this example, raw U–Pb isotope data, without any common-Pb correction, are presented on two separate diagrams (Figs. 5.22a, b), based on the *x* and *z* axes of the three-dimensional isochron diagram in Fig. 5.21. This is done to ease the plotting of the data, but the conclusions are the same as for the true three-dimensional diagram.

On the Pb–Pb isotope sub-diagram (Fig. 5.22a) the intercept of the chondrule array on the *y* axis gives the $^{207}Pb/^{206}Pb$ age of meteorites. Hence, the most precise ages are given by radiogenic-Pb data points near the axis. However, the inset shows the effects of Pb loss from meteorite phosphate grains (solid circles) at the radiogenic end of the array. This open-system behaviour limits the precision on the age. On the Tera–Wasserburg sub-diagram (Fig. 5.22b) whole-rock chondrules define an array with a concordia intersection age of 4561 Myr. This age approximates the correct age of chondrule formation (section 5.3.1), but many points in the array project towards a present-day terrestrial composition (solid diamond) rather than the expected primordial-solar-system composition. The conclusion from this analysis is that the chondrules must have been contaminated by terrestrial Pb. Therefore, to minimise these effects, chondrules should be washed with acid before analysis, in order to reduce this contamination (section 5.3.1).

Ludwig (2001) argued that another advantage of the total-Pb/U isochron is that it can eliminate mass-fractionation uncertainties from the age calculation. Again, this is more significant for samples with larger common-Pb contents. These calculations were included in a Microsoft Excel Geochronological Toolkit (Ludwig, 1999).

5.2.7 Alternative U–Pb dating materials

Zircon has been the mineral of choice for most U–Pb dating work since the earliest studies. However, other minerals may yield valuable U–Pb age data that complement U–Pb zircon ages. The most important of these other minerals are monazite, sphene (titanite) and baddeleyite. In addition, other minerals such as garnet can be used for U–Pb dating in particular circumstances.

Monazite is a light-rare-earth-element (LREE) phosphate that also incorporates a significant amount of Th and a minor amount of U. It is found in relatively Ca-poor and Al-rich granitoids and high-grade metamorphic rocks. It coexists with zircon but not with sphene in many of these rock types. Monazite can exhibit similar Pb-inheritance and Pb-loss behaviour to zircon (Copeland *et al.*, 1988), but its different chemistry means that these types of behaviour often occur under different conditions from those for coexisting zircon. Monazite has a lower blocking temperature than zircon (Dahl, 1997), which makes any inherited monazites in a crustal melt tend to lose their Pb during the melting event. Hence, monazites can be useful for dating aluminous granitoids with major zircon inheritance. Despite its lower blocking temperature, monazite seems to be more resistant to Pb loss during lower-temperature events. This is probably because, unlike zircon, monazite undergoes annealing at relatively low temperatures, thus healing radiation damage of the lattice (Smith and Giletti, 1997).

These properties of monazite were applied by Schärer (1984) to date the Himalayan Makalu granite,

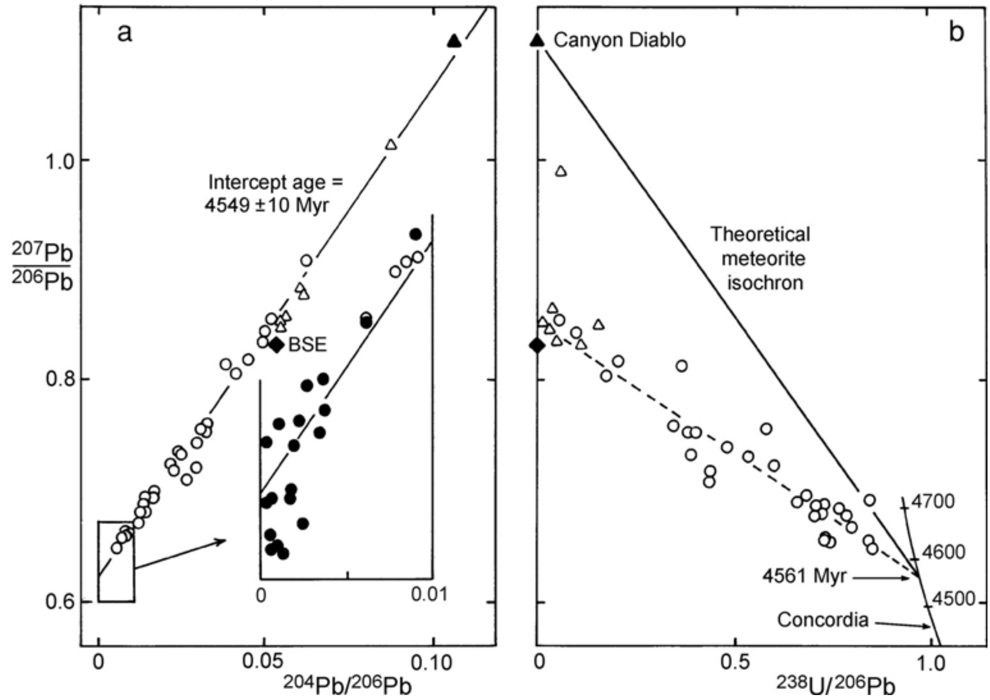

Fig. 5.22. Meteorite data on Tera–Wasserburg and Pb–Pb isotope diagrams, representing the *X* and *Z* axes of the total-Pb/U isochron diagram. The lower (radiogenic) end of the meteorite discordia shows the effect of Pb loss, while the upper (unradiogenic) end shows the effect of terrestrial contamination: (●) = whole-rock chondrules; (○) = phosphates; (▲) = irons. After Tera and Carlson (1999).

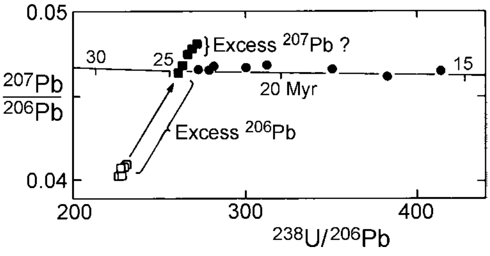

Fig. 5.23. Tera–Wasserburg concordia diagram for the Makalu leucogranite, Himalayas, showing zircon (●), which has lost Pb, and monazite (□, ■) before and after correction for inherited U–Th disequilibrium. After Schärer (1984).

whose zircon systematics were complicated by a combination of inherited Pb (Fig. 5.20) and Pb loss (Fig. 5.23). Monazites in this granite were not affected by these problems. However, a complication arose because the high Th content of monazite causes uptake of a significant content of the short-lived U-series isotope ^{230}Th. This subsequently decays to ^{206}Pb (Fig. 12.2a), causing an excess abundance of this isotope (Ludwig, 1977). Schärer demonstrated that a correction for this excess production caused apparently discordant analyses to fall properly on the concordia (Fig. 5.23), yielding a precise age of 24 ± 1 Myr for crystallisation of the Makalu pegmatitic granite. Several other applications were described by Parrish (1990), and details of the application of monazite to dating metamorphic events were described by Foster *et al.* (2002).

The large Th content of most monazites also allows the possibility of Th–Pb dating. This has been applied quite widely by using the electron microprobe to determine total Th–Pb ‘chemical age dates’ (e.g. Montel *et al.*, 1996). This method is based on the principle that Th abundances in monazite are so high that radiogenic ^{208}Pb totally dominates over uranogenic and non-radiogenic Pb. Chemical dating can be used only as a reconnaissance technique because significant errors arise from uranogenic Pb. However, more accurate Th–Pb dating of monazite can be carried out using the ion microprobe.

Unlike U–Pb dating, the Th–Pb dating method does not allow for an internal correction for Pb-loss events. However, *in situ* depth profiling of monazite grains by ion microprobe can allow cooling curves to be determined on the basis of Pb loss from the grain surface. Grove and Harrison (1999) demonstrated this technique on Tertiary monazites from the hanging wall of the Himalayan Main Central Thrust. By matching a model for diffusional Pb loss from the grain surface with the variation of Th–Pb ages against depth, Grove and Harrison were able to model the cooling history of the hanging wall since 12 Myr ago, the average Th–U age derived from the interiors of monazite grains. Additional applications of *in situ* monazite analysis were described by Catlos *et al.* (2002).

Sphene is a titanium silicate (hence often called titanite) with similar properties to zircon and monazite. It has a somewhat lower blocking temperature (about 625 °C) than monazite (about 715 °C) and zircon (about 900 °C; Dahl, 1997). Therefore, sphene may remain open to Pb diffusion during high-temperature cooling of metamorphic terranes. However, it is much less susceptible to low-temperature Pb loss than zircon because it easily recrystallises, allowing annealing of radiation damage. Sphene was first applied as a dating tool by Tilton and Grunenfelder (1968) and has since been applied widely to studies of polymetamorphic belts (e.g. Tucker *et al.*, 1987). A good example is the combined use of zircon and sphene ages to date both the formation age and the Caledonian metamorphic age of gneisses from western Norway (Fig. 5.24).

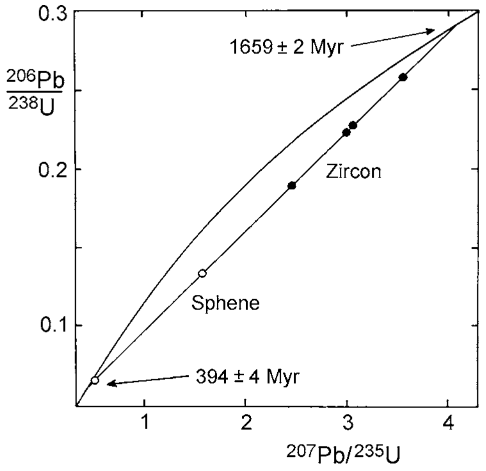

Fig. 5.24. Concordia diagram for migmatite of the Western Gneiss Region (Norway), showing a discordia line defined by zircons (●) that have suffered partial Pb loss, with a lower intercept anchored at the time of Caledonian metamorphism by sphene (○). After Tucker *et al.* (1987).

Mafic igneous rocks have very low contents of zircon, monazite and sphene, and therefore have always been difficult to date accurately. However, Krogh *et al.* (1987) showed that the zirconium oxide mineral baddeleyite could be used as a dating tool in these rock types. (In pronouncing 'baddeleyite', it should be remembered that the mineral is named after Baddeley!) This method has since been applied widely to U–Pb dating of mafic rocks (e.g. Heaman and LeCheminant, 1993). In addition, French *et al.* (2002) have shown that total U–Pb analysis of baddeleyite using the electron microprobe can also be used as a reconnaissance dating tool for dyke swarms, when supported by conventional U–Pb dating of selected samples.

Garnet is an important mineral in the geothermometry and barometry of metamorphic rocks. Therefore, the direct dating of this material would allow constraints to be placed on heating and cooling rates during regional metamorphism. Both the Sm–Nd system and the U–Pb system have potential for dating metamorphic garnets, but they have different strengths and weaknesses. Garnets grown under amphibolite-facies conditions (about 550 °C) can give concordant ages of prograde garnet growth from the two methods (section 4.1.4). However, Mezger *et al.* (1992) argued that the Sm–Nd system was opened at about 600 °C (upper amphibolite facies) in all but very large inclusion-free grains. Therefore, they suggested that garnet Sm–Nd ages usually date cooling rather than prograde mineral growth.

Mezger *et al.* (1991) proposed a higher closure temperature of about 800 °C for the U–Pb system in garnet. However, this system suffers from the tendency for uranium to be concentrated in minute inclusions, rather than in the garnet lattice. For example, in the first study of this type, on the Pikwitonei granulite terrane in northern Manitoba, Mezger *et al.* (1989) attempted to use the U–Pb system to date prograde garnet growth during prolonged Late Archean metamorphism. After correction for a small common-Pb component, radiogenic $^{206}Pb^*/^{238}U$ and $^{207}Pb^*/^{235}U$ ages were calculated using equations [5.7] and [5.8]. Unfortunately, most samples gave discordant ages for the two Pb systems, indicative of open-system behaviour. In a later study, DeWolf *et al.* (1996) showed that this was due to Pb loss from micrometre-sized monazite inclusions in the garnet grains.

5.3 Common (whole-rock) Pb–Pb dating

The whole-rock Pb–Pb dating method is based on rearranging the U–Pb decay equations [5.5] and [5.4] to bring the Pb/Pb terms to the left-hand side:

$$\left(\frac{^{207}\mathrm{Pb}}{^{204}\mathrm{Pb}}\right)_{\mathrm{P}} - \left(\frac{^{207}\mathrm{Pb}}{^{204}\mathrm{Pb}}\right)_{\mathrm{I}} = \frac{^{235}\mathrm{U}}{^{204}\mathrm{Pb}}(e^{\lambda_{235}t} - 1) \qquad [5.9]$$

$$\left(\frac{^{206}\mathrm{Pb}}{^{204}\mathrm{Pb}}\right)_{\mathrm{P}} - \left(\frac{^{206}\mathrm{Pb}}{^{204}\mathrm{Pb}}\right)_{\mathrm{I}} = \frac{^{238}\mathrm{U}}{^{204}\mathrm{Pb}}(e^{\lambda_{238}t} - 1) \qquad [5.10]$$

Nier *et al.* (1941) showed that, if these two equations refer to the same system, [5.9] can be divided by [5.10], whereupon the ^{204}Pb terms on the right-hand side of the equations cancel out, leaving the term ^{235}U/^{238}U (which has a constant value of 1/137.88 throughout the solar system). This yields the simplified equation:

$$\frac{\left(\frac{^{207}\mathrm{Pb}}{^{204}\mathrm{Pb}}\right)_{\mathrm{P}} - \left(\frac{^{207}\mathrm{Pb}}{^{204}\mathrm{Pb}}\right)_{\mathrm{I}}}{\left(\frac{^{206}\mathrm{Pb}}{^{204}\mathrm{Pb}}\right)_{\mathrm{P}} - \left(\frac{^{206}\mathrm{Pb}}{^{204}\mathrm{Pb}}\right)_{\mathrm{I}}} = \frac{1}{137.88}\,\frac{e^{\lambda_{235}t} - 1}{e^{\lambda_{238}t} - 1} \qquad [5.11]$$

If we consider a number of systems that have the same age and initial isotopic composition (e.g. whole-rock samples of a granite) then it can be seen from equations [5.9] and [5.10] that they will develop different Pb isotope compositions, according to their U/Pb ratios, at the present day. Therefore, if the present-day Pb isotope compositions of this suite are plotted (left-hand side of [5.11]), they should form a straight-line array, provided that they have remained closed systems. The slope of this array, which was first termed an 'isochrone' by Houtermans (1947), depends only on t, and does not require any knowledge of the U and Pb concentrations in the samples. It should be noted that the isochron equation [5.11] is 'transcendental'. In other words, the term on the right-hand side (equal to the slope) cannot be solved algebraically to yield the age, t, but must therefore be solved iteratively by computer.

Since the U–Pb closed-system requirement remains, it might be wondered what advantage this method offers over the discredited whole-rock U–Pb isochron method (section 5.1), in view of the known high mobility of uranium. However, this question can be answered empirically. Figure 5.25 shows a whole-rock Pb–Pb isochron diagram for the Granite Mountains, Wyoming (Rosholt and Bartel, 1969), which gives a geologically correct age of 2.82 Byr. However, it was shown in Fig. 5.1 that these samples had suffered disastrous uranium losses. This paradox can be explained by the fact that U–Pb whole-rock systems were effectively closed from the time of formation of the intrusion until very near the present day, when uranium was lost in recent weathering processes. This invalidates the U–Pb isochron method, but since the Pb isotope ratios in the rock reflect the pre-weathering U concentrations, they are not upset by the recent alteration event.

5.3.1 The geochron

The first application of the common Pb–Pb dating technique was actually to meteorites rather than terrestrial rocks. In this study, Patterson (1956) calculated a Pb–Pb age of 4.55 ± 0.07 Byr on a suite of three stony meteorites and two iron meteorites (Fig. 5.26). The least radiogenic of these samples was troilite (FeS) from the Canyon Diablo iron meteorite, which was responsible for Meteor Crater, Arizona. The U/Pb

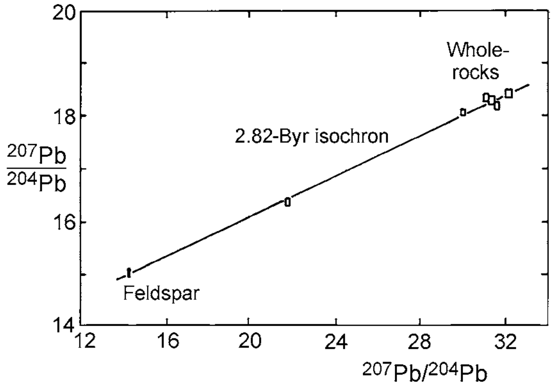

Fig. 5.25. Pb–Pb isochron diagram for whole-rock and mineral samples of the Granite Mountains batholith. After Rosholt and Bartel (1969).

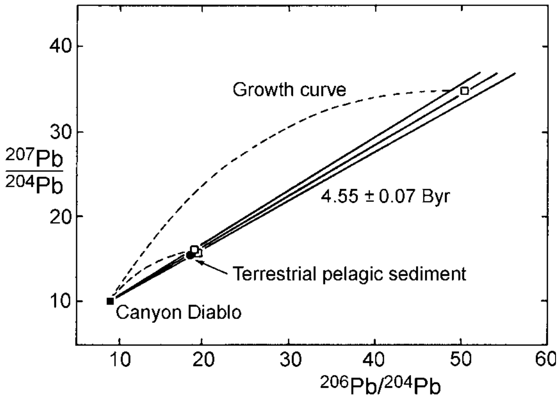

Fig. 5.26. Pb–Pb isochron diagram for iron and stony meteorites (■ □,) and a 'Bulk Earth' sample of oceanic sediment (●), showing that the Earth lies on the meteorite isochron, which is therefore also called the 'geochron'. After Patterson (1956).

ratio measured on this sample (0.025) was so low that Patterson concluded that 'no observable change in the isotopic composition of lead could have resulted from radioactive decay after the meteorite was formed'. Hence Canyon Diablo troilite represents the primordial Pb isotope composition of the solar system. This is an important benchmark for terrestrial Pb isotope evolution, just as the chondritic reservoir constrains terrestrial Nd isotope evolution.

Patterson also solved a problem that had occupied geochronologists for decades, namely the age of the Earth. A sample of recent oceanic sediment, regarded as the best estimate of the Bulk Earth Pb isotope composition, lay on the meteorite isochron, and furthermore had the appropriate U and Pb concentrations to be generated by radiogenic Pb growth from the Canyon Diablo composition in 4.55 Byr. This finding provided good evidence that the Earth has both the same age and the same ultimate origin as meteorites. The meteorite isochron was therefore termed the Geochron.

Subsequent work has shown that the interpretation of pelagic sediment as a Bulk Earth composition is only a rough approximation to the complexities of terrestrial Pb isotope evolution. Therefore the apparent Pb–Pb age of the Earth must now be revised downwards slightly (section 5.4.3). However, the new value is almost within experimental error of the determination of Patterson.

Because ^{235}U was relatively abundant in the early solar system, and because of its relatively short half-life of 704 Myr, Pb–Pb dating on meteorites can provide very accurate ages for the early evolution of the solar system. Based on evidence from extinct nuclides (section 15.4.1) calcium–aluminium inclusions from the Allende chondrite are regarded as the oldest solar-system objects, and are therefore of particular interest in dating the early evolution of the solar system. Inclusions and chondrules both have high U/Pb ratios, but a significant common-Pb component rules out direct application of the U–Pb method. Several Pb–Pb dating studies have therefore been performed, mostly on mixed suites of chondrules and inclusions. However, Chen and Wasserburg (1981) obtained the first precise age from inclusions alone, which gave an age of 4568 ± 5 Myr.

Two-point isochrons between Canyon Diablo and any individual inclusion can be calculated. These are termed model ^{207}Pb/^{206}Pb ages because they rely on the assumption that initial lead in the inclusion was the same as Canyon Diablo. However, Allègre *et al.* (1995a) showed that the ^{207}Pb/^{206}Pb ages in the inclusions were correlated with the ^{206}Pb/^{204}Pb ratio, which measures the amount of common Pb in each sample (Fig. 5.27). This suggests that the inclusions were contaminated with extraneous common Pb from outside the chondrules that did not match Canyon Diablo Pb. Therefore, Allègre *et al.* utilised a progressive leaching procedure to remove the common-Pb component. The results of this procedure gave ^{207}Pb–^{206}Pb ages within error of the most radiogenic data of Chen and Wasserburg, with an improved age of 4566 + 2/– 1 Myr.

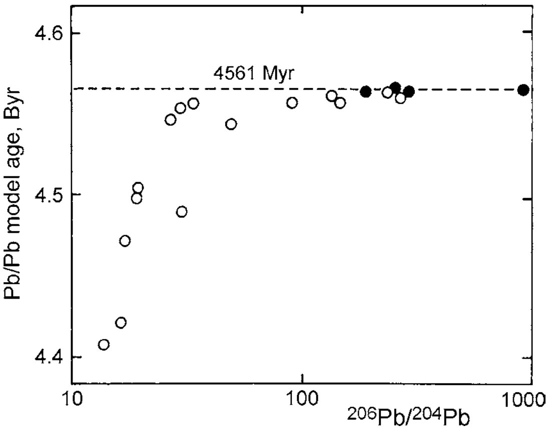

Fig. 5.27. Plot of 207/206 ages for Allende calcium–aluminium inclusions (CAI), showing an inverse correlation with common-Pb content: (○) = bulk samples; (●) = leached. After Allègre *et al.* (1995a).

A similar approach was used by Amelin *et al.* (2002) to achieve a high-quality Pb–Pb isochron on acid-washed whole-rock chondrules from the Acfer chondrite. The data are shown in Fig. 5.28 on an alternative form of the Pb–Pb isochron diagram, which is the same as the third dimension in the total-Pb/U isochron diagram (Fig. 5.21). On this diagram the intercept indicates the ^{207}Pb–^{206}Pb age for an infinitely radiogenic sample. Because the samples analysed by Amelin *et al.* were very radiogenic, they gave an excellent intercept, corresponding to an age of 4564.7 ± 0.6 Myr for chondrule formation (MSWD = 0.5). Acid-washed whole-rock fragments of two calcium–aluminium inclusions (CAIs) from the Efremovka chondrite also gave excellent Pb–Pb isochrons (MSWD = 0.9 and 1.1) with an average intercept age of 4567.2 ± 0.6 Myr, which is 2.5 Myr older than the chondrite isochron. This age difference is consistent with the age differences between CAIs and chondrules determined from extinct-nuclide (^{26}Al–^{26}Mg) systematics (section 15.4.1). Hence, this evidence provides a reliable anchor for the chronology of the early solar system.

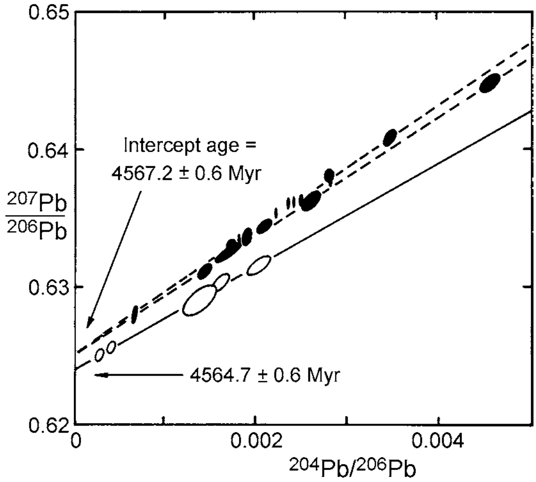

Fig. 5.28. Alternative Pb–Pb isochron diagram, showing 207/206 (intercept) ages for acid-washed chondrules (open ellipses) and calcium–aluminium inclusions (CAI, solid ellipses). After Amelin *et al.* (2002).

5.4 Model (galena) ages

As discussed above, different Pb isotope dating methods address the problem of uranium mobility in different ways. In the U–Pb zircon dating method, a mineral was chosen that held U well and in which Pb loss could be modelled and corrected. In common Pb–Pb dating the recent loss of U can be permitted, provided that the system was closed for most of its life. In the galena method discussed here, a phase that contains no U is analysed, so there is no problem associated with loss of U.

5.4.1 The Holmes–Houtermans model

Since there is no U decay in a galena, we are not measuring its age directly back from the present day, but are measuring the age of the galena source from the formation of the Earth until the isolation of the galena. This approach was conceived independently by Holmes (1946) and Houtermans (1946). They divided the isotopic evolution of galena Pb into two parts. The first was assumed to be a rock system, which must have remained closed to U and Pb from the formation of the Earth until galena separation. The second was in the galena itself, which must contain no significant amounts of uranium. This model for terrestrial Pb isotope evolution may be summarised as follows:

$$\underset{\text{age of earth}}{T} \xrightarrow[\text{in rock}]{\text{U decay}} \underset{\text{age of galena}}{t} \xrightarrow[\text{in galena}]{\text{no U decay}} \underset{\text{present}}{\mathrm{P}}$$

Given this model, the basic decay equation for ^{207}Pb is

$$^{207}\mathrm{Pb}_t = {}^{207}\mathrm{Pb}_T + {}^{235}\mathrm{U}(\mathrm{e}^{\lambda_{235}T} - \mathrm{e}^{\lambda_{235}t}) \qquad [5.12]$$

This decay equation is more complex than [5.2] because t is not zero. Each term is next divided through by ^{204}Pb and rearranged. The same procedure is applied to the corresponding equation for ^{206}Pb to yield the following results:

$$\left(\frac{^{207}\mathrm{Pb}}{^{204}\mathrm{Pb}}\right)_t - \left(\frac{^{207}\mathrm{Pb}}{^{204}\mathrm{Pb}}\right)_T = \frac{^{235}\mathrm{U}}{^{204}\mathrm{Pb}}(\mathrm{e}^{\lambda_{235}T} - \mathrm{e}^{\lambda_{235}t}) \qquad [5.13]$$

$$\left(\frac{^{206}\mathrm{Pb}}{^{204}\mathrm{Pb}}\right)_t - \left(\frac{^{206}\mathrm{Pb}}{^{204}\mathrm{Pb}}\right)_T = \frac{^{238}\mathrm{U}}{^{204}\mathrm{Pb}}(\mathrm{e}^{\lambda_{238}T} - \mathrm{e}^{\lambda_{238}t}) \qquad [5.14]$$

Equation [5.13] is now divided through by [5.14] and the result is simplified as follows:

(1) ^{204}Pb terms are cancelled out on the right-hand side of the equation. This leaves a factor for the U isotope ratio at the present day, which is a constant with the value 1/137.88.

(2) $(^{207}\mathrm{Pb}/^{204}\mathrm{Pb})_t$ and $(^{206}\mathrm{Pb}/^{204}\mathrm{Pb})_t$ represent the present-day compositions, since galena incorporates no U.

(3) The Pb isotope compositions at time 'T' represent the composition of the solar nebula; which is the primordial composition of the Earth, now represented by Canyon Diablo troilite (CD).

The equation can then be written as

$$\frac{\left(\frac{^{207}\mathrm{Pb}}{^{204}\mathrm{Pb}}\right)_\mathrm{P} - \mathrm{CD}}{\left(\frac{^{206}\mathrm{Pb}}{^{204}\mathrm{Pb}}\right)_\mathrm{P} - \mathrm{CD}} = \frac{1}{137.88}\,\frac{(\mathrm{e}^{\lambda_{235}T} - \mathrm{e}^{\lambda_{235}t})}{(\mathrm{e}^{\lambda_{238}T} - \mathrm{e}^{\lambda_{238}t})} \qquad [5.15]$$

If the isotope ratios on the left-hand side of the equation represent a sample extracted from the mantle at time t, then the term on the right-hand side corresponds to the slope of an 'isochron' line joining it to the solar-nebula composition (Fig. 5.29).

To apply the Holmes–Houtermans model, the galena source rock is assumed to be a closed system with a 'single-stage' Pb isotope history. A growth curve is then constructed for this galena source, which runs from the primordial Pb composition to that of the analysed galena, and is calibrated for various values of t. (Since this is a transcendental curve, t cannot be solved by direct algebra starting with a composition on the left-hand side of [5.15].) The shape of the

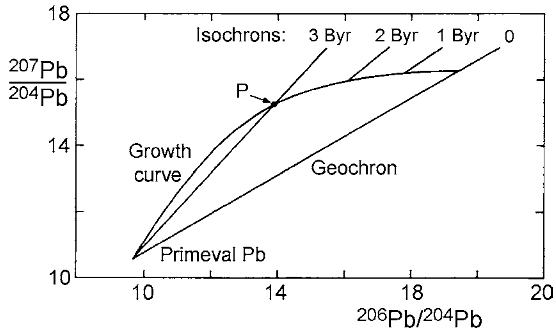

Fig. 5.29. Pb–Pb isochron diagram, showing present-day composition (P) of galena extracted from a Bulk Earth reservoir 3 Byr ago. After Russell and Farquhar (1960).

growth curve is determined by the two uranium decay constants, and its trajectory by the $^{238}U/^{204}Pb$ or 'μ' value of the closed-system galena source. For the single-stage model described, it is called the μ_1 value and would normally be between 7 and 9. According to the Holmes–Houtermans model, not every galena source rock need have the same growth curve, defined by the same μ value. Galena ore bodies were expected to have concentrated the metal from local continental basement in the vicinity. However, this presupposes that the basement in question has been in existence since near the time of formation of the Earth, which is now regarded as very unlikely (e.g. see section 4.4).

A major problem encountered using the Holmes–Houtermans model was that, as more galenas were analysed, they were found to scatter more and more widely on the Pb–Pb isochron diagram (Fig. 5.30). Some of the ages determined were clearly erroneous, since they were in the future. Others, which were outliers to the main trend, often gave ages that could be shown to be geologically impossible. Since galenas of these two types contradicted the Holmes–Houtermans model, they were called 'anomalous leads'. However, the crucial problem with this situation was the lack of an *a priori* test that could be performed to predict whether a galena would be anomalous, in the absence of other evidence of its age.

5.4.2 Conformable leads

Given the complexity of the Earth's evolution, it was realised even in the 1950s that the country-rock source of a given galena ore was unlikely to have been a closed system since the formation of the Earth. Alpher and Herman (1951) attempted to overcome this problem by attributing Pb isotope evolution in the galena source rock to a single world-wide homogeneous reservoir, regarded by Russell (1956) as the Earth's mantle. As an explanation of the observed galena Pb isotope variation this model is quite obviously inadequate, but it was the basis of a more geologically realistic model proposed by Stanton and Russell (1959).

A certain class of Pb ores was found by Stanton and Russell that did lie on a single closed-system growth curve. These were sulphides associated with sediments and volcanics in greenstone belts and island arcs, which were structurally conformable with the host rocks (in contrast to cross-cutting veins). Stanton and Russell regarded these ores as being formed by syngenetic deposition in sedimentary basins associated with volcanic centres, and therefore as representing galena derived

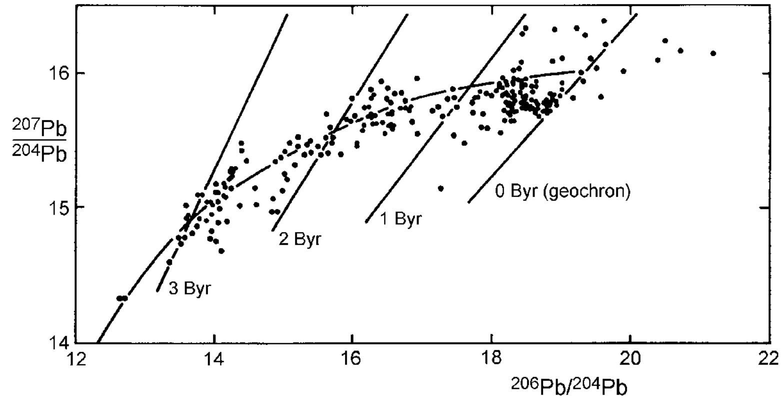

Fig. 5.30. Pb–Pb isochron diagram, showing a compilation of many analysed galenas from various environments. After Stanton and Russell (1959).

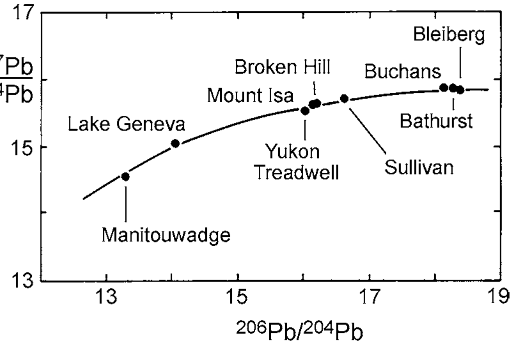

Fig. 5.31. Pb–Pb isochron diagram, showing galena ores that form the basis of the 'conformable' Pb model. After Stanton and Russell (1959).

directly from the upper mantle without crustal contamination.

Stanton and Russell selected nine deposits of various ages that satisfied these criteria, and fitted a single-stage (upper-mantle) growth curve with a μ_1 value of 9.0 (Fig. 5.31). These ores were termed 'conformable' leads because of their structural occurrence, and all galenas that didn't fit this curve were by inference 'anomalous'. Anomalous leads were divided into groups such as 'J-type leads' after a deposit at Joplin, Missouri, which gave ages in the future, and some other types such as the 'B' type, which gave ages in the past.

Unfortunately, due to the mobility of Pb during crustal processes, it is difficult to develop *a priori* criteria to recognise galenas that will fit the conformable Pb evolution model. Therefore, the galena method is largely discredited as a dating tool. Nevertheless, it may provide powerful constraints on the Earth's evolution, which will be examined below.

5.4.3 Open-system Pb evolution

As early as 1956, Russell considered the possibility that the mantle might not have been a closed system to U and Pb, but might have had a variable μ value over time, due to some kind of differentiation mechanism. However, the success of the conformable lead model to explain uncontaminated galena compositions with a closed-system mantle militated against such complications.

In the early 1970s, new measurements of the uranium decay constants (Jaffey *et al.*, 1971) and a better estimate of primordial Pb from Canyon Diablo necessitated a re-examination of the conformable Pb model. For example, using the new values, a curve calculated to yield a reasonable fit to conformable galenas gave a low apparent age for the Earth of 4.43 Byr (Doe and Stacey, 1974). Alternatively, a terrestrial age of 4.57 Byr based on Pb–Pb dating of meteorites (Tatsumoto *et al.*, 1973) caused the Geochron to lie to the left of most Phanerozoic galenas and young oceanic volcanics. This problem became known as the 'Pb paradox' and meant that single-stage Pb models gave 'future ages' up to 1 Byr in error for Phanerozoic rocks.

To rectify these problems, Oversby (1974) proposed a model for an evolving (mantle) source of galena Pb with a progressive increase in μ value over time (approximated by a series of small increments in μ). This model was elaborated upon by Cumming and Richards (1975), who modelled a galena source with a linear increase in μ value. Surprisingly perhaps, Cumming and Richards regarded the galena source as a regional average of the crust. However, this might not be as strange as it sounds, since later work would show that mantle and crustal Pb evolution are in fact coupled together, and that upper-mantle Pb is largely buffered by the crust (section 6.3.3). The model of Cumming and Richards yields a good fit to the ages of selected galena data, but still implies a young apparent age for the Earth of 4.50 Byr.

An alternative solution to this problem, proposed by Stacey and Kramers (1975), was to break terrestrial Pb isotope evolution into two parts. Stacey and Kramers used Canyon Diablo Pb and average modern Pb (from a mixture of manganese nodules, ocean sediments and island-arc rocks) to anchor the ends of a composite growth curve. This curve was produced by two closed systems (1 and 2) with different μ values (μ_1 and μ_2), separated in time by a world-wide differentiation event. The closed systems consisted of a combination of the upper mantle and upper crust (lower crust, lower mantle and core being isolated). The model gave the best fit to a selection of conformable galenas (dated by the enclosing sediments) when $\mu_1 = 7.2$, $\mu_2 = 9.7$ and the event was at 3.7 Byr (Fig. 5.32). This time was regarded as a peak of crust-forming events, an interpretation made particularly attractive by the 3.7 Byr age determined for the Amitsoq gneisses of western Greenland (section 5.5.1). However, Stacey and Kramers noted that their model was only an approximation of Pb isotope evolution in the real Earth. For example, the discrete event at 3.7 Byr in the model might actually represent a slow change in the Earth's evolution during the Early Archean.

The above observations suggested that the galena source evolved for the last 3.8 Byr along a higher-μ growth curve than the geochron, but the reason for this behaviour was not clear. Armstrong (1968) and

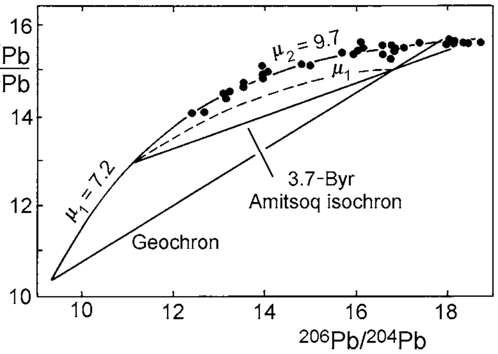

Fig. 5.32. Pb isotope diagram, showing a two-stage lead isotope evolution model proposed for the source of galenas (●). After Stacey and Kramers (1975).

Russell (1972) argued that these observations could be explained by recycling (bi-directional transport) of Pb between the crust and mantle. This concept was developed further by Doe and Zartman (1979) and presented as a computer program that modelled the Pb isotope evolution of the Earth, termed 'plumbotectonics'.

Doe and Zartman defined three reservoirs: upper crust, lower crust and upper mantle (<500 km depth). Given the evidence that continental accretion began about 4 Byr ago and that frequent orogenies mixed mantle and crustal sources to yield differentiated crustal blocks, they modelled orogenies at 400-Myr intervals, with a decreasing mantle contribution through time. Crustal contributions represented erosion and continental foundering. Orogenies instantaneously extracted U, Th and Pb from the three sources, mixed them, and re-distributed them back to the sources (Fig. 5.33). Fractionation of U into the upper crust represented granulite-facies metamorphism.

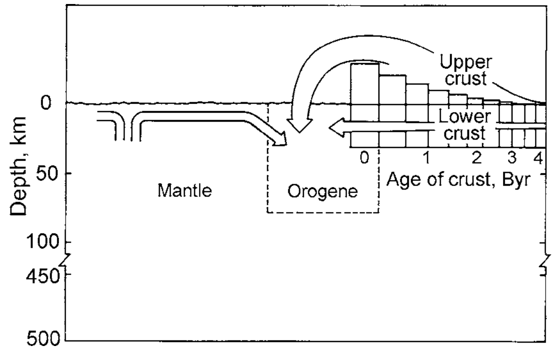

Fig. 5.33. Schematic illustration of the operation of the 'plumbotectonics' model, showing mixing of crustal and mantle reservoirs into the orogene (galena source) reservoir. After Doe and Zartman (1979).

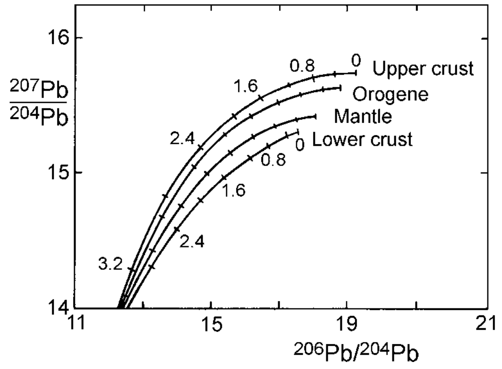

Fig. 5.34. Pb–Pb isochron diagram, showing isotopic evolution of the four reservoirs computed by the plumbotectonics model. After Doe and Zartman (1979).

The orogene composition generated by the plumbotectonics model was constrained empirically to fit galena ores, and consequent growth curves generated for the other reservoirs are shown in Fig. 5.34. The upper crust develops radiogenic Pb, which is balanced by the development of an unradiogenic lower-crustal reservoir, due to preferential retention of Pb relative to U during granulite-facies metamorphism of the lower crust. The calculated upper-mantle μ value is similar to that for the total crust, but recycling of radiogenic upper-crustal Pb into the mantle yields an *apparent* increase in mantle μ value with time. Despite this effect, it is important to note that the plumbotectonics model was not designed to solve the Pb paradox. Thus, in the first and second models (Zartman and Doe, 1981) Pb evolution started with an arbitrary isotope composition 4 Byr ago, whereas in the fourth model (Zartman and Haines, 1988) Pb evolution began 4.45 Byr ago from the Canyon Diablo composition (100 Myr after terrestrial accretion).

The curved arrays inherent in the two-isotope system make it hard to evaluate the goodness of fit of conformable Pb data to terrestrial Pb isotope evolution models, as well as making conceptual understanding of the system difficult. Therefore, Manhès *et al.* (1979) developed an alternative presentation that overcame the problem of non-linearity. However, their formulation was rather complex, which detracted from its usefulness. To simplify the data presentation, Albarède and Juteau (1984) analysed each of the U–Pb systems (and Th–Pb) on a separate diagram of Pb isotope ratio against time, as is done for Nd (section 4.2). However, because of the effectively finite half-lives of U and Th relative to the age of the Earth (unlike Nd), the time dimension must be presented as the exponent (Fig. 5.35) in order to achieve linear evolution lines.

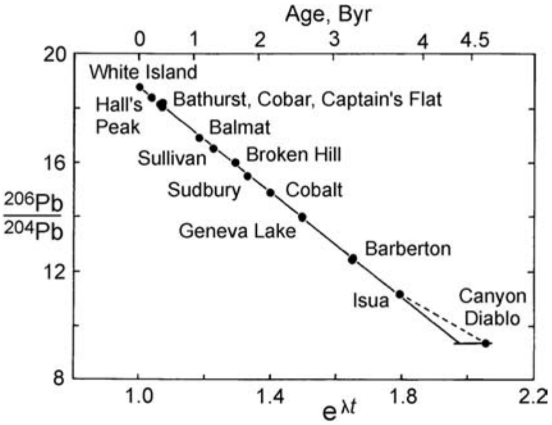

Fig. 5.35. Exponential plot of $^{206}Pb/^{204}Pb$ evolution against time, to test the fit of galena sources to a linear isotope evolution trend. After Albarède and Juteau (1984).

Albarède and Juteau utilised a combined galena data set from Stacey and Kramers (1975) and Cumming and Richards (1975), with the addition of the galena data from Isua (Appel *et al.*, 1978). This considerably strengthens the data-base, since it improves the constraints on early terrestrial Pb evolution. Fitting a linear growth line to the data (equivalent to a constant source μ value) causes this line to intersect the Canyon Diablo Pb composition at an apparent age of 4.4 Byr, in close agreement with Doe and Stacey (1974) and Manhès *et al.* (1979). This is seen most clearly for ^{206}Pb (Fig. 5.35) but also, albeit less strongly, for ^{207}Pb. However, terrestrial accretion at a date as late as 4.4 Byr is inconsistent with the 4.55 Byr age of differentiated meteorites (section 3.2.4). Therefore, as an alternative, an Early Archean reservoir with lower μ value was postulated. Hence the model of Stacey and Kramers is supported, but, due to noise in the data set, continuous Pb isotope evolution models could not be ruled out.

This situation remained essentially unchanged until some other research groups started to re-examine the behaviour of the U–Pb system during terrestrial accretion. For example, Allègre *et al.* (1995b) pointed out that the Bulk Silicate Earth (BSE) has a much higher μ value (about 9) than bulk chondrites (about 0.7), which are regarded as equivalent to the Bulk Earth composition. This difference could be due to volatilisation of Pb during terrestrial accretion, or to partition of Pb into the Earth's core. However, comparison of the partition coefficients of Pb and other siderophile–chalcophile elements suggested that core formation was the main cause of the high μ value in the BSE (e.g. Galer and Goldstein, 1996).

If this model is correct, terrestrial Pb isotope evolution can be constrained by the Hf–W extinct-nuclide system (section 15.5.4). The Hf–W couple has similar chemical affinities to the U–Pb couple, in that both parents are lithophile (rock-loving) and both daughters are siderophile (Fe-core-loving). The difference is that the parent isotope of Hf had a short half-life, which caused it to become extinct over approximately the same time period as that over which the Earth's core developed. Therefore, W isotope analysis can be used to estimate the time of terrestrial core formation.

Most Hf–W evidence appeared to favour late core formation, about 100 Myr after the main stage of terrestrial accretion (section 15.5.4). This model would then be consistent with the simplest interpretation of the Archean galena compositions (Fig. 5.35), involving a period of low μ values very early in the Earth's history. Therefore, it was argued that a period of core formation lasting 100 Myr could largely explain the Pb paradox, since it would cause the BSE, and hence average MORB, to lie to the right of the geochron (section 6.3.1).

Kramers and Tolstikhin (1997) challenged this explanation, arguing that delayed core formation could explain only one third of the Pb paradox. Instead, they further developed the plumbotectonics model by allowing enhanced recycling of uranium to the upper mantle over the last 1.5 Byr. This was caused by mobilisation of uranium in the sedimentary environment as a result of the gradual development of an oxygenated atmosphere. This modification of the plumbotectonics model also improves the solution to a 'second' Pb paradox, called the 'kappa conundrum' (section 6.3.3).

Kramers and Tolstikhin's rejection of the late-core model as an explanation of the Pb paradox turned out to be somewhat inspired, because subsequent W isotope work (section 15.5.4) implies significantly earlier core formation than the previous studies. Core formation can still have some effect on Pb if it is combined with a late giant impact, but the plumbotectonics (crustal-recycling) model must again be called upon to 'solve' at least part of the 'Pb paradox'.

It is concluded that the Kramers and Tolstikhin version of plumbotectonics is probably the most realistic terrestrial Pb isotope evolution model yet developed, but it still has significant limitations. Like all of the earlier models, it assumes direct recycling of crustal material into the MORB source, and also assumes no exchange of material with the lower mantle. The combination of these features causes the MORB reservoir in the model to have a somewhat unusual trajectory (e.g. Kamber and Collerson, 1999). A fully realistic model would need to direct a fraction of recycled crust into the lower mantle. After 1–2 Byr of isolation in the deep mantle, such reservoirs generate mantle plumes that mix with and fertilise the upper-mantle reservoir.

5.5 Pb–Pb dating and crustal evolution

Because the Pb–Pb whole-rock method depends only on isotopic compositions, it is comparatively resistant to metamorphic re-setting, and can also yield some age information for crustal reservoirs exhibiting complex mixing relationships. Good examples of these uses are provided by Pb–Pb dating studies of Archean crustal evolution in the North Atlantic region, particularly western Greenland.

5.5.1 Archean crustal evolution

A major crust-forming event in the Archean craton of western Greenland is represented by the Nuk gneisses. Gneisses in this association from Fiskanaesset, Nordland and Sukkertopen in western Greenland have Pb compositions (filled circles in Fig. 5.36) that fall on a reference line with slope age of 2900 Myr. If a single-stage mantle growth curve is calculated to fit this isochron, it yields a μ_1 value of 7.5 which is a typical value for the mantle source of juvenile Archean gneiss terranes (Moorbath and Taylor, 1981). This single-stage model mantle composition is not expected to represent the real Earth, since this was shown above to be an oversimplification; however, the μ_1 value provides a convenient yard-stick for comparison of different crust-forming events.

The Nuk gneisses approximate a two-stage Pb isotope evolution model, in which the first stage is in the mantle and the second is in each analysed whole-rock system. However, Taylor *et al.* proposed that there might be two extra short stages in the middle. The first of these short stages represents extraction of basalt from the mantle before subsequent re-melting to form tonalitic magmas, possibly at the base of the crust. The second short stage might occur between the time of tonalite emplacement in the crust and its high-grade metamorphism. The whole process was termed a crustal-accretion–differentiation super-event or CADS by Moorbath and Taylor (1981). More recently, trace-element studies have suggested that Archean tonalites may be produced by partial melting of amphibolitised ocean-floor basalt in the downgoing slabs of subduction zones (Drummond and Defant, 1990; Foley *et al.*, 2002). In this model, the first short stage would represent the time from oceanic crust formation at an ocean ridge until its consumption in a subduction zone. However, for either of these melting models, and for Pb evolution between magmatism and metamorphism, the short duration of these stages minimises their effect on long-term Pb isotope evolution.

Nuk gneisses from near Godthaab (open circles in Fig. 5.36) fall in a scatter below the 2900-Myr isochron. However, Taylor *et al.* (1980) argued that if these were age-corrected back to 2900 Myr ago, they would lie on a mixing line between 2900-Myr-old mantle (M), and the local crust, represented by Early Archean (3700-Myr-old) Amitsoq gneisses (A). Owing to their low U contents, the Amitsoq gneisses barely changed in Pb isotope ratio between 3700 and 2900 Myr ago. Given

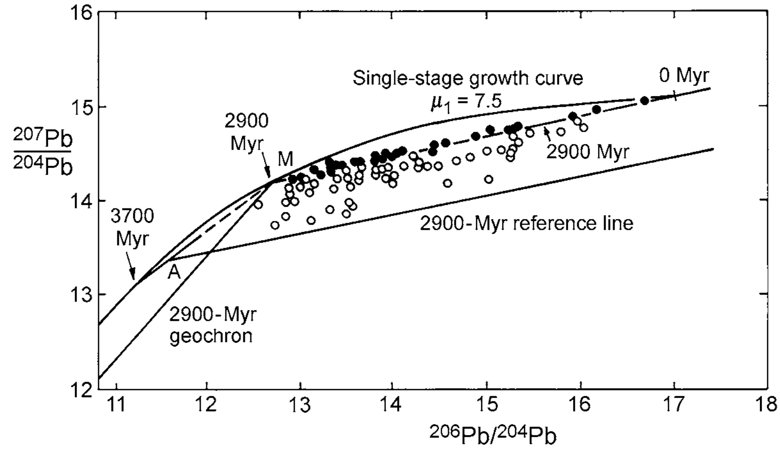

Fig. 5.36. Pb–Pb isochron diagram for basement gneisses from western Greenland: (●) = Nuk gneisses from Fiskanaesset, Nordland and Sukkertopen; (○) = contaminated Nuk gneisses from near Godthaab. M = mantle at 2900 Myr; A = range of Amitsoq gneiss compositions at 2900 Myr. After Taylor *et al.* (1980).

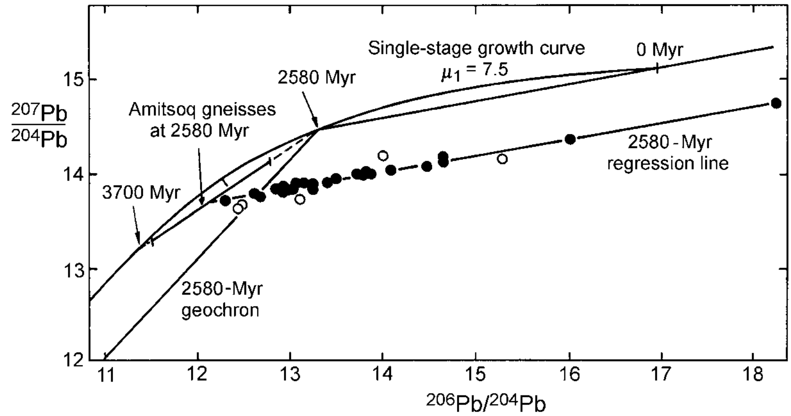

Fig. 5.37. Pb–Pb isochron diagram for Qorqut granite samples, showing the coincidence of their initial ratio with the average Amitsoq gneiss composition at 2580 Myr. (Open symbols were omitted from the regression.) After Moorbath and Taylor (1981).

these end-members, the distance down the mixing line from 'M' to 'A' indicates the fraction of crustal Pb incorporated into the magma. The variable pattern of crustal Pb contamination suffered by Late Archean Nuk magmas is consistent with the known extent of Early Archean crust. Thus, while Godthaab is known to lie on Amitsoq gneiss basement, such rocks are not exposed near Fiskanaesset, Nordland and Sukkertopen.

The Qorqut granite is also exposed within the Amitsoq gneiss terrane near Godthaab (Moorbath *et al.*, 1981). Whole-rock samples of this body define a linear array whose slope corresponds to an age of 2580 Myr (Fig. 5.37). However, if one attempts to fit a single-stage mantle growth curve to these data, an impossibly low μ_1 value of 6.23 is obtained, showing that the Qorqut granite cannot be a mantle-derived melt. In fact, the initial Pb isotope ratio of the Qorqut granite coincides closely with the average composition of analysed Amitsoq crust at 2580 Myr, indicating that the Qorqut granite is probably a partial melt of Amitsoq gneiss. It therefore approximates to three-stage Pb isotope evolution: stage1 = mantle; stage2 = Amitsoq crust; stage3 = Qorqut granite. The initial $^{87}Sr/^{86}Sr$ ratio of the Qorqut granite (0.7083 ± 4) supports this model (section 7.3.4).

5.5.2 Paleo-isochrons and metamorphic disturbance

It was argued above that comparatively short periods (less than 200 Myr) between the crustal extraction and metamorphic differentiation of a gneiss complex do not necessarily upset dating of the crustal formation event using Pb–Pb systematics. However, if the period between the two events is substantial, then spurious ages may be obtained. A good example is provided by the Vikan gneiss complex from Lofoten–Vesteralen in NW Norway. If we assume that these rocks behaved as closed systems after their generation from an isotopically homogeneous (mantle?) source, we determine a slope age of 3410 ± 70 Myr (Taylor, 1975). However, Nd model age dating yields ages of about 2.4–2.7 Byr (Jacobsen and Wasserburg, 1978).

Subsequent examination of present day U/Pb ratios in the gneisses (Griffin *et al.*, 1978) revealed that they were uniformly far too low to 'support' the observed range of Pb isotope compositions. Therefore, it is now believed that the Pb data reflect a 2680-Myr-old igneous protolith that suffered high-grade metamorphism about 1760 Myr ago. To illustrate this interpretation, Pb isotope compositions for the protolith are shown as a paleo-isochron at the time of metamorphism (Fig. 5.38). If the rocks were depleted in U to a nearly uniform level 1760 Myr ago, subsequent U decay would yield a 'transposed paleo-isochron' (Griffin *et al.*, 1978; Moorbath and Taylor, 1981) almost parallel to the original paleo-isochron.

The slope of the transposed paleo-isochron approximates Pb evolution from time T (protolith age) to t (metamorphic age). This is described by an equation analogous to [5.15] for galena evolution:

$$\frac{\left(\frac{^{207}\mathrm{Pb}}{^{204}\mathrm{Pb}}\right)_\mathrm{P} - \left(\frac{^{207}\mathrm{Pb}}{^{204}\mathrm{Pb}}\right)_\mathrm{I}}{\left(\frac{^{206}\mathrm{Pb}}{^{204}\mathrm{Pb}}\right)_\mathrm{P} - \left(\frac{^{206}\mathrm{Pb}}{^{204}\mathrm{Pb}}\right)_\mathrm{I}} = \frac{1}{137.88}\,\frac{e^{\lambda_{235}T} - e^{\lambda_{235}t}}{e^{\lambda_{238}T} - e^{\lambda_{238}t}} \qquad [5.16]$$

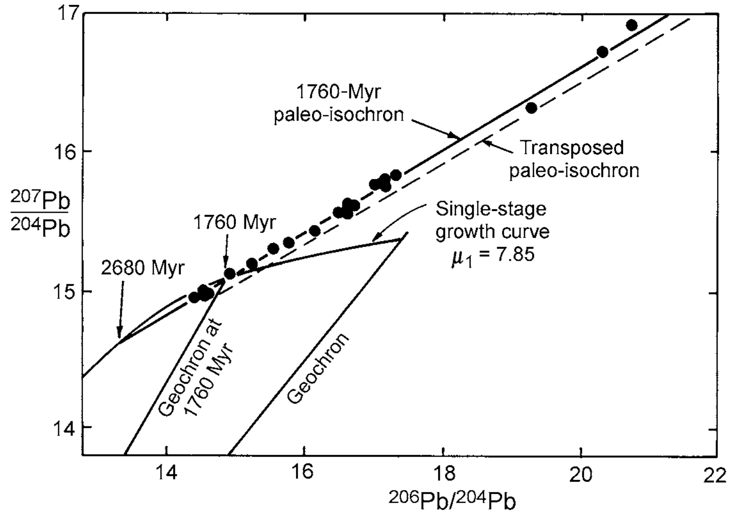

Fig. 5.38. Pb–Pb isochron diagram, showing a 'transposed paleo-isochron' defined by Vikan gneisses of NW Norway. These rocks were formed from 2680-Myr-old precursors, which were subjected to a granulite-facies uranium-depletion event at 1760 Myr. After Moorbath and Taylor (1981).

In contrast, the simple Pb–Pb isochron equation [5.11], describing evolution from *t* to the present, yields too large an age because it is based on the lower $^{235}U/^{238}U$ ratio prevailing at the present day compared with that 1760 Myr ago.

Transposed paleo-isochrons can be detected by checking concordancy of Pb with Sr or Nd ages and by checking that observed Pb isotope compositions are adequately supported by the U/Pb ratio in the samples. Another example of this phenomenon was found in upper amphibolite-facies gneisses of the Outer Hebrides, NW Scotland, by Whitehouse (1990). By substituting the 2660-Myr (Badcallian) Pb homogenisation event as *T* into [5.16], and assuming uniform U/Pb ratios after the second event, he was able to estimate the timing (*t*) of this second event. The calculated age of 1880 ± 270 Myr was consistent with the timing of the Laxfordian metamorphic event.

Another example where high-grade metamorphism occurred much later than protolith formation is provided by the Grenville Province of eastern North America. In this case, high-grade metamorphism (about 1.1 Byr ago) occurred up to 1.6 Byr after crustal formation. To investigate Pb isotope evolution in Grenville crust, DeWolf and Mezger (1994) measured Pb isotope ratios on K-feldspars from various rock types in the Grenville Province of Ontario and New York State. Data for Mid-Proterozoic rocks of the Adirondacks and Central Meta-sedimentary Belt formed a compact array of shallow slope, whereas data from the Central Gneiss Belt (CGB) defined a steeper but more scattered array (Fig. 5.39).

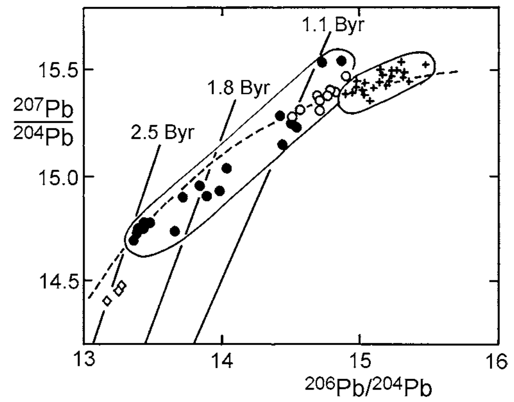

Fig. 5.39. Pb–Pb isotope diagram for Grenvillian gneisses with older crustal formation ages: (●) = Archean; (+) = Mid-Proterozoic; (○) = Early Proterozoic ages with ambiguous Pb isotope signatures. (◇) = Archean, Superior province. The growth curve is from Doe and Zartman (1979). Data from DeWolf and Mezger (1994).

DeWolf and Mezger attempted to use the Pb–Pb data set to test Nd isotope mapping of the extent of Archean crust in the CGB. However, the susceptibility of Pb isotope data to open-system behaviour during high-grade metamorphism makes Pb a less-sensitive tool than Nd for mapping crustal-formation ages in the Grenville province. A combination of Nd isotope and U–Pb data indicates the existence of a juvenile Early Proterozoic terrane in the CGB. However, meta-igneous rocks in this terrane have ambiguous Pb isotope signatures that cannot be resolved from the Archean or Mid-Proterozoic arrays. This applies both to the ^{207}Pb/^{204}Pb–^{206}Pb/^{204}Pb diagram (Fig. 5.39) and to the ^{208}Pb/^{204}Pb–^{206}Pb/^{204}Pb diagram (not shown).

The two case studies discussed above show that Pb–Pb isotope systems can be quite unreliable when a high-grade metamorphic event occurred some time after crustal formation. However, these were both cases in which a Late Archean crustal terrane was subjected to metamorphism in the Early-to-Mid Proterozoic. In contrast, Pb isotope systematics allow much tighter constraints on crustal evolution for Early Archean rocks, due to the rapid evolution of ^{207}Pb during the Earth's early history. Therefore, for Early Archean rocks, even Pb *model* ages can be used to test Pb–Pb isochron ages for metamorphic disturbance.

Kamber and Moorbath used this approach to test a Pb–Pb regression age for 83 Amitsoq gneisses from the coastal Godthabsfjord area, south of Nuk in western Greenland (Fig. 5.40). Because of the large size of the data set, a relatively precise age of 3.65 ± 0.07 Byr (2σ) was obtained. However, the regression gave a large MSWD of 18, suggesting either initial ratio heterogeneity or metamorphic disturbance. Both of these effects could have subtly influenced the errorchron slope to produce a meaningless age. Therefore, to test this possibility, the Amitsoq Pb–Pb regression line was compared with a depleted-mantle growth curve to determine a Pb model age for the rocks.

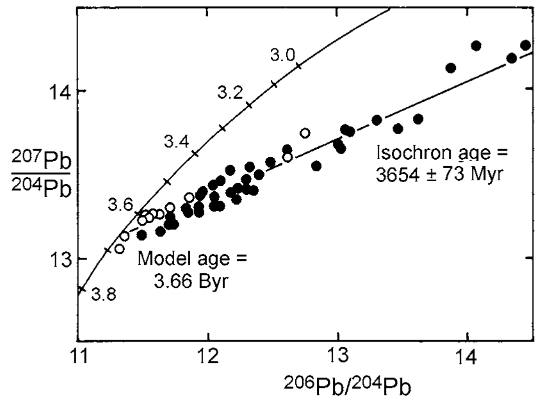

Fig. 5.40. Pb–Pb isochron for Amitsoq gneisses from the Godthabsfjord area of western Greenland, showing intersection with the depleted-mantle growth curve at a model Pb age of 3.66 Byr, in good agreement with the regression age: (●) = whole-rocks; (○) = feldspar. After Kamber and Moorbath (1998).

The growth curve used was that of Kramers and Tolstikhin (1997), but the curve of Stacey and Kramers (1975) gives almost identical results. The regression line was shown to intersect the growth curve at a point corresponding to a model Pb age of 3.66 Byr, in excellent agreement with the regression age. The inclusion of leached-feldspar analyses in the data set makes the model age particularly robust because these are very close to initial Pb isotope ratios. Hence, these data confirm that the Pb–Pb regression age gives the true age of crustal formation from a typical mantle Pb source. This suggests that, in the coastal Godthabsfjord area of western Greenland, there is no significant crustal prehistory before 3.66 Byr. However, this does not rule out such a prehistory for Amitsoq gneisses from the area further inland, near Isua (section 4.4.4).

5.6 Environmental Pb

Interest in the isotopic composition of Pb in environmental systems arose from attempts to date the age of the Earth by the Pb/Pb method. In order to determine a Bulk Earth composition for this dating work, Patterson investigated the composition of pelagic sediments, which were thought to provide an average composition of the whole crust. However, the analyses of pelagic sediments led to considerations about the distribution of Pb in the oceanic system.

A primary necessity in attempting to understand the distribution of Pb in the oceans is the accurate measurement of the Pb concentration of seawater. However, the very low levels of Pb in seawater presented a considerable analytical challenge. The first problem was to find an analytical method with detection limits as low as one part per billion (ppb). The only method that can routinely achieve these kinds of detection limits is isotope dilution (section 2.4), which allows the measurement of Pb isotope composition at the same time. The second problem is anthropogenic contamination of the samples during analysis, referred to as 'blank' (section 2.1.4). This was to pose a particular problem, because almost all laboratory materials and equipment have higher Pb levels than those in seawater.

The first workers to overcome both of these problems and achieve accurate analysis of the Pb content of seawater were Tatsumoto and Patterson (1963). They went to extreme lengths to minimise Pb contamination during analysis, and demonstrated the effectiveness of these measures by using the same analytical procedure to analyse seawater samples of various sizes. Since the amount of contamination is determined by

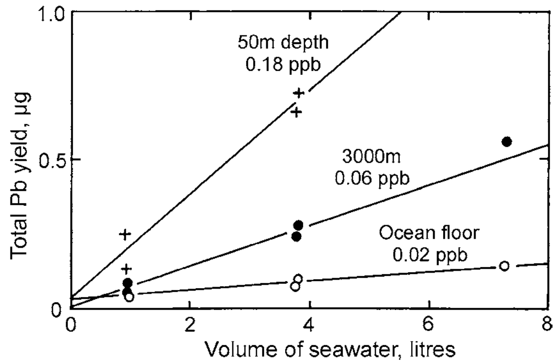

Fig. 5.41. Plot of analytical Pb yield (in micrograms) against volume of seawater (in litres), allowing the Pb content of seawater to be determined. After Tatsumoto and Patterson (1963).

the procedure, the application of an identical procedure to samples of various sizes should give rise to a constant Pb blank, whereas the total amount of Pb detected is dependent on the sample size. Hence, the two quantities can be separated (Fig. 5.41). This procedure showed that the Pb content of seawater varied within the range 0.02–0.18 ppb (μg/l), whereas the analytical blank was about 50 ng (0.05μg). Previous Pb determinations on seawater had been ten to fifty times higher (2–8 ppb), which must be attributed to analytical error.

The accurate measurement of Pb concentrations from different water depths resulted in some surprising observations (e.g. Fig. 5.41). These showed Pb concentrations in surface ocean water to be nearly an order of magnitude higher than those in deep ocean water (2000–4000 m). This behaviour was the opposite to that observed for many natural tracers, but resembled the distribution of nuclear fallout in the oceans. Hence, Tatsumoto and Patterson (1963) argued that the principal input of Pb to the oceans at the present day is anthropogenic. Following this discovery, the investigation of Pb in the oceans soon turned to focus on the origins and distribution of anthropogenic Pb in various near-surface environments.

5.6.1 Anthropogenic Pb

The first use of Pb isotopes to trace the sources and distribution of anthropogenic Pb was made by Chow and Johnstone (1965). Following an observation by Tatsumoto and Patterson (1963) that snow from Lassen Peak National Park had (relatively) very elevated Pb contents (1.6 parts per trillion), Chow and Johnstone made Pb isotope measurements on the snow for comparison with possible sources in Californian leaded gasoline. They found that the Pb isotope signature of Lassen snow was almost identical to that of atmospheric particulates recovered from their clean-laboratory filter in Pasadena (Los Angeles) and also fell within the range of Pb isotope compositions of local gasoline. This was due to the practice of adding tetra-ethyl lead to gasoline to prevent engine pre-ignition.

Chow (1970) followed up this work with a study of the world-wide compositional variations of leaded gasoline. He found large isotopic variations, and attributed them to the varying geological age of the Pb ores used for making tetra-ethyl lead in different countries. He then compared these Pb signatures with the isotopic compositions of locally collected pollutant leads, either from air filters or from soil samples. The results were presented on a graph that has often been used since (with minor variations) to compare the signatures of pollutant leads (Fig. 5.42). The data revealed a very strong correlation between the Pb isotope composition of gasoline Pb and that of local pollutant Pb, conclusively demonstrating that gasoline additives were the principal source of pollutant lead in the environment.

By the late 1960s, steps to convert American cars to lead-free gasoline were under way. Ironically, this was not to avoid poisoning the human population but to avoid poisoning catalytic converters, which were being fitted to car exhaust systems to control pollution haze (Harrison and Laxen, 1981). As a result of this policy,

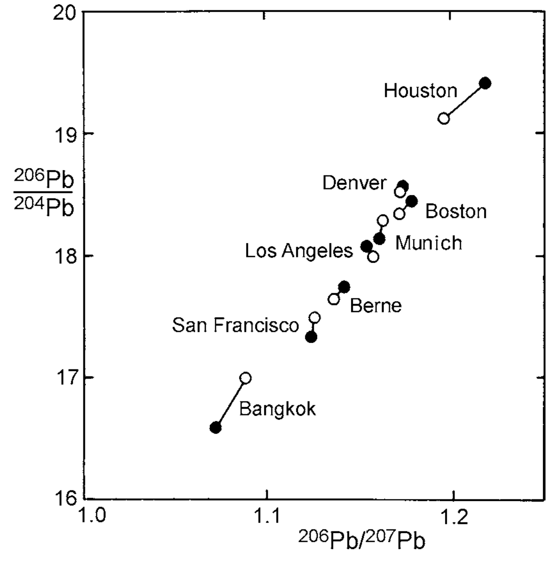

Fig. 5.42. Correspondence between lead ore compositions (●) and gasolines (○) from various countries on a Pb/Pb isotope plot. After Chow (1970).

the use of Pb in American gasoline peaked in 1970 and by 1990 had fallen to less than 5% of the peak level (Wu and Boyle, 1997). Therefore, after 1970, Pb isotope tracer studies were devoted to assessing the relative contributions of various different Pb pollution sources to the environment.

In an early example of this kind of work, Chow and Earl (1972) showed that atmospheric Pb pollution derived from the combustion of coal could be distinguished from that of leaded gasoline by the more radiogenic Pb signature in coal. This is because Pb in the sedimentary system (where coal is deposited) is more radiogenic than Pb in basement rocks, which are the sources of most Pb ore deposits. In a later study, Sturges and Barrie (1987) showed that the isotopic composition of atmospheric Pb pollution from Canadian and American sources could be distinguished, allowing the tracing of cross-border air pollution.

Some more recent studies have used the distinct Pb isotope signatures of North American and European Pb pollution to trace their relative contributions to the contamination of environmental systems far from their sources. For example, Rosman *et al.* (1993) measured the Pb isotope composition of Greenland snows between 1968 and 1988, and found relatively large variations during this period (Fig. 5.43). Since European leaded petrol generally had lower $^{206}Pb/^{207}Pb$ ratios than did American leaded gasoline, a decrease in the $^{206}Pb/^{207}Pb$ ratio of Greenland snow (accompanied by a seven-fold decrease in overall Pb concentration) was attributed to the earlier phase-out of leaded gasoline in North America.

A final example demonstrates the use of Pb isotopes to trace North American and European anthropogenic contributions to the Pb inventory of North Atlantic surface water (Fig. 5.44). In this study, American Pb sources were found to dominate the Pb isotope composition of North Atlantic surface waters off the North African coast in 1990–1992, despite the earlier phase-out of American leaded gasoline. This Pb was carried across the Atlantic, via the Sargasso Sea, by eastward-moving surface water currents. Hence, this study demonstrates that the signature of leaded gasoline will remain in environmental systems for many years to come, as anthropogenic Pb changes from a deadly health hazard to a useful marker of 1970s-age components in hydrological and sedimentary systems.

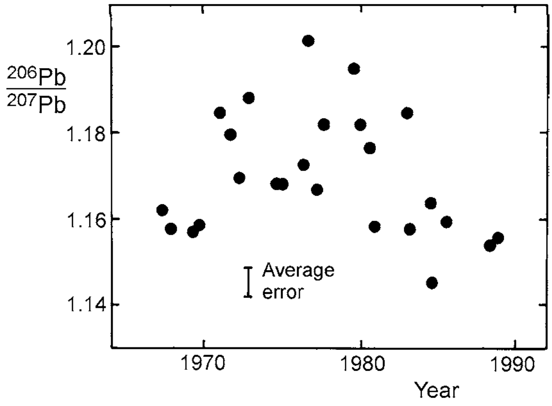

Fig. 5.43. Changing $^{206}Pb/^{207}Pb$ ratio in a twenty-year section of Greenland snow, attributed to the phase-out of American leaded gasoline. After Rosman *et al.* (1993).

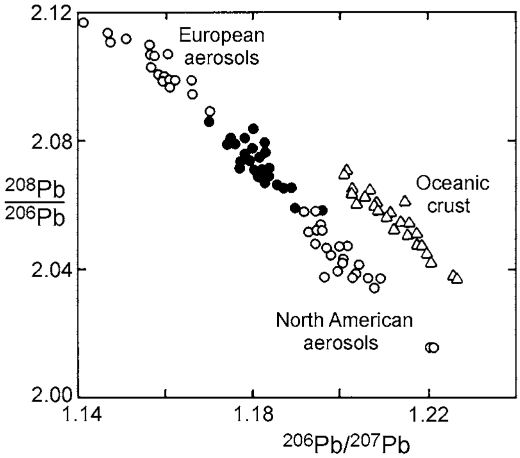

Fig. 5.44. Mixing of anthropogenic Pb components in the North Atlantic, shown on a Pb/Pb isotope diagram: (○) = aerosols carried from Europe and North America; (●) = North African surface waters; (△) = uncontaminated deep-sea sediments. After Hamelin *et al.* (1997).

5.6.2 Pb as an oceanographic tracer

The extent of anthropogenic Pb contamination of ocean water is so great that Pb isotope measurements of ocean water itself cannot give information about natural Pb circulation. Therefore, studies of Pb as a natural oceanic tracer must be based on inventories of past oceanic Pb, recorded in ferromanganese nodules and pelagic sediments, as well as on the behaviour of ^{210}Pb, a short-lived isotope in the U-series decay chain (section 12.1).

The use of Pb isotope analysis in oceanography was pioneered by the studies of Chow and Patterson (1959) on manganese nodules, and Chow and Patterson (1962) on pelagic sediments. These studies revealed a general distinction between the Pb isotope signatures of Atlantic and Pacific samples, but within each ocean basin manganese nodules and pelagic sediments gave relatively consistent results. From these observations, Chow and Patterson concluded that Pb had a relatively short residence time in seawater, and that the distinct Pacific and Atlantic Ocean signatures reflected the average Pb isotope composition of the continents surrounding each ocean basin.

From these inter-oceanic variations, Chow and Patterson estimated a residence time for dissolved Pb in seawater of about 10 kyr. However, Craig *et al.* (1973) showed that ^{210}Pb can be used to determine a much more accurate Pb residence time, by comparison with the relatively long-lived isotope ^{226}Ra, which acts as the parent of ^{210}Pb in seawater. They showed that ^{210}Pb was severely depleted relative to ^{226}Ra in deep ocean water, and hence that Pb must be very rapidly scavenged from seawater by adsorption onto particulate matter. Hence, from the degree of ^{210}Pb depletion in a vertical section through the North Pacific off Guadalupe, Craig *et al.* calculated a deep-water Pb residence time of only 50 yr (Fig. 5.45). This figure was confirmed as the average oceanic Pb residence time by a recent compilation of oceanic ^{210}Pb data, coupled with a general ocean-circulation model (Henderson and Maier-Reimer, 2002). However, variations in residence time of up to an order of magnitude were observed between areas of high and low biological productivity.

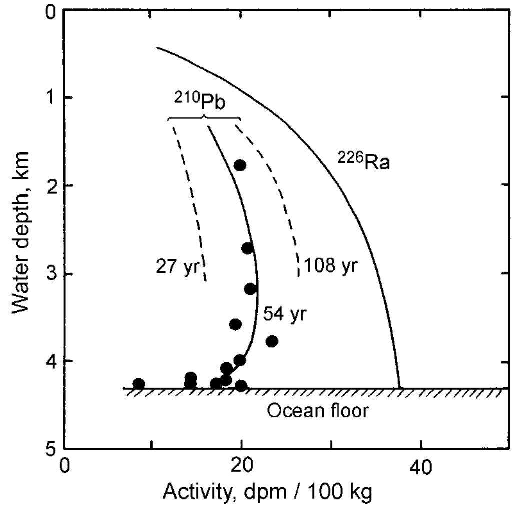

Fig. 5.45. Profiles of ^{210}Pb and ^{226}Ra activity against depth in the central Pacific Ocean, showing the good agreement between measured ^{210}Pb activity (●) and a water-column model with a Pb residence time of 54 yr. After Craig *et al.* (1973).

In the 1970s, interest in environmental Pb isotope analysis switched from natural to anthropogenic Pb, and relatively few studies of Pb isotopes as oceanic tracers were performed until the 1990s. However, a study by Reynolds and Dasch (1971) led to a better understanding of the sources of dissolved oceanic Pb. Reynolds and Dasch were able to obtain more accurate Pb isotope data than Chow and Patterson because of advances in mass spectrometry, including the use of a double-spiking technique to correct for instrumental mass fractionation (section 2.4.2). They showed that Mn nodules from the Atlantic Ocean had Pb signatures consistent with a source from continental erosion, whereas Mn nodules from the Pacific Ocean appeared to contain a mixture of continental Pb and a component of Pb from submarine volcanic activity.

The importance of submarine hydrothermal activity as a source of Pb in the oceans was confirmed by studies of metal-rich sediments near the East Pacific Rise (Dasch *et al.*, 1971). These sediments have very large Pb contents (about 200 ppm) and Pb isotope signatures that overlap the composition of Pacific MORB. On the other hand, Mn nodules not in the immediate vicinity of the ocean ridge were shown to have more-radiogenic Pb signatures indicative of mixing with continental sources (Reynolds and Dasch, 1971). This interplay between continental and hydrothermal Pb fluxes as sources for oceanic Pb was confirmed by O'Nions *et al.* (1978). They argued that, because the oceanic residence of Pb is so short, the isotopic composition of seawater Pb at any one point is essentially a dynamic equilibrium between these competing fluxes.

Despite its very short oceanic residence time, the behaviour of oceanic Pb somewhat resembles that of Sr (section 3.6.2) in resulting from competing continental and hydrothermal fluxes. The importance of ocean-floor hydrothermal activity as a source of Pb can be attributed to the solubility of Pb as high-temperature chloride complexes, despite its strong adsorption into particulate matter at low temperatures. In contrast, the solubility of Nd is low both at high and at low temperatures. Therefore Nd is not mobilised by sea-floor hydrothermal activity, and oceanic Nd is derived entirely from mixing of riverine and windblown components (section 4.5.1).

Much oceanographic evidence shows that Pacific and Atlantic water masses communicate via the circumpolar (Antarctic) ocean (e.g. section 14.1.7). Therefore, a good understanding of present-day oceanic Pb can be obtained from circumpolar Mn nodules. These were studied by Abouchami and Goldstein (1995), who found evidence for major mixing of Pb between different water masses, as shown on a Pb–Pb isotope diagram (Fig. 5.46). In this plot, the composition of East Pacific Rise metalliferous sediments overlaps the MORB field, while the Pb array in Mn nodules spans the range from the metalliferous sediments to radiogenic crustal sources.

The mixing relationships in Fig. 5.46 can be seen in a dynamic fashion by plotting the Pb isotope ratio of circumpolar Mn nodules against longitude (Fig. 5.47). This plot reveals two principal trends, involving progressive reduction in the Pb isotope ratio of Antarctic water across the south Pacific, and a progressive increase across the southern Atlantic–Indian oceans. These variations occur in response to mixing of these water masses with the eastward-moving circumpolar current, which has a circulation time of about 30 yr.

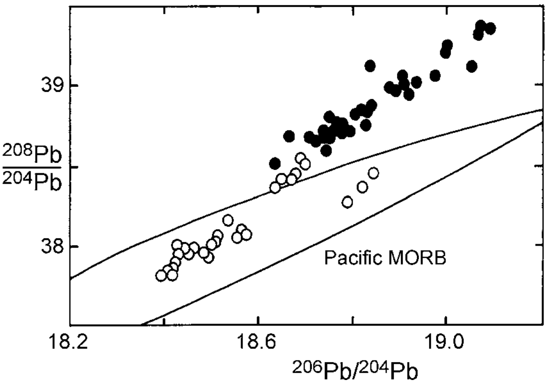

Fig. 5.46. Thorogenic–uranogenic Pb isotope diagram, showing circumpolar Mn nodules (●) resulting from mixing of Antarctic water with Pacific and Atlantic–Indian Ocean water. Pacific MORB and metalliferous sediments (○) are shown for reference. After Abouchami and Goldstein (1995).

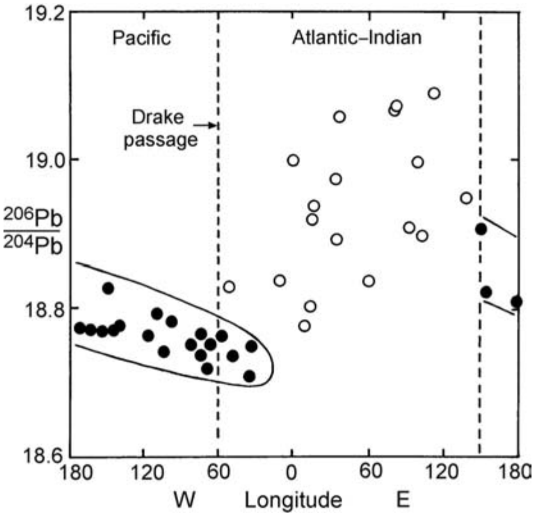

Fig. 5.47. Plot of Pb isotope ratio against longitude, showing the changing composition of circumpolar water due to mixing with water masses of the Pacific Ocean (●) and Atlantic–Indian Ocean (○). Modified after Abouchami and Goldstein (1995).

The Atlantic–Indian Pb trend in Fig. 5.47 is correlated with ϵ Nd, which Abouchami and Goldstein attributed to the southerly current that carries North Atlantic Deep Water (NADW) into the Antarctic Ocean. Here, NADW mixes with the Antarctic Bottom Water in which the Mn nodules grow. In contrast, the Pacific Pb trend does not correlate with ε Nd, which Abouchami and Goldstein attributed to the effect of many isolated mixing events between Pacific and Antarctic water as the circumpolar current moves across the southernmost Pacific. However, when this circumpolar water (CPW) reaches the Drake Passage between South America and Antarctica, the circumpolar current carries this water, with its distinct isotopic signature, half-way across the south Atlantic, until it suddenly meets the southward-moving NADW. A similar sudden transition occurs SE of Australia, where Pacific water first meets CPW in the Tasman Straits (Fig. 5.47).

Within the Atlantic, Indian and Pacific oceans, the Pb isotope compositions of Mn nodules are more homogeneous than they are in the circumpolar ocean (von Blanckenburg *et al.*, 1996). However, recent work has revealed isotopic provinciality in the Mn nodules from these oceans, with complex mixing relationships between Pb from different bodies of water. For example, the southern Indian Ocean is influenced by NADW and CPW, as discussed above, but the northern Indian Ocean carries a Pb signature from Himalayan erosion (Vlastélic *et al.*, 2001). Similarly, the south-central Pacific is dominated by hydrothermal input from the East Pacific Rise, but the north-central Pacific carries a Pb component derived from windblown sediment, largely composed of Chinese loess (Jones *et al.*, 2000). Finally, the marginal north Pacific bears Pb signatures from the erosion of circum-Pacific volcanic arcs.

5.6.3 Paleo-seawater Pb

Because of their slow growth over millions of years, ferromanganese nodules and crusts preserve a record of past variations of seawater Pb isotope composition, as well as geographical variations at the present time. The reliable dating of such material, which is critical in order to make accurate paleo-oceanographic reconstructions, is discussed in section 4.5.3.

In view of the very short residence time of Pb in the oceans, and the multitude of Pb sources discussed above, it might be expected that the records of past oceanic Pb isotope composition carried in ferromanganese crusts would show rapid changes. Rapid changes were indeed observed in the Northwest Atlantic over the past 2 Myr (Fig. 5.48). These were originally attributed to the closure of the Panama Gateway (Burton *et al.*, 1997). However, the observation of similar changes in the Arctic Ocean suggested that the changes were probably due to the input of very radiogenic Pb from the Canadian and Greenland shields as a result of intensified glacial erosion beginning about 3 Myr ago (von Blanckenburg and O'Nions, 1999).

In contrast to these rapid changes, the earlier evolution of North Atlantic Pb was somewhat less variable, while the central Pacific has maintained a practically constant Pb isotope composition over the past 30 Myr (Ling *et al.*, 1977). On the other hand, the northern Indian Ocean has experienced moderately large long-term Pb isotope variations over the past 25 Myr, attributed by Frank and O'Nions (1998) to the effects of Himalayan uplift and erosion. The sensitivity of Pb isotopes to these regional oceanographic processes, coupled with the power of MC-ICP-MS for producing large numbers of accurate measurements (section 2.5.4), means that Pb isotopes promise to be excellent tracers for detailed paleo-oceanography.

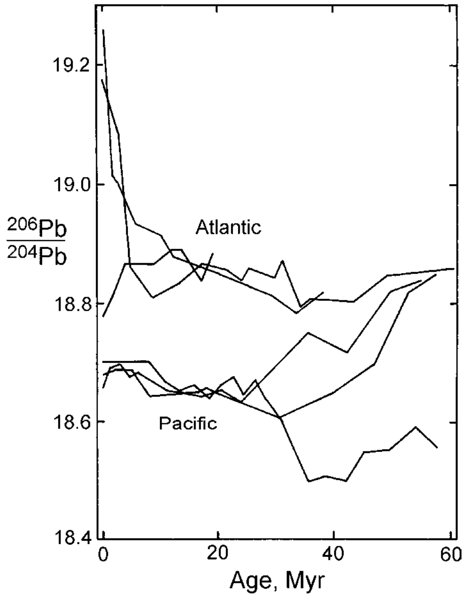

Fig. 5.48. Pb isotope variations in ferromanganese crusts from the major oceans over the past 30 Myr. After Frank and O'Nions (1998).

References

Abouchami, W. and Goldstein, S. L. (1995). A lead isotopic study of Circum-Antarctic manganese nodules. *Geochim. Cosmochim. Acta* **59**, 1809–20.

Ahrens, L. H. (1955). Implications of the Rhodesia age pattern. *Geochim. Cosmochim. Acta* **8**, 1–15.

Albarède, F. and Juteau, M. (1984). Unscrambling the lead model ages. *Geochim. Cosmochim. Acta* **48**, 207–12.

Aleinikoff, J. N., Winegarden, D. L. and Walter, M. (1990). U–Pb ages of zircon rims: a new analytical method using the air-abrasion technique. *Chem. Geol. (Isot. Geosci. Section)* **80**, 351–63.

Allègre, C. J., Manhès, G. and Göpel, C. (1995a). The age of the Earth. *Geochim. Cosmochim. Acta* **59**, 1445–56.

Allègre, C. J., Poirier, J.-P., Humler, E. and Hofmann, A. W. (1995b). The chemical composition of the Earth. *Earth Planet. Sci. Lett.* **134**, 515–26.

Alpher, R. A. and Herman, R. C. (1951). The primeval lead isotopic abundances and the age of the Earth's crust. *Phys. Rev.* **84**, 1111–14.

Amelin, Y., Krot, A. N., Hutcheon, I. D. and Ulyanov, A. A. (2002). Lead isotopic ages of chondrules and calcium–aluminum-rich inclusions. *Science* **297**, 1678–83.

Appel, P. W. U., Moorbath, S. and Taylor, P. N. (1978). Least radiogenic terrestrial lead from Isua, west Greenland. *Nature* **272**, 524–6.

Armstrong, R. L. (1968). A model for the evolution of Sr and Pb isotopes in a dynamic Earth. *Rev. Geophys.* **6**, 175–99.

Burton, K. W., Ling, H.-F. and O'Nions, R. K. (1997). Closure of the Central American Isthmus and its effect on deep-water formation in the North Atlantic. *Nature* **386**, 382–5.

Carl, C. and Dill, H. (1985). Age of secondary uranium mineralization in the basement rocks of the north eastern Bavaria F.R.G. *Chem. Geol. (Isot. Geosci. Section)* **52**, 295–316.

Carl, C., Wendt, I. and Wendt, J. I. (1989). U/Pb whole-rock and mineral dating of the Falkenburg granite in northeast Bavaria. *Earth Planet. Sci. Lett.* **94**, 236–44.

Catlos, E. J., Gilley, L. D. and Harrison, T. M. (2002). Interpretation of monazite ages obtained via *in situ* analysis. *Chem. Geol.* **188**, 193–215.

Chapman, H. J. and Roddick, J. C. (1994). Kinetics of Pb release during the zircon evaporation technique. *Earth Planet. Sci. Lett.* **121**, 601–11.

Chen, J. H. and Wasserburg, G. J. (1981). The isotopic composition of uranium and lead in Allende inclusions and meteoritic phosphates. *Earth Planet. Sci. Lett.* **52**, 1–15.

Chow, T. J. (1970). Isotopic identification of industrial pollutant lead. In: *Second International Clean Air Congress*. New South Wales University Press, pp. 348–52.

Chow, T. J. and Earl, J. L. (1972). Lead isotopes in North American coals. *Science* **176**, 510–11.

Chow, T. J. and Johnstone, M. S. (1965). Lead isotopes in gasoline and aerosols of Los Angeles Basin, California. *Science* **147**, 502–3.

Chow, T. J. and Patterson, C. C. (1959). Lead isotopes in manganese nodules. *Geochim. Cosmochim. Acta* **17**, 21–31.

Chow, T. J. and Patterson, C. C. (1962). The occurrence and significance of lead isotopes in pelagic sediments. *Geochim. Cosmochim. Acta* **26**, 263–308.

Compston, W., Williams, I. S. and Meyer, C. (1984). U–Pb geochronology of zircons from lunar breccia 73217 using a sensitive high mass-resolution ion microprobe. *Proc. 14th Lunar and Planet. Sci. Conf., J. Geophys. Res.* **89** *Suppl.*, B525–34.

Copeland, P., Parrish, R. R. and Harrison, T. M. (1988). Identification of inherited radiogenic Pb in monazite and its implications for U–Pb systematics. *Nature* **333**, 760–3.

Corfu, F. (1988). Differential response of U–Pb systems in coexisting accessory minerals, Winnipeg River Sub-province, Canadian Shield: implications for Archean crustal growth and stabilization. *Contrib. Mineral. Petrol.* **98**, 312–25.

Corfu, F. (2000). Extraction of Pb with artificially too-old ages during stepwise dissolution experiments on Archean zircon. *Lithos* **53**, 279–91.

Craig, H., Krishnaswami, S. and Somayajulu, B. L. K. (1973). ^{226}Pb–^{226}Ra: radioactive disequilibrium in the deep sea. *Earth Planet. Sci. Lett.* **17**, 295–305.

Cumming, G. L. and Richards, J. R. (1975). Ore lead isotope ratios in a continuously changing earth. *Earth Planet. Sci. Lett.* **28**, 155–71.

Dahl, P. S. (1997). A crystal-chemical basis for Pb retention and fission-track annealing systematics in U-bearing minerals, with implications for geochronology. *Earth Planet. Sci. Lett.* **150**, 277–90.

Dasch, E. J., Dymond, J. R. and Heath, G. R. (1971). Isotopic analysis of metalliferous sediment from the East Pacific Rise. *Earth Planet. Sci. Lett.* **13**, 175–80.

Davis, D. W. (1982). Optimum linear regression and error estimation applied to U–Pb data. *Can. J. Earth Sci.* **19**, 2141–9.

Davis, D. W. and Krogh, T. E. (2000). Preferential dissolution of ^{234}U and radiogenic Pb from alpha-recoil-damaged lattice sites in zircon: implications for thermal histories and Pb isotopic fractionation in the near surface environment. *Chem. Geol.* **172**, 41–58.

DeWolf, C. P. and Mezger, K. (1994). Lead isotope analyses of leached feldspars: constraints on the early crustal history of the Grenville Orogen. *Geochim. Cosmochim. Acta* **58**, 5537–50.

DeWolf, C. P., Zeissler, C. J., Halliday, A. N., Mezger, K. and Essene, E. J. (1996). The role of inclusions in U–Pb and Sm–Nd garnet geochronology: stepwise dissolution experiments and trace uranium mapping by fission track analysis. *Geochim. Cosmochim. Acta* **60**, 121–34.

Doe, B. R. and Stacey, J. S. (1974). The application of lead isotopes to the problems of ore genesis and ore prospect evaluation: a review. *Econ. Geol.* **69**, 757–76.

Doe, B. R. and Zartman, R. E. (1979). Plumbotectonics: the Phanerozoic. In: Barnes, H. L. (Ed.), *Geochemistry of Hydrothermal Ore Deposits*. Wiley, pp. 22–70.

Drummond, M. S. and Defant, M. J. (1990). A model for trondhjemite–tonalite–dacite genesis and crustal growth via slab melting: Archean to modern comparisons. *J. Geophys. Res.* **95**, 21 503–21 521.

Feng, R., Machado, N. and Ludden, J. (1993). Lead geochronology of zircon by laser probe–inductively coupled plasma mass spectrometry (LP–ICPMS). *Geochim. Cosmochim. Acta* **57**, 3479–86.

Foley, S., Tiepolo, M. and Vannucci, R. (2002). Growth of early continental crust controlled by melting of amphibolite in subduction zones. *Nature* **417**, 837–40.

Foster, G., Gibson, H. D., Parrish, R., Horstwood, M., Fraser, J. and Tindle, A. (2002). Textural, chemical and isotopic insights into the nature and behaviour of metamorphic monazite. *Chem. Geol.* **191**, 183–207.

Frank, M. and O'Nions, R. K. (1998). Sources of Pb for Indian Ocean ferromanganese crusts: a record of Himalayan erosion? *Earth Planet. Sci. Lett.* **158**, 121–30.

French, J. E., Heaman, L. M. and Chacko, T. (2002). Feasibility of chemical U–Th–total Pb baddeleyite dating by electron microprobe. *Chem. Geol.* **188**, 85–104.

Froude, D. O., Ireland, T. R., Kinny, I. S., Williams, I. S. and Compston, W. (1983). Ion microprobe identification of 4,100–4,200 Myr-old terrestrial zircons. *Nature* **304**, 616–18.

Galer, S. J. G. and Goldstein, S. L. (1996). Influence of accretion on lead in the Earth. In: Basu, A. and Hart, S. R. (Eds.), *Earth Processes: Reading the Isotopic Code. Geophysics. Monograph* **95**. American Geophysical Union, pp. 75–98.

Gentry, R. V., Sworski, T. J., McKown, H. S., Smith, D. H., Eby, R. E. and Christie, W. H. (1982). Differential lead retention in zircons: implications for nuclear waste containment. *Science* **216**, 296–7.

Goldrich, S. S. and Mudrey, M. G. (1972). Dilatancy model for discordant U–Pb zircon ages. In: Tugarinov, A. I. (Ed.), *Contributions to Recent Geochemistry and Analytical Chemistry.* Moscow Nauka Publication Office, pp. 415–18.

Griffin, W. L., Taylor, P. N., Hakkinea, J. W., *et al.* (1978). Archaean and Proterozoic crustal evolution in Lofoten–Vesteraalen, Norway. *J. Geol. Soc. Lond.* **135**, 629–47.

Grove, M. and Harrison, T. M. (1999). Monazite Th–Pb age depth profiling. *Geology* **27**, 487–90.

Halliday, A. N. (1984). Coupled Sm–Nd and U–Pb systematics in Late Caledonian granites and the basement under northern Britain. *Nature* **307**, 229–33.

Hamelin, B., Ferrand, J. L., Alleman, L., Nicolas, E. and Veron, A. (1997). Isotopic evidence of pollutant lead transport from North America to the subtropical North Atlantic gyre. *Geochim. Cosmochim. Acta* **61**, 4423–8.

Harrison, R. M. and Laxen, D. P. H. (1981). *Lead Pollution: Causes and Control.* Chapman and Hall.

Heaman, L. M. and LeCheminant, A. N. (1993). Paragenesis and U–Pb systematics of baddeleyite (ZrO_2). *Chem. Geol.* **110**, 95–126.

Henderson, G. M. and Maier-Reimer, E. (2002). Advection and removal of ^{226}Pb and stable Pb isotopes in the oceans: a general circulation model study. *Geochim. Cosmochim. Acta* **66**, 257–72.

Hinton, R. W. and Long, J. V. P. (1979). High-resolution ion-microprobe measurement of lead isotopes: variations within single zircons from Lac Seul, Northwestern Ontario. *Earth Planet. Sci. Lett.* **45**, 309–25.

Holmes, A. (1946). An estimate of the age of the Earth. *Nature* **157**, 680–4.

Holmes, A. (1954). The oldest dated minerals of the Rhodesian Shield. *Nature* **173**, 612–17.

Houtermans, F. G. (1946). Die Isotopen-Häufigkeiten im natürlichen Blei und das Alter des Urans. *Naturwissenschaften* **33**, 185–7.

Houtermans, F. G. (1947). Das Alter des Urans. *Z. Naturf.* **29**, 322–8.

Jacobsen, S. B. and Wasserburg, G. J. (1978). Interpretation of Nd, Sr and Pb isotope data from Archaean migmatites in Lofoten–Vesteraalen, Norway. *Earth Planet. Sci. Lett.* **41**, 245–53.

Jaffey, A. H., Flynn, K. F., Glendenin, L. E., Bentley, W. C. and Essling, A. M. (1971). Precision measurement of the half-lives and specific activities of U235 and U238. *Phys. Rev. C* **4**, 1889–907.

Jahn B.-M. and Cuvellier, H. (1994). Pb–Pb and U–Pb geochronology of carbonate rocks: an assessment. *Chem. Geol. (Isot. Geosci. Section)* **115**, 125–51.

Jones, C. E., Halliday, A. N. and Lohmann, K. C. (1995). The impact of diagenesis on high-precision U–Pb dating of ancient carbonates: an example from the Late Permian of New Mexico. *Earth Planet. Sci. Lett.* **134**, 409–23.

Jones, C. E., Halliday, A. N., Rea, D. K. and Owen, R. M. (2000). Eolian inputs of lead to the North Pacific. *Geochim. Cosmochim. Acta* **64**, 1405–16.

Kamber, B. S. and Collerson, K. D. (1999). Origin of ocean island basalts: a new model based on lead and helium systematics. *J. Geophys. Res.* **104**, 25 479–91.

Kamber, B. S. and Moorbath, S. (1998). Initial Pb of the Amitsoq gneiss revisited: implication for the timing of early Archean crustal evolution in West Greenland. *Chem. Geol.* **150**, 19–41.

Kober, B. (1986). Whole-grain evaporation for ^{207}Pb/^{206}Pb-age investigations on single zircons using a double-filament thermal ion source. *Contrib. Mineral. Petrol.* **93**, 482–90.

Kober, B. (1987). Single-zircon evaporation combined with Pb^{+} emitter bedding for ^{207}Pb/^{206}Pb-age investigations using thermal ion mass spectrometry, and implications to zirconology. *Contrib. Mineral. Petrol.* **96**, 63–71.

Kober, B., Pidgeon, R. T. and Lippolt, H. J. (1989). Single-zircon dating by stepwise Pb-evaporation constrains the Archean history of detrital zircons from the Jack Hills, Western Australia. *Earth Planet. Sci. Lett.* **91**, 286–96.

Kramers, J. D. and Tolstikhin, I. N. (1997). Two terrestrial lead isotope paradoxes, forward transport modelling, core formation and the history of the continental crust. *Chem. Geol.* **139**, 75–110.

Krogh, T. E. (1982a). Improved accuracy of U–Pb zircon dating by selection of more concordant fractions using a high gradient magnetic separation technique. *Geochim. Cosmochim. Acta* **46**, 631–5.

Krogh, T. E. (1982b). Improved accuracy of U–Pb zircon ages by the creation of more concordant systems using the air abrasion technique. *Geochim. Cosmochim. Acta* **46**, 637–49.

Krogh, T. E., Corfu, F., Davis, D. W. *et al.* (1987). Precise U–Pb isotopic ages of diabase dykes and mafic to ultramafic rocks using trace amounts of baddeleyite and zircon. In: Halls, H. C. and Fahrig, W. F. (Eds.), *Mafic Dyke Swarms. Geol. Assoc. Canada Spec. Pap.* **34**, 147–52.

Krogh, T. E. and Davis, G. L. (1975). Alteration in zircons and differential dissolution of altered and metamict zircon. *Carnegie Institute Washington Year Book* **74**, 619–23.

Ling., H. F., Burton, K. W., O'Nions, R. K. *et al.* (1997). Evolution of Nd and Pb isotopes in Central Pacific seawater from ferromanganese crusts. *Earth Planet. Sci. Lett.* **146**, 1–12.

Ludwig, K. R. (1977). Effect of initial radioactive daughter disequilibrium on U–Pb isotope apparent ages of young minerals. *J. Res. U.S. Geol. Surv.* **5**, 663–7.

Ludwig, K. R. (1998). On the treatment of concordant uranium–lead ages.*Geochim. Cosmochim. Acta* **62**, 665–76.

Ludwig, K. R. (1999). *Users, Manual for Isoplot/Ex Version 2, A Geochronological Toolkit for Microsoft Excel.* Berkeley Geochronology Centre Special Publication 1a, 47 pp.

Ludwig, K. R. (2000). Decay constant errors in U–Pb concordia-intercept ages. *Chem. Geol.* **166**, 315–18.

Ludwig, K. R. (2001). Eliminating mass-fractionation effects on U–Pb isochron ages without double spiking. *Geochim. Cosmochim. Acta* **65**, 3139–45.

Manhès, G., Allègre, C. J., Dupré, B. and Hamelin, B. (1979). Lead–lead systematics, the 'age of the Earth' and the chemical evolution of our planet in a new representation space. *Earth Planet. Sci. Lett.* **44**, 91–104.

Mattinson, J. M. (1987). U–Pb ages of zircons: a basic examination of error propagation. *Chem. Geol. (Isot. Geosci. Sect.)* **66**, 151–62.

Mattinson, J. M. (1994). A study of complex discordance in zircons using step-wise dissolution techniques. *Contrib. Mineral. Petrol.* **116**, 117–29.

Mattinson, J. M. (2001). Multi-step high-resolution Pb/U and Pb/Pb zircon age spectra: combined annealing, partial dissolution and TIMS analysis. *Eos Trans. AGU* **82** (47), Fall Meeting Suppl., abstract V22C–1056.

Mezger, K., Essene, E. J. and Halliday, A. N. (1992). Closure temperatures of the Sm–Nd system in metamorphic garnets. *Earth Planet. Sci. Lett.* **113**, 397–409.

Mezger, K., Hanson, G. N. and Bohlen, S. R. (1989). U–Pb systematics of garnet: dating the growth of garnet in the Late Archean Pikwitonei granulite domain at Cauchon and Natawahunan Lakes, Manitoba, Canada. *Contrib. Mineral. Petrol.* **101**, 136–48.

Mezger, K., Rawnsley, C. M., Bohlen, S. R. and Hanson, G. N. (1991). U–Pb garnet, sphene, monazite, and rutile ages: implications for the duration of high-grade metamorphism and cooling histories, Adirondack Mts., New York. *J. Geol.* **99**, 415–28.

Montel, J.-M., Foret, S., Veschambre, M., Nicollet, C. and Provost, A. (1996). Electron microprobe dating of monazite. *Chem. Geol.* **131**, 37–53.

Moorbath, S. and Taylor, P. N. (1981). Isotopic evidence for continental growth in the Precambrian. In: Kroner, A. (Ed.), *Precambrian Plate Tectonics*. Elsevier, pp. 491–525.

Moorbath, S., Taylor, P. N. and Goodwin, R. (1981). Origin of granite magma by crustal remobilisation: Rb–Sr and Pb/Pb geochronology and isotope geochemistry of the late Archaean Qorqut Granite complex of southern West Greenland. *Geochim. Cosmochim. Acta* **45**, 1051–60.

Nier, A. O., Thompson, R. W. and Murphy, B. F. (1941). The isotopic constitution of lead and the measurement of geological time III. *Phys. Rev.* **60**, 112–17.

O'Nions, R. K., Carter, S. R., Cohen, R. S., Evensen, N. M. and Hamilton, P. J. (1978). Pb, Nd and Sr isotopes in oceanic ferromanganese deposits and ocean floor basalts. *Nature* **273**, 435–8.

Oversby, V. M. (1974). A new look at the lead isotope growth curve. *Nature* **248**, 132–3.

Parrish, R. R. (1990). U–Pb dating of monazite and its application to geological problems.*Can. J. Earth Sci.* **27**, 1431–50.

Patterson, C. C. (1956). Age of meteorites and the Earth. *Geochim. Cosmochim. Acta* **10**, 230–7.

Pankhurst, R. J. and Pidgeon, R. T. (1976). Inherited isotope systems and the source region pre-history of early Caledonian granites in the Dalradian series of Scotland. *Earth Planet. Sci. Lett.* **31**, 55–68.

Pidgeon, R. T. and Aftalion, M. (1978). Cogenetic and inherited zircon U–Pb systems in granites: Palaeozoic granites of Scotland and England. In: Bowes, D. R. and Leake, B. E. (Eds.), *Crustal Evolution in Northwestern Britain and Adjacent Regions. Geol. Soc. Spec. Issue* **10**, 183–220.

Potts, P. J. (1987). *Handbook of Silicate Rock Analysis.* Blackie. 622 pp.

Rasbury, E. T., Hanson, G. N., Meyers, W. J. and Saller, A. H. (1997). Dating of the time of sedimentation using U–Pb ages for paleosol calcite. *Geochim. Cosmochim. Acta* **61**, 1525–9.

Reynolds, P. H. and Dasch, E. J. (1971). Lead isotopes in marine manganese nodules and the ore-lead growth curve. *J. Geophys. Res.* **76**, 5124–9.

Rogers, G., Dempster, T. J., Bluck, B. J. and Tanner, P. W. G. (1989). A high precision U–Pb age for the Ben Vuirich granite: implications for the evolution of the Scottish Dalradian Supergroup. *J. Geol. Soc. Lond.* **146**, 789–98.

Rosholt, J. N. and Bartel, A. J. (1969). Uranium, thorium and lead systematics in Granite Mountains, Wyoming. *Earth Planet. Sci. Lett.* **7**, 141–7.

Rosman, K. J. R., Chisholm, W., Boutron, C. F., Candelone, J. P. and Görlach, U. (1993). Isotopic evidence for the source of lead in Greenland snows since the late 1960s. *Nature* **362**, 333–5.

Russell, R. D. (1956). Lead isotopes as a key to the radioactivity of the Earth's mantle. *Ann. N.Y. Acad. Sci.* **62**, 435–48.

Russell, R. D. (1972). Evolutionary model for lead isotopes in conformable ores and in ocean volcanics. *Rev. Geophys. Space Phys.* **10**, 529–49.

Russell, R. D. and Ahrens, L. H. (1957). Additional regularities among discordant lead–uranium ages. *Geochim. Cosmochim. Acta* **11**, 213–18.

Russell, R. D. and Farquhar, R. M. (1960). *Lead Isotopes in Geology.* Interscience Publishers, 243 p.

Schärer, U. (1984). The effect of initial ^{230}Th disequilibrium on young U–Pb ages: the Makalu case, Himalaya. *Earth Planet. Sci. Lett.* **67**, 191–204.

Schärer, U. and Allègre, C. J. (1982). Uranium–lead system in fragments of a single zircon grain. *Nature* **295**, 585–7.

Schärer, U., Xu, R. H. and Allègre, C. J. (1984). U–Pb geochronology of Gangdese (Transhimalaya) plutonism in the Lhasa–Xigaze region, Tibet. *Earth Planet. Sci. Lett.* **69**, 311–20.

Silver, L. T. and Deutsch, S. (1963). Uranium–lead isotopic variations in zircons: a case study. *J. Geol.* **71**, 721–58.

Smith, H. A. and Giletti, B. J. (1997). Lead diffusion in monazite. *Geochim. Cosmochim. Acta* **61**, 1047–55.

Smith, P. E. and Farquhar, R. M. (1989). Direct dating of Phanerozoic sediments by the ^{238}U–^{206}Pb method. *Nature* **341**, 518–21.

Smith, P. E., Farquhar, R. M. and Hancock, R. G. (1991). Direct radiometric age determination of carbonate diagenesis using U–Pb in secondary calcite. *Earth Planet. Sci. Lett.* **105**, 474–91.

Stacey, J. S. and Kramers, J. D. (1975). Approximation of terrestrial lead isotope evolution by a two-stage model. *Earth Planet. Sci. Lett.* **26**, 207–21.

Stanton, R. L. and Russell, R. D. (1959). Anomalous leads and the emplacement of lead sulfide ores. *Econ. Geol.* **54**, 588–607.

Sturges, W. T. and Barrie, L. A. (1987). Lead 206/207 isotope ratios in the atmosphere of North America as tracers of US and Canadian emissions. *Nature* **329**, 144–6.

Tatsumoto, M., Knight, R. J. and Allègre, C. J. (1973). Time differences in the formation of meteorites as determined from the ratio of lead-207 to lead-206. *Science* **180**, 1279–83.

Tatsumoto, M. and Patterson, C. C. (1963). The concentration of common lead in sea water. In: Geiss, J. and Goldberg, E. D. (Eds.), *Earth Science and Meteoritics.* North-Holland Publishing. Co., pp. 74–89.

Taylor, P. N. (1975). An early Precambrian age for migmatitic gneisses from Vikan i Bo, Vesteraalen, North Norway. *Earth Planet. Sci. Lett.* **27**, 35–42.

Taylor, P. N., Moorbath, S., Goodwin, R. and Petrykowski, A. C. (1980). Crustal contamination as an indicator of the extent of early Archaean continental crust: Pb isotopic evidence from the late Archaean gneisses of West Greenland. *Geochim. Cosmochim. Acta* **44**, 1437–53.

Tera, F. and Carlson, R. W. (1999). Assessment of the Pb–Pb and U–Pb chronometry of the early solar system. *Geochim. Cosmochim. Acta* **63**, 1877–89.

Tera, F. and Wasserburg, G. J. (1973). A response to a comment on U–Pb systematics in lunar basalts. *Earth Planet. Sci. Lett.* **19**, 213–17.

Tera, F. and Wasserburg, G. J. (1974). U–Th–Pb systematics on lunar rocks and inferences about lunar evolution and the age of the Moon. *Proc. 5th Lunar Sci. Conf. (Suppl. 5, Geochim. Cosmochim. Acta)* **2**, 1571–99.

Tilton, G. R. (1960). Volume diffusion as a mechanism for discordant lead ages. *J. Geophys. Res.* **65**, 2933–45.

Tilton, G. R. and Grunenfelder, M. H. (1968). Sphene: uranium–lead ages. *Science* **159**, 1458–61.

Tucker, R. D., Raheim, A., Krogh, T. E. and Corfu, F. (1987). Uranium–lead zircon and titanite ages from the northern portion of the Western Gneiss Region, south–central Norway. *Earth Planet. Sci. Lett.* **81**, 203–11.

van Breemen, O., Davidson, A., Loveridge, W. D. and Sullivan, R. W., (1986). U–Pb zircon geochronology of Grenville tectonites, granulites and igneous precursors, Parry Sound, Ontario. In: Moore, J. M., Davidson, A. and Baer, A. J. (Eds.), *The Grenville Province. Geol. Assoc. Canada Spec. Pap.* **31**, 191–207.

Vlastélic, I., Abouchami, W., Galer, S. J. G. and Hofmann, A. W. (2001). Geographical control on Pb isotope distribution and sources in Indian Ocean Fe–Mn deposits. *Geochim. Cosmochim. Acta* **65**, 4303–19.

von Blanckenburg, F. and O'Nions, R. K. (1999). Response of beryllium and radiogenic isotope ratios in northern Atlantic deep water to the onset of Northern Hemisphere glaciation. *Earth Planet. Sci. Lett.* **167**, 175–82.

von Blanckenburg, F., O'Nions, R. K. and Hein, J. R. (1996). Distribution and sources of pre-anthropogenic lead isotopes in deep ocean water from Fe–Mn crusts. *Geochim. Cosmochim. Acta* **60**, 4957–63.

Watson, E. B. and Harrison, T. M. (1983). Zircon saturation revisited: temperature and composition effects in a variety of crustal magma types. *Earth Planet. Sci. Lett.* **64**, 295–304.

Wendt, I. (1984). A three-dimensional U–Pb discordia plane to evaluate samples with common lead of unknown isotopic composition. *Isot. Geosci.* **2**, 1–12.

Wetherill, G. W. (1956a). An interpretation of the Rhodesia and Witwatersrand age patterns. *Geochim. Cosmochim. Acta* **9**, 290–2.

Wetherill, G. W. (1956b). Discordant uranium–lead ages. *Trans. Amer. Geophys. Union* **37**, 320–7.

Whitehouse, M. (1990). Isotopic evolution of the southern Outer Hebridean Lewisian gneiss complex: constraints on Late Archean source regions and the generation of transposed Pb–Pb palaeoisochrons. *Chem. Geol. (Isot. Geosci. Section)* **86**, 1–20.

Wilde, S. A., Valley, J. W., Peck, W. H. and Graham, C. M. (2001). Evidence from detrital zircons for the existence of continental crust and oceans on the Earth 4.4 Gyr ago. *Nature* **409**, 175–8.

Williams, I. S., Compston, W., Black, L. P., Ireland, T. R. and Foster, J. J. (1984). Unsupported radiogenic Pb in zircon: a cause of anomalously high Pb–Pb, U–Pb and Th–Pb ages. *Contrib. Mineral. Petrol.* **88**, 322–7.

Wu, J. and Boyle, E. A. (1997). Lead in the western North Atlantic Ocean: completed response to leaded gasoline phase-out. *Geochim. Cosmochim. Acta* **61**, 3279–83.

Zartman, R. E. and Doe, B. R. (1981). Plumbotectonics – the model. *Tectonophysics* **75**, 135–62.

Zartman, R. E. and Haines, S. M. (1988). The plumbotectonic model for Pb isotopic systematics among major terrestrial reservoirs – a case for bi-directional transport. *Geochim. Cosmochim. Acta* **52**, 1327–39.

6 Isotope geochemistry of oceanic volcanics

Some of the most important questions in geology concern the processes which operate in the Earth's mantle. Mantle convection is clearly the driving force behind plate tectonics (e.g. Turcotte and Oxburgh, 1967), but the details of its operation are still unclear. The depth of mantle convection cells, the fate of subducted lithosphere and the source of upwelling mantle plumes are all questions that remain poorly understood. Isotope geochemistry may help to answer these questions by revealing the progress of mantle differentiation into different reservoirs and the extent to which these reservoirs are re-mixed by convective stirring.

The inaccessibility of the mantle presents a severe problem for geochemical sampling. However, mantle-derived basic magmas provide a prime source of evidence about the chemical structure of the mantle. Isotopic tracers are a particularly powerful tool for such studies, because, unlike elemental concentrations, isotope ratios are not affected by crystal fractionation. However, isotope ratios are susceptible to contamination in the continental lithosphere. Therefore the simplest approach to studying mantle chemistry through basic magmas is to analyse oceanic volcanics, which are expected to have suffered minimal contamination in the thin oceanic lithosphere.

Isotope analysis of ocean-island basalts (OIB) was first used to demonstrate the existence of mantle heterogeneity (Faure and Hurley, 1963; Gast *et al.*, 1964). Subsequently, variations were found between the isotopic compositions of mid-ocean-ridge basalts (MORB) and OIB (Tatsumoto, 1966). Isotopic analysis of oceanic basalts can be used both to probe the structure of the mantle and to model its evolution over time. The approach taken here will be to examine the constraints on mantle structure from single isotopic systems (mainly Sr and Pb), then to examine the constraints on mantle evolution from multiple isotopic systems (Sr–Nd, U–Th–Pb and Sr–Nd–Pb). Evidence from other systems will be examined in later chapters.

6.1 Isotopic tracing of mantle structure

6.1.1 Contamination and alteration

Before oceanic volcanics can be used to deduce mantle compositions, we must examine and quantify the amounts of alteration and contamination which could occur during magma transport and eruption on ocean islands or the ocean floor.

Sub-solidus alteration of analysed samples could result from hydrothermal interaction with seawater, in the case of submarine basalts, or sub-aerial weathering, in the case of ocean-island basalts. For example, Dasch *et al.* (1973) found a positive correlation between $^{87}Sr/^{86}Sr$ ratio and water content in dredged oceanic basalts of various ages (Fig. 6.1). Samples with more than 1% H_2O had almost invariably suffered contamination with Sr from seawater, but those with less than 1% alteration appeared to be uncontaminated.

Sub-solidus alteration in submarine samples can reliably be avoided by analysing 100%-fresh MORB glasses (Cohen *et al.*, 1980). Where crystalline rock must be analysed (e.g. White *et al.*, 1976), alteration can be avoided by analysing fresh material dredged from the median valley of the ocean ridges, where very young, unmetamorphosed basalts outcrop. Alternatively, leaching of crystalline samples before analysis may remove contaminated alteration minerals, also yielding results that are consistent with glasses (Dupré and Allègre, 1980). Unaltered OIB are easily obtained by sampling only fresh lavas.

Once sub-solidus alteration of samples has been excluded, the next possibility that must be considered is contamination in the oceanic lithosphere. Although this is normally much thinner than the continental lithosphere, some ocean islands could be located on micro-continents or some other kind of abnormal lithosphere.

In their early work on Ascension and Gough islands, Gast *et al.* (1964) considered the possibility of contamination of the analysed lavas by a crustal micro-plate.

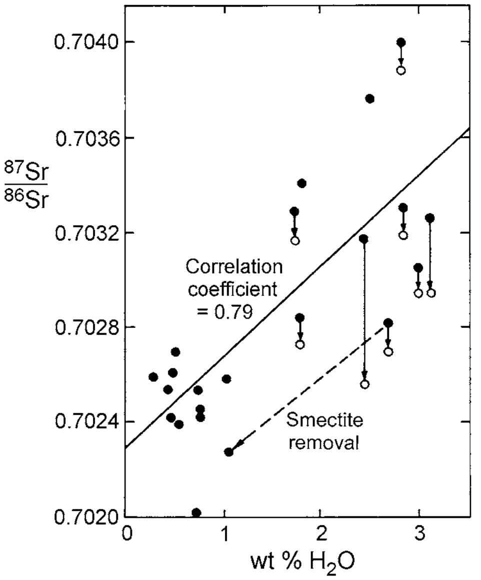

Fig. 6.1. Plot of strontium isotope ratio against water content in ocean-floor basalts. Vertical arrows show the effect of leaching before analysis. The dashed arrow shows the effect of removal of smectite from an altered sample. After Dasch *et al.* (1973).

They tested this possibility by analysing a range of lavas at variable degrees of magmatic differentiation (Fig. 6.2). The lack of any correlation in all but the most evolved rocks was argued to rule out crustal contamination. High Sr isotope ratios in the highly evolved rocks were attributed to radioactive growth after eruption, since these rocks have very high Rb/Sr ratios. No age corrections could be applied to these lavas since their ages were unknown. Similar problems have been encountered in more recent studies of Ascension lavas (Harris *et al.*, 1983). However, most oceanic basalts require no age correction since they have very low Rb/Sr ratios.

Some workers, most notably O'Hara, suggested that isotopic variations in MORB and OIB could be explained by fractionation or contamination processes affecting magmas during their ascent through oceanic crust. In his early papers on the subject, O'Hara (1973; 1975) suggested that variations in ^{87}Sr/^{86}Sr ratio could be generated by physical fractionation of the isotopes during magmatic differentiation. This is a misconception, since ^{87}Sr/^{86}Sr ratios are always fractionation-corrected to the standard ^{88}Sr/^{86}Sr ratio of 8.37521 (section 2.2.3) to eliminate both natural and analytical mass-dependent fractionation. Subsequently, O'Hara and Mathews (1981) argued that large-ion lithophile (LIL) elements (including strontium) could be perturbed by contamination with altered oceanic crust in a periodically tapped, periodically re-filled, long-lived magma chamber. This model is now ruled out by the evidence from U-series isotopes, which severely limits the time between generation and eruption of ocean-floor basalt, and hence the ability of an open-system magma chamber to overprint the source isotopic signatures in the erupted products (section 13.3).

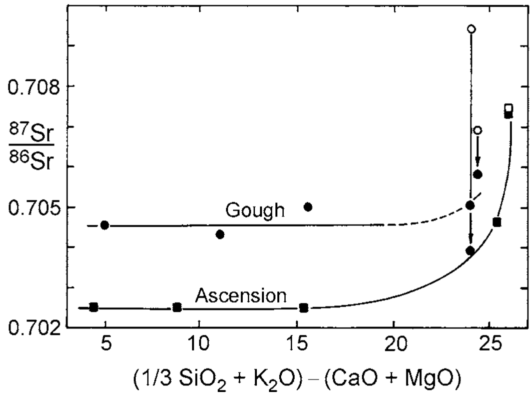

Fig. 6.2. Sr isotope ratios in lavas from Gough and Ascension islands plotted against an index of magmatic differentiation. Radiogenic Sr in highly evolved lavas (open symbols) is attributed to radioactive growth since eruption. Arrows show estimated age corrections. After Gast *et al.* (1964).

More recently, renewed attention has been paid to the possibility that some OIB may have been contaminated by mantle lithosphere. In the case of Hawaii it was proposed some time ago (Chen and Frey, 1983) that late magmatism on Oahu involved partial melting of the LIL-depleted oceanic lithosphere, and that these melts were variably mixed with melts from a plume source. However, it is only recently that strong evidence has been amassed for the contamination of some plume sources by old continental lithosphere. Within the ocean basins, other islands now thought to be underlain by fragments of old lithosphere include Grande Comore (Class *et al.*, 1998), São Miguel in the Azores (Widom *et al.*, 1997) and the Canaries (Widom *et al.*, 1999), all of which surround the African continent. Therefore, it has been suggested that fragments of African sub-continental lithosphere were delaminated during continental rifting and left as scattered remnants under new oceanic crust (Widom *et al.*, 1997; Moreira *et al.*, 1999). The case of São Miguel will be discussed in section 6.2.2.

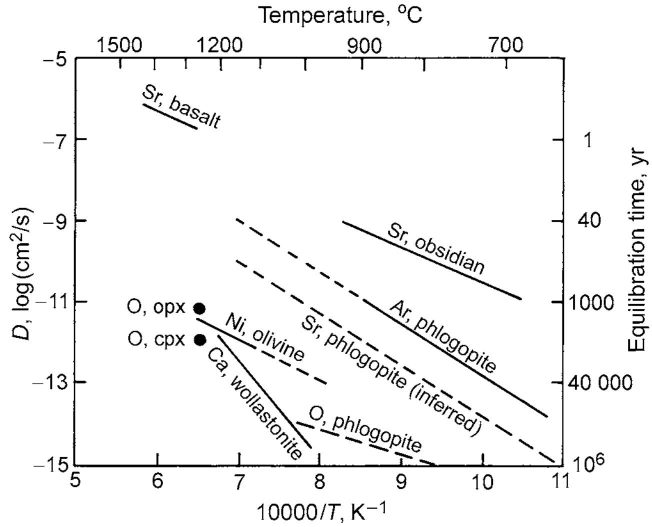

Fig. 6.3. Plot of diffusivity against 1/temperature, showing experimental results for the diffusion of Sr, Ar, Ni, Ca and oxygen in various types of material. Times for effective equilibration are based on a grain size of 1 cm. Modified after Hofmann and Hart (1978).

6.1.2 Disequilibrium melting

Following the discovery of 'mantle heterogeneity' under the oceans, various workers (e.g. Harris *et al.*, 1972; O'Nions and Pankhurst, 1973; Flower *et al.*, 1975) suggested that mantle temperatures might not be high enough to ensure diffusional homogenisation of Sr isotope ratios between different mantle minerals. In that case, grains with higher Rb/Sr ratios (such as the magnesian mica phlogopite) could develop more radiogenic $^{87}Sr/^{86}Sr$ compositions over geological time. 'Disequilibrium' melting of such phases could then bias the isotopic composition of a melt towards higher $^{87}Sr/^{86}Sr$ compositions. Small-degree partial melts would tend to be enriched in Rb/Sr and $^{87}Sr/^{86}Sr$ relative to large-degree partial melts, due to the tendency of high Rb/Sr phases such as phlogopite to enter the melt first.

Harris *et al.* (1972) argued in favour of disequilibrium melting during basalt genesis, based on evidence of isotopic disequilibrium in mantle xenoliths carried to the surface in basic magmas. Isotopic disequilibrium in ultramafic xenoliths is very widespread (section 7.1), but such cases represent samples of the solid lithosphere. It is questionable whether these observations can be extrapolated to the higher-temperature environment of basaltic magma genesis in the convecting asthenosphere.

Hofmann and Hart (1978) examined data for the diffusion of Sr in mantle silicates in order to determine the rates at which isotopic disequilibrium could be eradicated at various temperatures. In Fig. 6.3, values of diffusivity (D) are used to calculate times for effective equilibration of a species between a sphere of diameter 1 cm and an infinite reservoir such as a slowly moving melt. These times are roughly those taken for diffusion over a 'characteristic transport distance' of 0.25 cm, using the equation $X = (Dt)^{1/2}$.

Using the lower of the measured diffusivities, it would take millions of years to eradicate Sr isotope heterogeneity between large grains of phlogopite and clinopyroxene (cpx) in solid lithospheric mantle at, say, 600 °C. Even in a solid mantle at 1000 °C, equilibration could take millions of years if the phlogopite and clinopyroxene grains were separated by intervening olivine or orthopyroxene, which effectively contain no Sr but lengthen the diffusion pathways between phlogopite and cpx. However, as soon as a melt is present, the surface of each crystal is in diffusional contact with nearby (about 2 cm distant) grains over a period of a few years. Therefore isotopic disequilibrium between phlogopite and cpx could be eradicated in a few thousand years at temperatures above the basalt solidus (about 1000–1200 °C). Nevertheless, diffusion over long distances, even in a partially molten mantle, is still slow.

Hofmann and Hart (1978) concluded that the evidence favoured 'local equilibrium in a partially molten mantle, local disequilibrium in a completely crystalline mantle, and regional disequilibrium in any mantle that

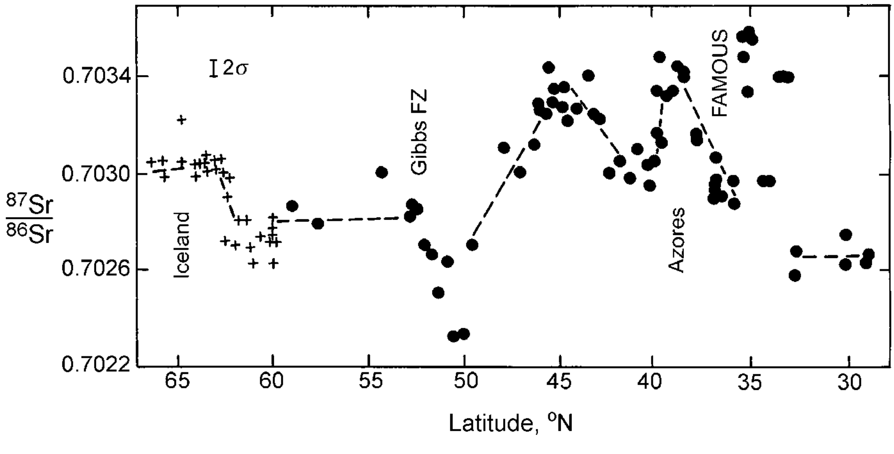

Fig. 6.4. Plot of Sr isotope ratio against latitude for basalts from the Mid-Atlantic Ridge: (+) = Iceland–Reykjanes ridge. Age correction of isotope data is unnecessary, due to the low Rb/Sr ratios and young ages of analysed material. After White *et al.* (1976).

convects only slowly in large convection cells'. This suggests that disequilibrium melting does not preferentially sample isotopic mantle heterogeneity at the mineralogical scale. However, it might well sample heterogeneity between different petrological source types, even if these are streaked out by convection into thin bands (see below).

6.1.3 Mantle plumes

Following the acceptance of the plate-tectonic model, it was realised that the tectonic setting of basic volcanism was a crucial factor in determining the nature of the mantle source being tapped, and consequent magma chemistry. Morgan (1971) proposed that the different chemistries of MORB and OIB could be explained if the former were derived directly from the asthenospheric upper mantle, whereas the latter were generated by upwelling plumes from the lower mantle. Evidence in support of this model was provided by elemental analysis of Icelandic basalts (Schilling, 1973). These data suggested a region of mixing between plume (OIB source) and depleted upper mantle (MORB source) on the Reykjanes Ridge south of Iceland. Sr isotope data for the Reykjanes Ridge (Hart *et al.*, 1973) were slightly more equivocal, since they showed a step-like feature in the data (Fig. 6.4). Hart *et al.* interpreted the data as a mixing phenomenon, but some workers (e.g. Flower *et al.*, 1975) interpreted this step as resulting from disequilibrium melting of a mantle with variable phlogopite contents.

White *et al.* (1976; 1979) extended the Sr isotope data set by analysing dredged samples from the axial valley of the Mid-Atlantic Ridge (MAR) between 29 and 63 °N and by sampling across the Azores platform. Isotopic data are plotted against latitude down the MAR in Fig. 6.4, and against longitude across the Azores Plateau in Fig. 6.5. There are large variations in the strontium isotope ratio of MORB samples along the MAR, but where MORB and OIB are erupted alongside each other (the Azores Plateau), they have very similar isotope ratios (with the exception of São Miguel). Because tholeiitic (MORB) and alkaline (OIB) magmas are attributed to different degrees

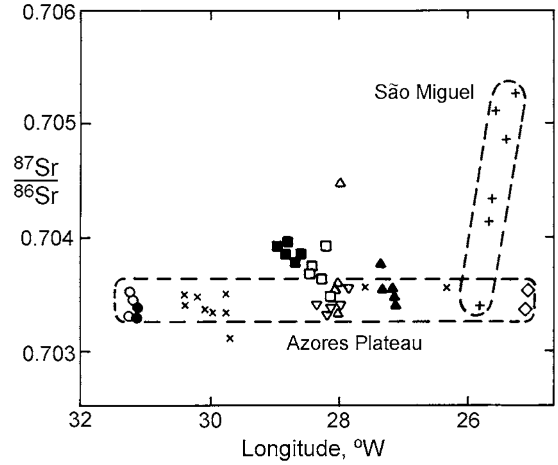

Fig. 6.5. Plot of strontium isotope ratio against longitude for basalt samples from the Azores Plateau: (×) = dredged basalts. Other symbols represent individual islands. After White *et al.* (1979).

of mantle melting, the overlap of their compositions across the Azores Plateau is evidence against sampling of isotopic heterogeneities on a mineralogical scale.

The plume–asthenosphere mixing model for the Reykjanes Ridge was strongly confirmed by Pb isotope analysis (Sun *et al.*, 1975), which revealed a smooth compositional variation down the ridge (Fig. 6.6a). In contrast, Pb isotope analysis of basalts from the Kolbeinsey Ridge, north of Iceland, did not reveal any contamination of this ridge segment with plume material (Mertz *et al.*, 1991). These differences in mixing style north and south of Iceland can be attributed to asymmetrical distortion of the plume by a regional southerly flow of asthenospheric mantle (Fig. 6.6b). Non-uniform Pb isotope contamination of ridge segments has also been observed in the South Atlantic, caused by the off-axis St Helena plume (Hanan *et al.*, 1986).

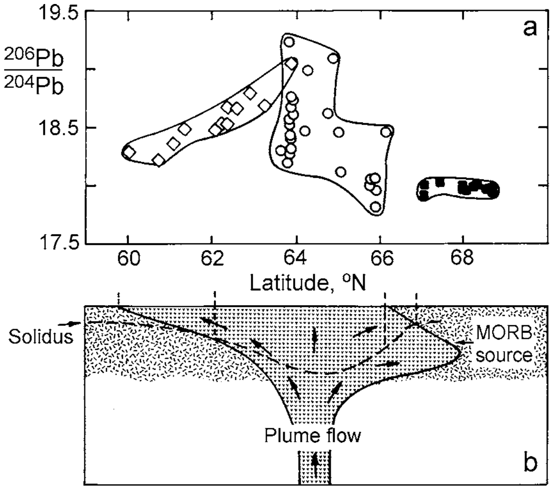

Fig. 6.6. Interpretation of isotopic data for the Iceland plume: (a) compilation of Pb data from Iceland (○), Reykjanes ridge (◇) and Kolbeinsey ridge (■); and (b) model cross-section of the upper mantle. After Mertz *et al.* (1991).

6.1.4 Plum-pudding mantle

Many workers have questioned whether there might be an intermediate scale of mantle heterogeneity between rare large plumes and mineralogical disequilibrium. Even in their early elemental studies of the Faeroes 'plume', Schilling and Noe-Nygaard (1974) recognised that this structure need not be a continuous column, but could have the form of a train of 'blobs'. Later workers (e.g. Allègre *et al.*, 1980) developed the idea that trains of blobs need not simply pass in streams from a (hypothetical) lower-mantle reservoir through the asthenosphere, but could be part of the convecting asthenosphere itself. Allègre identified three alternative models for 'blob heterogeneity' of the asthenosphere (Fig. 6.7).

In an analysis of basaltic glasses from the ocean basins, Cohen and O'Nions (1982) showed that the (comparatively) very large ranges of Pb isotope variation seen in Atlantic MORB were not equalled on the East Pacific Rise. Rather than attributing these differences to a smaller degree of mantle heterogeneity beneath the Pacific, Cohen and O'Nions argued that approximately equal degrees of heterogeneity in the Atlantic and Pacific upper mantle were homogenised in the large magma chamber associated with its fast-spreading ridge. Support for this model came from the observation by Zindler *et al.* (1984) that seamounts near the East Pacific Rise exhibited much more variation than did the adjacent ridge.

Batiza (1984) confirmed the inverse effect of ridge spreading rate on isotopic heterogeneity by plotting total ranges of $^{87}Sr/^{86}Sr$ ratio (Δ) for various mid-ocean ridges against their spreading rates (Fig. 6.8). He attributed the small range of compositions on the fast-spreading ridges to homogenisation, during the melting process, of a mantle that was 'ubiquitously heterogeneous on a small scale'. Low isotopic variation on some slow-spreading ridges (e.g. Juan de Fuca) was attributed to either their short length or limited sampling. Batiza adopted the more gastronomically elegant term of 'plum-pudding' mantle to describe this blob-bearing

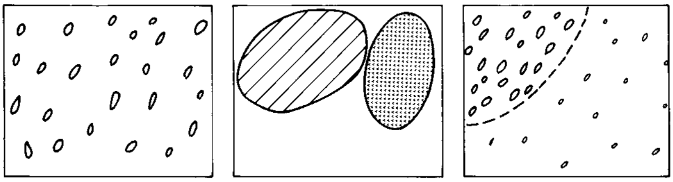
Model a Model b Model c

Fig. 6.7. Hypothetical scales of mantle heterogeneity: (a) small scale; (b) large scale; and (c) large and small scale. After Allègre *et al.* (1980).

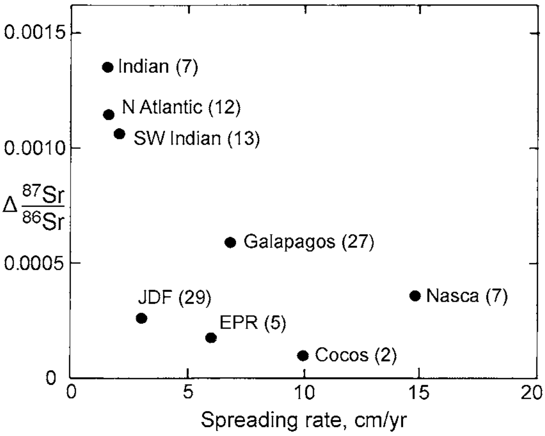

Fig. 6.8. Total ranges of Sr isotope ratio (△) for MORB glasses or leached whole-rocks from a given ridge, plotted against spreading rate on that ridge (JDF = Juan de Fuca; EPR = East Pacific Rise). Figures in brackets indicate numbers of analyses. After Batiza (1984).

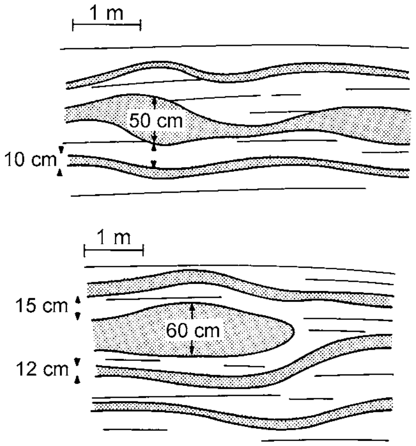

Fig. 6.9. Schematic illustration of 'marble-cake' mantle consisting of pyroxenite (shaded) and lherzolite layers in the Beni Bousera peridotite of Morocco. After Allègre and Turcotte (1986).

asthenosphere. Allègre *et al.* (1984) also found an inverse correlation between ridge spreading rate and isotopic variation, but argued that homogenisation must be primarily by (solid-state) mantle convection rather than magma mixing.

In order to express the idea that plume and plum-pudding models should not be thought of as mutually exclusive, but rather as a continuum of phenomena, Sun (1985) coined the term 'plume-pudding' mantle (*sic*). Plums and plumes might originate from a variety of phenomena. However, this question cannot effectively be answered by the application of single isotopic systems, and will be discussed below on the basis of co-variations in multiple isotopic systems.

6.1.5 Marble-cake mantle

Fluid-dynamic modelling of the convecting asthenosphere (e.g. Richter and Ribe, 1979; McKenzie, 1979) has suggested that discrete structures in the mantle (e.g. blobs, plums, etc.) cannot remain undeformed for long periods in the convecting asthenosphere. They will tend to be elongated and sheared until they are eventually physically homogenised with the depleted reservoir. Polvé and Allègre (1980) argued that evidence of this process was provided in orogenic lherzolites (Fig. 6.9), which contain alternating bands of (depleted) lherzolite and (enriched) pyroxenite. They suggested that this banding might have been generated by convective 'stirring' and stretching of a two-part sandwich of oceanic crust and underlying residual lherzolite, which is recycled back into the mantle by subduction. Allègre and Turcotte (1986) coined the term 'marble-cake' mantle to describe this concept, and argued that it is representative of the structure of much of the upper mantle.

Prinzhofer *et al.* (1989) argued that random mixing between partial melts of pyroxenite and peridotite in a marble-cake mantle could generate the large ranges of incompatible element concentrations and the moderate range of radiogenic isotope ratios seen in lavas from a small (40 km × 10 km) area of the East Pacific Rise. However, mixing in the magma chamber is not capable of explaining the length dependence of large-scale isotopic anomalies on ridges (Kenyon, 1990). For example, the isotopic 'texture' of the South Atlantic Ridge requires convective homogenisation over distances of up to 1000 km (Fig. 6.10). This is too large for a magma chamber, since it is more than the length of ridge segments between transform faults. Hence it follows that homogenisation must occur at a deeper level, either by solid-state convection of the marble-cake mantle, or during ascent of magma from the zone of partial melting under the ridge (e.g. section 13.3).

6.2 The Nd–Sr isotope diagram

In the mid 1970s, studies of the origins of mantle heterogeneity were revolutionised by the application of Nd isotope analysis to young volcanic rocks (DePaolo and Wasserburg, 1976; Richard *et al.*, 1976). DePaolo and Wasserburg plotted ^{143}Nd/^{144}Nd isotope ratios, in the form of ε Nd (section 4.2), against ^{87}Sr/^{86}Sr

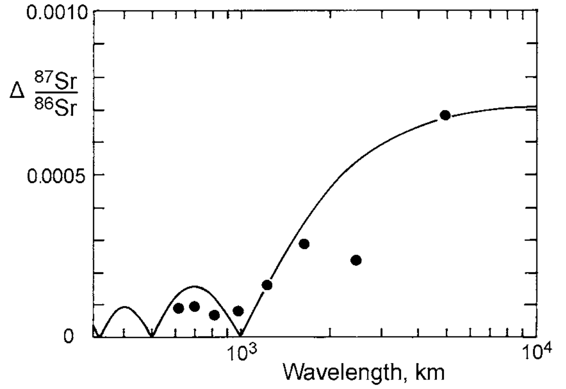

Fig. 6.10. Curve-fit for mixing of isotopic heterogeneity, compared with empirical data for amplitude *versus* wavelength of Sr isotope variation on the South Atlantic Ridge. After Kenyon (1990).

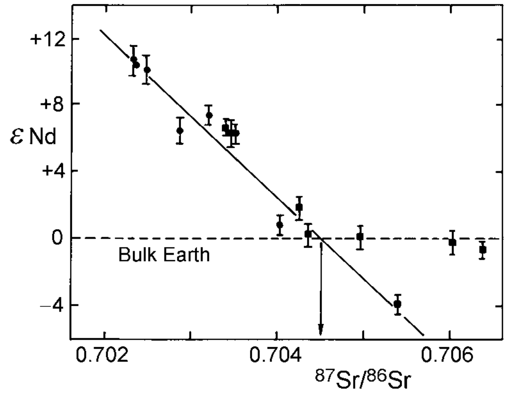

Fig. 6.11. Plot of ε Nd against Sr isotope ratio for ocean-floor, ocean-island and continental basalts analysed before 1976. The arrow shows estimated Bulk Earth strontium. After DePaolo and Wasserburg (1976).

ratios, and found a negative correlation between them in oceanic and some continental igneous rocks (Fig. 6.11). They suggested that the formation of magma *sources* in the mantle involved the coupled fractionation of Sm–Nd and Rb–Sr, whereas some continental samples (which lay to the right of the main correlation line) could have been contaminated by radiogenic Sr in the crust.

On the basis that the 'Bulk Earth' has a chondritic Sm/Nd ratio (section 4.2), DePaolo and Wasserburg used the intersection of the chondritic (zero) ε Nd line with the mantle Nd–Sr correlation line to calculate an unfractionated mantle (i.e. Bulk Earth) ^{87}Sr/^{86}Sr ratio of 0.7045 (Fig. 6.11). By using the initial ^{87}Sr/^{86}Sr ratio of the solar nebula (0.699), calculated from the 'basaltic achondrite best initial' (BABI, section 3.2.4), and the present-day value from Fig. 6.11, they deduced an Rb/Sr ratio for the unfractionated mantle (now referred to as the Bulk Silicate Earth) of 0.029.

O'Nions *et al.* (1977) extended the ^{143}Nd/^{144}Nd *versus* ^{87}Sr/^{86}Sr correlation line in oceanic volcanics by analysing a larger suite of OIB. This included two samples from Tristan da Cunha with ^{143}Nd/^{144}Nd ratios lower than the Bulk Earth, indicative of a mantle source which is slightly enriched in LREE relative to Bulk Earth. O'Nions *et al.* argued that enrichment of some mantle sources in Nd/Sm and Rb/Sr (and depletion of others such as MORB) could be explained by trace-element partition between the melt phase and residual mantle during partial melting. In view of the long half-lives of Rb and Sm, they concluded that these heterogeneities had existed for long periods of time.

6.2.1 Box models for MORB sources

The observed depleted nature of the MORB source relative to Bulk Earth has very important implications for the evolution of the mantle, and is attributed to the extraction of the continental crust from the mantle. This was first modelled by Jacobsen and Wasserburg (1979) and O'Nions *et al.* (1979), using calculations commonly termed 'box models'.

In a box model, the Earth is divided into chemical reservoirs, which may exchange matter, grow, shrink, etc., and whose evolution is modelled over the Earth's 4.5 Byr history. Typical reservoirs or 'boxes' are the crust, mantle and core, although these may be subdivided, e.g. into upper and lower mantle. The Earth's evolution is portrayed in some alternative box models in Fig. 6.12, which will be briefly discussed.

O'Nions *et al.* (1979) examined two models of mantle differentiation and crustal growth (1a and 1b in Fig. 6.12). These were based on the numerical solution of upward and downward transport coefficients for several elements in 90 steps, each corresponding to 50 Myr of the Earth's history. The model was constrained by boundary conditions in the form of the composition of the primitive chondritic mantle 4.55 Byr ago and the estimated composition of the outermost 50 km of the Earth (including the continental and oceanic crust) at the present day. In Fig. 6.13 the results for ^{87}Sr/^{86}Sr evolution are shown for cases in which (a) the whole mantle is depleted by the extraction of the upper 50-km layer; and (b) only the upper half of the mantle

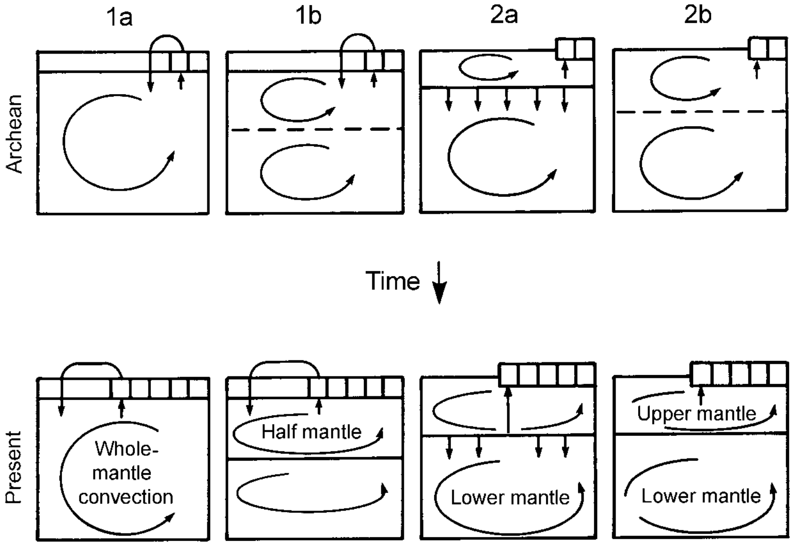

Fig. 6.12. Box models for the geochemical evolution of the mantle. Models 1a and 1b correspond to whole- or half-mantle depletion due to the extraction of continental crust. Models 2a and 2b show alternative types of mantle evolution: progressive growth of a constantly depleted mantle or progressive depletion of a constant-volume mantle.

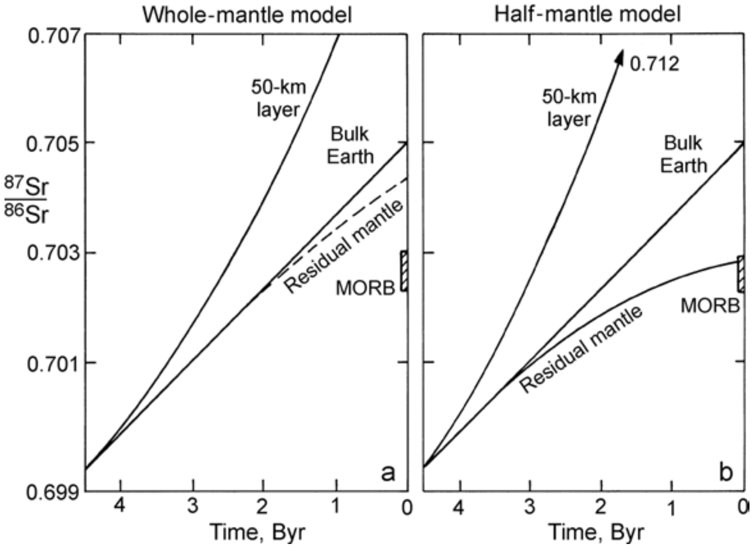

Fig. 6.13. Plots of Sr isotope evolution against time to compare the effects of (a) whole-mantle and (b) half-mantle convection on the degree of depletion predicted for the residual (MORB) reservoir. The hatched area is the present-day composition of MORB. After O'Nions *et al.* (1979).

is depleted. (These scenarios correspond to models 1a and 1b in Fig. 6.12.) Model (b) is found to yield a much better approximation to the present ^{87}Sr/^{86}Sr ratio of the depleted (MORB) source.

Jacobsen and Wasserburg (1979) used box models to examine another aspect of global differentiation (2a and 2b in Fig. 6.12). They simplified their treatment by considering only unidirectional transport of species from the mantle to generate the crust continuously over geological time, and solved the transport equations algebraically. In model 2a (Fig. 6.12) melts are extracted from the primitive mantle and generate the continental crust and a depleted mantle, both of whose *volumes* grow over geological time. However, the elemental *composition* of the depleted mantle remains constant through time. Mass-balance calculations based on Sm–Nd data led Jacobsen and Wasserburg to calculate that only 33% of the mantle need be depleted to generate the continental crust, corresponding to the formation of a depleted MORB reservoir occupying approximately the upper 650 km of the mantle.

In Jacobsen and Wasserburg's second model (2b in Fig. 6.12), the crust is extracted from a fixed *volume* of mantle, which therefore becomes more and more depleted through geological time. The mass of this depleted mantle needed to generate the crust was calculated as only 25% of the total. In this model the isotopic composition of new continental crust will reflect a derivation from depleted mantle, whereas in model 2a new continental crust will have a chondritic (primitive-mantle) isotopic signature. On the basis of Nd isotope data available to them at the time (section 4.2.1), Jacobsen and Wasserburg preferred model 2a. However, more recent Nd isotope evidence (section 4.2.2) strongly favours model 2b. The different estimates of O'Nions *et al.* (1979) and Jacobsen and Wasserburg (1979) for the volume of the depleted mantle reflect the uncertainties involved in estimating the trace-element and isotopic composition of the crust.

DePaolo (1980) studied a model similar to 2b, but with the possibility of crustal recycling into the mantle, and again concluded that only 25%–50% of the mantle need be depleted to generate the continental crust. It appears that modest amounts of crustal recycling have relatively little effect on mantle Nd–Sr isotope systematics, but a large effect on Pb (section 5.4.3).

The box-model approach has been used in numerous more recent papers, e.g. Allègre *et al.* (1983). These authors used the so-called 'total inversion method' to attempt to choose between different models, but the uncertainties in the data did not allow significant extra information to be gained. In fact, more recent work (see below and also section 4.4.3) has suggested that the subduction of oceanic crust and sea-floor sediments may have created an enriched reservoir in the lower mantle as important as continental crust. This suggests that the above modelling has probably under-estimated the size of the depleted reservoir at the present day, which may actually comprise more than 50% of the volume of the whole mantle.

6.2.2 The mantle array and OIB sources

The Nd–Sr isotope correlation in oceanic rocks was first referred to as the 'mantle array' by DePaolo and Wasserburg (1979). They attributed the OIB which form most of this array to a chondritic lower-mantle source contaminated by mixing with melts from the depleted MORB source during ascent. Indeed, much of the early discussion about the Nd isotope systematics of OIB attempted to explain their composition in terms of the two major reservoirs discussed above, namely Bulk Earth and depleted mantle. Little attention was given to the problem of generating enriched oceanic mantle, since Tristan da Cunha was regarded as more or less representing a primitive-mantle composition similar to the Bulk Earth (Allègre *et al.*, 1979; O'Nions *et al.*, 1980).

Kamber and Collerson (1999) recently 'rediscovered' and attempted to revive this model for OIB sources involving simple mixing between a primordial Bulk Earth reservoir and the MORB source mantle. This proposal was based largely on recent Pb isotope evolution models discussed in section 5.4.3. However, Kamber and Collerson also claimed that there was "growing geophysical and geochemical evidence in support of this original 'standard' model". Nevertheless, the present author is in complete disagreement with this claim, believing that a simplistic model of this type is not consistent with the geophysical and geochemical evidence reviewed below.

The first persuasive evidence against simple mixing between Bulk Earth and MORB source mantle was provided by the extension of the mantle array into the 'enriched' lower-right quadrant of the Nd–Sr isotope diagram. This was convincingly demonstrated in a study of the Kerguelen Islands (Dosso and Murthy, 1980), shown in Fig. 6.14. More recent work has shown that part of the Kerguelen Plateau is underlain by a fragment of continental lithosphere, which has imparted enriched isotopic signatures to the magmas which erupted through it (section 6.3.2). However, the lavas of the Kerguelen Islands themselves are not affected by this phenomenon, and are still attributed by most workers to an enriched source in the deep mantle (e.g. Neal *et al.*, 2002; Mattielli *et al.*, 2002).

Another enriched mantle source was revealed by alkali basalts from São Miguel in the Azores (Hawkesworth *et al.,* 1979a). However, in this case the data trended towards enriched ^{87}Sr/^{86}Sr compositions lying to the right of the mantle array. The São Miguel trend was subsequently extended by data from Samoa and the Society Islands (White and Hofmann, 1982), breaking the simple Nd–Sr isotope correlation in OIB

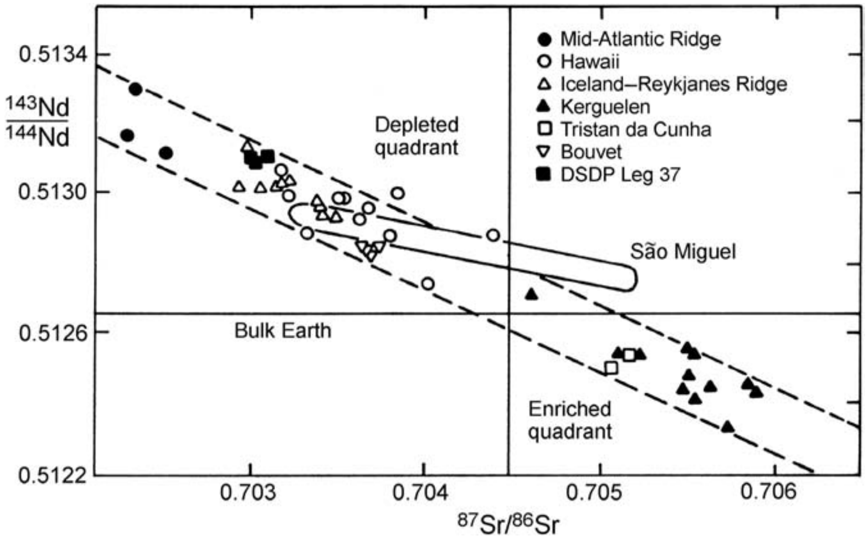

Fig. 6.14. Plot of Nd *versus* Sr isotope compositions for oceanic volcanics, showing extension of the 'mantle array' into the 'enriched' quadrant relative to Bulk Earth, based on Kerguelen data (▲), and the extension of São Miguel data into the upper-right quadrant. Modified from Dosso and Murthy (1980).

into a 'mantle disarray' (White, 1981). Further disarray is caused by the existence of other ocean islands with compositions to the left of the mantle array, such as St Helena (White and Hofmann, 1982).

Hawkesworth *et al.* (1979a) discovered an additional problem when they compared isotopic and trace-element data in OIB samples. Iceland, Hawaii and São Miguel basalts plot in the upper-left quadrant of the Nd–Sr isotope diagram, together with MORB (Fig. 6.14), indicating derivation from a source with a time-integrated depletion in light REE relative to Bulk Earth for all of these samples, and depletion in Rb (relative to Sr) for most. However, when trace-element abundance ratios in these samples are examined (Fig. 6.15), only MORB samples plot completely in the depleted quadrant relative to Bulk Earth. Iceland reaches into the LREE-enriched (i.e. low-Sm/Nd) quadrant, while some Hawaiian samples also reach into the Rb/Sr-enriched quadrant, and all São Miguel samples plot in the LREE- and Rb/Sr-enriched quadrant.

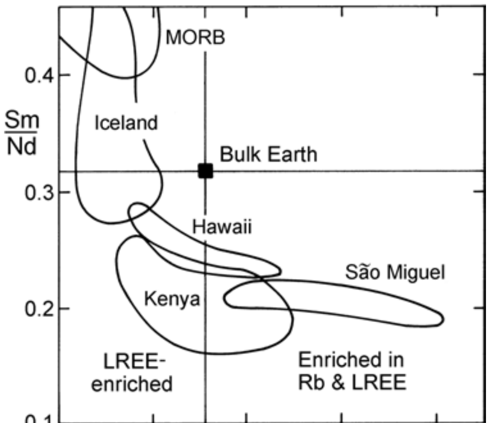

Fig. 6.15. Plot of Sm/Nd *versus* Rb/Sr elemental ratios for basic volcanic suites relative to the calculated ratios for Bulk Earth. After Norry and Fitton (1983).

Hawkesworth *et al.* examined several possible ways of generating the isotopic and trace-element features of the Azores data. They ruled out interaction with seawater because this would displace points horizontally to the right on the Nd–Sr isotope diagram (section 6.6). They recognised that ocean-floor sediments have suitable Nd and Sr isotope compositions to generate the São Miguel array by contamination, but they ruled out this model for two reasons. Firstly, a 1-km-deep hole drilled into the pillow lavas which build the island did not encounter any sediments. Secondly, the primitive chemistry of the basalts shows no sign of crustal contamination. Hence, by a process of elimination, Hawkesworth *et al.* attributed the isotopic signatures to the mantle sources of the basalts.

One model that can explain both the isotopic and the trace-element characteristics of the Azores data is mantle metasomatism. Hawkesworth *et al.* suggested that this caused LIL-element enrichment of the source a few tens of millions of years before generation of the Azores magmas. This can explain how a mantle source with a long-term depletion in LREE relative to Bulk Earth (as indicated by Nd isotope compositions, Fig. 6.14) can nevertheless be enriched in LIL trace elements (Fig. 6.15). If the source was only recently enriched in LREE, there would be insufficient time to affect its Nd isotope signature. On the other hand, if the metasomatising fluids came from a region with long-term Rb/Sr enrichment relative to Bulk Earth, they would also carry a radiogenic Sr isotope signature, which they could impart to the melting region of the São Miguel basalts.

In subsequent work, Hawkesworth *et al.* (1984) argued that mantle metasomatism could have widely affected the sources both of continental and of ocean-island basalts. This was a controversial proposal, and caused much debate at the time. Recent work (Widom *et al.*, 1997) has supported the metasomatism model for the mantle source of São Miguel, but has also indicated that this represents a delaminated fragment of African continental lithosphere, and is therefore not representative of OIB sources in general. Meanwhile, the paradox of deriving other LIL-enriched magmas from a source with long-term LIL depletion has been solved by new views of the nature of mantle melting. It is now proposed that very-small-degree (LIL-enriched) melts can be extracted from the mantle under conditions of low-degree partial melting (section 13.3.1). This avoids the need to invoke widespread metasomatic enrichment of mantle sources prior to magmatism.

As an alternative to the metasomatism model, Hofmann and White (1980; 1982) proposed that recycling of ancient oceanic crust into the OIB source could explain relatively enriched trace-element and isotopic compositions within the mantle array. Similarly, the deviation of Azores, Samoa and Society Islands basalts to the right of the mantle array could be explained by the addition of subducted sediment to the recycling of oceanic crust (Fig. 6.16).

In this model, subducted ocean crust was believed to descend to a density-compensation level where it was stored and reheated for 1–2 Byr before returning to the surface in a plume. Hofmann and White suggested that this was the core–mantle boundary, but Ringwood (1982) advocated the 670-km phase transition as the compensation depth at which oceanic crust resides. Seismic evidence for depression of the 670-km mantle phase boundary under subduction zones supports this model by suggesting that the descending slab may be deflected horizontally at this level (Shearer and Masters, 1992). However, other evidence suggests that the density contrast is too small to impede convective transport across this boundary and prevent slab penetration into the lower mantle (Morgan and Shearer, 1993). Furthermore, there is an increasing amount of tomographic evidence showing that some slabs sink to the bottom of the mantle (van der Hilst *et al.*, 1997) and that some plumes rise from the same place (e.g. Bijwaard and Spakman, 1999).

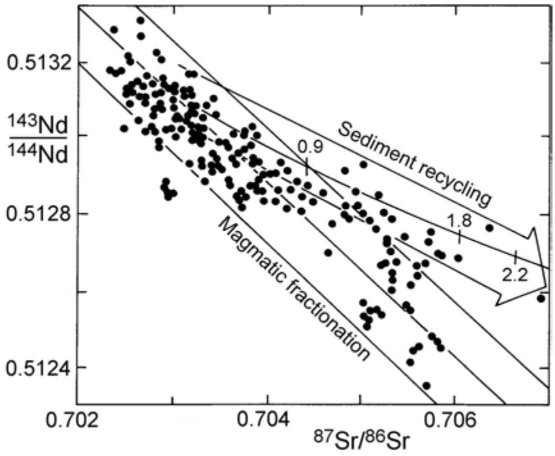

Fig. 6.16. Plot of Nd *versus* Sr isotope composition for oceanic volcanics, showing two arrays. The main mantle array is attributed to recycling of magmatically fractionated material such as oceanic crust. The shallow mixing line is attributed to recycling of sediment. After Hofmann and White (1982).

6.2.3 Mantle convection models

Over the past couple of decades, the convective structure of the mantle has been much debated, with geophysicists generally advocating a single layer of convection cells in the mantle, while geochemists have generally advocated two-layer convection. Some geochemists (e.g. Allègre, 1997) have continued to support a fairly rigid two-layer model, but there are increasing suggestions that a compromise position should be taken. This is based on new evidence that the viscosity of the mantle increases by nearly two orders of magnitude from top to bottom (e.g. Bunge *et al.*, 1996). This variable-viscosity model seems to imply a convective regime somewhere between the two extremes of single- and double-layer convection. In principle the lower mantle is part of the main convective system of the mantle, but in practice its high viscosity may isolate large bodies of it from the more rapidly convecting

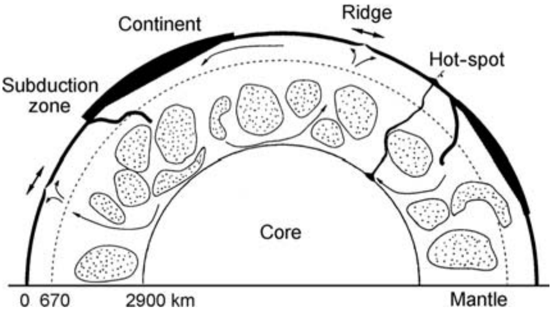

Fig. 6.17. The predicted effect of a variable-viscosity mantle, resulting in a homogeneous upper mantle and a more heterogeneous lower mantle where large 'blobs' of material can resist entrainment into the convective system. After Becker *et al.* (1999).

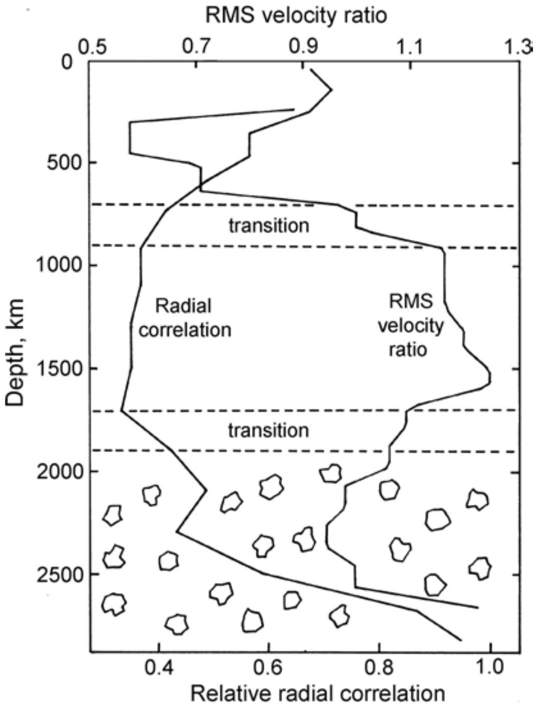

Fig. 6.18. Cross-section of the whole mantle, showing the variation of two measures of heterogeneity as a function of depth. Modified after van der Hilst and Karason (1999).

upper mantle. This style of mantle convection is illustrated by a conceptual diagram in Fig. 6.17.

In an early evaluation of variable-viscosity mantle circulation models, Manga (1996) suggested that lower-mantle blobs of high viscosity may actually aggregate together over time, unlike the convective regime in the upper mantle, which is able to streak out and homogenise heterogeneities over time. The 'blob' model of the lower mantle was also supported by Becker *et al.* (1999), who suggested that blobs of primitive mantle with a viscosity 100 times larger than that of the surrounding depleted mantle could be the *cause* of the variations of mantle viscosity with depth. However, they could not account for the origin of these blobs. The opposite view was taken by van Keken and Zhong (1999), who argued that mantle convection would efficiently mix and eradicate mantle 'blobs' so that it would not be possible for large volumes of the lower mantle to remain isolated over the lifetime of the Earth. These conflicting interpretations illustrate the limitations of theoretical modelling of mantle structure, since the models are not sufficiently well constrained to yield definitive results.

A model involving a heterogeneous lower mantle was supported by new tomographic evidence for the gross structure of the mantle (van der Hilst and Karason, 1999). Variations in seismic properties were represented by two measures of the radial (vertical) structure of the mantle (Fig. 6.18). The first (radial correlation) is a measure of the vertical continuity of structure, while the second (radial variation) is a measure of the variability of seismic velocities. These measures show that the mid mantle is relatively homogeneous, whereas the upper and lower mantle are more heterogeneous. In the upper mantle this is due to rapid phase changes with depth, and to the large temperature variations between plumes, slabs and asthenospheric mantle. In the lower mantle it is presumed to correspond to chemical heterogeneity among different domains of primordial, recycled and mixed material.

The model of van der Hilst and Karason (1999) was developed by Kellogg *et al.* (1999) to reinstate a sharper division between upper- and lower-mantle domains. The division between these domains was placed at 1600 km depth, at the top of the heterogeneous lower-mantle domain identified by van der Hilst and Karason. The main feature of the new model was a hypothetical reservoir of 'intrinsically dense' material at the bottom of the mantle, perhaps reflecting Fe enrichment. It was suggested that this material originated early in the Earth's history, perhaps from a magma ocean or by recycling of particularly mafic oceanic crust in the Archean. Subducted slabs could penetrate this material, but would normally collect on its upper surface, as illustrated in Fig. 6.19.

The greater density of the hypothetical lower layer obviously stabilises it against entrainment into the convective system of the upper mantle. Because this layer

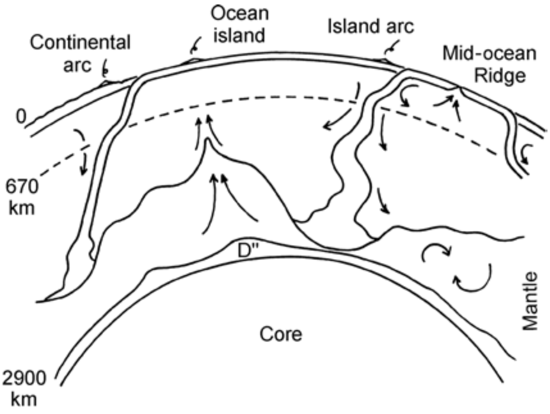

Fig. 6.19. A hypothetical mantle with 'intrinsically dense' material at its base, upon which recycled slab material would collect. After Kellogg *et al.* (1999).

is also enriched in incompatible elements relative to the upper mantle, it can supply large amounts of heat. It can also satisfy Nd isotope box models, because the large volume of enriched material at the base of the mantle compensates for the large volume of the depleted upper mantle. However, the main problem with this model is the vagueness of the nature and origin of the hypothetical 'intrinsically dense' reservoir. Until more concrete geochemical evidence is provided, this reservoir is only a convenient theoretical construct.

Forte and Mitrovica (2001) made a more quantitative evaluation of mantle structure by using global geophysical data to constrain convective-flow models. The data included global-scale free-air gravity anomalies, observed plate motions, and dynamic topography of the core–mantle boundary and the Earth's surface (in response to convective flow). Forte and Mitrovica were able to use these data to constrain convective flow in the mantle and thereby predict the depth dependence of mantle viscosity. The result was a surprising stratification of mantle viscosity (Fig. 6.20), with two zones of very high viscosity at depths of about 1000 and 2000 km . These results appear to support a 'megablob' model of the lower mantle by suggesting that some very viscous domains are present in the lower half of the mantle, some of which may represent primordial mantle. In addition, it is possible that the viscosity peak at 1000 km depth represents subducted 'megaliths' as suggested by Ringwood (1982). No doubt these new geophysical constraints will be further refined. However, they appear at present to leave plenty of room for the long-term preservation of primordial and recycled mantle domains, as implied by geochemical evidence.

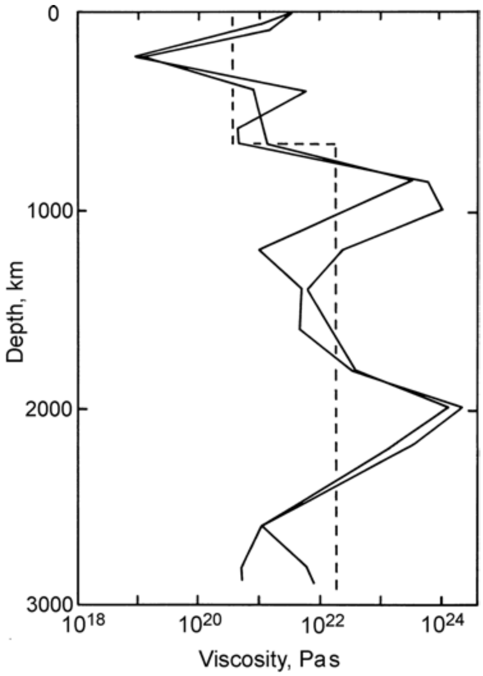

Fig. 6.20. Predicted variation of mantle viscosity with depth, based on geophysical constraints on two different mantle convective-flow models. The dashed line shows the average viscosity of upper and lower mantle. After Forte and Mitrovica (2001).

6.3 Pb isotope geochemistry

Pb isotopes are a powerful tool in studies of mantle and crustal evolution because the three different radiogenic isotopes are generated from parents with a wide span of half-lives, two of which are isotopes of the same element. By using the different isotopes in conjunction, it is possible not only to identify the nature of differentiation events, but also to place constraints on their timing.

Early inferences about the Pb isotopic evolution of the mantle were based on the analysis of galenas. These continue to give important information about Archean Pb isotope evolution. However, younger galena ores are plagued by the complex evolutionary history implied by the formation of ore deposits, involving both mantle and crustal residence times. As analytical methods improved, it became possible to analyse mantle-derived samples such as basic magmas. These have much lower lead contents, but usually a much simpler history, allowing inferences about the mantle source to be made with greater confidence.

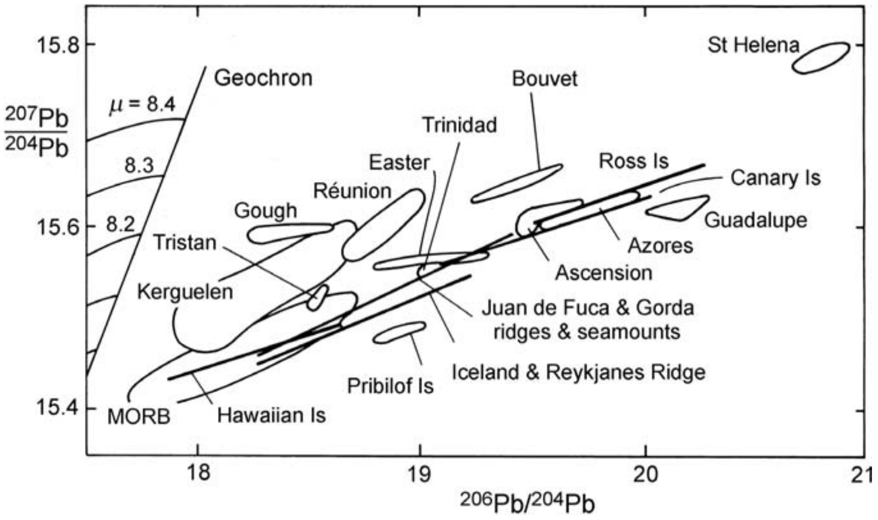

Fig. 6.21. Pb–Pb 'isochron' diagram showing linear arrays of data defined by ocean-island basalts. After Sun (1980).

6.3.1 Pb–Pb isochrons and the lead paradox

Ocean-island-basalt (OIB) leads were found by several workers (e.g. Gast *et al.*, 1964; Tatsumoto, 1966; Sun *et al.*, 1975; Tatsumoto, 1978) to define a series of arrays to the right of the geochron on the Pb–Pb 'isochron' diagram (Fig. 6.21). The slopes of these OIB arrays correspond to apparent ages of between 1 and 2.5 Byr, and can be interpreted in three principal ways: as the products of two-component mixing processes; as resulting from discrete mantle-differentiation events; or as resulting from continuous evolution of reservoirs with changing μ values. Each of these models may be applicable to different magmatic suites.

The mixing model was championed by Sun *et al.* (1975), who showed that the array of Pb isotope compositions in Reykjanes Ridge basalts was best explained by two-component mixing of 'plume' and 'low-velocity-zone' (upper-mantle) components under Iceland. They suggested that the linear Pb isotope arrays generated by several other ocean islands might be explained by the same mechanism. However, since these arrays have different slopes, a mixing model can work only if each array is attributed to mixing of the MORB reservoir with a different enriched source (Sun, 1980). Therefore, the problem of explaining the origin of these radiogenic sources still remains.

The differentiation model was studied by Chase (1981), who evaluated OIB data in terms of a two-stage Pb isotope evolution model. This allowed ^{238}U/^{204}Pb ratios to be calculated for an 'original' mantle reservoir (μ_1) and for the secondary sources (μ_2) which yield OIB Pb–Pb arrays. Chase found that values for μ_2 are variable within each island group and between groups, but the calculated μ_1 value was remarkably constant (7.84–7.96) for all of the data (Fig. 6.22). He therefore concluded that ocean islands were derived from

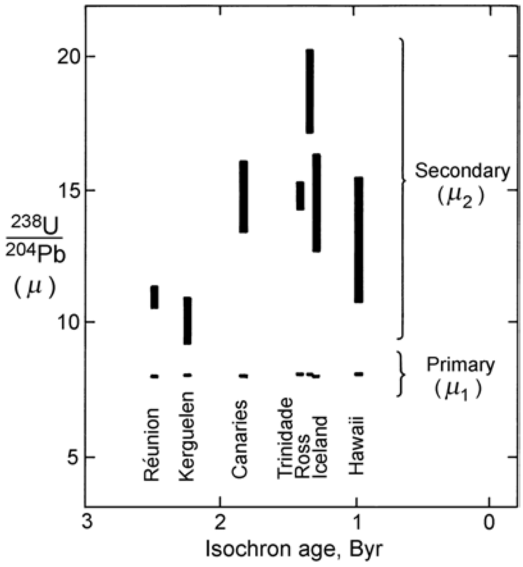

Fig. 6.22. Range of μ values required to explain OIB sources using a two-stage Pb evolution model. Parental mantle (μ_1) undergoes differentiation events at different times to yield discrete OIB source domains (μ_2). After Chase (1981).

separate OIB sources of variable age, but that these in turn were derived from a single long-lived primary reservoir.

The model of continuous mantle evolution with a changing μ value was adopted by Dupré and Allègre (1980) to explain the Pb isotope composition of leached basalt samples dredged from the Mid-Atlantic Ridge. The data define a linear array to the right of the geochron, whose slope yields an apparent Pb–Pb isochron of 1.7 Byr age. However, this result was interpreted, not as a world-wide mantle-differentiation event, but as an average age for continuous differentiation from about 3.8 Byr ago until the present. This could have occurred by the mixing of enriched components with depleted mantle in numerous small events.

The distribution of OIB Pb–Pb arrays to the right of the geochron presents a problem in understanding Pb evolution in the Earth as a whole, since it implies that the depleted mantle has an average composition more radiogenic than the Geochron (Bulk Earth). This is the opposite of the expected behaviour, since experimental evidence (e.g. Tatsumoto, 1988) suggests that U is more incompatible than Pb, and should generate low U/Pb ratios in the depleted mantle. This problem has been termed the 'lead paradox' (Allègre *et al.*, 1980). A complementary reservoir with unradiogenic Pb must exist to balance the radiogenic depleted mantle, but this other reservoir has proved hard to locate.

In the plumbotectonics model (section 5.4.3) unradiogenic Pb was located in the lower crust. However, this model was not actually intended to solve the Pb paradox, but simply to explain the distributions of U and Pb in various crustal and mantle reservoirs. In fact the earlier versions of the model did not deal at all with the Pb paradox, while the later versions assumed a young age for the Earth to solve the paradox.

These historical caveats notwithstanding, the plumbotectonics model can go some way towards solving the Pb paradox. By retaining unradiogenic Pb in the lower crust, recycling of upper-crustal Pb can partially explain the distribution of oceanic volcanic Pb to the right of the geochron. However, the U/Pb ratios of typical ocean-floor sediment (White *et al.*, 1985) are not great enough to explain the radiogenic Pb signatures of most OIB sources.

An alternative model proposed by Vidal and Dosso (1978) and Allègre (1982) suggested that fractionation of Pb from a lower-mantle OIB reservoir into the Earth's core could increase the μ value of OIB sources so as to generate the Pb–Pb arrays to the right of the geochron. These authors proposed that, while core segregation progressed very rapidly after the Earth's accretion, and was probably almost complete after 100 Myr, it nevertheless continued at a slow rate up to about 1.5 Byr ago, preferentially incorporating Pb.

Newsome *et al.* (1986) argued that this model could be tested by examining the distributions of other elements such as Mo and W that have much higher distribution coefficients from a lithophile (mantle) to siderophile (core) phase than Pb. Hence, if late partitioning of Pb into the core is invoked to explain radiogenic OIB sources (e.g. St Helena) then these sources should be very depleted in Mo and W.

The model was tested by comparing Pb isotope data in OIB sources with Mo elemental data. However, allowance must first be made for the behaviour of Mo during solid–liquid partitioning in OIB magma genesis. This is done by comparing Mo with another element with similar bulk partition coefficients for an upper-mantle mineralogy. Experimental evidence suggests that LREE such as Pr have this behaviour. After removing upper-mantle effects by normalising against Pr, Mo abundances exhibit no correlation with radiogenic Pb isotope ratios in OIB (Fig. 6.23). This suggested that the core-fractionation model for OIB leads should be rejected. More recently, the core-fractionation model has been reinstated in order to explain the *general* distribution of terrestrial Pb isotope reservoirs to the right of the geochron (section 5.4.3). However, it now appears that even this effect is weaker than first thought.

Since core fractionation has been reduced in importance as a solution for the Pb paradox, we are forced to return to explanations involving Pb partition between the mantle and crust. Following Hofmann and White (1980) and Chase (1981), it has been widely proposed

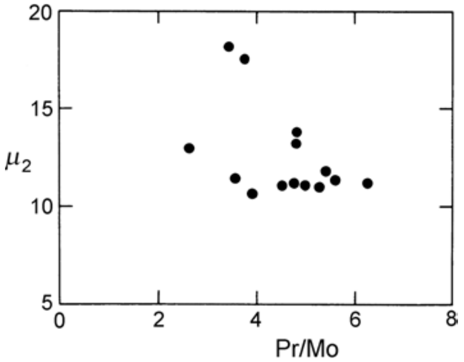

Fig. 6.23. Pb isotope data for OIB, expressed in terms of the μ_2 value of a two-stage evolution model. These exhibit no correlation with a trace-element index that measures possible fractionation of siderophile elements into the Earth's core. After Newsome *et al.* (1986).

that subducted oceanic crust can solve this paradox. U/Pb fractionation during the generation of MORB allows the creation of OIB sources with relatively high μ values, which can generate radiogenic Pb signatures after storage for 1–2 Byr. However, the U/Pb ratios of normal MORB are not high enough to explain the composition of strongly radiogenic OIB sources (termed HIMU by Zindler and Hart, 1986). Therefore, several mechanisms have been proposed to elevate the U/Pb ratios of subducted oceanic crust.

6.3.2 The development of HIMU

Seawater alteration has been invoked as one possible mechanism to elevate U/Pb ratios in oceanic crust (Michard and Albarède, 1985), but this might also elevate Rb/Sr ratios, generating more radiogenic strontium than is seen in the HIMU component. A better model (Weaver, 1991) is to invoke preferential extraction of Pb, relative to U, from the downgoing slab in subduction zones. Weaver argued that the characteristic trace-element signature necessary to generate the HIMU source could indeed be produced in the dehydration residue of subducted ocean crust, if fluids are enriched in Pb but depleted in U. This requires that uranium be held in a U^{4+} state, limiting the formation of soluble U^{6+} complexes. The model is supported by U/Pb ratios nearly an order of magnitude lower in island-arc tholeiites than in MORB (Sun, 1980). Mobilisation of Pb from the slab in a fluid phase could also explain the surprising degree of Pb isotope homogeneity in arc-related ‘conformable’ galena deposits (section 5.4.2).

This model was further developed by Chauvel *et al.* (1995), who suggested that Pb is removed from subducting oceanic crust by metasomatism and deposited in the overlying mantle wedge. It would then be incorporated into the continental crust via arc magmatism. This non-magmatic movement of Pb can account for the Pb paradox, but it can also explain the general decoupling of Pb from other isotope systems (section 6.4.1).

In order to create the most radiogenic Pb signatures with U/Pb ratios that are not unreasonably high, it is necessary for HIMU reservoirs to be isolated for 1–2.5 Byr. This is a problem, because the process of mantle convection naturally tends to streak out any heterogeneities into narrow *Schlieren* (Olsen, 1984), which would then be too small to source large volumes of enriched OIB magmas.

One way to avoid this problem is to involve the lithosphere. By definition this material is solid and non-convecting, and Nd model age dating (section 4.2.1) indicates its potentially long lifetime. Since the lithosphere is thought to be generally depleted, it would need to undergo secondary enrichment by the emplacement of LIL-rich metasomatic fluids in order to become a HIMU source. McKenzie and O’Nions (1983) suggested that sub-continental lithosphere has a greater density than the underlying Fe-depleted asthenosphere, so that over-thickening during continental collision might cause some of the lithosphere to constrict off and fall into the upper-mantle convection system. If this material were sampled within a few hundred million years then it might yield OIB magmas, before being homogenised into the MORB source by convection. The main objection to this model is simply that the magnitude of its effect is inadequate to create a major deep-mantle reservoir.

This has led most workers to return to the model of Hofmann and White (1980; 1982) and Chase (1981), who proposed that the radiogenic OIB reservoirs could be generated by subduction of U-enriched oceanic crust. The attraction of this model is the certain fact that vast amounts of this material *are* subducted back into the mantle, together with the fact that the oceanic crust is necessarily enriched in many incompatible elements relative to its depleted-mantle source. The main problem with this model is the possibility outlined above, namely that such heterogeneities would be re-homogenised into the mantle before the 1–2-Byr period necessary for high U/Pb ratios to generate radiogenic Pb isotope signatures elapsed.

Ringwood (1982) attempted to solve this problem by postulating that subducted oceanic crust and continental sediments collect in large blobs or ‘megaliths’ at the 670-km seismic discontinuity, which was also proposed by many workers as a boundary layer between upper- and lower-mantle convection. Alternatively, with the general acceptance of some form of whole-mantle convection, recent suggestions are that subducted oceanic lithosphere could form high-viscosity reservoirs resistant to convective homogenisation near the core–mantle boundary (e.g. Davies, 2002).

6.3.3 The terrestrial Th/U ratio

Over many years, the prime focus of Pb isotope analysis has been on the U–Pb system. However, the combination of ^{208}Pb and ^{206}Pb isotopes also allows constraints to be placed on the Th/U ratio or κ value of Earth reservoirs. This places new limits on models of terrestrial Pb isotope evolution that can help to constrain MORB and OIB sources. It should be noted that, in all of the following discussion, ancient Th/U values are normalised for subsequent radioactive decay and presented in terms of their 'present-day equivalent' κ value.

In order to use Pb isotope ratios to determine the Th/U ratio of a reservoir, it is necessary to know the age of the reservoir and its Pb isotope composition at the start and end of its evolution. For the Bulk Earth system the age is defined by the Geochron, and the initial ratio at time T (the age of the Earth) is given by the Canyon Diablo composition (Tatsumoto *et al.*, 1973). The Pb isotope ratio of a mantle reservoir at time t (the end of the period of mantle evolution considered) is determined from the initial Pb isotope composition of a mantle-derived magma at that time. Hence (following Allègre *et al.*, 1986), we can define the radiogenic ^{208}Pb/^{206}Pb ratio of a mantle reservoir as

$$\frac{^{208}\mathrm{Pb}^*}{^{206}\mathrm{Pb}^*} = \frac{\left(\dfrac{^{208}\mathrm{Pb}}{^{204}\mathrm{Pb}}\right)_t - \left(\dfrac{^{208}\mathrm{Pb}}{^{204}\mathrm{Pb}}\right)_T}{\left(\dfrac{^{206}\mathrm{Pb}}{^{204}\mathrm{Pb}}\right)_t - \left(\dfrac{^{206}\mathrm{Pb}}{^{204}\mathrm{Pb}}\right)_T} \qquad [6.1]$$

Given a closed system from time T to t, the Th/U ratio (κ value) of the reservoir can be calculated from the ^{208}Pb*/^{206}Pb* ratio by solving U–Th and U–Pb decay equations for T and t (chapter 5). However, we can also calculate the average or 'time-integrated' Th/U ratio of an open system from time T to t.

In the conformable Pb model (section 5.4.2), the closed-system assumption for the mantle implied a constant κ value against time, equal to the meteorite value of 3.9 ± 0.1 (Tatsumoto *et al.*, 1973). In contrast, the model of Cumming and Richards (1975) proposed a decrease in terrestrial Th/U ratio from an initial value of 4.13 to a present-day value of 3.84. This model was largely overlooked in constraining mantle Th/U evolution because of the near coincidence of κ values in Phanerozoic galenas with the meteorite value.

In a major new examination of this problem, Allègre *et al.* (1986) used initial Pb isotope ratios for Phanerozoic ophiolite complexes and Archean komatiites to calculate time-integrated Th/U ratios for the upper mantle from T (4.57 Byr ago) until the age of eruption (Fig. 6.24). They concluded that the upper mantle had higher Th/U ratios in the Archean than it has at present, and that this reservoir was progressively depleted in Th/U over time, in a similar way to its depletion in Rb/Sr and Nd relative to Sm (section 4.2.2). It follows that the κ value for the oldest rocks (about 4.3) might be expected to approximate the Bulk Silicate Earth value (i.e. before significant depletion of the upper-mantle reservoir). Similar κ values of 4.25 and 4.37 may be calculated from the Isua galenas analysed by Appel *et al.* (1978) and Frei and Rosing (2001). These data represent the oldest terrestrial galena analyses and provide strong support for the evolution curve of time-integrated κ values proposed by Allègre *et al.* (1986).

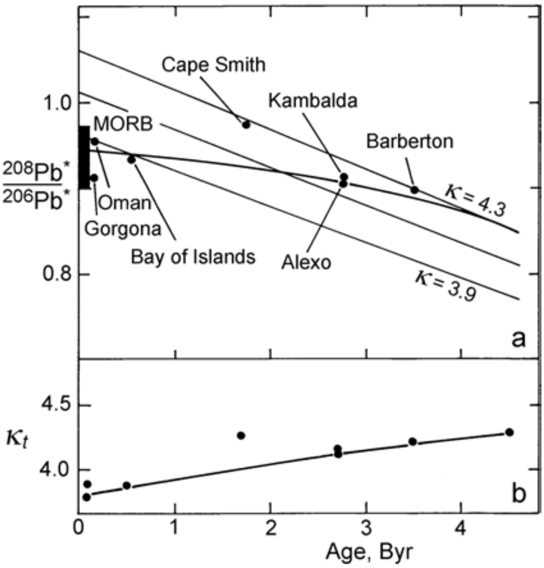

Fig. 6.24. Pb isotope evidence for time-integrated mantle Th/U ratio. (a) Radiogenic ^{208}Pb/^{206}Pb ratios for mantle-derived Pb, showing the best-fit open-system curve relative to closed-system evolution lines. (b) Calculated variations of time-integrated mantle Th/U ratio (κ_t) over the Earth's history. After Allègre *et al.* (1986).

The Bulk Silicate Earth κ value derived above was tested by an independent determination from recent oceanic volcanics (Allègre *et al.*, 1986). This is analogous to the determination of the Bulk Earth Sr isotope ratio from the Sr–Nd isotope 'mantle array'. Radiogenic ^{208}Pb*/^{206}Pb* ratios in oceanic volcanics define fairly good linear arrays when plotted against ^{143}Nd/^{144}Nd and ^{87}Sr/^{86}Sr (Fig. 6.25). The intersection of Bulk Earth Sr and Nd compositions with these correlation lines yields the Bulk Silicate Earth ^{208}Pb*/^{206}Pb* ratio, and hence time-integrated Bulk Earth κ values of 4.1–4.2. Thus, the two different approaches (old and modern leads) yield Bulk Earth κ values in good agreement, averaging 4.2. Allègre *et al.* argued that this value would also be consistent with the lower Th/U ratio of meteorites if early partition of U into the core is taken into account. The similarity between the time-integrated κ values of MORB and chondrites therefore appears to be a coincidence.

In addition to determining the time-integrated Th/U ratio of the upper mantle from Pb isotope data, we can also determine an 'instantaneous' present-day

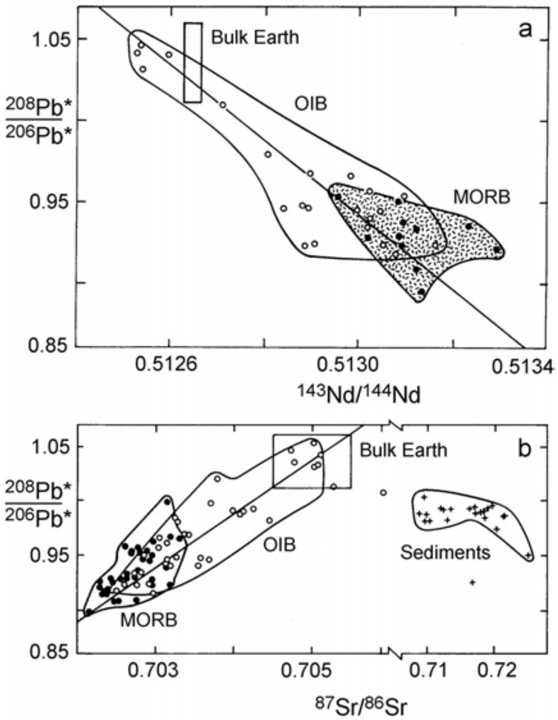

Fig. 6.25. Plots of radiogenic $^{208}Pb/^{206}Pb$ against Nd and Sr isotope ratio for modern oceanic volcanics, allowing a calculation of the time-integrated Th/U ratio of Bulk Earth: (●) = MORB; (○) = OIB. The box indicates the uncertainty of the Bulk Earth composition. After Allègre *et al.* (1986).

Th/U ratio for the mantle from oceanic volcanics. Tatsumoto (1978) estimated this value as about 2.5 in the MORB source by measuring elemental Th/U ratios in lavas. This value has been confirmed more recently by $^{232}Th/^{230}Th$ activity ratios in oceanic volcanics, which can also be used to calculate the instantaneous κ value for the mantle source (section 13.3). Compared with a Bulk Earth κ value near 4, these data indicate strong mantle depletion, which can be attributed to crustal extraction. However, this presents a problem, since the time-integrated κ value of about 3.75 in MORB is much higher than the instantaneous value, and only slightly less than the Bulk Earth value.

Galer and O'Nions (1985) solved this problem by proposing that the MORB reservoir was buffered over geological time by a less-depleted reservoir. In other words, Pb recently extracted from the MORB source only had a brief residence time in the depleted reservoir, and spent most of Earth history in a reservoir with a κ value near that of Bulk Earth. They calculated that a residence time of 600 Myr in a Th-depleted MORB reservoir with $\kappa = 2.5$ and residence for 4 Byr in a reservoir with $\kappa = 3.9$ would give the time-integrated κ value of 3.75 needed to explain MORB lead isotope compositions (Fig. 6.26). Galer and O'Nions examined three possible locations for their proposed Bulk Earth κ lead source: upper continental crust, sub-continental lithosphere and lower mantle. However, the short upper-mantle residence time for Pb calculated using their model was a severe test of the ability of all of these reservoirs to account for MORB Pb.

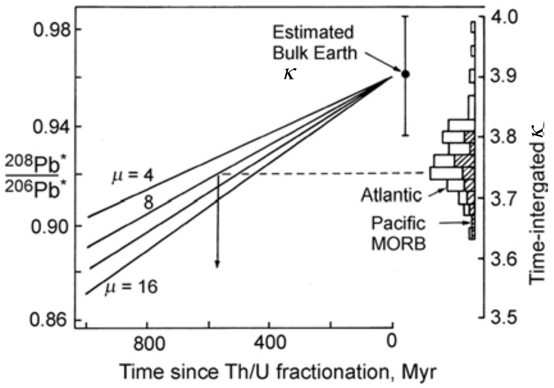

Fig. 6.26. Evolution of time-integrated κ values as a function of residence time in the MORB reservoir, starting at a value of 3.9. The histogram on the right indicates present-day compositions of Pacific (hatched) and Atlantic MORB. After Galer and O'Nions (1985).

The proposal to buffer MORB by upper-crustal Pb causes problems because the continental crust is characterized by a higher $^{207}Pb/^{204}Pb$ ratio than MORB, and due to the almost complete extinction of the ^{235}U parent of ^{207}Pb at the present day, these differences must be long-lived. On the other hand, the low Pb content and relatively small volume of sub-continental lithospheric mantle require an unreasonably rapid rate of exchange (complete exchange within 1 Byr) to buffer upper-mantle Pb. This is precluded by the old Sm–Nd model ages of inclusions in diamonds (section 4.2.1). Finally, buffering of MORB Pb by the lower mantle might be possible if the depleted upper mantle constituted only the upper 670 km, but more recent evidence for a larger volume of upper mantle makes it impossible to buffer this reservoir adequately with a Pb residence time of only 600 Myr.

These problems could be overcome by using a higher Bulk Earth κ value of 4.2, leading to an upper mantle Pb residence time of 1.8 Byr (Dickin, 1995).

An alternative approach to solving this 'kappa conundrum' (e.g. Kramers and Tolstikhin, 1997; Elliott

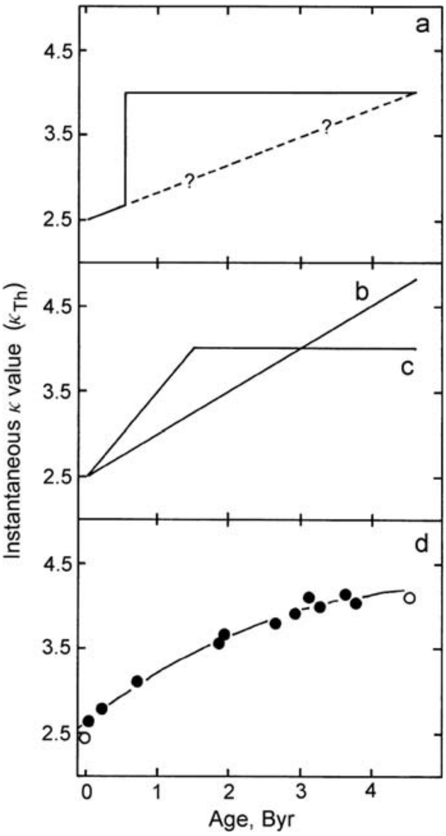

Fig. 6.27. Alternative evolution lines for the instantaneous κ value of the MORB source that can generate the observed Pb isotope distribution of MORB: (a) – (c) = model curves; (d) = average measured Th/U values. The area under each curve yields time-integrated κ (κ_t). For discussion, see the text. After Elliott *et al.* (1999) and Collerson and Kamber (1999).

et al., 1999) is to argue that the instantaneous κ value (Th/U ratio) of the MORB source upper mantle has itself evolved downwards over geological time, and that this has been the prime control on the time-integrated κ value of upper-mantle Pb. Models of this second type are compared with the model of Galer and O'Nions (1985) in Fig. 6.27. In this plot, instantaneous κ values of sources generating radiogenic Pb are plotted as a function of time, whereas the time-integrated κ value of Pb at the present day is determined by the area under the graph (Elliott *et al.*, 1999).

Of the four models shown in Fig. 6.27, (a) corresponds to that of Galer and O'Nions, in which Pb is held in a high-κ source until it enters a steady-state low-κ MORB reservoir only 600 Myr ago. Figure 6.27b shows a model in which the MORB source is not buffered by any other source, but undergoes progressive depletion though geological time due to crustal extraction. This causes a steady decrease in the upper-mantle Th/U value, whose average value determines the time-integrated κ value recorded by Pb isotope analysis. Figure 6.27c shows a model proposed by Elliott *et al.* (1999) in which the Th/U ratio of the upper mantle remains at a value of 4 until about 1.6 Byr ago, after which it decreases rapidly to the present-day value. This model is similar to a model proposed by Kramers and Tolstikhin (1997), and is based on the argument that crustal uranium would be locked up in an insoluble form in the sedimentary environment, until oxygenation of the atmosphere released this uranium into the sea, from where it could be recycled into the upper mantle. Recycling can occur by uranium enrichment of basaltic crust on the ocean floor, and subsequent release of uranium back to the mantle in subduction-related fluids (section 13.4). Finally, Fig. 6.27d shows the results of empirical analysis of elemental Th/U ratios in mafic/ultramafic rocks of various ages, averaged to reduce the scatter of individual data points. The curve is a polynomial fitted to the data, which could be explained by a combination of Th/U fractionation during melting and more recent recycling of dissolved crustal uranium.

The first three models in Fig. 6.27 all successfully yield a time-integrated κ value in the MORB source of about 3.75, but they have some problems. Model (a) proposes an upper-mantle residence for Pb that seems impossibly low in comparison with the roughly 1 Byr residence of helium, the most incompatible element (section 11.1). In addition, this model does not explain how the mantle arrived at its present day Th/U ratio. Model (b) addresses the latter point, but can only satisfy the time-integrated upper-mantle κ value by starting from a very high Th/U ratio of nearly 5. Model (c) addresses both of these problems by keeping a chondritic Th/U ratio in the MORB source until about 1.6 Byr ago, then causing a rapid decline. However, it ignores the possibility of exchange of Pb with primordial or recycled sources in the lower mantle, which could buffer upper-mantle Pb. Finally, the best-fit curve to the empirical data in Fig. 6.27d has resemblances to models (b) and (c) but the time-integrated κ value (area under the curve) is too low to support the Pb isotope composition of the MORB source (Collerson and Kamber, 1999). However, this is a good fault because it leaves room for some buffering of MORB source Pb by input from the lower mantle.

A Pb isotope model dominated by binary mixing between the MORB source and a lower-mantle Bulk Earth reservoir was proposed by Kamber and Collerson

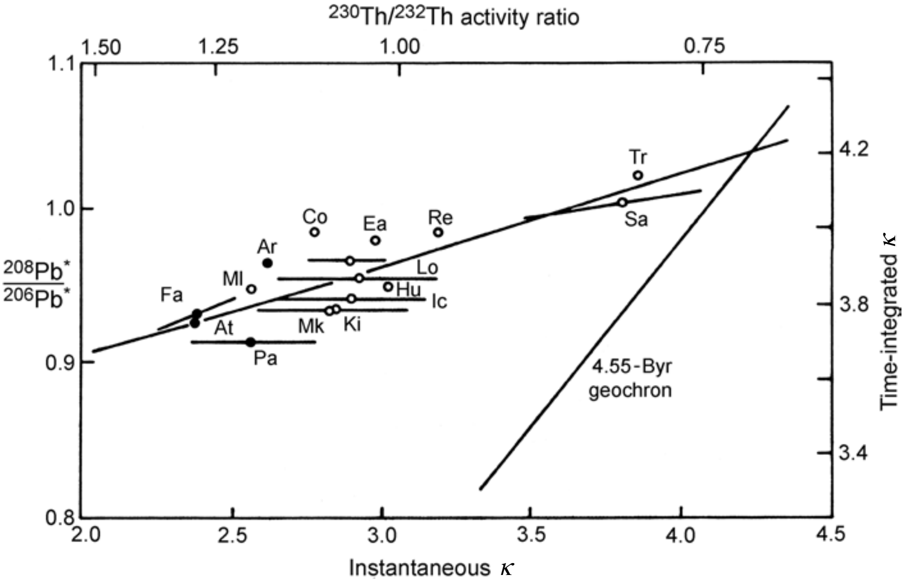

Fig. 6.28. Plot of time-integrated κ (κ_t) against instantaneous kappa (κ_p) values for oceanic volcanics: (●) = MORB; (○) = OIB. After Allègre *et al.* (1986).

(1999). However, these authors excluded the effect of any crustal recycling into the OIB reservoir, and permitted enrichment of the OIB source only in the direction of increasing μ value. In view of the clear evidence for OIB sources with Sr–Nd isotope signatures enriched relative to Bulk Earth (section 6.2.2), this model cannot be considered realistic. Nevertheless, this model can be valid if the concept of mixing between upper- and lower-mantle sources is broadened to include enriched lower-mantle sources resulting from crustal recycling. These enriched reservoirs (together with a primordial reservoir) can then buffer the κ value of the MORB source via the OIB source, allowing a Pb residence time of up to 1.8 Byr (Dickin, 1995). This possibility is demonstrated on a plot of instantaneous κ value against time-integrated κ value for oceanic volcanics (Fig. 6.28). The OIB samples define an array (interpreted as a mixing line) linking MORB compositions (solid symbols) and a Bulk Earth point with a κ value of about 4.2 (Allègre *et al.*, 1986).

6.3.4 The upper-mantle μ value re-examined

There has been much discussion about the time-integrated μ value of the mantle as revealed by Pb isotope analysis. It is now generally agreed that the *apparent* increase in μ value of the upper mantle over time may be an illusion caused by recycling of radiogenic Pb from the oceanic and continental lithosphere (sections 5.4.3 and 6.3.1). However, in order to quantify this process, it is necessary to determine the instantaneous (present-day) μ value of the upper mantle. Unfortunately, this cannot be determined directly from the U/Pb ratios of MORB glasses, since U/Pb fractionation during partial melting is poorly constrained. Neither is there any isotopic route to this quantity, as was possible for the κ value. However, White (1993) developed an indirect approach to the determination of upper mantle μ from the relationship between μ and uranium content in MORB glasses.

Analysis of U and Pb in 82 glasses from the Atlantic, Pacific and Indian oceans revealed a strong positive correlation between ^{238}U/^{204}Pb ratio and U content (Fig. 6.29). White (1993) attributed this correlation to fractionation (of uranium) during partial melting, and argued that it could be used to estimate the depleted-mantle μ value. Since U is incompatible, the U content of the Bulk Silicate Earth estimated from chondrites (0.018 ppm) must be an upper limit for U in the depleted mantle (MORB source). Applying this value to the μ *versus* U correlation line leads to a maximum instantaneous μ value of 4.5 in the MORB source (compared with a time-integrated μ value of about 8.5).

This discrepancy is exactly analogous to the kappa conundrum and, again, is due to the relatively short residence time of Pb in the upper mantle. White proposed that upper-mantle Pb is buffered by the entrainment of

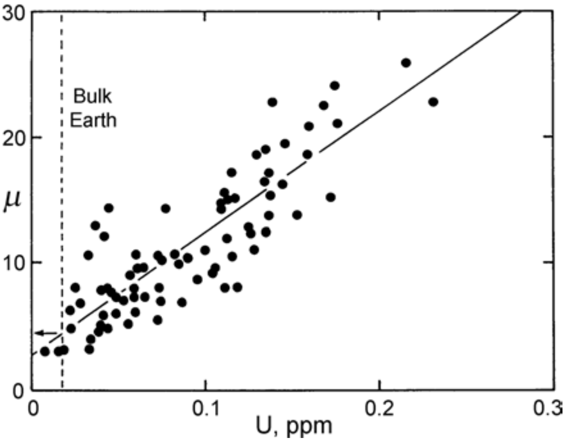

Fig. 6.29. Plot of $^{238}U/^{204}Pb$ (μ) in MORB glasses against uranium content, showing a positive correlation, from which a maximum upper-mantle μ value can be estimated. After White (1993).

radiogenic Pb from plumes. Therefore, the Pb isotope composition of the upper mantle reflects dynamic equilibrium between Pb fluxes into and out of this reservoir. In contrast, radiogenic Sr and Nd in the upper mantle are largely generated by *in situ* decay of Rb and Sm.

It is concluded that the U–Th–Pb isotope systematics of the upper mantle can be reasonably explained by recycling of various enriched sources (and a primordial source) via lower-mantle plumes. However, until such processes are incorporated into an improved 'plumbotectonics' model, a complete quantitative understanding of terrestrial U–Th–Pb systematics cannot be claimed.

6.4 Mantle reservoirs in isotopic multispace

6.4.1 The mantle plane

The unification of the *radiogenic* $^{208}Pb^*/^{206}Pb^*$ ratio with other isotope systematics (section 6.3.3) breaks down when Pb isotope ratios involving non-radiogenic Pb are plotted against other isotope systems on bivariate diagrams (e.g. Fig. 6.30). This indicates that the isotope systematics of the mantle cannot be explained by a two-component mixing model. An exception to this general observation is provided by Pb–Sr isotope systematics on the North Atlantic, which *do* define a coherent positive correlation (Dupré and Allègre, 1980). However, this can be attributed to coincidental contamination of the MORB reservoir in this area with a single compositional type of enriched plume material.

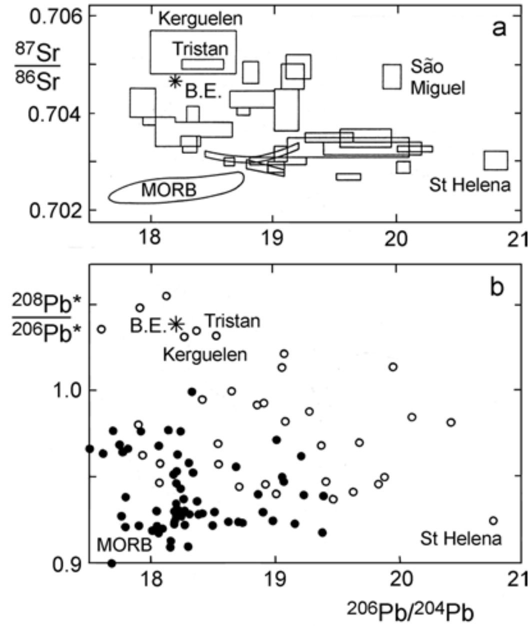

Fig. 6.30. Diagrams to show the decoupling of $^{206}Pb/^{204}Pb$ from other isotopic systems in oceanic volcanics: (a) Sr isotope data, after Sun (1980); and (b) radiogenic $^{208}Pb^*/^{206}Pb^*$ data, after Allègre *et al.* (1986). B.E. = Bulk Earth.

To explain the scatter of data on Fig. 6.30a, Zindler *et al.* (1982) argued that the Pb–Sr–Nd isotope compositions of oceanic volcanics must be caused by (solid-state?) mixing of three mantle components. The proposed end-members were a pristine chondritic mantle with a Pb composition on the geochron, a MORB source depleted by continental crustal extraction, and a reservoir containing recycled MORB. This made Kerguelen the best candidate for a primitive mantle source, while St Helena was regarded as having the greatest amount of recycled MORB material in its source. Zindler *et al.* argued that average isotopic compositions of ocean ridges and ocean islands displayed very little scatter away from a plane containing these three end-member components (Fig. 6.31).

Zindler *et al.* justified their three-component model by the high correlation coefficient of 0.98 calculated for their data set. However, such a limited scatter was achieved by excluding some ocean islands. For example, São Miguel was not included in the Azores average. However, this signature was argued by White (1985) to be part of a much wider compositional field, including data from the Society Islands, Samoa and the Marquesas which extend 'above' the 'mantle plane' of Zindler *et al.* (1982). Furthermore, the averaging

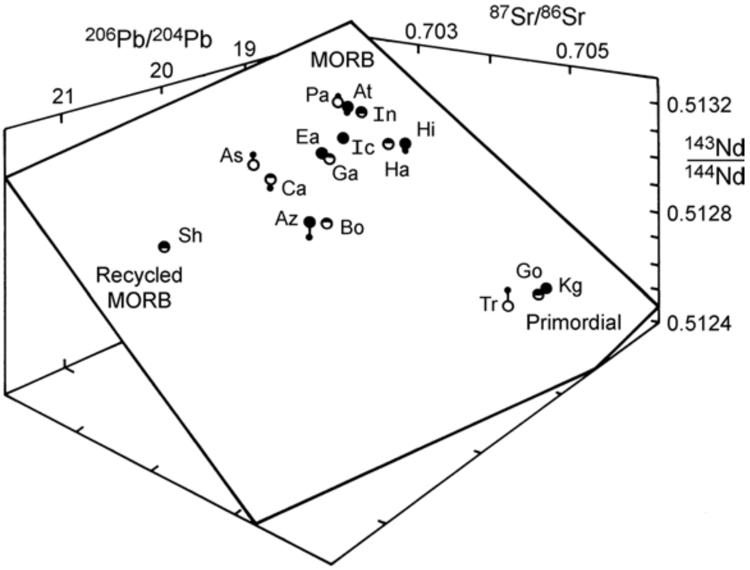

Fig. 6.31. Three-component mantle mixing model for MORB and OIB sources. Solid and open symbols indicate points above and below the mantle plane, respectively. Pa, At, In = Pacific, Atlantic and Indian MORB; Hi = Hiva Oa; Ha = Hawaii; Ic = Iceland; Ea = Easter; Ga = Galapagos; As = Ascension; Ca = Canaries; Az = Azores; Bo = Bouvet; Sh = St Helena; Tr = Tristan da Cunha; Go = Gough; Kg = Kerguelen. After Zindler *et al.* (1982).

process also obscured data that lay 'below' the mantle plane, such as the Walvis Ridge. Therefore, at least one additional component must be invoked to explain the data.

6.4.2 The mantle tetrahedron

Hart *et al.* (1986) considered that the mantle plane of Zindler *et al.* (1982) might really be a 'co-incidence of similar mixing proportions' of end-members with more extreme compositions, rather than a discrete entity in its own right. This is illustrated in Fig. 6.32, where samples are plotted in terms of parts per 10^5 deviation in Nd isotope ratio from the mantle plane, against Pb isotope composition.

Hart *et al.* proposed that the lower bound of individual ^{143}Nd/^{144}Nd sample compositions on the Nd–Sr isotope diagram (Fig. 6.33a) might be a more fundamental topological structure, which they termed the 'LoNd' array. The samples which define this array on the Nd–Sr isotope diagram also fall in a line on the Sr–Pb isotope plot (Fig. 6.33b), despite the fact that this cuts across the middle of the OIB field in this diagram. ^{208}Pb/^{204}Pb ratios in these samples are also coherent with the three other isotope systems.

The LoNd array was itself interpreted as a mixing line between 'HIMU' (high U/Pb) and 'EMI' (enriched mantle I) end-members (Zindler and Hart, 1986). Other important end-members were defined by the most extreme composition of the MORB field (DMM) and the Societies (EMII). In addition, Zindler and Hart (1986) suggested that three other components might be located inside the tetrahedral mixing space in Fig. 6.33. These are a 'primordial helium isotope reservoir', exemplified by Loihi seamount (section 11.1.3); a 'Bulk Earth' U–Th–Pb isotope reservoir, exemplified by Gough–Tristan (section 6.3.3); and a 'PREvalent MAntle' or PREMA component, justified on the grounds that the mixing of discrete components may have reached such a stage of completeness that this mixture itself becomes a recognisable entity. These possible components will be discussed further below.

One of the characteristics of the LoNd array (Hart, 1988) is that island groups are not generally elongated *along* the proposed mixing line, but often trend obliquely off the line. This was used as evidence that mixing within the LoNd array occurred a long time ago, before secondary mixing with other components lying off the array. In addition, Hart *et al.* (1986) argued that the straightness of the proposed LoNd mixing line places tight constraints on the nature of the two mixing end-members, by requiring them to have similar Nd–Sr–Pb ratios and an intimately related environment of formation. Since they believed that such

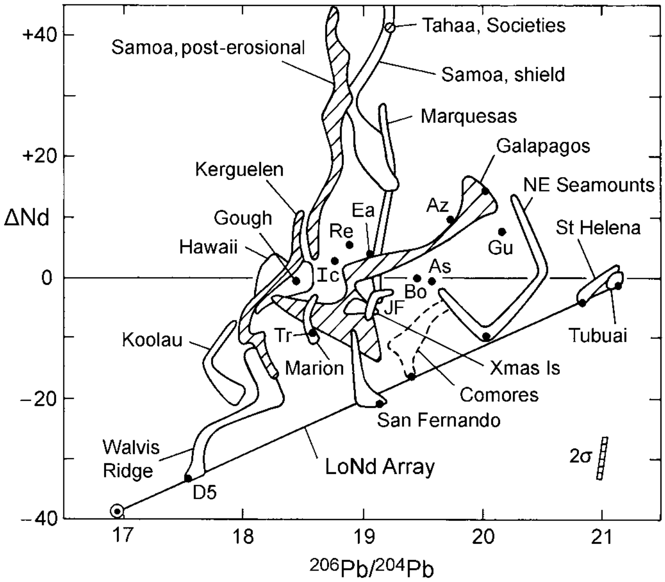

Fig. 6.32. Plot of Δ Nd (part per 10^5 deviation in $^{143}Nd/^{144}Nd$ ratio from the mantle plane of Zindler *et al.*, 1982) against Pb isotope ratio. OIB compositions are plotted both as fields and as discrete points. JF = Juan Fernández, Re = Réunion, Gu = Guadeloupe. Other abbreviations are as in Fig. 6.31. After Hart *et al.* (1986).

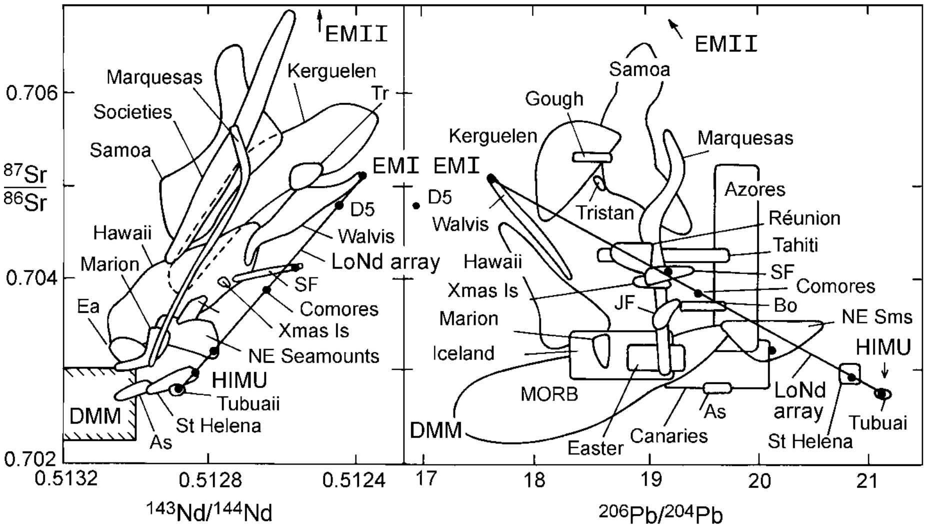

Fig. 6.33. Plots of (a) Sr *versus* Nd isotope ratio and (b) Sr *versus* Pb isotope ratio, showing the proposed end-members of a four-component mixing system: DMM, HIMU, EMI (= EM1) and EMII (= EM2). Dots are compositions argued to lie on an array between the HIMU and EMI end-members, termed the LoNd array. After Hart *et al.* (1986).

conditions would not be expected for mixing between recycled crustal and mantle components, Hart *et al.* argued that the two end-members must have resulted by different metasomatic enrichment processes in the sub-continental lithosphere.

Hart (1988) identified another two-component mixing line within the OIB data set, by using an upper $^{87}Sr/^{86}Sr$ ratio cut-off of 0.703 to exclude all samples with an enriched mantle component. On a diagram of $^{143}Nd/^{144}Nd$ ratio against $^{206}Pb/^{204}Pb$ ratio (Fig. 6.34),

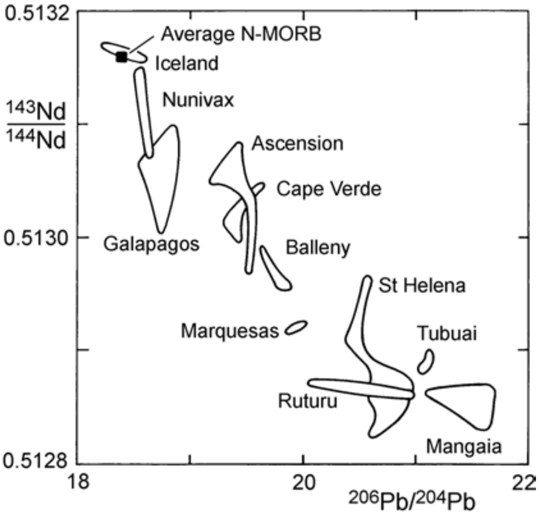

Fig. 6.34. Nd *versus* Pb isotope diagram, showing the linear array of OIB samples with $^{87}Sr/^{86}Sr$ ratios below 0.703, attributed to the 'No-EM' mixing line. After Hart (1988).

these island groups with low $^{87}Sr/^{86}Sr$ ratios define a so-called 'no-EM' array between the HIMU and DMM end-members. The straightness of this array again suggests that the end-members had similar Nd/Pb ratios, and hence that DMM, HIMU and EMI all have similar Nd/Pb ratios. However, the geochemical relationship between DMM and HIMU cannot easily be attributed to spatial proximity, as was the EMI–HIMU relationship, because the depleted mantle is a distinct reservoir. This therefore weakens Zindler and Hart's argument for an intimate genetic relationship between the end-members of the LoNd array. Instead, a more general relationship is possible, whereby the three components are generated by similar mantle-differentiation *processes*, but in different locations.

In contrast to the linear mixing lines described above, mixing with the EMII component tends to generate elongated curved arrays within island groups, as shown in Figs. 6.32 and 6.33. This suggests that elemental ratios between EMII and the other mantle domains were far from unity, which is consistent with a model in which DMM, HIMU and EMI are generated by mantle differentiation processes, but EMII represents recycled continental crust with a very different trace-element signature. Hart (1988) went further in his distancing of EMII from the other components, suggesting that mixing with this end-member was a late phenomenon that occurred after other mixing processes. However, Staudigel *et al.* (1991) found strong evidence for mixing between HIMU and EMII in the South Pacific Isotopic and Thermal Anomaly (SOPITA), particularly on the Sr–Pb isotope diagram (not shown here). In view of the intimate geographical association of HIMU and EMII in the SOPITA case, it is likely that this array was formed prior to mixing with MORB, and it may constitute one of a family of curved 'HiNd' mixing lines analogous to the LoNd array.

There is considerable danger in looking at isotope variations in a number of two-component systems, since arrays are projected onto these surfaces from a multi-dimensional mixing polygon, and in this process the true trends of the arrays may be misunderstood. In order to analyse the data in a more objective fashion, Allègre *et al.* (1987) ran a principal-component analysis on a large set of $^{87}Sr/^{86}Sr$, $^{143}Nd/^{144}Nd$, $^{206}Pb/^{204}Pb$, $^{207}Pb/^{204}Pb$ and $^{208}Pb/^{204}Pb$ data for MORB and OIB samples. This was also performed on an updated sample set by Hart *et al.* (1992).

Principal-component analysis resolves the oceanic data set into five eigenvectors, representing directions in multi-component space that show the greatest percentage of variance in the data. The magnitudes of these vectors (in the calculation by Hart *et al.*) are approximately 56%, 37%, 4%, 2% and 1%. The pre-eminence of the first two vectors demonstrates the largely planar form of the data set, as emphasised by Zindler *et al.* (1982). However, there is enough residual scatter in the data that a third vector is necessary in order to represent the mixing process properly. The sum of these three vectors is 97.5% in Hart's analysis and 99.2% in Allègre's analysis. Hence Hart *et al.* argued that a three-dimensional (four-component) analysis is appropriate to analyse the data with a fairly high degree of reliability. However, the eigenvectors are so divorced from the familiar isotope ratios that it becomes difficult to understand the data. Therefore, Hart *et al.* presented the data in the form of a three-dimensional isotope plot (of $^{143}Nd/^{144}Nd$, $^{87}Sr/^{86}Sr$ and $^{206}Pb/^{204}Pb$ ratios), but projected in such a way as to approximate the eigenvector directions (Fig. 6.35).

The focussing of data points at the lower corners of the mantle tetrahedron (Fig. 6.35) provides evidence that some of the proposed components are real entities, rather than merely theoretical end-members. This is exemplified by the intersection of the LoNd and No-EM arrays, which provide a relatively strong constraint on the composition of HIMU, suggesting that the 'pure end-member' has a composition very similar to the most radiogenic Pb already analysed, from the island of Mangaia. This conclusion is supported by the close agreement between the compositions of the widely separated HIMU islands from the South

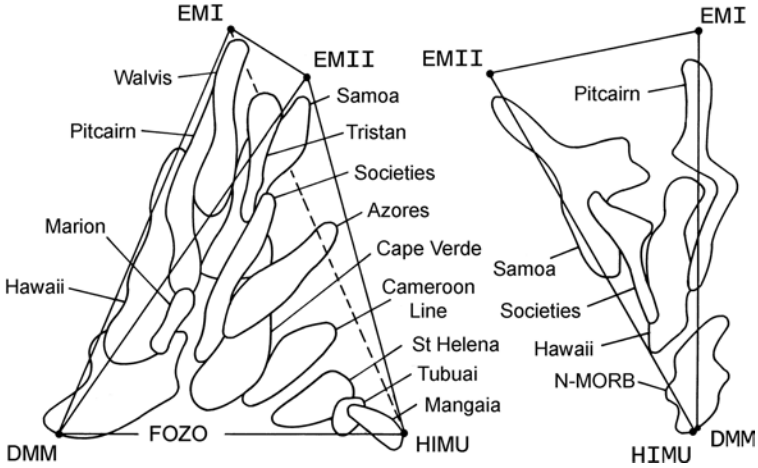

Fig. 6.35. Two views of a three-dimensional mantle tetrahedron representing the mixing relationships of four isotopically proposed mantle components seen in oceanic volcanics, together with a proposed 'focus zone', FOZO. Modified after Hart *et al.* (1992).

Atlantic and South Pacific. In contrast, the density of samples lying at the EMI and EMII end-member compositions is much lower, and may suggest that these are the most extreme products yet sampled of enrichment *processes*, rather than significant mantle reservoirs in their own right (Barling and Goldstein, 1990).

6.5 Identification of mantle components

Since the study of Hart *et al.* (1986), major efforts have been devoted to identifying the proposed mantle components in geological terms and explaining how they have interacted to generate OIB sources. To a large extent the debate has been polarised between those who invoke metasomatic enrichment models (e.g. Hart *et al.*, 1986) and those who invoke crustal-recycling models (e.g. Weaver, 1991) to explain the enriched components. Some of the arguments will be briefly examined for the various end-members.

6.5.1 HIMU

Many authors have proposed that HIMU represents subducted oceanic crust (e.g. Chase, 1981; Palacz and Saunders, 1986; Staudigel *et al.*, 1991; Chauvel *et al.*, 1992; Hauri *et al.*, 1993). The great advantage of this model is that it attributes HIMU to a known major subducted component.

The U/Pb ratios of normal MORB are not high enough to explain the composition of HIMU, but various means have been proposed to raise the U/Pb ratio of subducted oceanic crust (section 6.3.2). An alternative site for possible U/Pb enrichment in the subducted slab is the sub-oceanic lithosphere. For example, Halliday *et al.* (1990; 1992) argued that shallow Pb–Pb isotope arrays in the Cameroon Line volcanics and other Atlantic islands were best explained by recent strong U/Pb enrichment of the oceanic lithosphere (section 7.3.2). This process cannot directly explain the much steeper correlation between ^{206}Pb and ^{207}Pb in HIMU islands; however, after storage for about 1 Byr and mixing with less-radiogenic Pb from other parts of the subducted slab, this is an additional mechanism to generate the HIMU component.

This type of model has been adapted by several workers (e.g. Thirlwall, 1997) to suggest that OIB signatures with radiogenic Pb that are less extreme than the HIMU end-member could be attributed to 'young HIMU mantle', rather than to mixing with the specific HIMU reservoir seen at St Helena and Mangaia. However, it is worth noting a possible corollary of this model, by which the HIMU end-member itself was created as a special case within this general model. Perhaps HIMU was formed by subduction of very U-enriched oceanic crust about 2 Byr ago, reflecting the sudden release of uranium to the ocean in response to changing atmospheric conditions (section 6.3.3).

A rather different concept of the origin of some mantle plumes was suggested by Class *et al.* (1993; 1996), who proposed that plumes such as Ninetyeast–Kerguelen and Tristan–Walvis could undergo *in situ* growth of radiogenic Pb. This model was based on an observed correlation of Pb isotope ratio with age along

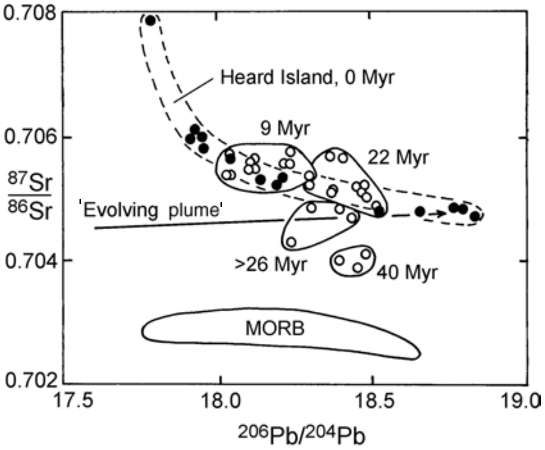

Fig. 6.36. Plot of Sr–Pb isotope signatures for volcanic units of the Kerguelen plateau (○) and Heard Island (●) relative to an 'evolving-plume' model based on Ninetyeast Ridge data. Numbers indicate approximate ages of volcanism in Myr. After Class *et al.* (1996).

the Ninetyeast Ridge, increasing from an unradiogenic composition similar to that of the Rajmahal traps of eastern India (about 120 Myr ago) to a composition at the radiogenic Pb end of the Heard Island array (at the present day). This trend is shown by the bold line in Fig. 6.36, and has been dubbed the 'evolving-plume' model. Class *et al.* envisaged that U/Pb enrichment occurred when sub-continental lithosphere was delaminated and recycled back into the convecting mantle, where it would reside for less than 1 Byr at a mantle boundary layer. New plumes would then be generated from this material, either at the 760-km discontinuity or at the core–mantle boundary.

Helium isotope data for Heard Island have indeed provided evidence for a plume signature at this island (section 11.1.5). However, isotope data for lavas of various ages in the Kerguelen islands appear to define an evolution line in the opposite direction to the 'evolving-plume' trend (Fig. 6.36). This led Frey and Weiss (1995; 1996) to argue that the evolving-plume model could not explain the Kerguelen data and could only partially explain the Ninetyeast Ridge data. Since that time a considerable amount of additional work has been done on the Kerguelen Plateau, as well as other features near the SE Indian Ridge. The picture that has arisen is very complex, with evidence for contamination by upper crust, lower crust, or lithospheric mantle in some localities, as well as evidence for a heterogeneous plume composition (e.g. Neal *et al.*, 2002; Mattielli *et al.*, 2002). Hence the overall consensus seems to be that the evolving-plume model is too simple to explain all the observed variability. Possibly, the unradiogenic Pb signatures in older Ninetyeast basalts were due to lithospheric contamination, whereas several different plume components with varying radiogenic Pb signatures are now involved.

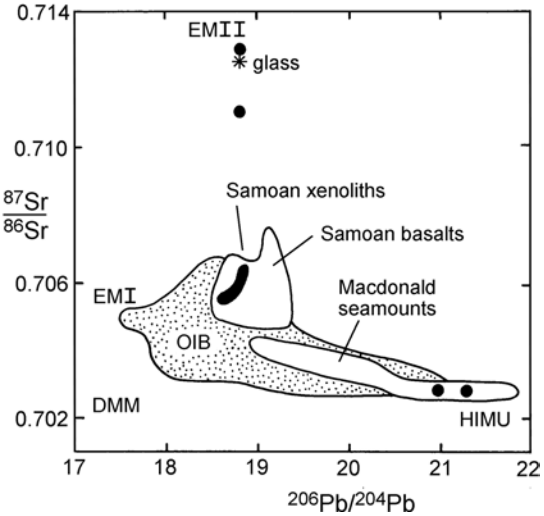

Fig. 6.37. Plot of Sr *versus* Pb isotope data for cpx grains (●) and glass inclusions (∗) in peridotite xenoliths from Savaii (Samoa) and Tubuai (Austral Islands), indicating affinity with the EMII and HIMU mantle end-members. After Hauri *et al.* (1993).

6.5.2 EMII

The case for EMII as subducted continental material is almost universally agreed, since this end-member is squarely located on mixing lines between depleted mantle and marine sediments. This model was further strengthened by evidence from peridotite xenoliths in Samoan lavas (Hauri *et al.*, 1993). Trace-element data for these xenoliths indicate an origin from carbonate-rich melts within the Samoan plume, and the isotopic compositions of the xenoliths are therefore taken as indicative of the EMII mantle component. These xenoliths extend the EMII array directly into the field of marine sediments (Fig. 6.37) and thus provide a compelling case for this material as the source of the EMII component. Similar xenoliths from Tubuai also support the concept of a discrete HIMU component, as previously observed in lavas from Mangaia, Tubuai and the nearby Macdonald seamount chain.

Further evidence for recycling of sediment into the EMII source comes from oxygen isotope measurements, which have consistently revealed elevated signatures in these plumes relative to MORB values. Other enriched mantle reservoirs have also appeared in the past to display oxygen isotope variations outside the range of MORB values, based on analysis of whole-rock basalts or basaltic glasses (see the review by Harmon and Hoefs, 1995). However, more recent analysis of olivine phenocrysts from a variety of plume sources gave a much more restricted range (Eiler *et al.*, 1997), suggesting that most of the earlier variations were due to shallow contamination effects, either at the magmatic stage by oceanic crust, or under sub-solidus conditions after eruption. In contrast, phenocryst analyses from EMII plumes continue to give elevated oxygen isotope ratios correlated with $^{87}Sr/^{86}Sr$ ratio, and are therefore considered to be a strong indicator of sediment recycling.

6.5.3 EMI

In their early synthesis on the nature of enriched-mantle sources, Hart *et al.* (1986) argued that both HIMU and EMI were derived from recycled sub-continental lithosphere. More recent work has supported the argument that these two components are very closely related (e.g. Chauvel *et al.*, 1992), but, with the increasing acceptance of oceanic crust/lithosphere as the origin of HIMU, a sub-continental origin for EMI became more problematical. Dickin (1995) attempted to resurrect this model by advocating the juxtaposition of oceanic and continental lithosphere in the plume source by subduction erosion. However, since that time there has been increasing evidence to support the suggestion of Weaver (1991) that subducted pelagic sediment is an important component in the EMI source (in contrast to EMII, which is attributed to recycled terrigenous sediment).

Some of this evidence comes from a re-evaluation of Hf isotope data, which were earlier believed to militate against the recycling of variable types of sediment into the plume source (section 9.2.5). Other evidence comes from stable-isotope analysis. However, this has had a checkered history.

Woodhead *et al.* (1993) re-initiated interest in this problem when they found significantly elevated oxygen isotope signatures in submarine glasses from the Pitcairn seamounts, which display the most extreme EMI signatures for several isotope systems. Unfortunately there are many ways in which oxygen isotope ratios can be perturbed by sea-floor processes to yield spurious signals. Nevertheless, Woodhead *et al.* argued that none of these processes could explain their data, which they attributed to isotopic variations in the plume source itself. Hence, their preferred explanation for this effect was the recycling of marine sediment into the EMI source by subduction.

Eiler *et al.* (1995) tested these findings by analysing the oxygen isotope compositions of olivine and plagioclase phenocrysts from Pitcairn Island. All olivines had $\delta^{18}O$ values close to 5.2, whereas plagioclase had $\delta^{18}O$ values near 6.1, consistent with mass-fractionation effects at magmatic temperatures. Therefore, it was concluded that the variations seen by Woodhead *et al.* are almost certainly due to local contamination of the glasses, either before or after solidification. Local contamination effects are also believed to explain oxygen isotope data from Iceland that lie well below the range of MORB values, although less-extreme oxygen signatures could originate from a plume source (Harmon and Hoefs, 1995).

In contrast to these negative results, more recent analysis of olivine phenocrysts from Hawaiian lavas has provided the first strong evidence in support of sediment contamination of the EMI source (Eiler *et al.*, 1996). In this study, oxygen isotope ratios were correlated with lithophile isotope tracers such as Nd, in addition to osmium and helium, consistent with the involvement of three end-members in the Hawaiian plume (Fig. 6.38). The Loihi component, with an oxygen signature similar to that of MORB, has helium and osmium signatures indicative of a core component (section 8.3.5). The Kea component, with a depleted $\delta^{18}O$ signature relative to MORB, is attributed to melting of recycled oceanic lithosphere. Finally, the Koolau component has an enriched $\delta^{18}O$ signature indicative of a component of recycled sediment, combined with unradiogenic Pb and Nd signatures characteristic of the EMI source. Additional evidence for this model comes from Hf isotope data (section 9.2.5).

This strong evidence for a pelagic-sediment signature in the EMI source is problematical for the alternative origin of EMI in the sub-continental lithosphere. However, the two models may be reconciled by proposing that the lithospheric mantle wedge above subduction zones takes on the isotopic signature of pelagic sediment by magmatic and metasomatic enrichment from sediments in the subducting slab (section 6.6.2).

A final note on EMI concerns basalts dredged from the Afanasy–Nikitin (A–N) rise (at the southern end of the non-seismic 85° E ridge), which may extend EMI to even more enriched compositions. Two samples analysed by Mahoney *et al.* (1996) were collinear with an extension of the Pitcairn seamount array in Nd–Pb, Sr–Pb and Pb–Pb isotope space. In addition, nine analyses quoted from a Russian source (Sushchevskaya *et al.*, 1996) define an array that is collinear with the data of

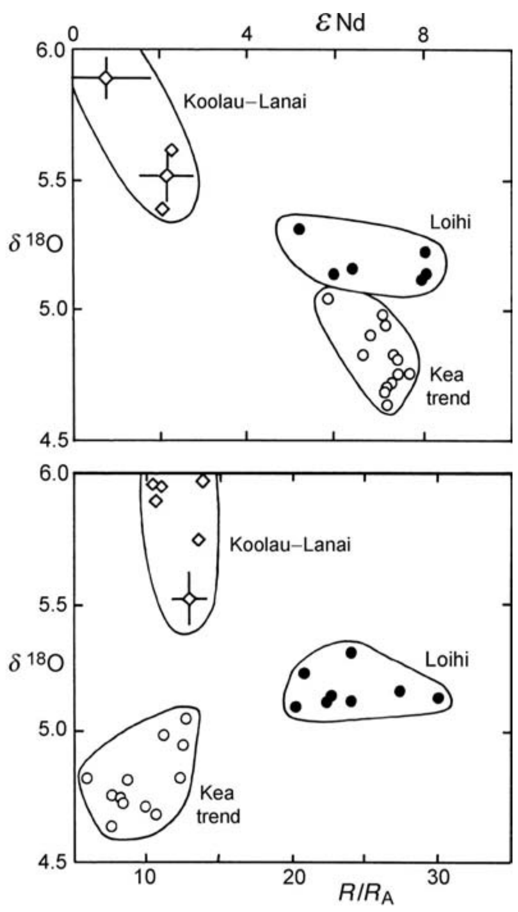

Fig. 6.38. Plots of ε Nd and He isotope data (R/R_A) against $\delta^{18}O$ for olivine phenocrysts in lavas from selected Hawaiian volcanos: (◇) = Koolau–Lanai; (○) = Mauna Kea; (●) = Loihi. Error bars represent suites where different tracers were determined on different samples, so the symbol shows the mean and standard deviation of the suite. Modified after Eiler *et al.* (1996).

Mahoney *et al.* (and Pitcairn data) in Nd–Pb and Sr–Pb isotope space. The Russian data are not collinear on a Pb–Pb isochron diagram (not shown), but this could be due to analytical fractionation effects. Mahoney *et al.* ruled out *in situ* lithospheric mantle as a source for the A–N data, because at the time of volcanism the A–N rise was situated on young oceanic crust, far from any continent. However, the data need not represent a lower-mantle source composition because they are quite distinct from the Crozet hot spot, to which the 85° E ridge and A–N rise are attributed. Hence, Mahoney *et al.* speculated that the A–N component may represent lithospheric mantle material entrained for a brief time into the Crozet plume.

6.5.4 Kinematic models for mantle recycling

If HIMU, EMII and EMI are attributed to recycling of oceanic crust, continental sediment, and mantle wedge plus pelagic sediment, respectively, a simple plate-tectonic model can explain recycling of these components into the deep mantle in two conjugate pairs: EMI–HIMU and EMII–HIMU. This is based on the two different tectonic settings of subduction zones recognised by Uyeda (1982). The Chilean-type setting (Fig. 6.39a) is characterised by a compressional stress regime across the arc–trench gap. This causes tectonic erosion of the underside of the arc lithosphere, which may then give rise to a composite sheet in the downgoing slab consisting of oceanic crust overlain by lithospheric mantle. If the mantle wedge carries an EMI signature introduced from subducted pelagic sediment, the combination with subducted oceanic crust can generate the conjugate pair HIMU–EMI in the OIB source.

In contrast to the Chilean type, the Mariana-type setting (Fig. 6.39b) is characterised by a tensional stress regime across the arc–trench gap. This causes

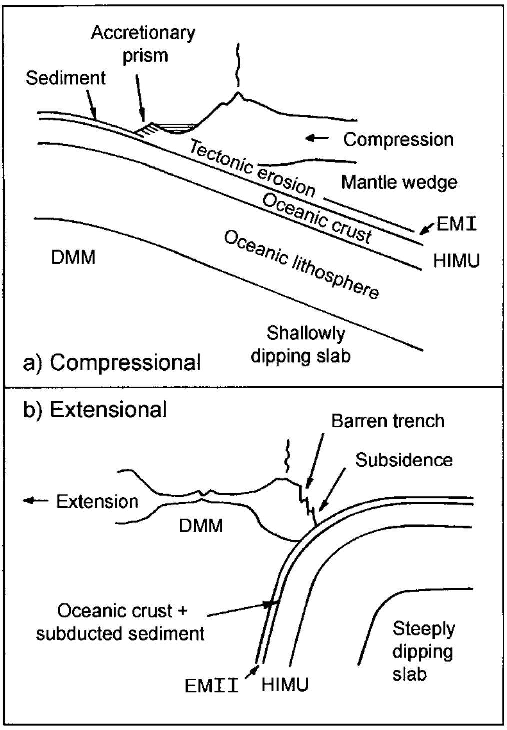

Fig. 6.39. Schematic illustrations of two different tectonic styles at subduction zones that may generate conjugate pairs of enriched mantle signatures: (a) HIMU–EMI and (b) HIMU–EMII. Modified after Uyeda (1982).

subsidence of the trench bottom so that ocean-floor sediments are efficiently subducted, but tectonic erosion of sub-arc lithospheric mantle does not occur. The results of this process can be seen in the Lesser Antilles arc (section 6.6). The north end of the arc (with a low sediment supply) subducts barren oceanic crust, which can form a pure HIMU component after storage in the lower mantle. In contrast, the south end of the arc (with a large sediment supply) subducts a composite sheet of oceanic crust and continental sediment, which can generate the conjugate pair HIMU–EMII in the lower mantle. Isotopic evidence for these alternative processes in subduction zones will be examined in section 6.6.

The subduction of oceanic crust, together with marine sediment or eroded sub-continental lithosphere, may give rise to large-scale isotopic structure in the mantle. For example, Hart (1984) argued that recycling into the asthenosphere was responsible for generating a Pb and Sr isotope anomaly of global scale, which he observed to form a small circle of approximately constant latitude encircling the southern hemisphere. He named it the 'Dupal' anomaly because its characteristic signature was first described in Indian Ocean volcanics by Dupré and Allègre (1983).

Hart quantified the Dupal anomaly in terms of its deviation from the typical Pb isotope signatures of MORB and OIB in the northern hemisphere, which form a series of coherent Pb/Pb arrays (Fig. 6.21). Hence, he defined the terms $\triangle$ 207/204 and $\triangle$ 208/204 as per mil deviations of Pb isotope ratio from a 'Northern Hemisphere Reference Line'. Not only are the southern tropics characterised by the Dupal anomaly with a positive $\triangle$ 208/204 value, but a HIMU source with negative $\triangle$ 208/204 is also seen in the same area.

Hart (1988) and Castillo (1988) argued that the configuration of these anomalies was an indicator of the convective structure of the deep mantle. Staudigel *et al.* (1991) further suggested that large-scale regional isotope signatures such as the Dupal anomaly could be explained by 'focussed subduction' from a group of destructive plate margins, such as are presently seen in SE Asia.

6.5.5 Depleted OIB sources

When Zindler and Hart (1986) integrated enriched-mantle signatures into a coherent model, and proposed the three well-known end-members discussed above, they also recognised that many OIBs were intermediate in composition between the end-members. However, rather than suggest that all such plumes represent complex mixing of all three end-members, they suggested the existence of a large reservoir of intermediate composition, which they called PREvalent MAntle (PREMA). Zindler and Hart also noticed that the group of islands exhibiting this signature included Hawaii and Iceland, with enriched helium isotope signatures, but with lithophile isotope signatures depleted relative to Bulk Earth. As a result of these observations, Zindler and Hart suggested two possible alternative origins for PREMA. It could either be a result of mixing of all the other mantle sources, or a kind of depleted mantle formed early in the Earth's history, before two-layered mantle convection established the existence of the MORB reservoir.

The increased amount of OIB data that became available over subsequent years led Hart *et al.* (1992) to argue that the most common feature in the isotope data from plume sources was a tendency to form linear arrays, which appeared to fan out from a 'focus zone' at the base of the mantle tetrahedron towards a variety of enriched mantle end-members. Hence Hart *et al.* named this common component FOZO. The proposed composition of FOZO was on the edge of the tetrahedron between the depleted mantle (DMM) and HIMU. However, it was clearly distinct from DMM. Therefore, Hart *et al.* proposed that it was a lower-mantle component that had been entrained around enriched mantle plumes rising from the core–mantle boundary.

Subsequent work showed that the location of FOZO as originally proposed was not satisfactory, since several island arrays (e.g. the Macdonald seamounts) trended from HIMU or DMM towards the middle of the mantle tetrahedron. Therefore, Hauri *et al.* (1994) revised the concept of FOZO to a somewhat less-depleted signature bearing a very strong resemblance to PREMA (Fig. 6.40). Again, this component was also identified with elevated levels of ^{3}He. In addition, fluid-dynamic modelling by Hauri *et al.* suggested that the extent of entrainment of lower mantle into plumes was very variable (between 5% and 90%).

Hauri *et al.* (1994) examined two alternative models for mixing between FOZO and enriched mantle in plumes. Since these plumes were argued to originate at the core–mantle boundary layer (CMBL), it was argued that one of the two end-members must be located at this point. Therefore, either plumes originate as enriched mantle at the CMBL and entrain FOZO as a kind of sheath, or they must originate as FOZO at the CMBL and entrain enriched blobs of lower mantle.

These and other alternative models were recently reviewed by van Keken *et al.* (2002), who re-examined the correlation between helium and lithophile isotope systems. They plotted ^{3}He data against a composite

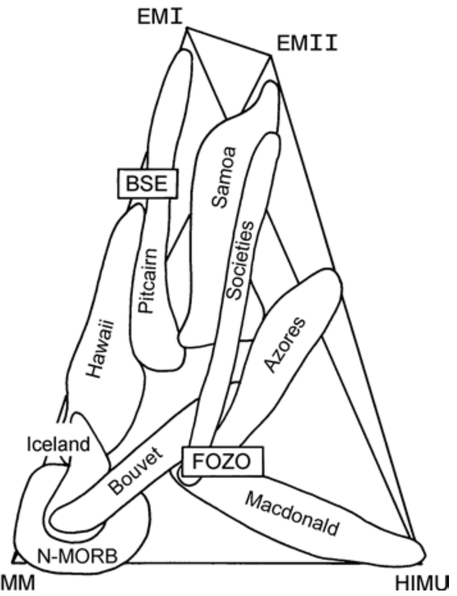

Fig. 6.40. View of the mantle tetrahedron, showing OIB arrays that converge on the revised composition of FOZO from many different directions. After Hauri *et al.* (1994).

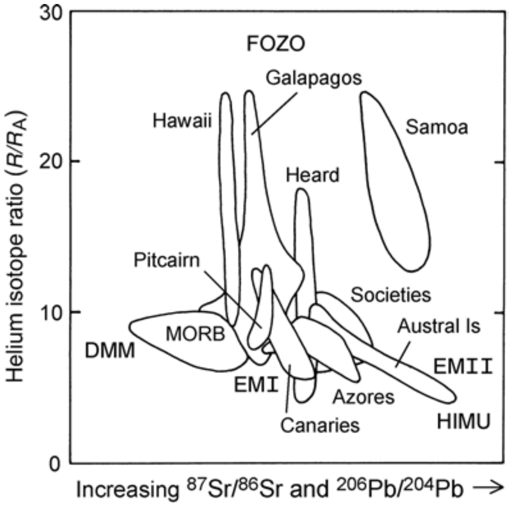

Fig. 6.41. Plot of helium isotope ratios relative to the atmospheric composition (section 11.1) against a composite index for Sr and Pb isotope variation. Several ocean islands exhibit vertical trends, which are attributed to FOZO. After van Keken (2002).

index of Sr and Pb isotope ratios (Fig. 6.41). Several ocean islands exhibit ^{3}He enrichment, but the degree of correlation between helium and lithophile isotope tracers is generally quite weak (except for Samoa, where helium variations are attributed to shallow mixing processes; see section 11.1). Therefore, the evidence in Fig. 6.41 suggests that the ^{3}He-enriched component is largely decoupled from and independent of the lithophile isotope signature of FOZO/PREMA.

The simplest solution to the problem of juxtaposing these sources would be that elevated ^{186}Os and ^{3}He signatures come from the core and then become one of a suite of distinct components at the CMBL. These components then all undergo variable mixing with FOZO/PREMA during their ascent and entrainment in the mantle convection system, as originally proposed. This would imply that FOZO/PREMA is dispersed in the lower mantle between blobs of enriched material. In this case it can most easily be produced by recycling of oceanic lithospheric mantle, in contrast to the enriched components, which represent recycled crust or subcontinental lithosphere.

Detailed examination of individual hot-spots may offer the best hope of determining the origins of 'non-enriched' lower-mantle sources such as FOZO, and the ways in which these sources are juxtaposed with enriched sources in rising plumes. For these purposes, the Iceland plume has been of particular interest.

Thirlwall *et al.* (1994) showed that Icelandic basalts and North Atlantic MORB display sub-parallel but distinct Pb isotope arrays. Hence, they argued that isotopic heterogeneity in the Iceland plume could not be caused by mixing with MORB. They speculated that the Iceland plume array might represent a 'young-HIMU'-type source. On the other hand, Kerr *et al.* (1995) suggested that the Iceland plume was formed from recycled 'lower-oceanic lithosphere'. This would generate a more depleted signature than recycled oceanic crust (the proposed source of HIMU). A component similar to this was proposed by Hanan and Graham (1996) as a 'common' mantle component, 'C'. This resembles FOZO/PREMA in some respects, since it has effectively the same Pb isotope ratio. However, the component C was envisaged as dispersed within the MORB reservoir. It could therefore represent FOZO/PREMA material in a 'marble-cake' mantle.

6.6 Island arcs and mantle evolution

Island arcs are central to the understanding of mantle evolution because they represent the site where lithospheric material of various types is returned to the deep mantle. Island-arc magmatism may allow us to sample this material which is in the process of being recycled. Dewey (1980) showed that the volcanic front is always located about 100 km above the descending slab, whatever the angle of subduction. This shows that dehydration of the slab, triggered by pressure, is central to the operation of island-arc magmatism. However, the petrology of island-arc basalts (IAB) precludes their genesis by fusion of subducted oceanic crust (since this would require nearly 100% melting). Therefore, they must be dominantly produced by melting of the 'mantle wedge' overlying the subduction zone (e.g. Wyllie, 1984). Hence, the central problem in interpreting IAB is that of identifying which signatures are derived from the slab (and subducted sediment) and which are derived from the overlying wedge. We will therefore examine this problem in terms of two-component mixing between the slab and wedge.

6.6.1 Two-component mixing models

Island-arc basalts have enhanced $^{87}Sr/^{86}Sr$ ratios relative to MORB. However, the origin of these differences is discernible only in the context of other isotope evidence. The first study using combined Sr and Nd isotope data was performed by Hawkesworth *et al.* (1977) on island-arc and back-arc tholeiites from the Scotia Sea (South Sandwich Islands). Analysis of back-arc material provides a control condition because it samples a mantle segment that should be similar to the wedge, but without any slab component.

Hawkesworth *et al.* found that island-arc and back-arc samples from the Scotia Sea had identical $^{143}Nd/^{144}Nd$ ratios, overlapping with those of MORB. However, the island-arc samples had significantly higher $^{87}Sr/^{86}Sr$ ratios (Fig. 6.42), which could not be explained by sub-aerial weathering. Therefore, Hawkesworth *et al.* suggested that the enhanced Sr isotope ratios of the IAB were a product of subducted ^{87}Sr from seawater or (alternatively) oceanic sediments. Possible mechanisms proposed were the direct partial melting of altered and subducted oceanic crust or, alternatively, metasomatic contamination of the mantle wedge with elements derived from the ocean crust. It is now generally accepted that the latter model is correct for the Scotia arc (e.g. Pearce, 1983).

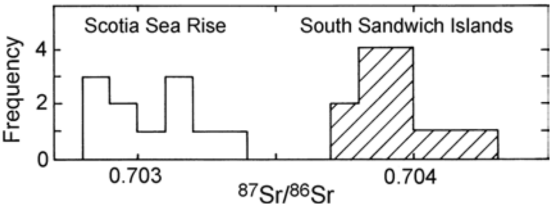

Fig. 6.42. Histogram to compare Sr isotope ratios of basalts from the South Sandwich arc and the (back-arc) Scotia Sea Rise. After Hawkesworth *et al.* (1977).

The Scotia arc provides an example of the role of slab-derived fluids in an arc with depleted chemistry. However, in arcs with less-depleted chemistry, material contributions from the slab and wedge are more difficult to resolve. The Lesser Antilles (Caribbean) arc provides a good test case for the behaviour of arcs with more-enriched signatures, since the chemistry of the arc changes along its length. This may help in resolving the origin of enriched components.

Grenada volcanics display variations in both $^{87}Sr/^{86}Sr$ and $^{143}Nd/^{144}Nd$, defining a range similar to those observed by Hawkesworth *et al.* (1979a) from São Miguel in the Azores, but further to the right of the main mantle correlation line (Fig. 6.43). In view of these parallels, Hawkesworth *et al.* (1979b) attributed the Grenada data to Sr contamination (from the slab) of a heterogeneous mantle wedge with a range of Nd and Sr isotope compositions along the mantle array. However, it is not clear why this particular piece of sub-oceanic lithosphere would display such large heterogeneities, since mantle plumes cannot penetrate above a subduction zone. It would be necessary to propose that the mantle wedge in this location happened

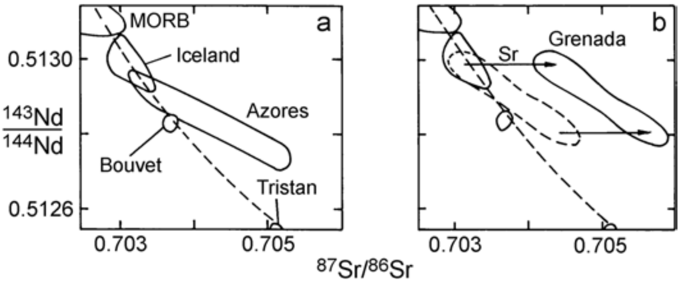

Fig. 6.43. Comparison of Sr–Nd isotope systematics in (a) the Azores and (b) Grenada, showing possible derivation from enriched mantle sources. After Hawkesworth *et al.* (1979b).

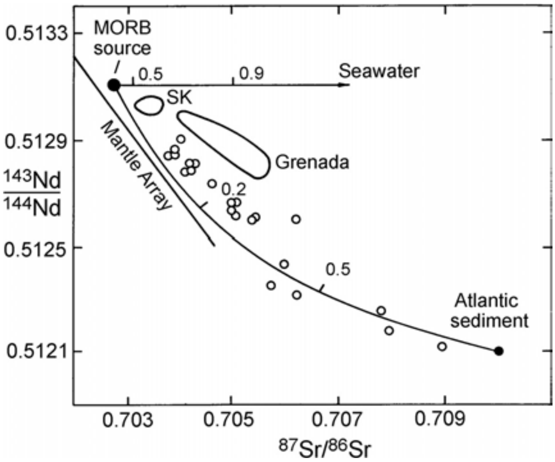

Fig. 6.44. Sr–Nd isotope diagram, showing extreme isotopic variation in Martinique lavas (○) compared with Grenada and St Kitts (SK). Mixing lines model the effects of contamination by sediments or seawater. After Davidson (1983).

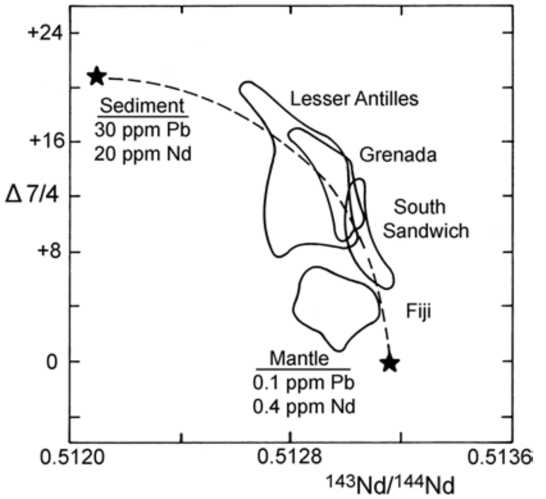

Fig. 6.45. Assessment of a sediment–asthenosphere mixing model for Lesser Antilles volcanics, in terms of Pb and Nd isotope systematics. Δ 7/4 measures deviations in ^{207}Pb/^{204}Pb ratio from the 'Northern Hemisphere Reference Line' of Hart (1984). After Ellam and Hawkesworth (1988).

to contain an enriched 'plum', as suggested for the Aleutian arc by Morris and Hart (1983).

Isotopic investigation of other islands in the Lesser Antilles (Davidson, 1983) revealed that St Kitts, situated at the northern end of the arc, has a very small range of isotopic composition close to MORB, whereas Martinique, in the centre of the arc, has an extremely large range of isotope composition (Fig. 6.44). If such variations were inherited from the mantle wedge, then 'gross heterogeneity on a scale of kilometres is implied'. Davidson initially ascribed the variations to contamination of the mantle source with subducted sediment. However, more detailed geochemical studies (Davidson, 1987) revealed positive correlations between Sr isotope ratio, oxygen isotope ratio and silica content in Martinique lavas. These are indicative of crustal contamination of ascending magma in the arc crust, which is thickest in the central region of the arc near Martinique. Such processes will not be detailed here, since they will be covered in the next chapter. However, they serve to exclude Martinique data from considerations of magma petrogenesis in the mantle.

White and Dupré (1986) presented Pb isotope data for representative samples from the whole length of the Lesser Antilles arc, showing that they were generally intermediate between MORB and sediment compositions. There is no evidence that these signatures are derived from magma contamination in the arc crust. For example, sedimentary xenoliths in Grenada lavas actually have unradiogenic Pb, inherited from an earlier location of the arc to the west, above the subducting Farallon plate. In contrast, Atlantic ocean-floor sediments in front of the present-day arc have radiogenic Pb signatures.

White and Dupré found a general increase in the Pb isotope ratio of Atlantic floor sediment when going southwards in front of the Lesser Antilles subduction zone, probably reflecting sediment carried onto the sea floor at the south end of the arc by the Orinoco river. This trend was matched by the composition of Lesser Antilles volcanics, suggesting the presence of a subducted-sediment component in the arc magmas. This model is supported by the co-variation of Pb and Nd isotope data in the volcanics (Fig. 6.45). Two-component mixing between a MORB source and average Atlantic sediment can therefore explain the observed Pb–Nd isotope systematics of Lesser Antilles magmas, avoiding the need to invoke an enriched-mantle wedge (Ellam and Hawkesworth, 1988).

Rare-earth concentration data may present a problem for this model, since LREE enrichment in some arc volcanics may be too great to be explained by simple mixing between a MORB source and subducted sediment (Hawkesworth *et al.* 1991). This problem is illustrated in Fig. 6.46 on a plot of Ce/Yb ratio (i.e. REE profile slope) against Sr isotope ratio. LREE-enriched basalts and andesites from Grenada, the Sunda arc and the Aeolian arc of southern Italy fall off the mixing

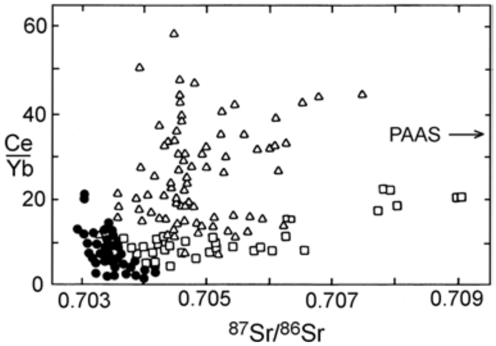

Fig. 6.46. Plot of Ce/Yb ratio against Sr isotope ratio for island-arc basalts and andesites: (●) = normal arc volcanics; (△) = LREE-enriched; (□) = Martinique lavas, contaminated during magma ascent. PAAS (post-Archean average shale) is a typical sediment composition. After Hawkesworth *et al.* (1991).

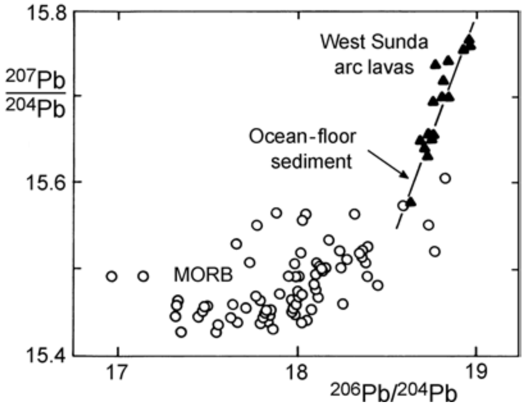

Fig. 6.47. Pb–Pb isotope plot, showing collinearity of the West Sunda arc (▲) with ocean-floor sediment in front of the trench (solid line). Indian MORB is shown by open symbols. After Ben Othman *et al.* (1989).

line between depleted arcs and a typical sediment represented by 'post-Archean average shale' (PAAS). However, White and Dupré (1986) argued that the Pb isotope evidence for involvement of sediment in arc-magma genesis was so conclusive that it over-rides these trace-element problems. Given this constraint, the very steep REE profiles must be due to some feature of the melting process. For example, *partial* melting of sediment in the presence of residual garnet could elevate LREE abundances in the melt while depressing the abundances of heavy REE.

Most workers now accept the supremacy of Pb isotope evidence for involvement of sediment in the genesis of IAB. For example, Ben Othman *et al.* (1989) observed perfect matching of Pb isotope systematics between the West Sunda arc and ocean-floor sediment in front of the arc (Fig. 6.47). Since the Pb contents of arc volcanics are nearly an order of magnitude lower than those of typical sediments, it is unlikely that the sediment signature is itself controlled by erosion of arc-volcanics. Therefore, it is most likely that the reverse relationship applies: arc-volcanic Pb is controlled by subducted sediment. Further evidence was provided by McDermott *et al.* (1993), who observed Pb isotopic variations along the North Luzon (Philippine) arc, which were correlated with the composition of sediment cores from the South China Sea, in front of the trench.

6.6.2 Three-component mixing models

In the above examples, two-component mixing between slab and wedge was examined for cases where the slab-derived component (SDC) was dominantly either a fluid or sediment. However, it is clear that in some cases both of these components must be present. Therefore, White and Dupré (1986) and Ellam and Hawkesworth (1988) expanded the two-component models described above into a three-component mixing model. This involves contamination of the depleted-mantle source of IAB with partial melts of subducted sediment *and* LIL-element-enriched slab-derived fluids. Evidence for such a process is seen when abundances of low-field-strength LIL elements such as Sr are ratioed against high-field-strength elements such as REE. Subsequently, it has been shown that the Ba/Th ratio is the perfect monitor of the slab-derived fluid component (e.g. Turner *et al.*, 1996). For example, arc basalts from the Lesser Antilles have elevated $^{87}Sr/^{86}Sr$ ratios relative to MORB, implying contamination with sediment, but they also have variable Ba/Th ratios that are higher than either MORB or average sediment compositions, implying the addition of a Sr-rich fluid (Fig. 6.48).

The slab-derived fluid has a relatively minor effect on radiogenic isotope signatures, apart from causing a modest increase in the Sr isotope composition of the source (Fig. 6.42). However, this component is very strongly resolved by boron isotope evidence (as well as cosmogenic ^{10}Be, section 14.3.6), which can then be plotted against radiogenic isotope tracers. The use of this technique was demonstrated by Smith *et al.* (1997) in a study of island-arc lavas from Martinique (Fig. 6.49). Since the mantle contains very little boron, mixing lines on this plot extend between the composition of the altered oceanic crust and that of the

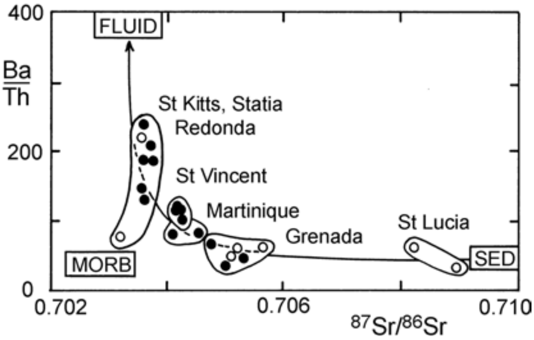

Fig. 6.48. Plot of Ba/Th ratio against Sr isotope ratio to show the necessity of invoking three-component mixing to explain the geochemistry of Lesser Antilles lavas. After Turner *et al.* (1996).

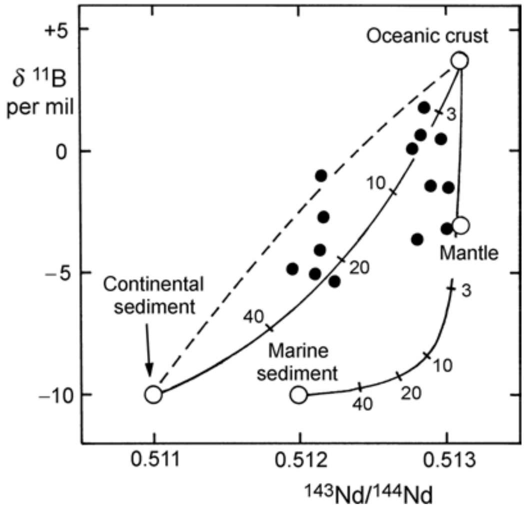

Fig. 6.49. Plot of boron isotope ratio against Nd isotope ratio to show how mixing models involving multiple fluid components can explain lava compositions from Martinique. Numbered ticks indicate percentages of sedimentary component. After Smith *et al.* (1997).

subducted-sediment component. Smith *et al.* modelled these mixing lines assuming that both signatures were carried by fluids. However, the availability of both subducted marine and continental sediment means that a fan of mixing lines is produced from three fluid components. In addition, further complexity is caused by subsequent contamination of the arc magmas during their ascent through the arc crust. Detailed analysis of various magma suites using several different tracers can be used to unravel these very complex petrogenetic processes involving multiple components (e.g. Thirlwall *et al.*, 1996). However, it will be more profitable here to examine crustal contamination processes involving fewer end-members. This will be done in the next chapter during a discussion of continental magmatism.

References

Allègre, C. J. (1982). Chemical geodynamics. *Tectonophysics* **81**, 109–32.

Allègre, C. J. (1997). Limitation on the mass exchange between the upper and lower mantle: the evolving convection regime of the Earth. *Earth Planet. Sci. Lett.* **150**, 1–6.

Allègre, C. J., Ben Othman, D., Polvé, M. and Richard, P. (1979). The Nd–Sr isotopic correlation in mantle materials and geodynamic consequences. *Phys. Earth Planet. Int.* **19**, 293–306.

Allègre, C. J., Brévart, O., Dupré, B. and Minster, J. F. (1980). Isotopic and chemical effects produced by a continuously differentiating convecting Earth mantle. *Phil. Trans. Roy. Soc. Lond. A* **297**, 447–77.

Allègre, C. J., Dupré, B. and Lewin, E. (1986). Thorium/uranium ratio of the Earth. *Chem. Geol.* **56**, 219–27.

Allègre, C. J., Hamelin, B. and Dupré, B. (1984). Statistical analysis of isotopic ratios in MORB: the mantle blob cluster model and the convective regime of the mantle. *Earth Planet. Sci. Lett.* **71**, 71–84.

Allègre, C. J., Hamelin, B., Provost, A. and Dupré, B. (1987). Topology in isotopic multispace and origin of mantle chemical heterogeneities. *Earth Planet. Sci. Lett.* **81**, 319–37.

Allègre, C. J., Hart, S. R. and Minster, J. F. (1983). Chemical structure and evolution of the mantle and continents determined by inversion of Nd and Sr isotopic data. I. Theoretical methods. *Earth Planet. Sci. Lett.* **66**, 177–90.

Allègre, C. J. and Turcotte, D. L. (1986). Implications of a two-component marble-cake mantle. *Nature* **323**, 123–7.

Appel, P. W. U., Moorbath, S. and Taylor, P. N. (1978). Least radiogenic terrestrial lead from Isua, west Greenland. *Nature* **272**, 524–6.

Barling, J. and Goldstein, S. L. (1990). Extreme isotopic variations in Heard Island lavas and the nature of mantle reservoirs. *Nature* **348**, 59–62.

Batiza, R. (1984). Inverse relationship between Sr isotope diversity and rate of oceanic volcanism has implications for mantle heterogeneity. *Nature* **309**, 440–1.

Becker, T. W., Kellog, J. B. and O'Connell, R. J. (1999). Thermal constraints on the survival of primitive blobs in the lower mantle. *Earth Planet. Sci. Lett.* **171**, 351–65.

Ben Othman, D., White, W. M. and Patchett, J. (1989). The geochemistry of marine sediments, island arc magma genesis, and crust–mantle recycling. *Earth Planet. Sci. Lett.* **94**, 1–21.

Bijwaard, H. and Spakman, W. (1999). Tomographic evidence for a narrow whole mantle plume below Iceland. *Earth Planet. Sci. Lett.* **166**, 121–6.

Bunge, H. P., Richards, M. A. and Baumgardner, J. R. (1996). Effect of depth-dependent viscosity on the planform of mantle convection. *Nature* **379**, 436–8.

Bunge, H.-P., Richards, M. A., Lithgow-Bertelloni, C., Baumgardner, J. R., Grand, S. P. and Romanowicz, B. A. (1998).

Time scales and heterogeneous structure in geodynamic Earth models. *Science* **280**, 91–5.

Castillo, P. (1988). The Dupal anomaly as a trace of the upwelling lower mantle. *Nature* **336**, 667–70.

Chase, C. G. (1981). Oceanic island Pb: two-stage histories and mantle evolution. *Earth Planet. Sci. Lett.* **52**, 277–84.

Chauvel, C., Goldstein, S. L. and Hofmann, A. W. (1995). Hydration and dehydration of oceanic crust controls Pb evolution in the mantle. *Chem. Geol.* **126**, 65–75.

Chauvel, C., Hofmann, A. W. and Vidal, P. (1992). HIMU–EM: the French Polynesian connection. *Earth Planet. Sci. Lett.* **110**, 99–119.

Chen, C. Y. and Frey, F. A. (1983). Origin of Hawaiian tholeiite and alkalic basalt. *Nature* **302**, 785–9.

Class, C., Goldstein, S. L., Altherr, R. and Bachèlery, P. (1998). The process of plume–lithosphere interactions in the ocean basins – the case of Grande Comore. *J. Petrol.* **39**, 937–52.

Class, C., Goldstein, S. L. and Galer, S. J. G. (1996). Discussion of "Temporal evolution of the Kerguelen plume: geochemical evidence from ~38 to 82 Ma lavas forming the Ninetyeast Ridge" by F. A. Frey and D. Weis. *Contrib. Mineral. Petrol.* **124**, 98–103.

Class, C., Goldstein, S. L., Galer, S. J. G. and Weis, D. (1993). Young formation age of a mantle plume source. *Nature* **362**, 715–21.

Cohen, R. S., Evensen, N. M., Hamilton, P. J. and O'Nions, R. K. (1980). U–Pb, Sm–Nd and Rb–Sr systematics of ocean ridge basalt glasses. *Nature* **283**, 149–53.

Cohen, R. S. and O'Nions, R. K. (1982). Identification of recycled continental material in the mantle from Sr, Nd and Pb isotope investigations. *Earth Planet. Sci. Lett.* **61**, 73–84.

Collerson, K. D. and Kamber, B. S. (1999). Evolution of the continents and the atmosphere inferred from Th–U–Nb systematics of the depleted mantle. *Science* **283**, 1519–22.

Cumming, G. L. and Richards, J. R. (1975). Ore lead isotope ratios in a continuously changing Earth. *Earth Planet. Sci. Lett.* **28**, 155–71.

Dasch, E. J., Hedge, C. E. and Dymond, J. (1973). Effect of seawater alteration on strontium isotope composition of deep-sea basalts. *Earth Planet. Sci. Lett.* **19**, 177–83.

Davidson, J. P. (1983). Lesser Antilles isotopic evidence of the role of subducted sediment in island arc magma genesis. *Nature* **306**, 253–6.

Davidson, J. P. (1987). Crustal contamination *versus* subduction zone enrichment: examples from the Lesser Antilles and implications for mantle source compositions of island arc volcanic rocks. *Geochim. Cosmochim. Acta* **51**, 2185–98.

Davies, G. F. (2002). Stirring geochemistry in mantle convection models with stiff plates and slabs. *Geochim. Cosmochim. Acta* **66**, 3125–42.

DePaolo, D. J. (1980). Crustal growth and mantle evolution: inferences from models of element transport and Nd and Sr isotopes. *Geochim. Cosmochim. Acta* **44**, 1185–96.

DePaolo, D. J. and Wasserburg, G. J. (1976). Inferences about magma sources and mantle structure from variations of ^{143}Nd/^{144}Nd. *Geophys. Res. Lett.* **3**, 743–6.

DePaolo, D. J. and Wasserburg, G. J. (1979). Petrogenetic mixing models and Nd–Sr isotopic patterns. *Geochim. Cosmochim. Acta* **43**, 615–27.

Dewey, J. (1980). Episodicity, sequence and style at convergent plate boundaries. In: Strangway, D. W. (Ed.), *The Continental Crust and Its Mineral Deposits. Geol. Assoc. Canada Spec. Pap.* **8**, pp. 553–73.

Dickin, A. P. (1995). *Radiogenic Isotope Geology*, 1st edn. Cambridge University Press.

Dosso, L. and Murthy, V. R. (1980) A Nd isotopic study of the Kerguelen islands: inferences on enriched oceanic mantle sources. *Earth Planet. Sci. Lett.* **48**, 268–76.

Dupré, B. and Allègre, C. J. (1980). Pb–Sr–Nd isotopic correlation and the chemistry of the North Atlantic mantle. *Nature* **286**, 17–22.

Dupré, B. and Allègre, C. J. (1983). Pb–Sr isotope variation in Indian Ocean basalts and mixing phenomena. *Nature* **303**, 142–6.

Eiler, J. M., Farley, K. A., Valley, J. W. *et al.* (1997). Oxygen isotope variations in ocean island basalt phenocrysts. *Geochim. Cosmochim. Acta* **61**, 2281–93.

Eiler, J. M., Farley, K. A., Valley, J. W., Hofmann, A. W. and Stolper, E. M. (1996). Oxygen isotope constraints on the sources of Hawaiian volcanism. *Earth Planet. Sci. Lett.* **144**, 453–68.

Eiler, J. M., Farley, K. A., Valley, J. W., Stolper, E. M., Hauri, E. H. and Craig, H. (1995). Oxygen isotope evidence against bulk recycled sediment in the mantle sources of Pitcairn Island lavas. *Nature* **377**, 138–41.

Ellam, R. M. and Hawkesworth, C. J. (1988). Elemental and isotopic variations in subduction related basalts: evidence for a three component model. *Contrib. Mineral. Petrol.* **98**, 72–80.

Elliot, T., Zindler, A. and Bourdon, B. (1999). Exploring the kappa conundrum: the role of recycling in the lead isotope evolution of the mantle. *Earth Planet. Sci. Lett.* **169**, 129–45.

Farnetani, C. G. and Richards, M. A. (1995). Thermal entrainment and melting in mantle plumes. *Earth Planet. Sci. Lett.* **136**, 251–67.

Faure, G. and Hurley, P. M. (1963). The isotopic composition of strontium in oceanic and continental basalt. *J. Petrol.* **4**, 31–50.

Flower, M. F. J., Schmincke, H. U. and Thompson, R. N. (1975). Phlogopite stability and the ^{87}Sr/^{86}Sr step in basalts along the Reykjanes Ridge. *Nature* **254**, 404–6.

Forte, A. M. and Mitrovica, J. X. (2001). Deep-mantle high-viscosity flow and thermochemical structure inferred from seismic and geodynamic data. *Nature* **410**, 1049–55.

Frei, R. and Rosing, M. T. (2001). The least radiogenic terrestrial leads; implications for the early Archean crustal evolution and hydrothermal–metasomatic processes in the Isua Supracrustal Belt (West Greenland). *Chem. Geol.* **181**, 47–66.

Frey, F. A. and Weis, D. (1995). Temporal evolution of the Kerguelen plume: geochemical evidence from ~38 to 82 Ma lavas forming the Ninetyeast Ridge. *Contrib. Mineral. Petrol.* **121**, 12–28.

Frey, F. A. and Weis, D. (1996). Reply to the Class *et al.* discussion of "Temporal evolution of the Kerguelen plume:

geochemical evidence from ~38 to 82 Ma lavas forming the Ninetyeast Ridge". *Contrib. Mineral. Petrol.* **124**, 104–10.

Galer, S. J. G. and O'Nions, R. K. (1985). Residence time of thorium, uranium and lead in the mantle with implications for mantle convection. *Nature* **316**, 778–82.

Gast, P. W., Tilton, G. R. and Hedge, C. (1964). Isotopic composition of lead and strontium from Ascension and Gough Islands. *Science* **145**, 1181–5.

Halliday, A. N., Davidson, J. P., Holden, P., DeWolf, C., Lee, D-C. and Fitton, J. G. (1990). Trace-element fractionation in plumes and the origin of HIMU mantle beneath the Cameroon Line. *Nature* **347**, 523–8.

Halliday, A. N., Davies, G. R., Lee, D-C. *et al.* (1992). Lead isotope evidence for young trace element enrichment in the oceanic upper mantle. *Nature* **359**, 623–7.

Hanan, B. B. and Graham, D. W. (1996). Lead and helium isotope evidence from oceanic basalts for a common deep source of mantle plumes. *Science* **272**, 991–5.

Hanan, B. B., Kingsley, R. H. and Schilling J.-G. (1986). Pb isotope evidence in the South Atlantic for migrating ridge–hotspot interactions. *Nature* **322**, 137–44.

Hanan, B. B. and Schilling, J.-G. (1997). The dynamic evolution of the Iceland mantle plume: the lead isotope perspective. *Earth Planet. Sci. Lett.* **151**, 43–60.

Harmon, R. S. and Hoefs, J. (1995). Oxygen isotope heterogeneity of the mantle deduced from global ^{18}O systematics of basalts from different geotectonic settings. *Contrib. Mineral. Petrol.* **120**, 95–114.

Harris, C., Bell, J. D. and Atkins, F. B. (1983). Isotopic composition of lead and strontium in lavas and coarse-grained blocks from Ascension Island, South Atlantic – an addendum. *Earth Planet. Sci. Lett.* **63**, 139–41.

Harris, P. G., Hutchison, R. and Paul, D. K. (1972). Plutonic xenoliths and their relation to the upper mantle. *Phil. Trans. Roy. Soc. Lond. A* **271**, 313–23.

Hart, S. R. (1984). A large-scale isotope anomaly in the Southern Hemisphere mantle. *Nature* **309**, 753–7.

Hart, S. R. (1988). Heterogeneous mantle domains: signatures, genesis and mixing chronologies. *Earth Planet. Sci. Lett.* **90**, 273–96.

Hart, S. R., Gerlach, D. C. and White, W. M. (1986). A possible new Sr–Nd–Pb mantle array and consequences for mantle mixing. *Geochim. Cosmochim. Acta* **50**, 1551–7.

Hart, S. R., Hauri, E. H., Oschmann, L. A. and Whitehead, J. A. (1992). Mantle plumes and entrainment: isotopic evidence. *Science* **256**, 517–20.

Hart, S. R., Schilling, J.-G. and Powell, J. L. (1973). Basalts from Iceland and along the Reykjanes Ridge: Sr isotope geochemistry. *Nature Phys. Sci.* **246**, 104–7.

Hauri, E. H., Shimizu, N., Dieu, J. J. and Hart, S. R. (1993). Evidence for hotspot-related carbonatite metasomatism in the oceanic upper mantle. *Nature* **365**, 221–7.

Hauri, E. H., Whitehead, J. A. and Hart, S. R. (1994). Fluid dynamic and geochemical aspects of entrainment in mantle plumes. *J. Geophys. Res.* **99**, 24 275–300.

Hawkesworth, C. J., Hergt, J. M., McDermott, F. and Ellam, R. M. (1991). Destructive margin magmatism and the contributions from the mantle wedge and subducted crust. *Australian J. Earth Sci.* **38**, 577–94.

Hawkesworth, C. J., Norry, M. J., Roddick, J. C. and Vollmer, R. (1979a). ^{143}Nd/^{144}Nd and ^{87}Sr/^{86}Sr ratios from the Azores and their significance in LIL element enriched mantle. *Nature* **280**, 28–31.

Hawkesworth, C. J., O'Nions, R. K. and Arculus, R. J. (1979b). Nd and Sr isotope geochemistry of island arc volcanics, Grenada, Lesser Antilles. *Earth Planet. Sci. Lett.* **45**, 237–48.

Hawkesworth, C. J., O'Nions, R. K., Pankhurst, R. J., Hamilton, P. J. and Evensen, N. M. (1977). A geochemical study of island-arc and back-arc tholeiites from the Scotia Sea. *Earth Planet. Sci. Lett.* **36**, 253–62.

Hawkesworth, C. J., Rogers, N. W., van Calsteren, P. W. C. and Menzies, M. A. (1984). Mantle enrichment processes. *Nature* **311**, 331–3.

Hofmann, A. W. and Hart, S. R. (1978). An assessment of local and regional isotopic equilibrium in the mantle. *Earth Planet. Sci. Lett.* **38**, 44–62.

Hofmann, A. W. and White, W. M. (1980). The role of subducted oceanic crust in mantle evolution. *Carnegie Institute Washington Yearbook* **79**, 477–83.

Hofmann, A. W. and White, W. M. (1982). Mantle plumes from ancient oceanic crust. *Earth Planet. Sci. Lett.* **57**, 421–36.

Jacobsen, S. B. and Wasserburg, G. J. (1979). The mean age of mantle and crustal reservoirs. *J. Geophys. Res.* **84**, 7411–27.

Kamber, B. S. and Collerson, K. D. (1999). Origin of ocean island basalts: a new model based on lead and helium isotope systematics. *J. Geophys. Res.* **104**, 25 479–91.

Kellogg, L. H., Hager, B. H. and van der Hilst, R. D. (1999). Compositional stratification in the deep mantle. *Science* **283**, 1881–4.

Kenyon, P. M. (1990). Trace element and isotopic effects arising from magma migration beneath mid-ocean ridges. *Earth Planet. Sci. Lett.* **101**, 367–78.

Kerr, A. C., Saunders, A. D., Tarney, J., Berry, N. H. and Hards, V. L. (1995). Depleted mantle–plume geochemical signatures: no paradox for plume theories. *Geology* **23**, 843–6.

Kramers, J. D. and Tolstikhin, I. N. (1997). Two terrestrial lead isotope paradoxes, forward transport modelling, core formation and the history of the continental crust. *Chem. Geol.* **139**, 75–110.

Mahoney, J. J., White, W. M., Upton, B. G. J., Neal, C. R. and Scrutton, R. A. (1996). Beyond EM–1: lavas from Afanasy–Nikitin Rise and the Crozet Archipelago, Indian Ocean. *Geology* **24**, 615–18.

Manga, M. (1996). Mixing of heterogeneities in the mantle: effect of viscosity differences. *Geophys. Res. Lett.* **23**, 403–6.

Mattielli, N., Weis, D., Blichert-Toft, J. and Albarède, F. (2002). Hf isotope evidence for a Miocene change in the Kerguelen mantle plume composition. *J. Petrol.* **43**, 1327–39.

McDermott, F., Defant, M. J., Hawkesworth, C. J., Maury, R. C. and Joron, J. L. (1993). Isotope and trace element evidence for three component mixing in the genesis of the North Luzon arc lavas (Philippines). *Contrib. Mineral. Petrol.* **113**, 9–23.

McKenzie, D. (1979). Finite deformation during fluid flow. *Geophys. J. Roy. Astron Soc.* **58**, 689–715.

McKenzie, D. P. and O'Nions, R. K. (1983). Mantle reservoirs and ocean island basalts. *Nature* **301**, 229–31.

Mertz, D. F., Devey, C. W., Todt, W., Stoffers, P. and Hofmann, A. W. (1991). Sr–Nd–Pb isotope evidence against plume–asthenosphere mixing north of Iceland. *Earth Planet. Sci. Lett.* **107**, 243–55.

Michard, A. and Albarède, F. (1985). Hydrothermal uranium uptake at ridge crests. *Nature* **317**, 244–6.

Moreira, M., Doucelance, R., Kurz, M. D., Dupré, B. and Allègre, C. J. (1999). Helium and lead isotope geochemistry of the Azores Archipelago. *Earth Planet. Sci. Lett.* **169**, 189–205.

Morgan, J. P. and Shearer, P. M. (1993). Seismic constraints on mantle flow and topography of the 660-km discontinuity: evidence for whole-mantle convection. *Nature* **365**, 506–11.

Morgan, W. J. (1971) Convection plumes in the lower mantle. *Nature* **230**, 42–3.

Morris, J. D. and Hart, S. R. (1983). Isotopic and incompatible element constraints on the genesis of island arc volcanics: Cold Bay and Amak Islands, Aleutians. *Geochim. Cosmochim. Acta* **47**, 2015–30.

Neal, C. R., Mahoney, J. J. and Chazey, W. J. III (2002). Mantle sources and the highly variable role of continental lithosphere in basalt petrogenesis of the Kerguelen Plateau and Broken Ridge LIP: results from ODP Leg 183. *J. Petrol.* **43**, 1177–205.

Newsome, H. E., White, W. M., Jochum, K. P. and Hofmann, A. W. (1986). Siderophile and chalcophile element abundances in oceanic basalts, Pb isotope evolution and growth of the Earth's core. *Earth Planet. Sci. Lett.* **80**, 299–313.

Norry, M. J. and Fitton, J. G. (1983). Compositional differences between oceanic and continental basic lavas and their significance. In: Hawkesworth, C. J. and Norry, M. J. (Eds.), *Continental Basalts and Mantle Xenoliths.* Shiva, pp. 5–19.

O'Hara, M. J. (1973). Non-primary magmas and dubious mantle plume beneath Iceland. *Nature* **243**, 507–8.

O'Hara, M. J. (1975). Is there an Icelandic mantle plume? *Nature* **253**, 708–10.

O'Hara, M. J. and Mathews, R. E. (1981). Geochemical evolution in an advancing, periodically replenished, periodically tapped, continuously fractionated magma chamber. *J. Geol. Soc. Lond.* **138**, 237–77.

Olson, P. (1984). Mixing of passive heterogeneities by mantle convection. *J. Geophys. Res.* **89**, 425–36.

O'Nions, R. K., Evensen, N. M. and Hamilton, P. J. (1979). Geochemical modelling of mantle differentiation and crustal growth. *J. Geophys. Res.* **84**, 6091–101.

O'Nions, R. K., Evensen, N. M. and Hamilton, P. J. (1980). Differentiation and evolution of the mantle. *Phil. Trans. Roy. Soc. Lond. A* **297**, 479–93.

O'Nions, R. K., Hamilton, P. J. and Evensen, N. M. (1977). Variations in ^{143}Nd/^{144}Nd and ^{87}Sr/^{86}Sr ratios in oceanic basalts. *Earth Planet. Sci. Lett.* **34**, 13–22.

O'Nions, R. K. and Pankhurst, R. J. (1973). Secular variation in the Sr-isotope composition of Icelandic volcanic rocks. *Earth Planet. Sci. Lett.* **21**, 12–21.

Palacz, Z. A. and Saunders, A. D. (1986). Coupled trace element and isotope enrichment in the Cook–Austral–Samoa islands, southwest Pacific. *Earth Planet. Sci. Lett.* **79**, 270–80.

Pearce, J. (1983). The role of sub-continental lithosphere in magma genesis at active continental margins. In: Hawkesworth, C. J. and Norry, M. J. (Eds.), *Continental Basalts and Mantle Xenoliths.* Shiva, pp. 230–49.

Polvé, M. and Allègre, C. J. (1980). Orogenic lherzolite complexes studied by ^{87}Rb$-^{87}$Sr: a clue to understand the mantle convection process? *Earth Planet. Sci. Lett.* **51**, 71–93.

Prinzhofer, A., Lewin, E. and Allègre, C. J. (1989). Stochastic melting of the marble-cake mantle: evidence from local study of the East Pacific Rise at 12° 50′ N. *Earth Planet. Sci. Lett.* **92**, 189–206.

Richard, P., Shimizu, N. and Allègre, C. J. (1976) ^{143}Nd/^{144}Nd, a natural tracer: an application to oceanic basalts. *Earth Planet. Sci. Lett.* **31**, 269–78.

Richter, F. M. and Ribe, N. M. (1979). On the importance of advection in determining the local isotopic composition of the mantle. *Earth Planet. Sci. Lett.* **43**, 212–22.

Ringwood, A. E. (1982). Phase transformations and differentiation in subducted lithosphere: implications for mantle dynamics, basalt petrogenesis, and crustal evolution. *J. Geol.* **90**, 611–43.

Schilling, J.-G. (1973). Iceland mantle plume: geochemical study of Reykjanes Ridge. *Nature* **242**, 565–71.

Schilling, J.-G. and Noe Nygaard, A. (1974). Faeroe–Iceland plume; rare-earth evidence. *Earth Planet. Sci. Lett.* **24**, 1–14.

Shearer, P. M. and Masters, T. G. (1992). Global mapping of topography on the 660-km discontinuity. *Nature* **355**, 791–6.

Smith, H. J., Leeman, W. P., Davidson, J. and Spivack, A. J. (1997). The B isotopic composition of arc lavas from Martinique, Lesser Antilles. *Earth Planet. Sci. Lett.* **146**, 303–14.

Staudigel, H., Park, K-H., Pringle, M. Rubenstone, J. L., Smith, W. H. F. and Zindler, A. (1991). The longevity of the South Pacific isotopic and thermal anomaly. *Earth Planet. Sci. Lett.* **102**, 24–44.

Sun, S. S. (1980). Lead isotopic study of young volcanic rocks from mid-ocean ridges, ocean islands and island arcs. *Phil. Trans. Roy. Soc. Lond. A* **297**, 409–45.

Sun, S. S. (1985). Ocean islands – plums or plumes? *Nature* **316**, 103–4.

Sun, S. S. and Hanson, G. N. (1975). Evolution of the mantle: geochemical evidence from alkali basalt. *Geology* **3**, 297–302.

Sun, S. S., Tatsumoto, M. and Schilling, J.-G. (1975). Mantle plume mixing along the Reykjanes ridge axis: lead isotopic evidence. *Science* **190**, 143–7.

Sushchevskaya, N. M., Ovchinnikova, G. V., Borisova, A. Y., Belyatsky, B. V. and Vasileva, I. M. (1996). Geochemical heterogeneity of the magmatism of the Afanasij Nikitin Rise, northeastern Indian Ocean. *Petrology* **4**, 119–36.

Tatsumoto, M. (1966). Genetic relations of oceanic basalts as indicated by lead isotopes. *Science* **153**, 1094–101.

Tatsumoto, M. (1978). Isotopic composition of lead in oceanic basalt and its implication to mantle evolution. *Earth Planet. Sci. Lett.* **38**, 63–87.

Tatsumoto, M. (1988). U, Th and Pb abundances in Hawaiian xenoliths. *Conf. Origin of the Earth.* Lunar & Planetary Institute, pp. 89–90.

Tatsumoto, M., Knight, R. J. and Allègre, C. J. (1973). Time differences in the formation of meteorites as determined from the ratio of lead-207 to lead-206. *Science* **180**, 1279–83.

Thirlwall, M. F. (1997). Pb isotopic and elemental evidence for OIB derivation from young HIMU mantle. *Chem. Geol.* **139**, 51–74.

Thirlwall, M. F., Graham, A. M., Arculus, R. J., Harmon, R. S. and Macpherson, C. G. (1996). Resolution of the effects of crustal assimilation, sediment subduction, and fluid transport in island arc magmas: Pb–Sr–Nd–O isotope geochemistry of Grenada, Lesser Antilles. *Geochim. Cosmochim. Acta* **60**, 4785–810.

Thirlwall, M. F., Upton, B. G. J. and Jenkins, C. (1994). Interaction between continental lithosphere and the Iceland plume – Sr–Nd–Pb isotope geochemistry of Tertiary basalts, NE Greenland. *J. Petrol.* **35**, 839–79.

Turcotte, D. L. and Oxburgh, E. R. (1967). Finite amplitude convective cells and continental drift. *J. Fluid. Mech.* **28**, 29–42.

Turner, S., Hawkesworth, C., van Calsteren, P., Heath, E., Macdonald, R. and Black, S. (1996). U-series isotopes and destructive plate margin magma genesis in the Lesser Antilles. *Earth Planet. Sci. Lett.* **142**, 191–207.

Uyeda, S. (1982). Subduction zones: an introduction to comparative subductology. *Tectonophysics* **81**, 133–59.

van der Hilst, R. D. and Karason, H. (1999). Compositional heterogeneity in the bottom 1000 kilometers of Earth's mantle: toward a hybrid convection model. *Science* **283**, 1885–8.

van der Hilst, R. D., Widiyantoro, S. and Engdahl, E. R. (1997). Evidence for deep mantle circulation from global tomography. *Nature* **386**, 578–84.

van Keken, P. E., Hauri, E. H. and Ballentine, C. J. (2002). Mantle mixing: the generation, preservation, and destruction of chemical heterogeneity. *Ann. Rev. Earth Planet. Sci.* **30**, 493–525.

van Keken, P. E. and Zhong, S. (1999). Mixing in a 3D spherical model of present-day mantle convection. *Earth Planet. Sci. Lett.* **171**, 533–47.

Vidal, P. and Dosso, L. (1978). Core formation: catastrophic or continuous? Sr and Pb isotope geochemistry constraints. *Geophys. Res. Lett.* **5**, 169–72.

Weaver, B. L. (1991). The origin of ocean island basalt end-member compositions: trace element and isotopic constraints. *Earth Planet. Sci. Lett.* **104**, 381–97.

White, W. M. (1981). *European Colloquium of Geochronology, Cosmochronology and Isotope Geology VII*, meeting abstract.

White, W. M. (1985). Sources of oceanic basalts: radiogenic isotopic evidence. *Geology* **13**, 115–18.

White, W. M. (1993). ^{238}U/^{204}Pb in MORB and open system evolution of the depleted mantle. *Earth Planet. Sci. Lett.* **115**, 211–26.

White, W. M. and Dupré, B. (1986). Sediment subduction and magma genesis in the Lesser Antilles: isotopic and trace element constraints. *J. Geophys. Res.* **91**, 5927–41.

White, W. M., Dupré, B. and Vidal, P. (1985). Isotope and trace element geochemistry of sediments from the Barbados Ridge–Demerara Plain region, Atlantic Ocean. *Geochim. Cosmochim. Acta* **49**, 1875–86.

White, W. M. and Hofmann, A. W. (1982). Sr and Nd isotope geochemistry of oceanic basalts and mantle evolution. *Nature* **296**, 821–5.

White, W. M., Schilling, J.-G. and Hart, S. R. (1976). Evidence for the Azores mantle plume from strontium isotope geochemistry of the Central North Atlantic. *Nature* **263**, 659–63.

White, W. M., Tapia, M. D. M. and Schilling, J.-G. (1979). The petrology and geochemistry of the Azores islands. *Contrib. Mineral. Petrol.* **69**, 201–13.

Widom, E., Carlson, R. W., Gill, J. B. and Schmincke, H.-U. (1997). Th–Sr–Nd–Pb isotope and trace element evidence for the origin of the São Miguel, Azores, enriched mantle source. *Chem. Geol.* **140**, 49–68.

Widom, E., Hoernle, K. A., Shirey, S. B. and Schmincke, H. U. (1999). Os isotope systematics in the Canary Islands and Madeira: lithospheric contamination and mantle plume signatures. *J. Petrol.* **40**, 279–96.

Woodhead, J. D., Greenwood, P., Harmon, R. S. and Stoffers, P. (1993). Oxygen isotope evidence for recycled crust in the source of EM-type ocean island basalts. *Nature* **362**, 809–13.

Wyllie, P. J. (1984). Constraints imposed by experimental petrology on possible and impossible magma sources and products. *Phil. Trans. Roy. Soc. Lond. A* **310**, 439–56.

Zindler, A. and Hart, S. R. (1986). Chemical geodynamics. *Ann. Rev. Earth Planet. Sci.* **14**, 493–571.

Zindler, A., Jagoutz, E. and Goldstein, S. (1982). Nd, Sr and Pb isotopic systematics in a three-component mantle: a new perspective. *Nature* **298**, 519–23.

Zindler, A., Staudigel, H. and Batiza, R. (1984). Isotope and trace element geochemistry of young Pacific seamounts: implications for the scale of upper mantle heterogeneity. *Earth Planet. Sci. Lett.* **70**, 175–95.

7 Isotope geochemistry of continental rocks

Oceanic volcanics, which erupted through thin, young lithosphere, provide a window on the asthenosphere and deep mantle. In contrast, continental basalts and mantle xenoliths, emplaced through thick, old lithosphere, may tell us about the nature of the deep crust and the lithospheric mantle, as well as the evolution of magmas during their ascent to the surface. Isotopic data are a powerful tool for such studies, firstly because of their ability to date geological events, and secondly because of their usefulness as tracers of complex mixing processes.

Unfortunately, continental igneous rocks are difficult to interpret. This is because they can derive an enriched elemental and isotopic signature from three possible sources: mantle plumes, sub-continental lithosphere, and the crust. Resolving these components from one another in continental volcanics and plutons has been a major subject of discussion in geochemistry for several decades. Much progress has been made, but the large number of variables tends to make each case a unique example; or, as Read (1948) put it, there are 'granites and granites'. This makes a generalised approach to continental magmas difficult, and forces us to adopt a case-study approach as an attempt to illustrate underlying principles.

Mantle xenoliths provide a more direct means of sampling the sub-continental lithosphere. Their texture provides evidence of a solid source, while the peridotite (i.e. lherzolite) petrology of the commonest types is readily distinguished from crustal xenoliths (which will not be dealt with here). Therefore, our approach in this chapter will be firstly to study the lithospheric mantle by means of xenoliths, secondly to examine crustal contamination processes, and lastly to look at some classic case studies on the genesis and evolution of continental igneous rocks.

7.1 Mantle xenoliths

The sub-continental lithosphere is distinguished from the underlying asthenosphere by its non-convecting, rigid state. Hence it was termed the 'tectosphere' by Jordan (1975; 1978). Jordan argued from seismic and heat-flow evidence that this tectosphere was 200–300 km thick under shield areas. Evidence from diamond inclusions in garnets (section 4.2.1) suggests a similar thickness of continental lithosphere in the Archean.

Alkaline magmas, kimberlites and carbonatites in many continental areas bring up peridotite xenoliths (also called nodules) from great depths. On the basis of their mineral chemistry, these must be samples of the mantle rather than the crust. Maaloe and Aoki (1977) analysed the major element composition of numerous such xenoliths in an attempt to estimate the bulk upper-mantle composition. They recognised compositional differences between spinel lherzolite xenoliths, derived from Proterozoic and younger lithosphere, and garnet lherzolites, derived from Archean cratons. Both types of xenolith had overlapping ranges of MgO content, but the (Archean) garnet peridotites had distinctly lower FeO contents. In view of their more exotic history, we will direct our main attention to this group.

The world's classic mantle xenolith suites come from South Africa, where they are obtained as by-products of diamond mining. Within this collection, two main textural types are observed: granular and sheared. Harte (1983) proposed that the former were samples of the lithosphere, whereas the latter, which are more often found around the margins of the Kaapvaal craton, were derived from the convecting asthenosphere. Of the granular types, Harte further sub-divided samples exhibiting obvious or 'modal' metasomatism (indicated by hydrous or other exotic minerals) from the more normal garnet peridotites. The latter samples came from the centre of the Kaapvaal craton, at Northern Lesotho and Bultfontein (hence NLB type), and were regarded as typical samples of the mantle lithosphere.

Various explanations have been proposed to account for the differing FeO contents of spinel and garnet peridotites. However, the most satisfactory was developed by Richter (1988). He proposed that garnet peridotites were residues of komatiite extraction in the Archean, and that the large degrees of melting associated with this process caused FeO depletion. This in turn lowered the density of the residuum, relative to fertile mantle, and allowed its stabilisation as sub-continental lithosphere. This material reached sufficient thicknesses (>150 km) for crystallisation of diamond to occur at its base. In contrast, Proterozoic lithosphere was stabilised only by conductive cooling of the upper mantle (a mechanism that would not have been possible in the hotter Archean mantle). Proterozoic mantle lithosphere may be residual from basalt extraction, or might not have been depleted by melt extraction at all; hence it has higher levels of FeO and other fertile components. The thickness of lithosphere formed in this way is insufficient to render diamond stable, while its high density makes it susceptible to delamination from the base of the crust during orogenic shortening of the lithosphere.

The major element compositional differences between garnet and spinel peridotite xenoliths, described above, are paralleled by isotopic differences. Figure 7.1 shows a compilation of Sr and Nd isotope data for the two groups (Hawkesworth *et al.*, 1990), which define fairly distinct fields. Spinel peridotite data are derived mainly from separated clinopyroxene (cpx), but garnet peridotite data are based on a combination of separated-mineral and whole-rock analyses. The latter are less reliable because they are susceptible to contamination by the host magma (usually kimberlite in the case of garnet peridotite).

Menzies (1989) adopted a terminology for interpreting mantle xenoliths (Fig. 7.2) that was based on the DMM, EMI and EMII end-members proposed for OIB sources by Zindler and Hart (section 6.4.2). He did not propose that the processes which formed these types of lithospheric 'domains' were necessarily the same as those which formed OIB end-members, but the use of such a terminology may imply a genetic relationship. Zindler and Hart did in fact propose (section 6.4.2) that the HIMU and EMI components (forming the LoNd array) were derived from recycled mantle lithosphere. However, the EMI component does not necessarily bear a direct relationship to any given segment of lithosphere. Furthermore, such a model does not fit well

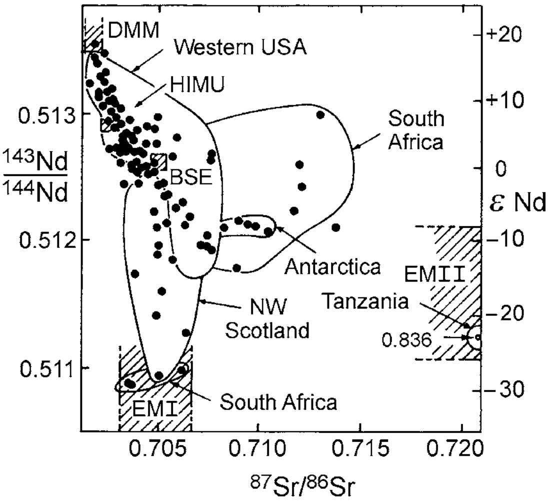

Fig. 7.2. Nd *versus* Sr isotope diagram, showing compositional fields for xenolith suites from different provinces, relative to enriched-mantle components identified in OIB sources (hatched fields). After Menzies (1989).

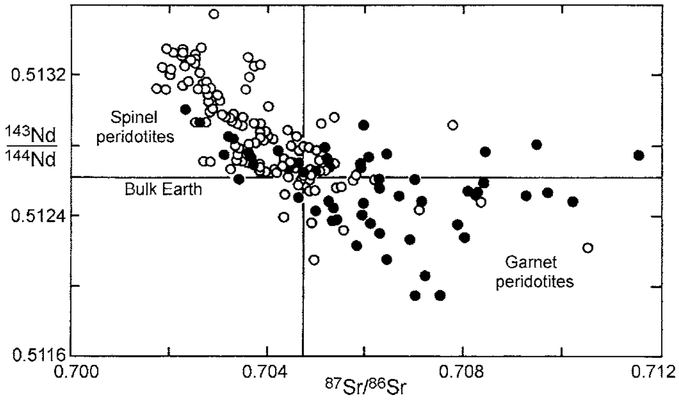

Fig. 7.1. Nd *versus* Sr isotope diagram, showing the largely distinct compositional fields of spinel peridotite (○) and garnet peridotite (●). After Hawkesworth *et al.* (1990).

to the EMII component of the OIB source, which is widely attributed to sediment subduction. Hence, the present author suggests the use of different names for domain types in plume sources and the lithosphere.

7.1.1 Mantle metasomatism

Spinel peridotite data in Fig. 7.1 are generally depleted relative to the Bulk Earth composition. Therefore, they may represent fairly normal samples of the upper mantle. However, garnet peridotites generally fall in the enriched quadrant relative to Bulk Earth, despite the fact that they are interpreted as residues of komatiite extraction. This demands a secondary enrichment process, which could be caused either by silicate melts, or by hydrous or carbonaceous fluids. Only the last two are examples of metasomatism in the strict sense, but, typically, mantle enrichment is regarded as more or less synonymous with mantle metasomatism.

Dawson and Smith (1977) described a suite of mafic xenoliths from kimberlites such as Bultfontein, whose hydrous mineralogy marked them as relics of ancient metasomatising fluids. These nodules, sometimes described as glimmerite, are characterised by the presence of phlogopite mica, together with various other hydrous minerals. Dawson and Smith distinguished an important sub-group of these nodules with a characteristic mineral assemblage of mica–amphibole–rutile–ilmenite–diopside, which they dubbed the 'MARID' suite. They suggested that these MARID xenoliths might have crystallised from a pegmatitic magmatic fluid, chemically similar to kimberlite, which would be capable of metasomatising its peridotite wall rocks.

This model was developed by Jones *et al.* (1982), who suggested that peridotite nodules from Bultfontein had been metasomatised by a fluid that, although not exactly like the parent of the MARID suite, was related to it in some way. This metasomatic process is recorded by different peridotite lithologies, which form a series. Starting from garnet peridotite, this progresses through garnet–pargasite peridotite and phlogopite peridotite to phlogopite–K-richterite peridotite in a suite represented as GP–GPP–PP–PKP (Erlank *et al.*, 1987).

Having established the role of mantle metasomatism in generating the incompatible-element enrichments of peridotite xenoliths, another important question is the timing of this process. Kramers (1979) analysed the Pb isotope composition of sulphide inclusions in diamonds (and also cpx from eclogite and peridotite xenoliths) in several Cretaceous kimberlite pipes. Both inclusion and cpx data lay close to a 2.5-Byr isochron line (Fig. 7.3), implying that diamonds and xenoliths are cogenetic, and that mineralogical heterogeneity has been preserved in the South African sub-continental lithosphere since the Archean. In particular, the very unradiogenic composition of the diamonds, which yield Pb model ages of over 2 Byr, would be very difficult to explain in terms of any recent metasomatic event. In contrast, Pb isotope compositions in other 'fertile' peridotites and cpx megacrysts were interpreted as evidence of fairly recent disturbance.

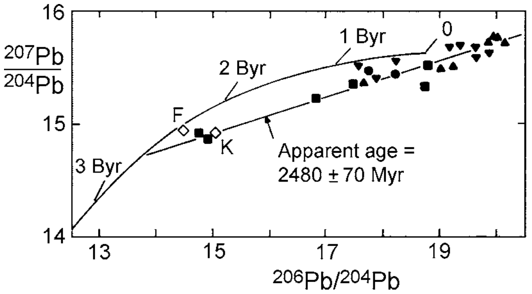

Fig. 7.3. Pb–Pb isochron diagram for nodules from South African kimberlites: (◇) = sulphide inclusions in diamonds (F = Finsch mine, K = Kimberley); filled symbols are for cpx from peridotite and cpx megacrysts (different symbols signify different mines). After Kramers (1979).

Menzies and Murthy (1980) analysed the Sr and Nd isotope compositions of diopsides in micaceous garnet lherzolite nodules from South African kimberlite pipes (Bultfontein and Kimberley). The diopsides exhibited a strong inverse correlation on the Sr–Nd isotope diagram (Fig. 7.4). This was attributed by Menzies and

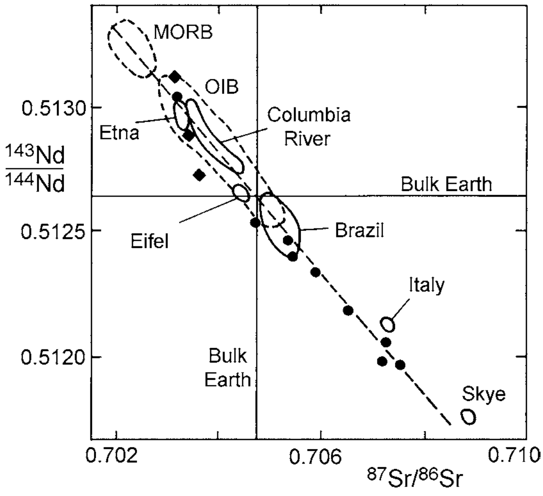

Fig. 7.4. Plot of Nd *versus* Sr isotope ratios for diopsides from South African kimberlite nodules (●), relative to the mantle array of oceanic basalts: (◆) = whole-rock peridotites. After Menzies and Murthy (1980).

Murthy to gross mantle heterogeneity, randomly sampled by kimberlite magmas. They suggested that these signatures were generated by an ancient metasomatic event, probably related to an upwelling mantle plume, which caused LIL-element enrichment of the mantle lithosphere.

Hawkesworth *et al.* (1983) estimated from Nd isotope data that the ancient enrichment event postulated by Menzies and Murthy probably occurred about 1–4 Byr ago. However, the Rb/Sr ratios of the analysed diopsides (and, indeed, any mantle diopsides) are much too low to 'support' their observed ^{87}Sr/^{86}Sr compositions (i.e. generate the required extra amount of ^{87}Sr by *in situ* decay of ^{87}Rb in the required time). This is demonstrated by the clustering of these points near the *y* axis in Fig. 7.5. Therefore, Hawkesworth *et al.* argued that the diopsides must have crystallised in a recent event, presumably during secondary metasomatism of the enriched mantle which was generated by the ancient metasomatic event. The enhanced Sr isotope ratios cannot be generated by contamination with the host kimberlite magma itself, because the latter has unradiogenic ^{87}Sr.

On the Rb–Sr isochron diagram in Fig. 7.5, whole-rock analyses of (garnet-free) phlogopite-bearing and K-richterite-bearing peridotites (PP and PKP) define a linear array with a slope age of 150 Myr. Since these radiogenic Sr signatures in the nodules could not be derived from the host kimberlite, Hawkesworth *et al.* attributed the array to a metasomatic event about 150 Myr ago, possibly associated with Karoo flood-basalt magmatism. In contrast, phlogopites separated from Bultfontein peridotites yield a well-fitted Rb–Sr mineral isochron with an age of 84 Myr (Kramers *et al.*, 1983), which is close to the emplacement age of 90 Myr determined from U–Pb data. However, this was regarded as a metamorphic age, reflecting the opening of mineral systems during the thermal event associated with kimberlite emplacement.

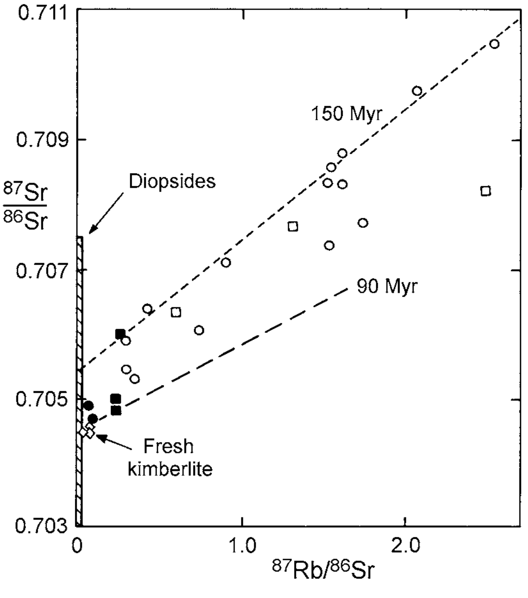

Fig. 7.5. Rb–Sr isochron diagram for South African kimberlite nodules, showing diopside field (hatched) relative to kimberlite host (◇) and nodules of various lithologies: (●) = garnet peridotite; (■) = garnet–pargasite peridotite; (□) = phlogopite peridotite; (○) = phlogopite–K-richterite peridotite. After Hawkesworth *et al.* (1983).

Kimberlites are actually known to have two distinct isotopic signatures, termed Group I and Group II, respectively (section 7.3.1). As noted above, the (Group-I) kimberlite host of the peridotite nodules was ruled out as the metasomatising agent because of its unradiogenic Sr signature. Therefore, Erlank *et al.* (1987) considered the possibility that the Sr signatures found in the peridotite nodules could have been generated by metasomatic fluids related to the more-radiogenic Group-II kimberlites. A compilation of Sr and Pb isotope data for kimberlites, MARID xenoliths and metasomatised peridotite shows that all three suites form a single array with negative slope, which could be a mixing line (Fig. 7.6). However, several problems led Erlank *et al.* to reject this model. The most important

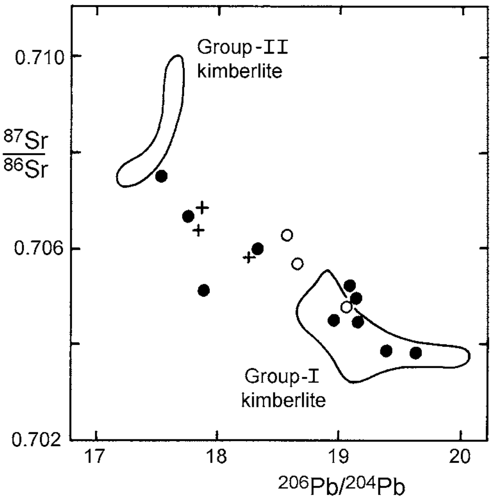

Fig. 7.6. Plot of initial Sr isotope ratio at 90 Myr (kimberlite emplacement age) against Pb isotope ratio for PKP whole-rocks (+), minerals from MARID xenoliths (○) and minerals from other Kimberley peridotites (●), compared with the fields for Group-I and -II kimberlites. After Erlank *et al.* (1987).

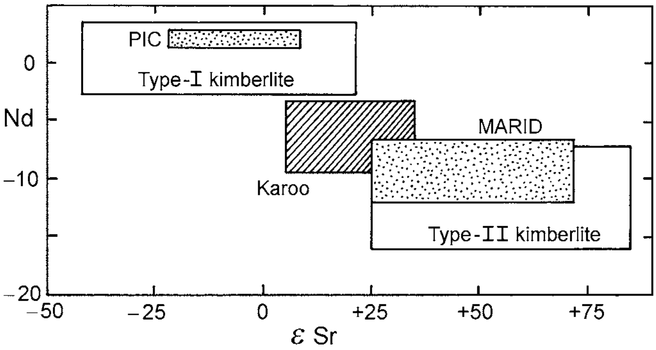

Fig. 7.7. Plot of ε Nd *versus* ε Sr at 90 Myr to show resemblances between the isotope signatures of various types of kimberlite magmas and glimmerite nodules. After Grégoire *et al.* (2002).

of these problems was an apparent lack of similarity in trace-element signatures of the metasomatised peridotites, MARID xenoliths and kimberlite magmas.

This problem was revisited by Grégoire *et al.* (2002), who identified another sub-group of richterite (amphibole)-free glimmerites with an assemblage characterised by phlogopite mica, minor rutile, ilmenite and diopsitic cpx. Grégoire *et al.* named these 'PIC' (phlogopite–ilmenite–cpx) xenoliths, although 'MID' (mica–ilmenite–diopside) would have been more consistent with the established term MARID. However, the important point is that the PIC xenoliths have isotope signatures resembling those of Group-I kimberlites. Grégoire *et al.* also argued that there were sufficient trace-element resemblances between the two respective suites of peridotites, glimmerites and kimberlites to suggest that mantle metasomatism in the Kimberley area was caused by fluids related to the two recognised kimberlite magma groups rather than the Karoo volcanism. In addition to the resemblances in Fig. 7.6, these similarities can also be seen on a Sr–Nd isotope plot (Fig. 7.7). It remains to be seen whether this simple unified model will bear detailed scrutiny.

7.2 Crustal contamination

Many continental igneous rocks have enriched chemical and isotopic signatures similar to those discussed in the previous section. However, the critical question is whether these signatures were inherited from the mantle or the crust. In principle, isotopic methods are ideal for solving this problem, since they are not upset by the crystal-fractionation processes which affect most magmas during ascent and emplacement. However, the high degrees of enrichment which can occur in plume or lithospheric mantle sources may generate isotopic signatures similar to those of the crust. Hence it has been argued (e.g. Thirlwall and Jones, 1983; Hawkesworth *et al.*, 1984) that mantle and crustal sources cannot be distinguished simply on the basis of 'isotopic discriminant diagrams' in which each component has a unique field. Instead, crustal or mantle contributions to magmatism must be recognised by observing the products of *processes* such as magma mixing and crustal assimilation.

Philosophically, one can examine contamination processes in two ways: using a predictive model (e.g. DePaolo, 1981a) or an inversion technique (e.g. Mantovani and Hawkesworth, 1990). In the former, we set conditions and then examine consequences. In the latter, we examine products and attempt to reconstruct the original conditions. The predictive model is well suited to two-component mixing processes, such as progressive contamination of a single magma batch by wall-rock assimilation. Some examples of such models will be examined below, followed by an examination of crustal melting processes pertinent to crustal-contamination models. However, volcanic lava piles often involve multi-component mixing. These processes are more difficult to examine using predictive models, because of the plethora of possible mixing scenarios. Therefore, it is more effective to model such suites using the inversion approach, bearing in mind the predictive models already developed for single magma batches. This approach will be illustrated using the classic British Tertiary Igneous Province as a case study.

7.2.1 Two-component mixing models

In its simplest form, contamination of mantle-derived magma by the continental crust can be regarded as a process of two-component mixing. However, magma–crust mixing processes usually have more than one degree of freedom (such as the compositions and proportions of mixed components). Therefore, to evaluate mixing relations adequately, it is usually necessary to apply two or more measured variables to the problem. These variables are usually isotope ratios, elemental ratios, and elemental abundances. In the context of isotope geology, it is logical to begin by examining the behaviour of isotopic tracers as a function of the elemental concentration of the same element. Therefore, we will begin by studying initial $^{87}Sr/^{86}Sr$ ratios as a function of Sr concentration.

Mixing of components with different isotopic and elemental compositions yields a hyperbolic curve on a diagram of initial $^{87}Sr/^{86}Sr$ ratio against Sr concentration (Fig 7.8a). Ideally, initial Sr isotope ratios should be plotted against the abundance of ^{86}Sr, since the total concentration of strontium is slightly perturbed by variations in ^{87}Sr. This would apply to old rocks, for which a large age correction is necessary in order to obtain the initial ratio. However, the decay constant of Rb is so low that ^{88}Sr makes up the bulk of strontium in most rocks. Therefore the abundance of ^{86}Sr can be approximated by total Sr without introducing significant errors. (This is not so for Pb in old rocks, where radiogenic Pb can easily swamp the non-radiogenic component.)

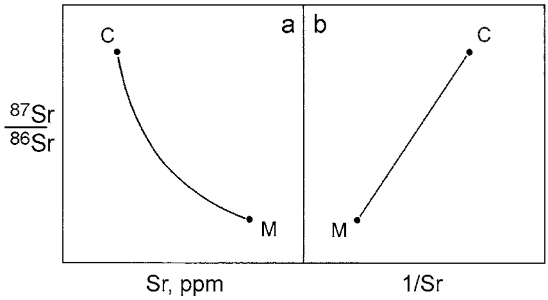

Fig. 7.8. Schematic illustration of two-component mixing on plots of Sr isotope ratio against (a) Sr concentration and (b) 1/Sr: C = crustal end-member; M = mantle-derived end-member.

A bivariate diagram for two ratios with common denominators must yield linear mixing lines. Therefore the hyperbolic mixing curve of Fig. 7.8a can be transformed into a straight line (Fig. 7.8b) by plotting the initial $^{87}Sr/^{86}Sr$ ratio against 1/Sr (approximating $1/^{86}Sr$). Briquet and Lancelot (1979) used this format to examine contamination and fractionation processes in a 'selective-contamination' model (Fig. 7.9), which envisages two-component mixing between a primary basic magma and a hypothetical Sr-rich extract from the crust. Following the contamination process, plagioclase fractionation may cause the Sr content of the magma to fall as it evolves to dacitic and then rhyolitic compositions (Fig. 7.9a). If these contamination and fractionation steps were repeated sequentially then they would create the effect seen in Fig. 7.9b. If the steps become very small, the result is simultaneous fractionation and contamination (Fig. 7.9c). However, Briquet and Lancelot's 'selective' model is probably not the most realistic for magma contamination, since Nd isotope evidence suggests that most contamination is by crustal melts (e.g. Thirlwall and Jones, 1983).

Crustal melting and assimilation is an endothermic process. If the magma is on or below the liquidus then it can obtain heat to power melting only by itself undergoing fractional crystallisation. Hence, we may expect these two processes to be coupled into a mechanism that DePaolo (1981a) termed 'assimilation fractional crystallisation' (AFC). In this model, the effect of fractionation on the mixing trajectory will depend on the relative importance of assimilation and fractional crystallisation, and also on the crystal–liquid bulk distribution coefficient (D) pertaining at the time.

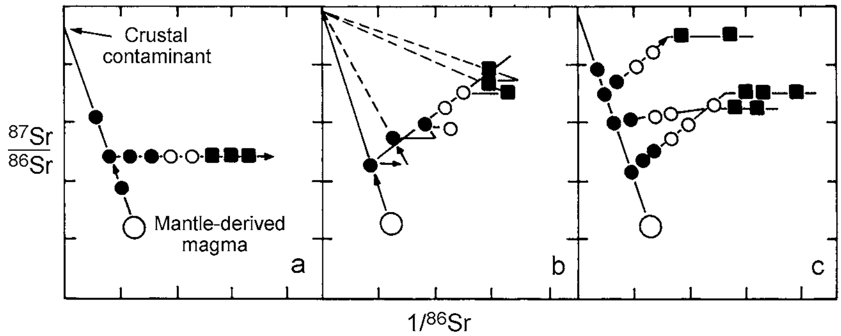

Fig. 7.9. Schematic modelling of selective Sr contamination and fractionation of magmas on plots of Sr isotope ratio against 1/Sr: (a) contamination followed by fractionation; (b) sequential contamination and fractionation events; and (c) simultaneous contamination and fractionation, followed by pure fractionation. After Briquet and Lancelot (1979).

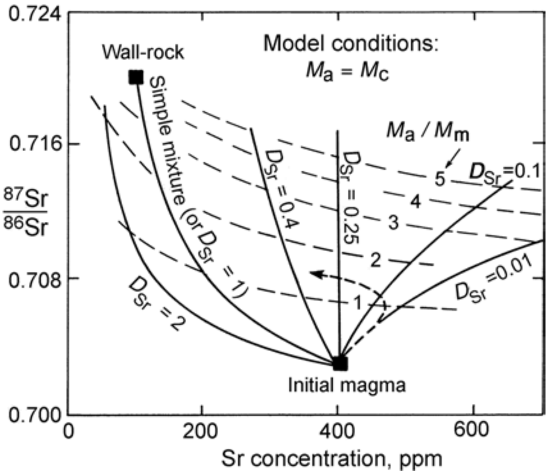

Fig. 7.10. Plot of Sr isotope ratio against concentration to show the effect of the solid/liquid bulk distribution coefficient (D_{Sr}) during the process of assimilation–fractional crystallisation (AFC) by a basic magma. For discussion, see the text. After DePaolo (1981a).

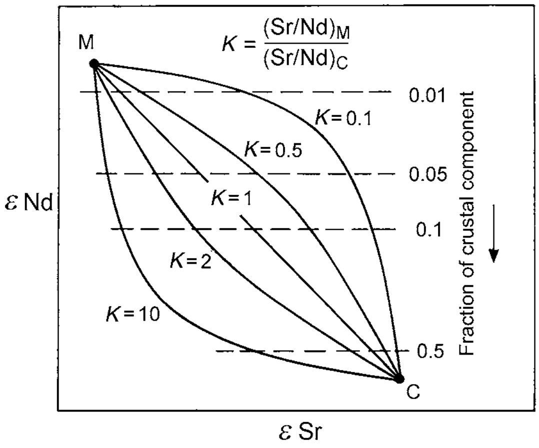

Fig. 7.11. Schematic illustration of two-component mixing on a plot of ε Nd *versus* ε Sr. M and C are mantle-derived and crustal end-members. *K* = Sr/Nd ratio in mantle-derived relative to crustal end-member. Normally *K* is between 2 and 10. After DePaolo and Wasserburg (1979a).

To illustrate these effects, Fig. 7.10 shows calculated mixing lines for various D_{Sr} values at increasing mass fractions of assimilate (M_a) relative to initial magma (M_m), for a fixed proportion of assimilation relative to crystallisation (M_a/M_c). (A smaller amount of fractionation relative to assimilation will cause less deviation from the simple mixing line; a larger relative amount of fractionation will cause more deviation.) When plagioclase joins the crystallising assemblage, this will have a very dramatic effect on D_{Sr} values, changing strontium from an incompatible element ($D_{Sr} \ll 1$) to a compatible element ($D_{Sr} > 1$) in the crystallising material. This may cause a magma to follow the bold dashed curve in Fig. 7.10 during its evolution.

The Sr *versus* Nd isotope diagram provides a useful means for assessing crustal-contamination models. DePaolo and Wasserburg (1979a) showed that simple two-component mixing on this diagram gives rise to hyperbolae whose trajectories depend on the relative Sr/Nd concentration ratio in the two end-members (Fig. 7.11). For the special case in which the the Sr/Nd ratio is the same in both end-members, the mixing line is straight. When the mantle-derived component (M) has a higher Sr/Nd ratio, Nd compositions are more readily affected by contamination than Sr compositions, yielding a concave-upward curve ($K > 1$). This is the normal situation when the mantle-derived component is more basic than the crustal end-member (whose Sr content has been lowered by plagioclase fractionation in its previous history). However, contamination by very-plagioclase-rich crust could yield a convex-upward curve ($K < 1$).

7.2.2 Melting in natural and experimental systems

The isotopic composition of a mantle-derived magma undergoing crustal contamination may be fairly predictable, but the composition of possible crustal melts is much more poorly constrained. Therefore several studies have been conducted on melting processes, both in the laboratory and in 'natural laboratories' in the field. Most of these studies have involved the melting of granitoid rocks, since this is believed to be the most important component of rock available for melting in the continental crust. A few of these studies will be reviewed here.

One of the first modern studies of this problem was made by Maury and Bizouard (1974) on partially melted biotite gneiss xenoliths in a basanitic melt from southern France. One of the most important findings was that more than one initial melt composition was present (represented by quenched glasses). The two principal melt compositions were a colourless rhyolitic glass resulting from melting on quartz–feldspar grain boundaries and a brown latite glass resulting from melting on biotite–feldspar grain boundaries. Most subsequent studies have confirmed these findings, but since the colourless and brown glasses tend to mix if the melting interval is prolonged, the 'starting compositions' have often not been found in sufficient quantity for geochemical analysis. For example, two studies on melting of the Sierra Nevada granite batholith at Rattlesnake Gulch by a trachyandesite plug (Kaczor *et al.*, 1988; Tommasini and Davies, 1997) both identified pale-brown and dark-brown melt glasses. However, it was not possible to separate the initial colourless and brown glasses for geochemical analysis.

A purely laboratory-based melting study was performed by Hammouda *et al.* (1996) on a synthetic mixture of plagioclase and phlogopite (i.e. Mg biotite). Preferential melting of the phlogopite was observed above 1200 °C. Since the phlogopite had been doped with radiogenic Sr to simulate the effects of Rb decay in an old granite, the melt glasses were much more radiogenic than the bulk rock. This experiment could simulate the melting behaviour of a tonalitic crustal rock, suggesting that partial melting of such material could cause 'selective contamination' of mafic magmas with radiogenic Sr. However, it had previously been suggested by Thompson *et al.* (1982) that the small amounts of fusible granitic rock in a crustal section would be more important in promoting crustal contamination of basaltic magmas than the relatively refractory tonalite component.

A combined field-based and laboratory-based melting study of granitic rocks was carried out by Knesel and Davidson (1999). The field component involved melting of the Sierra Nevada granite in the vicinity of a Pleistocene-age olivine basalt at Tungsten Hills, whereas the laboratory-based component involved melting relatively large 45 g cubes of a 1200-Myr-old Precambrian granite. Sr isotope results from the latter study (Fig. 7.12) revealed a progressive evolution in the composition of brown and colourless melt glasses as the melting temperature was increased (for a fixed 24-h duration). The isotope ratios of the two melts were initially very distinct but evolved towards the whole-rock composition of the source. In contrast, the Sr abundances of the two melts started relatively close to the whole-rock value, but evolved away from it, reflecting increasing Sr enrichment as melting progressed. This was attributed to the evolution of the restite towards a strontium-free quartz residue.

A somewhat different picture was obtained when the bulk composition of the experimental glass was calculated from the compositions and abundances of the two components. When the Sr isotope ratio of the bulk glass was plotted against the melt fraction, a monotonic decrease in (initial) Sr isotope ratio was observed as a function of melt fraction (Fig. 7.13a). Such a pattern was also observed in the field-based data from Tungsten Hills and Rattlesnake Gulch (Knesel and Davidson, 1999; Tommasini and Davies, 1997) shown in Fig. 7.13 (parts b and c).

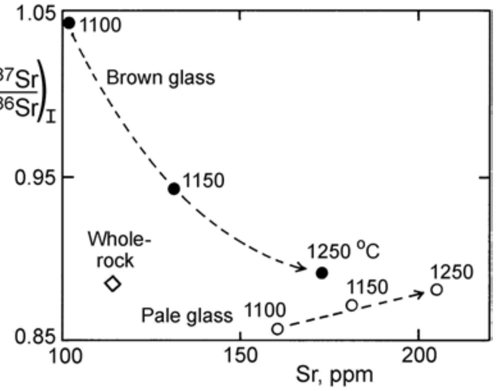

Fig. 7.12. Plot of Sr isotope ratio against concentration, showing the effect of increasing melting temperature (1100–1150–1250 °C) on colourless and brown melt glasses generated in laboratory experiments on a Precambrian granite. After Knesel and Davidson (1999).

The laboratory experiments described above were all performed at atmospheric pressure, and therefore under anhydrous conditions which do not accurately represent crustal melting in the deep crust. Therefore, Knesel and Davidson (2002) repeated the experiments on the same granite sample at a confining pressure of 600 MPa (6 kbar), equivalent to a depth of about 20 km within the Earth's crust. These conditions permitted runs of longer duration (up to 2 months), and also allowed the melt products to be 'extracted' from the source into a vacant pore space created by a bed of industrial diamonds at one end of the sample charge. The sample itself consisted of finely crushed granite (75–100 μm) that was intended to preserve the mineralogical proportions of the original rock. The only water in the system was derived from the hydrous minerals of the source rock.

Results of this experiment are shown in Fig. 7.14 for three melting temperatures in the range 850–950 °C. The surprising thing about these results is that, unlike the previously reported field and laboratory experiments, the initial melt was *less* radiogenic than the source, although it eventually reached Sr isotope equilibrium with the whole-rock composition. In contrast, an experiment at 1000 °C (not shown) gave results similar to the previous experiments, with an initial melt more radiogenic than the whole-rock. The unradiogenic Sr composition of the low-temperature melts was attributed to the melting of plagioclase in a

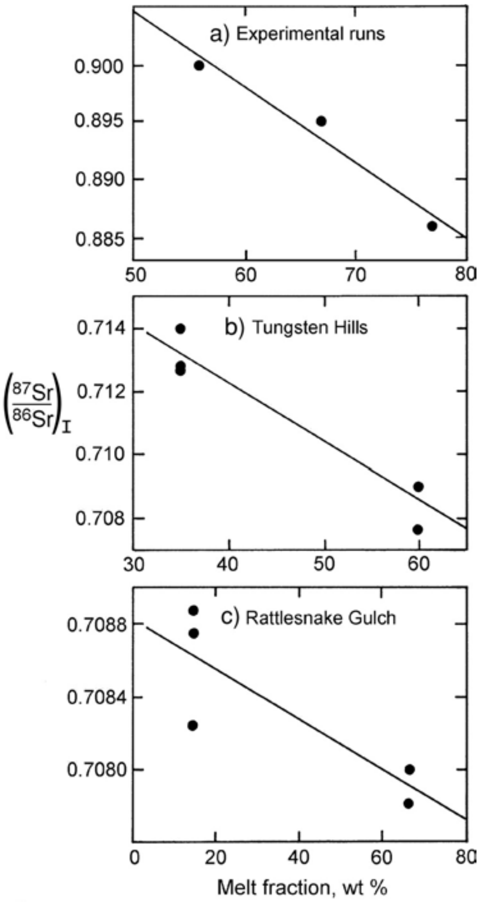

Fig. 7.13. Plots of initial Sr isotope compositions of bulk melts as a function of melt fraction in three studies of granitic melting described in the text. After Knesel and Davidson (1999).

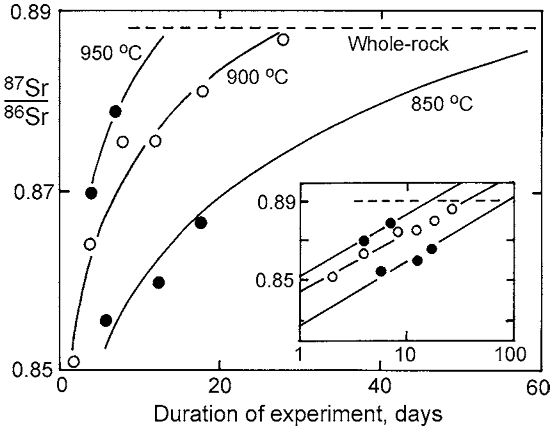

Fig. 7.14. Plot of Sr isotope ratio of granitic melts generated in piston–cylinder experiments over various durations and at various temperatures. (Pressure = 6 kbar.) The inset shows experimental duration on a log scale. After Knesel and Davidson (2002).

reaction involving the dehydration of a small amount of muscovite in the sample. In contrast, breakdown of biotite was the most important reaction above 950 °C. These results are interesting because they suggest that crustal contaminants are not necessarily enriched in radiogenic Sr relative to the source rock. However, the crushing of the original sample may have created artificial mineral contacts that do not accurately represent the original rock. Therefore, more experiments are clearly needed in order to test the behaviour of this material and other source compositions under similar melting conditions.

The general conclusion from all of these melting experiments is that the isotopic composition of a crustal melt evolves slowly towards the bulk composition of the rock as melting progresses. However, since the temperature and duration of melting are different for any given crustal-contamination event, it is not possible to make general predictions about the extent of disequilibrium melting to be expected in crustal contaminants. Each case must be investigated in its own context.

7.2.3 Inversion modelling of magma suites

The above modelling has considered the evolution of single batches of magma during melting, assimilation and/or fractionation processes. However, a suite of analysed lavas may represent magma batches that reached different stages of differentiation (and hence had different trace-element contents) before contamination. Just as different bivariate plots can be used to model progressive contamination of a single magma, the same variety of plots can be used to examine the evolution of magma suites. The Tertiary volcanic province of NW Scotland represents a good natural 'laboratory' in which to examine some of these processes for two main reasons. Firstly, magma–crust interaction was relatively intense, due to the volatile-poor nature of the magmas. This prevented them from punching through the crust quickly. Secondly, isotopic contrasts between mantle and crustal end-members are well developed, because old lithospheric mantle had been melted away from under the Tertiary volcanic centres by earlier magmatism.

An example of the co-variation of Sr isotope ratio with Sr concentration is provided by Tertiary basic-to-intermediate lavas from the Isle of Skye, NW Scotland (termed the Skye Main Lava Series). Moorbath and Thompson (1980) found a weak negative correlation

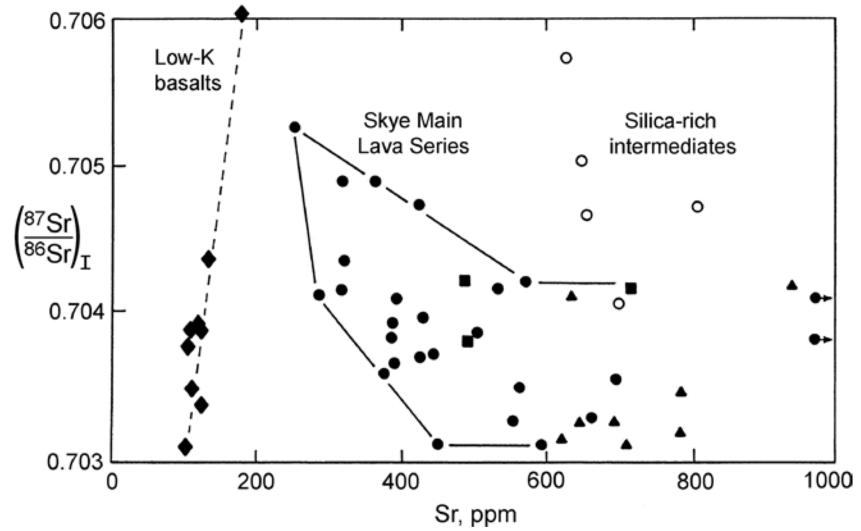

Fig. 7.15. Plot of initial Sr isotope ratio against concentration for Tertiary lavas from Skye, NW Scotland. Skye Main Lava Series: (●) = basalt; (▲) = hawaiite; (■) = mugearite–benmoreite. Other lavas: (○) = silica-oversaturated intermediates; (◆) = low-K basalts. After Moorbath and Thompson (1980).

between Sr isotope ratio and concentration in this suite, forming a hyperbolic trend (Fig. 7.15). However, any individual mixing line between a hypothetical mantle-derived precursor and the estimated crustal component has a slope perpendicular to the observed trend. Such a trajectory is displayed by a small suite of low-potassium (low-K) basalts in Fig. 7.15.

To explain the main data set, Moorbath and Thompson proposed that crystal fractionation had occurred in the upper mantle, yielding a series of magmas with variable Sr contents. These were then subjected to similar degrees of contamination with radiogenic crustal Sr, so that those with high Sr contents were less affected than those with low Sr contents, yielding a hyperbolic pattern for the suite as a whole. The scatter in the data probably results from somewhat variable degrees of contamination in different magma batches.

Thirlwall and Jones (1983) performed Nd isotope determinations on the same suite of Skye lavas. The data are shown (Fig. 7.16) on a plot of Nd isotope ratio against 1/concentration. Most of the basalts define an approximately linear array (equivalent to a hyperbola on a plot of $^{143}Nd/^{144}Nd$ ratio against Nd concentration). However, this linear array does not have the trajectory expected for two-component mixing (steep vectors in Fig. 7.16). Instead, it is attributed to contamination of a magma series with variable Nd contents, in which the most 'primitive' magmas, with lowest Nd contents, exhibit the greatest effects of contamination. On the other hand, a few basalts, together with silica-rich intermediate lavas, exhibit the effects of an AFC process, in which Nd contents rise rapidly as contamination progresses (Fig. 7.16).

Thirlwall and Jones confirmed this interpretation (Fig. 7.17) using a plot of Nd isotope ratio against the major-element differentiation index FeO/(FeO + MgO). They showed that the 'F/M' ratios of the Skye lavas must have been generated by fractionation at the base of the crust, since they were too high in most of the rocks to have been in equilibrium with mantle

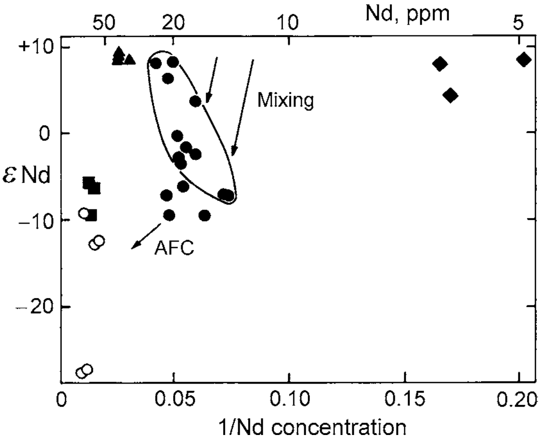

Fig. 7.16. Plot of initial Nd isotope ratio (ε Nd), against reciprocal Nd content in Skye lavas. Symbols are as in Fig. 7.15. Arrows show the effects of contamination by magma mixing and by AFC. After Thirlwall and Jones (1983).

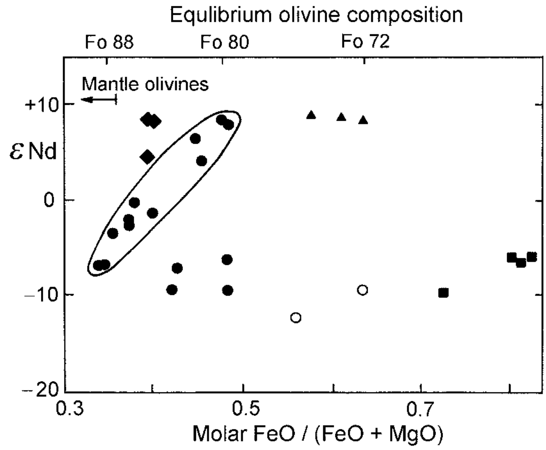

Fig. 7.17. Plot of ε Nd against 'F/M' ratio for Tertiary lavas from Skye, showing more intense crustal contamination in more magnesian basalts. Symbols are as in Fig. 7.15. After Thirlwall and Jones (1983).

olivines. It follows that the strong correlation of ε Nd with F/M must be the result of a subsequent process, i.e. contamination in the crust. The most primitive basalts (lowest F/M ratios) were the most contaminated, since their lower Nd contents rendered them more sensitive to contamination. Again, the linear array in this diagram does not correspond to a two-component mixing line. Crustal contaminants have low Fe and Mg concentrations, so they do not affect the F/M ratio of the contaminated magma. Hence, sub-vertical mixing vectors are generated in Fig. 7.17. The formation of the array of lava compositions at an oblique angle to these vectors can be ascribed to a regular and predictable contamination mechanism affecting a suite of related differentiates.

Huppert and Sparks (1985) attributed the type of contamination process seen in the Skye lavas to thermal erosion of wall rocks by turbulently flowing magma during its ascent through the crust. The more magnesian magmas were hotter and less viscous, therefore enhancing the turbulent flow of these magmas. This prevented the formation of a chilled margin by continually bringing fresh, hot magma into contact with the conduit walls, thereby allowing more wall-rock erosion. Huppert and Sparks imagined this process occurring in dykes, but a more probable site for such wall-rock assimilation may be sill complexes in the crust, where the longer magma residence time would allow more opportunity for contamination.

Kille *et al.* (1986) described an example of the possible effects of turbulent wall-rock assimilation from the Hebridean island of Mull, where inclined intrusive sheets are intruded into meta-sedimentary units of the Moine series. Large embayments were seen in the more fusible units of the sedimentary sequence, suggesting that 'excavation' by turbulently flowing magma had occurred. Subsequently, additional evidence was found from the Mull lava pile for wall-rock assimilation during turbulent ascent of magma (Kerr *et al.*, 1995). This study showed that lavas of the Mull Plateau Group had similar patterns of ε Nd against elemental concentration to those previously seen in Skye. Hence, it appears that this process is of quite widespread occurrence, prompting Kerr *et al.* to coin the expression 'assimilation during turbulent ascent'.

Isochron diagrams are a particular example of bivariate plots involving isotope ratios and trace-element ratios, and may therefore be useful for studying crustal-contamination processes. For old rock suites, initial isotope ratios are plotted on a pseudo-isochron diagram. Because the denominators on both axes are the same, two-component mixing must give rise to products that lie on a straight line between the end-members. However, a magma suite may again generate a data array that does not project to the mixing end-members. The Tertiary lavas from Skye provide a good example of this problem also.

Thirlwall and Jones (1983) found a linear array of ε Nd *versus* Sm/Nd ratios in Skye basalts (Fig. 7.18). They interpreted this array as a mixing line between

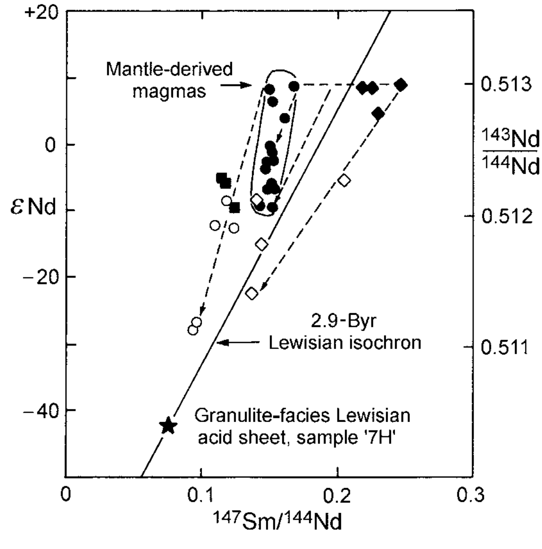

Fig. 7.18. Sm–Nd pseudo-isochron diagram for Tertiary lavas from Skye, showing proposed contamination vectors in comparison with the array of contaminated basalts. Symbols are as in Fig. 7.15. After Dickin *et al.* (1984).

a mantle-derived magma with constant Sm/Nd ratio and a partial melt of intermediate (tonalitic) Lewisian gneiss. The projection of the mixing line onto the Lewisian isochron then indicates an ε Nd value (at 60 Myr) of about −15. However, Dickin *et al.* (1984) argued that the basalt array was not a single mixing line, but was generated by a series of obliquely angled mixing lines involving mantle-derived magmas with different Sm/Nd ratios. These trajectories indicate a crustal end-member with ε Nd of about −40, corresponding to Lewisian granitic (acid) gneiss. This controversy may be resolvable by Ce isotope evidence (section 9.4.3), but it serves to reiterate the importance of distinguishing between individual mixing lines and magma-evolution trends on all plots where contamination models are considered.

Since the Sr and Nd isotope compositions of a contaminated lava suite may be a complex function of Sr and Nd concentrations, depending on the differentiation history of the suite, these factors must be borne in mind when interpreting the Nd *versus* Sr isotope diagram for a magma suite. For the data from Skye and Mull (Fig. 7.19), most samples define an array with a negative slope, implying coupled behaviour of Sr and Nd in the mixing process. However, it has been shown that contamination effects for each isotope system (^{87}Sr/^{86}Sr and ^{143}Nd/^{144}Nd) are individually controlled by the Sr and Nd concentrations of the differentiating magmas. Furthermore, these trace elements often do not behave coherently during magma differentiation, since Nd is always incompatible, whereas Sr becomes a compatible element once crystallisation of plagioclase begins. Therefore, we should expect some scatter in the Sr–Nd isotope correlation in order to reflect these complexities.

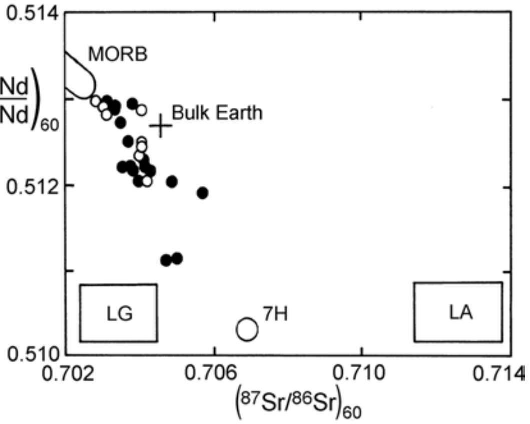

Fig. 7.19. Plot of Nd *versus* Sr isotope ratio for Skye (●) and Mull (○) lavas, showing a trend towards local crustal units: LG = Lewisian granulite-facies gneiss; LA = Lewisian amphibolite-facies gneiss; 7H = Archean pegmatite sheet. After Kerr *et al.* (1995).

A further problem with the interpretation of Skye and Mull data on the Sr–Nd isotope diagram is that the correlation line of Tertiary lavas trends half-way between the fields for Rb-depleted granulite-facies and Rb-rich amphibolite) facies Lewisian gneisses, argued to represent the lower and upper parts respectively of the present-day crust under Skye. However, the relative contributions of these crustal components can be resolved using Pb isotope data, as shown below.

Pb isotopes are a powerful tool in studies of mantle and crustal evolution, because the three different radiogenic isotopes are generated from parents with a wide span of half-lives, two of which are a common element. By using ^{206}Pb/^{204}Pb and ^{207}Pb/^{204}Pb ratios in conjunction, it is possible to measure not only the importance of crustal contamination, but also the age of the crustal component. On the other hand, by using ^{206}Pb/^{204}Pb and ^{208}Pb/^{204}Pb ratios in conjunction, it is sometimes possible to locate the depth of the crustal contaminant, since the crust may develop a stratified signature of these isotopes in response to high-grade metamorphism. Both of these possibilities are illustrated by the Tertiary magmatism of Skye and Mull.

Moorbath and Welke (1969) found that both acid and basic Tertiary igneous rocks from Skye lay on a strong linear array on the ^{207}Pb/^{204}Pb *versus* ^{206}Pb/^{204}Pb diagram, with a slope age of about 3 Byr. They interpreted the linear array as a mixing line between radiogenic mantle-derived Pb and very-unradiogenic Archean (Lewisian) crustal Pb. Dickin (1981) repeated this study with more modern techniques and found a mixing line with a slope age of 2920 ± 70 Myr (Fig. 7.20a), the same as the Sm–Nd age of the Lewisian complex (see section 4.1.3). By plotting ^{208}Pb/^{204}Pb *versus* ^{206}Pb/^{204}Pb ratios (Fig. 7.20b), it was possible to resolve three components in the Skye Tertiary igneous rocks. The lavas are interpreted as mantle-derived magmas that had suffered strong contamination in the granulite-facies lower crust, whereas gabbros of the Cuillins layered complex are attributed to contamination in amphibolite-facies upper crust. Finally, the Skye granites are attributed to differentiated basic magmas that suffered contamination in the lower crust, followed by further differentiation and contamination in the upper crust.

In this model, the crustal end-members were based on average compositions of gneisses from NW Scotland, supported by evidence from crustal xenoliths carried up in a Tertiary intrusion from Skye. The lower

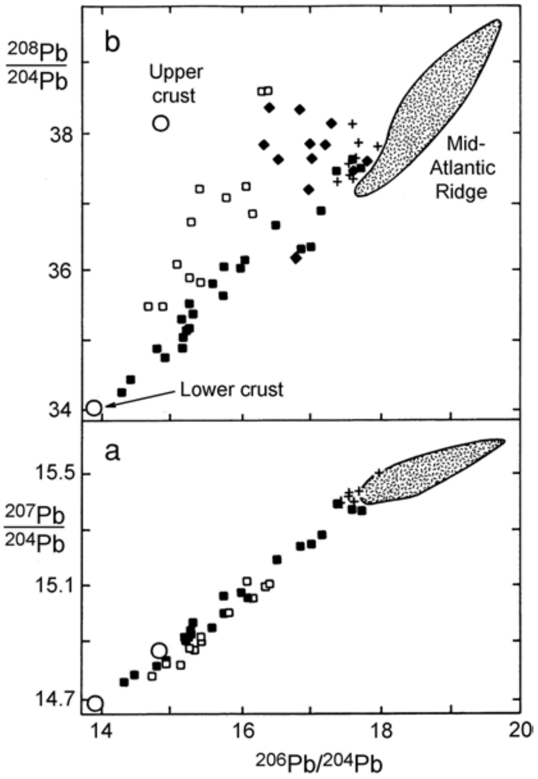

Fig. 7.20. Plot of initial Pb isotope ratios for Tertiary igneous rocks from Skye, showing evidence for three-component mixing: (■) = lava series; (□) = granites; (+) = low-K basalts; (◆) = layered gabbros. Mid-Atlantic Ridge approximates the local mantle composition. Modified after Thompson (1982).

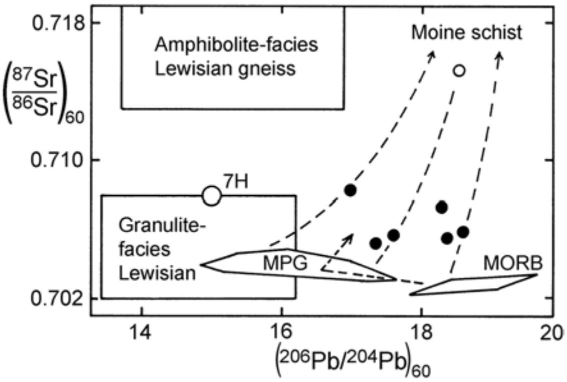

Fig. 7.21. Plot of initial Sr *versus* Pb isotope ratios in lava suites from Mull, showing the distinct contamination histories of the Mull Plateau Group (MPG) and the early erupting Staffa Magma Type (●). After Morrison *et al.* (1985).

crustal rocks were depleted in both U and Th relative to Pb during the 2.7-Byr-old Scourian granulite-facies metamorphism, while the present-day upper crust contains rocks that were depleted in U but not Th (relative to Pb) in the Archean middle crust. The original upper crust, enriched in U and Th relative to Pb, has largely been removed by erosion.

The combination of Pb with Sr isotope evidence allows additional constraints to be applied to the evolution of contaminated magma suites. For example, the shallow slope of the Sr–Pb isotope correlation line in Fig. 7.21 is consistent with contamination of the Skye and Mull lavas by granulite-facies lower crust. However, it must be remembered that (unlike the Pb–Pb isotope diagram) mixing lines on the Sr–Pb isotope diagram can be strongly hyperbolic. In fact, the lavas were probably contaminated by the most felsic components in the granulite-facies basement, which were more Rb-enriched than the bulk lower crust. Felsic minor intrusions were argued by Thompson *et al.* (1982) to be the most likely fraction in the crust to melt, leading to a kind of 'selective-contamination' mechanism due to melts of fusible rock types. One such rock (sample '7H') is shown in Fig. 7.19, where it is found to explain the Sr–Nd correlation line in the lavas.

A contrasting type of behaviour was seen in a distinct magma type from SW Mull, which was important in the very early eruptive history of the complex (Morrison *et al.*, 1985). These lavas of the so-called Staffa Magma Type lie far off the Sr–Pb correlation line formed by the later lavas (Fig. 7.21), and were therefore attributed to a two-stage contamination process. This began at the base of the crust, as seen in the other lavas, but was followed by a period of residence in the uppermost crust, where the magmas were contaminated by supracrustal meta-sediments of the Moine series. Thus, as more isotope tracers have become available, the application of multiple tracers to magma suites has allowed more complex magma-evolution histories in the crust to be modelled and understood.

7.2.4 Lithospheric mantle contamination

Isotopic tracers have been widely used to monitor crustal contamination of continental magmas during their ascent, and to some extent this process can now be quantified. In contrast, the relative importance of lithospheric and asthenospheric mantle sources continues to be a matter of debate. Thermal constraints (McKenzie and Bickle, 1988) suggest that the high melting rates necessary to erupt flood basalt provinces

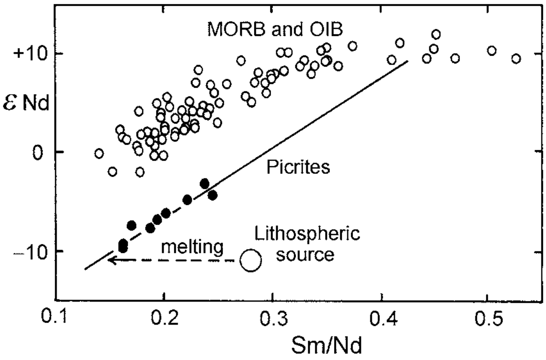

Fig. 7.22. Sm/Nd pseudo-isochron diagram, showing a linear array of Nuanetsi picrite compositions (●), which is interpreted as a mixing line between a primitive picritic magma and a hypothetical lamproite magma. Open symbols are for oceanic volcanics. After Ellam and Cox (1991).

can be satisfied only by melting of mantle plumes. On the other hand, lithospheric extension will cause small-volume melting of metasomatised lithosphere, generating mafic potassic magmas that may have extreme isotopic compositions. Several workers recognised that these processes might act together, leading to contamination of asthenospheric magmas by the mantle lithosphere, as well as by the overlying crust. Good examples of this process come from the Mesozoic flood-basalt province of Gondwana (Southern Africa, South America and Antarctica).

In the Karoo province of Southern Africa, picrite basalts from Nuanetsi define a Sm–Nd pseudo-isochron with an apparent age of 1 Byr. This was initially interpreted as a mantle isochron dating the age of a magma source in the lithosphere (Ellam and Cox, 1989). However, re-examination of the data (Ellam and Cox, 1991) suggested that the array was a mixing line, formed by contamination of picritic magmas (from a depleted plume source) by mafic potassic magmas (lamproites) from a lithospheric source (Fig. 7.22). Trace-element-mixing calculations suggested that the lamproite component made up about 20% of the mixed magma, but dominated its Nd and Pb isotope signature. On the other hand, osmium contents of the two end-members were about equal (section 8.4.4). A similar model may explain Nd–Os isotope data for the Stillwater Complex, Montana (Lambert *et al.*, 1994).

An important aspect of the Gondwana flood-basalt province is its geochemical provinciality, which provides strong evidence for lithospheric control of magma chemistry. One example of this provinciality is the identification of high-Ti and low-Ti flood-basalt provinces in Southern Africa and in the Paraná basin of South America (e.g. Hawkesworth *et al.*, 1984). If the same provinciality were found in mafic potassic rocks, this would support the lithospheric-contamination model for flood basalts. Such a case was observed for the high-Ti Paraná province (e.g. Hawkesworth *et al.*, 1992), but the absence of low-Ti alkali mafic rocks caused major uncertainty about the petrogenesis of low-Ti Paraná basalts (Hergt *et al.*, 1991). This problem was solved by the discovery of low-Ti alkali mafic rocks on the flanks of the Paraná basin (Gibson *et al.*, 1996).

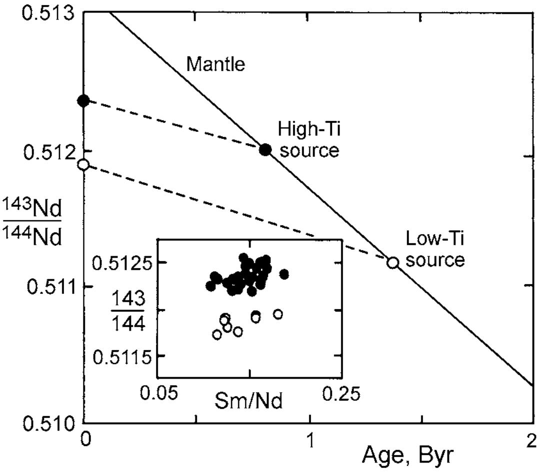

Fig. 7.23. Nd isotope evolution diagram, showing predicted evolution lines of the lithospheric sources of high-Ti (●) and low-Ti (○) alkali mafic magmas, with ages of about 0.8 and 1.4 Gyr, respectively. The inset shows the lava data on which the evolution lines are based. After Gibson *et al.* (1996).

Comparison of the Nd isotope systematics of high-Ti and low-Ti alkali mafic rocks from the Parana showed that, while the ranges of Sm/Nd ratios were identical, Nd isotope compositions were quite distinct (Fig. 7.23). This suggests that the lithospheric mantle underlying high-Ti and low-Ti provinces has distinct trace-element-enrichment ages, possibly reflecting the geographical extent of a Late Proterozoic crustal reworking event. Therefore, this confirms that the high-Ti and low-Ti suites reflect the provinciality of the subcontinental lithosphere.

If the isotopic signatures of the most enriched alkali mafic suites are used as end-members in a mixing model, the isotopic compositions of low-Ti flood basalts can be explained by roughly 20% contamination of a primitive plume end-member in the lithospheric mantle, followed by extensive contamination

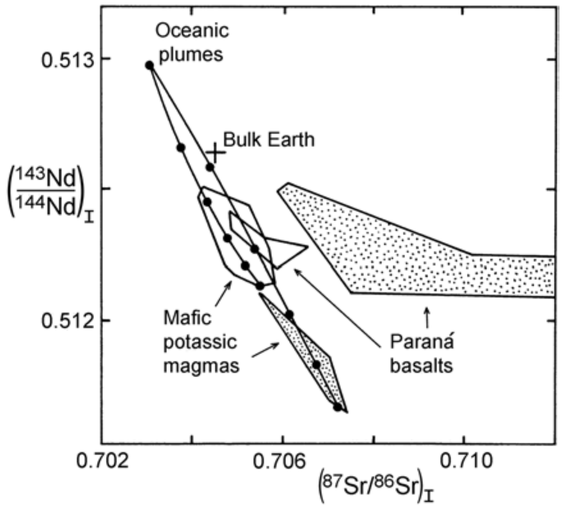

Fig. 7.24. Nd–Sr isotope diagram, showing fields for high-Ti rocks (white) and low-Ti rocks (shaded). Paraná basalts are explained by two-stage contamination of plume magmas, firstly in the sub-continental lithosphere and secondly in the crust. Mixing lines are marked in 20% increments. After Gibson *et al.* (1996).

in the crust (Fig. 7.24). On the other hand, the high-Ti flood basalts require about 50% contamination in the mantle lithosphere, but less crustal contamination. Such multi-stage models for the interaction of plumes with the mantle lithosphere are likely to be a continuing major focus in geochemical studies of continental basalts.

7.2.5 Phenocrysts as records of magma evolution

Inversion modelling is unavoidable when attempting to reconstruct the evolution of large magma suites during emplacement through the crust. However, when this is based only on the whole-rock composition of the final products, it may overlook internal mineralogical evidence that could help to constrain contamination models. Therefore, some recent studies have investigated the internal Sr isotope heterogeneity of feldspar phenocrysts in volcanic lavas in order to reconstruct near-surface magma plumbing. Early work (e.g. Davidson and Tepley, 1997) used a micro-drilling technique, followed by conventional ion-exchange chemistry, to study Sr zoning in plagioclase phenocrysts from three volcanic systems. However, the advent of MC-ICP-MS (section 2.2.2) has allowed *in situ* Sr isotope analysis of feldspar phenocrysts by laser ablation (Davidson *et al.*, 2001).

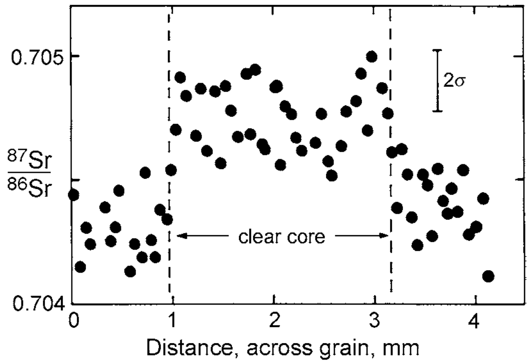

Fig. 7.25. Sr isotope profile along the length of a zoned plagioclase with a clear core and a patchy rim, reflecting two stages of feldspar growth. The width of each data point indicates the approximate size of each ablation pit. After Davidson *et al.* (2001).

Figure 7.25 shows a typical isotope profile from the study of Davidson *et al.* (2001), which was measured along the length of a plagioclase phenocryst from El Chichón volcano, Mexico. The data are in good agreement with micro-drill results from the same crystal (Davidson and Tepley, 1997), and clearly show two phases of magma evolution recorded by the crystal. The data are attributed to successive injections of mantle-derived magma with unradiogenic Sr into a magma chamber in the crust. Plating out of crystals on the walls is argued to protect subsequent magma injections from contamination, so that the bulk magma becomes less radiogenic with time.

7.3 Petrogenesis of continental magmas

It is impossible here to attempt a comprehensive review of continental magma suites. Instead, a few case studies will be examined for various magma types that illustrate a variety of approaches to problems of petrogenetic interpretation.

7.3.1 Kimberlites, carbonatites and lamproites

Kimberlites, carbonatites and lamproites are highly incompatible-element-enriched magmas that may be genetically related. Experimental evidence suggests that they are all products of very-small-degree partial melting in the deep mantle, and that CO_2 plays an important role in their genesis (e.g. Wendlandt and Mysen, 1980). The volatile-rich nature of these magmas causes rapid ascent through the crust. This,

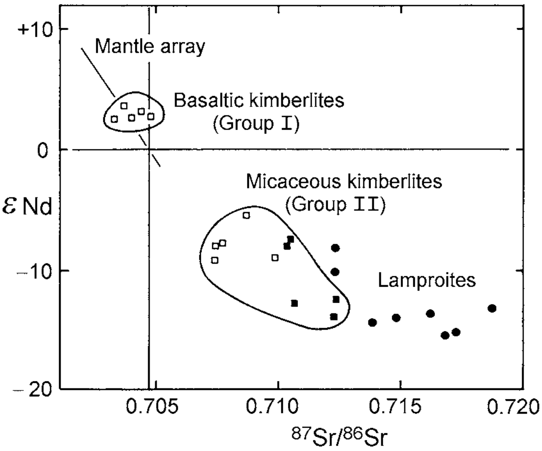

Fig. 7.26. Plot of ε Nd against Sr isotopic compositions of basaltic and micaceous kimberlites from South Africa (□) and western Australia (■), together with Australian lamproites (●). After DePaolo (1988).

coupled with their high incompatible-element concentrations, renders these magmas very resistant to isotopic modification by crustal contamination.

South African kimberlites are divided into two petrological types, basaltic and micaceous (phlogopitic), according to their groundmass mineralogy (Dawson, 1967). These two groups, referred to as types I and II, respectively, by Smith (1983), have distinct Sr and Nd isotope compositions. Basaltic (Group-I) kimberlites have isotopic compositions that cluster just within the depleted quadrant relative to Bulk Earth, whereas micaceous (Group-II) kimberlites fall well inside the enriched quadrant (Fig. 7.26).

Kimberlites of western Australia graduate from phlogopite kimberlite to lamproite, and were found by McCulloch *et al.* (1983) to extend the compositional range of micaceous kimberlites even further into the enriched quadrant in Fig. 7.26. McCulloch *et al.* calculated T_{DM} model ages for the source region of these rocks, on the assumption that fractionation of REE had not occurred during magma genesis. These were in the range 0.9–1.3 Byr. However, they recognised that the magmas might have been fractionated to more LREE-enriched compositions than the source, making these minimum ages that may substantially under-estimate the age of the enrichment event.

The resistance of carbonatites to crustal contamination makes them a potential source of data on the composition of the sub-continental lithosphere. Bell and Blenkinsop (1987) investigated this application by carrying out Sr and Nd isotope analysis of carbonatites from Ontario and Quebec, ranging in age from 110 to 2700 Myr. Sr isotope ratios lay along a depleted-mantle evolution line, which Bell and Blenkinsop attributed to the sub-continental lithosphere of the Superior province. However, Nd isotope data for the same samples were more scattered. They comprise part of a larger set of Nd data from different continents (Nelson *et al.*, 1988), which scatter between the depleted mantle and reservoirs at least as enriched as Bulk Earth (Fig. 7.27).

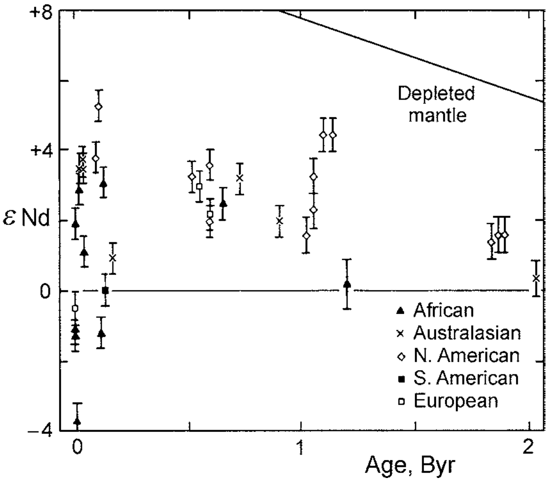

Fig. 7.27. Nd isotope evolution diagram in terms of ε Nd against time, showing derivation of carbonatite from variably depleted (or mixed) mantle sources. After Nelson *et al.* (1988).

Nelson *et al.* argued that the world-wide occurrence of these scattered data militated against an origin in the sub-continental lithosphere, and instead favoured a plume origin similar to that of OIB. This can explain the data in Fig. 7.27, but not the extreme signatures of the Australian lamproite data (Fig. 7.26). Therefore, the mixing model which Nixon *et al.* (1981) originally proposed for genesis of kimberlite can serve as a unifying petrogenetic model for kimberlites, carbonatites and lamproites. In this model, very-small-degree partial melts originate from comparatively 'fertile' asthenospheric sources (Group-I signature); they are subsequently contaminated to different degrees in the LIL-enriched but refractory sub-continental lithosphere (Group-II signature).

This mixing model essentially places kimberlites, carbonatites and lamproites on the same footing as other within-plate magmas. These magmas are now generally thought to originate from plume sources, and subsequently undergo variable degrees of contamination in the lithosphere. Therefore, each example must be investigated in its own context, just like other magmas.

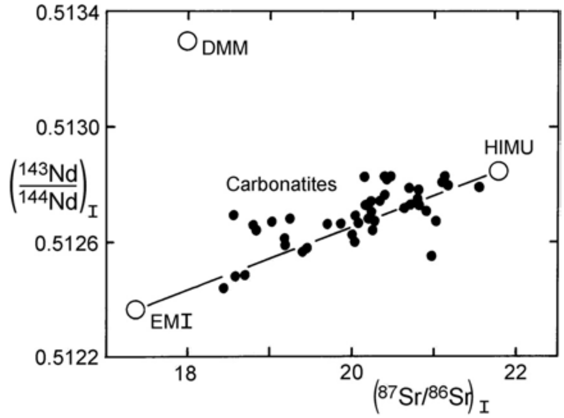

Fig. 7.28. Nd–Pb isotope plot, showing carbonatites from the East African Rift (●) relative to the end-members invoked to explain the compositions of OIB. After Bell and Tilton (2001).

One province that has always been important for the study of carbonatites and ultra-alkaline magmas is the East African Rift. Bell and Simonetti (1996) showed that the magmas of this province, including the active carbonatite volcano Oldoinyo Lengai, lie very close to the HIMU–EMI mixing line identified in OIB (Fig. 7.28). Bell and Simonetti (1996) attributed the mixing line to magmas from a HIMU-type plume that were subsequently contaminated by sub-continental lithospheric mantle with an isotopic signature resembling that of EMI (section 6.5.3). However, subsequent work on a larger number of carbonate and nephelinite volcanic centres from the East African Rift (Bell and Tilton, 2001) showed that this mixing line was a widespread phenomenon.

The discovery that the mixing line originally observed at Oldoinyo Lengai was also seen in carbonatites from elsewhere in the East African Rift caused Bell and co-workers to change their ideas about the origin of these components. The widespread occurrence of relatively coherent two-component mixing throughout the rift made a source in the lithosphere less likely, since this is expected to be laterally heterogeneous. Therefore, Bell and Tilton (2001) proposed that the signature of HIMU–EMI mixing in East African carbonatites reflected heterogeneity in the plume source itself, as seen in OIB.

Additional support for the importance of plume sources in carbonatite magmatism is provided by rare-gas evidence from carbonatites of the Kola Peninsula. For example, neon isotope data provide clear evidence for the involvement of a plume-type lower-mantle source (Tolstikhin *et al.*, 2002). However, individual provinces of kimberlite, carbonatite and lamproite magmatism are likely to exhibit variable degrees of contamination of plume-derived melts by enriched sources in the sub-continental lithosphere.

7.3.2 Alkali basalts

An interesting location to study alkali basalt genesis is provided by the Cameroon Line of western Africa. This volcanic chain, composed dominantly of alkali basalts with subordinate tholeiites, stretches from the Atlantic island of Pagalu (700 km SW of the Niger delta) to the Biu Plateau (800 km inland). Despite the fact that the volcanic chain is situated half on young oceanic crust and half on ancient continental crust, the ranges of trace-element contents and Sr isotope ratios in the two sections of the line are identical (Fitton and Dunlop, 1985). Given that oceanic and continental lithosphere would be expected to have different signatures, Fitton and Dunlop argued that the magma source must lie below the lithosphere.

The Cameroon Line exhibits no evidence of age progression along its length, and must therefore represent a 'hot zone' rather than a hot-spot trail generated by plate motion over a small plume. Fitton and Dunlop argued that because there is no evidence of migration of the area of volcanism over its 65-Myr history (despite movement of the African plate), 'the mantle source must be coupled to the lithosphere', rather than originating from a deep-mantle plume that tracked across the overlying plate. This was a surprising result, since the only explanation (at that time) for isotopic heterogeneity inherited from a shallow mantle source was disequilibrium melting (section 6.1.2).

To investigate this problem further, Halliday *et al.* (1988) performed a more detailed isotopic study on the Cameroon Line, including Pb and Nd isotope measurements (Fig. 7.29). A few samples were found to show evidence of contamination by continental basement; however, after excluding these samples, the most distinctive feature of the data was the very radiogenic Pb isotope compositions displayed by basic lavas from the continent–ocean boundary, about half-way along the volcanic chain. These compositions approach those of the St Helena hot-spot, but volcanics on either side (within the oceanic and continental segments) are less radiogenic.

Halliday *et al.* (1988) attributed these features to the 'impregnation' of the upper mantle under the Cameroon Line by material from the St Helena plume. This plume played a major role in promoting the initial opening of the South Atlantic, about 120 Myr ago. It was probably responsible for the actual location

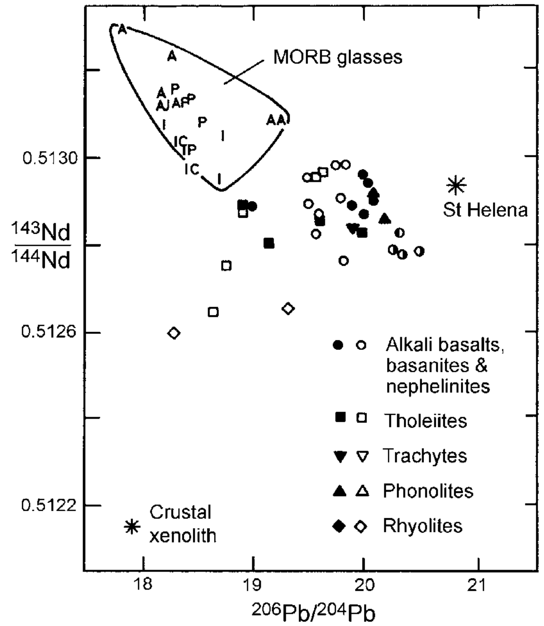

Fig. 7.29. Plot of Nd *versus* Pb isotope compositions for Cameroon Line volcanics. Solid symbols: continental lavas; open symbols: oceanic; half-filled: continental edge. A, I and P = Atlantic, Indian and Pacific MORB. After Halliday *et al.* (1988).

of rifting, which subsequently became the continental edge. With time, the African plate moved away from the St Helena plume, but a 'blob' of hot plume material became incorporated into the lithospheric mantle under Cameroon as the continental margin cooled after the rifting event. As the plume component was gradually dispersed laterally along the volcanic chain, its compositional effect was seen at volcanic centres progressively further from the continental edge.

Halliday *et al.* (1990) revised this model as a result of new observations on the Pb isotope data. These revealed that the radiogenic ^{206}Pb/^{204}Pb signatures at the continental edge were not accompanied by high enough ^{207}Pb/^{204}Pb ratios to represent direct mixing with the St Helena plume. Instead, a positive correlation between ^{206}Pb/^{204}Pb and U/Pb ratios was observed (Fig. 7.30), which Halliday *et al.* interpreted as a 200-Myr-old erupted isochron. However, it was shown in Fig. 7.29 that the ^{206}Pb/^{204}Pb ratio correlates with the Nd isotope ratio, which cannot develop large variations by decay of Sm over periods of only 200 Myr. Therefore the arrays of Pb isotope ratio are probably mixing lines. The radiogenic end-member must represent young lithosphere whose high ^{206}Pb/^{204}Pb signature was generated by magmas with high U/Pb ratios (μ) at the time of continental rifting. Mixing between this component and local asthenospheric upper mantle can explain the isotopic mixing process, which also satisfies more recent rare-gas evidence from the Cameroon Line (Barfod *et al.*, 1999).

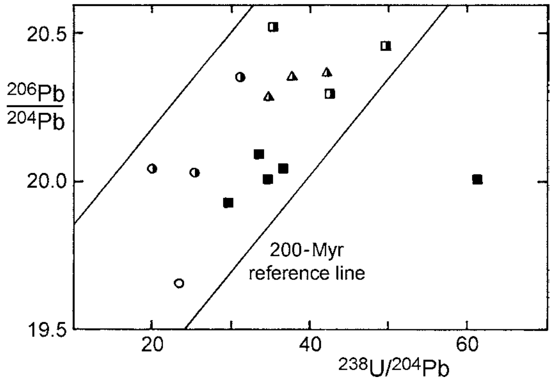

Fig. 7.30. U–Pb isochron diagram for young Cameroon Line lavas with over 4% MgO, yielding an apparent age of about 200 Myr. Half-open symbols denote individual volcanoes from the continental edge. Other symbols indicate continental (○) and oceanic segments (■). After Halliday *et al.* (1990).

This work has two important conclusions. Firstly, episodes of continental rifting can replace old subcontinental lithosphere with young lithosphere, which may have an exotic composition. Secondly, U is more incompatible than Pb in magmatic processes, so that preferential extraction of Pb from the mantle cannot be invoked to explain the lead paradox (section 6.3.1).

7.3.3 Flood basalts

The northwestern USA displays one of the world's major flood-basalt provinces, the Columbia River Basalt Group (CRBG). The controversies about the petrogenesis of these lavas serve very well to illustrate the complexities of modelling the genesis of flood basalts.

Early Nd isotope data on the Columbia River basalts clustered near ε Nd $= 0$, leading DePaolo and Wasserburg (1976) to propose an undepleted (primordial-type) source for these magmas, in contrast to the depleted mantle source of MORB (ε Nd $= +10$). This model was supported by DePaolo (1983) on the basis of a volume-weighted histogram of initial ε Nd values measured on the Columbia River basalts (Fig. 7.31). DePaolo argued that the marked concentration of data at slightly positive ε values and the sharp cut off at ε Nd $= 0$ constituted evidence for a chondritic source for the most voluminous Grande Ronde group of lavas, merging into a depleted-mantle source for the Imnaha

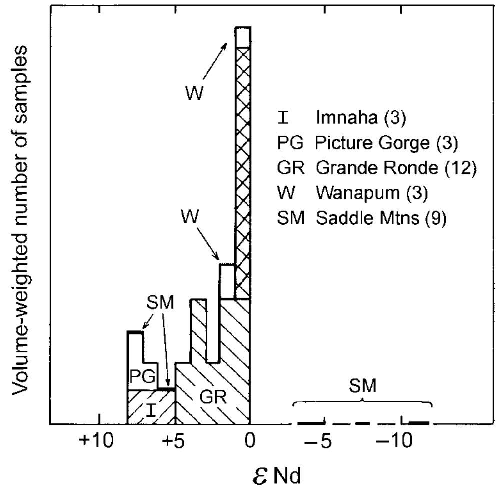

Fig. 7.31. Histogram of ε Nd compositions for Columbia River basalts, weighted according to eruptive volume. Double-hatched data are from DePaolo and Wasserburg (1976; 1979b). Modified after DePaolo (1983).

and Picture Gorge basalts. However, the abundance peak at ε Nd = 0 in Fig. 7.31 was partly a product of adding the data of DePaolo and Wasserburg (1976; 1979b) to those of Carlson *et al.* (1981), which caused ‘double sampling’ of some of the same flows.

A compilation of Sr and Nd isotope data for several basaltic suites from the northwestern USA appears to present a rather different picture. The samples display a very strong, almost continuous, curved trend, which fans out somewhat in the enriched quadrant (Fig. 7.32). These data imply that a relatively simple mixing process, such as crustal contamination, was involved in the genesis of the lavas (Carlson *et al.*, 1981). However, it has become apparent over the last few years that radiogenic isotopes alone may not be able to distinguish between enriched mantle and crustal sources. Incompatible-element ratios and stable-isotope data may be needed to assist in this distinction.

Carlson and Hart (1988) argued that the ratio of a highly incompatible element against a high-field-strength element (e.g. K_2O/P_2O_5) can be used as an index of (specifically) crustal contamination. This index is plotted against Sr isotope ratio in Fig. 7.33. Some Picture Gorge and Grande Ronde basalts of the CRBG, together with Steens Mountain basalts from the Oregon Plateau, have quite elevated K_2O/P_2O_5 ratios, despite having low-to-intermediate Sr isotope ratios. Carlson and Hart attributed this pattern to contamination of magmas from a ‘C-1’ mantle source by crustal units with a variety of ages. The C-1 source was identified as typical asthenospheric upper mantle, whose melting was probably caused by mantle convection behind the Cascades arc. In contrast to the above lavas, some

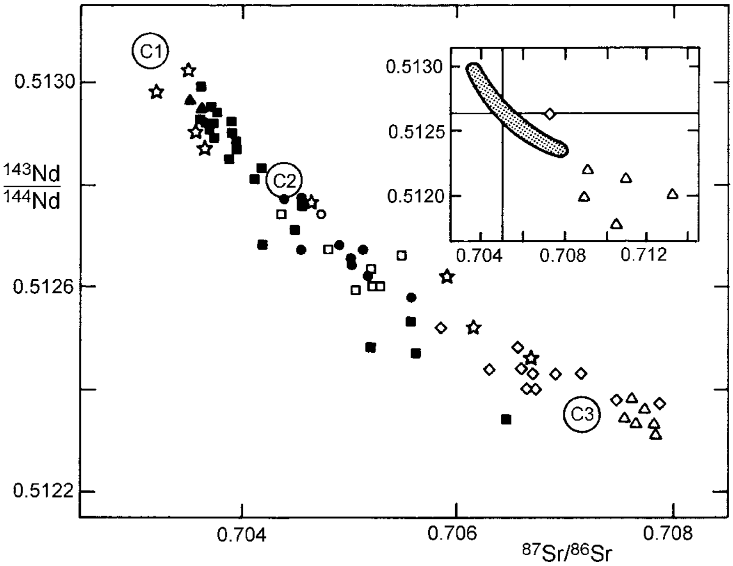

Fig. 7.32. Plot of Nd *versus* Sr isotope ratio for basalts from the northwestern USA: (■) = Grande Ronde; (●) = Picture Gorge; (□) = Wanapum; (▲) = Steens Mountain; (△) = Saddle Mountains; (☆) = HAOT; (◇) = SROT. C1 to C3 are possible sources discussed in the text. Data from the main diagram define the shaded field on the inset. After Carlson and Hart (1988).

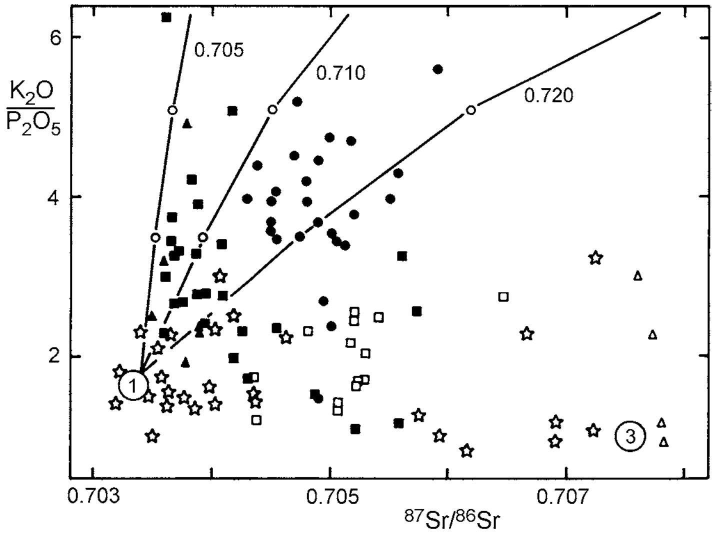

Fig. 7.33. Plot of K_2O/P_2O_5 ratio against Sr isotope ratio for basalts from the northwestern USA, showing mixing models between C-1 magmas and three crustal contaminants with various Sr isotope ratios. Symbols are as in Fig. 7.32. After Carlson and Hart (1988).

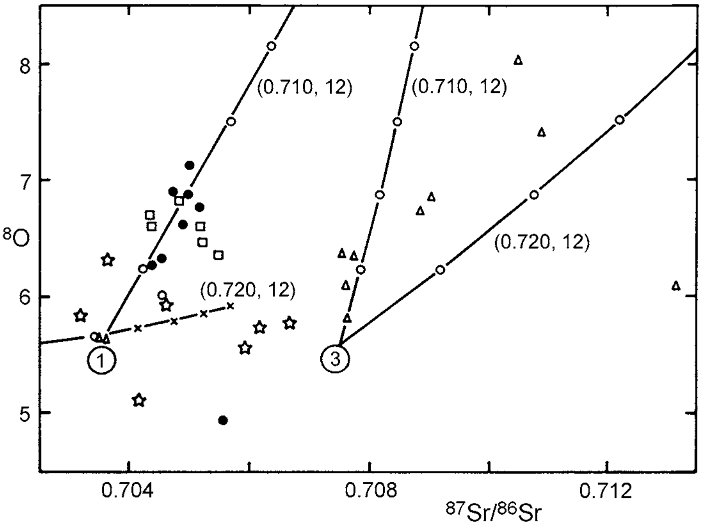

Fig. 7.34. Plot of $\delta^{18}O$ against Sr isotope ratio for basalts from the northwestern USA. Curves show effects of mixing with crust of a given Sr and ^{18}O composition. Steep mixing lines model contamination of magmas (○ = 10% increments); the shallow mixing line models contamination of MORB-type source with subducted sediment (× = 1% increments). Symbols are as in Fig. 7.32. After Carlson and Hart (1988).

Saddle Mountains CRBG flows, high-Al olivine tholeiites (HAOT) from the Oregon Plateau, and Snake River olivine tholeiites (SROT) have $^{87}Sr/^{86}Sr$ ratios up to 0.708, but low K_2O/P_2O_5 ratios. Carlson and Hart attributed these signatures to a lithospheric mantle source ('C-3').

A plot of $\delta^{18}O$ against Sr isotope ratio supports this model (Fig. 7.34). Steep vectors result from contamination of basaltic magmas by typical crustal units. In contrast, sub-horizontal vectors could be produced by mixing with old ^{87}Sr-enriched mantle, or possibly by recent contamination of the Sr-poor mantle

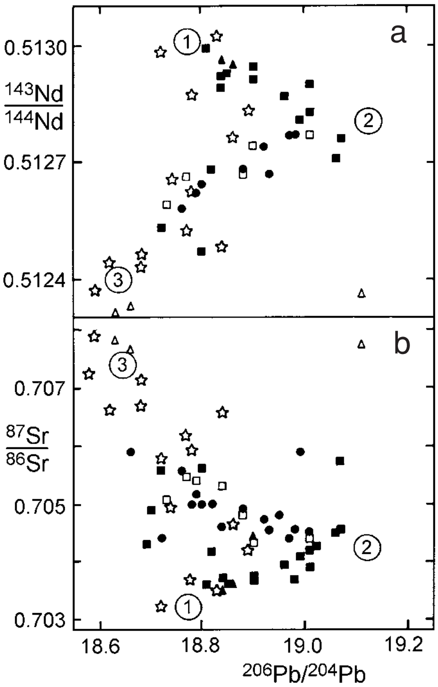

Fig. 7.35. Isotope compositions of basalts from the northwestern USA: (a) Nd *versus* Pb isotope plot; and (b) Sr *versus* Pb isotope plot. Three distinct mantle sources are resolved (C-1 to C-3). Symbols are as in Fig. 7.32. After Carlson and Hart (1988).

source by subducted sediment. Such a distinction between source and magma contamination vectors on the oxygen–strontium isotope diagram was investigated in detail by Taylor (1980) for granitic rocks (section 7.3.5).

Pb isotope data reveal one more level of complexity in this picture. Basalts with ^{87}Sr/^{86}Sr ratios below 0.708 display a triangular distribution on plots of Sr or Nd isotope ratio against ^{206}Pb/^{204}Pb ratio (Fig. 7.35). On this diagram, many Grande Ronde lavas trend towards an end-member (C-2) with radiogenic Pb that is distinct from the C-1 and C-3 mantle end-members recognised from other evidence. Carlson and Hart speculated that the C-2 source may have been derived by contamination of C-1 depleted mantle by subducted sediment.

Unlike DePaolo, Carlson and Hart did not invoke any lower-mantle plume source for the Columbia River basalts, which therefore makes this an unusual model for a flood basalt province. In contrast, authors of several subsequent studies of the Columbia River Basalt province have invoked a plume as one of the end-members. The first of these studies (Brandon and Goles, 1988) involved trace-element analysis only, whereas three subsequent studies used radiogenic isotope tracers. However, the analytical results obtained in these later isotope studies were largely the same as those of Carlson and Hart... just the conclusions differed. Therefore, these models will be discussed using the older isotope data in Fig. 7.35.

Hooper and Hawkesworth (1993) and Brandon and Goles (1995) used multiple isotope tracers (Pb–Sr–Nd) in their investigation, as well as elemental data. They broadly agreed with Carlson and Hart (1988) that C-1 is asthenospheric upper mantle and C-3 is lithospheric mantle. However, both groups re-interpreted C-2 as a plume source, identified as part of the track of the present-day Yellowstone plume. In contrast, Chamberlain and Lambert (1994) used Pb isotope only, and also divided both C-1 and C-2 into two sub-component reservoirs (R1–R2 and R4–R5, respectively). However, the main difference was that they identified the C-3 component (their R3) as the plume source and the C-2 component (i.e. R4–R5) as crustal.

These competing models were tested by Dodson *et al.* (1997) using helium and neon isotope evidence. Two samples were analysed, an Imnaha basalt (close to the C-2 end-member) and a Wanapum basalt (close to the C-3/R3 end-member). The Imnaha (C-2) basalt was found to have a much stronger plume (un-degassed lower-mantle) signature than the Wanapum basalt, thus confirming the models of Hooper and Hawkesworth (1993) and Brandon and Goles (1995). In so doing, this work also vindicated to some extent the early studies of DePaolo and Wasserburg, by showing that the Columbia River basalts do indeed contain a lower-mantle component. However, these results also demonstrate that no single isotope tracer (either Nd or Pb) is sufficient alone to distinguish between sources in such a complex multi-component system.

More recent investigation of the CRBP using the osmium isotope tracer has further quantified the degree of crustal contamination in the origin of these basalts (Chesley and Ruiz, 1998). These data do not distinguish between the alternative sources in the upper and lower mantle (C-1 and C-2), but they throw additional light on the identity of the C-3 source. Contrary to the arguments of Carlson and Hart (1988) based on trace-element and oxygen isotope data, Chesley and Ruiz argued that the C-3 end-member was represented by crustal rather than mantle lithosphere. After all of the argumentation above, this seems a surprising conclusion. However, Chesley and Ruiz claimed that initial osmium signatures in lavas from the Grande Ronde, Wanapum and Saddle Mountains groups were so radiogenic that only a crustal source could explain them (see section 8.3 for background).

Additional evidence for this interpretation comes from dykes of the Wanapum group that are intruded across a suture boundary between Precambrian and Mesozoic terranes. Analyses of lithophile isotope ratios revealed no change across this boundary, but initial $^{187}Os/^{188}Os$ ratios changed from 0.2 on the Mesozoic side to about 3 on the Precambrian side. Hence this provides strong support for a relatively shallow contamination process, attributed by Chesley and Ruiz to mafic lower crust. This material would have low values of $\delta^{18}O$ and possibly also low K_2O/P_2O_5 ratios, thus confounding the evidence from these tracers. This should serve as a warning that the composition of the lower continental crust is still not well understood, even for isotope tracer systems which have supposedly reached a mature stage of understanding.

7.3.4 Precambrian granitoids

One of the most fundamental questions about the continental crust is the extent to which any given block of sialic basement is the product of juvenile separation from the mantle or reworking of older cratonic material. Sr isotope data were originally applied to this problem on the grounds that crustal reservoirs, which have high Rb/Sr ratios, develop higher $^{87}Sr/^{86}Sr$ ratios over geological time than does the low-Rb/Sr mantle. Calculation of the initial Sr isotope composition of a plutonic crustal segment should then indicate whether it has a mantle or crustal source. The evolution line for Sr in the depleted mantle is constructed by drawing a linear growth curve from the 'basaltic achondrite best initial' (BABI) value of 0.69899 ± 5 (section 3.2.4) to the $^{87}Sr/^{86}Sr$ composition of recent ocean-ridge basalts in the range 0.702–0.704. Data for specific crustal provinces can then be compared with this evolution line to assess their petrogenesis.

A classic example of the application of the Sr isotope evolution diagram to the provenance of crustal basement is provided by studies of the Archean and Proterozoic gneisses of West Greenland by Moorbath and Pankhurst (1976). Figure 7.36 shows average growth lines for 3.7-Byr-old Amitsoq gneisses from four localities, 2.8–2.9-Byr-old Nuk gneisses from five localities, 1.8-Byr-old Ketilidian gneisses from two localities (in South Greenland) and the 2.52-Byr-old Qorqut granite. The initial ratios of these terranes are compared in Fig. 7.36 with a hypothetical linear upper-mantle growth line drawn between BABI and MORB.

Moorbath and Pankhurst argued that the Nuk (and Ketilidian) gneisses could not be derived by reworking of older (e.g. Amitsoq) gneiss, since the growth lines of the Amitsoq samples are much too steep to generate products with initial ratios of only 0.702–0.703. Instead they concluded that the igneous precursors of the Nuk gneisses represented a massive addition of juvenile calc-alkaline crust to the Archean basement of West Greenland. The slight elevation of the calculated initial ratios above the upper-mantle evolution line was attributed to a period of crustal Sr isotope evolution, lasting perhaps 100–200 Myr, between the separation of the igneous precursors from the mantle and their subjection to granulite-facies metamorphism (see section 5.5). In contrast, Moorbath and Pankhurst recognised the Qorqut granite as a good candidate for a pluton derived by reworking of older crust, since its initial ratio of 0.709 ± 0.007 is well within error of the compositions of Amitsoq gneisses at that time.

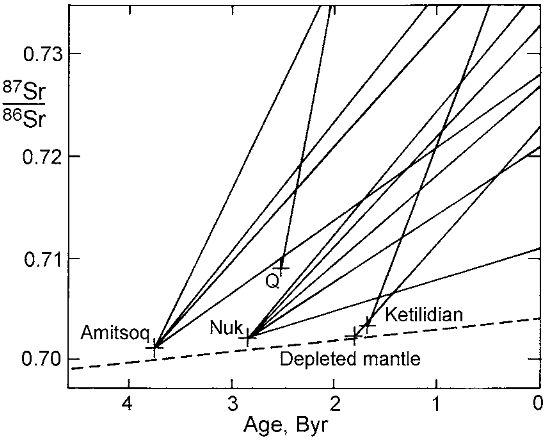

Fig. 7.36. Sr isotope evolution diagram showing the development of four crustal suites relative to the depleted-mantle evolution line. The Qorqut granite (Q) is attributed to crustal anatexis. After Moorbath and Taylor (1981).

Pb isotope analysis of the Nuk gneisses revealed a more complex picture than the Sr isotope data alone, by demonstrating that Nuk magmas emplaced into areas of Amitsoq crust had suffered significant contamination with old crustal Pb (section 5.5). In view of the lack of obvious crustal Sr contamination, selective contamination by Pb was invoked to explain these observations (Taylor *et al.*, 1980). In this situation, the application of Nd isotope analysis provides an ideal way of testing petrogenetic models for the Nuk gneisses.

Taylor *et al.* (1984) analysed a selection of Pb-contaminated and Pb-uncontaminated gneisses for Nd isotope composition (Fig. 7.37). The data indicate a good correlation between ε Nd and Rb, an

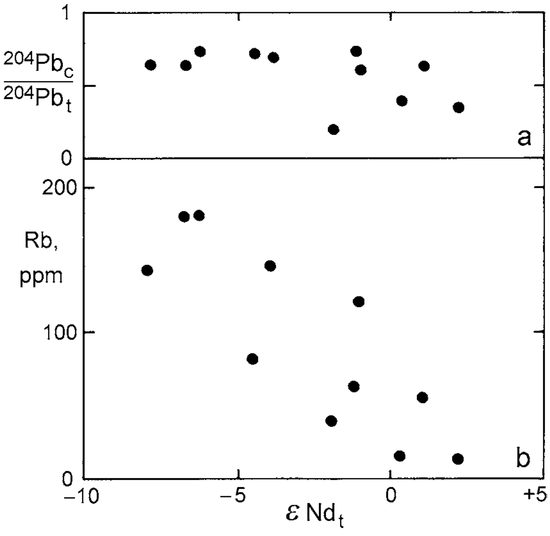

Fig. 7.37. Variation of ε Nd in Nuk gneisses, compared with (a) the fraction of isotopic contamination by Amitsoq Pb (from section 5.5); and (b) Rb content. After Taylor *et al.* (1984).

incompatible trace element expected to be enriched in the Amitsoq gneisses. Taylor *et al.* attributed these results to contamination of mantle-derived Nuk magmas by partial melts of Amitsoq gneiss in the lower crust. However, ε Nd does not correlate well with the degree of Pb isotopic contamination (represented by the index $^{204}Pb_{contaminant}/^{204}Pb_{total}$). This suggests that additional selective Pb contamination occurred, due to Pb-enriched fluids generated by crustal dehydration.

The paradox whereby substantial Pb and Nd contamination of the Nuk magmas was not accompanied by observable Sr isotope disturbance must be attributed to the stratified nature of the Amitsoq crust. Taylor *et al.* argued that the deep crust responsible for Pb and Nd contamination must have had lower Rb/Sr ratios than those analysed from the surface outcrops, presumably due to the flushing out of Rb from the lower crust during granulite-facies metamorphism. Hence it did not develop elevated Sr isotope ratios over geological time. It is concluded from this evidence and other studies that Sr isotope data often cannot readily distinguish between mantle and lower-crustal source regions. In this situation, Nd isotopes are a more powerful petrogenetic tracer because Sm/Nd is fractionated during crustal extraction from the mantle but is not significantly fractionated by intra-crustal processes (section 4.3).

The Pb isotope system comprises two coupled dating systems, whereas Sm–Nd normally offers only one. Therefore Pb–Pb data should theoretically provide more control than Nd data on mixing between crustal reservoirs of different ages. However, U–Pb isotope systems are quite susceptible to open-system behaviour over geological history, whereas whole-rock Sm–Nd systems are very resistant to such effects. Therefore, when Pb–Pb data are used to study ancient mixing events, the measured isotope ratios cannot normally be corrected to unique initial ratios. Instead, model initial $^{207}Pb/^{204}Pb$ ratios are usually determined by projecting the Pb–Pb data back along an isochron line corresponding to the age of the mixing event (e.g. Fig. 5.36). Hence, we are left with a single isotopic tracer, analogous to $^{143}Nd/^{144}Nd$.

Davis *et al.* (1996) compared the use of initial $^{207}Pb/^{204}Pb$ and $^{143}Nd/^{144}Nd$ ratios in late Archean granitoids as tracers of the extent of Early–Mid-Archean basement in the Slave Province of NW Canada. They found a relatively good correlation between the two tracers (Fig. 7.38), supporting a model of two-component mixing between juvenile (recently mantle-derived) and old crustal end-members. The mixing line is somewhat curved, indicating a Pb/Nd ratio in the old crustal end-member about three times higher than in the juvenile end-member. In principle this makes Pb a more sensitive tracer of hidden crust than Nd. However, evidence from Greenland (Fig. 7.37) suggests that Pb may behave less reproducibly. Hence, the scatter in Fig. 7.38 is probably due to non-stoichiometric mixing of Pb rather than Nd.

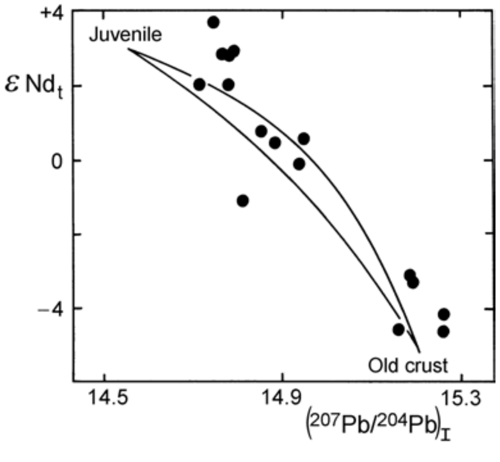

Fig. 7.38. Plot of calculated initial $^{143}Nd/^{144}Nd$ *versus* $^{207}Pb/^{204}Pb$ compositions of Late Archean granitoid magmas (●), explained by mixing of juvenile and ancient crustal end-members. After Davis *et al.* (1996).

7.3.5 Phanerozoic batholiths

Hurley *et al.* (1965) performed a strontium isotope study of the Sierra Nevada batholith and concluded that most of the intrusive bodies making up the batholith had initial $^{87}Sr/^{86}Sr$ ratios of about 0.7073 ± 0.001. They recognised that this value was intermediate between expected upper-mantle and Precambrian crustal values of about 0.703–0.705 and 0.71–0.73, respectively. However, they were unable to determine on the basis of the Sr isotope evidence whether the Sierra Nevada batholith represented mantle-derived magmas subsequently contaminated by the crust, or simply partial melting of geosynclinal sediments and volcanics.

DePaolo (1981b) performed a combined Sr and Nd isotope study of the Sierra Nevada and Peninsular Ranges batholiths in a further attempt to resolve the genesis of these bodies. The data define hyperbolic arrays on ε Sr *versus* ε Nd diagrams (Fig. 7.39), running from the island-arc basalt field towards the composition of a nearby Precambrian schist. The latter was regarded as representative of the source area which yielded the Paleozoic–Mesozoic geosynclinal sediments into which the batholiths are intruded. DePaolo recognised that the western Peninsular Ranges samples closely conformed to the Sr–Nd mantle array, and that they could therefore be products of a heterogeneous mantle without crustal contamination. However, in the context of the Sierra Nevada data, crustal contamination of magmas within the island-arc field seems much more likely.

This interpretation is supported by a comparison of strontium and oxygen isotope data (Taylor and Silver, 1978; DePaolo, 1981b), which together form another powerful tool for studies of granite petrogenesis. (For background to stable-isotope geology, see Hoefs, 1987.) Sierra Nevada and Peninsular Range granitoids form a hyperbolic array on the ε Sr *versus* $\delta^{18}O$ diagram (Fig. 7.40), between mantle-derived and Paleozoic sediment end-members. The shape of the hyperbola is determined by the relative strontium/oxygen concentrations in the two end-members, and is consistent with a simple mixture of high-$\delta^{18}O$ sedimentary crustal melts with basic magmas.

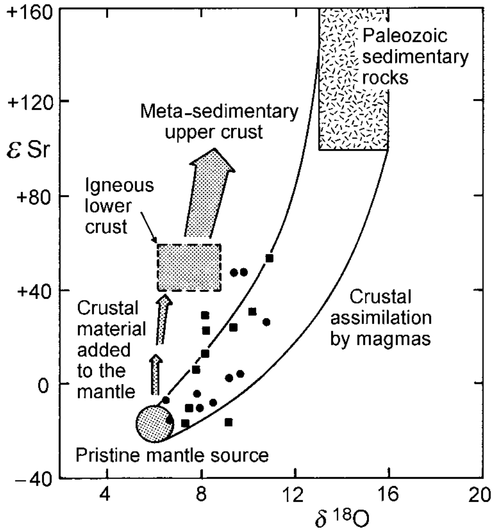

Fig. 7.40. Plot of ε Sr against $\delta^{18}O$, showing data for the Peninsula Ranges (●) and Sierra Nevada (■) batholiths, relative to possible magma sources and mixing models. After DePaolo (1981b).

Three alternative models can all be ruled out because they would cause vertical vectors in Fig. 7.40, in which Sr isotope increases would not be accompanied by appreciable change in $\delta^{18}O$. These models are the following:

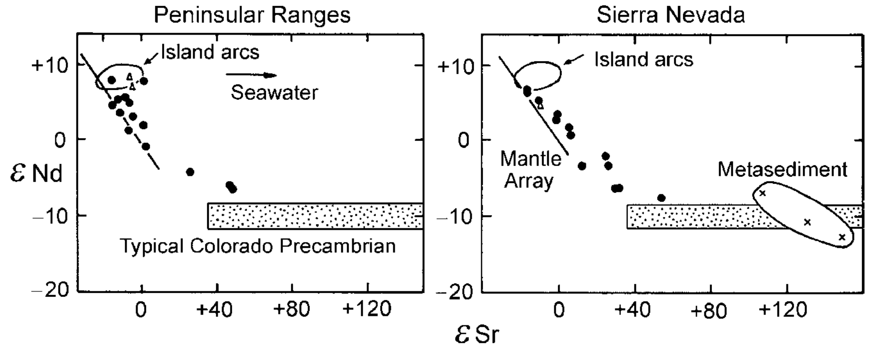

Fig. 7.39. Plots of ε Nd against ε Sr for granitoids (●) from the Peninsular Ranges and the Sierra Nevada. Compositions of crustal reservoirs and the effect of seawater alteration are also shown. After DePaolo (1981b).

(1) Sr (and Nd) isotopic enrichment of a mantle source along the mantle array in Fig. 7.39.

(2) Contamination of the mantle source by subduction of sediment. The much lower strontium content of mantle, relative to basic magmas, would make it much more susceptible to contamination by subducted sedimentary or seawater Sr, whereas the oxygen content of the mantle is the same as that of basic magmas. In other words, the mantle has a lower Sr/O ratio than basic magma, which would yield a mixing hyperbola of steeper slope in Fig. 7.40.

(3) Contamination of magmas by a hypothetical lower crustal component with low $\delta\,^{18}$O values.

Neither Fig. 7.39 nor Fig. 7.40 can distinguish between genesis of the Peninsula Ranges batholith as a direct mantle-derived differentiate or as a re-melt of young basic igneous rock at the base of the crustal geosyncline. However, the San Marcos gabbro unit of the Peninsular Ranges must be a direct mantle melt because of its basic major-element composition. Additional mantle-derived melts must have been present at depth to cause crustal melting. Therefore, the simplest, but not exclusive, model is that these melts contributed fractionated magmas to the rest of the batholith.

As important products of Phanerozoic crustal evolution, the California batholiths are paralleled by the Berridale and Kosciusko batholiths of the Lachlan fold belt of SE Australia. However, the genesis of these granitoid suites has proved particularly controversial. This debate began when Chappell and White (1974) distinguished two major types of granite on the basis of chemical and mineralogical criteria. 'S-type' granites with low Ca contents and a tendency to per-aluminous character ($Al_2O_3/(Na_2O + K_2O + CaO) > 1.05$) were regarded as partial melts of sedimentary rocks; 'I-type' granites with high Ca contents and $Al_2O_3/(Na_2O + K_2O + CaO) < 1.05$ were regarded as partial melts of young igneous crustal rocks.

McCulloch and Chappell (1982) tested this model by analysing a suite of samples from the Berridale and Kosciusko batholiths for Sr and Nd isotope compositions. The data formed two overlapping fields, which together define a hyperbolic array in the lower-right quadrant of the ε Nd *versus* ε Sr diagram (Fig. 7.41). McCulloch and Chappell interpreted these data in support of the crustal-melting model of Chappell and White (1974). However, Gray (1984; 1990) attributed them to contamination of mantle-derived basic magmas by mixing with a sedimentary crustal component. Possible end-members are represented by young basic rocks with a mantle-like signature, and Ordovician flysch with a model Nd age of about 1400 Myr. The left end of the array projects back to a depleted mantle-like end-member with ε Nd of + 6. The existence of 'rare gabbros' in the vicinity of the batholiths demonstrates that such magmas were available in the crust; their rarity at the surface can be attributed to the 'density problem' of raising basic magma through a felsic crust. The crustal end-member is well represented by the Cooma granodiorite, which displays strong structural evidence of being an *in situ* melt of Ordovician flysch.

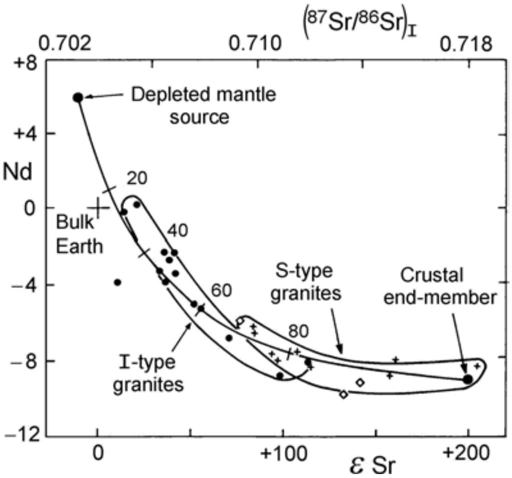

Fig. 7.41. Diagram of ε Nd against ε Sr for 'I-type' (●) and 'S-type' (+) granites and crustal xenoliths (◇) from SE Australia. A best-fit mixing line between hypothetical crustal and mantle-derived end-members is shown. After McCulloch and Chappell (1982).

Gray supported his model with major-element-variation diagrams and by examining Sr isotope compositions on a Rb–Sr isochron diagram (Fig. 7.42). Average initial $^{87}Sr/^{86}Sr$ and Rb/Sr ratios are plotted for two gabbros and for several plutons from the major 'S-type' and 'I-type' batholiths. Most of the data form a cone-shaped array, which Gray attributed to mixing between a low-Rb/Sr basaltic or andesitic end-member ($^{87}Sr/^{86}Sr \simeq 0.703$–$0.704$) and a somewhat heterogeneous crustal end-member, typified by the crustally derived Cooma granodiorite. Compositions to the right of this array were attributed to plagioclase fractionation subsequent to mixing, which would yield horizontal displacements.

McCulloch and Chappell (1982) and Chappell and White (1992) acknowledged that the isotopic data for the Lachlan Fold Belt could be explained by two-component mixing between mafic and sedimentary

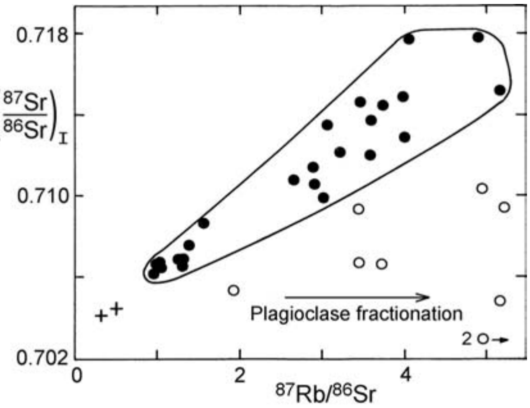

Fig. 7.42. Rb–Sr pseudo-isochron diagram for granites of SE Australia (●) showing a possible 'mixing fan': (+) = gabbros; (○) = granites argued to have fractionated plagioclase after contamination. After Gray (1984).

end-members. However, they rejected this model on the grounds that mixing of basic igneous and greywacke components could not explain the major-element signatures of the rocks (White and Chappell, 1988).

This problem was solved by a more detailed study of the most mafic granitoids of the Lachlan Fold Belt, comprising the Moruya granitoid suite (Keay *et al.*, 1997). A variety of rock types from this suite defined an elongated distribution with ε Nd values from +8 to +4, lying between the fields for Paleozoic mantle-derived magmas and Cambrian greenstones (Fig. 7.43) believed to be an important deep-crustal component of the fold belt. Hence, Keay *et al.* attributed these rocks to mixing between a mantle-derived basic magma and tonalitic partial melts of the Cambrian greenstones. These mixed magmas then provide one end-member for an additional mixing process involving melts of Ordovician turbidites, leading overall to a three-component mixing model. This model also explains the relatively greater abundance of the S-type granites (containing a large sedimentary component) in the western part of the belt, since the turbidite sequence is thickest in the west and dies out eastwards (Collins, 1998).

In response to this revised contamination model, Chappell *et al.* (1999) continued to assert one aspect of their earlier crustal-melting model, involving the importance of restite (the solid residue of crustal melting) as a component in the genesis of granite. However, this is largely a second-order problem because all workers agree that restite is present in the granitoids of the Lachlan Fold Belt; the disagreement is now about the relative importance of this solid component in the relatively late-stage evolution of granitoid magmas.

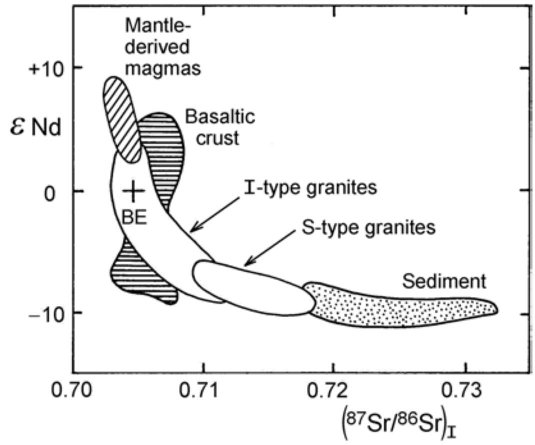

Fig. 7.43. Plot of ε Nd versus initial Sr isotope ratio for granitoids of the Lachlan Fold Belt, together with mantle-derived and crustal end-members (shaded) involved in a three-component mixing model. After Keay *et al.* (1997).

References

Barfod, D. N., Ballentine, C. J., Halliday, A. N. and Fitton, J. G. (1999). Noble gases in the Cameroon line and the He, Ne, and Ar isotopic composition of high mu (HIMU) mantle. *J. Geophys. Res.* **104**, 29 509–27.

Bell, K. and Blenkinsop, J. (1987). Archean depleted mantle: evidence from Nd and Sr initial isotopic ratios of carbonatites. *Geochim. Cosmochim. Acta* **51**, 291–8.

Bell, K. and Simonetti, A. (1996). Carbonatite magmatism and plume activity: implications from the Nd, Pb and Sr isotope systematics of Oldoinyo Lengai. *J. Petrol.* **37**, 1321–39.

Bell, K. and Tilton, G. R. (2001). Nd, Pn and Sr isotopic compositions of East African carbonatites: evidence for mantle mixing and plume heterogeneity. *J. Petrol.* **42**, 1927–45.

Brandon, A. D. and Goles, G. G. (1988). A Miocene subcontinental plume in the Pacific Northwest: geochemical evidence. *Earth Planet. Sci. Lett.* **88**, 273–83.

Brandon, A. D. and Goles, G. G. (1995). Assessing subcontinental lithospheric mantle sources for basalts: Neogene volcanism in the Pacific Northwest, USA as a test case. *Contrib. Mineral. Petrol.* **121**, 364–79.

Briqueu, L. and Lancelot, J. R. (1979). Rb–Sr systematics and crustal contamination models for calc-alkaline igneous rocks. *Earth Planet. Sci. Lett.* **43**, 385–96.

Carlson, R. W. and Hart, W. K. (1988). Flood basalt volcanism in the northwestern United States. In: MacDougall, J. D. (Ed.), *Continental Flood Basalts*. Kluwer, pp. 35–62.

Carlson, R. W., Lugmair, G. W. and MacDougall, J. D. (1981). Columbia River volcanism: the question of mantle heterogeneity or crustal contamination. *Geochim. Cosmochim. Acta* **45**, 2483–99.

Chamberlain, V. E. and Lambert, R. St. J. (1994). Lead isotopes and the sources of the Columbia River Basalt Group. *J. Geophys. Res.* **99**, 11 805–17.

Chappell, B. W. and White, A. J. R. (1974). Two contrasting granite types. *Pacific Geol.* **8**, 173–4.

Chappell, B. W. and White, A. J. R. (1992). I- and S-type granites in the Lachlan Fold Belt. *Trans. Roy. Soc. Edinburgh: Earth Sci.* **83**, 1–26.

Chappell, B. W., White, A. J. R., Williams, I. S., Wyborn, D., Hergt, J. M. and Woodhead, J. D. (1999). Discussion and reply: evaluation of petrogenetic models for Lachlan Fold belt granitoids: implications for crustal architecture and tectonic models. *Australian J. Earth Sci.* **46**, 827–36.

Chesley, J. T. and Ruiz, J. (1998). Crust–mantle interaction in large igneous provinces: implications from the Re–Os isotope systematics of the Columbia River flood basalts. *Earth Planet. Sci. Lett.* **154**, 1–11.

Collins, W. J. (1998). Evaluation of petrogenetic models for Lachlan Fold belt granitoids: implications for crustal architecture and tectonic models. *Australian J. Earth Sci.* **45**, 483–500.

Davidson, J. P. and Tepley, F. J. (1997). Recharge in volcanic systems; evidence from isotopic profiles of phenocrysts. *Science* **275**, 826–9.

Davidson, J., Tepley, F., Palacz, Z. and Meffan-Main, S. (2001). Magma recharge, contamination and residence times revealed by *in situ* laser ablation isotopic analysis of feldspar in volcanic rocks. *Earth Planet. Sci. Lett.* **184**, 427–42.

Davis, W. J., Gariepy, C. and van Breemen, O. (1996). Pb isotopic composition of late Archean granites and the extent of recycling early Archean crust in the Slave Province, northwest Canada. *Chem. Geol.* **130**, 255–69.

Dawson, J. B. (1967). A review of the geology of kimberlite. In: Wyllie, P. J. (Ed.), *Ultramafic and Related Rocks*. Wiley, pp. 241–51.

Dawson, J. B. and Smith, J. V. (1977). The MARID (mica–amphibole–rutile–ilmenite–diopside) suite of xenoliths in kimberlite. *Geochim. Cosmochim. Acta* **41**, 309–23.

DePaolo, D. J. (1981a). Trace element and isotopic effects of combined wallrock assimilation and fractional crystallisation. *Earth Planet. Sci. Lett.* **53**, 189–202.

DePaolo, D. J. (1981b). A neodymium and strontium isotopic study of the Mesozoic calc-alkaline granitic batholiths of the Sierra Nevada and Peninsular Ranges, California. *J. Geophys. Res.* **86**, 10 470–88.

DePaolo, D. J. (1983). Comment on 'Columbia River volcanism: the question of mantle heterogeneity or crustal contamination' by R. W. Carlson, G. W. Lugmair and J. D. Macdougall. *Geochim. Cosmochim. Acta* **47**, 841–4.

DePaolo, D. J. (1988). *Neodymium Isotopes in Geology*. Springer-Verlag, 187 pp.

DePaolo, D. J. and Wasserburg, G. J. (1976). Nd isotopic variations and petrogenetic models. *Geophys. Res. Lett.* **3**, 249–52.

DePaolo, D. J. and Wasserburg, G. J. (1979a). Petrogenetic mixing models and Nd–Sr isotopic patterns. *Geochim. Cosmochim. Acta* **43**, 615–27.

DePaolo, D. J. and Wasserburg, G. J. (1979b). Neodymium isotopes in flood basalts from the Siberian Platform and inferences about their mantle sources. *Proc. Nat. Acad. Sci. USA* **76**, 3056–60.

Dickin, A. P. (1981). Isotope geochemistry of Tertiary igneous rocks from the Isle of Skye, N. W. Scotland. *J. Petrol.* **22**, 155–89.

Dickin, A. P., Brown, J. L., Thompson, R. N., Halliday, A. N. and Morrison, M. A. (1984). Crustal contamination and the granite problem in the British Tertiary Volcanic Province. *Phil. Trans. Roy. Soc. Lond. A* **310**, 755–80.

Dodson, A., Kennedy, B. M. and DePaolo, D. J. (1997). Helium and neon isotopes in the Imnaha Basalt, Columbia River Basalt Group: evidence for a Yellowstone plume source. *Earth Planet. Sci. Lett.* **150**, 443–51.

Ellam, R. M. and Cox, K. G. (1989). A Proterozoic lithospheric source for Karoo magmatism: evidence from the Nuanetsi picrites. *Earth Planet. Sci. Lett.* **92**, 207–18.

Ellam, R. M. and Cox, K. G. (1991). An interpretation of Karoo picrite basalts in terms of interaction between asthenospheric magmas and the mantle lithosphere. *Earth Planet. Sci. Lett.* **105**, 330–42.

Erlank, A. J., Waters, F. G., Hawkesworth, C. J. *et al.* (1987). Evidence for mantle metasomatism in peridotite nodules from the Kimberly pipes, South Africa. In: Menzies, M. A. and Hawkesworth, C. J. (Eds.), *Mantle Metasomatism*. Academic Press, pp. 221–311.

Fitton, J. G. and Dunlop, H. M. (1985). The Cameroon line, West Africa, and its bearing on the origin of oceanic and continental alkali basalt. *Earth Planet. Sci. Lett.* **72**, 23–38.

Gibson, S. A., Thompson, R. N., Dickin, A. P. and Leonardos, O. H. (1996). High-Ti and low-Ti mafic potassic magmas: key to plume–lithosphere interactions and continental flood-basalt genesis. *Earth Planet. Sci. Lett.* **141**, 325–41.

Gray, C. M. (1984). An isotopic mixing model for the origin of granitic rocks in southeastern Australia. *Earth Planet. Sci. Lett.* **70**, 47–60.

Gray, C. M. (1990). A strontium isotopic traverse across the granitic rocks of southeastern Australia: petrogenetic and tectonic implications. *Australian J. Earth Sci.* **37**, 331–49.

Grégoire, M., Bell, D. R. and Le Roex, A. P. (2002). Trace element geochemistry of phlogopite-rich mafic mantle xenoliths: their classification and their relationship to phlogopite-bearing peridotites and kimberlites revisited. *Contrib. Mineral. Petrol.* **142**, 603–25.

Halliday, A. N., Davidson, J. P., Holden, P., DeWolf, C., Lee, D-C, and Fitton, J. G. (1990). Trace-element fractionation in plumes and the origin of HIMU mantle beneath the Cameroon line. *Nature* **347**, 523–8.

Halliday, A. N., Dickin, A. P., Fallick, A. E. and Fitton, J. G. (1988). Mantle dynamics: a Nd, Sr, Pb and O isotopic study of the Cameroon line volcanic chain. *J. Petrol.* **29**, 181–211.

Hammouda, T., Pichavant, M. and Chaussidon, M. (1996). Isotopic equilibration during partial melting: an experimental test of the behaviour of Sr. *Earth Planet. Sci. Lett.* **144**, 109–21.

Harte, B. (1983). Mantle peridotites and processes – the kimberlite sample. In: Hawkesworth, C. J. and Norry, M. J. (Eds.), *Continental Basalts and Mantle Xenoliths*. Shiva, pp. 46–91.

Hawkesworth, C. J., Erlank, A. J., Marsh, J. S., Menzies, M. A. and van Calsteren, P. W. C. (1983). Evolution of the continental lithosphere: evidence from volcanics and xenoliths in Southern Africa. In: Hawkesworth, C. J. and Norry, M. J. (Eds.), *Continental Basalts and Mantle Xenoliths*. Shiva, pp. 111–38.

Hawkesworth, C. J., Gallagher, K., Kelley, S. *et al.* (1992). Paraná magmatism and the opening of the South Atlantic. *Geol. Soc. Lond. Spec. Pub.* **68**, 221–40.

Hawkesworth, C. J., Kempton, P. D., Rogers, N. W., Ellam, R. M. and van Calsteren, P. W. C. (1990). Continental mantle lithosphere, and shallow level enrichment processes in the Earth's mantle. *Earth Planet. Sci. Lett.* **96**, 256–68.

Hawkesworth, C. J., Rogers, N. W., van Calsteren, P. W. C. and Menzies, M. A. (1984). Mantle enrichment processes. *Nature* **311**, 331–3.

Hergt, J. M., Peate, D. W. and Hawkesworth, C. J. (1991). The petrogenesis of Mesozoic Gondwana low-Ti flood basalts. *Earth Planet. Sci. Lett.* **105**, 134–48.

Hoefs, J. (1987). *Stable Isotope Geology*, 3rd edn. Springer-Verlag, 241 pp.

Hooper, P. R. and Hawkesworth, C. J. (1993). Isotopic and geochemical constraints on the origin and evolution of the Columbia River basalt. *J. Petrol.* **34**, 1203–46.

Huppert, H. E. and Sparks, R. S. J. (1985). Cooling and contamination of mafic and ultramafic magmas during ascent through continental crust. *Earth Planet. Sci. Lett.* **74**, 371–86.

Hurley, P. M., Bateman, P. C., Fairbairn, H. W. and Pinson, W. H. (1965). Investigation of initial Sr^{87}/Sr^{86} ratios in the Sierra Nevada plutonic province. *Bull. Geol. Soc. Amer.* **76**, 165–74.

Jones, A. P., Smith, J. V. and Dawson, J. B. (1982). Mantle metasomatism in 14 veined peridotites from Bultfontein Mine, South Africa. *J. Geol.* **90**, 435–53.

Jordan, T. H. (1975). The continental tectosphere. *Rev. Geophys. Space Phys.* **13** (3), 1–12.

Jordan, T. H. (1978). Composition and development of the continental tectosphere. *Nature* **274**, 544–8.

Kaczor, S. M., Hanson, G. N. and Peterman, Z. E. (1988). Disequilibrium melting of granite at the contact with a basic plug: a geochemical and petrographic study. *J. Geol.* **96**, 61–78.

Keay, S., Collins, W. J. and McCulloch, M. T. (1997). A three-component Sr–Nd isotopic mixing model for granitoid genesis, Lachlan fold belt, eastern Australia. *Geology* **25**, 307–10.

Kerr, A. C., Kempton, P. D. and Thompson, R. N. (1995). Crustal assimilation during turbulent magma ascent (ATA); new isotopic evidence from the Mull Tertiary lava succession, N.W. Scotland. *Contrib. Mineral. Petrol.* **119**, 142–54.

Kille, I. C., Thompson, R. N., Morrison, M. A. and Thompson, R. F. (1986). Field evidence for turbulence during flow of a basalt magma through conduits from southwest Mull. *Geol. Mag.* **123**, 693–7.

Knesel, K. M. and Davidson, J. P. (1999). Sr isotope systematics during melt generation by intrusion of basalt into continental crust. *Contrib. Mineral. Petrol.* **136**, 285–95.

Knesel, K. M. and Davidson, J. P. (2002). Insights into collisional magmatism from isotopic fingerprints of melting reactions. *Science* **296**, 2206–8.

Kramers, J. D. (1979). Lead, uranium, strontium, potassium and rubidium in inclusion-bearing diamonds and mantle-derived xenoliths from southern Africa. *Earth Planet. Sci. Lett.* **42**, 58–70.

Kramers, J. D., Roddick, J. C. M. and Dawson, J. B. (1983). Trace element and isotopic studies on veined, metasomatic and 'MARID' xenoliths from Bultfontein, South Africa. *Earth Planet. Sci. Lett.* **65**, 90–106.

Lambert, D. D., Walker, R. J., Morgan, J. W. *et al.* (1994). Re–Os and Sm–Nd isotope geochemistry of the Stillwater Complex, Montana: implications for the petrogenesis of the J–M reef. *J. Petrol.* **35**, 1717–35.

Maaloe, S. and Aoki, K. (1977). The major element composition of the upper mantle estimated from the composition of lherzolites. *Contrib. Mineral. Petrol.* **63**, 161–73.

Mantovani, M. S. M. and Hawkesworth, C. J. (1990). An inversion approach to assimilation and fractional crystallisation processes. *Contrib. Mineral. Petrol.* **105**, 289–302.

Maury, R. C. and Bizouard, H. (1974). Melting of acid xenoliths into a basanite: an approach to the possible mechanisms of crustal contamination. *Contrib. Mineral. Petrol.* **48**, 275–86.

McCulloch, M. T. and Chappell, B. W. (1982). Nd isotopic characteristics of S- and I-type granites. *Earth Planet. Sci. Lett.* **58**, 51–64.

McCulloch, M. T., Jaques, A. L., Nelson, D. R. and Lewis, J. D. (1983). Nd and Sr isotopes in kimberlites and lamproites from Western Australia: an enriched mantle origin. *Nature* **302**, 400–3.

McKenzie, D. and Bickle, M. J. (1988). The volume and composition of melt generated by extension of the lithosphere. *J. Petrol.* **29**, 625–79.

Menzies, M. A. (1989). Cratonic, circumcratonic and oceanic mantle domains beneath the Western United States. *J. Geophys. Res.* **94**, 7899–915.

Menzies, M. A. and Murthy, V. R. (1980). Enriched mantle: Nd and Sr isotopes in diopsides from kimberlite nodules. *Nature* **283**, 634–6.

Moorbath, S. and Pankhurst, R. J. (1976). Further rubidium–strontium age and isotope evidence for the nature of the late Archean plutonic event in West Greenland. *Nature* **262**, 124–6.

Moorbath, S. and Taylor, P. N. (1981). Isotopic evidence for continental growth in the Precambrian. In: Kroner, A. (Ed.), *Precambrian Plate Tectonics*. Elsevier, pp. 491–525.

Moorbath, S. and Thompson, R. N. (1980). Strontium isotope geochemistry and petrogenesis of the early Tertiary lava pile of the Isle of Skye, Scotland and other basic rocks of the British Tertiary Province: an example of magma crust interaction. *J. Petrol.* **21**, 217–231.

Moorbath, S. and Welke, H. (1969). Lead isotope studies on igneous rocks from the Isle of Skye, Northwest Scotland. *Earth Planet. Sci. Lett.* **5**, 217–30.

Morrison, M. A., Thompson, R. N. and Dickin, A. P. (1985). Geochemical evidence for complex magmatic plumbing during development of a continental volcanic center. *Geology* **13**, 581–4.

Nelson, D. R., Chivas, A. R., Chappell, B. W. and McCulloch, M. T. (1988). Geochemical and isotopic systematics in carbonatites and implications for the evolution of ocean-island sources. *Geochim. Cosmochim. Acta* **52**, 1–17.

Nixon, P. H., Rogers, N. W., Gibson, I. L. and Grey, A. (1981). Depleted and fertile mantle xenoliths from southern African kimberlites. *Ann. Rev. Earth Planet. Sci.* **9**, 285–309.

Read, H. H. (1948). Granites and granites. In: Gilluly, J. (Ed.), *Origin of Granite. Geol. Soc. Amer. Mem.* **28**, 1–19.

Richter, F. M. (1988). A major change in the thermal state of the Earth at the Archean–Proterozoic boundary: consequences for the nature and preservation of continental lithosphere. *J. Petrol. Spec. Vol.*, 39–52.

Smith, C. B. (1983). Pb, Sr and Nd isotopic evidence for sources of southern African cretaceous kimberlites. *Nature* **304**, 51–4.

Taylor, H. P. (1980). The effects of assimilation of country rocks by magmas on $^{18}O/^{16}O$ and $^{87}Sr/^{86}Sr$ systematics in igneous rocks. *Earth Planet. Sci. Lett.* **47**, 243–54.

Taylor, H. P. and Silver, L. T. (1978). Oxygen isotope relationships in plutonic igneous rocks of the Peninsula Ranges Batholith, southern and Baja California. *US Geol. Surv. Open File Rep.* **79–701**, 423–6.

Taylor, P. N., Jones, N. W. and Moorbath, S. (1984). Isotopic assessment of relative contributions from crust and mantle sources to the magma genesis of Precambrian granitoid rocks. *Phil. Trans. Roy. Soc. Lond. A* **310**, 605–25.

Taylor, P. N., Moorbath, S., Goodwin, R. and Petrykowski, A. C. (1980). Crustal contamination as an indicator of the extent of Early Archean continental crust: Pb isotopic evidence from the Late Archean gneisses of West Greenland. *Geochim. Cosmochim. Acta* **44**, 1437–53.

Thirlwall, M. F. and Jones, N. W. (1983). Isotope geochemistry and contamination mechanisms of Tertiary lavas from Skye, northwest Scotland. In: Hawkesworth, C. J. and Norry, M. J. (Eds.), *Continental Basalts and Mantle Xenoliths*. Shiva, pp. 186–208.

Thompson, R. N. (1982). Magmatism of the British Tertiary Volcanic Province. *Scott. J. Geol.* **18**, 49–107.

Thompson, R. N., Dickin, A. P., Gibson, I. L. and Morrison, M. A. (1982). Elemental fingerprints of isotopic contamination of Hebridean Palaeocene mantle derived magmas by Archean sial. *Contrib. Mineral. Petrol.* **79**, 159–68.

Tolstikhin, I. N., Kamensky, I. L., Marty, B. *et al.* (2002). Rare gas isotopes and parent trace elements in ultrabasic–alkaline–carbonatite complexes, Kola Peninsula: identification of lower mantle plume component. *Geochim. Cosmochim. Acta* **66**, 881–901.

Tommasini, S. and Davies, G. R. (1997). Isotope disequilibrium during anatexis: a case study of contact melting, Sierra Nevada, California. *Earth Planet. Sci. Lett.* **148**, 273–85.

Wendlandt, R. F. and Mysen, B. O. (1980). Melting phase relations of natural peridotite + CO_2 as a function of degree of partial melting at 15 and 30 kbar. *Amer. Mineral.* **65**, 37–44.

White, A. J. R. and Chappell, B. W. (1988). Some supracrustal (S-type) granites of the Lachlan Fold Belt. *Trans. Roy. Soc. Edinburgh: Earth Sci.* **79**, 169–81.

8 Osmium isotopes

Osmium is the least abundant member of the group of six elements called the platinum-group elements (PGE). Like lead, osmium is an element with siderophile–chalcophile affinities, but unlike lead, osmium appears to be a strongly ‘compatible’ element during melting in silicate systems (meaning that it is strongly retained in the mantle source mineralogy). These geochemical properties mean that osmium can be used as a dating tool and a tracer in different ways from lithophile isotope systems such as Sr, Pb and Nd, providing unique evidence that complements these other systems.

Osmium has seven naturally occurring isotopes, two of which (^{187}Os and ^{186}Os) are the decay products of long-lived radioactive isotopes, ^{187}Re and ^{190}Pt. Of these two decay schemes, the Re–Os method has been used as a dating tool and geochemical tracer for over twenty years. ^{187}Re has a half-life of about 42 Byr and makes up 62% of natural rhenium, a chalcophile element that behaves like molybdenum. The Pt–Os method has only recently been applied because the radioactive parent, ^{190}Pt, has an extremely long half-life of about 470 Byr and makes up only 0.013% of natural platinum. This means that the natural variations in ^{186}Os are extremely small and hard to measure. However, in combination with the Re–Os couple, the Pt–Os system provides unique information that justifies the effort of its analysis. Technically, ^{186}Os is itself radioactive, but the half-life is so long that it can be considered stable for geological purposes.

8.1 Osmium analysis

Despite its great potential as a geochemical tool, analytical difficulties initially limited the application of the osmium isotope method. The chief of these difficulties is the high ionisation potential of Os (about 9 eV) which prevents the formation of positive osmium ions at temperatures attainable in conventional thermal-ionisation mass spectrometry (TIMS). Alternative methods of excitation therefore had to be sought.

Hirt *et al.* (1963) analysed osmium isotopes as the gaseous species OsO_4, but precision was low (±10% on a 200-ng sample of pure radiogenic osmium). This was probably due to dissociation of OsO_4 during thermal ionisation of the molecule. Consequently, this method was not pursued for over twenty-five years. Instead, subsequent work focussed on the enhanced production of atomic osmium ions using more-energetic ion sources. One of the most successful of these methods was secondary-ion mass spectrometry (SIMS). In this technique, a beam of light negative ions (e.g. O^-) is used to bombard and sputter a purified solid concentrate of osmium metal to yield a positive Os ion beam, which is analysed in a double-focussing mass spectrometer (section 5.2.3). Other high-energy excitation methods used with success were ICP-MS (Russ *et al.*, 1987) and RIMS, involving laser (resonance) ionisation (Walker and Fassett, 1986).

All of these excitation methods for atomic osmium ions were rendered largely obsolete by the discovery that a solid osmium sample could yield negative Os-bearing molecular ions by conventional thermal ionisation (Volkening *et al.*, 1991). This N-TIMS method allows levels of precision over an order of magnitude better than the positive-ion techniques described above.

In the N-TIMS method Os is measured as the species OsO_3^-, using platinum filaments. These are coated with a barium salt to lower the work function of the filament, which enhances the emission of negative ions relative to electrons. The formation of the oxide species may also be enhanced by bleeding oxygen into the source (Walczyk *et al.*, 1991). The same N-TIMS method may be used to perform isotope-dilution analysis of other PGE, as well as rhenium, which forms the ReO_4^- species (Fig. 8.1). This method can generate beams large enough for analysis by Faraday detector from a few nanograms of osmium, while multiplier analysis allows picogram samples to be analysed (Creaser *et al.*, 1991). This technical advance has now brought the osmium isotope system to the same

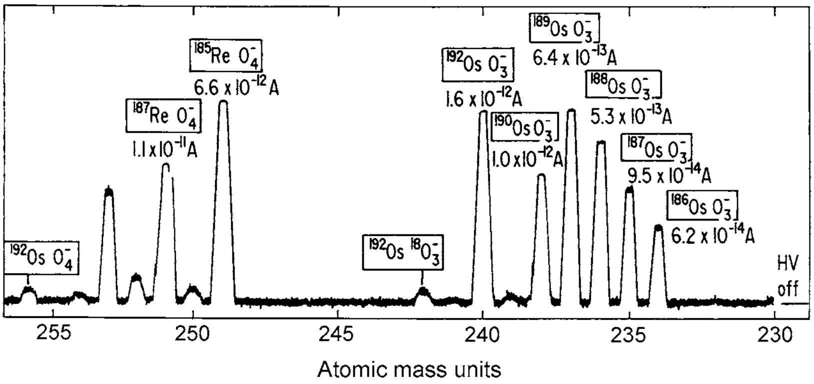

Fig. 8.1. Mass spectrum of Re and Os molecular ions produced from a Ba-doped Pt filament at 770 °C (about 2 A), loaded with 5 ng Os and 3 ng Re. After Creaser *et al.* (1991).

wide range of applications as the Sr, Nd and Pb isotope methods.

In addition to the difficulties of ionising osmium, another major problem with Re–Os analysis has been the chemical behaviour of osmium in solution, due to the existence of multiple oxidation states, including the volatile tetroxide species. The volatility of osmium tetroxide allowed Luck *et al.* (1980) to establish a chemical extraction method in which samples were oxidised after dissolution, allowing separation by distillation. However, the variable oxidation states of osmium have continually plagued the isotope-dilution analysis of osmium, by preventing complete homogenisation between sample and spike osmium.

This problem was finally resolved by the introduction of the somewhat hazardous 'Carius-tube' digestion method (Shirey and Walker, 1995) In this technique, samples are dissolved in sealed glass ampoules under high temperature and pressure. Reagents are typically either aqua regia or a mixture of sulphuric acid and chromium trioxide, and the samples are heated to 240 °C. Outer metal safety jackets are used, but the pressure is retained entirely by the sealed glass tube, which may quite often break! After a successful reaction, the products are frozen before the vial is broken to release the sample.

The development of MC-ICP-MS has reopened the possibility of performing high-precision osmium isotope analyses with the ICP source. However, the principal advantage of MC-ICP-MS is the ability to perform *in situ* analysis by laser ablation. Hirata *et al.* (1998) made the first demonstration of this method by performing *in situ* analysis of Os–Ir alloys. The rarity of this type of material limits the usefulness of the technique. However, Pearson *et al.* (2002) showed that laser ablation MC-ICP-MS could be also used to make *in situ* measurements of osmium isotope ratio and Re/Os ratios in sulphide inclusions within mantle olivines. Since most of the osmium inventory from mantle rocks is probably in sulphide inclusions, the ability to perform *in situ* analyses on this material offers a powerful technique for understanding the behaviour of the Re–Os system in the mantle.

8.2 The Re–Os and Pt–Os decay schemes

8.2.1 The Re decay constant

^{187}Re decays to ^{187}Os by β decay, but the decay energy of 2.65 keV is extremely low, even compared with that for ^{87}Rb (275 keV). This makes measurement of the decay constant by direct counting very difficult. Accurate counting of solid samples is almost impossible, due to absorption of β particles by surrounding Re atoms. An alternative technique is to use either a gaseous Re compound to replace the gas filling of a proportional counter, or a liquid Re compound in a scintillation detector. In both cases it is difficult to find compounds with suitable properties, but Brodzinski and Conway (1965) obtained a ^{187}Re half-life of 66 ± 13 Byr by the former method, and Naldrett (1984) obtained a value of 35 ± 4 Byr by the latter.

The difficulty with counting determinations has encouraged alternative measurements of the ^{187}Re half-life based on growth of the ^{187}Os daughter product, either in the laboratory or in geological samples. One of the most successful was by Lindner *et al.* (1986), who used the 'laboratory-shelf' technique to perform an independent half-life determination. A 1-kg sample of purified perrhenic acid ($HReO_4$) was spiked with two different non-radiogenic Os isotopes (190 and 192),

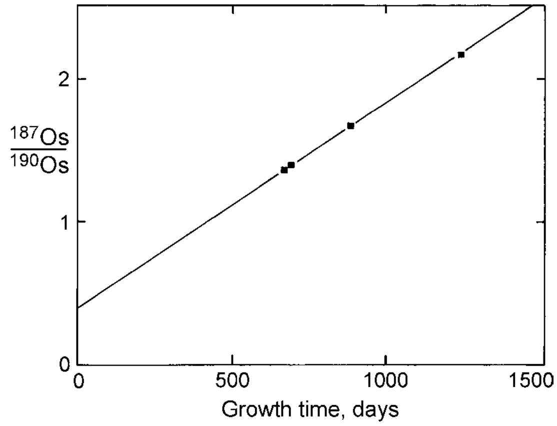

Fig. 8.2. Least-squares growth line of $^{187}Os/^{190}Os$ ratio as a function of time 'on the shelf' for a Re stock solution. Note the non-zero initial ratio. After Lindner *et al.* (1986).

set aside for two years to allow growth of radiogenic Os, and then sampled for Os isotope composition over a further two-year interval. Os isotope measurements by LAMMA and ICP-MS were of comparable precision, and in good agreement, although the two spikes gave results differing by 2%. Results for $^{187}Os/^{190}Os$ obtained by ICP-MS are shown in Fig. 8.2.

Unfortunately, the starting material used by Lindner *et al.* had a non-zero level of initial radiogenic Os, as indicated by the positive intercept in Fig. 8.2. Hence the first two years of storage were effectively wasted. Despite this setback, a precise half-life of 43.5 ± 1.3 Byr was determined. This was refined by Lindner *et al.* (1989), using five times as much data as the earlier work, to a half-life of 42.3 ± 1.3 Byr, equivalent to a decay constant of 1.64×10^{-11} yr^{-1}.

Geological measurements of the half-life are an attractive alternative to laboratory experiments, but these have also encountered technical difficulties. In view of the low concentrations of Re in normal rocks, early attempts at age determination (e.g. Hirt *et al.*, 1963) were made on molybdenite (MoS_2), which strongly concentrates Re at contents of about 10–50 ppm. Since molybdenites effectively incorporate no initial osmium, only the total abundance of the daughter need be measured, but this still involves mass spectrometry, since isotope dilution is the only method with enough sensitivity. Unfortunately, the data scattered significantly, yielding an imprecise half-life of 43 ± 5 Byr.

Luck and Allègre (1982) made further studies of the potential for Re–Os dating with molybdenite. They selected samples of known age over a wide range of geological time and analysed Re and Os concentrations by isotope dilution. Since insignificant amounts of common osmium were found, no isotope-ratio determination was necessary. High-precision results were obtained, sometimes in good agreement with published ages, but often giving older ages. This suggested that Re–Os dating of molybdenite is an unreliable geochronometer. However, more recent work has shown that the method can work, given careful sample selection (section 8.2.3).

8.2.2 Meteorite isochrons

In view of these problems, other attempts at geological half-life determination were focussed principally on iron meteorites. These have moderately large Re and Os contents, commonly in the high-ppb (parts-per-billion) to low-ppm range, and also display the good range of Re/Os ratios necessary for a precise age. Since these samples contain initial Os, the age must be calculated on an isochron diagram. Luck *et al.* (1980) ratioed radiogenic ^{187}Os against ^{186}Os, following Hirt *et al.* (1963). However, most other workers have normalised osmium isotope ratios with respect to ^{188}Os, because ^{186}Os can itself exhibit small variations in nature (see below). This leads to the following Re–Os isochron equation:

$$\left(\frac{^{187}\mathrm{Os}}{^{188}\mathrm{Os}}\right)_{\mathrm{P}} = \left(\frac{^{187}\mathrm{Os}}{^{188}\mathrm{Os}}\right)_{\mathrm{I}} + \frac{^{187}\mathrm{Re}}{^{188}\mathrm{Os}}(e^{\lambda t} - 1) \qquad [8.1]$$

Luck *et al.* (1980) determined a good isochron fit for 'whole-rock' (bulk) samples of five iron meteorites, suggesting that iron meteorites of different types were all formed during a narrow time interval. Good isochron fits were also obtained in subsequent work on iron meteorites by several workers. These isochrons can be used to calculate values for the Re half-life by substituting a value of t into equation [8.1]. Because group-II and group-III iron meteorites represent the cores of differentiated planetesimals, their age is constrained to be slightly younger than that of chondrites. However, iron meteorites cannot be more than about 20 Myr younger than chondrites, since they incorporated the short-lived nuclide ^{107}Pd with a half-life of 6.5 Myr (section 15.5). Hence t must be near 4.55 Byr.

Unfortunately, early meteoritic half-life determinations were also dogged by analytical problems, principally involving spike calibration. For example, Luck *et al.* (1980) determined a half-life of 42.8 ± 2.4 Byr (Fig. 8.3), in close agreement with the estimate of Hirt *et al.* (1963), but Luck and Allègre (1983) retracted this value on the grounds that isotope-dilution analysis

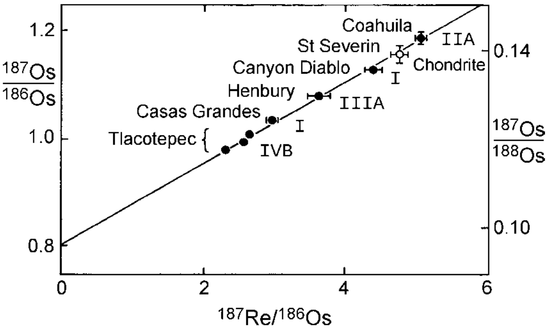

Fig. 8.3. Re–Os isochron diagram, showing best-fit regression for five iron meteorites (notation indicates sub-group) and one chondrite (○). For $T = 4.55$ Byr, $\lambda = 1.62 \pm 0.08 \times 10^{-11}\ \text{yr}^{-1}$ ($t_{1/2} = 42.8$ Byr). After Luck *et al.* (1980).

of Os in their 1980 data set was upset by a change of osmium species in the spike solution subsequent to its calibration. However, subsequent work has shown the original determination to be more nearly correct.

Problems with spike calibration were also encountered by Walker and Morgan (1989), but this time involving an over-estimate of the Re content of the spike, as later demonstrated by Morgan *et al.* (1992). However, Walker and Morgan also encountered problems with inadequate homogenisation between sample and spike. For example, analysis of seven chondrites gave results that did not lie on the isochron through iron meteorites (using the same spike calibration for both types of meteorite). This discrepancy was probably caused by the very different chemistries of the two types of meteorite during dissolution, since more recent work places the chondrites on the iron-meteorite isochron, although with a large degree of scatter attributed to later disturbance of Re–Os systems in chondrites (Walker *et al.*, 2002).

To avoid problems of inadequate spike homogenisation, the Carius-tube technique was used in subsequent studies aimed at more accurate dating of meteorites. In the most detailed of these studies, Smoliar *et al.* (1996) determined Re–Os isochrons for four different classes of iron meteorites, of which the IIIA group is the oldest. Evidence from extinct nuclides (section 15.5.1) suggests that these (group-IIIA) iron meteorites have ages within 5 Myr of the age of angrite meteorites (4558 Myr). Therefore, assuming this age for IIIA meteorites, the Re–Os isochron slope was used to determine a Re decay constant of $1.666 \times 10^{-11}\ \text{yr}^{-1}$, equivalent to a half-life of 41.6 ± 0.4 Byr. The error estimate was based on the possibility of a 1% error on the spike calibration. Although the error estimate itself is uncertain, 41.6 Byr is the best current value for the Re half-life.

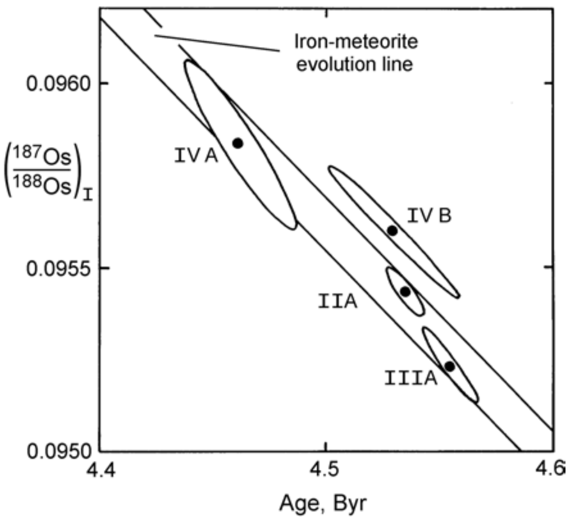

Fig. 8.4. Osmium isotope evolution diagram for ages and initial ratios of iron meteorite isochrons, used to infer the Re–Os evolution of the early solar system. After Smoliar *et al.* (1996).

Using this half-life, other iron-meteorite groups (except IVB) yield ages and initial ratios on a common osmium evolution curve (Fig. 8.4). The slope of this evolution curve represents the Re/Os ratio for the iron-meteorite source, and is within error of the H-chondrite Re/Os ratio. Hence, Smoliar *et al.* suggested that this source is probably the evolving solar nebula. The offset of the IVB initial ratio from the evolution line was later found to be caused by instrumental bias (Smoliar, personal communication). Shen *et al.* (1996) also carried out a precise isochron determination on group-IIAB irons, yielding a slope identical to the group-IIAB isochron of Smoliar *et al.* (within analytical error). The spread of Re–Os ratios in the other groups did not allow precise ages to be determined.

8.2.3 Dating ores and rocks

Very few dating methods have shown much success in the dating of ore deposits, despite the importance of such studies for economic geology. This is because most dating schemes involve lithophile elements that are not stable in ore minerals. In contrast, Re, and to some extent Os, display chalcophile chemistry, so both parent and daughter should occupy relatively stable lattice sites in sulphide minerals. Hence, many attempts at Re–Os dating of ore deposits have been made. However, following the problems encountered by Luck and Allègre (1982) in dating molybdenite, there has been continuing disagreement over the susceptibility of sulphide minerals to open-system behaviour.

Suzuki *et al.* (1993) claimed that recent Re–Os dates on molybdenite were usually concordant with those obtained by other methods, and suggested that errors in the earlier work might be due to poor sample–spike homogenisation rather than geological disturbance. However, other workers such as McCandless *et al.* (1993) maintained that open-system behaviour is a major problem, at least in old molybdenites. They suggested that a combination of microprobe analysis, electron back-scatter imaging and X-ray diffraction should be used to screen samples for alteration prior to analysis.

More success has been achieved in dating young ore deposits with molybdenite. For example, Selby *et al.* (2002) achieved perfect Re/Os isochrons (MSWD < 1) for molybdenites associated with Mesozoic gold deposits from Alaska. The ages were close to the time of igneous intrusion (from U–Pb dating) and older than Ar–Ar dates on hydrothermal muscovite and sericite.

In an attempt to widen the usefulness of the Re–Os method as a geochronometer, Luck and Allègre (1984) applied it to the dating of a Ni–Cu sulphide ore from the Cape Smith komatiite of NE Quebec. This material has moderate concentrations of Re and Os (about 0.4 ppm of each) and can be used to calculate a model Re–Os isotope age in a manner analogous to model Nd ages. Using the then-current decay constant, Luck and Allègre calculated a model Os age of 1740 ± 60 Myr for the sulphide ore, in reasonable agreement with the Sm–Nd isochron age of 1871 ± 75 Myr. However, using the $1.666 \times 10^{-11}\,\text{yr}^{-1}$ decay constant of Smoliar *et al.* (1996), the Re–Os model age is reduced to 1590 Myr, 250 Myr younger than the Sm–Nd age. This suggests that Ni–Cu sulphides are susceptible to re-setting in the same way as Mo sulphide. Similar evidence of open-system behaviour was found by Walker *et al.* (1989b) in Archean schists from India.

Laboratory experiments (Brenan *et al.*, 2000) confirmed the susceptibility of pyrrhotite to re-setting by diffusional gain or loss of osmium. An Arrhenius relationship was observed in high-temperature diffusion experiments. This allowed a pyrrhotite 'blocking' or closure temperature to be calculated (sections 3.3.2 and 10.5; equation [10.15]). The resulting estimates of blocking temperature for a variety of grain sizes were between 300 and 400 °C, similar to the blocking temperature for Rb–Sr and K–Ar in biotite. This means that pyrrhotite as a dating tool is easily re-set by metamorphic events. In contrast, Brenan *et al.* found diffusion rates over an order of magnitude lower in pyrite, implying a blocking temperature over 500 °C.

A recent study on sulphide-rich ores of the Sudbury nickel deposit in Ontario exemplifies the problems of trying to date pyrrhotite-rich ores (Morgan *et al.*, 2002). Suites of sulphide ore from two different mines gave errorchrons with large MSWD values, although the resulting isochron ages were within error of the known age of the complex from U–Pb dating. Similarly, most of the Sudbury ore samples analysed by Dickin *et al.* (1999) appeared to be relatively undisturbed, but a few samples gave impossible (negative) initial ratios indicative of major disturbance. Hence, it is concluded that ages and initial ratios based on pyrrhotite must be treated with caution and substantiated by the analysis of large sample suites.

In contrast to these difficulties, several recent studies have generated good isochrons from sulphide-poor material. One example is a dating study on the Deccan basalts (Allègre *et al.*, 1999). A suite of ten whole-rock basalt samples formed an excellent Re–Os isochron with a good spread of data points. Using a decay constant of $1.663 \times 10^{-11}\,\text{yr}^{-1}$, the isochron gave a precise age of 65.6 ± 0.3 Myr, in excellent agreement with previous K–Ar and Ar–Ar ages averaging 64.5 ± 1.5 Myr. This shows that young whole-rock suites are capable of generating Re–Os isochrons, although older material may be more problematical.

In another recent dating study, Kirk *et al.* (2002) successfully determined a Re–Os isochron age for gold samples from the Witwatersrand Supergroup of South Africa (Fig. 8.5). Gold from the Vaal Reef had moderate Re/Os ratios, and despite the authigenic appearance of some of the grains, gave an age of 3016 ± 110 Myr (MSWD =1.9) which was older than

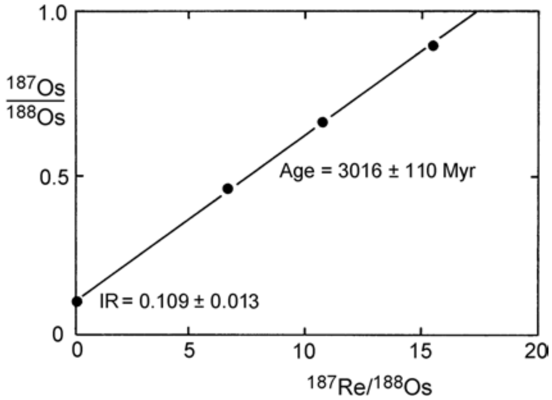

Fig. 8.5. Re–Os isochron defined by gold samples from the Vaal Reef in the Witwatersrand Supergroup of South Africa. After Kirk *et al.* (2002).

the maximum age of sedimentary deposition. This age provides powerful evidence that the gold is of detrital origin, and was not introduced by later hydrothermal fluid circulation.

A final example of the potential of Re–Os geochronology is its application to dating the depositional ages of organic-rich sediments. Sedimentary deposition is one of the most difficult events to date, and attempts to apply the Rb–Sr and U–Pb methods have met with mixed success (sections 3.5 and 5.1.1). However, it was shown by Ravizza and Turekian (1992) that carbonaceous shales could be used to recover seawater osmium signatures (section 8.5), and more recent work (e.g. Cohen *et al.*, 1999) has shown that this material can also be used for dating sedimentary deposition.

Evidence for open Re–Os systems in sulphides suggests that open-system behaviour might also be a problem in dating black shales. However, a study of Paleozoic black shales from the Western Canada sedimentary basin (Creaser *et al.*, 2002) suggested that Re–Os systems remain closed over a variety of degrees of hydrocarbon maturation. On the other hand, contamination of some samples with detrital osmium led to a large scatter on the isochron diagram (MSWD = 103). Therefore, Creaser *et al.* selected samples with total organic carbon contents over 5% in order to sample only seawater-derived (hydrogenous) osmium. These samples formed a much tighter array (MSWD = 1.8) with an age of 358 ± 9 Myr. This suggests that the hydrogenous osmium component in the rock can be successfully isolated to determine depositional ages.

8.2.4 Os normalisation and the Pt–Os decay scheme

Hirt *et al.* (1963) established the convention of ratioing ^{187}Os data against ^{186}Os, and were followed in this practice by Luck and Allègre (1983), who normalised Os data for within-run fractionation with respect to a ^{192}Os/^{188}Os ratio of 3.0827. However, ^{186}Os is itself the α-decay product of the rare long-lived unstable isotope ^{190}Pt. This is not a significant problem in most geological applications, since ^{190}Pt makes up only 0.013% of total platinum. However, in view of the growing importance of the Pt–Os decay scheme for understanding mantle evolution (section 8.3), it now seems best to use an alternative normalising isotope for both decay schemes, and most workers are now using ^{188}Os for this purpose. Hence, in this book ^{188}Os will be used in all cases as the normalising isotope, and isotope ratios previously quoted as ^{187}Os/^{186}Os ratios are now quoted in terms of ^{187}Os/^{188}Os ratios. However, in such cases the original ^{187}Os/^{186}Os ratios are given in brackets and these ratios are shown where possible on figures (when ^{186}Os was the original normalising isotope). ^{187}Os/^{186}Os ratios can be converted to ^{187}Os/^{188}Os ratios by multiplying by 0.12034.

The Pt–Os decay scheme was first applied by Walker *et al.* (1991), who analysed a suite of Pt-rich Fe–Cu–Ni sulphide ores from the Strathcona mine of the Sudbury nickel deposit. They constructed a Pt–Os isochron by substituting into the general decay equation as follows:

$$\left(\frac{^{186}\mathrm{Os}}{^{188}\mathrm{Os}}\right)_{\mathrm{P}} = \left(\frac{^{186}\mathrm{Os}}{^{188}\mathrm{Os}}\right)_{\mathrm{I}} + \frac{^{190}\mathrm{Pt}}{^{188}\mathrm{Os}}(\mathrm{e}^{\lambda t} - 1) \qquad [8.2]$$

By using the known age of the complex, Walker *et al.* were able to use the isochron for a rough determination of the ^{190}Pt decay constant, obtaining a value similar to the counting determination of 1×10^{-12} yr^{-1} (Macfarlane and Kohman, 1961).

A much more precise determination of the ^{190}Pt decay constant was made by Walker *et al.* (1997) by analysis of Fe–Ni sulphide ores with very high Pt/Os ratios from the Noril'sk complex in Siberia. Using the isochron shown in Fig. 8.6 and a published U–Pb age of 251.2 ± 0.3 Myr, Walker *et al.* determined a precise value for the decay constant. After modification of the abundance of ^{190}Pt to 0.01296% (Brandon *et al.*, 1999), this gave a decay constant of $1.477 \times 10^{-12}\ \mathrm{yr}^{-1}$, equivalent to a half-life of 469 Byr.

An alternative osmium isotope notation proposed by Walker *et al.* (1989a) is in the form of percentage deviations (γ) from a chondritic reference point. However, the Bulk Silicate Earth does not have an exactly chondritic Os signature (see below), so the CHUR reference point is less powerful for Os than it is for the Sm–Nd system (section 4.2). Nevertheless, if we wish to com-

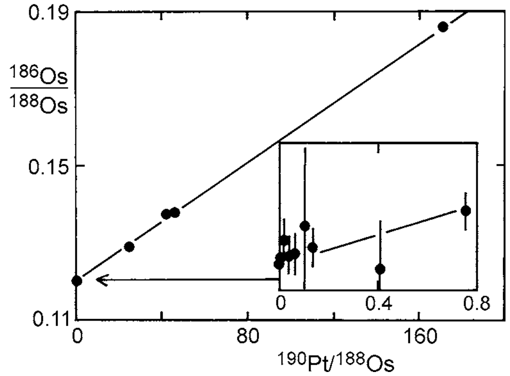

Fig. 8.6. Pt–Os isochron diagram for Fe–Ni sulphide ores from the Noril'sk complex, Siberia. The inset shows data for samples with low Pt/Os ratios. After Walker *et al.* (1997).

pare Os isotope data of different ages, we may need to use this notation, so it will be used here to a limited extent. The present-day average chondrite reference values chosen by Walker *et al.* were $^{187}\mathrm{Os}/^{188}\mathrm{Os} = 0.127$ and $^{187}\mathrm{Re}/^{188}\mathrm{Os} = 0.40186$ (after conversion to the new normalisation).

8.3 Mantle osmium

Given the siderophile chemistry of Re and Os, most of the inventory of these elements originally accreted to the Earth must have been partitioned into the core. Since it is very unlikely that Re and Os should have identical partition coefficients between the mineralogies of the mantle and core, we should expect to see Re/Os fractionation during core formation. Therefore, if Re and Os in the mantle represent the residue from core formation, we would not expect them to display a Bulk Earth (i.e. chondritic) ratio. Therefore, many recent Os isotope studies of mantle-derived rocks have been devoted to establishing a 'Bulk Mantle' osmium evolution line.

8.3.1 Bulk Silicate Earth

The first determination of the terrestrial osmium evolution line was made by Allègre and Luck (1980) on placer samples of the platinoid alloy osmiridium, whose crystallisation ages could be estimated. Not only can osmiridium be analysed directly on the ion probe, but also, since its Re content is zero, no age correction was necessary to obtain initial ratios. These analyses were combined with the initial Os isotope ratio of the iron-meteorite isochron to estimate an evolution line for the Bulk Silicate Earth (even though the mantle evolution line cannot be constrained from meteorite analysis, the initial ratio of the meteorite isochron is a valid starting point for the osmium isotope evolution of the Earth's mantle). The data defined a single evolution line for all samples except the Urals, suggesting that the mantle system was effectively closed for Re–Os over the Earth's history (Fig. 8.7). In other words, the mantle does not display evidence of progressive depletion in Re/Os ratio due to the extraction of the crust, as seen for Nd.

Allègre and Luck showed from concentration data that Re was strongly partitioned into the crust relative to Os, since the former is an incompatible element in the mantle whereas the latter is not. Therefore they attributed the apparent closed-system osmium isotope evolution of the mantle to the small total osmium budget of the crust relative to the mantle. The Re–Os analysis of whole-rock chondrites by Walker and Morgan (1989) allowed a meaningful comparison between chondritic osmium and the mantle-growth curve of Allègre and Luck. This showed that the average chondritic growth curve falls close to the mantle-growth curve in Fig. 8.7. This was surprising, in view of the expectation of mantle Re/Os fractionation by partition into the core. To explain this coincidence, Morgan (1985) suggested that the Re–Os budget of the mantle was produced by late accretion of chondritic material to the Earth, after core formation.

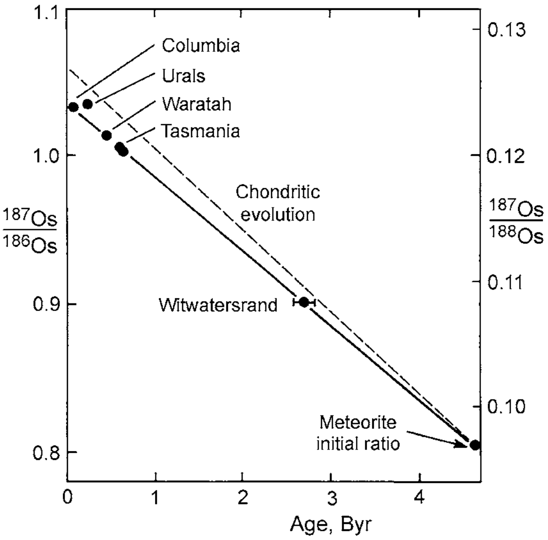

Fig. 8.7. Os isotope evolution diagram, showing the first determination of the mantle-growth curve, compared with the evolution line for average chondrites (Walker and Morgan, 1989). The Witwatersrand point has subsequently been discredited (Hart and Kinloch, 1989). After Allègre and Luck (1980).

Several attempts were then made to determine the composition of the upper-mantle reservoir from young mantle-derived products. For example, Martin *et al.* (1991) presented data on oceanic peridotites from various localities. These data were supplemented by Luck and Allègre (1991), who analysed whole-rock samples of Phanerozoic ophiolites. Both of these types of sample are thought to represent the composition of the uppermost oceanic upper mantle, i.e. the asthenosphere.

In another study of the oceanic mantle, Hattori and Hart (1991) analysed platinum-group minerals in placer deposits derived from zoned and un-zoned ultramafic bodies. The former are attributed to ultramafic magmas, whereas the latter are interpreted as tectonically uplifted pieces of asthenospheric mantle, solidified to become new lithosphere. Since magmas may be susceptible to minor contamination by crustal Os,

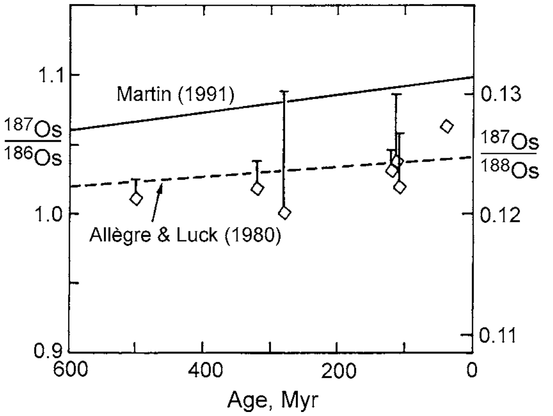

Fig. 8.8. Ranges of initial Os isotope ratio in Phanerozoic placer deposits derived from massive ultramafic bodies, relative to proposed mantle-evolution lines. Diamonds provide the best estimates of depleted-mantle osmium. After Hattori and Hart (1991).

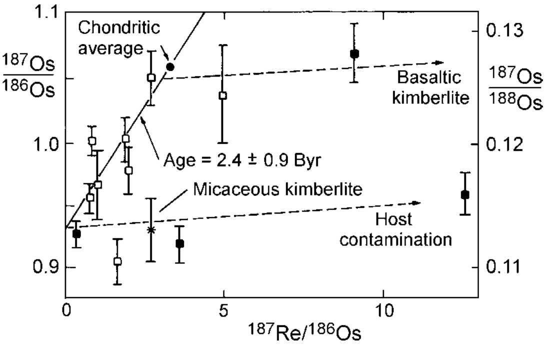

Fig. 8.9. Re–Os isochron diagram for South African peridotite xenoliths: (□) = high-temperature peridotite: (■) = low-temperature peridotite; (*) = group-II (micaceous) kimberlite. After Walker *et al.* (1989a).

the tectonically emplaced bodies are more reliable as indicators of mantle composition. If the lower limit from each locality is accorded greatest significance (diamond symbols in Fig. 8.8), then we can obtain the composition of the most depleted upper mantle. However, this leaves uncertainty about the meaning of the more radiogenic samples, and hence the degree of heterogeneity in the upper mantle.

The approaches described above provide reasonable evidence on the composition of the most depleted asthenospheric mantle, but it is evident that the upper mantle displays considerable osmium isotope heterogeneity. The osmium signatures of mantle-derived magmas are not a reliable guide to upper-mantle osmium because of the possibility of sampling plume-derived components with radiogenic osmium (section 8.3.4). Therefore, the best understanding of the evolution and differentiation of the asthenosphere can be obtained by detailed studies of lithospheric mantle peridotite suites. Because this mantle has been preserved in the solid state for long periods, it offers the opportunity of studying ancient upper-mantle differentiation events, as well as the effects of more recent mantle enrichment.

8.3.2 Lithospheric evolution

The first osmium isotope signatures of ancient subcontinental lithosphere were determined by Walker *et al.* (1989a), who analysed peridotite xenoliths from South African kimberlites. The Re–Os isochron diagram (Fig. 8.9) allowed the effects of contamination by the host (group-I-type) basaltic kimberlite to be assessed. Walker *et al.* argued that the process of contamination caused samples to move along a sub-horizontal vector towards high Re/Os ratios characteristic of the host magma. Samples argued not to have suffered this effect define a steep array in Fig. 8.9, corresponding to an age of 2.4 ± 0.9 Byr.

Walker *et al.* attributed the relatively coherent Re–Os isotope systematics of the peridotite xenoliths to separation of South African lithosphere from the convecting asthenosphere in the Archean. Their unradiogenic compositions, relative to Allègre and Luck's upper mantle $^{187}Os/^{188}Os$ ratio of 0.125 ($^{187}Os/^{186}Os = 1.04$), suggested that these peridotites represent residues from partial melting, which is consistent with gross incompatible-element depletion of the subcontinental lithosphere (Jordan, 1978). Hence, Walker *et al.* suggested that the Re–Os system could provide insights into mantle-depletion events in a manner distinct from LIL tracers such as Sr and Nd, which commonly chart secondary *enrichment* of the subcontinental lithosphere by metasomatism.

The first attempt to determine a Re–Os isochron on a section of lithospheric mantle was made by Reisberg *et al.* (1991) for the Ronda 'orogenic lherzolite' massif in southern Spain. The massif contains both mafic and ultramafic layers, which Reisberg *et al.* interpreted as relics of old recycled oceanic mantle ('marble-cake mantle', section 6.1.5), which had later been incorporated into the continental lithosphere. Whole-rock samples of mafic and ultramafic layers defined Re–Os errorchrons with similar apparent ages (Fig. 8.10), which were interpreted as the time when this piece of mantle was accreted to the continental lithosphere. However,

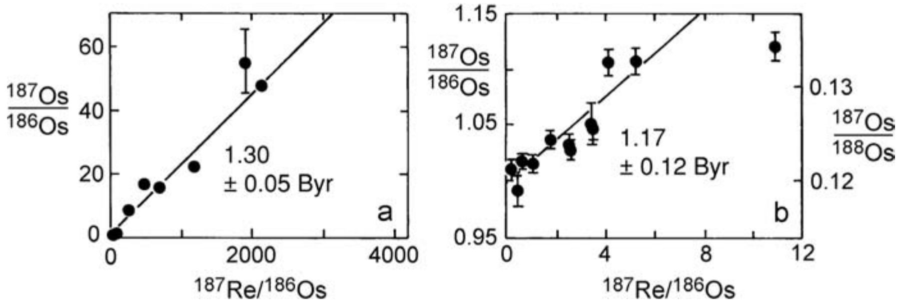

Fig. 8.10. Re–Os isochron diagrams for the Ronda ultramafic complex: (a) mafic units and (b) ultramafic units. After Reisberg *et al.* (1991).

the ranges of isotopic composition are very different: ultramafic units displayed both isotopic enrichment and depletion relative to the chondritic composition, whereas the mafic units displayed extreme isotopic enrichment. The significance of the latter component will be discussed further below.

Reisberg and Lorand (1995) attempted to apply the Re–Os isochron technique to date a similar mantle-differentiation event in the East Pyrenees lherzolite, but the data were badly scattered on the Re–Os isochron diagram. The scattered data were attributed to open-system behaviour of rhenium during mantle metasomatism. However, Reisberg and Lorand (1995) observed good correlations between osmium isotope ratios and aluminium contents of whole-rock peridotite samples, both for the East Pyrenees and the Rhonda lherzolite. Hence, they proposed that these plots are isochron analogues, in which aluminium, an immobile and incompatible element, is a proxy for rhenium. Because the Re/Al ratio of the original rock before metasomatism is unknown, the slope cannot be solved directly to yield an age. However, if Re and Al behaved coherently in the original rock, the intercept on the *y* axis will yield the initial osmium isotope ratio in the usual way. This quantity can be used to date mantle-differentiation events using Os model ages. However, the Al–Os pseudo-isochron diagram was also found to be useful in determining the composition of the primitive upper mantle (section 8.3.3).

Because the Re–Os system can effectively date mantle-depletion events, as well as the mantle-enrichment events normally dated by lithophile isotope systems, osmium model ages may be particularly useful for dating sub-continental lithospheric mantle. Samples of depleted mantle can be used to calculate conventional osmium model ages, based on the intersection of sample and Bulk Earth evolution lines (Fig. 8.11). However, the Re/Os ratio of mantle samples may be disturbed by metasomatic addition of rhenium after the initial crust-forming Re-depletion event. An alternative approach (Walker *et al.*, 1989a) is to assume that the depletion event generated Re/Os ratios of zero in the samples. Rhenium-depletion model ages (T_{RD}) can then be calculated by projecting a horizontal line back to the Os mantle-growth curve (Fig. 8.11).

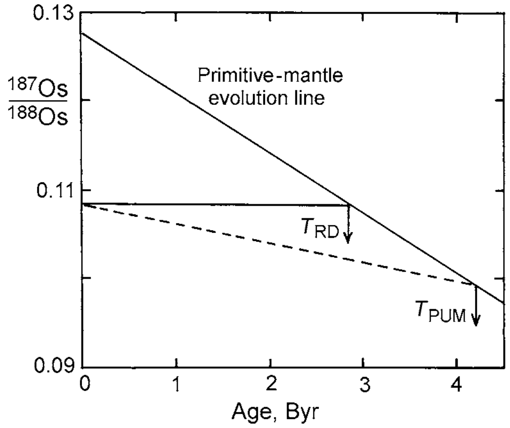

Fig. 8.11. Comparison of a rhenium-depletion model age (T_{RD}) with a conventional model age relative to the Primitive Upper-Mantle reservoir (T_{PUM}).

Rhenium-depletion ages are minimum ages for lithospheric formation. However, they can be calculated directly from the osmium isotope ratios of peridotites, allowing the accumulation of reasonably large data sets (e.g. Carlson and Irving, 1994). From these data (Fig. 8.12) we can deduce that the Wyoming, Kaapvaal and Siberian cratons all possess mantle keels with minimum formation ages of about 3 Byr. Where osmium data are available for enriched samples from the same locality, these can further constrain the age of the lithospheric mantle. For example, eclogites from Siberian kimberlites yield Re–Os model ages of about 3 Byr, which are consistent with a Re–Os isochron age

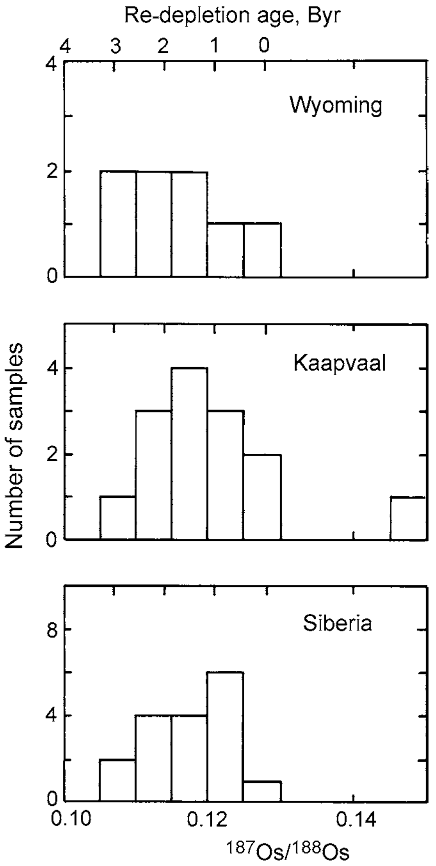

Fig. 8.12. Histograms showing the ages of lithospheric mantle keels under the Wyoming, Kaapvaal and Siberian cratons, based on Rhenium-depletion model ages for peridotites. Carlson and Irving (1994).

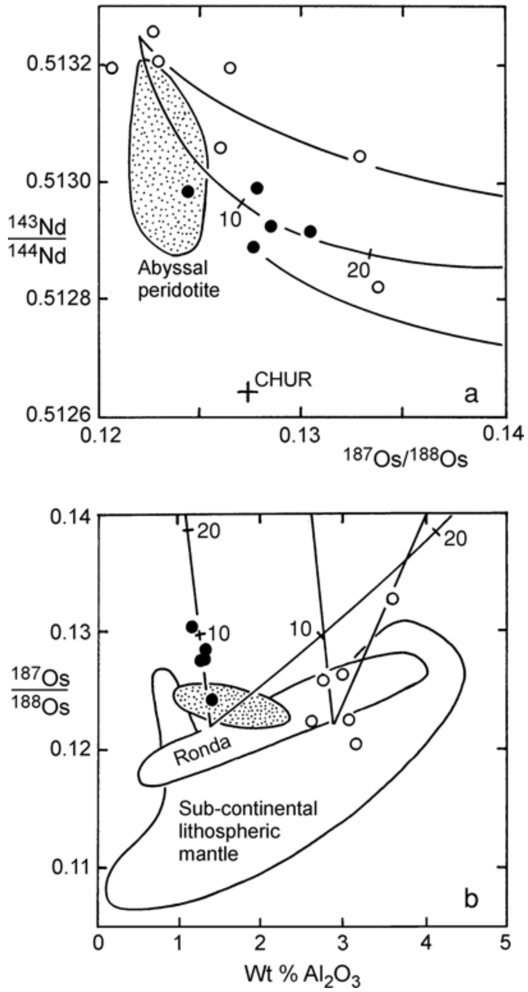

Fig. 8.13. Osmium isotope data for xenoliths from subduction-related magmas, compared with (a) Nd isotope data and (b) Al_2O_3 contents: (●) = Simcoe; (○) = Ichinomegata. Mixing lines show the effect of contamination with subduction-related fluids (percentage increments are shown). After Brandon *et al.* (1996).

of 2.9 Byr for the same rocks and with the (minimum) mantle-depletion age of 3 Byr (Pearson *et al.*, 1995b).

Several other studies have also documented osmium isotope signatures less radiogenic than the chondritic evolution line in samples of lithospheric mantle (e.g. Olive *et al.*, 1997; Chesley *et al.*, 1999). However, it is also known that lithospheric mantle can undergo secondary enrichment processes, causing the development of more-radiogenic osmium signatures. An important example of this process comes from lherzolite and harzburgite xenoliths in arc lavas (Brandon *et al.*, 1996). These xenoliths have low osmium concentrations of 0.1–2.1 ppb, and are believed to sample the mantle wedge which overlies a subduction zone.

Brandon *et al.* determined osmium isotope ratios in whole-rock xenoliths which ranged up to 5% above and below the chondritic composition, from a minimum near the field of abyssal peridotites to a maximum ^{187}Os/^{188}Os ratio of 0.134 (^{187}Os/^{186}Os = 1.12). Os and Nd isotope ratios displayed a broad negative correlation (Fig. 8.13a), which could be explained by mixing of depleted upper mantle with 5%–15% of a subduction-related component derived from 80%–95% basalt and 5%–20% sediment. This model is supported by the relatively low Al_2O_3 ratios of the xenoliths (especially those from Simcoe, Washington). These define a vertical trend (Fig. 8.13b) distinct from the diagonal enrichment–depletion trend seen in orogenic lherzolites. Brandon *et al.* suggested that their results reflected metasomatic transport of osmium in a chloride-rich slab-derived fluid or melt.

Additional examples of metasomatic osmium-enrichment events overprinted on earlier lithospheric extraction (Re-depletion) events have been demonstrated in several different localities. For example, Peslier *et al.* (2000) described peridotite xenoliths in the Canadian cordillera that displayed ancient Re depletion, followed by later enrichment with radiogenic Os, probably also from the cordilleran subduction zone. Similarly, Becker *et al.* (2001) described Alpine peridotite bodies that had undergone melt percolation by subduction-related magmas, causing variable introduction of rhenium and radiogenic osmium. These melts were believed to be associated with a Paleozoic subduction zone in this area.

A final question about lithospheric samples that needs to be discussed is the location of osmium in mantle minerals. To investigate this issue, Burton *et al.* (1999b) performed a detailed petrographic and geochemical examination of a spinel lherzolite xenolith from Kilburn Hole, New Mexico. This revealed that most osmium was contained in Fe–Ni sulphide minerals, which contained about 4 ppm osmium, two thousand times as much as the bulk xenolith. These findings have been confirmed in subsequent studies (e.g. Burton *et al.*, 2002), showing that osmium is not really a compatible element in mantle minerals such as olivine, but is contained in sulphide phases that tend to crystallise at the same time as olivine.

Of the sulphide material in the Kilburn Hole xenoliths, Burton *et al.* found that 80%–90% was interstitial between the silicate minerals, while the remainder was mostly in small inclusions 5–10 μm in diameter, enclosed in pyroxenes. Isotopic analysis showed that the interstitial sulphide was in equilibrium with the silicate minerals of the xenolith and with the host basalt. However, the sulphide inclusions within the pyroxenes were out of isotopic equilibrium with the rest of the system. It was concluded that these inclusions were protected from diffusional communication with the rest of the rock by the high sulphide/silicate partition coefficient of osmium, which tends to keep osmium 'locked up' in the inclusions.

Similar results were obtained by Alard *et al.* (2002), using the laser-probe MC-ICP-MS to study peridotite xenoliths from the Massif Central of France. They demonstrated that there was isotopic disequilibrium between interstitial sulphides and sulphide inclusions in silicates, but the interstitial sulphides were also out of equilibrium with the host magma. The sulphide inclusions in silicates (termed 'Type 1') had unradiogenic osmium, which is consistent with ancient mantle depletion. However, interstitial sulphides ('Type 2') had variable isotope compositions, usually more radiogenic than Type 1, which is consistent with recent metasomatism. Therefore, Alard *et al.* cautioned that whole-rock osmium analyses of mantle peridotites are really sampling isotopic mixtures from different types of sulphide grains.

8.3.3 Primitive upper mantle

Since mantle depletion events are quantitatively the most important processes affecting the osmium evolution of lithospheric mantle, Meisel *et al.* (1996) argued that the most fertile (Al-rich) lherzolites from the subcontinental lithosphere could be used to constrain the osmium isotope evolution of the 'primitive upper mantle' (PUM). Mantle xenoliths from Kilburn Hole (New Mexico), West Eifel (Germany) and the Baikal Rift (Mongolia) formed a linear array on a plot of Os isotope ratio against Al_2O_3 (Fig. 8.14). The most Al-rich samples were consistent with an estimated Al_2O_3 content of 4.2% in PUM, and gave an average $^{187}Os/^{188}Os$ ratio of 0.129 ($^{187}Os/^{186}Os = 1.08$), in good agreement with the most Al-rich of the massive peridotites analysed by Reisberg and Lorand (1995). This PUM value is in agreement with the average for ordinary chondrites, but is significantly more radiogenic than the mantle value of Allègre and Luck (1980).

The composition of PUM determined by Meisel *et al.* (1996) was further refined by Meisel *et al.* (2001)

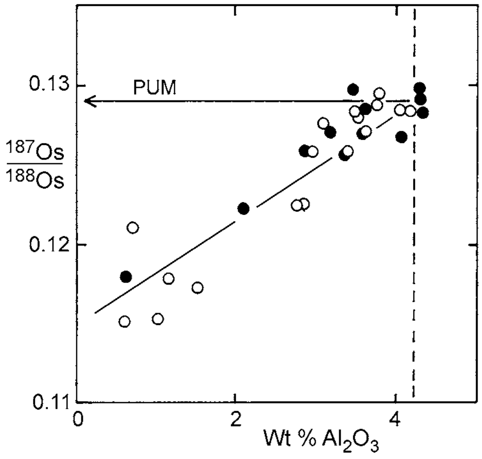

Fig. 8.14. Al–Os 'isochron' diagram used to determine the composition of PUM: (○) = old data; (●) = new data. After Meisel *et al.* (1996).

using a much larger data set of spinel- and garnet-lherzolites from around the world. Again using Al–Os pseudo-isochrons, they obtained a PUM osmium composition of 0.1296 ± 0.0008. When this value is compared with a compilation of data for various kinds of chondrites, it is a good match for the composition of ordinary chondrites but slightly more radiogenic than carbonaceous chondrites. Analysis of Early Archean peridotites from western Greenland and western Australia has also given initial osmium ratios close to that of PUM (Bennett *et al.*, 2002), suggesting that the upper mantle has had this composition since very early in the Earth's history.

The choice of value for PUM has profound implications for terrestrial Re–Os evolution. For example Martin *et al.* (1991) used a more radiogenic estimate for the undepleted mantle that was based on plume compositions (^{187}Os/^{188}Os = 0.132; ^{187}Os/^{186}Os = 1.10). However, using this mantle osmium value, the extraction of the continental crust from the mantle was insufficient or barely sufficient to balance Re/Os depletion in the sub-continental lithosphere, let alone to balance a Re-depleted asthenospheric upper mantle. Hence, they argued that depletion of the upper mantle from a primitive ^{187}Os/^{188}Os ratio of 0.132 to an asthenospheric ratio of 0.126 could be achieved only by storage (somewhere in the mantle) of oceanic crust equal to ten times the volume of the continental crust.

The primitive-mantle composition of Martin *et al.* (1991) is now believed to be an over-estimate. However, this 'osmium problem' still persists, albeit at a slightly reduced level. This can be seen by ratioing estimated Re concentrations in various Earth reservoirs against Yb, which has a similar solid/liquid distribution coefficient in silicate systems (Fig. 8.15). On this figure, both depleted upper mantle (DMM) and continental crust have lower Re concentrations than PUM, requiring a hidden reservoir to balance them. Righter and Hauri (1998) proposed that this reservoir was represented by the garnet component of subducted oceanic crust. They also performed mass-balance calculations to estimate the necessary quantity of this recycled crustal component and its Re content. For a recycled crustal reservoir equal to 6% of the mantle, this would need to contain 650 ppb Re. This material would also need to make up 30% of the source of HIMU plumes in order to explain their highest Os isotope ratio (see below).

Becker (2000) performed direct measurements on the Re contents of ancient garnet-bearing meta-basic rocks to evaluate their ability to act as sources of HIMU magmas. The measured Re contents varied very widely from 3 to 1689 ppb, with a median of 331 ppb. This was too low to satisfy the modelling described above. However, the mean value for the eclogites and mafic granulites in their data set is about 530 ppb. In view of the extreme scatter of the data, this seems to represent a reasonable fit to the first-order modelling described above. However, new data published by Sun *et al.* (2003) suggest that crustal Re/Yb ratios may also have been under-estimated.

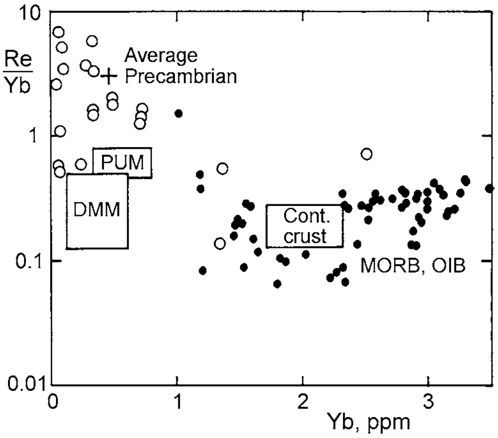

Fig. 8.15. Plot of Re/Yb ratio against Yb concentration to show the need for a component with high Re/Yb ratio to balance the derivation of the crust and upper mantle from PUM. Precambrian komatiites and basalts (○) may represent the missing component. After Righter and Hauri (1998).

8.3.4 Enriched plumes

The first osmium isotope analyses of OIB were performed on samples from Iceland and Hawaii (Martin, 1991). These exhibited modest enrichment in ^{187}Os relative to the values seen in ophiolites and peridotite xenoliths (see above). However, as was seen for lithophile isotope systems (section 6.5), the best understanding of mantle enrichment processes in OIB is obtained by the analysis of extreme examples. For example, Hauri and Hart (1993) determined initial (^{187}Os/^{188}Os ratios approaching 0.15) ^{187}Os/^{186}Os ratios as high as 1.25 in lavas from the HIMU island of Mangaia. These radiogenic compositions are best explained by the recycling of enriched crustal material back into the upper mantle. Thus, Hauri and Hart calculated that 16% of recycled 2.1-Byr-old oceanic crust can explain the osmium signature of the HIMU component. On the other hand, 1%–2% of recycled continental crust in the EMII source does not markedly affect its osmium isotope signature.

Reisberg *et al.* (1993) found even more radiogenic osmium in the HIMU islands of the Comores and St Helena, with initial $^{187}Os/^{188}Os$ ratios as high as 0.2. However, they cautioned that, because these signatures were carried by osmium-poor lavas (10–30 parts per trillion (ppt) = 0.01–0.03 ppb), their elevated ^{187}Os signatures could have been introduced by processes in the oceanic lithosphere. This could involve contamination of OIB magmas with ocean-floor sediments included in the volcanic edifice, or by accumulated lithospheric olivine xenocrysts. However, work on the Canaries (Marcantonio *et al.*, 1995) established that samples with more than about 30–50 ppt (0.03–0.05 ppb) osmium are generally immune to sea-floor contamination processes. Such effects were also ruled out in Mauna Kea lavas by strong correlations between Os and Sr, Nd and Pb isotope ratios, showing that the osmium signatures must be derived from primary mantle sources (Hauri *et al.*, 1996).

Although sea-floor contamination was ruled out for the Canaries samples, they nevertheless gave evidence of complex mixing processes in the plume source, since they had radiogenic osmium signatures, coupled with Pb isotope ratios intermediate between HIMU and EMI (Fig. 8.16). This cannot be explained by simple mixing between DMM and HIMU (Marcantonio *et al.*, 1995). Therefore, the Canaries data were tentatively attributed to mixing between DMM and a HIMU–EMI mix. This model is also consistent with lithophile isotope evidence, which suggests that there is an intimate relationship between HIMU and EMI in plume sources (section 6.5).

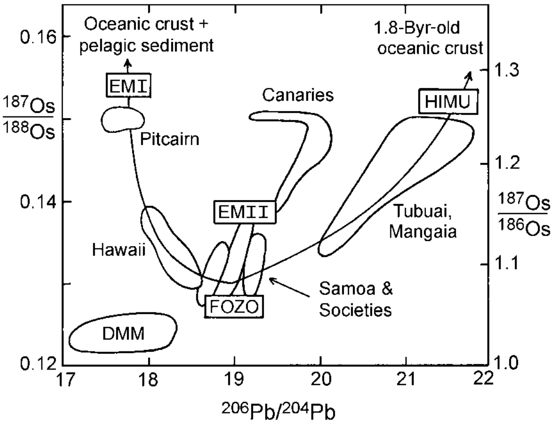

Fig. 8.16. Plot of Os against Pb isotope ratios for various plume sources to show possible mixing lines between a depleted lower-mantle end-member (FOZO) and distinct enriched end-members. Data were from OIB samples with more than 45 ppt osmium. Hauri *et al.* (1996).

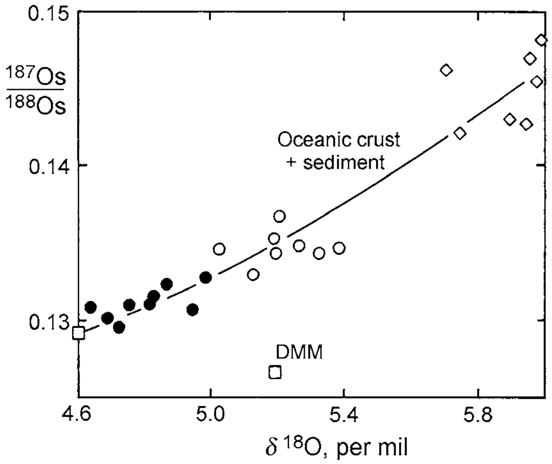

Fig. 8.17. Plot of osmium against oxygen isotope composition for Hawaiian lavas, showing a positive correlation attributed to recycling of ancient sediment into the Hawaiian plume source: (◇) = Koolau; (●) = Mauna Kea; (○) = Mauna Loa. After Lassiter and Hauri (1998).

New data for the Koolau volcano, Hawaii (Bennet *et al.*, 1996) extended the Hawaiian Os–Sr–Pb correlation line to more enriched compositions, approaching the composition of Pitcairn (Fig. 8.17). This is thought to approximate the isotopic composition of the EMI mantle component. However, the trajectory of the Hawaiian array in Fig. 8.16 cannot be explained by simple two-component mixing between EMI and DMM mantle. Therefore, Hauri *et al.* (1996) identified the other mixing component as entrained lower mantle (FOZO, section 6.5.5) with unradiogenic osmium. In contrast, post-erosional alkaline mafic rocks of the Honolulu volcanic series define a mixing line with a quite different trajectory that does trend towards DMM. This suite is best explained by interaction of the plume source with partial melts of the oceanic lithosphere under Hawaii (Class and Goldstein, 1997).

An important discovery by Lassiter and Hauri (1998) is that radiogenic osmium in Koolau basalts is associated with elevated $\delta^{18}O$ signatures (Fig. 8.17). Since elevated oxygen isotope compositions are normally produced only in the sedimentary system, these workers attributed the enriched (EMI) signature to a mixture of recycled oceanic crust and pelagic sediment, a model also supported by Hf isotope evidence (section 9.2.5). A similar osmium–oxygen isotope correlation was also obtained for the Iceland plume (Skovgaard *et al.*, 2001) and attributed to melting of a mixed source involving various components of ancient recycled oceanic lithosphere. One end-member with an osmium signature at the bottom end of the MORB array was attributed to a mixture of recycled lower-oceanic crust and mantle lithosphere, whereas the more radiogenic end-member was attributed to a mixture of recycled upper-oceanic crust and mantle lithosphere.

With the development of methods to analyse Os isotope ratios at very low abundance (Birck *et al.*, 1997), the analysis of subduction-related magmas allows the opportunity of 'direct monitoring' of the material being subducted into the deep-mantle. Such an investigation was performed by Alves *et al.* (1999) on volcanic rocks of the Sunda arc in Java. On successfully analysing samples with extremely low Os concentrations (0.1–17 ppt), Alves *et al.* found extreme ranges of osmium isotope ratio in Miocene and Pliocene subduction-related magmas. Os isotope ratios were inversely correlated with osmium contents, suggesting the occurrence of binary mixing. However, the correlation of osmium isotope ratios with Sr and Pb signatures suggested that the osmium variations did not originate from contamination with seawater osmium during ascent through the oceanic lithosphere.

Instead, Alves *et al.* attributed the mixing lines to contamination of the mantle wedge overlying the subduction zone. For example, lavas of different ages defined two distinct mixing lines (Fig. 8.18), implying the involvement of two different radiogenic end-members, each mixing with a common non-radiogenic end-member. Thus, Alves *et al.* attributed a steeper array in Miocene lavas to mixing of osmium from primitive mantle and subducted oceanic crust. However, they suggested that post-Miocene entry of terrigenous sediment into the subduction zone caused a change in the radiogenic end-member from oceanic crust to continental sediment. However, these isotopic variations could be due to crustal contamination effects, since even individual lavas exhibited significant isotopic heterogeneity. Similar mixing arrays between mantle wedge and slab-derived components were subsequently found in several other volcanic arc systems (Alves *et al.*, 2002).

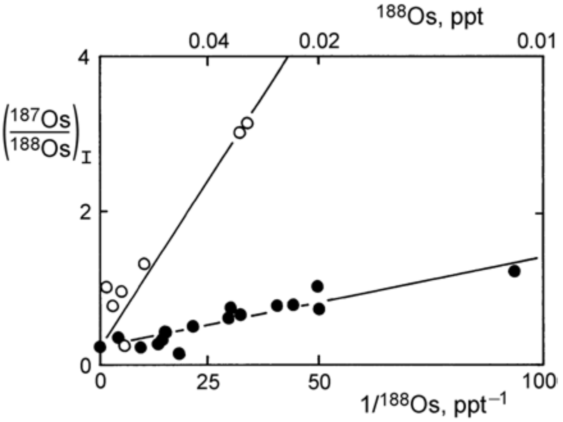

Fig. 8.18. Plot of initial Os isotope ratio against reciprocal of Os concentration to show evidence for mixing between mantle wedge and subduction components in two suites of arc volcanics from Java. After Alves *et al.* (1999).

8.3.5 Osmium from the core

Walker *et al.* (1995) and Widom and Shirey (1996) proposed an alternative model for isotopic enrichment of OIB, which derives the radiogenic osmium signatures of some plumes directly from the core. They suggested that a metallic core component could be incorporated into plumes at the core–mantle boundary, such that its high osmium content would overprint the isotopic signature of the deep-mantle source with radiogenic osmium from the outer core. However, the existing isotope tracer evidence was inadequate to test this model.

The development of the Pt–Os decay scheme provided an additional isotopic tracer to test the possibility of contamination of plumes by material from the outer core. To provide a basis for interpretation, Walker *et al.* (1997) predicted the behaviour of Re–Os and Pt–Os systems in the core and mantle from known silicate–metal partition coefficients, and by comparison with the isotope and PGE systematics of iron meteorites. It is well known that all PGE were strongly partitioned from the mantle to the core during the early history of the Earth. However, the meteorite evidence also suggests that the PGE were partitioned between the liquid and solid core once the latter had begun to crystallise, such that the outer core was enriched in Pt and Re relative to Os. This was attributed to the very strong partitioning of Os into the solid metal phase. Over time, this would lead to correlated enrichments in ^{186}Os and ^{187}Os in the outer core.

The first evidence in support of this predictive model came from analysis of the Noril'sk complex, which revealed a significant enrichment of ^{186}Os relative to other terrestrial and meteorite samples (Walker *et al.*, 1997). This is consistent with the derivation of the Noril'sk complex from a plume source. These findings were supported by Brandon *et al.* (1998), who found similar enrichments of ^{186}Os in Hawaiian picrites from the Loihi, Mauna Loa and Koolau volcanoes. However,

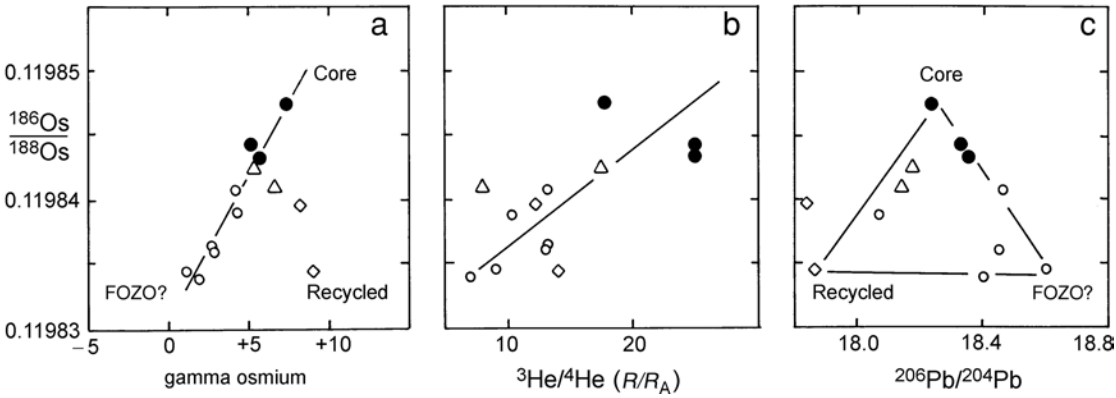

Fig. 8.19. Enrichments of ^{186}Os in Hawaiian picrites relative to other isotope tracers: (a) ^{187}Os, (b) ^{3}He and (c) ^{206}Pb. (◇) = Koolau; (●) = Loihi & Hualalai; (△) = Mauna Loa; (○) = Mauna Kea and Kilauea. After Brandon *et al.* (1999).

evidence that the most ^{186}Os-enriched sample came from the Koolau volcano caused great consternation, because other workers provided very strong evidence that the enriched signature of this volcano was derived from lithospheric recycling into the mantle (Lassiter and Hauri, 1998). The combination of such a recycled signature with an osmium contribution from the core would require a peculiar coincidence.

Fortunately, these problems were resolved by the more detailed investigation of Brandon *et al.* (1999). This replicated the elevated ^{186}Os signatures in Loihi and Mauna Loa, but showed that the original Koolau analysis was in error, probably due to small molecular-ion interferences on the ^{186}Os peak. The new Koolau data exhibited a small enrichment in ^{186}Os, but lay below a correlation line formed by the Noril'sk plume and other Hawaiian samples (Fig. 8.19a). When the ^{186}Os data from the latter samples were compared with helium isotope data (Fig. 8.19b), the observed positive correlation provided powerful support for the core-derivation model of Walker *et al.* (1995; 1997). This is because the enriched ^{3}He signatures seen in Loihi are generally regarded as indicative of primordial helium from the deep interior of the Earth, possibly the core itself. Therefore, the observation that some of the highest ^{186}Os signatures are found in Loihi is very persuasive.

The geochemical picture of the Hawaiian plume is completed in Fig. 8.19c by plotting ^{186}Os against Pb isotope ratio. In this plot the data fall within a triangular field which requires three end-members. In the bottom right is the so-called Kea component, derived from a relatively depleted plume source (FOZO?). In the bottom left is the Koolau component with a signature of recycled Pb resembling EMI (section 6.5.3). The slightly elevated ^{186}Os signatures in this material can be explained by recycling of old lithosphere with moderate enrichment of Pt relative to Os. Finally, the Loihi–Hualali component has an intermediate Pb isotope signature, possibly representative of primordial lower mantle that was 'fertilised' by radiogenic ^{186}Os from the outer core.

The advent of this persuasive evidence for a flux of siderophile elements from the core to the mantle requires a reconsideration of the Os–Pt–Re budget of the mantle. Hauri and Hart (1997) examined this problem by analysing Re abundances in MORB and OIB samples. Since Re has the same degree of incompatibility as Yb during mantle melting processes, the Re/Yb ratio is independent of solid/liquid partition processes, and can be used to compare the relative abundances of Re in the sources of MORB and OIB. A plot of Re/Yb ratio against Yb showed essentially no difference between Re/Yb ratios in MORB and OIB, leading Hauri and Hart to suggest that plume sources have not been enriched by a significant flux of Re from the core. (A similar argument was used to place limits on late partition of Pb into the core, section 6.3.1.)

However, it was pointed out by Brandon *et al.* (1999) that the lower mantle was depleted in siderophile elements when these were first partitioned into the core, early in the Earth's history. Because of this depletion, Brandon *et al.* calculated that less than 0.2% of outer-core material would be needed to modify the osmium isotope signature of the Hawaiian plume. In contrast, it was argued on the basis of Re–Os evidence (section 8.3.1) that the upper-mantle budget of siderophile elements was derived by a late addition of material with a chondritic siderophile-element signature. This model is supported by Pt–Os evidence (Brandon *et al.*, 2000), which suggests that the upper mantle has a homogeneous ^{186}Os/^{188}Os signature that overlaps with the chondritic composition. Hence the upper mantle has been approximately chondritic regarding both its Re/Os ratio and its Pt/Os ratio over most of the Earth's history.

One problem remaining for this model was to explain how osmium in the dense metallic core could possibly rise into the light oxide-dominated mantle. However, an explanation was provided by an experimental petrologist (Walker, 2000). He cited the work of Ito *et al.* (1995), who suggested that crystallisation of the inner core might drive the oxygen content of the liquid outer core past the level of saturation, so that oxide species might exsolve at the core–mantle boundary (termed the D″ layer). This process would provide an ideal mechanism by which to reimplant osmium and other PGE back into the lower mantle, whence they originated before the formation of the core.

Most osmium isotope analyses of Archean and Proterozoic mantle-derived rocks have come from so-called 'Large Igneous Provinces' attributed to mantle plumes. A compilation of some of these data (Fig. 8.20) shows that most have initial ratios above the chondritic evolution line. This plot shows two models for ^{187}Os evolution in the outer core, assuming either early or continuous crystallisation of the inner core. Most of the provinces analysed have initial ratios within error of one or other of these evolution lines. However, an outer-core contribution to osmium in these plumes can be verified only by very demanding ^{186}Os analysis. Otherwise, plumes of recycled ocean crust are an alternative possibility.

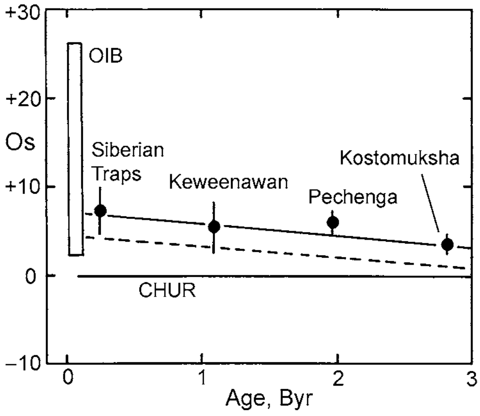

Fig. 8.20. Compilation of initial osmium isotope data for Large Igneous Provinces of various ages, using the gamma notation. These are compared with osmium evolution lines for the outer core, assuming either early (solid) or continuous (dotted) inner-core crystallisation. After Puchtel *et al.* (2001).

8.3.6 Asthenospheric mantle heterogeneity

Roy-Barman and Allègre (1994) made a detailed comparison between ocean-ridge basalts and abyssal peridotites from different ridges. These two types of sample are expected to have the same osmium isotope ratios, since they are thought to represent (respectively) the eruptive product and the residue from melting. Samples were leached with oxalic acid (and then HBr) to remove ferromanganese coatings, which have radiogenic seawater osmium signatures. Leached peridotites from the flanks of the Mid-Atlantic Ridge (MAR) had a very narrow range of ^{187}Os/^{188}Os ratios, in good agreement with previous work. However, leached MORB samples had elevated ratios of 0.128–0.133, within the range of North Atlantic OIB. (Roy-Barman and Allègre interpreted the MORB values as magmatic because they found good agreement between leached-glass and crystalline-basalt compositions.) They proposed two alternative models to explain the differences between MORB and peridotites: contamination of MAR basaltic magmas by assimilation of hydrothermally altered oceanic crust; or contamination of the MAR magma source with isotopically enriched osmium, either from the Azores plume or from enriched streaks in a marble-cake mantle (Roy-Barman *et al.* 1996).

Further work on this problem by Schiano *et al.* (1997) confirmed the earlier results using pristine MORB glasses from the MAR, with additional samples from the Pacific and Indian ridges. Extreme care was necessary in order to obtain accurate Os data from these samples with very low Os concentrations of 1–30 ppt. This involved the hand picking of large samples, followed by a four-step sequential leaching procedure to remove any Fe–Mn coatings, together with very careful correction for analytical blanks.

Schiano *et al.* discovered correlations between the signatures of osmium and lithophile isotope systems (Sr, Nd and Pb), which suggested that the osmium data were representative of long-term DMM sources rather than being due to recent seawater contamination of these sources or MORB magmas. However, the range of osmium isotope signatures measured in these samples (Fig. 8.21) was almost as large as for HIMU samples of OIB (Fig. 8.17). Assuming that these elevated signatures represent recycled oceanic crust in the mantle magma sources, this would imply a huge component of recycled crust in the upper mantle (as much

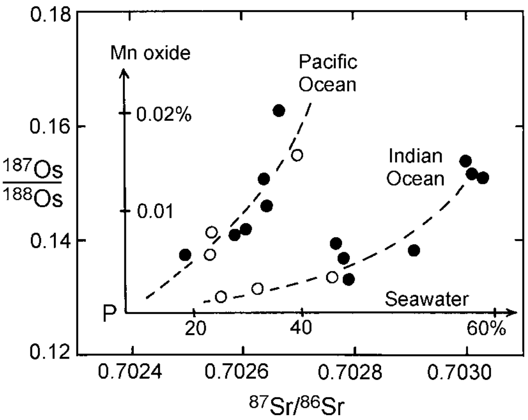

Fig. 8.21. Plot of osmium isotope ratio against Sr isotope ratio for pristine MORB glasses. Pacific and Indian Ocean samples define distinct trends: (○) = Atlantic; P = peridotite source. After Schiano *et al.* (1997).

as 40%). However, if eclogitic streaks in a 'marble-cake mantle' were allowed to melt preferentially in the production of new MORB, the fraction of recycled oceanic crust required in the MORB source would be reduced to less than 5%, which seems more reasonable. These findings are supported by recent U-series isotope data (section 13.3.4).

Another interesting feature in Fig. 8.21 is the existence of two distinct trends, which are even more clearly separated on a plot of Os against Pb isotope ratio (not shown here). One trend is defined principally by Pacific Ocean MORB and one trend by Indian Ocean MORB, consistent with previous lithophile isotope evidence for distinct isotopic signatures in these ocean basins. On the other hand, the Atlantic Ocean samples span both trends, suggesting that two sources of enriched material are available in this ocean basin.

We infer that the regional geochemical differences between the upper mantle under different ocean basins, normally attributed to contamination of the MORB source by various types of plume ('plume-pudding mantle'), are continuous with the much smaller-scale heterogeneities of the 'marble-cake mantle', in a seamless manner. Hence, these data help to resolve a long-standing question about the relative importance of these alternative models.

8.4 Petrogenesis and ore genesis

As one of the PGE, osmium is uniquely suited as a tracer of petrogenetic and ore-forming processes of noble-metal deposits. PGE deposits are generally associated with major mafic complexes, and have been attributed to mixing between mantle-derived and crustal components (e.g. Naldrett, 1989). The strong fractionation between Re and Os in crust-forming processes, which generates very radiogenic osmium in the crust relative to the mantle, makes osmium a powerful tracer for such studies. Several of the world's largest basic–ultrabasic intrusions have been subjected to Re–Os analysis; however, the complexities of their chemistry have typically required several studies in order to gain a reasonable understanding of their genesis.

8.4.1 The Bushveld Complex

The Bushveld Complex is the world's largest layered mafic intrusion and principal PGE producer. Historically, most of these PGE came from the famous Merensky Reef, but the UG1 and UG2 chromite layers (chromitites) are now also major sources. Hart and Kinloch (1989) performed an ion-microprobe study of PGE sulphides from the Merensky Reef on the western lobe of the intrusion. They found consistent initial ^{187}Os/^{188}Os ratios of about 0.175 (^{187}Os/^{186}Os = 1.45) for grains of laurite (RuS_2) from the Rustenburg, Union and Amandelbult mining areas. These values are far above the mantle growth line for osmium at the time of intrusion of the Bushveld Complex (2.05 Byr ago), indicating that there is a large crustal component in the ore. However, two grains of erlichmanite (OsS_2) from Rustenburg and Union gave low ^{187}Os/^{186}Os ratios, lying on the chondritic evolution line (^{187}Os/^{188}Os = 0.112).

The Bushveld laurites can be interpreted as the products of crustally contaminated magmas, as has been proposed to explain Sr isotope data for the Bushveld Complex (Sharpe, 1985). However, the erlichmanite results pose a major problem for this interpretation. They cannot be attributed to open-system perturbation of Re–Os, since these minerals contain no rhenium. Hence, if the osmium isotope variations in the laurites are attributed to magmatic processes, then the erlichmanites must represent mantle-derived PGE phases that were somehow carried into the intrusion (which seems unlikely). Alternatively, osmium isotope variations in the laurites must be hydrothermal in origin, and some component of the Merensky Reef mineralisation must therefore be attributed to hydrothermal introduction of PGE.

In an attempt to solve this conundrum, Schoenberg *et al.* (1999) analysed separated minerals from the 'Critical Zone' underlying the Merensky Reef and the 'Bastard Unit' of the Main Zone above it (Fig. 8.22).

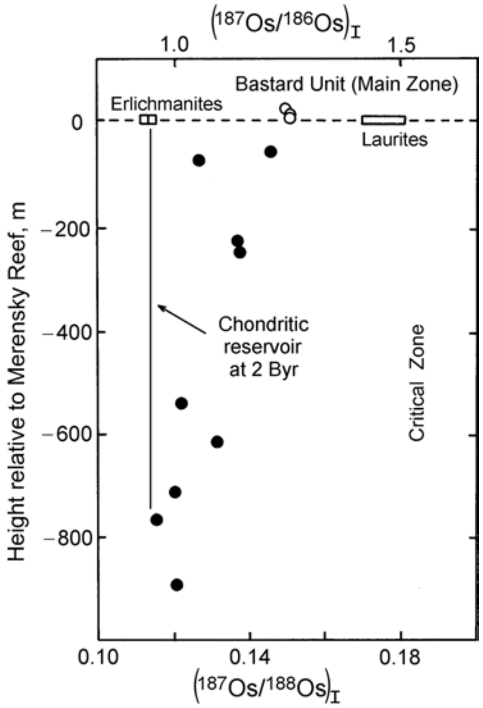

Fig. 8.22. Plot of initial osmium isotope ratios in the Bushveld Complex against stratigraphic height relative to the Merensky Reef: (○) = pyroxene; (□) = sulphide; (●) = chromite. After Schoenberg *et al.* (1999).

Powerful evidence against the 'metasomatic contamination model' came from four analyses of the Bastard Unit. Four poikilitic pyroxenites collected from 4–20 m above the Reef gave a perfect Re–Os isochron with an age of 2043 ± 11 Myr (MSWD $= 0.7$). When we take into account the uncertainty of about 1% in the Re decay constant, this is in excellent agreement with an intrusive age of 2059 ± 1 Myr from U–Pb dating (Buick *et al.*, 2001). Schoenberg *et al.* argued that such a good isochron would have been very unlikely if pervasive introduction of osmium by metasomatism had occurred in the vicinity of the Merensky Reef.

Support for the alternative 'magma-mixing model' came from analysis of chromitites of the Critical Zone (Schoenberg *et al.*, 1999; McCandless *et al.*, 1999). These chromitites were found to have variable initial ratios (Fig. 8.22), including some unradiogenic values near the chondritic evolution line that confirmed the erlichmanite analyses of Hart and Kinloch (1989). Since crystallisation of chromite is attributed to magma mixing, the variable initial ratios of the Critical Zone chromitites suggest that two magmas mixed several times in the history of the magma chamber, in different proportions. The same magma-mixing process which pushed the mixed magma into the field of chromite crystallisation probably also caused the separation of immiscible sulphide droplets. The chromite grains and sulphide droplets would then have settled at the same time, forming cumulate chromitites with interstitial sulphide. However, the composition of the sulphide droplets thus formed might have been quite variable, as they scavenged PGE from different pockets of an isotopically heterogeneous magma. Hence the data of Hart and Kinloch (1989) are reasonably explained within the overall framework of the magma-mixing model.

8.4.2 The Stillwater Complex

The Stillwater Complex in Montana has similarities to the Bushveld Complex, and has also produced some puzzling Re–Os results that have only recently been resolved. As in the Bushveld case, two distinct magmas have been proposed to explain the petrology and chemistry of the pluton. An ultramafic liquid apparently gave rise to the lower Ultramafic Series (UMS), whereas a magma similar to high-Al basalt formed most of the overlying Banded Series. The PGE-bearing J–M reef is located near the stratigraphic boundary between these two liquids, whose mixing may have promoted the segregation of a PGE-bearing sulphide liquid to form the reef. However, chromite-rich layers scattered through the ultramafic series may also reflect small influxes of a high-Al basaltic liquid into a magma chamber crystallising an ultramafic liquid. These chromitites are identified by letters (A, B, G etc.).

Despite the initial ratio heterogeneity of the complex, Lambert *et al.* (1989) obtained a Re–Os isochron from four Re-rich whole-rock samples, comprising two sulphide-rich cumulates, a bronzite pegmatite, and the K-seam chromitite band. The isochron had a low MSWD of 0.03, although this was achieved at the expense of throwing out a fifth data point from a hydrothermally altered harzburgite (Fig. 8.23a). Using a decay constant of 1.64×10^{-11} yr^{-1}, the isochron gave an age of 2.66 ± 0.08 Byr, but recalibration of the spike (Lambert *et al.*, 1994) increased this to 2.74. Nevertheless, the age is revised back down to 2.69 ± 0.08 Byr using the new decay constant of 1.666×10^{-11} yr^{-1}. This result is in good agreement with U–Pb and Sm–Nd ages for the intrusion (section 4.1.2), and suggests that fresh whole-rock samples from the Stillwater Complex generally remained as closed systems for Re and Os during a thermal event that re-set Rb–Sr *mineral* systems in the complex.

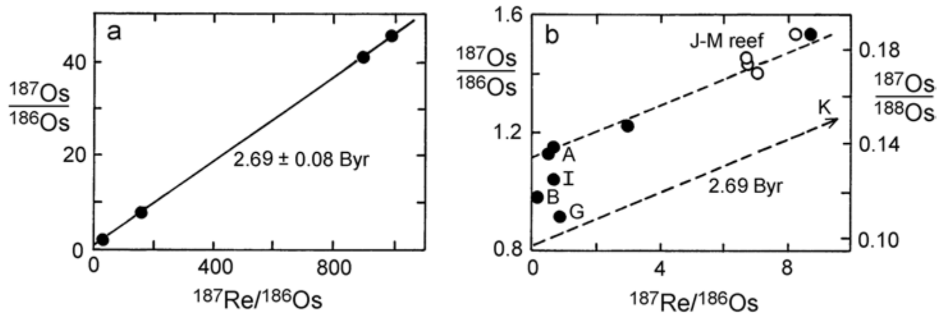

Fig. 8.23. Re–Os isochron diagrams for whole-rock samples from the Stillwater Complex: (a) rhenium-rich samples used to construct an isochron and (b) Re-poor samples, including the J-M reef (○), chromitite bands A to K, and un-named chromitites (●). After Lambert *et al.* (1989).

Analysis of whole-rock samples with low Re/Os ratios by Lambert *et al.* revealed a degree of initial ratio heterogeneity similar to that of the Bushveld Complex (Fig. 8.23b). Chromitite bands from the ultramafic series had initial ^{187}Os/^{188}Os compositions ranging from a late Archean chondritic value of 0.109 to a maximum initial ratio of 0.145 in the J–M reef. Similar results were also obtained on a smaller suite of samples by Martin (1989). Lambert *et al.* attributed the variable initial Os ratios in the chromitites to crustal contamination of mantle-derived magmas by an enriched crustal component, whereas Martin (1989) attributed isotopic variation in the reefs to variable mixing between chromite cumulates and contaminated intercumulus liquid.

Further study of fresh Stillwater chromites by Marcantonio *et al.* (1993) gave puzzling results. Chromite separates and chromitite whole-rocks from four horizons had initial ^{187}Os/^{188}Os ratios within error of the 'chondritic' mantle ratio of 0.109 at the time of intrusion. On the other hand, samples from the fifth horizon (G chromitite) gave very variable initial ratios, ranging from below the chondritic evolution line to well above it (initial ^{187}Os/^{188}Os = 0.79) in a molybdenite-bearing sample. The simplest explanation for the latter sample would be later disturbance of the Re–Os system, but the molybdenite from this sample gave a Re–Os age of 2.74 ± 0.08 Byr, suggesting that re-distribution of osmium occurred soon after emplacement of the complex. Therefore, Marcantonio *et al.* attributed the elevated initial ratios in this and other chromitite samples to hydrothermal introduction of radiogenic Os immediately after crystallisation. They also suggested that the Sm–Nd system might have been similarly upset by hydrothermal re-mobilisation, but this seems extremely unlikely.

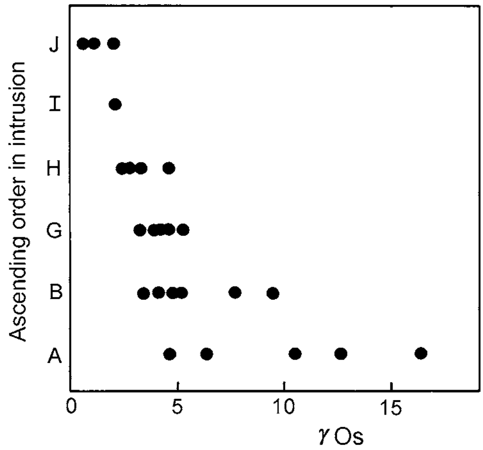

Fig. 8.24. Plot of initial Os isotope ratios (γ Os) for massive chromite layers of the Stillwater Complex against stratigraphic height in the ultramafic series (UMS). After Horan *et al.* (2001).

Subsequent work by Lambert *et al.* (1994) and Horan *et al.* (2001) helped to resolve some of these problems. For example, analysis of additional chromitite samples gave a more coherent picture in which initial osmium isotope ratios of massive chromitites gradually decreased upwards through the ultramafic series (Fig. 8.24). Horan *et al.* attributed this effect to the mixing of two magmas in changing proportions; an osmium-rich melt with a chondritic isotope signature that was probably derived from a mantle plume, and a second magma probably contaminated by upper crustal rocks. According to this model, the fraction of the second (contaminated) magma must have decreased with time. However, the lack of a complete Nd data set on all samples analysed for Os makes the model speculative.

The J–M reef itself represents a reversal of this trend, which is difficult to explain (Lambert *et al.*, 1994). However, as in the Bushveld Complex, it seems most likely that a much larger influx of crustally contaminated melt, mixing with the plume-derived magma, caused major precipitation of immiscible sulphide, which then took on the relatively radiogenic osmium signature of the mixed liquid. Additional Os and Nd analyses on the same samples are needed in order to test and clarify these models.

8.4.3 The Sudbury Igneous Complex

The Sudbury Igneous Complex (SIC) in Ontario, Canada, is a large mafic body which also hosts the world's largest nickel reserves. However, isotopic evidence indicates a unique origin for the magmas which gave rise to this mineralisation. This can be attributed to the genesis of the Sudbury structure in a meteorite impact, a model first proposed by Dietz (1964) and now confirmed by numerous lines of evidence.

Nd isotope data for the silicate rocks of the SIC were presented by Faggart *et al.* (1985) and Naldrett *et al.* (1986). Both groups showed that the silicate rocks had a remarkably strong crustal signature, with ε Nd at 1.85 Byr averaging about -7.5, although Naldrett *et al.* found a range of ε values from -5 to -9. Faggart *et al.* argued that their data could be explained by an exclusively crustal origin for the SIC, whereas Naldrett *et al.* preferred a model involving gross crustal contamination of a mantle-derived magma. However, because Nd is a lithophile element, this evidence cannot reliably be extrapolated to deduce such an origin for the nickel-bearing sulphide ores of the complex. Furthermore, the enrichment of Nd in crustal relative to mantle-derived melts makes it an insensitive tracer for a small mantle-derived source component, which would tend to be swamped by crustal Nd. In this situation, Os data may be more diagnostic.

Walker *et al.* (1991) demonstrated approximate agreement between Re–Os isochron ages for sulphide ores and the 1.85 Byr U–Pb age of the silicate rocks (Krogh *et al.*, 1984). This substantiated previous geochemical evidence indicating that the sulphide and silicate melts were co-genetic. However, age correction of measured isotope ratios in ores from the Levack West, Falconbridge and Strathcona mines gave rise to variable initial Os isotope ratios 1.85 Byr ago. This was attributed to a heterogeneous magma body, formed by variable mixing between mantle-derived osmium and radiogenic crustal osmium.

In contrast to these results, Dickin *et al.* (1992) observed relatively good homogeneity of initial osmium isotope ratios for sulphide ores from the Creighton, Falconbridge and Levack West mines. Tails to lower initial ratios in two of these mines, and the large scatter of initial ratios from the Strathcona mine, were attributed to post-intrusive open-system behaviour of the Re–Os system, possibly in response to the Grenville orogeny. The consensus of initial ratios for Sudbury mines falls within the range of estimated crustal compositions at 1.85 Byr, and was attributed by Dickin *et al.* to an entirely crustal source for osmium in the Sudbury ores. This is consistent with an origin of the SIC as an impact melt sheet (Dietz, 1964). However, no evidence of material contribution from the meteorite itself is seen.

Further work by Dickin *et al.* (1999), Cohen *et al.* (2000), and Morgan *et al.* (2002) has resulted in some convergence between the previous positions. It is now recognised that the complex probably had a 100% crustal origin, but it is also recognised that there is considerable Os isotope heterogeneity in the complex due to incomplete mixing between the melted target rocks. The degree of osmium heterogeneity in the complex is demonstrated by the compilation of data in Fig. 8.25. This histogram shows that there is good agreement between the initial ratios of Creighton and Falconbridge ores, but much larger variations in mineralised 'inclusions' from the Whistle mine. These 'inclusions' are mafic–ultramafic xenoliths whose elemental chemistry is indicative of an origin as cumulates from the SIC magma. However, their isotopic signatures are indicative of an origin from locally melted crustal rocks, at least some being of basaltic composition. Hence

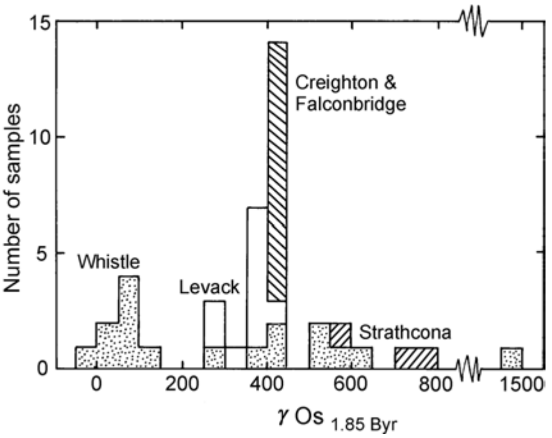

Fig. 8.25. Histogram of initial Os isotopic ratios (γ Os) for Sudbury ores 1.85 Byr ago. Some mines display homogeneous osmium, whereas others (e.g. Whistle) are very heterogeneous. After Cohen *et al.* (2000).

it appears that the SIC magma was very poorly homogenised at an early stage in its evolution when these cumulates were formed, but became much better homogenised as it cooled and differentiated (Dickin *et al.*, 1999).

The evidence from the Whistle mine for impact melting of mafic as well as felsic crustal rocks is supported by ^{190}Pt–^{186}Os isotope evidence (Morgan *et al.*, 2002). Comparison of initial ^{186}Os and ^{187}Os abundances in three mines revealed a rough inverse correlation, consistent with the mixing of distinct lithologies. Thus, Strathcona samples had radiogenic ^{187}Os but unradiogenic ^{186}Os, indicative of a large component of melted felsic rocks with high Re/Pt ratios. On the other hand, samples from Falconbridge and McCreedy West had less radiogenic ^{187}Os, but more radiogenic ^{186}Os, indicative of a component of melted basic rocks with lower Re/Pt ratios. This mixing model is supported by Sr isotope evidence (e.g. Dickin *et al.*, 1999). However, Pb isotope evidence provides a different slant, by revealing distinct contributions to the impact melt sheet from different crustal depths (Dickin *et al.*, 1996; 1999). Thus, most Pb in North Range ores came from Archean crust, whereas most Pb in South Range ores came from Huronian supracrustals.

Hence it is concluded that the melt sheet formed by the Sudbury meteorite impact was a complex mixture of shock-melted crustal rocks. Mixing of mafic and felsic lithologies probably caused the melt to enter the field of immiscibility between silicate and sulphide melts (Naldrett *et al.*, 1986). This sulphide melt was of crustal origin and probably did not originally contain high levels of PGE. However, the melt must have been in intimate contact with the pool of fused crustal material for considerable time. During this time, PGE were partitioned from the bulk crustal melt into the sulphide phase in a process analogous to the nickel sulphide fire-assay method (e.g. Hofmann *et al.*, 1978). Hence, Sudbury represents ‘nature’s largest fire assay’.

8.4.4 Flood-basalt provinces

A combination of Os and Nd isotope data has been used to study mixing between source components of the picritic Karoo flood basalts from southern Africa (Ellam *et al.*, 1992). Initial Os–Nd isotope data for these samples (at 190 Myr) are shown relative to possible source reservoirs in Fig. 8.26. These data reveal some of the potential advantages of Os isotope data, relative to other tracers such as Nd, in discriminating between components involved in basalt genesis. Nd isotope compositions in the continental crust and sub-continental lithosphere may be similar, making these components hard to resolve. In addition, the greater incompatible-element inventories of lithospheric reservoirs, relative to asthenospheric melts, make it hard to quantify the contamination processes which may occur during ascent of magma through the lithosphere. On the other hand, Os isotope data can resolve these components because the Re-depleted sub-continental lithosphere typically has an unradiogenic signature relative to plume sources and crustal units (Walker *et al.*, 1989a). The model mixing lines in Fig. 8.26 suggest that there were variable contributions of material to magma genesis from asthenospheric and lithospheric mantle (see section 7.2.4).

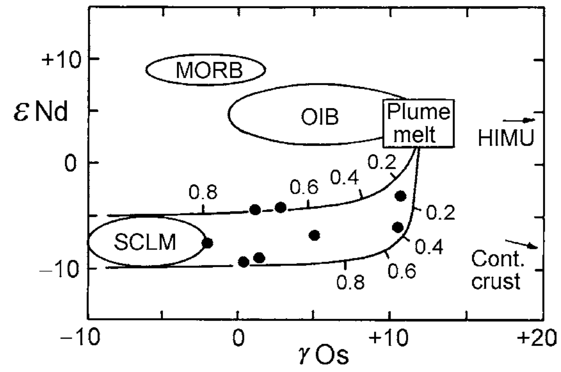

Fig. 8.26. Plot of ε Nd against γ Os for Karoo basalts and possible source reservoirs. Mixing lines between plume and lithospheric components are shown. After Ellam *et al.* (1992).

Another flood-basalt province from which osmium isotope data have been obtained is the Deccan trap province of southern India (Allègre *et al.*, 1999). Samples collected from a wide range of stratigraphic heights in the lava pile nevertheless had very homogeneous initial ratios close to the chondritic evolution line. This is in contrast to lithophile isotope tracers, which record significant effects of crustal contamination. This contrast in behaviour reflects the known enrichment of osmium in primitive mantle-derived magmas relative to continental crust.

8.5 Seawater osmium

A comparison with Sr isotope systematics suggests that the large differences in osmium isotope composition between crustal and mantle reservoirs should generate large seawater Os isotope variations through time. Seawater itself contains very little osmium, but chemical sediments act to pre-concentrate osmium by scavenging it from seawater, thus reaching quite high abundances. Ravizza and Turekian (1992) showed that this 'hydrogenous' osmium component could be extracted from the substrate by leaching. Hence, they demonstrated that modern seawater has radiogenic $^{187}Os/^{186}Os$ ratios of about 8.5 ($^{187}Os/^{188}Os = 1.0$). In contrast, residues from leaching have significantly lower Os isotope ratios due to the presence of a micrometeorite (cosmic-dust) component that is constantly raining down upon the Earth.

It is most convenient to review this subject under the same categories that were used for seawater Sr (section 3.6). Therefore, we first examine the evidence used to reconstruct a seawater osmium curve, before considering the competing fluxes which cause changes in seawater osmium through time.

8.5.1 Seawater Os isotope evolution

Pegram *et al.* (1992) analysed leached carbonaceous sediments of various ages in the first study of seawater osmium isotope evolution through the Cenozoic. Osmium was extracted by acid hydrogen peroxide leaching of pelagic black shales from a large piston core recovered from the North Pacific. Pegram *et al.* interpreted the measured osmium isotope ratios as primary signatures of the sediments, reflecting seawater osmium, rather than the product of secondary mixing between re-mobilised terrestrial and meteoritic osmium. Given this assumption, the data implied a sharp increase in seawater osmium isotope composition during the Tertiary period, mimicking the seawater Sr profile for this period (section 3.6.1).

These preliminary findings were confirmed by Ravizza (1993), who used metalliferous sediments deposited near mid-ocean ridges as recorders of seawater osmium. Because these sediments have greater rates of deposition than the pelagic clays used previously, the fraction of hydrogenous (seawater-derived) osmium dominates over the cosmic-dust fraction. The results were in good agreement with leached pelagic clay data, and revealed a rapid increase in seawater Os isotope ratio over the last 15 Myr, but relatively constant ratios between 18 and 28 Myr ago (Fig. 8.27). Sr isotope ratios from the same samples were in good agreement with published data, but when they were compared with osmium data they revealed significant decoupling between the two systems. This is not surprising, in view of the very different chemistries of the two elements.

Peucker-Ehrenbrink *et al.* (1995) extended the detailed seawater osmium record to 80 Myr, using a combination of leached and bulk sediment analyses. However, they showed that for slowly deposited pelagic clays, a more gentle leaching procedure was necessary in order to remove hydrogenous osmium without releasing the cosmic-dust fraction. Data from sediments with a relatively high deposition rate were in good agreement between different studies, but data from slowly deposited sediments were less reliable. Leached 80-Myr-old sediment showed for the first time a radiogenic osmium isotope signature below the K–T boundary (Fig. 8.27). In addition, gently leached samples on either side of the boundary constrained a sharp drop in osmium isotope ratio to the immediate vicinity of the boundary. To explain this dip at the K–T boundary, Peucker-Ehrenbrink *et al.* calculated that a meteorite impact could have released a pulse of dissolved osmium into the oceans equivalent in size to that provided by 5 Myr of the global run-off flux (see below).

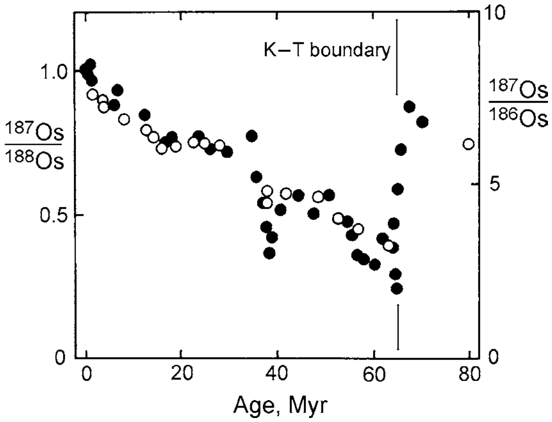

Fig. 8.27. Plot of Os isotope ratio of sediment leachates against age, attributed to increasing seawater Os isotope ratio during the Tertiary. Data sources: (○) = Ravizza (1993) and Peucker-Ehrenbrink *et al.* (1995); (●) = Pegram and Turekian (1999).

Data from the above studies were augmented by Pegram and Turekian (1999) in a larger study of the same sediment core as that used by Pegram *et al.* (1992). The bottom of the core was dated using cobalt accumulation rates (section 4.5.3), and the accuracy of Os measurements on bulk sediment was improved by correcting for the cosmogenic Os component in the sediment on the basis of ^3He measurements. The result was a more detailed profile for the early Tertiary, which was largely consistent with earlier work but also reached to even less radiogenic compositions at the K–T boundary. A similar dip was seen at the Eocene–Oligocene boundary (Fig. 8.27).

The first attempt to extend the seawater osmium curve back into the Jurassic was made by Cohen *et al.*

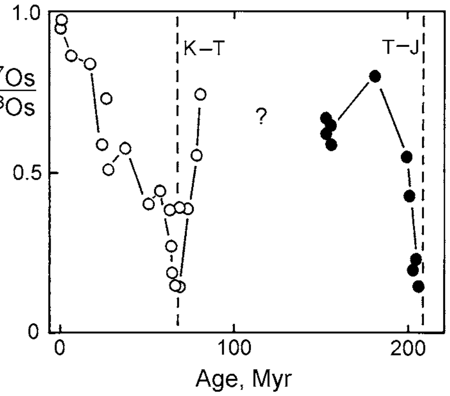

Fig. 8.28. Plot of inferred Os isotope ratios of seawater through the Jurassic to Tertiary periods. After Cohen *et al.* (1999). Open symbols are data of Peucker-Ehrenbrink *et al.* (1995).

(1999). This was based on analysis of relatively very-Os-rich, organic-rich mud-rocks with total Os contents between 0.2 and 3 ppb. Samples were analysed by bulk dissolution techniques on the grounds that the meteoritic component was insignificant in these continental-shelf sediments, which have deposition rates several orders of magnitude faster than those of pelagic sediments. Unlike the cases discussed above, these organic-rich mud-rocks also have high Re/Os ratios, so relatively large age corrections were necessary in order to recover initial Os isotope ratios indicative of seawater osmium. This was achieved by means of three Re–Os isochrons, with ages of intervening samples estimated by interpolation.

The results from this study (Fig. 8.28) revealed very unradiogenic osmium near the Triassic–Jurassic boundary, with a subsequent very rapid rise, reminiscent of the K–T boundary. Despite the relatively proximal (near-shore) deposition site of the sediments, the osmium isotope signatures were taken to be indicative of seawater osmium on the grounds that only the open ocean could supply the relatively very large amounts of Os necessary to support the deposition flux in these Os-rich sediments. However, Cohen *et al.* attributed the presumed variations in seawater osmium to varying terrestrial osmium fluxes (see below), rather than a meteoritic source.

One case where a continental weathering model seems justified is the Os isotope peak in the early Jurassic, which was shown by Cohen *et al.* (2004) to be much sharper than previously realised, with a duration of only 1 Myr. The Os peak is correlated with the 'Toarcian oceanic anoxic event', a global warming event that caused a sharp increase in continental weathering. This could have released a spike of radiogenic osmium to the oceans.

8.5.2 Os fluxes and residence times

In order to understand seawater osmium evolution it is important to quantify the fluxes which control its composition. A comparison between these fluxes and the oceanic osmium inventory will then allow a calculation of the residence time of osmium in seawater. The principal source of radiogenic osmium is river-borne run-off from old continental crust. On the other hand, possible sources of unradiogenic osmium are low-temperature hydrothermal alteration of ultramafic rocks (Sharma *et al.*, 2000) and the dissolution of cosmic dust. The magnitude of the unradiogenic component is unknown, but its composition is well constrained. Therefore, a major objective has been to constrain the size and composition of the river-water budget.

In early work on this subject, Pegram *et al.* (1994) argued that the oxidising conditions of river water would cause osmium to be adsorbed on the ferromanganese coatings of particulate sediment, rather than remaining in solution. They speculated that when this sediment reached the sea, reducing conditions would break down the ferromanganese oxides, releasing osmium to seawater. By analysing leaches of river sediment, Pegram *et al.* found very variable $^{187}Os/^{188}Os$ ratios, ranging from 0.17 to 0.85 in rivers draining ultramafic rocks to values of 1.4–2.8 in more typical drainage basins. However, large rivers such as the Mississippi and Ganges had ratios close to 2.2, a best estimate for the global average. This was substantially more radiogenic than an estimate of 1.26 in average upper crust (Esser and Turekian, 1993).

The first direct measurements on dissolved river-water osmium were made by Sharma and Wasserburg (1997). Because these concentrations are so low, it is convenient to quote them in pg/kg (10^{-15} g/g). Analysis of four major rivers suggested a concentration range from 2.8 to 8.5 pg/kg and a range of $^{187}Os/^{188}Os$ ratio from 1.2 to 2.0. Hence Sharma and Wasserburg estimated the total riverine supply of dissolved osmium at 320 kg/yr. These results were refined by Levasseur *et al.* (1999), using data for seventeen of the world's largest rivers. The average dissolved osmium concentration was estimated as 7.9 pg/kg, with a $^{187}Os/^{188}Os$ ratio of 1.5, leading to an estimated global riverine flux of 295 kg/yr, in good agreement with Sharma and Wasserburg (1997). In addition, the flux of non-dissolved Os carried on particulate matter was estimated at less than 25% of the dissolved flux.

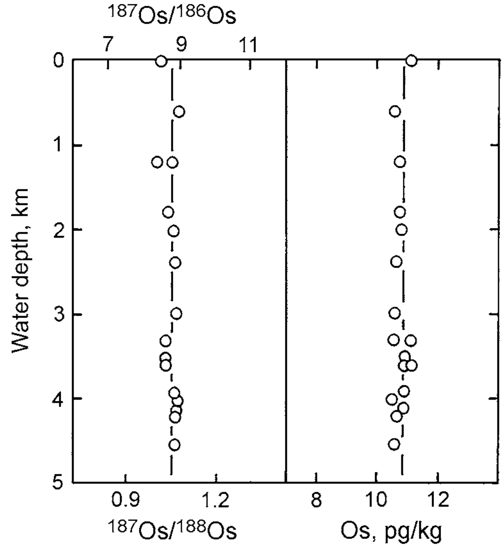

Fig. 8.29. Profiles of (a) osmium isotope ratio and (b) concentration, in sections through the SW Indian Ocean. After Levasseur *et al.* (1998).

The first direct measurements of seawater osmium concentration were made by Sharma *et al.* (1997), yielding a best estimate of 3.6 pg/kg, with an isotope ratio of 1.04 ($^{187}Os/^{186}Os = 8.7$). Subsequent work by Levasseur *et al.* (1998) and Woodhouse *et al.* (1999) confirmed the mean isotope ratio of modern seawater as 1.06 (8.8), but suggested that the concentration determined by Sharma *et al.* was an underestimate, due to a failure to achieve complete isotopic homogenisation between sample and spike osmium. Thus, Levasseur *et al.* determined a constant concentration of 10.9 pg/kg in a 5-km-deep section from the southwest Indian ridge (Fig. 8.29). A similar experiment by Woodhouse *et al.* (1999), on a 3-km-deep section from the eastern Pacific, gave identical isotope ratios but suggested some variations in osmium concentration. Below 2 km depth, these ranged from 8.5 to 9.5 pg/kg, but at 500 m depth the concentration dropped as low as 6.5 pg/kg.

A comparison between the isotopic compositions of average river water and seawater allows the relative fluxes of riverine osmium and unradiogenic osmium (meteoritic and mantle-derived) to be estimated. Estimates of the size of the riverine flux vary from a low of 50% (using the riverine $^{187}Os/^{188}Os$ ratio of 2.2 from Pegram *et al.*, 1994) to a high of 81% (using the value of 1.5 from Sharma and Wasserburg, 1997). The intermediate riverine value of 1.8 from Levasseur *et al.* (1999) corresponds to a 70% contribution. Ignoring the redissolution of particulate osmium from rivers, this implies a global osmium flux to the oceans (riverine and unradiogenic) of 420 kg/yr.

Assuming that the system is in a steady-state condition, comparison of the seawater osmium inventory with the total input flux allows the oceanic residence time of osmium to be calculated. An average seawater concentration of 10 pg/kg, divided by the mass of the oceans (1.4×10^{21} kg), leads to an oceanic osmium inventory of 1.4×10^{7} kg. Given a total input flux of 420 kg/yr, this leads to a residence time (τ) of 33 kyr. This residence time is near the middle of many estimates made over the past ten years. It is much shorter than that of strontium (section 3.6.2), but also substantially longer than those of non-conservative elements such as Nd, Th and Be. In fact it is similar to the time taken for river water to fill the oceans (37 kyr).

Despite the efforts described above to place constraints on global osmium fluxes, there are still major uncertainties. One of these concerns the fate of dissolved osmium in the estuarine and coastal zone. As noted above, Pegram *et al.* (1994) initially proposed that particulate riverine osmium would be released into solution in estuaries. On the other hand, a study of the Lena river in Siberia (Levasseur *et al.*, 2000) showed that nearly 30% of dissolved riverine osmium was *lost* from solution in the estuary by adsorption onto suspended particles. If this process occurred on a world-wide scale, the seawater residence time of osmium would have to be increased by 30%. However, a study of the Fly and Sepik rivers in Papua New Guinea (Martin *et al.*, 2001) suggested that *both* riverine osmium and seawater osmium were removed by adsorption in the estuary and the near-shore zone. This was demonstrated in a 200-km-long ‘salinity transect’ (Fig. 8.30).

When the osmium isotope ratios are plotted against salinity (Fig. 8.30a), they provide evidence of fairly simple mixing between seawater and the unradiogenic osmium carried by the river (reflecting its source in young ultramafic rocks). However, the plot of osmium *concentration* against salinity (Fig. 8.30b) shows that removal of dissolved osmium has occurred, particularly at the seaward end of the transect. This implies that seawater osmium may be lost at a similar rate to, or greater rate than, riverine osmium. The relative magnitude remains unknown, certainly at the global scale, but it suggests that 33 kyr may be a maximum rather than a minimum value for residence of osmium in seawater.

The tentative consensus of seawater osmium residence times around 30–40 kyr was shattered by evidence for very rapid changes in seawater osmium isotope composition during the Quaternary period (Oxburgh, 1998). This evidence comes from two

200-kyr sediment cores from the East Pacific Rise, which display osmium isotope variations in step with glacial cycles, as represented by oxygen isotope analysis (Fig. 8.31). The two cores yielded consistent results, suggesting that they might be recording real changes in the seawater osmium signature. However, the sharpness of the changes (particularly during deglaciations 140 kyr and 20 kyr ago) implied an extremely short seawater osmium residence time, possibly as low as 3000 yr. Given such a short residence time, the apparent sharp drops in the isotope signature during the last two glacial periods were attributed to a reduction in chemical weathering at these times. However, in order to reconcile these data with the box-model estimate of seawater residence, it is necessary to postulate a riverine flux at least three times greater than that estimated by Sharma and Wasserburg (1997) and Levasseur *et al.* (1999).

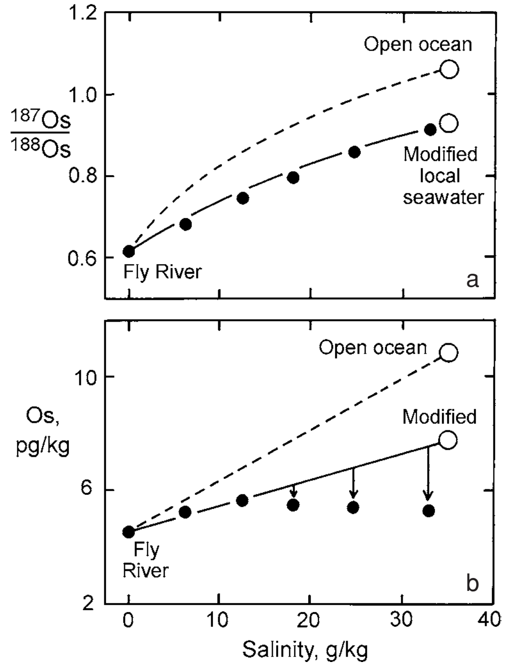

Fig. 8.30. Salinity profiles from the estuary of the Fly River, Papua New Guinea: (a) against isotope ratio and (b) against Os concentration. After Martin *et al.* (2001).

Further evidence for very rapid changes in seawater osmium was presented by Oxburgh (2001) for the Cariaco Basin in the Caribbean (Fig. 8.32). This basin shows annual varves that have been calibrated against radiocarbon ages (section 14.1.5). This data set gave much better time resolution for seawater osmium evolution and appeared to reveal a sudden jump from a steady state during the last glacial maximum to a new steady state during the Holocene.

The data are compared in Fig. 8.32 with three of the data points from core V19-55 in the Pacific (Oxburgh, 1998). This comparison reveals some positive and some negative points (for an interpretation of these signals as real seawater osmium variations). On the positive side, the core-top analyses from the Pacific and the Caribbean samples are consistent with osmium analysis of young Fe–Mn crusts from the Pacific and Atlantic oceans (Burton *et al.*, 1999a), as shown in Fig. 8.32. However, on the negative side, the Cariaco basin records a very early rise in the osmium signature, largely in advance of the oxygen isotope profile, and while the Pacific core is still displaying a 'glacial' signature. Hence it is concluded that more work must be undertaken before these findings can be accepted as genuine reflections of seawater osmium isotope evolution.

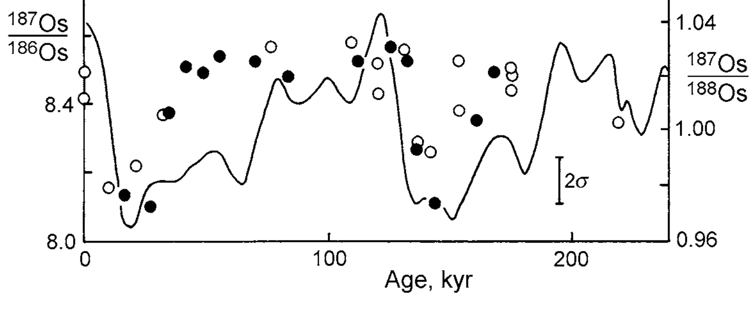

Fig. 8.31. Plot of osmium isotope ratio against age for two sediment cores (●, ○) from the flanks of the East Pacific Rise. These are compared with a record of oxygen isotope variations, which are representative of glacial cycles. After Oxburgh (1998).

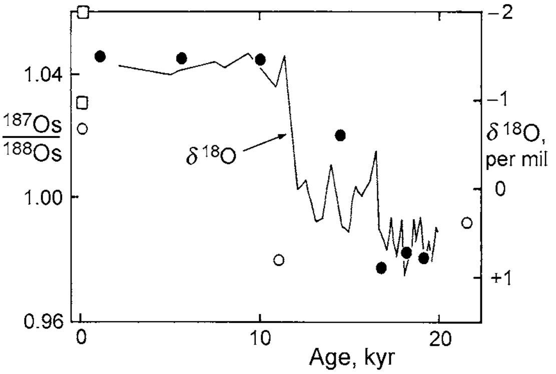

Fig. 8.32. Plot of Os isotope ratio against age for sediment cores from the Cariaco Basin (●) and the East Pacific Rise (○), compared with an oxygen isotope record from the Cariaco Basin. Recent Fe–Mn crusts from the Atlantic and Pacific Ocean are also shown (□). Modified after Oxburgh (2001).

References

Alard, O., Griffin, W. L., Pearson, N. J., Lorand, J.-P. and O'Reilly, S. Y. (2002). New insights into the Re–Os systematics of sub-continental lithospheric mantle from *in situ* analysis of sulphides. *Earth Planet. Sci. Lett.* **203**, 651–63.

Allègre, C. J., Birck, J.-L., Capmas, F. and Courtillot, V. (1999). Age of the Deccan traps using ^{187}Re–^{187}Os systematics. *Earth Planet. Sci. Lett.* **170**, 197–204.

Allègre, C. J. and Luck, J. M. (1980). Osmium isotopes as petrogenetic and geological tracers. *Earth Planet. Sci. Lett.* **48**, 148–54.

Alves, S., Schiano, P. and Allègre, C. J. (1999). Rhenium–osmium isotopic investigation of Java subduction zone lavas. *Earth Planet. Sci. Lett.* **168**, 65–77.

Alves, S., Schiano, P., Capmas, F. and Allègre, C. J. (2002). Osmium isotope binary mixing arrays in arc volcanism. *Earth Planet. Sci. Lett.* **198**, 355–69.

Becker, H. (2000). Re–Os fractionation in eclogites and blueschists and the implications for recycling of oceanic crust into the mantle. *Earth Planet. Sci. Lett.* **177**, 287–300.

Becker, H., Shirey, S. B. and Carlson, R. W. (2001). Effects of melt percolation on the Re–Os systematics of peridotites from a Paleozoic convergent plate margin. *Earth Planet. Sci. Lett.* **188**, 107–21.

Bennett, V. C., Esat, T. M. and Norman, M. D. (1996). Two mantle-plume components in Hawaiian picrites inferred from correlated Os–Pb isotopes. *Nature* **381**, 221–3.

Bennett, V. C., Nutman, A. P. and Esat, T. M. (2002). Constraints on mantle evolution from ^{187}Os/^{188}Os isotopic compositions of Archean ultramafic rocks from southern West Greenland (3.8 Ga) and Western Australia (3.46 Ga). *Geochim. Cosmochim. Acta* **66**, 2615–30.

Birck, J.-L., Roy-Barman, M. and Capmas, F. (1997). Re–Os isotopic measurements at the femtomole level in natural samples. *Geostand. Newslett.* **20**, 19–27.

Brandon, A. D., Creaser, R. A., Shirey, S. B. and Carlson, R. W. (1996). Osmium recycling in subduction zones. *Science* **272**, 861–4.

Brandon, A. D., Norman, M. D., Walker, R. J., and Morgan, J. W. (1999). ^{186}Os–^{187}Os systematics of Hawaiian picrites. *Earth Planet. Sci. Lett.* **174**, 25–42.

Brandon, A. D., Snow, J. E., Walker, R. J., Morgan, J. W. and Mock, T. D. (2000). ^{190}Pt–^{186}Os and ^{187}Re–^{187}Os systematics of abyssal peridotites. *Earth Planet. Sci. Lett.* **177**, 319–35.

Brandon, A. D., Walker, R. J., Morgan, J. W., Norman, M. D. and Prichard, H. M. (1998). Coupled ^{186}Os and ^{187}Os evidence for core–mantle interaction. *Science* **280**, 1570–3.

Brenan, J. M., Cherniak, D. J. and Rose, L. A. (2000). Diffusion of osmium in pyrrhotite and pyrite: implications for closure of the Re–Os isotopic system. *Earth Planet. Sci. Lett.* **180**, 399–413.

Brodzinski, R. L. and Conway, D. C. (1965). Decay of rhenium-187. *Phys. Rev.* **138**, B1368–71.

Buick, I. S., Maas, R. and Gibson, R. (2001). Precise U–Pb titanite age constraints on the emplacement age of the Bushveld Complex, South Africa. *J. Geol. Soc. Lond.* **158**, 3–6.

Burton, K. W., Bourdon, B., Birck, J.-L., Allègre, C. J. and Hein, J. R. (1999a). Osmium isotope variations in the oceans recorded by Fe–Mn crusts. *Earth Planet. Sci. Lett.* **171**, 185–97.

Burton, K. W., Gannoun, A., Birk, J.-L. *et al.* (2002). The compatibility of rhenium and osmium in natural olivine and their behaviour during mantle melting and basalt genesis. *Earth Planet. Sci. Lett.* **198**, 63–76.

Burton, K. W., Schiano, P., Birck, J.-L. and Allègre, C. J. (1999b). Osmium isotope disequilibrium between mantle minerals in a spinel-lherzolite. *Earth Planet. Sci. Lett.* **172**, 311–22.

Carlson, R. W. and Irving, A. J. (1994). Depletion and enrichment history of subcontinental lithospheric mantle: an Os, Sr, Nd and Pb isotopic study of ultramafic xenoliths from the northwestern Wyoming Craton. *Earth Planet. Sci. Lett.* **126**, 457–72.

Chesley, J. T., Rudnick, R. and Lee, C.-T. (1999). Re–Os systematics of mantle xenoliths from the East African Rift: age, structure, and history of the Tanzanian craton. *Geochim. Cosmochim. Acta* **63,** 1203–17.

Class, C. and Goldstein, S. L. (1997). Plume–lithosphere interactions in the ocean basins: constraints from the source mineralogy. *Earth Planet. Sci. Lett.* **150**, 245–60.

Cohen, A. S., Burnham, O. M., Hawkesworth, C. J. and Lightfoot, P. C. (2000). Pre-emplacement Re–Os ages from ultramafic inclusions in the sublayer of the Sudbury Igneous Complex, Ontario. *Chem. Geol.* **165**, 37–46.

Cohen, A. S., Coe, A. L., Harding, S. M. and Schwark, L. (2004). Osmium isotope evidence for the regulation of atmospheric CO_2 by continental weathering. *Geology* **32**, 157–60.

Cohen, A. S., Coe, A. L., Bartlett, J. M. and Hawkesworth, C. J. (1999). Precise Re–Os ages of organic-rich mudrocks and the Os isotope composition of Jurassic seawater. *Earth Planet. Sci. Lett.* **167**, 159–73.

Creaser, R. A., Papanastassiou, D. A. and Wasserburg, G. J. (1991). Negative thermal ion mass spectrometry of osmium, rhenium, and iridium. *Geochim. Cosmochim. Acta* **55**, 397–401.

Creaser, R. A., Sannigrahi, P., Chacko, T. and Selby, D. (2002). Further evaluation of the Re–Os geochronometer in organic-rich sedimentary rocks: a test of hydrocarbon maturation effects in the Exshaw Formation, Western Canada Sedimentary Basin. *Geochim. Cosmochim. Acta* **66**, 3441–52.

Dickin, A. P., Artan, M. A. and Crocket, J. H. (1996). Isotopic evidence for distinct crustal sources of North and South Range ores, Sudbury Igneous Complex. *Geochim. Cosmochim. Acta* **60**, 1 605–13.

Dickin, A. P., Nguyen, T. and Crocket, J. H. (1999). Isotopic evidence for a single impact melting origin of the Sudbury Igneous Complex. *Geol. Soc. Amer. Spec. Paper* **339**, pp. 361–71.

Dickin, A. P., Richardson, J. M., Crocket, J. H., McNutt, R. H. and Peredery, W. V. (1992). Osmium isotope evidence for a crustal origin of platinum group elements in the Sudbury nickel ore Ontario, Canada. *Geochim. Cosmochim. Acta* **56**, 3531–7.

Dietz, R. S. (1964). Sudbury structure as an astrobleme. *J. Geol.* **72**, 412–34.

Ellam, R. M., Carlson, R. W. and Shirey, S. B. (1992). Evidence from Re–Os isotopes for plume–lithospheric mixing in Karoo flood basalt genesis. *Nature* **359**, 718–21.

Esser, B. K. and Turekian, K. K. (1993). The osmium isotopic composition of the continental crust. *Geochim. Cosmochim. Acta* **57**, 3093–104.

Faggart, B. E., Basu, A. R. and Tatsumoto, M. (1985). Origin of the Sudbury Complex by meteoritic impact: neodymium isotope evidence. *Science* **230**, 436–9.

Hart, S. R. and Kinloch, E. D. (1989). Osmium isotope systematics in Witwatersrand and Bushveld ore deposits. *Econ. Geol.* **84**, 1651–5.

Hattori, K. and Hart, S. R. (1991). Osmium-isotope ratios of platinum-group minerals associated with ultramafic intrusions: Os-isotopic evolution of the oceanic mantle. *Earth Planet. Sci. Lett.* **107**, 499–514.

Hauri, E. H. and Hart, S. R. (1993). Re–Os isotope systematics of HIMU and EMII oceanic island basalts from the south Pacific Ocean. *Earth Planet. Sci. Lett.* **114**, 353–71.

Hauri, E. H. and Hart, S. R. (1997). Rhenium abundances and systematics in oceanic basalts. *Chem. Geol.* **139**, 185–205.

Hauri, E. H., Lassiter, J. C. and DePaolo, D. J. (1996). Osmium isotope systematics of drilled lavas from Mauna Loa, Hawaii. *J. Geophys. Res.* **101**, 11 793–806.

Hirata, T., Hattori, M. and Tanaka, T. (1998). In-situ osmium isotope ratio analyses of iridosmines by laser ablation–multiple collector–inductively coupled plasma mass spectrometry. *Chem. Geol.* **144**, 269–80.

Hirt, B., Tilton, G. R., Herr, W. and Hoffmeister, W. (1963). The half life of ^{187}Re. In: Geiss, J. and Goldberg, E. (Eds.), *Earth Science Meteoritics*. North Holland Publishers, pp. 273–80.

Hofmann, E. L., Naldrett, A. J., van Loon, J. C., Hancock, R. G. V. and Manson, A. (1978). The determination of all the platinum group elements and gold in rocks and ore by neutron activation analysis after preconcentration by a nickel sulfide fire-assay technique on large samples. *Anal. Chim. Acta* **102**, 157–66.

Horan, M. F., Morgan, J. W., Walker, R. J. and Cooper, R. W. (2001). Re–Os isotopic constraints on magma mixing in the Peridotite Zone of the Stillwater Complex, Montana, USA. *Contrib. Mineral. Petrol.* **141**, 446–57.

Ito, E., Morooka, K., Ujike, O. and Katsura, T. (1995). Reactions between molten iron and silicate at high pressure: implications for the chemical evolution of the Earth's core. *J. Geophys. Res.* **100**, 5901–10.

Jordan, T. H. (1978). Composition and development of the continental tectosphere. *Nature* **274**, 544–8.

Kirk, J., Ruiz, J., Chesley, J., Walshe, J. and England, G. (2002). A major Archean, gold- and crust-forming event in the Kaapvaal Craton, South Africa. *Science* **297**, 1856–8.

Krogh, T. E., Davis, D. W. and Corfu, F. (1984). Precise U–Pb zircon and baddeleyite ages from the Sudbury area. In: Pye, E. G., Naldrett, A. J. and Giblin, P. E. (Eds.), *The Geology and Ore Deposits of the Sudbury Structure. Ont. Geol. Surv. Spec. Pub. Vol. 1*, pp. 431–47.

Lambert, D. D., Morgan, J. W., Walker, R. J. *et al.* (1989). Rhenium–osmium and samarium–neodymium isotopic systematics of the Stillwater Complex. *Science* **244**, 1169–74.

Lambert, D. D., Walker, R. J., Morgan, J. W. *et al.* (1994). Re–Os and Sm–Nd isotope geochemistry of the Stillwater Complex, Montana: implications for the petrogenesis of the J–M reef. *J. Petrol.* **35**, 1717–53.

Lassiter, J. C. and Hauri, E. H. (1998). Osmium-isotope variations in Hawaiian lavas: evidence for recycled oceanic lithosphere in the Hawaiian plume. *Earth Planet. Sci. Lett.* **164**, 483–94.

Levasseur, S., Birk, J.-L. and Allègre, C. J. (1998). Direct measurement of femtomoles of osmium and the ^{187}Os/^{186}Os ratio in seawater. *Science* **282**, 272–4.

Levasseur, S., Birk, J.-L. and Allègre, C. J. (1999). The osmium riverine flux and the oceanic mass balance of osmium. *Earth Planet. Sci. Lett.* **174**, 7–23.

Levasseur, S., Rachold, V., Birk, J.-L. and Allègre, C. J. (2000). Osmium behaviour in estuaries: the Lena River example. *Earth Planet. Sci. Lett.* **177**, 227–35.

Lindner, M., Leich, D. A., Borg, R. J. *et al.* (1986). Direct laboratory determination of the ^{187}Re half-life. *Nature* **320**, 246–8.

Lindner, M., Leich, D. A., Russ, G. P., Bazan, J. M. and Borg, R. J. (1989). Direct determination of the half-life of ^{187}Re. *Geochim. Cosmochim. Acta* **53**, 1597–606.

Luck, J. M. and Allègre, C. J. (1982). The study of molybdenites through the ^{187}Rep^{187}Os chronometer. *Earth Planet. Sci. Lett.* **61**, 291–6.

Luck, J. M. and Allègre, C. J. (1983). ^{187}Rep^{187}Os systematics in meteorites and cosmochemical consequences. *Nature* **302**, 130–2.

Luck, J. M. and Allègre, C. J. (1984). ^{187}Re–^{187}Os investigation in sulphide from Cape Smith komatiite. *Earth Planet. Sci. Lett.* **68**, 205–8.

Luck, J. M. and Allègre, C. J. (1991). Osmium isotopes in ophiolites. *Earth Planet. Sci. Lett.* **107**, 406–15.

Luck, J. M., Birck, J. L. and Allègre, C. J. (1980). ^{187}Re$-^{187}$Os systematics in meteorites: early chronology of the solar system and the age of the galaxy. *Nature* **283**, 256–9.

Macfarlane, R. D. and Kohman, T. P. (1961). Natural α radioactivity in medium–heavy elements. *Phys. Rev.* **121**, 1758–69.

Marcantonio, F., Zindler, A., Elliot, T. and Staudigel, H. (1995). Os isotope systematics of La Palma, Canary Islands: evidence for recycled crust in the mantle source of HIMU ocean islands. *Earth Planet. Sci. Lett.* **133**, 397–410.

Marcantonio, F., Zindler, A., Reisberg, L. and Mathez, E. A. (1993). Re–Os isotopic systematics in chromitites from the Stillwater Complex, Montana, USA. *Geochim. Cosmochim. Acta* **57**, 4029–37.

Martin, C. E. (1989). Re–Os isotopic investigation of the Stillwater Complex, Montana. *Earth Planet. Sci. Lett.* **93**, 336–44.

Martin, C. E. (1991). Osmium isotopic characteristics of mantle-derived rocks. *Geochim. Cosmochim. Acta* **55**, 1421–34.

Martin, C. E., Esser, B. K. and Turekian, K. K. (1991). Re–Os isotopic constraints on the formation of mantle and crustal reservoirs. *Australian J. Earth Sci.* **38**, 569–76.

Martin, C. E., Peucker-Ehrenbrink, B., Brunskill, G. and Szymczak, R. (2001). Osmium isotope geochemistry of a tropical estuary. *Geochim. Cosmochim. Acta* **65**, 3193–200.

McCandless, T. E., Ruiz, J. R., Adair, B. I. and Freydier, C. (1999). Re–Os isotope and Pd/Ru variations in chromitites from the critical Zone, Bushveld Complex, South Africa. *Geochim. Cosmochim. Acta* **63**, 911–23.

McCandless, T. E., Ruiz, J. and Campbell, A. R. (1993). Rhenium behaviour in molybdenite in hypogene and near-surface environments: implications for Re–Os geochronometry. *Geochim. Cosmochim. Acta* **57**, 889–905.

Meisel, T., Walker, R. J., Irving, A. J. and Lorand, J.-P. (2001). Osmium isotopic compositions of mantle xenoliths: a global perspective. *Geochim. Cosmochim. Acta* **65**, 1311–23.

Meisel, T., Walker, R. J. and Morgan, J. W. (1996). The osmium isotopic composition of the Earth's primitive upper mantle. *Nature* **383**, 517–20.

Morgan, J. W. (1985). Osmium isotope constraints on Earth's accretionary history. *Nature* **317**, 703–5.

Morgan, J. W., Walker, R. J. and Grossman, J. N. (1992). Rhenium–osmium isotope systematics in meteorites I: magmatic iron meteorite groups IIAB and IIIAB. *Earth Planet. Sci. Lett.* **108**, 191–202.

Morgan, J. W., Walker, R. J., Horan, M. F., Beary, E. S. and Naldrett, A. J. (2002). ^{190}Pt–^{186}Os and ^{187}Re–^{187}Os systematics of the Sudbury Igneous Complex, Ontario. *Geochim. Cosmochim. Acta* **66**, 273–90.

Naldrett, A. J. (1989). *Magmatic Sulphide Deposits.* Oxford University Press, 186 pp.

Naldrett, A. J., Rao, B. V. and Evensen, N. M. (1986). Contamination at Sudbury and its role in ore formation, In: Gallagher, M. J., Ixer, R. A., Neary, C. R. and Pritchard, H. M. (Eds.), *Metallogeny of Basic and Ultrabasic Rocks.* Special Publication of the Institute Mining & Metallurgy, pp. 75–92.

Naldrett, S. N. (1984). Half-life of rhenium: geologic and cosmologic ages. *Can. J. Phys.* **62**, 15–20.

Olive, V., Ellam, R. M. and Harte, B. (1997). A Re–Os isotope study of ultramafic xenoliths from the Matsoku kimberlite. *Earth Planet. Sci. Lett.* **150**, 129–40.

Oxburgh, R. (1998). Variations in the osmium isotope composition of sea water over the past 200,000 years. *Earth Planet. Sci. Lett.* **159**, 183–91.

Oxburgh, R. (2001). Residence time of osmium in the oceans. *Geochem. Geophys. Geosys.* **2**, 2000GC000104.

Pearson, D. G., Shirey, S. B., Carlson, R. W., Boyd, F. R., Pokhilenko, N. P. and Shimizu, N. (1995a). Re–Os, Sm–Nd, and Rb–Sr isotope evidence for thick Archean lithospheric mantle beneath the Siberian craton modified by multistage metasomatism. *Geochim. Cosmochim. Acta* **59**, 959–77.

Pearson, D. G., Snyder, G. A., Shirey, S. B., Taylor, L. A., Carlson, R. W. and Sobolev, N. V. (1995b). Archean Re–Os age for Siberian eclogites and constraints on Archean tectonics. *Nature* **374**, 711–13.

Pearson, N. J., Alard, O., Griffin, W. L., Jackson, S. E. and O'Reilly, S. Y. (2002). *In situ* measurement of Re–Os isotopes in mantle sulfides by laser ablation multicollector–inductively coupled plasma mass spectrometry: analytical methods and preliminary results. *Geochim. Cosmochim. Acta* **66**, 1037–50.

Pegram, W. J., Esser, B. K., Krishnaswami, S. and Turekian, K. K. (1994). The isotopic composition of leachable osmium from river sediments. *Earth Planet. Sci. Lett.* **128**, 591–9.

Pegram, W. J., Krishnaswami, S., Ravizza, G. E. and Turekian, K. K. (1992). The record of seawater ^{187}Os/^{186}Os variation through the Cenozoic. *Earth Planet. Sci. Lett.* **113**, 569–76.

Pegram, W. J. and Turekian, K. K. (1999). The osmium isotopic composition change of Cenozoic sea water as inferred from deep-sea core corrected for meteoritic contributions. *Geochim. Cosmochim. Acta* **63**, 4053–8.

Peslier, A. H., Reisberg, L., Ludden, J. and Francis, D. (2000). Re–Os constraints on harzburgite and lherzolite formation in the lithospheric mantle: a study of Northern Canadian Cordillera xenoliths. *Geochim. Cosmochim. Acta* **64**, 3061–71.

Peucker-Ehrenbrink, B., Ravizza, G. and Hofmann, A. W. (1995). The marine ^{187}Os/^{186}Os record of the past 80 million years. *Earth Planet. Sci. Lett.* **130**, 155–67.

Puchtel, I. S., Brügmann, G. E. and Hofmann, A. W. (2001). ^{187}Os-enriched domain in an Archean mantle plume: evidence from 2.8 Ga komatiites of the Kostomuksha greenstone belt, NW Baltic Shield. *Earth Planet. Sci. Lett.* **186**, 513–26.

Ravizza, G. (1993). Variations of the ^{187}Os/^{186}Os ratio of seawater over the past 28 million years as inferred from metalliferous carbonates. *Earth Planet. Sci. Lett.* **118**, 335–48.

Ravizza, G. and Turekian, K. K. (1992). The osmium isotopic composition of organic-rich marine sediments. *Earth Planet. Sci. Lett.* **110**, 1–6.

Reisberg, L. C., Allègre, C. J. and Luck, J. M. (1991). The Re–Os systematics of the Ronda Ultramafic Complex of southern Spain. *Earth Planet. Sci. Lett.* **105**, 196–213.

Reisberg, L. and Lorand, J.-P. (1995). Longevity of sub-continental mantle lithosphere from osmium isotope systematics in orogenic peridotite massifs. *Nature* **376**, 159–62.

Reisberg, L. C., Zindler, A., Marcantonio, F., White, W., Wyman, D. and Weaver, B. (1993). Os isotope systematics in ocean island basalts. *Earth Planet. Sci. Lett.* **120**, 149–67.

Righter, K. and Hauri, E. H. (1998). Compatibility of rhenium in garnet during mantle melting and magma genesis. *Science* **280**, 1737–41.

Roy-Barman, M. and Allègre, C. J. (1994). ^{187}Os/^{186}Os ratios of mid-ocean ridge basalts and abyssal peridotites. *Geochim. Cosmochim. Acta* **58**, 5043–54.

Roy-Barman, M., Luck, J.-M. and Allègre, C. J. (1996). Os isotopes in orogenic lherzolite massifs and mantle heterogeneities. *Chem. Geol.* **130**, 55–64.

Russ, G. P., Bazan, J. M. and Date, A. R. (1987). Osmium isotopic ratio measurements by inductively coupled plasma source mass spectrometry. *Anal. Chem.* **59**, 984–9.

Schiano, P., Birck, J.-L. and Allègre, C. J. (1997). Osmium–strontium–neodymium–lead isotopic covariations in mid-ocean ridge basalt glasses and the heterogeneity of the upper mantle. *Earth Planet. Sci. Lett.* **150**, 363–79.

Schoenberg, R., Kruger, F. J., Nägler, T. F., Meisel, T. and Kramers, J. D. (1999). PGE enrichment in chromite layers in the Merensky Reef of the western Bushveld Complex; a Re–Os and Rb–Sr isotope study. *Earth Planet. Sci. Lett.* **172**, 49–64.

Selby, D., Creaser, R. A., Hart, C. J. R. *et al.* (2002). Absolute timing of sulfide and gold mineralization: a comparison of Re–Os molybdenite and Ar–Ar mica methods from the Tintina Gold Belt, Alaska. *Geology* **30**, 791–4.

Sharma, M., Papanastassiou, D. A. and Wasserburg, G. J. (1997). The concentration and isotopic composition of osmium in the oceans. *Geochim. Cosmochim. Acta* **61**, 3287–99.

Sharma, M. and Wasserburg, G. J. (1997). Osmium in the rivers. *Geochim. Cosmochim. Acta* **61**, 5411–16.

Sharma, M., Wasserburg, G. J., Hofmann, A. W. and Butterfield, D. A. (2000). Osmium isotopes in hydrothermal fluids from the Juan de Fuca Ridge. *Earth Planet. Sci. Lett.* **179**, 139–52.

Sharpe, M. R. (1985). Strontium isotope evidence for preserved density stratification in the main zone of the Bushveld Complex, South Africa. *Nature* **316**, 119–26.

Shen, J. J., Papanastassiou, D. A. and Wasserburg, G. J. (1996). Precise Re–Os determinations and systematics of iron meteorites. *Geochim. Cosmochim. Acta* **60**, 2887–900.

Shirey, S. B. and Walker, R. J. (1995). Carius tube digestion for low-blank Re–Os analyses. *Anal. Chem.* **67**, 2136–41.

Skovgaard, A. C., Storey, M., Baker, J., Blusztajn, J. and Hart, S. (2001). Osmium–oxygen isotopic evidence for a recycled and strongly depleted component in the Iceland mantle plume. *Earth Planet Sci. Lett.* **194**, 259–75.

Smoliar, M. I., Walker, R. J. and Morgan, J. W. (1996). Re–Os ages of group IIA, IIIA, IVA, and IVB iron meteorites. *Science*, **271**, 1099–102.

Sun, W., Bennett, V. C., Eggins, S. M., Kamenetsky, V. S., and Arculus, R. J. (2003). Enhanced mantle-to-crust rhenium transfer in undegassed arc magmas. *Nature* **422**, 294–7.

Suzuki, K., Lu, Q., Shimizu, H. and Masuda, A. (1993). Reliable Re–Os age for molybdenite. *Geochim. Cosmochim. Acta* **57**, 1625–8.

Volkening, J., Walczyk, T. and Heumann, K. G. (1991). Osmium isotope ratio determinations by negative thermal ionization mass spectrometry. *Int. J. Mass Spectrom. Ion Proc.* **105**, 147–59.

Walczyk, T., Hebeda, E. H. and Heumann, K. G. (1991). Osmium isotope ratio measurements by negative thermal ionization mass spectrometry (NTI–MS). *Fres. J. Anal. Chem.* **341**, 537–41.

Walker, D. (2000). Core participation in mantle geochemistry: Geochemical Society Ingerson Lecture, GSA Denver, October 1999. *Geochim. Cosmochim. Acta* **64**, 2897–911.

Walker, R. J., Carlson, R. W., Shirey, S. B. and Boyd, F. R. (1989a). Os, Sr, Nd, and Pb isotope systematics of southern African peridotite xenoliths: implications for the chemical evolution of subcontinental mantle. *Geochim. Cosmochim. Acta* **53**, 1583–95.

Walker, R. J. and Fassett, J. D. (1986). Isotopic measurement of sub-nanogram quantities of rhenium and osmium by resonance ionization mass spectrometry. *Anal. Chem.* **58**, 2923–7.

Walker, R. J., Horan, M. F., Morgan, J. W., Becker, H., Grossman, J. N. and Rubin, A. E. (2002). Comparative ^{187}Re–^{187}Os systematics of chondrites: implications regarding early solar system processes. *Geochim. Cosmochim. Acta* **66**, 4187–201.

Walker, R. J. and Morgan, J. W. (1989). Rhenium–osmium isotope systematics of carbonaceous chondrites. *Science* **243**, 519–22.

Walker, R. J., Morgan, J. W., Beary, E. S., Smoliar, M. I., Gzamanske, G. K. and Horan, M. F. (1997). Applications of the ^{190}Pt–^{186}Os isotope system to geochemistry and cosmochemistry. *Geochim. Cosmochim. Acta* **61**, 4799–807.

Walker, R. J., Morgan, J. W. and Horan, M. F. (1995). Osmium-187 enrichment in some plumes: evidence for core–mantle interaction? *Science* **269**, 819–22.

Walker, R. J., Morgan, J. W., Naldrett, A. J., Li, C. and Fassett, J. D. (1991). Re–Os isotopie systematics of Ni–Cu sulfide ores, Sudbury Igneous Complex, Ontario: evidence for a major crustal component. *Earth Planet. Sci. Lett.* **105**, 416–29.

Walker, R. J., Shirey, S. B., Hanson, G. N., Rajamani, V. and Horan, M. F. (1989b). Re–Os, Rb–Sr, and O isotopic systematics of the Archean Kolar schist belt, Karnataka, India. *Geochim. Cosmochim. Acta* **53**, 3005–13.

Widom, E. and Shirey, S. B. (1996). Os isotope systematics in the Azores: implications for mantle plume sources. *Earth Planet. Sci. Lett.* **142**, 451–65.

Woodhouse, O. B., Ravizza, G., Falkner, K. K., Statham, P. J. and Peucker-Ehrenbrink, B. (1999). Osmium in seawater: vertical profiles of concentration and isotopic composition in the eastern Pacific ocean. *Earth Planet. Sci. Lett.* **173**, 223–33.

9 Lu–Hf and other lithophile isotope systems

Lutetium lies at the end of the lanthanide series as the 'heaviest' of the REE. It has two isotopes, ^{175}Lu and ^{176}Lu, whose respective abundances are 97.4% and 2.6%. ^{176}Lu, displays a branched isobaric decay, by β^- emission to ^{176}Hf and by electron capture to ^{176}Yb. However, the latter makes up only a few per cent at most of the total activity and can be more or less ignored (Dixon *et al.*, 1954). ^{176}Hf is left in an excited state after β emission, and decays to the ground state by γ emission. It is one of six isotopes and makes up 5.2% of total hafnium, an element which is not a rare earth but resembles Zr very closely in its crystal chemical behaviour.

9.1 Lu–Hf geochronology

The decay scheme

$$^{176}_{71}\mathrm{Lu} \rightarrow {}^{176}_{72}\mathrm{Hf} + \beta^- + \nu + Q$$

yields a decay equation

$$^{176}\mathrm{Hf} = {}^{176}\mathrm{Hf}_\mathrm{I} + {}^{176}\mathrm{Lu}(e^{\lambda t} - 1) \qquad [9.1]$$

This is conveniently divided through by ^{177}Hf:

$$\frac{^{176}\mathrm{Hf}}{^{177}\mathrm{Hf}} = \left(\frac{^{176}\mathrm{Hf}}{^{177}\mathrm{Hf}}\right)_\mathrm{I} + \frac{^{176}\mathrm{Lu}}{^{177}\mathrm{Hf}}(e^{\lambda t} - 1) \qquad [9.2]$$

The first Lu–Hf geochronological measurement was made by Herr *et al.* (1958), who attempted to determine the half-life of ^{176}Lu by analysing the isotopic composition of Hf in the heavy-REE-rich mineral gadolinite (containing several thousand ppm Lu). However, routine Hf isotope analysis was prevented until 1980 by the difficulties of low-blank chemical separation and by the poor ionisation efficiency of Hf during thermal-ionisation mass spectrometry (TIMS). These problems were finally overcome by Patchett and Tatsumoto (1980a), using a modified form of triple-filament analysis with a very hot centre filament (section 2.2.1). After this breakthrough, TIMS analysis of Hf continued to be limited by poor ionisation efficiency, although improvements were achieved by various methods. For example, one technique involved bombarding the heated sample with an ion beam during TIMS analysis, hence 'hot SIMS' (Salters and Zindler, 1995). However, TIMS analysis of Hf has now been superseded by MC-ICP-MS (section 2.5.2).

9.1.1 The Lu decay constant and the CHUR composition

Patchett and Tatsumoto (1980b) presented the first Lu–Hf isochron, using data from a suite of eucrite meteorites (achondrites). These have an estimated age of about 4.55 Byr, from which Patchett and Tatsumoto were able to make a geological determination of the ^{176}Lu decay constant. Their original ten-point whole-rock isochron was improved by the addition of three extra points (Tatsumoto *et al.*, 1981) to yield a half-life of 35.7 ± 1.2 Byr (equivalent to a decay constant of 1.94×10^{-11} yr^{-1}) and an initial ^{176}Hf/^{177}Hf ratio of 0.27978 ± 9 (2σ), Fig. 9.1. This half-life compared very well with the value of 35.4 ± 1.1 Byr which Patchett and Tatsumoto (1980b) calculated as a weighted mean of five physical half-life determinations made since 1960 (Faure, 1977). However, it should be noted that the good isochron fit obtained from achondrites was achieved by rejecting one sample, the Antarctic meteorite ALHA.

More recent physical determinations yield significantly higher values of the half-life, averaging 37.3 ± 0.1 Byr (Nir-El and Lavi, 1998), equivalent to a decay constant of $1.86 \pm 0.005 \times 10^{-11}$ yr^{-1}. This value has been supported by geological half-life determinations based on four Proterozoic rock samples (Scherer *et al.*, 2001). Three of these samples comprised pegmatites, whereas the fourth was a monazite–xenotime gneiss from Grenville-age rocks of the Hudson Highlands, New York State. All four samples were dated by U–Pb, yielding an overall value for the ^{176} Lu decay constant of 1.867×10^{-11} yr^{-1}($t_{1/2} = 37.1$ Byr) which is in excellent agreement with the value of 1.86×10^{-11} yr^{-1} determined by counting experiments.

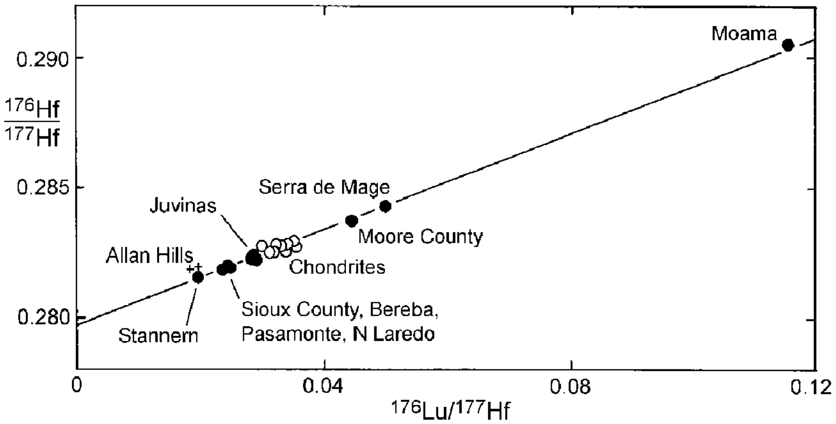

Fig. 9.1. Lu–Hf isochron for eucrite meteorites. Allan Hills samples (+) were omitted from the regression; (○) = chondrites analysed in later work. Modified after Blichert-Toft and Albarède (1997).

Pettingill and Patchett (1981) attempted to test their Lu decay constant in a dating study on the Amitsoq gneisses of west Greenland. Despite metamorphic events that occurred 2.9 and 1.7 Byr ago, zircon separates and whole-rock gneiss samples formed a coherent array on a Lu–Hf isochron diagram. However, the relatively large scatter on the isochron prevented its use as a critical test of the decay constant. The regression gave a somewhat low age of 3.58 ± 0.22 Byr (2σ) using the ^{176}Lu decay constant of 1.94×10^{-11} yr^{-1}, but this is increased to 3.70 Byr using the new decay constant of 1.867×10^{-11} yr^{-1} (Fig. 9.2).

Similarly low Lu–Hf isochron ages were also obtained in a more recent dating study on the Isua supracrustals of western Greenland, and on Early Proterozoic (Birimian) metamorphic rocks of western Africa (Blichert-Toft *et al.*, 1999). In this case the relatively large discrepancy between Lu–Hf and Sm–Nd ages was attributed to open-system behaviour of the Lu–Hf system. However, the Lu–Hf and Sm–Nd ages in this study can be reconciled using the new decay constant (Villa *et al.*, 2001).

The low Hf abundances in chondrites, coupled with the poor efficiency of Hf analysis by TIMS, prevented a direct determination of their Hf isotope composition until recently. Therefore, Patchett and Tatsumoto (1981) determined the composition of the chondritic uniform reservoir (CHUR) from the intersection of the eucrite meteorite isochron and the ^{176}Lu/^{177}Hf ratio of 0.0334 derived from the carbonaceous chondrites Murchison and Allende. This gave a present-day chondritic ^{176}Hf/^{177}Hf ratio of 0.28286.

Direct analysis of chondritic Hf was finally made possible by MC-ICP-MS (Blichert-Toft and Albarède, 1997). This work yielded a cluster of data points very close to the eucrite isochron of Patchett and Tatsumoto, but the average present-day CHUR value was lowered slightly to 0.28277 ± 3. Both values compare quite well with the Bulk Earth Hf isotope ratio determined from the intersection of chondritic ^{143}Nd/^{144}Nd with the Nd–Hf isotope array defined by OIB. However, the new value does not fit quite as well as the old one.

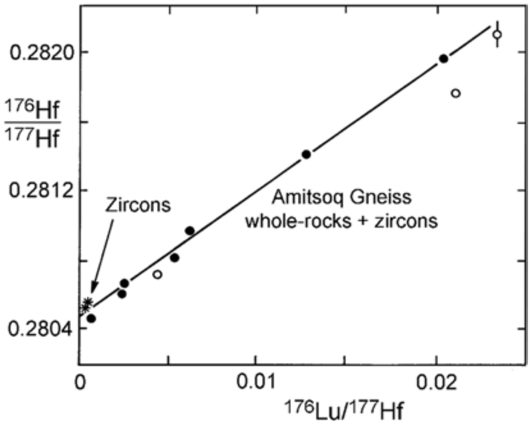

Fig. 9.2. Lu–Hf errorchron for a suite of whole-rock Amitsoq gneisses and separated zircons. Open symbols were omitted from the regression. After Pettingill and Patchett (1981).

Hf isotope ratios can be expressed using the ε notation developed for Nd (parts per 10 000 deviation from the chondritic evolution line). Unfortunately, changes in the Lu decay constant also have a major impact on the calculation of ε Hf values because they change the slope of the chondritic growth line. As a result, the new decay constant described above gives rise to a CHUR evolution line that is approximately three epsilon units higher than the old value. This has major ramifications for the use of Hf initial ratios as a tracer of crust and mantle evolution, as discussed in more detail in section 9.2.

Following the studies described above, additional work was done on the Lu–Hf systematics of meteorites, with somewhat perplexing results. The first of these studies, by Blichert-Toft *et al.* (2002), re-examined the suite of eucrites analysed by Patchett and Tatsumoto. The second study focussed on ordinary chondrites and carbonaceous chondrites, with a few eucrite analyses for comparison (Bizzarro *et al.*, 2003).

Blichert-Toft *et al.* analysed a suite of twenty-one whole-rock eucrites, including most of the samples in Fig. 9.1. This suite actually comprises two different petrological types, the cumulate eucrites (with Lu/Hf ratios greater than chondrites) and the basaltic eucrites, also called basaltic achondrites (with lower Lu/Hf ratios, similar to those of chondrites). Basaltic achondrites have been dated successfully by Sm–Nd mineral isochrons (section 4.1.1), but Sm–Nd analysis of the cumulate eucrites shows evidence of major disturbance, especially for Moama, the high-Lu/Hf-ratio sample that controls the eucrite Lu–Hf isochron in Fig. 9.1. On the other hand, if the Lu–Hf data set is restricted to basaltic eucrites (achondrites), the spread in Lu/Hf ratios is not sufficient to obtain a precise regression.

After rejecting Moama and two other samples from a composite Sm–Nd data set of cumulus and basaltic eucrites, Blichert-Toft *et al.* obtained an age of 4464 ± 75 Myr. Using the old ^{176}Lu decay constant of 1.94×10^{-11} yr^{-1} then gave a similar age of 4470 ± 22 Myr for the three most radiogenic eucrites in Fig. 9.1 (Moama, Moore County and Serra de Mage). However, this agreement was obtained only by selecting different samples for the two isochrons, and is not therefore very meaningful.

Alternatively, the basaltic eucrite suite alone yields a Lu–Hf 'errorchron age' of 4604 ± 39 Myr (MSWD $= 4.52$) using the old decay constant, which is within error of the latest estimate of 4565 Myr ago for the time of differentiation of the eucrite parent body (section 15.5.2). On this basis, Blichert-Toft *et al.* argued that their data supported the old decay constant. However, if analytical errors on the basaltic eucrite errorchron are expanded to equal the geological scatter (MSWD $= 1$), the errorchron then provides a relatively weak constraint on the decay constant. For example, an age of about 4.75 ± 0.18 Byr would be obtained using the new ^{176}Lu decay constant, which is just within error of the earliest solar-system ages of 4.57 Byr. On this basis, the eucrite data cannot definitely exclude the new decay constant.

Apparently stronger evidence against the new decay constant was obtained from the study of Bizzarro *et al.* (2003) on chondrites. For example, a composite suite of ordinary chondrites, carbonaceous chondrites and a few eucrites gave an isochron fit with a reported MSWD of 1.04. Assuming an age of 4.56 Byr for the chondrite-forming event, the isochron implied a high ^{176}Lu decay constant of 1.98×10^{-11} yr^{-1}, equivalent to a half-life of 35.0 Byr. In addition, the steeper slope on the isochron gave a less radiogenic chondritic initial ratio of 0.27963 ± 2. Combining this value with the high decay constant leads to a CHUR evolution line about three epsilon units *lower* than Patchett's original value (in contrast to the new 'terrestrial' value that is three epsilon units higher).

The discrepancy between the new 'terrestrial' and 'meteorite' decay constants obviously introduces a lot of uncertainty into the interpretation of hafnium isotope data, both in terms of dating and in terms of crust–mantle evolution models. Faced with this dilemma, the present author believes that the terrestrial value is to be preferred, because it causes fewer problems for several dating studies on terrestrial rock suites. It is also supported by the new study of Söderlund *et al.* (2004). However, until the meteorite initial ratio is clarified, the interpretation of Hf isotope data must be regarded as provisional. Hence the CHUR line used in the rest of this chapter will largely follow the old value of Patchett and Tatsumoto (1981).

9.1.2 Dating metamorphism

The high Lu/Hf ratios found in garnets make these minerals useful for Lu–Hf dating of metamorphic events in a manner analogous to Sm–Nd. In particular, the spread of Lu/Hf ratios measured in metamorphic garnets is typically greater than for the Sm/Nd ratio. When coupled with the lower half-life of Lu, this allows more precise dating of young (Cenozoic) metamorphic events. Applications have included the dating of garnet granulite lower-crustal xenoliths (Scherer *et al.*, 1997) and the dating of high-pressure metamorphism in the Alps (Duchêne *et al.*, 1997).

Scherer *et al.* (2000) performed a detailed study of the application of Lu–Hf garnet geochronology, including the effects of Hf-rich accessory minerals and an estimation of the blocking temperature of the Lu–Hf system in garnet. Of the major accessory minerals apatite, monazite and zircon, only the last contains high

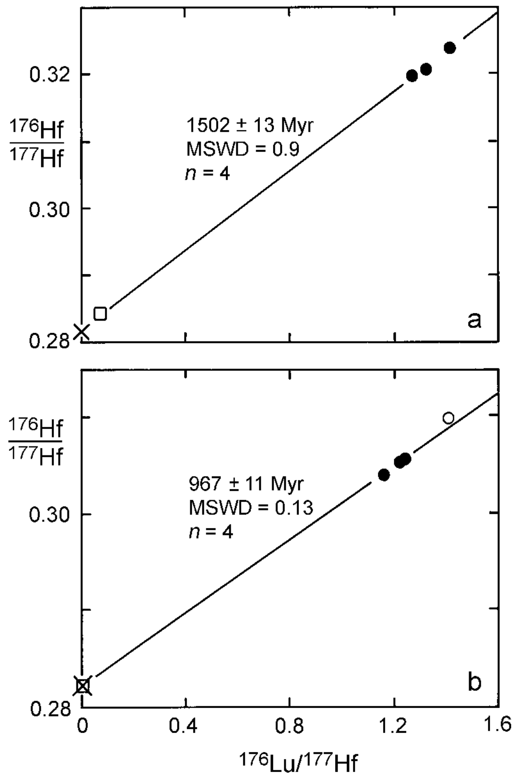

Fig. 9.3. The effects of zircon on Lu–Hf ages of metamorphic garnet growth: (a) involving groundmass zircons only; and (b) involving zircon inclusions in garnet grains: (●) = garnet; (○) = leached garnet; (□) = whole-rock; (×) = zircon. After Scherer *et al.* (2000).

levels of Hf, whereas monazite contains high levels of Nd. This means that comparison of Lu–Hf and Sm–Nd ages can be used to test for the perturbation of garnet–whole-rock isochrons by these minerals. This is important because zircon may contain as much as 95% of the total Hf inventory of a rock, so any discordance between zircon and garnet will have a large effect on the Lu–Hf age. Such discordance is quite likely when we are trying to date the growth of metamorphic garnet, because the rock will probably contain pre-metamorphic zircon grains which do not equilibrate with garnet under peak metamorphic conditions.

Two alternative scenarios involving discordant zircon are shown in Fig. 9.3. The first rock (Fig. 9.3a) has zircon grains in the groundmass, but not in the garnet. Comparison between zircon and whole-rock compositions shows that the zircon grains bias the whole-rock point to give an apparent isochron age that is slightly too old. In the other case (Fig. 9.3b) there are zircon inclusions in the garnet as well as zircon grains in the groundmass. In this case, comparison of leached and unleached garnets shows that the apparent age will be too young. To avoid these problems, Scherer *et al.* recommended that inclusion-free garnets should be selected by hand picking. In addition, the analysis of other zircon-free minerals such as hornblende or clinopyroxene can be used (instead of the whole-rock point) to avoid the effects of groundmass zircon.

Having applied such corrections, Scherer compared the resulting Lu–Hf ages with Sm–Nd ages on the same samples. Their published ages should also be corrected for the new decay constant. The result is that the Lu–Hf ages are either within error of or older than the Sm–Nd ages, so the blocking temperature of the Lu–Hf system in garnet appears to be greater than or equal to that of the Sm–Nd system. However, because metamorphic garnets have large variations in texture and chemistry, both isotope systems will have a fairly wide range of blocking temperatures.

9.2 Mantle Hf evolution

9.2.1 Hf zircon analysis

Patchett *et al.* (1981) investigated the usefulness of initial Hf isotope ratios as a tracer of mantle Hf through time, using crustal rocks with a clear mantle derivation. In order to calculate accurate initial $^{176}Hf/^{177}Hf$ ratios for many rock bodies without making numerous isochron determinations, Patchett *et al.* principally analysed zircon separates. These provided excellent material for Hf isotope analysis for several reasons:

(1) Hf forms an integral part of the zircon lattice, which is therefore very resistant to Hf mobility and contamination.
(2) The very high Hf concentrations in zircon (about 10 000 ppm) yield very low Lu/Hf ratios and consequently minute age corrections.
(3) There are large quantities of zircon separates previously prepared for U–Pb analysis, which yield accurate dates for the same material.
(4) Any metamorphic overprinting or zircon inherited from a previous crustal history are clearly revealed by the U–Pb data.

Initial $^{176}Hf/^{177}Hf$ ratios of presumed mantle-derived igneous rocks of various ages were plotted on a hafnium isotope evolution diagram by Patchett *et al.* (1981). All of the igneous rocks with a mantle-derived signature lay within error of, or above, the chondrite evolution line (Fig. 9.4). However, only one sample, a

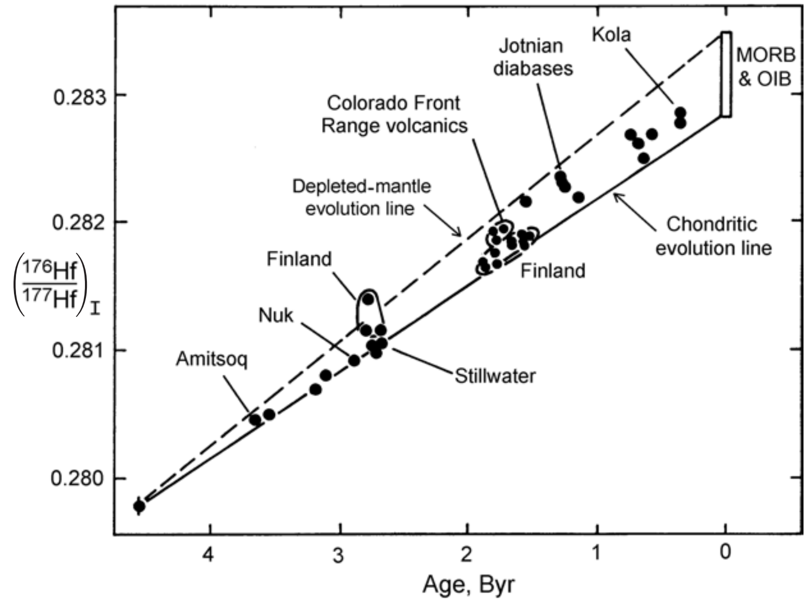

Fig. 9.4. Diagram of Hf isotope evolution over geological time. Initial ratios of uncontaminated mantle-derived magmas show them to be derived from a slightly depleted source relative to chondrites. Data from Patchett *et al.* (1981).

meta-tholeiite dyke cutting the Suomussalmi–Kuhmo greenstone belt in Finland, had an initial ^{176}Hf/^{177}Hf ratio above a linear depleted-mantle evolution line drawn from the primordial solar-system value to the most radiogenic MORB analysis (Fig. 9.4).

One explanation for the fan of Hf data in Fig. 9.4 is their derivation from a heterogeneous mantle exhibiting variable trace-element depletion of Hf relative to Lu through space and time. An alternative would be to derive magmas from a more depleted homogeneous source (such as defined by the dashed evolution line in Fig. 9.4) and subject them to contamination by older crustal basement. Patchett *et al.* (1981) preferred this model for the 1.4-Byr-old Silver Plume and 1.0-Byr-old Pikes Peak batholiths of Colorado, which have Nd *and* Hf initial ratios near the chondritic evolution line, and were argued to contain large fractions of 1.7-Byr-old crust by DePaolo (section 4.2.2). Two 1.8-Byr-old post-tectonic granites intruded into the Archean craton of north Finland had spectacularly low initial ratios, corresponding to ε Hf values of -10 and -12. These two samples are clearly of crustal derivation on the basis of Pb and Sr isotope data, and were selected to demonstrate the effects of crustal reworking on Hf isotope systematics.

It is important to remember that when this paper was published (in 1981), the only conclusive Nd isotope evidence for depleted mantle in the Proterozoic was provided by the work of DePaolo on the Front Ranges of Colorado (see section 4.2.2). Nd isotope evidence from komatiites for Archean depleted mantle (section 4.4.3) was not yet available. Hence the major significance of this paper at the time.

9.2.2 Archean sediments

Because Hf involves greater analytical difficulties than Nd, the latter has been the primary tool for studying continental growth through geological time (section 4.4). However, the resistance of zircon to weathering and to metamorphic re-setting means that Hf isotope analysis of this mineral provides a good test for Nd isotope data in studies of the Earth's early evolution, involving both ancient sediments and mantle-derived igneous rocks. These data have then been used to constrain models of crustal growth or recycling in the early Archean (section 4.4.2).

Stevenson and Patchett (1990) performed the first Lu–Hf study on Archean and Proterozoic sedimentary zircons from the Canadian, Wyoming, North Atlantic and South African cratons. The samples were mainly from the Late Archean and Early Proterozoic, and are summarised on a diagram of Lu–Hf model age *versus* stratigraphic age (Fig. 9.5), using the old CHUR value.

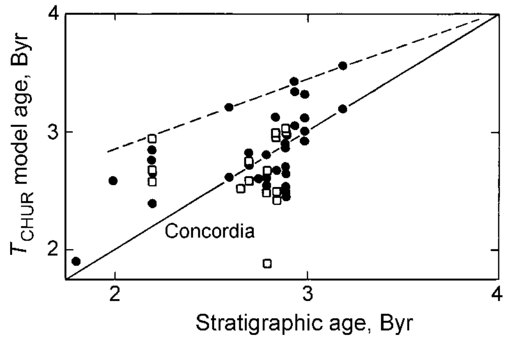

Fig. 9.5. Model age *versus* stratigraphic age diagram for sedimentary zircons to constrain crustal-growth models for the Archean: (●) = Hf data; (□) = Nd data. The dashed line accents the upper envelope of the data. After Stevenson and Patchett (1990).

A significant number of samples gave model ages in excess of stratigraphic age (i.e. above the 'concordia' line). The excess of model age over stratigraphic age was less in older sediments, leading Stevenson and Patchett to argue that there were 'no great quantities of continental crust in the early Earth providing ancient zircons . . . '. However, a significant number of points lie below the concordia line in Fig. 9.5, indicating that the chondritic mantle model is an under-estimate of the provenance ages of these samples.

The use of a depleted-mantle model implies provenance ages about 200 Myr older than those obtained with the CHUR model, suggesting a significant volume of Early Archean crust. Nevertheless, there is no evidence for a 'big-bang' model in which the volume of Early Archean crust was as great as that at the present day. Consequently, the data provide some support for a model involving progressive crustal growth with time, but are nevertheless ambiguous.

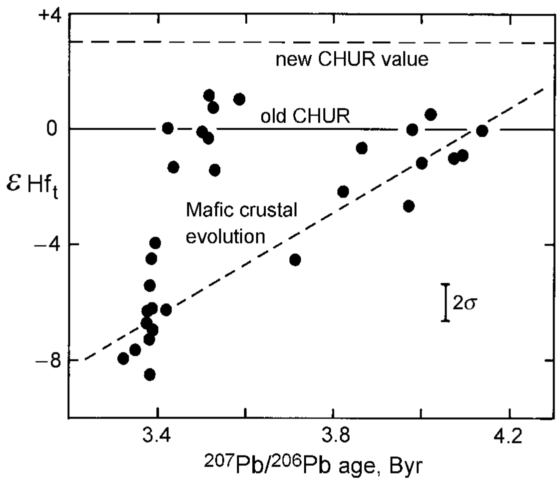

Fig. 9.6. Plot of ε Hf against 207/206 lead ages for 37 detrital zircon grains from the Jack Hills meta-conglomerate of the Narryer gneiss complex of western Australia. Error bar indicates average precision. Modified after Amelin *et al.* (1999).

Amelin *et al.* (1999) extended the study of Hf in detrital zircons to the early Archean. This was based on zircons from the Jack Hills meta-conglomerate in western Australia, which have yielded U–Pb ages as old as 4.28 Byr. The greater sensitivity of MC-ICP-MS (section 2.5.2) allowed the Hf analysis of single grains rather than bulk zircon separates, and therefore permitted a better understanding of this detrital zircon population with variable U–Pb ages. Results for thirty-seven individual grains fell into three groups on a plot of ε Hf against lead 207/206 age (Fig. 9.6). However, two of the groups lay on an isotopic growth line (dashed) with a ^{176}Lu/^{177}Hf ratio (0.022) typical of mafic rocks. This implies that the zircon grains in these two groups (whose elemental chemistry is indicative of felsic magmas) might be derived from granitoid rocks of various Early Archean ages, derived by melting of mafic crustal rocks.

Back projection of the Hf isotope crustal-growth line to an intersection with the chondritic evolution line allowed the age of formation of this mafic crustal terrane to be estimated. The result obtained using the conventional chondritic evolution line suggested a crustal formation age of about 4.1 Byr for this terrane. However, the new low decay constant would imply a chondritic evolution line about three epsilon units higher, and therefore a crustal formation age of about 4.4 Byr (Amelin *et al.*, 2000). This implies that at least some crustal fragments were in existence almost immediately after the last giant impact event led to the formation of the Moon (section 15.5.4). On the other hand, the new high decay constant implies a chondritic line two or three epsilon units lower than the old value. This would imply that mantle depletion was occurring very early in the Earth's history.

9.2.3 Western Greenland

Another important application of Hf isotope data was to test Nd evidence for early crustal evolution in western Greenland. Nd isotope analysis of Amitsoq gneisses by Bennett *et al.* (section 4.4.4) had previously implied a large range of ε Nd values, based on initial ratios calculated at the U–Pb ages of the rocks. This included some strongly positive ε values,

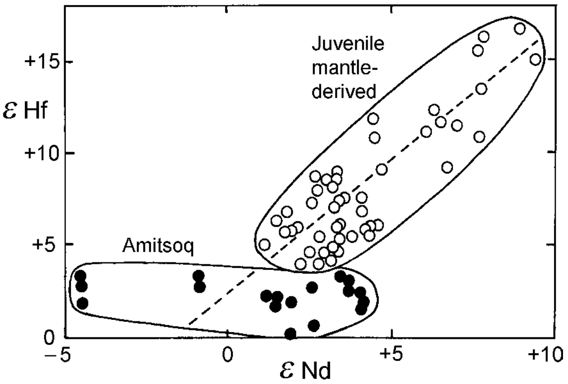

Fig. 9.7. Plot of initial ε Hf against ε Nd (using values of *t* from U–Pb ages) for Amitsoq gneisses (●) compared with a variety of juvenile samples less than 3.5 Byr old (○). After Vervoort and Blichert-Toft (1999).

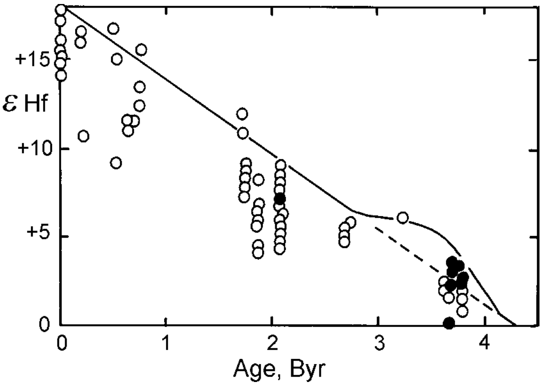

Fig. 9.8. Hf isotope evolution plot showing initial ratios of juvenile mantle-derived rocks. Samples with low Lu/Hf ratios are shown by solid symbols. After Vervoort and Blichert-Toft (1999).

suggesting strong mantle depletion in the Early Archean. To test these results, Vervoort *et al.* (1996) analysed zircon separates from a selection of the samples analysed by Bennett *et al.* However, the ε Hf values fell in a narrower range than ε Nd, suggesting to Vervoort *et al.* that whole-rock Sm–Nd systems in some of these rocks had probably been disturbed.

In a continuation of this study, Vervoort and Blichert-Toft (1999) analysed Hf both in whole-rock samples and in additional zircon separates. The results bore out the earlier work, showing that whole-rock Hf–Nd isotope systematics in the West Greenland samples depart from the mantle array defined by juvenile samples younger than 3.5 Byr (Fig. 9.7). Hence, the whole-rock Hf isotope data support the earlier data on zircon separates in implying that the Nd isotope system was somewhat disturbed. It should also be noted at this point that these conclusions apply to samples from the heavily reworked southern area of the Itsaq gneiss terrane (as it is now called), as well as the less reworked northern area (see section 4.4.4).

When initial Hf isotope ratios are plotted against U–Pb ages, the resulting Hf isotope evolution plot shows essentially linear depletion with time, supporting the model of progressive continental growth through time (Fig. 9.8). An exception to this linear evolution trend is exhibited by some zircon data from the Amitsoq gneisses, with ^{176}Lu/^{177}Hf values less than 0.1, which are shown by solid symbols. However, these samples are the most susceptible to perturbation by any errors in the decay constant, because their evolution lines depart most strongly from the chondritic evolution curve. In view of the uncertainties in the decay constant, these samples should be given less significance in interpreting the depleted-mantle composition against time, suggesting that this is essentially a linear evolution trend.

Despite the results previously obtained, Blichert-Toft *et al.* (1999) reversed their earlier position on gradual Hf mantle depletion in the Early Archean as a result of new Hf isotope analysis on the Isua supracrustal sequence of western Greenland. As described in section 9.1, this sample suite, and one from western Africa, gave apparent Lu–Hf isochron ages consistently lower than Sm–Nd isochron ages on the same whole-rock samples. This led Blichert-Toft *et al.* (1999) to invoke mobility of Hf in these samples, whose effects they tried to 'see through' by a fairly complex modelling procedure. The result of this modelling was to create strongly positive ε Hf and ε Nd values, implying strong mantle depletion. However, in a scientific comment on this paper, Villa *et al.* (2001) pointed out that the use of the new Lu decay constant causes the Sm–Nd and Lu–Hf isochron ages to agree within error, avoiding the necessity for wholesale Hf isotope re-setting in these rocks. In the meantime, however, Albarède *et al.* came up with a different explanation of the Hf data. This was based on the Lu/Hf *versus* Sm/Nd diagram, which has been used quite widely in Hf isotope studies.

Firstly, Albarède *et al.* plotted measured ratios of Lu/Hf against Sm/Nd for Early Archean rocks of western Greenland, and compared them with these ratios in modern volcanic rocks (Fig. 9.9). They showed that a moderate number of Amitsoq gneisses and Isua metavolcanic rocks lay along the array of modern volcanic rocks, whereas samples of the Garbenschiefer unit of the Isua sequence lay well off the array. They

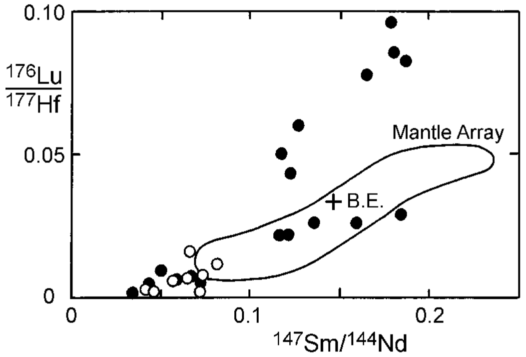

Fig. 9.9. Plot of measured concentration ratios of Lu/Hf and Sm/Nd for Amitsoq gneisses (○) and Isua metavolcanics (●), compared with a 'mantle array' of modern volcanic rocks. After Albarède *et al.* (2000).

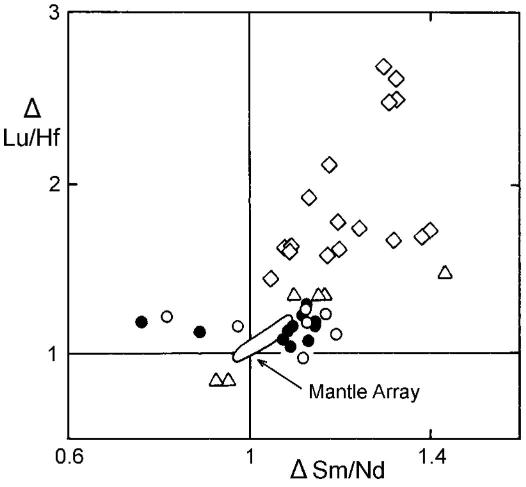

Fig. 9.10. Plot of model (time-integrated) Lu/Hf versus Sm/Nd (Δ) necessary to generate calculated initial Hf and Nd isotope ratios of igneous rocks at the time of their crystallisation. The ratios are chondrite-normalised using the new Hf decay constant: (◇) = Moon; (△) = Mars; (●) = Isua; (○) = Amitsoq. After Albarède *et al.* (2000).

interpreted this to mean that the latter unit (which is REE-depleted) has disturbed Lu–Hf and Sm–Nd systems, whereas the samples that plot within the modern array are undisturbed.

Having thus 'screened' the Early Archean samples for disturbance, Albarède *et al.* then plotted the 'successful' samples on a graph of time-integrated Lu/Hf *versus* Sm/Nd ratios (Fig. 9.10). The significance of the plotted ratios of Lu/Hf and Sm/Nd is that these are *model* values necessary to generate the initial isotope ratios of the samples (at the time of igneous crystallisation given by their U–Pb age) by isotopic evolution in a closed system starting from a chondritic composition 4.56 Byr ago. In essence, this is equivalent to plotting ε Hf against ε Nd. When the Early Archean samples from western Greenland are compared with modern oceanic volcanics, lunar samples, and Martian (SNC) meteorites, it appears that the Greenland rocks exhibit similar variations to other solar system bodies (the Moon and Mars) that were characterised by very heterogeneous isotope signatures in their early history. Hence, Albarède *et al.* inferred that the Greenland magmas were sampling a heterogeneous terrestrial mantle.

Because the argument put forward by Albarède *et al.* is quite complex, it is difficult to evaluate. However, there are a couple of hidden assumptions. The first is that collinearity with modern volcanics in Fig. 9.9 implies a lack of disturbance. This need not be true if the manner of disturbance of the gneisses was isotopic homogenisation between different types of rock, as was suggested by Moorbath *et al.* (section 4.4.4).

The second assumption is that the spread of time-integrated Lu/Hf and Sm/Nd ratios in the Greenland rocks is similar to those of the other solar-system bodies, and may therefore have originated in the same way. However, an examination of Fig. 9.10 shows that some of the Greenland rocks (in the top-left quadrant) have much lower time-integrated Sm/Nd ratios than lunar or Martian samples. These compositions represent sources that are very enriched relative to the chondritic evolution line (i.e. ε Nd values well below the chondritic line). It is much more likely that these are disturbed crustal signatures rather than enriched-mantle reservoirs. However, if we admit that these disturbed crustal rocks could nevertheless lie on the modern volcanic array in Fig. 9.9 then samples in the top-right quadrant of Fig. 9.10 could likewise be disturbed. Hence, the present author agrees with Kramers (2001) that the balance of evidence does not support the existence of strongly depleted sources in the Early Archean Earth.

9.2.4 Mantle depletion and recycling

Patchett and Tatsumoto (1980c) made the first Hf isotope measurements on selected MORB and OIB samples (that had previously been analysed for ^{143}Nd/^{144}Nd and ^{87}Sr/^{86}Sr). These data, augmented by Patchett (1983) show that the ^{176}Hf/^{177}Hf ratio very closely parallels the ^{143}Nd/^{144}Nd ratio in OIB (Fig. 9.11). However, MORB samples display a proportionally greater degree of spread in ^{176}Hf/^{177}Hf ratio

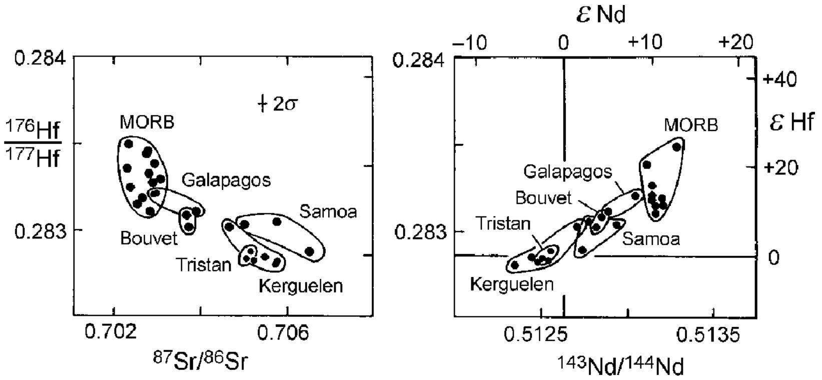

Fig. 9.11. Hf *versus* Sr and Nd isotope diagrams, showing early data for oceanic volcanics. OIB samples define a mantle array, but MORB samples exhibit some decoupling of Hf systematics from Sr and Nd. After Patchett (1983).

(60% of the total range for oceanic basalts) than they do in ^{143}Nd/^{144}Nd (only 30% of the total range). Hence the MORB arrays in Fig. 9.11 are nearly three times steeper than the OIB arrays. Patchett and Tatsumoto attributed these differences to stronger fractionation of Lu/Hf than of Sm/Nd and Sr/Rb in very trace-element-depleted source regions such as MORB, due to the greater incompatibility displayed by Hf relative to Lu than Nd/Sm or Rb/Sr.

Compared with their radiogenic Hf isotope signatures (indicative of a depleted source), many MORB samples are enriched in Hf/Lu (corresponding to a low Lu/Hf ratio). This phenomenon has also been observed for other incompatible-element systems such as Sm/Nd and U/Th, and is generally attributed to sequential extraction of very-small-degree melts (sections 6.2.2 and 13.3.1); however, it is more marked in the Lu–Hf system than the Sm–Nd system. Salters and Hart (1989) attributed this 'hafnium paradox' to residual garnet in the MORB source. Because Hf is not a true REE, its chemistry is not coherent with that of the heavy rare earths. This is illustrated by the mineral–magma partition coefficients shown in Fig. 9.12. Hence there is an opportunity for more extreme fractionation in Lu/Hf than in Sm/Nd ratio when low-degree melting occurs at depths greater than 80 km, within the garnet stability zone.

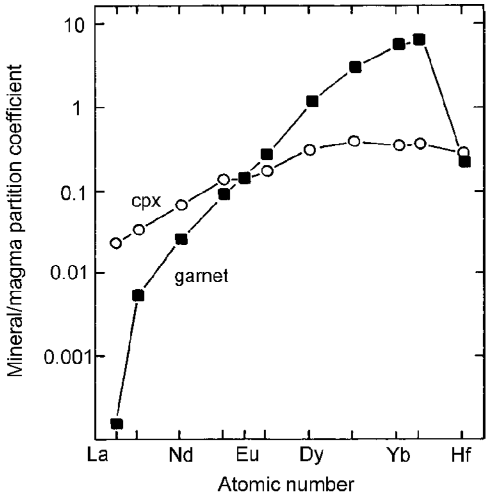

Fig. 9.12. Partition coefficients for REE and Hf between minerals (cpx, garnet) and kimberlite magma. After Fujimaki *et al.* (1984).

Gruau *et al.* (1990) analysed 3.5-Byr-old komatiites from the Onverwacht Group of South Africa to see whether Archean depleted mantle displayed extreme ranges of Lu/Hf depletion due to fractionation of garnet. They compared Al-depleted and Al-enriched komatiites, whose contrasting chemistries are attributed to fractionation of garnet in the mantle source. However, calculated initial Hf and Nd isotope ratios were indicative of similar degrees of mantle depletion (ε from 0 to +2) in both Al-enriched and Al-depleted types. Hence there is no evidence for widespread fractionation of garnet in the early Earth, such as might have resulted from a magma ocean. Consequently the major-element composition of the magma was attributed to fractionation of garnet in the source during the komatiite melting event itself, a conclusion supported by Blichert-Toft and Arndt (1999).

Although the concept of garnet fractionation from an ancient magma ocean has been rejected, Salters and Hart (1991) argued that variable garnet contents in ancient melting events could nevertheless explain the partial decoupling of Hf–Nd isotope systematics in MORB. When garnet is present in the residue from melting, this residue develops high Lu/Hf ratios, and hence, over time, a radiogenic Hf isotope signature. On the other hand, the melting residues of (garnet-free) spinel peridotites will have lower Lu/Hf ratios, resulting in less radiogenic Hf isotope signatures over geological time. Johnson and Beard (1993) termed these two types of depleted-mantle signature DMM-I and DMM-II, respectively, and showed that the latter type was also represented in the source of Tertiary basalts in the southern Rio Grande rift (USA). They argued that the DMM-I and DMM-II components were generated by ancient depletion events, and that intermediate MORB compositions were generated by mixing between them (Beard and Johnson, 1993).

Salters (1996) presented an enlarged Hf–Nd data set for MORB samples in order to re-examine the 'hafnium paradox' in ocean-ridge magmatism. Trace-element fractionation during melting is quantified using the Δ value, which compares the actual Lu/Hf and Sm/Nd ratios in MORB samples with the time-integrated ratios necessary to generate observed isotopic signatures by evolution from a 2-Byr-old chondritic source (Fig. 9.13).

Almost all MORBs and OIBs have significantly more extreme Δ (Lu/Hf) values than Δ (Sm/Nd) in Fig. 9.13, which implies melting in the garnet stability zone. In addition, average Δ values from four different ridges (interpreted as garnet signatures) gave a positive correlation with the depth of water over the ridge (Fig. 9.14), which in turn is *inversely* dependent on the rate of magma generation at the ridge. In other words, the ridge with the lowest rate of magma generation had the largest garnet signature. This is the opposite of what would be predicted for peridotite melting, since ridges with high magma-generation rates should begin melting at greater depth, allowing a longer melting interval in the garnet zone.

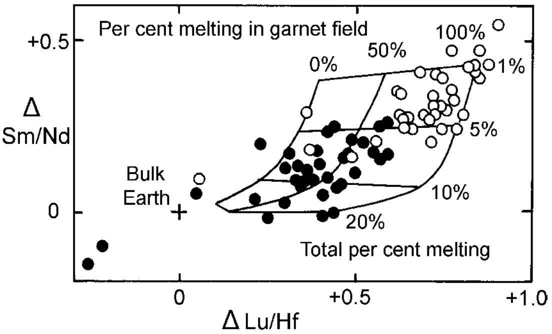

Fig. 9.13. Plot of time-integrated ratios of Sm/Nd and Lu/Hf (Δ) necessary to generate observed isotope ratios in MORB (○) and OIB (●) over 2 Byr. Curves show model melting conditions that can explain the calculated Δ ratios. After Salters (1996).

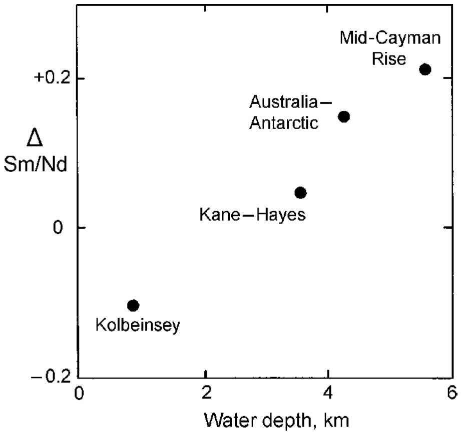

Fig. 9.14. Plot of calculated Δ values for Sm/Nd (Fig. 9.13) against water depth for a selection of ridge segments. Δ Lu/Hf shows a similar pattern. After Salters (1996).

To explain this paradox, Hirschmann and Stolper (1996) argued that Lu/Hf fractionation in MORB results from melting of garnet pyroxenite (rather than garnet peridotite) in a marble-cake mantle. According to this model, the 'garnet signature' from melting of pyroxenite is preserved under deep ridges with low melting rates, but under shallow ridges this signature is diluted by large-scale melting of spinel peridotite. Evidence from other isotopic systems may help to resolve this debate (sections 8.3.6 and 13.3.4).

The advent of MC-ICP-MS offered the opportunity to test the earlier work on MORB samples by the analysis of larger sample suites at levels of precision nearly an order of magnitude better. At first, it appeared that the large spread of Hf isotope analyses originally measured by Patchett *et al.* on Atlantic MORB samples might not be reproduced (e.g. Nowell *et al.*, 1998; Kempton *et al.*, 2000). However, subsequent work by Chauvel and Blichert-Toft (2001) was able to reproduce most of the range of Hf isotope ratios seen in the early work on MORB.

Hf analyses of OIB samples were presented by Salters and Hart (1991) and Salters and White (1998) in order to establish the locations of the end-member components proposed by Zindler and Hart (section 6.4.2). The results (Fig. 9.15) showed that EMI and EMII were strongly collinear. On the other hand, the isolation of HIMU below the main trend suggests a possible connection with the DMM-II component, which

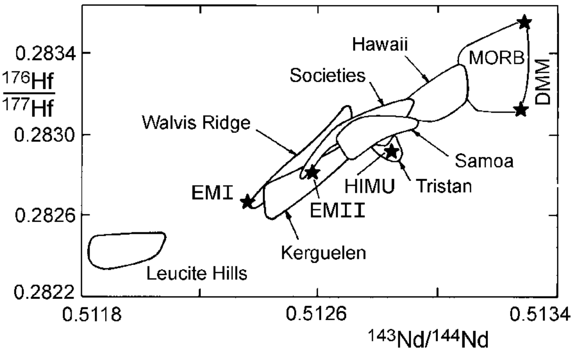

Fig. 9.15. Hf–Nd isotope diagram, showing fields for geochemically important ocean islands, together with the estimated compositions of end-members. The Leucite Hills represent sub-continental lithosphere. Modified after Salters and Hart (1991).

was attributed by Johnson and Beard (1993) to ancient depleted spinel peridotite. In other words, if we take into account the location of the HIMU field below the main OIB array, the degree of decoupling between Hf and Nd isotope signatures in OIB mirrors that seen in MORB.

9.2.5 Sediment recycling

Another geological environment where Lu/Hf can undergo strong fractionation relative to Sm/Nd is the sedimentary system. Patchett *et al.* (1984) plotted Lu/Hf ratios against Sm/Nd for various types of marine sediment (Fig. 9.16). While ^{147}Sm/^{144}Nd ratios are more or less constant at about 0.12–0.14 in most samples analysed, ^{176}Lu/^{177}Hf is strongly fractionated between sandstones and clays. Patchett *et al.* attributed this fractionation to the very strong affinity of Hf for zircon, which, because of its resistance to mechanical and chemical attack, becomes enriched in sand-grade sediments. Hf is correspondingly depleted in the fine-grained clay fraction.

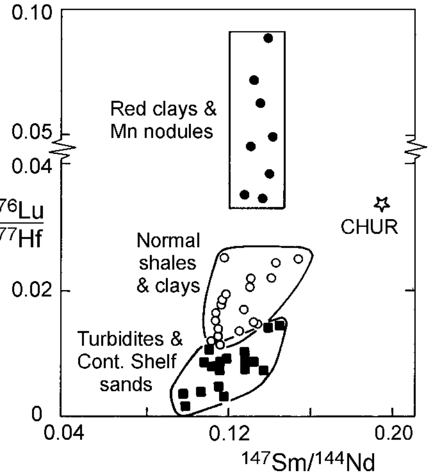

Fig. 9.16. Plot of Lu/Hf *versus* Sm/Nd ratio in various types of sediment, showing that large fractionations in Lu/Hf are not accompanied by significant changes in Sm/Nd ratio. After Patchett *et al.* (1984).

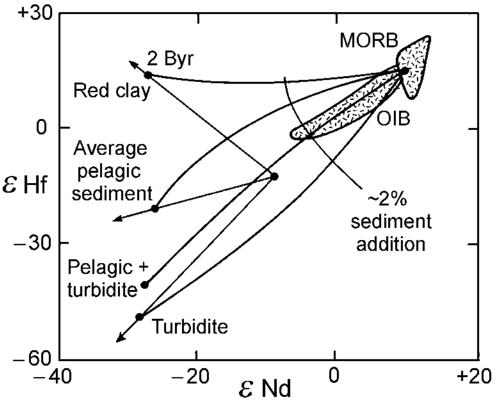

Fig. 9.17. Trends in OIB data predicted to result from the subduction of various types of sediment into the deep mantle, followed by storage for 1–2 Byr. After Patchett *et al.* (1984).

The sorting of marine sediments according to grain size is expected to yield low-Lu/Hf-ratio sands and turbidites on the continental shelf and continental slope, medium-Lu/Hf-ratio shales and clays, and very-high-Lu/Hf-ratio red clays and Mn nodules in the deep ocean, where terrigenous sediment is lacking. These variations in sediment Lu/Hf ratios were in turn predicted to generate large variations in Hf isotope ratio after recycling and storage in deep-mantle reservoirs. Hence, Patchett *et al.* (1984) calculated that any individual type of sediment subducted (e.g. red clay, average pelagic sediment, or turbidite) would yield distinctive isotopic compositions after 2 Byr of residence in the mantle (Fig. 9.17). Since such dramatic divergences are not seen in OIB samples, Patchett *et al.* concluded that the magnitude of sediment recycling into the mantle must be strictly limited.

Island-arc basalts (IAB) offer a means of monitoring the composition of material actually being recycled into the mantle, in order to test theoretical models such as that of Patchett *et al.* (1984). Hf–Nd isotope data were presented by White and Patchett (1984) for arc basalts sampling depleted and enriched sources

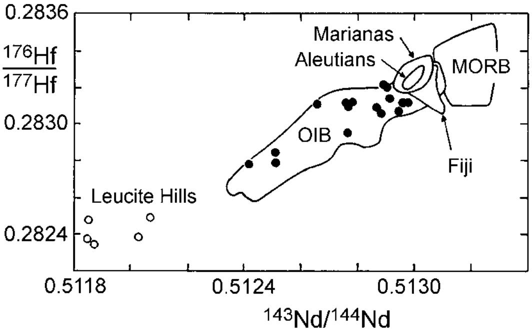

Fig. 9.18. Hf–Nd isotope plot, showing the composition of island-arc basalts (●, and marked fields) relative to MORB, OIB and sub-continental lithosphere. After Salters and Hart (1991).

(solid symbols in Fig. 9.18). These data fall within the field of OIB samples, showing that old sedimentary material now being subducted into the mantle has appropriate Hf–Nd systematics to explain the composition of OIB magmas. Therefore, contrary to the prediction of Patchett (1984), this implies that non-extreme mixtures of various types of sediment *can* explain the composition of OIB sources with moderate ease.

This conclusion was supported by MC-ICP-MS analysis of Hf in a much larger suite of sediment samples by Vervoort *et al.* (1999). This work showed that Hf–Nd isotope systematics in the global sedimentary system were more coherent than had previously been expected. Apart from a very few extreme samples, the vast majority of sediments (of a wide variety of ages) lie along the same trend as the OIB mantle array (Fig. 9.19). This is particularly true for sediments from active margins, which are much more likely to be recycled into the mantle than are passive-margin sediments. Therefore, it is concluded that Hf isotope data provide a weaker constraint on recycling of sediment into the mantle than had originally been expected, so models involving recycling of terrigenous or pelagic sediment into various OIB reservoirs are no longer ruled out.

With the advent of new high-precision Hf data sets from MC-ICP-MS, more subtle trends have been observed within the OIB data set, which can give a better understanding of the origins of OIB sources from various types of recycled crustal material. For example, a detailed Hf isotope study of Hawaiian lavas (Blichert-Toft *et al.*, 1999) revealed two *en échelon* arrays formed, respectively, by the Koolau volcano and by a composite of several other volcanoes (Fig. 9.20). These arrays cut across the main Nd–Hf isotope array in OIB, with significantly lower slopes and were attributed to a significant fraction of recycled pelagic sediment in parts of the Hawaiian plume, mixed in different proportions with a component of recycled oceanic lithosphere. This model is supported by osmium and oxygen isotope evidence (section 8.3.4). A similar shallow trend, consistent with a subducted sediment component, was subsequently found in Pitcairn samples (Eisele *et al.*, 2002). Since Pitcairn is the most extreme example of the EMI mantle reservoir, this supports the model involving recycling of pelagic sediment into this OIB source (section 6.5.3).

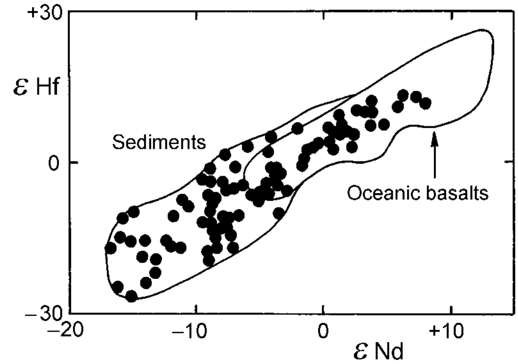

Fig. 9.19. Hf–Nd isotope data for a large suite of sediments of various ages (●), to show variation relative to the field of oceanic volcanics. After Vervoort *et al.* (1999).

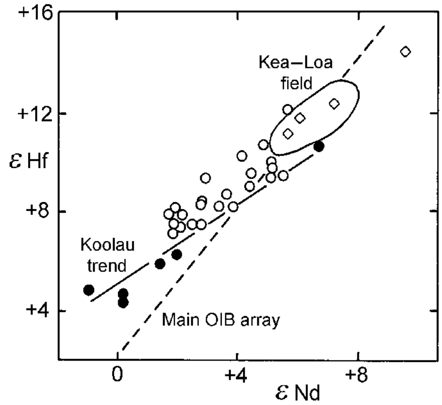

Fig. 9.20. Plot of ε Hf versus ε Nd compositions for several Hawaiian volcanos relative to the main trend of the Hf–Nd OIB array: (●) = Koolau volcano; (○) = Lanai and Kahoolawe; (◇) = Haleakala. After Blichert-Toft *et al.* (1999).

9.3 Seawater hafnium

The first study of seawater hafnium was performed by White *et al.* (1986), by analysis of four Fe–Mn nodules from the Pacific and one each from the Atlantic and Indian Oceans. In contrast to the wide range of Hf isotope signatures in marine sediments, ferromanganese nodules were found to have homogeneous ε Hf values around +2, with little variation outside analytical error, despite the observed wide range of Nd isotope compositions (Fig. 9.21). White *et al.* interpreted the isotope signatures of the nodules as indicative of seawater hafnium, which therefore appears to resemble seawater strontium in being homogeneous in the world's oceans.

White *et al.* attributed the homogeneous seawater hafnium signature to mixing between crustal and mantle sources of dissolved hafnium. This implies that the crustal source should reflect the composition of non-zircon-bearing sediments, with ε Hf about −9, probably carried in river water. On the other hand, the mantle-like end-member was attributed to low-temperature alteration of basaltic ocean-floor crust, with a MORB ε Hf signature of about +16. This implies approximately equal mixing between the two end-members. However, because the deduced range of seawater Hf is much smaller than the range between the end-members, it also suggests that hafnium must have a long residence time in seawater, to allow such a high degree of homogenisation. This was surprising, since the concentration of hafnium in seawater is low. However, White *et al.* suggested that hafnium would be present in seawater as the hydrolysed species $Hf(OH)_5^-$, making it resistant to the process of particulate scavenging that gives rise to the short seawater residence time of the REE.

The relatively large errors in Hf analysis by TIMS prevented the development of this work until the advent of MC-ICP-MS. In the first study with this instrument, Godfrey *et al.* (1997) used ferromanganese crusts as archives of recent seawater Hf compositions, and revealed a weak correlation with Pb isotope ratio. This was attributed to the mixing of continental and hydrothermal Hf in the global ocean system. Within this array the Atlantic had less radiogenic Hf, implying domination by sedimentary Hf, whereas the Pacific had more radiogenic Hf, suggesting domination by a sea-floor hydrothermal Hf flux. However, the range of seawater Hf isotope signatures was more restricted than that of Pb (relative to the end-member compositions), which led Godfrey *et al.* to suggest that Hf has a longer seawater residence time than Pb.

Albarède *et al.* (1998) analysed a larger suite of ferromanganese nodules from the Atlantic and Pacific oceans, and confirmed that these did show some degree of Hf isotope variation. In addition, they found that samples with over 7.5 ppm Hf displayed a significant co-variation with Nd isotope composition, both in the Atlantic and in the Pacific Ocean (Fig. 9.22). On the other hand, aberrant signatures in samples with lower Hf contents were attributed to the incorporation of less radiogenic Hf of a detrital or diagenetic origin. The trajectory of the right-hand end of the mixing line is not precisely defined, but it converges on the general

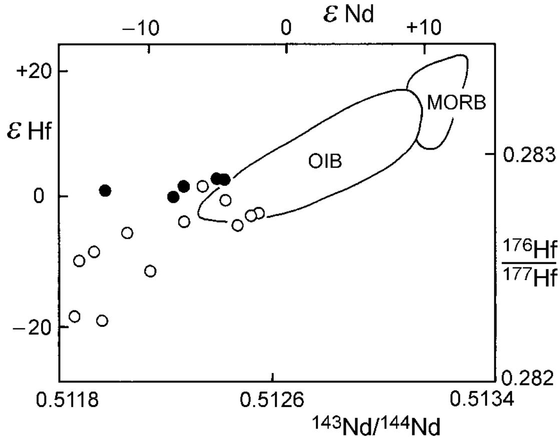

Fig. 9.21. Plot of hafnium isotope compositions against Nd and Sr, to show variations in Fe–Mn nodules (●) and marine sediments (○) relative to oceanic volcanics. After White *et al.* (1986).

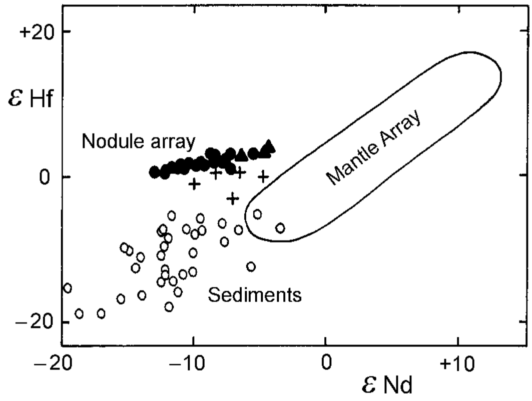

Fig. 9.22. Plot of Hf *versus* Nd isotope composition for ferromanganese nodules from the Atlantic Ocean (●) and Pacific Ocean (▲), compared with sedimentary rocks (○) and the oceanic mantle array; (+) = Mn nodules with low Hf contents. After Albarède *et al.* (1998).

field of ocean-floor basalts, and is therefore compatible with a source in low-temperature hydrothermal fluids, as proposed by White *et al.* (1986). On the other hand, the left-hand end of the mixing line in Fig. 9.22 points to an end-member distinctly more radiogenic than most sediments. Similar results were obtained by David *et al.* (2001). Putting all the evidence together, it appears that the seawater residence time of Hf is somewhat longer than that of Nd, but much shorter than that of Sr.

The first record of paleo-seawater Hf isotope variations for the Cenozoic was presented by Lee *et al.* (1999). This record came from two Pacific ferromanganese crusts from about 2 km depth. These have been dated by ^{10}Be over the past 20 Myr, with extrapolated growth rates back to 50 Myr. The two crusts were found to have flat ε Hf evolution profiles for the past 20 Myr, ranging from +6 to +8, with more variations in the period 20–50 Myr ago that were partially correlated between the two crusts. However, there was essentially no correlation with Nd isotope ratio.

More complex paleo-seawater Hf variations were observed in ferromanganese crusts from the North Atlantic Ocean by Piotrowski *et al.* (2000). Using a composite record from two different crusts, Piotrowski *et al.* observed a positive correlation between Hf and Nd isotope signatures over the past 5 Myr (Fig. 9.23). However, between 30 and 5 Myr ago, Hf and Nd were decoupled, as ε Nd gradually increased while ε Hf decreased and then increased again. Piotrowski *et al.* invoked changes in the weathering of the non-zircon component of the continental crust to explain these variations. However, they rejected a suggestion by Albarède *et al.* (1998) that this end-member might reflect the input of zircon-deficient wind-borne material to the oceans. This was because suggested indices of the windborne flux, such as the Al contents of the crusts, were not correlated with changes in Hf isotope ratio. Therefore, Piotrowski suggested that the zircon-deficient continental Hf flux was mostly carried by rivers. This model is supported by Hf isotope data from Pacific ferromanganese crusts, which do not show a marked change in isotopic composition 3.5 Myr ago, when there was a marked increase in the flux of aeolian dust from the loess deposits of eastern Asia (Pettke *et al.*, 2002).

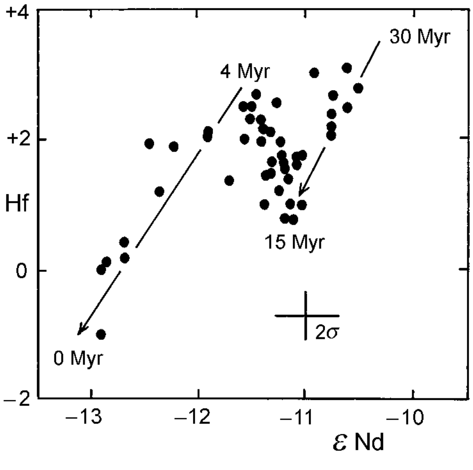

Fig. 9.23. Plot of ε Hf against ε Nd, showing a magnified (composite) record from two North Atlantic Fe–Mn crusts, attributed to temporal variations in the isotope composition of Hf and Nd of seawater due to varying riverine fluxes. After Piotrowski *et al.* (2000).

9.4 The La–Ce and La–Ba systems

^{138}La exhibits branched decay; by β emission to ^{138}Ce and by electron capture to ^{138}Ba. The La–Ce decay scheme is a potentially useful isotopic tracer, and the La–Ba scheme may form a useful geochronometer, but their application has been greatly hindered by the very low abundance of the parent isotope (0.089% of natural lanthanum) and its very long half-life (over 100 Byr, totalled for both routes). Nevertheless, both methods have been applied to geological problems.

In addition to the general problems mentioned above, counting determinations of the La decay constants are hampered by the low energy of emitted particles. Hence, early measurements, particularly of the β-decay branch, were scattered. To overcome this problem, the counting experiments actually measure the γ decay of isomers (excited states) of the product nuclide, rather than the isobaric decay process itself.

A further complication for counting experiments is the hygroscopic nature of La_2O_3, the material usually used in these studies. Transformations to the hydroxide or carbonate result in weight gains of 17% and 2.5%, respectively, but in ten out of twelve recent counting determinations on La, no volatile data were reported (Tanaka and Masuda, 1982). However, despite a large variation in absolute values, all counting determinations since 1970 yield a ratio for β/electron-capture decay constants near 0.51. In addition, two recent counting experiments on anhydrous La oxide yielded average values for the β decay constant of 2.29×10^{-12} and 2.22×10^{-12} yr^{-1}, respectively (Sato and Hirose, 1981; Norman and Nelson, 1983). The La–Ce system was the first of the two methods to be applied geologically, but since the La–Ba case is simpler, it will be discussed first.

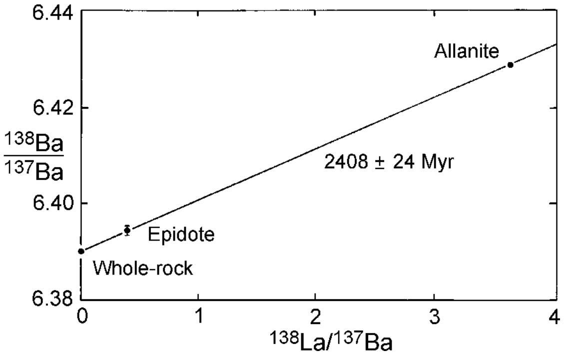

Fig. 9.24. La–Ba isochron diagram for a sample of Amitsoq gneiss, western Greenland. The isochron yields an age of 2408 ± 24 Myr, which dates a metamorphic event rather than the age of the rock. The initial ratio of 6.3897 is invariant in whole-rock systems. After Nakai *et al.* (1986).

9.4.1 La–Ba geochronology

^{138}Ba, the daughter product of the electron capture decay of ^{138}La, is also the most abundant isotope of barium, making up 88% of the natural element. In view, therefore, of the very low abundance of the parent nuclide, significant variations in the abundance of ^{138}Ba are found only in REE-rich and Ba-poor minerals. The first geological measurements were made by Nakai *et al.* (1986) on epidote, allanite and sphene from Precambrian rocks (Fig. 9.24). Nakai *et al.* ratioed ^{138}Ba against ^{137}Ba to yield the following decay equation:

$$\frac{^{138}\mathrm{Ba}}{^{137}\mathrm{Ba}} = \left(\frac{^{138}\mathrm{Ba}}{^{137}\mathrm{Ba}}\right)_{\mathrm{I}} + \frac{^{138}\mathrm{La}}{^{137}\mathrm{Ba}}\frac{\lambda_{\mathrm{EC}}}{\lambda_{\mathrm{total}}}(e^{\lambda_{\mathrm{total}}t} - 1) \qquad [9.3]$$

Ba isotope analyses were normalised with respect to a ^{136}Ba/^{137}Ba ratio of 0.6996.

Nakai *et al.* found that all analysed whole-rock samples had ^{138}Ba/^{137}Ba initial ratios within error of 6.3897, which they attributed to the very low ^{138}La/^{137}Ba ratios of all such materials. Since the Ba isotope ratio of whole-rock systems is effectively invariant over time, a La–Ba mineral age can be based simply on the analysis of one or more La-enriched minerals. Using the electron-capture decay constant of 4.44×10^{-12} determined by Sato and Hirose (1981), Nakai *et al.* obtained relatively good agreement between the La–Ba and Sm–Nd ages of a pegmatite from Mustikkamaki (Finland) and Amitsoq gneiss from Greenland.

9.4.2 La–Ce geochronology

The relative harmony between counting and geological determinations of the La electron-capture decay branch was not matched by the La β-decay route to cerium. This branch is beset by much larger analytical problems, but has more geochemical applications. Tanaka and Masuda (1982) determined the first La–Ce isochron, ratioing ^{138}Ce against ^{142}Ce and normalising with respect to a ^{136}Ce/^{142}Ce ratio of 0.0172 . The decay equation is

$$\frac{^{138}\mathrm{Ce}}{^{142}\mathrm{Ce}} = \left(\frac{^{138}\mathrm{Ce}}{^{142}\mathrm{Ce}}\right)_{\mathrm{I}} + \frac{^{138}\mathrm{La}}{^{142}\mathrm{Ce}}\frac{\lambda_{\beta}}{\lambda_{\mathrm{total}}}(e^{\lambda_{\mathrm{total}}t} - 1) \qquad [9.4]$$

Because the half-lives of both decay branches are so long, they have very little effect on each other. For example, simplifying the equation to

$$\frac{^{138}\mathrm{Ce}}{^{142}\mathrm{Ce}} = \left(\frac{^{138}\mathrm{Ce}}{^{142}\mathrm{Ce}}\right)_{\mathrm{I}} + \frac{^{138}\mathrm{La}}{^{142}\mathrm{Ce}}(e^{\lambda_{\beta}t} - 1) \qquad [9.5]$$

causes only a 0.5% over-estimate in age.

Two further technical problems are encountered in Ce isotope analysis. One is the extreme size of the ^{140}Ce peak relative to the small ^{136}Ce and ^{138}Ce peaks (e.g. $^{140}\mathrm{Ce}/^{136}\mathrm{Ce} = 464.65$). Collision of the ^{140}Ce ion beam with gas molecules in the vacuum system causes down-mass peak tailing, whose effect on the small peaks must be corrected.

A second major problem is the isobaric interference of ^{138}Ba onto ^{138}Ce. ^{138}Ba is six times more abundant than any other natural Ba isotope that could be used to monitor Ba interference. Therefore any interference correction for ^{138}Ba (even if near zero) will amplify detector noise six-fold. The solution to this problem is to analyse Ce as the oxide species CeO^+. Because barium is divalent, the BaO^+ species is very unfavourable. Therefore, provided that overall Ba levels are kept low by good chemistry, the Ba interference can be taken to be zero without correction. Analysing Ce as the oxide introduces other isobaric interference problems, but these are easily overcome by good chemistry (section 2.1.2).

Tanaka and Masuda (1982) attempted to date separated minerals from the Bushveld pluton, but because of the geological similarity between La and Ce, a limited range of La/Ce ratios was available and the isochron had a large analytical error. Further isochron determinations were made by Masuda *et al.* (1988). However, using the β decay constant of $2.29 \times 10^{-12}\ \mathrm{yr}^{-1}$ obtained by Sato and Hirose (1981), the La–Ce isochrons gave old ages outside error of the corresponding Sm–Nd isochrons. If ages are taken

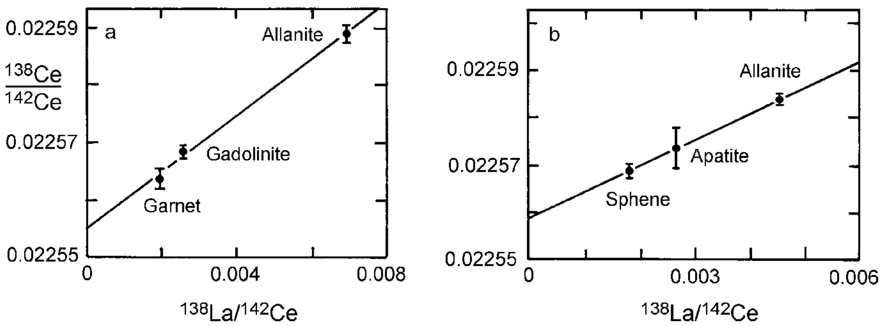

Fig. 9.25. La–Ce isochrons for (a) the Lovbole and (b) the Mustikkamaki pegmatites of Finland. When combined with Sm–Nd data, they imply La β decay constants of 2.70 ± 0.25 and 2.93 ± 0.41 $\times 10^{-12}\ yr^{-1}$, respectively. After Masuda *et al.* (1988).

from the Sm–Nd data then the La–Ce isochron slopes can be used to make a geological decay-constant determination. Using the Bushveld result and mineral isochrons from two Finnish pegmatites (Fig. 9.25), Masuda *et al.* calculated an average β decay constant of $2.77 \times 10^{-12}\ yr^{-1}$, about 20% higher than the counting determinations.

In an attempt to provide further geological constraints on the La β decay constant, Dickin (1987a) determined a La–Ce isochron on a suite of Lewisian whole-rock gneisses from northwest Scotland. ^{138}Ce was ratioed against ^{136}Ce, since this gives rise to more manageable isotope ratios, but an equivalent normalising factor was used to correct for fractionation. It was argued that whole-rock REE systems were more advantageous for calibrating the decay constant than mineral systems, due to the greater resistance of the former to metamorphic re-setting. The original sample suite contained two basic granulites and four intermediate-to-acid granulites. Using the decay constant of Sato and Hirose (1981), the La–Ce isochron age of 2.99 Byr was in good agreement with the Lewisian Sm–Nd age of 2.91 Byr (section 4.1.3).

However, further work on the Sm–Nd systematics of Lewisian gneisses has shown that the samples analysed by Dickin (1987a) comprise two suites with different geological histories. Basic gneisses preserve crustal formation ages of 2.9 Byr, whereas intermediate-to-acid whole-rock gneisses have been re-set by granulite-facies metamorphism at 2.60 Byr (section 4.1.3). Using the decay constant of Sato and Hirose, the four intermediate-to-acid granulites yield a La–Ce age of 2.65 ± 0.3 Byr (2σ), which is in agreement with the Sm–Nd result on this suite. No meaningful La–Ce age can be calculated on the basic granulites alone.

The most recent geological determination of the La β decay constant (Makishima *et al.*, 1993) has also supported the value of Sato and Hirose. Two La–Ce mineral isochrons were determined on Archean granites from western Australia, which gave more or less concordant U–Pb zircon and Rb–Sr mineral isochron ages. Sm–Nd mineral suites also yielded ages within error of the other methods, but with higher error due to large MSWD values. Using a decay constant of $2.29 \times 10^{-12}\ yr^{-1}$, the granites gave La–Ce mineral ages of 2.76 ± 0.41 and 2.69 ± 0.38 Byr, which agree well with U–Pb ages of 2.665 and 2.692 Byr, respectively.

9.4.3 Ce isotope geochemistry

Since La and Ce are LREE, Ce isotope data form a tracer for time-integrated LREE enrichment or depletion of geological reservoirs. Similarly, Nd isotope data are a tracer for time-integrated fractionation between the middle REE. Therefore, a combination of Ce and Nd isotope data provides a unique control of the time-integrated light-to-middle REE evolution of complex geological reservoirs in the mantle or crust. Together they may form a powerful petrogenetic tool.

Ce isotope analyses of eight OIB from the Atlantic, Pacific and Indian oceans were presented by Dickin (1987b). When plotted against published Nd isotope analyses, the data defined a linear array that fell within error of the meteoritic Bulk Earth point of Shimizu *et al.* (1984). The linearity of this 'mantle array' can be attributed to the coherent behaviour of the REE during processes of mantle evolution.

Subsequently, Tanaka *et al.* (1987) reported Ce isotope data on eleven more ocean-island, ocean-ridge and island-arc basalts (Fig. 9.26). Most of these were very consistent with the data of Dickin (1987b), but three samples lay outside of error of a best-fit mantle array calculated by Dickin (1988). Tanaka *et al.* (1987; 1988)

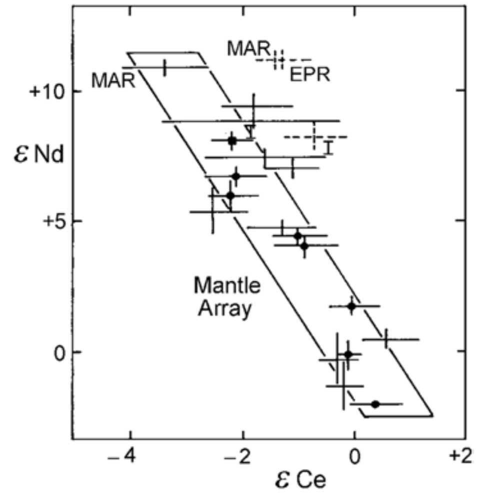

Fig. 9.26. Plot of ε Nd against ε Ce (parts per 10^4 deviation from Bulk Earth) for young oceanic volcanics. Error bars represent 2 SDM within-run precision. Plain crosses and those with solid centres denote data from two different laboratories. The solid square is for a Skye plateau lava, relative to 60-Myr-old Bulk Earth. Dotted error bars denote samples whose error bars do not overlap the mantle array. After Dickin (1988).

attributed these outliers to incoherent behaviour of the La–Ce and Sm–Nd systems during the evolution of the depleted upper mantle. However, the fact that Nd, Sr and Pb isotope systems in the Ce-anomalous samples were perfectly normal led Dickin (1988) to suggest that larger analytical errors might be responsible. In contrast, Makishima and Masuda (1994) found high ε Ce in MORB and rejected the low value of Tanaka *et al.* (1987), implying a mantle array twice as steep.

Because of the gradual variation of chemical properties along the lanthanide series, chondrite-normalised REE patterns for large rock reservoirs tend to define approximately linear profiles. Tanaka *et al.* (1987) considered the behaviour of an idealised group of rocks that underwent Ce and Nd isotope evolution starting at the Bulk Earth isotope composition. If these rocks all had linear REE profiles then their Ce–Nd isotope compositions must lie on a linear array whose slope is solely a function of the relative decay constants of the parent nuclides, irrespective of age. Ideally, if such a rock suite were analysed for Ce and Nd isotope composition, the relative decay constants could be calculated without the need to know any concentration or age information.

Tanaka *et al.* attempted to apply this model in practice, by determining the La β decay constant by the analysis of four unrelated continental rocks from around the world with approximately linear REE profiles. An almost perfect linear array was found, but unfortunately this must be attributed to coincidence, since the calculated initial ratios of these samples are actually *more* dispersed than their present-day compositions. Therefore the linearity of this particular data set is coincidental, and its slope cannot be used to determine the La β decay constant. This concept is probably destined to remain a theoretical construct, since the principal difficulty in determining the decay constant is not determination of the La/Ce ratio, but the Ce isotope ratio itself.

A combination of Ce and Nd isotope data was used by Dickin *et al.* (1987) to study mixing relations during crustal contamination of continental magmas. Twelve Tertiary igneous rocks from Skye in northwest Scotland were analysed for Ce isotope composition. These were compared with theoretical mixing models based on analysed crustal end-members. The Ce *versus* Nd isotope diagram (Fig. 9.27) provides one way to evaluate the merits of various mixing models for analysed lavas. This immediately allows the exclusion of the trondhjemitic mixing line as a relevant petrogenetic model. However, the data allow a more elegant test of the end-members involved in magma mixing.

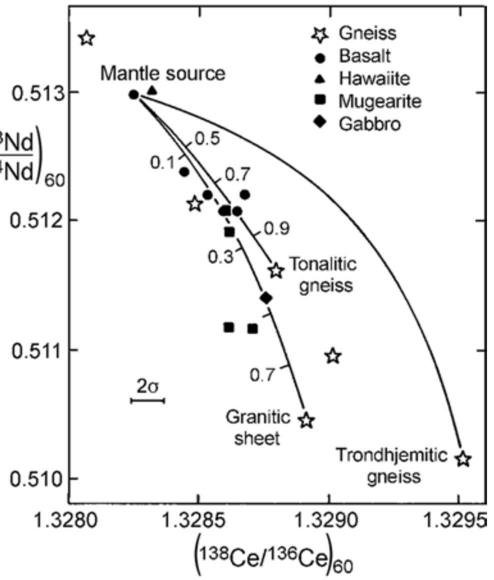

Fig. 9.27. Plot of initial Nd *versus* Ce isotope composition of Skye lavas (solid symbols), relative to Archean basement gneisses at 60 Myr (stars). The array of lava compositions excludes mixing of mantle-derived and trondhjemitic crustal melts. After Dickin *et al.* (1987).

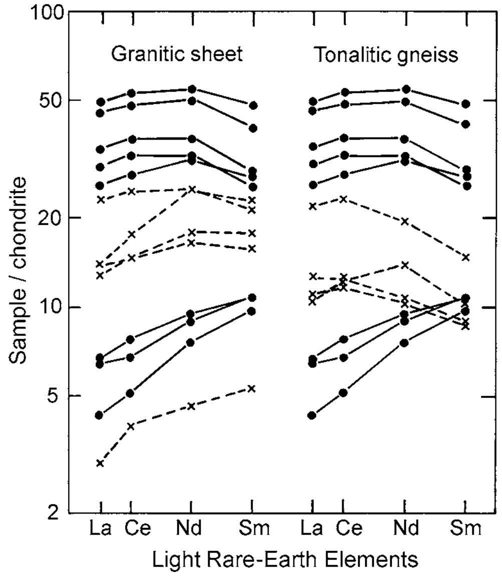

Fig. 9.28. LREE profiles for isotopically uncontaminated lavas (solid lines) compared with model LREE profiles for mantle-derived precursors of contaminated lavas (dashed). The 7H model yields more consistent profiles for the two types of lava. After Dickin *et al.* (1987).

By taking the Ce isotope compositions of competing crustal end-members, linear mixing lines can be projected back through the analysed product lavas on diagrams of Ce isotope ratio against 1/Ce concentration and La/Ce ratio to model the elemental composition of the mantle-derived precursor prior to contamination. By performing the same calculation for the Sm/Nd data, a complete model LREE profile can be determined for each precursor. These model profiles (dashed) are compared in Fig. 9.28 with a variety of REE profiles for lavas whose isotopic compositions are effectively uncontaminated (solid lines). In this way it was possible to show that the granitic sheet end-member is better able to explain the isotopic composition of the contaminated lavas than is the intermediate tonalitic gneiss end-member.

The oceans constitute another environment where combined Ce and Nd isotope analysis can be used to study mixing processes. Ce–Nd isotope data for Atlantic and Pacific ferromanganese nodules were presented by Tanaka *et al.* (1986) and Amakawa *et al.* (1991). These isotope ratios are argued to be indicative of the composition of the ocean water from which the nodules grew. In the light of Nd and Sr isotope data (section 4.5), the Ce–Nd data are expected to reflect mixing between continental and MORB-type REE fluxes into the ocean system. However, the data were widely scattered, and did not lie on a single mixing line between reasonable MORB and continental end-members.

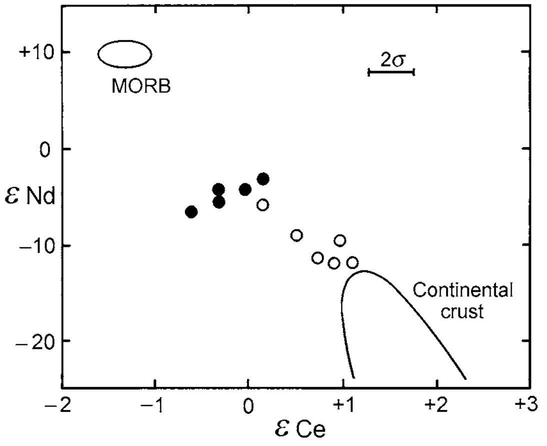

Fig. 9.29. Plot of ε Nd versus ε Ce, showing data for Pacific (●) and Atlantic (○) manganese nodules that can be explained by mixing of REE from MORB and continental end-members. After Amakawa *et al.* (1996).

New Ce isotope analyses on ocean-floor manganese nodules from the Atlantic Ocean (Amakawa *et al.*, 1996) gave values that were much less scattered than previous data. Hence, the scatter of the old data may have been due to analytical error. On a plot of ε Nd *versus* ε Ce (Fig. 9.29), the new data fall close to a mixing line between MORB and continental crust, which is consistent with simple mixing of REE from these sources.

9.5 The K–Ca system

The K–Ca couple was actually the first isotopic system to be suggested as a geochemical tracer for granite petrogenesis (Holmes, 1932). However, this was on the assumption that the major isotope of potassium, ^{41}K, was the radioactive nuclide. (Fortunately this is not really the case or the Earth would have melted from the heat.) When it was realised that ^{40}K was actually the radioactive nuclide, the idea of pursuing the K–Ca system was abandoned, since it was expected that radiogenic ^{40}Ca would be swamped by the dominant non-radiogenic ^{40}Ca component. The method finally became viable with the development of modern high-precision mass spectrometers, but has not been applied widely.

Russell *et al.* (1978) used Ca isotope analysis to investigate mass-dependent fractionation processes, but the first geochronological application of the method was made by Marshall and DePaolo (1982). Because of the large relative differences between Ca nuclide masses, isotope ratios must be corrected for natural and instrumental mass fractionation using a more complex procedure than the simple linear law (section 2.2.3). In practice, an exponential mass-fractionation correction was used in the two studies mentioned above. Marshall and DePaolo quoted their Ca isotope data as ^{40}Ca/^{42}Ca ratios, corrected by reference to a value of 0.31221 for the non-radiogenic ^{42}Ca/^{44}Ca ratio.

A variety of meteorites, lunar samples and mantle-derived materials was analysed by Russell *et al.* (1978) and Marshall and DePaolo (1982). When age-corrected to yield initial Ca isotope ratios at various times between 1.3 and 4.6 Byr ago, all of the measurements fell within analytical uncertainty of a ^{40}Ca/^{42}Ca ratio of 151.016. This tells us that, because of its very low K/Ca ratio, the Earth's mantle demonstrates negligible growth of radiogenic Ca with time.

Rather than quoting raw isotope ratios, Ca isotope compositions can be reported in terms of ε units (parts per 10^4 deviation from the mantle composition). However, this is more a matter of convenience than necessity, in view of the zero Ca isotope evolution of the mantle reservoir with time. In contrast, granitic crustal reservoirs have high K/Ca ratios of about 5–10, which can generate appreciable growth in ^{40}Ca with time. For reservoirs more than 1 Byr old these may give rise to isotope ratios outside error of the mantle value (Fig. 9.30). Because of the relatively short half-life of ^{40}K compared with the age of the Earth, isotopic growth lines are curved in this diagram.

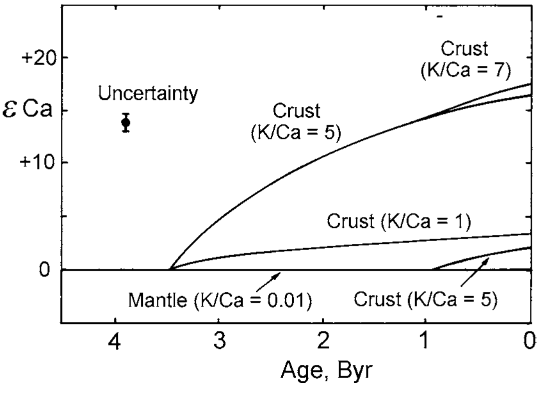

Fig. 9.30. Plot of Ca isotope evolution against time in terms of ε units (parts per 10^4 deviation from the constant mantle composition). Growth lines are shown for intermediate crust (K/Ca = 1) and granitic crust (K/Ca = 5). After Marshall and DePaolo (1982).

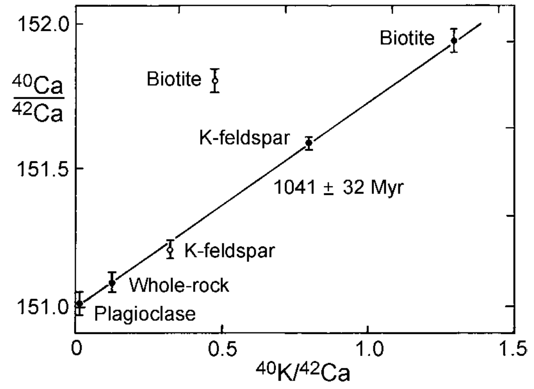

Fig. 9.31. K–Ca isochron plot for separated minerals from the Pikes Peak batholith. Note erroneous results of spiking aliquots (○) rather than the whole dissolution (●). After Marshall and DePaolo (1982).

Bearing in mind the branched decay of ^{40}K, we can substitute into the general decay equation [1.10] to derive the following isochron equation for the K–Ca system:

$$\frac{^{40}\mathrm{Ca}}{^{42}\mathrm{Ca}} = \left(\frac{^{40}\mathrm{Ca}}{^{42}\mathrm{Ca}}\right)_{\mathrm{I}} + \frac{^{40}\mathrm{K}}{^{42}\mathrm{Ca}}\frac{\lambda_\beta}{\lambda_{\mathrm{total}}}(e^{\lambda_{\mathrm{total}}t} - 1) \qquad [9.6]$$

The branching ratio of β to total decays is 0.8952, and the total decay constant is $5.543 \times 10^{-10}\ \mathrm{yr}^{-1}$ (section 10.1).

Marshall and DePaolo tested the K–Ca system as a dating tool by analysing a small suite of separated minerals from the Pikes Peak batholith of Colorado. Plagioclase, whole-rock, K-feldspar and biotite define an isochron array (Fig. 9.31), whose slope yields an age of 1041 ± 32 Myr (2σ). This is within error of other age determinations on this largely unmetamorphosed pluton. The initial ratio of the Pikes Peak batholith (151.024) is within error of the mantle value.

One severe analytical problem that was encountered during this work (other than the mass-fractionation behaviour mentioned above) was that samples divided into aliquots before mixing with spike gave erroneous K/Ca ratios. Marshall and DePaolo speculated that this might have been due to some precipitation of potassium from the rock solutions. It is avoided by spiking the whole sample before dissolution.

Marshall and DePaolo (1989) went on to apply the K–Ca method as a petrogenetic tracer in a study of Cenozoic plutons from the western USA. Granites emplaced into Paleozoic crust on the continental margin had a similar range of Ca isotope ratios to island-arc volcanics, from values within error of the MORB composition to just outside error (see also Nelson and

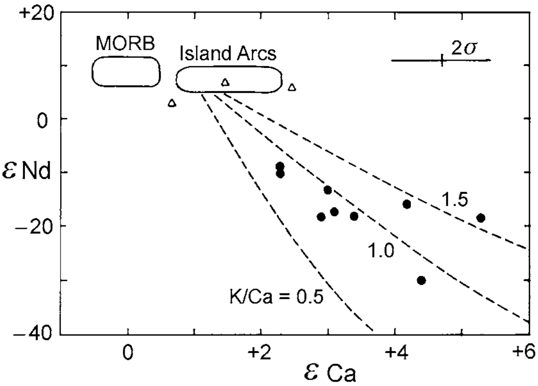

Fig. 9.32. Plot of ε Nd against ε Ca, showing compositions of Cenozoic granitoids emplaced into young basement (△) and old basement (●), relative to island-arc volcanics and MORB. Curves show model K/Ca ratios for basement with ^{147}Sm/^{144}Nd = 0.1. After Marshall and DePaolo (1989).

McCulloch, 1989). In contrast, granites emplaced into Lower Proterozoic basement exhibited larger Ca isotope enrichments which were correlated with ε Nd (Fig. 9.32). Hence, the Ca isotope ratios of the plutons must be inherited from the crustal source at depth.

Marshall and DePaolo compared the ε Ca – ε Nd compositions of the plutons with crustal-evolution models shown by dashed curves in Fig. 9.32. Given a crustal ^{147}Sm/^{144}Nd ratio of 0.1 (determined using the known Nd isotope signature of Colorado basement), Ca–Nd isotope evolution curves were drawn for various crustal K/Ca ratios. If we assume the granites to be total crustal melts, then the data in Fig. 9.32 imply a K/Ca ratio of about unity in the source. However, this is higher than most estimates for bulk crust, so a more likely explanation is that ε Ca ratios were fractionated during the melting processes by preferential extraction of the most fusible components of the crust. The usefulness of these constraints for petrogenetic modelling suggests that Ca isotopes have promise as a tracer for crust–mantle mixing, and may find more exploitation in the future.

References

Albarède, F., Blichert-Toft, J., Vervoort, J. D., Gleason, J. D. and Rosing, M. (2000). Hf–Nd isotope evidence for a transient dynamic regime in the early terrestrial mantle. *Nature* **404**, 488–90.

Albarède, F., Simonetti, A., Vervoort, J. D., Blichert-Toft, J. and Wafa, A. (1998). A Hf–Nd isotopic correlation in ferromanganese nodules. *Geophys. Res. Lett.* **25**, 3895–8.

Amakawa, H., Ingri, J., Masuda, A. and Shimizu, H. (1991). Isotopic compositions of Ce, Nd and Sr in ferromanganese nodules from the Pacific and Atlantic Oceans, the Baltic and Barents Seas and the Gulf of Bothnia. *Earth Planet. Sci. Lett.* **105**, 554–65.

Amakawa, H., Nozaki, Y. and Masuda, A. (1996). Precise determination of variations in the ^{138}Ce/^{142}Ce ratios of marine ferromanganese nodules. *Chem. Geol.* **131**, 183–95.

Amelin, Y., Lee, D.-C. and Halliday, A. N. (2000). Early–middle Archaean crustal evolution deduced from Lu–Hf and U–Pb isotopic studies of single zircon grains. *Geochim. Cosmochim. Acta* **64**, 4205–25.

Amelin, Y., Lee, D.-C., Halliday, A. N. and Pidgeon, R. T. (1999). Nature of the Earth's earliest crust from hafnium isotopes in single detrital zircons. *Nature* **399**, 252–5.

Beard, B. L. and Johnson, C. M. (1993). Hf isotope composition of late Cenozoic basaltic rocks from northwest Colorado, USA: new constraints on mantle enrichment processes. *Earth Planet. Sci. Lett.* **119**, 495–509.

Bizzarro, M., Baker, J. A., Haack, H., Ulfbeck, D. and Rosing, M. (2003). Early history of Earth's crust–mantle system inferred from hafnium isotopes in chondrites. *Nature* **421**, 931–3.

Blichert-Toft, J. and Albarède, F. (1997). The Lu–Hf isotope geochemistry of chondrites and the evolution of the mantle–crust system. *Earth Planet. Sci. Lett.* **148**, 243–58.

Blichert-Toft, J., Albarède, F. Rosing, M., Frei, R. and Bridgwater, D. (1999). The Nd and Hf isotopic evolution of the mantle through the Archean. Results from the Isua supracrustals, West Greenland, and from the Birimian terranes of West Africa. *Geochim. Cosmochim. Acta* **63**, 3901–14.

Blichert-Toft, J. and Arndt, N. T. (1999). Hf isotope compositions of komatiites. *Earth Planet. Sci. Lett.* **171**, 439–51.

Blichert-Toft, J., Boyet, M., Télouk, P. and Albarède, F. (2002). ^{147}Sm–^{143}Nd and ^{176}Lu–^{176}Hf in eucrites and the differentiation of the HED parent body. *Earth Planet. Sci. Lett.* **204**, 167–81.

Blichert-Toft, J., Frey, F. A. and Albarède, F. (1999). Hf isotope evidence for pelagic sediments in the source of Hawaiian basalts. *Science* **285**, 879–82.

Chauvel, C. and Blichert-Toft, J. (2001). A hafnium isotope and trace element perspective on melting of the depleted mantle. *Earth Planet. Sci. Lett.* **190**, 137–51.

David, K., Frank, M., O'Nions, R. K., Belshaw, N. S. and Arden, J. W. (2001). The Hf isotope composition of global seawater and the evolution of Hf isotopes in the deep Pacific Ocean from Fe–Mn crusts. *Chem. Geol.* **178**, 23–42.

Dickin, A. P. (1987a). La–Ce dating of Lewisian granulites to constrain the ^{138}La β-decay half-life. *Nature* **325**, 337–8.

Dickin, A. P. (1987b). Cerium isotope geochemistry of ocean island basalts. *Nature* **326**, 283–4.

Dickin, A. P. (1988). Mantle and crustal Ce/Nd isotope systematics. *Nature* **333**, 403–4.

Dickin, A. P., Jones, N. W., Thirlwall, M. F. and Thompson, R. N. (1987). A Ce/Nd isotope study of crustal contamination processes affecting Palaeocene magmas in Skye, northwest Scotland. *Contrib. Mineral. Petrol.* **96**, 455–64.

Dixon, D., McNair, A. and Curran, S. C. (1954). The natural radioactivity of lutetium. *Phil. Mag.* **45**, 683–4.

Duchene, S., Blichert-Toft, J., Luais, B., Télouk, P. and Albarède, F. (1997). The Lu–Hf dating of garnets and the ages of the Alpine high-pressure metamorphism. *Nature* **387**, 586–9.

Eisele, J., Sharma, M., Galer, S. J. G., Blichert-Toft, J., Devey, C. W. and Hofmann, A. W. (2002). The role of sediment recycling in EM-1 inferred from Os, Pb, Hf, Nd, Sr isotope and trace element systematics of the Pitcairn hotspot. *Earth Planet. Sci. Lett.* **196**, 197–212.

Faure, G. (1977). *Principles of Isotope Geology.* Wiley, 464 pp.

Fujimaki, H., Tatsumoto, M. and Aoki, K. (1984). Partition coefficients of Hf, Zr and REE between phenocryst phases and groundmass. *Proc. 14th Lunar Planet. Sci. Conf., J. Geophys. Res.* **89** (suppl.), B662–72.

Godfrey, L. V., Lee, D.-C., Sangrey, W. F. *et al.* (1997). The Hf isotopic composition of ferromanganese nodules and crusts and hydrothermal manganese deposits: implications for seawater Hf. *Earth Planet. Sci. Lett.* **151**, 91–105.

Gruau, G., Chauvel, C., Arndt, N. T. and Cornichet, J. (1990). Aluminum depletion in komatiites and garnet fractionation in the early Archean mantle: hafnium isotopic constraints. *Geochim. Cosmochim. Acta* **54**, 3095–101.

Herr, W., Merz, E., Eberhardt, P. and Signer, P. (1958). Zur Bestimmung der β Halbwertszeit des ^{176}Lu durch den Nachweis von radiogenem ^{176}Hf. *Z. Naturf.* **13a**, 268–73.

Hirschmann, M. M. and Stolper, E. M. (1996). A possible role for garnet pyroxenite in the origin of the 'garnet signature' in MORB. *Contrib. Mineral. Petrol.* **124**, 185–208.

Holmes, A. (1932). The origin of igneous rocks. *Geol. Mag.* **69**, 543–58.

Johnson, C. J. and Beard, B. L. (1993). Evidence from hafnium isotopes for ancient sub-oceanic mantle beneath the Rio Grande rift. *Nature* **362**, 441–4.

Kempton, P. D., Fitton, J. G., Saunders, A. D. *et al.* (2000). The Iceland plume in space and time: a Sr–Nd–Pb–Hf study of the North Atlantic rifted margin. *Earth Planet. Sci. Lett.* **177**, 255–71.

Kramers, J. (2001). The smile of the Cheshire Cat. *Science* **293**, 619–20.

Lee, D.-C., Halliday, A. N., Hein, J. R., Burton, K. W., Christensen, J. N. and Günther, D. (1999). Hafnium isotope stratigraphy of ferromanganese crusts. *Science* **285**, 1052–4.

Makishima, A. and Masuda, A. (1994). Ce isotope ratios of N-type MORB. *Chem. Geol.* **118**, 1–8.

Makishima, A., Nakamura, E., Akimoto, S., Campbell, I. H. and Hill, R. I. (1993). New constraints on the ^{138}La β-decay constant based on a geochronological study of granites from the Yilgarn Block, Western Australia. *Chem. Geol. (Isot. Geosci. Section)* **104**, 293–300.

Marshall, B. D. and DePaolo, D. J. (1982). Precise age determination and petrogenetic studies using the K–Ca method. *Geochim. Cosmochim. Acta* **46**, 2537–45.

Marshall, B. D. and DePaolo, D. J. (1989). Calcium isotopes in igneous rocks and the origin of granite. *Geochim. Cosmochim. Acta* **53**, 917–22.

Masuda, A., Shimizu, H., Nakai, S., Makishima, A. and Lahti, S. (1988). ^{138}La β-decay constant estimated from geochronological studies. *Earth Planet. Sci. Lett.* **89**, 316–22.

Nakai, S., Shimizu, H. and Masuda, A. (1986). A new geochronometer using lanthanum-138. *Nature* **320**, 433–5.

Nelson, D. R. and McCulloch, M. T. (1989). Petrogenetic applications of the ^{40}K–^{40}Ca radiogenic decay scheme – a reconnaissance study. *Chem. Geol. (Isot. Geosci. Section)* **79**, 275–93.

Nir-El, Y. and Lavi, N. (1998). Measurement of the half-life of ^{176}Lu. *Appl. Radiat. Isot.* **49**, 1653–5.

Norman, E. B. and Nelson, M. A. (1983). Half-life and decay scheme of ^{138}La. *Phys. Rev. C* **27**, 1321–4.

Nowell, G. M., Kempton, P. D., Noble, S. R. *et al.* (1998). High precision Hf isotope measurements of MORB and OIB by thermal ionisation mass spectrometry: insights into the depleted mantle. *Chem. Geol.* **149**, 211–33.

Patchett, P. J. (1983). Hafnium isotope results from mid-ocean ridges and Kerguelen. *Lithos* **16**, 47–51.

Patchett, P. J., Kouvo, O., Hedge C. E. and Tatsumoto M. (1981). Evolution of continental crust and mantle heterogeneity: evidence from Hf isotopes. *Contrib. Mineral. Petrol.* **78**, 279–97.

Patchett, P. J. and Tatsumoto, M. (1980a). A routine high-precision method for Lu–Hf isotope geochemistry and chronology. *Contrib. Mineral. Petrol.* **75**, 263–7.

Patchett, P. J. and Tatsumoto, M. (1980b). Lu–Hf total-rock isochron for the eucrite meteorites. *Nature* **288**, 571–4.

Patchett, P. J. and Tatsumoto, M. (1980c). Hafnium isotope variations in oceanic basalts. *Geophys. Res. Lett.* **7**, 1077–80.

Patchett, P. J. and Tatsumoto, M. (1981). Lu/Hf in chondrites and definition of a chondritic hafnium growth curve. *Lunar Planet. Sci.* **12**, 822–4.

Patchett, P. J., White W. M., Feldmann, H., Kielinczuk, S. and Hofmann, A. W. (1984). Hafnium/rare earth element fractionation in the sedimentary system and crustal recycling into the Earth's mantle. *Earth Planet. Sci. Lett.* **69**, 365–78.

Pettingill, H. S. and Patchett, P. J. (1981). Lu–Hf total rock age for the Amitsoq gneisses, West Greenland. *Earth Planet. Sci. Lett.* **55**, 150–6.

Pettke, T., Lee, D.-C., Halliday, A. N. and Rea, D. K. (2002). Radiogenic Hf isotopic compositions of continental aeolian dust from Asia, its variability and its implications for seawater Hf. *Earth Planet. Sci. Lett.* **202**, 453–64.

Piotrowski, A. M., Lee, D.-C., Christensen, J. N. *et al.* (2000). Changes in erosion and ocean-circulation recorded in the Hf isotopic compositions of North Atlantic and Indian Ocean ferromanganese crusts. *Earth Planet. Sci. Lett.* **181**, 315–25.

Russell, W. A., Papanastassiou, D. A. and Tombrello, T. A. (1978). Ca isotope fractionation on the Earth and other solar system materials. *Geochim. Cosmochim. Acta* **42**, 1075–90.

Salters, V. J. M. (1996). The generation of mid-ocean ridge basalts from the Hf and Nd isotope perspective. *Earth Planet. Sci. Lett.* **141**, 109–23.

Salters, V. J. and Hart, S. R. (1989). The hafnium paradox and the role of garnet in the source of mid-ocean-ridge basalts. *Nature* **342**, 420–2.

Salters, V. J. and Hart, S. R. (1991). The mantle sources of ocean ridges, islands and arcs: the Hf-isotope connection. *Earth Planet. Sci. Lett.* **104**, 364–80.

Salters, V. J. M. and White, W. M. (1998). Hf isotope constraints on mantle evolution. *Chem. Geol.* **145**, 447–60.

Salters, V. J. M. and Zindler, A. (1995). Extreme ^{176}Hf/^{177}Hf in the sub-oceanic mantle. *Earth Planet. Sci. Lett.* **129**, 13–30.

Sato J. and Hirose T. (1981). Half-life of ^{138}La. *Radiochem. Radioanal. Lett.* **46**, 145–52.

Scherer, E. E., Cameron, K. L. and Blichert-Toft, J. (2000). Lu–Hf garnet geochronology: closure temperature relative to the Sm–Nd system and the effects of trace mineral inclusions. *Geochim. Cosmochim. Acta* **64**, 3413–32.

Scherer, E. E., Cameron, K. L., Johnson, C. M., Beard, B. L., Barovich, K. M. and Collerson, K. D. (1997). Lu–Hf geochronology applied to dating Cenozoic events affecting lower crustal xenoliths from Kilburn Hole, New Mexico. *Chem. Geol.* **142**, 63–78.

Scherer, E., Munker, C. and Mezger, K. (2001). Calibration of the lutetium–hafnium clock. *Science* **293**, 683–8.

Shimizu, H., Tanaka, T. and Masuda, A. (1984). Meteoritic ^{138}Ce/^{142}Ce ratio and its evolution. *Nature* **307**, 251–2.

Söderlund, U., Patchett, P. J., Vervoort, J. D. and Isachsen, C. E. (2004). The ^{176}Lu decay constant determined by Lu–Hf and U–Pb isotope systematics of Precambrian mafic intrusions. *Earth Planet. Sci. Lett.* **219**, 311–24.

Stevenson, R. K. and Patchett, P. J. (1990). Implications for the evolution of continental crust from Hf isotope systematics of Archean detrital zircons. *Geochim. Cosmochim. Acta* **54**, 1683–97.

Tanaka, T. and Masuda, A. (1982). The La–Ce geochronometer: a new dating method. *Nature* **300**, 515–18.

Tanaka, T., Shimizu, H., Kawata, Y. and Masuda, A. (1987). Combined La–Ce and Sm–Nd isotope systematics in petrogenetic studies. *Nature* **327**, 113–17.

Tanaka, T., Shimizu, H., Kawata, Y. and Masuda, A. (1988). Reply to: Dickin, A. P. (1988). Mantle and crustal Ce/Nd isotope systematics. *Nature* **333**, 403–4.

Tanaka, T., Usui, A. and Masuda, A. (1986). Oceanic Ce and continental Nd: multiple sources of REE in oceanic ferromanganese nodules. *Terra Cognita* **6**, 114 (abstract).

Tatsumoto, M., Unruh, D. M. and Patchett, P. J. (1981). U–Pb and Lu–Hf systematics of Antarctic meteorites. *Nat. Inst. Polar Res. Tokyo.*

Vervoort, J. D. and Blichert-Toft, J. (1999). Evolution of the depleted mantle: Hf isotope evidence from juvenile rocks through time. *Geochim. Cosmochim. Acta* **63**, 533–56.

Vervoort, J. D., Patchett, P. J., Blichert-Toft, J. and Albarède, F. (1999). Relationships between Lu–Hf and Sm–Nd isotopic systems in the global sedimentary system. *Earth Planet. Sci. Lett.* **168**, 79–99.

Vervoort, J. D., Patchett, P. J., Gehrels, G. E. and Nutman, A. P. (1996). Constraints on early Earth differentiation from hafnium and neodymium isotopes. *Nature* **379**, 624–7.

Villa, I. M., Kamber, B. Z. and Nägler, T. F. (2001). Comment on "The Nd and Hf isotopic evolution of the mantle through the Archean. Results from the Isua supracrustals, West Greenland, and from the Birimian terranes of West Africa" by Blichert-Toft *et al.* (1999). *Geochim. Cosmochim. Acta* **65**, 2017–21.

White, W. M. and Patchett, J. (1984). Hf–Nd–Sr isotopes and incompatible element abundances in island arcs: implications for magma origins and crust–mantle evolution. *Earth Planet. Sci. Lett.* **67**, 167–85.

White, W. M., Patchett, J. and Ben Othman, D. (1986). Hf isotope ratios of marine sediments and Mn nodules: evidence for a mantle source of Hf in seawater. *Earth Planet. Sci. Lett.* **79**, 46–54.

10 K–Ar and Ar–Ar dating

Potassium is one of the eight most abundant chemical elements in the Earth's crust and a major constituent of many rock-forming minerals. However, the radioactive isotope, ^{40}K, makes up only 0.012% of total potassium, so it effectively falls in the low-ppm concentration range. ^{40}K exhibits a branched decay scheme to ^{40}Ca and ^{40}Ar. The major branch leads to ^{40}Ca, but in most rocks the daughter product is swamped by common (non-radiogenic) ^{40}Ca, which makes up 97% of total calcium. Because variations in abundance of radiogenic ^{40}Ca are very limited in most rock systems, this method has a restricted application as a dating tool (section 9.5). Only 11% of ^{40}K decays lead to ^{40}Ar, but since this is a rare gas, the radiogenic component is dominant. It makes up 99.6% of atmospheric argon, equal to 0.93% of dry air by volume.

Decay to ^{40}Ar is by three different routes (section 1.3.1), two of which involve capture of an orbital electron by the nucleus. The third route (positron emission) makes up only 0.01% of decays to ^{40}Ar. Therefore, the electron capture (EC) decay constant can be taken to represent all of the routes from ^{40}K to ^{40}Ar. This decay constant has a recommended value of $0.581 \times 10^{-10}\,\mathrm{yr}^{-1}$, equivalent to a half-life of 11.93 Byr (Steiger and Jäger, 1977), based on a weighted mean of the six best counting determinations evaluated by Beckinsale and Gale (1969).

Decay to ^{40}Ca is by emission of a β particle, and the β decay constant has a recommended value of $4.962 \times 10^{-10}\,\mathrm{yr}^{-1}$, equivalent to a half-life of 1.397 Byr. The sum of the decay constants for the two branches yields the total ^{40}K decay constant of $5.543 \times 10^{-10}\,\mathrm{yr}^{-1}$, equivalent to a half-life of 1.25 Byr. The possible need for revision to this value is discussed in section 10.4.3.

10.1 The K–Ar dating method

The fraction of ^{40}K atoms that decay into ^{40}Ar is given by the expression $\lambda_{\mathrm{EC}}/(\lambda_{\mathrm{EC}} + \lambda_{\beta})$. Hence, substituting into the general decay equation [1.10], the growth of ^{40}Ar in a K-bearing rock or mineral can be written as

$$^{40}\mathrm{Ar}_{\mathrm{total}} = {}^{40}\mathrm{Ar}_{\mathrm{I}} + \frac{\lambda_{\mathrm{EC}}}{\lambda_{\mathrm{total}}}\,{}^{40}\mathrm{K}(e^{\lambda_{\mathrm{total}}t} - 1) \qquad [10.1]$$

However, if the system was completely outgassed of Ar at the time of formation, the initial Ar term disappears, and the equation is simplified to

$$^{40}\mathrm{Ar}^{*} = (\lambda_{\mathrm{EC}}/\lambda_{\mathrm{total}})\,{}^{40}\mathrm{K}(e^{\lambda_{\mathrm{total}}t} - 1) \qquad [10.2]$$

where ^{40}Ar* signifies radiogenic argon only. As will be seen below, this is the situation which is normally assumed in K–Ar dating.

10.1.1 Analytical techniques

The isotopic composition of naturally occurring potassium has been found to be effectively constant in all types of rock throughout the Earth, with a few minor exceptions (e.g. Garner *et al.*, 1976). Therefore the ^{40}K content of a mineral or rock is usually found by straightforward chemical analysis for total potassium, followed by multiplication by 1.2×10^{-4} to derive the concentration of the radioactive isotope. Various methods can be used to determine potassium, including ICP-OES (inductively coupled plasma–optical emission spectrometry), X-ray fluorescence, and isotope dilution. In the past, a commonly used method was flame photometry (Vincent, 1960), a form of optical emission spectrometry especially suitable for the alkali metals. This technique was less accurate than isotope dilution but could achieve precisions of about 1% and was quick and inexpensive.

Argon trapped in a geological sample is released and purified in an argon-extraction line, 'spiked' with an enriched isotope, and then fed into a mass spectrometer for isotopic analysis (Fig. 10.1). Samples must have the minimum possible surface area for absorption of atmospheric argon; therefore mineral separates or whole-rock chips are not powdered. After loading the sample(s) in the extraction line, the whole line, and especially the sample itself, must be baked under

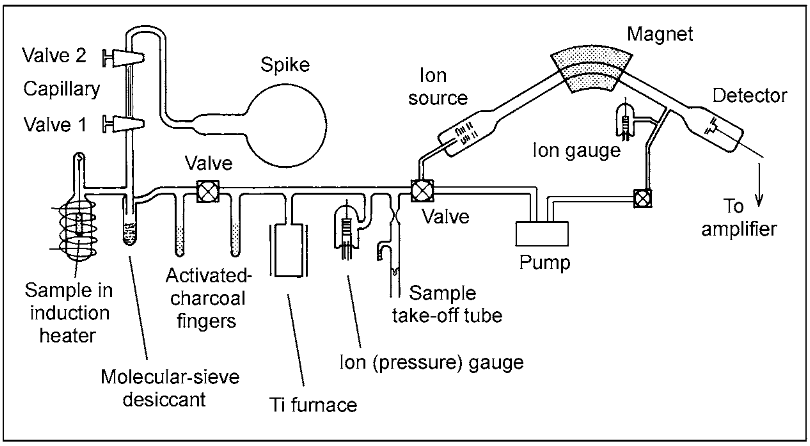

Fig. 10.1. Schematic diagram of an argon extraction line coupled to a static gas mass spectrometer. After Dalrymple and Lanphere (1969).

vacuum to extract all possible atmospheric argon from the system. Next, after isolating the pump, the sample is manoeuvred into a disposable molybdenum crucible, which is positioned in a radio-frequency induction furnace. The crucible is heated to about 1400 °C, whereupon the sample melts and releases all of the trapped gases. These consist mostly of H_2O and CO_2, with a very small amount of argon and other rare gases. All gases except the rare gases can be removed by reaction with titanium vapour in a Ti-sublimation pump or by using a zeolite ‘getter’. Activated charcoal fingers may be used for temporary absorption of gases during their manipulation.

Highly enriched ^{38}Ar spike is usually stored in a large glass reservoir bulb. This is connected to a length of capillary tube of fixed volume, between two valves with low dead-space (Fig. 10.1). The capillary is opened to the reservoir while valve 1 is closed. Valve 2 is then closed, and the known volume of spike between the two valves is added to the sample by opening valve 1. Because the reservoir pressure falls with each gas withdrawal, successive spike aliquots contain smaller and smaller fractions of ^{38}Ar. However, aliquots are periodically calibrated by mixing with a known volume of atmospheric argon and performing an isotope-dilution analysis. The amount of ^{38}Ar spike added to each sample is determined by noting its order in the sequence and interpolating between the calibration runs (Lanphere and Dalrymple, 1966). The amount of argon released from a typical sample of a few hundred milligrams is very small, generally less than 10^{-6} cm^3 at STP (standard temperature and pressure = 25 °C at 1 atm). For this reason the isotopic analysis is performed statically; in other words, the entire sample is fed into the mass spectrometer at once, after isolation from the pumps. The ^{40}Ar/^{36}Ar ratio in the air may be measured between unknown samples as a check on the calibration of the machine, and normally has a value of 295.5 ± 0.5.

Two different types of mass spectrometer are in common use. Modern rare-gas machines tend to be very similar to solid-source TIMS machines, with a high accelerating potential of several kilovolts and peak-switching by changing the magnetic field. The problem with this type of machine is that the high velocities of the ions make them implant into metal components in the vacuum system whenever these are struck by the ion beam. Such ions diffuse back out of the metal surfaces during analysis of the next sample, and this memory effect must be carefully corrected. The effect may be reduced by polishing metal components that the beam is likely to strike. Many older instruments used a low accelerating potential of a few hundred volts and a small permanent-field magnet. The accelerating potential was then switched to focus different nuclides into the collector. This type of machine suffered from very little memory effect but was capable of much poorer precision in the measurement of isotope ratios. Since the source is gaseous, there is no problem of mass-dependent fractionation in either type of machine.

A typical argon isotope mass spectrum is shown in Fig. 10.2. The presence of any ^{36}Ar signal shows that common or non-radiogenic argon is present. This is almost inevitable, because of the great difficulty of removing all atmospheric argon from the system.

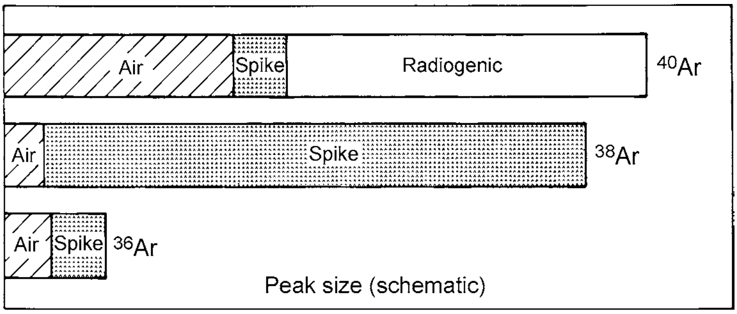

Fig. 10.2. Schematic argon isotope mass spectrum, showing fractions of each peak due to radiogenic Ar (white), spike (stippled) and atmospheric contamination (hatched). Size fractions are not shown to scale. After Dalrymple and Lanphere (1969).

However, if the sample was completely outgassed at the time of its formation, it will not contain any inherited non-radiogenic Ar. In this case the measured ^{40}Ar peak can be corrected for atmospheric contamination by subtracting 295.5 times the ^{36}Ar peak:

$$^{40}\mathrm{Ar}^* = {}^{40}\mathrm{Ar}_{\mathrm{total}} - 295.5\,{}^{36}\mathrm{Ar} \qquad [10.3]$$

A value of 0.063% of atmospheric argon is similarly subtracted from the ^{38}Ar peak. The ^{40}Ar and ^{36}Ar peaks must also be corrected for small fractions of these isotopes in the spike. The amount of radiogenic ^{40}Ar* in the sample is then found by comparison with the size of the net ^{38}Ar peak, formed by a known quantity of spike. (In other words, this is an isotope-dilution determination.) Given the abundances of ^{40}Ar and ^{40}K in the sample, the age is calculated by rearranging equation [10.2]:

$$t = \frac{1}{\lambda_{\mathrm{total}}} \ln\left(\frac{^{40}\mathrm{Ar}^*}{^{40}\mathrm{K}} \frac{\lambda_{\mathrm{total}}}{\lambda_{\mathrm{EC}}} + 1 \right) \qquad [10.4]$$

K–Ar ages depend on closed-system behaviour of the sample for K and Ar throughout its history. In addition, it is necessary to assume that the sample contains no initial argon (usually called ‘excess’ argon), because this might have a ^{40}Ar/^{36}Ar ratio different from that of atmospheric argon. This would lead to a mixture with indeterminate ^{40}Ar/^{36}Ar ratio that could not be corrected for atmospheric contamination.

The ^{36}Ar/^{40}Ar ratio must be analysed to very high precision because the atmospheric Ar correction magnifies any errors in this measurement by a factor of nearly 300. The importance of this effect is shown in Fig 10.3, where the effect of error in the measurement of ^{36}Ar is shown in terms of the resulting error on the calculated age (Cox and Dalrymple, 1967). Once atmospheric contamination exceeds 70% of total argon, errors in ^{36}Ar have serious consequences for the age measurement. This correction is not a problem for old and/or K-rich samples, but is the principal limitation to dating young material.

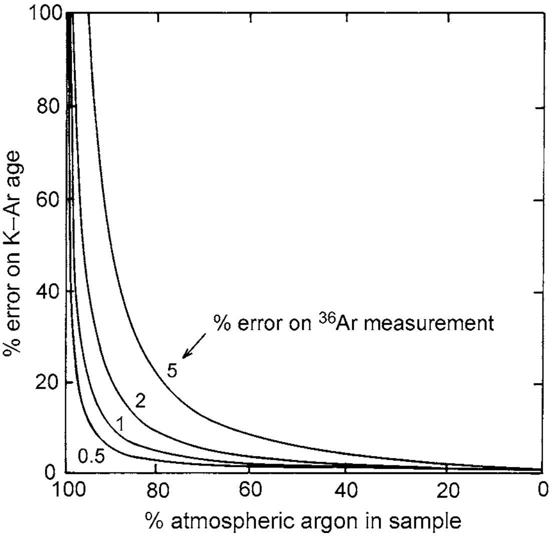

Fig. 10.3. Error magnification in K–Ar dating (*y* axis) resulting from atmospheric argon contamination. Curves are calculated for 0.5%, 1%, 2% and 5% errors in the measurement of ^{36}Ar. After Cox and Dalrymple (1967).

Since 1967, great improvements in measurement precision have been made, allowing the dating of very young rocks. However, Mussett and Dalrymple (1968) showed that volcanic rocks contain ‘locked-in’ atmospheric (non-radiogenic) argon, some of which cannot be removed even by baking in a vacuum. Hence, even with a low-blank analytical system, a small residual atmospheric fraction is almost unavoidable in terrestrial lavas.

10.1.2 Inherited argon and the K–Ar isochron diagram

Since ^{36}Ar is used as a monitor of atmospheric contamination, there is no facility in K–Ar dating to correct for initial argon incorporated into minerals or rocks at the time of crystallisation. Hence, it must be assumed to be absent. However, early work by Damon and Kulp (1958) showed the presence of initial or 'excess' argon in beryl, cordierite and tourmaline. Since these minerals all have a ring structure, it was initially assumed that the stacking of rings created channels in which excess argon inherited from fluids could reside. Hence, Damon and Kulp suggested that this problem might also occur in hornblende, where partial vacancy of the alkali-cation site might provide a location for excess argon.

However, excess argon was subsequently also found in pyroxenes by Hart and Dodd (1962). Since the pyroxene structure does not have any suitable voids for accommodation of argon, Hart and Dodd argued that it must be located in crystal dislocations and defect structures. This implies that excess argon is a product of the environment of crystallisation rather than the host mineral. Hart and Dodd noted that their analysed pyroxenes were from originally deep-seated rocks, unlike the volcanic or shallow intrusive rocks normally used in K–Ar dating. Hence they warned that excess argon might be a common feature in samples from deep-seated (plutonic) environments.

The known occurrence of excess argon was extended to submarine lavas by Dalrymple and Moore (1968). They dated glassy pillow rims and whole-rock pillow cores from flows at 500–5000 m depth on the northeast ridge of Kilauea volcano, Hawaii. Various geological lines of evidence suggested a historical age for the samples, but K–Ar ages of up to 43 Myr were found. Furthermore, a series of samples from rim to interior of one pillow (from 2590 m depth) showed an inverse correlation of apparent K–Ar age with distance from the rim (Fig. 10.4). The results were attributed to entrapment of initial or excess argon that had been inherited from the mantle source by the magmas. Dalrymple and Moore concluded that because these magmas were quenched under substantial hydrostatic pressure, inherited argon was not completely outgassed at the time of eruption, as usually occurs in terrestrial lavas. It was subsequently able to escape from the slowly crystallising core of the pillow, but was retained in the glassy rim.

Even some sub-aerially erupted lavas were subsequently found to contain inherited argon. For example, McDougall *et al.* (1969) encountered measurable radiogenic ^{40}Ar contents in historical-age sub-aerial basalts from New Zealand. Lavas shown by ^{14}C dating of wood inclusions to be less than 1 kyr old nevertheless gave K–Ar ages of up to 465 kyr. This led McDougall *et al.* to consider whether such cases of inherited argon could be detected and/or corrected.

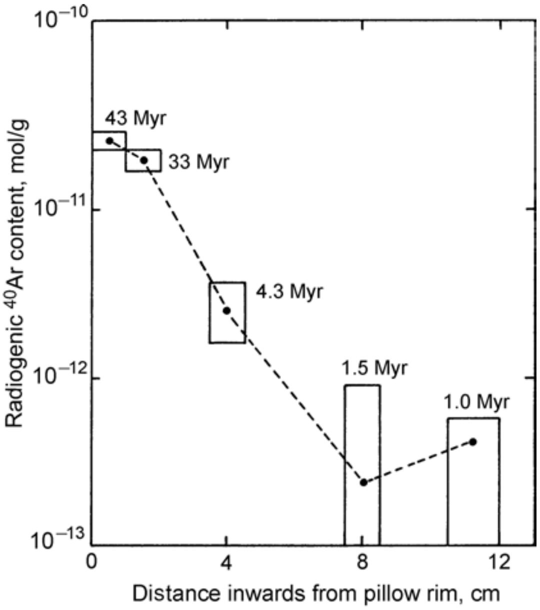

Fig. 10.4. Contents of (excess) radiogenic ^{40}Ar in submarine pillows from Hawaii, plotted against inward distance from the pillow rim. Apparent K–Ar ages for each sample are noted in Myr. After Dalrymple and Moore (1968).

They proposed that the raw ^{40}Ar signal (uncorrected for atmospheric contamination) be divided by ^{36}Ar and plotted against the K/Ar ratio to form an isochron diagram analogous to that for Rb–Sr (Fig. 10.5). This is achieved by expanding the initial Ar term in [10.1] to include both atmospheric and excess components, and by dividing throughout by ^{36}Ar:

$$\left(\frac{^{40}\mathrm{Ar}}{^{36}\mathrm{Ar}}\right)_{\mathrm{total}} = \left(\frac{^{40}\mathrm{Ar}}{^{36}\mathrm{Ar}}\right)_{\mathrm{atm+excess}} + \frac{^{40}\mathrm{K}}{^{36}\mathrm{Ar}}\,\frac{\lambda_{\mathrm{EC}}}{\lambda_{\mathrm{EC}}+\lambda_{\beta}}\left(e^{\lambda_{\mathrm{total}}t}-1\right) \qquad [10.5]$$

This equation has the form

$$y = c + xm \qquad [10.6]$$

When a suite of samples is analysed from a single completely outgassed system such as a lava flow, the *c* term is entirely atmospheric. Therefore, the analysed points,

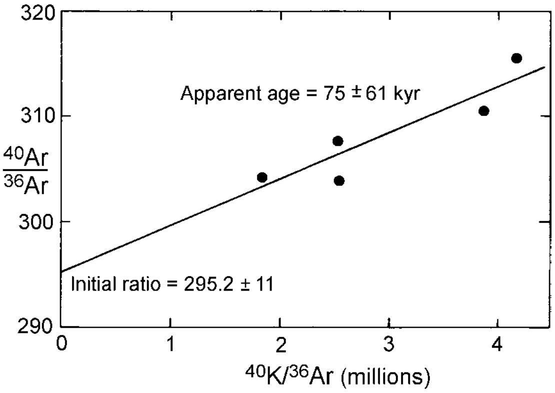

Fig. 10.5. K–Ar isochron plot for a lava of historical age from Mount Wellington, New Zealand, showing a best-fit slope age of 75 kyr. After McDougall *et al.* (1969).

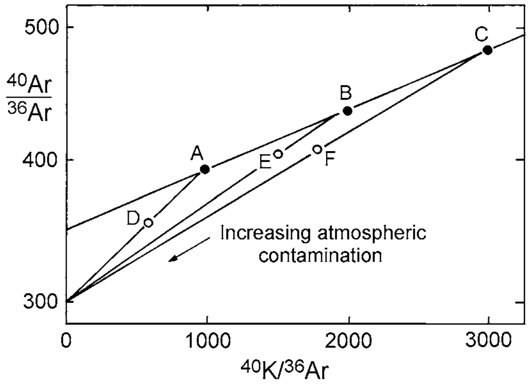

Fig. 10.6. Schematic K–Ar isochron diagram to show the effect of mixing inherited and radiogenic argon (A, B and C), coupled with variable atmospheric contamination (D, E and F). After Roddick and Farrar (1971).

when plotted on an isochron diagram, should define a straight line with an intercept of 295.5, whose slope yields the age of eruption. In fact, this array is merely a mixing line between the samples and atmospheric argon. When the atmospheric correction is performed on a single analysis, we effectively make 295.5 the origin and determine the slope.

In the case studied by McDougall *et al.* (1969), the lavas are of approximately zero age. Hence, the analyses which make up their 'isochrons' (e.g. Fig. 10.5) represent argon trapped in the magma and later variably mixed with atmospheric argon. McDougall *et al.* speculated that the trapped argon might originate from partially digested crustal xenocrysts.

Roddick and Farrar (1971) considered the case of a geologically old sample suite displaying both inherited argon and atmospheric contamination (Fig. 10.6). With inherited and radiogenic argon only, the array ABC is defined, but if variable atmospheric contamination occurs, a scatter (DEF) may result. In principle, a good linear array on the K–Ar isochron diagram should indicate that both the age and the initial Ar isotope ratio are meaningful. However, it may be possible for the slope of the line to swing round in a systematic way due to complex mixing processes, so that it yields a good array of meaningless slope. Nevertheless, the isochron diagram is a useful test of K–Ar data where the presence of inherited Ar is suspected.

Lanphere and Dalrymple (1976) drew a distinction between inherited argon and excess argon. They defined the former as argon that 'originates within mineral grains by decay of ^{40}K prior to the rock-forming event'. Hence, this definition applies to the examples given above. However, excess argon has a wider definition that also includes sources of extraneous argon that diffuse into a system from outside. Lanphere and Dalrymple (1971; 1976) pioneered the use of the ^{40}Ar/^{39}Ar method to identify excess argon in rocks (section 10.2.5).

10.1.3 Argon loss

The K–Ar method is unique amongst the major radiometric dating methods in having a gaseous daughter product. This means that the K–Ar system reacts differently from lithophile isotope systems such as Rb–Sr in response to thermal and hydrothermal events. Because argon is a non-reactive gas, its partition into the fluid phase is limited. Therefore, the K–Ar system may be more resistant than Rb–Sr to hydrothermal metamorphism. On the other hand, no mineral phase preferentially takes up argon when it is lost from the mineral where it was originally produced. This means that in K–Ar dating, whole-rock analysis confers no additional resistance to metamorphic re-setting (as it does for the Rb–Sr method). On the contrary, in K–Ar analysis a whole-rock sample is only as resistant to re-setting as its *least* retentive phase. Consequently whole-rock K–Ar analysis is a last resort, when all mineral phases in the rock are too fine-grained for mineral separation.

A good comparison of argon loss from various minerals during a thermal event is provided by contact metamorphism associated with the Eldora stock in the Colorado Front Ranges (Hart, 1964). The 54-Myr-old quartz monzonite stock is intruded into roughly 1350-Myr-old amphibolites and schists. Hart analysed biotite, hornblende and K-feldspar at increasing

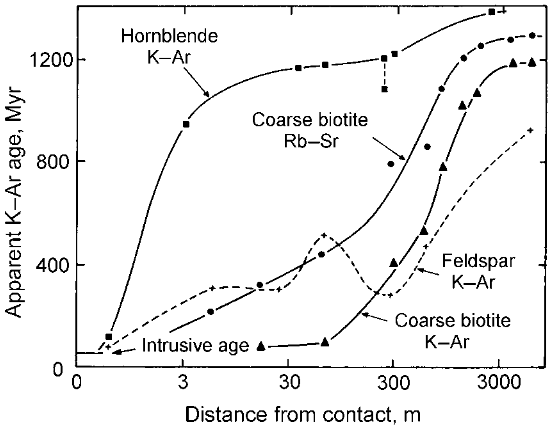

Fig. 10.7. Plot of apparent K–Ar mineral ages against outward distance from the contact of the 60-Myr-old Eldora stock, Colorado. After Hart (1964).

distances from the intrusive contact (Fig. 10.7), and found that despite the limited extent of petrographic alteration, K–Ar mineral ages were re-set at large distances from the stock. Hornblende displayed good Ar-retention properties, with loss of argon confined primarily to within ten feet (about 3 m) of the contact. However, coarse biotites were largely re-set at distances up to 1000 ft (300 m) from the contact, while K-feldspars had lost a substantial fraction of argon even 20 000 ft (6 km) from the contact. The latter can hardly be said to be within the thermal aureole of the stock, and reflects the now widely accepted view that K-feldspars may lose argon by diffusion even at ambient temperatures. It is now recognised that systems such as these, that have suffered open-system behaviour of argon, must be studied by the ^{40}Ar–^{39}Ar technique (see below).

10.2 The ^{40}Ar–^{39}Ar dating technique

The very different chemical affinities of potassium and argon cause limitations in the K–Ar dating method. However, these limitations can be overcome by converting ^{39}K into ^{39}Ar in a nuclear reactor, by irradiation with fast neutrons. This causes an n, p (neutron capture, proton emission) reaction

$${}^{39}_{19}\text{K} + \text{n} \rightarrow {}^{39}_{18}\text{Ar} + \text{p}$$

This reaction permits the potassium determination for a K–Ar age to be made as part of the argon isotope analysis, thus opening up many new opportunities for the K–Ar dating technique.

10.2.1 ^{40}Ar–^{39}Ar measurement

The comparatively long half-life of ^{39}Ar ($t_{1/2}$ = 269 yr) means that it can be regarded as a stable isotope for mass-spectrometric analysis, which was first applied to ^{40}Ar–^{39}Ar dating by Merrihue and Turner (1966). It is interesting to note, however, that the concept of combined irradiation and mass-spectrometric analysis was applied to the I–Xe system in meteorite studies five years earlier (section 15.3).

The production of ^{39}Ar from ^{39}K during the irradiation is expressed as

$${}^{39}\text{Ar} = {}^{39}\text{K}\,\Delta t \int_{\min e}^{\max e} \varphi_e \sigma_e \, \mathrm{d}e \qquad [10.7]$$

where Δt is the irradiation time, φ_e is the flux density of neutrons with energy e, and σ_e is the capture cross-section of ^{39}K for neutrons of energy e. The production must be integrated over the total range of neutron energies, which is a very difficult calculation in practice. Therefore, the normal procedure is to use a sample of known age as a flux monitor.

Taking the K–Ar decay equation [10.2], which is reproduced here,

$${}^{40}\text{Ar}^* = (\lambda_{\text{EC}}/\lambda_{\text{total}})\,{}^{40}\text{K}(\mathrm{e}^{\lambda_{\text{total}}t} - 1)$$

and dividing through on both sides by [10.7] yields

$$\frac{{}^{40}\text{Ar}^*}{{}^{39}\text{Ar}} = \left(\frac{\lambda_{\text{EC}}}{\lambda_{\text{total}}} \frac{{}^{40}\text{K}}{{}^{39}\text{K}\,\Delta t \int \varphi_e \sigma_e \, \mathrm{d}e}\right)(\mathrm{e}^{\lambda_{\text{total}}t} - 1) \qquad [10.8]$$

However, the term in large parentheses is the same for sample and standard. Therefore it is customary to refer to it as a single quantity, whose reciprocal J can be evaluated as a constant (Mitchell, 1968). Hence, for the standard,

$$J = \frac{\mathrm{e}^{\lambda t} - 1}{{}^{40}\text{Ar}^*/{}^{39}\text{Ar}} \qquad [10.9]$$

where t is known. Rearranging [10.8] for samples of unknown age yields

$$t = \frac{1}{\lambda} \ln\left[J\left(\frac{{}^{40}\text{Ar}^*}{{}^{39}\text{Ar}}\right) + 1\right] \qquad [10.10]$$

In order to obtain an accurate value of J for each unknown sample, several standards need to be run, representing known spatial positions relative to the unknown samples within the reactor core (Mitchell, 1968). Hence J values for each of the samples can be interpolated.

10.2.2 Irradiation corrections

During the irradiation of ^{39}K, interfering Ar isotopes are generated from calcium and other potassium isotopes by neutron reactions (Fig. 10.8). Brereton (1970) and Dalrymple and Lanphere (1971) made detailed studies of the magnitudes of these effects and their correction. However, it appears in practice that many workers have simply ignored the interferences.

Mitchell (1968) suggested that acceptable results could be obtained without interference correction on minerals over 1 Myr old, provided that the K/Ca ratio was greater than unity. In such circumstances, a simple atmospheric correction may be considered adequate:

$$\frac{^{40}\mathrm{Ar}^*}{^{39}\mathrm{Ar}} = \left(\frac{^{40}\mathrm{Ar}}{^{39}\mathrm{Ar}}\right)_{\mathrm{meas}} - 295.5\left(\frac{^{36}\mathrm{Ar}}{^{39}\mathrm{Ar}}\right)_{\mathrm{meas}} \qquad [10.11]$$

Turner (1971a) showed that Ar interferences could be kept to a minimum by variation of certain irradiation parameters. The principal interferences which must be considered (Fig. 10.8) are

$$\begin{aligned} &^{40}\mathrm{K}\ \ \mathrm{n,p} &&\rightarrow\ ^{40}\mathrm{Ar} \\ &^{40}\mathrm{Ca}\ \mathrm{n,n}\alpha &&\rightarrow\ ^{36}\mathrm{Ar} \\ &^{42}\mathrm{Ca}\ \mathrm{n},\alpha &&\rightarrow\ ^{39}\mathrm{Ar} \end{aligned}$$

Other interferences occur but may be omitted as insignificant.

The approaches suggested by Turner were the following:

(1) Optimisation of neutron dose according to age (Fig. 10.9a) to maximise ^{39}Ar production, without generating significant artificial ^{40}Ar from ^{40}K. (K content is not considered as a factor because the intended target and interfering one are both K isotopes.)
(2) Optimisation of sample size according to age and K content in order to obtain the total ^{40}Ar and ^{39}Ar yields necessary to achieve the desired counting statistics during mass-spectrometric analysis.
(3) The K/Ca ratio in the sample also dictates an optimum neutron dose to generate enough ^{39}Ar without significant interfering ^{36}Ar (Fig. 10.9b). However, the optimum values largely overlap with those prescribed by criterion (1).

Theoretically, very young rocks can be activated with less than 1% interferences by following these rules. However, this may require an immense sample size. In practice, a better alternative may be to use more irradiation but apply corrections. The complete correction formula (in terms of Ar isotope ratios) is

$$\frac{^{40}\mathrm{Ar}^*}{^{39}\mathrm{Ar}} = \left[\frac{^{40}\mathrm{Ar}}{^{39}\mathrm{Ar}} - 295.5\frac{^{36}\mathrm{Ar}}{^{39}\mathrm{Ar}} + 295.5\frac{^{37}\mathrm{Ar}}{^{39}\mathrm{Ar}}\left(\frac{^{36}\mathrm{Ar}}{^{37}\mathrm{Ar}}\right)_{\mathrm{Ca}} - \left(\frac{^{40}\mathrm{Ar}}{^{39}\mathrm{Ar}}\right)_{\mathrm{K}}\right] \Big/ \left[1 - \frac{^{37}\mathrm{Ar}}{^{39}\mathrm{Ar}}\left(\frac{^{39}\mathrm{Ar}}{^{37}\mathrm{Ar}}\right)_{\mathrm{Ca}}\right] \qquad [10.12]$$

where ^{37}Ar/^{39}Ar is the interference monitor ratio measured for the unknown, which must be corrected for decay of ^{37}Ar from the time of irradiation until analysis ($t_{1/2}$ = 35 days); and $(^{36}\mathrm{Ar}/^{37}\mathrm{Ar})_{\mathrm{Ca}}$, $(^{39}\mathrm{Ar}/^{37}\mathrm{Ar})_{\mathrm{Ca}}$ and $(^{40}\mathrm{Ar}/^{39}\mathrm{Ar})_K$ are production ratios of Ar isotopes from the subscripted elements. These production ratios are determined by irradiating pure salts of Ca and K, respectively, in the reactor of interest, and are characteristic of the neutron flux of that reactor. Values for these production ratios measured by various authors for different reactors have typical ranges of 2.1–2.7, 6.3–30 and 0.006–0.031, respectively (Dalrymple and Lanphere, 1971).

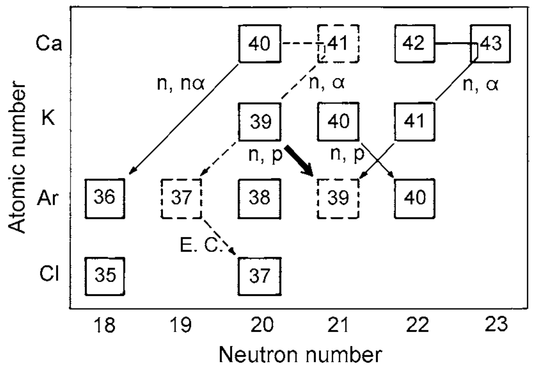

Fig. 10.8. Part of the chart of the nuclides in the region of potassium, showing the production reaction (heavy arrow) and major interfering reactions (solid) during neutron activation. The dashed reaction to ^{37}Ar is the interference monitor. Data from Mitchell (1968).

10.2.3 Step heating

Because the potassium signature of a sample is converted *in situ* into an argon signature by the 40–39 technique, it is possible to liberate argon in stages

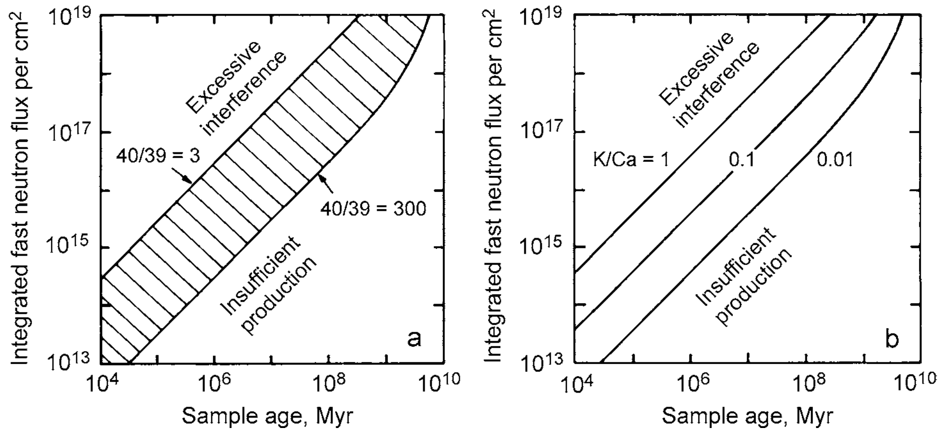

Fig. 10.9. Optimisation of neutron dose for (a) K content and (b) K/Ca ratio. The hatched area in (a) and bold lines in (b) indicate regions of acceptable compromise between sufficient ^{39}Ar production and minimal ^{40}Ar or ^{36}Ar interference in typical rocks. After Turner (1971a).

from different domains of the sample and still recover full age information from each step. Merrihue and Turner (1966) demonstrated the effectiveness of this 'step-heating' technique in their original Ar–Ar dating study of meteorites, adapting the method from its previous application to I–Xe analysis of meteorites (section 15.3.1).

The great advantage of the step-heating technique over the conventional 'total-fusion' technique is that progressive outgassing allows the possibility that anomalous sub-systems within a sample may be identified, and, ideally, excluded from an analysis of the 'properly behaved' parts of the sample. This can apply both to separated minerals and to whole-rock samples. Most commonly the technique is used to understand samples that have suffered argon loss, but it may also be a help in interpreting samples with inherited argon.

In the case of partially disturbed systems, the domains of a sample that are most susceptible to diffusional argon loss (such as the rim of a crystal) should be outgassed at relatively low temperatures, whereas domains with tightly bound argon (which are more resistant to disturbance) should release argon at higher temperature. In order to understand the history of disturbed samples, results of the step-heating analysis are normally presented in one of two ways: as a K–Ar isochron diagram, analogous to a suite of samples analysed by conventional K–Ar; or as an age-spectrum plot.

Step-heating results from the meteorite Bjurbole (Merrihue and Turner, 1966) are plotted on an isochron diagram in Fig. 10.10. The straight-line array indicates a simple one-stage closed-system history for the meteorite. However, the initial ^{40}Ar/^{36}Ar ratio may be only partially meaningful, since it is a mixture of initial Ar and atmospheric contamination. The isochron plot can be useful to see the relative amounts of radiogenic argon and atmospheric/inherited argon in the sample. However, it conceals one of the most useful pieces of information about a step-heating analysis, which is the position of each argon-release step in the overall heating experiment. This information is displayed in the argon spectrum plot.

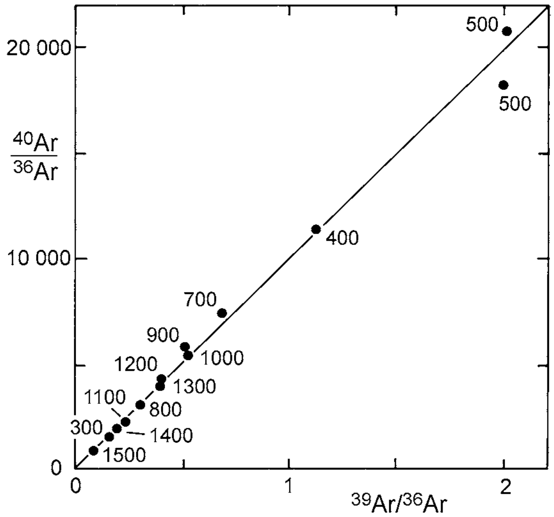

Fig. 10.10. Step-heating data for the Bjurbole meteorite presented on the Ar–Ar isochron diagram. Numbers by data points signify temperatures of each release step in °C. After Merrihue and Turner (1966).

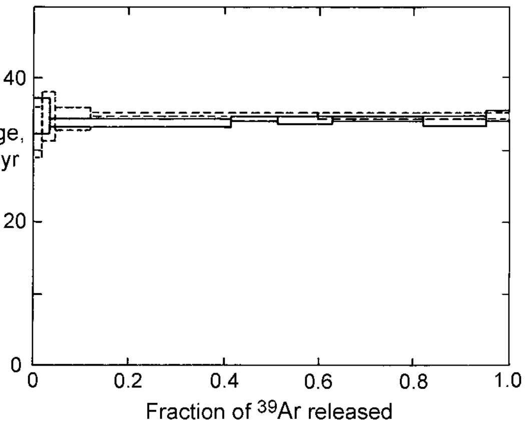

Fig. 10.11. Ideal ^{40}Ar/^{39}Ar age spectra for two Texas tektites, distinguished by solid and dashed boxes. After York (1984).

To construct a spectrum plot, the size of each gas release at successively higher temperature is measured in terms of the magnitude of the ^{39}Ar ion beam produced. Each gas release can then be plotted as a bar, whose length represents its volume as a fraction of the total ^{39}Ar released from the sample, and whose value on the y axis is the corrected ^{40}Ar/^{39}Ar ratio from equation [10.12]. The latter is proportional to age, which is sometimes plotted on a log scale, and sometimes linear. Determination of a reliable crystallisation age from the spectrum plot depends on the identification of an age 'plateau'. A rigorous criterion for a plateau age is the identification of a series of adjacent steps that together comprise more than 50% of the total argon release, each of which yields an age within two standard deviations of the mean (Dalrymple and Lanphere, 1974; Lee *et al.* 1991). However, plateaus have been 'identified' in many instances on the basis of weaker evidence.

The age spectrum plot displays the ideal behaviour of the K–Ar system in tektite glasses. These are objects that were completely melted during flight through the atmosphere and then rapidly quenched on landing. Thus, young tektites that have not been affected by weathering yield perfect plateaus (Fig. 10.11). However, the most useful application of the 40–39 method is on samples with a complex geological history that *does* involve secondary argon loss.

10.2.4 Argon-loss events

In order to assess the usefulness of 40–39 dating on disturbed systems, Turner *et al.* (1966) applied the method to chondritic meteorites. Many of these objects yield conventional K–Ar ages below 4.5 Byr, with U–He ages clustering around 500 Myr (Anders, 1964). For example, step-heating results from a whole-rock sample of the Colby meteorite generate a complex age spectrum (Fig. 10.12), which was attributed to argon loss at about 500 Myr (Turner *et al.*, 1966; Turner, 1968).

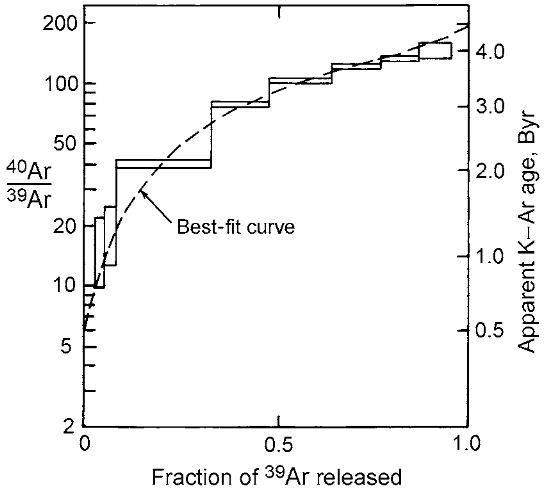

Fig. 10.12. The 40–39 argon-release pattern for the Colby meteorite, showing evidence for disturbance after formation. The best-fit curve is consistent with a model in which 40% of argon was lost during a thermal event (see below). After Turner (1968).

Turner *et al.* suggested that when these meteorites were subjected to an ancient heating event (possibly in a collision between planetesimals), Ar loss occurred from the surface of mineral grains, and its transport within grains was by volume diffusion. This argon-loss model is illustrated schematically in Fig. 10.13. Turner *et al.* argued that step-heating analysis of the sample in the vacuum system would mimic the natural thermal event, so that domains near the surface of minerals, which had suffered geological disturbance, would outgas first in the experiment. In contrast, domains near the cores of grains would be resistant to geological disturbance, and would also outgas at the highest temperatures in the laboratory. (Although these meteorites are chondrites, it is the minerals in the chondrules that retain argon, rather than the chondrules themselves.)

In order to test their diffusion model, Turner *et al.* calculated theoretical age spectrum plots, assuming that the meteorites were formed at 4500 Myr and metamorphosed in a single event at 500 Myr. Argon loss was modelled by assuming volume diffusion from spherical

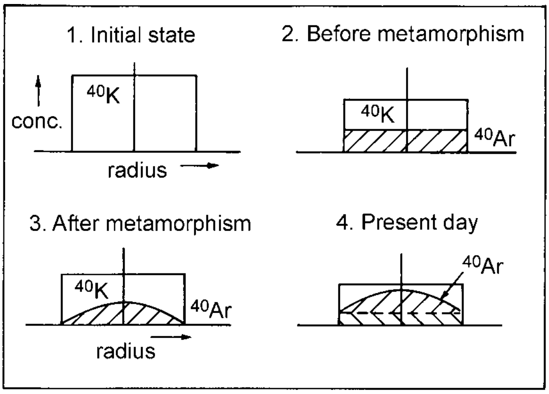

Fig. 10.13. Schematic illustration of the geological history of a mineral grain in a partially disturbed meteorite: (1) at 4500 Myr; (2) 500 Myr ago, before the thermal event; (3) immediately after the event; and (4) at the present day. After Turner (1968).

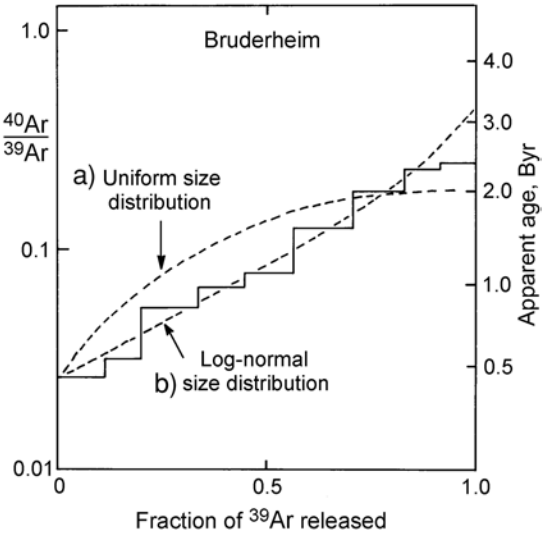

Fig. 10.14. Argon-release profile of the Bruderheim meteorite, compared with calculated argon-loss profiles from spherical mineral grains formed at 4.5 Byr and disturbed at 0.5 Byr: (a) assuming a uniform size distribution; and (b) a log-normal size distribution with $\sigma = 0.20$. After Turner (1968).

K-bearing mineral grains (probably mainly feldspar). The results of two different models are compared with the measured argon-release profile of the Bruderheim meteorite in Fig. 10.14. The first model assumed that argon was lost from spherical grains of uniform size, but this gave a bad fit to the measured profile (curve a). However, thin-section analysis of the meteorite revealed the existence of variably sized feldspar grains. Therefore, Turner *et al.* calculated the result of diffusion of argon from grains with a log-normal size distribution. This model generates a family of solutions according to the amount of grain-size variation allowed. Curve b in Fig. 10.14 shows the best result, assuming a standard deviation (σ [log radius]) of 0.20, equivalent to four-fifths of grains falling within a factor of two from the mean radius.

The shape of best-fitting curve in Fig. 10.14 is also dependent on the fraction of total Ar that was lost in the heating event. Thus, the concave upwards shape of curve b indicates that Bruderheim suffered more than 80% argon loss. In this case the low-temperature part of the profile yields the age of metamorphism (0.5 Byr) but the formation age is lost because even the highest-temperature release steps give ages well below 4.5 Byr. On the other hand, the shape of the Colby release profile (Fig. 10.12) approximates to about 40% argon loss, so that the high-temperature argon-release steps still preserve an indication of the age of formation. For samples that lost less than 20% (not shown), the high-temperature plateau still records a good crystallisation age but the metamorphic age is badly constrained.

The relatively good agreement between the analysed and the log-normal model pattern in Fig. 10.14 suggests that the diffusional loss mechanism is a good description of the thermal disturbance of meteorites. This might be expected, since both the geological event and laboratory measurements were based on heating of anhydrous phases in a vacuum. Turner (1972) demonstrated a similar good fit to the diffusional model for experimental data from a lunar anorthosite. In contrast, terrestrial 40–39 dating generally involves hydrated minerals such as biotite and hornblende. In this case, the diffusional argon-loss mechanism might not provide such an accurate model. An assessment can be made by examining 40–39 data for the Eldora stock (Berger, 1975), for which conventional K–Ar data were described above. Figure 10.15 shows age spectrum plots for hornblendes, biotites and feldspars in the vicinity of the stock.

Of the three minerals studied, hornblende (Figs. 10.15a and b) displays the type of pattern most similar to Turner's thermal-diffusion degassing model, although this resemblance may be misleading. The most distant sample (not shown) yields an excellent plateau age of about 1400 Myr. Samples at 1130, 950 and 248 ft (about 350, 290 and 75 m) display serious Ar loss from the outside of grains, but approach the 'true' age in the highest-temperature fractions. However, Berger recognised that the pattern of Ar loss might reflect alteration to biotite, rather than diffusional loss of Ar from

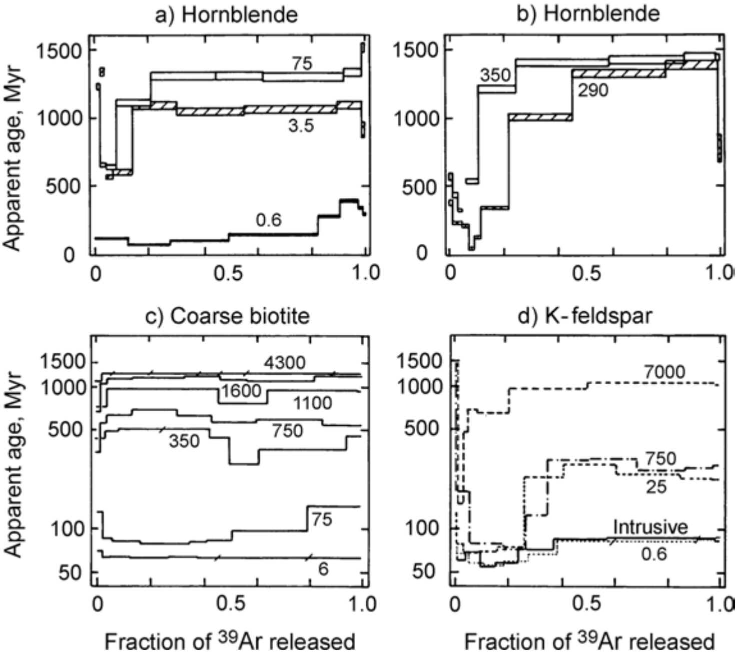

Fig. 10.15. Ar–Ar age spectrum plots for mineral phases at different distances from the Eldora stock. Figures beside age spectra indicate distances in metres: (a) and (b) a hornblende, (c) biotite and (d) K-feldspar. Release steps with identical ages are separated by slashes. After Berger (1975).

hornblende. This interpretation is supported by dating experiments on synthetic hornblende–biotite mixtures (Rex *et al.*, 1993). Another problematical observation is that the sample 11 ft (3.5 m) from the contact displays an intermediate 'false' plateau of high quality. Finally, the sample 2 ft (0.6 m) from the contact displays a saddle-shaped pattern, in which the lowest-age fraction approaches the age of metamorphism.

Coarse biotite (Fig. 10.15c) behaves somewhat differently. Its maximum age at infinite distance from the stock (1250 Myr) is lower than the hornblende age. At intermediate distances the spectra are irregular, but exhibit a general decrease in 'plateau' age as the stock is approached. Hence, it appears that biotites can be partially but uniformly outgassed, possibly because of enhanced diffusion parallel to the cleavage. Finally, K-feldspar suffers irregular and disastrous Ar losses, as is known from conventional K–Ar analysis (Fig. 10.15d).

Berger concluded that hornblendes were able to generate plateaus of high quality that were nevertheless meaningless. This may make hornblende a dangerous material on which to base geological interpretations of age, in the absence of independent confirmatory evidence. On the other hand, partially re-set biotites were always identifiable by their irregular patterns, making biotite ages a more reliable tool for age interpretation. The exact meaning of the plateaus in the biotite and hornblende samples distant from the stock is equivocal, since the country-rocks are paragneisses with a long history of thermal events. Subsequent studies have indeed generated many examples of meaningless plateaus in hornblende and, more rarely, in biotite.

10.2.5 Excess argon

As well as detecting argon loss, step-heating analysis can also be used to evaluate cases in which excess argon is present in a ^{40}Ar–^{39}Ar analysis. Following early work by Lanphere and Dalrymple (1971), a more detailed examination of this problem was made by Lanphere and Dalrymple (1976). In this study, step-heating analyses were done on separated mineral phases from several rocks that were known from earlier work to contain excess (inherited) argon. The data were presented on K/Ar isochron diagrams and age spectrum plots for comparison. The example shown in Fig. 10.16 (a and b) comes from a sample of Mg-rich biotite separated from a kimberlite dyke that intrudes

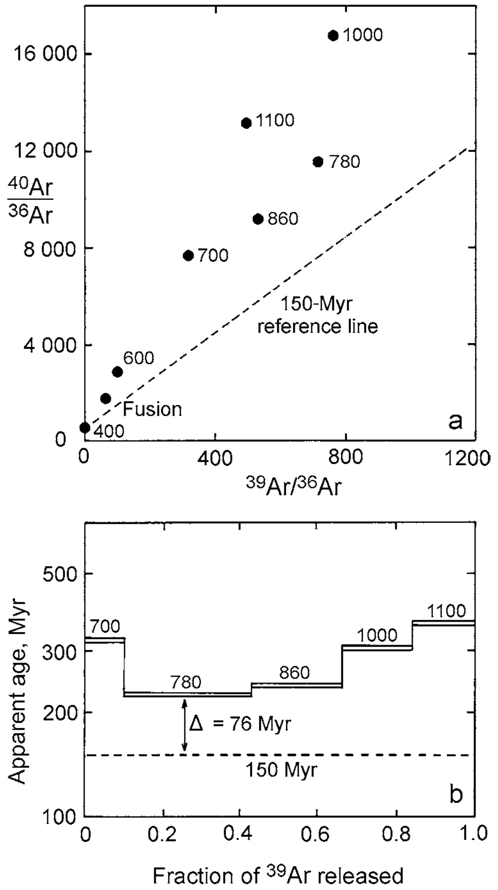

Fig. 10.16. Comparison between the K/Ar isochron plot and age-spectrum plot for 150-Myr-old biotite with excess argon. Note the characteristic 'saddle-shaped' profile. Numbers indicate the temperature of each heating step in °C. After Lanphere and Dalrymple (1976).

Devonian sediments in New York state. Results of previous studies had suggested that these minerals might be xenocrysts, since K–Ar ages were variable.

On the K–Ar isochron diagram, it can be seen that the data scatter badly above a 150-Myr reference line. This line was based on the estimated age of the kimberlite, with an intercept equal to the atmosphere point. The scatter of the data provides evidence of excess argon, but is not further diagnostic. However, when the data are plotted on the spectrum plot, they form a 'saddle-shaped' pattern that was found to be characteristic of all of the samples with excess argon analysed by Lanphere and Dalrymple (1976). Unfortunately, the minimum age from the saddle does not give the age of intrusion, since it is still above this estimated age. Therefore, such minima must be regarded only as maximum ages for the rock, as argued by Kaneoka (1974).

In seeking an explanation for the saddle-shaped age spectrum associated with excess (inherited) argon, Kelley (2002) suggested that this feature was caused by inclusions of various types. For example, fluid inclusions in mineral grains are expected to release argon at low temperature, whereas mineral inclusions may release argon at high temperature. A special case of the former type is exhibited by anorthoclase grains in a lava from Mt Erebus, Antarctica (Esser *et al.*, 1997). The lava is of zero age, but the anorthosite phenocrysts contain excess argon. ^{40}Ar–^{39}Ar analysis showed that this argon was inherited by melt inclusions in the phenocrysts, which were not completely outgassed during eruption. A different type of excess argon observed in some other cases is caused by back-diffusion into a mineral of argon from the surrounding rock. This will be discussed below (section 10.5.2).

10.2.6 Dating paleomagnetism: a case study

Paleomagnetic measurements are a vital tool in the reconstruction of ancient plate-tectonic motions, by comparison of 'apparent polar wander paths' (APWPs) for various continental fragments. One essential step in the construction of an APWP 'track' for a given terrane is to date the time when magnetic remanence was inherited by the rock. However, the magnetic remanence is relatively easily overprinted because it has a comparatively low blocking temperature.

The dating of magnetic remanence took a major step forwards when York (1978) showed from theoretical principles that the processes of thermal demagnetisation and argon loss from a mineral grain were related. This is because they are both almost exclusively the products of thermal kinetics, in contrast to loss of ^{87}Sr (for example), which may be dependent on the presence or absence of aqueous fluids. Hence, the 40–39 method is ideal for dating paleomagnetic remanence.

A good example of such work is provided by the oldest reliable Ar–Ar age for terrestrial rocks (Lopez Martinez *et al.*, 1984), on the Barberton komatiites. Although the time of eruption was constrained by Sm–Nd dating, knowledge of their subsequent thermal history was required in order to interpret paleomagnetic data. Analyses were performed on whole-rock powders, which were irradiated alongside the '3 GR' hornblende standard to determine neutron fluxes. Figure 10.17 shows an age spectrum from the best sample analysed, with three separate release stages. At low temperatures

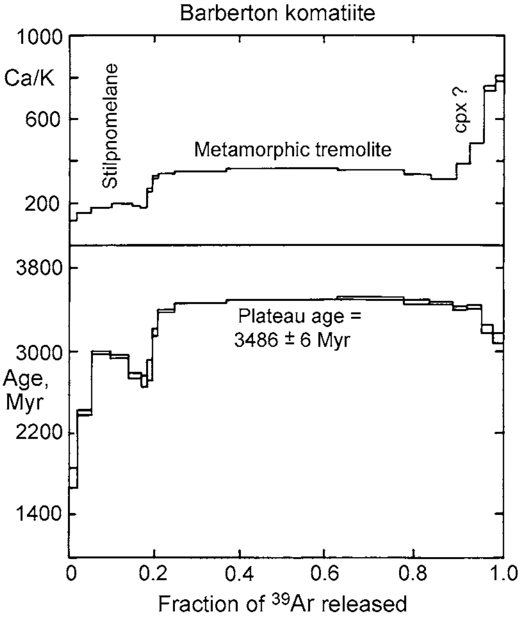

Fig. 10.17. Age spectrum and Ca/K spectrum from Barberton komatiite sample B40A. Mineral phases responsible for gas releases are identified. Error boxes, where visible, are 1σ. After Lopez Martinez *et al.* (1984).

(600–800 °C) and high temperatures (> 1100 °C) argon loss was observed, resulting in low ages. However, at intermediate temperatures (925–1035 °C) a very stable plateau was observed, from which an age of 3486 ± 6 Myr (2σ) was obtained. The integrated (total-fusion) age of 3336 Myr was significantly younger, due to the effects of the low- and high-temperature steps.

The top half of Fig. 10.17 reports Ca/K ratios calculated from the measured ^{37}Ar/^{39}Ar ratio (section 10.2.2), which help characterise the mineral phases in the sample which gave rise to various parts of the age spectrum. By microprobe analysis, the authors were able to deduce that the mineral giving rise to the age plateau was metamorphic tremolite, while the low-temperature, low-Ca/K-ratio phase was stilpnomelane. The high-Ca/K-ratio phase may represent pyroxene relics of the original igneous mineralogy.

A K–Ar isochron diagram was plotted (Fig. 10.18) in order to examine the composition of the non-radiogenic end-member and test for inherited argon. In this case the isochron diagram was plotted in the alternative form ^{36}Ar/^{40}Ar *versus* ^{39}Ar/^{40}Ar (Turner, 1971b). This representation helps to curtail the strong correlation between the two ordinates which occurs with the conventional K–Ar isochron diagram, making error estimates easier. An initial ^{40}Ar/^{36}Ar ratio of 281 ± 18 (2σ) is calculated from the inverse of the y-axis intercept, after expansion of analytical errors to absorb a small amount of geological scatter. This is within error of the atmospheric value of 295.5, so an insignificant amount of initial argon was probably present. These data are from a sample that was stored under vacuum between irradiation and analysis. This was found to be necessary in order to prevent a strong absorption of atmospheric argon by the sample. The reciprocal of the x intercept yields the radiogenic ^{40}Ar/^{39}Ar ratio, equivalent to an age of 3489 ± 68 Myr (2σ). This is almost identical to the plateau age.

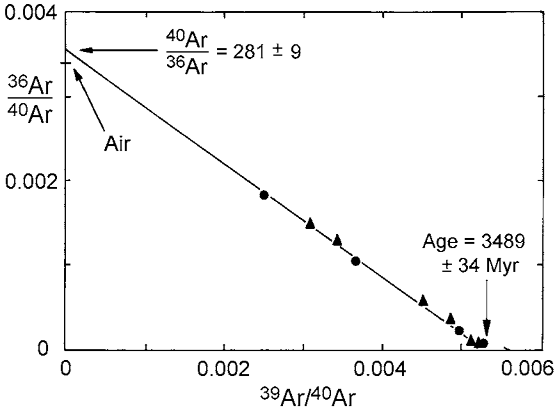

Fig. 10.18. Inverse argon–argon isochron plot for two Ar–Ar runs (●, ▲) on the Barberton komatiite B40A. The age is determined from the intersection on the x axis. After Lopez Martinez *et al.* (1984).

Age spectrum results from the better of two basaltic komatiite samples are shown in Fig. 10.19. In contrast to the komatiites, these samples display significant excess argon in the low- and high-temperature gas releases, with an integrated age of 3778 Myr. Nevertheless, the best plateau age of 3447 Myr is in close agreement with the best komatiite results. The saddle-shaped form is well known for samples containing excess argon.

The Ca/K plot for the basaltic komatiite suggests that the plateau is due to hornblende, while the disturbed parts of the spectrum are again related to stilpnomelane. Lopez Martinez *et al.* speculated that K–Ar systematics in this mineral might have been disturbed during oxidation from ferro- to ferric-stilpnomelane. Since the plateau ages are in all cases identified with metamorphic minerals, they must be dating a thermal event that occurred less than 100 Myr after eruption. Hale (1987) tentatively identified this event as the intrusion of the nearby Threespruit granitoid pluton.

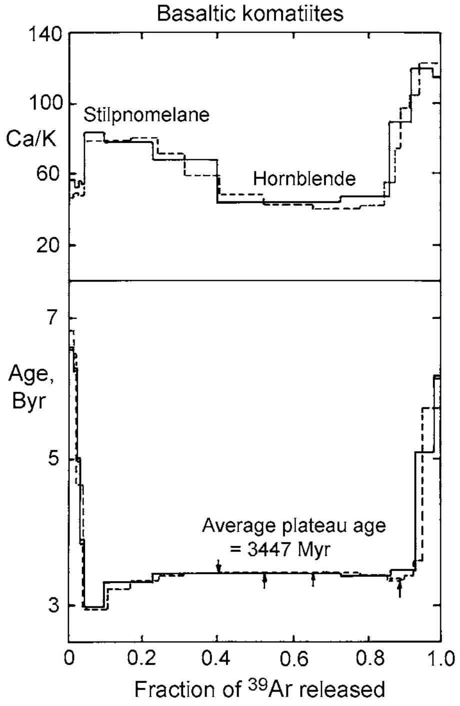

Fig. 10.19. Age and Ca/K spectrum for two runs on a basaltic komatiite, showing evidence of inherited Ar during low- and high-temperature emission from high-Ca/K domains. Arrows separate successive gas releases with identical ages. After Lopez Martinez *et al.* (1984).

10.2.7 ^{39}Ar recoil

The Ar–Ar dating technique was found to be particularly useful for dating small whole-rock samples of lunar material, especially fine-grained mare basalts. The dashed profile in Fig. 10.20 shows a typical release pattern (Turner and Cadogan, 1974), attributed to 8% radiogenic Ar loss from K-rich sites with low Ar retentivity. However, other samples gave either a sharp decrease in apparent age in the high-temperature fractions, or, particularly in fine-grained rocks, a progressive decrease in apparent age over most of the gas release. The latter examples led workers to suspect that re-distribution of Ar was occurring within the sample, possibly during the irradiation process.

It was proposed by Mitchell (in Turner and Cadogan, 1974) that recoil of ^{39}Ar during the n, p reaction from ^{39}K could cause small-scale re-distribution of this nuclide. Turner and Cadogan calculated that this effect could deplete argon from the surface of a K-bearing mineral to a mean depth of 0.08 μm (Fig. 10.21). In order to test the practical effects of this process on fine-grained material, they powdered a sample of medium-grained ferrobasalt to a grain size of 1–10 μm before irradiation. This was expected to bring about 10% of K-bearing lattice sites to within 0.1 μm of a grain boundary, whereupon ^{39}Ar could recoil out of the lattice. It was thought that the ^{39}Ar released would enter low-K minerals such as plagioclase, pyroxene and

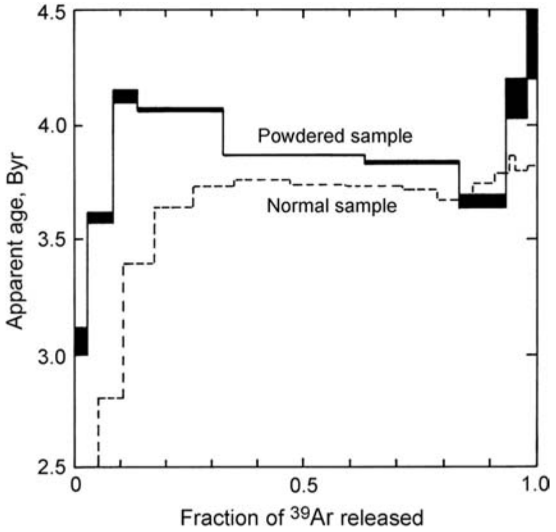

Fig. 10.20. The effect of fine crushing on a 40–39 age spectrum, due to ^{39}Ar recoil. Dashed profile = analysed rock chip of a lunar mare basalt. Solid profile = similar sample activated after fine powdering. After Turner and Cadogan (1974).

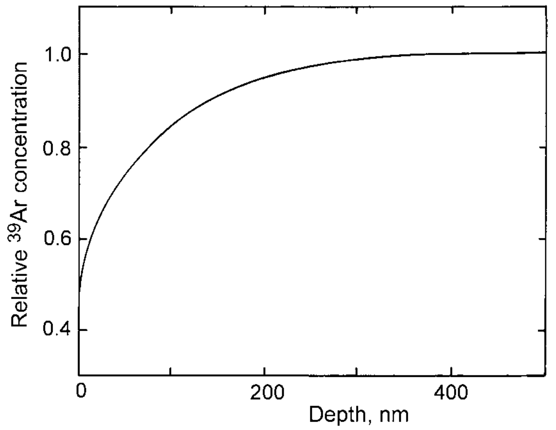

Fig. 10.21. Plot showing calculated drop in ^{39}Ar concentration at the surface of a K-bearing mineral due to recoil, in response to bombardment with an isotropic neutron flux. After Turner and Cadogan (1974).

ilmenite, leading to an old apparent age during low-temperature release (K-bearing minerals) and a young apparent age during high-temperature release.

The results from this experiment (Fig. 10.20) showed that, while abnormally old ages were produced at low temperature, the data approached the 'true' plateau age at intermediate temperatures. Therefore, Turner and Cadogan argued that ^{39}Ar released by recoil must have been lost from the sample altogether, rather than absorbed by low-K phases. This is probably due to the fact that adjacent grains are in less intimate contact in a powdered sample than they are in a fine-grained rock sample. The unusually high ages in the highest-temperature fraction (Fig. 10.20) were tentatively attributed to an incorrect Ca correction, due to recoil of the monitor isotope ^{37}Ar during the n, α reaction from ^{40}Ca. This transformation should result in four times more recoil than proton emission from ^{39}K.

Argon recoil has important implications for minerals whose diffusional history is explained in terms of micro-domains (section 10.5.3). The most important examples are feldspars, which have exsolution lamellae about 0.01–0.3 μm thick, but show little evidence for recoil effects in their plateau ages or Arrhenius plots. The lack of any such evidence led McDougall and Harrison (1988) to speculate that a large fraction of ^{39}Ar recoils might occur at low energy, with reduced displacements.

Onstott *et al.* (1995) re-examined this question using theoretical calculations and ion-implantation experiments, but these continued to support a mean ^{39}Ar recoil distance of 0.082 μm. The implications were examined for three minerals showing exsolution of K-rich and K-poor lamellae (amphibole, plagioclase and K-feldspar). In all three cases, calculations indicated that ^{39}Ar concentrations would be significantly homogenised and ^{37}Ar almost totally homogenised between adjacent lamellae (Fig. 10.22). Therefore, Onstott *et al.* concluded that the lamellae were too small to be the domains controlling volume diffusion of argon in the samples of amphibole and plagioclase studied. The situation for K-feldspar was less clear, but they suggested that some re-interpretation of results might be necessary for the smallest domain sizes of K-feldspar used in thermal-history analysis.

The calculations of Onstott *et al.* were tested by a direct determination of the ^{39}Ar recoil distance by Villa (1997). A thin slab of KCl was sandwiched between two sheets of silica, but on one side the silica layer was shielded by a silicon coating 95 nm thick. The whole assembly was then irradiated to simulate a 40–39 argon analysis. After irradiation, the ^{39}Ar concentration on the inner surface of each silica sheet was analysed, and, from the difference between the shielded and unshielded surface, a mean ^{39}Ar recoil distance of 80 ± 20 nm in silicon was calculated. From the relative densities of silicon and K-feldspar, the recoil distance in the mineral was estimated as about 70 nm. This measurement supported the theoretical calculations of Onstott *et al.* (1995), and therefore led Villa (1997; 1998) to question the meaning of K-feldspar thermochronometry using the multi-diffusion domain (MDD) model (section 10.5.3). This question remains controversial.

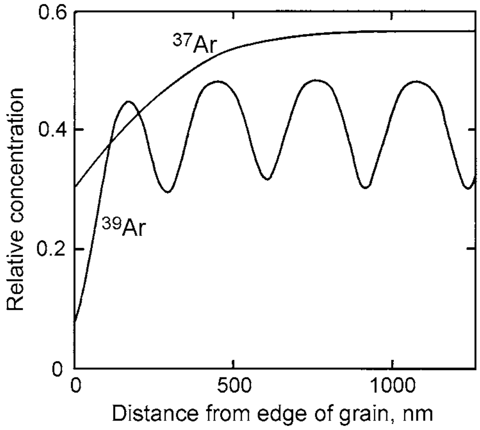

Fig. 10.22. Predicted argon isotope distribution after neutron irradiation of a plagioclase grain. The grain has alternating lamellae of calcic plagiocase (60 nm wide) and 50% plagioclase and K-feldspar (320 nm wide). After Onstott *et al.* (1995).

10.2.8 Dating glauconite and clay minerals

The problem of ^{39}Ar recoil was found to be particularly severe in attempts to apply ^{40}Ar–^{39}Ar dating to the authigenic sedimentary mineral glauconite (e.g. Foland *et al.*, 1984). This is probably due to the very small grain size of the glauconite crystallites which make up the grains of a pellet. Smith *et al.* (1993) showed that this problem might be overcome by encapsulating glauconite grains in small glass ampoules prior to irradiation. The recoil products can then be collected for analysis, in order to correct the Ar release from the rest of the grain. However, this method is applicable only to a whole-sample degassing analysis (analogous to a conventional K–Ar age) and cannot be used with the step-heating method.

Smith *et al.* (1998) applied the method of microencapsulation to the analysis of suites of single glauconite grains of three different ages. However, when the data were used to construct age frequency diagrams, Smith *et al.* found multiple age peaks, suggesting several episodes of glauconitisation. Nevertheless, it appeared that the oldest of these episodes was in each case close to the time of sediment deposition, so that the analysis of a large sample suite may give a reasonable estimate of the time of deposition. It remains to be seen whether such ages are sufficiently reliable for calibration of the stratigraphic column.

The small grain size of clay minerals (typically 5–1000 nm thick) makes them also very susceptible to ^{39}Ar loss by recoil effects. To combat this process, the technique of encapsulation was also applied by Smith *et al.* (1993) to clay minerals. ^{39}Ar that escaped from the sample due to recoil was held in an ampoule so that it could be collected and analysed with argon released during laser heating. However, experiments by Dong *et al.* (1995) suggested that the escaping argon fraction is not lost from illite and smectite by direct recoil, but by thermal degassing of low-retentivity sites that have picked up recoiling nuclides. These low-retentivity sites are actually the two free surfaces of the clay mineral grain, and the amount of ^{39}Ar loss is inversely proportional to thickness. For example, a grain of illite 100 nm (1000 Å) thick, made of 100 silicate–cation–silicate composite layers, will lose about 1% of its ^{39}Ar (2 out of 200 surfaces); on the other hand, a grain 10 nm thick might lose as much as 10% of its ^{39}Ar budget during irradiation.

Dong *et al.* argued that ^{39}Ar loss during irradiation may match ^{40}Ar loss during geological heating (diagenesis). They measured the ^{39}Ar signal retained by encapsulation, then subtracted this fraction from the total gas release of the sample (including all encapsulated argon). The resulting 'argon-retention age' should be the same as a non-encapsulated age, and was argued to be a better estimate of the time of deposition or early diagenesis than the encapsulated age. However, retention ages measured on Paleozoic clays were older to varying degrees than the non-encapsulated ages. This suggests that ^{39}Ar loss by recoil was indeed causing a bias to the data, even if this was superimposed on an argon-loss process during diagenesis. The fact that recoil loss of ^{39}Ar *is* a problem in the analysis of many clay samples is indicated by excess ages for the high-temperature release fraction, which is not affected by low-temperature argon-loss events (Kapusta *et al.*, 1997).

Kapusta *et al.* (1997) proposed a new method whereby step-heating experiments could be performed on fine-grained material such as glauconite or clay. This approach involves irradiating two aliquots of the sample to be dated. The first is used for the step-heating analysis, whereas the second is encapsulated and used to determine a total release age (relative to a standard of known age). The standard of known age is used to determine the *J* value of the irradiation in the usual way. The total release age of the encapsulated aliquot is then used in turn to calculate a 'J_C' correction for the step-heated aliquot, modified from [10.9]:

$$J_C = \frac{e^{\lambda t} - 1}{(^{40}\mathrm{Ar}^*/^{39}\mathrm{Ar})_{\mathrm{total\ release}}} \qquad [10.13]$$

The J_C value allows normalisation of both the neutron flux and recoil loss, provided that the encapsulated sample has the same grain-size distribution and crystal make-up as the step-heated sample. Kapusta *et al.* (1997) demonstrated the method on a glauconite standard (Fig. 10.23). However, it should be applicable to clay minerals that have suffered a combination of radiogenic ^{40}Ar loss over geological time and ^{39}Ar loss during irradiation.

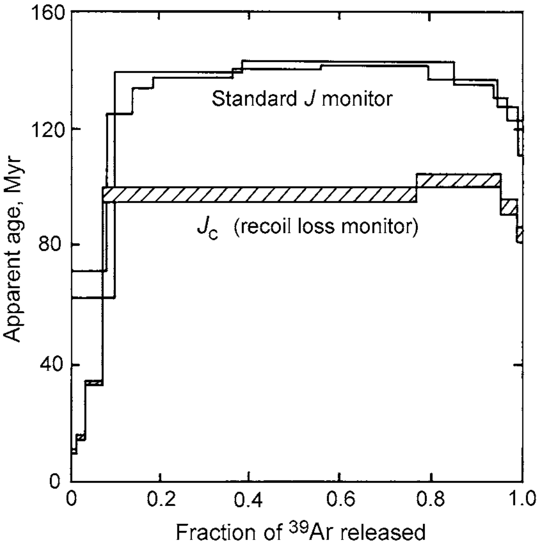

Fig. 10.23. Ar spectrum plot on a 95-Myr-old glauconite standard showing the results of conventional step heating (top two profiles) as well as a step-heating analysis corrected using the J_C recoil loss monitor (hatched). Modified after Kapusta *et al.* (1997).

10.3 Laser-probe dating

10.3.1 Method development

The application of the laser probe to K–Ar dating is now becoming an important technique, but surprisingly, the method was slow in development. Megrue

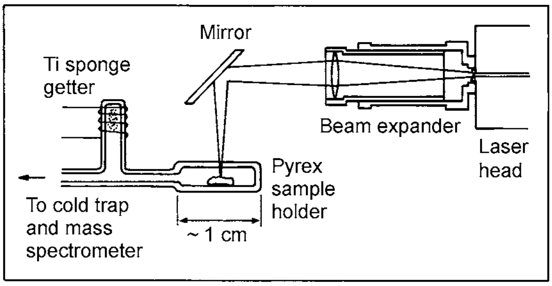

Fig. 10.24. Schematic illustration of laser ablation Ar–Ar dating equipment. After York *et al.* (1981).

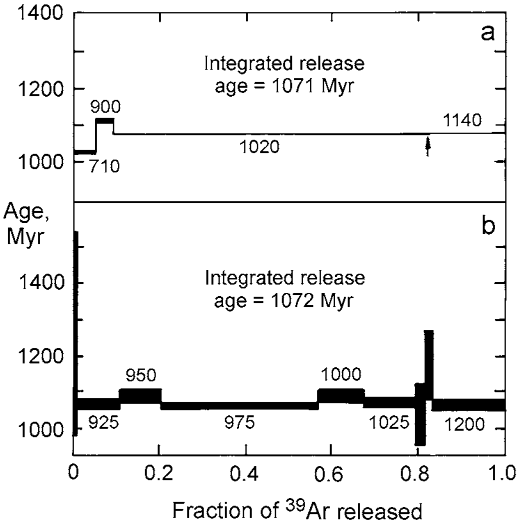

Fig. 10.25. Step-heating results for the Hb3GR standard: (a) conventional and (b) laser single grain. Quoted ages are average (integrated release) ages. After Layer *et al.* (1987).

(1967) pioneered the use of laser ablation for rare-gas analysis, but did not apply the method to geochronology until six years later (Megrue, 1973). This study made use of the laser probe in order to date small clasts in a polymict lunar breccia. After activation, spots 100 μm in diameter were irradiated with single pulses from a ruby laser. Each pulse ablated a pit about 30 μm deep, equivalent to about 1 μg of rock, representing a miniature total-fusion analysis of the exposed surface. The aggregate gas fraction from several nearby spots was gettered and cryogenically trapped, before admission to the mass spectrometer for analysis. (Typical equipment is shown in Fig. 10.24.) Analysis of ten different clasts revealed two arrays of data on a K–Ar isochron diagram with ages of approximately 3.7 and 2.9 Byr.

York *et al.* (1981) developed the laser-microprobe technique by showing that a de-focussed continuous-wave laser could be used to perform step-heating analysis in a manner analogous to conventional 40–39 dating. The technique was demonstrated on a whole-rock sample of slate from the Kidd Creek mine, near Timmins, Ontario. The laser beam was focussed to generate a spot 0.6 mm in diameter, which caused progressive release of argon from the surface after a few minutes, using a 1-W power setting. The laser step-heating analysis produced results consistent with conventional step heating of the same sample, representing the timing of a thermal event that opened the K–Ar system in the slate.

The low sensitivity of the MS-10 mass spectrometer used by York *et al.* (1981) limited application of the method, but in subsequent development a purpose-built continuous laser system was coupled to a high-sensitivity mass spectrometer. Layer *et al.* (1987) tested this system by analysing the hornblende standard Hb3GR. This is known from previous step-heating analysis (Turner, 1971a) to yield a perfect plateau age (Fig. 10.25a). After activation, single grains up to 0.5 mm across were heated within the laser beam for 30 s at increasing power levels. After each heating episode, argon was gettered and then analysed. Excellent plateaus were generated (e.g. Fig. 10.25b), and the integrated release ages fell within error of the conventional step-heating result.

Laser-probe dating was developed using continuous-wave infra-red lasers, either de-focussed for step heating, or focussed for spot analysis. These lasers are effective for heating most samples, but cannot be focussed below a spot size of 50 μm, and are not effective for analysing pale-coloured minerals such as feldspar. To overcome these problems, ultra-violet lasers have been introduced (e.g. Kelley *et al.*, 1994). Ultra-violet laser light is obtained by frequency doubling, which necessitates using pulsed lasers. The power available with such a system is much lower, but it is effective for spot ablation because the energy is more efficiently concentrated in a 10-μm-diameter spot. The ultra-violet laser-ablation microprobe (UVLAMP) offers the opportunity for *in situ* analysis of thin sections with high spatial precision, both laterally and with depth in the sample. Kelley *et al.* demonstrated the depth resolution by using a rastered beam to ablate successive 2-μm-deep steps into the surface of a K-feldspar grain. The resulting isotopic depth profile shows the diffusion of atmospheric argon into the surface of the grain (Fig. 10.26). The method shows great potential for detailed studies of argon diffusion in minerals (section 10.5.2).

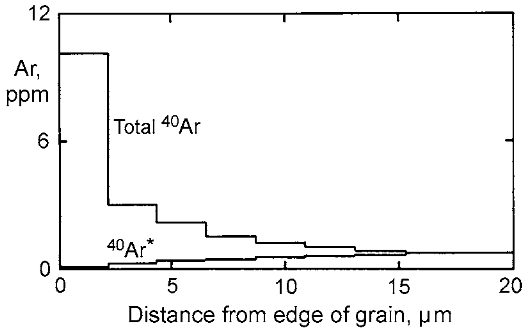

Fig. 10.26. UVLAMP depth-profiling measurements of total ^{40}Ar concentration and radiogenic ^{40}Ar in a K-feldspar grain. The data fit a model involving diffusion of radiogenic Ar out of the grain and of atmospheric Ar into the grain, except for a high value at the surface, which is probably due to adsorption. After Kelley *et al.* (1994).

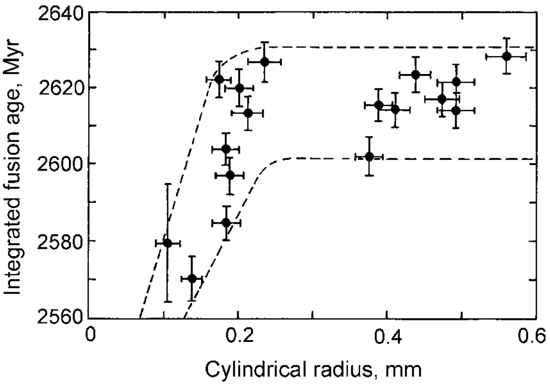

Fig. 10.27. Plot of integrated release ages against grain size for single biotite grains from the Trout Lake batholith, Ontario. The plateau is attributed to loss of Ar from sub-domains within large biotite grains. After Wright *et al.* (1991).

10.3.2 Applications of laser-probe dating

In order to test the laser step-heating method on a slowly cooled geological system, Layer *et al.* (1987) analysed biotites from the Trout Lake batholith, NW Ontario. Laser step heating of a small (0.25 mm) biotite grain yielded an age of 2600 Myr, which was identical to the result obtained with a conventional step-heating analysis on 13 mg of biotite. However, laser step heating of a large (1 mm) biotite from the same hand specimen yielded a significantly older age. The total release age for this grain (2654 ± 5 Myr) was closer to the U–Pb intrusive age for the batholith of 2699 ± 2 Myr. This shows that the larger biotites probably closed earlier during metamorphic cooling.

Wright *et al.* (1991) developed this study on the Trout Lake batholith by using the laser step-heating method to date a range of single biotite grains of various sizes. Only grains having a regular shape similar to a thin cylinder were analysed. After measurement of the grain radii and activation in the reactor, each specimen was subjected to laser step-heating analysis, during which the whole grain was bathed in the laser beam at increasing intensities. For samples displaying normal plateaus, their integrated ages were plotted against grain size (Fig. 10.27). The results display a positive correlation between grain size (cylindrical radius) and integrated age. This was attributed to diffusional loss of argon during the original cooling history of the batholith. Wright *et al.* speculated that the scatter of data points to the right of the main array might represent large grains that either had been damaged during sample crushing or consisted of natural aggregates of smaller sub-domains.

The positive correlation in Fig. 10.27 is explained by the larger surface-area/volume ratio of smaller grains, resulting in a lower effective blocking temperature than for larger grains. Geological determinations of Ar diffusion in biotite (e.g. Onstott *et al.*, 1989) can be used to calculate the size dependence of blocking temperature (0.1 mm = 275 °C; 0.23 mm = 295 °C). Hence, the array in Fig. 10.27 translates into a cooling curve for the batholith, of temperature against time. This yields a calculated cooling rate between 295 and 275 °C of about 0.33 °C/Myr. The high-temperature cooling curve of the pluton can be calculated between the older biotite ages and the U–Pb zircon age of 2700 Myr (with a blocking temperature estimated to be about 750 °C). This segment of the cooling curve is much steeper, at about 5 °C/Myr.

Lee *et al.* (1990) tested the laser step-heating method on biotite and hornblende grains that had suffered a thermal disturbance long after initial cooling. The sample consisted of baked Archean gneiss adjacent to an Early Proterozoic dyke, and both minerals were analysed by three methods: conventional step heating; single-grain laser step heating; and laser spot dating. Biotite ages for the three methods clustered closely around 2050 Myr, which was interpreted as the time of dyke intrusion. On the other hand, hornblende produced very different results from the three techniques. Conventional step heating of a multi-grain population and laser spot dating generated very variable ages (Fig. 10.28), whereas laser step heating generated a good plateau with an apparent age of 2430 Myr. However, this does not correspond to a known geological event.

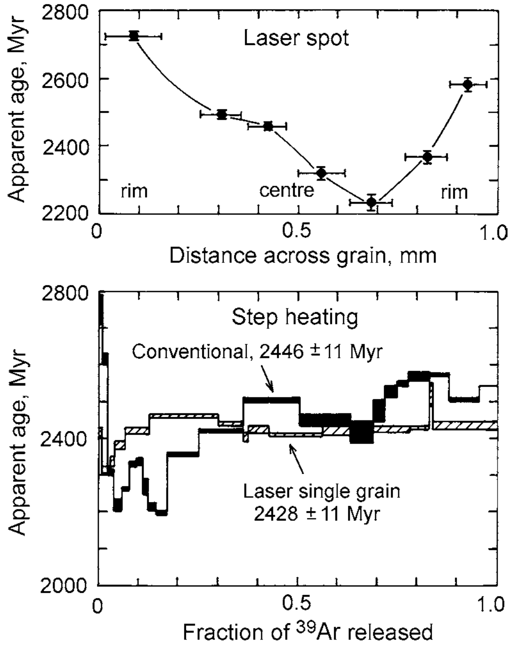

Fig. 10.28. Comparison of spot and step-heating ages for a disturbed hornblende sample: a profile of laser spot ages across a single grain; and laser and conventional step-heating profiles. After Lee *et al.* (1990; 1991).

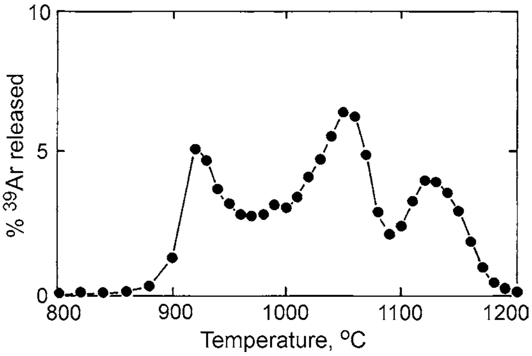

Fig. 10.29. Argon-release pattern observed in response to heating of the hornblende standard Mmhb-1. After Lee *et al.* (1991).

Lee *et al.* (1991) speculated that the plateau could result from mixing of argon from different domains in the mineral before release. Heating experiments on the hornblende standard Mmhb-1 showed that argon was released in three principal pulses (Fig. 10.29). The first of these, at 930 °C, was correlated with the onset of structural breakdown at the margins of grains. However, the main phase of breakdown occurred at 1050 °C, forming a strong fabric parallel to cleavage and accompanied by the breakdown of titanite lamellae in the crystal. Finally, at 1130 °C the grains melted. The laser step-heating plateau in Fig. 10.28 was formed by release of argon between 960 and 1250 °C, suggesting that it may result from homogenisation of the argon distribution in the grain during structural breakdown. Therefore, although laser step heating is a powerful technique, it is necessary to check data from disturbed systems by a second technique such as laser spot dating or laser depth profiling (e.g. Roberts *et al.*, 2001).

10.4 Timescale calibration

The high precision that is obtainable in K–Ar dating, particularly using the ^{40}Ar–^{39}Ar step-heating method or the laser-probe method, makes this method very useful for timescale calibration. This applies particularly to the Tertiary period, for which K–Ar dating can exceed the precision of U–Pb zircon geochronology. The following sections will review some of the most important applications.

10.4.1 The magnetic-reversal timescale

One of the most important applications of the K–Ar method has been to calibrate the magnetic-reversal timescale defined by sea-floor magnetic-anomaly 'stripes'. The amount of ocean-floor material recovered which is fresh (unaltered) enough for dating is limited, so most attention has been focussed on dating terrestrial sections (such as basic lavas) which yield a good magnetostratigraphy. The K–Ar method is really the only geochronometer capable of dating young basic rocks. Since its establishment, the reversal timescale has been subject to almost continuous revision, and some landmarks are reviewed here.

Pioneering work was performed by Cox *et al.* (1963) on 0–3-Myr-old lavas from California, and by McDougall and Tarling (1964) on 0–3-Myr-old lavas from the Hawaiian islands. Cox *et al.* used K–Ar dates on sanidine, obsidian, biotite and whole-rocks, whereas McDougall and Tarling worked on basalt whole-rocks. Good agreement between the two data sets confirmed that the reversal timescale is due to world-wide changes in the polarity of the Earth's magnetic field, rather than to post-crystallisation alteration phenomena, as had been suggested by some workers.

A comprehensive compilation of data for 354 terrestrial lavas (mostly from ocean islands) was used by Mankinen and Dalrymple (1979) to constrain the polarity timescale for the last 5 Myr more precisely,

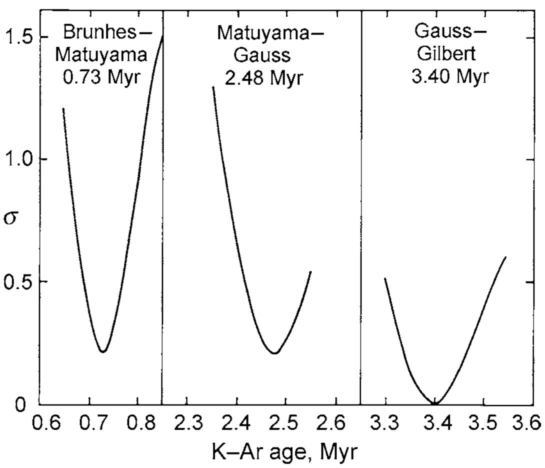

Fig. 10.30. Standard deviation of apparent dating inconsistencies as a function of 'trial' values for polarity boundaries. The best estimate of each boundary age is where the error is a minimum. After Mankinen and Dalrymple (1979).

using the new K–Ar decay constants (Steiger and Jäger, 1977). Not all of the available data were in perfect agreement; therefore Mankinen and Dalrymple used a statistical technique to calculate the most probable ages of the three most recent polarity-epoch boundaries, such that the standard deviation of apparent dating inconsistencies was minimised (Fig. 10.30).

Unfortunately, the geological record of terrestrial lavas is too fragmented to extend the technique of detailed epoch-boundary dating back beyond 5 Myr. Therefore, Heirtzler *et al.* (1968) used sea-floor magnetic-anomaly patterns to extend the terrestrial timescale to about 80 Myr by extrapolation. They took as a fixed point an age of 3.35 Myr for the epoch boundary between Gilbert (reversed) and Gauss (normal), based on the Sierra Nevada data of Doell *et al.* (1966). Heirtzler *et al.* extrapolated from the present day, through the Gilbert–Gauss point, to calibrate the older part of the timescale, by assuming a constant spreading rate for the South Atlantic ridge over the last 80 Myr. This may seem a crude assumption, but Heirtzler *et al.* justified it on the basis of the good correlation between S Atlantic and N Pacific spreading rates.

During the next two decades, improvements to the reversal timescale were achieved by adding additional fixed points. LaBrecque *et al.* (1977) made the first major revision by using two fixed points to avoid the extreme extrapolation of Heirtzler *et al.* (1968). The younger point was again the Gilbert (R)–Gauss (N) boundary, while the older (marine anomaly 29) was tied by magnetostratigraphy of Paleocene limestones near Gubbio, Italy, to the Cretaceous–Tertiary (K–T) boundary. Tying the reversal timescale to the geological column was advantageous in harmonising the timescales, but problematical in that it revealed the poor constraints on the K–T boundary itself. For example, sources cited by LaBrecque *et al.* (1977) for a K–T boundary age of 65 Myr were a poster published by Elsevier (van Eysinga, 1975) and a paper by van Hinte (1976). The latter was merely a citation of Berggren (1972), whose only constraints were a minimum of 57.1 ± 3 Myr from Belgium and a maximum of 68.1 ± 4 Myr from SE England. Fortunately the age of 65 Myr for the K–T boundary has proved so robust in the long run that it has not even been affected by changes in the decay constants used! (This is a coincidence, of course.)

The next major step in calibrating the reversal timescale was made by Lowrie and Alvarez (1981), who used magnetostratigraphy on the 25–130 Myr-old Gubbio limestones of Italy to interpolate between eleven fixed points. However, the large number of fixed points generated a kinked line, due to errors in the absolute age calibrations of some points. Harland *et al.* (1982) ironed out some of these inflections to produce a useful 'working timescale' (Fig. 10.31). However,

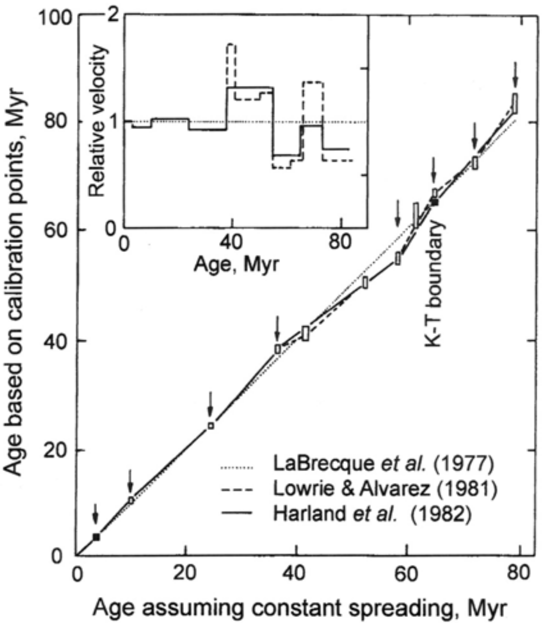

Fig. 10.31. Diagram to show the fixed points that constrain the reversal timescales of LaBrecque *et al.* (■); Lowne and Awarex (▣); and Harland *et al.* (↓). Inset shows consequences for Atlantic spreading rate. After Harland *et al.* (1982).

Harland's approach had probably now reached its technical limit, since the absolute ages of the fixed points, being based mainly on K–Ar glauconite ages, were not reliable enough for more accurate calibration.

10.4.2 The astronomical timescale

Johnson (1982) proposed a completely new approach to the calibration of the geomagnetic-polarity timescale, which was based on planetary mechanics (Milankovich forcing, section 12.4.2). According to this theory, small variations in the Earth's orbit have led to variations in the intensity of solar radiation reaching the Earth, which were responsible for the glacial–interglacial cycles of the Quaternary period. These glacial cycles caused variations in the oxygen isotope composition of seawater, which were recorded in fossil forams.

Because the Earth's orbital variations can be projected back into the past very accurately, it is possible to 'tune' the oxygen isotope record in deep-sea cores with a precision of better than 1%. From coherent patterns in two high-quality cores from the western Pacific, Johnson was able to date the Brunhes–Matuyama magnetic-reversal signature, which was preserved in sediment 7.25 m below the surface of core V28-239 (Fig. 10.32). He estimated a date of 790 kyr for the boundary, with a probable uncertainty of less than 5 kyr. However, this work did not receive much attention because of the large discrepancy between this date and the younger value of 730 kyr determined by Mankinen and Dalrymple (1979).

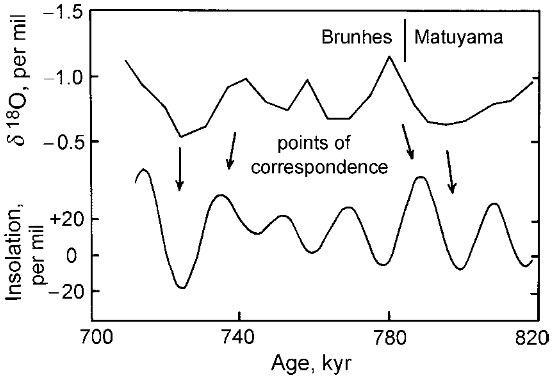

Fig. 10.32. Section of a DSDP core displaying the Brunhes–Matuyama reversal boundary. This is dated by tuning oxygen isotope variations (caused by glacial cycles) to the history of northern-hemisphere insolation, calculated from orbital mechanics. Arrows show suggested correlation points. After Johnson (1982).

The publication of a new high-resolution oxygen isotope record for the Pleistocene (Shackleton *et al.*, 1990) focussed attention back onto the discrepancy between the astronomical and K–Ar calibrations. A slight revision of the orbital tuning calculation placed the Brunhes–Matuyama boundary at 780 kyr and suggested that the date of Mankinen and Dalrymple (1979) might indeed be in error. Therefore, several high-resolution K–Ar and ^{40}Ar–^{39}Ar studies were undertaken to test the age of this and other important reversal boundaries. The first of these studies were conducted simultaneously by Baksi *et al.* (1992), Spell and McDougall (1992) and Tauxe *et al.* (1992).

Baksi *et al.* (1992) calibrated the Brunhes–Matuyama boundary using ^{40}Ar–^{39}Ar ages of whole-rock samples of basalt lava exposed in the caldera wall of Haleakala volcano on the island of Maui. The magnetic signature of the section had previously been studied, and gives such detailed coverage of the reversal boundary that several flows actually have magnetic signatures that are transitional between normal and reversed polarities. Samples were analysed in two different laboratories, yielding consistent results with an average age for the reversal boundary of 783 ± 11 kyr, in excellent agreement with the astronomical calibration.

Tauxe *et al.* (1992) re-examined the data analysis of Mankinen and Dalrymple (1979). The K–Ar ages used to constrain the Brunhes–Matuyama boundary exhibited significant internal disagreement (Fig. 10.33), as was shown in fact by the 'error-function' plot of Mankinen and Dalrymple (Fig. 10.30). The failure of the error function to reach a zero value should have been a warning that the raw data were unreliable, but the scientific community (including the present author) was 'bewitched' by the statistical treatment of the data. In hindsight we can see that the low ages for the reversed (Matuyama) chron were probably caused by argon loss. In such cases, the appropriate remedy is to collect new high-precision data rather than statistically filtering old data. Therefore Spell and McDougall (1992) performed a new dating study on the Valles Caldera, New Mexico, where the anomalous samples had come from. They used the ^{40}Ar–^{39}Ar laser-fusion technique to date sanidine crystals from the critical section, and obtained older ages, confirming that the Brunhes–Matuyama boundary should be located at 780 ± 10 kyr.

The use of the astronomical timescale reached a mature stage in 1994 when it was used to back calibrate

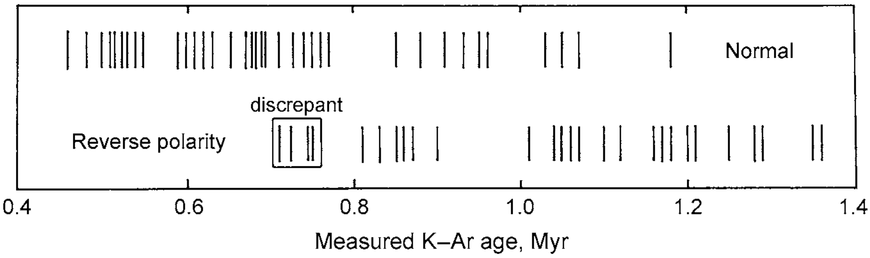

Fig. 10.33. Chart showing raw data used by Mankinen and Dalrymple to date the Brunhes–Matuyama reversal boundary. The best-fit age for the boundary was biassed downwards by some data (boxed) that had evidently been affected by argon loss. Modified after Tauxe *et al.* (1992).

the Fish Canyon sanidine standard, one of the primary ^{40}Ar/^{39}Ar dating standards (Renne *et al.*, 1994). Sanidine crystals from Fish Canyon tuff had been used in several earlier studies to calibrate Ar–Ar ages for six important reversal boundaries. However, with the advent of a precise astronomical calibration of these boundaries, it was possible to reverse the calibration in order to determine an absolute geological age of 27.95 ± 0.18 Myr for the eruption of the Fish Canyon tuff.

Absolute ages cannot be determined directly by the Ar–Ar method because a standard must always be used to calculate the neutron flux. However, high-precision conventional K–Ar ages on undisturbed material allow absolute calibration of Ar–Ar standards such as Fish Canyon sanidine. Intercalibration studies by Baksi *et al.* (1996) and Renne *et al.* (1998b) were based on K–Ar dating of three older standards (SB3, GA-1550 and GHC-305). The resulting calibration ages for Fish Canyon tuff were 27.95, 28.02 and 28.15 Myr, respectively, using the recommended ^{40}K half-life. All of these values fall within error of the astronomical calibration, but the median value is probably most reliable.

10.4.3 Intercalibration of decay constants

Despite the great advances made in K–Ar and Ar–Ar dating in the past few years, there remains one outstanding problem in the use of this method for high precision dating of older rocks. This is the observation that calibrated Ar–Ar ages are consistently slightly younger than U–Pb ages for the same rock unit. This has raised the question of whether the decay-constant determination of Beckinsale and Gale (1969), adopted by Steiger and Jäger (1977) as a recommended value, is significantly in error.

U–Pb dating is regarded as the ‘gold standard’ for geochronology (Lugmair, section 5.2.2), because the uranium decay constants are based on the best laboratory determinations, and because of the built-in check for disturbance. However, even U–Pb ages have non-negligible uncertainties arising from decay-constant errors, and these now exceed the analytical uncertainty of high-precision ages. Despite these difficulties, high-precision measurements have been made on a few ‘geologically ideal’ samples to test for concordance between U–Pb and Ar–Ar ages. Some of these results are presented in Table 10.1. All errors are quoted at the 2σ level and include uncertainties in the decay constants. Unfortunately, it can be seen that, although the Ar–Ar ages are about 1% less than the U–Pb age on each occasion, these two results are actually within error if the uncertainties in the decay constants are fully propagated into the age determination. This problem is complicated by the branched nature of ^{40}K decay, which means that two different

Table 10.1. *Comparison between U–Pb and Ar–Ar ages of ‘ideal’ samples*

Material	U–Pb age (Myr)	Ar–Ar age (Myr)	Reference
Fish Canyon tuff	28.4 ± 0.1	28.0 ± 0.4	Renne *et al.* (1998b)
Siberian traps	251.3 ± 1	250.0 ± 4	Renne *et al.* (1998a)
Palisade rhyolite	1098 ± 4	1088 ± 15	Min *et al.* (2000)
Acapulco meteorite	4554 ± 12	4507 ± 50	Renne (2000)

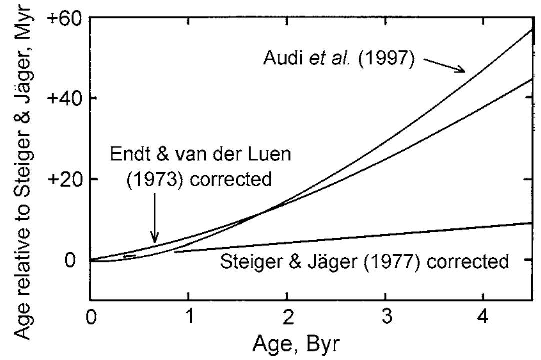

Fig. 10.34. Effect on calculated geological ages of using alternative experimentally determined potassium decay constants. Deviations are very small below 1 Byr. After Min *et al.* (2000).

decay constants have to be considered in any geological calibration.

As part of their study of this problem, Min *et al.* (2000) also reviewed the counting experiments of Beckinsale and Gale (1969) and compared them with two other determinations. These values are compared in Fig. 10.34 (after some minor corrections to the Beckinsale and Gale value adopted by Steiger and Jäger, 1977). The results show that the divergence of the three curves is not really significant for ages below 1 Byr, although it is quite large for very old rocks. Unfortunately, it remains unclear whether the young K–Ar age for the Acapulco meteorite is due to an error in the ^{40}K half-life or due to slow cooling of the meteorite from 4.55 to 4.50 Byr ago (Trieloff *et al.*, 2001; Renne, 2001).

Schmitz and Bowring (2001) recently performed a new U–Pb dating study on the Fish Canyon tuff, which confirmed the U–Pb age quoted in Table 10.1. However, the discrepancy between the U–Pb and K–Ar ages might not be due to an error in the decay constant. Hence, it is concluded that the ^{40}K decay constant of Steiger and Jäger should probably still be used until more data are obtained to resolve this problem.

10.5 Thermochronometry

The thermal history of meteorites was interpreted in section 10.2.4 in terms of short-lived thermal events, including their initial cooling and any subsequent collisions, separated by long periods under cold conditions. However, Turner (1969) recognised that, in different circumstances, slow cooling from a single event could yield an age spectrum rather similar to that produced by episodic thermal events.

10.5.1 Arrhenius modelling

A special feature of the Ar–Ar step-heating method is that argon release in the laboratory should be controlled by the same diffusional properties of minerals as those that cause argon loss in nature. The long timescales of geological events obviously preclude laboratory analysis under natural conditions. However, if diffusion obeys the Arrhenius law, a rapid argon-release experiment at high temperature in the laboratory can mimic much slower argon release at lower temperatures in the crust. Hence, step-heating data may be used to reconstruct thermal histories such as post-orogenic cooling.

The result of slow cooling in a young intrusive body is illustrated by the age spectrum of a biotite from La Encrucijada pluton in Venezuela (Fig. 10.35). Unfortunately, this approach can rarely be used on terrestrial rocks because the low-temperature part of the profile, which is critical in the determination of a precise

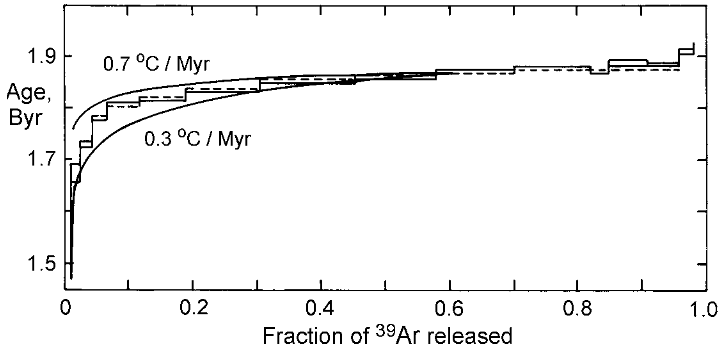

Fig. 10.35. ^{40}Ar/^{39}Ar age spectrum of La Encrucijada biotite, Venezuela, compared with predicted cooling curves based on modelling of diffusion of Ar in biotite. After York (1984).

cooling rate, becomes 'corrupted' by minor diffusional loss of argon at ambient temperatures over geological time.

A more useful approach to quantifying the cooling history of crustal rocks is the blocking-temperature concept (section 3.3.2), whose theoretical basis was examined by Dodson (1973). Argon loss from a mineral can be described by the thermal diffusion coefficient

$$D = D_0 e^{-E/(RT)} \qquad [10.14]$$

where D_0 is the thermal diffusivity of the mineral, E is the activation energy for diffusion of argon, R is the gas constant and T is the absolute temperature. The exponent makes D a very strong function of temperature. Therefore a small drop in temperature can cause a transition from a state in which Ar loss by diffusion is rapid to a state in which Ar loss by diffusion is very slow. This relatively sharp transition constitutes the process of blocking. The blocking temperature T_B is defined by Dodson (1973) as follows:

$$T_B = \frac{E}{R \ln(A\tau D_0/a^2)} \qquad [10.15]$$

where A is a geometrical parameter that takes account of the crystal form of the argon-bearing mineral (55, 27 or 9 for a sphere, cylinder or sheet, respectively), a is the length of the average diffusion pathway from the interior to the surface of the grain, and τ is the cooling time constant. The latter in turn is defined as follows:

$$\tau = RT_B^2/(-C_B E) \qquad [10.16]$$

where $-C_B$ is the cooling rate at the blocking temperature T_B. Hence, substituting equation [10.15] into [10.14] yields

$$T_B R = E \Big/ \ln\left(A \frac{RT_B^2}{-C_B E}\frac{D_0}{a^2}\right) \qquad [10.17]$$

A method to calculate blocking temperatures from Ar–Ar spectrum plots was proposed by Buchan *et al.* (1977) and developed by Berger and York (1981a). A plateau age must be available on a mineral from a slowly cooled terrane. For each heating step in the plateau, the volume of radiogenic ^{40}Ar released in a given time is used to calculate D/a^2. For planar minerals such as biotite the diffusion equation has the following general form (e.g. Harrison and McDougall, 1981):

$$\frac{D}{a^2} = \frac{(qf)^2}{t} \qquad [10.18]$$

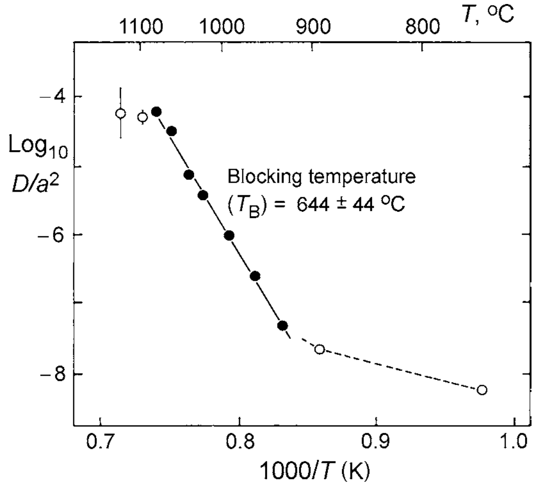

Fig. 10.36. Arrhenius plot for hornblende from a Grenville diorite, Haliburton Highlands, Ontario. The blocking temperature was determined from the array of seven solid data points. Error bars are 1σ. After Berger and York (1981a).

where f is the fractional loss of argon, t is the heating time and q is a geometrical factor.

The results are plotted on a log scale against the reciprocal temperature of each step, forming an Arrhenius plot (e.g. Fig. 10.36). If diffusional Ar loss obeys the Arrhenius law as expected, then the steps in the plateau should define a straight line whose slope is the activation energy E and whose y intercept is the frequency factor D_0/a^2. These values allow equation [10.17] to be solved, provided that the cooling rate $-C_B$ at the blocking temperature (T_B) can be estimated. Fortunately, the temperature solution has a weak dependence on the cooling rate, such that an order-of-magnitude change in this value causes only a 10% change in the calculated blocking temperature. Because T_B appears on both sides of equation [10.17], it must be solved iteratively, but it converges quickly. The power of this technique is that the blocking temperature of a mineral is calculated directly on the dated material, rather than having to depend on generalised blocking temperatures for various types of mineral from the literature, which might not be applicable to the specific cooling conditions under study.

Berger and York (1981a) applied this 'thermochronometry' method to a study of post-orogenic cooling in the Grenville province of southern Ontario, Canada. Plutonic ages in the Grenville belt vary from 1.0 to 2.7 Byr, but most K–Ar dates fall below 1 Byr and are attributed to uplift and cooling after

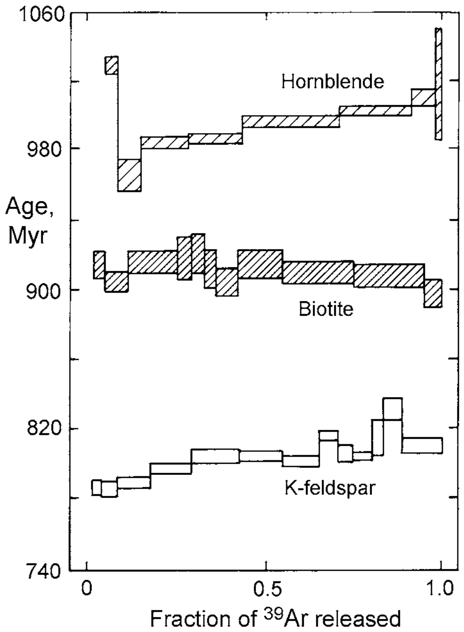

Fig. 10.37. The 40–39 age spectra for hornblende, biotite and K-feldspar analyses used to determine blocking temperatures in Figs. 10.36 and 10.38. Modified after Berger and York (1981a).

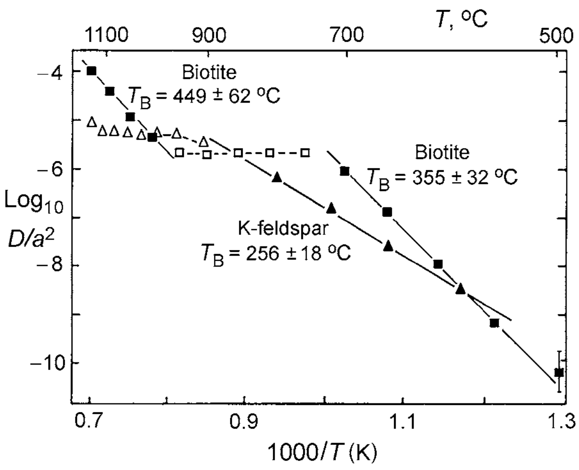

Fig. 10.38. Arrhenius plot for Grenville K-feldspar (▲, △) and biotite (■, □) dated in Fig. 10.36. Blocking-temperature calculations were based on solid data points only. After Berger and York (1981a).

collisional orogeny (Harper, 1967). Berger and York studied dioritic and gabbroic plutons from the Haliburton Highlands, both to determine a detailed cooling curve for the area and to interpret paleomagnetic data on these rocks.

Typical 40–39 profiles from Haliburton diorites that gave reasonable plateaus are shown in Fig. 10.37. These samples are plotted on Arrhenius plots in Figs. 10.36 and 10.38. The hornblende displays a relatively simple array in Fig. 10.36, although low-temperature and high-temperature points must be excluded from the regression. K-feldspar displays coherent low-temperature behaviour, but high-temperature data are irregular, possibly due to disruption of the lattice above 900 °C. The most unusual behaviour was demonstrated by biotite, which in many cases gave rise to two heating pulses that defined sub-parallel arrays (such as in Fig. 10.38). Nevertheless, the blocking temperatures calculated from the two segments were usually within error. Berger and York speculated that the break in regular behaviour was due to structural breakdown.

Results from all of the analysed minerals are shown on a diagram of blocking temperature against age (Fig. 10.39). Points without error bars failed a reliability criterion that required both the age plateau and the Arrhenius correlation line to have four or five statistically well-fitting data points. The data show a clear picture of fairly rapid cooling (at about 5 °C/Myr) from the hornblende blocking temperature of about 700 °C at 980 Myr to the biotite blocking temperature of about 380 °C at 900 Myr. Thereafter, the data are mainly from plagioclase, which displays considerable scatter. Berger and York's original interpretation (solid line in Fig. 10.39) called for very slow cooling (under 1 °C/Myr) for a further 300 Myr. However, in a study of gabbro from the Hastings Basin of the Grenville (about 80 km east of the Haliburton Highlands), Berger and York (1981b) recognised that the apparently slow cooling curve after 900 Myr might really represent a more recent thermal event.

The latter interpretation of the plagioclase data was supported by Hanes *et al.* (1988), on the basis of Ar–Ar dating of the Elzevir and Skootamata plutons of the Hastings basin. Hanes *et al.* analysed three plagioclases, which displayed a range of rather mediocre plateau ages between 400 and 600 Myr. Variations in ^{37}Ar/^{39}Ar ratio with the fraction of ^{39}Ar released were used as an index of the Ca/K ratios of various domains within the minerals. A pronounced hump in the middle of these profiles indicated that the analysed plagioclases were multi-phase systems. They display two different types of alteration, which may be of different ages. Hanes *et al.* suggested that scattered coarse

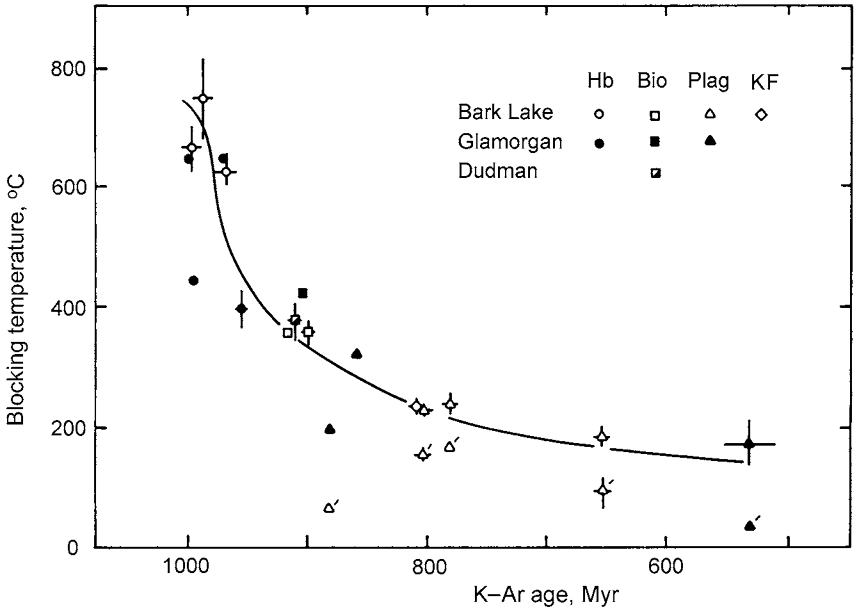

Fig. 10.39. Plot of calculated mineral blocking temperatures against plateau ages to show a model for crustal cooling after the Grenville orogeny. Solid and open symbols indicate minerals from different plutons. After Berger and York (1981a).

epidote and muscovite alteration might have formed at high temperatures soon after plutonism, while fine-grained sericitic alteration probably represents an event younger than 400 Myr.

The evidence for structural breakdown in biotite points to a weakness in the thermochronometry method of Berger and York. Because biotite is a hydrous mineral, diffusional loss of Ar during vacuum heating may not accurately mimic Ar loss in nature under (probable) hydrothermal conditions, as suggested by Giletti (1974). This problem was confirmed by Gaber *et al.* (1988), who showed that there were large divergences in argon diffusivity between hydrothermal and vacuum-heating experiments on biotite and hornblende.

The susceptibility of these hydrous minerals to structural breakdown during vacuum heating has largely discredited the application of step-heating analysis to determine their blocking temperatures. Instead, attention has switched to K-feldspar, the most common anhydrous K-bearing mineral. As an anhydrous phase, the behaviour of this mineral during vacuum degassing can mimic argon loss in nature with some accuracy (section 10.5.3). However, studies of diffusional loss of argon from hydrous minerals have been continued using laser spot analysis. For example, this method has been applied to the study of complex argon-diffusion models in micas and amphiboles.

10.5.2 Complex diffusion models

The traditional approach to mineral blocking temperatures is based on 'Fickian' behaviour, which means that diffusion of argon in minerals is assumed to occur by volume diffusion, obeying Fick's first law (e.g. McDougall and Harrison, 1999). However, detailed analysis of Ar–Ar ages in minerals has revealed breakdowns in this simple model, requiring more complex models of argon diffusion to be proposed. The advent of the laser probe has allowed the detailed spatial analysis of minerals in order to test these more complex models.

It has long been known that large biotite grains can lose radiogenic strontium or argon more rapidly than predicted by volume diffusion (e.g. section 3.3.2). This behaviour was also seen in argon-diffusion experiments using hydrothermal bombs, and can be explained if biotite has an 'effective diffusion radius' of about 150 μm (e.g. Harrison *et al.*, 1985). This implies that biotite grains consist of domains of about

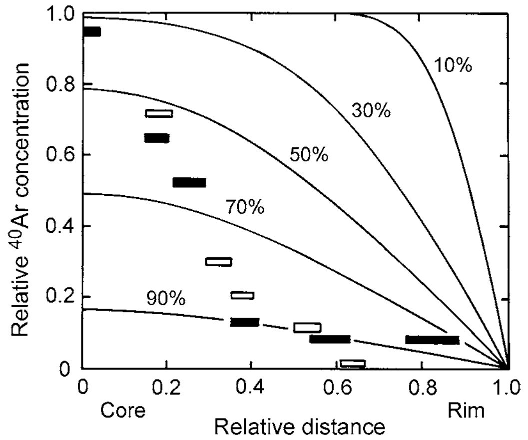

Fig. 10.40. Plot of ^{40}Ar concentrations along two transects (solid and open boxes) from core to rim of a metamorphosed phlogopite grain. Predicted argon-loss curves based on volume diffusion fail to explain the data. After Phillips and Onstott (1988).

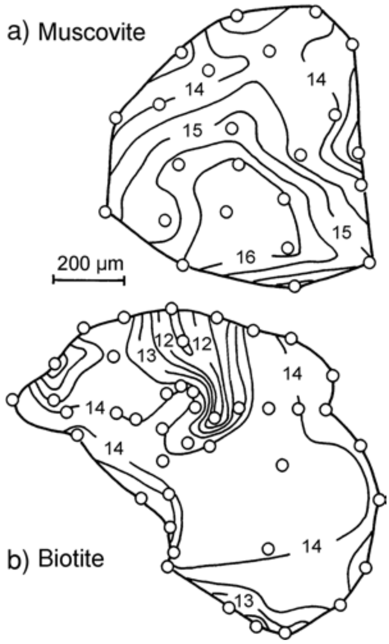

Fig. 10.41. Comparison between 'chrontour' age maps for muscovite and biotite determined from laser spot dating. Numbers indicate ages in hundreds of Myr. After Hodges *et al.* (1994).

150 μm radius, within which argon moves by volume diffusion, but between which there is a mechanism of enhanced transport along crystallographic defects.

The increased amount of spatial argon data available from the laser probe has allowed complex diffusion models to be tested using natural mineral systems. Phillips and Onstott (1988) performed the first such study, which was based on mantle-derived phlogopites from the Premier kimberlite, South Africa. 'Chrontour' mapping of 75 laser spots revealed apparent ages of 1.2–1.4 Byr in the rim of a large grain, rising to a maximum of 2.4 Byr in the core. This pattern was attributed to the loss of inherited mantle argon from the rim of the grain during emplacement of 1.2-Byr-old kimberlite. However, the shape of the argon-loss profile (boxes in Fig. 10.40) did not fit a volume-diffusion model (curves in Fig. 10.40). Phillips and Onstott attributed the observed patterns to enhanced diffusive loss of argon from a wide band (round the rim of the grain) due to structural defects. However, the nature of these defects was unknown.

Hodges *et al.* (1994) compared argon-diffusion patterns in muscovite and biotite using the laser probe. Single mica grains were analysed from the 1700-Myr-old Crazy Basin monzogranite of central Arizona, which has been argued to display either very slow cooling or multiple metamorphic events. Laser step heating of both muscovite and biotite gave very similar plateau ages of 1412 and 1410 Myr. However, for muscovite, the gas-release steps which form the plateau occurred after melting had begun. Therefore, this plateau undoubtedly results from argon homogenisation during melting, and the similarity to the biotite plateau age is probably a coincidence. These findings are consistent with the work described above, in which argon homogenisation was shown to be a greater problem in laser step heating than it is in conventional step heating (section 10.3.2).

Laser spot dating revealed very different age patterns in other muscovite and biotite grains from the same sample. Muscovite spot ages ranged from 1270 Myr at the rim to 1650 Myr (the 'true' age) in a small core area, with a roughly concentric pattern (Fig. 10.41a). This age distribution fits a simple volume-diffusion model for cylindrical geometry with an effective diffusion radius similar to the grain size. On the other hand, laser spot ages in the biotite grain had a quite different distribution, with ages ranging from 1150 Myr at the rim to 1420 Myr in a large core area (Fig. 10.41b). The large area with (re-set) ages of 1400 Myr, together with an asymmetrical zone of young ages approaching the core, was evidence of the operation of fast diffusion pathways. Hodges *et al.* interpreted the data in terms of small domains with an effective diffusion

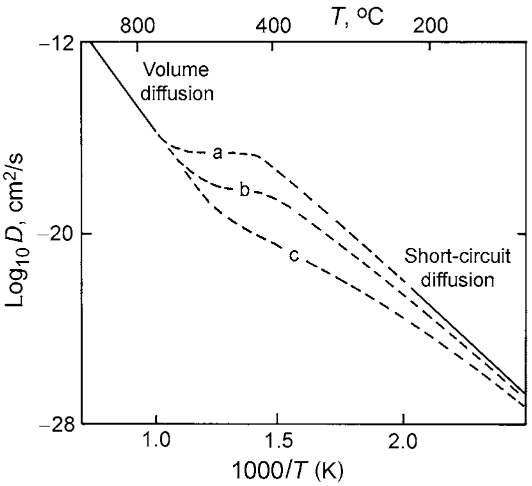

Fig. 10.42. Predicted effect of an 'exchange coefficient' (*D*) in changing the dominant diffusive mechanism from volume to short-circuit diffusion. Curves a, b and c represent exchange coefficients of -10^{-13}, -10^{-14} and -10^{-15} for the transfer of species from the crystal lattice to high-diffusivity paths. After Lee (1995b).

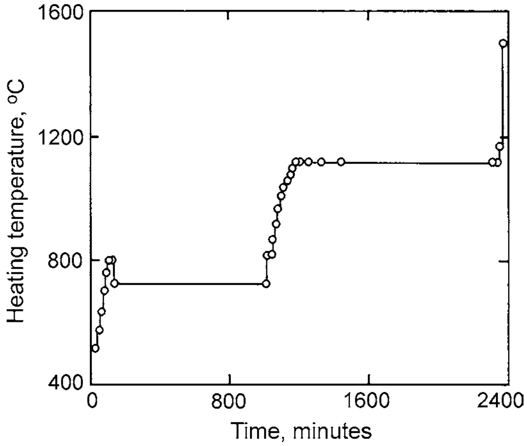

Fig. 10.43. Demonstration of a cyclic heating schedule for Ar–Ar analysis. After Richter *et al.* (1991).

radius of 150 μm, as postulated in hydrothermal experiments.

Lee and Aldama (1992) attempted to explain complex diffusion behaviour by combining mechanisms for diffusion within the crystal lattice with enhanced ('short-circuit') diffusion between lattice domains into a general model termed 'multi-path' diffusion. In this model, diffusion in both of the pathways (lattice and short-circuit) is Fickian, but is of very different magnitudes in the two pathways. In addition, the transfer of species from the crystal lattice to the high-diffusivity paths, and vice-versa, is attributed to two exchange coefficients, termed K_2 and K_1 respectively. The magnitudes of these coefficients are critical in determining whether multi-path diffusion will occur in a given situation.

The operation of the multi-path diffusion model can be examined on an Arrhenius plot (Fig. 10.42). At high temperatures (>800 °C), volume diffusion in the crystal lattice is the dominant mechanism for loss of argon from a mineral. However, if the exchange coefficient (K_2) is relatively large, this causes a sudden change from lattice-dominated to short-circuit argon transport as temperature falls, forming a sigmoidally shaped diffusion curve. On the other hand, smaller values of K_2 inhibit the role of short-circuit diffusion, maintaining a lattice-dominated diffusion mechanism to lower temperatures (<500 °C).

Although the multi-path model is an attempt to create a realistic representation of the physical movement of argon in minerals, McDougall and Harrison (1999) argued that it is of limited use in analysing thermal histories from geological samples, because the postulated exchange coefficients cannot be determined by laboratory measurement. In addition, the model cannot explain the results of 'cycling step heating', a method developed by Lovera *et al.* (1991) for K-feldspar thermochronometry (see below). In this method, the heating schedule in an Ar–Ar degassing experiment is not increased monotonically as in a conventional analysis, but is increased in short 'bursts' with a period in between when the temperature is either reduced or maintained at a constant level for a relatively long time. An example of such a heating schedule is shown in Fig. 10.43.

According to the multi-path diffusion model, the short-circuit diffusion path should be 'replenished' by volume diffusion out of the lattice during the backward-cycling stage of the step-heating procedure, so that the subsequent increasing-temperature cycles reproduce the low-temperature behaviour from the beginning of the experiment. However, such behaviour was not seen (McDougall and Harrison, 1999). Therefore, if the short-circuit pathway exists, it may be more like an independent reservoir of stored argon, perhaps sampling argon from defect sites, than a pathway fed by lattice diffusion. In fact, McDougall and Harrison (1999) pointed out that, if the exchange coefficients are ignored, the multi-path diffusion model is mathematically equivalent to diffusion of argon from two

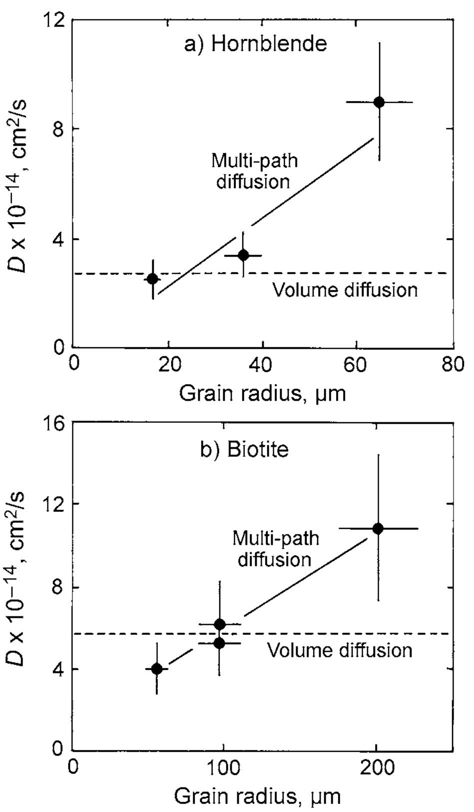

Fig. 10.44. Plots of bulk argon diffusion coefficients against grain radius. Measurements from hydrothermal experiments on (a) hornblende and (b) biotite are compared with the predicted results of volume and multi-path diffusion models. After Lee (1995b).

different domain sizes in the multi-domain model (section 10.5.3). In other words, extraction of argon over relatively long distances along high-diffusivity pathways is equivalent to volume diffusion from very small lattice domains.

Complex diffusion models can be tested against the results of hydrothermal diffusion experiments on hornblende and biotite at different grain sizes (Fig. 10.44). Lee (1995b) argued that the enhanced diffusivities for large grain sizes favour the multi-path model over simple volume diffusion. However, the data can also be explained by a domain model, in which the lattice domains controlling volume diffusion are smaller than the complete crystal.

In the hydrothermal experiments, the behaviour of hornblende and biotite may result from similar styles of alteration, both in the laboratory and in natural systems. For example, Onstott *et al.* (1991) suggested that fast diffusion pathways in hydrothermal biotite may be created during the experiment by the breakdown of chlorite layers, whereas Kelley and Turner (1991) attributed fast diffusion pathways in natural hornblende to biotite alteration.

Recent experiments using the ultra-violet laser ablation microprobe (UVLAMP) suggest that, in pristine, unaltered grains of biotite, most diffusion of argon out of (or into) the grains occurs by volume diffusion. For example, Pickles *et al.* (1997) demonstrated such behaviour in biotite grains of various sizes (50–4500 µm diameter) in a pegmatite affected by Alpine metamorphism. During the metamorphic event, excess ^{40}Ar diffused into the grains from the grain-boundary fluid and created diffusion profiles. In several grains, diffusion profiles up to 100 µm long were successfully modelled by volume diffusion. In the largest grain, the diffusion profile spanned a distance of nearly 300 µm, although the outermost 90 µm of the profile was disrupted by argon loss during a later alteration event.

Results of other experiments suggest that short-circuit diffusion is principally a feature of low temperatures of argon release. For example, Lo *et al.* (2000) found low-temperature argon diffusivities two to four orders of magnitude faster than the values that would result from extrapolation of hydrothermal experiments to low-temperature conditions. However, they suggested that this low-temperature release might be of argon that had accumulated in radiation-induced lattice defects. Evidence for this interpretation comes from the fact that the outgassing of ^{39}Ar usually exceeds that of ^{40}Ar during very-low-temperature argon release (about 400 °C), which would be consistent with the preferential release of recoiled ^{39}Ar atoms residing in defect sites. In this case the occurrence of short-circuit diffusion might be to some extent an artefact of the irradiation procedure involved in the Ar–Ar method. Similar doubts have been expressed about the meaning of the lowest-temperature emission step from K-feldspars (section 10.2.7 and below).

10.5.3 K-feldspar thermochronometry

K-feldspars have long been known to exhibit complex diffusion behaviour. Because of the unpredictable effects of perthitic exsolution, K-feldspars have very variable blocking temperatures, which must be determined for individual dated samples by the step-heating method. Heizler *et al.* (1988) demonstrated

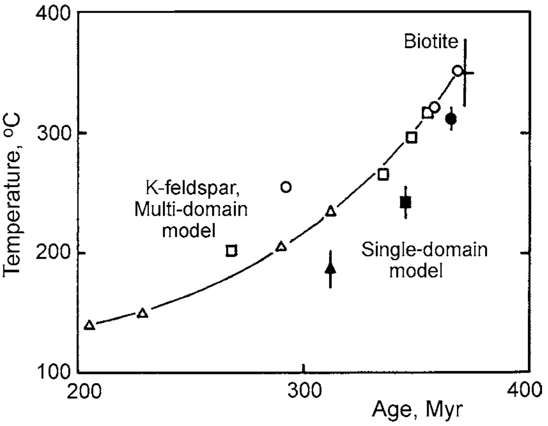

Fig. 10.45. Plot of calculated K-feldspar blocking temperature against plateau age to model cooling of the Chain of Ponds pluton, NW Maine. Solid symbols show the single-plateau analysis of Heizler *et al.* (assuming uniform domain size). Open symbols show the sub-plateau analysis of Lovera *et al.* (assuming variable domain size). After Harrison (1990).

this technique in determining the cooling curve of the Chain of Ponds pluton, NW Maine. They obtained quite distinct blocking temperatures and ages on three feldspar separates, establishing a post-Appalachian cooling curve from 330 to 180 °C (solid symbols in Fig. 10.45).

Other workers (e.g. Foland, 1974) suggested that diffusion in K-feldspars is controlled by microstructural domains of variable size, rather than on a whole-grain scale. The variable domain sizes invoked by this model can explain the traditional reputation of K-feldspars for having such poor retentivity of argon as to be useless as a dating tool. The smallest of the domains do indeed suffer argon loss at near ambient temperatures. However, the larger domains, sampled in a step-heating analysis, can have blocking temperatures as high as that of biotite. Therefore, if this variation in blocking temperatures can be exploited using the step-heating method, K-feldspar can be a powerful tool in thermochronometry. Because this method is based on the assumption of domains of various sizes, it is termed the multi-diffusion domain (MDD) model.

Adopting the MDD model, Lovera *et al.* (1989) re-interpreted the data of Heizler *et al.* (1988) by breaking each Ar–Ar analysis into a series of sub-plateaux with distinct ages and blocking temperatures. They attributed these sub-plateaux to diffusional domains within each feldspar grain, varying in size by two orders of magnitude. This model was tested by comparing measured step-heating data with model spectra based on different domain-size distributions, as applied by Turner *et al.* (1966) to meteorite studies (section 10.2.4). The variable-domain-size model was shown to fit the experimental data much better than the uniform model, thus confirming its usefulness. The result of this approach was that each analysis yielded a separate but overlapping cooling-curve *segment* (open symbols in Fig. 10.45), rather than a single point on the cooling curve. Further experiments on single feldspar crystals by Lovera *et al.* (1991) showed that domains of varying size are an intrinsic property of alkali feldspars, which therefore cannot be separated by hand picking of material for analysis.

Conventional thermochronometry is based on linear Arrhenius relationships observed when ^{39}Ar is released from diffusion domains of uniform size and K content that obey a simple diffusion law. In their development of the K-feldspar method, Lovera *et al.* (1989) showed that non-linear Arrhenius trends produced by conventional step heating could be resolved into separate linear segments by cycling the heating schedule up and down.

Subsequent work on a variety of samples showed that these line segments were effectively parallel, indicating relative constancy of diffusional activation energies. The vertical separation between different linear segments on the Arrhenius diagram can then be interpreted in terms of relative domain size. If the effective diffusion radius of the domain which generates the first, low-temperature array is set arbitrarily to be r_0 ('r' is the equivalent of 'a' in section 10.5.1), then the relative diffusion dimension of each subsequent gas-release point can be calculated using the following relation:

$$\log\left(\frac{r}{r_0}\right) = \frac{\log\left(\frac{DT}{r^2}\right) - \log\left(\frac{DT}{r_0^2}\right)}{2} \qquad [10.19]$$

Because we are interested only in the relative diffusion dimension, the exact geometry assumed (slab, sphere etc.) has little effect on the calculations. Richter *et al.* (1991) proposed that each value of $\log(r/r_0)$ should be plotted against cumulative ^{39}Ar release in a manner analogous to an age spectrum plot (Fig. 10.46b). This plot therefore bridges the gap between the age spectrum diagram and the Arrhenius diagram.

The working of the 'Richter plot' was demonstrated on an analysis from the Quxu pluton of the Himalayas. The diagram gave evidence of four plateaus, of which the three highest-temperature ones correspond

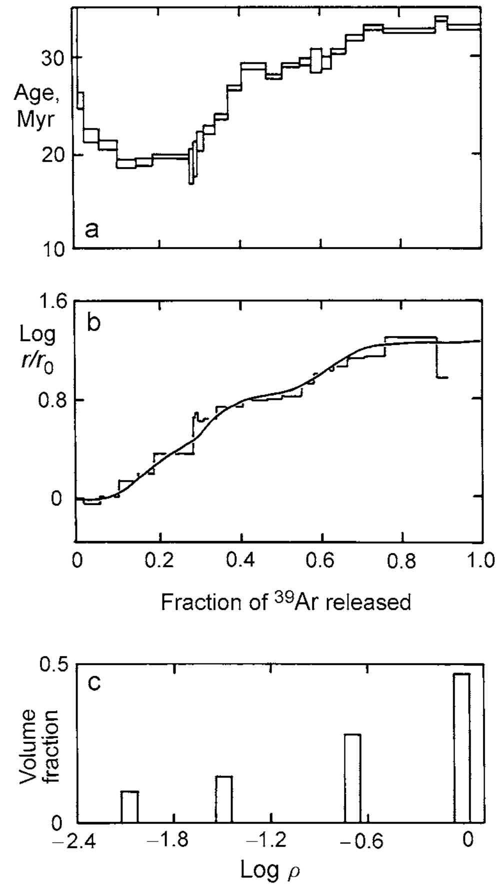

Fig. 10.46. Comparison of different ways of presenting data for K-feldspar thermochronometry: (a) the traditional age-spectrum plot; (b) an r/r_0 plot; and (c) the resulting solution of volume fraction against relative domain size. After Richter *et al.* (1991).

to plateaus on the age spectrum plot (Fig. 10.46a). The lowest-temperature plateau had no corresponding age because the first five steps were perturbed by excess ^{40}Ar, which had probably diffused into the grains after cooling of the pluton. However, this did not affect the ^{39}Ar released during this part of the analysis, which can still be used to obtain diffusional data. On the other hand, the highest-temperature step gave an age, but no diffusional information, because it occurred during melting of the sample. After the gas release has been broken into plateaux, the volume fraction of each is calculated, and an iterative program is used (Lovera, 1992) to determine the actual radius ratios of the domains which will model the observed profile of relative diffusion dimensions. The solution is shown in Fig. 10.46c. Finally, a cooling curve is determined (iteratively), which will yield the observed age spectrum.

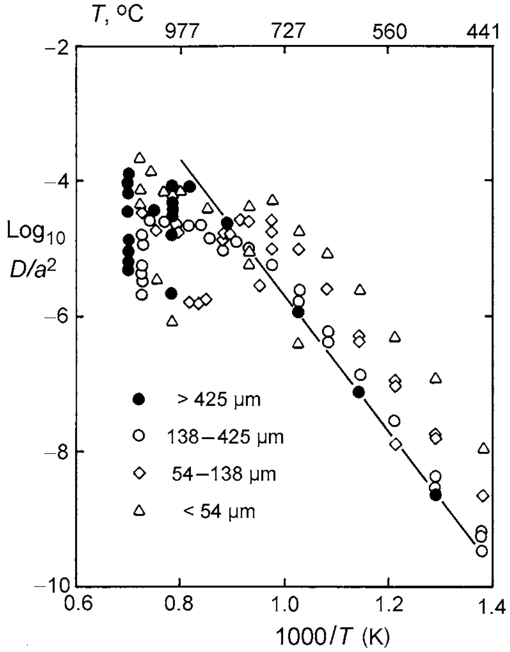

Fig. 10.47. Arrhenius plot for K-feldspar from the Chain of Ponds pluton, Maine. Parallel linear arrays were obtained from the low-temperature gas releases, after crushing to four different grain sizes. After Lovera *et al.* (1993).

In several experiments on K-feldspars from different orogens, the radius ratio of largest to smallest domains was determined to be between 100 and 500. Lovera *et al.* (1993) performed step-heating experiments on the Chain of Ponds pluton, Maine (sample MH-10) in an attempt to find the absolute sizes of these domains. After crushing, K-feldspar grains were separated into four size fractions, averaging 425, 138, 54 and 42 μm in diameter. Following irradiation, a full step-heating analysis was performed on each size fraction, and the resulting Arrhenius plots were compared (Fig. 10.47). The results revealed a dramatic decrease in retentivity of argon between the 138- and 54-μm size fractions, attributed to the ‘breaking open’ of the largest diffusion domain in crushing to 54 μm. Hence, the diameter of this domain was inferred to be 50–100 μm. On the basis of relative domain-size ratios, the smallest domain size was then estimated to be about 0.1 μm.

In an accompanying optical and TEM study, FitzGerald and Harrison (1993) attempted to determine the crystallographic identities of the different domain sizes. They tentatively correlated the largest domains with blocks of K-feldspar surrounded by fractured and turbid zones, and the smallest with the distance of 0.1 μm (100 nm) between albite exsolution lamellae. However, they were unable to identify any intermediate-sized domains.

Authors of more recent studies have attempted to achieve a better understanding of argon diffusion in K-feldspar by studying gem-quality crystals, which are expected to display simpler diffusional behaviour. Two of these studies were performed on the same gem-quality orthoclase from Madagascar. The first study (Arnaud and Kelley, 1997) primarily used cyclic step-heating experiments to investigate the argon-release behaviour of the orthoclase. This experiment revealed that Ar release occurred in two stages with different activation energies. The main release was consistent with simple volume diffusion from a single domain size. However, the low-temperature release could be explained by invoking either rapid diffusion pathways (e.g. short-circuit diffusion) or multi-diffusion domains. However, this release stage represented only 0.5% of the total ^{39}Ar inventory of the sample, so Arnaud and Kelley speculated that it actually represented release of argon from the surface of the sample, which had possibly been damaged during sample preparation.

The second study of this material used the ultraviolet laser-ablation microprobe to perform depth profiles of the sample surface (Wartho *et al*., 1999). This study revealed that argon release from the surfaces of the orthoclase crystal was controlled by volume diffusion, just like in the crystal's interior. In fact, calculations of the effective diffusion radius for the low-temperature release and the main argon release gave values of 1.8 and 1.3 mm, respectively, both of which were consistent with the 2–3-mm dimensions of the analysed fragments. Therefore, despite the different activation energies of the different release stages, they both reflected volume diffusion from a single domain, which is consistent with the unflawed nature of the analysed fragments. Possibly, the low-temperature release was of argon from vacancy sites in the mineral. It was concluded from these experiments that cyclic step heating faithfully measured the diffusion parameters of the sample. However, they could not provide further help in understanding complex metamorphic K-feldspars.

Because the estimated size of the smallest diffusion domains in the MDD model is similar to the ^{39}Ar recoil distance, doubts have been expressed (section 10.2.7) about the meaning of the lowest-temperature argon-emission data. In addition, Parsons *et al*. (1999) argued that many K-feldspars display microstructural complexity that is meta-stable during step-heating experiments. Therefore, they suggested that alkali-feldspar thermochronology using the MDD model is a 'mathematical mirage' rather than a method that can be used to recover real thermal histories. However, there have been several empirical demonstrations that cooling curves based on K-feldspar thermochronology are in good agreement with other geochronological evidence. For example, Lee (1995a) demonstrated that there was good agreement of K-feldspar cooling curves with 40–39 muscovite ages and fission-track apatite ages in a study of tectonic uplift in the Snake Range, Nevada (Fig. 10.48).

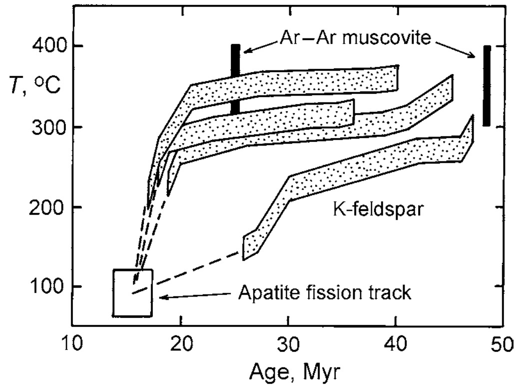

Fig. 10.48. Comparison of cooling data for the Snake Range, Nevada. Shaded fields derived from K-feldspar thermochronometry are consistent with control points from apatite fission-track analysis and Ar–Ar muscovite analysis (boxes). After Lee (1995a).

To provide a more objective test of the reliability of K-feldspar thermochronology as a technique for recovering real thermal histories, Lovera *et al.* (1997; 2002) analysed the argon-release patterns of a suite of nearly 200 basement samples. They found that the most common obstacle to the derivation of thermal histories from step-heating results was inherited argon. This has long been recognised as a problem in K–Ar and Ar–Ar dating, and in the study of Lovera *et al.* it was manifested by saddle-shaped profiles (intermediate age minimum) on the age spectrum diagram. On the other hand, a second type of anomalous behaviour was manifested as an intermediate age *maximum*, which was attributed to low-temperature alteration. Together, these problems affected about one-half of the total sample suite of 194 K-feldspars studied. The remaining half of the sample suite was considered to be 'well behaved', and therefore suitable for analysis by the

MDD model. In addition, the activation energies in these samples had a normal distribution (average = 46 ± 6 kcal/mol), so a standard protocol could be used to analyse all samples, thereby minimising subjectivity in the interpretation of the data.

Lovera *et al.* (2002) argued that the effectiveness of the MDD model at explaining the real thermal history of a sample could be assessed by the goodness of fit between the step-heating age spectrum and the pattern of changing effective diffusion-radius ratio (r/r_0). If these two profiles matched in a K-feldspar analysis, this was held to be evidence that the laboratory argon-release experiment successfully mimicked the diffusional loss of argon over the cooling history of the sample. However, in order to demonstrate the quality of fit between the two profiles, it was necessary to develop quantitative indices for comparing their shapes. Two indices were calculated for the middle part of the argon-release curve, after low-temperature inherited argon had essentially disappeared and before the sample started to melt. These indices are compared in Fig. 10.49, which shows the analysis spectra from two K-feldspars, one with an ideal argon-release pattern and one of poor quality.

The first index is a correlation coefficient, derived by fitting a polynomial function to each of the two patterns, extracting a series of discrete points at evenly spaced intervals, then calculating the correlation coefficient between the two series. This is shown in the lower right of each spectrum plot in Fig. 10.49. The second index is obtained simply by determining the average value of each series, and then determining where this point is achieved in the cumulative argon-release pattern. For the ideal experiment (Fig. 10.49a) the correlation coefficient was 0.98 and the mean points coincided. For the poor experiment the correlation coefficient was very poor (0.5) and the mean points did not coincide. On several other occasions, one or other of the criteria was satisfied, but not both.

The result of applying this analysis to the complete sample suite was that 40% of the samples had correlation coefficients above 0.9, leading Lovera *et al.* (2002) to suggest that most of the alteration-free samples without large inventories of inherited argon were suitable for thermal-history analysis by the MDD model. In response to the criticism that the postulated multi-diffusion domains cannot be identified structurally, Lovera *et al.* argued that the empirical results are adequate in themselves to demonstrate the effectiveness of the method for recovering thermal histories, and that understanding the structural basis of the model was of secondary importance. Doubtless, this debate will continue.

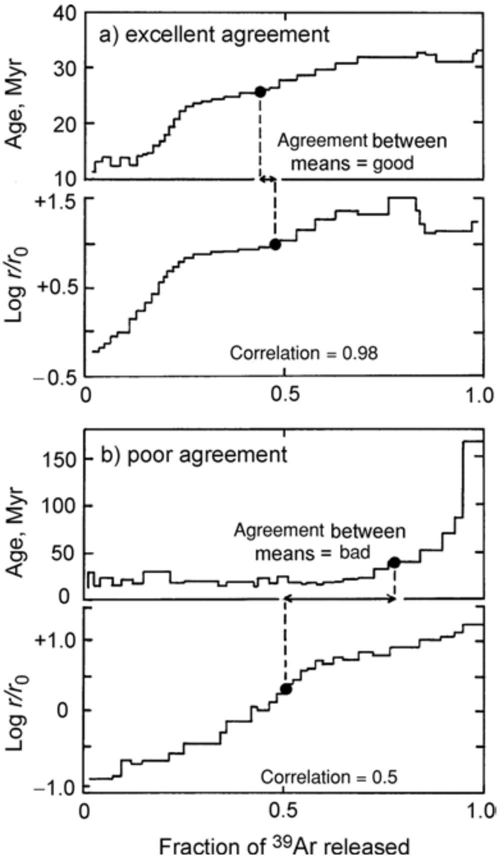

Fig. 10.49. Age spectra and profiles of changing effective diffusion radius ratio (r/r_0) in two step-heating experiments on basement samples of K-feldspar showing: (a) excellent agreement between the two profile shapes; and (b) poor agreement between profile shapes. After Lovera *et al.* (2002).

References

Anders, E. (1964). Meteorite ages. *Rev. Mod. Phys.* **34**, 287–325.

Arnaud, N. O. and Kelley, S. P. (1997). Argon behaviour in gem-quality orthoclase from Madagascar: experiments and some consequences for ^{40}Ar/^{39}Ar geochronology. *Geochim. Cosmochim. Acta* **61**, 3227–55.

Baksi, A. K., Archibald, D. A. and Farrar, E. (1996). Intercalibration of ^{40}Ar/^{39}Ar dating standards. *Chem. Geol.* **129**, 307–24.

Baksi, A. K., Hsu, V., McWilliams, M. O. and Farrar, E. (1992). ^{40}Ar/^{39}Ar dating of the Brunhes–Matuyama geomagnetic field reversal. *Science* **256**, 356–7.

Beckinsale, R. D. and Gale, N. H. (1969). A reappraisal of the decay constants and branching ratio of ^{40}K. *Earth Planet. Sci. Lett.* **6**, 289–94.

Berger, G. W. (1975). ^{40}Ar/^{39}Ar step heating of thermally overprinted biotite, hornblende and potassium feldspar from Eldora, Colorado. *Earth Planet. Sci. Lett.* **26**, 387–408.

Berger, G. W. and York. D. (1981a). Geothermometry from ^{40}Ar/^{39}Ar dating experiments. *Geochim. Cosmochim. Acta* **45**, 795–811.

Berger, G. W. and York. D. (1981b). ^{40}Ar/^{39}Ar dating of the Thanet gabbro, Ontario: looking through the metamorphic veil and implications for paleomagnetism. *Can. J. Earth Sci.* **18**, 266–73.

Berggren, W. A. (1972). A Cenozoic time-scale – some implications for regional geology and paleobiogeography. *Lethaia* **5**, 195–215.

Brereton, N. R. (1970). Corrections for interfering isotopes in the ^{40}Ar/^{39}Ar dating method. *Earth Planet. Sci. Lett.* **8**, 427–33.

Buchan, K. L., Berger, G. W., McWilliams, M. O., York, D. and Dunlop, D. J. (1977). Thermal overprinting of natural remanent magnetization and K/Ar ages in metamorphic rocks. *J. Geomag. Geoelectr.* **29**, 401–10.

Cox, A. and Dalrymple, G. B. (1967). Statistical analysis of geomagnetic reversal data and the precision of potassium–argon dating. *J. Geophys. Res.* **72**, 2603–14.

Cox, A., Doell, R. R. and Dalrymple, G. B. (1963). Geomagnetic polarity epochs and Pleistocene geochronology. *Nature* **198**, 1049–51.

Dalrymple, G. B. and Lanphere, M. A. (1969). *Potassium–Argon Dating*. Freeman, 258 pp.

Dalrymple, G. B. and Lanphere, M. A. (1971). ^{40}Ar/^{39}Ar technique of K–Ar dating: a comparison with the conventional technique. *Earth Planet. Sci. Lett.* **12**, 300–8.

Dalrymple, G. B. and Lanphere, M. A. (1974). ^{40}Ar/^{39}Ar age spectra of some undisturbed terrestrial samples. *Geochim. Cosmochim. Acta* **38**, 715–38.

Dalrymple, G. B. and Moore, J. G. (1968). Argon 40: excess in submarine pillow basalts from Kilauea Volcano, Hawaii. *Science* **161**, 1132–5.

Damon, P. E. and Kulp, J. L. (1958). Excess helium and argon in beryl and other minerals. *Amer. Mineral.* **43**, 433–59.

Dodson, M. H. (1973). Closure temperature in cooling geochronological and petrological systems. *Contrib. Mineral. Petrol.* **40**, 259–74.

Doell, R. R., Dalrymple, G. B. and Cox, A. (1966). Geomagnetic polarity epochs: Sierra Nevada data, 3. *J. Geophys. Res.* **71**, 531–41.

Dong, H., Hall, C. M., Peacor, D. R. and Halliday, A. N. (1995). Mechanisms of argon retention in clays revealed by laser ^{40}Ar–^{39}Ar dating. *Science* **267**, 355–9.

Esser, R. P., McIntosh, W. C., Heizler, M. T. and Kyle, P. R. (1997). Excess argon in melt inclusions in zero-age anorthoclase feldspar from Mt Erebus, Antarctica, as revealed by the ^{40}Ar/^{39}Ar method. *Geochim. Cosmochim. Acta* **61**, 3789–801.

FitzGerald, J. D. and Harrison, T. M. (1993). Argon diffusion domains in K-feldspar I: microstructures in MH-10. *Contrib. Mineral. Petrol.* **113**, 367–80.

Foland, K. A. (1974). Ar^{40} diffusion in homogeneous orthoclase and an interpretation of Ar diffusion in K-feldspars. *Geochim. Cosmochim. Acta* **38**, 151–66.

Foland, K. A., Linder, J. S., Laskowski, T. E. and Grant, K. (1984). ^{40}Ar–^{39}Ar dating of glauconies: measured ^{39}Ar recoil loss from well-crystallized specimens. *Chem. Geol. (Isot. Geosci. Section)* **46**, 241–64.

Gaber, L. J., Foland, K. A. and Corbato, C. E. (1988). On the significance of argon release from biotite and amphibole during ^{40}Ar/^{39}Ar vacuum heating. *Geochim. Cosmochim. Acta* **52**, 2457–65.

Garner, E. L., Machlan, L. A. and Barnes, I. L. (1976). The isotopic composition of lithium, potassium, and rubidium in some Apollo 11, 12, 14, 15, and 16 samples. In: *Proceedings of the 6th Lunar Science Conference*. Pergamon, pp. 1845–55.

Giletti, B. J. (1974). Diffusion related to geochronology. In: Hofmann, A. W., Giletti, B. J., Yoder, H. S. and Yund, R. A. (Eds.), *Geochemical Transport and Kinetics*. Carnegie Institute Washington, pp. 61–76.

Hale, C. J. (1987). The intensity of the geomagnetic field at 3.5 Ga: paleointensity results from the Komati Formation, Barberton Mountain Land, South Africa. *Earth Planet. Sci. Lett.* **86**, 354–64.

Hanes, J. A., Clark, S. J. and Archibald, D. A. (1988). An ^{40}Ar/^{39}Ar geochronological study of the Elzevir batholith and its bearing on the tectonothermal history of the southwestern Grenville Province, Canada. *Can. J. Earth Sci.* **25**, 1834–45.

Harland, W. B., Cox, A. V., Llewellyn, P. G., Pickton, C. A. G., Smith, A. G. and Walters, R. (1982). *A Geologic Time Scale 1982*. Cambridge University Press, 131 pp.

Harper, C. T. (1967). On the interpretation of potassium–argon ages from Precambrian shields and Phanerozoic orogens. *Earth Planet. Sci. Lett.* **3**, 128–32.

Harrison, T. M. (1990). Some observations on the interpretation of feldspar ^{40}Ar/^{39}Ar results. *Chem. Geol. (Isot. Geosci. Section)* **80**, 219–29.

Harrison, T. M., Duncan, I. and McDougall, I. (1985). Diffusion of ^{40}Ar in biotite: temperature, pressure and compositional effects. *Geochim. Cosmochim. Acta* **49**, 2461–8.

Harrison, T. M. and McDougall, I. (1981). Excess ^{40}Ar in metamorphic rocks from Broken Hill, New South Wales: implications for ^{40}Ar/^{39}Ar age spectra and the thermal history of the region. *Earth Planet. Sci. Lett.* **55**, 123–49.

Hart, S. R. (1964). The petrology and isotopic–mineral age relations of a contact zone in the Front Range, Colorado. *J. Geol.* **72**, 493–525.

Hart, S. R. and Dodd, R. T. (1962). Excess radiogenic argon in pyroxenes. *J. Geophys. Res.* **67**, 2998–9.

Heirtzler, J. R., Dickson, G. O., Herron, E. M., Pitman, W. C. and LePichon, X. (1968) Marine magnetic anomalies, geomagnetic field reversals, and motions of the ocean floor and continents. *J. Geophys. Res.* **73**, 2119–36.

Heizler, M. T., Lux, D. R. and Decker, E. R. (1988). The age and cooling history of the Chain of Ponds and Big Island Pond plutons and the Spider Lake granite, west-central Maine and Quebec. *Amer. J. Sci.* **288**, 925–52.

Hodges, K. V., Hames, W. E. and Bowring, S. A. (1994). ^{40}Ar/^{39}Ar age gradients in micas from a high-temperature–low-pressure metamorphic terrane: evidence for very slow cooling and implications for the interpretation of age spectra. *Geology* **22**, 55–8.

Johnson, R. G. (1982). Brunhes–Matuyama magnetic reversal dated at 790,000 yr B.P. by marine–astronomical correlations. *Quaternary Res*. **17**, 135–47.

Kaneoka, I. (1974). Investigation of excess argon in ultramafic rocks from the Kola peninsula by the ^{40}Ar/^{39}Ar method. *Earth Planet. Sci. Lett*. **22**, 145–56.

Kapusta, Y., Steinitz, G., Akkerman, A., Sandler, A., Kotlarsky, P. and Nägler, A. (1997). Monitoring the deficit of ^{39}Ar in irradiated clay fractions and glauconites: modelling and analytical procedure. *Geochim. Cosmochim. Acta* **61**, 4671–8.

Kelley, S. P. (2002). Excess argon in K–Ar and Ar–Ar geochronology. *Chem. Geol*. **188**, 1–22.

Kelley, S. P., Arnaud, N. O. and Turner, S. P. (1994). High spatial resolution ^{40}Ar/^{39}Ar investigations using an ultra-violet laser probe extraction technique. *Geochim. Cosmochim. Acta* **58**, 3519–25.

Kelley, S. P. and Turner, G. (1991). Laser probe ^{40}Ar–^{39}Ar measurements of loss profiles within individual hornblende grains from the Giants Range granite, northern Minnesota, USA. *Earth Planet. Sci. Lett*. **107**, 634–48.

LaBrecque, J. L., Kent, D. V. and Cande, S. C. (1977). Revised magnetic polarity time scale for Late Cretaceous and Cenozoic time. *Geology* **5**, 330–5.

Lanphere, M. A. and Dalrymple, G. B. (1966). Simplified bulb tracer system for argon analysis. *Nature* **209**, 902–3.

Lanphere, M. A. and Dalrymple, G. B. (1971). A test of the ^{40}Ar/^{39}Ar age spectrum technique on some terrestrial materials. *Earth Planet. Sci. Lett*. **12**, 359–72.

Lanphere, M. A. and Dalrymple, G. B. (1976). Identification of excess ^{40}Ar by the ^{40}Ar/^{39}Ar age spectrum technique. *Earth Planet. Sci. Lett*. **32**, 141–8.

Layer, P. W., Hall, C. M. and York, D. (1987). The derivation of ^{40}Ar/^{39}Ar age spectra of single grains of hornblende and biotite by laser step-heating. *Geophys. Res. Lett*. **14**, 757–60.

Lee, J. (1995a). Rapid uplift and rotation of mylonitic rocks from beneath a detachment fault: insights from potassium feldspar ^{40}Ar/^{39}Ar thermochronology, northern Snake Range, Nevada. *Tectonics* **14**, 54–77.

Lee, J. K. W. (1995b). Multipath diffusion in geochronology. *Contrib. Mineral. Petrol*. **120**, 60–82.

Lee, J. K. W. and Aldama, A. A. (1992). Multipath diffusion: a general numerical model. *Comput. Geosci*. **18**, 531–55.

Lee, J. K. W., Onstott, T. C., Cashman, K. V., Cumbest, R. J. and Johnson, D. (1991). Incremental heating of hornblende *in vacuo*: implications for ^{40}Ar/^{39}Ar geochronology and the interpretation of thermal histories. *Geology* **19**, 872–6.

Lee, J. K. W., Onstott, T. C. and Hanes, J. A. (1990). An ^{40}Ar/^{39}Ar investigation of the contact effects of a dyke intrusion, Kapuskasing Structural Zone, Ontario. *Contrib. Mineral. Petrol*. **105**, 87–105.

Lo, C.-H., Lee, J. K. W. and Onstott,. T. C. (2000). Argon release mechanisms of biotite *in vacuo* and the role of short-circuit diffusion and recoil. *Chem. Geol*. **165**, 135–66.

Lopez Martinez, M., York, D., Hall, C. M. and Hanes, J. A. (1984). Oldest reliable ^{40}Ar/^{39}Ar ages for terrestrial rocks: Barberton Mountain komatiites. *Nature* **307**, 352–4.

Lovera, O. M. (1992). Computer programs to model ^{40}Ar/^{39}Ar diffusion data from multidomain samples. *Comput. Geosci*. **18**, 789–813.

Lovera, O. M., Grove, M. and Harrison, T. M. (2002). Systematic analysis of K-feldspar ^{40}Ar/^{39}Ar step heating results II: relevance of laboratory argon diffusion properties to nature. *Geochim. Cosmochim. Acta* **66**, 1237–55.

Lovera, O. M., Grove, M., Harrison, T. M. and Mahon, K. I. (1997). Systematic analysis of K-feldspar ^{40}Ar/^{39}Ar step heating results: I. Significance of activation energy determinations. *Geochim. Cosmochim. Acta* **61**, 3171–92.

Lovera, O. M., Heizler, M. T. and Harrison, T. M. (1993). Argon diffusion domains in K-feldspar II: kinetic properties of MH-10. *Contrib. Mineral. Petrol*. **113**, 381–93.

Lovera, O. M., Richter, F. M. and Harrison, T. M. (1989). The ^{40}Ar/^{39}Ar thermochronometry for slowly-cooled samples having a distribution of domain sizes. *J. Geophys. Res*. **94**, 17 917–35.

Lovera, O. M., Richter, F. M. and Harrison, T. M. (1991). Diffusion domains determined by ^{39}Ar released during step heating. *J. Geophys. Res*. **96**, 2057–69.

Lowrie, W. and Alvarez, W. (1981). One hundred million years of geomagnetic polarity history. *Geology* **9**, 392–7.

Mankinen, E. A. and Dalrymple, G. B. (1979). Revised geomagnetic polarity time scale for the interval 0 to 5 m.y. B.P. *J. Geophys. Res*. **84**, 615–26.

McDougall, I. and Harrison, T. M. (1988). *Geochronology and Thermochronology by the ^{40}Ar/^{39}Ar Method*. Oxford University Press, 212 p.

McDougall, I. and Harrison, T. M. (1999). *Geochronology and Thermochronology by the ^{40}Ar/^{39}Ar Method*, 2nd edn. Oxford University Press, 269 pp.

McDougall, I., Polach, H. A. and Stipp, J. J. (1969). Excess radiogenic argon in young subaerial basalts from the Auckland volcanic field, New Zealand. *Geochim. Cosmochim. Acta* **33**, 1485–520.

McDougall, I. and Tarling, D. H. (1964). Dating geomagnetic polarity zones. *Nature* **202**, 171–2.

Megrue, G. H. (1967). Isotopic analysis of rare gases with a laser microprobe. *Science* **157**, 1555–6.

Megrue, G. H. (1973). Spatial distribution of ^{40}Ar/^{39}Ar ages in lunar breccia 14 301. *J. Geophys. Res*. **78**, 3216–21.

Merrihue, C. and Turner, G. (1966). Potassium–argon dating by activation with fast neutrons. *J. Geophys. Res*. **71**, 2852–7.

Min, K., Mundil, R., Renne, P. R. and Ludwig, K. R. (2000). A test for systematic errors in ^{40}Ar/^{39}Ar geochronology through comparison with U/Pb analysis of a 1.1-Ga rhyolite. *Geochim. Cosmochim. Acta* **64**, 73–98.

Mitchell, J. G. (1968). The argon-40/argon-39 method for potassium–argon age determination. *Geochim. Cosmochim. Acta* **32**, 781–90.

Mussett, A. E. and Dalrymple, G. B. (1968). An investigation of the source of air Ar contamination in K–Ar dating. *Earth Planet. Sci. Lett*. **4**, 422–6.

Onstott, T. C., Hall, C. M. and York, D. (1989). ^{40}Ar/^{39}Ar thermochronometry of the Imataca complex, Venezuela. *Precamb. Res.* **42**, 255–91.

Onstott, T. C., Miller, M. L., Ewing, R. C., Arnold, G. W. and Walsh, D. S. (1995). Recoil refinements: implications for the ^{40}Ar/^{39}Ar dating technique. *Geochim. Cosmochim. Acta* **59**, 1821–34.

Onstott, T. C., Phillips, D. and Pringle-Goodell, L. (1991). Laser microprobe measurement of chlorine and argon zonation in biotite. *Chem. Geol.* **90**, 145–68.

Parsons, I., Brown, W. L. and Smith, J. V. (1999). ^{40}Ar/^{39}Ar thermochronology using alkali feldspars: real thermal history or mathematical mirage of microtexture? *Contrib. Mineral. Petrol.* **136**, 92–110.

Phillips, D. and Onstott, T. C. (1988). Argon isotopic zoning in mantle phlogopite. *Geology* **16**, 542–6.

Pickles, C. S., Kelley, S. P., Reddy, S. M. and Wheeler, J. (1997). Determination of high spatial resolution argon isotope variations in metamorphic biotites. *Geochim. Cosmochim. Acta* **61**, 3809–33.

Renne, P. R. (2000). ^{40}Ar/^{39}Ar age of plagioclase from Acapulco meteorite and the problem of systematic errors in cosmochronology. *Earth Planet. Sci. Lett.* **175**, 13–26.

Renne, P. R. (2001). Reply to comment on "^{40}Ar/^{39}Ar age of plagioclase from Acapulco meteorite and the problem of systematic errors in cosmochronology" by Paul. R. Renne. *Earth Planet. Sci. Lett.* **190**, 271–3.

Renne, P. R., Deino, A. L., Walter, R. C. *et al.* (1994). Intercalibration of astronomical and radioisotopic time. *Geology* **22**, 783–6.

Renne, P. R., Karner, D. B. and Ludwig, K. R. (1998a). Absolute ages aren't exactly. *Science* **282** 1840–1.

Renne, P. R., Swisher, C. C., Deino, A. L., Karner, D. B., Owens, T. L. and DePaolo, D. J. (1998b). Intercalibration of standards, absolute ages and uncertainties in ^{40}Ar/^{39}Ar dating. *Chem. Geol.* **145**, 117–52.

Rex, D. C., Guise, P. G. and Wartho, J.-A. (1993). Disturbed ^{40}Ar/^{39}Ar spectra from hornblendes: thermal loss or contamination? *Chem. Geol. (Isot. Geosci. Section)* **103**, 271–81.

Richter, F. M., Lovera, O. M., Harrison, T. M. and Copeland, P. (1991). Tibetan tectonics from ^{40}Ar/^{39}Ar analysis of a single K-feldspar sample. *Earth Planet. Sci. Lett.* **105**, 266–78.

Roberts, H. J., Kelley, S. P. and Dahl, P. S. (2001). Obtaining geologically meaningful ^{40}Ar–^{39}Ar ages from altered biotite. *Chem. Geol.* **172**, 277–90.

Roddick, J. C. and Farrar, E. (1971). High initial argon ratios in hornblendes. *Earth Planet. Sci. Lett.* **12**, 208–14.

Schmitz, M. D. and Bowring, S. A. (2001). U–Pb zircon and titanite systematics of the Fish Canyon Tuff: an assessment of high-precision U–Pb geochronology and its application to young volcanic rocks. *Geochim. Cosmochim. Acta* **65**, 2571–87.

Shackleton, N. J., Berger, A. and Peltier, W. R. (1990). An alternative astronomical calibration of the lower Pleistocene timescale based on ODP Site 677. *Trans. Roy. Soc. Edinburgh: Earth Sci.* **81**, 251–61.

Smith, P. E., Evensen, N. M. and York, D. (1993). First successful ^{40}Ar/^{39}Ar dating of glauconies: argon recoil in single grains of cryptocrystalline material. *Geology* **21**, 41–4.

Smith, P. E., Evensen, N. M., York, D. and Odin, G. S. (1998). Single-grain ^{40}Ar–^{39}Ar ages of glauconies: implications for the geologic time scale and global sea level variations. *Science* **279**, 1517–9.

Spell, T. L. and McDougall, I. (1992). Revisions to the age of the Brunhes–Matuyama boundary and the Pleistocene geomagnetic polarity timescale. *Geophys. Res. Lett.* **19**, 1181–4.

Steiger, R. H. and Jäger, E. (1977). IUGS Subcommission on Geochronology: convention on the use of decay constants in geo- and cosmochronology. *Earth Planet. Sci. Lett.* **36**, 359–62.

Tauxe, L., Deino, A. D., Behrensmeyer, A. K. and Potts, R. (1992). Pinning down the Brunhes/Matuyama and upper Jaramillo boundaries: a reconciliation of orbital and isotopic time scales. *Earth Planet. Sci. Lett.* **109**, 561–72.

Trieloff, M., Jessberger, E. K. and Fiéni, C. (2001). Comment on "^{40}Ar/^{39}Ar age of plagioclase from Acapulco meteorite and the problem of systematic errors in cosmochronology" by Paul. R. Renne. *Earth Planet. Sci. Lett.* **190**, 267–9.

Turner, G. (1968). The distribution of potassium and argon in chondrites. In: Ahrens, L. H. (Ed.), *Origin and Distribution of the Elements*. Pergamon, pp. 387–97.

Turner, G. (1969). Thermal histories of meteorites by the ^{39}Ar–^{40}Ar method. In: Millman, P. M. (Ed.), *Meteorite Research*. Reidel, pp. 407–17.

Turner, G. (1971a). Argon 40–argon 39 dating: the optimisation of irradiation parameters. *Earth Planet. Sci. Lett.* **10**, 227–34.

Turner, G. (1971b). ^{40}Ar/^{39}Ar ages from the lunar maria. *Earth Planet. Sci. Lett.* **11**, 169–91.

Turner, G. (1972). ^{40}Ar–^{39}Ar age and cosmic ray irradiation history of the Apollo 15 anorthosite, 15 415. *Earth Planet. Sci. Lett.* **14**, 169–75.

Turner, G. and Cadogan, P. H. (1974). Possible effects of ^{39}Ar recoil in ^{40}Ar/^{39}Ar dating. In: *Proceedings of the 5th Lunar Science Conference*. Pergamon, pp. 1601–15.

Turner, G., Miller, J. A. and Grasty, R. L. (1966). Thermal history of the Bruderheim meteorite. *Earth Planet. Sci. Lett.* **1**, 155–7.

van Eysinga, F. W. B. (1975). *Geological Time Table, 3rd edn.* Elsevier.

van Hinte, J. E. (1976). A Cretaceous time scale. *Amer. Assoc. Petroleum Geol. Bull.* **60**, 498–516.

Villa, I. M. (1997). Direct determination of ^{39}Ar recoil distance. *Geochim. Cosmochim. Acta* **61**, 689–91.

Villa, I. M. (1998). Reply to the comment by T. M. Harrison, M. Grove, and O. M. Lovera on "Direct determination of ^{39}Ar recoil distance". *Geochim. Cosmochim. Acta* **62**, 349.

Vincent, E. A. (1960). Analysis by gravimetric and volumetric methods, flame photometry, colorimetry and related techniques. In: Smales, A. A. and Wager, L. R. (Eds.), *Methods in Geochemistry.* Interscience, pp. 33–80.

Wartho, J.-A., Kelley, S. P., Brooker, R. A., Carroll, M. R., Villa, I. M. and Lee, M. R. (1999). Direct measurement of Ar diffusion profiles in a gem-quality Madagascar K-feldspar using the ultra-violet laser ablation microprobe (UVLAMP). *Earth Planet. Sci. Lett.* **170**, 141–53.

Wright, N., Layer, P. W. and York, D. (1991). New insights into thermal history from single grain ^{40}Ar/^{39}Ar analysis of biotite. *Earth Planet. Sci. Lett.* **104**, 70–9.

York, D. (1978). A formula describing both magnetic and isotopic blocking temperatures. *Earth Planet. Sci. Lett.* **39**, 89–93.

York, D. (1984). Cooling histories from ^{40}Ar/^{39}Ar age spectra: implications for Precambrian plate tectonics. *Ann. Rev. Earth Planet. Sci.* **12**, 383–409.

York, D., Hall, C. M., Yanase, Y., Hanes, J. A. and Kenyon, W. J. (1981). ^{40}Ar/^{39}Ar dating of terrestrial minerals with a continuous laser. *Geophys. Res. Lett.* **8**, 1136–8.

11 Rare-gas geochemistry

The elements known as the rare, inert or noble gases possess unique properties that make them important in isotope geology. The low abundance of these rare gases allows them to sensitively record several types of nuclear process, even including rare nuclear-fission reactions. (In contrast, the relatively larger abundance of other fission-product nuclides such as the 'rare' earths swamps fissiogenic production.) Another property of these gases is their inertness, which allows unique insights into the Earth's interior because of their lack of interaction with other materials. Finally, as isotopic tracers, rare gases can give information about the degassing history of the mantle, the formation of the atmosphere, and mixing relationships between different mantle reservoirs.

11.1 Helium

Helium has two isotopes, ^{4}He and ^{3}He. The former was recognised by Rutherford (1906) to be the α-decay product of actinide elements, and hence comprised the first radiometric dating method. However, the great diffusivity of helium made the method very susceptible to thermal disturbance, and it has therefore been abandoned in all but the most specialised applications (e.g. Wernicke and Lippolt, 1993).

Non-radiogenic ^{3}He was first discovered in nature by Alvarez and Cornog (1939). Alvarez and Cornog estimated (using a cyclotron) that atmospheric helium had a ^{3}He/^{4}He ratio ten times greater than that of natural oil-well gases from the Earth's crust. Aldrich and Nier (1948) confirmed this observation by mass-spectrometric measurements, and determined atmospheric and well-gas ^{3}He/^{4}He ratios of about 1.2×10^{-6} and 1×10^{-7}, respectively. They concluded that there must be independent sources of the two isotopes, one of which could be primordial.

11.1.1 Mass spectrometry

Mass-spectrometric analysis of helium is broadly similar to argon isotope analysis in K–Ar dating (section 10.1.1). However, in helium isotope analysis there are no 'extra' isotopes available to allow accurate correction for atmospheric contamination. Therefore it is critical to minimise the *extent* of this contamination during helium extraction and analysis. Uncertainties in the atmospheric 'blank' may contribute the principal error in helium isotope analysis, especially for rock samples. Well-gas samples, being larger, are less susceptible to atmospheric contamination during analysis, but may have come from an open system in the natural environment. In the case of rock analysis, absorbed atmospheric helium is usually driven off by heating overnight at 200–300 °C. The sample gas may then be extracted by melting the rock or by crushing under vacuum. A combination of the two techniques (e.g. Kurz and Jenkins, 1981) provides an extra check against the possibility of atmospheric contamination, both in the laboratory and in the environment.

Two steps are necessary in order to reduce blank levels in the mass spectrometer for all rare-gas analyses. One is to polish all internal surfaces of a metal instrument to minimise absorption of gas onto the walls of the vacuum system. Another is to reduce the internal surface area of the instrument as much as possible, for example by boring the flight tube out of a solid piece of steel rather than using welded pipe. A low internal volume also yields better sensitivity for very small samples.

All rare-gas analyses are performed in the static gas mode (i.e. with vacuum pumps isolated). As a result, hydrogen tends to build up in the instrument, so that its molecular ions HD$^+$ and H_3^+ cause isobaric interferences onto ^{3}He$^+$. Therefore, the vacuum system in some older machines contains a small titanium 'getter', designed to absorb H_2 released inside the instrument (Clarke *et al.*, 1969). Nevertheless the peak composed of HD and H_3 may still be much larger than that of ^{3}He, so it is essential to separate them by mass. This can be done by making use of the 0.006-atomic-mass-unit difference between ^{3}He and the other two species

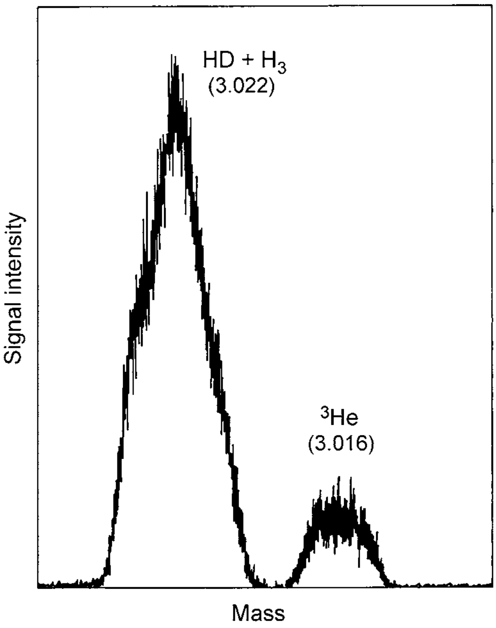

Fig. 11.1. Scan of peaks in the region of mass 3 during helium isotope analysis, showing the separation of molecular interference using high spectral resolution. Masses are quoted relative to $^{12}C = 12.000$. After Lupton and Craig (1975).

(Fig. 11.1) which results from their different nuclear binding energies. In order to achieve this separation at mass 3, a resolution of one mass unit in 600 is necessary, which can be achieved with an instrument of about 25 cm radius (Clarke *et al.*, 1969; Kurz and Jenkins, 1981).

In order to measure the very large difference in intensity between ^{3}He and ^{4}He signals, it is most convenient to measure the former on a multiplier detector and the latter by Faraday detector. These can only be used in the static collection mode if a branched flight tube is available, because of the extreme divergence of the mass-3 and mass-4 ion beams (Lupton and Craig, 1975). Alternatively, peak switching is performed by changing the accelerating potential or magnetic field (e.g. Clarke *et al.*, 1969; Poreda and Farley, 1992).

11.1.2 Helium production in nature

In order to determine whether primordial helium is an important constituent in the Earth, it is necessary to determine the ^{3}He/^{4}He ratio of primordial solar-system helium, and also the production ratio in nuclear and cosmogenic processes. A good indication of the composition of primordial helium is provided by the ^{3}He/^{4}He ratio of $(2\text{–}4) \times 10^{-4}$ measured in gas-rich carbonaceous chondrites (Pepin and Signer, 1965). These meteorites have such high primordial gas contents that their composition is not significantly perturbed by 'cosmogenic' helium (a product of cosmic-ray spallation effects). In contrast, most ^{3}He in iron meteorites is cosmogenic.

Early calculations of the nuclear ^{3}He/^{4}He production ratio in igneous rocks were made by Morrison and Pine (1955). Radiogenic production of ^{4}He is obvious, since the α particle is synonymous with a ^{4}He nucleus. However, 'nucleogenic' ^{3}He can also be generated by neutron bombardment of light atoms. Radioactive decay of uranium generates a neutron flux in rocks by two mechanisms. Spontaneous fission is a minor source, but by far the dominant source of neutrons is the collision of α particles with nuclei of light elements. Some of these neutrons reach epithermal energies, where they can induce the (n, α) reaction on lithium. The tritium thus produced decays to ^{3}He:

$$^6\text{Li} + \text{n} \rightarrow {}^3\text{H} + \alpha$$

$$^3\text{H} \rightarrow {}^3\text{He} + \beta \quad (t_{1/2} = 12\,\text{yr})$$

Kunz and Schintlmeister (1965) calculated that ^{3}He generation by this reaction is at least three orders of magnitude more efficient than all other neutron-induced reactions. Given the uranium (plus thorium) and lithium content of a rock, the ^{3}He/^{4}He yield can be calculated (Gerling *et al.*, 1971). The results are consistent with the range of $(1\text{–}3) \times 10^{-8}$ measured empirically in old granites. The calculations were also confirmed by experimental irradiation of ultrabasic rocks in a reactor (Tolstikhin *et al.*, 1974). Some other possible sources of ^{3}He (via tritium) are

$$^{238}\text{U} \rightarrow \text{fission products} + (2 \times 10^{-4})\,{}^3\text{H}$$

$$^7\text{Li} + \alpha \rightarrow {}^8\text{Be} + {}^3\text{H}$$

$$^7\text{Li} + \gamma \rightarrow {}^4\text{He} + {}^3\text{H}$$

However, Mamyrin and Tolstikhin (1984) calculated total ^{3}He/^{4}He production ratios of 8×10^{-12}, $<7 \times 10^{-9}$ and about 10^{-13}, respectively, for these reactions, making them insignificant compared with the main (n, α) reaction. It was concluded from these observations and calculations that no nuclear process is capable of generating ^{3}He/^{4}He ratios significantly greater than 10^{-8} in normal rocks. However, uranium ores generate lower ratios, while Li-rich *minerals* generate abnormally high ratios.

Another mineral in which high ^{3}He/^{4}He ratios have been observed is diamond. Values up to 3×10^{-4} were interpreted by Ozima and Zashu (1983) as indicative of primordial mantle reservoirs, but have been attributed by later workers to either nucleogenic or cosmogenic ^{3}He production. For example, Lal *et al.* (1987) attributed high ^{3}He/^{4}He ratios in alluvial diamonds from Zaire to cosmogenic production while the diamonds had been exposed at the surface.

On the other hand, Kurz *et al.* (1987) and Zadnik *et al.* (1987) measured ^{3}He/^{4}He ratios as high as 1.4×10^{-3} in diamonds mined directly from kimberlite pipes at depths of about 26 and 200 m, respectively. Since cosmic rays cannot penetrate to such depths, these helium signatures were attributed to nucleogenic production. Evidence for this interpretation came from the observation of isotopic variability within individual diamonds, and the determination of ^{3}He/^{4}He ratios higher than solar in the latter study. In both cases, ^{3}He production was attributed to the (n, α) reaction on lithium. For this process to occur, the diamond and its inclusions must be irradiated by neutrons from outside the crystal, so that radiogenic ^{4}He production in the diamond itself is suppressed.

In situ cosmogenic helium production in terrestrial rocks was proposed by Jeffrey and Hagan (1969), but was not identified unambiguously until work by Kurz (1986a) and Craig and Poreda (1986). In a detailed helium isotope study of sub-aerial lavas from Haleakala volcano, Kurz discovered very high ^{3}He/^{4}He ratios released by step heating of some near-surface 0.5–0.8-Myr-old alkali basalts. Low-temperature gas releases from samples within 0.5 m of the weathered surface gave ^{3}He/^{4}He ratios over 10^{-3} (Fig. 11.2). These values are even higher than those for primordial meteoritic or solar-wind helium.

In contrast, step heating of samples from a similar stratigraphic horizon that were buried under about 160 m of younger flows yielded MORB-like helium (^{3}He/^{4}He $= 1.2 \times 10^{-5}$). Helium released by crushing of phenocrysts also gave a MORB signature, both for the buried and for the surface samples. Therefore, Kurz argued that crushing released magmatic helium from vesicles, but step heating of old surface samples released dispersed cosmogenic helium from the rock matrix. Young surface samples such as the 1790 flow on Haleakala do not show these effects, ruling out anthropogenic bomb tritium as the source of the ^{3}He.

Kurz (1986b) went on to examine cosmogenic ^{3}He production as a function of depth below the surface of a lava flow. Spallation reactions caused by cosmogenic neutrons are the dominant source of ^{3}He at the surface, but neutron fluxes are attenuated exponentially downwards. Nevertheless, ^{3}He abundances exhibited less attenuation with depth than expected. This was attributed to production by cosmic-ray muons, which have a greater penetration depth than neutrons. Muon capture by nuclei causes neutron emission, which in turn produces ^{3}He via the (n, α) reaction on lithium. The depth dependences of different production routes for ^{3}He are summarised in Fig. 11.3 (Lal, 1987).

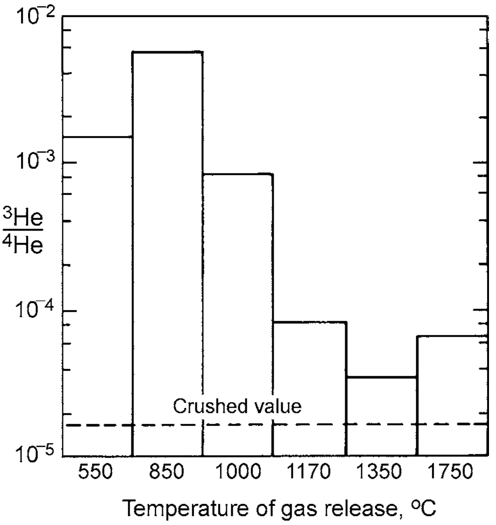

Fig. 11.2. Step-heating helium isotope analysis of a surface sample of Haleakala lava, showing a large cosmogenic component, especially in the low-temperature release steps. Crushed vesicles yield the 'true' mantle value. After Kurz (1986a).

Cosmogenic isotopes constitute a useful tool for determining exposure ages of rock surfaces (section 14.6). However, the great diffusivity of helium may be a problem in using ^{3}He in such studies. For example, Cerling (1989) showed that helium was often not quantitatively retained in quartz, the most widely used material in surface-exposure dating. On the other hand, ^{21}Ne displays cosmogenic production with an attenuation depth similar to that of ^{3}He (Sarda *et al.*, 1993). The lower diffusivity of neon may therefore make it more widely useful in surface-exposure dating (section 11.2.1).

11.1.3 Terrestrial primordial helium

The first accurate determinations of the atmospheric ^{3}He/^{4}He ratio were made by Mamyrin *et al.* (1970) and Clarke *et al.* (1976), yielding ratios of 1.40×10^{-6} and 1.38×10^{-6}. Because atmospheric helium is universally used as a mass-spectrometric standard, it is convenient to express ^{3}He/^{4}He ratios in unknown samples relative to the atmospheric ratio in the form $R_{\text{unknown}}/R_{\text{air}}$ (R/R_A). However, because cosmogenic ^{3}He production in the atmosphere is difficult to

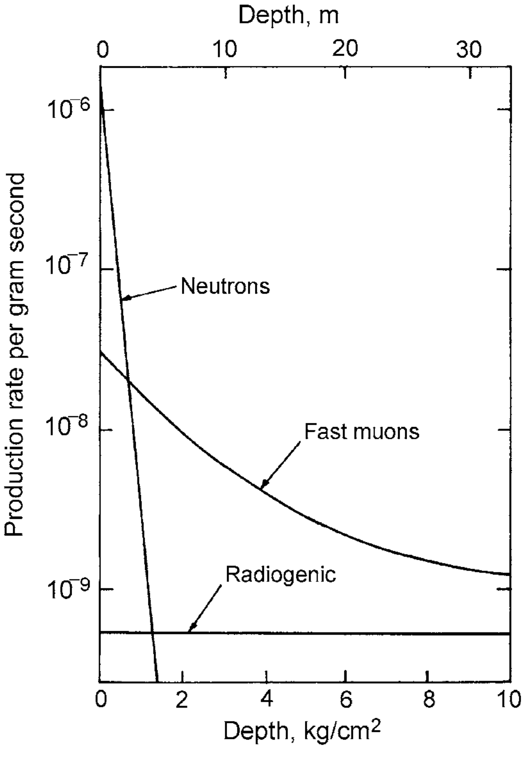

Fig. 11.3. Calculated rates for production of ^{3}He by different processes as a function of depth in a rock surface. Depths are expressed as kg/cm^2, which is approximately equal to 1/3 × depth in metres. After Lal (1987).

quantify accurately, it is not possible to prove the existence of a primordial helium source in the Earth *simply* by the fact that the atmosphere is two orders of magnitude richer in ^{3}He than the radioactive production in rocks.

Stronger evidence of a primordial helium signature in the Earth was provided by Clarke *et al.* (1969), when they discovered that deep water from the Pacific Ocean was enriched in ^{3}He by up to 20% relative to the atmosphere. However, Sheldon and Kern (1972) and Lupton and Craig (1975) hypothesised that this could conceivably be due to a temporary weakening of the Earth's magnetic field, during which the atmospheric ^{3}He/^{4}He ratio was elevated by greater penetration of cosmic rays.

Convincing evidence of primordial helium in the Earth was first provided by Mamyrin *et al.* (1969), who found ^{3}He/^{4}He ratios ten times the atmospheric ratio in thermal fluids from the Kurile Islands. Subsequently, ^{3}He/^{4}He ratios as high as twenty times atmospheric were found in hot springs from Iceland (Mamyrin *et al.*, 1972). Even higher R/R_A values have been found in oceanic volcanic rocks: up to 26 in sub-glacial basaltic glasses from Iceland and up to 32 in basaltic glass from Loihi Seamount off Hawaii (Kurz *et al.*, 1982). These values are regarded as reliable indicators of primordial helium because they come from rocks that have been shielded from *in situ* cosmogenic production, either by water or by ice.

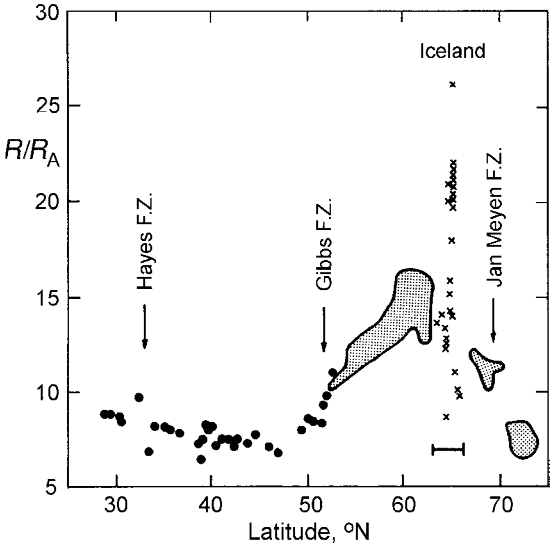

Fig. 11.4. Plot of helium isotope ratios along the Mid-Atlantic Ridge, expressed as deviations from the atmospheric value (R/R_A). The primordial ^{3}He signature of the Iceland plume (×) is elevated relative to MORB (●). Shaded fields display mixing of sources. After Kurz *et al.* (1985).

The highest R/R_A value for any plume source (38) was found in crushed phenocrysts from an olivine basalt in the neovolcanic zone of NW Iceland (Hilton *et al.*, 1999). These rocks are not shielded from cosmogenic production, but it was argued that the possibility of cosmogenic contamination of the data could be excluded. This was based on the observation that the *residues* from crushing (which should contain any dispersed cosmogenic component) had *less*-elevated ^{3}He/^{4}He ratios than the gases released by crushing. The helium signature of the Iceland plume can also be seen spreading out over a large area of the North Atlantic as the plume head contaminates the asthenospheric upper mantle (Fig. 11.4).

11.1.4 The 'two-reservoir' model

In contrast to the variable helium isotope signatures in OIB, Craig and Lupton (1976) found a relatively narrow range of R/R_A ratios around 9 in MORB glasses from various ocean basins. Subsequent data have confirmed this narrow helium isotope range in MORB, relative to the large variations in plumes (e.g. Fig. 11.4). The intermediate helium isotope composition of MORB, between those of atmospheric and plume sources, can be explained by partial outgassing of primordial helium from the upper mantle, followed by radiogenic helium production. This caused the upper mantle to develop a lower ^{3}He/^{4}He composition than the un-degassed lower mantle, where radiogenic production is swamped by primordial helium.

This partial-degassing or 'two-reservoir' model for the mantle was originally proposed to explain argon isotope systematics (Hart *et al.*, 1979), and was applied to helium by Kaneoka and Takaoka (1980). Unfortunately, Kaneoka and Takaoka based their case on rare-gas compositions in phenocrysts from Haleakala volcano, Hawaii, which were subsequently shown to be contaminated with atmospheric argon and cosmogenic helium (Fisher, 1983; Kurz, 1986a). However, more recent data from OIB samples have confirmed the elevated R/R_A value of the plume source, as noted above. Hence the two-reservoir model for mantle helium has been widely accepted.

An early test of the two-reservoir model was performed by comparing helium and heat fluxes from the Earth (O'Nions and Oxburgh, 1983). These fluxes must be related because the decay of uranium and thorium produces both radiogenic helium (alpha particles) and also radioactive heating. Taking account of the small amount of heat also derived from ^{40}K decay, O'Nions and Oxburgh (1983) calculated that 10^{12} atoms of ^{4}He would be generated in the mantle per joule of heat production. They then calculated the concentration of U necessary to generate the observed helium and heat fluxes. The results were somewhat surprising, because the amount of uranium required to generate 88% of the Earth's oceanic helium flux can produce only 3% of the oceanic heat flow.

The logical source for some of the remaining heat flux is crystallisation of the inner core, which releases heat through the outer core and mantle by convection. However, this convection must operate in such a way that the reservoir of primordial ^{3}He in the Earth's interior is not completely exhausted. Therefore, O'Nions and Oxburgh proposed that a boundary layer inhibits upward transport of helium from the 'primordial' reservoir much more effectively than it inhibits the transport of heat. They envisaged this boundary layer at 700 km depth, separating the upper and lower mantle. This would imply that the whole of the lower mantle is a kind of primordial helium reservoir. Other workers have preferred the core–mantle boundary, although it is not clear whether the core could represent the repository of primordial Earth helium. This question will be discussed further below.

Another challenge for the two-reservoir model is to explain the respective concentrations of helium and other rare gases in the two reservoirs. Thus, if OIB come from the un-degassed source, we would expect them to contain more helium than MORB glasses from the degassed upper mantle. However, OIB glasses actually have ten times *less* ^{3}He than MORB glasses (Fisher, 1985). This observation has sometimes been called the helium paradox (e.g. Hilton *et al.*, 2000). However, although this evidence is problematical, it is not definitive, due to the poorly constrained behaviour of rare gases during the melting process. For example, the dynamics of mantle convection and melt segregation under ridges must be different from those of plumes; so that ridge magmas collect helium from a greater volume of mantle during the melting process (section 13.3.6). Hence, most workers have taken the isotopic evidence in favour of the two-reservoir model for helium as definitive, and over-riding any problems involving rare-gas abundances. The case for the heavy rare gases will be discussed later.

The existence of a primordial helium reservoir in the Earth was challenged more recently by Anderson (1993), who attributed this signature to the subduction of cosmic (interplanetary) dust particles. These particles were found to accumulate in ocean-floor sediments by Merrihue (1964). Cosmic dust has ^{3}He/^{4}He ratios similar to those of gas-rich meteorites (about 3×10^{-4}), but unlike meteorites, these particles can fall to Earth without burning up in the atmosphere (Nier and Schlutter, 1990). Hence, ocean-floor sediments develop a 'primordial' helium isotope signature (Fig. 11.5a).

The rare gases in cosmic dust particles are encapsulated in magnetite grains, which are relatively resistant to thermal degassing (Matsuda *et al.*, 1990). Therefore, the cosmic helium in ocean-floor sediments might survive the subduction process and be transported into the deep mantle. In contrast, *atmospheric* rare gases trapped in ocean-floor sediments are very susceptible to thermal degassing. Staudacher and Allègre (1988) argued that subduction-related volcanism is at least 98% efficient at scavenging these atmospheric gases from subducted sediments before they can reach the deep mantle.

Because cosmic dust might survive the 'subduction barrier' against atmospheric rare gases, it has the potential to deliver helium with a primordial signature into the deep mantle. This possibility was recognised

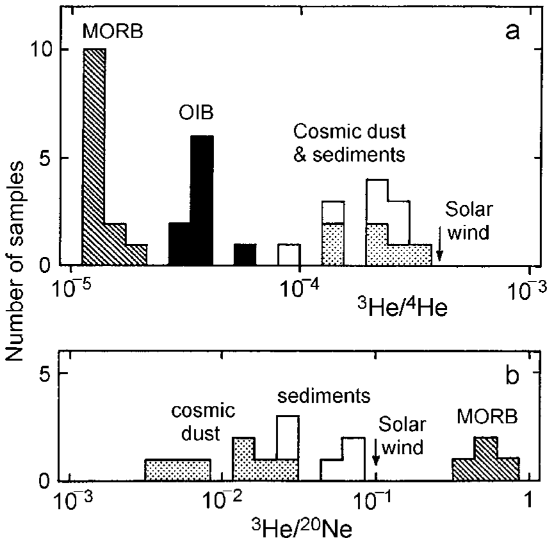

Fig. 11.5. Histograms of (a) $^3He/^4He$ and (b) $^3He/^{20}Ne$ in cosmic dust particles (stipple) and ocean-floor sediments (white) compared with the rare-gas composition of MORB (hatched) and OIB (black). The solar-wind composition is shown for reference. Data from Allègre *et al.* (1993).

by several workers (e.g. Allègre *et al.*, 1993), but Anderson (1993) took the model a step further by attributing *most* of the primordial helium signal in mantle hotspots to subducted cosmic dust. However, Allègre *et al.* (1993) used neon isotope data to place upper limits on the amount of cosmic ^3He which can enter plume sources. They noted that the $^3He/^{20}Ne$ ratio in cosmic dust is one to two orders of magnitude *lower* than the $^3He/^{20}Ne$ ratio in the upper mantle (Fig. 11.5b). Furthermore, helium has a much greater diffusivity than neon, which would promote its preferential degassing from grains of cosmic dust during subduction (Hiyagon, 1994). Therefore it appears that subduction of cosmic dust cannot contribute more than a small fraction of the mantle ^3He budget without causing excessive enrichment of ^{20}Ne in submarine glasses.

Although helium isotope ratios provide the best evidence for a primordial gas reservoir in the Earth, this single isotope ratio cannot provide enough degrees of freedom to constrain the complex mixing processes expected to occur in the mantle. Hence, various attempts have been made to compare helium isotope signatures with other isotope ratios in oceanic volcanics, in order to provide extra constraints on mantle processes.

One such approach is the comparison of helium and strontium isotope data (Kurz *et al.*, 1982; Lupton, 1983). MORB samples define a restricted range of compositions on a plot of helium isotope ratio against $^{87}Sr/^{86}Sr$ ratio, but ocean islands are widely scattered (Fig. 11.6). While Loihi defines the most primordial helium composition, some ocean islands such as Tristan, Gough and the Azores have $^3He/^4He$ ratios *lower* (more radiogenic) than MORB. Similar low ratios have subsequently been found in the HIMU islands of the SW Pacific (Hanyu and Kaneoka, 1997). These low $^3He/^4He$ ratios require a component of radiogenic helium from a long-lived U- or Th-rich source, which can most easily be satisfied by the recycling of oceanic crust and sediments into the mantle, as inferred from lithophile isotope data (section 6.5). Finally, a possible third type of plume source is exemplified by the data distribution from Samoa in Fig. 11.6. This was originally attributed to mixing of primordial and recycled helium in the deep mantle, but more recent work suggests a mixing process in the shallow mantle as the cause (section 11.1.5).

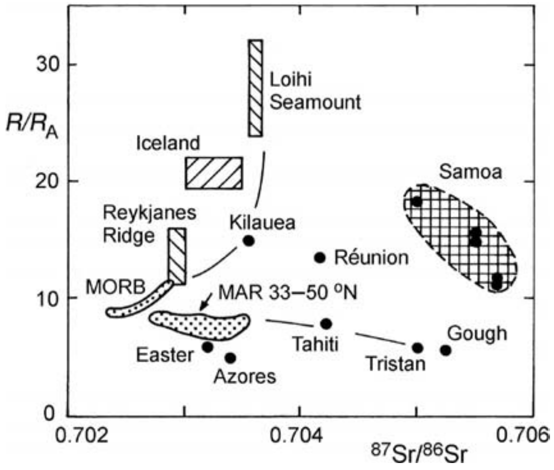

Fig. 11.6. Plot of $^3He/^4He$ against Sr isotope ratio to show mixing between the MORB reservoir and primordial and recycled plume sources. For discussion, see the text. After Lupton (1983).

The MORB field in Fig. 11.6 breaks into two lobes with geographical boundaries. The main field trends slightly towards the primordial source, while the Mid-Atlantic Ridge between 33 and 50 °N defines a subsidiary field with more radiogenic helium, which is consistent with contamination by the nearby Azores plume. This evidence suggests that plumes break into trains of blobs that locally contaminate the MORB source. According to the nature of the plume material contaminating any given ridge segment, the MORB array can trend towards either the primordial or the recycled type of plume.

Models that involve large-scale recycling of crustal sources back into the mantle imply that the upper mantle has a short residence time for many elements, and would therefore have reached a steady-state condition at the present day (e.g. sections 6.3.3 and 13.3.7). In view of the ease with which helium can escape from any system at elevated temperatures, it represents the ultimate incompatible element, and should therefore have the shortest residence time. Since it was argued above that subduction of helium is negligible, input to the upper mantle must be restricted to primordial helium escaping from the lower mantle, plus *in situ* production of radiogenic helium from U-series isotopes.

Kellogg and Wasserburg (1990) assumed a steady state between supply and degassing in order to determine the residence time of helium in the upper mantle. They argued that ridges are the principal sites where helium escapes from the upper mantle (whereas hotspots dominate in outgassing the lower mantle). Hence, they used a simple calculation to estimate the residence time of helium in the upper mantle:

$$\tau = \text{mass of upper mantle/rate of outgassing}$$

Assuming a depth of 670 km, the upper mantle has a mass of 1×10^{27} g. Also, assuming ocean-floor production at 3.5 km^3/yr and a melting depth of 60 km, the rate of mantle outgassing is estimated at 7×10^{17} g/yr. Hence, Kellogg and Wasserburg calculated a helium residence time of 1.4 Byr in the upper mantle. On the other hand, O'Nions and Tolstikhin (1994) estimated a somewhat shorter residence time of 1.1 Byr, assuming an upper mantle mass of 1.1×10^{27} g and an outgassing rate of 1×10^{18} g/yr (corresponding to a melting depth of 90 km). These relatively short residence times suggest that the upper mantle has been completely outgassed of primordial helium. However, in view of the extreme volatility of helium, they also represent a minimum for the upper-mantle residence times of lithophile elements (section 6.3.3).

Contamination of the MORB source by OIB sources can occur at various scales, from plumes to isolated blobs and sheets. To evaluate this process, Allègre *et al.* (1995) examined the dispersion of helium isotope data in MORB as a function of the spreading rates of various ridges. They found that several ridges defined a strong inverse correlation between isotopic dispersion and spreading rate (Fig. 11.7). This led them to suggest that the MORB source has a stirring time for helium about four times shorter than the mean residence time of helium in this source. Other authors have examined isotopic variations of particular ridge segments in more detail, and shown how these can be explained by local contamination by plums or plumes. For example, Graham *et al.* (1996) observed correlated He–Pb and He–Sr isotope systematics in the South Atlantic.

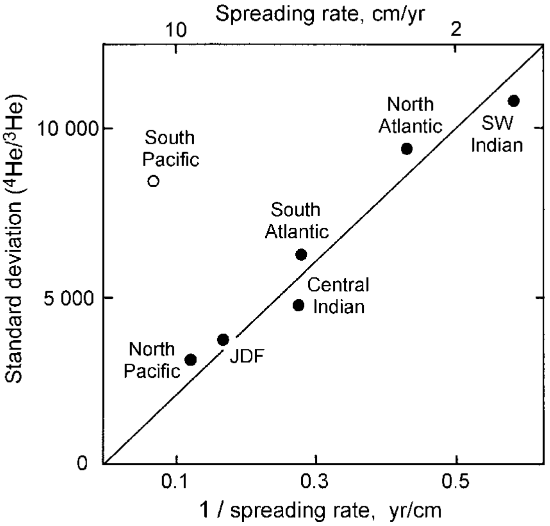

Fig. 11.7. Plot of the standard deviation of helium isotope ratios for various ridges against the reciprocal of spreading rate, showing a good correlation for several ridges. The South Pacific displays more isotope heterogeneity than expected. After Allègre *et al.* (1995).

The relatively coherent account of the two-reservoir model given above has been threatened more recently by increasing geophysical evidence for single-layer mantle convection (section 6.2.3). This militates against traditional box models, which make the lower mantle the source of primordial helium signatures. Several alternative approaches have been proposed to deal with this problem.

An attractive way of preserving the two-reservoir model in a mantle with single-layer convection is to invoke increasing mantle viscosity with depth. It is argued that this could cause large lumps of the lower mantle to be preserved intact, without being streaked out and homogenised by convection. This model was tested by two-dimensional numerical modelling of one-layer convection in such a mantle (van Keken and Ballentine, 1998; 1999). However, these workers argued that models which were realistically close to the real Earth in terms of viscosity and phase transformations could not preserve lower-mantle domains large enough to retain a significant primordial helium reservoir. Opinion about the effect of three-dimensional modelling is divided: van Keken and Ballentine (1999) argued that this would cause more rapid homogenisation, whereas other workers (e.g. Schmalzl *et al.*, 1995) suggested that it would cause less rapid homogenisation.

A second approach to preserving the two-reservoir model is to place the primordial reservoir in the core. Work by Matsuda *et al.* (1993) suggested that the core would have only a limited helium budget, but on the other hand, osmium isotope data (section 8.3.5) support this model. A recent review of the evidence (Porcelli and Halliday, 2001) is equivocal.

A third approach to this problem is to dismantle, at least partially, the two-reservoir model. For example, studies by Coltice and Ricard (1999), Anderson (2001) and Seta *et al.* (2001) suggested that the 'primordial' or 'relatively un-degassed' helium reservoir does not exist. Instead, they argued that all of the mantle is equally degassed, but some parts (e.g. the MORB reservoir) are more enriched in radiogenic helium due to U recycling via enriched OIB plumes. Anderson again took the most extreme position, suggesting that OIB are actually derived from a shallow mantle reservoir. In contrast, other workers still require a lower-mantle plume source, with a relatively high ^{3}He/^{4}He ratio which must be preserved against convective homogenisation with the more radiogenic upper mantle. However, Seta *et al.* argued that such a distinction is easier to preserve than a primordial helium reservoir, because it needs to be preserved only for about 2 Byr, whereas a primordial reservoir must be preserved for 4.5 Byr. This argument is illustrated in more detail in Fig. 11.8.

Although this model can be represented numerically, this does not necessarily mean that it is a realistic Earth model. Indeed it has several problems. Firstly, the new helium data from Iceland ($R/R_A = 38$) suggest that some plume sources are less degassed than had previously been thought, placing tighter limits on the amount of degassing possible from this source. Furthermore, evidence for a relatively un-degassed mantle source is supported by new neon data (section 11.2.2). Finally, new data from some plume sites with low R/R_A values suggest that some of these may be due to shallow mixing with radiogenic sources. Therefore, the average R/R_A value of the plume source is higher than proposed by Anderson. It is concluded that a genuine primordial helium source is probably still present in the Earth. To the present author, the evidence now favours the core.

11.1.5 Crustal helium

Of the continental helium flux, 99% is radiogenic, and can be sustained by a U equivalent concentration of 6 ppm in the upper 8 km of the crust. This can also explain 50% of the continental heat flux. Hence, the other 50% of continental heat flow must be subcontinental, whereas less than 1% (primordial plus radiogenic) of the continental helium flux comes from the mantle. In this case it is clear that the continental crust is a boundary layer. Mantle-derived heat can be carried across it conductively, but mantle-derived helium only leaks through the crust in certain discrete areas. These are normally areas of active magmatism.

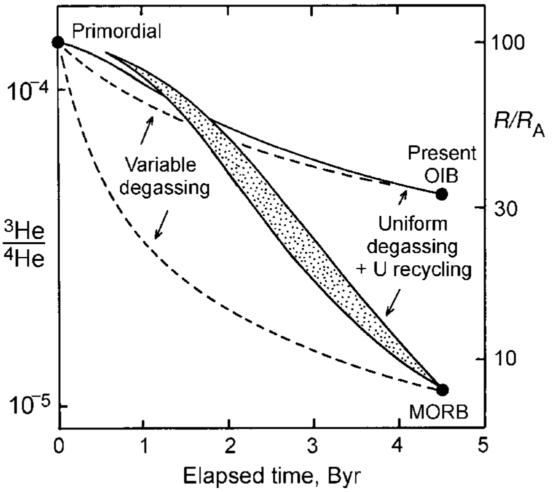

Fig. 11.8. Plot of helium isotope ratios against time to show how uniform degassing plus excess production of radiogenic helium in the MORB reservoir (from recycled uranium) could give rise to present-day signatures similar to those of the traditional variable-degassing model (dashed lines). After Seta *et al.* (2001).

Well-gas studies demonstrate the local nature of mantle helium transport through the crust. Oxburgh *et al.* (1986) showed that sedimentary basins resulting from crustal loading, such as the Alpine Molasse basin, yield helium with very low R/R_A values around 0.05, whereas sedimentary basins formed by extensional tectonics, such as the Rhine Graben and the Pannonian basin of Hungary, may yield helium with much higher R/R_A values around unity (Fig. 11.9a). The huge 'Panhandle' gas field in the southern USA is particularly interesting. It is one of the world's largest gas fields, and has helium contents of up to 2%. In the south, the reservoir is draped over uplifted Proterozoic–Paleozoic basement, and in this region R/R_A values as low as 0.06 have been measured (Fig. 11.9b). In contrast, the northern part of the reservoir is in an area of recent igneous activity. Here, R/R_A values up to 0.2 have been measured, corresponding to 2% MORB-type helium (Oxburgh *et al.*, 1986).

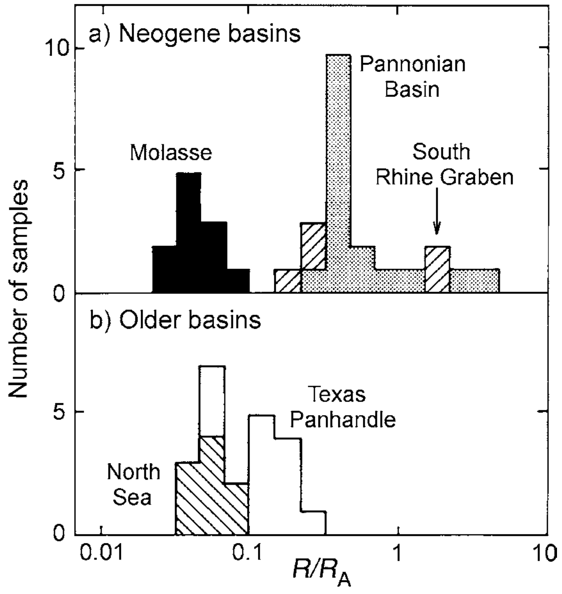

Fig. 11.9. Histograms showing variation in R/R_A values (on a log scale) in different types of sedimentary basin. After Oxburgh *et al.* (1986).

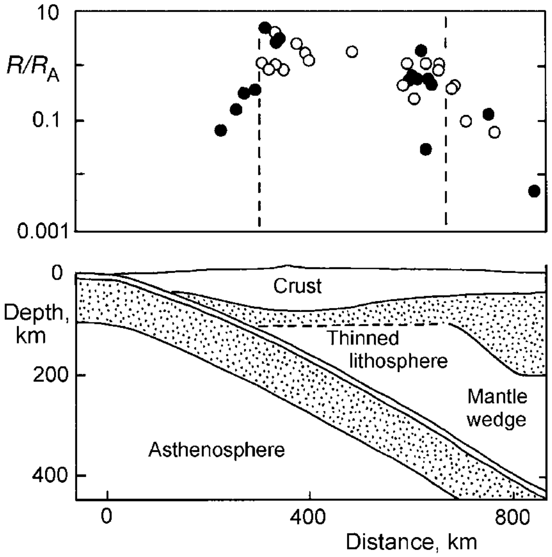

Fig. 11.10. Variation of R/R_A values across the Central Andes, compared with a 1/1 cross section showing proposed thinning of the lithosphere within the mantle wedge: (○) = gas sample; (●) = water sample. After Hoke *et al.* (1994).

More recently, helium analysis of geothermal fluids was used by Hilton *et al.* (1993b) and Hoke *et al.* (1994) to probe the width of the mantle melting zone behind the Andean subduction zone. Both studies revealed high R/R_A values (indicative of a significant fraction of mantle helium) in the magmatic zone centred on the Altiplano. In contrast, R/R_A values below 0.5 were found in the trench zone in front of the magmatic arc, and behind the Eastern Cordillera (Fig. 11.10). Hilton *et al.* found good agreement between helium analyses of geothermal fluids and phenocrysts from nearby volcanoes. However, because of the high altitude of these volcanoes, special rapid-crushing procedures were necessary in order to minimise contamination from a large *in situ* cosmogenic component. Hoke *et al.* attributed high R/R_A values in the central section of the Andes to thinned lithosphere resulting from subduction erosion. The lower R/R_A values behind the Eastern Cordillera probably mark the transition from hot thin lithosphere above the subduction zone to the thick cold lithosphere of the Brazilian shield.

It is now widely understood that heavy rare gases in OIB magmas are very susceptible to shallow-level contamination in magmatic systems (sections 11.2–11.4). However, recent work shows that helium isotope signatures in OIB may also be susceptible to such contamination processes. These processes can potentially be mistaken for the signature of deep-mantle sources in OIB.

For example, Hilton *et al.* (1993a) found a strong correlation between R/R_A value and petrology in submarine volcanic glasses from the Lau back-arc basin, situated behind the Tongan arc. Basaltic samples from the centre of the basin had relatively high helium contents (up to 10 μcc/g), and normal MORB-like R/R_A values of 8 (Fig. 11.11). However, more differentiated glasses from just behind the magmatic arc had much lower helium contents (<0.2 μcc/g) and R/R_A values as low as unity. Given this correlation between ^{3}He/^{4}He ratio, helium content, and petrology, Hilton *et al.* attributed the lower R/R_A values in differentiated glasses to shallow-level contamination, probably due to crustal assimilation by magmas that had largely been degassed of mantle helium.

Hilton *et al.* (1995) observed similar evidence in phenocryst phases from two different lava series on Heard Island, in the Kerguelen Archipelago. Phenocrysts from the Laurens Peninsula series had a plume-type helium signature with R/R_A of 16–18. However, phenocrysts from the Big Ben series had MORB-like R/R_A values in helium-rich samples, but lower R/R_A values in helium-poor samples (Fig. 11.12a). In the latter sample suite, isotopic disequilibrium between olivine and cpx phenocrysts was

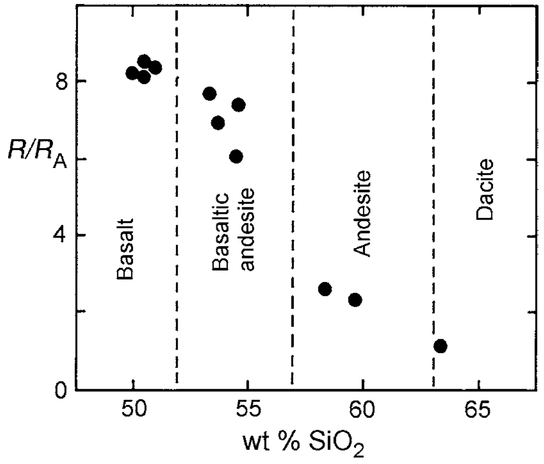

Fig. 11.11. Plot of helium isotope composition (in vesicles) against the silica content of Lau Basin submarine volcanics, showing an inverse correlation. After Hilton *et al.* (1993a).

observed. Therefore, Hilton *et al.* suggested that contamination with radiogenic helium occurred immediately before eruption, probably during phenocryst growth in shallow magma chambers.

Several other hot-spots with R/R_A values lower than MORB and elevated Sr isotope ratios (up to 0.705) have been attributed to crustal recycling into the OIB source reservoir (Fig. 11.6). However, Hilton *et al.* observed that low R/R_A values in these islands were also associated with low total helium contents (Fig. 11.12b). Hence, they suggested that the radiogenic helium signatures in these islands also result from contamination within the oceanic lithosphere, rather than recycling of sediment into the deep mantle.

A different scenario is seen in Samoan basalts, which have a unique combination of elevated R/R_A and radiogenic Sr (Fig. 11.6). Peridotite xenoliths in these lavas have very radiogenic Sr isotope signatures, which are attributed to metasomatism by an EMII mantle component (section 6.5.2). However, helium isotope analysis of fluid inclusions from the xenoliths revealed high R/R_A values of around 12 (Farley, 1995a). This was unexpected, since a recycled sediment component should have radiogenic helium with low R/R_A values. However, the fluids also had $C/^3He$ ratios of about 3×10^9 that were typical of mantle values and distinct from ratios of over 10^{11} seen in sediments (see below). The combined evidence suggests that the volatile component of the metasomatic fluid was derived from the deep mantle and only recently mixed with a volatile-poor melt of subducted sediment.

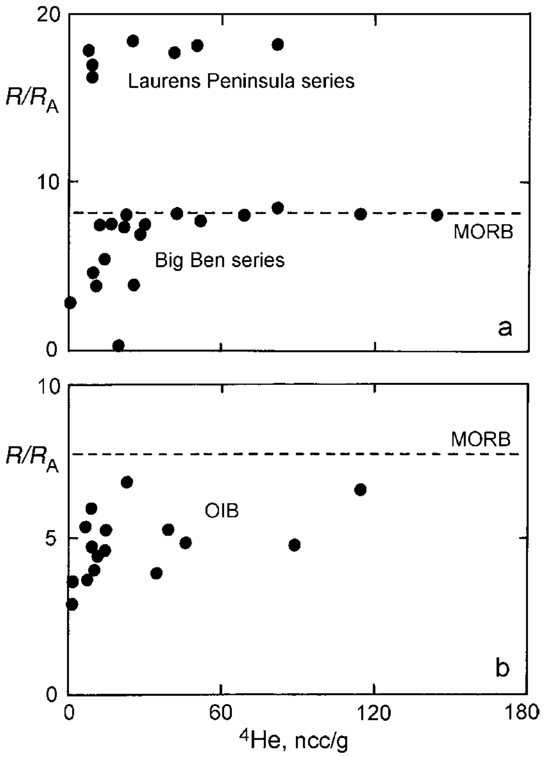

Fig. 11.12. Plot of helium isotope ratio against abundance, showing (a) depressed R/R_A values in helium-poor samples from Big Ben volcano, Heard Island; and (b) similar features in other OIB. After Hilton *et al.* (1995).

Because subducted sediment accumulates radiogenic helium from uranium decay, the high R/R_A value of the metasomatic fluid places limits on the mantle residence time of the sediment since subduction. On the basis of binary strontium–helium mixing calculations, Farley estimated a residence time of only 10 Myr, suggesting that the sediments were incorporated into the plume from the nearby Tongan trench.

11.1.6 Helium and volatiles

The comparison of helium isotope data with other rare-gas tracers will be discussed below. However, helium isotope compositions can also be used to place important constraints on the interpretation of other volatile species, the most important of which are carbon dioxide and methane.

Carbon fluxes in the Earth are difficult to constrain because of the reactivity of this element. However, Marty and Jambon (1987) argued that, if the abundance

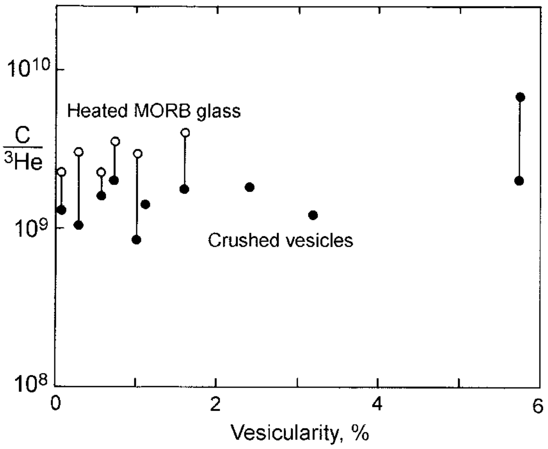

Fig. 11.13. Plot of C/^{3}He ratio against glass vesicularity for MORB samples: (○) = heated glass; (●) = crushed vesicles. After Marty and Jambon (1987).

of carbon could be tied to ^{3}He in major mantle products such as MORB, helium fluxes might be usable as a measure of the carbon flux in a variety of environments. They collated C/^{3}He data for MORB from various ocean basins and found a relatively narrow range with an average C/^{3}He ratio of about 2×10^9.

In a parallel study, Jambon and Zimmerman (1987) showed that the C/^{3}He ratios measured by heating MORB glass and by crushing of vesicles were similar (Fig. 11.13), suggesting that the measured ratios are indicative of the basaltic magma itself, and are not severely fractionated relative to one another during eruption. This is attributed to the similar solubilities of helium and carbon dioxide in basaltic magma. Taken together, these pieces of evidence suggest that the measured ratio is typical of the C/^{3}He flux from the upper mantle on a world-wide scale.

O'Nions and Oxburgh (1988) took these deductions further, by arguing that the oceanic upper-mantle flux of C/^{3}He could also be applied to mantle-derived volatile fluxes through the continental lithosphere. They examined as an example the Pannonian basin of Hungary, which has an R/R_A value as high as 6, suggesting that mantle-derived helium comprises up to 90% of the total helium flux in parts of the basin. This is attributed to its extensional tectonic setting. Measurements of helium abundance for a major aquifer in the Pannonian basin were used by Martel *et al.* (1989) to estimate a mantle ^{3}He flux of 8×10^4 atoms/m^2 per s for the basin as a whole, which is greater than the globally averaged oceanic flux. Hence, O'Nions and Oxburgh concluded that, if extensional zones such as the Pannonian basin make up a significant fraction of the lithosphere, they must also make a major contribution to the global carbon inventory of the crust.

11.1.7 Helium and interplanetary dust

It is well established that high ^{3}He/^{4}He ratios in ocean-floor sediments reflect the accumulation of interplanetary dust particles (IDPs). However, the question of temporal variability in the IDP flux has only recently been examined (Takayanagi and Ozima, 1987). These authors studied ^{3}He variability in a 10-m pelagic clay core from the Central Pacific and a 150-m nanofossil ooze core from the South Atlantic. The former spanned 0–3 Myr, whereas the latter, with generally higher sedimentation rates, spanned 0–40 Myr. Sedimentation rates were determined in both cases by paleomagnetism, supplemented in the 3-Myr-old core with ^{10}Be data (section 14.3.4). The observed range of ^{3}He/^{4}He ratios was attributed to mixing of 0.1–1 ppm of IDPs with terrestrial sediment (Fig. 11.14).

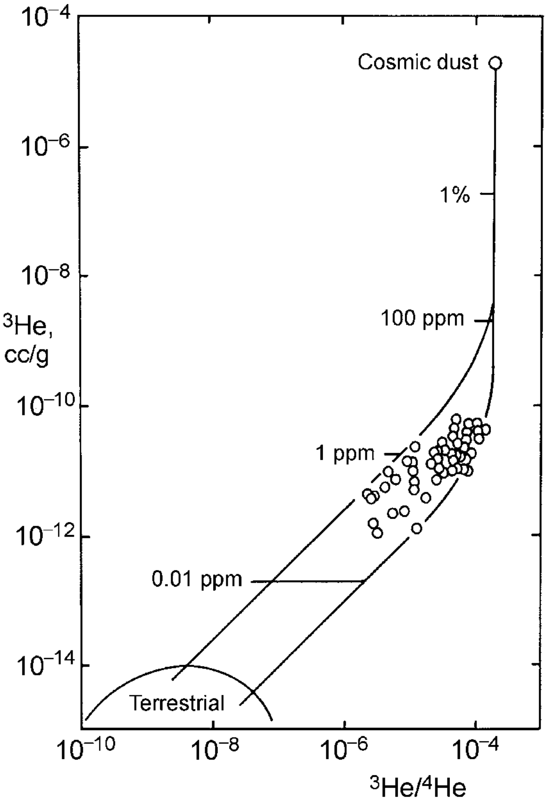

Fig. 11.14. Plot of ^{3}He abundance against isotope ratio in pelagic clays from the Central Pacific, compared with mixing lines between cosmic dust and terrestrial sediments. After Takayanagi and Ozima (1987).

However, the ^{3}He content of IDPs is ten orders of magnitude higher than that of terrestrial sediment, so the IDP fraction totally dominates the ^{3}He budget of the samples.

In both cores studied by Takayanagi and Ozima, ^{3}He contents were inversely correlated with sedimentation rate. The ^{3}He deposition flux was therefore determined by multiplying the ^{3}He content by the sediment-mass accumulation rate (mass is used because ocean-floor sediments undergo compaction after deposition). The results suggested flux variations over time, but did not display any overall trend. The average ^{3}He flux over the past 40 Myr was estimated as 1.5 (±1) × 10^{-15} cc/cm^2 per yr (at STP).

Generally similar results were obtained by Farley (1995b) on a 22-m core of pelagic clay from the central North Pacific, spanning the past 72 Myr. During the Quaternary, the sedimentation rate was high, yielding a ^{3}He flux of about 1.1 × 10^{-15} cc/cm^2 per yr, in good agreement with Takayanagi and Ozima (1987). However, in the deeper part of the core, the calculated ^{3}He flux was lower, averaging about 0.5 × 10^{-15} cc/cm^2 per yr. It is not clear whether this represents a real variation in the flux of interplanetary dust over time, or a reduction in the retentivity of ^{3}He with depth. In a detailed study, Mukhopadhyay *et al.* (2001) observed no ^{3}He peak at the K–T boundary, indicating that the extra-terrestrial signals from iridium and helium are decoupled (Fig. 11.15). This was attributed to impact-induced vaporisation and outgassing of the K–T bolide. In contrast, Farley *et al.* (1998) discovered a spike of ^{3}He in the late Eocene (35–36 Myr ago) that *did* correlate with the iridium signal (Fig. 11.15). This was attributed to a comet shower.

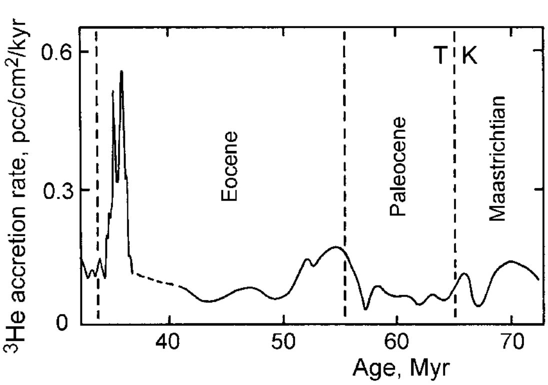

Fig. 11.15. Record of ^{3}He abundances in Cretaceous to Paleogene sediments, showing a ^{3}He peak in the late Eocene, but no peak at the K–T boundary. After Mukhopadhyay *et al.* (2001).

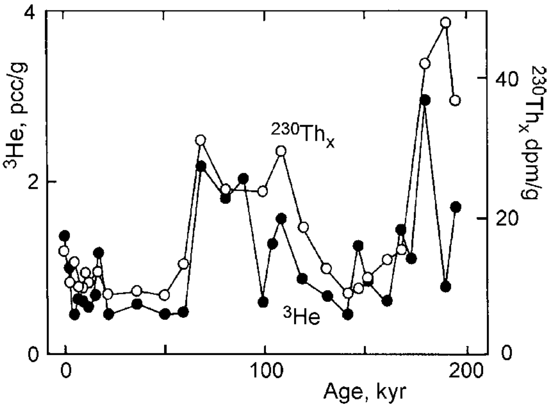

Fig. 11.16. Isotope stratigraphy of a carbonate-rich sediment from the Central Pacific, showing strong co-variation between ^{3}He abundance (●) and excess initial ^{230}Th activity (○). After Marcantonio *et al.* (1995).

A more controversial question concerns the evidence for variation of the ^{3}He flux during the glacial cycles of the Quaternary period. A detailed study in this time range was performed by Marcantonio *et al.* (1995) on a 4-m core of carbonate-rich sediment from the Central Pacific, spanning the last 200 kyr. After correcting for dilution by biogenic carbonate, their ^{3}He/^{4}He data lay on the same mixing line as that observed by Takayanagi and Ozima between terrigenous and IDP components. However, Marcantonio also determined initial excess ^{230}Th activities on the same samples. Normalisation of ^{3}He with respect to ^{230}Th can remove the effects of variable sediment dilution, because ^{230}Th is constantly produced in seawater from ^{234}U, and is rapidly transported to the ocean floor by adsorption onto sinking particulate matter (section 12.3.3). When plotted against ages from oxygen isotope stratigraphy, ^{3}He and ^{230}Th exhibited strong co-variation, with peak signals during interglacial periods (Fig. 11.16). These peaks were attributed, not to variations of the IDP flux, but to intensified dissolution of carbonate during interglacial periods. Hence, from the ratio of ^{230}Th activity to ^{3}He content, an average ^{3}He deposition flux of 0.96 × 10^{-15} cc/cm^2 per yr was determined for the past 200 kyr.

Farley and Patterson (1995) performed a similar study of Quaternary ^{3}He variation on a 9-m core of foram-nano-fossil ooze from the flank of the Mid-Atlantic Ridge, spanning the period 250–450 kyr BP. ^{3}He contents were inversely correlated with δ^{18}O variations, which were interpreted as monitors of glacial–interglacial cycles. Similar results were found by Patterson and Farley (1998) for a Pacific core.

The 100-kyr cycle of ^{3}He abundance variations observed in these studies, if interpreted as a proxy of IDP flux variations, ties in with a proposal by Muller and MacDonald (1995; 1997) that Quaternary climate variations might be due to a 100-kyr cycle of variations in the Earth's orbital inclination, causing periodic encounters with a cloud of IDPs that could partially block out solar radiation. Hence, Farley and Patterson speculated that the helium isotope data might be recording a causal relationship between IDP accumulation and climate. However, according to this model, interglacial periods should be characterised by the lowest ^{3}He flux, whereas Farley and Patterson found the opposite relationship. Therefore, an alternative interpretation of the data (Marcantonio *et al.*, 1995) is that climatically induced variations in sedimentation rate caused apparent variations in the ^{3}He flux, which could not be adequately corrected with the available age data for the core.

Curiously enough, new modelling of the orbits of IDPs and the Earth (Kortenkamp and Dermott, 1998) confirmed the 100-kyr periodicity of the IDP flux predicted by Muller and MacDonald, but attributed this periodicity to variations in the eccentricity of the Earth's orbit. However, the predicted IDP flux variations were still anti-correlated with the ocean-floor ^{3}He record, and their magnitude was also judged to be too small to cause climatic cycles.

Confirmation that Quaternary ^{3}He variations in ocean-floor sediments are due to variations in sedimentation rate rather than the IDP flux was provided in new work (Marcantonio *et al.*, 1996; 1999) on cores from the Atlantic and Indian Oceans, respectively. In both studies ^{3}He abundances were again correlated with ^{230}Th data, which Marcantonio *et al.* attributed to variations in the amount of sediment focussing during different climatic periods. After using ^{230}Th data to correct for these effects, constant ^{3}He accumulation rates were found, with magnitudes of 0.8, 1.2 and 1.1 × 10^{-15} cc/cm^2 per yr for the equatorial Pacific, Atlantic and Indian Oceans, respectively. Hence, it is concluded that the ^{3}He flux has been essentially uniform and constant over the past 200 kyr.

11.2 Neon

Until recently, neon was the most problematical of the rare gases. Of its three isotopes, ^{21}Ne and ^{22}Ne are nucleogenic and their variations are well understood. In contrast, ^{20}Ne is non-nucleogenic, and the causes of its variation in the Earth were hotly debated. However, the resolution of this debate has now made neon isotopes a kind of 'Rosetta Stone' for understanding the behaviour of the other rare gases in mantle sources.

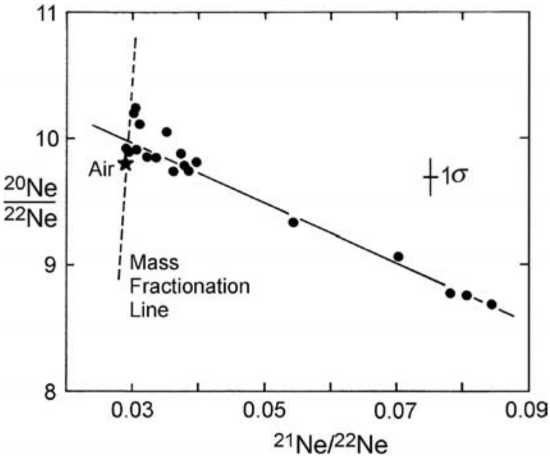

Fig. 11.17. Neon three-isotope correlation diagram, showing well gases from the Alberta basin on a mixing line between atmospheric and nucleogenic neon. After Kennedy *et al.* (1990).

11.2.1 Neon production

The principal nuclear reactions which generate neon isotopes are n, α reactions on ^{24}Mg and ^{25}Mg, which produce ^{21}Ne and ^{22}Ne, respectively. Subsidiary pathways are α, n reactions on ^{18}O and ^{19}F, which produce ^{21}Ne and ^{22}Na, the latter undergoing β decay to ^{22}Ne. The α, n reaction on ^{17}O to yield ^{20}Ne is unimportant, due to the low abundance of the parent. All α particles are derived from the U-series decay chains, while the neutrons are mostly produced by secondary reactions from α particles.

These reactions were first studied by Wetherill (1954), and have been refined in subsequent work (e.g. Kennedy *et al.*, 1990). The net result of these reactions is to yield a trend towards lower ^{20}Ne/^{22}Ne and higher ^{21}Ne/^{22}Ne ratios, which is most clearly seen in uranium-rich rocks such as granites. Figure 11.17 shows isotopic data for gas wells from Alberta, Canada, plotted on the commonly used neon three-isotope diagram. The data form a linear array which was attributed to mixing between atmospheric and nucleogenic neon. This is consistent with helium isotope data for these gases, which show a strong radiogenic signature with no mantle-derived component.

Isotopic analysis of exposed terrestrial rocks has also demonstrated the cosmogenic production of ^{21}Ne (Marty and Craig, 1987). This isotope is produced by spallation reactions on Mg, Na, Si and Al, generating a sub-horizontal array on the three-isotope plot. By analysing all three isotopes, the cosmogenic component can resolved from trapped (magmatic) neon and nucleogenic neon. Graf *et al.* (1991) applied the cosmogenic-neon method to quartz separates from Antarctic rocks that had previously been dated by ^{26}Al and ^{10}Be (section 14.6.2). They demonstrated coherent behaviour of ^{21}Ne with these other cosmogenic isotopes, suggesting that neon will be a useful tool in determining cosmic exposure ages of surficial rocks.

11.2.2 Solar neon in the Earth

The first evidence for non-atmospheric neon in the mantle was presented by Craig and Lupton (1976) for samples of MORB and volcanic gases. These are enriched in ^{20}Ne, as well as nucleogenic ^{21}Ne, relative to ^{22}Ne contents. Subsequently, Harding County well gas was also found to have a composition well removed from atmospheric (Phinney *et al.*, 1978). These ^{20}Ne-enriched components were attributed to exotic primordial rare-gas components in the Earth, possibly representing solar neon. In contrast, Kyser and Rison (1982) speculated that ^{20}Ne enrichment in the analysed samples might be due to mass fractionation of neon from an original mantle composition similar to that of the atmosphere. They compared a compilation of mantle-derived neon analyses with neon data from geothermal gases in Japan (Nagao *et al.*, 1979). These gases display a mass-fractionation trend (Fig. 11.18), which is explained by preferential diffusion of light neon through the soil to the sampling sites.

Elevated ^{20}Ne abundances were also found in diamonds (Fig. 11.19) by Honda *et al.* (1987) and Ozima and Zashu (1988; 1991). These analyses disproved the ^{20}Ne-'enrichment' model of Kyser and Rison, since diamonds are *in situ* solid samples of the mantle. Therefore, Ozima and Zashu reversed the mass-fractionation argument of Kyser and Rison, suggesting that diamonds sample a solar neon reservoir in the Earth, whereas the present-day atmosphere has been *depleted* in ^{20}Ne by mass fractionation. They argued that bombardment of the early Earth by radiation caused the massive blow-off of a primitive solar-type atmosphere, leaving a residue enriched in heavy neon.

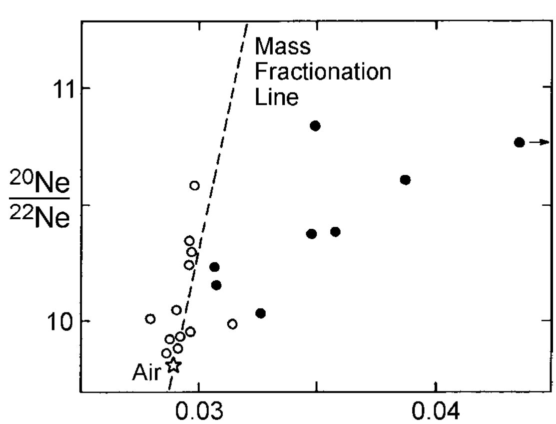

Fig. 11.18. Comparison of mantle samples (●), and mass-fractionated geothermal gases (○), on a neon three-isotope diagram. After Kyser and Rison (1982).

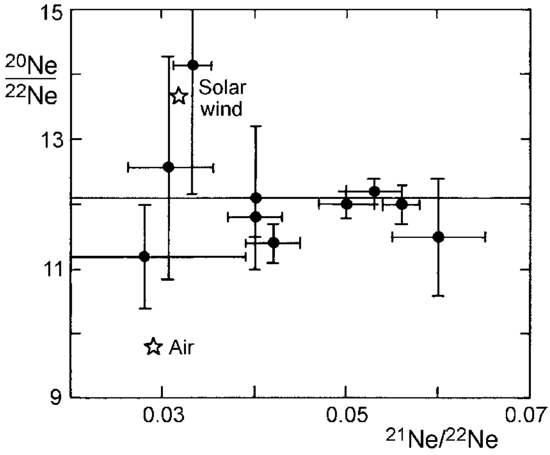

Fig. 11.19. Neon isotope data for diamonds compared with the signatures of other solar-system components. (The solar-wind composition was determined by analysis of lunar soil.) For data sources, see the text.

Fractionation of the proposed magnitude between mantle and atmosphere should be accompanied by fractionation of the non-radiogenic isotopes of argon, krypton and xenon. Therefore, it should be possible to test the atmospheric-fractionation model by isotopic analysis of the heavy rare gases. However, two factors make such tests difficult to perform. Firstly, the heavier rare gases respond to fractionation effects to a lesser degree; and secondly, the heavy rare gases are more likely to be recycled back into the mantle, masking the effect of any mantle–atmosphere fractionation of such gases. This subject will be re-examined below.

Additional insights into terrestrial neon systematics have been sought from the analysis of submarine basaltic glasses. Sarda *et al.* (1988) demonstrated the existence of a MORB correlation line passing through the atmosphere point, which has been confirmed by several subsequent studies (e.g. Marty, 1989; Hiyagon *et al.*, 1992; Moreira *et al.*, 1998). This array (Fig. 11.20) can be explained by three-component mixing of solar-type, atmosphere-type and nucleogenic neon, as discussed below.

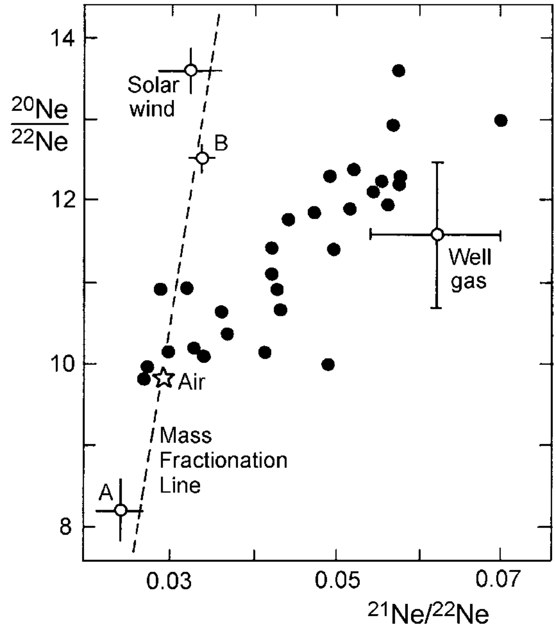

Fig. 11.20. Compilation of MORB neon data (●) on a three-isotope plot. A and B represent the 'planetary' neon compositions seen in some meteorites. After Hiyagon *et al.* (1992).

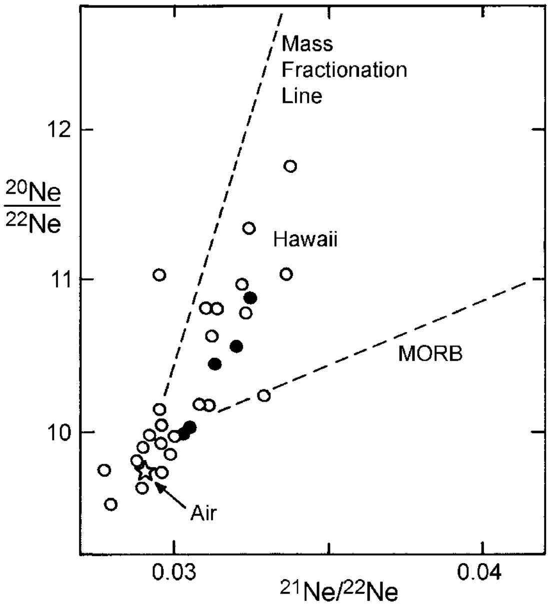

Fig. 11.21. Compilation of Hawaiian neon data on a three-isotope plot: (○) = Loihi; (●) = Kilauea. The MORB array is shown by a dashed line. After Hiyagon *et al.* (1992).

Sarda *et al.* (1988) also determined neon isotope ratios in several Loihi glasses, which fell within error of the atmospheric ratio. They believed that these signatures represented a genuine primordial-mantle signature, consistent with this reservoir being the principal source of atmospheric neon. However, subsequent analyses of submarine basalt glasses from Loihi and nearby Kilauea revealed a wider range of neon isotope ratios, stretching from the atmospheric composition towards ^{20}Ne-enriched compositions (Honda *et al.*, 1991; Hiyagon *et al.*, 1992). The enriched end of this array approaches the solar-wind composition, but the array has a slope intermediate between the pure mass-fractionation line and the MORB correlation line (Fig. 11.21). In order to explain these results, Honda *et al.* and Hiyagon *et al.* attributed all neon in the Earth's interior to mixing between solar and nucleogenic isotopes. The sloping arrays of MORB and OIB were then attributed to variable atmospheric contamination of this solar-plus-radiogenic mantle neon, whereas the Loihi neon samples originally analysed by Sarda *et al.* (1988) were attributed almost entirely to atmospheric contamination.

Allègre *et al.* (1993) attempted to reinstate the 'planetary model' for neon in the deep mantle by invoking a new mechanism to explain high ^{20}Ne/^{22}Ne ratios of solar type in the Earth's mantle. They attributed these signatures to the subduction of cosmic-dust particles accumulated in deep-sea sediments. These dust particles become implanted with neon from the solar wind during their exposure in space. Analysis of this material in the atmosphere and in deep-sea sediment reveals ^{20}Ne/^{22}Ne ratios spanning the range between atmospheric and solar compositions (e.g. Nier and Schlutter, 1990). Matsuda *et al.* (1990) suggested that these particles could survive the 'noble-gas subduction barrier' and deliver cosmic (solar) neon to the deep mantle. This could explain the high ^{20}Ne/^{22}Ne ratios of submarine glasses without having to invoke solar-type primordial neon in the Earth. However, experimental studies by Hiyagon (1994) suggested that neon would be completely extracted from cosmic dust within three years at 500 °C, which is insufficient to sustain this model.

Ozima and Igarashi (2000) also rejected the 'solar-neon' model. Their argument was based on the distribution of data in a histogram of ^{20}Ne/^{22}Ne ratios from MORB, OIB and diamonds (Fig. 11.22). They argued that, since the distribution tailed away to nothing at the solar-wind composition, solar neon could not be a major component of the terrestrial rare-gas inventory.

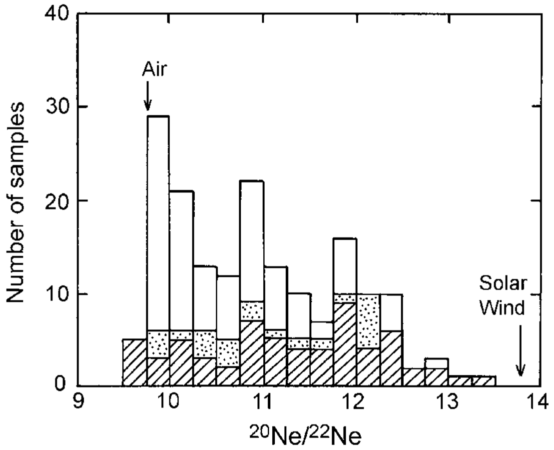

Fig. 11.22. Histogram of neon isotope data for MORB (hatched); diamonds (stipple) and OIB (clear) to show the distribution of data between the atmospheric and solar-wind values. After Ozima and Igarashi (2000).

However, it should be noted that the tailing effect in Fig. 11.22 is mainly due to OIB data. The MORB distribution is essentially flat, indicating relatively equal mixing of solar and atmospheric neon in these samples. The distribution of OIB data in Fig. 11.22 is mainly a historical artefact, representing the great difficulties encountered in excluding atmospheric contamination in earlier work. However, improved methods to combat atmospheric contamination have gradually been developed, as seen in recent data presented by Harrison *et al.* (1999) while the paper by Ozima and Igarashi was under revision. These new neon isotope data from Iceland reached ^{20}Ne/^{22}Ne ratios above 13.5 for the first time, overlapping with the solar-wind composition.

Further evidence from Iceland in support of the solar-neon model was provided by Dixon *et al.* (2000) and Moreira *et al.* (2001). For the first time, these studies revealed a correlation steeper than the L–K line on the three-isotope plot, falling within error of the mass-fractionation line between atmospheric and solar neon (Fig. 11.23). This discovery provides important support for the two-reservoir model for terrestrial noble gases (section 11.1.4), because it implies that the Earth does contain an essentially primordial neon reservoir.

11.2.3 Neon and helium

Following widespread acceptance of the solar-neon model for the Earth, neon and helium isotope data can now be placed in a unified model. This is because helium does not suffer significant atmospheric contamination, while atmospheric contamination of neon can be corrected using the three-isotope plot. Relationships between neon and heavy rare gases will be discussed in the next section.

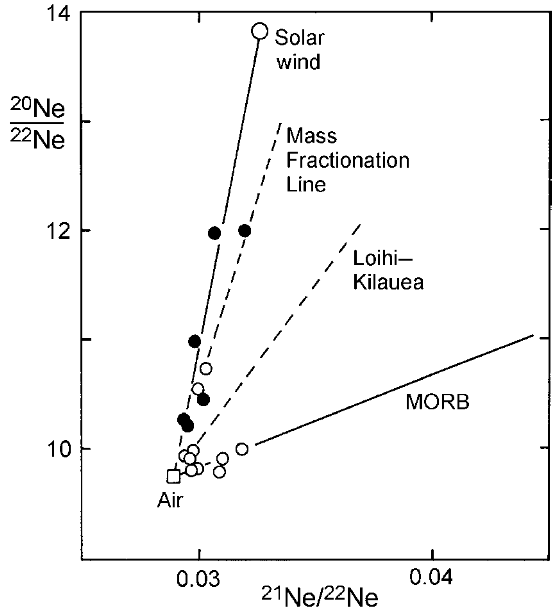

Fig. 11.23. Neon three-isotope plot showing new Iceland data, some of which lie within error of the mass-fractionation line between atmospheric and solar neon: (●) = olivine; (○) = glass. After Dixon *et al.* (2000).

One way of correcting for atmospheric neon contamination is to calculate the slopes of data arrays on the three-isotope plot by forcing a regression line through the atmospheric composition. The gradient of this regression line is then equal to the ratio $\delta\ ^{20}\text{Ne}/\delta\ ^{21}\text{Ne}$. Poreda and Farley (1992) used this notation to compare the neon compositions of various mantle sources, categorised according to ^{3}He/^{4}He ratio (expressed as R/R_{A}). The results of this analysis are presented in Fig. 11.24. In addition to data from Loihi and MORB, new data were obtained from ultramafic xenoliths from Réunion and two different localities in the Samoan islands, which were found to define neon isotope arrays with slopes intermediate between those for Hawaii and MORB (Staudacher *et al.*, 1990; Poreda and Farley, 1992). Overall, the data suggest a correlation between neon and helium isotope ratios, which can be explained by the addition of a nucleogenic–radiogenic neon–helium component to a variably degassed primordial component.

An alternative way of correcting for atmospheric neon contamination is to project data away from the atmosphere point to the solar ^{20}Ne/^{22}Ne ratio,

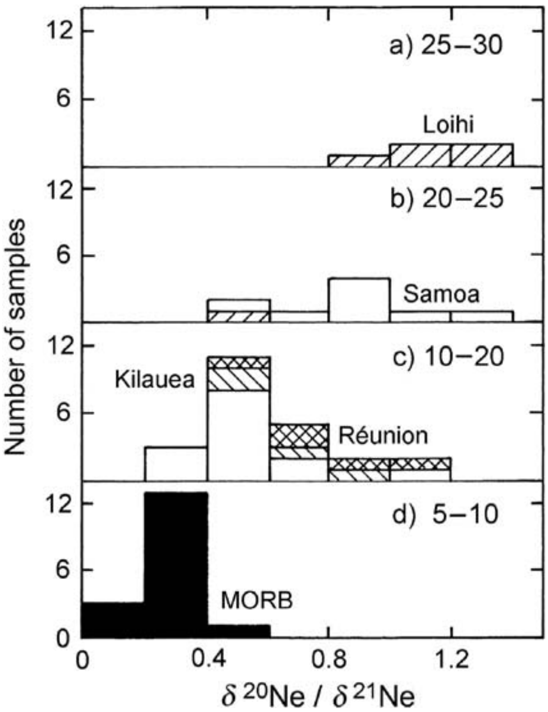

Fig. 11.24. Correlation of neon and helium isotope signatures in mantle sources, expressed as histograms of $\delta\,^{20}Ne/\delta\,^{21}Ne$, categorised by R/R_A ratio. Different OIB samples are distinguished by hatching. After Poreda and Farley (1992).

whereupon the neon data are presented as normalised $^{21}Ne/^{22}Ne$ ratios. Porcelli and Wasserburg (1995b) used this notation to compare neon and helium data for depleted mantle, lower-mantle plumes, and meteorites (representing the initial Earth). These reservoirs form an approximately linear growth curve on a diagram of $^{21}Ne/^{22}Ne$ ratio against $^{4}He/^{3}He$ ratio. This is consistent with the common progenitors U and Th, which produce radiogenic helium and nucleogenic neon. Porcelli and Wasserburg (1995b) also argued that the linear Ne–He growth curve is consistent with a steady-state model for mantle rare gases.

The atmospheric-contamination model successfully explains the neon isotope arrays in submarine glasses, but it brings us back to the problem of explaining the origin of the atmospheric neon signature itself. Most workers now support the hypothesis that fractionation of neon occurred during the burn-off of an early terrestrial atmosphere of solar composition (as proposed by Ozima and Zashu, 1988; 1991). This question was re-evaluated by Pepin (1997), who argued that a giant impact in the early history of the Earth would have fractionated all rare-gas isotope ratios, including those for neon and the heavy rare gases. Nevertheless, he argued that atmospheric burn-off powered by extreme ultra-violet solar radiation was still necessary in order to explain the observed atmospheric neon signatures. An alternative model proposed by Marty (1989) is that the atmosphere was formed by late accretion of gas-rich meteorites with planetary neon (e.g. neon A in Fig. 11.20). These could have been accreted to the surface of the Earth subsequent to the formation of the mantle with a solar neon budget.

11.3 Argon

Initial, 'excess' or 'inherited' argon is normally regarded as a problem to be avoided in K–Ar and Ar–Ar dating (section 10.1.2). However, the isotopic composition of this argon can be used as a powerful geochemical tracer, especially alongside other rare-gas data.

Atmospheric contamination is a much more serious problem in the isotopic analysis of 'heavy' rare gases than it is for helium and neon. Atmospheric helium has a very low abundance due to its complete escape from the atmosphere, and even atmospheric neon is believed to have been depleted significantly in the atmosphere by intense solar irradiation. Furthermore, the neon three-isotope plot allows atmospheric contamination to be monitored. On the other hand, the heavy rare gases (argon, krypton and xenon) have accumulated in the atmosphere over the Earth's history, and corrections for atmospheric contamination are much more difficult. Because of this problem, the first clear evidence for inherited argon was provided by the analysis of beryl, whose ring-type structure accommodates unusually large quantities of initial argon, swamping the effects of atmospheric contamination. 'Excess' argon was first found in beryl by Aldrich and Nier (1948) and studied in more detail by Damon and Kulp (1958). The latter workers discovered Archean beryls containing more than 99% of excess argon and with $^{40}Ar/^{36}Ar$ ratios as high as 10^5.

11.3.1 Terrestrial primordial argon

The ^{40}Ar contents of beryl were observed to decrease over geological time (Fig. 11.25), leading Damon and Kulp to propose extensive early degassing of the Earth in the Archean, decreasing exponentially towards the present. The beryl data shown in Fig. 11.25 were also used by Fanale (1971) to support a more extreme model of catastrophic early degassing of the Earth. He argued that they were not consistent with models of constant

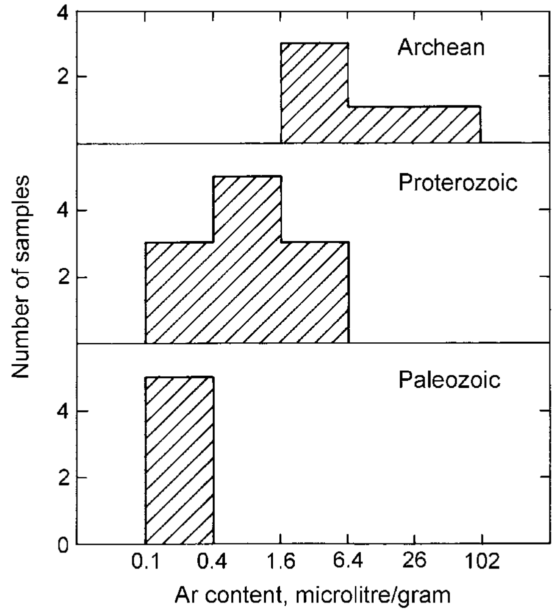

Fig. 11.25. Histograms of the argon content of beryl samples grouped by age to show the decrease in measured ^{40}Ar contents with time. After Damon and Kulp (1958).

degassing intensity through the Earth's history, such as that proposed by Turekian (1964).

Schwartzman (1973) supported the early-degassing model using Ar isotope data from the 2.7-Byr-old Stillwater complex. Because this is a basic magma it can yield more direct information about the Archean mantle than beryl-bearing pegmatites with a potentially large crustal input. A Stillwater pyroxene had an excess $^{40}Ar/^{36}Ar$ ratio of at least 17 900, corresponding to a calculated maximum $^{36}Ar/Si$ ratio of 3×10^{-11} for the 2.7-Byr-old mantle source. The ratio of atmospheric ^{36}Ar to mantle silicon at the present day is 1×10^{-10}, so the Earth was apparently outgassed to at least 70% of its present extent by the end of the Archean.

Ocean-floor basalt glasses are an important source of information about the rare-gas budget of the present-day mantle because the high water pressure at the site of eruption retains initial magmatic argon in the sample (section 10.1.2). Furthermore, rapid quenching reduces contamination by atmospheric argon dissolved in seawater. In contrast, the crystalline cores of basalt pillows are largely outgassed of magmatic rare gases and contaminated with atmospheric gases during crystallisation (Fisher, 1971).

Hart *et al.* (1979) used the maximum ^{40}Ar content of 3×10^{-6} ml/g in ocean-floor basalt glasses as an estimate of the present-day ^{40}Ar concentration in the upper-mantle (UM) source. By subtracting this value from the average ^{40}Ar concentration in the Bulk Silicate Earth (estimated from its K abundance) and comparing this with the total ^{40}Ar budget of the atmosphere and crust, Hart *et al.* were able to calculate the mass of mantle which must have been be outgassed. This calculation is shown in equation [11.1], where square brackets denote concentrations:

$$\text{mass of mantle outgassed} = \frac{^{40}Ar_{atm} + ^{40}Ar_{crust}}{[^{40}Ar_{BSE}] - [^{40}Ar_{UM}]} \qquad [11.1]$$

Using this equation, a potassium abundance of 660 ppm in the Bulk Silicate Earth implies that only 25% of the total mass of the mantle need be outgassed.

Hart *et al.* proposed that the upper mantle was also thoroughly degassed of ^{36}Ar, so that subsequent radiogenic ^{40}Ar production generated high $^{40}Ar/^{36}Ar$ ratios of up to 16 000. In contrast, the lower mantle was not significantly degassed of argon, such that radiogenic ^{40}Ar production was swamped by the primordial component, allowing only a modest rise in $^{40}Ar/^{36}Ar$ ratio above the atmospheric value. Hart *et al.* noted the similarity of these model predictions to the $^{40}Ar/^{36}Ar$ ratios observed in ocean-floor glasses from ridges and mantle plumes, respectively (Fig. 11.26). This suggested to them that these data were not seriously perturbed by atmospheric contamination.

The concept of a relatively less degassed or 'undegassed' mantle reservoir with respect to heavy rare gasses was strongly contested by Fisher (1983; 1985). He argued that the low $^{40}Ar/^{36}Ar$ ratios measured in plume environments were a result of atmospheric contamination. This argument was initially aimed at data on xenolithic inclusions in lavas (e.g. Kaneoka and Takaoka, 1980). These appeared to contain primordial argon and helium, but were subsequently shown to be contaminated by atmospheric argon and cosmogenic helium (section 11.1.2). Submarine glasses may be more resistant to such effects, but the interpretation of these data has nevertheless provoked intense controversy.

Experience has shown that all mantle-derived rare-gas samples are contaminated to some extent by atmospheric gases. Therefore, it is necessary to take stringent experimental precautions to minimise as far as possible the extent of this contamination. Samples and equipment are thoroughly baked before analysis, and frequent blanks are determined to verify the effectiveness of these procedures. It may be possible to derive a mantle signature from a contaminated sample by

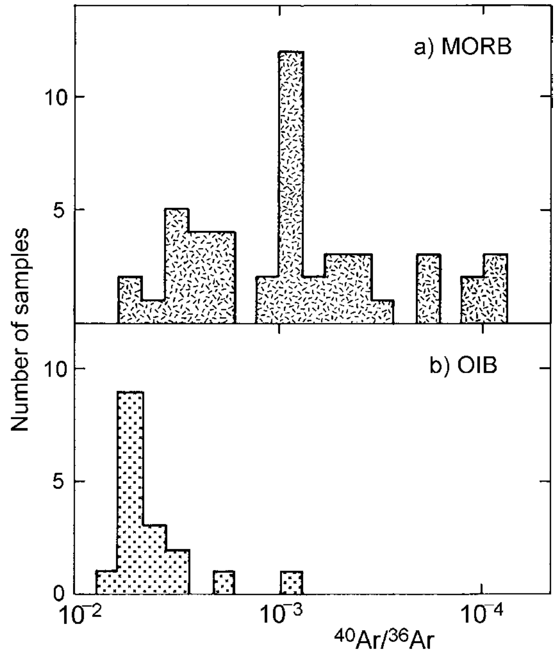

Fig. 11.26. Histograms of early $^{40}Ar/^{36}Ar$ data for MORB and OIB, showing contrasting ranges of isotope composition. After Hart *et al.* (1979).

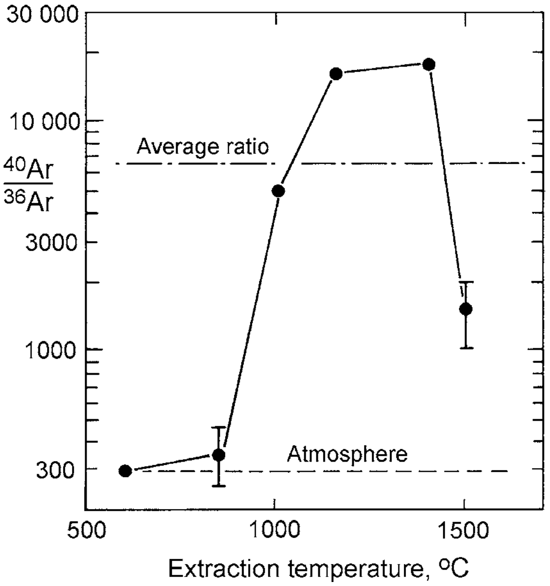

Fig. 11.27. Plot of measured argon isotope ratio against extraction temperature for MORB glass, showing heavy atmospheric contamination of the low-temperature (<1000 °C) fractions. After Staudacher and Allègre (1982).

extracting argon from the sample in separate aliquots, which could sample isotopic heterogeneities within the sample. One approach is to perform the rare-gas analysis by step heating (e.g. Staudacher and Allègre, 1982). This procedure is demonstrated for a MORB sample in Fig. 11.27. Absorbed atmospheric rare gases are released in the low-temperature heating steps, allowing an estimate of the severity of contamination effects to be made. Another approach (Hart *et al.*, 1983) is to do separate experiments by thermal degassing and by crushing. The latter method releases gases from vesicles, which may have undergone less (but sometimes more) contamination than the rock matrix. Staudacher *et al.* (1986) used both step heating and crushing to carry out the most rigorous search for sample contamination.

In other early work on this subject, there were attempts to use elemental rare-gas ratios (e.g. $^{4}He/^{40}Ar$) to distinguish between atmospheric and primordial signatures in MORB and OIB samples (e.g. Hart *et al.*, 1983; 1985). However, it has become apparent that elemental fractionation of rare gases can occur during several phases of the evolution of the samples, including partial meting, magmatic differentiation and solidification. Hence, it appears that isotope signatures are the only reliable discriminant between atmospheric and primordial signatures, and even these can be misleading.

In an attempt to resolve these components in the argon isotope signatures of MORB and OIB samples, Allègre *et al.* (1983) and Staudacher *et al.* (1986) compared argon and helium isotope ratios in glasses from ocean ridges and from the Hawaiian plume. Loihi Seamount gave the highest $^{3}He/^{4}He$ ratios for uncontaminated mantle-derived materials (presented in inverted form as the $^{4}He/^{3}He$ ratio in Fig. 11.28). Since this helium signature of Loihi glasses is regarded as primordial, Allègre *et al.* interpreted the low argon isotope ratio in these samples as likewise indicative of an un-degassed mantle source. In Fig. 11.28, the MORB field has a forked shape, attributed by Staudacher *et al.* (1986) to mixing with primordial and atmospheric helium reservoirs. Both mixing branches exhibited very strong curvature, which was attributed to the very low argon content of the degassed MORB reservoir, relative to both the atmosphere and plume reservoirs. In contrast, a dunite xenolith from Loihi lay far off the MORB–plume mixing line. The argon signature of this sample is consistent with a source in oceanic lithosphere. The high ^{3}He content of this sample cannot be cosmogenic (as for some other xenoliths), since it is

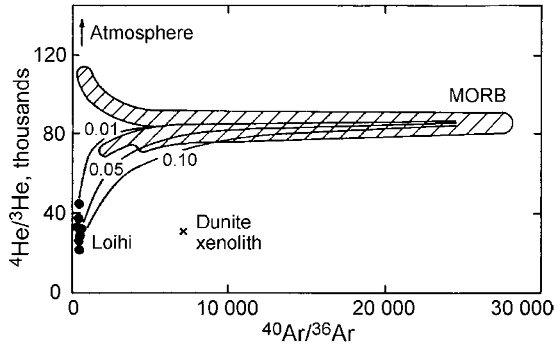

Fig. 11.28. Plot of helium *versus* argon isotope ratio for submarine glasses from MORB and plume environments. Mixing lines for various $^3He/^{36}Ar$ ratios in Loihi relative to MORB sources are shown. After Staudacher *et al.* (1986).

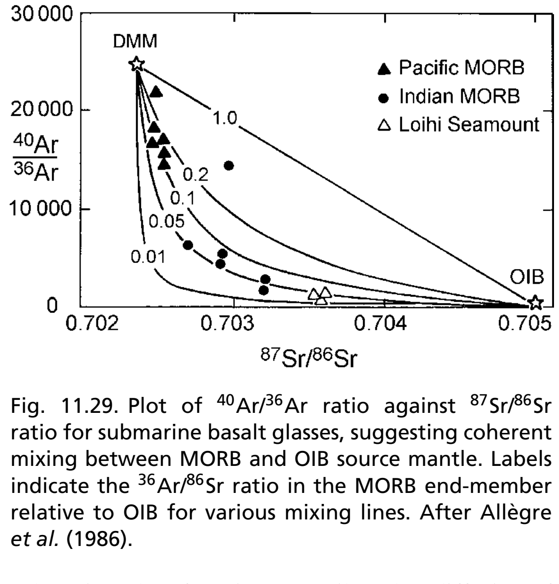

Fig. 11.29. Plot of $^{40}Ar/^{36}Ar$ ratio against $^{87}Sr/^{86}Sr$ ratio for submarine basalt glasses, suggesting coherent mixing between MORB and OIB source mantle. Labels indicate the $^{36}Ar/^{86}Sr$ ratio in the MORB end-member relative to OIB for various mixing lines. After Allègre *et al.* (1986).

submarine; therefore, it was attributed to diffusion of helium from the host magma into the xenolith before eruption.

Allègre *et al.* (1983) observed that MORB glasses also fell on reasonable mixing lines between degassed and un-degassed (plume) sources on a plot of $^{40}Ar/^{36}Ar$ ratio against strontium isotope ratio (Fig. 11.29). They argued that these mixing lines had a different trajectory from what would be expected from surficial contamination processes, and therefore that the isotope data were indicative of processes in the mantle source. However, because rare gases may be decoupled from lithophile-element systems, the trajectory of mixing lines might not be a reliable indicator of the end-member compositions.

Patterson *et al.* (1990) argued that helium isotope systematics in Loihi glasses might also be decoupled from argon, due to the extreme difference in He/Ar ratio between the end-members (as demonstrated, for example, by the hyperbolic form of proposed mixing lines in Fig. 11.29). They pointed out that seawater has between two and four orders of magnitude more ^{36}Ar than Loihi glasses, but two orders of magnitude less ^3He. Hence, argon isotope ratios in Loihi magmas might have been contaminated by seawater without affecting their helium signature. In MORB glasses, variable contamination of this kind generates correlations between $^{40}Ar/^{36}Ar$ ratio and $1/^{36}Ar$ abundances, indicative of simple mixing between atmospheric and mantle argon (Fisher, 1986). However, Loihi data do not display such a correlation. Hence, the atmospheric contamination model is hard to evaluate critically in plume environments.

Farley and Craig (1994) made a new examination of this problem, using helium and argon measurements in olivine phenocrysts from a tholeiitic plume basalt. In this sample from the Juan Fernandez hot-spot, Farley and Craig were able to demonstrate a positive correlation between ^4He and ^{40}Ar abundances released from fluid inclusions by crushing of phenocrysts (Fig. 11.30a). This correlation line is inconsistent with significant atmospheric contamination involving these isotopes, since the atmosphere has negligible ^4He. Therefore, the correlation must be attributed to variable gas inventories sampled from a mantle source with constant $^4He/^{40}Ar$ ratio.

In contrast, Farley and Craig observed no correlation between ^4He and ^{36}Ar abundances (Fig. 11.30b). Therefore, they argued that ^{36}Ar abundances must have been perturbed by atmospheric contamination. However, since even gas-rich samples showed this behaviour, analytical blank was an unlikely cause. Instead, Farley and Craig attributed the effect to contamination of the magma by seawater argon within the oceanic crust. Hence, they argued that the mantle source sampled by the Juan Fernandez hot-spot had a minimum $^{40}Ar/^{36}Ar$ ratio equal to the maximum observed $^{40}Ar/^{36}Ar$ ratio of 7700. However, this does not place strong constraints on the argon isotope ratio of the lower mantle (un-degassed reservoir) because the Juan Fernandez plume may have been contaminated with radiogenic argon during its ascent through the MORB source.

If this seawater-contamination model is correct, it casts doubt on the reliability of basaltic glasses *in general* as samples of primordial argon from the lower mantle. However, it does not disprove the 'two-reservoir' model for mantle rare gases; it simply

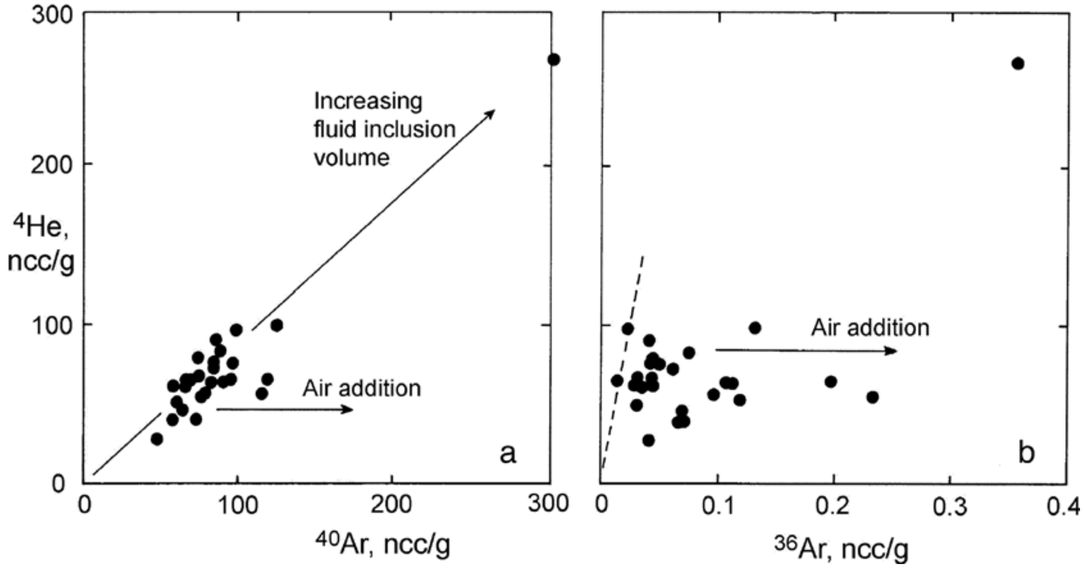

Fig. 11.30. Plots of gas release (10^{-9} cc/g) during crushing of olivine phenocrysts from a Juan Fernandez basalt: (a) ^{4}He against ^{40}Ar and (b) ^{4}He against ^{36}Ar, showing effects of atmospheric contamination. Modified after Farley and Craig (1994).

implies that the ^{40}Ar/^{36}Ar ratio of the deep mantle cannot be determined directly. In this situation, neon isotope evidence may help to narrow the range of possible values by acting as a monitor for atmospheric contamination.

11.3.2 Neon–argon

Starting from the 'atmospheric-contamination' model for neon, Farley and Poreda (1993) suggested that ^{20}Ne/^{22}Ne ratios could be used to monitor and correct atmospheric contamination in other rare gases such as argon. However, because the end-members will have different rare-gas abundance ratios (e.g. Ne/Ar), mixing will generate hyperbolic rather than linear arrays, leading to somewhat greater uncertainty in the calculation of uncontaminated end-members.

In order to constrain the curvature of mixing lines, Farley and Poreda first examined Ne–Ar isotope systematics in MORB glasses (Fig. 11.31a). Two sources of data were used. Solid symbols represent directly measured data from Hiyagon *et al.* (1992), whereas open symbols represent less-accurate argon data calculated indirectly from Marty (1989). Mixing lines were calculated between the atmosphere point and the best estimate (at the time) of terrestrial primordial neon and argon. These were based on the composition of planetary neon (^{20}Ne/^{22}Ne = 12.5) and the highest ^{40}Ar/^{36}Ar ratio (near 30 000) measured in a volatile-rich 'popping rock' from the Mid-Atlantic Ridge (Staudacher *et al.*, 1989). The very high volatile contents of these magmas were thought to render them relatively immune to atmospheric contamination. Using these end-members, most MORB analyses lay between mixing lines with ^{22}Ne/^{36}Ar ratios (r) of 0.06 and 0.6 in atmospheric relative to mantle components.

The OIB data set (Fig. 11.31b) can be modelled in a similar way. However, from the slightly different Ne/Ar ratios in OIB and MORB, Farley and Poreda estimated that simple two-component mixing between plume and atmospheric rare gases should fall between mixing lines with relative ^{22}Ne/^{36}Ar ratios of 0.07 and 0.7. Many of the Samoan samples in Fig. 11.31b have radiogenic argon signatures similar to the MORB data. However, the Samoan plume had already been shown to have a radiogenic neon isotope signature (section 11.2.3). Therefore, these data should be excluded from a search for the composition of the primordial argon reservoir. On the other hand, by fitting the mixing curves to the OIB samples with lowest argon isotope ratio, Farley and Poreda calculated a 'revised' ^{40}Ar/^{36}Ar ratio for primordial terrestrial argon, with a value of about 3500. This compares with the ^{40}Ar/^{36}Ar ratio of 400 proposed by Allègre *et al.* (1983). The higher value would then imply substantial radiogenic argon growth in this 'primordial' reservoir.

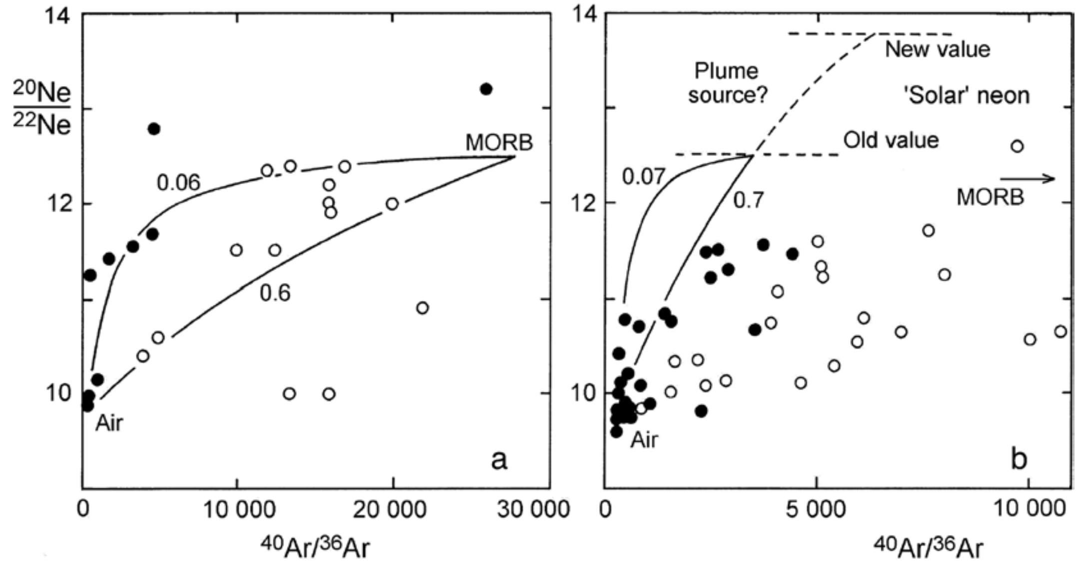

Fig. 11.31. Plots of neon *versus* argon isotope compositions in submarine glasses, showing possible mixing lines due to atmospheric contamination: (a) MORB (open symbols = indirect measurements) and (b) OIB (open symbols = Samoa). Modified after Farley and Poreda (1993).

The neon–argon diagram forms the basis of ongoing efforts to pin-point the argon isotope compositions of pristine mantle sources. However, new argon data for the 'popping rock' from the Mid-Atlantic Ridge (Burnard *et al.*, 1997) showed that even this very volatile-rich sample had suffered severe atmospheric contamination. Burnard *et al.* released the gases from vesicles in a section of rock 0.3 mm thick, using short pulses from a Nd : YAG laser. They found that ^{40}Ar abundances in individual vesicles were well correlated with ^{4}He and CO_2, indicating a mantle-derived source. In contrast, ^{36}Ar abundances were generally poorly correlated with these other quantities, leading Burnard *et al.* to suggest that perhaps none of the measured ^{36}Ar was mantle-derived. This seems to be a rather extreme interpretation, because a cluster of ^{40}Ar/^{36}Ar ratios was observed at a value of about 40 000. Nevertheless, this places a new lower limit on the ^{40}Ar/^{36}Ar ratio of the MORB source.

This new ^{40}Ar/^{36}Ar ratio for the MORB source was supported by additional studies of the argon–neon systematics of the popping rock, using gases extracted by stepwise crushing (Moreira *et al.*, 1998). This work yielded a good correlation line consistent with previous MORB data on the neon three-isotope plot, which was attributed to mantle–atmosphere mixing. However, an excellent hyperbolic mixing line was also observed on the argon–neon isotope diagram (Fig. 11.32), which allows the most accurate determination yet of the argon isotope ratio of the MORB source. From the intersection of the mixing line with the solar composition (rather than the planetary neon composition used by Farley and Poreda), a ^{40}Ar/^{36}Ar ratio of 44 000 was determined.

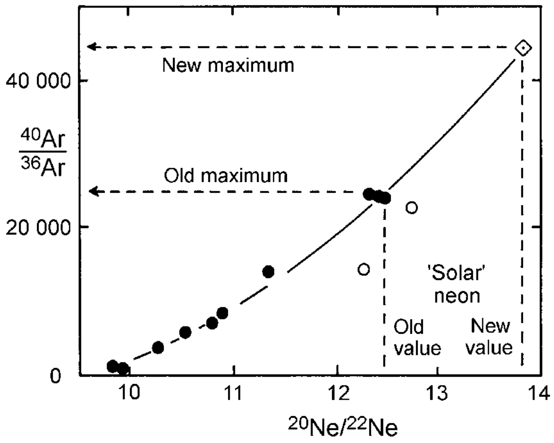

Fig. 11.32. Argon–neon isotope plot, showing a determination of the argon isotope ratio of the MORB source. Open points were omitted from the calculation of the mixing line because they had high argon blanks. After Moreira *et al.* (1998).

Since the work of Farley and Poreda (1993), several new studies have been performed on argon–neon isotope systematics in OIB glasses. Most of the data fall fairly close to the mixing line observed by Farley and Poreda. However, if the mixing line is extrapolated to a solar neon isotope ratio (^{20}Ne/^{22}Ne $= 13.8$) rather than the neon-B planetary value (^{20}Ne/^{22}Ne $= 12.5$), it necessarily implies that the ^{40}Ar/^{36}Ar ratio of the plume source will be more radiogenic.

Valbracht *et al.* (1997) performed such a study on glassy pillow rims and olivine phenocrysts, collected from water depths of 3–5 km on Loihi seamount. The best results were obtained by step heating, and reached ^{20}Ne/^{22}Ne ratios as high as 13. These authors plotted argon isotope data against the ^{21}Ne/^{22}Ne ratio, but the result is equivalent to using the ^{20}Ne/^{22}Ne ratio. Two mixing lines were drawn, with the minimum and maximum curvatures that could fit the data. Using a solar ^{21}Ne/^{22}Ne ratio of 0.41 (calculated from the three-isotope plot), the inferred ^{40}Ar/^{36}Ar composition of the plume source is between 2500 and 6000.

In a somewhat different approach, Marty *et al.* (1998) were able to sample plume-type rare gases from 380-Myr-old carbonatites in the Kola region of northern Russia. Neon and argon were extracted from a variety of rock types by crushing, and defined an array on the neon three-isotope plot with a slope slightly lower than that for Loihi. On a neon–argon isotope plot the data define an array with ^{20}Ne/^{22}Ne ratios as high as 12. Extrapolation to the solar neon composition led to estimated ^{40}Ar/^{36}Ar ratios between 5000 and 6000, depending on the curvature of the mixing line drawn through the data. These results clearly show the important role of deep-mantle plumes in carbonatite magmatism, as well as supporting the argon isotope composition of the plume source obtained from ocean islands.

Additional argon–neon isotope data were obtained by Trieloff *et al.* (2000) from sub-glacially erupted basalt glasses from Iceland and volatile-rich dunite xenoliths from Loihi. These sample suites defined arrays slightly steeper than previous Loihi data on the neon three-isotope plot, but on the neon–argon plot (Fig. 11.33) the results were similar to previous work. The upper ends of these data arrays (^{20}Ne/^{22}Ne $= 12.5$) fell within error of the neon-B composition, leading Trieloff *et al.* to suggest that this was the composition of 'solar neon' in the Earth. However, subsequent data (section 11.2.2) have exceeded this value, showing that the Earth contains true solar neon with ^{20}Ne/^{22}Ne ratios as high as those in the solar wind. Using this value to determine the argon isotope composition of the plume source leads to a ^{40}Ar/^{36}Ar ratio of about 7000 for Iceland. On this occasion the Loihi data indicated a higher ^{40}Ar/^{36}Ar ratio of about 15 000.

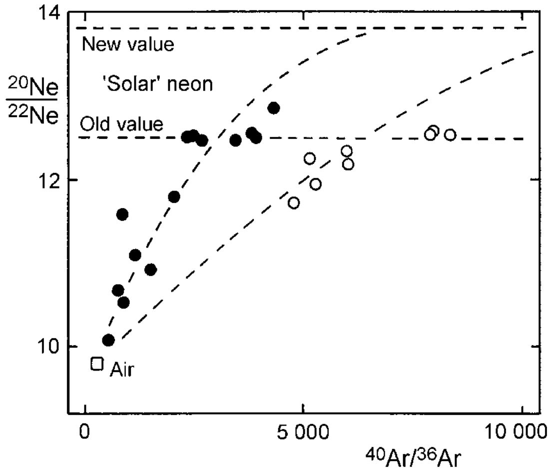

Fig. 11.33. Neon–argon isotope plot for Icelandic subglacial basalts (●) and Loihi dunites (○), showing mixing lines between atmospheric and plume-source (solar) rare gases. Modified after Trieloff *et al.* (2000).

Unfortunately these data leave the argon isotope composition of the plume source in a certain amount of doubt. It is demonstrably higher than that of air and lower than that in the MORB source, but a precise value remains elusive. The steady-state model of Porcelli and Wasserburg (1995b) predicts that the ^{40}Ar/^{36}Ar ratio of the (lower-mantle?) primordial rare-gas source should be about one-third of the upper-mantle value. Given a ^{40}Ar/^{36}Ar ratio of about 45 000 for the latter reservoir, a ratio between 5000 and 15 000 may be reasonable for the lower mantle.

11.3.3 Argon-38

In principle, ^{38}Ar data could be combined with ^{36}Ar and ^{40}Ar data to make a three-isotope system analogous to that of neon. Unfortunately, ^{38}Ar is about five times less abundant than ^{36}Ar, which is itself a very rare isotope. Furthermore, the total variation between atmospheric and solar compositions is only 5%. Therefore, until recently, no ^{38}Ar/^{36}Ar ratios had been observed that were distinct from the air composition. Two research groups have recently claimed to find such deviations (Valbracht *et al.*, 1997; Pepin, 1998). However, in a third study of comparable methodology (Kunz, 1999) no such deviations were found, so these positive signals remain disputable.

Valbracht *et al.* (1997) observed a weak correlation between ^{38}Ar/^{36}Ar ratios and ^{20}Ne/^{22}Ne ratios

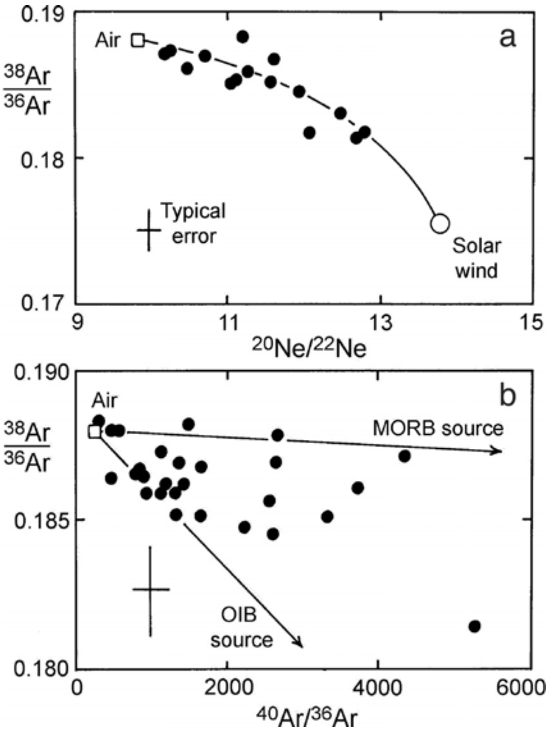

Fig. 11.34. Plots showing claimed variations of ^{38}Ar/^{36}Ar ratio in mantle-derived samples: (a) MORB samples on the argon–neon plot; and (b) MORB and OIB samples on the argon three-isotope plot. Error bars are 1σ. After Pepin (1998).

in Loihi glasses, which they interpreted as a mixing line between atmospheric and solar rare gases. Niederman *et al.* (1997) also presented ^{38}Ar/^{36}Ar data for MORB glasses from the East Pacific Rise (EPR), but did not discuss the data in detail, believing them to be within error of the atmospheric composition. However, Pepin (1998) pointed out that the EPR argon data define a relatively strong correlation with neon isotope data, between the atmospheric and solar compositions (Fig. 11.34a). Pepin also plotted the Loihi and EPR data on the argon three-isotope plot (Fig. 11.34b), on which mixing lines are linear. On this plot, both MORB and OIB data display a fan between the predicted mixing lines from atmospheric argon to upper- and lower-mantle sources.

Kunz (1999) pointed out a problem with the EPR data on the argon three-isotope plot, which is that these data lie not on the mixing line to MORB sources, but below that line, trending towards OIB. This could be attributed to contamination of the MORB source with plume material, but some of the EPR data lie surprisingly close to the atmosphere–plume-source mixing line to be explained in this way. Therefore, Kunz argued that these analyses are simply MORB samples with heavy atmospheric contamination, and that the low ^{38}Ar/^{36}Ar ratios (which have large error bars) are products of analytical noise. Furthermore, in a test for variations of ^{38}Ar/^{36}Ar ratio in the popping rock sample from the Mid-Atlantic Ridge, Kunz found no data outside error of the atmospheric composition, even though ^{20}Ne/^{22}Ne ratios were as high as 12.5. Therefore, the suggested variations in ^{38}Ar/^{36}Ar ratio remain unproven.

11.4 Xenon

Xenon is a heavy rare gas with nine stable isotopes. Reynolds (1960) first demonstrated variations in the meteoritic abundance of ^{129}Xe, which had been produced from the extinct nuclide ^{129}I (section 15.3.1). In addition, the four heaviest isotopes are fission products of both ^{238}U (Wetherill, 1953), and the extinct nuclide ^{244}Pu (Kuroda, 1960). It is convenient to ratio xenon isotope abundances against ^{130}Xe, which is non-radiogenic and is also shielded from spallation production. Hence, xenon isotope data are usually presented on a plot of either ^{134}Xe/^{130}Xe or ^{136}Xe/^{130}Xe (uranogenic and plutogenic xenon) against ^{129}Xe/^{130}Xe (iodogenic xenon), as shown in Fig. 11.35.

11.4.1 Iodogenic xenon

Because Xe is a tracer for two extinct nuclides, meteorite 'xenology' is a powerful tool for studying the condensation of the solar system (Reynolds, 1963). However, 'terrestrial xenology' is also a powerful tool for understanding terrestrial differentiation (Staudacher and Allègre, 1982). The first evidence for excess ^{129}Xe in the Earth (relative to atmospheric xenon) was found in CO_2 well gases from Harding County, New Mexico (Butler *et al.*, 1963). This evidence has such far-reaching implications, that numerous subsequent studies have been devoted to Harding County well gases (e.g. Hennecke and Manuel, 1975; Phinney *et al.*, 1978; Staudacher, 1987).

Studies of xenon isotope data from granitic rocks (Butler *et al.*, 1963) showed that, unlike the heavy xenon isotopes, ^{129}Xe is not generated in significant amounts (relative to non-radiogenic xenon) by fission or neutron-activation reactions (Fig. 11.35). Therefore Butler *et al.* concluded that the excess ^{129}Xe in mantle-derived gases must have been due to decay, soon after the formation of the Earth, of extinct ^{129}I. The presence of this extinct nuclide ($t_{1/2}$ = 16 Myr) in the

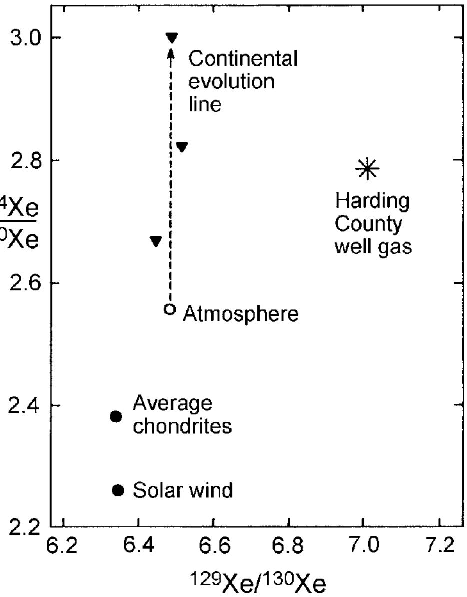

Fig. 11.35. Plot of fissiogenic ^{134}Xe/^{130}Xe ratio against iodogenic ^{129}Xe/^{130}Xe ratio for granites and well gases analysed prior to 1978. Modified after Staudacher and Allègre (1982).

Earth demonstrates that its accretion must have occurred within a few million years of meteorites, which also commonly display ^{129}Xe anomalies (section 15.3.1).

Further advances in terrestrial xenology required the well-gas data to be put into the wider perspective of major terrestrial reservoirs. Technical developments, allowing the xenon analysis of submarine glasses, made this possible. In early work, Staudacher and Allègre (1982) found correlated enrichments of ^{129}Xe and other heavy xenon isotopes in MORB glasses. This was confirmed by Staudacher (1987), who showed that the most ^{129}Xe-enriched well-gas analyses lay on the same correlation line as MORB (Fig. 11.36a). Well-gas and MORB compositions were also coherent on a plot of ^{40}Ar/^{36}Ar ratio against ^{129}Xe/^{130}Xe ratio (Fig. 11.36b). This provides strong evidence that the Harding County well gases sample an upper-mantle reservoir similar to the depleted MORB source.

Staudacher and Allègre (1982) argued that the excess ^{129}Xe in MORB (relative to a Bulk Earth with atmospheric xenon) could be explained by degassing of the upper mantle very early in the Earth's history. Primordial rare gases including ^{130}Xe would also have been lost to the atmosphere, while ^{129}I still remained in the mantle. The high I/Xe ratios generated by this process would allow the small amount of ^{129}I remaining in the upper mantle to generate measurable excesses in ^{129}Xe after its decay. Hence, upper-mantle degassing must have occurred much earlier than lithophile depletion (by crust formation), although these two processes seem to affect roughly similar fractions of the mantle. These data will be discussed further in section 11.4.2.

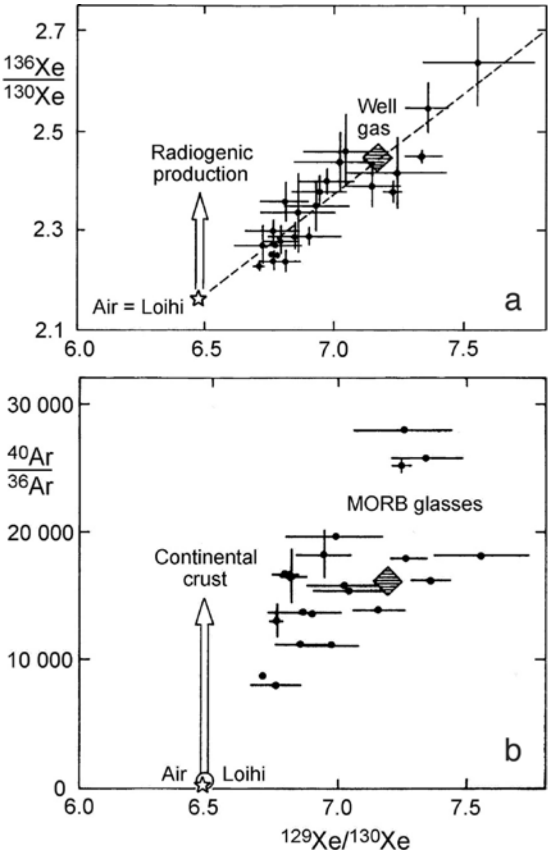

Fig. 11.36. Plots of (a) ^{136}Xe/^{130}Xe ratio and (b) ^{40}Ar/^{36}Ar ratio against ^{129}Xe/^{130}Xe ratio for MORB glasses, compared with other terrestrial components. After Staudacher (1987).

Additional evidence for the xenon isotope evolution of the upper mantle has been obtained from the analysis of 'coated' diamonds (Ozima and Zashu, 1991). The coats of these diamonds contain relatively large rare-gas contents, and are thus suited to isotopic analysis. Ozima and Zashu found xenon isotope ratios identical to the MORB correlation line (Fig. 11.37), suggesting that the same evolution processes gave rise to the mantle sources of MORB and diamonds. In the light

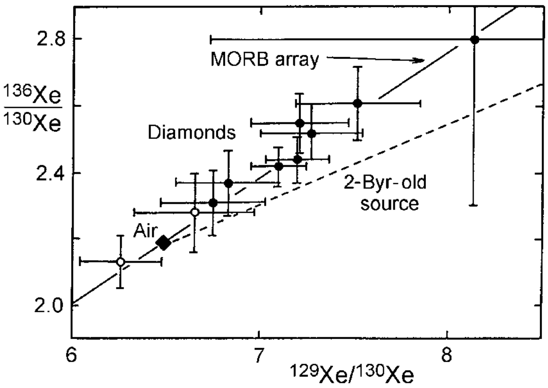

Fig. 11.37. Plot of $^{136}Xe/^{130}Xe$ ratio against $^{129}Xe/^{130}Xe$ ratio for coated diamonds, compared with the MORB correlation line of Staudacher (1987): (○) = cores; (●) = coats. The dashed line shows the result of uranogenic production from a 2-Byr-old source. After Ozima and Zashu (1991).

of neon and argon isotope evidence (sections 11.2 and 11.3), the MORB array is best attributed to atmospheric contamination of magmas with radiogenic xenon. Similarly, Ozima and Zashu attributed the diamond array to mixing between a radiogenic xenon source and atmospheric xenon contamination (represented by the cores).

Analysis of xenon isotope compositions in glasses from Loihi Seamount and the Reykjanes Ridge gave results within error of atmospheric rare gases, but the origin of this signature was widely disputed. Allègre *et al.* (1983) and Hart *et al.* (1983) attributed it to a less-degassed mantle source, in which radiogenic ^{129}Xe and ^{40}Ar are swamped by large primordial rare-gas contents. Alternatively, Ozima *et al.* (1985) proposed that atmospheric xenon is recycled into the deep mantle, whereas Patterson *et al.* (1990) argued that the xenon isotope ratios of Loihi glasses (together with argon ratios) are due to atmospheric contamination, introduced directly into plume magmas from seawater.

Poreda and Farley (1992) suggested that the relatively shallow ocean depths at which Loihi basalts had erupted allowed much of the magmatic gas content to be lost, making them very susceptible to contamination by rare gases in seawater. To avoid these problems, Poreda and Farley analysed two suites of very volatile-rich harzburgite xenoliths from the Samoan hot-spot, which are more resistant to atmospheric contamination. The helium and neon isotope signatures of these rocks were somewhat more radiogenic than those for Loihi (section 11.2.3), but still well below the levels in MORB. Therefore, these samples clearly contain a large plume-derived component. Xenon isotope ratios were found to be elevated by up to 6% relative to the atmospheric point, providing the first evidence for a non-atmospheric xenon signature from the lower mantle.

Using this evidence for non-atmospheric xenon in plumes, Porcelli and Wasserburg (1995a) extended the steady-state helium model of Kellogg and Wasserburg (1990) to xenon. They argued that the radiogenic signature of upper-mantle xenon (relative to the atmosphere) is not a residue of early degassing of the Earth, as had previously been proposed, but is the result of input from the lower mantle, along with minor *in situ* production. The supply of rare gases from lower to upper mantle was attributed to mass transfer in plumes. A fraction of the plume is degassed at the hot-spot, but the bulk is mixed into the upper mantle. In this mass-transfer model, rare gases are not fractionated from one another, so they are all thought to have the same upper-mantle residence time of about 1.4 Byr.

Since the upper mantle is argued to be in steady state, it bears no memory of its early history. Hence, variations of $^{129}Xe/^{130}Xe$ ratio in the upper mantle (attributed to extinct iodine) are explained solely by mixing of lower-mantle and atmospheric xenon. The atmosphere is at the unradiogenic end of the MORB array, and must therefore have been outgassed from the Earth before a substantial amount of the iodine budget had decayed. However, Porcelli and Wasserburg suggested that some of the atmosphere was probably contributed by late accretion of volatile-rich material after degassing of the deep Earth. In contrast to this composition, the lower mantle is predicted to be at the radiogenic end of the MORB range.

Experimental confirmation that the xenon isotope composition of the plume source has a radiogenic signature resembling that of MORB came from new analyses of Loihi and Iceland samples (Trieloff *et al.*, 2000). These were the first Loihi data to be clearly distinct from the atmospheric composition, and extended half-way up the MORB array (Fig. 11.38). These data therefore confirm the similarities between rare-gas signatures of the plume source and the upper mantle, providing strong support for the steady-state model of Porcelli and Wasserburg (1995a). However, the evidence continues to support the two-reservoir model for terrestrial rare gases by maintaining the need for a primordial rare-gas reservoir in the deep Earth, at the same time as a strongly degassed upper mantle. It remains unknown whether the primordial rare-gas reservoir is located in the deep mantle or the core. However, Jephcoat (1998) suggested that heavy rare gases could actually be in the solid phase at lower mantle pressures.

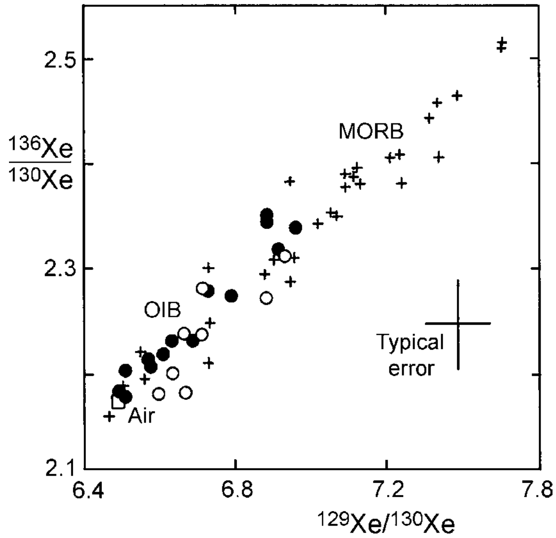

Fig. 11.38. Comparison of new data from Loihi (○) and Iceland (●) with the location of the MORB array (+) on the xenon three-isotope plot. Modified after Trieloff *et al.* (2000).

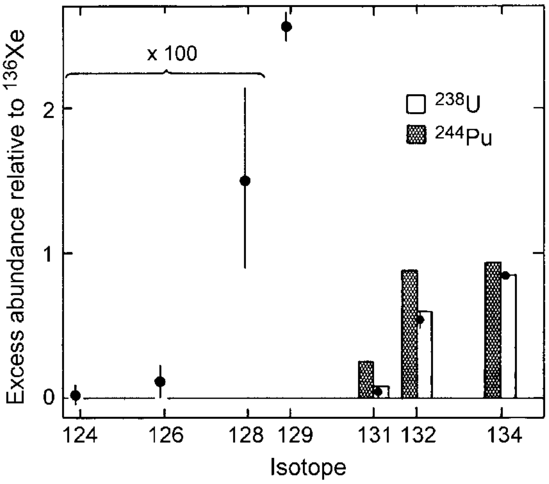

Fig. 11.39. Plot of excess abundances of xenon isotopes in well gas relative to the atmosphere, ratioed against excess ^{136}Xe. The data (●) are compared with modelled production of fissiogenic xenon from ^{238}U and ^{244}Pu. After Phinney *et al.* (1978).

11.4.2 Fissiogenic xenon

Variations in fissiogenic xenon are more complex than variations in iodogenic xenon because there are components from fission of both extinct plutonium and extant uranium. The early work by Butler *et al.* (1963) and Hennecke and Manuel (1975) suggested that some fissiogenic xenon in Harding County well gases was plutogenic. However, more precise analysis by Phinney *et al.* (1978) showed that the excess abundances of ^{131}Xe, ^{132}Xe and ^{134}Xe relative to ^{136}Xe in well gas are a better match to the calculated isotope production from spontaneous fission of ^{238}U rather than ^{244}Pu (Fig. 11.39).

The heavy xenon isotope signatures in diamonds can also be used to test for plutogenic or uranogenic production, as demonstrated above for well gases. Ozima and Zashu (1991) showed that production from ^{238}U yields the best fit to the xenon data on diamond coats, which in turn places a tight constraint on the time of formation of these coats. Uranogenic xenon (unlike iodogenic and plutogenic xenon) grows in the mantle over the Earth's history. Therefore, if the rare gases in diamonds have been isolated from the silicate upper mantle for the past few billion years, they should have developed less ^{136}Xe than young MORB samples (dashed line in Fig. 11.34). The fact that MORB, diamond coats, and well gases all lie on the same array (if not a coincidence) suggests that all of these samples were formed relatively recently in geological time. This presents a problem, since other studies have indicated ancient formation ages for diamonds (section 4.2.1). However, it is possible that old diamond cores were overgrown by younger coats shortly before or during kimberlite magmatism (about 100 Myr ago).

Ozima *et al.* (1985) showed that fissiogenic xenon data can be evaluated in a more quantitative manner on a plot in which two different fissiogenic xenon isotopes are ratioed against ^{130}Xe. Any one of ^{131}Xe, ^{132}Xe or ^{134}Xe can be compared with ^{136}Xe, but the last two isotopes are usually compared because they have the best analytical precision. These isotopes are plotted in Fig. 11.40, from a re-evaluation of published data by Tolstikhin and O'Nions (1996). The errors on the MORB data available at the time this plot was drawn were too large to resolve these components reliably, but it appeared that MORB xenon resembles well-gas xenon in having a uranogenic signature. More recently, xenon isotope analysis of carbonatites from Brazil and Canada gave a signature that was distinctly uranogenic (Sasada *et al.*, 1997). However, new analyses of MORB by Kunz *et al.* (1998) suggested a mixture of uranogenic and plutogenic xenon.

The evolution of fissiogenic and iodogenic xenon in the steady-state model of Porcelli and Wasserburg (1995a) is shown in Fig. 11.41. In response to decay of iodine and plutonium, it is thought that lower-mantle xenon evolved from an initial solar or planetary

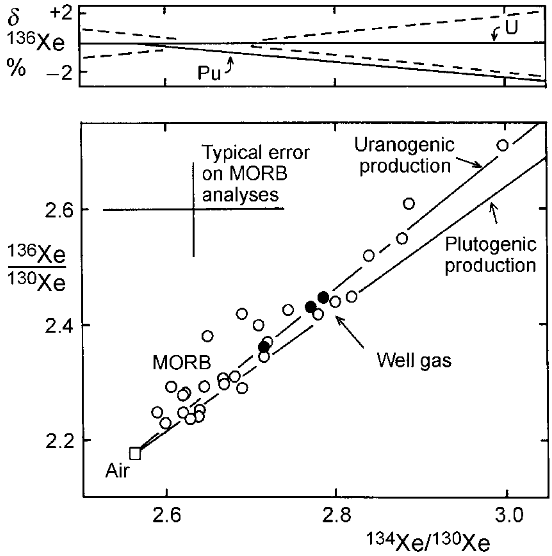

Fig. 11.40. Plot of two fissiogenic xenon isotopes, ratioed against ^{130}Xe, to compare data for well gas (●) and MORB (○) with alternative uranogenic and plutogenic production routes. The δ ^{136}Xe diagram above shows the 95% confidence envelope for the best-fit regression of MORB data (dashed lines), relative to the alternative production routes. After Tolstikhin and O'Nions (1996).

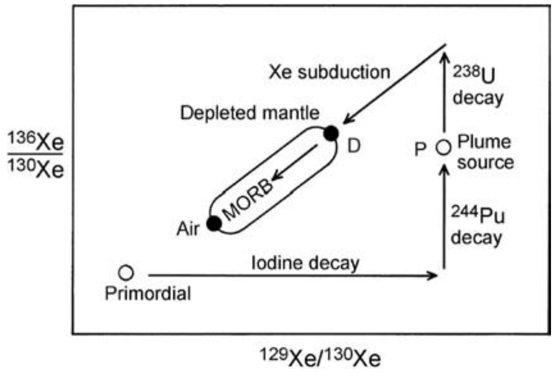

Fig. 11.41. Conceptual model showing the evolution of fissiogenic xenon in the Earth, sub-divided into plutogenic and uranogenic components: (○) = hypothetical compositions. After Porcelli and Wasserburg (1995a).

composition to the hypothetical composition of present-day lower mantle (P). In the steady-state model, xenon escaping from the lower mantle is supplemented by decay of uranium in the upper mantle, and then mixed with subducted atmospheric xenon, to reach the upper-mantle composition (D). The MORB xenon array is then attributed to mixing between D and the atmosphere, due to contamination of magmas at the sea floor.

Plume sources should define a similar array of gentler slope, between the atmosphere and P. However, this prediction cannot yet be tested reliably, due to the difficulty of obtaining definitive non-atmospheric xenon signatures from hot-spots. The available data for plume sources (Fig. 11.38) do not appear to support the model, since all data appear to be collinear with the MORB array. However, two processes may act to homogenise the plume and MORB signatures: firstly, ongoing contamination of the upper mantle by plume material; and secondly, contamination of ascending plumes by entrainment of upper-mantle xenon. It should also be borne in mind that many plume sources (e.g. Samoa) contain recycled lithospheric material, almost certainly including subducted atmospheric xenon.

Further uncertainties in fissiogenic Xe systematics arise from the findings of Meshik *et al.* (1995), who suggested that variations in the relative abundances of heavy xenon isotopes could be due to open-system conditions during the β decay of uranium fission products. High-temperature conditions could allow preferential escape of some short-lived intermediates, affecting the isotopic composition of xenon isotopes, which are the final decay products. In the light of all the above problems, fissiogenic xenon systematics remain in considerable doubt.

11.4.3 Solar xenon

The non-radiogenic light isotopes of xenon are potentially very useful for unravelling the mysteries of terrestrial xenology. These isotopes should be usable in the same way as the non-radiogenic neon isotopes to assess the relationship between atmospheric xenon and primordial xenon in the Earth. However, because of the low abundances of the light isotopes, analytical errors have prevented their application until fairly recently.

Well-gas ^{128}Xe data presented by Caffee *et al.* (1988) provided the first evidence for a correlation between the iodogenic ^{129}Xe/^{130}Xe ratio and the non-radiogenic ^{128}Xe/^{130}Xe ratio. This implies that the atmosphere and the (upper) mantle reservoir sampled by well gases exhibit relative fractionation of xenon isotopes, in a manner analogous to neon. These systematics were investigated in more detail by Jacobsen and Harper (1996), Tolstikhin and O'Nions (1996) and Caffee *et al.* (1999), as illustrated in Fig. 11.42. By showing that

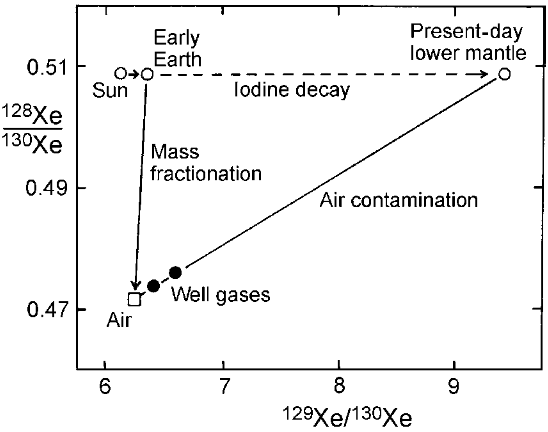

Fig. 11.42. Plot of non-radiogenic $^{128}Xe/^{130}Xe$ ratio against iodogenic $^{129}Xe/^{130}Xe$ ratio, showing the evolution of mantle and atmospheric xenon and their mixing in well gases. Modified after Jacobsen and Harper (1996).

the Earth's mantle is slightly enriched in ^{128}Xe relative to the atmosphere, the data support the model of Pepin (1991), who argued that the atmosphere has undergone mass fractionation of xenon relative to an original solar composition.

It is generally agreed that the compositions of solar xenon, the present-day Earth's atmosphere, and well gases in Fig. 11.42 can be related by mass fractionation and by iodine decay but there is some disagreement about the order of events. This author proposes to follow the 'classical' view that the order of events was (1) accretion of the Earth, (2) early degassing, (3) atmospheric fractionation and (4) decay of iodine deep in the Earth.

Ozima and Igarashi (1989) suggested that mass fractionation occurred during accretion (and therefore before degassing). However, the distinct solar composition of the Earth's mantle seems to rule out this model. Similarly, Caffee *et al.* (1999) suggested that substantial decay of iodine occurred before accretion. However, this would require extreme variation in the I/Xe ratios of accreted components in order to create large inherited xenon isotope heterogeneity between the mantle and atmosphere. This also seems unlikely. Therefore, the best explanation (as shown in Fig. 11.41) is that the atmosphere was degassed after only *minor* decay of iodine in the Earth and then underwent mass fractionation.

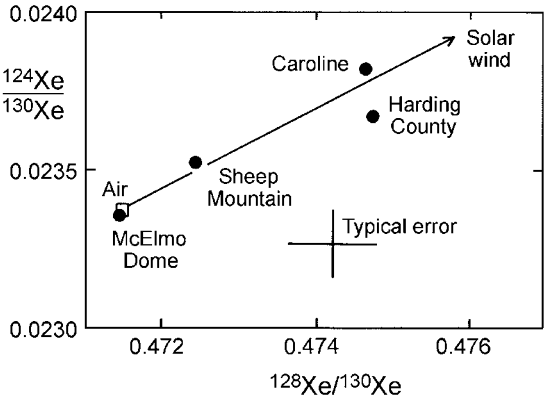

Fig. 11.43. Plot of non-radiogenic xenon isotope systematics, showing that well gases lie on a mixing line between atmospheric and solar xenon. After Caffee *et al.* (1999).

The analysis of additional non-radiogenic light xenon isotopes by Caffee *et al.* (1999) provided further support for the 'solar-xenon' model by revealing a correlation between $^{124}Xe/^{130}Xe$ and $^{128}Xe/^{130}Xe$ ratios (Fig. 11.43). This array, formed entirely by non-radiogenic xenon isotopes, trends from the atmospheric composition towards the solar-wind composition. This confirms that the Earth's mantle has a solar xenon signature, and continues to suggest that the atmosphere underwent mass fractionation of xenon, probably from a combination of giant impact and solar radiation (section 11.2.2).

In conclusion, much progress has been made in understanding terrestrial xenology. The overall pattern of degassing of the early Earth, the evolution of the plume source, and upper-mantle buffering now constitute a fairly robust model. However, many details remain to be worked out.

References

Aldrich, L. T. and Nier, A. O. (1948). The occurrence of He^3 in natural sources of helium. *Phys. Rev.* **74**, 1590–4.

Allègre, C. J., Moreira, M. and Staudacher, T. (1995). $^4He/^3He$ dispersion and mantle convection. *Geophys. Res. Lett.* **22**, 2325–8.

Allègre, C. J., Sarda, P. and Staudacher, T. (1993). Speculations about the cosmic origin of He and Ne in the interior of the Earth. *Earth Planet. Sci. Lett.* **117**, 229–33.

Allègre, C. J., Staudacher, T. and Sarda, P. (1986). Rare gas systematics: formation of the atmosphere, evolution and structure of the Earth's mantle. *Earth Planet. Sci. Lett.* **81**, 127–50.

Allègre, C. J., Staudacher, T., Sarda, P. and Kurz, M. (1983). Constraints on evolution of Earth's mantle from rare gas systematics. *Nature* **303**, 762–6.

Alvarez, L. W. and Cornog, R. (1939). Helium and hydrogen of mass 3. *Phys. Rev.* **56**, 613.

Anderson, D. L. (1993). Helium-3 from the mantle: primordial signal or cosmic dust? *Science* **261**, 170–6.

Anderson, D. L. (2001). A statistical test of the two reservoir model for helium isotopes. *Earth Planet. Sci. Lett.* **193**, 77–82.

Burnard, P., Graham, D. and Turner, G. (1997). Vesicle-specific noble gas analyses of "popping rock": implications for primordial noble gases in Earth. *Science* **276**, 568–71.

Butler, W. A., Jeffery, P. M., Reynolds, J. H. and Wasserburg, G. J. (1963). Isotopic variations in terrestrial xenon. *J. Geophys. Res.* **68**, 3283–91.

Caffee, M. W., Hudson, G. B., Velsko, C., Alexander, E. C., Huss, G. R. and Chivas, A. R. (1988). Non-atmospheric noble gases from CO_2 well gases. *Lunar Planet. Sci.* **19**, 154–5 (abstract).

Caffee, M. W., Hudson, G. B., Velsko, C., Huss, G. R., Alexander, E. C. and Chivas, A. R. (1999). Primordial noble gases from Earth's mantle: identification of a primitive volatile component. *Science* **285**, 2115–18.

Cerling, T. E. (1989). Dating geomorphologic surfaces using cosmogenic ^{3}He. *Quaternary Res.* **33**, 148–56.

Clarke, W. B., Beg, M. A. and Craig, H. (1969). Excess ^{3}He in the sea: evidence for terrestrial primordial helium. *Earth Planet. Sci. Lett.* **6**, 213–20.

Clarke, W. B., Jenkins, W. J. and Top, Z. (1976). Determination of tritium by mass-spectrometric measurement of ^{3}He. *Int. J. Appl. Rad. Isot.* **27**, 515–22.

Coltice, N. and Ricard, Y. (1999). Geochemical observations and one layer mantle convection. *Earth Planet. Sci. Lett.* **174**, 125–37.

Craig, H. and Lupton, J. E. (1976). Primordial neon, helium, and hydrogen in oceanic basalts. *Earth Planet. Sci. Lett.* **31**, 369–85.

Craig, H. and Poreda, R. J. (1986). Cosmogenic ^{3}He in terrestrial rocks: the summit lavas of Maui. *Proc. Nat. Acad. Sci. USA* **83**, 1970–4.

Damon, P. E. and Kulp, L. (1958). Excess helium and argon in beryl and other minerals. *Amer. Miner.* **43**, 433–59.

Dixon, E. T., Honda, M., McDougall, I., Campbell, I. H. and Sigurdsson, I. (2000). Preservation of near-solar neon isotopic ratios in Icelandic basalts. *Earth Planet. Sci. Lett.* **180**, 309–24.

Fanale, F. P. (1971). A case for catastrophic early degassing of the Earth. *Chem. Geol.* **8**, 79–105.

Farley, K. A. (1995a). Rapid cycling of subducted sediments into the Samoan mantle plume. *Geology* **23**, 531–4.

Farley, K. A. (1995b). Cenozoic variations in the flux of interplanetary dust recorded by ^{3}He in a deep-sea sediment. *Nature* **376**, 153–6.

Farley, K. A. and Craig, H. (1994). Atmospheric argon contamination of ocean island basalt olivine phenocrysts. *Geochim. Cosmochim. Acta* **58**, 2509–17.

Farley, K. A., Montanari, A., Shoemaker, E. M. and Shoemaker, C. S. (1998). Geochemical evidence for a comet shower in the late Eocene. *Science* **280**, 1250–3.

Farley, K. A. and Patterson, D. B. (1995). A 100-kyr periodicity in the flux of extraterrestrial ^{3}He to the sea floor. *Nature* **378**, 600–3.

Farley, K. A. and Poreda, R. J. (1993). Mantle neon and atmospheric contamination. *Earth Planet. Sci. Lett.* **114**, 325–39.

Fisher, D. E. (1971). Incorporation of Ar in East Pacific basalts. *Earth Planet. Sci. Lett.* **12**, 321–4.

Fisher, D. E. (1983). Rare gases from the undepleted mantle? *Nature* **305**, 298–300.

Fisher, D. E. (1985). Noble gases from oceanic island basalts do not require an undepleted mantle source. *Nature* **316**, 716–18.

Fisher, D. E. (1986). Rare gas abundances in MORB. *Geochim. Cosmochim. Acta* **50**, 2531–41.

Gerling, E. K., Mamyrin, B. A., Tolstikhin, I. N. and Yakovleva, S. S. (1971). Isotope composition of helium in some rocks. *Geokhimiya* **10**, 1209–17.

Graf, T., Kohl, C. P., Marti, K. and Nishiizumi, K. (1991). Cosmic-ray-produced neon in Antarctic rocks. *Geophys. Res. Lett.* **18**, 203–6.

Graham, D. W., Castillo, P. R., Lupton, J. E. and Batiza, R. (1996). Correlated He and Sr isotope ratios in South Atlantic near-ridge seamounts and implications for mantle dynamics. *Earth Planet. Sci. Lett.* **144**, 491–503.

Hanyu, T. and Kaneoka, I. (1997). The uniform and low ^{3}He/^{4}He ratios of HIMU basalts as evidence for their origin as recycled materials. *Nature* **390**, 273–6.

Harrison, D., Burnard, P. and Turner, G. (1999). Noble gas behaviour and composition in the mantle: constraints from the Iceland Plume. *Earth Planet. Sci. Lett.* **171**, 199–207.

Hart, R., Dymond, J. and Hogan, L. (1979). Preferential formation of the atmosphere–sialic crust system from the upper mantle. *Nature* **278**, 156–9.

Hart, R., Dymond, J., Hogan, L. and Schilling, J. G. (1983). Mantle plume noble gas component in glassy basalts from Reykjanes Ridge. *Nature* **305**, 403–7.

Hart, R., Hogan, L. and Dymond, J. (1985). The closed-system approximation for evolution of argon and helium in the mantle, crust and atmosphere. *Chem. Geol. (Isot. Geosci. Section)* **52**, 45–73.

Hennecke, E. W. and Manuel, O. K. (1975). Noble gases in CO_2 well gas, Harding County, New Mexico. *Earth Planet. Sci. Lett.* **27**, 346–55.

Hilton, D. R., Barling, J. and Wheller, G. E. (1995). Effect of shallow-level contamination on the isotope systematics of ocean-island lavas. *Nature* **373**, 330–3.

Hilton, D. R., Grönvold, K., Macpherson, C. G. and Castillo, P. R. (1999). Extreme ^{3}He/^{4}He ratios in northwest Iceland: constraining the common component in mantle plumes. *Earth Planet. Sci. Lett.* **173**, 53–60.

Hilton, D. R., Hammerschmidt, K., Loock, G. and Friedrichsen, H. (1993a). Helium and argon isotope systematics of the central Lau Basin and Valu Fa Ridge: evidence of crust/mantle interactions in a back-arc basin. *Geochim. Cosmochim. Acta* **57**, 2819–41.

Hilton, D. R., Hammerschmidt, K., Teufel, S. and Friedrichsen, H. (1993b). Helium isotope characteristics of Andean geothermal fluids and lavas. *Earth Planet. Sci. Lett.* **120**, 265–82.

Hilton, D. R., Thirlwall, M. F., Taylor, R. N., Murton, B. J. and Nichols, A. (2000). Controls on magmatic degassing along the Reykjanes Ridge with implications for the helium paradox. *Earth Planet. Sci. Lett.* **183**, 43–50.

Hiyagon, H. (1994). Retention of solar helium and neon in IDPs in deep sea sediment. *Science* **263**, 1257–9.

Hiyagon, H., Ozima, M., Marty, B., Zashu, S. and Sakai, H. (1992). Noble gases in submarine glasses from mid-ocean ridges and Loihi seamount: constraints on the early history of the Earth. *Geochim. Cosmochim. Acta* **56**, 1301–16.

Hoke, L., Hilton, D.R., Lamb, S.H., Hammerschmidt, K. and Friedrichsen, H. (1994). ^{3}He evidence for a wide zone of active mantle melting beneath the Central Andes. *Earth Planet. Sci. Lett.* **128**, 341–55.

Honda, M., McDougall, I., Patterson, D.B., Doulgeris, A. and Clague, D.A. (1991). Possible solar noble-gas component in Hawaiian basalts. *Nature* **349**, 149–51.

Honda, M., Reynolds, J.H., Roedder, E. and Epstein, S. (1987). Noble gases in diamonds: occurrences of solar-like helium and neon. *J. Geophys. Res.* **92**, 12 507–21.

Jacobsen, S.B. and Harper, C.L. (1996). Accretion and early differentiation history of the Earth based on extinct radionuclides. In: Basu, A. and Hart, S.R. (Eds.), *Earth Processes: Reading the Isotopic Code. Geophysics Monograph* **95**, pp. 47–74.

Jambon, A. and Zimmermann, J.L. (1987). Major volatiles from an Atlantic MORB glass: a size fraction analysis. *Chem. Geol.* **62**, 177–89.

Jeffrey, P.M. and Hagan, P.J. (1969). Negative muons and the isotopic composition of the rare gases in the Earth's atmosphere. *Nature* **223**, 1253.

Jephcoat, A.P. (1998). Rare-gas solids in the Earth's deep interior. *Nature* **393**, 355–8.

Kaneoka, I. and Takaoka, N. (1980). Rare gas isotopes in Hawaiian ultramafic nodules and volcanic rocks: constraints on genetic relationships. *Science* **208**, 1366–8.

Kellog, L.H. and Wasserburg, G.J. (1990). The role of plumes in mantle helium fluxes. *Earth Planet. Sci. Lett.* **99**, 276–89.

Kennedy, B.M., Hiyagon, H. and Reynolds, J.H. (1990). Crustal neon: a striking uniformity. *Earth Planet. Sci. Lett.* **98**, 277–86.

Kortenkamp, S.J. and Dermott, S.F. (1998). A 100,000-year periodicity in the accretion rate of interplanetary dust. *Science* **280**, 874–6.

Kunz, J. (1999). Is there solar argon in the Earth's mantle? *Nature* **399**, 649–50.

Kunz, J., Staudacher, T. and Allègre, C.J. (1998). Plutonium-fission xenon found in the Earth's mantle. *Science* **280**, 877–80.

Kunz, W. and Schintlmeister, I. (1965). *Tabellen der Atomkerne, Teil II, Kernreaktionen*. Akademie-Verlag, 1022 pp.

Kuroda, P.K. (1960). Nuclear fission in the early history of the Earth. *Nature* **187**, 36–8.

Kurz, M.D. (1986a). Cosmogenic helium in a terrestrial igneous rock. *Nature* **320**, 435–9.

Kurz, M.D. (1986b). *In-situ* production of terrestrial cosmogenic helium and some applications to geochronology. *Geochim. Cosmochim. Acta* **50**, 2855–62.

Kurz, M.D., Gurney, J.J., Jenkins, W.J. and Lott, D.E. (1987). Helium isotopic variability within single diamonds from the Orapa kimberlite pipe. *Earth Planet. Sci. Lett.* **86**, 57–68.

Kurz, M.D. and Jenkins, W.J. (1981). The distribution of helium in oceanic basalt glasses. *Earth Planet. Sci. Lett.* **53**, 41–54.

Kurz, M.D., Jenkins, W.J. and Hart, S.R. (1982). Helium isotopic systematics of oceanic islands and mantle heterogeneity. *Nature* **297**, 43–6.

Kurz, M.D., Meyer, P.S. and Sigurdsson, H. (1985). Helium isotopic systematics within the neovolcanic zones of Iceland. *Earth Planet. Sci. Lett.* **74**, 291–305.

Kyser, T.K. and Rison, W. (1982). Systematics of rare gas isotopes in basic lavas and ultramafic xenoliths. *J. Geophys. Res.* **87**, 5611–30.

Lal, D. (1987). Production of ^{3}He in terrestrial rocks. *Chem. Geol. (Isot. Geosci. Section)* **66**, 89–98.

Lal, D., Nishiizumi, K., Klein, J., Middleton, R. and Craig, H. (1987). Cosmogenic ^{10}Be in Zaire alluvial diamonds: implications to ^{3}He excess in diamonds. *Nature* **328**, 139–41.

Lupton, J.E., (1983). Terrestrial inert gases: isotope tracer studies and clues to primordial components in the mantle. *Ann. Rev. Earth Planet. Sci.* **11**, 371–414.

Lupton, J.E. and Craig. H. (1975). Excess ^{3}He in oceanic basalts: evidence for terrestrial primordial helium. *Earth Planet. Sci. Lett.* **26**, 133–9.

Mamyrin, B.A., Anufriyev, G.S., Kamenskiy, I.L. and Tolstikhin, I.N. (1970). Determination of the composition of atmospheric helium. *Geochem. Int.* **7**, 498–505.

Mamyrin, B.A. and Tolstikhin, I.N. (1984). *Helium Isotopes in Nature*. Elsevier, 273 pp.

Mamyrin, B.A., Tolstikhin, I.N. Anufriyev, G.S. and Kamenskiy, I.L. (1969). Anomalous isotopic composition of helium in volcanic gases. *Dokl. Akad. Nauka SSSR* **184**, 1197–9.

Mamyrin, B.A., Tolstikhin, I.N. Anufriyev, G.S. and Kamenskiy, I.L. (1972). Isotopic composition of helium in Icelandic hot springs. *Geokhimiya* **11**, 1396.

Marcantonio, F., Anderson, R.F., Stute, M., Kumar, N., Schlosser, P. and Mix, A. (1996). Extraterrestrial ^{3}He as a tracer of marine sediment transport and accumulation. *Nature* **383**, 705–7.

Marcantonio, F., Kumar, N., Stute, M. *et al.* (1995). A comparative study of accumulation rates derived by He and Th isotope analysis of marine sediments. *Earth Planet. Sci. Lett.* **133**, 549–55.

Marcantonio, F., Turekian, K.K., Higgins, S., Anderson, R.F., Stute, M. and Schlosser, P. (1999). The accretion rate of extraterrestrial ^{3}He based on the oceanic ^{230}Th flux and the relation to Os isotope variation over the past 200,000 years in an Indian Ocean core. *Earth Planet. Sci. Lett.* **170**, 157–68.

Martel, D.J., Deak, J., Dovenyi, P. *et al.* (1989). Leakage of helium from the Pannonian basin. *Nature* **342**, 908–12.

Marty, B. (1989). Neon and xenon isotopes in MORB: implications for the Earth–atmosphere evolution. *Earth Planet. Sci. Lett.* **94**, 45–56.

Marti, B. and Craig, H. (1987). Cosmic-ray-produced neon and helium in the summit lavas of Maui. *Nature* **325**, 335–7.

Marty, B. and Jambon, A. (1987). C/^{3}He in volatile fluxes from the solid Earth: implications for carbon geodynamics. *Earth Planet. Sci. Lett.* **83**, 16–26.

Marty, B., Tolstikhin, I., Kamensky, I.L., Nivin, V., Balaganskaya, E. and Zimmermann, J.-L. (1998). Plume-derived rare gases in 380 Ma carbonatites from the Kola region (Russia) and the argon isotopic composition in the deep mantle. *Earth Planet. Sci. Lett.* **164**, 179–192.

Matsuda, J., Murota, M. and Nagao, K. (1990). He and Ne isotopic studies on the extraterrestrial material in deep-sea sediments. *J. Geophys. Res.* **95**, 7111–17.

Matsuda, J., Sudo, M., Ozima, M., Ito, K., Ohtaka, O. and Ito, E. (1993). Noble gas partitioning between metal and silicate under high pressures. *Science* **259**, 788–90.

Merrihue, C. (1964). Rare gas evidence for cosmogenic dust in modern Pacific red clay. *Ann. N. Y. Acad. Sci.* **119**, 351–67.

Meshik, A. P., Shukolyukov, Y. A. and Jeβberger, E. K. (1995). Chemically fractionated fission xenon (CFF-Xe) on the Earth and in meteorites. In: Busso, M. *et al.* (Eds.), *Nuclei in the Cosmos III*, *Amer. Inst. Phys. Conf. Proc.* **327**, 603–6.

Moreira, M., Breddam, K., Curtice, J. and Kurz, M. D. (2001). Solar neon in the Icelandic mantle: new evidence for an undegassed lower mantle. *Earth Planet. Sci. Lett.* **185**, 15–23.

Moreira, M., Kunz, J. and Allègre, C. J. (1998). Rare gas systematics in popping rock: isotopic and elemental compositions in the upper mantle. *Science* **279**, 1178–81.

Morrison, P. and Pine, J. (1955). Radiogenic origin of the helium isotopes in rocks. *Ann. N.Y. Acad. Sci.* **62**, 69–92.

Mukhopadhyay, S., Farley, K. A. and Montanari, A. (2001). A 35 Myr record of helium in pelagic limestones from Italy: implications for interplanetary dust accretion from the early Maastrichtian to the middle Eocene. *Geochim. Cosmochim. Acta* **65**, 653–69.

Muller, R. A. and Macdonald, G. J. (1995). Glacial cycles and orbital inclination. *Nature* **377**, 107–8.

Muller, R. A. and Macdonald, G. J. (1997). Glacial cycles and astronomical forcing. *Science* **277**, 215–18.

Nagao, K., Takaoka, N. and Matsubayashi, O. (1979). Isotopic anomalies of rare gases in the Nigorikawa geothermal area, Hokkaido, Japan. *Earth Planet. Sci. Lett.* **44**, 82–90.

Niedermann, S., Bach, W. and Erzinger, J. (1997). Noble gas evidence for a lower mantle component in MORBs from the southern East Pacific Rise: decoupling of helium and neon isotope systematics. *Geochim. Cosmochim. Acta* **61**, 2697–715.

Nier, A. O. and Schlutter, D. J. (1990). Helium and neon isotopes in stratospheric particles. *Meteoritics* **25**, 263–7.

O'Nions, R. K. and Oxburgh, E. R. (1983). Heat and helium in the Earth. *Nature* **306**, 429–36.

O'Nions, R. K. and Oxburgh, E. R. (1988). Helium volatile fluxes and the development of continental crust. *Earth Planet. Sci. Lett.* **90**, 331–47.

O'Nions, R. K. and Tolstikhin, I. N. (1994). Behaviour and residence times of lithophile and rare gas tracers in the upper mantle. *Earth Planet. Sci. Lett.* **124**, 131–8.

Oxburgh, E. R., O'Nions, R. K. and Hill, R. I. (1986). Helium isotopes in sedimentary basins. *Nature* **324**, 632–5.

Ozima, M. and Igarashi, G. (1989). Terrestrial noble gases: constraints and implications on atmospheric evolution. In: Atreya, S. K., Pollack, J. B. and Matthews, M. (Eds.), *Origin and Evolution of Planetary and Satellite Atmospheres*. University Arizona Press, pp. 306–27.

Ozima, M. and Igarashi, G. (2000). The primordial noble gases in the Earth: a key constraint on Earth evolution models. *Earth Planet. Sci. Lett.* **176**, 219–32.

Ozima, M., Podosek, F. A. and Igarashi, G. (1985). Terrestrial xenon isotope constraints on the early history of the Earth. *Nature* **315**, 471–4.

Ozima, M. and Zashu, S. (1983). Primitive helium in diamonds. *Science* **219**, 1067–8.

Ozima, M. and Zashu, S. (1988). Solar-type Ne in Zaire cubic diamonds. *Geochim. Cosmochim. Acta* **52**, 19–25.

Ozima, M. and Zashu, S. (1991). Noble gas state of the ancient mantle as deduced from noble gases in coated diamonds. *Earth Planet. Sci. Lett.* **105**, 13–27.

Patterson, D. B. and Farley, K. A. (1998). Extraterrestrial ^{3}He in seafloor sediments: evidence for correlated 100 kyr periodicity in the accretion rate of interplanetary dust, orbital parameters, and Quaternary climate. *Geochim. Cosmochim. Acta* **62**, 3669–82.

Patterson, D. B., Honda, M. and McDougall, I. (1990). Atmospheric contamination: a possible source for heavy noble gases in basalts from Loihi Seamount, Hawaii. *Geophys. Res. Lett.* **17**, 705–8.

Pepin, R. O. (1991). On the origin and early evolution of terrestrial planet atmospheres and meteoritic volatiles. *Icarus* **92**, 2–79.

Pepin, R. O. (1997). Evolution of Earth's noble gases: consequences of assuming hydrodynamic loss driven by giant impact. *Icarus* **126**, 148–56.

Pepin, R. O. (1998). Isotopic evidence for a solar argon component in the Earth's mantle. *Nature* **394**, 664–7.

Pepin, R. O. and Signer, P. (1965). Primordial rare gases in meteorites. *Science* **149**, 253–65.

Phinney, D., Tennyson, J. and Frick, U. (1978). Xenon in CO_2 well gas revisited. *J. Geophys. Res.* **83**, 2313–19.

Porcelli, D. and Halliday, A. N. (2001). The core as a possible source of mantle helium. *Earth Planet. Sci. Lett.* **192**, 45–56.

Porcelli, D. and Wasserburg, G. J. (1995a). Mass transfer of xenon through a steady-state upper mantle. *Geochim. Cosmochim. Acta* **59**, 1991–2007.

Porcelli, D. and Wasserburg, G. J. (1995b). Mass transfer of helium, neon, argon, and xenon through a steady-state upper mantle. *Geochim. Cosmochim. Acta* **59**, 4921–37.

Poreda, R. J. and Farley, K. A. (1992). Rare gases in Samoan xenoliths. *Earth Planet. Sci. Lett.* **113**, 129–44.

Reynolds, J. H. (1960). Determination of the age of the elements. *Phys. Rev. Lett.* **4**, 8–10.

Reynolds, J. H. (1963). Xenology. *J. Geophys. Res.* **68**, 2939–56.

Rutherford, E. (1906). The production of helium from radium and the transformation of matter. In: Rutherford, E., *Radioactive Transformations*. Yale University Press, pp. 187–93.

Sarda, P., Staudacher, T. and Allègre, C. J. (1988). Neon isotopes in submarine basalts. *Earth Planet. Sci. Lett.* **91**, 73–88.

Sarda, P., Staudacher, T., Allègre, C. J. and Lecomte, A. (1993). Cosmogenic neon and helium at Réunion: measurement of erosion rate. *Earth Planet. Sci. Lett.* **119**, 405–17.

Sasada, T., Hiyagon, H., Bell, K. and Ebihara, M. (1997). Mantle-derived noble gases in carbonatites. *Geochim. Cosmochim. Acta* **61**, 4219–28.

Schmalzl, J., Houseman, G. A. and Hansen, U. (1995). Mixing properties of 3-dimensional (3-D) stationary convection. *Phys. Fluids* **7**, 1027–33.

Schwartzman, D. W. (1973). Argon degassing models of the Earth. *Nature Phys. Sci.* **245**, 20–1.

Seta, A., Matsumoto, T. and Matsuda, J.-I. (2001). Concurrent evolution of ^{3}He/^{4}He ratio in the Earth's mantle reservoirs for the first 2 Ga. *Earth Planet. Sci. Lett.* **188**, 211–19.

Sheldon, W. R. and Kern, J. W. (1972). Atmospheric helium and geomagnetic field reversals. *J. Geophys. Res.* **77**, 6194–201.

Staudacher, T. (1987). Upper mantle origin for Harding County well gases. *Nature* **325**, 605–7.

Staudacher, T. and Allègre, C. J. (1982). Terrestrial xenology. *Earth Planet. Sci. Lett.* **60**, 389–406.

Staudacher, T. and Allègre, C. J. (1988). Recycling of oceanic crust and sediments: the noble gas subduction barrier. *Earth Planet. Sci. Lett.* **89**, 173–83.

Staudacher, T., Kurz, M. D. and Allègre, C. J. (1986). New noble-gas data on glass samples from Loihi Seamount and Hualalai and on dunite samples from Loihi and Réunion Island. *Chem. Geol.* **56**, 193–205.

Staudacher, T., Sarda, P. and Allègre, C. J. (1990). Noble gas systematics of Réunion Island, Indian Ocean. *Chem. Geol.* **89**, 1–17.

Staudacher, T., Sarda, P., Richardson, S. H., Allègre, C. J., Sagna, I. and Dmitriev, L. V. (1989). Noble gases in basalt glasses from a Mid-Atlantic Ridge topographic high at 14 °N: geodynamic consequences. *Earth Planet. Sci. Lett.* **96**, 119–33.

Takayanagi, M. and Ozima, M. (1987). Temporal variation of ^{3}He/^{4}He ratio recorded in deep-sea sediment cores. *J. Geophys. Res.* **92**, 12 531–8.

Tolstikhin, I. N., Mamyrin, B. A., Khabarin, L. V. and Erlikh, E. N. (1974). Isotopic composition of helium in ultrabasic xenoliths from volcanic rocks of Kamchatka. *Earth Planet. Sci. Lett.* **22**, 75–84.

Tolstikhin, I. N. and O'Nions, R. K. (1996). Some comments on isotopic structure of terrestrial xenon. *Chem. Geol.* **129**, 185–99.

Trieloff, M., Kunz, J., Clague, D. A., Harrison, D. and Allègre, C. J. (2000). The nature of pristine noble gases in mantle plumes. *Science* **288**, 1036–8.

Turekian, K. K. (1964). Outgassing of argon and helium from the Earth. In: Brancazio, P. and Cameron, A. G. W. (Eds.), *The Origin and Evolution of Atmospheres and Oceans*. Wiley, pp. 74–83.

Valbracht, P. J., Staudacher, T., Malahoff, A. and Allègre, C. J. (1997). Noble gas systematics of deep rift zone glasses from Loihi Seamount, Hawaii. *Earth Planet. Sci. Lett.* **150**, 399–411.

van Keken, P. E. and Ballentine, C. J. (1998). Whole-mantle versus layered mantle convection and the role of a high-viscosity lower mantle in terrestrial volatile evolution. *Earth Planet. Sci. Lett.* **156**, 19–32.

van Keken, P. E. and Ballentine, C. J. (1999). Dynamical models of mantle volatile evolution and the role of phase transitions and temperature-dependent rheology. *J. Geophys. Res.* **104**, 7137–51.

Wernicke, R. S. and Lippolt, H. J. (1993). Botryoidal hematite from the Schwarzwald (Germany): heterogeneous uranium distributions and their bearing on the helium dating method. *Earth Planet. Sci. Lett.* **114**, 287–300.

Wetherill, G. W. (1953). Spontaneous fission yields from uranium and thorium. *Phys. Rev.* **82**, 907–12.

Wetherill, G. W. (1954). Variations in the isotopic abundances of neon and argon extracted from radioactive materials. *Phys. Rev.* **96**, 679–83.

Zadnik, M. G., Smith, C. B., Ott, U. and Begemann, F. (1987). Crushing of a terrestrial diamond: ^{3}He/^{4}He higher than solar meteorites. *Meteoritics* **22**, 540–41.

12 U-series dating

The intermediate nuclides in the U–Pb and Th–Pb decay series have very short half-lives in comparison with their parents, and are usually ignored in the Pb isotope dating methods. However, their short half-lives make these nuclides useful for dating Pleistocene geological events that are too old to be well resolved by the radiocarbon method and too young to be well resolved by decay schemes with long half-lives. The manner in which U-series nuclides can fill this 'dating gap' is shown in Fig. 12.1. Generally they are most useful for dating events of similar age to their half-life.

12.1 Secular equilibrium and disequilibrium

A distinctive property of the U-series nuclides that sets them apart from other isotope dating schemes is that the radiogenic daughters are themselves radioactive. Hence, in a uranium-bearing system that has remained undisturbed for a few million years, a state of 'secular equilibrium' becomes stablished between the abundances of successive parent and daughter nuclides in the U and Th decay chains, such that the decay rate (or 'activity') of each daughter nuclide in the chain is equal to that of the parent:

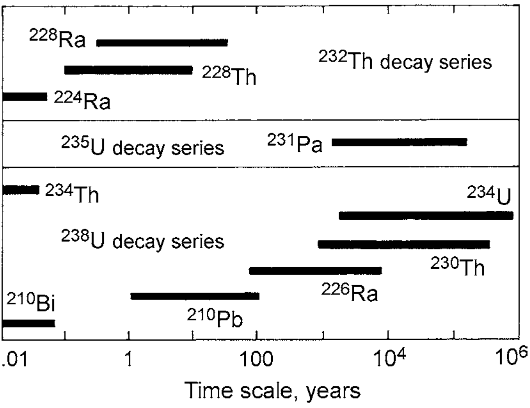

Fig. 12.1. Diagram showing the dating ranges of various nuclides within the three U-series decay chains to demonstrate their utility. After Potts (1987).

$$\text{Activity} = \lambda_0 n_0 = \lambda_1 n_1 = \lambda_2 n_2 = \lambda_N n_N \qquad [12.1]$$

where λ_0 is the decay constant and n_0 is the number of atoms of the original parent, λ_1 and n_1 are the decay constant and abundance of the first daughter, and so on. It follows that the abundance of each nuclide will be directly proportional to its half-life (i.e. inversely proportional to its decay constant). The relevant parts of the decay chains are shown in Fig. 12.2.

During geological processes such as erosion, sedimentation, melting, and crystallisation, nuclides in the decay series can become fractionated relative to one another, due to variations in their chemistry or the structural site they occupy. This results in a state of secular disequilibrium. Such a situation can be utilised in two different ways as a dating tool, called, respectively, the 'daughter-excess' and 'daughter-deficiency' dating methods.

In the daughter-excess method, a deposit is formed with an excess of the daughter beyond the level which can be sustained by the abundance of its parent nuclide. Over time, the excess or 'unsupported' daughter decays back until secular equilibrium with its parent is restored. If the original fractionation can be estimated, the age of the deposit can be calculated by the progress of decay of the excess.

In the daughter-deficiency method, chemical fractionation during the formation of a deposit causes it to take up a radioactive parent but effectively none of its daughter. The age of the deposit can then be determined by measuring the growth of the daughter, up to the point when its abundance is within error of secular equilibrium of the parent.

Using high-precision mass-spectrometric data (section 12.2.1) the useful dating range of U-series nuclides may be up to seven half-lives, but other factors may impose lower limits. Table 12.1 summarises some of the

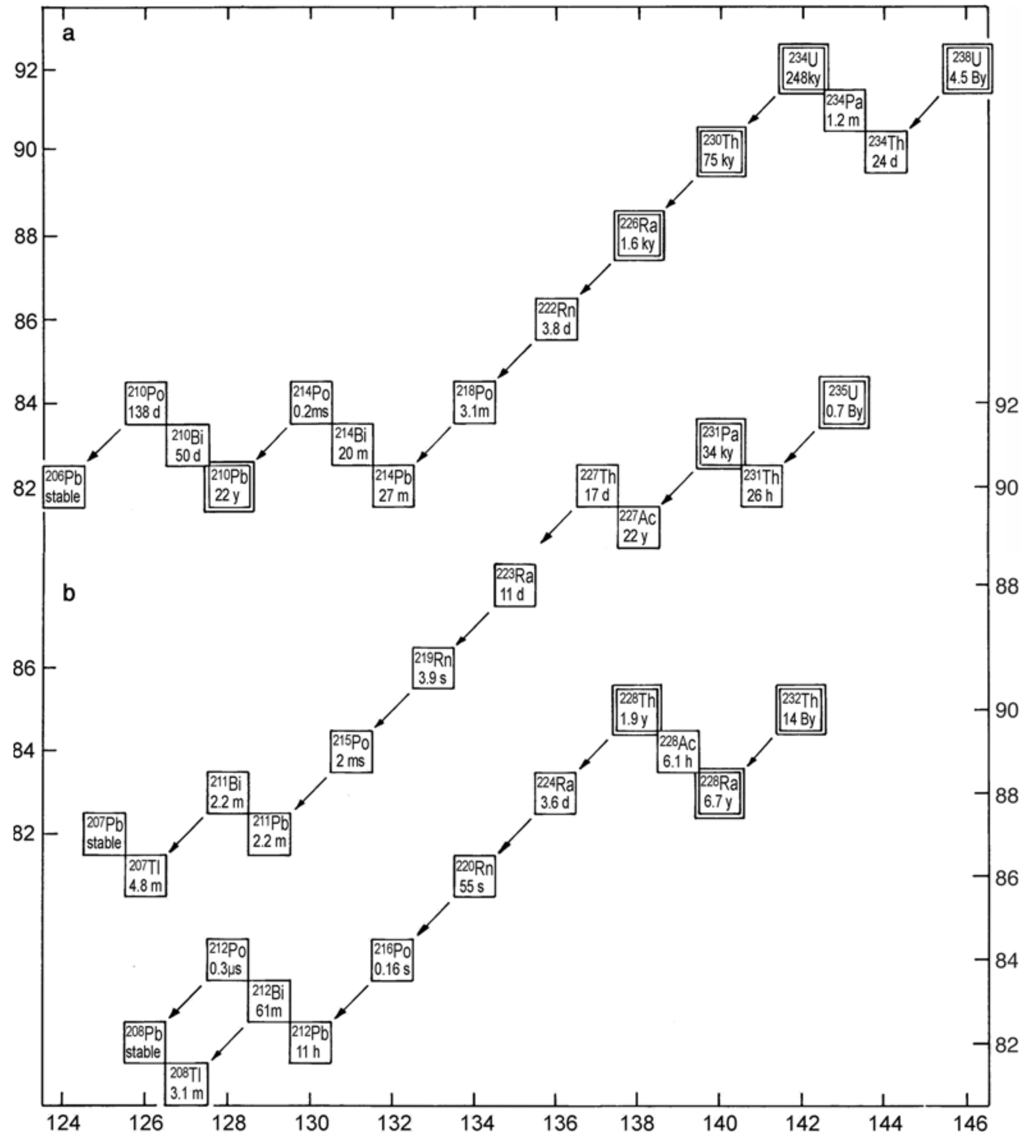

Fig. 12.2. Part of the chart of the nuclides, in terms of Z against N, to show species in the Th- and U-series decay chains and their half-lives. Useful species are indicated by double boxes. In early research on decay-series nuclides, some species were given special names (e.g. ^{230}Th = ionium). However, these are now obsolete.

more important U-series dating methods. ***Note that, in this chapter, all nuclide abundances are given as activities unless stated otherwise.***

12.2 Analytical methods

As noted above, the atomic abundance of a U-series nuclide in secular equilibrium is proportional to its half-life. Therefore, the very variable half-lives of the U-series radionuclides cause them to have extreme abundance ratios. Until recently, this discouraged mass-spectrometric determination of U-series nuclides for dating purposes. In contrast, species in secular equilibrium have equal activities (by definition), so radioactive counting is an obvious method for their determination. Counting techniques utilising β and γ

Table 12.1. *U-series dating methods*

Method	Measurement	$t_{1/2}$, kyr	Range, kyr	Application
Daughter excess				
^{234}U–^{238}U	^{234}U decay	245.3	<1500	Coral
^{230}Th	^{230}Th decay	75.7	<500	Deep-sea sedimentation rates
^{231}Pa	^{231}Pa decay	32.8	<200	Ditto
^{210}Pb	^{210}Pb decay	0.022	<0.1	Recent sedimentation
Daughter deficiency				
^{230}Th–^{234}U	^{230}Th accumulation	75.7	<500	Marine and fresh-water carbonate, volcanics
^{231}Pa–^{235}U	^{231}Pa accumulation	32.8	<200	Closed-system test for ^{230}Th
^{226}Ra–^{238}U	^{226}Ra accumulation	1.6	<10	Ditto

particles are not favoured because of the low energies of β transitions and the complexity of γ-ray spectra (Yokoyama and Nguyen, 1980). Therefore, the traditional technique for measurement of U-series nuclides has been α spectrometry.

Because of the very short range of α particles in matter, samples to be counted are made into a thin film and placed under vacuum in a gridded ion chamber (a type of gas-ionisation chamber with a short dead-time). If the potential applied between cathode and anode is within a certain range, the electrical pulses generated by α-particle emission will be proportional in size to the kinetic energy of those particles. The output is then fed to a multi-channel analyser in order to register count rates as a function of energy level. This allows the α particles from different decay transitions to be distinguished as separate 'peaks' in the energy spectrum. To obtain 1σ counting errors of 1%, total counts of 10^4 are required on each peak ($\sigma = \sqrt{n}$). To achieve this, counting times of at least a week are required for most natural samples. Recoil effects gradually contaminate the counter over time with U-series nuclides, raising its background. Hence the counter has a finite effective life, which is shortened if higher-than-normal count rates are measured.

Because α counting only measures the abundances of atoms that actually decay during the measurement period, it is a very inefficient measurement technique, especially for long-lived nuclides. In contrast, mass spectrometry offers the opportunity of counting every atom in the sample, and is therefore much more sensitive. In the case of U-series nuclides, mass spectrometry offers approximately an order-of-magnitude improvement, both in sensitivity and in precision, and has therefore largely replaced α spectrometry as a measurement technique. However, these advances also throw the emphasis of U-series dating work back onto sample collection and preparation, since open-system behaviour of samples becomes more obvious with improvements in analytical precision. These problems will be discussed below.

Given the low abundances of the U-series nuclides to be measured in natural materials (in the part-per-trillion to part-per-million range), chemical purification is essential, both for α counting and for mass spectrometry. This normally involves dissolution of the sample in HNO_3 (carbonates) or HF (silicates) followed by anion-exchange separation (section 2.1.4). Anion exchange is also used to separate between U and Th. Since chemical extractions are not expected to give a 100% yield, the sample is 'spiked' before chemistry with a known quantity of artificially enriched isotopes, allowing an isotope-dilution determination of isotope abundances in the sample (section 2.4). In α-counting analysis, short-lived radioactive species were usually chosen as spikes. For example, a widely used U–Th spike was ^{232}U($t_{1/2} = 72$ yr), which had been allowed to generate its daughter ^{228}Th ($t_{1/2} = 1.9$ yr). The short half-life of the latter nuclide meant that it reached secular equilibrium with its parent within about twenty years (Ivanovich, 1982a). For mass spectrometry, the longer-lived isotopes ^{229}Th and ^{236}U, with half-lives of about 6 kyr and 70 kyr, respectively, are preferred.

A pre-requisite to precise and accurate dating with U-series nuclides is the availability of good half-life determinations. However, the attainment of secular equilibrium allows these half-lives to be determined relative to the very-well-constrained ^{238}U half-life. For example, the half-life of ^{234}U can be determined very accurately relative to that of ^{238}U, by measurement of the ^{234}U/^{238}U ratio on a sample in secular equilibrium, such as uraninite ore. Using this technique, De Bièvre *et al.* (1971) determined a value of 244.6 ± 0.7 kyr by α spectrometry, which was revised to 245.3 ± 0.14 kyr by mass spectrometry (Ludwig *et al.*, 1992). The latter result was confirmed by Cheng *et al.* (2000), who determined a value of 245.25 ± 0.49 kyr.

The ^{230}Th half-life can also be determined by analysis of uraninite in secular equilibrium, using a mixed ^{229}Th–^{236}U spike. However, this determination has a larger uncertainty because it incorporates the errors of spike calibration, based on gravimetric U and Th standards. (Many laboratories calibrate their spikes against uraninite, which would lead to a circular argument in this case.) Meadows *et al.* (1980) determined a half-life of 75.4 ± 0.6 kyr from α counting, which was revised to 75.69 ± 0.23 kyr by mass spectrometry (Cheng *et al.*, 2000) using four different types of sample considered to be in secular equilibrium. Fortunately, the two half-life determinations increased by a similar proportion (on moving from the α-counting to the mass-spectrometric values), so the overall effect on calculated ages is small.

12.2.1 Mass spectrometry

Uranium-series dating by mass spectrometry was one of the missed opportunities of 1970s isotope geology, since the analytical equipment available at that time was equal to this task, but was not applied until the late 1980s. This omission can be explained by a communications gap between workers in the two fields, and by exaggerated estimates of the problems which might be posed by large nuclide-abundance ratios. The gap was closed in two stages, by Chen *et al.* (1986), who performed the first precise mass-spectrometric analysis on ^{234}U, and by Edwards *et al.* (1987), who made the first ^{230}Th measurements. These workers showed that mass-spectrometric U-series dating offered great improvements in precision over the best α-counting determinations.

Edwards *et al.* avoided the difficulty of measuring large ^{238}U/^{234}U ratios by measuring ^{235}U/^{234}U ratios instead. Since the ^{238}U/^{235}U ratio has a constant value of 137.88 in normal rocks, the conversion is simple. Furthermore, by analysing pure corals with a low detrital ^{232}Th content (see below), it was possible to obtain a ^{232}Th/^{230}Th atomic abundance ratio as low as 1.1 (compared with typical ratios of over 250 000 in silicate rocks). These techniques allowed Edwards *et al.* to determine the age of a typical Pleistocene coral to a precision of 123 ± 1.5 kyr (2σ), compared with an α-counting determination of 129 ± 9 kyr.

Thorium has a relatively high ionisation potential. Therefore TIMS analysis of this element is relatively inefficient. Li *et al.* (1989) used the conventional double-filament technique employed for Nd isotope analysis (section 2.2.1), with a very hot centre filament to promote the formation of Th metal ions. This method is not very demanding of chemical purity but is relatively inefficient. Edwards *et al.* loaded both U and Th (separately) onto graphite-coated single rhenium filaments, and analysed them as the metal species. This method is more efficient for very small samples, but the ionisation efficiency drops rapidly as the size of sample increases (Fig. 12.3), from 0.1% with very small samples to 0.001% with large samples. This is due to a failure to make proper contact with the heated metal filament as the size of the sample load increases. Asmerom and Edwards (1995) described a new method for loading Th as the fluoride. When used with a normal double-filament technique, this method improved the ionisation efficiency of large thorium samples (such as igneous rocks). Using the new method, a 200-ng Th sample had an ionisation efficiency of 2×10^{-4}, an order of magnitude better than had been achieved with the previous technique (Fig. 12.3).

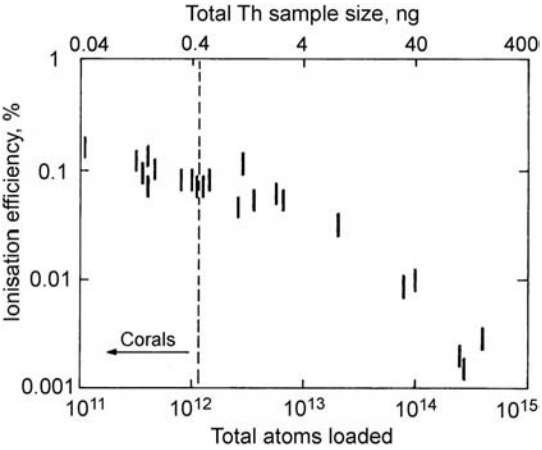

Fig. 12.3. Plot of ionisation efficiency for Th isotope analysis against the total amounts of Th loaded on single Re filaments. The typical sample size of clean corals is shown. After Edwards *et al.* (1987).

Ionisation problems are avoided using an ICP source, which achieves nearly complete ionisation of all elements (section 2.2.2). As a result, MC-ICP-MS seems likely to supersede TIMS for Th analysis (section 2.5.3). It also has the capability of performing *in situ* U-series analysis of uranium-rich samples using the laser microprobe (Stirling *et al.*, 2000). However, sampling of the plasma by the mass spectrometer is only about 1% efficient, so MC-ICP-MS offers only a moderate advantage over TIMS. Therefore, TIMS analysis is expected to find continued use for some time into the future.

12.3 Daughter-excess methods

12.3.1 ^{234}U dating of carbonates

^{238}U decays via two very-short-lived intermediates to ^{234}U (Fig. 12.2). Since ^{234}U and ^{238}U have the same chemical properties, it might be expected that they would not be fractionated by geological processes. However, Cherdyntsev *et al.* (1965) and Cherdyntsev (1969) showed that such fractionation does occur. In fact, natural waters exhibit a considerable range in ^{234}U/^{238}U activities from unity (secular equilibrium) to values of 10 or more (e.g. Osmond and Cowart, 1982). Cherdyntsev *et al.* (1961) attributed these fractionations to radiation damage of crystal lattices, caused both by α emission and by recoil of parent nuclides. In addition, radioactive decay may leave ^{234}U in a more soluble +6 charge state than its parent (Rosholt *et al.*, 1963). These processes (termed the 'hot-atom' effect) facilitate preferential leaching of the two very-short-lived intermediates and the longer-lived ^{234}U nuclide into groundwater. The short-lived nuclides have a high probability of decaying into ^{234}U before they can be adsorbed onto a substrate, and ^{234}U is itself stabilised in surface waters as the soluble UO_2^{2+} ion, due to the generally oxidising conditions prevalent in the hydrosphere.

The variety of weathering conditions prevailing in the terrestrial environment leads to very variable ^{234}U/^{238}U activity ratios in fresh water systems. However, the long residence time of uranium in seawater (>300 kyr, Ku *et al.*, 1977) maintains the seawater ^{234}U/^{238}U ratio within narrow limits, corresponding to an activity ratio of about 1.14 (Goldberg and Bruland, 1974). A major uranium sink in the oceans is calcium carbonate, with which uranium is co-precipitated. This is deposited in shallow water by marine organisms, and in deep water as an authigenic mineral (i.e. by direct chemical precipitation). At the time of deposition, this material takes on the 'daughter-excess' ^{234}U/^{238}U activity ratio of seawater, but once isolated, the excess decays away until secular equilibrium with the parent is regained (Fig. 12.4). Given an estimate of the original ^{234}U/^{238}U fractionation, and given subsequent closed-system behaviour, the system can be used as a dating tool until it returns to within analytical error of secular equilibrium.

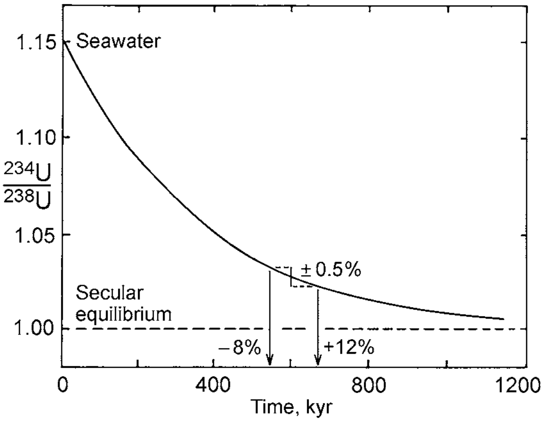

Fig. 12.4. Plot of ^{234}U/^{238}U activity against time, showing the return to secular equilibrium after isolation from seawater. Arrows show the amplification of analytical errors as the system approaches equilibrium.

Unfortunately, many problems are encountered in the practical application of this method. As noted above, the variable uranium isotope fractionations observed in fresh-water systems preclude its application there. In addition, pelagic sediments are ruled out by open-system behaviour of uranium after deposition (Ku, 1965), while mollusc shells also tend to take up uranium after deposition (Kaufman *et al.*, 1971). However, the method has been applied with reasonable success to the dating of corals (e.g. Thurber *et al.*, 1965).

The decay of excess ^{234}U can be expressed by the fundamental decay equation [1.5]. Although this equation was derived in section 1.4 for atomic abundances, it is also true for activities (on dividing both sides by the decay constant, e.g. $\lambda\,^{234}$U):

$$\frac{n}{\lambda} = \frac{n_0}{\lambda} e^{-\lambda t} \qquad [12.2]$$

$$A = A_0 e^{-\lambda t} \qquad [12.3]$$

In order to date a carbonate sample by the decay of excess ^{234}U (Fig. 12.4), we can substitute into [12.3] to yield

$$^{234}U^{X}_{\text{present}} = {}^{234}U^{X}_{\text{initial}}\, e^{-\lambda_{234} t} \qquad [12.4]$$

where 'X' signifies excess activities above secular equilibrium and 'initial' signifies the activity at the time of precipitation.

As noted above, *all nuclide quantities in this chapter will be presented in terms of activities* (unless stated otherwise). However, absolute activities are not as readily measurable as activity ratios, so it is convenient to divide through by ^{238}U activities. However, because of the very long half-life of ^{238}U, the activity of $^{238}U_{\text{present}}$ is the same as that of $^{238}U_{\text{initial}}$. So

$$({}^{234}U^{X}/{}^{238}U)_{\text{present}} = ({}^{234}U^{X}/{}^{238}U)_{\text{initial}}\, e^{-\lambda_{234} t} \qquad [12.5]$$

Since these quantities are in the form of activities, the excess ^{234}U/^{238}U activity is equal to the total activity ratio minus one (that part corresponding to secular equilibrium). So

$$\left(\frac{^{234}\mathrm{U}}{^{238}\mathrm{U}}\right)^{\text{total}}_{\text{present}} - 1 = \left[\left(\frac{^{234}\mathrm{U}}{^{238}\mathrm{U}}\right)^{\text{total}}_{\text{initial}} - 1\right] \mathrm{e}^{-\lambda_{234}t} \qquad [12.6]$$

Hence, if we assume that the initial activity ratio of the sample is given by present-day seawater, we can calculate the age of a coral simply by measuring its present-day activity ratio. Chen *et al.* (1986) showed that modern seawater in the Pacific and Atlantic Oceans has a homogeneous ^{234}U/^{238}U activity ratio, with values of 1.143 and 1.144, respectively. Given the >300-kyr residence time of uranium in seawater (Ku *et al.*, 1977), this gives us a strong expectation that the activity ratio should have been close to this value within the 1.2 Myr theoretical dating range of the method. This was indeed demonstrated by more recent work (Henderson, 2002), which indicated a ^{234}U/^{238}U activity ratio of 1.145 for the last 350 kyr. This value is often expressed as δ (excess ^{234}U), with a value of 145 per mil (Fig. 12.4).

Because the seawater ^{234}U/^{238}U ratio is relatively close to secular equilibrium, a small error in the ^{234}U measurement leads to a large error in the calculated age (Fig. 12.4). Hence, the ^{230}Th-deficiency method (section 12.4) yields more precise ages below 400 kyr. However, using mass-spectrometric analysis, the ^{234}U method allows the possibility of dating back to 1 Myr with tolerable precision. This was demonstrated by Ludwig *et al.* (1991), who used ^{234}U to date submerged coral terraces off NW Hawaii. Comparison of ^{234}U ages with terrace depth led to a subsidence curve that is approximately linear for the last 500 kyr, at a rate of 2.6 mm/yr (Fig. 12.5). Small undulations on the subsidence curve represent the calculated effect of eustatic sea-level fluctuations. These cause development of coral terraces by periodically neutralising subsidence (to create a sea-level 'stand') and then exacerbating subsidence, to drown the reef.

The good fit of data points to a linear subsidence model in Fig. 12.5 provides evidence of the reliability of the ^{234}U/^{238}U dating method, including the closed-system assumption for uranium systems in coral. This is attributed to the good preservation of submarine coral systems. In contrast, coral that has suffered freshwater percolation is very susceptible to open-system behaviour. For example, Bard *et al.* (1991) found that many coral specimens over 50 kyr old that had been dated by ^{230}Th at the Lamont laboratory had calculated initial ^{234}U activities above the seawater value of 1.14 (Fig. 12.6). These corals come from raised terraces on the island of Barbados, which is undergoing net tectonic uplift with time.

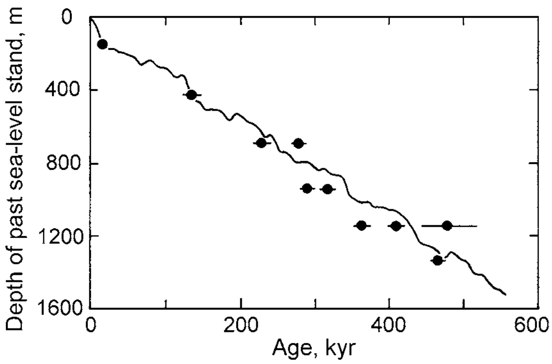

Fig. 12.5. Plot of terrace depth against mass-spectrometric ^{234}U age for corals off NW Hawaii, showing the good fit to a cooling subsidence curve (modulated by eustatic variations). After Ludwig *et al.* (1991).

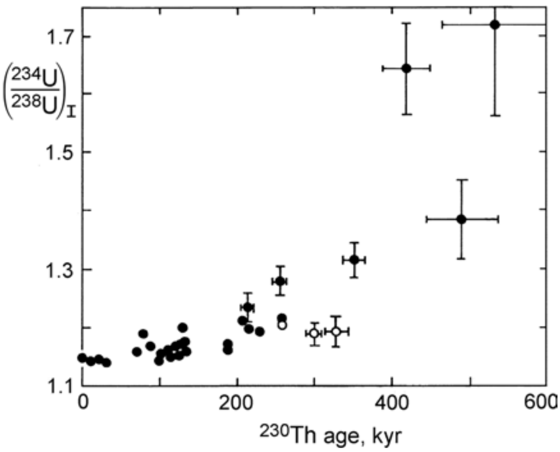

Fig. 12.6. Plot of initial ^{234}U/^{238}U activities in Barbados coral terraces, against calculated ^{230}Th ages, to show apparent initial ratios above the seawater value of 1.15. After Bard *et al.* (1991).

Since the evidence from Hawaii is consistent with a constant ^{234}U activity in seawater (at least for the past 500 kyr), the high apparent initial ratios found by Bard *et al.* must be attributed to open-system behaviour of uranium. Unfortunately this sub-aerial redistribution of uranium will also affect the ^{230}Th ages calculated from these samples. For example, the sample with an apparent age of 528 kyr in Fig. 12.6 comes from a lower terrace on Barbados, and hence must be younger than the samples with apparent ages of 230 and 418 kyr.

12.3.2 ^{234}U dating of Fe–Mn crusts

Another application of ^{234}U is to the dating of ocean-floor ferromanganese crusts. These crusts grow over long periods of time on the ocean floor, and provide very useful archives of past seawater chemistry if they can be dated accurately. In the first U-series dating study on this material, Chabaux *et al.* (1995) analysed two crusts dredged from 1900 m depth on a West Pacific seamount. For both crusts, the ^{234}U and ^{230}Th daughter-excess methods gave consistent growth rates of about 7.6 and 6.7 mm/Myr, respectively (Fig. 12.7). This suggested that closed-system conditions were preserved, and that initial uranium and thorium isotope ratios remained constant (within error) during the 150-kyr period of deposition.

A problem with the sampling of Fe–Mn crusts is that the outer surface can be abraded during dredging operations, preventing a determination of the absolute age of the crust from its growth rate. This is specifically a problem with the ^{230}Th method, because the initial thorium isotope ratio of seawater is variable. Therefore, in the absence of an 'initial-ratio' determination from the surface of the crust, an absolute date is not possible. On the other hand, the initial ^{234}U/^{238}U ratio of seawater is constant in space and time. Therefore, it should be possible to use ^{234}U to determine the original growth surface of the crust by projecting the excess ^{234}U activity back to the known seawater composition (Fig. 12.7b).

Fe–Mn crusts are quite porous and have very slow growth rates. Therefore, there was concern that diffusion could cause open-system behaviour of U-series nuclides in the crust after deposition. The work of Chabaux *et al.* (1995) appeared to allay these fears, but subsequent work by Chabaux *et al.* (1997), Neff *et al.* (1999) and Henderson and Burton (1999) has confirmed that diffusion of U is a problem in Fe–Mn crusts. These later studies gave Fe–Mn growth rates of 7–19 mm/Myr, based on measurements of excess ^{234}U, but only 3–4 mm/Myr based on excess ^{230}Th. The discrepancy between these growth rates, especially for the very high value of 19 mm/Myr, must be explained by diffusional re-distribution of uranium. By comparing the observed decay profile of ^{234}U with a theoretical decay curve based on excess ^{230}Th dates, Henderson and Burton were able to calculate effective diffusion coefficients for uranium in various Fe–Mn crusts (e.g. Fig. 12.8). These values were in the range from 10^{-6} to 5×10^{-8} cm^2/yr.

Henderson and Burton argued that the magnitude of U diffusion in the crust must be controlled by the ability of uranium to be exchanged from the solid crust into pore water within the crust. Hence, the diffusion coefficient must be dependent on the partition coefficient of uranium between seawater and the Fe–Mn crust. The solubility of U in surface water has already been discussed. In contrast, thorium is said to be 'particle-reactive', meaning that it is readily adsorbed onto the surface of detrital grains, and has a very short residence time in natural waters.

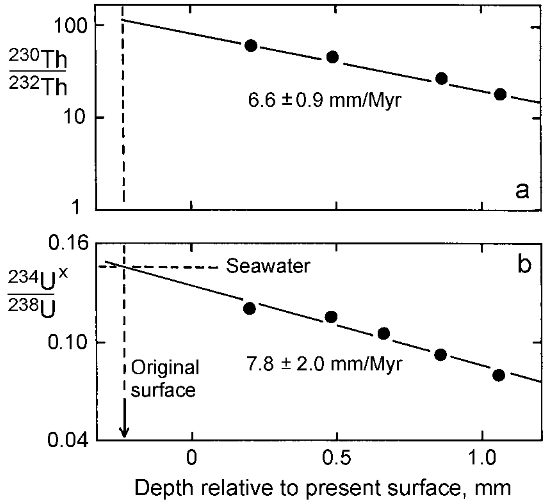

Fig. 12.7. The use of ^{230}Th/^{232}Th and excess ^{234}U activities in a ferromanganese crust to determine the growth rate and the zero-age surface of the crust before abrasion. Modified after Chabaux *et al.* (1995).

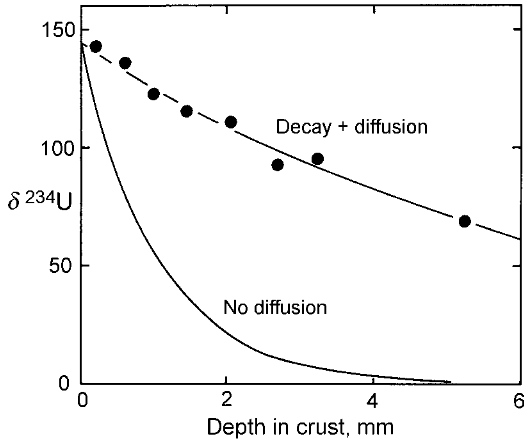

Fig. 12.8. Plot of ^{234}U activity (parts per mil above secular equilibrium) against depth in an Fe–Mn crust from the North Atlantic. The measured ^{234}U 'decay curve' is compared with the predicted decay curve for zero diffusion. After Henderson and Burton (1999).

Table 12.2. *Partition and diffusion coefficients in Fe–Mn crusts*

Element	Crust/seawater partition coefficient	Diffusion coefficient in crust, cm^2/yr
Particle-reactive species		
Th	2.0×10^9	2×10^{-12}
Nd	2.6×10^8	2×10^{-11}
Pb	1.6×10^8	3×10^{-11}
Be	4.0×10^7	1×10^{-10}
Hf	5.2×10^6	9×10^{-10}
Os	1.7×10^5	3×10^{-8}
Conservative species		
U	4.0×10^3	1×10^{-6}
Sr	2.1×10^2	2×10^{-5}

Thus, uranium has a seawater residence time exceeding 300 kyr, whereas thorium has a seawater residence time more than 1000 times shorter than this.

Using these principles, Henderson and Burton estimated the diffusion coefficients of other elements from their relative concentrations in the crust and in seawater. This calculation places these species into two groups (Table 12.2; Henderson, personal communication). Uranium, together with strontium, has a relatively large diffusion coefficient in crusts, which is consistent with these elements being non-particle-reactive, and hence conservative in seawater. At the other extreme, thorium has a partition coefficient about six orders of magnitude lower than that of uranium, which is consistent with it being the most particle-reactive of its group. In addition, other members of the particle-reactive group also have sufficiently low diffusion coefficients in Fe–Mn crusts that they can be considered immobile. This is encouraging for the use of Fe–Mn crusts as an inventory of the past seawater signatures of these tracers (sections 4.5, 5.6, 9.3 and 14.3). However, it is concluded that the ^{234}U method is not reliable for dating this material.

Another area where excess ^{234}U activity data would be very useful is in the dating of planktonic foraminifera, since these are the basis of the seawater oxygen isotope record (section 12.4.2). However, forams have low U contents (typically 20 ppb), which tend to be swamped by the U contents of ferromanganese diagenetic overgrowths. Henderson and O'Nions (1995) showed that dithionite solution (a reducing agent) could be used to clean recent forams in order to recover normal seawater uranium isotope ratios. However, a test on 2-Myr-old forams detected excess ^{234}U activities above the seawater value, which must have been introduced from pore waters after sedimentation. This suggests that forams do not remain a closed system for uranium, and therefore cannot be used for dating or to constrain the uranium isotope evolution of seawater.

12.3.3 ^{230}Th sediment dating

The differing behaviour of uranium and thorium in seawater causes U/Th fractionation during the formation of various types of sediment, leading to systems out of secular equilibrium. As noted above, ^{238}U decays via two very short-lived intermediates to ^{234}U in seawater. This in turn decays to ^{230}Th, but the latter is almost immediately adsorbed onto the sediment surface. Because it is preferentially enriched on the sediment surface, relative to its (^{234}U) parent, ^{230}Th is 'unsupported' and out of secular equilibrium. However, after isolation from the sediment–water interface, this unsupported ^{230}Th begins to decay back to secular equilibrium with its parent. Hence, this method should allow the dating of sedimentary deposition.

Adsorption of thorium onto detrital grains is so much more effective than adsorption of uranium that, for young sediments, the uranium-supported component (i.e. the component in secular equilibrium) can be effectively ignored. In other words,

$$^{230}\mathrm{Th}_{\mathrm{excess}} \approx {}^{230}\mathrm{Th}_{\mathrm{total}} \qquad [12.7]$$

Therefore we can use the method as a dating tool by means of the simple decay equation

$$^{230}\mathrm{Th}_{\mathrm{present}} = {}^{230}\mathrm{Th}_{\mathrm{initial}}\, e^{-\lambda_{230} t} \qquad [12.8]$$

Since the ^{230}Th excess method is used to study sedimentation, it is convenient to formulate t in terms of sediment depth, D (in a core), and sedimentation rate, R:

$$t = D/R \qquad [12.9]$$

If we substitute this into [12.8] and take the natural log of both sides, we obtain

$$\ln {}^{230}\mathrm{Th}_{\mathrm{P}} = \ln {}^{230}\mathrm{Th}_{\mathrm{I}} - D(\lambda_{230}/R) \qquad [12.10]$$

This corresponds to the equation for a straight line:

$$y = c - xm \qquad [12.11]$$

Hence, if the natural log of the present-day ^{230}Th activity is plotted against depth in the core, the sedimentation rate can be obtained from the reciprocal of the slope (the solid line in Fig. 12.9):

$$R = -\lambda_{230} \frac{D}{\ln {}^{230}\mathrm{Th}_{\mathrm{P}} - \ln {}^{230}\mathrm{Th}_{\mathrm{I}}} \qquad [12.12]$$

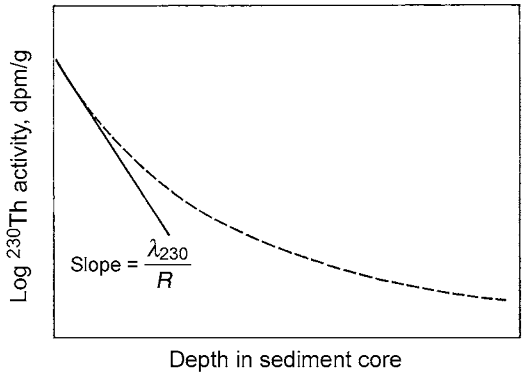

Fig. 12.9. Schematic plot of log ^{230}Th activity (decays per minute/gram) against depth, to show behaviour expected in a core formed by a constant sedimentation rate. Solid line = young sediments; dashed line = older sediments with U-supported ^{230}Th.

Although the effects of U-supported ^{230}Th may be negligible near the sediment surface, this component becomes increasingly important as the system approaches secular equilibrium with increasing burial depth (dashed line in Fig. 12.9). Two possible sources of U-supported ^{230}Th may be present. Authigenic minerals such as calcite contain no ^{230}Th at the sediment surface, but their uranium budget generates ^{230}Th until this reaches secular equilibrium with the parent. This fraction is best removed physically by mineral separation. On the other hand, detrital grains contain ^{230}Th that is in secular equilibrium with ^{234}U and ^{238}U, even at the sediment surface. This fraction is removed by subtracting ^{234}U activity (in secular equilibrium with the ^{230}Th daughter) from total ^{230}Th activity (e.g. Ku, 1976). This leaves the 'excess' ^{230}Th activity of the clay fraction:

$$^{230}\mathrm{Th}_{\mathrm{excess}} = {}^{230}\mathrm{Th}_{\mathrm{total}} - {}^{234}\mathrm{U} \qquad [12.13]$$

The corrected (excess) activities determined in this way are substituted into [12.10] and [12.12] above to determine sedimentation rates. Since the concentration of ^{230}Th in the oceans is expected to be constant through time, and the adsorption process is expected to be of constant efficiency, the initial concentration of ^{230}Th in the detrital-sediment fraction should be constant. Then, if the bulk sedimentation rate (R) remains constant with time, excess ^{230}Th activity will decrease as a logarithmic function with depth. Figure 12.10a shows data from a Caribbean core that fit this model (Ku, 1976), yielding a linear fit (of log activity against depth). The regression slope yields a sedimentation rate R of 25 ± 1 mm/kyr for the last 300 kyr.

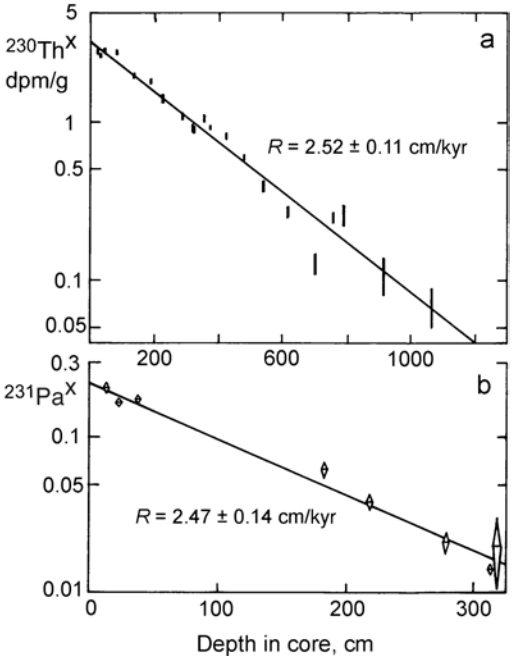

Fig. 12.10. Plots of (a) excess ^{230}Th activity and (b) excess ^{231}Pa activity against depth in a sediment core, yielding two independent estimates of the average sedimentation rate. After Ku (1976).

Within the decay chain of ^{235}U, the species ^{231}Pa (protactinium) is another particle-reactive species that behaves very similarly to thorium in seawater. Therefore it also develops excess activities at the sediment surface relative to its parent isotope of uranium. ^{231}Pa has a half-life of 32.76 kyr (Roberts *et al.*, 1969), and is therefore used in an analogous way to ^{230}Th. However, because the parent (^{235}U) has a much lower abundance than ^{238}U, analytical errors are larger. Therefore, ^{231}Pa is usually used only as a concordance test for ^{230}Th dates, to check that the dating assumptions have been upheld. This application is shown in Fig. 12.10b.

12.3.4 ^{230}Th–^{232}Th

Unfortunately, not all cores yield such good results as that in Fig. 12.10, because ^{230}Th and ^{231}Pa are sometimes variably diluted in sediments. Picciotto and Wilgain (1954) suggested that this problem could be avoided by using ^{232}Th as a reference isotope to normalise for variable absolute levels of adsorbed Th. They justified this approach on the basis that ^{230}Th and ^{232}Th ($t_{1/2}$ = 14 Byr) are chemically identical, so they should be removed from seawater at the same rate. Because ^{232}Th has such a long half-life, it suffers no significant decay within the dating range of ^{230}Th. Therefore, if we assume that initial ^{230}Th/^{232}Th activities at the sediment surface remain constant at any given locality through time, we can divide both sides of equation [12.8] by ^{232}Th (where X signifies excess activities):

$$\left(\frac{^{230}\mathrm{Th}^{\mathrm{X}}}{^{232}\mathrm{Th}}\right)_{\text{present}} = \left(\frac{^{230}\mathrm{Th}^{\mathrm{X}}}{^{232}\mathrm{Th}}\right)_{\text{initial}} \mathrm{e}^{-\lambda_{230}t} \qquad [12.14]$$

On applying this to the activity *versus* depth plot, we obtain

$$\ln\left(\frac{^{230}\mathrm{Th}^{\mathrm{X}}}{^{232}\mathrm{Th}}\right)_{\mathrm{P}} = \ln\left(\frac{^{230}\mathrm{Th}^{\mathrm{X}}}{^{232}\mathrm{Th}}\right)_{\mathrm{I}} - D\frac{\lambda_{230}}{R} \qquad [12.15]$$

Picciotto and Wilgain pointed out that, for this method to work, effectively all of the Th in the sediment must have been chemically precipitated, rather than being detrital. However, 30% or more of the total ^{232}Th budget in a pelagic sediment is normally within the detrital phases (Goldberg and Koide, 1962). Consequently, Ku *et al.* (1972) argued that the effect of dividing by ^{232}Th is similar to the effect of dividing by the detrital (non-carbonate) fraction in the analysed sample. If the detrital fraction in the sediment is constant then this does not cause a problem, but if it varies with depth, this will perturb the initial ^{230}Th/^{232}Th ratios and hence lead to erroneous ages and sedimentation rates. This problem is illustrated in Fig. 12.11 using data for a core from the Mid-Atlantic Ridge. The ^{230}Th/^{232}Th plot (Fig. 12.11a) yields an age for the 12-cm-deep horizon (arrowed) that is more discordant from the ^{14}C age of 17 kyr than the simple ^{230}Th plot (Fig. 12.11b).

In order to reduce the perturbing effect of the detrital component on ^{230}Th/^{232}Th ages, Goldberg and Koide (1962) used a technique by which authigenic minerals and adsorbed Th were leached from the detrital component with hot hydrochloric acid. This led them also to adopt a different correction for U-supported ^{230}Th. On the assumption that no detrital ^{230}Th component was leached, they excluded the component in secular equilibrium. Instead they corrected for U-supported ^{230}Th in the authigenic (carbonate) component, which is expected to grow with time. This is equivalent to the ^{230}Th daughter-deficiency method, and will be dealt with in detail below (section 12.4.1). If the immediate parent (^{234}U) is assumed to be in equilibrium with ^{238}U (an approximation) then the growth of U-supported Th is given by equation [12.25]. This is subtracted from total ^{230}Th activity to determine excess ^{230}Th:

$$^{230}\mathrm{Th}_{\text{excess}} = {}^{230}\mathrm{Th}_{\text{total}} - {}^{238}\mathrm{U}(1 - \mathrm{e}^{-\lambda_{230}t}) \qquad [12.16]$$

Ku (1976) argued that this method also had drawbacks, since thorium leaks from detrital phases during the acid leaching. Hence, it is concluded that normalising with respect to ^{232}Th can sometimes improve ^{230}Th data, but sometimes has a degrading effect. Therefore, it tends to be used on an *ad hoc* empirical basis.

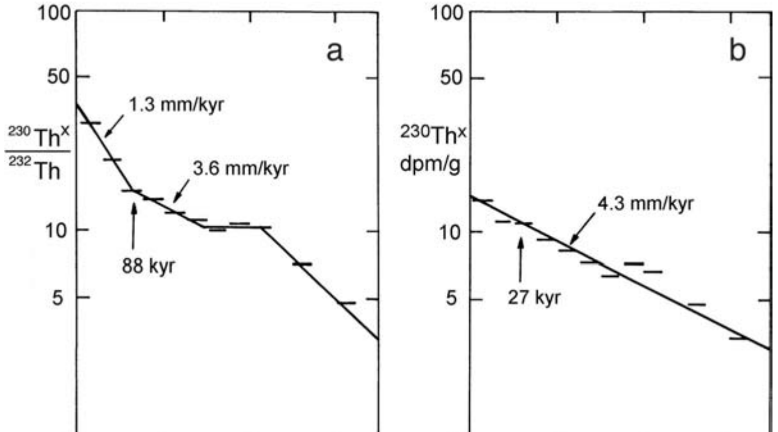

Fig. 12.11. Thorium isotope results from the ZEP 15 core (Mid-Atlantic Ridge), showing interpretations of sedimentation history using (a) the ^{230}Th/^{232}Th method and (b) the simple ^{230}Th method. After Ku (1976).

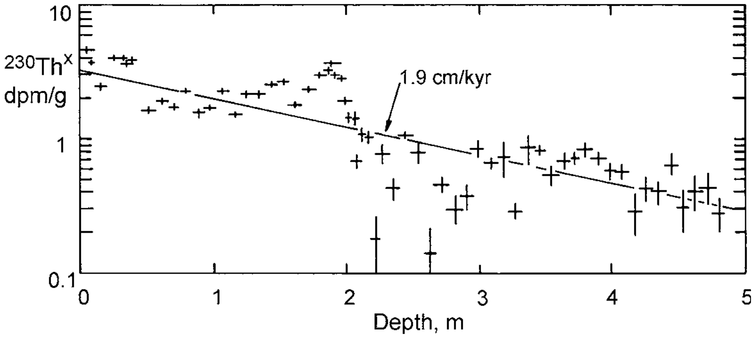

Fig. 12.12. Plot of excess ^{230}Th activity (on a log scale) against depth in core 23059 from the Norwegian Sea. The regression line indicates the average sedimentation rate. After Scholten *et al.* (1990).

12.3.5 ^{230}Th sediment stratigraphy

In view of the difficulties described above, the ^{230}Th dating method should probably be regarded as semi-quantitative in most circumstances. However, ^{230}Th data may be a powerful tool for stratigraphic correlation of Quaternary sediments. An example of this application is provided by the study of Scholton *et al.* (1990) on a 5-m core from the Norwegian Sea near Jan Mayen (Fig. 12.12). In general, excess ^{230}Th activity data from this study fitted an average decay curve equivalent to a sedimentation rate of 1.9 cm/kyr. This is in reasonable agreement with the rate of 1.6 cm/kyr calculated from oxygen isotope stratigraphy. However, the data display large short-term variations superimposed on the mean decay curve.

Traditionally, variations of this type have been attributed to changes in sedimentation rate. However, this is clearly impossible for some segments of core 23059, which define a positive slope of excess activity against depth (opposite to the effect of radioactive decay). In order to examine these short-term activity variations, Scholten *et al.* corrected the data for radioactive decay since burial (using the mean decay curve), and then ratioed these *initial* (excess) ^{230}Th activities against ^{232}Th to correct for variable carbonate contents. The resulting values display variations with depth that are correlated with $\delta\,^{18}O$ (Fig. 12.13). Scholten *et al.* attributed these variations to the influence of climatic factors on the ^{230}Th deposition rate. Climatic changes affect the productivity of plankton, and hence the amount of sinking organic matter.

Biogenic particle fluxes were argued by Mangini and Diester-Haass (1983) to control the downward flux of radionuclides off NW Africa, and hence ^{230}Th activity variations in sediment cores. Therefore Scholten *et al.* argued that the low initial excess ^{230}Th/^{232}Th activity ratios in isotope stages 2 and 6 (Fig. 12.13) were due to a widespread reduction of biogenic paleo-productivity during these cold periods. This regional climatic control of radionuclide deposition allows the opportunity of correlating ^{230}Th variations between different sites in an ocean system. Similar results may be obtained using ^{231}Pa/^{230}Th activity ratios (Kumar *et al.*, 1993) and using the cosmogenic isotope ^{10}Be (section 14.3.4).

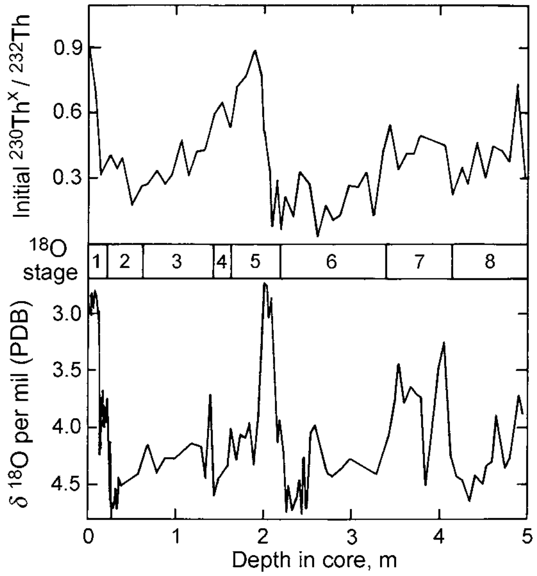

Fig. 12.13. Comparison of the depth dependences of excess initial ^{230}Th/^{232}Th ratio and $\delta\,^{18}O$ in core 23059. Numbered intervals are stages based on ^{18}O stratigraphy. Stages 1 and 5 represent the Holocene and the 120–130-kyr interglacials. After Scholten *et al.* (1990).

The rapid adsorption of ^{230}Th onto particulate matter makes it a very useful oceanographic tracer. Hence,

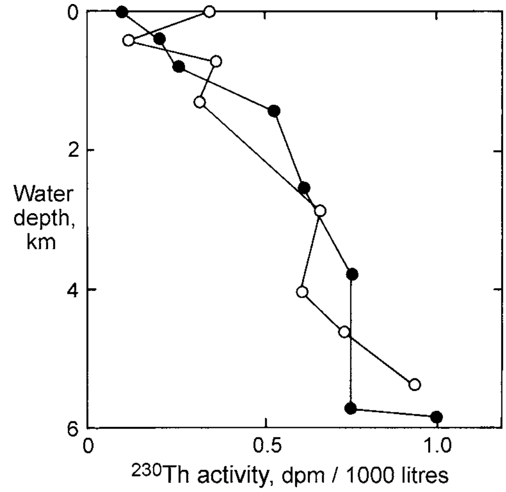

Fig. 12.14. Plot of total ^{230}Th activity as a function of depth in waters off Cape Hatteras (○) and north of Puerto Rico (●). After Cochran *et al.* (1987).

several studies have been directed at understanding its behaviour in seawater, including its ocean residence time. The activity of ^{230}Th in North Atlantic seawater was determined by Cochran *et al.* (1987) by pumping large volumes of seawater, at various depths, through a filter system designed to scavenge ^{230}Th. Two profiles showed increasing activity with depth, both on particulates and in solution (Fig. 12.14). High levels of dissolved ^{230}Th at depth were attributed to attainment of sorption equilibrium between particulates and seawater. In addition, riverine supply of ^{230}Th causes slight enrichment in shallow seawater off Cape Hatteras, but makes a negligible contribution to the total ^{230}Th inventory.

Yu *et al.* (1996) used these results to make a new estimate of the ^{230}Th residence time in North Atlantic seawater. This value can be determined from the ^{230}Th inventory per unit volume of water (n = activity/λ_{230}), divided by the supply flux per unit volume. Since riverine supply of ^{230}Th is considered insignificant, the supply flux is equal to oceanic ^{234}U decay. Hence, in terms of activities:

$$\tau_{\text{Th-230}} = \frac{1}{\lambda_{230}} \frac{^{230}\text{Th}}{^{234}\text{U}} \qquad [12.17]$$

Using profiles of activity against depth, Yu *et al.* estimated an average ^{230}Th activity of 0.65 dpm/m^3 in the North Atlantic at 25 °N. This compares with a ^{234}U activity of 2700 dpm/m^3, which is constant throughout the oceans due to the long residence time of uranium. Plugging these values into the above equation gave a τ value of only 26 yr, much shorter than had previously been estimated.

12.3.6 ^{231}Pa–^{230}Th

Similarities between the chemistries of Pa and Th prompted Sackett (1960) and Rosholt *et al.* (1961) to suggest their use in conjunction as a dating tool. Three factors suggested that the adsorbed initial ^{230}Th/^{231}Pa activity ratio should be a constant ($\sim$11) defined by the production ratio of the two species: firstly, the isotope ratio of their parents is relatively constant in seawater (as demonstrated by the concordance of ^{231}Pa and ^{230}Th dates); secondly, they are both adsorbed rapidly compared with their half-lives; and thirdly, the direct river-borne contribution of ^{231}Pa and ^{230}Th to the oceans is negligible (Scott, 1968). In this case, equation [12.8] can be divided by the corresponding equation for protactinium, yielding

$$\left(\frac{^{230}\text{Th}}{^{231}\text{Pa}}\right)_{\text{P}}^{\text{excess}} = \left(\frac{^{230}\text{Th}}{^{231}\text{Pa}}\right)_{\text{I}}^{\text{excess}} e^{-(\lambda_{230}-\lambda_{231})t} \qquad [12.18]$$

Equation [12.18] can then be solved for t by assuming the initial (production) ratio to be 11. The early work of Sackett (1960) and Rosholt *et al.* (1961) appeared to bear out the assumption. However, subsequent work has yielded variable excess ^{230}Th/^{231}Pa activities at the sediment surface. Sediments often have surface ratios much higher than 11 (e.g. Sackett, 1964), while manganese nodules may have ratios much lower than 11 (e.g. Sackett, 1966). Hence, it is concluded that variable fractionation between ^{231}Pa and ^{230}Th occurs during sedimentation, rendering the method useless as a dating tool.

The variable fractionation between ^{231}Pa and ^{230}Th can now be explained by the different seawater residence times of these species. Because of its extremely particle-reactive behaviour, very little ^{230}Th can be transported laterally (advected) before it is scavenged and sedimented. In contrast, ^{231}Pa can be advected by ocean currents before it is scavenged in locations with a high flux of sinking particles. As a result, ^{230}Th/^{231}Pa ratios vary across ocean basins, normally with high ratios in the centre of the basin, where sedimentation rates are low, and low ratios near the margins, where sedimentation rates are high (Yang *et al.*, 1986).

Yu *et al.* (1996) proposed that the different seawater residence times of Pa and Th should allow their activity ratios to be used as monitors of ocean circulation. For example, the present-day Atlantic Ocean is dominated by a 'conveyor belt' that transports North Atlantic Deep Water (NADW) southwards to the Antarctic.

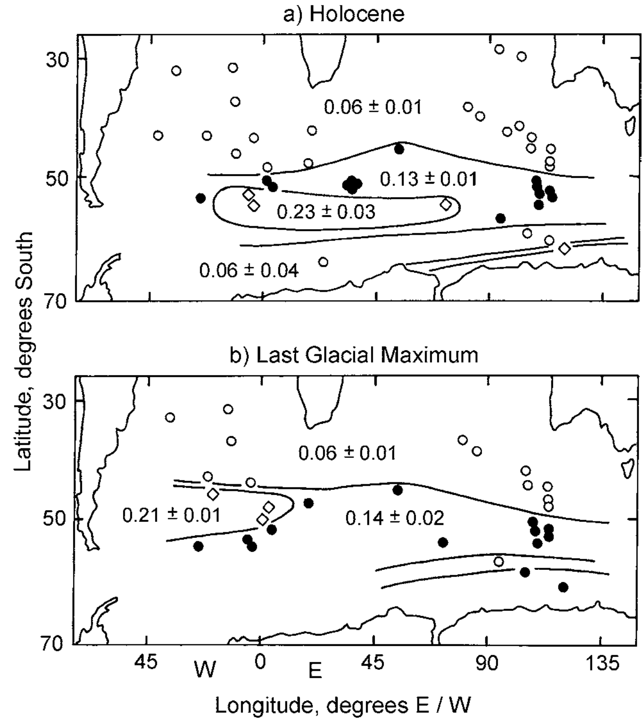

Fig. 12.15. ^{231}Pa/^{230}Th activity ratios for the South Atlantic and the Southern Ocean, showing values both above and below the production ratio of 0.09: (a) present day and (b) last glacial maximum. ^{231}Pa/^{230}Th values: (○) = below 0.1; (●) = 0.1–0.2; (◇) = over 0.2. After Yu *et al.* (1996).

Radiocarbon evidence (section 14.1.6) suggests that NADW has a residence time of 200–300 yr in the Atlantic. Comparison of this value with the ocean residence times of ^{231}Pa and ^{230}Th indicates that about 50% of ^{231}Pa, but only 10% of ^{230}Th produced in the Atlantic will be exported to the Southern Ocean. These predictions were supported by activity measurements on (recent) core tops from ocean-floor sediment (Fig. 12.15). These data are presented in the reciprocal form (^{231}Pa/^{230}Th), and reveal an average activity ratio of only 0.06 in the Atlantic, but 0.17 in the Southern Ocean (relative to a production ratio of 0.09).

Yu *et al.* made the critical observation that sediments deposited at the time of the last glacial maximum had exactly the same distribution pattern of ^{231}Pa/^{230}Th activity ratios (Fig. 12.15b) as present-day sediments. From this observation they concluded that the ocean conveyor belt operated at a very similar rate during the glacial maximum. This result cast doubt on the widely favoured model in which the conveyer belt was thought to have partially or completely ceased during the last glacial maximum (section 14.1.7). Hence, it was critically important to evaluate the result obtained by Yu *et al.*, to see whether the conclusions were robust, or whether factors other than ocean currents could have produced similar patterns at the present day and during the last glacial maximum.

The circulation model of Yu *et al.* (1996) made a prediction that could be tested, as one way of assessing its robustness. Because the high ^{231}Pa/^{230}Th ratios in sediments from the Southern Ocean were attributed to high sedimentation rates from Circum-Polar Deep Water (CPDW), it should be expected that sediment ^{231}Pa/^{230}Th ratios should decrease again near the Antarctic shore, where sedimentation rates are low.

Walter *et al.* (1997) tested this expectation by collecting a much larger set of data from waters and sediments right across the Antarctic Circumpolar Current (ACC), which extends from 50° S to 60° S, and is equivalent to the range of CPDW. Their data (Fig. 12.16a) showed that high ratios of excess ^{231}Pa/^{230}Th in sediments continued south of 60° into the Weddell Sea, despite the low sedimentation rates in this area near the Antarctic continent. However, analysis of suspended particulates revealed very high

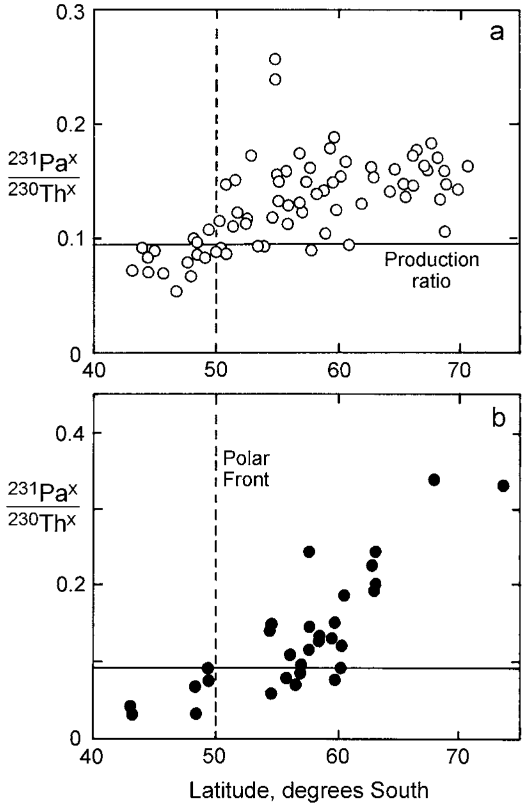

Fig. 12.16. Plot of excess $^{231}Pa/^{230}Th$ activity ratios as a function of latitude across the Southern Ocean, showing values increasing towards the Antarctic coast: (a) recent sediments and (b) particulate matter in water. After Walter *et al.* (1997).

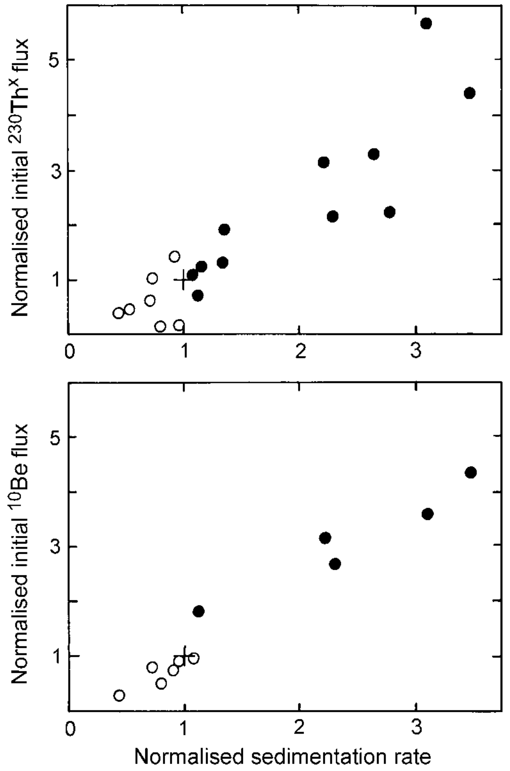

Fig. 12.17. Plots of normalised fluxes of excess ^{230}Th and ^{10}Be against normalised sedimentation rate to show similar correlation lines for the two nuclides: (○) = glacial, isotope stages 2, 5d and 6; (●) = interglacial, stages 1, 5e and 7. After Frank *et al.* (1995).

$^{231}Pa/^{230}Th$ activity ratios in this zone (Fig. 12.16b), which were related to the presence of biogenic opal. Therefore, Walter *et al.* suggested that biogenic opal was much more effective at scavenging Pa than clay minerals. Hence, it is concluded that $^{231}Pa/^{230}Th$ ratios can be influenced by sediment type, so that they are a less reliable measure of paleo-productivity and ocean circulation than had previously been expected (Luo and Ku, 1999; Chase *et al.*, 2002).

The short ocean residence time of ^{230}Th also makes this tracer useful in constraining the deposition fluxes of other species such, as ^{10}Be, with longer residence times. Frank *et al.* (1995) illustrated this approach in a study of sediment stratigraphy from the Weddell Sea, Antarctica. Samples were collected at intermediate water depths to avoid contamination by resuspended sediment (>1500 m below the surface and >500 m above the sea floor). Both ^{10}Be abundances and excess initial ^{230}Th activities exhibited large variations in concentration between glacial periods (stages 2, 4 and 6) and interglacials (stages 1, 5e and 7).

Frank *et al.* calculated average burial fluxes for each climatic stage, using initial radionuclide abundances, dry bulk density and sedimentation rate. These fluxes were positively correlated with sedimentation rate (Fig. 12.17), and varied by more than an order of magnitude. Since ^{230}Th activities vary to the same extent as the abundance of ^{10}Be, these variations cannot be attributed principally to boundary scavenging of advected nuclides (although this may play some role). Instead, Frank *et al.* attributed the variations to sediment transport. High radionuclide fluxes during interglacial periods were attributed to focussing of 'marine snow' (radionuclide-bearing diatoms) by strong bottom currents. Low radionuclide fluxes during glaciations were attributed to 'bulldozing' of sediments by grounded ice shelves, which replaced young (isotopically hot) sediment by old (isotopically dead) material.

12.3.7 ^{210}Pb

Within the ^{238}U decay chain, the daughter product of ^{226}Ra is the rare gas ^{222}Rn. This escapes into the atmosphere from the whole land surface. However, ^{222}Rn has a half-life of only three days, and is followed by four intermediates with half-lives of minutes to seconds, ultimately yielding longer-lived ^{210}Pb. This is estimated to remain in the upper atmosphere for a few days, before the majority returns to the surface in precipitation. Thereafter, unsupported ^{210}Pb decays away with a half-life of 22.3 yr. The use of ^{210}Pb to date accumulation of snow was first suggested by Goldberg (1963). However, it can also be used to date very recent fresh-water and marine sedimentation (e.g. Krishnaswamy *et al.*, 1971; Koide *et al.*, 1972) because ^{210}Pb has an aqueous residence time of only a year or two before adsorption onto sediment.

If the ^{210}Pb concentration in newly precipitated snow or sediment remains more or less constant with time at a given locality (as expected), then the system will behave in exactly the same way as the ^{230}Th excess method. We can then use ^{210}Pb activity at the present-day surface to determine initial ^{210}Pb, and solve for the age of a buried ice or sediment sample:

$$^{210}\text{Pb} = {}^{210}\text{Pb}_{\text{initial}}\, e^{-\lambda_{210} t} \qquad [12.19]$$

As with ^{230}Th, if we plot the log of ^{210}Pb activity against depth, the slope yields the sedimentation rate. The first application of the method was to snow chronology (Crozaz *et al.*, 1964). The calculated sedimentation rate of snow at the South Pole in water equivalents (6 ± 1 cm/yr) compared well with a rate determined from yearly 'ice varves'.

The short half-life of ^{210}Pb also makes it ideally suited to the dating of historical-age sediments. For example, the method has become important in studying the history of heavy-metal pollution of coastal waters and lakes. Bruland *et al.* (1974) used the method in a study of metal pollution of the Santa Monica basin off Los Angeles. A log plot of total ^{210}Pb activity against depth (Fig. 12.18) yields a linear fit at shallow depths, but the profiles flatten out at about 8 cm depth due to the effect of ^{210}Pb supported by ^{226}Ra. However, this can be corrected by subtracting ^{226}Ra activity, yielding excess ^{210}Pb activities:

$$^{210}\text{Pb}_{\text{excess}} = {}^{210}\text{Pb}_{\text{total}} - {}^{226}\text{Ra} \qquad [12.20]$$

When the data are plotted in this form, the usable range of the method is extended to about 150 yr. For the Santa Monica basin the corrected (excess) ^{210}Pb data yield a sedimentation rate of 0.7 mm/yr (Fig. 12.18).

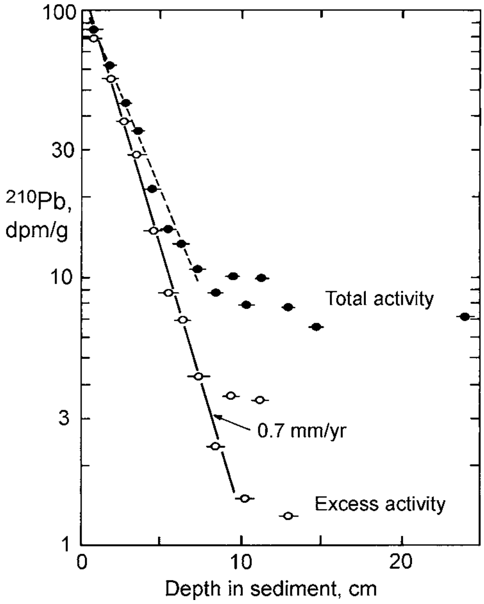

Fig. 12.18. Plot of ^{210}Pb activity against depth in recent sediments of the Santa Monica basin. Solid symbols: total ^{210}Pb activity, including ^{226}Ra-supported fraction. Open symbols: excess ^{210}Pb only. After Bruland *et al.* (1974).

A particularly appropriate application of the ^{210}Pb method is to studies of anthropogenic Pb contamination of sediments. Shirahata *et al.* (1980) applied the method to a remote sub-alpine pond in Yosemite National Park, in order to assess the regional atmospheric fallout of Pb from car exhausts. A sedimentation rate of 0.6 mm/yr was calculated from ^{210}Pb data (Fig. 12.19). Bioturbation of the sediment was ruled out because all bomb-produced radionuclides remained within about 2 cm of the sediment surface. Total Pb concentrations in the sediment were found to have increased four-fold over the past hundred years, and this change was accompanied by a change in ^{206}Pb/^{207}Pb ratio from a natural local value of 1.15 to an exotic value of 1.2 . The latter was typical of the sources of Pb ore used in the USA for the manufacture of leaded gasoline (section 5.6.1).

Despite these achievements with the ^{210}Pb method, caution must be exercised in the interpretation of data, since some studies (e.g. Santschi *et al.*, 1983; Benoit and Hémond, 1991) have shown that ^{210}Pb can be remobilised from the surfaces of sediment grains into sediment pore waters, and thence into the overlying water column. Benoit and Hémond showed from theoretical modelling that re-distribution of ^{210}Pb could

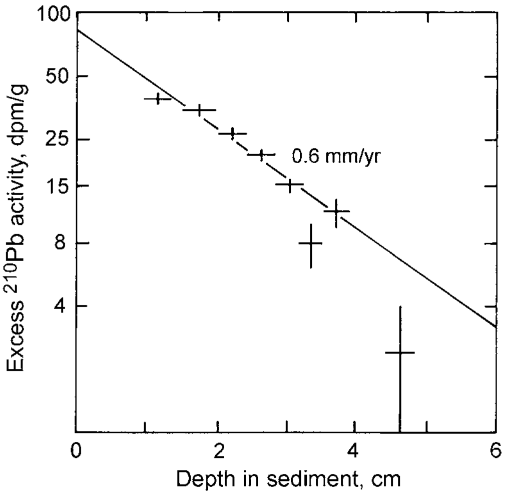

Fig. 12.19. Plot of excess ^{210}Pb activity against depth in a sub-alpine pond from Yosemite National Park, California. After Shirahata *et al.* (1980).

occur by pore-water diffusion, without the need for particle reworking.

12.4 Daughter-deficiency methods

12.4.1 ^{230}Th: theory

The tendency described above for thorium to become adsorbed onto clay minerals leads to low Th levels in groundwaters, in contrast to their moderate U levels. Thus, when biogenic or authigenic calcite is formed, it tends to contain appreciable U concentrations (a few ppm) but negligible Th. This leads to a situation in which ^{230}Th is strongly deficient relative to its parent, ^{234}U. The subsequent regeneration of ^{230}Th can then be used as a dating tool.

The first application of this '^{230}Th-deficiency' technique was made as early as 1926 by Khlapin, who used short-lived ^{226}Ra as a measure of ^{230}Th activity. Khlapin (1926) assumed that the ^{234}U parent taken up by calcite was itself in secular equilibrium with ^{238}U and that Th uptake was negligible. Under these conditions, we can treat ^{230}Th production from ^{234}U as if it were derived directly from ^{238}U. To calculate the net accumulation of ^{230}Th, we must then subtract the fraction which has decayed to ^{226}Ra. On substituting into the relevant Bateman equation [1.13], the abundance (not activity) of ^{230}Th after time t is given as follows:

$$n\,^{230}\mathrm{Th} = \frac{\lambda_{238}}{\lambda_{230} - \lambda_{238}}\, n\,^{238}\mathrm{U}_\mathrm{I}(\mathrm{e}^{-\lambda_{238}t} - \mathrm{e}^{-\lambda_{230}t}) \qquad [12.21]$$

where I signifies the initial ratio. These abundances may easily be converted into activities by dividing by the relevant decay constants:

$$\frac{^{230}\mathrm{Th}}{\lambda_{230}} = \frac{\lambda_{238}}{\lambda_{230} - \lambda_{238}}\,\frac{^{238}\mathrm{U}_\mathrm{I}}{\lambda_{238}}(\mathrm{e}^{-\lambda_{238}t} - \mathrm{e}^{-\lambda_{230}t}) \qquad [12.22]$$

Now, on cancelling out λ_{238} and multiplying both sides by λ_{230},

$$^{230}\mathrm{Th} = \frac{\lambda_{230}}{\lambda_{230} - \lambda_{238}}\,^{238}\mathrm{U}_\mathrm{I}(\mathrm{e}^{-\lambda_{238}t} - \mathrm{e}^{-\lambda_{230}t}) \qquad [12.23]$$

However, because of the very long half-life of ^{238}U relative to the other species, its activity is effectively constant over time. Therefore initial ^{238}U activity can be approximated by ^{238}U, $\mathrm{e}^{-\lambda_{238}t}$ is approximately 1 and $\lambda_{230} - \lambda_{238}$ is approximately λ_{230}, which then cancels out to yield

$$^{230}\mathrm{Th} = {}^{238}\mathrm{U}(1 - \mathrm{e}^{-\lambda_{230}t}) \qquad [12.24]$$

Finally, dividing through by ^{238}U activity yields the decay equation which can be used for dating:

$$\frac{^{230}\mathrm{Th}}{^{238}\mathrm{U}} = 1 - \mathrm{e}^{-\lambda_{230}t} \qquad [12.25]$$

However, it was noted above that ^{234}U and ^{238}U activities in natural waters are very rarely in secular equilibrium. This introduces a complication into the decay equation, since there is an extra contribution to ^{230}Th activity by excess ^{234}U, until the latter has decayed away. ^{230}Th production by excess ^{234}U(X) is given by an equation analogous to [12.23]:

$$^{230}\mathrm{Th}^\mathrm{X} = \frac{\lambda_{230}}{\lambda_{230} - \lambda_{234}}\,^{234}\mathrm{U}_\mathrm{I}^\mathrm{X}(\mathrm{e}^{-\lambda_{234}t} - \mathrm{e}^{-\lambda_{230}t}) \qquad [12.26]$$

However, excess ^{234}U activities can conveniently be measured only as a ratio against ^{238}U. Therefore we divide both sides of [12.26] by ^{238}U activity. This is effectively constant over time, due to the long half-life of ^{238}U, so that present and initial ^{238}U activities are interchangeable:

$$\left(\frac{^{230}\mathrm{Th}}{^{238}\mathrm{U}}\right)^\mathrm{X} = \frac{\lambda_{230}}{\lambda_{230} - \lambda_{234}}\left(\frac{^{234}\mathrm{U}}{^{238}\mathrm{U}}\right)^\mathrm{X}_\mathrm{I}(\mathrm{e}^{-\lambda_{234}t} - \mathrm{e}^{-\lambda_{230}t}) \qquad [12.27]$$

But, the excess activity ratio is equal to the total activity ratio minus one (corresponding to secular equilibrium).

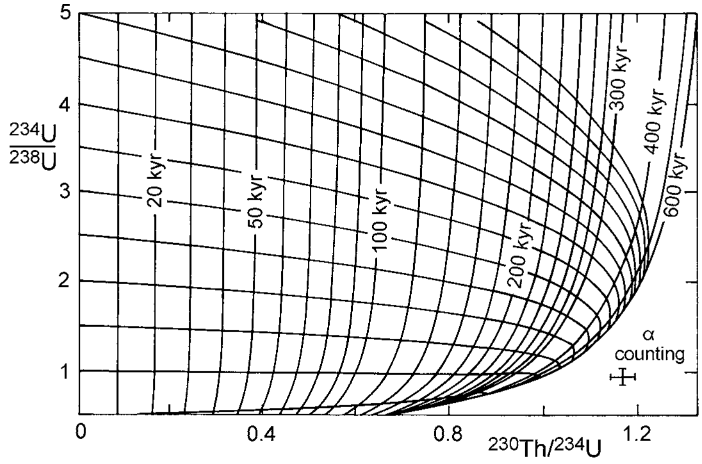

Fig. 12.20. Th–U isochron diagram for systems containing no ^{232}Th. Labelled, steeply dipping lines are isochrons; lateral lines are growth lines. The error bar shows the typical uncertainty for α spectrometry. After Kaufman and Broecker (1965).

So

$$\left(\frac{^{230}\mathrm{Th}}{^{238}\mathrm{U}}\right)^{\mathrm{X}} = \frac{\lambda_{230}}{\lambda_{230}-\lambda_{234}}\left[\left(\frac{^{234}\mathrm{U}}{^{238}\mathrm{U}}\right)_{\mathrm{I}} - 1\right] \times (\mathrm{e}^{-\lambda_{234}t} - \mathrm{e}^{-\lambda_{230}t}) \qquad [12.28]$$

We can substitute [12.6] into this equation in order to convert initial ^{234}U/^{238}U activities into the present-day measured activities (P):

$$\left(\frac{^{230}\mathrm{Th}}{^{238}\mathrm{U}}\right)^{\mathrm{X}} = \frac{\lambda_{230}}{\lambda_{230}-\lambda_{234}}\left[\left(\frac{^{234}\mathrm{U}}{^{238}\mathrm{U}}\right)_{\mathrm{P}} - 1\right] \times \frac{\mathrm{e}^{-\lambda_{234}t} - \mathrm{e}^{-\lambda_{230}t}}{\mathrm{e}^{-\lambda_{234}t}} \qquad [12.29]$$

The final term simplifies to yield

$$\left(\frac{^{230}\mathrm{Th}}{^{238}\mathrm{U}}\right)^{\mathrm{X}} = \frac{\lambda_{230}}{\lambda_{230}-\lambda_{234}}\left[\left(\frac{^{234}\mathrm{U}}{^{238}\mathrm{U}}\right)_{\mathrm{P}} - 1\right] \times (1 - \mathrm{e}^{-(\lambda_{230}-\lambda_{234})t}) \qquad [12.30]$$

Finally, on adding the ^{230}Th production from equilibrium and excess ^{234}U ([12.25] and [12.30]), we obtain

$$\frac{^{230}\mathrm{Th}}{^{238}\mathrm{U}} = 1 - \mathrm{e}^{-\lambda_{230}t} + \frac{\lambda_{230}}{\lambda_{230}-\lambda_{234}}\left(\frac{^{234}\mathrm{U}}{^{238}\mathrm{U}} - 1\right)(1 - \mathrm{e}^{-(\lambda_{230}-\lambda_{234})t}) \qquad [12.31]$$

This equation could be used directly to solve ages, but it has become normal procedure to rearrange it by multiplying through by the ^{238}U/^{234}U ratio. This yields

$$\frac{^{230}\mathrm{Th}}{^{234}\mathrm{U}} = \frac{1 - \mathrm{e}^{-\lambda_{230}t}}{^{234}\mathrm{U}/^{238}\mathrm{U}} + \frac{\lambda_{230}}{\lambda_{230}-\lambda_{234}} \times \left(1 - \frac{1}{^{234}\mathrm{U}/^{238}\mathrm{U}}\right)(1 - \mathrm{e}^{-(\lambda_{230}-\lambda_{234})t}) \qquad [12.32]$$

This equation was plotted as an isochron diagram (Fig. 12.20) by Kaufman and Broecker (1965). Effectively, the calibration line for ^{234}U/^{238}U activity = 1 (secular equilibrium) yields the age in terms of ^{230}Th build-up, while the near-vertical isochron lines apply the correction for non-equilibrium U isotope compositions. As can be seen on the diagram, this correction is unnecessary for samples less than about 30 kyr old. The maximum dating range of the ^{230}Th method is about 300 kyr by α counting, but this may be extended to over 400 kyr by mass spectrometry.

12.4.2 ^{230}Th: applications

The ^{230}Th–^{234}U method is applicable to the dating of any closed-system carbonate that is free of contamination by initial detrital thorium. It can provide far better precision for coral dating than the ^{234}U–^{238}U method alone. This is illustrated in Fig. 12.21 by a compilation of high-precision α-spectrometry data for unrecrystallised corals (Veeh and Burnett, 1982). It can be seen that typical measurement errors in ^{234}U/^{238}U ratio lead to age uncertainties of over 100%, whereas errors in ^{230}Th/^{234}U ratio lead to age errors of only 10%.

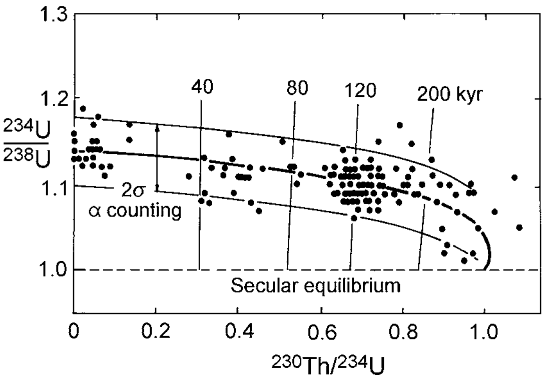

Fig. 12.21. Plot of $^{234}U/^{238}U$ *versus* $^{230}Th/^{234}U$ activity ratio for un-recrystallised coral data with 2σ errors better than 5% . The heavy near-horizontal curve shows the decay path starting from present-day seawater. Vertical lines are isochrons. After Veeh and Burnett (1982).

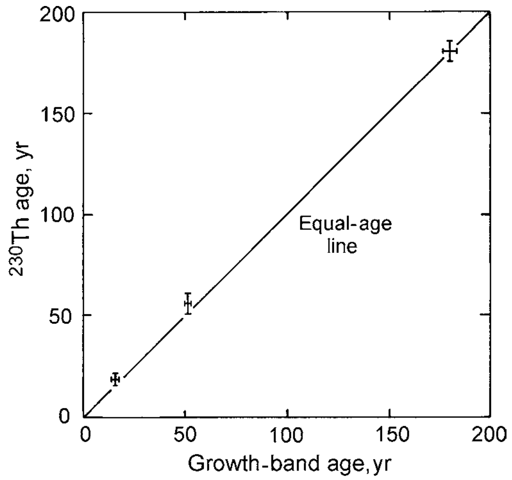

Fig. 12.22. Comparison of mass-spectrometric ^{230}Th ages of living corals with historical ages based on annual growth bands. After Edwards *et al.* (1988).

The precision of ^{230}Th coral dating has been further enhanced by the mass-spectrometric method, as demonstrated by the analysis of live reef-forming corals from the Vanuatu arc, east of Australia (Edwards *et al.*, 1988). In these specimens, ^{230}Th ages were compared with historical ages based on yearly growth bands. The latter are about 1 cm wide, and can be accurately counted in specimens at least 200 yr old. ^{230}Th ages were determined with errors as low as ± 3 yr (2σ), and were in excellent agreement with the historical age of the corals (Fig. 12.22). ^{230}Th dating of corals between 9000 and 40 000 yr old has been used very effectively to calibrate the radiocarbon timescale (section 14.1.5).

One of the most important applications of ^{230}Th dating is in the study of Pleistocene (Quaternary-age) climatic variations associated with glacial cycles. These cycles caused periodic variations in the global ice mass at the expense of seawater, and therefore left two types of record. The first is the direct variation of sea-level through time, while the second is an indirect record of sea-level variations, due to the fractionation of oxygen isotopes as various amounts of seawater were converted into ice. These oxygen isotope variations can be seen in marine and terrestrial carbonate deposits, as well as in ice records. The ^{230}Th (daughter-deficiency) method can be used to date both of these climatic records: direct sea-level variations and oxygen isotope variations recorded in terrestrial carbonates. These dates can then be used to test the third main record of Quaternary climatic variation, the so-called SPECMAP record of marine oxygen isotope variations.

The SPECMAP model (Imbrie *et al.*, 1984) attributes Pleistocene glacial cycles, recorded as the oxygen isotope variations in marine forams, to variations in the intensity of solar radiation. This is based on the theory of Milankovitch (1941), who suggested that changes in Pleistocene climate were largely due to changes of 'insolation' in the northern hemisphere caused by variations in the Earth's orbit. Because the Earth's orbital variations can be precisely calculated and projected back in time, it is possible to model insolation variations back though several million years. Then, if the Milankovitch theory is correct, these orbital variations can be used to 'tune' the climatic record of oxygen isotope variations in order to date glacial cycles precisely ('Milankovitch forcing').

Reef-building corals provide a useful record of past sea-level variations, because sea-level highs during interglacial periods become marked by coral terraces that are stranded when sea-level falls again. In general there is a good correlation between sea-level highs and northern-hemisphere insolation, providing support for the Milankovitch theory. However, α-counting dates revealed inconsistencies at the beginning of the last interglacial, (marked by high sea-level stage 5e in the stable isotope record). Ages for this sea-level stand spread over a very large range, from 120 to 140 kyr, causing it to be divided into two sub-parts. However, this uncertainty was partly due to the large size of the error bars on α-counting ages, which were almost of equal magnitude to the duration of glacial cycles.

This problem is illustrated in Fig. 12.23 by comparing α-spectrometry dates with the calculated insolation curve at the time of the last interglacial (stage 5e). A 129-kyr coral terrace date is correctly centred on the insolation high, corresponding to an interglacial.

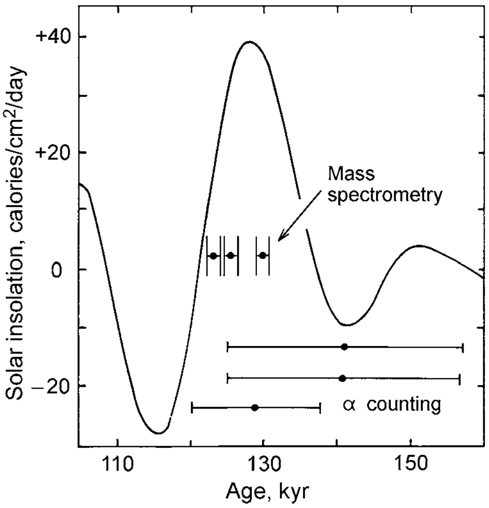

Fig. 12.23. Plot of solar insolation against time, to compare the duration of glacial cycles with analytical uncertainties for mass-spectrometric and α-counting U-series ages. Dates shown are for coral terraces from the last interglacial (oxygen isotope stage 5e). After Edwards *et al.* (1987).

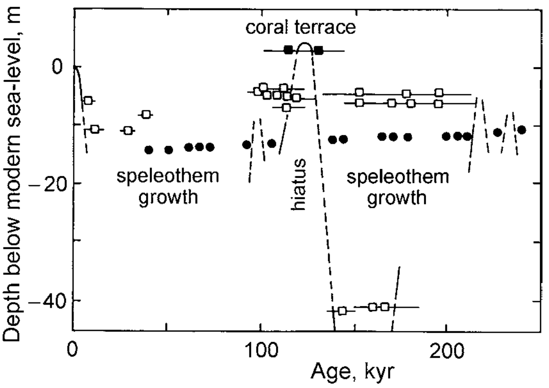

Fig. 12.24. Pleistocene sea-level curve for the Bahamas (dashed lines), based on U-series ages on drowned speleothems: (●) = mass-spectrometric data; (□, ■) = speleothem and coral terrace ages determined by α spectrometry. After Li *et al.* (1989).

However, two other α-counting dates on coral terraces, from the Huon Peninsula of Papua New Guinea (Bloom *et al.*, 1974), were situated between two insolation highs, on the intervening insolation low. Mass-spectrometic dates on the same samples were in all three cases within 2σ error of the α-counting determinations, but are now centred unequivocally on the insolation high at 127 kyr (Edwards *et al.*, 1987).

Another approach for constraining Pleistocene sea-level variations is ^{230}Th dating of speleothems (stalactites, stalagmites etc.) from submarine caves. These formations grow during periods of low sea-level stand, when they are exposed sub-aerially to percolating calcareous solutions. When sea-level rises and they become drowned, growth stops, and an erosional hiatus occurs. The densely crystalline form of speleothem deposits is conducive to good closed-system behaviour, so this material is ideal for U-series dating. Therefore, drowned speleothem and coral terraces form a complementary couple for Pleistocene sea-level studies. The first mass-spectrometric dating study on such material was performed by Li *et al.* (1989) on a sample from 12 m depth in a Bahamas 'blue hole'. A detailed sequence of U-series age determinations on the 12-cm-thick flowstone showed that carbonate deposition had occurred over 280 kyr (Fig. 12.24). Within this period, there were four internal hiatuses corresponding to sea-level stands above −12 m (relative to present-day sea-level). These data supported the orbitally tuned SPECMAP record in suggesting that the last interglacial began *after* 140 kyr ago.

Winograd (1990) challenged this evidence on the grounds of apparent conflict with the older α-counting ages from coral terraces (Bloom *et al.*, 1974). However, Lundberg *et al.* (1990) showed that, if careful attention is paid to the quoted analytical error limits of the α-counting and mass-spectrometric data, then there is no conflict between the speleothem and coral ages. In other words, the α-counting ages on coral terraces are consistent with sea-level rise after 140 kyr when their large error bars are taken into account. In this connection, it is important to remember that the 1σ error limits traditionally quoted for α spectrometry correspond to only 68% confidence that the 'true' age is within the quoted limits. Therefore, all such error limits should be doubled to generate (more realistic) 2σ error limits (95% confidence), which is the accepted practice in other fields of isotopic dating.

Speleothems can also be used as inventories of past atmospheric oxygen isotope variations, which are also linked to glacial cycles. These records are well suited to dating by the ^{230}Th (daughter-deficiency) method. Hence, climatic variations can be dated by measuring δ^{18}O signatures and U-series ages on the same cave deposits. For example, Winograd *et al.* (1992) performed a combined U-series and stable-isotope study on the calcite lining of a water-filled cavern in Nevada (USA) called Devils Hole. The results of this study suggested similar glacial cycles to the SPECMAP oceanic record, but, like the data of Bloom *et al.* (1974), the

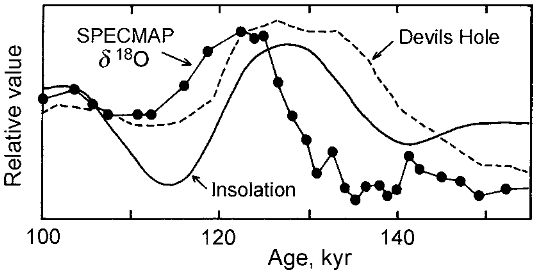

Fig. 12.25. Comparison of various lines of evidence for the onset of the last interglacial, based on Devils Hole, northern-hemisphere insolation and the SPECMAP oxygen isotope record. After Zhao *et al.* (2001).

warming trend associated with the last interglacial (about 140 kyr ago) appeared to precede the increase in solar insolation which should have driven this warming (Fig. 12.25). This led Winograd *et al.* to question the SPECMAP model.

In response to these difficulties, numerous explanations have been proposed. One possibility was that the Devils Hole age measurements were biased by a breakdown in the dating assumptions. For example, Edwards and Gallup (1993) suggested that the incorporation of unusually large amounts of initial ^{230}Th from the water reservoir in the Devils Hole fracture system could bias the ages in an unforeseen manner. However, this possibility was excluded by additional dating work (Edwards *et al.*, 1997), which demonstrated concordance between ^{230}Th and ^{231}Pa ages for two Devils Hole calcites.

Another suggestion (Imbrie *et al.*, 1993), was that the mis-match between the Devils Hole and SPECMAP chronologies was caused by a more complex relationship between δ^{18}O and paleoclimate in continental groundwater than in seawater. This suggestion prompted new dating measurements on the Huon Peninsula coral terraces which first began this debate. The new data (Esat *et al.* 1999) suggested that the main peak of high stand VII occurred 130 kyr ago, but that an earlier but probably smaller sea-level rise occurred beginning about 140 kyr ago. Because this earlier sea-level rise was lower, it was not recorded in the Bahamas blue-hole stalagmite at –12 m depth (Fig. 12.24), and the two records are therefore not in contradiction. The Devils Hole signal apparently records the earlier event, but this was followed by a glacial re-advance similar to the Younger Dryas event of the last deglaciation (13 kyr ago). Subsequently, deglaciation resumed, with the beginning of the last interglacial (*sensu stricto*) about 130 kyr ago.

This work was confirmed by more detailed sampling of coral terraces from Barbados (Gallup *et al.*, 2002). The occurrence of sea-level rise in two stages with a retreat in between suggests that this warming event was quite complex, possibly with more than one orbital forcing mechanism. This may therefore explain the difficulty in accurately modelling the causes of glacial advance and retreat, as discussed by Karner and Muller (2000).

12.4.3 ^{230}Th: dirty calcite

Because fossil bones may be encased by subsequent tufa deposits, U-series analysis of such material has been very useful for dating Pleistocene human and animal remains (e.g. Schwarcz and Blackwell, 1991). However, the most interesting tufas are often impure, for the very reason that, if they contain bones, they will probably contain other detrital material. This introduces initial ^{230}Th, which, if not corrected for, may cause serious errors in calculated ages.

In cases where detrital contamination is minor, the same laboratory technique may be used as for clean material: the sample is leached with dilute nitric acid in an attempt to dissolve the carbonate fraction without disturbing the detrital component. This may diminish the contamination to a level at which it is swamped by other errors. However, the detrital component is not usually inert in nitric acid, but often contains a certain fraction of loosely bound uranium and thorium which is removed by the leaching process. The extent of this leakage may be monitored by measuring the activity of ^{232}Th. If this reaches a level of more than a few per cent of ^{230}Th activity then it may be necessary to correct the carbonate data for leaching of radionuclides from the contaminating detrital phase (Ku and Liang, 1984).

U-series data for dirty calcites are best visualised on an isochron diagram. The most common form involves ratioing both ^{230}Th and ^{234}U against ^{232}Th (Fig. 12.26). If all U and Th isotopes are leached from the residue with equal efficiency then a cord joining the leachate and residue points can be interpreted as an isochron line. The slope will then yield the ^{230}Th/^{234}U ratio of the carbonate component, which can be used to calculate the sample age in the same way as for clean material (Fig. 12.20).

Przybylowicz *et al.* (1991) performed leaching experiments on artificial mixtures of pure calcite speleothems and mud in order to test the reliability of the leaching method in dating dirty calcites (e.g. Fig. 12.26). The results show that residues are displaced slightly (occasionally substantially) above the array of leachate compositions. This is probably due

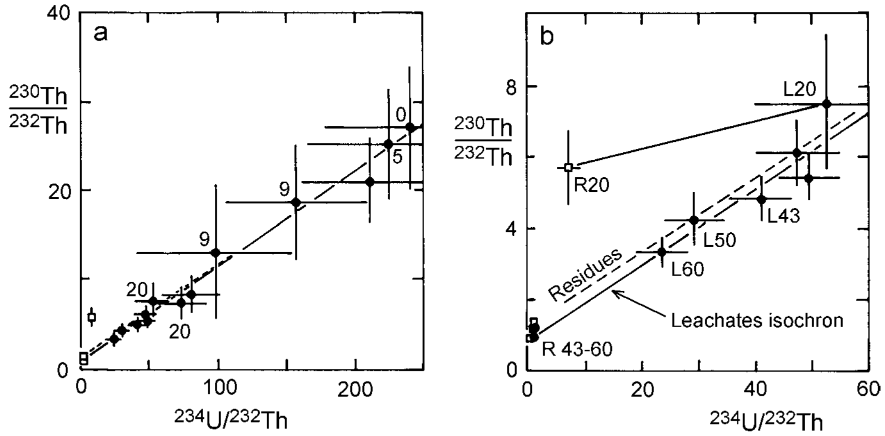

Fig. 12.26. U–Th isochron diagrams showing results from leaching artificial mixtures of calcite and mud with 5–7-M nitric acid: (●) = leachates; (□) = residues from leaching; numbers indicate the percentage of mud in the sample. Diagram (b) is a blow-up of the lower left corner of (a). After Przybylowicz *et al.* (1991).

to slight preferential leaching of uranium relative to thorium from the detrital phase during the leaching process, and may yield apparent ages somewhat below the true value. Schwarcz and Latham (1989) argued that this problem could be diminished by regressing leachate analyses alone. In this case it is no longer necessary to assume a lack of differential isotopic fractionation during the leaching process. Isotopic fractionation is permitted, provided that the amount of such fractionation is the same in all samples. This has the effect of shifting the isochron line sideways in Fig. 12.26b but not changing its slope.

A similar type of correlation diagram can also be used to correct the ^{234}U/^{238}U ratio for detrital contamination. Figure 12.27 shows these data for the experiment described above. However, this is less important, since the ^{230}Th age is only weakly dependent on the ^{234}U/^{238}U ratio in samples less than 300 kyr old.

An application of the 'leach–leach' technique to dating natural mixtures is shown in Fig. 12.28 for contaminated travertines that enclose the 'Mousterian cultural layer' at Tata, Hungary (Schwarcz and Skoflek, 1982). Regression of four leachates leads to an age of 101 ± 4 kyr for carbonate enclosing the cultural layer, which is bracketed between the ages of 78 ± 5 and 118 ± 37 kyr in overlying and underlying clean travertine layers.

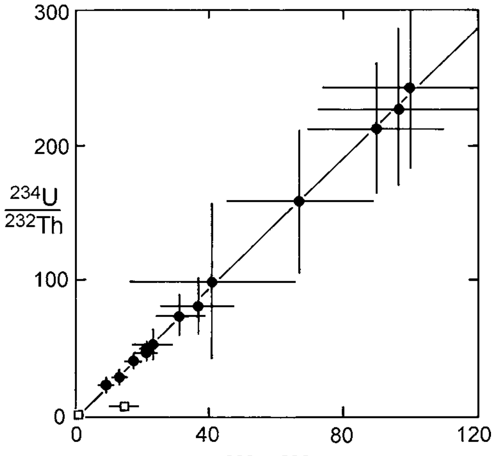

Fig. 12.27. Correlation plot to correct for detrital perturbation of uranium isotope ratios in impure carbonates: (●) = leachates; (□) = residues. After Przybylowicz *et al.* (1991).

In order to achieve a high-precision result from the leach–leach technique it is desirable to leach three or more samples with variable detrital contents from the horizon to be dated. However, under these circumstances it is possible that different samples might undergo variable degrees of isotopic fractionation during leaching. This problem can be avoided by total digestion of a suite of variably contaminated samples from the same deposit. If they all contain the same detrital component (i.e. have the same initial ^{230}Th/^{232}Th ratio) and have remained as closed systems, then they will define a perfect isochron line.

Bischoff and Fitzpatrick (1991) tested the relative performance of the total-dissolution, leach–leach and leachate–residue methods on a series of artificial mixtures of natural detritus and carbonate. (They also tested the effect of leaching with various strengths of

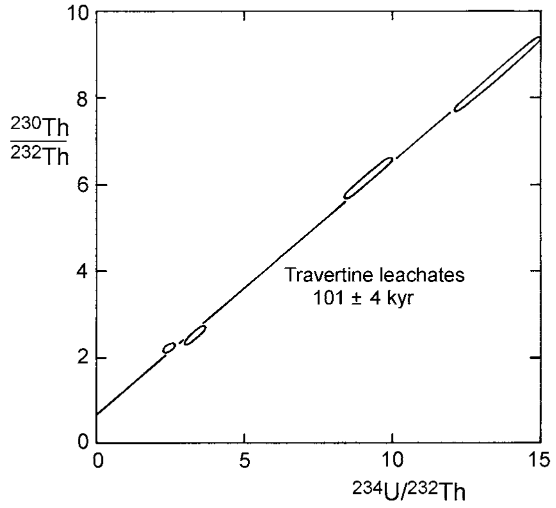

Fig. 12.28. ^{230}Th/^{232}Th *versus* ^{234}U/^{232}Th isochron diagram for leachates of contaminated travertine from Tata, Hungary. Ellipses portray correlated error limits. Modified after Schwarcz and Latham (1989).

acid.) Typical results showed that the total-dissolution method was superior to the other two techniques for artificial mixtures (Fig. 12.29). The total-dissolution method is also more versatile, in that it can be applied to the dating of any type of Pleistocene material with a homogeneous initial ratio and showing closed-system behaviour (Luo and Ku, 1991). However, it may be difficult to obtain a large enough range of detrital–carbonate variations to define a good regression line. Furthermore, in the pursuit of such a range of mixtures, samples with variable initial ratios may be analysed. Therefore, the total-dissolution, leach–leach and leach–residue methods may all be viable alternatives for dating dirty calcite in different circumstances.

One problem with the data presentation in Figs. 12.26 and 12.27 is that the two variables become very highly correlated as the ^{232}Th fraction diminishes in size. The large error bars should therefore be represented by elongated error ellipses (e.g. Fig. 12.28) rather then rectangular error boxes. Similarly, a regression program utilising correlated errors should be used to calculate isochron slopes.

An alternative isochron presentation, utilised by Kaufman (1971) but not shown here, involves plotting the ^{230}Th/^{234}U ratio against ^{232}Th/^{234}U. On this 'Th–U' isochron diagram, the age of the sample is represented by the intercept on the y axis, and increasing detrital contamination is indicated by displacement away from the y axis. Similar plots have been used more widely in U-series studies of silicate systems

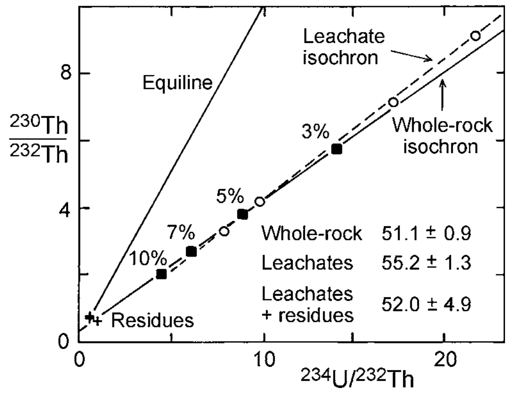

Fig. 12.29. U–Th isochron diagram showing tests of different dating approaches on artificial mixtures of carbonate and detritus: (■) = whole-rock (total dissolution); (○) = leachate; (+) = residue. After Bischoff and Fitzpatrick (1991).

(section 13.1.2.). Th/U isochrons offer some advantages over the more popular U/Th isochron presentation because Th/U isochrons minimise the problem of error correlation between the variables. To show how Th/U isochrons yield the composition of the detrital-free component in a dirty calcite system, Ludwig and Titterington (1994) plotted synthetic data in three dimensions. They also presented a maximum-likelihood method for calculation of the best-fit isochron, an approach already applied to some other isotopic systems (section 2.6.2).

12.4.4 ^{231}Pa

The build-up of ^{231}Pa in carbonates can be used as a dating tool in a way analogous to ^{230}Th. The immediate parent of ^{231}Pa (^{231}Th) is assumed to be always in equilibrium with its parent (^{235}U) due to its short half-life of 26 h. Hence, the age relationship is analogous to the simple form of equation [12.25] for build-up of ^{230}Th:

$$\frac{^{231}\mathrm{Pa}}{^{235}\mathrm{U}} = 1 - e^{-\lambda_{231} t} \qquad [12.33]$$

Because ^{235}U is so much less abundant than ^{238}U, measured α-counting rates for ^{231}Pa and its daughters are twenty times lower than for ^{230}Th. Since counting statistics are the major source of uncertainty in U-series dating, the ^{230}Th method has been much preferred to ^{231}Pa as a practical dating tool. However, the ^{231}Pa technique is potentially valuable as a concordance test for ^{230}Th dates, and the two systems can be used together to date partially open systems (section 12.5.1).

Mass spectrometry potentially offers the same advantages for ^{231}Pa analysis as for ^{230}Th, involving an order-of-magnitude improvement in precision. However, a problem encountered in this work is the lack of any long-lived nuclides for use as spike isotopes. Apart from ^{231}Pa, with a half-life of 32.76 kyr, the most long-lived isotope of protactinium is ^{233}Pa, with a half-life of 27.4 days. This must be prepared anew every few months and must be repeatedly calibrated so that its concentration is known on the exact day of its analysis!

Two methods of preparing ^{233}Pa are in use. The first, described by Pickett *et al.* (1994), involves periodically 'milking' ^{233}Pa from a solution of ^{237}Np. This is done by ion-exchange chemical separation, but it must be done under a stringent radiological protection regime because the parent isotope is very highly active. An alternative method, described by Bourdon *et al.* (1999), is much less hazardous. This involves periodic neutron activation of ^{232}Th in a reactor, to produce ^{233}Th. This short-lived species (half-life 22 min) then decays into ^{233}Pa. Because the parent (^{232}Th) has low activity, the ion-exchange purification can be done under normal laboratory conditions, after allowing short-lived by-products of the activation process to die away.

12.5 U-series dating of open systems

12.5.1 ^{231}Pa–^{230}Th

Because the ^{231}Pa and ^{230}Th (daughter-deficiency) dating methods share a common parent element (uranium), they form a single U–Th–Pa system that is analogous to the U–Pb dating system. This similarity was first discussed by Allègre (1964), who showed that the U–Th–Pa system can be studied using the same 'concordia' diagram as that used for U–Pb zircon dating (section 5.2). The significance of this observation is that a combination of U–Th and U–Pa analyses can be used to date systems that have been partially opened during their history, rather than just as a concordance test to check for closed-system behaviour.

Because the U–Th–Pa system involves three different elements, rather than two, it is necessarily more complex than the U–Pb system. However, this does not have a large effect on the method in practice, because the daughter nuclides Th and Pa are largely immobile, and behave essentially as if they were the same element. On the other hand, the principal cause of open-system behaviour is the mobility of uranium, which is the common element between the two systems.

Despite the fact that the U–Th and U–Pa sub-systems have the same parent element, the U–Th–Pa system is more complex than the U–Pb system because the parent uranium isotopes (^{234}U and ^{235}U) can undergo fractionation in the environment (section 12.3.1). As a result, the U–Th–Pa system actually gives rise to a family of curves in a concordia diagram. This complication was ignored in the analysis of Allègre (1964) and in later studies by Kaufmann and Ku (1989) and Kaufmann *et al.* (1995), but was treated in the more detailed discussion of Cheng *et al.* (1998). As a result, two different concordia diagrams can be plotted, one involving the ultimate parent (^{238}U, Fig. 12.30a) and one involving the immediate parent (^{234}U, Fig. 12.30b). On

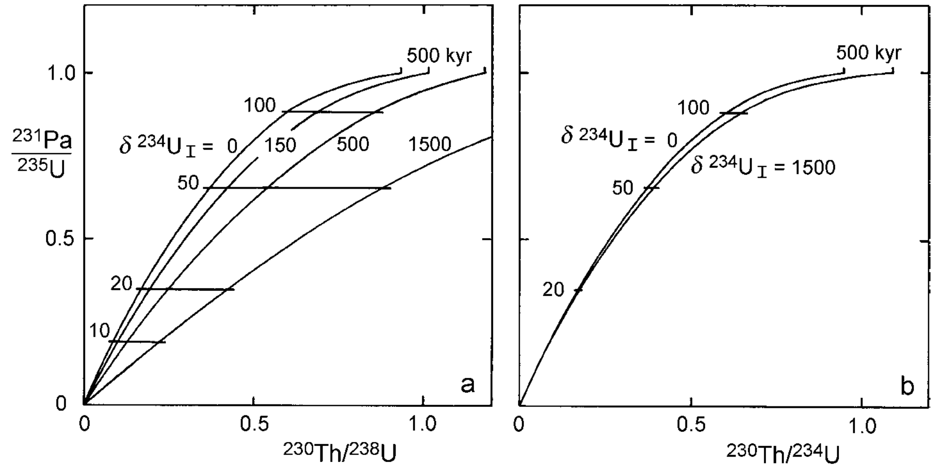

Fig. 12.30. Concordia diagrams for the U–Th–Pa system: (a) against ^{238}U and (b) against ^{234}U. Concordia curves are shown for a variety of δ^{234}U values. After Cheng *et al.* (1998).

each of these diagrams, concordia curves can then be shown for different $^{234}U/^{238}U$ activities, presented in the form of $\delta\,^{234}U$. For reference, it should be remembered that $\delta\,^{234}U = 0$ signifies secular equilibrium, while $\delta\,^{234}U = 150$ is the uranium isotope composition of seawater, corresponding to a $^{234}U/^{238}U$ activity ratio of 1.15.

The final complicating factor in the U–Th–Pa system, relative to U–Pb, is the fact that the daughter products are themselves radioactive. Indeed, this is actually the feature which makes the combined system useful for dating partially open systems in the age range 0–200 kyr. It is the return of ^{230}Th and ^{231}Pa activities to secular equilibrium with their parents, at different rates, which allows age information to be recovered from partially open systems. As a result, when the concordia diagram is plotted (Fig. 12.30), the curvature is in the opposite sense to that of the U–Pb concordia, with the longer-lived nuclide (^{230}Th) along the x axis and the shorter-lived (^{231}Pa) on the y axis.

Uranium gain is probably the most important type of open-system behaviour in U–Th–Pa dating, and causes the data points to move towards the origin in a similar way to Pb loss in the U–Pb system. The simplest scenario is a single episode of U gain. This forms a linear array through the origin at the time of open-system behaviour, and the array then rotates as the system ages under closed-system conditions. The result at the present time is a discordia array similar to a U–Pb discordia (Fig. 12.31). The upper intercept with the concordia line then gives the true age of the system. However, the lower intercept only gives the age of U gain for the special case in which $\delta\,^{234}U = 0$ (secular equilibrium of parent uranium isotopes).

The case of continuous open-system uranium gain is more complex, and gives rise to a curved 'discordia' array. However, as in the case of U–Pb dating, the upper end of this continuous U-gain line is relatively straight and can give a fairly precise upper intercept age. A special case of this scenario is 'linear uptake' of uranium through the life of the system, which is shown on the ^{234}U–Pa–Th diagram in Fig. 12.32. As for U–Pb dating, the best estimate for the upper intercept age is obtained by having a suite of samples with variable degrees of U gain, but with some samples near the concordia (minor late U gain). However, a minimum estimate of the upper intercept age can be calculated by dividing the U–Pa equation [12.33] by the U–Th equation [12.32], as suggested by Ivanovich (1982b). The resulting Pa–Th age is analogous to a 207/206 lead age.

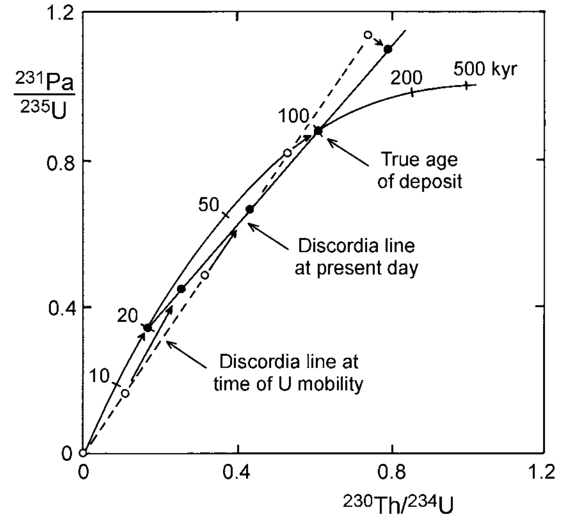

Fig. 12.31. ^{234}U–Pa–Th plot showing the evolution of a discordia line generated by a single episode of uranium mobility. After Cheng *et al.* (1998).

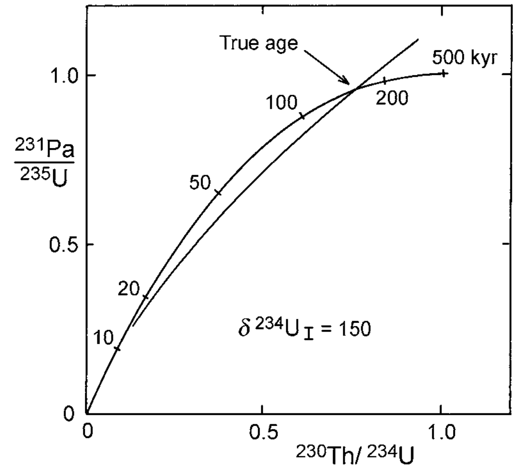

Fig. 12.32. U–Pa–Th plot showing a discordia line generated by continuous uranium uptake. after Cheng *et al.* (1998).

12.5.2 ESR–^{230}Th

Some of the most interesting applications of U-series dating involve human bones and cultural deposits, but these materials are notorious for their open-system behaviour of U-series isotopes, as well as their small sample size. In the past, the ages of this type of material were based on speleothem deposits that pre-dated and post-dated a 'cultural' layer (e.g. Schwarcz, 1989). However, with the advent of mass-spectrometric

U-series analysis, ^{230}Th ages can be used in combination with electron spin resonance (ESR) to obtain reliable dates for teeth (Grün *et al.*, 1988; Grün and McDermott, 1994). Human teeth are not dated directly, but human bones are often found in deposits with large numbers of bovoid teeth (from the cow family). The relatively large size of these teeth provides sufficient material for ESR and U-series dating.

Both ^{230}Th (daughter-deficiency) and ESR dating are based on U-series isotopes, but in different ways. ESR measures the accumulation of trapped electrons at defect sites, caused by the time-integrated radiation dose experienced by the sample, mainly derived from ^{238}U. (For reviews of ESR dating see Jonas (1997) and Rink (1997).) On the other hand, ^{230}Th dating measures the return of this nuclide to secular equilibrium with ^{238}U, *via* its daughter product ^{234}U. In both cases, a dating signal is derived largely from a common parent (^{238}U), and in both cases the dating signal itself is largely immobile (trapped electrons *versus* ^{230}Th nuclides). On the other hand, the dating signal has a different half-life in the two methods: infinite for trapped electrons but 72.5 kyr for ^{230}Th. Therefore, the combined ESR–^{230}Th method can be used to date systems that are partially open to uranium mobility in a similar way to the U–Th–Pa dating system.

Actually, ESR–^{230}Th dates are based on a system that is almost completely open to uranium, because the entire uranium inventory of a tooth is acquired after deposition (live teeth have essentially no uranium). However, experience has shown that the U-uptake history of a tooth can be approximated by three types of model, termed early uptake (EU), linear uptake (LU) and recent uptake (RU), as shown in Fig. 12.33. Of these three models, early uptake is the best scenario for dating because it approximates a case of closed-system evolution, whereby the age of the tooth is essentially the same as that of the uptake event that occurred soon after burial. In this case, the ESR and U-series (^{230}Th) ages will be concordant. On the other hand, a recent-uptake scenario is the worst for dating because the U-series method cannot see back any further than the recent uranium-enrichment event. ESR dating can give a useful date in these circumstances only if the majority of the radiation dose experienced by the tooth comes from the sedimentary environment *outside* the tooth. Linear uptake is the approximation which represents all scenarios between these two extremes. It generates relatively large uncertainties, but may be susceptible to analysis if a large enough data set is available. In detail, the uptake histories of three uranium reservoirs must be considered: tooth enamel, tooth dentine, and surrounding sediment. The ESR measurement is made on the enamel and dentine, and its signal is a time-integrated function of the radiation dose from the three reservoirs.

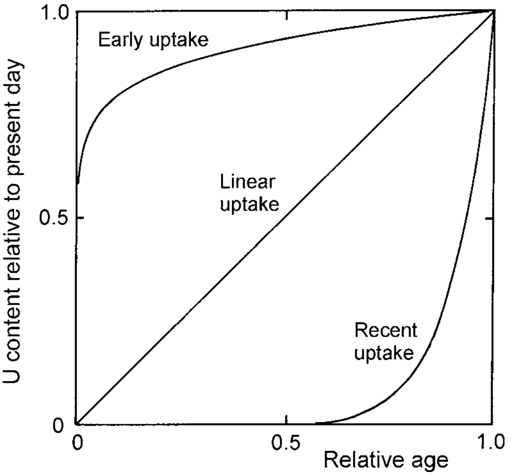

Fig. 12.33. Schematic illustration of different uptake models experienced by buried teeth.

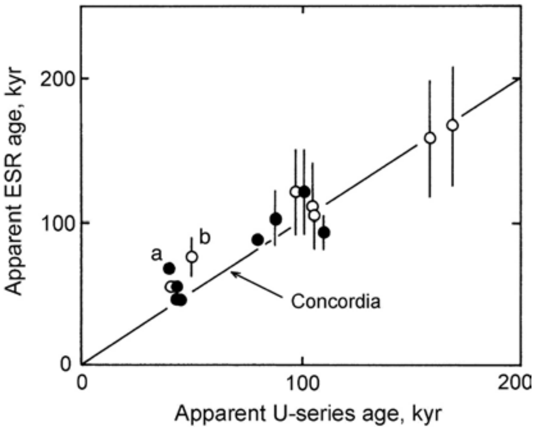

Fig. 12.34. Plot of apparent ESR and U-series ages for enamel (●) and dentine (○) samples of bovoid teeth from Israel, assuming an early-uptake model. Error bars are 1σ. After Grün and McDermott (1994).

An example of age concordance between U-series analyses and ESR ages is provided by a study of bovoid dental fragments associated with the skeletons of early modern humans (Fig. 12.34). In this case, agreement between most of the U-series and ESR dates indicated that uranium uptake occurred soon after deposition. Hence the U-series ages confirmed ESR dates for the appearance of early modern humans at least 100 kyr ago in Israel (McDermott *et al.,* 1993). Two points in Fig. 12.34 (samples a and b) display markedly lower

U-series ages relative to their ESR ages, outside the limits of error. These are indicative of a model of approximately linear uptake (Grün and McDermott, 1994).

Grün *et al.* (1988) proposed a complex parametric calculation to model the uptake history of a tooth using the relative ESR and U-series ages of open-system samples. They demonstrated the effectiveness of this technique on samples from Hoxne, England, which have very young U-series ages relative to their ESR ages, and are therefore indicative of relatively recent U uptake. However, Grün and McDermott (1994, p. 123) admitted that 'The mathematical formulation of these steps is very complex and we have not yet been able to establish a rigorous error calculation procedure'. Therefore, for practical purposes, a simpler method used by Rink *et al.* (2001) may be adequate. These authors categorised the uptake model (Fig. 12.35) using the ratio between the U-series age and the ESR age calculated from an early-uptake model. They then interpolated between the different uptake models to obtain a best estimate of the age of the tooth.

An alternative approach might be to plot a concordia diagram of the ^{230}Th/^{234}U ratio against the ESR age. The upper intercept of this concordia diagram should give the approximate age of the tooth, in a similar way to the U–Th–Pa and U–Pb concordia diagrams. Unfortunately, the quality of experimental data has not yet been adequate to demonstrate this approach.

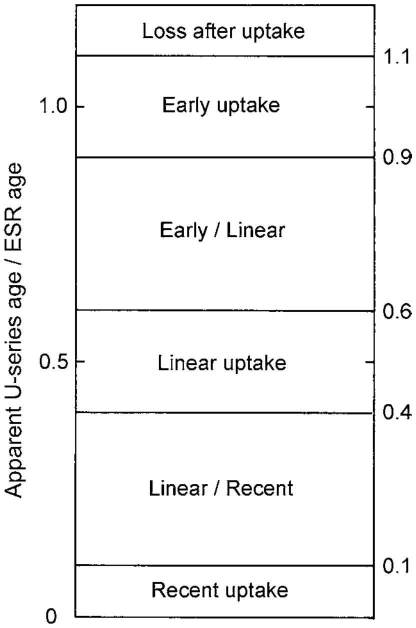

Fig. 12.35. Categories of uranium-uptake model based on the ratio between apparent U-series and ESR ages (calculated assuming early uptake for both systems). After Rink *et al.* (2001).

References

Allègre, C. (1964). De l'extension de la méthode de calcul graphique concordia aux mesures d'ages absolus effectués à l'aide du déséquilibre radioactif. *C. R. Acad. Sci. Paris* **259**, 4086–9.

Asmerom, Y. and Edwards, R. L. (1995). U-series isotope evidence for the origin of continental basalts. *Earth Planet. Sci. Lett.* **134**, 1–7.

Bard, E., Fairbanks, R. G., Hamelin, B., Zindler, A. and Hoang, C. T. (1991). Uranium-234 anomalies in corals older than 150,000 years. *Geochim. Cosmochim. Acta* **55**, 2385–90.

Benoit, G. and Hémond, H. F. (1991). Evidence for diffusive redistribution of ^{210}Pb in lake sediments. *Geochim. Cosmochim. Acta* **55**, 1963–75.

Bischoff, J. L. and Fitzpatrick, J. A. (1991). U-series dating of impure carbonates: an isochron technique using total-sample dissolution. *Geochim. Cosmochim. Acta* **55**, 543–54.

Bloom, A. L., Broecker, W. S., Chappell, J. M. A., Matthews, R. K. and Mesolella, K. J. (1974). Quaternary sea level fluctuations on a tectonic coast: new ^{230}Th/^{234}U dates from the Huon Peninsula, New Guinea. *Quaternary Res.* **4**, 185–205

Bourdon, B., Joron, J.-L. and Allègre, C. J. (1999). A method for ^{231}Pa analysis by thermal ionization mass spectrometry in silicate rocks. *Chem. Geol.* **157**, 147–51.

Bruland, K. W., Bertine, K., Koide, M. and Goldberg, E. D. (1974). History of metal pollution in Southern California coastal zone. *Envir. Sci. Technol.* **8**, 425–32.

Chabaux, F., Cohen, A. S., O'Nions, R. K. and Hein, J. R. (1995). ^{238}U–^{234}U–^{230}Th chronometry of Fe–Mn crusts: growth processes and recovery of thorium isotopic ratios of seawater. *Geochim. Cosmochim. Acta* **59**, 633–8.

Chabaux, F., O'Nions, R. K., Cohen, A. S. and Hein, J. R. (1997). ^{238}U–^{234}U–^{230}Th disequilibrium in hydrogenous oceanic Fe–Mn crusts: palaeoceanographic record or diagenetic alteration? *Geochim. Cosmochim. Acta* **61**, 3619–32.

Chase, Z., Anderson, R. F., Fleisher, M. Q. and Kubik, P. W. (2002). The influence of particle composition and particle flux on scavenging of Th, Pa and Be in the ocean. *Earth Planet. Sci. Lett.* **204**, 215–29.

Chen, J. H., Edwards, R. L. and Wasserburg, G. J. (1986). ^{238}U, ^{234}U and ^{232}Th in seawater. *Earth Planet. Sci. Lett.* **80**, 241–51.

Cheng, H., Edwards, R. L., Hoff, J., Gallup, C. D., Richards, D. A. and Asmerom, Y. (2000). The half-lives of uranium-234 and thorium-230. *Chem. Geol.* **169**, 17–33.

Cheng, H., Edwards, R. L., Murrell, M. T. and Benjamin, T. M. (1998). Uranium thorium protoactinium dating systematics. *Geochim. Cosmochim. Acta* **62**, 3437–52.

Cherdyntsev, V. V. (1969). *Uranium-234*. Atomizdat. Translated by Schmorak, J. *Israel Prog. Sci. Trans.* (1971), 234 pp.

Cherdyntsev, V. V., Kazachevskii, I. V. and Kuz'mina, E. A. (1965). Dating of Pleistocene carbonate formations by the thorium and uranium isotopes. *Geochem. Int.* **2**, 794–801.

Cherdyntsev, V. V., Orlov, D. P., Isabaev, E. A. and Ivanov, V. I. (1961). Isotopic composition of uranium in minerals. *Geochemistry* **10**, 927–36.

Cochran, J. K., Livingston, H. D., Hirschberg, D. J. and Surprenant, L. D. (1987). Natural and anthropogenic radionuclide distributions in the northwest Atlantic Ocean. *Earth Planet. Sci. Lett.* **84**, 135–52.

Crozaz, G., Picciotto, E. and De Brèuck, W. (1964). Antarctic snow chronology with Pb-210. *J. Geophys. Res.* **69**, 2597–604.

De Bièvre, P., Lauer, K. F., Le Duigou, Y. *et al.* (1971). In: Hurrell, M. L. (Ed.), *Proceedings of the International Conference on Chemical and Nuclear Data*, Institution of Civil Engineers London, pp. 221–25.

Edwards, R. L., Chen, J. H. and Wasserburg, G. J. (1987). ^{238}U–^{234}U–^{230}Th–^{232}Th systematics and the precise measurement of time over the past 500,000 years. *Earth Planet. Sci. Lett.* **81**, 175–92.

Edwards, R. L., Cheng, H., Murrell, M. T. and Goldstein, S. J. (1997). Protactinium-231 dating of carbonates by thermal ionization mass spectrometry: implications for Quaternary climate change. *Science* **276**, 782–6.

Edwards, R. L. and Gallup, C. D. (1993. Dating of the Devils Hole calcite vein. *Science* **259**, 1626–7.

Edwards, R. L., Taylor, F. W. and Wasserburg, G. J. (1988). Dating earthquakes with high-precision thorium-230 ages of very young corals. *Earth Planet. Sci. Lett.* **90**, 371–81.

Esat, T. M., McCulloch, M. T., Chappell, J., Pillans, B. and Omura, A. (1999). Rapid fluctuations in sea level recorded at Huon Peninsula during the penultimate deglaciation. *Science* **283**, 197–201.

Frank, M., Eisenhauer, A., Bonn, W. J. *et al.* (1995). Sediment redistribution versus paleoproductivity change: Weddell Sea margin sediment stratigraphy and biogenic particle flux of the last 250 000 years deduced from ^{230}Th$_{ex}$, ^{10}Be and biogenic barium profiles. *Earth Planet. Sci. Lett.* **136**, 559–73.

Gallup, C. D., Cheng, H., Taylor, F. W. and Edwards, R. L. (2002). Direct determination of the timing of sea level change during termination II. *Science* **295**, 310–13.

Goldberg, E. D. (1963). Geochronology with Pb-210. In: *Radioactive Dating*. IAEA, pp. 121–31.

Goldberg, E. D. and Bruland, K. (1974) Radioactive geochronologies. In: Goldberg, E. D. (Ed.), *The Sea*, vol. 5. Wiley Interscience, pp. 451–89.

Goldberg, E. D. and Koide, M. (1962). Geochronological studies of deep sea sediments by the ionium/thorium method. *Geochim. Cosmochim. Acta* **26**, 417–50.

Grün, R. and McDermott, F. (1994). Open system modelling for U-series and ESR dating of teeth. *Quaternary Geochron. (Quaternary Sci. Rev.)* **13**, 121–5.

Grün, R., Schwarcz, H. P. and Chadam, J. (1988). ESR dating of tooth enamel: coupled correction for U-uptake and U-series disequilibrium. *Nucl. Tracks Radiat. Meas.* **14**, 237–41.

Henderson, G. M. (2002). Seawater (^{234}U/^{238}U) during the last 800 thousand years. *Earth Planet Sci. Lett.* **199**, 97–110.

Henderson, G. M. and Burton, K. W. (1999). Using (^{234}U/^{238}U) to assess diffusion rates of isotopic tracers in ferromanganese crusts. *Earth Planet. Sci. Lett.* **170**, 169–79.

Henderson, G. M. and O'Nions, R. K. (1995). ^{234}U/^{238}U ratios in Quaternary planktonic foraminifera. *Geochim. Cosmochim. Acta* **59**, 4685–94.

Imbrie, J., Hays, J. D., Martinson, D. G. *et al.* (1984). The orbital theory of Pleistocene climate: support from a revised chronology of the marine δ^{18}O record. In: Berger, A. L. *et al.* (Eds.), *Milankovitch and Climate, Part 1*. Reidel, pp. 269–305.

Imbrie, J., Mix, A. C. and Martinson, D. G. (1993). Milankovitch theory viewed from Devils Hole. *Nature* **363**, 531–3.

Ivanovich, M. (1982a). Spectroscopic methods. In: Ivanovich, M. and Harmon, R. S. (Eds.), *Uranium Series Disequilibrium Applications to Environmental Problems*. Oxford University Press, pp. 107–44.

Ivanovich, M. (1982b). Uranium series disequilibria applications in geochronology. In: Ivanovich, M. and Harmon, R. S. (Eds.), *Uranium Series Disequilibrium Applications to Environmental Problems*. Oxford University Press, pp. 56–78.

Jonas, M. (1997). Concepts and methods of ESR dating. *Radiat. Meas.* **27**, 943–73.

Karner, D. B. and Muller, R. A. (2000). A causality problem for Milankovitch. *Science* **288**, 2143–4.

Kaufman, A. (1971). U-series dating of Dead Sea carbonates. *Geochim. Cosmochim. Acta* **35**, 1269–81.

Kaufman, A. and Broecker, W. S. (1965). Comparison of Th-230 and C-14 ages for carbonate materials from lakes Lahontan and Bonneville. *J. Geophys. Res.* **70**, 4039–54.

Kaufman, A., Broecker, W. S., Ku, T. L. and Thurber, D. L. (1971). The status of U-series methods of mollusc dating. *Geochim. Cosmochim. Acta* **35**, 1155–83.

Kaufman, A. and Ku, T.-L. (1989). The U-series ages of carnotites and implications regarding their formation. *Geochim. Cosmochim. Acta* **53**, 2675–81.

Kaufman, A., Ku, T.-L. and Luo, S. (1995). Uranium-series dating of carnotites: concordance between ^{230}Th–^{231}Pa ages. *Chem. Geol. (Isot. Geosci. Section)* **120**, 175–81.

Khlapin, V. G. (1926). *Dokl. Akad. Nauk SSSR* 178.

Koide, M., Soutar, A. and Goldberg, E. D. (1972). Marine geochronology with Pb-210. *Earth Planet. Sci. Lett.* **14**, 442–6.

Krishnaswamy, S., Lal, D., Martin, J. M. and Meybek, M. (1971). Geochronology of lake sediments. *Earth Planet. Sci. Lett.* **11**, 407–14.

Ku, T. L. (1965). An evaluation of the U^{234}/U^{238} method as a tool for dating pelagic sediments. *J. Geophys. Res.* **70**, 3457–74.

Ku, T. L. (1976). The uranium series methods of age determination. *Ann. Rev. Earth Planet. Sci.* **4**, 347–79.

Ku, T. L., Bischoff, J. L. and Boersma, A. (1972). Age studies of Mid-Atlantic Ridge sediments near 42 °N and 20 °N. *Deep-Sea Res.* **19**, 233–47.

Ku, T. L., Knauss, K. G. and Mathieu, G. G. (1977). Uranium in open ocean: concentration and isotopic composition. *Deep-Sea Res.* **24**, 1005–17.

Ku, T. L. and Liang, Z. C. (1984). The dating of impure carbonates with decay-series isotopes. *Nucl. Instr. Meth. Phys. Res. A* **223**, 563–71.

Kumar, N., Gwiazda, R., Anderson, R.F. and Froelich, P.N. (1993). ^{231}Pa/^{230}Th ratios in sediments as a proxy for past changes in Southern Ocean productivity. *Nature* **362**, 45–8.

Li, W. X., Lundberg, J., Dickin, A. P. *et al.* (1989). High-precision mass-spectrometric uranium-series dating of cave deposits and implications for palaeoclimate studies. *Nature* **339**, 534–6.

Ludwig, K. R., Simmons, K. R., Szabo, B. J. *et al.* (1992). Mass-spectrometric ^{230}Th–^{234}U–^{238}U dating of the Devils Hole calcite vein. *Science* **258**, 284–7.

Ludwig, K. R., Szabo, B. J., Moore, J. G. and Simmons, K. R. (1991). Crustal subsidence rate off Hawaii determined from ^{234}U/^{238}U ages of drowned coral reefs. *Geology* **19**, 171–4.

Ludwig, K. R. and Titterington, D. M. (1994). Calculation of ^{230}Th/U isochrons, ages, and errors. *Geochim. Cosmochim. Acta* **58**, 5031–42.

Lundberg, J., Ford, D. C., Schwarcz, H. P., Dickin, A. P. and Li, W. X. (1990). Dating sea level in caves: reply. *Nature* **343**, 217–18.

Luo, S. and Ku, T. L. (1991). U-series isochron dating: a generalised method employing total-sample dissolution. *Geochim. Cosmochim. Acta* **55**, 555–64.

Luo, S. and Ku, T.-L. (1999). Oceanic ^{231}Pa/^{230}Th ratio influenced by particle composition and remineralization. *Earth Planet. Sci. Lett.* **167**, 183– 95.

Mangini, A. and Diester-Haass, L. (1983). Excess Th-230 in sediments off NW Africa traces upwelling in the past. In: Suess, A. E. and Thiede, J. (Eds.), *Coastal Upwelling, Part A*. Plenum, pp. 455–70.

McDermott, F., Grün, R., Stringer, C. B. and Hawkesworth, C. J. (1993). Mass-spectrometric U-series dates for Israeli Neanderthal/early modern hominid sites. *Nature* **363**, 252–5.

Meadows, J. W., Armani, R. J., Callis, E. L. and Essling, A. M. (1980). Half-life of ^{230}Th. *Phys. Rev. C* **22**, 750–4.

Milankovitch, M. M. (1941). Canon of insolation and the ice age problem. Koniglich Serbische Akademie, Belgrade. Translation, *Israel Prog. Sci. Trans.*

Neff, U., Bollhöfer, A., Frank, N. and Mangini, A. (1999). Explaining discrepant depth profiles of ^{234}U/^{238}U and ^{230}Th$_{\text{exc}}$ in Mn-crusts. *Geochim. Cosmochim. Acta* **63**, 2211–18.

Osmond, J. K. and Cowart, J. B. (1982). Ground water. In: Ivanovich, M. and Harmon, R. S. (Eds.), *Uranium Series Disequilibrium Applications to Environmental Problems*. Oxford University Press, pp. 202–45.

Picciotto, E. G. and Wilgain, S. (1954). Thorium determination in deep-sea sediments. *Nature* **173**, 632–3.

Pickett, D. A., Murrell, M. T. and Williams, R. W. (1994). Determination of femtogram quantities of protactinium in geological samples by thermal ionization mass spectrometry. *Anal. Chem.* **66**, 1044–9.

Potts, P. J. (1987). *Handbook of Silicate Rock Analysis*. Blackie, 602 pp.

Przybylowicz, W., Schwarcz, H. P. and Latham, A. G. (1991). Dirty calcites. 2. Uranium-series dating of artificial calcite–detritus mixtures. *Chem. Geol. (Isot. Geosci. Section)* **86**, 161–78.

Rink, W. J. (1997). Electron spin resonance (ESR) dating and ESR applications in Quaternary science and archaeometry. *Radiat. Meas.* **27**, 975–1025.

Rink, W. J., Schwarcz, H. P., Lee, H. K., Rees-Jones, J., Rabinovich, R. and Hovers, E. (2001). Electron spin resonance (ESR) and thermal ionization mass-spectrometric (TIMS) ^{230}Th/^{234}U dating of teeth in Middle Paleolithic layers at Amud Cave, Israel. *Geoarchaeology* **16**, 701–17.

Roberts, J., Miranda, C. F. and Muxart, R. (1969). Mesure de la période du protoactinium-231 par microcalorimétrie. *Radiochim. Acta* **11**, 104–8.

Rosholt, J. N., Emiliani, C., Geiss, J., Koczy, F. F. and Wangersky, P. J. (1961). Absolute dating of deep-sea cores by the Pa-231/Th-230 method. *J. Geol.* **69**, 162–85.

Rosholt, J. N., Shields, W. R. and Garner, E. L. (1963). Isotopic fractionation of uranium in sandstone. *Science* **139**, 224–6.

Sackett, W. M. (1960). Protoactinium-231 content of ocean water and sediments. *Science* **132**, 1761–2.

Sackett, W. M. (1964). Measured deposition rates of marine sediments and implications for accumulation rates of extraterrestrial dust. *Ann. N.Y. Acad. Sci.* **119**, 339–46.

Sackett, W. M. (1966). Manganese nodules: thorium-230 : protoactinium-231 ratios. *Science* **154**, 646–7.

Santschi, P. H., Li, Y. H., Adler, D. M., Amdurer, M., Bell, J. and Nyffeler, U. P. (1983). The relative mobility of natural (Th, Pb and Po) and fallout (Pu, Am, Cs) radionuclides in the coastal marine environment: results from model ecosystems (MERL) and Narragansett Bay. *Geochim. Cosmochim. Acta* **47**, 201–10.

Scholten, J. C., Botz, R., Mangini, A., Paetsch, H., Stoffers, P. and Vogelsang, E. (1990). High resolution ^{230}Th$_{ex}$ stratigraphy of sediments from high-latitude areas (Norwegian Sea, Fram Strait). *Earth Planet. Sci. Lett.* **101**, 54–62.

Schwarcz, H. P. (1989). Uranium series dating of Quaternary deposits. *Quaternary Int.* **1**, 7–17.

Schwarcz, H. P. and Blackwell, B. (1991). Archaeological applications. In: Ivanovich, M. and Harmon, R. S. (Eds.), *Uranium Series Disequilibrium Applications to Environmental Problems*, 2nd edn. Oxford University Press, pp. 513–52.

Schwarcz, H. P. and Latham, A. G. (1989). Dirty calcites. 1. Uranium-series dating of contaminated calcite using leachates alone. *Chem. Geol. (Isot. Geosci. Section)* **80**, 35–43.

Schwarcz, H. P. and Skoflek, I. (1982). New dates for the Tata, Hungary archaeological site. *Nature* **295**, 590–1.

Scott, M. R. (1968). Thorium and uranium concentrations and isotope ratios in river sediments. *Earth Planet. Sci. Lett.* **4**, 245–52.

Shirahata, H., Elias, R. W., Patterson, C. C. and Koide, M. (1980). Chronological variations in concentrations and isotopic compositions of anthropogenic atmospheric lead in sediments of a remote subalpine pond. *Geochim. Cosmochim. Acta* **44**, 149–62.

Stirling, C. H., Lee, D.-C., Christensen, J. N. and Halliday, A. N. (2000). High-precision *in situ* ^{238}U–^{234}U–^{230}Th isotopic analysis using laser ablation multiple-collector ICP–MS. *Geochim. Cosmochim. Acta* **64**, 3737–50.

Thurber, D. L., Broecker, W. S., Blanchard, R. L. and Potratz, H. A. (1965). Uranium-series ages of Pacific atoll coral. *Science* **149**, 55–8.

Veeh, H. H. and Burnett, W. C. (1982). Carbonate and phosphate sediments. In: Ivanovich, M. and Harmon, R. S. (Eds.), *Uranium Series Disequilibrium Applications to Environmental Problems*. Oxford University Press, pp. 459–80.

Walter, H.J., Rutgers van der Loeff, M.M. and Hoeltzen, H. (1997). Enhanced scavenging of ^{231}Pa relative to ^{230}Th in the South Atlantic south of the Polar Front: implications for the use of the ^{231}Pa/^{230}Th ratio as a paleoproductivity proxy. *Earth Planet. Sci. Lett.* **149**, 85–100.

Winograd, I.J. (1990). Dating sea level in caves: comment. *Nature* **343**, 217–18.

Winograd, I.J., Coplen, T.B., Landwehr, J.M. *et al.* (1992). Continuous 500,000-year climate record from vein calcite in Devils Hole, Nevada. *Science* **258**, 284–7.

Yang, H.-S., Nozaki, Y., Sakai, H. and Masuda, A. (1986). The distribution of ^{230}Th and ^{231}Pa in the deep-sea surface sediments of the Pacific Ocean. *Geochim. Cosmochim. Acta* **50**, 81–9.

Yokoyama, Y. and Nguyen H.V. (1980). Direct and non-destructive dating of marine sediments, manganese nodules, and corals by high resolution γ-ray spectrometry. In: Goldberg, E. D., Horibe, Y. and Saruhashi, K. (Eds.), *Isotope Marine Chemistry.* Uchida Rokkaku, Ch. 14.

Yu, E.-F., François, R. and Bacon, M.P. (1996). Similar rates of modern and last-glacial ocean thermohaline circulation inferred from radiochemical data. *Nature* **379**, 689–94.

Zhao, J.-x., Xia, Q. and Collerson, K.D. (2001). Timing and duration of the Last Interglacial inferred from high resolution U-series chronology of stalagmite growth in Southern Hemisphere. *Earth Planet. Sci. Lett.* **184**, 635–44.

13 U-series geochemistry of igneous systems

U-series dating of sedimentary rocks was discussed in the previous chapter. These isotopes can also be used as dating tools for igneous rocks; however, their application as isotopic tracers is probably more important. The short half-lives of the decay-series nuclides make them ideally suited to studies on magma segregation from the mantle and magma evolution in the crust, since these processes operate over similar time periods. With a half-life of 75.4 kyr, ^{230}Th is by far the most important of these geological tracers, and will be the main focus of this chapter. However, attention will also be paid to other shorter-lived isotopes used in conjunction with thorium. ***Note that all isotopic abundances of U-series nuclides referred to in this chapter are expressed as activities, unless specifically stated to be atomic.***

Until recently, all U-series measurements on igneous rocks were made by α spectrometry, as for sedimentary rocks (section 12.2). Following the application of mass spectrometry to U-series dating of carbonates, it was quickly applied to igneous systems (Goldstein *et al.*, 1989). However, analysis of ^{230}Th in silicate rocks is made more difficult by their very large atomic ^{232}Th/^{230}Th ratios. For example, a basalt with a typical Th/U concentration ratio of 4, and in secular equilibrium, will have a ^{232}Th/^{230}Th atomic ratio of 240 000. For a single-sector mass spectrometer with an abundance sensitivity of 1 ppm at 2 a.m.u. (section 2.3.1), the ^{232}Th peak will then generate a peak tail at mass 230 which is one-quarter of the size of the ^{230}Th peak. Normally, the abundance sensitivity is improved using an energy filter (e.g. Cohen *et al.*, 1992; section 2.3.1). However, McDermott *et al.* (1993) showed that relatively accurate ^{230}Th data can be obtained without a filter if the exponentially curved baseline shape is carefully interpolated under the ^{230}Th peak.

In addition to ^{230}Th, there are five shorter-lived nuclides in the U and Th decay schemes that may be useful in the study of igneous systems. These are shown in Fig. 12.2, but for convenience they are summarised here. The equilibration times shown (t_{Eq}) represent the maximum useful range of each species, on the assumption that its activity will be within error of secular equilibrium after five half-lives. Each arrow represents a decay transition, but only nuclides relevant to volcanic systems are shown.

^{238}U > > > >	^{230}Th >	^{226}Ra > > > > > >	^{210}Pb > > >	^{206}Pb
$t_{1/2}$, yr	75 200	1600	22	
t_{Eq}, yr	400 000	8000	100	

^{235}U > >	^{231}Pa > > > > > > > > > >	^{207}Pb
$t_{1/2}$, yr	34 300	
t_{Eq}, yr	170 000	

^{232}Th >	^{228}Ra > >	^{228}Th > > > > > > > >	^{208}Pb
$t_{1/2}$, yr	5.77	1.91	
t_{Eq}, yr	30	10	

Disequilibrium between short-lived nuclei in volcanic rocks was discovered very early (e.g. Joly, 1909), but has only recently been the subject of detailed study. ^{210}Pb was observed to be out of secular equilibrium with ^{230}Th in ocean-island lavas by Oversby and Gast (1968). This demonstrated the occurrence of Th/Pb fractionation within 100 yr of eruption. However, the chemistry of Pb is so different from the other nuclides that it is difficult to use in petrogenetic interpretations. It will not be discussed in detail here. ^{228}Ra and ^{228}Th can be used to measure even shorter-period changes in magma chemistry, but have only rarely been found out of isotopic equilibrium.

Of the other short-lived nuclides, ^{226}Ra has been the most widely used. It has traditionally been measured by radioactive counting (sometimes *via* its shorter-lived decay products), but despite its short half-life, recent advances have allowed its measurement by mass spectrometry (e.g. Cohen and O'Nions, 1991). This permits ^{226}Ra abundances in the femtogram range (10^{-9} ppm) to be determined to better than 1% precision. ^{231}Pa abundances in igneous rocks are too low to measure by α spectrometry because of the low abundance of the parent isotope, ^{235}U. However, with the application of mass spectrometry, ^{231}Pa measurements are also possible in the femtogram range. Hence this nuclide also shows promise as a useful geochemical and chronological tool (Goldstein *et al.*, 1993).

13.1 Geochronology of volcanic rocks

In some ways, U-series systems in igneous rocks are simpler than carbonates, because ^{234}U and ^{238}U are always effectively in secular equilibrium. On the other hand, igneous systems are more complex than pure carbonates in that they invariably contain initial Th at the time of cooling. Hence, a U–Th isochron diagram must normally be used to date igneous rocks by the ^{230}Th method.

13.1.1 The U–Th isochron diagram

After time *t*, the net ^{230}Th activity in a silicate sample is the sum of ^{230}Th growth from U decay and the residue of partially decayed initial ^{230}Th. In other words, we sum equations [12.8] and [12.24]:

$$^{230}\mathrm{Th_P} = {}^{230}\mathrm{Th_I}\,\mathrm{e}^{-\lambda_{230}t} + {}^{238}\mathrm{U}(1 - \mathrm{e}^{-\lambda_{230}t}) \qquad [13.1]$$

It is convenient to divide through by ^{232}Th, whose activity is effectively constant between *t* initial and the present:

$$\left(\frac{^{230}\mathrm{Th}}{^{232}\mathrm{Th}}\right)_\mathrm{P} = \left(\frac{^{230}\mathrm{Th}}{^{232}\mathrm{Th}}\right)_\mathrm{I}\mathrm{e}^{-\lambda_{230}t} + \frac{^{238}\mathrm{U}}{^{232}\mathrm{Th}}(1 - \mathrm{e}^{-\lambda_{230}t}) \qquad [13.2]$$

This is the equation for a straight line, and is plotted on a diagram of ^{230}Th/^{232}Th activity ratio against ^{238}U/^{232}Th activity ratio (Fig. 13.1) which is analogous to the Rb–Sr isochron diagram. As with the Rb–Sr system, a suite of co-genetic samples of the same age defines a linear array whose slope yields the age. However, because the ^{230}Th daughter product is itself subject to decay, this leads to more complex isotope systematics.

The evolution of igneous systems on the U–Th isochron diagram depends on their composition with respect to a state of secular equilibrium. Samples in secular equilibrium must, by definition, have equal ^{230}Th and ^{238}U activities. Hence, they must have equal ^{230}Th/^{232}Th and ^{238}U/^{232}Th activity ratios in Fig. 13.1. Such samples lie on a slope of unity in this diagram, called the 'equiline' by Allègre and Condomines (1976).

Now, considering a suite of rock or mineral samples; at the time of their crystallisation they have variable U/Th ratios but a constant (initial) ^{230}Th/^{232}Th activity ratio, forming a horizontal line in Fig. 13.1. The point of intersection of this array with the equiline must by definition remain invariant, since it starts its closed-system evolution already in secular equilibrium. However, all other samples in the suite evolve with time. Those to the right of the invariant point are daughter (^{230}Th) deficient relative to ^{238}U, and ^{230}Th therefore builds up with time. They move vertically upwards until they also reach the equiline (secular equilibrium). Those to the left of the equiline have daughter (^{230}Th) excess relative to the parent. They move vertically downwards with time until they reach the equiline. The more initial thorium that is present, the higher the intersection between the initial composition and the equiline. Conversely, when no initial Th is present (as in pure carbonates), evolution begins along the *x* axis. Hence, in a co-genetic suite that has not yet reached secular equilibrium, the initial Th isotope ratio is given by the intersection of the isochron array with the equiline. It is not the intercept on the *y* axis.

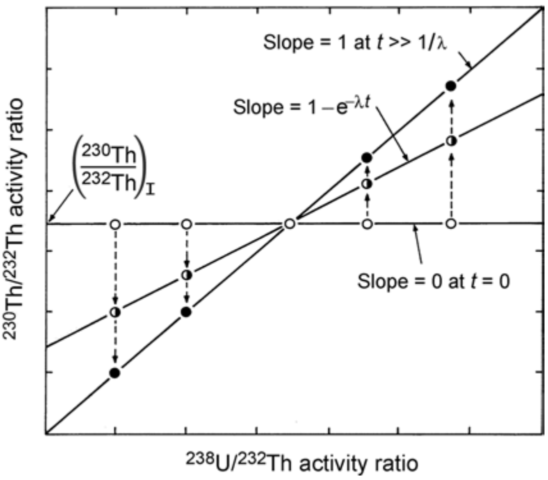

Fig. 13.1. Isotopic evolution of igneous rocks on the ^{230}Th/^{232}Th *versus* ^{238}U/^{232}Th isochron diagram. Symbols: (○) time t = 0; (◑) samples after elapsed time *t*; (●) samples after effectively infinite time ($t \gg 1/\lambda$).

The U–Th isochron method was first applied to the dating of igneous minerals by Cerrai *et al.* (1965) and subsequently tested by Kigoshi (1967). Kigoshi used the method to date three igneous rocks of different ages: a Cretaceous granite (effectively of infinite age), a 35.7-kyr-old pumice (dated by ^{14}C on a wood inclusion) and a lava of historical (effectively zero) age. His results (Fig. 13.2) demonstrated the method to be effective. The old granite samples lie on the equiline, the pumice samples yield a U–Th isochron age of 38 kyr, and the historical lava yields a zero slope.

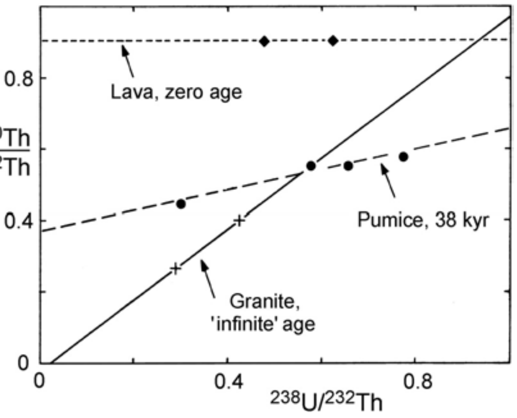

Fig. 13.2. $^{230}Th/^{232}Th$ *versus* $^{238}U/^{232}Th$ isochron diagram for three suites of leachates from whole-rock samples. After Kigoshi (1967).

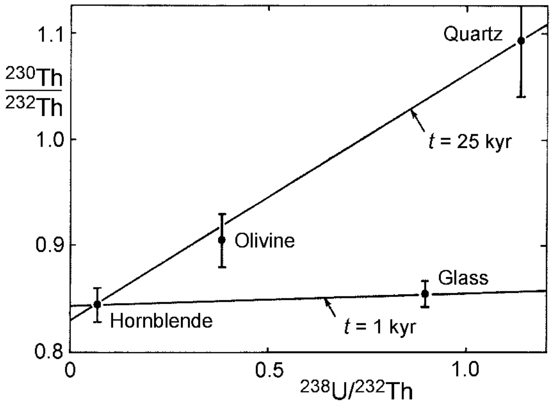

Fig. 13.3. $^{230}Th/^{232}Th$ *versus* $^{238}U/^{232}Th$ isochron diagram for hornblende–olivine–quartz phenocryst assemblages and glass matrix from a Mono Craters rhyolite (California), showing isotopic discordancy between phenocrysts and glass. After Allègre (1968).

To achieve a high-precision age from the U–Th method, a reasonable spread of $^{238}U/^{232}Th$ activity ratios is needed within each sample suite. Kigoshi carried over the leaching techniques of carbonate dating in order to maximise this spread of U/Th activity ratios. However, this is a potentially dangerous technique, since in the leaching process disequilibrium may be introduced between different parents and daughters in the decay series. For example, ^{230}Th may be preferentially leached relative to ^{238}U from radiation-damaged lattice sites, yielding spuriously old ages. This is called the 'hot-atom effect', which also gives rise to variable $^{234}U/^{238}U$ ratios in natural waters (section 12.3.1).

Taddeucci *et al.* (1967) avoided the complexities of the 'hot-atom' effect by using conventional physical separation and total dissolution of minerals to date five rhyolitic tuffs from the Mono Craters of California. However, U–Th dates on phenocryst–glass pairs did not display good agreement with other methods. For example, the hornblende–glass pair gave an apparent U–Th age of only 1 kyr, whereas K–Ar dating yielded an age of about 7 kyr and ^{14}C dating of undisturbed lake sediments near the volcano gave a minimum eruptive age of 2.2 kyr.

Allègre (1968) subsequently showed that separated phenocryst phases from one of the rocks studied by Taddeucci *et al.* defined an isochron age of 25 kyr (Fig. 13.3). The implication of these results is that the different analytical methods are dating different events. U–Th ages on phenocryst minerals probably date their crystallisation in a magma chamber, whereas the K–Ar method dates the time of eruption (if outgassing of volatiles during eruption was effective). The hornblende–glass age is meaningless, since these two systems did not close at the same time. The discordance between dating methods is therefore caused by the relatively long residence period of magma in the chamber, after phenocryst formation.

In contrast to the Mono Craters case, Allègre and Condomines (1976) and Condomines and Allègre (1980) were able to achieve good linearity of phenocryst and whole-rock points in dating studies of the Irazu volcano (Costa Rica) and Stromboli volcano (Italy). This implies that, in these systems, phenocryst growth only briefly preceded eruption. On the other hand, Capaldi and Pece (1981) claimed to find gross Th isotope disequilibrium between different mineral phases in modern lavas from Etna, Vesuvius and Stromboli. This led Capaldi *et al.* (1982) to completely write off the U–Th method as a dating tool. However, in repeat analyses of the samples from the same Etna and Vesuvius lavas, Hémond and Condomines (1985) were unable to find mineralogical disequilibrium of Th isotope ratios. This suggests that Capaldi *et al.* (1982) over-reacted when they dismissed the method. It is true that there are quite a number of instances in which Th isotope disequilibrium has been found on a mineralogical scale (Capaldi *et al.*, 1985). However, if phenocryst phases are screened by petrographic examination to exclude entrained xenocrysts then many young lavas can yield accurate U–Th crystallisation ages (e.g. Condomines *et al.*, 1982).

The analysis of zircon as a mineral phase for U–Th dating was proposed in very early work (e.g. Cerrai *et al.*, 1965), but not exploited much due to the low abundances of zircons in most rocks. However, the high uranium content of zircons often generates high U/Th ratios, which can yield good isochron fits. Hence, there has been renewed interest in U–Th dating of zircons with the development of mass-spectrometric methods for the analysis of small samples.

Condomines (1997) used conventional TIMS analysis to demonstrate the usefulness of U–Th zircon analysis on a young trachytic rock in the Puy de Dôme area of France. In this sample, the zircon analysis lay on the same isochron as several other mineral phases, and the isochron slope was consistent with the known age of eruption from other methods. However, more commonly, U–Th dating of zircon has produced more complex age relationships. For example, Charlier and Zellmer (2000) found that zircon fractions from a rhyolite in the Taupo Volcanic Zone (New Zealand) gave variable whole-rock-zircon ages, depending on the size fraction of the zircon analysed. This suggested that the zircon grains were probably zoned, with cores about 27 kyr older than the age of eruption, overgrown by rims only 2 kyr older than the age of eruption.

Problems of internal zircon heterogeneity can be avoided by using *in situ* micro-analysis. This was first demonstrated by Reid *et al.* (1997), using the ion microprobe to analyse zircons from the Long Valley Caldera (California). Zircons were analysed from two domes, one 115 kyr old and one less than 1 kyr old, located a few kilometres apart. Each zircon analysis was combined with the whole-rock composition to determine a two-point isochron that Reid *et al.* termed a 'zircon model age'. These model ages were somewhat scattered, due to a combination of relatively large analytical errors and some geological scatter. However, it was observed that the average zircon model age for the two domes was the same (Fig. 13.4), despite their different eruption ages. This suggests that the two domes might be sampling the same relatively long-lived magma chamber, which cooled through the zircon saturation temperature about 230 kyr ago, causing the crystallisation of a crop of zircon grains that subsequently remained entrained in the viscous magma. In view of the ability of ion-microprobe analysis to analyse many grains from complex heterogeneous systems, this would appear to be a technique with strong potential for studying the evolution of shallow felsic magma chambers.

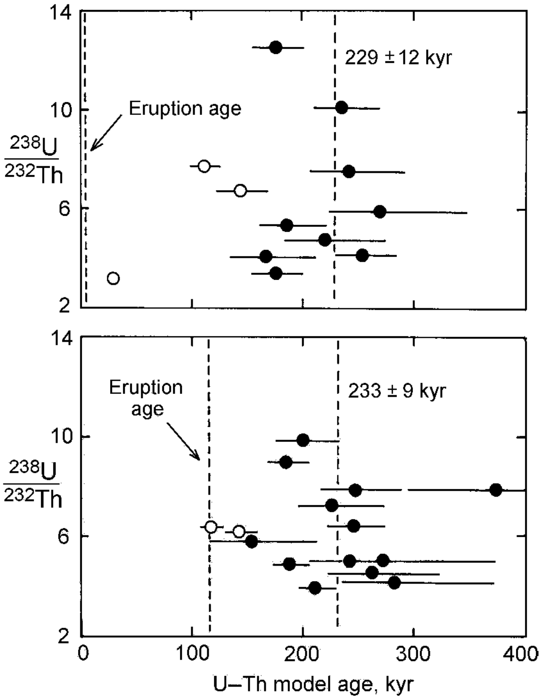

Fig. 13.4. Comparison of 'zircon model ages' in two domes of different eruption ages from the Long Valley Caldera, California. Open symbols were omitted from the calculations of averages. Errors are 1σ. After Reid *et al.* (1997).

13.1.2 Ra–Th isochron diagrams

In view of its short equilibration time of 8000 yr, ^{226}Ra is useful in studies of geologically rapid magmatic processes. However, a disadvantage is the lack of a longer-lived radium isotope to normalise against, in order to exclude chemical fractionation. Williams *et al.* (1986) proposed that this problem might be overcome by using barium as a proxy for a stable radium isotope. For this to be useful, the two elements must have similar distribution coefficients, so that they behave in the same way during partial melting and crystal fractionation.

If barium is an accurate analogue for stable radium, the Th–Ra/[Ba] method can be used in conventional isochron dating of magma-fractionation events. Reagan *et al.* (1992) applied this method to the dating of anorthosite phenocrysts in phonolitic magmas of Mount Erebus volcano, Antarctica. The data are used here to demonstrate the use of the Th–Ra/[Ba] isochron diagram for radium (which is analogous to the U–Th isochron diagram). This is based on the equation

$$\frac{(^{226}\mathrm{Ra})_\mathrm{P}}{[\mathrm{Ba}]} = \frac{(^{226}\mathrm{Ra})_\mathrm{I}}{[\mathrm{Ba}]}\mathrm{e}^{-\lambda_{226}t} + \frac{^{230}\mathrm{Th}}{[\mathrm{Ba}]}(1 - \mathrm{e}^{-\lambda_{226}t}) \qquad [13.3]$$

where square brackets denote concentrations. This is analogous to equation [13.2] for the U–Th system.

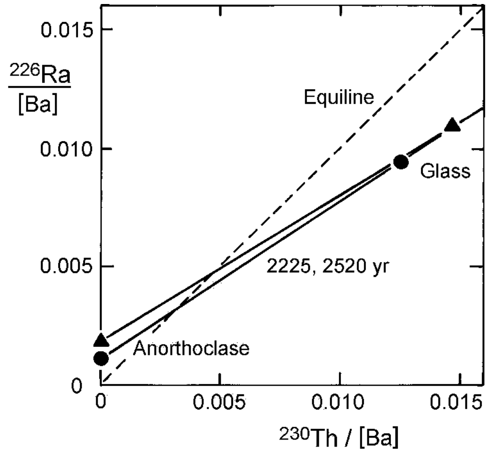

Fig. 13.5. Th–Ra/[Ba] isochron diagram for anorthosite–glass pairs from the 1984 and 1988 phonolite eruptions of Mt Erebus, Antarctica. After Reagan *et al.* (1992).

Because anorthoclase readily takes up divalent but not trivalent ions, it has Th/Ba ratios of effectively zero. The isochron age is then determined by the glass points, yielding crystallisation ages of about 2.5 kyr for samples from two recent eruptions (Fig. 13.5). However, it may be dangerous to rely on two-point phenocryst–glass ages without other supporting evidence (section 13.1.1). A more complete example of a Th–Ra/[Ba] isochron was provided by Schaefer *et al.* (1993) on the 1985 pumice eruption of Nevado del Ruiz volcano, Colombia. In this case the glass point was collinear with three different mineral phases (and the whole-rock), yielding a best-fit age of 6.1 ± 0.5 kyr. This result was interpreted as the average age of an extended period of crystal fractionation, rather than a discrete magmatic differentiation event.

Ra–Th isotope data can also be presented on an 'alternative' isochron diagram that was first used by Kaufman (section 12.4.3) for dating dirty calcite. We will take the opportunity here to examine this format and compare it with the conventional isochron plot, using data for MORB glasses from the East Pacific Rise (Rubin and Macdougall, 1990).

If a magma suite is extracted from a source in secular equilibrium and with homogeneous trace-element chemistry, then all zero-age lavas should have a constant ratio of ^{226}Ra activity/Ba concentration. This is equivalent in the alternative isochron diagram to a straight line through the origin (Fig. 13.6). Distribution along the line is due to fractionation of ^{226}Ra and Ba relative to Th, which is presumed to have occurred during partial melting. The intersection of this zero-age fractionation line with the equiline defines the Ba/Th ratio of the source (on the x axis). After separation from the source, magmas evolve vertically towards the equiline. Since the half-life of ^{226}Ra is much less than that of the parent (^{230}Th), the latter can be considered effectively stable over the time periods under consideration (<10 kyr). Therefore, for a theoretical sample with zero initial thorium, the decay equation is as follows:

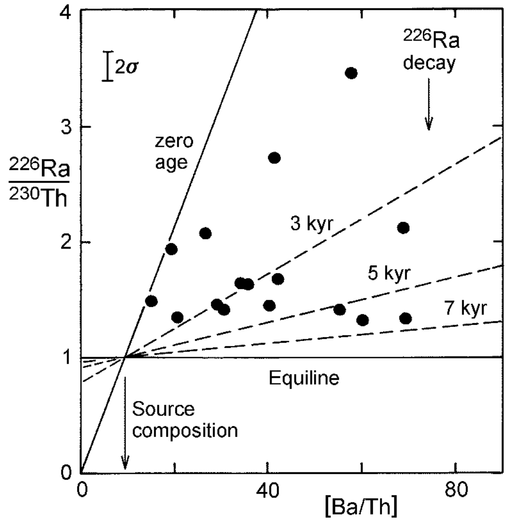

Fig. 13.6. Ra/Th–[Ba/Th] alternative isochron diagram for MORB glasses from the East Pacific Rise. For discussion, see the text. After Rubin and Macdougall (1990).

$$\frac{^{226}\mathrm{Ra}}{^{230}\mathrm{Th}} = 1 - \mathrm{e}^{-\lambda_{226}t} \qquad [13.4]$$

Therefore, ages are given by the intersection of isochrons on the y axis. However, since all samples have Ba/Th ratios greater than that of the source, isotopic evolution is by decay of excess ^{226}Ra. Therefore, it is convenient to show the ages as isochron lines for a given source composition (Fig. 13.6).

A problem with this study is that somewhat abnormal U–Th analyses were obtained on the same samples. However, the radium data have subsequently been confirmed by mass-spectrometric ^{226}Ra analysis of MORB glasses from the Juan de Fuca, Gorda, and East Pacific ridges (Volpe and Goldstein, 1993). Glasses from the ridge axis yield excess ^{226}Ra activities up to 2.5 times greater than the ^{230}Th activity. In contrast, off-axis glasses from these ridges yield ^{226}Ra/^{230}Th activity ratios of 1.00, as expected from their greater age. This gives us confidence that radium has not been mobilised in these glasses by sea-floor alteration, and that the disequilibrium data reflect processes of generation and evolution of magma.

13.1.3 U-series model age dating

The application of 'zircon model ages' to igneous systems was discussed in section 13.1.1. However, the first application of U-series model ages was actually to the dating of MORB samples. It is not practical to date these using the U–Th isochron technique, since MORB glasses have a narrow range of U–Th ratios, and phenocryst phases are rare. However, the consistency of mass-spectrometric Th isotope data from the crests of the Juan de Fuca and Gorda ridges prompted Goldstein *et al.* (1991) to apply a model age method as a dating tool for young off-axis MORB glasses. In this approach the *initial* activity ratio of the off-axis samples is estimated by analysing on-axis samples from the same ridge segment. Goldstein *et al.* demonstrated this approach for three ridge segments, of which two Juan de Fuca ridge segments are shown in Fig. 13.7.

In order to be sure that these older MORB glasses remained as closed systems for U and Th, and were not affected by sea-floor alteration, the samples were subjected to chemical screening, in addition to the normal processes of hand picking and surface leaching of glass chips (Goldstein *et al.*, 1989; 1991). Sensitive chemical screening was provided by boron analysis, since fresh glasses have boron levels of about 1 ppm, whereas altered glasses have boron contents more than an order of magnitude higher (Spivak and Edmond, 1987). In addition, samples were analysed for the $^{234}U/^{238}U$ activity, since alteration may cause this ratio to increase or decrease (Macdougall *et al.*, 1979). However, this test is probably less sensitive, since seawater has a $^{234}U/^{238}U$ activity ratio only slightly above unity.

Goldstein *et al.* (1991) compared model U–Th ages from samples on both sides of the ridge axis with the spreading rate determined from magnetic data. Generally, the fit was found to be quite good, although some asymmetry is apparent in the U–Th ages. Because the two ridges have the same sense of asymmetry, it is possible that this is a real feature of the spreading geometry. However, there are presently insufficient data for one to be confident of this interpretation. On the other hand, complexity in the age structure of the ridge is suggested by low apparent U–Th ages just below the summit of the Endeavour segment (open symbols in Fig. 13.7). Goldstein *et al.* attributed these ages to young lavas that had erupted near the ridge summit and flowed down over its flanks.

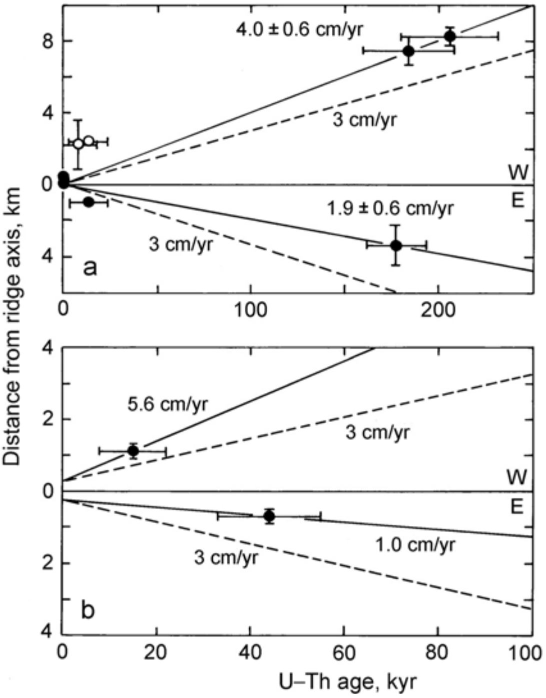

Fig. 13.7. Plot of U–Th model ages compared with distance from the axis of the Juan de Fuca ridge, East Pacific: (a) the Endeavour segment and (b) the Southern segment. Magnetically determined spreading rates are shown by dashed lines. Open symbols indicate abnormally young ages. After Goldstein *et al.* (1991).

Volpe and Goldstein (1993) showed that, within a given ocean-ridge segment, $^{230}Th/[Ba]$ ratios were constant in lavas of different ages (below 10 kyr). This implies that elemental fractionation effects were constant over this time. Hence, it is also reasonable to assume that constant $^{226}Ra/^{230}Th$ ratios pertained at the time of eruption. In this case, $^{226}Ra/^{230}Th$ ratios can be used to determine model ages for very young ocean-ridge basalts, in a similar way to the use of U–Th data. With this approach, the variation of $^{226}Ra/^{230}Th$ ratios in a suite of lavas from the axial valley of the Juan de Fuca ridge allowed the calculation of relative age differences of up to 1200 yr between different eruptions.

The first precise ^{231}Pa analyses of igneous rocks were performed by Goldstein *et al.* (1993) on MORB glasses from the East Pacific Rise and the Juan de Fuca and Gorda ridges. On-axis samples yielded $^{231}Pa/^{235}U$ activity ratios of up to 2.9, whereas off-axis samples returned to secular equilibrium over about 150 kyr. Protactinium data cannot be plotted on an isochron diagram because no suitable stable analogue to ^{231}Pa has yet been identified. However, Goldstein *et al.* argued that, within single ridge segments, U–Pa model ages could be determined in a manner analogous to U–Th and Th–Ra model ages. By assuming a zero age in the sample from each axial valley with highest ^{231}Pa/^{235}U activity, Goldstein *et al.* calculated model ages for other axial and off-axis samples that were within error of their U–Th model ages.

13.2 Magma-chamber evolution

Just as initial Sr isotope compositions are useful as a geochemical tracer when using the Rb–Sr method, initial Th isotope compositions are also a useful product of the U–Th dating method. One area where they have proved particularly valuable is in studying magma-chamber evolution.

In the same way that Th isotope evolution in a volcanic rock can be used to date crystallisation, Th isotope evolution between successive eruptions can be used to date the residence of magma in a chamber. We can use the same equation as for the rock system, except that what we input as the 'final composition' on the left-hand side is actually the initial Th activity ratio of a magma at the time of eruption (E), while the Th activity ratio on the right-hand side of the equations is the composition of the magma in the chamber at the time of influx (I), simplistically, from the mantle. The quantity t then represents the residence time of the magma batch in the chamber (with all nuclide ratios in activities):

$$\left(\frac{^{230}\text{Th}}{^{232}\text{Th}}\right)_{\text{E}} = \left(\frac{^{230}\text{Th}}{^{232}\text{Th}}\right)_{\text{I}} \text{e}^{-\lambda_{230}t} + \frac{^{238}\text{U}}{^{232}\text{Th}}\left(1 - \text{e}^{-\lambda_{230}t}\right) \qquad [13.5]$$

It is best to rearrange [13.5] to gather the exponent terms in one place:

$$\left(\frac{^{230}\text{Th}}{^{232}\text{Th}}\right)_{\text{E}} = \left[\left(\frac{^{230}\text{Th}}{^{232}\text{Th}}\right)_{\text{I}} - \frac{^{238}\text{U}}{^{232}\text{Th}}\right]\text{e}^{-\lambda_{230}t} + \frac{^{238}\text{U}}{^{232}\text{Th}} \qquad [13.6]$$

Allègre and Condomines (1976) preferred to refer all times to the present, introducing T as the age of influx into the chamber and t as the time of eruption. Then

$$\left(\frac{^{230}\text{Th}}{^{232}\text{Th}}\right)_{t} = \left[\left(\frac{^{230}\text{Th}}{^{232}\text{Th}}\right)_{T} - \frac{^{238}\text{U}}{^{232}\text{Th}}\right]\text{e}^{\lambda_{230}(t-T)} + \frac{^{238}\text{U}}{^{232}\text{Th}} \qquad [13.7]$$

Just as we make a closed-system assumption in the case of rock dating, so we must assume that the magma in the chamber remains a closed system to U and Th during its evolution and eruption. This assumption should not be upset by Rayleigh crystal fractionation, since the distribution coefficients of U and Th are so low that both elements normally remain entirely in the liquid.

13.2.1 The Th isotope evolution diagram

The ^{230}Th evolution of magmas can be shown on U–Th isochron diagrams, but it is also convenient to display isotopic evolution on a plot of Th activity ratio against time (Fig. 13.8). This plot is analogous to the evolution diagrams of Sr or Nd isotope composition against time (e.g. section 4.2), but because the half-life of ^{230}Th is short relative to the time periods under study, the x axis must be calibrated in log time.

A magma body in secular equilibrium must maintain its ^{230}Th/^{232}Th activity ratio. Hence, such evolution is described by a horizontal line in Fig. 13.8. If the system undergoes U/Th fractionation (horizontal displacement from M_0 to M or M' on the inset diagrams) then the ^{230}Th/^{232}Th activity ratio of the magma will evolve over time to regain secular equilibrium. A magma enriched in ^{238}U/^{230}Th (to the right of the equiline on the inset, with activity M) defines a line of negative slope on the main diagram. Similarly, a

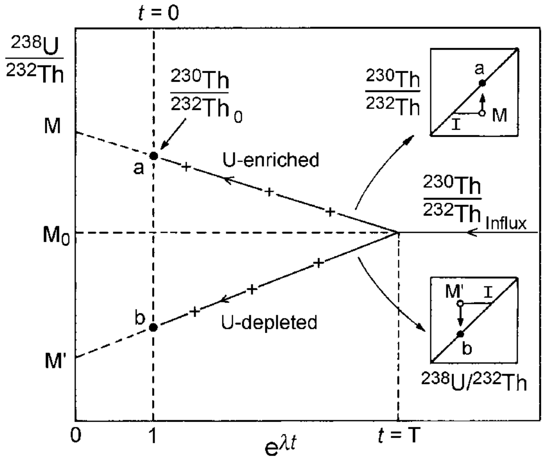

Fig. 13.8. Schematic diagram of Th isotope evolution against time for two closed-system magma chambers, displaying (a) daughter deficiency and b) daughter excess. Insets show U/Th fractionation and subsequent evolution on U–Th isochron diagrams. After Condomines *et al.* (1982).

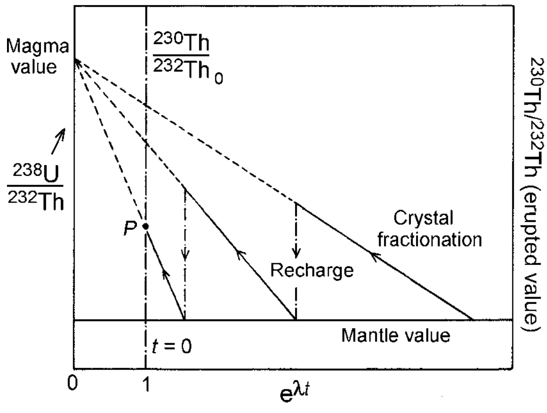

Fig. 13.9. Schematic illustration of the thorium isotope evolution of a periodically tapped and re-filled magma chamber with a constant magmatic U/Th ratio (defined by the intercept on the *y* axis). *P* = present-day Th activity ratio. After Condomines *et al.* (1982).

magma depleted in $^{238}U/^{230}Th$ (activity ratio M' on the inset) defines an evolution line of positive slope on the main diagram. If we extrapolate the growth lines to $e^{\lambda t} = 0$, then we can see from equation [13.6] that the y ordinate in the main diagram describes the $^{238}U/^{232}Th$ activity ratio of the evolving magma.

The U–Th isotope system is a very powerful tool for studying magma-chamber evolution because the half-life of ^{230}Th (75.4 kyr) is of the same order of magnitude as the time interval between magma-chamber events. However, a significant data-base is needed to unravel the history of most volcanoes, which usually involve repeated magma injection and eruption events. A simple scenario of this type is illustrated in Fig. 13.9. In this case a primary mantle source in secular equilibrium supplies (over a period of time) a series of magma batches that have a constant disequilibrium $^{238}U/^{232}Th$ activity ratio generated by the partial melting process (see below). After a period of magma evolution in a high-level chamber (sloping line), the chamber is emptied by eruption and re-filled, causing a kick back to the starting composition. However, in the real world, mixing of magmas of different ages is likely to occur, and this will generate a more complex pattern of magma evolution.

Early studies (Allègre and Condomines, 1976; Condomines and Allègre, 1980) lacked sufficient data to resolve the magmatic history of long-lived volcanoes; hence, their results were ambiguous. However, a later study by Condomines *et al.* (1982) provided enough data to interpret the history of the Etna volcano in Sicily. Thirteen mineral–whole-rock U–Th isochrons were determined, together with analyses of recent lavas. The results were plotted on a Th isotope evolution diagram (Fig. 13.10) and an isochron diagram (Fig. 13.11).

On the Th isotope evolution diagram (Fig. 13.10) the Etna data provide evidence for four episodes of eruption and replenishment of magma, the last three of which (numbered) tie in with known dates of major caldera-collapse events. Between these events, small magma tappings monitor Th isotope evolution in the high-level chamber. However, $^{230}Th/^{232}Th$ activities fall too rapidly during these periods to be explained by closed-system evolution, given the observed range of U/Th activity ratios (the hatched band on the left-hand axis). Therefore, Condomines *et al.* invoked a magma-mixing model to explain these steep trends, suggesting that the sub-horizontal evolution line represented a deep, long-lived alkali basalt reservoir that continually supplied magma to higher levels, where a low-$^{230}Th/^{232}Th$ tholeiitic component was added intermittently.

Initial ratios of lavas at the time of eruption are plotted on a U–Th isochron diagram in Fig. 13.11. The data suggest mixing between an old magma nearly in secular equilibrium and a young one substantially out of equilibrium. Condomines *et al.* argued that the low-$^{230}Th/^{232}Th$-ratio (young) component could not be a crustal contaminant, since this should be close to secular equilibrium, whereas Fig. 13.10 indicates it to be far from equilibrium. However, this does not exclude the possibility of sediment contamination of the mantle source of these magmas. The straight line (1) represents an instantaneous-mixing model whereas the curved lines (2 and 3) model progressive mixing over a time interval. Present-day ratios (of old lavas) are not plotted on Fig. 13.11 because they do not yield any useful information about magma evolution.

13.2.2 Short-lived species in magma evolution

The first detailed application of very-short-lived species to magma evolution was made by Capaldi *et al.* (1976) on the volcanoes of Etna and Stromboli. However, one of the most interesting applications of these species is in studying the genesis of carbonatite magma, as exemplified in Oldoinyo Lengai volcano, in the East African Rift of Tanzania. The 1960 and 1988 carbonatite eruptions from this volcano were studied, respectively, by Williams *et al.* (1986) and Pyle *et al.* (1991). Both of these eruptions exhibited strong disequilibrium between ^{228}Ra ($t_{1/2} = 5.77$ yr) and its

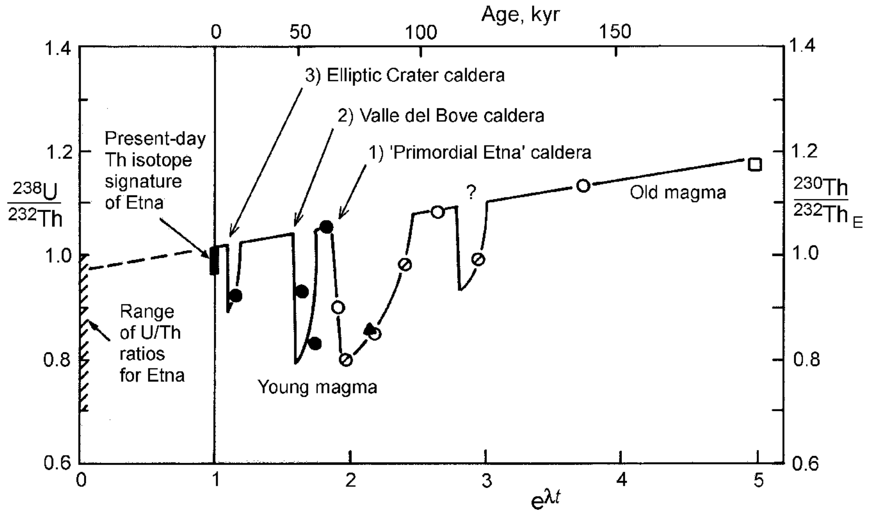

Fig. 13.10. Thorium isotope evolution diagram, showing the history of Etna volcano. Three magma-influx–mixing events correspond to known episodes of caldera formation, possibly preceded by an earlier fourth event. Symbols indicate erupted products of different ages. After Condomines *et al.* (1982).

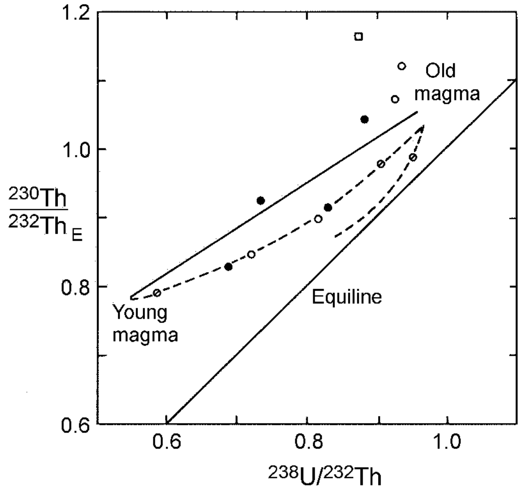

Fig. 13.11. U–Th isochron diagram showing activity data for Etna lavas at the time of eruption. The data array implies mixing between an old U-rich magma and a young U-depleted magma. Symbols are as in Fig. 13.10. After Condomines *et al.* (1982).

ultimate parent, ^{232}Th. The 1988 eruption also demonstrated ^{228}Th disequilibrium ($t_{1/2} = 1.91$ yr); however, it was not possible to test for this phenomenon in the 1960 eruption, since the samples had reached secular equilibrium in the twenty years between sampling and analysis! The so-called '1963' eruption of Williams *et al.* (1986) is also excluded from this discussion because of uncertainty about its eruption age (Williams *et al.*, 1988).

It is now generally agreed that carbonatites are formed by the evolution of per-alkaline magmas under conditions of strong CO_2 enrichment, probably involving the segregation of immiscible droplets of carbonate magma from a silicate magma host (e.g. Pyle *et al.*, 1991). The discovery of ^{228}Ra disequilibrium in the Oldoinyo carbonatites suggests that the segregation process probably occurred shortly before eruption. Over this timescale, ^{226}Ra ($t_{1/2} = 1620$ yr) can be treated effectively as a stable isotope. Therefore the ^{228}Ra decay equation can be divided by ^{226}Ra to yield an isochron relation analogous to equation [13.2] (Capaldi *et al.*, 1976):

$$\left(\frac{^{228}\mathrm{Ra}}{^{226}\mathrm{Ra}}\right)_{\mathrm{P}} = \left(\frac{^{228}\mathrm{Ra}}{^{226}\mathrm{Ra}}\right)_{\mathrm{I}} e^{-\lambda_{228}t} + \frac{^{232}\mathrm{Th}}{^{226}\mathrm{Ra}}(1 - e^{-\lambda_{228}t}) \qquad [13.8]$$

The effects of a hypothetical Ra/Th fractionation event are shown in Fig. 13.12. A reservoir previously in secular equilibrium (e.g. a long-lived magma body) becomes enriched in radium relative to thorium, due to some form of differentiation event. After this enrichment event, excess ^{226}Ra and ^{228}Ra activities decay away at different rates. ^{228}Th is initially in equilibrium with its ultimate parent (^{232}Th), but subsequently builds to a peak and then decays as it approaches equilibrium with its immediate parent (^{228}Ra).

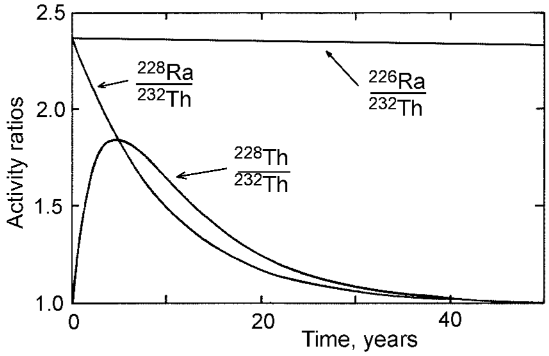

Fig. 13.12. Schematic illustration of the effects of a Ra/Th fractionation event on the activity ratios of a system previously in secular equilibrium. After Capaldi *et al.* (1976).

Williams *et al.* (1986) preferred to use the alternative isochron diagram, on which ages are defined by the intercept on the left-hand axis, using the following equation, which is analogous to [13.4]:

$$\left(\frac{^{228}\mathrm{Ra}}{^{232}\mathrm{Th}}\right)_{\mathrm{P}} = 1 - e^{-\lambda_{228}t} \qquad [13.9]$$

This activity ratio is plotted in Fig. 13.13a against ^{226}Ra/^{232}Th activity. The zero-age line passes through the origin and represents a Ra/Th fractionation line. The slope of this line is the ^{228}Ra/^{226}Ra activity ratio, which is equal in turn to the ^{232}Th/^{238}U activity ratio, since ^{226}Ra and ^{228}Ra are in separate decay chains. For Oldoinyo Lengai, this ratio was found to be unity. Radioactive decay of a system located on the fractionation line causes it to move vertically downwards towards the equiline and permits an age to be assigned.

The initial activity of the 1960 carbonatite is plotted on Fig. 13.13a. If this magma is attributed to a single instantaneous event that caused Ra/Th fractionation, it follows that this event occurred seven years before eruption. However, more complex models are also possible. For example, if segregation occurred in two events, ^{228}Ra formed in the first event might decay before the second event (Fig. 13.13a). In this case, the time from the second event to eruption is less than seven years. Alternatively, carbonatite segregation might have occurred over a period of time. In Fig. 13.13b, this process is modelled by drawing Ra/Th growth curves for different rates of Ra enrichment in the carbonatite magma (relative to the conjugate silicate liquid). These growth curves are then calibrated by determining the time necessary for enrichment of the effectively stable ^{226}Ra isotope. A simple model of constant enrichment rate yields a calculated duration of this process for the 1960 magma of about 18 yr, if this was occurring immediately prior to eruption (Fig. 13.13b).

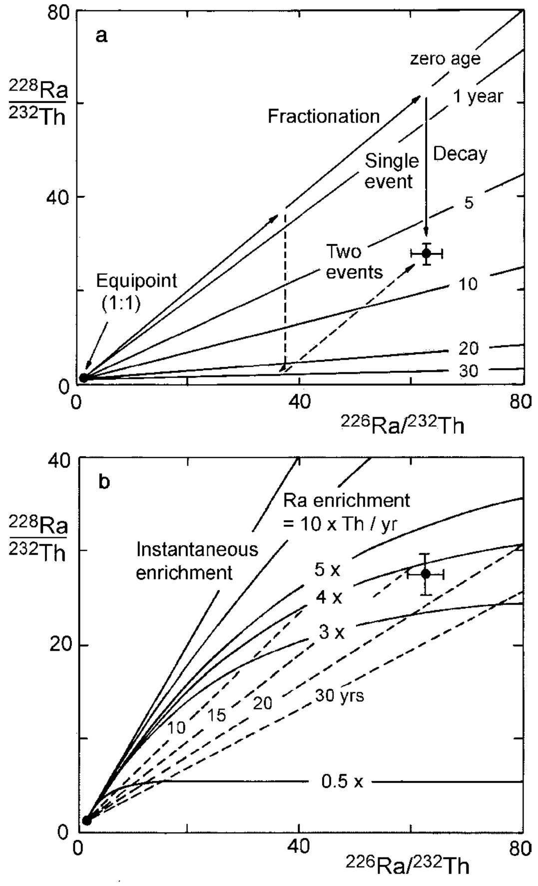

Fig. 13.13. Ra–Ra–Th isochron diagrams showing alternative models to explain the 1960 carbonatite of Oldoinyo Lengai: (a) involving one or two discrete Ra/Th fractionation events and (b) involving a continuous radium-enrichment process of specified intensity and duration. After Williams *et al.* (1986).

The addition of ^{228}Th data can potentially allow selection between short-term differentiation models such as those outlined above, because of its dependence on very recent events. These data were collected by Pyle *et al.* (1991) for the 1988 carbonatite of Oldoinyo Lengai, but, due to analytical difficulties, Ra/Th activity ratios could not be measured. Therefore, the advantage of the combined systems was lost.

Capaldi *et al.* (1976) attempted to use the ^{228}Ra and ^{228}Th systems to study the recent eruptive history of Mt Etna. However, Condomines *et al.* (1995) showed that these systems were in secular equilibrium in all

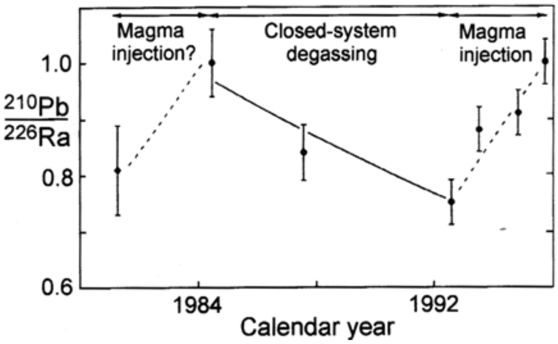

Fig. 13.14. Evolution of ^{210}Pb/^{226}Ra activity ratios as a function of time in Merapi volcano, Java. After Gauthier and Condomines (1999).

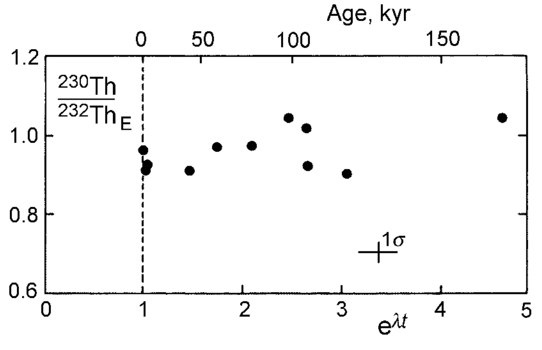

Fig. 13.15. Plot of erupted (initial) Th activity ratios against time for Piton de la Fournaise volcano (Réunion Island), showing that the magma composition has remained constant over time, within error. After Condomines *et al.* (1988).

Etna lavas. They also found that ^{210}Pb was in secular equilibrium with its parent (^{226}Ra) in all Etna lavas except the 1991 and 1992 flows. However, Gauthier and Condomines (1999) found significant ^{210}Pb disequilibrium in lavas from Merapi volcano in Java, Indonesia. Between 1984 and 1992, the initial ^{210}Pb/^{226}Ra activity ratio of erupted products decreased from unity (secular equilibrium) to a value of 0.75 (Fig. 13.14). This decrease was attributed to degassing of radon, which is the immediate daughter of ^{226}Ra, and is the only gaseous species in the ^{226}Ra–^{210}Pb decay chain (Fig. 12.2a). This radon probably escaped from a shallow magma chamber under otherwise closed-system conditions. A major eruption in 1992 marked the end of this period of closed-system evolution, as new magma was added to the chamber and gradually mixed with its contents, bringing them progressively back to secular equilibrium.

13.3 Mantle-melting models

Volcanoes located on continental crust often exhibit complex ^{230}Th evolution patterns, probably because mantle-derived magmas become trapped during their rise through low-density sialic basement. In contrast, oceanic volcanoes might be expected to exhibit simpler behaviour, since oceanic crust is easily punctured by rising magma. Therefore, oceanic volcanics provide a window to study Th isotope fractionation processes in the mantle.

The first detailed U-series measurements on oceanic volcanics were made by Oversby and Gast (1968) on recent ocean-island lavas. This study revealed disequilibrium between isotopes of the ultra-incompatible elements, radium and thorium. Oversby and Gast suggested that these fractionations were probably inherited from a melting event in the mantle source of the magmas. ^{230}Th activities were observed to be higher than ^{238}U activities, suggesting that thorium was a more incompatible element than uranium. This conclusion was supported more than ten years later (Condomines *et al.*, 1981) in studies of MORB magma genesis (see below).

In view of the short half-life of ^{226}Ra, Oversby and Gast attributed disequilibrium of this species to rapid ascent of ocean-island magmas from the source area (<10 000 yr). This conclusion has also been supported by radium analysis of MORB (section 13.3.5). In addition, the rapid ascent of ocean-island magmas has been confirmed by studies of their Th isotope chemistry over time. For example the volcanoes of Mauna Kea (Hawaii), Marion Island (SW Indian Ocean) and Piton de la Fournaise (Fig. 13.15) all have constant initial ^{230}Th/^{232}Th ratios (within error) over the last 250 kyr (Newman *et al.*, 1984; Condomines *et al.*, 1988). This suggests that transport of magma from the melting zone to the surface probably occurred within a few thousand years, without storage in a deep crustal reservoir that would have perturbed the observed ratios. Therefore, the calculated initial Th isotope ratio for each eruption is probably very close to the source value.

13.3.1 Melting under ocean ridges

Mid-ocean ridges present the minimum crustal thickness which must be traversed by ascending mantle-derived magmas. Therefore, in this environment we should have the best opportunity to see back through the processes of magma evolution during ascent, to study source processes and chemistry. However, some workers (e.g. O'Hara and Mathews, 1981) have suggested that MORB magmas spend many eruptive cycles in periodically re-filled, periodically tapped magma chambers under the ridge, which then grossly perturb the incompatible-element and isotopic signatures of the product magmas. In this case, they argued, it would be almost impossible to 'invert' the data (see section 7.2.3) to reconstruct the source chemistry.

The short half-life of ^{230}Th has provided a powerful tool to test these models of MORB magma evolution. In the first detailed study of MORB samples, Condomines *et al.* (1981) found that fresh, young crystalline basalts and glasses from the 'FAMOUS' area on the Mid-Atlantic Ridge (37 °N) had a narrow range of ^{230}Th/^{232}Th and U/Th activity ratios. Because these samples were all less than 5 kyr old, their present Th activity ratios can be taken as initial ratios at the time of eruption.

When plotted on a U–Th isochron diagram, the FAMOUS data fall well to the left of the equiline, showing them to be far from isotopic equilibrium. This U–Th disequilibrium must have been inherited during the melting process (Fig. 13.16), because U and Th are both ultra-incompatible elements, and cannot be fractionated from each other during Raleigh crystallisation in a magma chamber. If the residence time of magma in such chambers lasted more than a few tens of thousands of years, U–Th activities would again reach equilibrium (Fig. 13.16). Because this has not happened, we can deduce that the transport of magma from the melting zone to the surface was relatively rapid, which is not consistent with prolonged evolution in an open-system magma chamber. This conclusion has subsequently been supported by evidence of isotopic disequilibrium of even-shorter-lived U-series nuclides in MORB glasses (section 13.3.5).

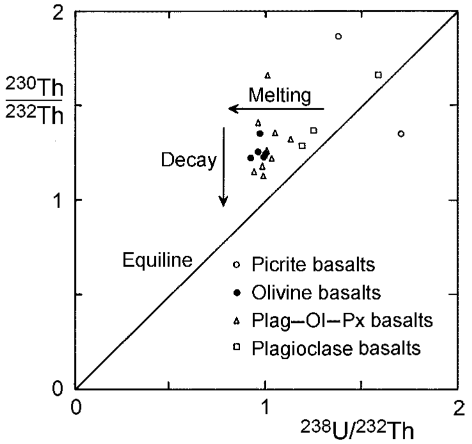

Fig. 13.16. U–Th isochron diagram, showing activity ratios in young lavas from the FAMOUS area of the Mid-Atlantic Ridge, to the left of the equiline. Arrows show the effects of partial melting and radioactive decay. After Condomines *et al.* (1981).

In addition to the FAMOUS area, Condomines *et al.* (1981) showed that other young ridge basalts and OIB also fell on the left-hand side of the equiline (Fig. 13.17). Hence, in all of these cases, melts were enriched in Th/U relative to the source. This implies greater incompatibility of Th over U during melting. Allègre and Condomines (1982) expressed this Th/U fractionation during melting by the quantity 'k':

$$k = \frac{(^{238}\mathrm{U}/^{232}\mathrm{Th})_{\mathrm{magma}}}{(^{238}\mathrm{U}/^{232}\mathrm{Th})_{\mathrm{source}}} \qquad [13.10]$$

However, it is more useful to express this ratio as its reciprocal, termed 'r', as used by McKenzie (1985a). In addition to facilitating the algebra, this formulation avoids confusion of k with κ (the atomic ^{232}Th/^{238}U ratio):

$$r = \frac{(^{238}\mathrm{U}/^{232}\mathrm{Th})_{\mathrm{source}}}{(^{238}\mathrm{U}/^{232}\mathrm{Th})_{\mathrm{magma}}} \qquad [13.11]$$

Since the source is assumed to be on the equiline, its ^{238}U/^{232}Th activity is equal to its ^{230}Th/^{232}Th activity. Furthermore, if the analysed sample was extracted from the source in less than a few thousand years, the source Th isotope activity is equal to that measured in the magma:

$$\left(\frac{^{238}\mathrm{U}}{^{232}\mathrm{Th}}\right)_{\mathrm{source}} = \left(\frac{^{230}\mathrm{Th}}{^{232}\mathrm{Th}}\right)_{\mathrm{source}} = \left(\frac{^{230}\mathrm{Th}}{^{232}\mathrm{Th}}\right)_{\mathrm{magma}} \qquad [13.12]$$

Hence, by substituting into [13.11], we obtain

$$r = \frac{(^{230}\mathrm{Th}/^{232}\mathrm{Th})_{\mathrm{magma}}}{(^{238}\mathrm{U}/^{232}\mathrm{Th})_{\mathrm{magma}}} = \left(\frac{^{230}\mathrm{Th}}{^{238}\mathrm{U}}\right)_{\mathrm{magma}} \qquad [13.13]$$

This is represented in Fig. 13.17 by the gradient of lines projecting from the origin. Hence we can determine U/Th fractionation during melting from a U-series analysis of the magmatic product.

Corroboration of the Mid-Atlantic Th isotope results came from a similar study on the East Pacific Rise by Newman *et al.* (1983). These data lie to the left of the equiline and fall within error of unaltered basalts from the FAMOUS area, but with more scatter, particularly in ^{238}U/^{232}Th activity. Since U and Th are both ultra-incompatible elements, Newman *et al.* recognised that it was very difficult to generate the required U/Th fractionations at the degrees of melting normally expected for MORB (about 10%). Hence, they suggested that,

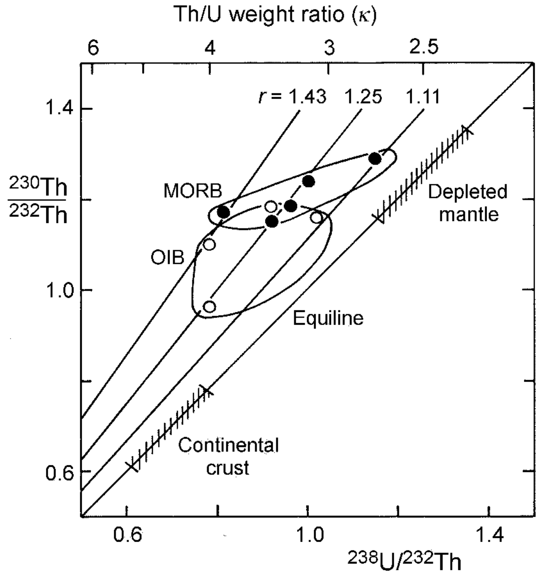

Fig. 13.17. U–Th isochron diagram, showing fields for MORB and OIB relative to the Th/U fractionation factor during melting (r). Modified after Allègre and Condomines (1982).

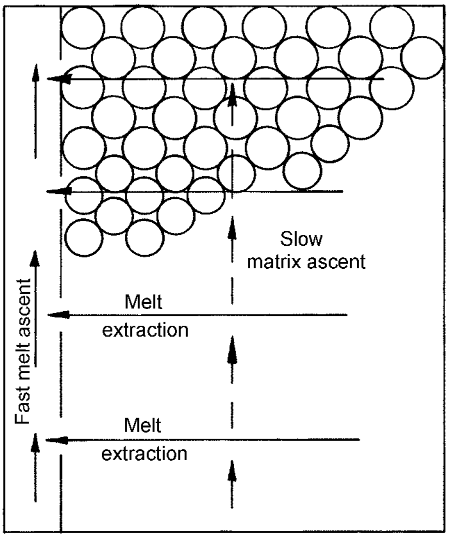

Fig. 13.18. Schematic view of a dynamic melting model for the generation of MORB, involving fast ascent and mixing of magmas, with slow ascent of the source. After McKenzie (1985a).

under these conditions, a U–Th-rich accessory phase might be required in order to explain the data.

Thompson *et al.* (1984) reversed this problem, arguing that the incompatible-element signatures of MORB rocks, including U–Th disequilibrium data, could be generated only by very low degrees of mantle melting. They noted that such an explanation was consistent with observations for other isotope systems on MORB glasses (e.g. Cohen *et al.*, 1980), which showed the observed Rb/Sr, Sm/Nd and U/Pb ratios in MORB magmas to be fractionated relative to the ratios required in the source to generate observed isotope compositions (see section 6.2.2).

13.3.2 The effect of source convection

This line of argument was developed by McKenzie (1985a), who performed calculations to determine the maximum percentage of partial melting that was consistent with the observed U/Th fractionations. For this purpose he assumed that Th was perfectly incompatible (i.e. its bulk distribution coefficient between solid and liquid, D, is zero), and that there was no residence time of magma in a ridge chamber before eruption. In order to generate a ^{230}Th/^{238}U enrichment (r) of 1.25 using a batch-melting model and a D value of 0.005 for uranium, the maximum degree of melting permitted was 2%. However, this result is not consistent with major-element considerations, which require MORB to be a large-degree (about 15%) melt of the mantle. Hence, McKenzie ruled out the simple batch-melting model for MORB genesis, and adopted instead the dynamic melting model of Langmuir *et al.* (1977).

In the dynamic melting model, melts are extracted simultaneously from a vertical thickness of perhaps 60 km of mantle (horizontal lines in Fig. 13.18). The melts ascend quickly to the surface in a conduit, mixing as they go (solid vertical lines in Fig. 13.18). Meanwhile the source itself moves slowly upwards through the melting zone (dashed vertical lines). At any given point the source contains less than 2% melt (termed the ‘porosity’), but as it moves upwards and melts are tapped off, the source becomes more and more depleted in incompatible elements. If melts mix equally from the whole melting zone, the effect of dynamic partial melting on incompatible-*element* abundances is similar to that of batch melting. This is because (in the extreme case) the source is completely exhausted of these elements by the time it reaches the top of the melting zone. In other words, incompatible-element extraction is 100% efficient. However, for short-lived *nuclides*, the two melting models can yield quite different results.

If the rate of mantle upwelling is rapid relative to the half-life of the nuclide in question (e.g. ^{230}Th), then

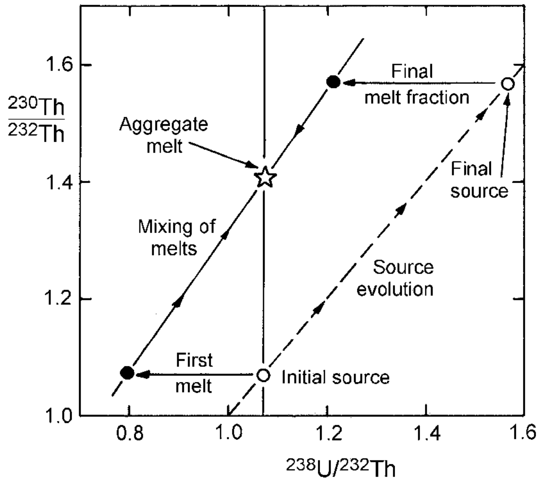

Fig. 13.19. Consequences of very slow mantle upwelling under the ridge for the Th activity systematics of MORB magmas. Note that the rate of *magma* upwelling is very rapid relative to the ^{230}Th half-life.

this nuclide behaves like a stable element. In that case, dynamic melting will yield an aggregate melt similar to that produced by batch melting, and the 15% melt fraction necessary to explain major-element data cannot satisfy the Th activity data. However, if the rate of mantle upwelling is very slow relative to the half-life of ^{230}Th, then ^{230}Th removed from the source at the base of the melting column is replenished in the source as it ascends, by decay from residual uranium (which is less incompatible than thorium). Consequently, as upwelling progresses, the ^{238}U/^{232}Th activity of the source increases, but it remains on the equiline. After extraction of all U and Th from the source (15% total melt) the ^{238}U/^{232}Th activity of the aggregate melt (star in Fig. 13.19) will be the same as that of the initial source, but the ^{230}Th/^{238}U activity ratio (r) is still the same as in the first increment of melting at the base of the melting zone.

In between these two extremes (simple batch and dynamic melting), it is possible to determine the rate of mantle upwelling which will yield the observed r value in MORB, given the bulk distribution coefficients (D) for U and Th. Williams and Gill (1989) presented these relationships in diagrammatic form, using the equations developed by McKenzie (1985a). This information is shown in Fig. 13.20. The values of D chosen by McKenzie (1985a) lead to a calculated mantle upwelling rate of only 1 cm/yr. In contrast, Williams and Gill (1989) argued for a much higher D value for uranium (Fig. 13.20). This implies a more rapid rate of upwelling (about 7 cm/yr).

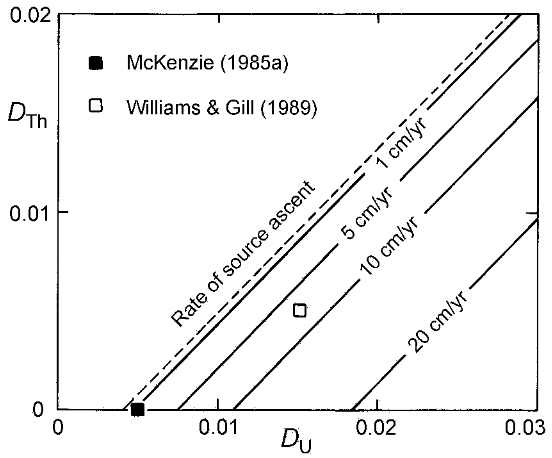

Fig. 13.20. Diagram showing the relationship between calculated mantle upwelling rate (cm/yr) and bulk distribution coefficients (D) for U and Th, assuming a dynamic-melting model with 2% porosity and yielding a ^{230}Th/^{238}U activity (r) of 1.2 in MORB. After Williams and Gill (1989).

These two different upwelling rates make very different predictions about mantle processes under the ridge. A value of 1 cm/yr is less than the rate of plate motion, which led McKenzie (1985b) to argue that the melting zone under the ridge is funnel-shaped. Trace elements are then extracted from a wide swath of mantle near the base of the funnel, while major elements are dominated by the melt extracted from the apex of the funnel (Fig. 13.21a). Because the trace-element-extraction zone is larger, this lower domain dominates the U–Th systematics of the melt, which acts like a small-degree batch melt of the original mantle source.

In contrast, with the higher upwelling rate of Williams and Gill (1989), melt extraction occurs from a vertical slice under the ridge, yielding a result closer to the simple dynamic model. However, the consequence is that the ^{230}Th/^{232}Th activity of the erupted products is substantially higher than that of the source (Fig. 13.19), while the ^{238}U/^{232}Th activity is similar to that of the source. O'Nions and McKenzie (1993) pointed out that, in this case, the Th/U ratio (κ value) of the source (sections 6.3.3 and 13.3.7) should be determined *not* from the Th isotope ratio of MORB (equation [13.12] above), but directly from the elemental U/Th ratio of MORB. Hence, this model predicts that short-lived isotopes *are* fractionated by the melting process under ridges, but stable incompatible elements are *not* fractionated under these conditions.

The real situation may be somewhere between the two extremes described above; however, several lines

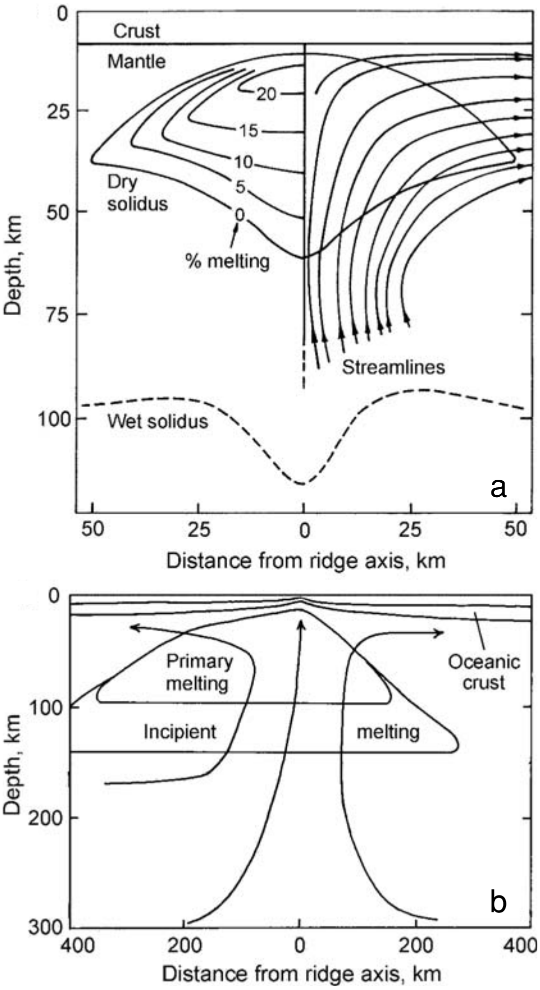

Fig. 13.21. Predicted and observed distributions of melting zones under a mid-ocean ridge: (a) the model predicted by Galer and O'Nions (1986); and (b) a cross-section of the East Pacific Rise based on results of the MELT seismic experiment. After Forsyth *et al.* (1998).

of evidence tend to support the slow-upwelling model. Perhaps the most important piece of evidence comes from the so-called Mantle Electromagnetic and Tomography (MELT) experiment, in which geophysical methods were used to image the distribution of partial melt zones under the East Pacific Rise (Forsyth *et al.*, 1998). Seismic evidence collected in this experiment showed that the zone of incipient melting under the ridge extended to depths of over 150 km and to a width of nearly 800 km, matching the shape of the melting zone predicted in Fig. 13.21a but having an extent 3–4 times greater in each direction (Fig. 13.21b). Other lines of evidence in support of slow upwelling with an extended zone of incipient melting are the continuing need to explain the trace-element signatures of long-lived isotopic systems (section 6.2.2) and evidence for preferential melting in the garnet stability zone, to be discussed below.

13.3.3 The effect of melting depth

As noted above, ^{230}Th/^{238}U enrichment (increased r) is only possible if thorium is more incompatible than uranium. Therefore, to model Th/U fractionation more accurately, it was necessary to refine the determinations of the crystal–melt distribution coefficients for U and Th. Since the only mineral phases that host significant inventories of U and Th are clino-pyroxene (cpx) and garnet, these minerals have been the focus of attention.

In the first detailed work on this subject, Beattie (1993a) measured solid/liquid partition coefficients (D) for cpx that were *greater* for Th than for U, implying that melting in the spinel peridotite stability field (above 70 km depth) could not generate the observed Th/U fractionations. On the other hand, Beattie (1993b) showed that garnet has solid/liquid partition coefficients that *are* suitable for generating the observed ^{230}Th/^{238}U enrichments. This was confirmed by LaTourrette *et al.* (1993), who determined $D_{\mathrm{Th}}/D_{\mathrm{U}}$ values of 0.1 for garnet. Hence, it was concluded that the Th/U fractionations observed in MORB must originate from melting at greater than 70 km depth, and the resulting liquids must be transported to the surface quickly, before substantial decay of ^{230}Th can occur.

These conclusions were questioned by Wood *et al.* (1999), who based their argument on modelling the pressure dependence of cpx/liquid partition coefficients for U and Th. With increasing pressure, cpx becomes more aluminous, shrinking the size of the M2 cation site where U and Th are housed. This should favour the smaller uranium ion, causing the ratio of U/Th partition coefficients between cpx and liquid to increase with pressure. Wood *et al.* predicted that at pressures slightly above 1 GPa (=10 kbar, equivalent to 35–50 km depth) the $D_{\mathrm{U}}/D_{\mathrm{Th}}$ ratio should rise above unity, allowing Th/U excesses to be generated by MORB melting in the spinel peridotite field. These predictions were confirmed by experimental work (Landwehr *et al.*, 2001), and their possible consequences are shown in Fig. 13.22.

This plot shows the excess ^{230}Th activity that can be generated by partial melting of lherzolite in the plagioclase, spinel- and garnet-peridotite stability fields. These results show that significant Th isotope excesses can be generated in the spinel-peridotite field, but only

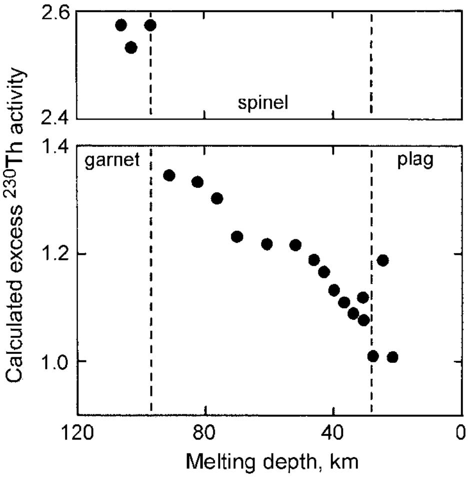

Fig. 13.22. Predicted excess ^{230}Th activity as a function of melting depth, based on measured cpx/liquid and garnet/liquid partition coefficients for U and Th, and assuming a very low porosity (incremental melt fraction) of 0.001%. Note the change in scale on the *y* axis. After Landwehr *et al.* (2001).

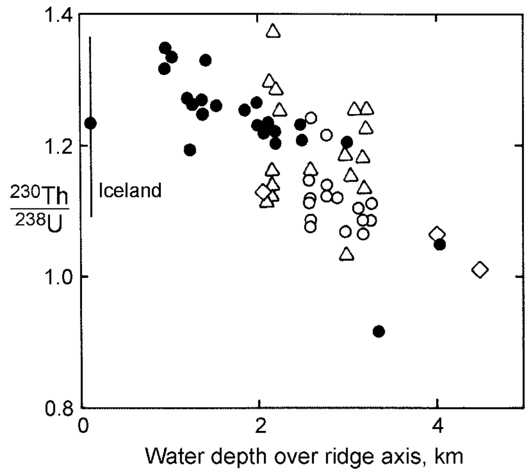

Fig. 13.23. Plot of ^{230}Th/^{238}U activity ('*r*') for MORB against depth to the ridge axis: (●) = Mid Atlantic; (△) = Gorda, JDF; (○) = EPR; (◇) = Australia–Antarctic. After Bourdon *et al.* (1996b).

at extremely low porosity. In fact, the excess ^{230}Th values presented in Fig. 13.22 were calculated assuming a porosity of 10^{-5}, equivalent to a melt fraction of only 0.001%! A somewhat more realistic porosity of 0.1% yields $D_{\mathrm{Th}}/D_{\mathrm{U}}$ values for cpx that are 75% as large as those shown, but these values are still only one-half the value obtained in the garnet stability field. In conclusion therefore, these findings do permit limited Th isotope excesses to be obtained at shallower depths than the garnet stability field, but melting in the garnet zone is still likely to be the major source of such disequilibrium.

Further light is thrown on the question of melting depths under ridges by the observation of a relationship between U-series activity ratios and ridge depth. In a study of MORB glasses from the Azores plateau, Bourdon *et al.* (1996a) demonstrated an inverse correlation between ^{230}Th/^{238}U activity ratio and depth of water above the axis of the Mid-Atlantic Ridge. This correlation was subsequently extended by Bourdon *et al.* (1996b) to other ridge segments (Fig. 13.23). However, in view of the great sensitivity of Th/U disequilibrium to melting porosity, one would not expect to see the greatest disequilibrium in samples from the shallowest part of the ridge, which has the highest melting rate.

The observation of an inverse correlation between isotope disequilibrium and depth led Bourdon *et al.* (1996a; 1986b) to suggest that the main control on Th/U disequilibrium across the Azores plateau must be the depth at which melting is *initiated.* If melting is initiated at greater depths, the longer melting column leads to greater overall melt fractions, but the longer melting interval within the garnet zone increases Th/U disequilibrium. Bourdon *et al.* attributed the greater melting depth across the Azores plateau to increased heating associated with the mantle plume. An alternative explanation is enhanced contamination of the mantle by eclogite or garnet pyroxenite from the plume (Hirschmann and Stolper, section 9.2.4). However, Bourdon *et al.*, argued that this could not account for the Azores observations, since Th/U excesses do not correlate with isotopic or trace-element evidence for source enrichment.

Data from Iceland constitute an exception to the generally good correlation between ridge depth and isotopic disequilibrium, since they lie well below the main trend. However, Iceland obviously represents an extreme example of plume contamination of a ridge, since the ridge actually emerges above sea-level. Therefore, Bourdon *et al.* attributed this anomalous behaviour to the much larger upwelling velocity under Iceland. This was confirmed by a more detailed study of Iceland and the Reykjanes Ridge (Peate *et al.*, 2001). Data for Iceland itself were again found to lie well below the main array. However, samples from greater than 1km depth on the Reykjanes Ridge south of Iceland exhibited a positive correlation between excess Th activity and depth, consistent with the rest of the MORB array.

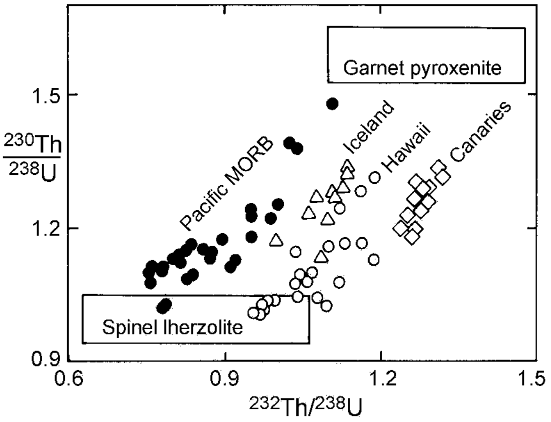

Fig. 13.24. Plot of ^{230}Th/^{238}U activity ('r') against ^{232}Th/^{238}U activity (or Th/U concentration, κ) to show sub-linear arrays for various ocean-ridge and ocean-island suites, lying between the fields for spinel lherzolite and garnet pyroxenite melts. After Sigmarsson *et al.* (1998).

13.3.4 The effect of source composition

The relative importance of source composition *versus* melt fraction as a control of isotope disequilibium has continued to be a matter of debate. Sigmarsson *et al.* (1998) investigated this question by plotting ^{230}Th/^{238}U activity ratios ('r' values) against ^{232}Th/^{238}U activity ratios. The latter can be converted to κ by multiplying by the ratio of the half-lives (3.134). The κ value is, in turn, almost identical to the overall Th/U weight ratio. This plot (Fig. 13.24) is actually equivalent to the Th–U 'alternative-isochron' plot (section 12.4.3) which was also used for presenting Ra–Th isotope data (section 13.1.2); however, that is not the purpose here. Sigmarsson *et al.* argued that the correlation between r values and κ values showed that Th isotope disequilibrium is caused by variations in source composition. However, since the apparent κ value can itself be fractionated by the melting process, this could be a circular argument.

A more conclusive determination of the effect of source composition on U-series disequilibrium is to compare Th isotope data with long-lived isotope tracers that are known to be affected by source variations. Lundstrom *et al.* (1999) made such a study on the East Pacific Rise in the vicinity of the Siqueiros Fracture Zone, north-west of the Galapagos Islands. From trace-element data and long-lived-isotope signatures (Sr–Nd) they identified magmas from an enriched source (E-MORB), a depleted source (D-MORB), and mixtures between these components (N-MORB).

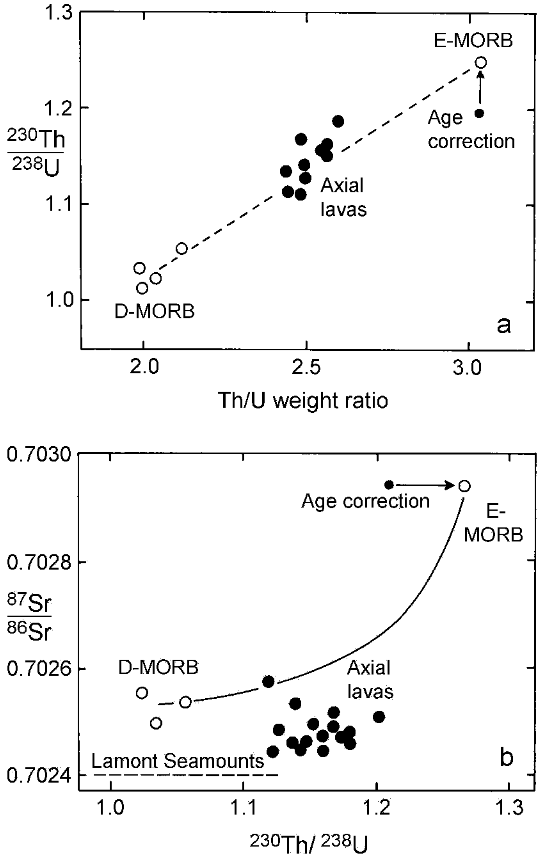

Fig. 13.25. Plots of isotope data for the axial graben of the East Pacific Rise (●) compared with D-MORB and E-MORB samples from the Siqueiros Fracture Zone (○): (a) Th activity ratios and (b) Th activity as a function of Sr isotope ratio. Modified after Sims *et al.* (2002).

These three types of sources also gave rise to distinct differences in Th isotope disequilibrium, with E-MORB exhibiting excess ^{230}Th activities, whereas D-MORBs were essentially in secular equilibrium (Fig. 13.25a). Hence, Lundstrom *et al.* concluded that E-MORBs were sampling garnet-bearing veins that were distributed in a source with 'marble-cake' structure (section 6.1.5), whereas D-MORBs sampled the garnet-free peridotite 'host'. N-MORBs were then attributed to mixing between these two end-members.

Unfortunately, further study of this area (Sims *et al.*, 2002) suggested that melting processes were more complex than had previously been realised. Sims *et al.* analysed a suite of samples collected from the axial graben of the East Pacific Rise, just north of the Siqueiros Fracture Zone studied by Lundstrom *et al.* (1999). On the plot of Th isotope disequilibrium

'r' (^{230}Th/^{238}U activity) against κ, they found that their axial graben samples lay on the mixing line between the E-MORB and D-MORB of Lundstrom *et al.* (Fig. 13.25a). However, on a plot of Th isotope disequilibrium ('r') against long-lived isotope tracers, they found that the axial graben samples did not lie on mixing lines between the E-MORB and D-MORB end-members defined by the Siqueiros Fracture Zone (Fig. 13.25b). Sims *et al.* therefore concluded that variations of U-series isotope activities were due to polybaric melting of a homogeneous source, rather than to mixing between melts from compositionally distinct sources.

This interpretation is problematical because it contradicts nearly twenty years' work on the origin of Pacific MORB, which suggested that the homogeneous signatures of long-lived isotope tracers are due to mixing of magma under the ridge, rather than to the sampling of a homogeneous mantle source (section 6.1.4). However, a re-examination of the Sims *et al.* paper suggests that basalts from the Lamont Seamounts (Fornari *et al.*, 1988) are a much better indicator of the nature of D-MORB in the axial graben segment studied by Sims *et al.* than are the basalts of the Siqueiros Fracture Zone. Firstly, the Lamont Seamounts are much closer to the study area than the Siqueiros Fracture Zone, and secondly, Pb isotope data from the axial graben samples actually form an array that falls within the larger envelope of the Lamont Seamount array (not shown here). The Lamont Seamounts have Sr isotope signatures indicative of a more depleted source (Fig. 13.25b), which would much better explain the compositions of the axial graben samples by mixing with E-MORB. Hence it appears that, as proposed by Lundstrom *et al.* (1999), axial graben samples of the East Pacific Rise are indeed the products of mixing between isotopically heterogeneous magmas from a 'marble-cake' or 'plum-pudding' mantle.

13.3.5 Evidence from short-lived species

Observations of ^{226}Ra/^{230}Th disequilibrium in MORB place even tighter constraints on melting models beneath ridges than those provided by Th/U data. Measured ^{226}Ra/^{230}Th activity ratios in MORB glasses are as high as 2.5, despite the short (8000 yr) equilibration time of ^{226}Ra. In principle, the dynamic melting model of McKenzie (1985a) can explain the Ra–Th data at very low porosities, assuming a Ra distribution coefficient of zero, because it assumes instantaneous melt extraction from all levels in the melting column. In this model, most of the radium must come from the base of the melting column, because ultra-incompatible elements are very efficiently extracted at low degrees of melting. Chabaux and Allègre (1994) showed that this model is applicable to OIB, whose small ^{226}Ra excesses may be preserved in a rapidly upwelling plume. This generates a positive correlation between ^{226}Ra/^{230}Th and ^{230}Th/^{238}U activity ratios, which is expressed as an inverse correlation on the 'reverse' plot of ^{230}Th/^{226}Ra *versus* ^{230}Th/^{238}U activity ratio used by Chabaux and Allègre (Fig. 13.26).

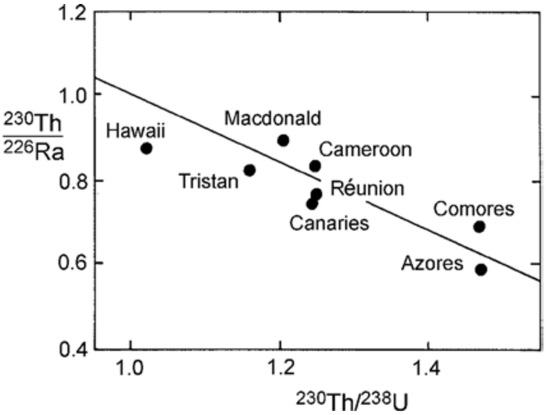

Fig. 13.26. Reverse plot of ^{230}Th/^{226}Ra *versus* ^{230}Th/^{238}U activity ratios, showing a correlation for OIB magmas that is consistent with a simple melting model. After Chabaux and Allègre (1994).

Unlike OIB magmas, it seems unlikely that MORB melts can ascend from 80 km depth with sufficient velocity to avoid decay of the excess ^{226}Ra inventory of the magma. Therefore, Spiegelman and Elliott (1993) proposed that small melt fractions cannot easily escape from the base of the melting zone, but only ascend slowly to the surface by a mechanism they termed equilibrium porous flow (EPF). They proposed that this process was also accompanied by an increase in the porosity of the melting system, from a value of zero at the base of the melting column to a maximum of about 0.5% at the top of the melting column. This model has the effect of holding back the complete release of Th, which can then decay to Ra as the source ascends. The ^{226}Ra extracted from these shallower levels in the melting column can then reach the surface without undergoing significant decay. This model gives mathematically acceptable solutions to the Th–U and Ra–Th data, but it is questionable whether melt extraction can begin at the porosities of less than 0.1% required in this model. An alternative approach (Rubin and Macdougall, 1988; Qin, 1992) is to invoke disequilibrium melting.

A disequilibrium melting model differs from all of the models discussed above, in which the inventory of trace elements within each mineral grain undergoing melting is believed to be homogenised by diffusion before any melt is removed from the surface of the grain. Hence, in an equilibrium melting model, ultra-incompatible elements can be stripped out from the entire grain by very small degrees of melting. However, Qin argued that, if the melting rate is of the same order of magnitude as the volume diffusion rate of cations in mineral grains (e.g. garnet and cpx), then incompatible elements will be stripped out from grains in layers, like the shells of an onion.

Qin (1992) argued that disequilibrium melting is almost unavoidable in the generation of ^{226}Ra excesses, since the secular equilibration time of this nuclide (8000 yr) is comparable to the diffusional equilibration time of 10^4 yr for cations in a mineral grain at the temperature of basaltic melting (section 6.1.2). Qin took this argument further, by suggesting that differing rates of volume diffusion for different cations could cause *diffusional fractionation* of U-series nuclides and other incompatible-element couples. However, this overlooks the fact that the source spends a minimum of 100 kyr in the melting zone, for a 50-km-deep melting zone upwelling at 5 cm/yr. These figures suggest that disequilibrium melting cannot be maintained over the whole depth of the melting column under ridges, but might occur at the base of the column in such a way as to hold back complete release of ultra-incompatible elements into the melt.

Kelemen *et al.* (1995) took a different approach, by examining the petrology of ophiolite complexes for evidence of the type of magma-flow mechanisms that might have occurred under ocean ridges. They suggested that the dunite pods which make up 5%–15% of the Oman ophiolite (Fig. 13.27) were formed by the partial equilibration of basic magmas with upper-mantle harzburgite, causing the replacement of pyroxene by olivine. Hence, these pods seem to represent 'fossilised' melt conduits, up which magma migrated by porous flow and possibly also by channel flow. Evidence for porous flow is provided by the pervasive replacement of pyroxene, which requires magma–wall-rock interaction. On the other hand, evidence of focussed channel flow is provided by the occurrence of chromitite rafts within the dunite pods. Because of the relatively low solubility of Cr in basaltic melts, Kelemen suggested that the chromitites must have scavenged Cr from over 300 times their own mass of liquid. This implies that the dunite pods experienced time-integrated melt/rock ratios over 300, which is consistent with a function as magma conduits.

Evidence that places tighter constraints on the alternative models of dynamic partial melting (channel flow) and EPF (porous flow) comes from a comparison of excess ^{226}Ra and ^{230}Th activities. Beginning with the work of Volpe and Goldstein (1993), it was observed that ^{226}Ra/^{230}Th activity ratios appeared to be *inversely* correlated with ^{230}Th/^{238}U activities in MORB. However, because of the very short half-life of ^{226}Ra, it could not be proven that the ^{226}Ra/^{230}Th activity ratios measured in the early studies were initial ratios at the time of eruption. In contrast, the samples analysed by Lundstrom *et al.* (1999) and Sims *et al.* (2002) from the axial graben of the EPR provided the first conclusive evidence of initial ^{226}Ra/^{230}Th activity ratios. These samples were collected by submersible rather than dredge (used in most previous studies). This allowed very young samples to be precisely selected from the narrow axial graben, in part from an eruption that was actually in progress on the sea floor in 1992. In addition, Po–Pb dating of other samples also indicated ages of less than 200 yr (Rubin *et al.*, 1994).

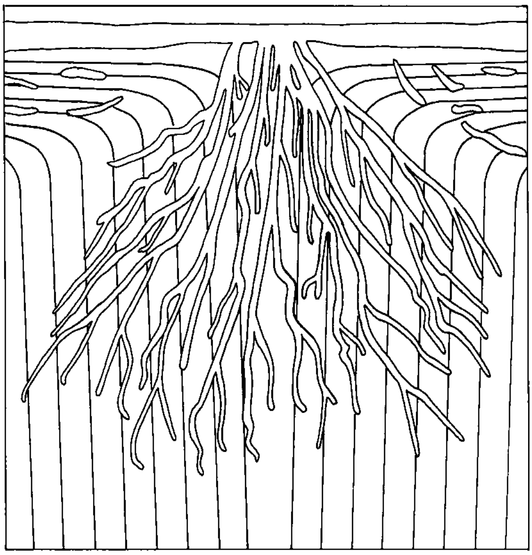

Fig. 13.27. Reconstruction of the magma conduit system under a mid-ocean ridge, based on the distribution of dunite pods in the Oman ophiolite. Streamlines show the direction of solid-state flow of the peridotite source material. After Kelemen *et al.* (2000).

An inverse correlation between ^{226}Ra/^{230}Th and ^{230}Th/^{238}U activity ratios from the axis of the EPR (Fig. 13.28) suggests that these magmas were produced by mixing between D-MORB and E-MORB end-members with distinct origins. The latter have large ^{230}Th excesses but little excess ^{226}Ra, indicating an origin from deep melting in the garnet zone,

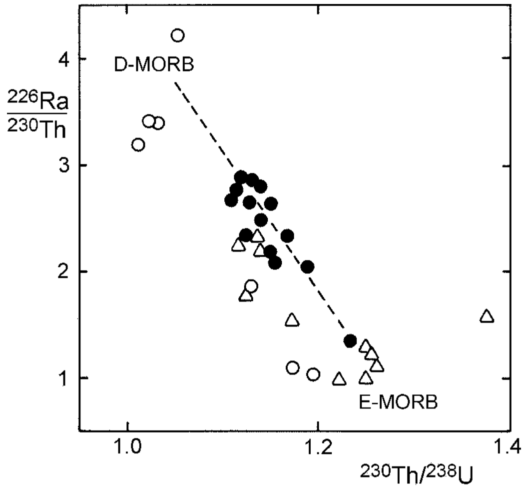

Fig. 13.28. Plot of $^{226}Ra/^{230}Th$ *versus* $^{230}Th/^{238}U$ activity ratios to show an inverse correlation in MORB, attributed to mixing between D-MORB and E-MORB melting products: (●) = EPR; (△) = JDF–Gorda; (○) = Siqueiros Fracture Zone. After Sims *et al.* (2002).

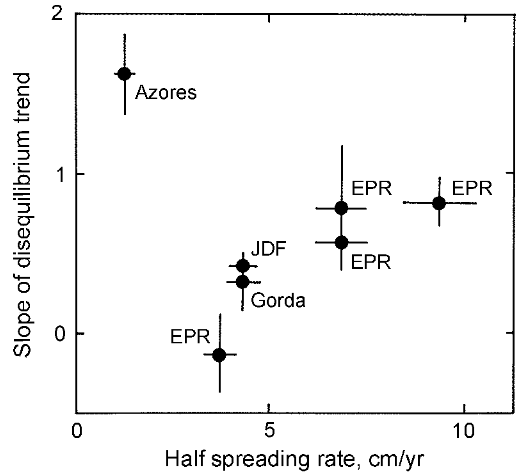

Fig. 13.29. Plot of the slope of the ^{230}Th 'disequilibrium trend' against half the spreading rate (i.e. the model upwelling rate), showing a positive correlation for various ridge segments in the East Pacific Rise. Subsequent work (Lundstrom, 2003) has added more points near the origin. After Lundstrom *et al.* (1998).

whereas the former have large ^{226}Ra excesses, but little excess ^{230}Th, implying a shallow origin from a source that did not lose its radium inventory at depth. Hence, Lundstrom *et al.* (1999) suggested that E-MORB were derived principally by a channel-flow melting process, whereas D-MORB were generated by a porous-flow melting process. These two processes must have been going on at the same time under the ridge, and could simply reflect heterogeneity in the melting process. For example, garnet-pyroxenite veins melt preferentially to form ^{230}Th-enriched E-MORB melts. These rise to the surface along channels that begin as zones of porous flow (hence extracting a ^{226}Ra-enriched D-MORB fraction from their wall-rocks). As melt focussing increases, a few of the zones of porous flow probably evolved into open magma conduits (Kelemen *et al.*, 2000).

13.3.6 Evidence for mantle upwelling rates

Lundstrom *et al.* (1998) argued that if most MORBs are the result of mixing between more depleted and less depleted sources, the average amount of Th isotope enrichment ('*r*') observed on a ridge segment might not be a fundamental property of that ridge, but could merely reflect the chance selection of more or less depleted samples. For example, the correlation between ridge depth and the average '*r*' value on a ridge segment (Bourdon *et al.*, 1996a; 1996b) should be expected to be a very noisy correlation. On the other hand, Lundstrom *et al.* argued that the *slope* of the 'disequilibrium trend' on the U–Th isochron ('equiline') diagram might be a more fundamental property of a particular ridge segment.

When Lundstrom *et al.* (1998) plotted the slope of this U–Th 'disequilibrium trend' against the half-spreading rate for seven ridge segments, they observed a good correlation for all examples except the Azores plateau (Fig. 13.29). They attributed this correlation to the effect of mantle upwelling velocity. Thus, on a fast-spreading ridge, the limited time for Th ingrowth during the ascent of the source through the melting zone leads to limited excess Th, whereas on the slowly spreading ridges the slow ascent of the source allows maximum Th ingrowth. This appears to support the EPF model, whereby Th ingrowth is the main source of isotopic disequilibrium. However, on the equiline diagram, most of the disequilibrium trends pirot round the E-MORB field, rather than the D-MORB end-member proposed by Lundstrom *et al.* (1998), so their argument is not conclusive.

Analysis of both protactinium and thorium allows the effects of the mantle upwelling rate to be evaluated at the same time as the effect of source composition (Fig. 13.30). Bourdon *et al.* (1998) used this figure to compare the degrees of source enrichment and upwelling rate in MORB with different plume sources. Plumes exhibit a lower $^{231}Pa/^{230}Th$ activity

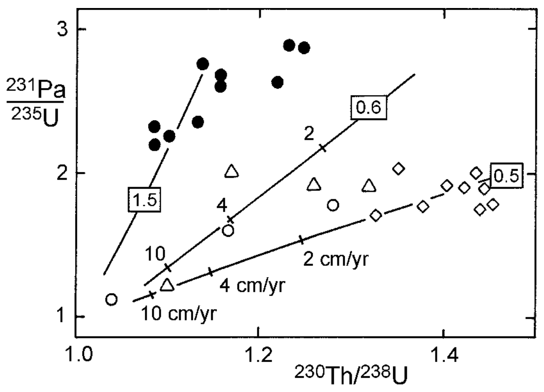

Fig. 13.30. Plot of excess ^{231}Pa *versus* ^{230}Th activity to compare MORB (●) with various ocean islands: (○) = Hawaii; (△) = Iceland; (◇) = Grande Comore. Lines represent constant ^{231}Pa/^{230}Th activity ratios (in boxes) and are labelled with upwelling rates in cm/yr, modelled assuming a melting porosity of 0.1% and an integrated melt fraction of 4%. After Bourdon *et al.* (1998).

ratio than does MORB, which is attributed to a greater fraction of garnet in their sources. However, plume-derived lavas appear to reflect more variable upwelling rates, even within a single hot-spot. For example, Hawaii and Iceland have very variable upwelling rates, from about 2 to 30 cm/yr. On the other hand, the Grande Comore plume exhibits a more consistent but lower upwelling rate coupled with an enriched source. In a more detailed study of the Hawaiian plume, using combined Pa–Th analysis, Sims *et al.* (1999) calculated upwelling rates as high as 20–80 cm/yr for Kilauea and Mauna Loa, but only 2–6 cm/yr for Hualalai and Mauna Kea. They attributed these variations in upwelling velocity to the radial distances of these volcanoes from the centre of upwelling, which is believed to lie under the southeast coast of the main island.

13.3.7 Evidence from Th–Sr and Th–U mantle arrays

U-series isotopes can be used in conjunction with long-lived isotope systems such as Rb–Sr and U–Pb to yield additional information about long-term mantle-enrichment processes. However, before examining the question of long-term mantle evolution, it is important to re-examine the mantle-melting process using a combination of U–Th and Rb–Sr evidence.

Condomines *et al.* (1981) first demonstrated that MORB and OIB samples formed a strong mantle array on a Th activity ratio *versus* Sr isotope ratio plot that is analogous to the Nd *versus* Sr isotope mantle array. Downward displacements of data from this array can be caused by prolonged magma evolution in the crust, as seen in Iceland and in the Canaries. On the other hand, some altered ocean-floor basalts from the FAMOUS area of the Mid-Atlantic Ridge fall above the Th–Sr isotope array due to contamination with ^{230}Th-enriched seawater. If these types of samples are removed from the data array, we can then examine the residual data to see whether ^{230}Th/^{232}Th activities or ^{238}U/^{232}Th activities (Fig. 13.19) are better correlated with Sr isotope ratios. This can help to test the alternative models of dynamic melting and EPF.

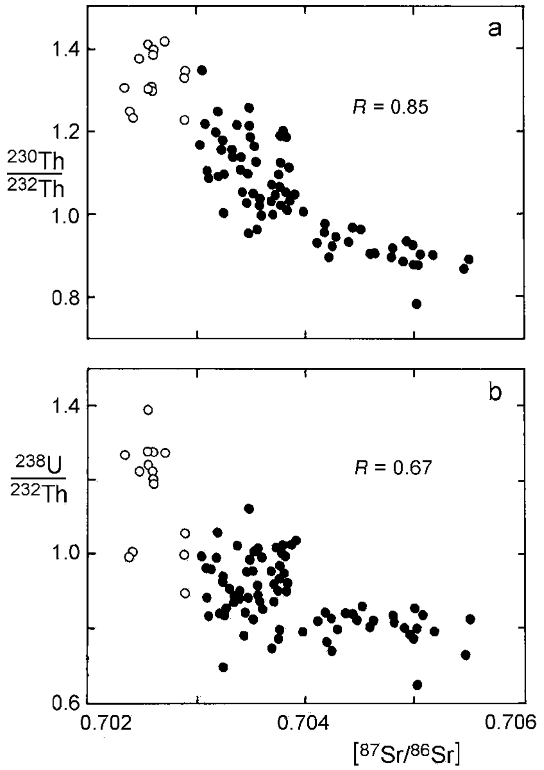

Fig. 13.31. Comparison between the strengths of Th–Sr isotope mantle arrays based on (a) ^{238}U/^{232}Th activities and (b) ^{230}Th/^{232}Th activities, plotted against (atomic) Sr isotope ratios for MORB (○) and OIB (●). After Condomines and Sigmarsson (2000).

If Th isotope ingrowth during source upwelling is the principal origin of excess Th activities, the Th/U (κ) value of the source should be best determined from the ^{238}U/^{232}Th activity ratio of the products (Fig. 13.31b). On the other hand, if U/Th fractionation during partial melting in the garnet zone is the principal origin of excess Th activities, the κ value of the source should best be determined from the $^{230}Th/^{232}Th$ activity ratio of the products (Fig. 13.31a). Both of these U-series activity ratios are compared with the Sr isotope ratios of MORB and OIB samples in Fig. 13.31. The best correlation is observed in Fig. 13.31a, which supports the dynamic melting (garnet-source) model rather than the ingrowth (EPF) model. However, most of the correlation line is defined by OIB rather than MORB, so the test is strictly relevant only to OIB. Since most plumes exhibit greater upwelling rates than MORB, the EPF model is not in any case expected to provide a good fit to plumes.

U–Th isotope data yield an 'instantaneous' κ value for the source; in other words the value pertaining in the source at the time of volcanism. However, we can also calculate a 'time-integrated' κ value for a given reservoir, such as the upper mantle, from Pb isotopes (section 6.3.3). The 'time-integrated' ratio is the average ratio over the Earth's history for a sample from that reservoir. OIB lie on a 'mantle array' (Fig. 13.32) between MORB and the U–Th geochron (representing the Bulk Earth). It is thought that the enriched plumes sampled by OIB buffer the MORB reservoir, which has a relatively short Pb residence time (section 6.3.3).

Williams and Gill (1992) proposed that one of the enriched reservoirs which buffers the U–Th systematics of OIB and MORB is sub-continental lithosphere. They argued that the signature of this component is exemplified by alkali basalts from Nyamuragira volcano in Eastern Zaire and Gaussberg volcano, Antarctica (see also Williams *et al.*, 1992). Both of these volcanoes display low $^{230}Th/^{232}Th$ activity ratios, yielding instantaneous κ values of about 5, well above the Bulk Earth value, but within the mantle array defined by oceanic volcanics (Fig. 13.32). In contrast, basalts from the Craters of the Moon volcanic field (Idaho) fall far from the mantle array of OIB samples (Reid, 1995). This cannot be explained by crustal contamination or *in situ* decay, but can be explained by a uranium-enrichment event that was too recent to affect Pb isotopes, yet sufficiently ancient for ^{234}U to decay to ^{230}Th. This enrichment event may have been caused by CO_2 metasomatism associated with the Yellowstone Plume. A similar model was proposed by Williams and Gill (1992) to explain less extreme U enrichment of the source of Nyiragongo volcano.

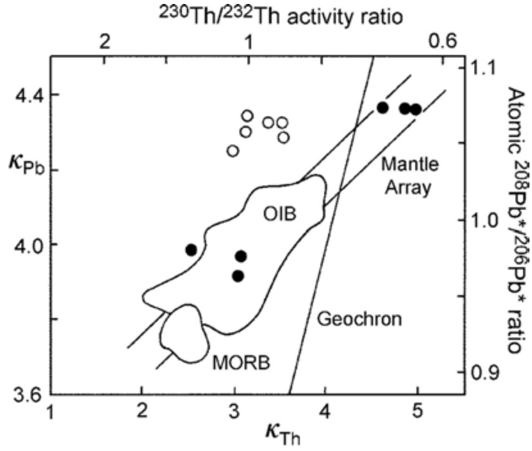

Fig. 13.32. Plot of time-integrated κ (Pb) against instantaneous κ (Th) for oceanic and continental (●) volcanics in the mantle array, together with the Craters of the Moon volcanic field (○), which lies off the array. After Reid (1995).

13.3.8 Evidence for crustal melting and contamination

Work on Icelandic lavas by Sigmarsson *et al.* (1991) has shown that Th isotope data can also be used to investigate the genesis of felsic rocks in oceanic environments. Two alternative models for these rocks involve either direct fractionation of mafic magmas or partial melting of pre-existing mafic crust. However, because of the young age of this crust, conventional radiogenic tracers such as Sr and Nd cannot resolve these models. In contrast, the short half-life of ^{230}Th may allow the solution of this problem.

Rift-zone tholeiites from Iceland are displaced to the left of the equiline by partial melting, but after 0.5 Myr, when their excess ^{230}Th activity has decayed back to secular equilibrium, they are displaced downwards to a different range of Th activity ratios on the equiline (Fig. 13.33). Consequently, historical-age felsic melts produced by anatexis of Icelandic crust will have a lower $^{230}Th/^{232}Th$ activity than will direct magmatic differentiates of juvenile basic magma. Sigmarsson *et al.* found that dacitic volcanics from the Hekla volcano in southern Iceland had $^{230}Th/^{232}Th$ activities too low to be derived from contemporaneous mantle-derived magmas (horizontal single arrows), but consistent with the melting of older crust (double arrow). Hekla rhyolites were then modelled by magmatic fractionation of the dacite melts (Fig. 13.33).

Th isotope studies of volcanic systems in Iceland have also been able to show the effect of contamination of basic magmas by crust a few million years old (Hémond *et al.*, 1988; Sigmarsson *et al.*, 1992). In major volcanic centres, where the oxygen isotope composition of the pre-existing crust has been overprinted by meteoric hydrothermal convection, Th activity ratios also correlate with $\delta\ ^{18}O$. An example of this behaviour is shown in Fig. 13.34 for contaminated quartz tholeiites from the active rift zones of Iceland.

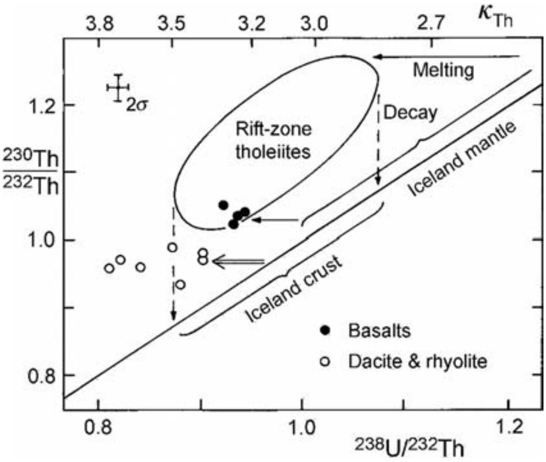

Fig. 13.33. U–Th isochron diagram showing the development of distinct Th activity ratios for Icelandic mantle and crust. These show that the dacitic and rhyolitic magmas from Hekla volcano are formed by crustal melting. After Sigmarsson *et al.* (1991).

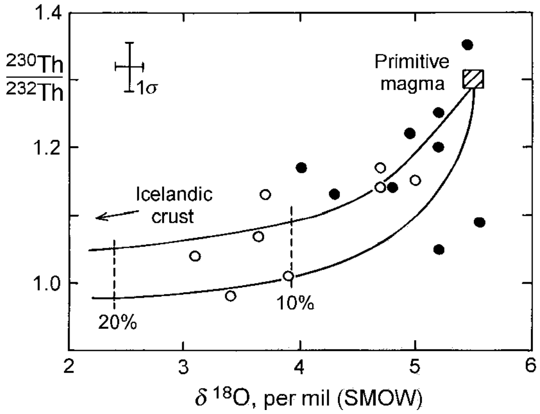

Fig. 13.34. Diagram of Th activity ratio against δ^{18}O (relative to SMOW), showing the effect of contamination of mafic magmas by young crust: (●) = olivine tholeiite; (○) = quartz tholeiite. After Hémond *et al.* (1988).

13.3.9 Sources of continental magmas

The evidence that excess ^{230}Th activities require the presence of garnet except at very low melting porosities (section 13.3.3) has provided a basis for understanding U-series systematics in young continental lavas. Asmerom and Edwards (1995) demonstrated this approach in comparing young (<10 kyr) basalts from the Pincate volcanic field of the Basin and Range province in Mexico, with the 'San Francisco' volcanic field of the Colorado Plateau.

Nd isotope and geochemical data are consistent with an asthenospheric origin for basalts of the Basin and Range, but a lithospheric origin for those of the Colorado Plateau. U-series analysis was performed to see whether basalts from these different sources would possess different ^{230}Th signatures, reflecting melting at different depths. The results showed that magmas regarded as asthenospheric had excess ^{230}Th activities typical of MORB magmas ($r = 1.2$–1.35), whereas those attributed to lithospheric melting had no excess ^{230}Th activity ($r = 0.99$–1.02). Two possible explanations for equilibrium ^{230}Th/^{238}U activity ratios are large degrees of mantle melting or slow ascent to the surface. However, both of these possibilities were ruled out by the observation of large excess ^{231}Pa activities in these rocks (^{231}Pa/^{235}U activity $= 2.0$). Melting in the spinel-peridotite field can generate excess ^{231}Pa, but cannot generate significant excess ^{230}Th activity (section 13.3.3). Therefore Asmerom and Edwards suggested that alkali basalts of the Colorado Plateau were probably generated by shallow melting of sub-continental lithosphere within the spinel-peridotite field, whereas Basin and Range magmas were produced by deeper asthenospheric melting in the garnet field (Fig. 13.35).

Subsequent work (Asmerom *et al.*, 2000) widened this study to include two samples from the Rio Grande Rift (RGR). The Zumi Band tholeiite is on the margin of the RGR and is attributed to a lithospheric source under the Colorado Plateau, whereas the Potrillo basalts are located in the southern central part of the RGR and attributed to an asthenospheric source. U-series data

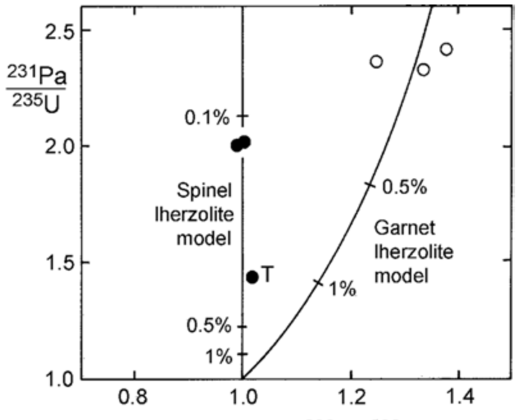

Fig. 13.35. Plot of excess ^{231}Pa *versus* ^{230}Th activity, showing distinct signatures in lithospheric (●) and asthenospheric (○) magmas from the western USA; T = tholeiite. Curves show the result of simple batch melting of spinel or garnet peridotite using reasonable partition coefficients. After Asmerom *et al.* (2000).

(Fig. 13.35) are consistent with these predictions. All of the alkali basalts have large excess ^{231}Pa activities consistent with small-degree melting and rapid ascent of magma. In contrast, the tholeiite has a smaller excess, due to either a larger degree of melting or slower ascent. On the other hand, excess ^{230}Th activities are again grouped according to source type, with the asthenospheric suite yielding large excess activities, whereas the lithospheric suite yields data within error of the equiline.

13.4 Subduction-zone processes

Subduction-related magmatism is one of the most complex environments of magma genesis, since there are numerous potential sources of magmas and fluids in the subducting slab, the mantle wedge, and the overlying arc crust (section 6.6). In this situation, evidence from U-series data can provide additional constraints, especially on the timing of fluid metasomatism and magma genesis.

13.4.1 U–Th evidence

The first comprehensive study of Th isotope systematics in subduction-related magmas was undertaken by Hémond (1986). This work revealed a distribution clustering near the equiline on the U–Th isochron diagram, but with strong departures from the Th–Sr isotope mantle array.

The incoherent behaviour of Th–Sr isotope systematics suggested more complex processes at subduction zones, compared with ridges and plumes. With additional work (Gill and Williams, 1990; McDermott and Hawkesworth, 1991) systematic variations began to emerge on the U–Th isochron diagram (Fig. 13.36), where continental arcs tend to lie on the U-depleted side of the equiline, whereas oceanic arcs lie to the U-enriched side. High elemental U/Th ratios (low Th/U ratios) have long been known in the island-arc tholeiite series (Jakes and Gill, 1970), so the distribution of these data to the right of the equiline is not surprising. This effect is seen clearly in oceanic arcs such as Tonga and the Marianas, but is small or absent for associated back-arc volcanics. For these reasons, the effect is best explained by U metasomatism from the subducted slab into the melting zone in the overlying mantle wedge.

The slab-derived uranium flux can be seen most clearly when the overlying wedge is LIL-depleted (e.g. Tonga, Marianas), but in arcs with a more enriched wedge, the uranium flux may be swamped by U and Th derived from normal partial-melting processes. Hence, continental arcs, underlain by enriched mantle lithosphere, tend to exhibit U/Th behaviour similar to that of within-plate basalts. This effect can be seen by plotting the ^{238}U/^{230}Th activity ratio ($1/r$ in section 13.3.1) against the total Th content of the rock (Fig. 13.37), thus showing that arcs with strong U/Th enrichment are characterised by low total Th contents (McDermott and Hawkesworth, 1991).

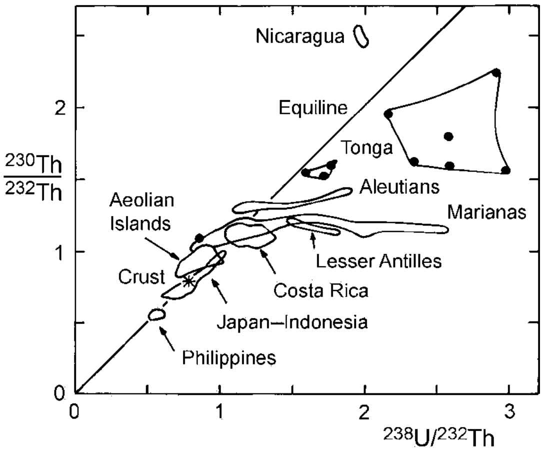

Fig. 13.36. U–Th isochron diagram, showing representative data for subduction-related magmas: * = average crust. After Hawkesworth *et al.* (1991).

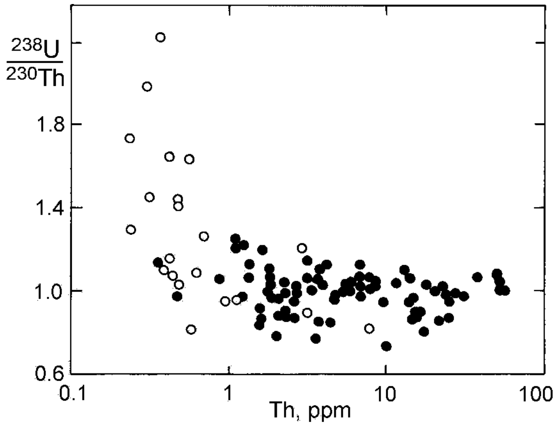

Fig. 13.37. Plot of ^{238}U/^{230}Th activity (= U/Th fractionation from the equiline) against total Th content of arc volcanics. Open symbols are from the Tonga and Marianas arcs. After McDermott and Hawkesworth (1991).

Magmas to the right of the equiline in Fig. 13.36 must reflect U/Th fractionation shortly before

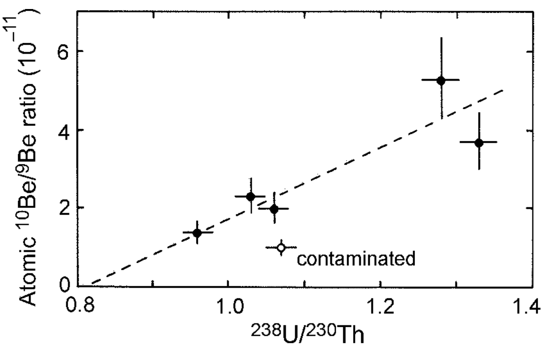

Fig. 13.38. Plot of ^{10}Be/^{9}Be ratio against ^{238}U/^{230}Th activity ratio in the Southern Volcanic Zone of the Andes, showing correlated enrichments. The open circle indicates a sample that has been perturbed by contamination in the continental crust. Modified after Sigmarsson *et al.* (1990).

eruption, in order to preserve isotopic disequilibrium. Independent evidence for the role of slab-derived fluids in this process comes from correlated ^{10}Be/^{9}Be and ^{238}U/^{230}Th ratios in the Southern Volcanic Zone of the Andes (Sigmarsson *et al.*, 1990). Because ^{10}Be is a cosmogenic isotope, it can only be introduced into the melting zone of arc magmas by subduction of ocean-floor crust and sediment (section 14.3.6). Therefore, a positive correlation between ^{10}Be/^{9}Be and ^{238}U/^{230}Th ratios suggests a similar location for uranium enrichment of arc magmas.

Several of the Southern Volcanic Zone samples have ^{238}U/^{230}Th activity ratios close to the equiline (in common with other continental arcs), but these all have elevated levels of cosmogenic beryllium (Fig. 13.38). Therefore, if we project the array in Fig. 13.38 back to zero cosmogenic beryllium, we can estimate the ^{238}U/^{230}Th activity of the wedge-derived component in subduction-related magmas. This has a value of 0.8–0.9, which is typical of asthenosphere-derived magmas from ocean ridges. This implies that the type of decompression melting seen at ridges (due to mantle diapirism) also occurs to some extent under arcs. This model is supported by ^{231}Pa data, which reveal Pa/U enrichments resembling MORB in most arcs (Pickett and Murrell, 1997). These ^{231}Pa/^{235}U enrichments can be explained by mild mantle upwelling (about 1 cm/yr), and may reflect gravitational instability in the source caused by fluid metasomatism (Turner, 2002).

A second distinct feature of subduction-related magmas on the U–Th isochron diagram is the extension of some arc suites to ^{232}Th-enriched compositions towards the origin (e.g. Philippines, Indonesia, Fig. 13.36). Because these suites lie close to the equiline, it appears that U/Th fractionation was relatively ancient. This is confirmed on a plot of κ_{Pb} against κ_{Th} in Fig. 13.39. Correlated increases in these values must reflect ancient U–Th fractionation events, since κ_{Pb} is controlled by long-lived U and Th isotopes. The best explanation of these data is contamination of arc magmas by partial melts of subducted sediments, which have appropriate compositions on both the U–Th isochron diagram and the κ–κ diagram (McDermott and Hawkesworth, 1991). Some sediment inevitably escapes the melting process, and is then recycled into the deep mantle.

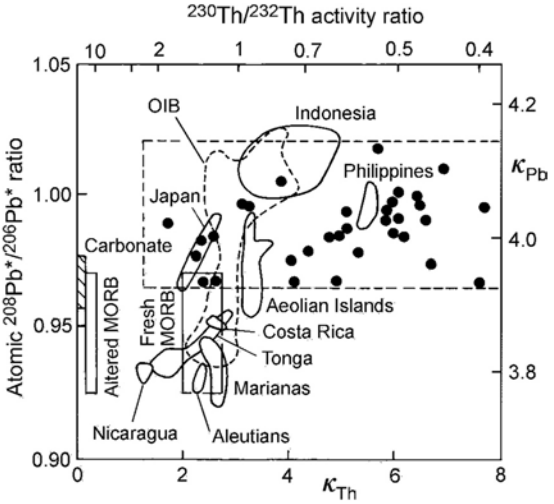

Fig. 13.39. Plot of κ_{Th} against κ_{Pb} to show correlated high values in some arcs and in ocean-floor sediments (●). Fields for OIB, MORB, altered MORB and marine sediments are shown for reference. After McDermott and Hawkesworth (1991).

Processes of fluid metasomatism and sediment contamination in arcs can be summarised on a Th activity *versus* Sr isotope plot (Fig. 13.40). On this diagram, the Aeolian arc defines a horizontal array that is consistent with two-component mixing between normal depleted mantle and subducted sediment. In contrast, Tongan data trend upwards towards altered MORB and marine carbonate, whence the U-enriched fluid flux is probably derived. A final note must be made regarding the Nicaraguan data. These have very high ^{230}Th contents, reminiscent of a metasomatised source, but actually fall on the U-depleted side of the equiline (Fig. 13.36). This unusual signature is probably best attributed to a source that suffered U metasomatism some time prior to magma generation.

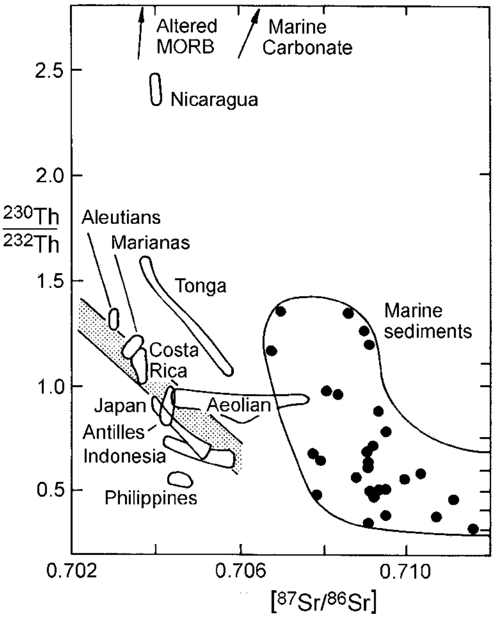

Fig. 13.40. Th–Sr isotope diagram showing possible mixing models to explain the departure of arc magmas from the mantle array of MORB and OIB compositions (shaded). After McDermott and Hawkesworth (1991).

Authors of recent studies on arc lavas have attempted to put tighter limits on the timing of fluid influx and magma genesis in the mantle wedge. Evidence relevant to the timing of fluid influx came from new studies by Turner *et al.* (1997) and Elliott *et al.* (1997) on the Tonga–Kermadec and Marianas arcs. These new data sets revealed low positive slopes on the U–Th isochron diagram, especially when the lower bound to each data set was considered (Fig. 13.41). This lower bound is believed to be most indicative of the typical time from fluid metasomatism of the mantle source to the time of eruption. In contrast, individual data points lying above the line are attributed to magma batches that had longer residence times in crustal magma chambers. The lower bounds to each data set gave slope ages of 30, 50 and 30 kyr, respectively, for the Tonga, Kermadec and Marianas arcs, suggesting that processes of magma genesis and ascent in oceanic arcs are quite rapid. However, because of its half-life of only 1600 yr, ^{226}Ra analysis offers the opportunity of seeing even more short-term processes in arc magmas.

13.4.2 Ra–Th evidence

Early work on the Ra–Th systematics of arc lavas (Gill and Williams, 1990) revealed large ^{226}Ra excesses in many lavas, with a weak positive correlation between ^{226}Ra and ^{230}Th enrichment. This led Gill and Williams to speculate that ^{226}Ra enrichment might be linked to subduction-related fluids. However, results of subsequent studies (e.g. Chabaux and Allègre, 1994) were equivocal. Furthermore, the discovery of tight correlation lines on the U–Th isochron diagram, implying that fluid enrichment occurred about 30 kyr ago, suggested that any ^{226}Ra introduced by subduction-related fluids would have decayed away before eruption. Therefore, Turner *et al.* (1997) suggested that the ^{238}U and ^{226}Ra excesses in arc magmas were due to separate processes: the former due to enrichment of the mantle wedge by subduction-related fluids, and the latter from the subsequent melting of this metasomatised mantle.

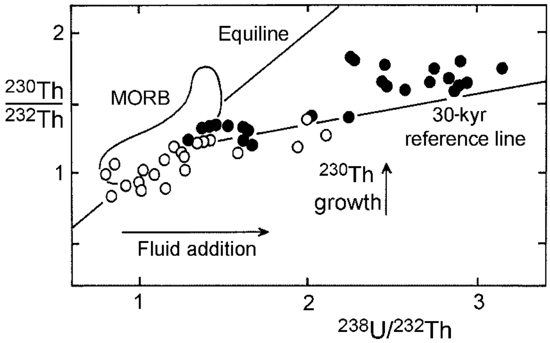

Fig. 13.41. Data arrays from the Tongan arc (●) and Kermadec arc (○) on a U–Th isochron diagram, showing arrays with possible age significance. After Turner *et al.* (1997).

A study on several different volcanic centres from the Lesser Antilles arc (Chabaux *et al.*, 1999) reversed this interpretation by showing that variations between ^{226}Ra/^{230}Th and ^{238}U/^{230}Th activity ratios were well correlated, suggesting that both ^{238}U and ^{226}Ra enrichment were caused by the subduction-related fluids themselves. This model was confirmed in a study of the Tonga–Kermadec arc (Turner *et al.*, 2000), which showed that the largest ^{226}Ra excesses were found in the most depleted basalts with the highest Ba/Th ratios (Fig. 13.42). Turner *et al.* also found that, as the silica contents of the magmas increased, ^{226}Ra excesses declined, reflecting increasing residence times in differentiating magma chambers.

Evidence that ^{226}Ra enrichment is caused by fluid metasomatism is problematical because the earlier U–Th evidence from the Tongan arc suggested that fluid enrichment occurred about 30 kyr ago. To overcome this problem, Turner *et al.* suggested that multiple fluid injections could have invaded the mantle wedge (Fig. 13.43). According to this model, an earlier event would have introduced both ^{238}U and ^{226}Ra into

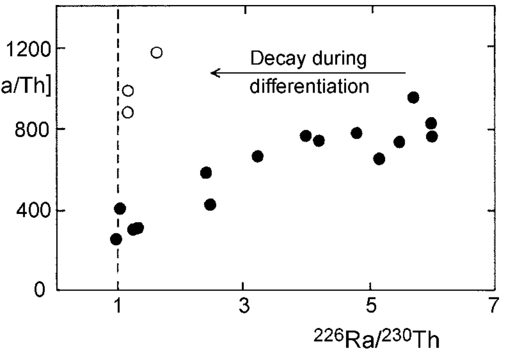

Fig. 13.42. Plot of Ba/Th weight ratio against ^{226}Ra/^{230}Th activity ratio for Tongan lavas, showing a positive correlation between ^{226}Ra enrichment and a trace-element indicator of subduction-related fluids. Open symbols are attributed to decay of ^{226}Ra in long-lived magma chambers. After Turner *et al.* (2000).

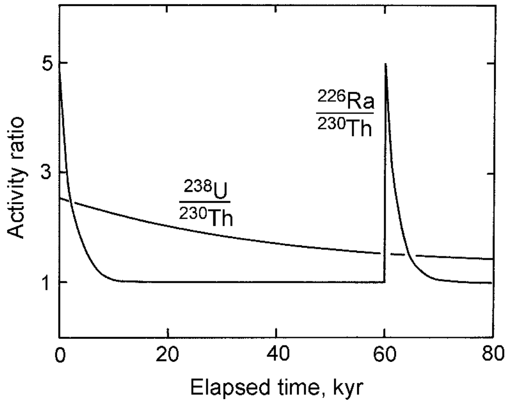

Fig. 13.43. Plot of excess activities of ^{226}Ra and ^{238}U against time to show the two-stage metasomatism proposed to explain the enrichment of Tongan lavas in U-series nuclides by subduction-related fluids. After Turner *et al.* (2000).

the wedge, but the latter nuclide soon decayed away. Meanwhile, as ^{226}Ra was decaying in the wedge, it was being replenished in the Th-rich subducting slab. Therefore, when a second episode of fluid metasomatism occurred, the replenished inventory of ^{226}Ra was again released into the mantle wedge. On this second occasion the metasomatic event was quickly followed by the extraction of a basaltic melt, which therefore picked up ^{238}U from the first event and ^{226}Ra from the second event.

Further confirmation of the role of fluid metasomatism in causing ^{226}Ra enrichments was provided by the observation of a positive correlation with beryllium isotope ratios in Andean lavas (Fig. 13.44).

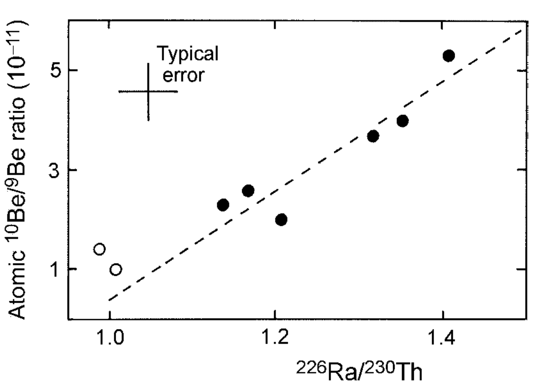

Fig. 13.44. Plot of atomic beryllium isotope ratio against ^{226}Ra/^{230}Th activity ratio for lavas from the Southern Volcanic Zone of the Andes. Open symbols are thought to have lost their excess ^{10}Be and ^{226}Ra during a complex magmatic history in the crust. After Sigmarsson *et al.* (2002).

Since cosmogenic ^{10}Be can originate only from subducted pelagic sediment (section 14.3.6), the correlation with ^{226}Ra provides strong evidence for the origin of these enrichments in subduction-related fluids (Sigmarsson *et al.*, 2002). However, Sigmarsson suggested that the data arrays with shallow slopes on the U–Th isochron diagram might be mixing lines produced by a multi-stage extraction of fluids from the slab, rather than isochrons dating the first stage of a two-phase process of fluid metasomatism.

As well as throwing more light on the timing of fluid metasomatism, ^{226}Ra evidence from arc basalts also provides new constraints on the rates of ascent of basic magmas. This is because the process of fluid metasomatism must occur at nearly 100 km depth, since the fluids are released by pressure-induced breakdown of amphibole in the subducting slab (section 6.6). In contrast, it is widely argued that ^{226}Ra enrichments under ocean ridges occur at quite shallow depths, due to ingrowth in the upwelling mantle source as a result of equilibrium porous flow (section 13.3.5).

To investigate these constraints in more detail, Turner *et al.* (2001) measured Ra–Th activities in seven additional arc systems, for comparison with the Tongan data. It was found that these other arc systems display behaviour similar to that of the Tongan arc, but less extreme in magnitude. Thus the other arcs also displayed positive correlations of initial ^{226}Ra/^{230}Th activity ratios with ^{238}U/^{230}Th activity and with Ba/Th weight ratio, and inverse hyperbolic relationships with silica content. These findings confirm that ^{226}Ra enrichments in arcs are a general product of metasomatism by slab-derived fluids, but they also place tight constraints on rates of magma ascent, suggesting that primary subduction-related magmas probably rise at rates approaching 1 km/yr from their mantle source at about 100 km depth. This implies that these magmas rise through open channel-ways rather than by melt percolation. However, it is not known whether this behaviour is peculiar to fluid-rich subduction-related magmas, or whether MORB melts might also ascend more rapidly than had previously been thought.

References

Allègre, C. J. (1968). ^{230}Th dating of volcanic rocks: A comment. *Earth Planet. Sci. Lett.* **5**, 209–10.

Allègre, C. J. and Condomines, M. (1976). Fine chronology of volcanic processes using ^{238}U/^{230}Th systematics. *Earth Planet. Sci. Lett.* **28**, 395–406.

Allègre, C. J. and Condomines, M. (1982). Basalt genesis and mantle structure studied through Th-isotopic geochemistry. *Nature* **299**, 21–4.

Asmerom, Y., Cheng, H., Thomas, R., Hirschmann, M. and Edwards, R. L. (2000). Melting of the Earth's lithospheric mantle inferred from protactinium thorium uranium isotopic data. *Nature* **406**, 293–6.

Asmerom, Y. and Edwards, R. L. (1995). U-series isotope evidence for the origin of continental basalts. *Earth Planet. Sci. Lett.* **134**, 1–7.

Beattie, P. (1993a). The generation of uranium series disequilibria by partial melting of spinel peridotite: constraints from partitioning studies. *Earth Planet. Sci. Lett.* **117**, 379–91.

Beattie, P. (1993b). Uranium–thorium disequilibria and partitioning on melting of garnet peridotite. *Nature* **363**, 63–5.

Bourdon, B., Joron, J.-L., Claude-Ivanaj, C. and Allègre, C. J. (1998). U–Th–Pa–Ra systematics for the Grande Comore volcanics: melting processes in an upwelling plume. *Earth Planet. Sci. Lett.* **164**, 119–33.

Bourdon, B., Langmuir, C. H. and Zindler, A. (1996a). Ridge–hotspot interaction along the Mid-Atlantic Ridge between 37° 30′ and 40° 30′ N: the U–Th disequilibrium evidence. *Earth Planet. Sci. Lett.* **142**, 175–89.

Bourdon, B., Zindler, A., Elliot, T. and Langmuir, C. H. (1996b). Constraints on mantle melting at mid-ocean ridges from global ^{238}U–^{230}Th disequilibrium data. *Nature* **384**, 231–5.

Capaldi, G., Cortini, M., Gasparini, P. and Pece, R. (1976). Short-lived radioactive disequilibria in freshly erupted volcanic rocks and their implications for the pre-eruption history of a magma. *J. Geophys. Res.* **81**, 350–8.

Capaldi, G., Cortini, M. and Pece, R. (1982). Th isotopes at Vesuvius: evidence for open system behaviour of magma-forming processes. *J. Volc. Geotherm. Res.* **14**, 247–60.

Capaldi, G., Cortini, M. and Pece, R. (1985). On the reliability of the ^{230}Th/^{238}U dating method applied to young volcanic rocks – (reply). *J. Volc. Geotherm. Res.* **26**, 369–76.

Capaldi, G. and Pece, R. (1981). On the reliability of the ^{230}Th–^{238}U dating method applied to young volcanic rocks. *J. Volc. Geotherm. Res.* **11**, 367–72.

Cerrai, E., Dugnani Lonati, R., Gazzarini, F. and Tongiorgi, E. (1965). Il metodo iono–uranio per la determinazione dell'età dei minerali vulcanici recenti. *Rend. Soc. Mineral. Ital.* **21**, 47–62

Chabaux, F. and Allègre, C. J. (1994). ^{238}U–^{230}Th–^{226}Ra disequilibria in volcanics: a new insight into melting conditions. *Earth Planet. Sci. Lett.* **126**, 61–74.

Chabaux, F., Hémond, C. and Allègre, C. J. (1999). ^{238}U–^{230}Th–^{226}Ra disequilibria in the Lesser Antilles arc: implications for mantle metasomatism. *Chem. Geol.* **153**, 171–85.

Charlier, B. and Zellmer, G. (2000). Some remarks on U–Th mineral ages from igneous rocks with prolonged crystallisation histories. *Earth Planet. Sci. Lett.* **183**, 457–69.

Cohen, A. S., Belshaw, N. S. and O'Nions, R. K. (1992). High precision uranium, thorium and radium isotope ratio measurements by high dynamic range thermal ionisation mass spectrometry. *Int. J. Mass Spectrom. Ion Processes* **116**, 71–81.

Cohen, A. S. and O'Nions, R. K. (1991). Precise determination of femtogram quantities of radium by thermal ionization mass spectrometry. *Anal. Chem.* **63**, 2705–8.

Cohen, R. S., Evensen, N. M., Hamilton, P. J. and O'Nions, R. K. (1980). U–Pb, Sm–Nd and Rb–Sr systematics of mid-ocean ridge basalt glasses. *Nature* **283**, 149–53.

Condomines, M. (1997). Dating recent volcanic rocks through ^{230}Th–^{238}U disequilibrium in accessory minerals: example of the Puy de Dôme (French Massif Central). *Geology* **25**, 375–8.

Condomines, M. and Allègre, C. J. (1980). Age and magmatic evolution of Stromboli volcano from ^{230}Th–^{238}U disequilibrium data. *Nature* **288**, 354–7.

Condomines, M., Hémond, Ch. and Allègre, C. J. (1988). U–Th–Ra radioactive disequilibria and magmatic processes. *Earth Planet. Sci. Lett.* **90**, 243–62.

Condomines, M., Morand, P. and Allègre, C. J. (1981). ^{230}Th–^{238}U radioactive disequilibria in tholeiites from the FAMOUS zones (Mid-Atlantic Ridge, 36° 50′ N): Th and Sr isotopic geochemistry. *Earth Planet. Sci. Lett.* **55**, 247–56.

Condomines, M. and Sigmarsson, O. (2000). ^{238}U–^{230}Th disequilibria and mantle melting processes: a discussion. *Chem. Geol.* **162**, 95–104.

Condomines, M., Tanguy, J. C., Kieffer, G. and Allègre, C. J. (1982). Magmatic evolution of a volcano studied by ^{230}Th–^{238}U disequilibrium and trace elements systematics: the Etna case. *Geochim. Cosmochim. Acta* **46**, 1397–416.

Condomines, M., Tanguy, J.-C. and Michand, V. (1995). Magma dynamics at Mt Etna: constraints from U–Th–Ra–Pb radioactive disequilibria and Sr isotopes in historical lavas. *Earth Planet. Sci. Lett.* **132**, 25–41.

Elliott, T., Plank, T., Zindler, A., White, W. and Bourdon, B. (1997). Element transport from slab to volcanic front at the Mariana arc. *J. Geophys. Res.* **102**, 14 991–15 019.

Fornari, D. J., Perfit, M. R., Allan, J. F. and Batiza, R. (1988). Small-scale heterogeneities in depleted mantle sources: near-ridge seamount lava geochemistry and implications for mid-ocean-ridge magmatic processes. *Nature* **331**, 511–13.

Forsyth, D. W., Scheirer, D. S., Webb, S. C. *et al.* (1998). Imaging the deep seismic structure beneath a Mid-Ocean Ridge: the MELT experiment. *Science* **280**, 1215–18.

Galer, S. J. G. and O'Nions, R. K. (1986). Magma genesis and the mapping of chemical and isotopic variations in the mantle. *Chem. Geol.* **56**, 45–61.

Gauthier, P.-J. and Condomines, M. (1999). ^{210}Pb–^{226}Ra radioactive disequilibria in recent lavas and radon degassing: inferences on the magma chamber dynamics at Stromboli and Merapi volcanoes. *Earth Planet. Sci. Lett* **172**, 111–126.

Gill, J. B. and Williams, R. W. (1990). Th isotope and U-series studies of subduction-related volcanic rocks. *Geochim. Cosmochim. Acta* **54**, 1427–42.

Goldstein, S. J., Murrell, M. T. and Janecky, D. R. (1989). Th and U isotopic systematics of basalts from the Juan de Fuca and Gorda Ridges by mass spectrometry. *Earth Planet. Sci. Lett.* **96**, 134–46.

Goldstein, S. J., Murrell, M. T., Janecky, D. R., Delaney, J. R. and Clague, D. A. (1991). Geochronology and petrogenesis of MORB from the Juan de Fuca and Gorda ridges by ^{238}U–^{230}Th disequilibrium. *Earth Planet. Sci. Lett.* **107**, 25–41; see also *Earth Planet. Sci. Lett.* **109**, 255–72 (erratum).

Goldstein, S. J., Murrell, M. T. and Williams, R. W. (1993). ^{231}Pa and ^{230}Th chronology of mid-ocean ridge basalts. *Earth Planet. Sci. Lett.* **115**, 151–9.

Hawkesworth, C. J., Hergt, J. M., McDermott, F. and Ellam, R. M. (1991). Destructive margin magmatism and the contributions from the mantle wedge and subducted crust. *Australian J. Earth Sci.* **38**, 577–94.

Hémond, Ch. (1986). *Géochimie isotopique du thorium et du strontium dans la série tholeiitique d'Islande et dans des séries calco-alcalines diverses.* Thèse Troisième Cycle, Université de Paris VII, 151 pp.

Hémond, Ch. and Condomines, M. (1985). On the reliability of the ^{230}Th–^{238}U dating method applied to young volcanic rocks – discussion. *J. Volc. Geotherm. Res.* **26**, 365–9.

Hémond, Ch., Condomines, M., Fourcade, S., Allègre, C. J., Oskarsson, N. and Javoy, M. (1988). Thorium, strontium and oxygen isotopic geochemistry in recent tholeiites from Iceland: crustal influence on mantle-derived magmas. *Earth Planet. Sci. Lett.* **87**, 273–85.

Jakes, P. and Gill, J. B. (1970). Rare earth elements and the island arc tholeiitic series. *Earth Planet. Sci. Lett.* **9**, 17–28.

Joly, J. (1909). On the radioactivity of certain lavas. *Phil. Mag.* **18**, 577.

Kelemen, P. B., Brann, M. and Hirth, G. (2000). Spatial distribution of melt conduits in the mantle beneath oceanic spreading ridges: observations from the Ingalls and Oman ophiolites. *Gcnbed* **1**, 000012.

Kelemen, P. B., Shimizu, N. and Salters, V. J. M. (1995). Extraction of mid-ocean-ridge basalt from the upwelling mantle by focused flow of melt in dunite channels. *Nature* **375**, 747–53.

Kigoshi, K. (1967). Ionium dating of igneous rocks. *Science* **156**, 932–4.

Landwehr, D., Blundy, J., Chamorro-Perez, E. M., Hill, E. and Wood, B. (2001). U-series disequilibria generated by partial melting of spinel lherzolite. *Earth Planet. Sci. Lett.* **188**, 329–48.

Langmuir, C. H., Bender, J. F., Bence, A. E. and Hanson, G. N. (1977). Petrogenesis of basalts from the FAMOUS area: Mid-Atlantic Ridge. *Earth Planet. Sci. Lett.* **36**, 133–56.

LaTourrette, T. Z., Kennedy, A. K. and Wasserburg, G. J. (1993). Thorium–uranium fractionation by garnet: evidence for a deep source and rapid rise of oceanic basalts. *Science* **261**, 739–42.

Lundstrom, C. C. (2003). Uranium series disequilibria in Mid-Ocean Ridge basalts: observations and models of basalt genesis. In: Bourdon, B., Henderson, G. M., Lundstrom, C. C. and Turner, S. P. *Uranium Series Geochemistry. Reviews in Mineralogy and Geochemistry*, vol. **52**. Mineralogical Society of America.

Lundstrom, C. C., Sampson, D. E., Perfit, M. R., Gill, J. and Williams, Q. (1999). Insights into mid-ocean ridge basalt petrogenesis: U-series disequilibria from Siqueiros Transform, Lamont Seamounts, and East Pacific Rise. *J. Geophys. Res.* **104**, 13 035–48.

Lundstrom, C. C., Williams, Q. and Gill, J. B. (1998). Investigating solid mantle upwelling rates beneath mid-ocean ridges using U-series disequilibria. 1: a global approach. *Earth Planet. Sci. Lett.* **157**, 151–65.

Macdougall, J. D., Finkel, R. C., Carlson, J. and Krishnaswami, S. (1979). Isotopic evidence for uranium exchange during low-temperature alteration of oceanic basalt. *Earth Planet. Sci. Lett.* **42**, 27–34.

McDermott, F., Elliott, T. R., van Calsteren, P. and Hawkesworth, C. J. (1993). Measurement of ^{230}Th/^{232}Th ratios in young volcanic rocks by single-sector thermal ionisation mass spectrometry. *Chem. Geol. (Isot. Geosci. Section)* **103**, 283–92.

McDermott, F. and Hawkesworth, C. (1991). Th, Pb, and Sr isotope variations in young island arc volcanics and oceanic sediments. *Earth Planet. Sci. Lett.* **104**, 1–15.

McKenzie, D. (1985a). ^{230}Th–^{238}U disequilibrium and the melting processes beneath ridge axes. *Earth Planet. Sci. Lett.* **72**, 149–57.

McKenzie, D. (1985b). The extraction of magma from the crust and mantle. *Earth Planet. Sci. Lett.* **74**, 81–91.

Newman, S., Finkel, R. C. and Macdougall, J. D. (1983). ^{230}Th–^{238}U disequilibrium systematics in oceanic tholeiites from 21 °N on the East Pacific Rise. *Earth Planet. Sci. Lett.* **65**, 17–33.

Newman, S., Finkel, R. C. and Macdougall, J. D. (1984). Comparison of ^{230}Th–^{238}U disequilibrium systematics in lavas from three hot spot regions: Hawaii, Prince Edward and Samoa. *Geochim. Cosmochim. Acta* **48**, 315–24.

O'Hara, M. J. and Mathews, R. E. (1981). Geochemical evolution in an advancing, periodically replenished, periodically tapped, continuously fractionated magma chamber. *J. Geol. Soc. Lond.* **138**, 237–77.

O'Nions, R. K. and McKenzie, D. (1993). Estimates of mantle thorium/uranium ratios from Th, U and Pb isotope abundances in basaltic melts. *Phil. Trans. Roy. Soc. Lond. A* **342**, 65–77.

Oversby, V. M. and Gast, P. W. (1968). Lead isotope compositions and uranium decay series disequilibrium in recent volcanic rocks. *Earth Planet. Sci. Lett.* **5**, 199–206.

Peate, D. W., Hawkesworth, C. J., van Calsteren, P. W., Taylor, R. N. and Murton, B. J. (2001). ^{238}U–^{230}Th constraints on mantle upwelling and plume–ridge interaction along the Reykjanes Ridge. *Earth Planet. Sci. Lett.* **187**, 259–72.

Pickett, D. A. and Murrell, M. T. (1997). Observations of ^{231}Pa/^{235}U disequilibrium in volcanic rocks. *Earth Planet. Sci. Lett.* **148**, 259–71.

Pyle, D. M., Dawson, J. B. and Ivanovich, M. (1991). Short-lived decay series disequilibria in the natrocarbonatite lavas of Oldoinyo Lengai, Tanzania: constraints on the timing of magma genesis. *Earth Planet. Sci. Lett.* **105**, 378–96.

Qin, Z. (1992). Disequilibrium partial melting model and its implications for trace element fractionations during mantle melting. *Earth Planet. Sci. Lett.* **112**, 75–90.

Reagan, M. K., Volpe, A. M. and Cashman, K. V. (1992). ^{238}U- and ^{232}Th-series chronology of phonolite fractionation at Mount Erebus, Antarctica. *Geochim. Cosmochim. Acta* **56**, 1401–7.

Reid, M. R. (1995). Processes of mantle enrichment and magmatic differentiation in the eastern Snake River Plain: Th isotope evidence. *Earth Planet. Sci. Lett.* **131**, 239–54.

Reid, M. R., Coath, C. D., Harrison, T. M. and McKeegan, K. D. (1997). Prolonged residence times for the youngest rhyolites associated with Long Valley Caldera: ^{230}Th–^{238}U ion microprobe dating of young zircons. *Earth Planet. Sci. Lett.* **150**, 27–39.

Rubin, K. H. and Macdougall, J. D. (1988). ^{226}Ra excesses in mid-ocean-ridge basalts and mantle melting. *Nature* **335**, 158–61.

Rubin, K. H. and Macdougall, J. D. (1990). Dating of neovolcanic MORB using (^{226}Ra/^{230}Th) disequilibrium. *Earth Planet. Sci. Lett.* **101**, 313–22.

Rubin, K. H., Macdougall, J. D. and Perfit, M. R. (1994). ^{210}Po–^{210}Pb dating of recent volcanic eruptions on the sea floor. *Nature* **368**, 841–4.

Schaefer, S. J., Sturchio, N. C., Murrell, M. T. and Williams, S. N. (1993). Internal ^{238}U-series systematics of pumice from the November 13, 1985, eruption of Nevado del Ruiz, Colombia. *Geochim. Cosmochim. Acta* **57**, 1215–19.

Sigmarsson, O., Carn, S. and Carracedo, J. C. (1998). Systematics of U-series nuclides in primitive lavas from the 1730–36 eruption of Lanzarote, Canary island, and implications for the role of garnet pyroxenites during oceanic basalt formations. *Earth Planet. Sci. Lett.* **162**, 137–51.

Sigmarsson, O., Chmeleff, J., Morris, J. and Lopez-Escobar, L. (2002). Origin of ^{226}Ra–^{230}Th disequilibria in arc lavas from southern Chile and implications for magma transfer time. *Earth Planet. Sci. Lett.* **196**, 189–96.

Sigmarsson, O., Condomines, M. and Fourcade, S. (1992). Mantle and crustal contribution in the genesis of recent basalts from off-rift zones in Iceland: constraints from Th, Sr and O isotopes. *Earth Planet. Sci. Lett.* **110**, 149–62.

Sigmarsson, O., Condomines, M., Morris, J. D. and Harmon, R. S. (1990). Uranium and ^{10}Be enrichments by fluids in Andean arc magmas. *Nature* **346**, 163–5.

Sigmarsson, O., Hémond, Ch., Condomines, M., Fourcade, S. and Oskarsson, N. (1991). Origin of silicic magma in Iceland revealed by Th isotopes. *Geology* **19**, 621–4.

Sims, K. W. W., DePaolo, D. J., Murrell, M. T. *et al.* (1999). Porosity of the melting zone and variations in the solid mantle upwelling rate beneath Hawaii: inferences from ^{238}U– ^{230}Th–^{226}Ra and ^{235}U–^{231}Pa disequilibria. *Geochim. Cosmochim. Acta* **63**, 4119–38.

Sims, K. W. W., Goldstein, S. J., Blichert-Toft, J. *et al.* (2002). Chemical and isotopic constraints on the generation and transport of magma beneath the East Pacific Rise. *Geochim. Cosmochim. Acta* **66**, 3481–504.

Spiegelman, M. and Elliott, T. (1993). Consequences of melt transport for uranium series disequilibrium in young lavas. *Earth Planet. Sci. Lett.* **118**, 1–20.

Spivak, A. J. and Edmond, J. M. (1987). Boron isotope exchange between seawater and the oceanic crust. *Geochim. Cosmochim. Acta* **51**, 1033–43.

Taddeucci, A., Broecker, W. S. and Thurber, D. L. (1967). ^{230}Th dating of volcanic rocks. *Earth Planet. Sci. Lett.* **3**, 338–42.

Thompson, R. N., Morrison, M. A., Hendry, G. L. and Parry, S. J. (1984). An assessment of the relative roles of crust and mantle in magma genesis: an elemental approach. *Phil. Trans. Roy. Soc. Lond. A* **310**, 549–90.

Turner, S. (2002). On the time-scales of magmatism at island-arc volcanoes. *Phil. Trans. Roy. Soc. Lond. A* **360**, 2853–71.

Turner, S., Bourdon, B., Hawkesworth, C. J. and Evans, P. (2000). ^{226}Ra–^{230}Th evidence for multiple dehydration events, rapid melt ascent and the time scales of differentiation beneath the Tonga Kermadec island arc. *Earth Planet. Sci. Lett.* **179**, 581–93.

Turner, S., Evans, P. and Hawkesworth, C. (2001). Ultra-fast source-to-surface movement of melt at island arcs from ^{226}Ra–^{230}Th systematics. *Nature* **292**, 1363–6.

Turner, S., Hawkesworth, C., Rogers, N. *et al.* (1997). ^{238}U–^{230}Th disequilibria, magma petrogenesis, and flux rates beneath the depleted Tonga–Kermadec island arc. *Geochim. Cosmochim. Acta* **61**, 4855–84.

Volpe, A. M. and Goldstein, S. J. (1993). ^{226}Ra–^{230}Th disequilibrium in axial and off-axis mid-ocean ridge basalts. *Geochim. Cosmochim. Acta* **57**, 1233–41.

Williams, R. W., Collerson, K. D., Gill, J. B. and Deniel, C. (1992). High Th/U ratios in subcontinental lithospheric mantle: mass spectrometric measurement of Th isotopes in Gaussberg lamproites. *Earth Planet. Sci. Lett.* **111**, 257–68.

Williams, R. W. and Gill, J. B. (1989). Effects of partial melting on the uranium decay series. *Geochim. Cosmochim. Acta* **53**, 1607–19.

Williams, R. W. and Gill, J. B. (1992). Th isotope and U-series disequilibria in some alkali basalts. *Geophys. Res. Lett.* **19**, 139–42.

Williams, R. W., Gill, J. B. and Bruland, K. W. (1986). Ra–Th disequilibria systematics: timescale of carbonatite magma formation at Oldoinyo Lengai volcano, Tanzania. *Geochim. Cosmochim. Acta* **50**, 1249–59.

Williams, R. W., Gill, J. B. and Bruland, K. W. (1988). Ra–Th disequilibria: timescale of carbonatite magma formation at Oldoinyo Lengai volcano, Tanzania. *Geochim. Cosmochim. Acta* **52**, 939. (Reply to Gittins, J. (1988). Comment on 'Ra–Th disequilibria systematics: timescale of carbonatite magma formation at Oldoinyo Lengai volcano, Tanzania'. *Geochim. Cosmochim. Acta* **52**, 937.)

Wood, B. J., Blundy, J. D. and Robinson, J. A. C. (1999). The role of clinopyroxene in generating U-series disequilibrium during mantle melting. *Geochim. Cosmochim. Acta* **63**, 1613–20.

14 Cosmogenic nuclides

The Earth undergoes continuous bombardment by cosmic rays from the galaxy. These are atomic nuclei (mainly protons) travelling through interstellar and interplanetary space at relativistic speeds. The net flux of cosmic-ray energy intercepted by the Earth is low, and roughly equivalent in intensity to visible starlight. However, the energy of each particle is very high, averaging several billion electron volts (the kinetic energy of a gas molecule at 10 000 K is about one electron volt). Cosmic rays can therefore interact strongly with matter.

Cosmic rays generate unstable nuclides in two principal ways: by direct bombardment of target atoms (causing atomic fragmentation or 'spallation'), and by the agency of cosmic-ray-generated fast neutrons. The latter are produced by the collision of cosmic rays with target molecules and slowed by further collisions to thermal kinetic energies. These 'thermal' neutrons are able to interact with the nuclei of stable atoms, causing transformations to radioactive nuclei. The 'cosmogenic' nuclides thus produced can be used as dating tools and as radioactive tracers.

Terrestrial cosmogenic nuclides ('TCN') are produced in two principal sites. The first is the atmosphere, where cosmic rays interact with nitrogen, oxygen and rare gases. The resulting 'atmospheric cosmogenic nuclides' include radiocarbon and other cosmogenic isotopes such as ^{10}Be, ^{36}Cl and ^{129}I that are useful as environmental tracers. The second site of production is within the surfaces of terrestrial rocks, termed *in situ* production. These nuclides, including ^{26}Al, ^{10}Be and ^{36}Cl, are useful for dating the surface exposure of rocks.

The measurement of cosmogenic nuclides falls into two developmental stages. Early work, almost entirely on ^{14}C, was by radioactive counting. More recently, accelerator mass spectrometry (AMS) has revolutionised the field of cosmogenic nuclides, allowing ^{14}C measurement on very small samples and allowing the utilisation of several other cosmogenic nuclides for the first time.

14.1 Carbon-14

The collision of cosmic-ray-produced thermal neutrons with nitrogen nuclei has a reasonable probability of generating radiocarbon by the n, p reaction:

$$^{14}_{7}\mathrm{N} + \mathrm{n} \rightarrow {}^{14}_{6}\mathrm{C} + \mathrm{p}$$

Oxidation to carbon dioxide follows rapidly, and this radioactive CO_2 joins the carbon cycle. It may be absorbed photosynthetically by plants, or may exchange with CO_2 in water and ultimately be deposited as carbonate.

^{14}C decays by β emission back to ^{14}N with a half-life of about 5700 yr. Hence, atmospheric ^{14}C activity is the result of an equilibrium between cosmogenic production, radioactive decay (and exchange with other reservoirs). During their lifetime, living tissues will exchange CO_2 with the atmosphere, and hence remain in radioactive equilibrium with it. However, on death this exchange is expected to stop, whereupon ^{14}C in the tissue decays with time. If the initial level of ^{14}C activity in a carbon sample at death (A_0) can be predicted, and if it has subsequently remained a closed system, then by measuring its present level of activity (A), its age (t) can be determined. This can be expressed as the radioactive-decay law (from equation [1.5])

$$A = A_0 e^{-\lambda t} \qquad [14.1]$$

The idea of using radiocarbon as a dating tool was conceived by W. F. Libby, for which he received the Nobel Prize for Chemistry in 1960. The early history of the field is described by Kamen (1963), and a twenty-five-year review was given by Ralph and Michael (1974). Taylor (1987) has written an account of its archaeological applications.

The Earth's magnetic field deflects incoming charged particles so that the equatorial cosmic-ray flux is four times less than the polar flux (Fig. 14.1). Therefore, one of the first questions which Libby and his co-workers investigated was whether the present-day activity of ^{14}C was uniform over the Earth's surface. No latitude dependence was found in modern wood (Anderson and Libby, 1951), and the average specific activity found was 15.3 disintegrations per minute per gram of carbon (dpm/g). Hence, geographical homogenisation of ^{14}C in the atmosphere (before its uptake by plants) appears to be a justifiable assumption.

More recent evidence for the rate of homogenisation of atmospheric ^{14}C came from atmospheric nuclear explosions. Figure 14.2 shows the levels of ^{14}C at various locations around the world after the addition of excess ^{14}C from atmospheric tests (Libby, 1970). World-wide atmospheric homogenisation occurs after only two or three years. The recovery rate of the Mojave Desert samples after 1965 suggests that the timescale for buffering of the atmosphere by surface ocean water is somewhat longer (17 yr), but this is still very short relative to the half-life of ^{14}C.

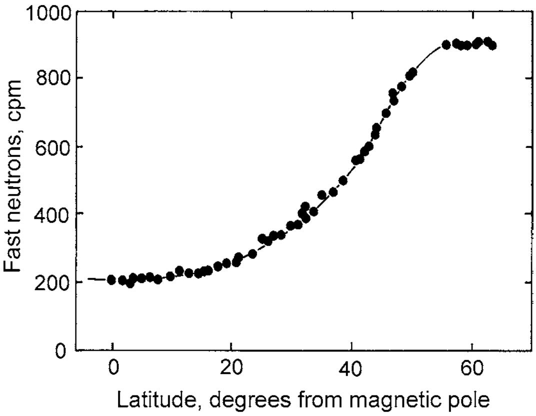

Fig. 14.1. Plot of cosmogenic neutron flux as a function of latitude to show the geographical variation in cosmic-ray intensity. After Simpson (1951).

Libby (1952) also assumed that the atmosphere had a constant ^{14}C activity through time, as a result of equilibrium between constant rates of production and decay. Hence, the ^{14}C activity of recent organic tissue was taken to be equal to the 'initial' activity of carbon samples formed in the past. A closed-system assumption was also argued, on the basis that complex organic molecules cannot exchange carbon with the environment after death. (However, such exchange can occur in many carbonates, making them less reliable as dating material.) The above-mentioned assumptions were supported (Arnold and Libby, 1949) by a good concordance between ^{14}C dates and historical ages for a suite of test samples (Fig. 14.3). These ages were based on a ^{14}C half-life of 5568 ± 30 yr obtained from a weighted mean of the four most precise laboratory counting determinations, all of which clustered closely around the mean.

In the natural reduction of CO_2 to carbon by photosynthesis, and during laboratory preparation for analysis (e.g. combustion of carbon to CO_2), isotopic fractionation between carbon isotopes can occur. This is due to the weaker bonding, and hence greater reactivity, of the lighter isotope (section 2.2.3). In order to assess the fractionation between ^{14}C and ^{12}C in natural and laboratory processes, Craig (1954) proposed that the ^{13}C/^{12}C ratio of samples be measured by mass spectrometry. Because fractionation is mass-dependent, ^{14}C/^{12}C fractionation will be twice as great as ^{13}C/^{12}C fractionation. The latter is normally expressed relative to the PeeDee belemnite (PDB) standard

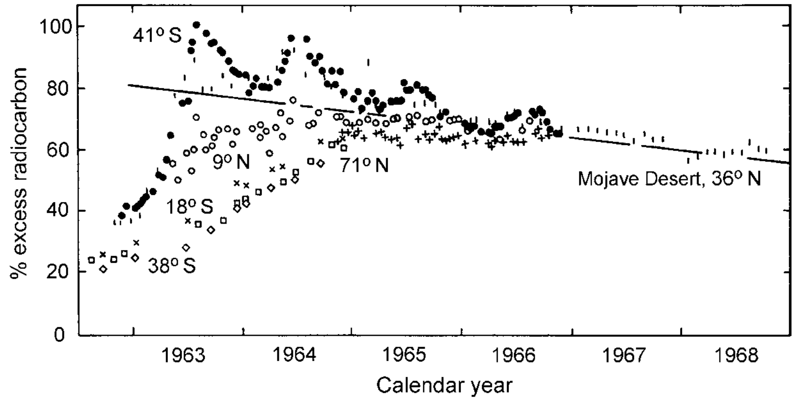

Fig. 14.2. Excess (bomb-produced) atmospheric ^{14}C measured at various latitudes round the world, during and after the peak of atmospheric nuclear testing. The regression line shows the result of carbon exchange with seawater. After Libby (1970).

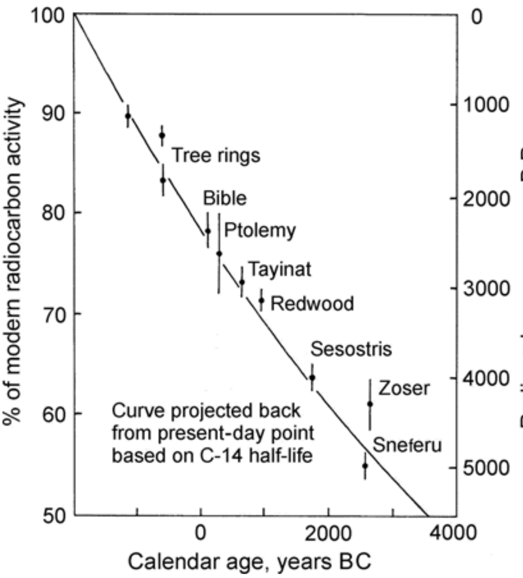

Fig. 14.3. Plot of ^{14}C activity in archaeological samples of known age, relative to the predicted decay curve based on modern wood and a half-life of 5568 yr. After Libby (1952).

(Craig, 1957):

$$\delta\,^{13}\mathrm{C} = \left(\frac{(^{13}\mathrm{C}/^{12}\mathrm{C})_{\mathrm{sample}}}{(^{13}\mathrm{C}/^{12}\mathrm{C})_{\mathrm{PDB}}} - 1\right) \times 10^3 \qquad [14.2]$$

This fractionation factor can be directly converted into a correction to the ^{14}C age using Fig. 14.4 (Mook and Streurman, 1983). In this diagram, normal $\delta\,^{13}$C compositions for various types of sample are shown. Because 'modern wood' is established as the reference point for calibrating the efficiency of ^{14}C counting equipment, age corrections must be applied relative to this type of material (Fig. 14.4), which has a normal or 'calibration' value of $\delta\,^{13}\mathrm{C} = -25$ per mil (relative to PDB). In marine carbonates, this effect is offset by the 400 yr ^{14}C age of ocean surface water, which must be subtracted from measured ages (section 14.1.6).

14.1.1 ^{14}C measurement by counting

The development of the radiocarbon method went hand in hand with the development of low-level counting techniques. The specific activity of ^{14}C is small, yielding a maximum count-rate of 13.6 decays per minute per gram (dpm/g) for modern wood, but only 0.03 dpm/g for a sample 50 kyr old. Furthermore, the maximum β energy is low (156 keV), so that, in a solid source of non-zero thickness, a significant fraction of emitted β particles would be absorbed by other carbon atoms in the sample.

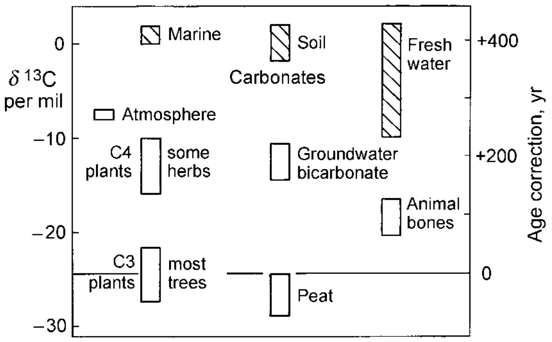

Fig. 14.4. Carbon isotope fractionation effects in various materials, and necessary corrections to calibrated ^{14}C ages for C3 plants (wood). Carbonates are hatched. After Mook and Streurman (1983).

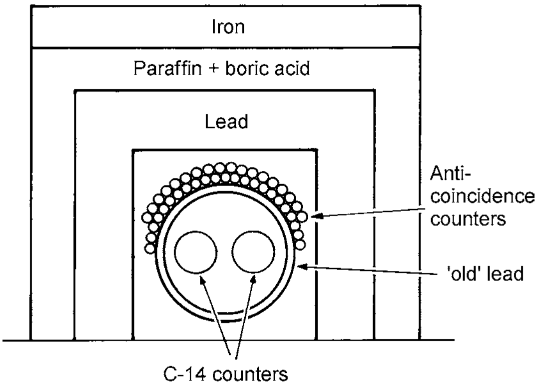

Fig. 14.5. Components in passive and active screening of a CO_2 gas counter. After Mook and Streurman (1983).

Libby's early determinations of ^{14}C activity were made on samples of solid carbon using a 'screen-wall' Geiger counter. However, this method was soon replaced by the analysis of CO_2 in a gas counter (de Vries and Barendsen, 1953). CO_2 is very readily prepared, and in the gas counter there is no risk of losing counts (due to absorption) before the β particles reach the detector.

Unfortunately the natural background level of activity which will be measured by a gas counter (cosmic rays and gamma emission from natural materials) is far larger than the level of activity from the sample itself. Hence, two screening techniques are used (Fig. 14.5). The first involves a thick wall of material which itself has a low level of activity (e.g. 'old' lead). The second component is an array of geiger tubes arranged immediately round the gas proportional counter. The geiger tubes are electronically connected in anti-coincidence to the proportional counter. If a high-energy particle such as a cosmic ray enters the shielding, it will trigger the geiger tubes at almost the same time as the proportional counter, and the two signals will cancel out. The dramatic effects of these shielding techniques on the counting background were demonstrated by Ralph (1971) using a counter filled with 'dead' CO_2 made from anthracite coal. Count rates (dpm) were as follows:

No shielding	1500
Shielded by iron and mercury	400
Shielded and with anti-coincidence counters turned on	8

Subsequently to Libby's work, his dating assumptions and half-life value have been re-examined. However, it was decided to continue to publish radiocarbon ages using Libby's atmospheric composition and half-life (Godwin, 1962). These are called 'conventional ages'. Correction factors are subsequently applied to determine a true 'historical' age. We will now re-examine two of the most important assumptions.

14.1.2 The closed-system assumption

Loss of carbon from a system during its geological lifetime is not usually a problem in radiocarbon dating. However, contamination with extraneous environmental carbon may be a major problem. To exclude such contamination, rigorous sample-preparation procedures have been developed.

When dating wood or charcoal for archaeological purposes, the objective is to determine the time when the tree was cut down. Hence, it is only necessary to exclude post-mortem exchange with the environment. For this, an acid–alkali–acid leaching treatment referred to as the AAA treatment was found to be effective (Olsson, 1980). The three steps are as follows:

(1) Leach with 4% HCl at 80 °C for 24 h to remove sugars, resins, soil carbonate and infiltrated humic acids.
(2) Leach with up to 4% NaOH at up to 80 °C for at least 24 h to remove infiltrated tannic acids (this step also removes part of the lignin).
(3) Repeat step (1) to remove any atmospheric CO_2 absorbed during the alkali step.

The overall process removes about 50% of the original carbon.

When dating tree rings for calibration studies (see below), the objective is quite different. In this case it is essential to sample only material laid down in the year of growth corresponding to the annual ring. This requires that all material deposited during the subsequent life of the tree (e.g. lignin) must be leached away. This is accomplished by inserting a step (1a) into the above procedure, in which the wood chips are bleached by progressive addition of an almost equal weight of sodium perchlorate powder in dilute acetic acid at 70 °C. The procedure removes up to 75% of the carbon, leaving a residue of pure cellulose for analysis (Mook and Streurman, 1983).

When dating bones, all of the inorganic carbonate fraction must be removed by leaching with very dilute HCl, because this fraction invariably exchanges carbon with groundwater. The organic carbon fraction in the bone is in the form of collagen, which is resistant to post-mortem exchange. Various methods for the treatment of bones are described by Olsson *et al.* (1974). Leaching with acid has also been shown to improve the accuracy of radiocarbon ages on corals (see below).

14.1.3 The initial-ratio assumption

As radiocarbon measurements became more precise, systematic age discrepancies between historical material and radiocarbon dates began to suggest that the level of ^{14}C activity in the atmosphere had varied with time. The first evidence for such temporal variations in ^{14}C activity was provided by Suess (1955), who found that twentieth-century wood was 2% depleted in activity relative to nineteenth-century wood. This was attributed to dilution of radioactive carbon by 'dead' carbon introduced into the atmosphere by burning fossil fuel (nuclear tests later drove the equilibrium in the other direction by adding ^{14}C to the atmosphere). Subsequently, de Vries (1958) found that late-seventeenth-century wood had about 2% *higher* activity than nineteenth-century wood. These two 'anomalies' are sometimes called the 'Suess' and 'de Vries' effects.

The discovery of secular variations in ^{14}C activity has elicited various models attempting to explain these variations. Forbush (1954) observed that the eleven-year cycle of sunspot activity was inversely correlated with cosmic-ray intensity. This is because high levels of solar activity (marked by increased sunspot activity) cause an increase in the solar wind of ionised particles, which extends the Sun's magnetic field and deflects galactic cosmic rays away from the Earth. Calculations by Oeschger *et al.* (1970) suggest that the stratospheric cosmic-ray flux may be nearly doubled at solar minima, relative to maxima.

Because historical records for sunspot frequency are available, this provided a means of predicting past cosmic-ray intensity, and hence ^{14}C production, over the last few hundred years. Stuiver (1961) performed these calculations and suggested that a sunspot minimum in the late seventeenth century could explain the 'de Vries effect', namely the ^{14}C activity maximum at that time. This was confirmed by Stuiver (1965) using more detailed ^{14}C data (Fig. 14.6).

Extension of the ^{14}C activity curve to well before the time of Christ revealed large long-term variations, in addition to the short-term effects attributed to changes in solar cosmic-ray modulation (Suess, 1965). Elsasser *et al.* (1956) had predicted that if the strength of the Earth's magnetic field displayed secular variations, as suggested by Thellier (1941), then this would have affected the paleo-cosmic-ray flux incident on the atmosphere, and hence ^{14}C production. However, strong evidence of a causal relationship with the Earth's field strength was not established until Bucha and Neustupny (1967) provided more extensive paleomagnetic intensity measurements. These data revealed sinusoidal variations in the Earth's magnetic field strength that matched the sinusoidal deviations between radiocarbon and absolute ages.

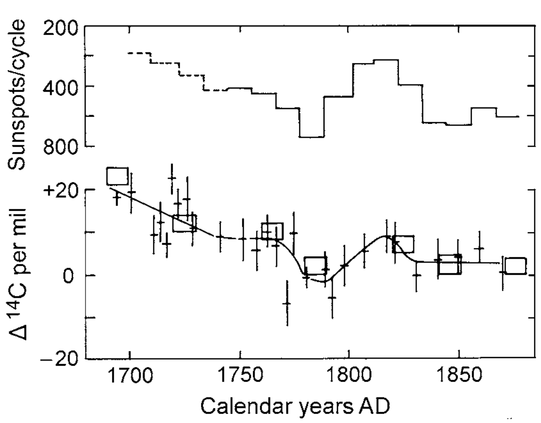

Fig. 14.6. Plots of sunspot activity and relative ^{14}C activity, expressed as Δ, parts per mil, to show coherent anti-correlation in the eighteenth and nineteenth centuries. A best-fit curve is drawn using two ^{14}C data sets (early error boxes and later bars). After Stuiver (1965).

By modelling the effect of paleomagnetic intensity variations on ^{14}C activity, Bucha and Neustupny were able to match the deviations between tree-ring and radiocarbon timescales almost exactly (Fig. 14.7). A comparison with historically dated wood gave a very similar result, except that this curve was translated upwards by about 100 yr. This can be attributed to the average time delay between wood growth and utilisation. Because the model of Bucha and Neustupny linked the long-time-period deviations between radiocarbon and absolute ages to variations in the global magnetic field, it also implied that the deviations should be of a systematic world-wide nature. Hence it gave grounds for the establishment of very precise calibration sequences, which could then be used for world-wide correction of 'conventional' radiocarbon ages to calendar ages.

14.1.4 Dendrochronology

It was quickly realised that the most accurate way to calibrate the 'conventional' ^{14}C timescale for initial ^{14}C variations was to integrate radiocarbon dates with tree-ring chronologies. Great efforts have been expended on this task over the last thirty years.

The longest dendrochronology calibration range has been achieved using the stunted bristlecone pine. When

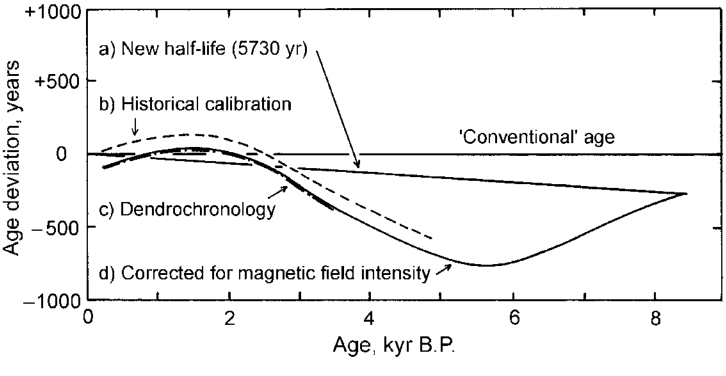

Fig. 14.7. Plot of age deviation between 'conventional' radiocarbon ages (half-life = 5568 yr) and other age determinations: (a) radiocarbon method using a half-life of 5730 yr; (b) historical timescale; (c) dendrochronology timescale; and (d) using a half-life of 5730 yr and correction for variations of the Earth's magnetic field intensity. After Bucha and Neustupny (1967).

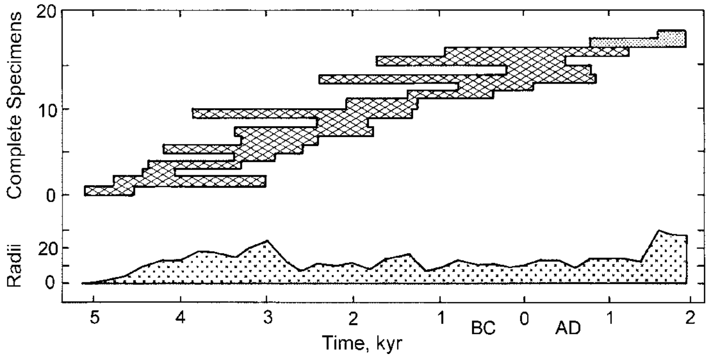

Fig. 14.8. A 'master' tree-ring chronology based on living and dead specimens of Bristlecone pine with overlapping age ranges. The upper chart shows the range of each specimen. The lower chart shows the total number of radii from which raw data were derived. After Ferguson (1970).

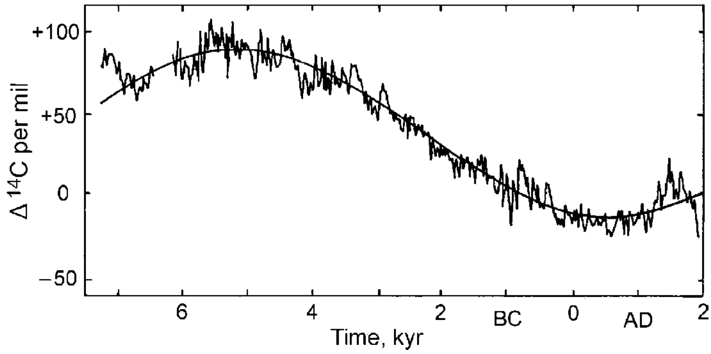

Fig. 14.9. Changes in atmospheric ^{14}C activity during the last 9000 years, presented in the form of isotopic fractionation per mil, based on 'continuous' bristlecone pine and 'floating' European oak chronologies. The apparent fit to a sinusoidal function is now known to be coincidental. After Bruns *et al.* (1983).

this work began the species was known as *Pinus aristata*. However, the great longevity of some populations of the bristlecone pine was subsequently recognised by placing these populations in a new species named *Pinus longaeva*. The semi-desert habitat of this tree gives rise to its great longevity and also permits good preservation of the dry wood after death. Thus, Ferguson (1970) erected a continuous master chronology reaching back over 7000 yr, which was based on several living trees and seventeen specimens of dead wood from the White Mountains of eastern–central California (Fig. 14.8). This suite now extends nearly 8700 yr (to 6700 BC) and includes the oldest living tree, which is more than 4600 yr old! (Ferguson and Graybill, 1983).

Suess (1970) presented a data set of 315 radiocarbon measurements for bristlecone pine from Ferguson's collection, and used this data set to construct a continuous calibration curve from 5200 BC to the present. One of the prominent features of this curve was the presence of numerous 'wiggles', with wavelengths of 100–300 yr, superimposed on the longer-term variations discussed above. Suess attracted much criticism because his calibration curve was drawn by eye through the measured points (with 'cosmic Schwung'), rather than using a statistical curve fit. Many other workers, as late as Pearson et al. (1977), maintained that the second-order 'wiggles' identified by Suess were an artefact of statistical uncertainties in the data and had no real meaning. However, this was illogical, since the known 'de Vries effect' wiggles of the seventeenth century AD were of similar magnitude. The reality of the 'Suess' wiggles in the ancient radiocarbon record (around 3500 BC) was finally established by De Jong *et al.* (1979). These wiggles are seen superimposed on long-term ^{14}C variations in the 9000-yr calibration curve shown in Fig. 14.9.

Comparatively large (20 per mil) ^{14}C variations between tree rings from single sunspot cycles have been claimed by some workers (e.g. Baxter and Farmer, 1973; Fan *et al.*, 1986). However, atmospheric ^{14}C variations on this timescale are not consistent with the experimental data of Stuiver and Quay (1981). The latter workers modelled small (4 per mil) ^{14}C variations over sunspot cycles, which are at the limits of measurement precision.

The convoluted shape of the calibration curve introduces ambiguities into ^{14}C dating within many periods, since a single radiocarbon age can correspond to more than one historical age. These ambiguities may sometimes be resolved by applying historical constraints (see section 14.2.1). Alternatively, they may be avoided in the dating of wood samples, if a piece spanning more than about fifty growth rings can be dated. This ring sequence then forms a small 'floating' calibration curve, which can be 'wiggle-matched' with the known calibration curve to yield a much more accurate time-span for the growth of the sample wood. Suess and Strahm (1970) demonstrated this technique when they dated a floating tree-ring sequence from Auvernier (Switzerland) against the bristlecone pine calibration curve (Fig. 14.10). This procedure allowed the age uncertainties on the Auvernier material to be reduced from hundreds of years to decades.

In order to obtain the highest-quality calibration curve, it is desirable to analyse samples representing single annual rings. However, the small size of the bristlecone pine limits the precision which can be obtained, because of the limited amount of sample for analysis. Therefore, other work has been devoted to obtaining a more detailed calibration curve from larger trees (e.g. De Jong *et al.*, 1979).

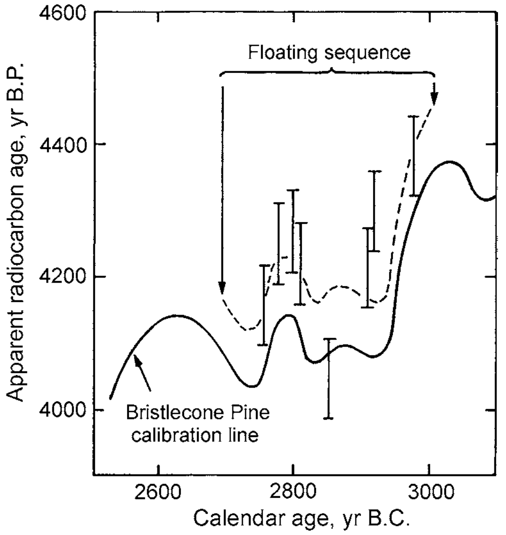

Fig. 14.10. Comparison of ^{14}C data for a wood sample and the calibration curve to show the application of 'wiggle matching'. The dashed line is the proposed fit to the measured data, which are shown with error bars. After Suess and Strahm (1970).

In Europe, the most important tree for detailed calibration purposes is the oak (*Quercus petraea*). This is partly because the oak very rarely has missing annual growth rings. In contrast, the widespread alder may lack up to 45% of its annual rings (Huber, 1970). The oak is also ideal because it is a long-lived, large tree that displays good resistance to decay after death. In North America, the last 1500 yr of the ^{14}C timescale has been calibrated in great detail (Stuiver and Pearson, 1986) using large trees such as the Douglas fir (*Pseudotsuga menziesii*) and giant redwood (*Sequoia gigantea*). This curve was adopted as a new international standard in 1985 (Mook, 1986). Part of this curve is used below (section 14.2.1).

Even more exact dates are possible if the floating chronology comes from an area geographically near to the calibration chronology. Having 'wiggle-matched' the radiocarbon data to obtain historical ages with uncertainties of a few decades, the widths of the tree-rings themselves are then matched between the floating and calibration material, to obtain an exact date. However, this procedure is only possible if the two chronologies come from areas with the same weather pattern, thus giving rise to similar growth variations.

Hillam *et al.* (1990) used this procedure to date a Neolithic wooden walkway from Somerset (England) to the probable year of its construction (3806 BC). This age is based on the fact that ten timbers had bark surfaces with ages of 3807/3806 BC, and must therefore have been cut down in that calendar year. A single sample with a bark age of 3800 BC probably represents a later repair to the walkway. This work suggests that, as dendrochronologies are completed for more areas of the world, it should increasingly be possible to date large wood samples to the exact age of their felling.

In principle, it should also be possible to create a floating radiocarbon sequence by the analysis of several plant macro-fossils (such as seeds) from a soil sequence. Such a sequence could then be wiggle-matched to the dendro-calibration to determine a much more reliable calendar age than is possible from the calibration of single radiocarbon ages.

14.1.5 Production and climatic effects

Many attempts have been made to extend the calibrated radiocarbon timescale beyond the limit of dendrochronology. Early work was mainly based on varved lake sediments (e.g. Tauber, 1970) or ice cores (e.g. Hammer *et al.*, 1986). Sediment varves are usually caused by a change in the type of minerals being deposited at different times of the year, but are not as reproducible as tree-rings. For example, if sediment from the bottom is stirred up by strong winds and then redeposited, it may be possible for more than one varve layer to be deposited in a year. As a result, many different and conflicting calibration lines were proposed, which largely discredited this approach.

Bard *et al.* (1990a) took a major step forwards in extending the radiocarbon calibration using mass-spectrometric U-series analysis (section 12.2.1). This method was used to assign absolute ages to Barbados corals that had previously been analysed for ^{14}C. In view of uncertainties about closed-system behaviour in carbonates, the method was tested by analysis of samples less than 10 kyr old. These gave ages in good agreement with the dendrochronology timescale, after applying a 400-yr correction for equilibration of ^{14}C between atmospheric and surface seawater (the 'reservoir age').

Results for older samples were presented on a plot of $\Delta\,^{14}$C activity (relative to modern wood) against U–Th age (Fig. 14.11). Samples in the range 10–15 kyr gave $\Delta\,^{14}$C activities well within error of those predicted from geomagnetic field-strength data. Samples older than 15 kyr initially gave more scattered data. However, repeat analysis of the ^{14}C measurements after strong acid leaching gave more consistent results (Bard *et al.*, 1993; 1998).

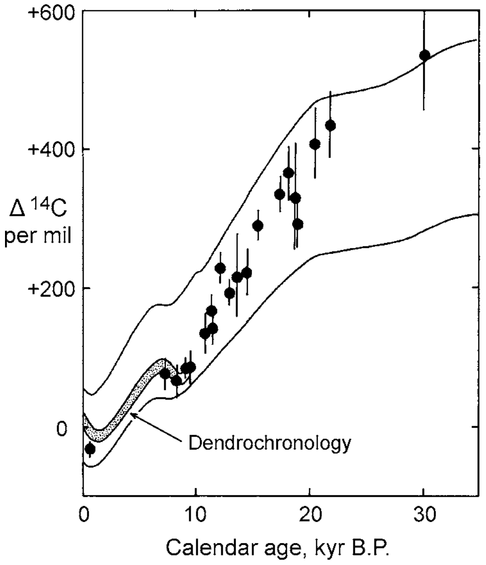

Fig. 14.11. Plot of $\Delta\,^{14}$C activity in corals (relative to modern wood) against U–Th ages. Shaded curve = dendrochronological calibration. Inflected curves show the envelope of ^{14}C activity predicted from geomagnetic modulation of cosmogenic production. After Bard *et al.* (1993).

Because the atmosphere contains only 5% of the carbon budget of the ocean–atmosphere system, climatic changes might have had a major influence on atmospheric ^{14}C abundances, modifying the effects of cosmogenic radiocarbon production. Large effects are not expected during the Holocene period covered by the dendrochronological timescale, due to its relatively consistent climate. However, much larger climatic effects are expected during the last glacial cycle. Therefore, the use of U-series dating to extend the calibrated timescale further back in time allows a test of these effects on atmospheric ^{14}C abundances.

Mazaud *et al.* (1991) compared the coral data of Bard *et al.* (1990a; 1990b) with a ^{14}C production model based on an improved geomagnetic intensity record. The good agreement between the coral data and the predicted ^{14}C activity curve means that long-term activity variations in the atmosphere and hydrosphere can largely be explained by variable cosmogenic production (in response to secular variations in the magnetic field). Hence, climatic effects, which can affect the ^{14}C equilibrium between atmospheric and marine carbonate reservoirs, must play a subordinate role. However, Stuiver *et al.* (1991) argued that climate could have a second-order effect on atmospheric ^{14}C/^{12}C activity ratios by releasing ^{12}C from oceanic carbonate sinks through changes in ocean circulation.

A continuous record of atmospheric radiocarbon through the period of the last glacial cycle was obtained by Beck *et al.* (2001) from a cave stalagmite, precisely dated by U-series analysis. The stalagmite records atmospheric radiocarbon signatures through the medium of dead plant material in soils, which provides the majority of dissolved carbon in cave groundwater. However, it was necessary to correct for contamination by a subordinate amount of dead radiocarbon leached from the limestone wall-rocks of the cave. Nevertheless, comparison with coral-, varve-, and dendrochronologies over ranges of several thousand years gave relatively constant offsets, which could then be corrected. The results in the period from 30 to 45 kyr ago revealed very dramatic variations of $\Delta\,^{14}$C. These results were broadly consistent with evidence for enhanced cosmogenic nuclide production during this period from ^{10}Be data (section 14.3.4). However, variation of climatic parameters (in addition to geomagnetic variation) was necessary in order to explain the full magnitude of the enhanced atmospheric ^{14}C abundance peak between 30 and 40 kyr BP.

The most recent climatic event which may have caused a perturbation in the ocean–atmosphere carbon balance is the Younger Dryas event, a brief glacial re-advance that occurred between 13 and 11.5 kyr BP. Hence, this event has proved to be a testing ground of high-precision ^{14}C measurements designed to compare atmospheric ^{14}C abundances with production rates. The first of these detailed studies was performed by Edwards *et al.* (1993a) using a coral record from 8 to 14 kyr BP. They found a markedly rapid decrease in ^{14}C activity between 12 and 11 kyr BP, which they attributed to dilution of atmospheric ^{14}C with 'dead' carbon as a result of the Younger Dryas event. Hence, it was argued that climatic changes *could* perturb the overall control of the geomagnetic field on atmospheric ^{14}C activity for short periods of time.

This problem was further investigated using two new varved sediment records. The first example is from Lake Suigetsu, near the coast of central Japan (Kitagawa and van der Plicht, 1998). This small fresh-water lake has a water depth of 34 m, but contains a 75-m-deep thickness of sediment at its bottom. The sediment exhibits annual varves about 1 mm thick, formed by variation from a winter season of dark clay deposition to a spring season of white (siliceous) diatom deposition. The sediments were cored, and the most clearly banded section from 10 to 30 m depth exhibited 29 100 varves. From within this section, 250 samples of windblown plant debris and insect wings were dated by radiocarbon analysis, allowing this section to be anchored to the tree-ring calibration curve between 9000 and 11 000 years BP.

The second new calibrated varve section was formed by sediments in the (marine) Cariaco Basin of the Caribbean (Hughen *et al.*, 1998). The dated points in this sediment core showed exceptionally good agreement with the tree-ring calibration curve and with dated coral samples in the range from 9000 to 12 000 yr BP (Fig. 14.12). Unfortunately there was some minor disagreement with U–Th-dated coral determinations around 13 000 yr BP. However, the Cariaco basin results agree with Lake Suigetsu data in predicting a sharp spike in Δ ^{14}C at this time.

These data were compared with new predictions of atmospheric radiocarbon production during the Younger Dryas by Muscheler *et al.* (2000). This prediction was obtained from a record of ^{10}Be production from the GISP2 ice core in central Greenland (section 14.3.3) using a box model for radiocarbon exchange between the atmosphere and oceans. The results were in good agreement with predicted variations in Δ ^{14}C back to 12 kyr BP, but failed to explain the magnitude of the observed radiocarbon spike during the Younger Dryas (Fig. 14.12). Hence, Muscheler suggested that additional climatic effects were needed in order to explain the Younger Dryas peak, possibly involving changes in ocean circulation.

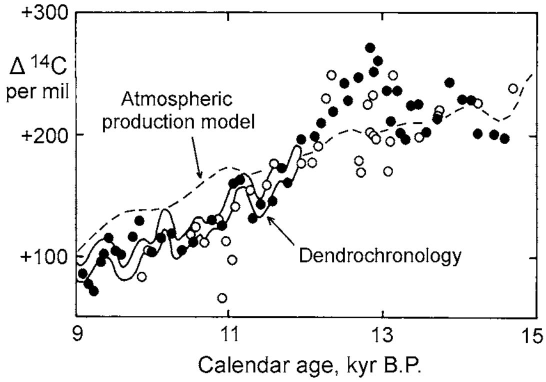

Fig. 14.12. Radiocarbon measurements for the Cariaco basin varve section (●), showing excellent agreement with the dendrochronology calibration line (band) and U–Th dates on corals (○). Dotted line = production model. After Hughen *et al.* (1998).

The opposite case was argued by Goslar *et al.* (2000) on the basis of varve records from Polish lakes. The radiocarbon data from these lakes are more scattered than the two examples cited above. However, a large clump of data was found in the time interval between 13 000 and 12 500 yr PB which lay below the varve record in Fig. 14.12, but in agreement with U–Th coral data (open symbols in Fig. 14.12). On this basis, Goslar *et al.* argued that the model of radiocarbon production based on the ^{10}Be ice-core record *was* capable of explaining most of the observed radiocarbon variation, and therefore that it was not necessary to invoke changes in ocean–atmosphere partition of ^{14}C due to ocean circulation. Further modelling by Marchal *et al.* (2001) supported the arguments of Muscheler *et al.* (2000), but it was admitted that a decisive conclusion was not yet possible.

14.1.6 Radiocarbon in the oceans

Radiocarbon is a very useful tracer in oceanography because it allows quantitative estimates of the residence times of water at various depths, mixing between different water bodies, and the magnitude of ocean currents. Radiocarbon evolution in the oceans begins with 'ventilation' of surface water to the atmosphere, which allows this water to reach equilibrium with atmospheric radiocarbon. After a water body moves away from the surface it can be dated by the decay of this radiocarbon, and hence its flow path and mixing history can be traced.

Studies of the radiocarbon budget of the oceans began in the 1950s at the same time as the first atmospheric nuclear tests, which produced large quantities of ^{14}C by neutron activation of nitrogen. This 'bomb' radiocarbon complicates the interpretation of natural radiocarbon variations in the oceans, but the entry of this 'spike' of anthropogenic radiocarbon into the oceans also provides a useful tracer of the very recent movement of water bodies. However, because the radiocarbon method was in its infancy when atmospheric nuclear testing began, there was an inadequate data set of pre-bomb measurements on seawater to provide a proper baseline to evaluate the magnitude of the bomb signature. Hence, a full understanding of the early data sets was not achieved until later studies revealed the composition of pre-bomb radiocarbon inventories. For example, the analysis of corals provides a means of sampling pre-bomb radiocarbon signatures of the surface oceans (Druffel, 1996).

The first major programme for the radiocarbon analysis of ocean water, called the Geochemical Ocean Sections Study (GEOSECS) was undertaken in the mid 1970s, near the peak of bomb radiocarbon in the atmosphere. Hence, surface water analyses from this programme provide a dramatic picture of the effects of ocean currents on the bomb radiocarbon signature (Fig. 14.13). The highest values of bomb radiocarbon were found in the sub-tropics, where water has the longest surface-residence time. In contrast, Antarctic water was found to have essentially no bomb radiocarbon signature, which was attributed to strong mixing between surface water and deep water (e.g. Nydal, 2000). Comparison of radiocarbon data from the GEOSECS programme with those from more recent sampling programmes such as WOCE (in the early 1990s) revealed a diminution with time of the bomb signature in the surface ocean (Fig. 14.13), but also a concomitant increase of the bomb signature in the deep ocean (e.g. Ostlund and Rooth, 1990).

Natural radiocarbon variations in the oceans provide evidence about ocean circulation on a longer timescale. The first detailed radiocarbon study of the Atlantic Ocean was undertaken by Broecker *et al.* (1960). After correction for anthropogenic contamination, tropical waters were found to have a $\Delta\,^{14}$C composition of −50 per mil (relative to nineteenth-century wood), equivalent to an apparent ^{14}C age of about 400 yr. As they flow north, these waters impart the same apparent ^{14}C age to North Atlantic surface water. After mixing with cold Arctic water, they feed North Atlantic Deep Water (NADW) with $\Delta\,^{14}$C values beginning around −70 parts per mil. However, as this deep water moves southwards, ^{14}C activities fall progressively as the water body ages, reaching a Δ value of −160 in Antarctic bottom water (Fig. 14.14).

These results are consistent with the established oceanographic model for the Atlantic (Fig. 4.40). In this model, tropical waters are transported (advected) to the North Atlantic, where they cool and, because

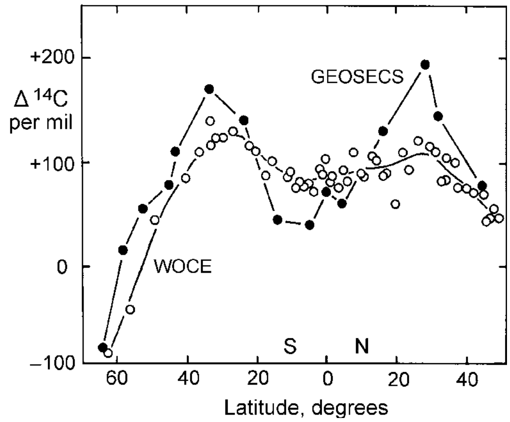

Fig. 14.13. Radiocarbon variations in surface ocean waters of the Pacific as a function of latitude, attributed to atmospheric nuclear tests: (●) = GEOSECS; (○) = WOCE. After Key *et al.* (1996).

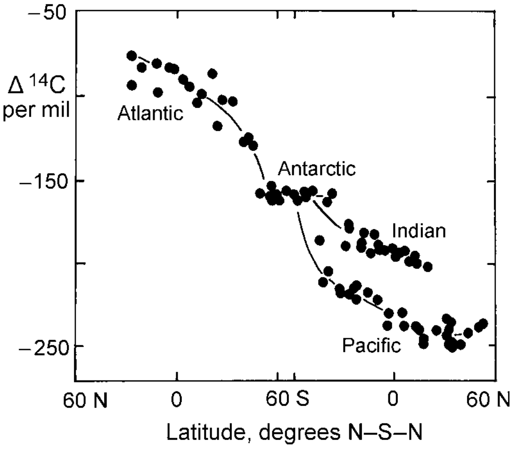

Fig. 14.14. Plot of $\Delta\,^{14}$C against latitude, showing the progressive drop in radiocarbon activity from the North Atlantic, through the Antarctic mixing zone, to the Pacific and Indian oceans. After Stuiver *et al.* (1983).

of their high salinity, sink to form NADW. This body of deep salty water flows southwards to the Antarctic, and after mixing with Antarctic bottom water, ultimately reaches the Pacific. The role of the Antarctic Ocean as a mixing zone between young Atlantic water (NADW) and older deep water from the Pacific and Indian Oceans was confirmed by the large radiocarbon data set from the GEOSECS programme (Stuiver *et al.*, 1983), as shown in Fig. 14.14.

If the change in $\Delta\,^{14}C$ from North Atlantic surface water to Pacific Deep Water were due entirely to radiocarbon decay (at about 11 dpm/century), this would imply a total age of about 1700 yr since the time when this water was last at the sea surface. However, the 'true' age of a water body, defined as the average time since the water in that package was at the sea surface, is considerably less. This is demonstrated by the use of a general circulation model (Campin *et al.*, 1999). The results of this modelling for the present-day Atlantic Ocean are shown in Fig. 14.15. At the top, Fig. 14.15a shows that the model successfully recreates the radiocarbon age structure of NADW and the old radiocarbon age of Antarctic Bottom Water (AABW). However, Fig. 14.15b shows that the true age of AABW is much lower. The difference is due to the presence of sea ice, which prevents the ventilation of radiocarbon from Antarctic surface water to the atmosphere. Furthermore, the average mixing time in each individual ocean basin is much shorter than the radiocarbon age: about 200–300 yr in the Atlantic, 500 yr in the Pacific, and only 80 yr in the Antarctic.

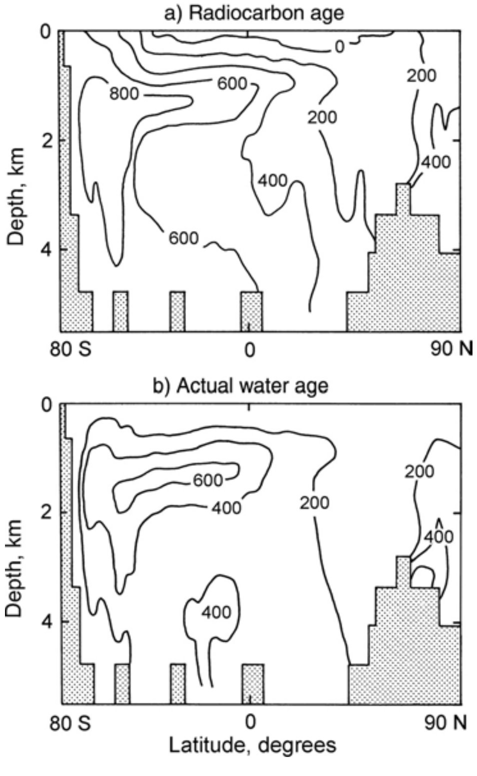

Fig. 14.15. Predicted ages of Atlantic water (contoured) based on a general circulation model for the oceans: (a) apparent radiocarbon age (in excess of the surface-water value of 360 yr); and (b) actual water age since surface residence. After Campin *et al.* (1999).

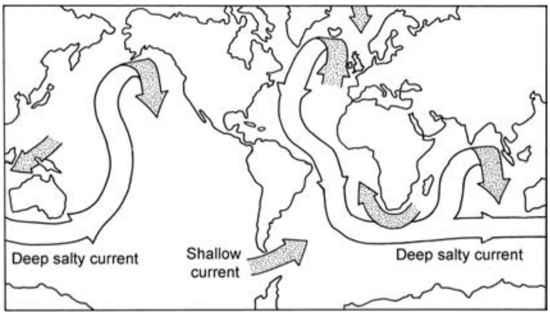

Fig. 14.16. World map showing the deep-water 'ocean conveyer belt' connecting major world oceans. Shaded arrows = surface water currents. After Broecker and Denton (1989).

14.1.7 The 'Ocean Conveyor Belt'

The global system of deep-water transport from the North Atlantic, via the Antarctic, to the Pacific has been termed the oceanic thermohaline circulation ('THC') or the Ocean Conveyor Belt (Broecker and Denton, 1989). These authors suggested that this thermohaline circulation (Fig. 14.16) played a critical role in controlling climate switches between glacial and interglacial periods. For example, evidence from elemental tracers suggested that the conveyer belt might have been 'turned off' during glacial periods, which would have tended to amplify the cooling effect in the North Atlantic by preventing the export of cold NADW and the import of warm tropical water. Broecker and Denton also speculated that a similar effect occurred during the Younger Dryas event, the temporary glacial re-advance which interrupted the last deglaciation.

Radiocarbon analysis of biogenic carbonates of various ages can be used to study changes in the operation of the Ocean Conveyor Belt by comparing the apparent ages of a given water mass at different times. For example, comparison between the radiocarbon ages of benthic and planktonic forams in a given deposit allows the relative radiocarbon ages of local surface and deep water bodies to be compared. This work was not possible until the advent of accelerator mass spectrometry (see below) because of the small amount of sample material available. The first study was attempted by Andree *et al.* (1985) but was complicated by the effects of bioturbation because the core under study had a sedimentation rate of only 1.5 cm/kyr.

Shackleton *et al.* (1988) avoided these problems by working on a core from the Central Pacific with a sedimentation rate of 10 cm/yr. For each sampled increment of the core (typically 2–3 cm) the difference between the radiocarbon ages of benthic and planktonic forams gave a 'ventilation age' for Pacific Deep Water, representing the time since this water body equilibrated with the atmosphere at the sea surface. These values were plotted against the radiocarbon age of surface water, which was determined by subtracting a 'reservoir age' of 650 yr (representing the apparent radiocarbon age of Pacific surface water) from the 'conventional age' determined analytically. The data are compared in Fig. 14.17 with the 1500 yr ventilation age of for present-day Pacific Deep Water measured in the GEOSECS programme. The results of Andree *et al.* (1986) are also shown for comparison. The ventilation ages measured by Shackleton *et al.* were quite variable, especially during the period of deglaciation 18–12 kyr BP. However, they argued that it was possible to identify a 'glacial mean value' that was about 500 yr older than the ventilation age of Pacific Deep Water at the present day. Subsequent workers have also reported considerable scatter in ages, but have generally agreed with this conclusion.

While benthic–pelagic (B–P) ages give a reasonable approximation to the ventilation age of ocean water masses, Adkins and Boyle (1997) pointed out that there were inaccuracies in this method, particularly when atmospheric radiocarbon abundances were changing rapidly in response to changing cosmogenic production. For example, during a period of decreasing atmospheric ^{14}C abundance (as seen for much of the past 20 kyr), the initial radiocarbon activity of an old deep-water sample would have been higher (when that water body was at the sea surface) than the activity level in surface water by the end of the period of evolution of the deep water body. This causes B–P ages to under-estimate the true ventilation age of the water body.

To avoid this inaccuracy, Adkins and Boyle proposed an improved calculation method, which they termed the 'projection' age method. This involves projecting the evolution line of the deep-water sample back in time until it reaches the atmospheric evolution curve (Fig. 14.18). The ventilation age is then calculated by subtracting the 'reservoir age' of surface ocean water. The method is based on the premise that the principal cause of changes in atmospheric ^{14}C abundance is variation in production, rather than changes in ventilation (since the latter would create a circular argument). In addition, it must be assumed that mixing of waters has not occurred. The result of applying this method to previously determined ventilation ages was a slight increase in the average ventilation age for Pacific Deep Water during the last glacial maximum, to a value of 600 yr above the present-day value.

Another consequence of a slow-down in the Ocean Conveyor Belt would be a reduction in the northward flow of tropical water to the North Atlantic, causing the apparent 'equilibration age' of North Atlantic surface water to rise. Bard *et al.* (1994) attempted to test this

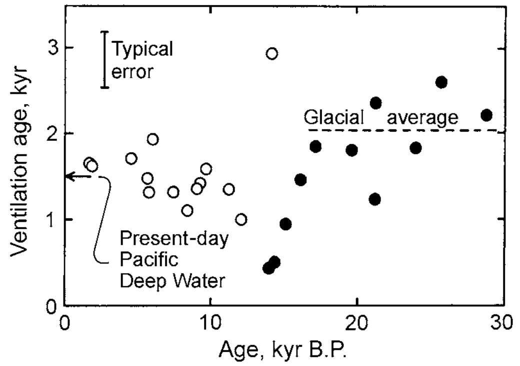

Fig. 14.17. Plot of apparent 'ventilation' age for Pacific Deep Water based on differences in radiocarbon ages between planktonic and benthic forams from a Central Pacific core: (○) = data of Andree *et al.* (1986); (●) = new data, after Shackleton *et al.* (1988).

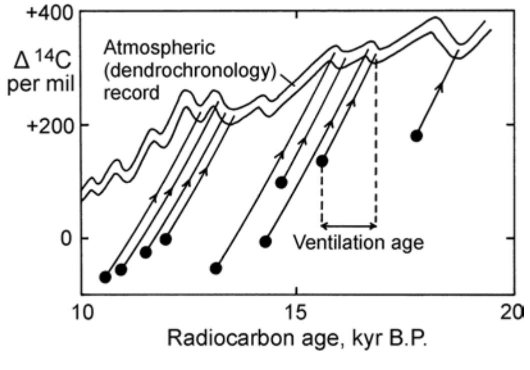

Fig. 14.18. Plot of Δ ^{14}C against time, to illustrate the 'projection method' for calculating ventilation ages of deep water bodies relative to atmospheric radiocarbon. After Adkins and Boyle (1997).

prediction for the Younger Dryas period by comparing the ^{14}C ages of plant fossils and planktonic forams of this age, marked by the distinctive Vede ash bed. The difference between terrestrial and planktonic radiocarbon ages would yield the equilibration age for North Atlantic surface water during the Younger Dryas period.

Data from four North Atlantic cores gave an average ^{14}C age 1400 yr older than the terrestrial section. However, because the 'control' samples of plant material used to determine atmospheric radiocarbon abundances did not come from the same cores as the forams, a 650-yr correction was necessary in order to account for marine bioturbation of the foram samples (despite the relatively high sedimentation rate in the core). This left a net age difference of about 750 yr, representing the estimated 'reservoir age' during the Younger Dryas. It compares with a present-day reservoir age of 400 yr for the North Atlantic, as described above. The increased North Atlantic reservoir age during the Younger Dryas was attributed by Bard *et al.* to reduced ventilation of North Atlantic surface water to the atmosphere. Some of this difference could be accounted for by an increase in sea-ice cover during the Younger Dryas, but the preferred model of Bard *et al.* was a reduction in the formation of NADW.

Deep-sea corals provide an alternative source of information about the radiocarbon signatures of deep water masses. These corals are slow-growing solitary corals that do not rely on symbiotic algae for an energy source, and can therefore grow outside the range of reef-building corals, in the deep sea and in polar regions. These corals can offer high-resolution climatic records because, unlike deep-sea sediments, they are not affected by bioturbation. As with the B–P method, ventilation ages from deep-sea coral analysis have been somewhat scattered (e.g. Goldstein *et al.*, 2001). However, this may partly reflect the variable 'reservoir' ages of surface water, which must be subtracted from the apparent radiocarbon ages of deep-water corals in order to calculate the ventilation age. For example, ventilation ages of very young deep-sea corals from the South Pacific gave results that were sometimes in agreement with data for the corresponding water masses and sometimes not (Fig. 14.19). Agreement between coral and GEOSECS data was very good for the sample from 950 m depth, but less good for samples from 100 and 350 m depth. However, Goldstein *et al.* suggested that part of the mis-fit for the shallowest point may be due to contamination of the coral sample by bomb radiocarbon in the water mass in which it grew.

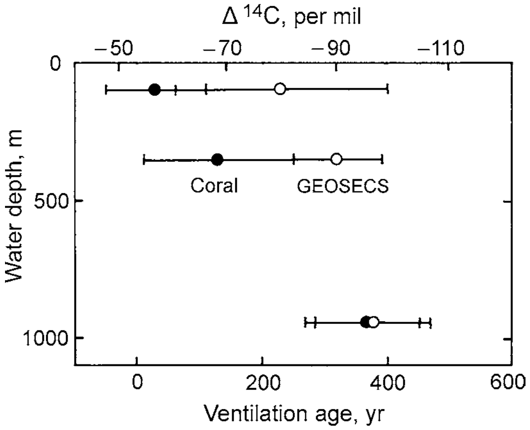

Fig. 14.19. Plot of ventilation age against depth for the south Pacific, to compare ages for deep-sea corals (●) with GEOSECS data on seawater (○). After Goldstein *et al.* (2001).

Because of these problems, it is likely that ventilation ages from both corals and forams are subject to considerable sampling 'noise'. However, averaging from several different sampling sites can help to overcome this noise. Using such an approach, Goldstein *et al.* (2001) determined that glacial bottom water from the Last Glacial Maximum ('LGM') had an average ventilation age 350 yr older than that of present-day bottom waters sampled in the GEOSECS programme. This supports the proposal of Broecker and Denton (1989) that the Ocean Conveyor Belt operated at a slower pace during glacial periods.

14.2 Accelerator mass spectrometry

Mass spectrometry is potentially a powerful alternative to radioactive counting in the determination of cosmogenic nuclides because it utilises every atom of the nuclide in the sample. In contrast, counting determinations utilise only the small number of atoms which decay during the measurement experiment. If decay rates are very high (corresponding to half-lives of less than a thousand years) then counting may be most efficient. However, for longer-lived nuclides, mass spectrometry has the ability to out-perform counting.

Cosmogenic nuclides are characterised by very low abundances, both relative to other isotopes of the same element and to isobaric interferences from other elements. The first problem is exemplified by the fact that even modern carbon, with the highest $^{14}C/^{12}C$ ratio (1.2×10^{-12}), would yield a ^{14}C peak too small to see above the tail of the very large ^{12}C peak in the

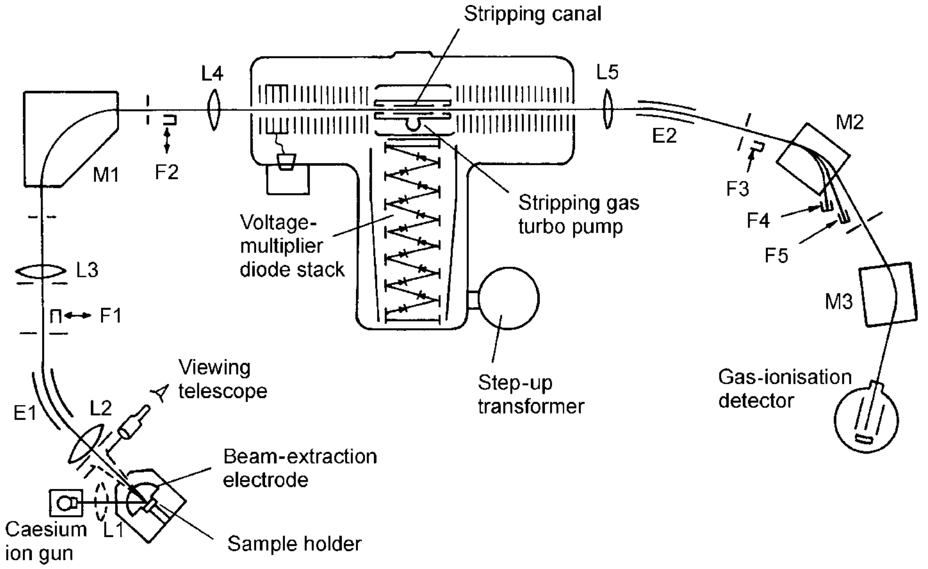

Fig. 14.20. Schematic illustration of the Toronto tandem accelerator, showing typical features of such instruments: M1–M3, magnetic analysers; E1 and E2, electrostatic analysers; L1–L5, electrostatic lenses; F1–F5, Faraday cups. After Kieser *et al.* (1986).

mass spectrum of a 'conventional' mass spectrometer used by geologists. Such machines typically have 'abundance sensitivities' (peak tail at one mass unit distance) of 10^{-6} at the uranium mass, which may decrease to about 10^{-9} at the mass of carbon.

Abundance sensitivity might be improved sufficiently to measure ^{14}C in a 'conventional' mass spectrometer by increasing the radius of the magnet, introducing electrostatic filters, and increasing the accelerating potential and magnet current. The last two approaches respectively filter and overwhelm the spread in energies of the ions emitted by the source. Accelerator mass spectrometers usually have all of these features (Fig. 14.20), but they are not central to accelerator mass spectrometry (AMS). In contrast, the three principal attributes of the tandem accelerators used in AMS are the positive-ion source, the charge-exchange process and the very high ion energies achieved (which allow use of special detectors).

It was suggested by Lal (1988) that the principal impetus for the development of AMS was the fact that accelerators became available for this purpose as their applications in physics diminished. As with many techniques, AMS began as a method looking for an application, but quickly took off as a useful tool in its own right. An alternative method of excluding isobaric interferences is laser-induced resonance ionisation (e.g. Labrie and Reid, 1981). However, this method has not lived up to its early promise.

The essence of the tandem accelerator is the initial acceleration of negative ions by a positive potential in the megavolt range, followed by charge exchange of the ion beam, after which positive ions are accelerated back to zero potential. During the charge-stripping process, isobars of different elements often adopt different charge states, allowing their subsequent separation, while molecular-ion isobaric interferences are destroyed.

Charge stripping may be performed by passing the ion beam through an electron-stripping gas (e.g. argon), a thin graphite film, or (in very-high-energy accelerators) a thin metal foil. Experience with carbon has shown that charge stripping to a 3+ state is often most effective, since CH_2 (the principal molecular-ion interference) breaks apart rather than forming triply charged ions (Litherland, 1987). This avoids the need for a high-resolution magnetic analyser to resolve molecular ions by their mass defect. By using only a low-resolution magnetic analyser, the transmission of the instrument for rare isotopes (e.g. ^{14}C) is maximised.

14.2.1 Radiocarbon dating by AMS

Most ^{14}C analyses by AMS are nowadays performed on solid graphite samples. A typical preparation method is the catalytic reduction of CO_2. In order to achieve a ^{14}C ion beam of fifteen ions per second from modern carbon, an 'intense' ^{12}C ion beam of 2 μA must be generated. This is normally achieved using a caesium sputter source, which ejects negative carbon ions by bombarding the sample with Cs^+ from an ion gun. The efficiency of AMS radiocarbon measurement is illustrated by the fact that it yields the same count rate from 1 mg of carbon as the β count rate from a whole gram of carbon. Nevertheless, a 55-kyr-old carbon sample yielding a 2-μA ^{12}C beam still has a ^{14}C count rate of only one ion per minute (corresponding to a $^{14}C/^{12}C$ ratio of about 1.2×10^{-15}).

The determination of ^{14}C (and ^{26}Al and ^{129}I) can be performed on a 'low-energy' tandem accelerator (Litherland, 1980; 1987), because the direct atomic isobars of these species (^{14}N, ^{26}Mg and ^{129}Xe) do not form stable negative ions. Therefore, complete separation from these species occurs in the source (e.g. Purser *et al.*, 1977). However, separation of the atomic $^{14}C^-$ ion from the molecular ion $^{12}CH_2^-$ depends on the charge-stripping stage of the tandem accelerator.

The sputter source generates an ion beam with variable ion energies. After acceleration to a few tens of kilovolts, this beam must be 'cleaned up' using an electrostatic analyser before the beam is ready for the accelerator. In addition, it is necessary to split the major and minor ion beams with a magnetic analyser before the accelerator, in order to minimise scattering of the ^{14}C beam by collision of the ^{12}C beam with gas molecules.

In ^{14}C dating, the most effective charge-stripping medium is provided by a relatively higher gas pressure in the central ultra-high-voltage 'stripping canal' of the tandem accelerator (Fig. 14.20). Differential pumping of the acceleration tubes at either end of the tandem generator can maintain a pressure 5000 times lower here than in the stripping canal (Litherland, 1987). The charge-stripping process generates a range of charge states in the positive-ion beam, such that only about 50% of ions have the selected charge. Therefore, the accelerator system must be calibrated against standards of known $^{14}C/^{12}C$ ratio before unknown samples are run. Production of $^{14}C^{3+}$ using a 3-MV accelerator is ideal for radiocarbon measurement, but $^{14}C^{2+}$ ions from a 1.4-MV accelerator can also be used (Lee *et al.*, 1984).

The very high energy of the positive-ion beam at the collector end of the instrument (normally > 1 MeV) allows the use of ionisation counters that can *identify* collected ions as well as measuring their abundance. This is done by measuring the energy loss of the ions in a 'collision cell', in which the ion beam is gradually decelerated by collision with gas molecules. Different kinds of ions lose energy at different rates in the collision cell. Hence, this provides a final means of resolving any residual ^{12}C molecular ions in the ^{14}C beam (possibly generated by recombination after the accelerator). Figure 14.21 shows that the molecular-ion beams of ^{13}C and ^{12}C are barely significant in modern carbon, but dominant in 47-kyr-old carbon.

A good example of the application of AMS to radiocarbon analysis is provided by the dating of the Shroud of Turin (Damon *et al.*, 1989). This was believed to be possibly the burial cloth of Christ, although its sudden appearance in the 1350s raised the probability that it was instead a medieval 'icon'. The advent of AMS analysis provided the opportunity to determine

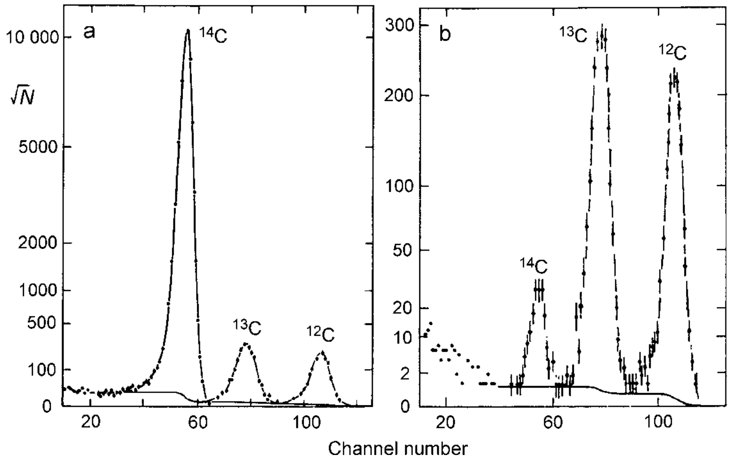

Fig. 14.21. Multi-channel pulse-height (energy-loss) analysis of radiocarbon samples from an ionisation detector: (a) modern carbon and (b) 47.4-kyr-old carbon. Typical error bars are shown. After Litherland (1987).

an absolute date on the fabric of the shroud, using a total of only 7 cm^2 (150 mg) of cloth. This was divided between university laboratories at Arizona, Oxford and Zürich. A major worry was that the fabric might have been contaminated during its long history as a relic. Therefore, a variety of different cleaning procedures was performed by each group on different sub-samples of cloth. In addition, each group dated three control fabric samples of different known ages to form a general impression of the between-laboratory reproducibility.

The results from the three laboratories, which were collated independently at the British Museum, were in good agreement. However, the shroud itself yielded poorer reproducibility than the controls, possibly due to contamination. The 'conventional' radiocarbon age of the shroud (BP) was translated into a calendar age using the calibration curve of Stuiver and Pearson (1986). The 95% confidence limits on the conventional age were found to bracket an inflection in the calibration curve, which technically creates two possible calendar-age ranges, AD 1262–1312 and 1353–1384 (Fig. 14.22). However, since the shroud went on view in the 1350s, the latter range can fortunately be excluded on historical grounds. It is concluded that the linen of the shroud was derived from cotton that grew in AD 1290 ± 25 yr, and it is therefore a medieval artefact.

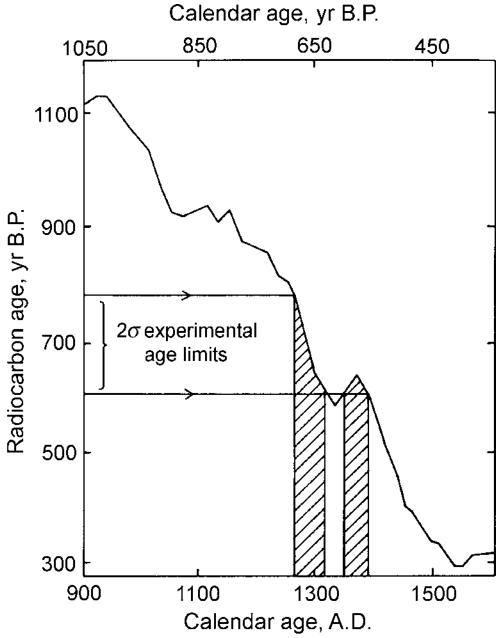

Fig. 14.22. Translation of the 'conventional' radiocarbon age for the Shroud of Turin into a calendar age. Age limits are at the 95% confidence level (2σ). Of the two possible calendar-age ranges (shaded), the more recent is excluded by historical data. After Damon *et al.* (1989).

14.3 Beryllium-10

Cosmic rays interact directly with nitrogen and oxygen atoms in the atmosphere, causing spallation (fragmentation) into the light atoms Li, Be and B. Amongst these, one of the nuclides produced is the unstable isotope ^{10}Be. Cosmogenic ^{10}Be can also be generated in the surface layer of exposed rocks by *in situ* production. However, this subject will be dealt with in section 14.6.

^{10}Be decays by pure β emission to ^{10}B. It was first observed in naturally occurring material by radioactive counting (Arnold, 1956). However, even at that time Arnold recognised that mass spectrometry might supplant radioactive counting as a method for the determination of ^{10}Be. This is because the relatively long half-life of 1.51 Myr (Hofmann *et al.*, 1987) makes counting a very inefficient process for ^{10}Be analysis of natural samples. For example, McCorkell *et al.* (1967) used 1200 tonnes of ice-water to make ^{10}Be (and ^{26}Al) measurements by β counting on Greenland ice. In contrast, Raisbeck *et al.* (1978) made the first AMS measurement on similar material using only 10 kg of ice-water.

Analytically, ^{10}Be determination by AMS is similar to ^{14}C, but involves some additional complications. Because Be does not form stable negative ions, the BeO$^-$ species must be used, upon which the isobaric interference of ^{10}BO is a serious problem. This is overcome by passing the ion beam through an absorber gas (in front of the detector) whose pressure is adjusted to stop transmission of ^{10}B. The high ion energy of the ^{10}Be beam generated by AMS allows this species to pass through to the detector, which consists of a gas-ionisation counter in front of a surface-barrier detector, which finally absorbs the ion beam. The first detector measures energy loss (ΔE) of the ions as they collide with gas molecules in the chamber (this property of the ions is inversely proportional to their atomic number). The second detector measures residual energy. Using this bivariate discriminant, ^{10}Be ions can be resolved from all other signals (Fig. 14.23) to yield a very low background. ^{10}Be contents of samples are measured relative to added ^{9}Be spike, and normalised for machine mass discrimination by frequent standard analysis.

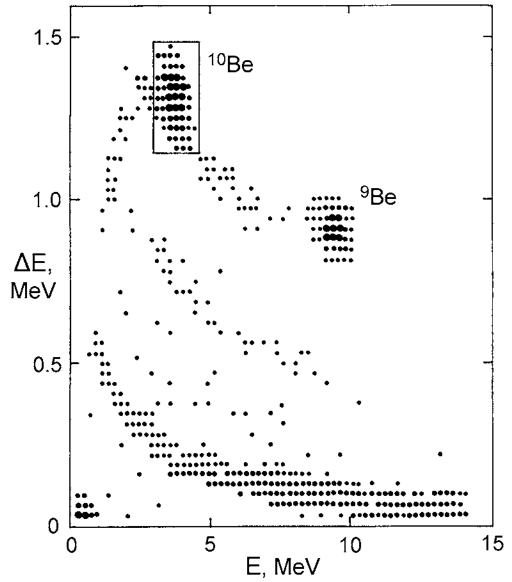

Fig. 14.23. Plot of ΔE against E for a typical geological sample, to show resolution of ^{10}Be from other species. Dot size indicates the number of counts in each bin (smallest = one count). After Brown *et al.* (1982).

14.3.1 ^{10}Be in the atmosphere

^{10}Be enters the hydrological cycle by attachment to aerosols, from which it is scavenged by precipitation. Consequently, it has a very short (about 1 week to 2 yr) residence time in the atmosphere and, unlike ^{14}C, is not homogenised within the atmosphere prior to its fallout.

It was originally intended (Raisbeck *et al.*, 1979) that ^{10}Be analysis of rainwater would allow accurate constraints to be placed on the global average ^{10}Be production rate. However, two factors complicate a determination of the ^{10}Be flux in rainwater. One is the tendency for comparatively Be-rich soil particulates to be caught up in the atmosphere and cause secondary contamination of rain (Stensland *et al.*, 1983). Once this effect has been removed, individual depositional events still turn out to have very variable ^{10}Be contents (Brown *et al.*, 1989).

One way of gauging the effect of soil resuspension on ^{10}Be abundances is to compare them with ^{7}Be data. The latter species has relatively similar atmospheric production rates to ^{10}Be, but much lower levels in soils due to its very short half-life (53 days). It is measured by γ counting. An alternative way of assessing the effects of soil resuspension is to compare continental and oceanic ^{10}Be deposition rates. Brown *et al.* (1989) used both of these approaches in an analysis of ^{10}Be precipitation in Hawaii and the continental USA to test its behaviour at temperate latitudes. Average ^{10}Be contents of Hawaiian rain, in which atmospheric soil suspension is negligible, are very similar to ^{7}Be in rain from Illinois in the USA (Fig. 14.24), but in both cases a few events yield very large relative contents.

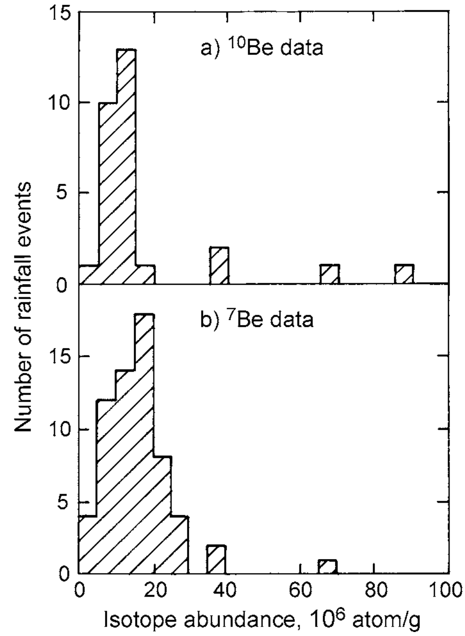

Fig. 14.24. Histograms of ^{10}Be and ^{7}Be concentration in rainfall from Mauna Loa, Hawaii and Bondville, Illinois, respectively. The former are weekly rainfall aggregates; the latter represent individual showers. After Brown *et al.* (1989).

The variability of ^{10}Be contents in individual rain showers makes it difficult to determine accurate annual fluxes for mid-latitudes. A summary of these data as a function of latitude (Fig. 14.25) shows the variability of these estimates (Brown *et al.*, 1992). However, at high and low latitudes the estimates of annual ^{10}Be flux are more reproducible. The latter are in good agreement with a global ^{10}Be flux estimate of 10^{6} atoms/cm^{2} per yr based on cosmic-ray intensity as a function of latitude (Lal and Peters, 1967). Therefore, at the present time, the curve in Fig. 14.25 represents the best available estimate of the atmospheric ^{10}Be flux.

14.3.2 ^{10}Be in soil profiles

Beryllium is partitioned very strongly from rainwater onto the surface of soil particles such as clay minerals.

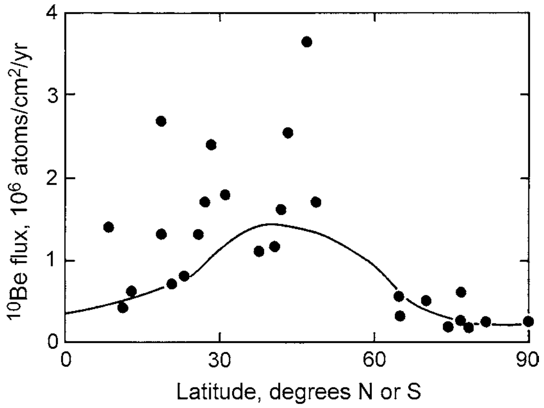

Fig. 14.25. Summary of empirical estimates of annual ^{10}Be flux in rainfall, as a function of latitude. These are compared with a theoretical production curve based on cosmic-ray intensity. After Brown *et al.* (1992).

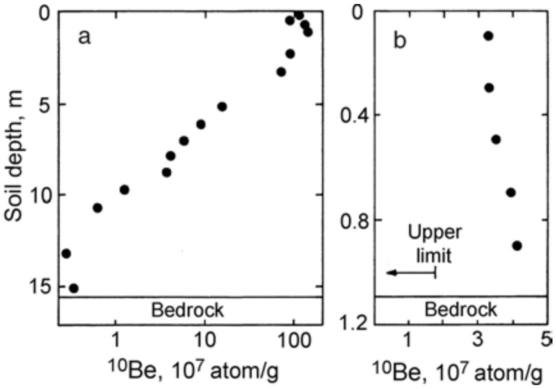

Fig. 14.26. Plots of ^{10}Be activity as a function of depth in two soil profiles: (a) Virginia Piedmont, after Pavich *et al.* (1985); and (b) Orinoco Basin, after Brown *et al.* (1992).

If we assume that ^{10}Be adsorption is perfect, and that a given soil section is developed by weathering of rock or rock debris without the addition or removal of sediment during the weathering process, the soil section should contain a complete inventory of all deposited ^{10}Be that has not yet decayed. This process offers the opportunity of dating a soil profile by measuring the total accumulation of ^{10}Be in the section, but it is apparent that there are many assumptions.

The ^{10}Be inventory of a soil profile in Virginia represents a case where beryllium uptake appears to be nearly 100% efficient (Pavich *et al.*, 1985). ^{10}Be activities display a smooth decay curve against depth (Fig. 14.26a), with a total inventory of 9×10^{11} atoms/cm^2. We can compare this value with a theoretical inventory, N, assuming 100% uptake over a given period of time. This is given by the equation

$$N = \frac{q}{\lambda}(1 - e^{-\lambda t}) \qquad [14.3]$$

where q is the input flux from rainfall and t is the accumulation time. If the profile is infinitely old, relative to the 1.5-Myr half-life of ^{10}Be, it will reach saturation, whereupon the input flux from rainfall is balanced by the rate of decay (λ). Equation [14.3] then simplifies to $N = q/\lambda$. Given an annual deposition flux of 1.3×10^6 atoms/cm^2 at this latitude, the saturation inventory will be 3×10^{12} atoms/cm^2, which is three times the observed inventory. The discrepancy can be explained by loss of ^{10}Be-enriched soil from the top of the profile by erosion, and its replacement at the bottom of the profile by weathering of bedrock with no ^{10}Be. Solving equation [14.3] for t (using the observed inventory) yields the residence time of ^{10}Be in the profile, which is 800 kyr.

Very different behaviour of ^{10}Be is demonstrated by a soil profile from the Orinoco Basin (Fig. 14.26b), which has a total inventory of only 5×10^9 atoms/cm^2. Assuming an annual ^{10}Be flux for this latitude of 0.4×10^6 atoms/cm^2, we obtain a ^{10}Be residence period in the soil profile of only 12 kyr (because t is short relative to the half-life of ^{10}Be, it can be approximated by N/q). This low value is best explained by 'breakthrough' of ^{10}Be from the base of the profile by leaching (Brown *et al.*, 1992).

Differences in ^{10}Be retention between the two cases described above can be understood in the light of laboratory experiments on partition of beryllium between soil and water (You *et al.*, 1989). The results showed that retention of beryllium on soil particles is strongly pH-dependent, with distribution coefficients of about 10^5 under neutral conditions (pH 7), but less than 100 at pH 2. Hence the more acidic conditions in tropical soils are less favourable for beryllium retention.

In alkaline soils, mobility of beryllium within the soil profile may be very limited, and under these conditions ^{10}Be may be used as a stratigraphic tool. An example is provided by a ^{10}Be study of Chinese loess, in which carbonate-rich conditions yield a pH value of 8 (Chengde *et al.*, 1992). The profile was dated magnetically back to 800 kyr, and represents the products of wind-borne deposition through varying climatic conditions. Chengde *et al.* tuned their profile to the Quaternary climatic record provided by sea-floor ^{18}O variations. They concluded that, during arid periods, rapid deposition of loess was accompanied by high fluxes of ^{10}Be adsorbed onto windblown particles. These sections were interspersed with wetter periods with lower depositional fluxes of ^{10}Be.

14.3.3 ^{10}Be in snow and ice

Atmospheric ^{10}Be accumulates in snow and ice, but its half-life is too long to date such deposits. However, it can be used as a tracer of climatic changes and to understand the processes modulating cosmogenic ^{14}C production in the atmosphere. The first detailed study of this type was performed by Raisbeck *et al.* (1981a) on a 906-m-long ice core from the Dome C station, eastern Antarctica. This core had been dated on the basis of oxygen isotope correlations with ^{14}C-dated marine sediments. A detailed analysis of the top 40 m of core revealed a ^{10}Be maximum around 1700 AD, which correlated with the ^{14}C 'de Vries effect' maximum (section 14.1.3) and the 'Maunder' sunspot minimum at this time (Eddy, 1976). Consequently these data supported the model of solar modulation of cosmic-ray intensity.

Subsequent studies of Greenland ice cores from the Camp Century and Milcent stations (Beer *et al.*, 1984) confirmed the ^{10}Be maximum associated with the Maunder sunspot minimum. In addition, Beer *et al.* (1985) performed a Fourier-transform analysis of very detailed isotopic data from the Milcent core. This revealed second-order ^{10}Be variations with a 9–11-year cycle time equal to the 'sunspot cycle', both before and during the Maunder Minimum. Hence, Beer *et al.* concluded that solar activity continues to vary, even when sunspots are not actually visible.

Investigations of the solar modulation of ^{10}Be production were extended to a 1000-year period in a more recent study of an ice core from the South Pole (Bard *et al.*, 1997). This section was precisely dated using twenty impurity layers which were correlated with known volcanic eruptions. In this section, the peak at the Maunder Minimum (1700 AD) is seen very sharply, but similar peaks are also visible at other periods, particularly around 1050 AD (Fig. 14.27). Measurement of ^{10}Be in polar ice is a particularly effective way to study solar modulation of cosmogenic production because the shielding effect of the Earth's magnetic field is reduced at the poles, enhancing the sensitivity of cosmogenic production to the effects of the solar wind. Furthermore, these local production effects are fully transmitted into the ice-core record because ^{10}Be is not well homogenised in the atmospheric system. In contrast, the radiocarbon signal from tree-rings is strongly damped, due to the buffering of atmospheric radiocarbon abundances by exchange with the oceans. However, Bard *et al.* used a box model to unravel these effects in the carbon system and calculate a synthetic record of 'undamped' radiocarbon production. As expected, this was well correlated with the ^{10}Be record (Fig. 14.27).

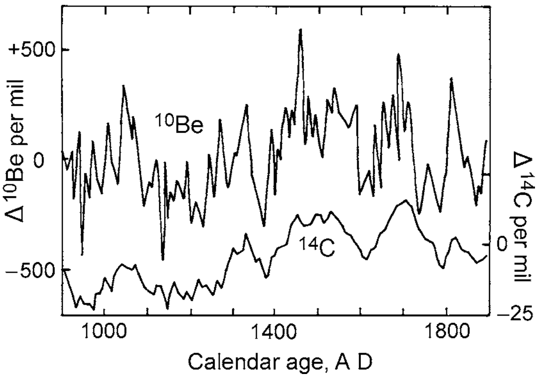

Fig. 14.27. Plot of ^{10}Be variation in a South Pole ice core during a 1000-yr period from c. 1900 to 900 compared with age-corrected ^{14}C levels in tree-rings. After Bard *et al.* (1997).

In contrast to the successful use of ice-core material to study *solar* modulation of cosmogenic nuclide production, attempts to use ice-core records of ^{10}Be to chart *geomagnetic* modulation of cosmogenic production were much less successful. For example, a reconnaissance study of the long Dome C core (Raisbeck *et al.*, 1981a) revealed a strong correlation of ^{10}Be with δ^{18}O, which was attributed to the climatic effect of the last ice age. No significant correlation was observed with geomagnetic field strength, which reached a minimum value 6000 yr ago and is argued to control long-term ^{14}C variations. Yiou *et al.* (1985) suggested a partial solution to this problem by attributing the ^{10}Be maximum during the last glaciation to lower precipitation at that time. This would sweep the same amount of ^{10}Be out of the atmosphere, but concentrate it in a lower volume of ice, causing the ^{10}Be record to be compressed.

The long-term Antarctic Dome C data were again matched by results from Camp Century in Greenland (Fig. 14.28). Beer *et al.* (1988) suggested two alternatives to explain the lack of correlation between the ^{10}Be and geomagnetic-intensity data. One idea was that ^{10}Be ice-core data are recorded at high latitudes where the field strength has a weak influence on atmospheric cosmic-ray intensity. A more radical suggestion was that the long-term variations in ^{10}Be and ^{14}C activities are not actually caused by changes in geomagnetic field, but by a complex interplay of climatic effects and solar cosmic-ray modulations. However, more recent

U–Th calibration of the radiocarbon timescale (section 14.1.5) suggests that ^{14}C variations up to 30 kyr old *can* largely be explained by variations in the Earth's magnetic field. Hence, the 'climate' modulation theory is now largely discredited (but see section 14.3.4).

It is now realised that the dramatic variations in abundance of ^{10}Be over the last glacial cycle are almost entirely a result of variable ice-accumulation rates. Indeed, the method has more recently been used to chart paleo-accumulation rates in central Greenland, with a correction for variable atmospheric production based on geomagnetic field-intensity data (Wagner *et al.*, 2001). Such a correction would not be necessary if all of the ^{10}Be signal were entirely local, since geomagnetic field intensity has little effect on cosmogenic production at the poles. Therefore, in order to study the effect of geomagnetic modulation of ^{10}Be production, it is necessary to study equatorial production records from deep-sea sediments. These records are subject to perturbation by oceanic currents, but if these effects are quantified, suitable cores can yield reliable records of paleo ^{10}Be production (section 14.3.4).

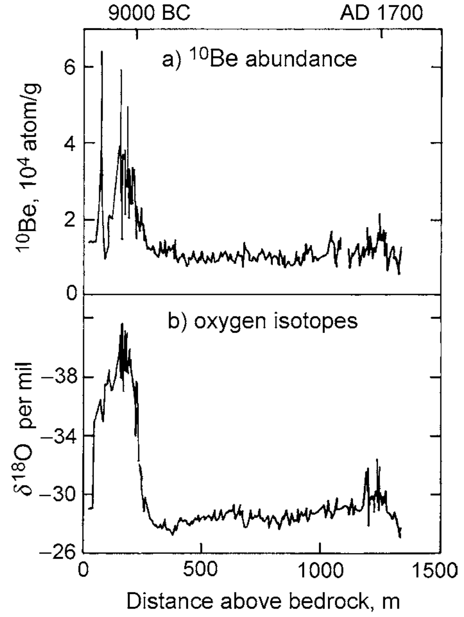

Fig. 14.28. Plots of (a) ^{10}Be and (b) δ ^{18}O variations in the Camp Century ice core (Greenland) over a depth of 1400 m, corresponding to about 10 kyr. After Beer *et al.* (1988).

14.3.4 ^{10}Be in the oceans

Marine sediments were some of the first materials to be successfully analysed for ^{10}Be, since they have concentrations measurable by β counting. The objective was to use ^{10}Be as a dating tool for oceanic sediments. However, early studies, in which ^{10}Be abundances at various depths were simply compared with theoretical cosmogenic production rates, gave unreliable results. A more rigorous study, on paleomagnetically dated sediment cores from the Pacific ocean, was performed by Tanaka and Inoue (1979). These workers showed that absolute ^{10}Be concentrations varied from site to site, but that values at a given depth, relative to the sediment surface, were consistent with a theoretical decay path (Fig. 14.29). The good agreement between ^{10}Be activities and a reference decay trajectory suggests that cosmogenic ^{10}Be production has been constant to within about 30% over the last 2.5 Myr.

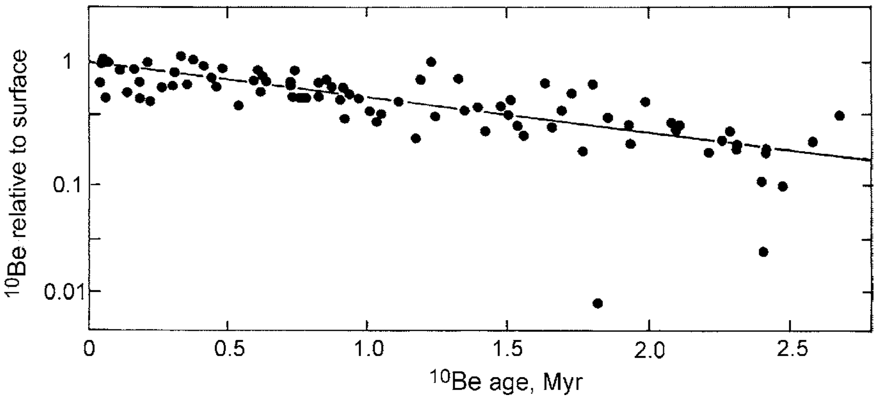

Fig. 14.29. Compilation plot of ^{10}Be activity (normalised relative to the sediment surface) against burial age (depth) for five cores from the North Pacific. After Tanaka and Inoue (1979).

An important application of ^{10}Be as a dating tool has been in studies of ferromanganese crusts. These deposits represent an ideal archive for particle-reactive species in the ocean system, such as Nd and Pb (section 4.5). Because the crusts grow into free space, they are resistant to contamination by clastic sediment particles, and can accurately record long-term seawater isotope variations, provided that their growth rates can be accurately measured. For the past 500 kyr, the dating of crusts can be performed using U-series isotopes (section 12.3.2), but beyond the range of this method, ^{10}Be is the best technique. This was first applied by Turekian *et al.* (1979) and is now used as a standard technique in oceanographic paleo-tracer analysis (section 4.5.3).

Early studies of the behaviour of stable ^{9}Be in the oceans suggested that it was one of the class of elements that very quickly precipitate from seawater (Merrill *et al.*, 1960). This implies that fine particulates are the principal carrier of ^{10}Be. This model was tested by Tanaka and Inoue (1979) by plotting the ^{10}Be precipitation rate against the sedimentation rate at various sites in the Pacific (Fig. 14.30). The good positive correlation displayed by most of the data suggests that the particulate model is valid. Therefore, the net ^{10}Be deposition flux at any given locality is dependent on the sedimentation rate rather than the cosmogenic flux. ^{10}Be deposition rates are actually seen to vary by a factor of three above and below the theoretically predicted flux from the atmosphere. These variations in the ^{10}Be depositional flux at different localities were attributed by Tanaka and Inoue to the lateral transport (advection) of fine particulates by ocean currents.

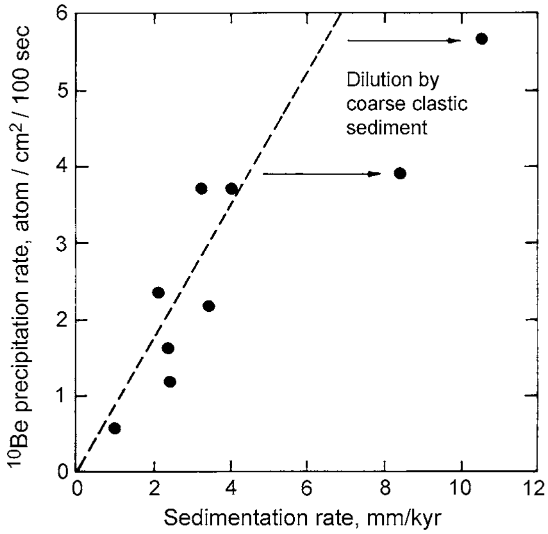

Fig. 14.30. Plot of ^{10}Be precipitation rate against particulate sedimentation rate for various Pacific Ocean sites. The dashed line represents a constant ^{10}Be concentration in different cores. Arrows show the effect of dilution by excess clastic material. After Tanaka and Inoue (1979).

A detailed understanding of the behaviour of ^{10}Be in the aqueous system requires a consideration of the oceanic residence time. Merrill *et al.* (1960) estimated the residence time of beryllium using equation [14.4] (Goldberg and Arrhenius, 1958):

$$\text{residence time} = \frac{\text{total oceanic inventory}}{\text{total rate of introduction}} \qquad [14.4]$$

This equation holds for a steady-state (equilibrium) system, which is approximated if the flux is constant for three residence times. For ^{10}Be the equation can conveniently be calculated per unit area:

$$\text{residence time} = \frac{\text{total water column budget/unit area}}{\text{supply flux/unit area}} \qquad [14.5]$$

Merrill *et al.* determined a residence time for ^{9}Be attached to particulate matter of only 150 yr, but they estimated a longer residence time of 570 yr for the dissolved beryllium budget.

The first estimate of the soluble ^{10}Be budget of the oceans was made by Yokoyama *et al.* (1978) on the basis of ^{10}Be/^{9}Be ratios in manganese nodules. By assuming that these incorporated dissolved beryllium directly from seawater, and using published ^{9}Be abundances in the oceans, they calculated the dissolved ^{10}Be budget as 2×10^{9} atoms/g. Almost identical concentrations were determined by Raisbeck *et al.* (1980) in the first direct ^{10}Be determinations on deep ocean waters, but their estimated residence time (630 yr) differed markedly from that of Yokoyama *et al.* (1600 yr) due to the use of different cosmogenic flux estimates. Raisbeck *et al.* used their own estimate of the cosmogenic ^{10}Be flux, which was based on one year's rain from a single locality in France, uncorrected for resuspension of soil. This can now be seen to be an over-estimate. Using the theoretical production rate of Reyss *et al.* (1981), both studies imply a soluble ^{10}Be residence time in the oceans of about 1200 yr.

Arnold (1958) divided the behaviour of elements such as beryllium in the oceanic system into three categories: soluble/sorbed ions; pelagic particulate-controlled ions; and inshore particulate-controlled ions. All three types of behaviour can be seen to control ^{10}Be. Despite its tendency to be adsorbed onto particulates, dissolved ^{10}Be has a longer residence time in the oceans than similar adsorbable species such as ^{230}Th (section 12.3.2). This difference can be explained by

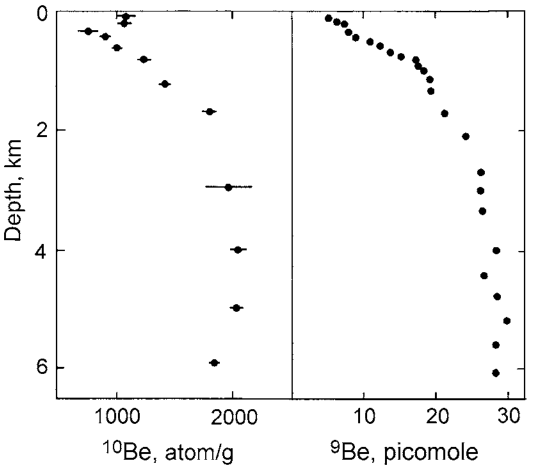

Fig. 14.31. Concentrations of dissolved ^{10}Be (atom/g) and ^{9}Be (picomole) plotted as a function of water depth in the open ocean of the east Pacific. After Kusakabe *et al.* (1987).

the nutrient-like behaviour of beryllium (Measures and Edmond, 1982). Profiles of dissolved beryllium concentration in Pacific ocean water (Fig. 14.31) show strong depletion near the surface (where beryllium is adsorbed onto organic matter) but relative enrichment at depth, due to the breakdown of dead organic matter (releasing Be) as it falls through the water column (Kusakabe *et al.*, 1987). These Pacific Ocean data yield a deep-water ^{10}Be concentration of 2 × 10^9 atoms/g, which is in agreement with the earlier results quoted above. However, Atlantic Ocean water displays a different signature, which may reflect the large river-water input into this ocean basin.

The behaviour of ^{10}Be in the near-shore environment is very different from that in the open ocean, as proposed in Arnold's model. Sediment cores from the continental rises off western Africa and western North America show that ^{10}Be accumulation rates are at least an order of magnitude larger than the theoretical cosmogenic flux (Mangini *et al.*, 1984; Brown *et al.*, 1985). This is attributed to the advection of large quantities of ^{10}Be, by ocean currents, into areas of high deposition. The high deposition rates may be caused by continental erosion or excess biological production, and in these localities the transported ^{10}Be is effectively scavenged and carried to the bottom.

Similar excess ^{10}Be sedimentation rates have been seen in fresh-water lakes (Raisbeck *et al.*, 1981b). In this case, soil erosion in the drainage basin which supplied the lake caused the introduction of beryllium-rich sediment. Lundberg *et al.* (1983) proposed that the excess ^{10}Be was introduced dominantly on organic matter rather than silicate particles, which is consistent with the nutrient-like behaviour of ^{10}Be proposed for the oceanic system.

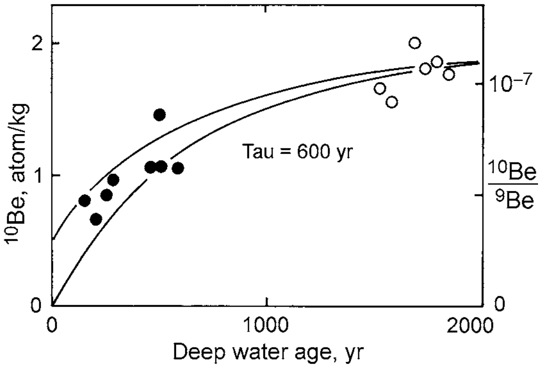

Fig. 14.32. Plot of ^{10}Be concentration against radiocarbon age in oceanic deep water to show the build-up of ^{10}Be along the Ocean Conveyer Belt: (●) = NADW; (○) = Pacific deep water. After von Blankenburg *et al.* (1996).

Comparisons between the Be isotope ratios of modern ocean masses were first made by Ku *et al.* (1990). These revealed a consistent global pattern of increasing ^{10}Be/^{9}Be ratio along the Ocean Conveyer Belt, with values ranging from 0.6 × 10^{-7} in NADW, through 1 × 10^{-7} in the Antarctic, to values as high as 1.6 × 10^{-7} in Pacific Deep Water (Ku *et al.*, 1990). This trend is shown in terms of increasing ^{10}Be content with water age in Fig. 14.32. The positive trend is due to the low particulate sedimentation rate from NADW, which allows ^{10}Be to be advected to the Pacific, and implies a beryllium residence time similar to the circulation age of the ocean water masses. The precise residence time is difficult to constrain because of the different sources of the two isotopes: ^{10}Be from global rain and ^{9}Be from river water. However, the curve shown in Fig. 14.32 was modelled assuming a residence time of 600 yr (von Blankenburg *et al.* (1996).

Beryllium isotope ratios in the 10^{-7} range are less extreme than most cosmogenic isotope ratios, offering the possibility of analysis by conventional (non-accelerator) mass spectrometry. Such a method was developed by Belshaw *et al.* (1995) and applied by von Blankenburg *et al.* (1996) to the beryllium isotope analysis of ocean-floor ferromanganese crusts. Uranium isotope ratios were used to date the surface layer of the crust in order to apply an age correction in cases where the original growth surface had been removed by abrasion (section 12.3.2). Crusts of various ages (0–300 kyr) gave very consistent initial Be isotope ratios within each ocean basin, which were also consistent with the beryllium composition of overlying deep-ocean water. This suggests that the oceans have generally maintained the same circulation pattern over the past 300 kyr. However, more detailed comparisons of glacial and interglacial $^{10}Be/^{9}Be$ ratios are needed in order to test for any interruptions to the conveyer belt during glacial maxima.

14.3.5 Comparison of ^{10}Be with other tracers

Ku *et al.* (1995) made the first comparison of the abundances of ^{26}Al and ^{10}Be in ocean water. They found $^{26}Al/^{27}Al$ ratios in surface water that were consistent with the expected ^{26}Al flux from atmospheric production (by spallation of argon). Therefore, contributions of *in situ* cosmogenic ^{26}Al from cosmic dust or windblown continental dust do not appear to be significant in seawater. However, the $^{26}Al/^{10}Be$ ratio measured in surface water was an order of magnitude lower than the atmospheric production ratio. This was therefore attributed to the much shorter ocean residence time of ^{26}Al.

Wang *et al.* (1996) compared ^{26}Al, ^{10}Be and ^{230}Th records in ocean-floor sediments. The authigenic (seawater-derived) fractions of these nuclides were removed from core samples by leaching with NaOH. $^{10}Be/^{9}Be$ ratios in the leachates were in good agreement with the composition of overlying (North Pacific) deep water, whereas $^{10}Be/^{9}Be$ ratios in the bulk sediment were 50% lower, due to input from detrital continental beryllium. The ^{26}Al budget in the sediment column was also in good agreement with the atmospheric production flux and with ^{26}Al in ocean water (Ku *et al.*, 1995).

Comparison of authigenic ^{26}Al, ^{10}Be and excess initial ^{230}Th revealed $^{26}Al/^{230}Th$ ratios consistent with the estimated production ratio, but excess abundances of ^{10}Be relative to both the other nuclides (Fig. 14.33). Hence, it was concluded that ^{26}Al and ^{230}Th have similar (very short) residence times in ocean water, whereas the longer residence time of ^{10}Be allows advection of ^{10}Be into the North Pacific, where it is scavenged by high biogenic production. Similar effects are seen in the $^{231}Pa/^{230}Th$ system (section 12.3.6), but the effect on the $^{10}Be/^{26}Al$ ratio is larger, due to the longer ocean residence of ^{10}Be. On the other hand, $^{231}Pa/^{230}Th$ ratios are easier to measure, so both methods are likely to be very useful in paleo-oceanography.

Despite the complexities which may be introduced into ^{10}Be sediment profiles by advection, marine sediments offer a better prospect than snow deposits for studying variations in paleo ^{10}Be production. To overcome the problem of advection, Lao *et al.* (1992) compared ^{10}Be abundances with the U-series nuclides ^{230}Th and ^{231}Pa. These nuclides have similar ocean chemistry to that of beryllium, but are produced at a constant rate from uranium in solution. Lao *et al.* compared ^{10}Be production at the present day and 20 kyr ago (corresponding to the last glacial maximum, when the ^{14}C flux was 140% of its present value). They normalised both ^{10}Be and ^{231}Pa fluxes against ^{230}Th. However, based on a comparison of ocean residence times (section 12.3.6), we can best normalise climatic effects on ^{10}Be deposition by comparing the $^{10}Be/^{231}Pa$ ratio at the present day and 20 kyr ago. After excluding one site with abnormal chemistry, seventeen sites in the Pacific gave an average ^{10}Be flux enhancement of 144% during the last

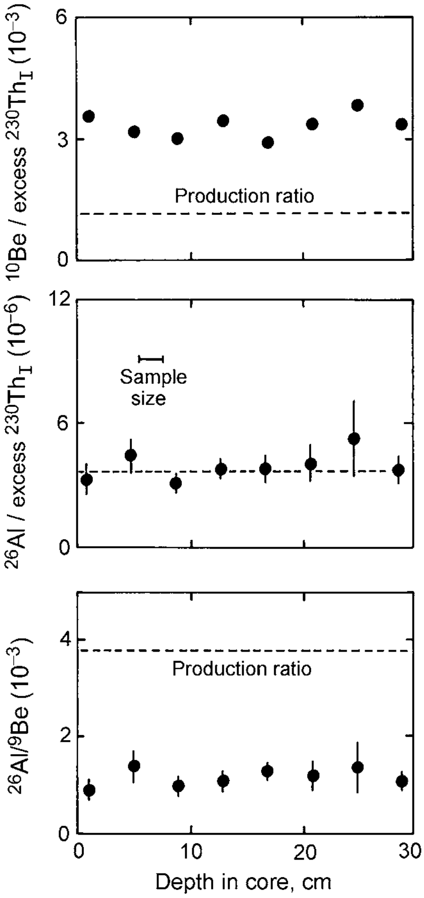

Fig. 14.33. Relative abundances of radionuclides in a sediment core from the North Pacific, showing ratios close to the production ratio for $^{26}Al/^{230}Th$, but out of equilibrium with ^{10}Be. After Wang *et al.* (1996).

glacial maximum, in excellent agreement with ^{14}C data.

Comparisons between the geomagnetic field strength and ^{10}Be deposition have also been made by observing their variation over time at a single site. However, the existence of a direct (inverse) relationship between these variables depends on the neutralisation of climatic effects. In the absence of U-series data for normalisation, this may happen only by chance. Thus, Robinson *et al.* (1995) observed a good inverse relationship between ^{10}Be and magnetic intensity in an 80-kyr-old sediment core from the central North Atlantic. However, Raisbeck *et al.* (1994) observed no such relationship in a 600–800-kyr-old section from the equatorial Pacific Ocean (beyond the range of the ^{230}Th dating method).

To avoid this type of problem, Frank *et al.* (1997) used only ^{230}Th-dated cores to compile a global average of ^{10}Be inventories for the past 200 kyr. This was based on nineteen long cores, which covered most of this age range, supplemented by eighteen shorter cores covering the last 25 kyr. The global stack of ^{10}Be abundance data (Fig. 14.34a) was then inverted to determine relative geomagnetic field intensity (Fig. 14.34b), which was found to correlate very well with a globally stacked paleointensity record (Fig. 14.34c).

Kok (1999) expressed concern that both the ^{10}Be and the paleointensity records might still not be completely free of climatically induced variations in sedimentation rate, despite the use of the ^{230}Th dating method to calibrate the sections. This concern was prompted by the observation that the magnetic paleointensity records exhibit a significant correspondence to the SPECMAP record of oxygen isotope variations (Figs. 14.35a, and b). However, two alternative explanations have since been offered for this correspondence. The first suggestion (Yamazaki and Oda, 2002) is that the geomagnetic field intensity is *itself* modulated by the Earth's orbital eccentricity (which is thought to modulate climatic cycles). In that case, we would expect to see a correlation between variations in climate and the measured paleointensity.

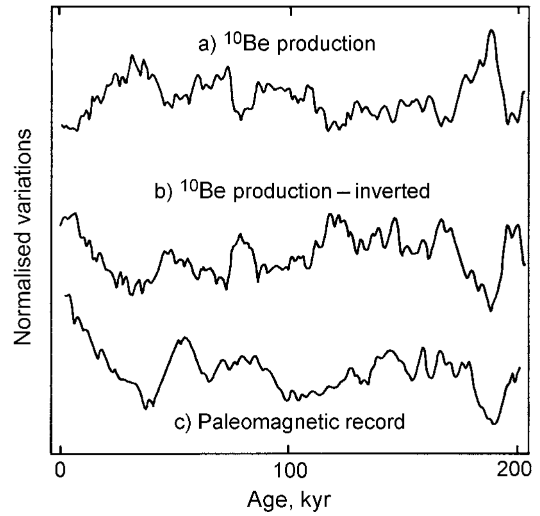

Fig. 14.34. Comparison of a global stack of ^{10}Be paleointensity data (a, b) with a similar stack of magnetic paleointensity (c), demonstrating the paleomagnetic modulation of global cosmogenic isotope production. After Frank *et al.* (1997).

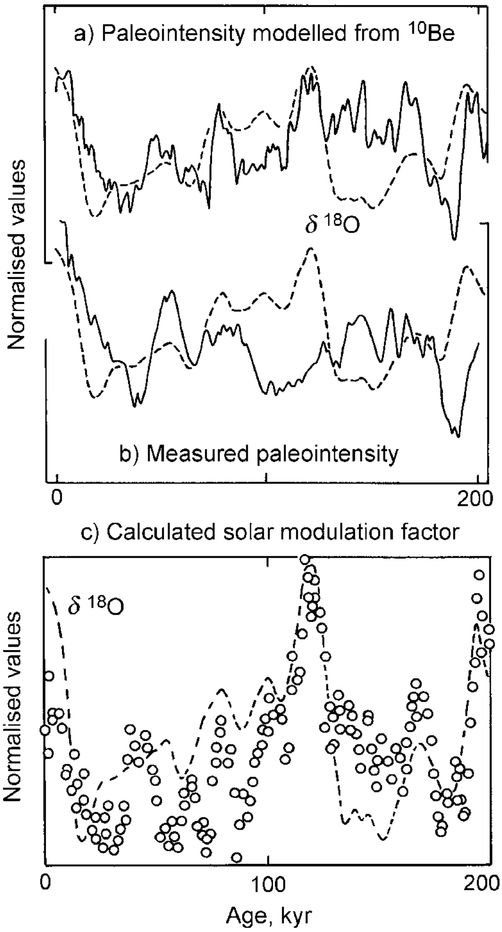

Fig. 14.35. Comparison of paleointensity records with the SPECMAP δ^{18}O record (dashed line): (a) magnetic paleointensity from inversion of ^{10}Be data; (b) directly measured magnetic paleointensity; and (c) normalised residual ^{10}Be modulation, attributed to solar magnetic field effects. After Kok (1999) and Sharma (2002).

However, close examination of Fig. 14.35 shows that the ^{10}Be-derived magnetic paleointensity stack (Fig. 14.35a) exhibits a stronger correspondence to the SPECMAP δ^{18}O record than does the directly measured magnetic record. This suggests that it is the ^{10}Be record, rather than the magnetic record, that contains a component with a climatic linkage.

Sharma (2002) examined this problem in more detail by extracting a residual ^{10}Be modulation effect, after subtraction of the geomagnetic modulation. This quantity was then normalised with respect to its present-day value, and is plotted in Fig. 14.35c together with the SPECMAP record. The controversial aspect of Sharma's analysis was that he attributed the residual modulation effect to solar magnetic activity, which he suggested was also responsible for the 100-kyr glacial climate cycles during this period. This would then provide a 'rival' explanation for glacial cycles, relative to the widely accepted Milankovitch model of 'orbital tuning' (section 12.4.2). The great success of the 'astronomical timescale' (section 10.4.2), obtained by orbital tuning of the oxygen isotope record, makes it hard to disbelieve the fundamental importance of the Milankovitch model. However, there may be room for more than one influence on glacial cycles. Therefore, as one reviewer commented, Sharma's model 'could just be right'. Unfortunately, it will take time to accumulate the high-quality ^{10}Be and paleomagnetic records needed to test this question further. In the meantime, it should be remembered that the Earth's geomagnetic field is the *principal* modulating influence on cosmogenic isotope production.

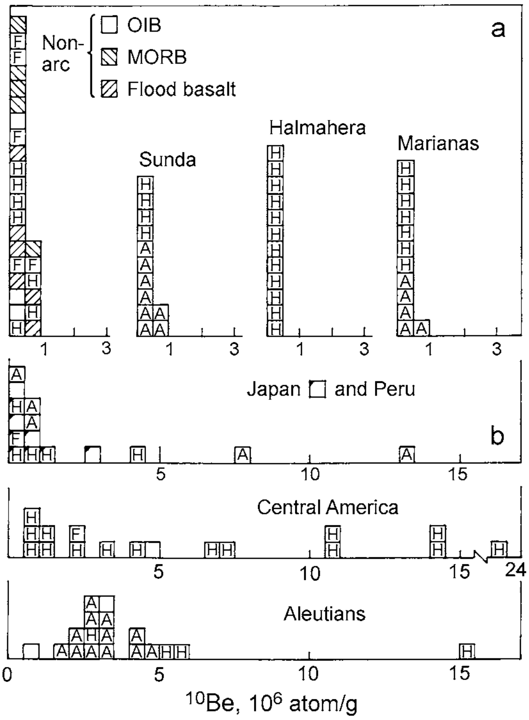

Fig. 14.36. Histograms of ^{10}Be abundance in volcanic rocks: (a) non-arc control group and low-^{10}Be arcs; and (b) high-^{10}Be arcs. Symbols: A = sample from 'active' volcano; H = historic flow; F = fresh sample collected during or immediately after eruption. After Tera *et al.* (1986).

14.3.6 ^{10}Be in magmatic systems

The most important application of ^{10}Be as a petrogenetic tracer is in studies of the relationship between sediment subduction and island-arc volcanism. In a reconnaissance study, Brown *et al.* (1982) demonstrated that ^{10}Be concentrations in island-arc volcanics, in the range $(2.7-6.9) \times 10^6$ atoms/g, were generally much higher than the levels seen in a control group of continental and oceanic flood basalts. Brown *et al.* argued against high-level contamination of the analysed volcanics on the grounds that the short half-life of ^{10}Be renders it extinct in all but surficial deposits, while ^{10}Be levels in rainwater are too low to cause the observed enrichments. In contrast, it has long been known (e.g. Arnold, 1956) that pelagic sediments have very large ^{10}Be contents, in excess of 10^9 atoms/g. Brown *et al.* therefore attributed their data to the involvement of subducted ocean-floor sediment in the genesis of island-arc magmatism.

Subsequent studies (e.g. Tera *et al.*, 1986) confirmed the general observation of high ^{10}Be contents in island-arc volcanics and low ^{10}Be contents in the non-arc control group (Fig. 14.36). Detailed studies were also undertaken to assess the effects of weathering on the ^{10}Be contents of lavas. Samples collected during or immediately after eruption were shown to contain the same range of ^{10}Be contents as historical lavas. Contamination of non-arc samples by radiogenic ^{10}Be was observed only in severely altered samples. The possibility of *in situ* cosmogenic production of ^{10}Be in lavas at depths over 1 cm was also excluded, given the low ^{10}Be abundances in 16-Myr-old Columbia River basalts.

A surprising result of the detailed study of Tera *et al.* was that several arcs have ^{10}Be levels as low as the maximum of 1×10^6 atoms/g in the control group. These included all samples from the Mariana, Halmahera (Moluccan) and Sunda arcs. To explain these observations, Tera *et al.* suggested four requirements for a positive ^{10}Be signal in arc volcanics:

(1) adequate ^{10}Be inventory in trench sediments;
(2) subduction rather than accretion of uppermost Be-enriched sediments;
(3) incorporation of sediment in the magma source area;
(4) transport time from sedimentation to magma source area <10 Myr.

Failure to satisfy any one of these criteria could preclude a positive ^{10}Be signal. However, Tera *et al.* did not observe simple correlations between ^{10}Be and geophysical parameters such as the age of the subducting plate.

In an attempt to harmonise their data from different arcs, Tera *et al.* plotted ^{10}Be contents against a model parameter involving sedimentation rate, sediment thickness, plate velocity and distance from trench to magma source. This quantity is specified as

$$\text{Predicted } {}^{10}\text{Be abundance} = \frac{\eta_0 s}{\lambda h}\exp\left(-\frac{\lambda l}{v}\right) \qquad [14.6]$$

where η_0 is the abundance of ^{10}Be in the sediment, s is the Pliocene–Pleistocene sedimentation rate, h is the sediment thickness, l is the arc–trench gap and v is the plate velocity. Since the volcanic front is always located about 100 km above the seismic plane, the arc–trench gap is inversely proportional to the dip of the Benioff zone. Using this model, the contrast between the ^{10}Be-rich Central American data and other arcs is explained by the high sedimentation rate and steep subduction angle of the former. However, the Japanese and Aleutian arcs both have a single ^{10}Be-rich data point (shown by the dashed ranges in Fig. 14.37) that does not fit the model.

A further step in rationalising the ^{10}Be systematics of arc volcanics was achieved by considering the data relative to non-cosmogenic (^{9}Be) abundances (Monaghan *et al.*, 1988; Morris and Tera, 1989). Within the different minerals of a single rock sample, ^{10}Be is normally strongly correlated with total Be content (Fig. 14.38), implying that radiogenic and non-radiogenic Be were mixed before magmatic differentiation occurred. This further strengthens the arguments against surficial contamination of the lavas by ^{10}Be, and also argues against crustal ^{10}Be assimilation by magmas. Finally, the enriched Be contents of the groundmass, relative to phenocrysts, show that Be behaves as an incompatible element during magmatic differentiation.

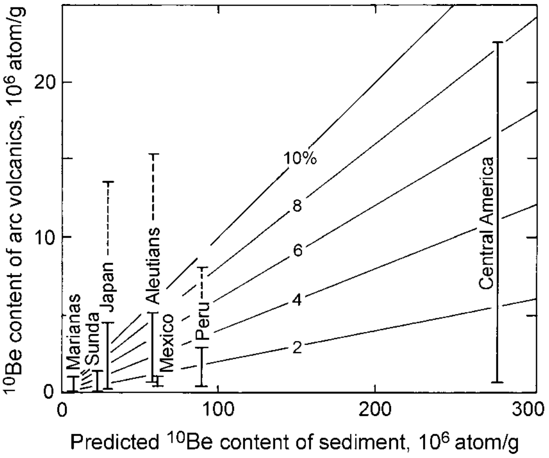

Fig. 14.37. Plot of ^{10}Be data for seven arcs against a model parameter for the efficiency of ^{10}Be supply to arc magma sources. ^{10}Be signals are modelled for various bulk percentage sediment contributions to magmas, shown by fanning lines. After Tera *et al.* (1986).

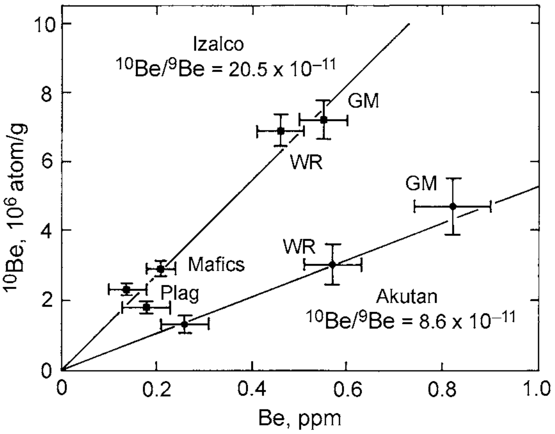

Fig. 14.38. Plot of ^{10}Be against total Be content for separated mineral phases, plus whole-rock (WR) and groundmass (GM) from two young lavas. Samples are from the Izalco volcano (Central America) and Akutan (Aleutians). After Morris and Tera (1989).

In contrast to Be mineral systematics, most whole-rock samples analysed by Morris and Tera did not show a strong correlation between ^{10}Be and total Be. However, they did exhibit a good correlation between ^{10}Be/^{9}Be ratios and absolute ^{10}Be abundances (Fig. 14.39). These findings suggest that most of the rocks analysed, which were basalts, did not have their ^{10}Be contents perturbed by magmatic differentiation. However, some andesites lie significantly to the right of the main trend, including the Japanese and Aleutian samples with abnormally high ^{10}Be contents in Fig. 14.37 (Tera *et al.*, 1986).

Further constraints on the timing of subduction-related processes were obtained by combining $^{10}Be/^{9}Be$ and $^{238}U/^{230}Th$ data. Sigmarsson *et al.* (1990) observed that these ratios were correlated in the Southern Volcanic Zone of the Andes (section 13.4). Given this correlation, and the much shorter half-life of ^{230}Th, Sigmarsson *et al.* suggested that the timescale for dehydration, melting and eruption of these arc magmas was probably less than 20 kyr.

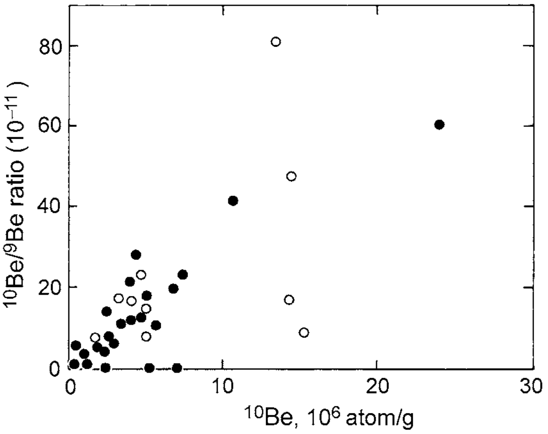

Fig. 14.39. Plot of $^{10}Be/^{9}Be$ ratio against ^{10}Be abundance for basalts (●) and evolved rocks (○) from various arc and non-arc environments. After Morris and Tera (1989).

A further step in understanding subduction-zone processes was achieved by comparing $^{10}Be/^{9}Be$ and B/Be ratios in arc lavas (Morris *et al.*, 1990). Several arcs displayed a strong positive correlation between these two variables (Fig. 14.40), despite the fact that the two beryllium isotopes and boron have different distributions in the subducted slab. ^{10}Be is concentrated in the uppermost sediment layers and diminishes rapidly downwards, ^{9}Be is distributed throughout the sediment column, whereas B is principally concentrated in the hydrothermally altered basaltic crust. Hence, there is no *a priori* reason why these three species should display coherent behaviour in arc volcanics. The fact that they do behave coherently in widely separated volcanoes along the length of an arc suggested a very thorough homogenisation mechanism for Be and B during the process of subduction-related magma genesis. While such a process could occur in the solid state, it is easiest to conceive of the mixing of fluids driven off from different parts of the subducted slab. The convergence

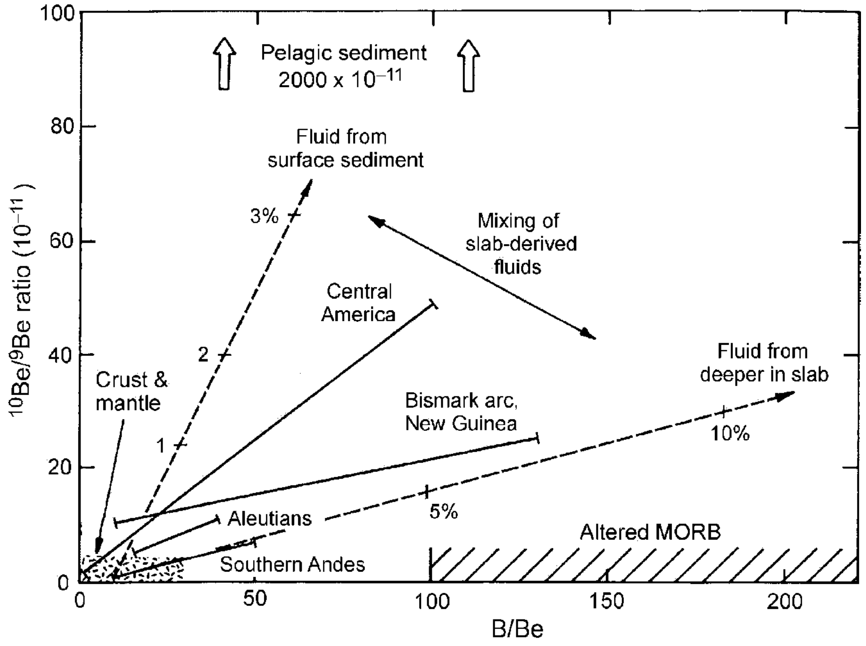

Fig. 14.40. Plot of $^{10}Be/^{9}Be$ ratio against elemental B/Be ratio, showing correlation lines for arc volcanics relative to possible mixing end-members. Numbered ticks denote calculated percentages of slab-derived fluids necessary to generate the observed arrays by contamination of the mantle source. After Morris *et al.* (1990).

of all of the correlation lines at the origin points to complete stripping out of all boron from the subduction zone, with no long-term residence of this element in the mantle.

The observed correlation between ^{10}Be/^{9}Be ratio and elemental B/Be ratio suggests that the latter may be a useful proxy for the former. This is important because it widens the applicability of beryllium data. Firstly, the elemental B/Be ratio can be used as a tracer of the slab component in arcs with low subduction rates, where ^{10}Be is extinct by the time of eruption. Secondly, elemental ratios can be measured with less-sophisticated analytical equipment such as ICP-MS. These advantages were demonstrated by Edwards *et al.* (1993b) in a study of basaltic lavas from the Indonesian arc. Edwards *et al.* were able to combine B/Be ratios with other radiogenic isotope systems in order to specify uniquely the Pb, Sr and Nd isotope signatures of the slab-derived component, which was modelled as an 80%–20% mixture of basaltic crust and Indian Ocean sediment. This signature was also distinguishable from enriched and depleted reservoirs in the mantle wedge. The use of elemental B/Be data made these deductions possible despite the fact that ^{10}Be abundances were at baseline, showing this nuclide to be extinct in the analysed lavas.

14.4 Chlorine-36

^{36}Cl is analogous to ^{10}Be in its atmospheric production, in this case by spallation of ^{40}Ar rather than ^{14}N, and like ^{10}Be, it is quickly swept from the atmosphere by precipitation. However, unlike ^{10}Be, ^{36}Cl is not removed from groundwater by adsorption onto particulates, but remains in the aqueous medium as it travels through geological strata. This fact, coupled with its relatively short half-life of 0.301 Myr, makes ^{36}Cl potentially very useful in the dating or tracing of Quaternary groundwater systems. Cosmogenic ^{36}Cl can also be generated in the surfaces of exposed rocks by *in situ* production. However, this subject will be covered in section 14.6.

The principal obstacle in AMS analysis of ^{36}Cl is isobaric interference by ^{36}S. This forms abundant negative ions and is not removed by the charge-stripping process. This requires a high-purity chemical separation before analysis. Residual ^{36}S can be resolved by its lower energy loss in the gas counter, but this is most effective at energy levels above 48 MeV, requiring an accelerator of at least 6 MV potential. This rules out ^{36}Cl analysis with lower-energy (2 MV) tandetrons (Wölfli, 1987). A 'time-of-flight' analyser may also be used before the gas counter (Fig. 14.41) in order to eliminate peak tailing from the relatively very large ^{35}Cl and ^{37}Cl

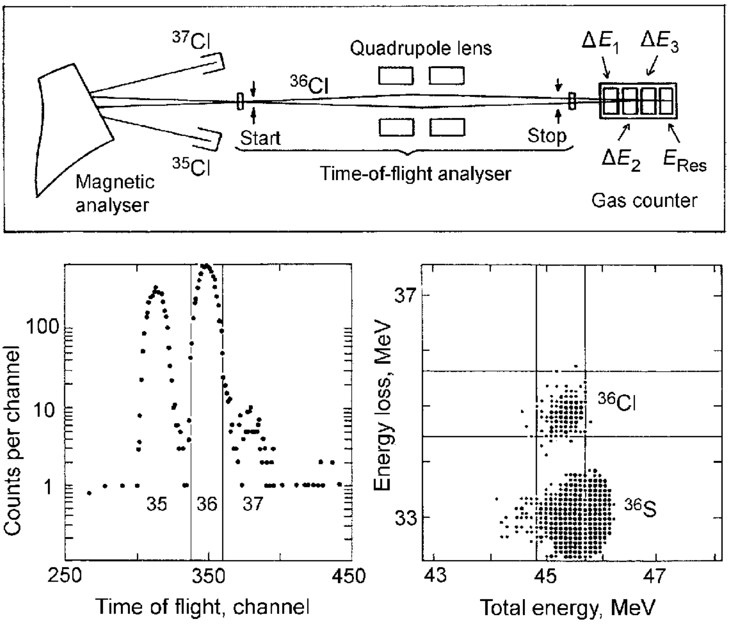

Fig. 14.41. Analyser segment and output data of an AMS instrument designed for ^{36}Cl determination, showing the use of time-of-flight analysis to resolve ^{36}Cl from ^{35}Cl and ^{37}Cl, and energy-loss detection to resolve ^{36}Cl from ^{36}S. After Wölfli (1987).

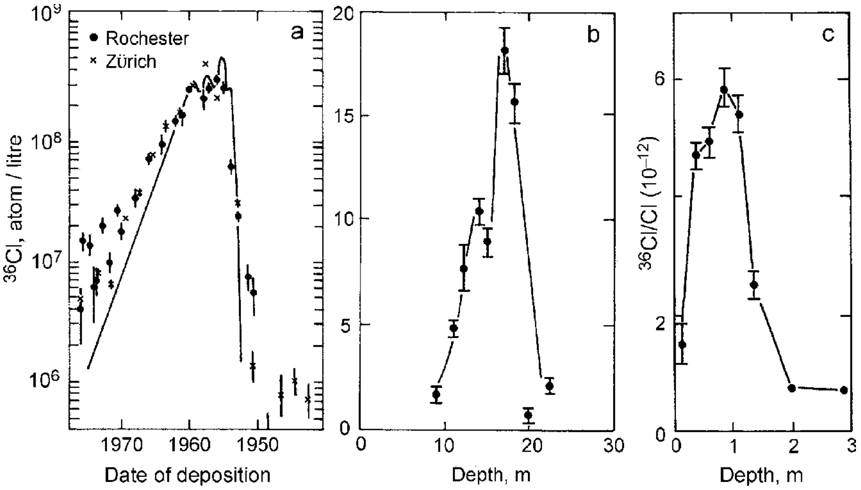

Fig. 14.42. Profiles of anthropogenic ^{36}Cl as a function of depth in various environments: (a) ice (Dye 3 station, central south Greenland); (b) groundwater (Borden landfill, Ontario); and (c) desert soil (New Mexico). After Gove (1987) and Fabryka-Martin *et al.* (1987).

ion beams, which are not adequately resolved by the preceding magnetic and electrostatic analysers in the system. Time-of-flight analysis can be performed only on pulsed ion beams, which are controlled by pulsing the sputter source. This analysis relies on the fact that lighter masses are accelerated to slightly higher velocities than heavier ones, so that, after traversing a distance of a metre or so, they arrive at the detector a few nanoseconds earlier. Hence ^{36}Cl is resolved from ^{36}S, ^{35}Cl and ^{37}Cl (Fig. 14.41).

The first use of ^{36}Cl as a hydrological tracer was not based on the cosmogenic isotope at all, but on anthropogenic bomb-produced ^{36}Cl. This resulted from seven large nuclear tests conducted on the sea surface from 1952 to 1958, which caused neutron activation of marine chlorine. Profiles of anthropogenic ^{36}Cl against time were determined in a Greenland ice core (Elmore *et al.*, 1982), in Canadian groundwater (Bentley *et al.*, 1982) and in a soil profile from New Mexico (Phillips *et al.*, 1988). All of these measurements revealed a very sharp spike in ^{36}Cl, with a duration of 15–20 yr (Fig. 14.42). It is expected that anthropogenic ^{36}Cl will be a useful hydrological tracer in the near future, replacing bomb-produced tritium as the latter becomes extinct.

As seen for other cosmogenic isotopes, the production of natural ^{36}Cl is expected to have varied in the past due to modulation of the cosmic-ray flux by the solar wind and the Earth's magnetic field. The most easily measured inventories of ^{36}Cl were the ice cores from Greenland and Antarctica which were also studied for several other environmental tracers. However, it was shown that ^{36}Cl and ^{10}Be abundances in these cores are better correlated with climatic variations than with past variations in geomagnetic field intensity (e.g. Beer *et al.*, 1988). This result caused considerable puzzlement at the time, but is not really surprising since the cosmogenic isotope flux in polar snow is largely of local (polar) origin, where cosmic-ray intensity is not significantly shielded by the Earth's magnetic field. Therefore, to obtain more representative records of past changes in global ^{36}Cl production, it was necessary to find a suitable inventory from a non-polar source. Such an inventory was discovered by Plummer *et al.* (1997) in the form of fossil packrat urine from Nevada.

Packrats obtain all of their water from the desert plants that they eat, and these plants in turn derive their water from surface-infiltrated rainfall. Therefore, the abundant chlorine in packrat urine accurately reflects the ^{36}Cl/Cl ratio of recent rainfall. Furthermore, this urine may be preserved for thousands of years in underground middens, and can be dated by the radiocarbon method. Hence, this material provides an ideal inventory of past cosmogenic ^{36}Cl production. ^{36}Cl/Cl ratios for packrat urine up to 40 kyr old are presented in Fig. 14.43, together with a record of past ^{14}C production compiled from several sources. The two data sets are relatively well correlated, especially at the present day and at the peak of cosmogenic isotope production about 30 kyr ago. Since geomagnetic modulation is the principal cause of past ^{14}C variations, it follows that ^{36}Cl production is subject to the same controls.

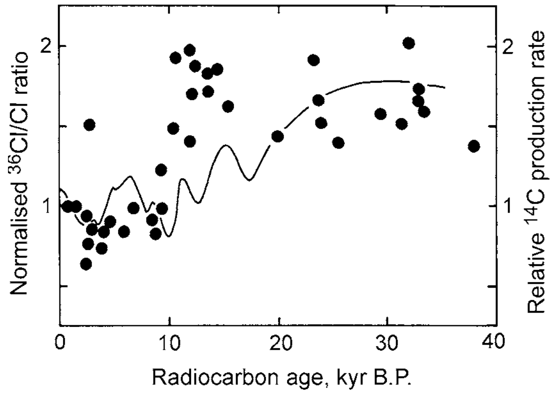

Fig. 14.43. Plot of chlorine isotope variation against age in samples of packrat urine from Nevada, USA. The data are compared with a normalised curve of radiocarbon production compiled from several sources. After Plummer *et al.* (1997).

Following this evidence for the geomagnetic modulation of global ^{36}Cl production, it was found that appropriate corrections for the variable accumulation rates of Greenland snow *did* yield a record of past ^{36}Cl variations that was well correlated with geomagnetic field strength (Baumgartner *et al.*, 1998). This suggests that a significant fraction of the precipitation in Greenland is actually derived from more temperate latitudes. However, the large corrections that must be applied for variable snow-accumulation rates mean that ice cores are not reliable as prime records of past cosmogenic isotope production. Instead, the known variations in past cosmogenic isotope production may be more useful to calibrate the variable ice-accumulation rates in these cores (Wagner *et al.*, 2001).

The most important application of cosmogenic ^{36}Cl (as opposed to anthropogenic ^{36}Cl) is the dating of ancient groundwater, hundreds of thousands of years in age. For simple sedimentary aquifers this has been quite successful, as demonstrated by studies on the Great Artesian Basin of eastern Australia by Bentley *et al.* (1986) and Torgersen *et al.* (1991). These authors presented a total of five ^{36}Cl transects across the basin, reaching up to 800 km from the recharge area. Comparisons were made with average groundwater ages from hydrological modelling, and three different ways of calculating the ^{36}Cl age were examined. However, the simplest method is probably the most reliable in most circumstances. This involves calculating the groundwater age from the total abundance of ^{36}Cl (above secular equilibrium) in an unknown sample relative to the total ^{36}Cl abundance above secular equilibrium at the recharge site (where water enters the aquifer):

$$t = -\frac{1}{\lambda_{36}} \ln \left(\frac{^{36}\mathrm{Cl}_{\mathrm{sample}} - {^{36}\mathrm{Cl}_{\mathrm{equilib}}}}{^{36}\mathrm{Cl}_{\mathrm{recharge}} - {^{36}\mathrm{Cl}_{\mathrm{equilib}}}} \right) \qquad [14.7]$$

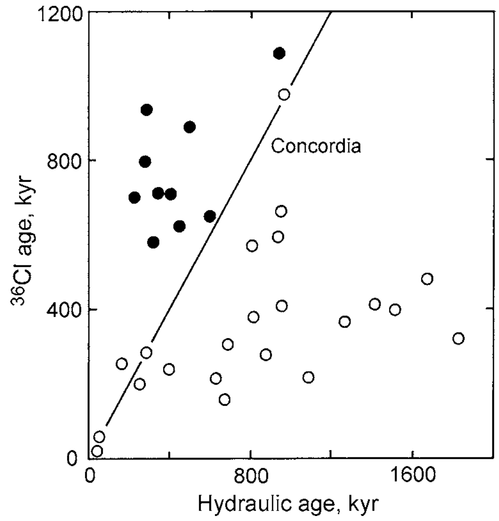

Fig. 14.44. Plot of ^{36}Cl groundwater ages for four transects across the Great Artesian Basin against average age since recharge based on hydraulic modelling. (○) = N–S transects; (●) = E–W transects. Data from Torgersen *et al.* (1991).

The ^{36}Cl groundwater ages calculated from this equation are shown in Fig. 14.44 for four transects across the basin, two approximately N–S and two E–W, and compared with the predicted age profile from hydraulic measurements. These results show that the two N–S transects, which are in the westerly part of the basin (open symbols), generally have younger ^{36}Cl ages than predicted. This can be explained by additional input of water into the system along the length of the basin, which dilutes old basin water with young recharge water. On the other hand, the E–W transects (solid symbols), which span the easterly half of the basin, generally have older ^{36}Cl ages than predicted. This implies that basin water tends to accumulate in this area, provided that these ages were not biased by *in situ* radiogenic production (section 14.5).

The ages from the transects are used to calculate a contour diagram of ^{36}Cl groundwater age in Fig. 14.45, where the results are compared with streamlines based on hydraulic measurements. The latter data imply that water flows mainly in a NE to SW direction across the basin from Queensland to South Australia. However, the contour plot shows the presence of old ages in the middle of the basin, implying that water tends to

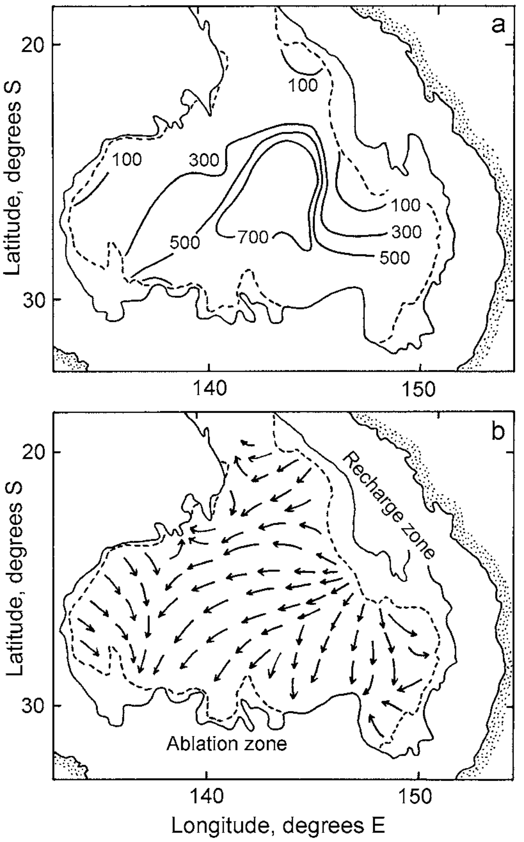

Fig. 14.45. Map of the Great Artesian Basin, showing (a) groundwater age contours from ^{36}Cl dating and (b) groundwater flow directions based on hydraulic modelling. After Torgersen *et al.* (1991).

pool here in what is also the deepest part of the basin. Coupled with the evidence for younger groundwaters in the western part of the basin, this implies that a somewhat radial water flow from basin margins to centre is imposed on the general NE–SW flow direction deduced from hydrological modelling.

The ^{36}Cl method has been more problematical in studying groundwater ages in igneous rocks, due to interference by local radiogenic ^{36}Cl production. These problems have been evaluated in a case study of the Stripa granite, Sweden, which has unusually high uranium contents of about 40 ppm. This generates a substantial neutron flux, which produces ^{36}Cl by the n, γ reaction on ^{35}Cl. The U content of meta-sedimentary country rocks (5 ppm) also generates significant, if much lower, levels of radiogenic ^{36}Cl. Analysis of Stripa groundwater yields ^{36}Cl/Cl ratios between the signatures of *in situ* radiogenic production in the two dominant rock types (Andrews *et al.*, 1989). These values are so high that they exceed and swamp normal cosmogenic ^{36}Cl/Cl ratios. The ^{36}Cl method is therefore only viable for dating waters in uranium-poor rocks such as sedimentary aquifers.

14.5 Iodine-129

There are over 100 cosmogenic isotopes with masses over 40 and half-lives over one year, which are therefore potentially useful geochemical tracers or dating tools (Henning, 1987). However, most of these elements are metals, and they are not suited to AMS analysis due to the difficulty of forming negative ions. One of the few heavy isotopes to have found significant application is ^{129}I, which is formed in modest quantities in the atmosphere by spallation of Xe, and which, being a non-metal, forms good negative-ion beams.

^{129}I analysis by AMS is relatively straightforward, since the only isobaric interference (^{129}Xe) does not form stable negative ions (Elmore *et al.*, 1980). The principal interference is ^{127}I, which at isotope ratios above 10^{12} forms a peak tail that must be removed by time-of-flight analysis in addition to magnetic and electrostatic analysers. The ^{129}I/^{127}I detection limit under these conditions is about 10^{-14}.

As in the case of ^{36}Cl, the ^{129}I tracer has been used to study the entry of anthropogenic material into natural systems. In a study of a marine sediment core from the continental slope off Cape Hatteras (North Carolina), Fehn *et al.* (1986) found ^{129}I/^{127}I ratios at the sediment surface that were two orders of magnitude higher than the relatively constant abundances at depth. This has been confirmed by more recent studies. For example, studies of Mississippi delta sediments (Oktay *et al.*, 2000) gave ^{129}I depth profiles very similar to those for ^{36}Cl. However, ^{129}I also differs from anthropogenic ^{14}C and ^{36}Cl because it is still being released to the environment at the present day by nuclear reprocessing plants (Fehn and Snyder, 2000). These ongoing emissions yield ^{129}I/I ratios up to one million times the natural background (Fig. 14.46).

^{129}I has a much longer half-life (15.7 Myr) than the other scientifically useful cosmogenic nuclides. It is therefore applicable to much older systems, but its geological applications are complicated by the significant radiogenic iodine production from *in situ* uranium fission. This was examined in case studies of the Great Artesian Basin of Australia and the Stripa granite of Sweden (Fabryka-Martin *et al.*, 1985; 1989).

Groundwaters in the Great Artesian Basin range up to about 1 Myr in age on the basis of hydrological and

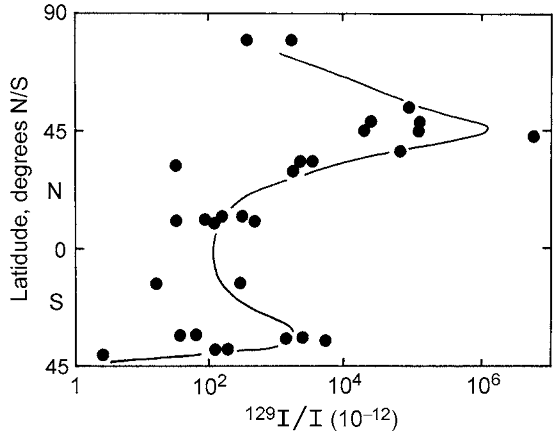

Fig. 14.46. Plot of iodine isotope ratio against latitude for meteoric surface waters, showing signals of anthropogenic iodine from nuclear reprocessing plants. After Fehn and Snyder (2000).

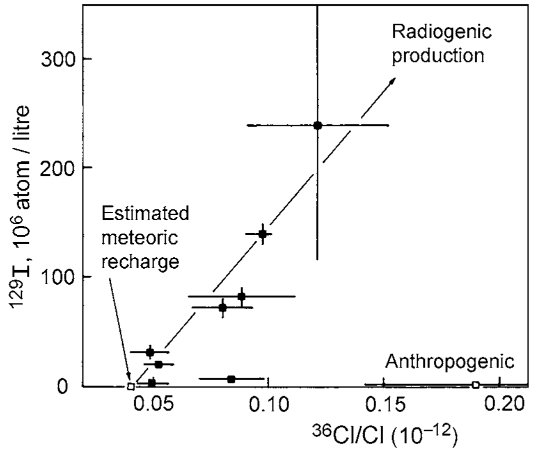

Fig. 14.47. Plot of absolute ^{129}I abundance against the ^{36}Cl/total Cl ratio for groundwaters from the Stripa mine, Sweden. Radiogenic and anthropogenic signatures are shown. After Fabryka-Martin *et al.* (1989).

^{36}Cl evidence (see above), so negligible decay of ^{129}I is expected. Therefore, in the absence of contamination by radiogenic iodine or extraneous water sources, $^{129}I/^{127}I$ ratios should be constant across the basin. Analytical data bear out this prediction to a reasonable extent, which is consistent with the very low uranium content of the aquifer rocks and the hydrostatic overpressure of the artesian basin relative to potential contaminant water bodies. Since the near-surface water is itself old relative to human activity, there is no anthropogenic signature. However, excess $^{129}I/^{127}I$ ratios (above normal cosmogenic levels) were seen in two water samples with ages of 150 and 500 kyr. Fabryka-Martin *et al.* attributed the latter result to contamination by radiogenic ^{129}I from granitic basement, which forms the floor of the aquifer at its distal end. The cause of the other high value is unknown.

Very different conditions were found in groundwaters from the Stripa granite, Sweden (Fabryka-Martin *et al.*, 1989). In this case, radiogenic ^{129}I is present at levels two orders of magnitude higher than cosmogenic iodine. The ^{129}I systematics at Stripa can be seen most clearly when plotted against the $^{36}Cl/Cl$ ratio (Fig. 14.47). Except for one shallow-water sample with a prominent anthropogenic ^{36}Cl signature, the data form an array trending from estimated meteoric recharge towards a pure radiogenic component. This array could result from mixing between two end-members, but it could also result from variable, but correlated, production of radiogenic ^{129}I and ^{36}Cl in the granite, since both are controlled by the uranium content of the rock. Hence, the main role for ^{129}I is to gauge *in situ* radiogenic perturbation of ^{36}Cl ages in groundwater systems.

14.6 *In situ* cosmogenic isotopes

14.6.1 Al-26 meteorite exposure ages

Atmospheric production of ^{26}Al is much lower than that of ^{14}C or ^{10}Be because the progenitor, ^{40}Ar, constitutes only about 1% of atmospheric gases. *In situ* production at the Earth's surface is also low, due to atmospheric attenuation of cosmic rays. Consequently, the first measurements of cosmogenic ^{26}Al were made in studies of the Moon and meteorites. After the breakup of their parent bodies, meteorite fragments are exposed to intense cosmic-ray bombardment during their travels through space, causing substantial ^{26}Al production. If these fragments have cosmic exposure ages of at least a few million years, their surfaces will reach saturation in ^{26}Al ($t_{1/2} = 0.7$ Myr).

After they have fallen to Earth, atmospheric shielding protects meteorite fragments from significant further ^{26}Al production, and decay of this inventory can then be used to determine a terrestrial residence age. Because the abundances of ^{26}Al in meteorites are comparatively high, they do not demand AMS analysis. Instead, they are measured using non-destructive γ counting, by putting the whole meteorite fragment into a large shielded detector. Attenuation of γ particles by the sample itself is corrected by empirical modelling (e.g. Evans *et al.*, 1979).

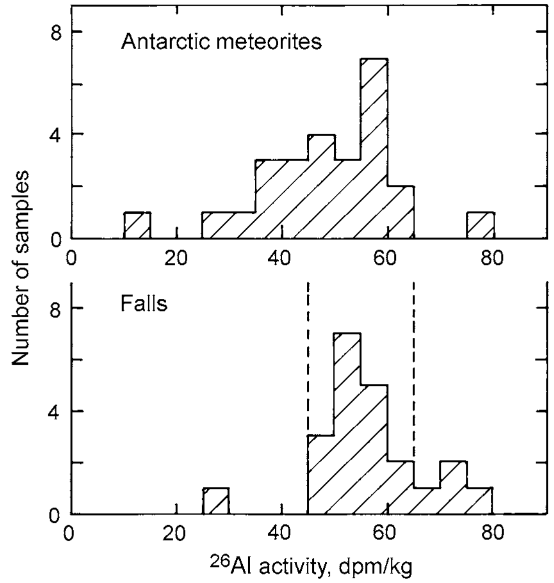

Fig. 14.48. Histogram of ^{26}Al activities in Antarctic meteorites, compared with American 'falls'. After Evans *et al.* (1979).

In the first large-scale survey of Antarctic meteorites, Evans *et al.* (1979) compared the ^{26}Al activities in these samples with those in 'falls' (observed at impact), which have a zero terrestrial residence age. The falls had a moderately well-defined range of ^{26}Al activities for a given compositional class of meteorites (Fig. 14.48). The outlier from this class can be attributed to a failure to reach ^{26}Al saturation, due to the short cosmic-ray exposure history of the fragment. In contrast, Antarctic meteorites ranged to substantially lower activities, indicating significant terrestrial residence ages in several cases. Unfortunately, these values are only semi-quantitative, due to the relatively long half-life of ^{26}Al and uncertainties in production. The latter problem arises because of the poor penetrative capacity of the low-energy cosmic rays which generate ^{26}Al, making the cosmic production rate susceptible to depth within the fragment.

Although ^{26}Al is a good reconnaissance tool for terrestrial age determination (e.g. Evans and Reeves, 1987), ^{36}Cl provides a more precise method (Nishiizumi *et al.*, 1979). This arises from its shorter (0.3 Myr) half-life and more accurately known saturation values, due to its generation by penetrative high-energy cosmic rays. However, the analysis is more technically demanding, and must be performed by AMS. Results of a large ^{36}Cl study of Antarctic meteorite ages are shown in Fig. 14.49 (Nishiizumi *et al.*, 1989a).

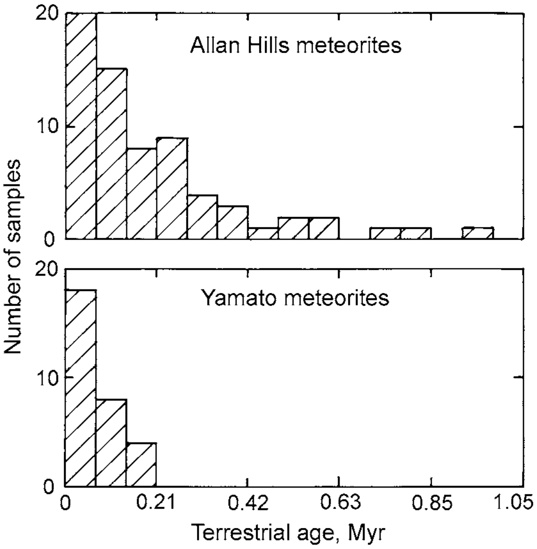

Fig. 14.49. Histograms of calculated terrestrial residence age for Antarctic meteorites from the Allan Hills and Yamato Mountains areas, based on the decay of cosmogenic ^{36}Cl. After Nishiizumi *et al.* (1989a).

The high quality of terrestrial ^{36}Cl ages for Antarctic meteorites has led to their use to determine the half-life of another cosmogenic nuclide, ^{41}Ca. With a half-life of only 0.1 Myr, this shows promise as a precise dating tool, but an efficient AMS analysis method has only recently been developed (Fink *et al.*, 1990). Another problem limiting the application of ^{41}Ca has been uncertainty in the half-life. To solve this problem, Klein *et al.* (1991) performed ^{41}Ca analyses on aliquots of Antarctic iron meteorites that had already been dated by ^{36}Cl measurements. The results revealed a strong linear correlation between the abundances of the two species, whose slope corresponds to the ratio of the half-lives. Taking a ^{36}Cl half-life of 301 ± 4 kyr yields a precise ^{41}Ca half-life of 103 ± 7 kyr.

14.6.2 Al–Be terrestrial exposure ages

Because of atmospheric attenuation of cosmic rays, most terrestrial materials have ^{26}Al/^{27}Al ratios less than 10^{-14}. However, in some aluminium-poor minerals such as quartz, the content of (non-cosmogenic) ^{27}Al may be as low as a few ppm. In this case, ^{26}Al/^{27}Al ratios of 10^{-11} to 10^{-13} may be generated after a few thousand years of exposure to cosmic rays, within the measurement range of AMS. These data can then be used to calculate exposure ages of terrestrial rock surfaces.

The principal obstacle to AMS analysis of ^{26}Al is the formation of sufficient negative Al ions during sputtering, which is only about 25% efficient (Middleton and Klein, 1987). The metal species must be used rather than the oxide because the latter suffers a severe interference from MgO. However, Mg does not form negative metal ions at all, so there are no isobaric interferences on the Al metal-ion signal.

The principal application of ^{26}Al as a geochronometer is in the measurement of rock exposure ages. It would be possible to use this nuclide alone for this purpose, but in view of the many possible permutations of exposure and erosion history, the use of two nuclides with different half-lives provides a more powerful constraint on these models. The normal choice is to combine ^{26}Al measurements ($t_{1/2} = 0.705$ Myr) with ^{10}Be measurements ($t_{1/2} = 1.51$ Myr).

The atmospheric ^{26}Al/^{10}Be production ratio has been determined as about 4×10^{-3} by sampling from high-flying aircraft, but the *in situ* production ratio in quartz has been measured as 6 (Nishiizumi *et al.*, 1989b). Because the atmospheric ^{10}Be production rate is comparatively high, great care must be taken to ensure that rock samples to be used for exposure dating are not contaminated by the atmospheric or so-called 'garden variety' of ^{10}Be (Nishiizumi *et al.*, 1986). Because of its resistance to chemical weathering, quartz is comparatively resistant to contamination by 'garden-variety' ^{10}Be. This, together with its low ^{27}Al content, makes it an excellent material for exposure dating. In quartz, ^{10}Be is derived from spallation of ^{16}O, whereas ^{26}Al is produced by spallation of ^{28}Si and mu-meson capture by the same species. Most of this production occurs in the top half-metre of the rock surface, but limited ^{26}Al production can occur at depths of up to 10 m (Middleton and Klein, 1987).

There are two limiting models for the interpretation of surface exposure data (e.g. Nishiizumi *et al.*, 1991a). These are illustrated on a plot of ^{26}Al/^{10}Be ratio against absolute ^{10}Be abundance (Fig. 14.50). The upper curve shows the effect of increasing exposure age, for the case where the erosion rate is zero. The lower curve shows the effect of various steady-state erosion rates, for the case where the exposure age is infinite (relative to the half-lives of ^{26}Al and ^{10}Be). At the point of saturation (after a few half-lives), the ^{26}Al/^{10}Be ratio is 2.88. Unfortunately, the limited (factor of two) difference between the half-lives of ^{26}Al and ^{10}Be causes only a relatively small separation between the curves for the two end-member models. This places limits on the resolving power of the Al–Be method, given the relatively large analytical errors on the AMS measurements.

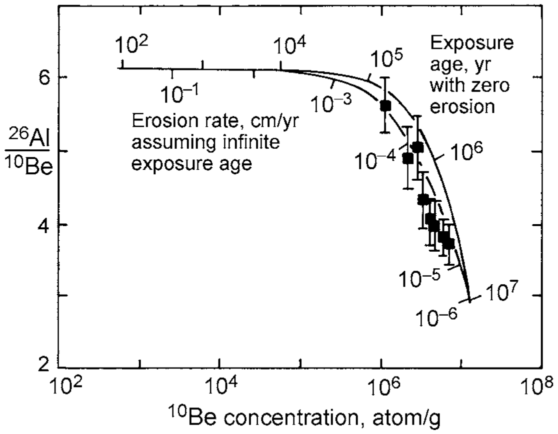

Fig. 14.50. Plot of analysed ^{26}Al/^{10}Be ratio against ^{10}Be abundance (corrected to production at sea-level) for Allan Hills quartz samples, used as a measure of minimum exposure age and/or maximum erosion rate. After Nishiizumi *et al.* (1991a).

Application of the Al–Be exposure method is demonstrated in Fig. 14.50 using data from nunataks of the Allan Hills area of Antarctica (Nishiizumi *et al.*, 1991a). The results display a range of Al/Be ratios close to the steady-state erosion curve. However, the zero-erosion-rate (variable-exposure-age) model cannot be ruled out. The lowest ^{26}Al/^{10}Be ratio yields the strongest constraint, representing a minimum exposure age of 1.4 Myr or a maximum erosion rate of 0.24 mm/kyr. Samples to the left of the erosion line in Fig. 14.50 may be explained by burial under ice for some period in the past. During times of burial, points move downwards to the left, due to the greater rate of decay of ^{26}Al relative to ^{10}Be.

The combination of these two cosmogenic isotopes can also be used to date sediment burial, as demonstrated by Granger *et al.* (2001) in a dating study on cave sediments from Mammoth Cave, Kentucky. Sediments entered this cave system from the Green River, a tributary of the Ohio River, which cut down into a karst landscape. There is a very strong likelihood that sediments were exposed on the land surface prior to their transport and deposition in the cave system. Therefore, quartz grains in the sediment are expected to have reached steady-state abundances of cosmogenic Al and Be, with a ^{26}Al/^{10}Be ratio of about 6 (Fig. 14.51).

After burial in the cave system, radioactive decay begins, and the samples follow a trend to the lower left in Fig. 14.51. This allows the dating of sediments at different levels in the cave system, so that the

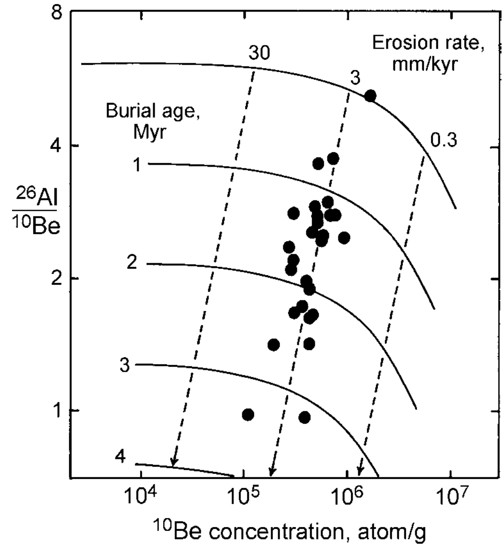

Fig. 14.51. Plot of analysed $^{26}Al/^{10}Be$ ratio against ^{10}Be in sediments from various levels in Mammoth Cave, Kentucky. Vertical displacements allow the dating of cave deposits from their burial ages, while the intersection with the exposure curve indicates an erosion rate of 3 mm/kyr for the sediment source. After Granger *et al.* (2001).

down-cutting of the river can be traced against time. Projection of the decay trend back to the steady-state line also allows the erosion rate of the surficial sediment source to be estimated at around 3 m/Myr. The combination of ^{26}Al and ^{10}Be is particularly suitable for burial dating because the pre-burial cosmogenic production of the two nuclides occurs under similar conditions. Accurate modelling of isotope production during the surface-exposure history of the sediment is a pre-requisite to obtaining accurate burial ages (Granger and Muzikar, 2001).

14.6.3 Chlorine-36 exposure ages

The concept of exposure dating using *in situ*-produced cosmogenic ^{36}Cl was suggested by Davis and Schaeffer (1955), but could not be effectively applied until the advent of AMS analysis (Phillips *et al.*, 1986). Although it was developed after the ^{10}Be and ^{26}Al methods, ^{36}Cl dating offers several advantages. It is applicable to a variety of rock types because ^{36}Cl is generated from three parents (K, Ca and Cl) with different chemistries, while most rocks have low background levels of chlorine. Furthermore, interferences by nucleogenic ^{36}Cl are minimal, and contamination from atmospheric ^{36}Cl is a problem only in severely weathered material.

The three main sources of *in situ* cosmogenic ^{36}Cl are neutron activation of ^{35}Cl and neutron-induced spallation of ^{40}K and ^{40}Ca. A subordinate source is from negative-muon capture by ^{40}Ca. The relative importance of these production routes depends on the relative abundances of K, Ca and Cl in the target and the degree of shielding by overlying rock. Zreda *et al.* (1991) made an empirical study of spallation production, while Liu *et al.* (1994) studied the depth dependence of the neutron-activation reaction. Spallation reactions are caused by fast neutrons, whose penetration decreases exponentially with depth. However, activation reactions require (slow) thermal neutrons, which are produced when fast neutrons undergo glancing collisions with substrate atoms. Hence, slow neutrons reach a peak intensity at about 15 cm depth in rocks (Fig. 14.52). The occurrence of multiple routes makes the calculation of total production rates more complex, but it also offers the possibility of greater age control, as will be shown below.

The simplest scenario for cosmogenic dating is the instantaneous transport of rock from below the cosmic-ray penetration depth to the surface, followed by exposure without shielding by other material (such as snow cover) and without significant erosion. In this case, all production routes for ^{36}Cl can be summed. However, corrections must be made for the latitude dependence of cosmic-ray intensity and the altitude dependence of atmospheric shielding.

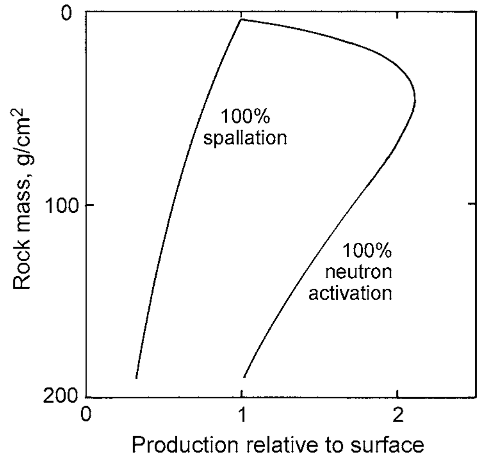

Fig. 14.52. Calculated production profiles for ^{36}Cl by spallation and neutron activation (normalised to equal values at the surface) as a function of rock mass per unit area. After Liu *et al.* (1994).

A relatively simple scenario is provided by surface-exposure dating of rocks at Meteor Crater, Arizona (Nishiizumi *et al.*, 1991b). Samples were taken from the upper few centimetres of large blocks in the ejecta blanket of the impact. The lithology of these blocks shows that they were from strata buried at depths of over 10 m before the impact. On the other hand, their large size suggests that they were unroofed of any overlying ash blanket soon after the impact event. The surfaces of the sampled ejecta blocks were found to be coated with 'rock varnish', which takes thousands of years to develop. Therefore, erosion was probably negligible in the arid climate of Arizona, so ^{36}Cl abundances translate directly into an exposure age. Good agreement between ^{36}Cl ages and Al–Be ages was found, with a consensus of ages around 50 kyr. A few younger ages (e.g. Monument Rock) may indicate more recent exposure of these blocks above the ash blanket.

Another type of simple scenario is achieved in relatively young lava flows, which are instantaneously exposed at the surface and have not yet suffered significant weathering. However, in many geological environments, erosion is a significant factor. In this case, a single cosmogenic isotope determination only allows the solution of exposure age at known erosion rate or erosion rate at known exposure age. For example, using a lava flow from Nevada of known age, Shepard *et al.* (1995) were able to estimate the weathering rate from ^{36}Cl/^{35}Cl ratios.

A more complex scenario arises when both the exposure age and the erosion rate of a deposit are unknown. This applies particularly to rapidly eroding sedimentary deposits. To investigate the constraints which may be applied to such a system, Zreda *et al.* (1994) considered a theoretical model for the erosional exposure of a deposit with buried clasts. These clasts, initially buried within the deposit, are gradually exposed at the surface by erosion of the fine-grained matrix (Fig. 14.53). This model applies to the problem of dating glacial moraines from exposure ages of boulders on the moraine surface, and also to dating meteorite impacts using blocks exposed on the ejecta blanket. Zreda *et al.* argued that, if ^{36}Cl dates are available from several different boulders on a moraine or ejecta blanket, the spread of ages (outside analytical error) could be used to model the exposure history of the deposit.

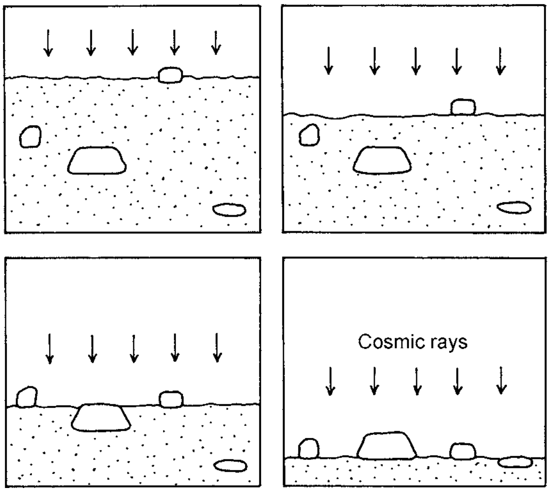

Fig. 14.53. Schematic illustration of the exhumation of clasts from a heterogeneous deposit by erosion of the matrix. After Zreda *et al.* (1994).

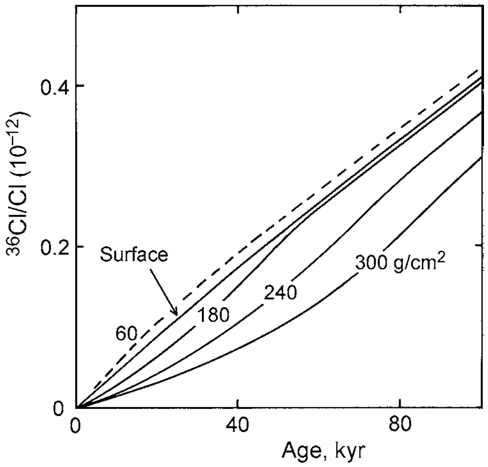

Fig. 14.54. Modelled ^{36}Cl/Cl inventories for rock boulders buried at various depths in an eroding deposit, showing peak cosmogenic production just below the surface. After Zreda and Phillips (1994).

To demonstrate these effects, Zreda and Phillips (1994) modelled ^{36}Cl/Cl ratios for several boulders buried at depths from zero to 300 g/cm^2 (approximately 1.5 m depth in soil of density equal to 2 g/cm^3). Total ^{36}Cl production was attributed 50% to spallation reactions and 50% to neutron activation. The erosion rate was set so that the deepest boulder just reaches the surface at the present day. The modelling results show a wide range of ^{36}Cl/Cl ratios, both below and slightly above the growth curve for zero depth (Fig. 14.54). The growth curves for deeply buried boulders start with slow production, due to the shielding effect of the overlying matrix. As the boulder approaches the surface, the rate of production accelerates, but the total ^{36}Cl inventory remains well below that of a surface

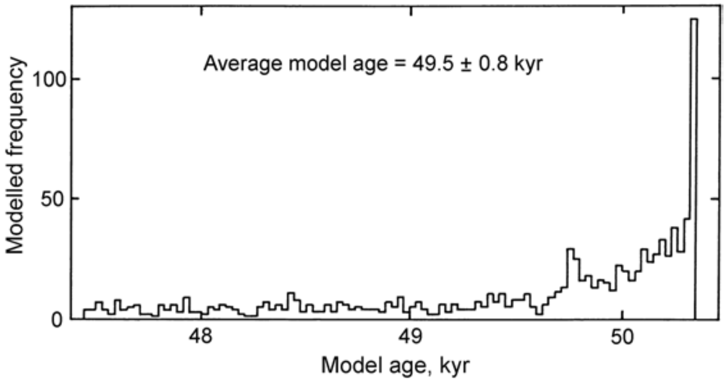

Fig. 14.55. Histogram of model ^{36}Cl exposure ages for 1000 rock clasts exhumed from depths of up to about 1.5 m in a deposit with a formation age of 50 kyr. Data for a few samples over-estimate the real age due to greater cosmogenic production just below the surface. After Zreda and Phillips (1994).

sample. On the other hand, boulders that were initially subject to shallow burial can actually exhibit greater total ^{36}Cl production than that at the surface, due to the peak of neutron-activation production at a depth of 50 g/cm^2.

Zreda and Phillips (1994) modelled the erosion history of ejecta blocks from Meteor Crater, Arizona, in a similar way. However, in this case the spread of apparent exposure ages was based on 1000 model points randomly buried from zero to a chosen maximum depth (Fig. 14.55). The model results were compared with the actual spread of ages in four blocks at Meteor Crater, with a mean age of 49.7 ± 0.9 kyr (Monument Rock was excluded). The best fit was obtained by assuming burial to a maximum depth of 300 g/cm^2 (about 1.5 m), removed at 30 g/cm^2 per kyr (0.15 mm/yr), so that all boulders reached the surface within 10 kyr. Such modelling cannot yield a unique solution to the erosion process, and the model results should ideally be compared with a larger set of measured ages. Nevertheless, the modelling does suggest that the four blocks yield exposure ages close to the estimated time of impact.

In principle, the use of two spallogenic nuclides (e.g. ^{10}Be and ^{26}Al) allows the deconvolution of exposure ages and erosion rates. However, as noted above, the closely spaced trajectories of the constant-erosion and the constant-exposure saturation lines make the deconvolution weak (e.g. Fig. 14.50). A more powerful application of the ^{36}Cl technique makes use of the neutron-activation route to ^{36}Cl, in comparison with the purely spallogenic nuclides (^{10}Be or ^{26}Al). Because spallation and neutron activation yield peak nuclide production at different depths in a geological surface, they should yield a clear resolution of exposure histories involving different rates of erosion (Liu *et al.*, 1994). With this objective in mind, Bierman *et al.* (1995) described a method for isolating the neutron-activation component of ^{36}Cl, by releasing chlorine from fluid inclusions within rock samples. However, the method has not been demonstrated in practice. Alternatively, a crude assessment of the rate of erosion can be obtained by simply ignoring spallogenic ^{36}Cl production.

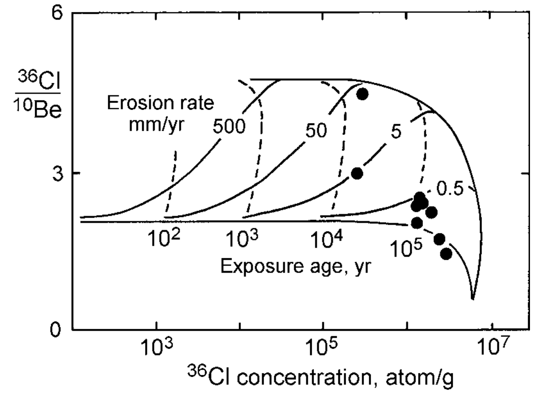

Fig. 14.56. Plot of analysed ^{36}Cl/^{10}Be ratio against ^{36}Cl abundance for boulders from glacial moraines of the Wind River Range, Wyoming. Solid lines indicate erosion rates; dashed lines are exposure-age isochrons. See the text for discussion. After Phillips *et al.* (1997).

This approach was taken by Phillips *et al.* (1997) in a study on glacial deposits of the Wind River Range, Wyoming. Ten boulders from glacial moraines were analysed for ^{36}Cl and ^{10}Be, and results are plotted on the Cl–Be plot in Fig. 14.56. The limits for zero erosion and for infinite age (erosional equilibrium) are given, as in the Al–Be plot. However, they are now much further apart, allowing easy resolution between the two models. Most of the data lie below the line corresponding to 0.5 mm/kyr erosion, indicating that the surfaces of these boulders are not undergoing significant loss by erosion. The boulders were sampled from six different moraines, and their ages indicate that one moraine dates from the last glaciation (about 20 kyr ago), three from the penultimate glaciation (about 130–100 kyr ago) and two from older glaciations, assuming rapid exposure of the boulders on the moraine surface.

A different application of the ^{36}Cl method was proposed by Stone *et al.* (1996), using ^{40}Ca spallation as a tool for exposure dating of calcite. The abundance of the target nuclide, together with the relatively low abundance of chlorine in calcite, makes this an analytically favourable method with great promise for exposure dating of karst landscapes. For example, two recent studies (Zreda and Noller, 1998; Mitchell *et al.*, 2001) used ^{36}Cl abundances in fault scarps to date the displacement of fault systems in carbonate rocks. In both cases, ^{36}Cl measurements were made at several points down the face of the fault scarp. ^{36}Cl accumulation was then used to determine the date when each sample was first exposed at the surface, allowing a reconstruction of past movement on the fault.

References

Adkins, J. F. and Boyle, E. A. (1997). Changing atmospheric Δ ^{14}C and the record of deep water paleoventilation ages. *Paleoceanography* **12**, 337–44.

Anderson, E. C. and Libby, W. F. (1951). World-wide distribution of natural radiocarbon. *Phys. Rev.* **81**, 64–9.

Andree, M., Oeschger, H., Broecker, W. *et al.* (1986). Limits on ventilation rates for the deep ocean over the last 12,000 years. *Climate Dynamics* **1**, 53–62.

Andrews, J. N., Davis, S. N., Fabryka-Martin, J. *et al.* (1989). The *in situ* production of radioisotopes in rock matrices with particular reference to the Stripa granite. *Geochim. Cosmochim. Acta* **53**, 1803–15.

Arnold, J. R. (1956). Beryllium-10 produced by cosmic rays. *Science* **124**, 584–5.

Arnold, J. R. (1958). Trace elements and transport rates in the ocean. *Second UN Conference on Peaceful Uses of Atomic Energy* **18**. IAEA, pp. 344–6.

Arnold, J. R. and Libby, W. F. (1949). Age determinations by radiocarbon content: checks with samples of known age. *Science* **110**, 678–80.

Bard, E., Arnold, M., Fairbanks, R. G. and Hamelin, B. (1993). ^{230}Th/^{234}U and ^{14}C ages obtained by mass spectrometry on corals. *Radiocarbon* **35**, 191–9.

Bard, E., Arnold, M., Hamelin, B., Tisnerat-Laborde, N. and Cabioch, G. (1998). Radiocarbon calibration by means of mass spectrometric ^{230}Th/^{234}U and ^{14}C ages of corals: an updated database including samples from Barbados, Mururoa and Tahiti. *Radiocarbon* **40**, 1085–92.

Bard, E., Arnold, M., Mangerud, J. *et al.* (1994). The North Atlantic atmosphere–sea surface ^{14}C gradient during the Younger Dryas climatic event. *Earth Planet. Sci. Lett.* **126**, 275–87.

Bard, E., Hamelin, B., Fairbanks, R. G. and Zindler, A. (1990a). Calibration of the ^{14}C timescale over the past 30,000 years using mass spectrometric U–Th ages from Barbados corals. *Nature* **345**, 405–10.

Bard, E., Hamelin, B., Fairbanks, R. G., Zindler, A., Mathieu, G. and Arnold, M. (1990b). U/Th and ^{14}C ages of corals from Barbados and their use for calibrating the ^{14}C timescale beyond 9000 years B. P. *Nucl. Instr. Meth. Phys. Res. B* **52**, 461–8.

Bard, E., Raisbeck, G. M., Yiou, F. and Jouzel, J. (1997). Solar modulation of cosmogenic nuclide production over the last millennium: comparison between ^{14}C and ^{10}Be records. *Earth Planet. Sci. Lett.* **150**, 453–62.

Baumgartner, S., Beer, J., Masarik, J., Wagner, G., Meynadier, L. and Synal, H.-A. (1998). Geomagnetic modulation of the ^{36}Cl flux in the GRIP ice core, Greenland. *Science* **279**, 1330–2.

Baxter, M. S. and Farmer, J. G. (1973). Radiocarbon: short-term variations. *Earth Planet. Sci. Lett.* **20**, 295–9.

Beck, J. W., Richards, D. A., Edwards, R. L. *et al.* (2001). Extremely large variations of atmospheric ^{14}C concentration during the last glacial period. *Science* **292**, 2453–8.

Beer, J., Andree, M., Oeschger, H. *et al.* (1984). The Camp Century ^{10}Be record: implications for long-term variations of the geomagnetic dipole moment. *Nucl. Instr. Meth. Phys. Res. B* **5**, 380–4.

Beer, J., Oeschger, H., Finkel, R. C. *et al.* (1985). Accelerator measurements of ^{10}Be: the 11 year solar cycle. *Nucl. Instr. Meth. Phys. Res. B* **10**, 415–18.

Beer, J., Siegenthaler, U., Bonani, G. *et al.* (1988). Information on past solar activity and geomagnetism from ^{10}Be in the Camp Century ice core. *Nature* **331**, 675–9.

Belshaw, N. S., O'Nions, R. K. and von Blankenburg, F. (1995). A SIMS method for ^{10}Be/^{9}Be ratio measurement in environmental materials. *Int. J. Mass Spectrom. Ion Phys.* **142**, 55–67.

Bentley, H. W., Phillips, F. M., Davis, S. N. *et al.* (1982). Thermonuclear ^{36}Cl pulse in natural water. *Nature* **300**, 737–40.

Bentley, H. W., Phillips, F. M., Davis, S. N. *et al.* (1986). Chlorine 36 dating of very old groundwaters, 1, The Great Artesian Basin, Australia. *Water Resources Res.* **22**, 1991–2002.

Bierman, P., Gillespie, A., Caffee, M. and Elmore, D. (1995). Estimating erosion rates and exposure ages with ^{36}Cl produced by neutron activation. *Geochim. Cosmochim. Acta* **59**, 3779–98.

Broecker, W. S. and Denton, G. H. (1989). The role of ocean–atmosphere reorganizations in glacial cycles. *Geochim. Cosmochim. Acta* **53**, 2465–501.

Broecker, W. S., Gerard, R., Ewing, M. and Heezen, B. C. (1960). Natural radiocarbon in the Atlantic Ocean. *J. Geophys. Res.* **65**, 2903–31.

Brown, E. T., Edmond, J. M., Raisbeck, G. M., Bourles, D. L., Yiou, F. and Measures, C. I. (1992). Beryllium isotope geochemistry in tropical basins. *Geochim. Cosmochim. Acta* **56**, 1607–624.

Brown, L., Klein, J. and Middleton, R. (1985). Anomalous isotopic concentrations in the sea off Southern California. *Geochim. Cosmochim. Acta* **49**, 153–7.

Brown, L., Klein, J., Middleton, R., Sacks, I. S. and Tera, F. (1982). ^{10}Be in island-arc volcanoes and implications for subduction. *Nature* **299**, 718–20.

Brown, L., Stensland, G. J., Klein, J. and Middleton, R. (1989). Atmospheric deposition of ^{7}Be and ^{10}Be. *Geochim. Cosmochim. Acta* **53**, 135–42.

Bruns, M., Rhein, M., Linick, T. W. and Suess, H. E. (1983). The atmospheric ^{14}C level in the 7th millennium BC. *P.A.C.T. (Physical and Chemical Techniques in Archaeology)* **8**, 511–16.

Bucha, V. and Neustupny, E. (1967). Changes in the Earth's magnetic field and radiocarbon dating. *Nature* **215**, 261–3.

Campin, J.-M., Fichefet, T. and Duplessy, J.-C. (1999). Problems with using radiocarbon to infer ocean ventilation rates for past and present climates. *Earth Planet. Sci. Lett.* **165**, 17–24.

Chengde, S., Beer, J., Tungsheng, L. *et al.* (1992). ^{10}Be in Chinese loess. *Earth Planet. Sci. Lett.* **109**, 169–77.

Craig, H. (1954). Carbon-13 in plants and the relationships between carbon-13 and carbon-14 variations in nature. *J. Geol.* **62**, 115–49.

Craig, H. (1957). Isotopic standards for carbon and oxygen and correction factors for mass-spectrometric analysis of carbon dioxide. *Geochim. Cosmochim. Acta* **12**, 133–49.

Damon, P. E., Donahue D. J., Gore, B. H. *et al.* (1989). Radiocarbon dating of the Shroud of Turin. *Nature* **337**, 611–15.

Davis, R. and Schaeffer, O. A. (1955). Chlorine-36 in Nature. *Ann. N.Y. Acad. Sci.* **62**, 105–22.

De Jong, A. F. M., Mook, W. G. and Becker, B. (1979). Confirmation of the Suess wiggles: 3200–3700 BC. *Nature* **280**, 48–9.

de Vries, H. (1958). Variation in concentration of radiocarbon with time and location on Earth. *Proc. Koninkl. Ned. Akad. Wetenschap B* **61**, 94–102.

De Vries, H. and Barendsen, G. W. (1953). Radiocarbon dating by a proportional counter filled with carbon dioxide. *Physica* **19**, 987–1003.

Druffel, E. M. (1996). Post-bomb radiocarbon records of surface corals from the tropical Atlantic Ocean. *Radiocarbon* **38**, 563–72.

Eddy, J. A. (1976). The Maunder minimum. *Science* **192**, 1189–202.

Edwards, R. L., Beck, J. W., Burr, G. S. *et al.* (1993a). A large drop in atmospheric ^{14}C/^{12}C and reduced melting in the Younger Dryas, documented with ^{230}Th ages of corals. *Science* **260**, 962–8.

Edwards, C. M. H., Morris, J. D. and Thirlwall, M. F. (1993b). Separating mantle from slab signatures in arc lavas using B/Be and radiogenic isotope systematics. *Nature* **362**, 530–3.

Elmore, D., Gove, H. E., Ferraro, R. *et al.* (1980). Determination of ^{129}I using tandem accelerator mass spectrometry. *Nature* **286**, 138–40.

Elmore, D., Tubbs, L. E., Newman, D. *et al.* (1982). ^{36}Cl bomb pulse measured in a shallow ice core from Dye 3, Greenland. *Nature* **300**, 735–7.

Elsasser, W., Ney, E. P. and Winckler, J. R. (1956). Cosmic-ray intensity and geomagnetism. *Nature* **178**, 1226–7.

Evans, J. C., Rancitelli, L. A. and Reeves, J. H. (1979). ^{26}Al content of Antarctic meteorites: implications for terrestrial ages and bombardment history. *Proceedings of the 10th Lunar Planetary Science Conference*. Lunar and Planetary Institute, pp. 1061–72.

Evans, J. C. and Reeves, J. H. (1987). ^{26}Al survey of Antarctic meteorites. *Earth Planet. Sci. Lett.* **82**, 223–30.

Fabryka-Martin, J., Bentley, H., Elmore, D. and Airey, P. L. (1985). Natural iodine-129 as an environmental tracer. *Geochim. Cosmochim. Acta* **49**, 337–47.

Fabryka-Martin, J., Davis, S. N. and Elmore, D. (1987). Applications of ^{129}I and ^{36}Cl in hydrology. *Nucl. Instr. Meth. Phys. Res. B* **29**, 361–71.

Fabryka-Martin, J., Davis, S. N., Elmore, D. and Kubik, P. W. (1989). *In situ* production and migration of ^{129}I in the Stripa granite, Sweden. *Geochim. Cosmochim. Acta* **53**, 1817–23.

Fan, C. Y., Chen, T. M., Yun, S. X. and Dai, K. M. (1986). Radiocarbon activity variation in dated tree rings grown in Mackenzie delta. *Radiocarbon* **28**, 300–5.

Fehn, U., Holdren, G. R., Elmore, D., Brunelle, T., Teng, R. and Kubik, P. W. (1986). Determination of natural and anthropogenic ^{129}I in marine sediments. *Geophys. Res. Lett.* **13**, 137–9.

Fehn, U. and Snyder, G. (2000). ^{129}I in the Southern Hemisphere: global redistribution of an anthropogenic isotope. *Nucl. Instr. Meth. Phys. Res. B* **172**, 366–71.

Ferguson, C. W. (1970). Dendrochronology of Bristlecone pine, *Pinus aristata*. Establishment of a 7484-year chronology in the White Mountains of eastern-central California, USA. In: Olsson, I. U. (Ed.), *Radiocarbon Variations and Absolute Chronology, Proceedings of the 12th Nobel Symposium*. Wiley, pp. 571–93.

Ferguson, C. W. and Graybill, D. A. (1983). Dendrochronology of Bristlecone pine: a progress report. *Radiocarbon* **25**, 287–8.

Fink, D., Middleton, R., Klein, J. and Sharma, P. (1990). ^{41}Ca measurement by accelerator mass spectrometry and applications. *Nucl. Instr. Meth. Phys. Res. B* **47**, 79–96.

Forbush, S. E. (1954). Worldwide cosmic-ray variations, 1937–1952. *J. Geophys. Res.* **59**, 525–42.

Frank, M., Schwarz, B., Baumann, S., Kubik, P. W., Suter, M. and Mangini, A. (1997). A 200 kyr record of cosmogenic radionuclide production rate and geomagnetic field intensity from ^{10}Be in globally stacked deep-sea sediments. *Earth Planet. Sci. Lett.* **149**, 121–9.

Godwin, H. (1962). Half-life of radiocarbon. *Nature* **195**, 984.

Goldberg, E. D. and Arrhenius, G. O. S. (1958). Chemistry of Pacific pelagic sediments. *Geochim. Cosmochim. Acta* **13**, 153–212.

Goldstein, S. J., Lea, D. W., Chakraborty, S., Kashgarian, M. and Murrell, M. T. (2001). Uranium-series and radiocarbon geochronology of deep-sea corals: implications for Southern Ocean ventilation rates and the ocean carbon cycle. *Earth Planet. Sci. Lett.* **193**, 167–82.

Goslar, T., Arnold, M., Tisnerat-Laborde, N., Czernik, J. and Wieckowski, K. (2000). Variations of Younger Dryas atmospheric radiocarbon explicable without ocean circulation changes. *Nature* **403**, 877–80.

Gove, H. E. (1987). Tandem-accelerator mass-spectrometry measurements of ^{36}Cl, ^{129}I and osmium isotopes in diverse natural samples. *Phil. Trans. Roy. Soc. Lond. A* **323**, 103–19.

Granger, D. E., Fabel, D. and Palmer, A. N. (2001). Pliocene–Pleistocene incision of the Green river, Kentucky, determined from radioactive decay of cosmogenic ^{26}Al and ^{10}Be in Mammoth Cave sediments. *GSA Bull.* **113**, 825–36.

Granger, D. E. and Muzikar, P. F. (2001). Dating sediment burial with *in situ*-produced cosmogenic nuclides: theory, techniques, and limitations. *Earth Planet. Sci. Lett.* **188**, 269–81.

Hammer, C. U., Clausen, H. B. and Tauber, H. (1986). Ice-core dating of the Pleistocene/Holocene boundary applied to a calibration of the ^{14}C time scale. *Radiocarbon* **28**, 284–91.

Henning, W. (1987). Accelerator mass spectrometry of heavy elements: ^{36}Cl to ^{205}Pb. *Phil. Trans. Roy. Soc. Lond. A* **323**, 87–99.

Hillam, J., Groves, C. M., Brown, D. M., Baillie, M. G. L., Coles, J. M. and Coles, B. J. (1990). Dendrochronology of the English Neolithic. *Antiquity* **64**, 210–20.

Hofmann, H. J., Beer, J., Bonani, G. *et al.* (1987). ^{10}Be half-life and AMS-standards. *Nucl. Instr. Meth. Phys. Res. B* **29**, 32–6.

Huber, B. (1970). Dendrochronology of central Europe. In: Olsson, I. U. (Ed.), *Radiocarbon Variations and Absolute Chronology, Proceedings of the 12th Nobel Symposium.* Wiley, pp. 233–5.

Hughen, K. A., Overpeck, J. T., Lehman, S. J. *et al.* (1998). Deglacial changes in ocean circulation from an extended radiocarbon calibration. *Nature* **391**, 65–8.

Kamen, M. D. (1963). Early history of carbon-14. *Science* **140**, 584–90.

Key, R., Quay, P. D., Jones, G. A., McNichol, A. P., Von Reden, K. F. and Schneider, R. J. (1996). WOCE AMS radiocarbon I: Pacific Ocean results (P6, P16, P17). *Radiocarbon* **38**, 425–518.

Kieser, W. E., Beukens, R. P., Kilius, L. R., Lee, H. W. and Litherland, A. E. (1986). Isotrace radiocarbon analysis – equipment and procedures. *Nucl. Instr. Meth. Phys. Res. B* **15**, 718–21.

Kitagawa, H. and van der Plicht, J. (1998). Atmospheric radiocarbon calibration to 45,000 yr B.P.: late glacial fluctuations and cosmogenic isotope production. *Science* **279**, 1187–90.

Klein, J., Fink, D., Middleton, R., Nishiizumi, K. and Arnold, J. (1991). Determination of the half-life of ^{41}Ca from measurements of Antarctic meteorites. *Earth Planet. Sci. Lett.* **103**, 79–83.

Kok, Y. S. (1999). Climatic influence in NRM and ^{10}Be-derived geomagnetic paleointensity data. *Earth Planet. Sci. Lett.* **166**, 105–19.

Ku, T. L., Kusakabe, M., Measures, C. I. *et al.* (1990). Beryllium isotope distribution in the western North Atlantic: a comparison to the Pacific. *Deep-Sea Res.* **37**, 795–808.

Ku, T. L., Wang, L., Luo, S. and Southon, J. R. (1995). ^{26}Al in seawater and ^{26}Al/^{10}Be as paleo-flux tracer. *Geophys. Res. Lett.* **22**, 2163–6.

Kusakabe, M., Ku, T. L., Southon, J. R. *et al.* (1987). The distribution of ^{10}Be and ^{9}Be in ocean water. *Nucl. Instr. Meth. Phys. Res. B* **29**, 306–10.

Labrie, D. and Reid, J. (1981). Radiocarbon dating by infrared laser spectroscopy. *Appl. Phys.* **24**, 381–6.

Lal, D. (1988). *In situ*-produced cosmogenic isotopes in terrestrial rocks. *Ann. Rev. Earth Planet. Sci.* **16**, 355–88.

Lal, D. and Peters, B. (1967). Cosmic-ray produced radioactivity on the Earth. In: *Handbook of Physics*, **46/2**. Springer-Verlag, pp. 551–612.

Lao, Y., Anderson, R. F., Broecker, W. S., Trumbore, S. E., Hofmann, H. J. and Wölfli, W. (1992). Increased production of cosmogenic ^{10}Be during the Last Glacial Maximum. *Nature* **357**, 576–8.

Lee, H. W., Galindo-Uribarri, A., Chang, K. H., Kilius, L. R. and Litherland, A. E. (1984). The $^{12}CH_2^{+2}$ molecule and radiocarbon dating by accelerator mass spectrometry. *Nucl. Instr. Meth. Phys. Res. B* **5**, 208–10.

Libby, W. F. (1952). *Radiocarbon Dating.* University of Chicago Press, 124 pp.

Libby, W. F. (1970). Ruminations on radiocarbon dating. In: Olsson, I. U. (Ed.), *Radiocarbon Variations and Absolute Chronology, Proceedings of the 12th Nobel Symposium.* Wiley, pp. 629–40.

Litherland, A. E. (1980). Ultra-sensitive mass spectrometry with accelerators. *Ann. Rev. Nucl. Part. Sci.* **30**, 437–73.

Litherland, A. E. (1987). Fundamentals of accelerator mass spectrometry. *Phil. Trans. Roy. Soc. Lond. A* **323**, 5–21.

Liu, B., Phillips, F. M., Fabryka-Martin, J. T., Fowler, M. M. and Stone, W. D. (1994). Cosmogenic ^{36}Cl accumulation in unstable landforms 1. Effects of the thermal neutron distribution. *Water Resources Res.* **30**, 3115–25.

Lundberg, L., Ticich, T., Herzog, G. F. *et al.* (1983). ^{10}Be and Be in the Maurice River–Union Lake system of Southern New Jersey. *J. Geophys. Res.* **88**, 4498–504.

Mangini, A., Segl, M., Bonani, G. *et al.* (1984). Mass-spectrometric ^{10}Be dating of deep-sea sediments applying the Zürich tandem accelerator. *Nucl. Instr. Meth. Phys. Res. B* **5**, 353–8.

Marchal, O., Stocker, T. F. and Muschler, R. (2001). Atmospheric radiocarbon during the Younger Dryas: production, ventilation, or both? *Earth Planet. Sci. Lett.* **185**, 383–95.

Mazaud, A., Laj, C., Bard, E., Arnold, M. and Tric, E. (1991). Geomagnetic field control of ^{14}C production over the last 80 kyr: implications for the radiocarbon time-scale. *Geophys Res. Lett.* **18**, 1885–8.

McCorkell, R., Fireman, E. L. and Langway, C. C. (1967). Aluminium-26 and beryllium-10 in Greenland ice. *Science* **158**, 1690–2.

Measures, C. I. and Edmond, J. M. (1982). Beryllium in the water column of the central North Pacific. *Nature* **297**, 51–3.

Merrill, J. R., Lyden, E. F. X., Honda, M. and Arnold, J. R. (1960). The sedimentary geochemistry of the beryllium isotopes. *Geochim. Cosmochim. Acta* **18**, 108–29.

Middleton, R. and Klein, J. (1987). ^{26}Al: measurement and applications. *Phil. Trans. Roy. Soc. Lond. A* **323**, 121–43.

Mitchell, S. G., Matmon, A., Bierman, P. R., Enzel, Y., Caffee, M. and Rizzo, D. (2001). Displacement history of a limestone normal fault scarp, northern Israel, from cosmogenic ^{36}Cl. *J. Geophys. Res.* **106**, 4247–64.

Monaghan, M. C., Klein, J. and Measures, C. I. (1988). The origin of ^{10}Be in island-arc volcanic rocks. *Earth Planet. Sci. Lett.* **89**, 288–98.

Mook, W. G. (1986). Business meeting: recommendations/ resolutions adopted by the Twelfth International Radiocarbon Conference. *Radiocarbon* **28**, 799.

Mook, W. G. and Streurman, H. J. (1983). Physical and chemical aspects of radiocarbon dating. *P.A.C.T. (Physical and Chemical Techniques in Archaeology)* **8**, 31–55.

Morris, J. D., Leeman, W. P. and Tera, F. (1990). The subducted component in island arc lavas: constraints from Be isotopes and B–Be systematics. *Nature* **344**, 31–6.

Morris, J. D. and Tera, F. (1989). ^{10}Be and ^{9}Be in mineral separates and whole-rocks from volcanic arcs: implications for sediment subduction. *Geochim. Cosmochim. Acta* **53**, 3197–206.

Muscheler, R., Beer, J., Wagner, G. and Finkel, R. C. (2000). Changes in deep-water formation during the Younger Dryas event inferred from ^{10}Be and ^{14}C records. *Nature* **408**, 567–70.

Nishiizumi, K., Arnold, J. R., Elmore, D. *et al.* (1979). Measurements of ^{36}Cl in Antarctic meteorites and Antarctic ice using a van de Graaff accelerator. *Earth Planet. Sci. Lett.* **45**, 285–92.

Nishiizumi, K., Elmore, D. and Kubik, P. W. (1989a). Update on terrestrial ages of Antarctic meteorites. *Earth Planet. Sci. Lett.* **93**, 299–313.

Nishiizumi, K., Kohl, C. P., Arnold, J. R., Klein, J., Fink, D. and Middleton, R. (1991a). Cosmic-ray produced ^{10}Be and ^{26}Al in Antarctic rocks: exposure and erosion history. *Earth Planet. Sci. Lett.* **104**, 440–54.

Nishiizumi, K., Kohl, C. P., Shoemaker, J. R. *et al.* (1991b). *In situ* ^{10}Be and ^{26}Al exposure ages at Meteor Crater, Arizona. *Geochim. Cosmochim. Acta* **55**, 2699–703.

Nishiizumi, K., Lal, D., Klein, J., Middleton, R. and Arnold, J. R. (1986). Production of ^{10}Be and ^{26}Al by cosmic rays in terrestrial quartz *in situ* and implications for erosion rates. *Nature* **319**, 134–6.

Nishiizumi, K., Winterer, E. L., Kohl, C. P. *et al.* (1989b). Cosmic ray production rates of ^{10}Be and ^{26}Al in quartz from glacially polished rocks. *J. Geophys. Res.* **94**, 17 907–15.

Nydal, R. (2000). Radiocarbon in the ocean. *Radiocarbon* **42**, 81–98.

Oeschger, H., Houtermans, J., Loosli, H. and Wahlen, M. (1970). The constancy of cosmic radiation from isotope studies in meteorites and on the Earth. In: Olsson, I. U. (Ed.), *Radiocarbon Variations and Absolute Chronology, Proceedings of the 12th Nobel Symposium.* Wiley, pp. 471–98.

Oktay, S. D., Santschi, P. H., Moran, J. E. and Sharma, P. (2000). The ^{129}I bomb pulse recorded in Mississippi River Delta sediments: results from isotopes of I, Pu, Cs, Pb, and C. *Geochim. Cosmochim. Acta* **64**, 989–96.

Olsson, I. U. (1980). ^{14}C in extractives from wood. *Radiocarbon* **22**, 515–24.

Olsson, I. U., El-Daoushy, M. F. A. F., Abdel-Mageed, A. I. and Klasson, M. (1974). A comparison of different methods for pretreatment of bones. *Geol. Foren. Stockh. Forhandl.* **96**, 171–81.

Ostlund, H. G. and Rooth, C. G. H. (1990). The North Atlantic tritium and radiocarbon transients 1972–1983. *J. Geophys. Res.* **95**, 20 147–65.

Pavich, M. J., Brown, L., Valette-Silver, J. N., Klein, J. and Middleton, R. (1985). ^{10}Be analysis of a Quaternary weathering profile in the Virginia Piedmont. *Geology* **13**, 39–41.

Pearson, G. W., Pilcher, J. R., Baillie, M. G. L. and Hillam, J. (1977). Absolute radiocarbon dating using a low altitude European tree-ring calibration. *Nature* **270**, 25–8.

Phillips, F. M., Leavy, B. D., Jannik, N. O., Elmore, D. and Kubik, P. W. (1986). The accumulation of cosmogenic chlorine-36 in rocks: a method for surface exposure dating. *Science* **231**, 41–3.

Phillips, F. M., Mattick, J. L. and Duval, T. A. (1988). Chlorine 36 and tritium from nuclear weapons fallout as tracers for long-term liquid and vapour movement in desert soils. *Water Resource Res.* **24**, 1877–91.

Phillips, F. M., Zreda, M. G., Gosse, J. C. *et al.* (1997). Cosmogenic ^{36}Cl and ^{10}Be ages of Quaternary glacial and fluvial deposits of the Wind River Range, Wyoming. *GSA Bull.* **109**, 1453–63.

Plummer, M. A., Phillips, F. M., Fabryka-Martin, J., Turin, H. J., Wigand, P. E. and Sharma P. (1997). Chlorine-36 in fossil rat urine: an archive of cosmogenic nuclide deposition during the past 40,000 years. *Science* **277**, 538–41.

Purser, K. H., Liebert, R. B., Litherland, A. E. *et al.* (1977). An attempt to detect stable N-ions from a sputter ion source and some implications of the results for the design of tandems for ultra-sensitive carbon analysis. *Rev. Phys. Appl.* **12**, 1487–92.

Raisbeck, G. M., Yiou, F., Fruneau, M., Lieuvin, M. and Loiseaux, J. M. (1978). Measurements of ^{10}Be in 1,000- and 5,000-year-old Antarctic ice. *Nature* **275**, 731–3.

Raisbeck, G. M., Yiou, F., Fruneau, M., Loiseaux, J. M., Lieuvin, M. and Ravel, J. C. (1979). Deposition rate and seasonal variations in precipitation of cosmogenic ^{10}Be. *Nature* **282**, 279–80.

Raisbeck, G. M., Yiou, F., Fruneau, M. *et al.* (1980). ^{10}Be concentration and residence time in the deep ocean. *Earth Planet. Sci. Lett.* **51**, 275–8.

Raisbeck, G. M., Yiou, F., Fruneau, M. *et al.* (1981a). Cosmogenic ^{10}Be concentrations in Antarctic ice during the past 30,000 years. *Nature* **292**, 825–6.

Raisbeck, G. M., Yiou, F., Lieuvin, M., Ravel, J. C., Fruneau, M. and Loiseaux, J. M. (1981b). ^{10}Be in the environment: some recent results and their application. *Proceedings of the Symposium on Accelerator Mass Spectrometry.* Argonne National Laboratory, pp. 228–43.

Raisbeck, G. M., Yiou, F. and Zhou, S. Z. (1994). Palaeointensity puzzle. *Nature* **371**, 207–8.

Ralph, E. K. (1971). Carbon-14 dating. In: Michael, H. N. and Ralph, E. K. (Eds.), *Dating Techniques for the Archaeologist*. M.I.T. Press, pp. 1–48.

Ralph, E. K. and Michael, H. N. (1974). Twenty-five years of radiocarbon dating. *Amer. Scient.* **62**, 553–60.

Reyss, J. L., Yokoyama, Y. and Guichard, F. (1981). Production cross sections of ^{26}Al, ^{22}Na, ^{7}Be from argon and of ^{10}Be, ^{7}Be from nitrogen: implications for the production rates of ^{26}Al and ^{10}Be in the atmosphere. *Earth Planet. Sci. Lett.* **53**, 203–10.

Robinson, C., Raisbeck, G. M., Yiou, F., Lehman, B. and Laj, C. (1995). The relationship between ^{10}Be and geomagnetic field strength records in central North Atlantic sediments during the last 80 ka. *Earth Planet. Sci. Lett.* **136**, 551–7.

Shackleton, N. J., Duplessy, J.-C., Arnold, M., Maurice, P., Hall, M. A. and Cartlidge, J. (1988). Radiocarbon age of last glacial Pacific deep water. *Nature* **335**, 708–11.

Sharma, M. (2002). Variations in solar magnetic activity during the last 200 000 years: is there a Sun–climate connection? *Earth Planet. Sci. Lett.* **199**, 459–72.

Shepard, M. K., Arvidson, R. E., Caffee, M., Finkel, R. and Harris, L. (1995). Cosmogenic exposure ages of basalt flows: Lunar Crater volcanic field, Nevada. *Geology* **23**, 21–4.

Sigmarsson, O., Condomines, M., Morris, J. D. and Harmon, R. S. (1990). Uranium and ^{10}Be enrichments by fluids in Andean arc magmas. *Nature* **346**, 163–5.

Simpson, J. A. (1951). Neutrons produced in the atmosphere by cosmic radiations. *Phys. Rev.* **83**, 1175–88.

Stensland, G. J., Brown, L., Klein, J. and Middleton, R. (1983). Beryllium-10 in rain. *EOS* **64**, 283 (abstract).

Stone, J. O., Allan, G. L., Fifield, L. K. and Cresswell, R. G. (1996). Cosmogenic chlorine-36 from calcium spallation. *Geochim. Cosmochim. Acta* **60**, 679–92.

Stuiver, M. (1961). Variations in radiocarbon concentration and sunspot activity. *J. Geophys. Res.* **66**, 273–6.

Stuiver, M. (1965). Carbon-14 content of 18th- and 19th-century wood: variations correlated with sunspot activity. *Science* **149**, 533–5.

Stuiver, M., Braziunas, T. F., Becker, B. and Kromer, B. (1991). Climatic, solar, oceanic and geomagnetic influences on late-glacial and Holocene atmospheric ^{14}C/^{12}C change. *Quaternary Res.* **35**, 1–24.

Stuiver, M. and Pearson, G. W. (1986). High-precision radiocarbon time-scale calibration from the present to 500 BC. In: Stuiver, M. and Kra, R. S. (Eds.), *Calibration Issue, 12th International Radiocarbon Conference. Radiocarbon* **28**, 805–38.

Stuiver, M. and Quay, P. D. (1981). Atmospheric ^{14}C changes resulting from fossil fuel CO_2 release and cosmic-ray flux variability. *Earth Planet. Sci. Lett.* **53**, 349–62.

Stuiver, M., Quay, P. D. and Ostlund, H. G. (1983). Abyssal water carbon-14 distribution and the age of the world oceans. *Science* **219**, 849–51.

Suess, H. E. (1955). Radiocarbon concentrations in modern wood. *Science* **122**, 415–17.

Suess, H. E. (1965). Secular variations of the cosmic-ray-produced carbon 14 in the atmosphere and their interpretations. *J. Geophys. Res.* **70**, 5937–52.

Suess, H. E. (1970). Bristlecone-pine calibration of the radiocarbon time-scale 5200 B.C. to the present. In: Olsson, I. U. (Ed.), *Radiocarbon Variations and Absolute Chronology, Proceedings of the 12th Nobel Symposium*. Wiley, pp. 303–11.

Suess, H. E. and Strahm, C. (1970). The Neolithic of Auvernier, Switzerland. *Antiquity* **44**, 91–9.

Tanaka, S. and Inoue, T. (1979). ^{10}Be dating of North Pacific sediment cores up to 2.5 million years B.P. *Earth Planet. Sci. Lett.* **45**, 181–7.

Tauber, H. (1970). The Scandinavian varve chronology and C-14 dating. In: Olsson, I. U. (Ed.), *Radiocarbon Variations and Absolute Chronology, Proceedings of the 12th Nobel Symposium*. Wiley, pp. 173–96.

Taylor, R. E. (1987). *Radiocarbon Dating, an Archaeological Perspective*. Academic Press, 212 pp.

Tera, F., Brown, L., Morris, J., Sacks, I. S., Klein, J. and Middleton, R. (1986). Sediment incorporation in island-arc magmas: inferences from ^{10}Be. *Geochim. Cosmochim. Acta* **50**, 535–50.

Thellier, E. O. (1941). Sur la vérification d'une méthode permettant de déterminer l'intensité du champ magnétique terrestre dans le passé. *C. R. Acad. Sci. Paris* **212**, 281.

Torgersen, T., Habermehl, M. A., Phillips, F. M. *et al.* (1991). Chlorine 36 dating of very old groundwater 3. Further studies in the Great Artesian Basin, Australia. *Water. Resources Res.* **27**, 3201–13.

Turekian, K. K., Cochran, J. K., Krishnaswami, S., Lanford, W. A., Parker, P. D. and Bauer, K. A. (1979). The measurement of ^{10}Be in manganese nodules using a tandem van de Graaff accelerator. *Geophys. Res. Lett.* **6**, 417–20.

von Blanckenburg, F., O'Nions, R. K., Belshaw, N. S., Gibb, A. and Hein, J. R. (1996). Global distribution of beryllium isotopes in deep ocean water as derived from Fe–Mn crusts. *Earth Planet. Sci. Lett.* **141**, 213–26.

Wagner, G., Laj, C., Beer, J. *et al.* (2001). Reconstruction of the paleoaccumulation rate of central Greenland during the last 75 kyr using the cosmogenic radionuclides ^{36}Cl and ^{10}Be and geomagnetic field intensity data. *Earth Planet. Sci. Lett.* **193**, 515–21.

Wang, L., Ku, T. L., Luo, S., Southon, J. R. and Kusakabe, M. (1996). ^{26}Al–^{10}Be systematics in deep-sea sediments. *Geochim. Cosmochim. Acta* **60**, 109–19.

Wölfli, W. (1987). Advances in accelerator mass spectrometry. *Nucl. Instr. Meth. Phys. Res. B* **29**, 1–13.

Yamazaki, T. and Oda, H. (2002). Orbital influence on Earth's magnetic field: 100,000-year periodicity in inclination. *Science* **295**, 2435–8.

Yiou, F., Raisbeck, G. M., Bourles, D., Lorius, C. and Barkov, N. I. (1985). ^{10}Be in ice at Vostok Antarctica during the last climatic cycle. *Nature* **316**, 616–17.

Yokoyama, Y., Guichard, F., Reyss, J. L. and Van, N. H. (1978). Oceanic residence times of dissolved beryllium and aluminium deduced from cosmogenic tracers ^{10}Be and ^{26}Al. *Science* **201**, 1016–17.

You, C. F., Lee, T. and Li, Y. H. (1989). The partition of Be between soil and water. *Chem. Geol.* **77**, 105–18.

Zreda, M. and Noller, J. S. (1998). Ages of prehistoric earthquakes revealed by cosmogenic chlorine-36 in a bedrock fault scarp at Hebgen Lake. *Science* **282**, 1097–9.

Zreda, M. G. and Phillips, F. M. (1994). Surface exposure dating by cosmogenic chlorine-36 accumulation. In: Beck, C. (Ed.), *Dating in Exposed and Surface Contexts*, University of New Mexico Press, pp. 161–83.

Zreda, M. G., Phillips, F. M. and Elmore, D. (1994). Cosmogenic ^{36}Cl accumulation in unstable landforms 2. Simulations and measurements on eroding moraines. *Water Resources Res*. **30**, 3127–36.

Zreda, M. G., Phillips, F. M., Elmore, D., Kubik, P. W., Sharma, P. and Dorn, R. I. (1991). Cosmogenic chlorine-36 production rates in terrestrial rocks. *Earth Planet. Sci. Lett.* **105**, 94–109.

15 Extinct radionuclides

15.1 Production and decay

An 'extinct radionuclide' is understood to be one that was formed by a process of stellar nucleosynthesis prior to the coalescence of the solar system, and which has subsequently decayed away to zero. Most extinct nuclides have very short half-lives, but a few have long half-lives in the millions-of-years range. These may have persisted in solar-system materials at high enough concentrations to generate observable variations in the isotopic composition of daughter products. These parent–daughter pairs are of interest to cosmochemists because they can provide information about the origin of the solar system and its early history.

The production rate of an arbitrary solar-system nuclide as a function of time is shown schematically in Fig. 15.1. After the 'big bang' about 13.7 Byr ago, nucleosynthetic production in stars proceeded at a rate p, which may be steady or very variable, depending on the process. However, prior to condensation in the new solar nebula, it is thought that much or all solar-system matter was out of nucleosynthetic 'circulation' for a period of time in some form of interstellar cloud. The time between last nucleosynthesis ('star death') and major condensation ('glob formation') is termed Δ (Fig. 15.1). Determination of Δ for various extinct nuclides may reveal information about the process which led to solar-system coalescence. Therefore, it is one of the major goals of isotope cosmochemistry.

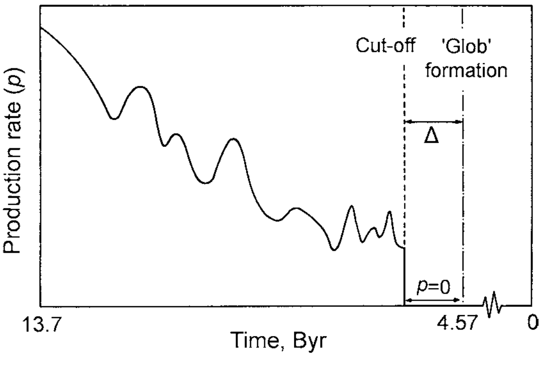

Fig. 15.1. Schematic illustration of the variation in production rate (p) of a given nuclide between the 'big bang' and termination of nucleosynthesis, followed by a period 'Δ' prior to solar-system coalescence. After Wasserburg (1985).

In order to derive useful information from the daughter products of extinct radionuclides, it is necessary to study material that has not been significantly reworked during the life of the solar system. Hence, chondritic meteorites, which appear to represent most nearly the original accretion components of the solar system, are the main objects of study. However, for some nuclide pairs, iron and stony meteorites, which were subject to early planetary differentiation processes, may also be useful. Cosmic-ray bombardment is one process to which meteorites are particularly susceptible. This can cause nuclear transformations, which must be excluded as a mechanism for generating daughter-product anomalies before the latter are attributed to extinct parents.

Most of the scientifically important extinct radionuclides with half-lives over 10^5 years are shown in Table 15.1 in order of decreasing stability, and will be discussed below. Mean lives ($1/\lambda$) are quoted in Table 15.1, in addition to half-lives, because they are helpful in understanding the production history of extinct nuclides. The most long-lived of these species is the extinct p-process nuclide ^{146}Sm ($t_{1/2} = 103$ Myr). This will be discussed briefly for the constraints it can place on very early terrestrial evolution, rather than solar-system condensation. However, another p-process nuclide (^{92}Nb, $t_{1/2} = 36$ Myr) is omitted because of the relatively weak constraints it provides (Schonbachler *et al.*, 2002).

15.2 Extant actinides

The age of the universe was estimated at between 12 and 15 Byr, based on application of the Hubble

Table 15.1. *Some important extinct radionuclides*

Parent	Daughter	Decay mode	Mean life (Myr)	Half-life (Myr)	λ (yr^{-1})
^{146}Sm	^{142}Nd	α	149	103	6.7×10^{-9}
^{244}Pu	Various	Fission	119	82	8.5×10^{-9}
^{129}I	^{129}Xe	β	23	16	4.3×10^{-8}
^{247}Cm	^{235}U	3α, 2β	22.5	15.6	4.4×10^{-8}
^{182}Hf	^{182}W	2β	13	9.0	7.7×10^{-8}
^{107}Pd	^{107}Ag	β	9.4	6.5	1.1×10^{-7}
^{53}Mn	^{53}Cr	β	5.3	3.7	1.9×10^{-7}
^{60}Fe	^{60}Ni	2β	2.1	1.5	4.7×10^{-7}
^{26}Al	^{26}Mg	β	1.0	0.7	9.8×10^{-7}
^{41}Ca	^{41}K	β	0.15	0.1	6.7×10^{-6}

constant to quasar red-shifts, and on the ages of the oldest stars calculated from nucleosynthetic models (e.g. Lineweaver, 1999). More recently, evidence from the anisotropy of the cosmic microwave background has been used to determine a much more precise age of 13.7 ± 0.2 Byr (Bennett, 2003). Therefore, the age of the galaxy at the time of solar-system condensation was about 9 Byr, which is of the same order as the lifetime of a typical star like the Sun. However, large stars have much shorter lifetimes, which may even be less than 1 Myr in duration. Since the solar system coalesced from the debris of 'dead' stars, it is theoretically possible that any given atom in the solar system could have been processed through only one previous star, or through numerous previous stars.

This indeterminacy leads to uncertainty in the production rate of solar-system nuclides over the life of the galaxy. This uncertainty is particularly severe for r-process nuclides, which are generated solely in the supernova explosions which terminate the life-histories of large stars (section 1.2.1). Uncertainties in the production rates of extinct nuclides are a major source of uncertainty in the determination of Δ. However, the best constraints on long-term r-process production rates are provided by long-lived 'extant' nuclides. Therefore the extant actinides ^{235}U, ^{238}U and ^{232}Th will be examined before discussion of individual extinct nuclides.

The gulf of unstable nuclides between the end of the s-process nucleosynthetic ladder and the actinide elements (section 1.2.2) means that these nuclides can only be generated by the r-process. The seed nuclei for this process are clearly the nuclei at the top of the s-process ladder, but these nuclides, especially Pb, have small neutron-capture cross-sections, creating a nucleosynthetic barrier. As a result, the production *ratios* of the actinides are constrained to be close to unity. This factor is critical in using them to model r-process production rates over the lifetime of the galaxy.

We begin with the abundances of these nuclides in chondritic meteorites. On normalising with respect to $^{235}\text{U} = 1$, ^{238}U and ^{232}Th have present-day abundances of about 138 and 520, respectively, in carbonaceous chondrites. On correcting for decay to initial abundances at 4.55 Byr and re-normalising with respect to $^{235}\text{U} = 1$, we obtain lower relative abundances of 3.45 and 8.18 for ^{238}U and ^{232}Th, respectively, but these are still higher than estimated production ratios (relative to ^{235}U) of 0.66 and 1.27, respectively (e.g. Broecker, 1986). Therefore, we can use these differences, together with the different half-lives of the three nuclides, to test alternative production models. Two of the extreme models are shown in Fig. 15.2 (a and b), and will be examined.

If all uranium formation were attributed to a single supernova event (Fig. 15.2a), then we could calculate the apparent timing of this event by the subsequent decay of short-lived ^{235}U (half-life about 700 Myr) relative to longer-lived ^{238}U (half-life about 4500 Myr). The calculation based on uranium isotopes alone may be somewhat more reliable than that involving thorium, because U/Th ratios could have been fractionated during solar-system coalescence. The 'single event' model leads to a calculated Δ value of 2.1 Byr before solar-system coalescence. However, evidence for the presence of the short-lived actinide ^{244}Pu in the early solar system rules out a model with such a large Δ value.

The other extreme model involves 'continuous' supernova production (Fig. 15.2b). Taken to its limit, this is an impossibility, since each supernova event terminates the evolution of a star, and the scattered debris must be incorporated into a new star before nucleosynthesis can continue. However, for nuclides with half-lives of hundreds of millions of years, a supernova

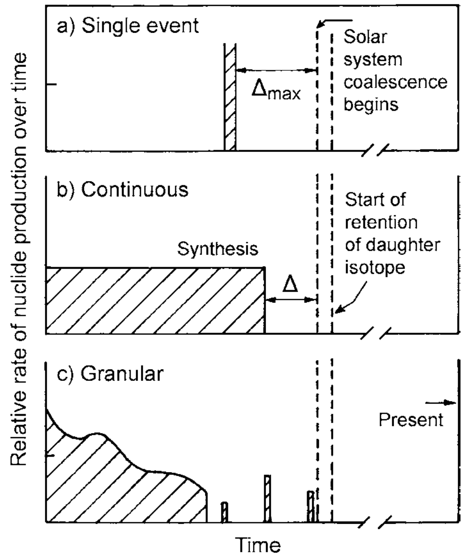

Fig. 15.2. Schematic illustration of the relationship between production models and Δ calculation: (a) a single supernova event yielding a maximum value of Δ; (b) 'continuous' production followed by a short Δ period; and (c) complex variation in production rate (the 'granular model'). After Wasserburg and Papanastassiou (1982).

frequency as low as one per 100 Myr in the production history of an element will be a close approximation to continuous production. Under this model, the abundance of an unstable nuclide builds up until it reaches a level at which the rate of synthesis is equalled by the rate of decay. This point of saturation is reached sooner for short-lived than for long-lived nuclides (Fig. 15.3).

The growth curves in Fig. 15.3 can be presented in the form of isotope ratios (Fig. 15.4) of ^{238}U and ^{232}Th against ^{235}U. The time at which the curves intersect the primordial solar-system composition (calculated above) yields a crude estimate for the age of the galaxy at solar-system coalescence. By adding 4.55 Byr, we obtain estimates for the age of the galaxy of 16.5 and 13.5 Byr from Figs. 15.4a and 15.4b, respectively. Given the many assumptions made, these estimates for the age of the galaxy agree surprisingly well with the estimated 13–14 Byr age of the universe, and therefore provide strong support for the 'continuous-supernova' model. With this model, the extant actinides provide a very poor constraint on the value of Δ. However, that is the role of the *extinct* nuclides.

In between the two extreme models described above, there is an infinite number of intermediate models in which discrete production events of variable size occur at variable intervals (e.g. Fig. 15.2c). These are termed 'granular' models. Ideally, we would like to use the actinide data to put an upper limit on the 'granularity' of these models. However, the indeterminacy of the system prevents the application of precise limits. Many workers have used rather arbitrary models involving a combination of 'continuous' production and late 'discrete' events. However, Trivedi (1977) suggested

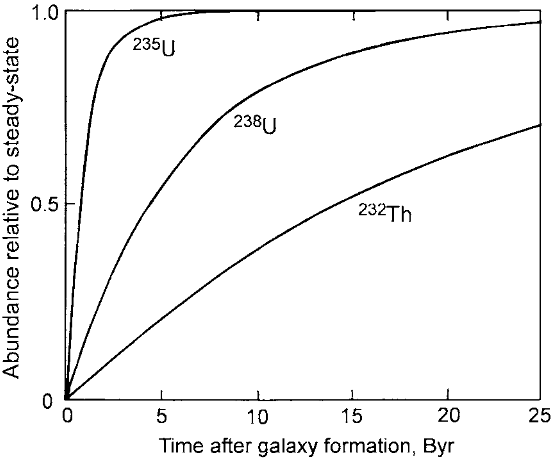

Fig. 15.3. Contrasting rates of approach of U and Th isotopes to the steady-state abundance in a model of 'continuous' supernova actinide production. After Broecker (1986).

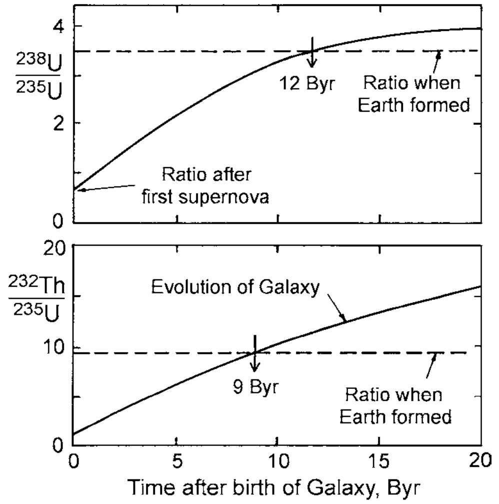

Fig. 15.4. Growth curves for $^{238}U/^{235}U$ and $^{232}Th/^{235}U$ ratios in a 'continuous' supernova production model, relative to the primordial solar-system value. After Broecker (1986).

that it was more reasonable to assume that supernova events occur at regular intervals. He proposed a simple model in which fifty supernova spikes of equal size were equally spaced with an interval of 140 Myr (assuming a galactic age at solar-system formation of 7 Byr). Relative to a theoretical 'stable' actinide, this means that the most recent supernova products would undergo 50-fold dilution by isotopically 'cold' material generated in previous events. This model represents a useful yardstick for comparison with the dilution factors proposed for extinct nuclides.

15.3 Xenon isotopes

Like terrestrial xenon, meteoritic xenon is an important isotopic tracer because it is the product of two independent decay routes. In addition, non-radiogenic xenon isotopes are of very low abundance, making radiogenic xenon from these decay routes easier to detect. Hence, xenon is a sensitive tracer of extinct radionuclide abundances.

15.3.1 I–Xe

The nuclide ^{129}I has a half-life of 16 Myr, and decays by β emission to ^{129}Xe (Fig. 15.5). Wasserburg and Hayden (1955) searched for ^{129}Xe anomalies, but were unsuccessful. However, ^{129}Xe excesses were eventually demonstrated by Reynolds (1960), making this the first extinct nuclide to be 'found'.

If the excess ^{129}Xe signatures discovered by Reynolds were due to the decay of now-extinct ^{129}I in the meteorite samples, it would be expected that stable ^{127}I would still be present. Therefore, to test this model, it was necessary to look for correlations between the abundance of ^{127}I and excess ^{129}Xe in each sample. To do this by chemical analysis would have been laborious and inaccurate. However, Jeffrey and Reynolds (1961) conceived of an elegant means of measuring the $^{129}\mathrm{Xe}_{\mathrm{excess}}/^{127}\mathrm{I}$ ratio in a single mass-spectrometric analysis. By irradiating whole-rock samples of a meteorite with slow neutrons in a reactor, it was possible to generate the stable isotope ^{128}Xe from ^{127}I by the following n, γ and β decay reactions:

$$^{127}\mathrm{I} + \mathrm{n} \rightarrow {}^{128}\mathrm{I} + \gamma$$
$$^{128}\mathrm{I} \rightarrow {}^{128}\mathrm{Xe} + \beta + \bar{\nu}$$

Hence, the I/Xe ratio could be determined by isotopic analysis of xenon alone.

Jeffery and Reynolds made a further technical advance in their method of sample analysis. Rather than one-step outgassing of xenon from each meteorite sample by melting it (to produce a single data point), they outgassed the sample in a series of increasing temperature steps, admitting each new gas-release separately to the mass spectrometer for analysis. A very similar neutron-irradiation and 'step-heating' mass-spectrometric method was applied to K–Ar geochronology five years later, revolutionising it to the ^{40}Ar–^{39}Ar method (section 10.2).

It is convenient to display the xenon isotope data on a plot somewhat analogous to an Ar–Ar isochron diagram (section 10.2.3). Jeffrey and Reynolds demonstrated a correlation between ^{129}Xe and ^{128}Xe abundances in the Richardton chondrite, ratioing both of these against the non-radiogenic isotope ^{132}Xe (e.g.

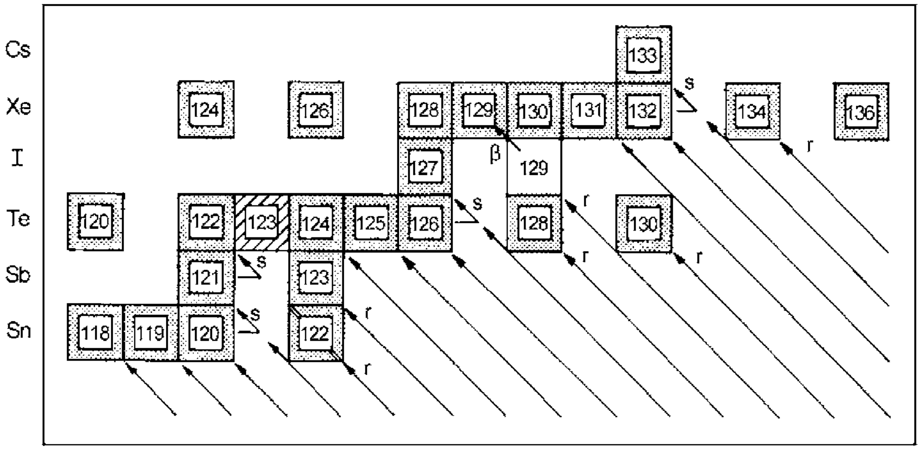

Fig. 15.5. Part of the chart of the nuclides in the region of iodine, showing nucleosynthetic production and radioactive decay routes. Arrows labelled 'r' indicate nuclides generated entirely by the r-process.

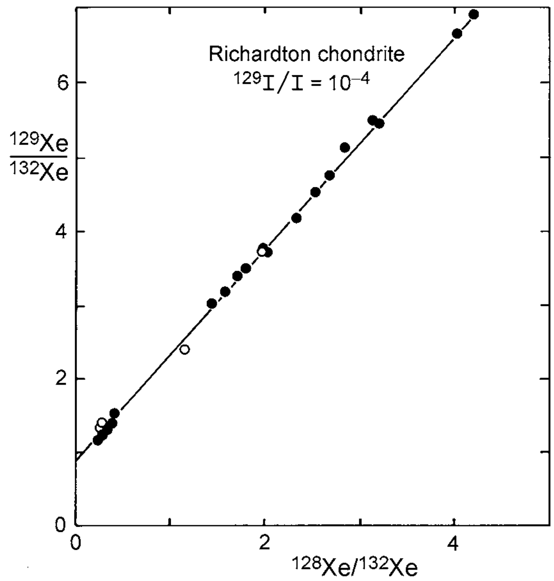

Fig. 15.6. Xe–Xe plot for stepwise-degassed samples of the Richardton meteorite, showing the line of constant initial $^{129}I/^{127}I$ ratio. Solid and open symbols indicate gas fractions released above and below 1100 °C, respectively. After Hohenberg *et al.* (1967).

Fig. 15.6). If the efficiency of the activation process is calibrated, the excess ^{128}Xe abundance translates into the abundance of the non-radioactive iodine isotope, ^{127}I. Similarly, because every ^{129}I atom has by now been converted into ^{129}Xe by radioactive decay, the excess ^{129}Xe abundance translates into the ^{129}I abundance at the time when meteorite components were isolated from a common reservoir. Hence, the slope of any array of data points observed in this diagram ($^{129}Xe_{excess}/^{128}Xe_{excess}$) has no direct age significance. Instead, it indicates the initial $^{129}I/^{127}I$ ratio when the meteorite cooled to the point at which its minerals became closed to diffusional loss of xenon into space. Meanwhile, the intercept of the correlation line on the y axis represents the initial $^{129}Xe/^{132}Xe$ ratio before the decay of extinct ^{129}I began.

The slope of the array for the Richardton chondrite (Fig. 15.6) corresponds to an initial $^{129}I/^{127}I$ ratio of 1×10^{-4}. Subsequent work on a wide variety of meteorites has confirmed this value with only small variations. This suggests that ^{129}I was widely distributed through the solar nebula (e.g. Podosek, 1970; Wasserburg *et al.*, 1977; Niemeyer, 1979). Excess ^{129}Xe is also found in terrestrial rocks and magmas, but in the Earth, ^{129}Xe abundances are not correlated with ^{127}I abundances. This observation is attributed to the outgassing of noble gases from a deep Earth reservoir that also once contained 'live' ^{129}I (section 11.4.1).

The $^{129}I/^{127}I$ ratio calculated from meteorite studies can be used as a 'model age' chronometer to measure the time interval (Δ) between last nucleosynthesis and coalescence of the solar nebula. However, as with model ages in general, several major assumptions must be made in any attempt to calculate a Δ value. In particular, estimates must be made of the following quantities:

(1) the $^{129}I/^{127}I$ ratio originally produced by nucleosynthesis;
(2) the rate of nucleosynthesis over time, prior to the Δ period;
(3) in a granular model, any dilution of the last addition of radioactively 'hot' iodine by 'cold' iodine from earlier events.

These questions are best examined by comparing some extreme solutions that were summarised by Wasserburg (1985).

It has traditionally been assumed that iodine is generated by the r-process (Fig. 15.5). Production ratios (p_{127}/p_{129}) can be determined only by theoretical calculation; hence there are large uncertainties. However, they are generally assumed to be near unity. For example, values that have been used in the literature are unity (Wasserburg *et al.*, 1960; Wasserburg, 1985), 1.3 (Cameron, 1962; quoted by Hohenberg, 1969) and $2.9 + 1/ -2$ (Seeger *et al.*, 1965; quoted by Schramm and Wasserburg, 1970).

The model originally conceived by Reynolds (1960) involved synthesis of iodine with a $^{129}I/^{127}I$ ratio of unity in a single event. This would decay to a ratio of 10^{-4} over about twelve half-lives, yielding a maximum Δ value of about 200 Myr (Fig. 15.7a). However, if all iodine were generated in a single supernova (i.e. zero dilution of 'hot' supernova iodine by 'cold' ^{127}I), then all other r-process elements would need to have formed at this time, which is incompatible with actinide evidence (as well as some short-lived extinct nuclides).

The other extreme model assumes that there has been more or less constant supernova activity throughout the lifetime of the galaxy. If their products were kept mixed, then r-process production of solar-system material might be regarded as relatively constant (Dicke, 1969). With this model, the total number of atoms of stable ^{127}I after time T (at the termination of nucleosynthesis, Fig. 15.1) is defined as

$$n_T^{127} = p^{127} T \qquad [15.1]$$

where p is the average production rate. Similarly, the total number of ^{129}I atoms after time T can be

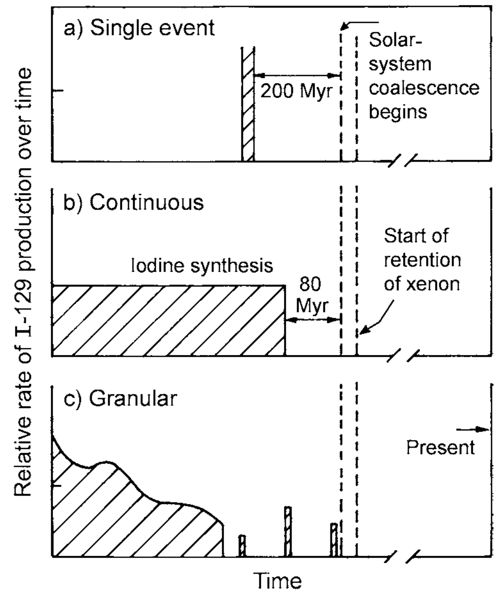

Fig. 15.7. Schematic illustration of iodine production models and consequent Δ calculation: (a) a single supernova event yielding a maximum value of Δ (about 200 Myr); (b) constant 'continuous' production followed by a period Δ of about 80 Myr; and (c) complex variation in production rate (the 'granular model'). After Wasserburg and Papanastassiou (1982).

approximated as

$$n_T^{129} = p^{129}/\lambda = p^{129} \times \text{mean life} \qquad [15.2]$$

On dividing [15.2] by [15.1] we obtain

$$\left(\frac{n^{129}}{n^{127}}\right)_T = \frac{p_{129}}{p_{127}}\,\frac{\text{mean life}}{T} \qquad [15.3]$$

Therefore, assuming a production ratio of unity in a model in which iodine is formed by frequent and well-mixed supernovae over a period of 10 Byr, the ^{129}I/^{127}I ratio when nucleosynthesis is interrupted is 2.3×10^{-3}. This would take nearly five half-lives to decay to a value of 1×10^{-4}, yielding a Δ value of about 80 Myr (Fig. 15.7b). However, this model has a major conceptual problem. It is very sensitive to the contributions of iodine from 'late' supernovae near the end of the nucleosynthetic period. If these form a significant fraction of the total iodine budget, then they are apt to destabilise the smooth growth model, giving rise to a 'granular' model (Wasserburg and Papanastassiou, 1982), as illustrated in Fig 15.7c.

In reality, consideration of the rate of supernova occurrence in the whole galaxy (about one every hundred years) relative to the size of the galaxy suggests that, in our corner of the galaxy, a granular model is almost inevitable, relative to the relatively short half-life of ^{129}I. In this case, the most critical quantity is the dilution factor for the last addition of hot iodine (^{129}I/^{127}I $\approx$ 1) by cold or nearly cold iodine from earlier events (^{129}I/^{127}I $\approx$ 0). A dilution factor of 100 has been proposed by Cameron and Truran (1977). Coupled with a production ratio of unity, this would yield a Δ value of about 110 Myr. However, as the dilution factor approaches 10^4, Δ can approach zero. Not until the review of Wasserburg (1985) was it explicitly pointed out that such 'extreme' solutions are possible.

In addition to uncertainties about the dilution factor, there are also questions about the site of nucleosynthetic production of ^{129}I. Because iodine is not greatly separated from the s-process nucleosynthetic pathway, there remains a possibility that ^{129}I might be produced in less extreme environments than supernovae. Furthermore, it must not be forgotten that ^{127}I is certainly generated by the s-process, so that uncertainties about the relative s- and r-process contribution to total iodine production are also present. Therefore, ^{129}I cannot place tight constraints on the relative timing of nucleosynthesis and solar-system condensation (contrary to early claims). For this we must turn to other systems. However, ^{129}I may be useful in dating the very early evolution of solar-system objects (section 15.3.3).

15.3.2 Pu–Xe

^{244}Pu has a half-life of 82 Myr. The clearest evidence of extinct ^{244}Pu in meteorite materials is provided by fission products, most notably a large excess abundance of ^{132}Xe, ^{134}Xe and ^{136}Xe, which has been matched to the signature of laboratory Pu fission products (Fig. 15.8). ^{244}Pu is always compared with the abundances of other actinide elements in drawing conclusions about solar-system origins.

^{244}Pu is most conveniently ratioed against ^{238}U, but this involves elemental as well as isotopic abundances, and the former are susceptible to chemical fractionation after condensation of the nebula. Hence, representative analysis has been very difficult. The first determination of the initial ^{244}Pu/^{238}U ratio, which was based on meteoritic phosphate (Wasserburg *et al.*, 1969), gave a value of about 0.035. However, this value might not be representative of the bulk (whole-rock) meteorite due to partition effects. Whole-rock analysis of various meteorites has yielded a large range of values, but the best consensus is for a chondritic value near 0.007 (Fig. 15.9).

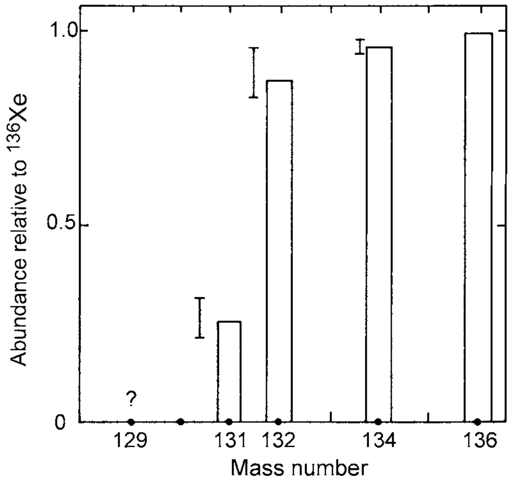

Fig. 15.8. Histogram of measured meteoritic Xe isotope abundance ratios relative to ^{136}Xe, compared with ratios observed in laboratory fission products (tie bars). After Wasserburg and Papanastassiou (1982).

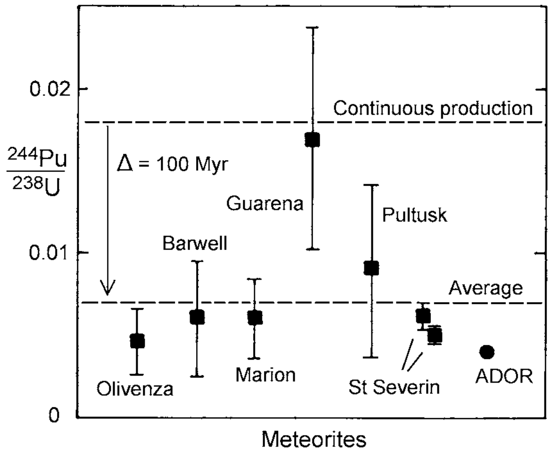

Fig. 15.9. Summary of Pu/U ratios for whole-rock samples of various meteorites (which are always named after their discovery site), relative to a model production ratio. ADOR = Angra dos Reis. After Hagee *et al.* (1990).

Plutonium data alone are not able to apply tight constraints to Δ, for the same reasons as were given for iodine. However, if we assume that ^{129}I and ^{244}Pu were added at the same time, we can use the data together to constrain Δ. For example, a continuous model yields an equilibrium ^{244}Pu/^{238}U ratio of 0.018, which can decay to 0.007 after a Δ period of about 100 Myr. This is in reasonable agreement with the continuous model for ^{129}I, which yields a Δ value of 80 Myr. Similarly, if we take a granular model in which both elements undergo 50-fold dilution of the last r-process addition with cold material, both plutonium and iodine yield Δ values of about 130 Myr. Both of these results argue against very late addition of very dilute material (which was able to explain the iodine data alone). On the other hand, if ^{129}I is not an r-process nuclide, then its addition does not have to be accompanied by ^{244}Pu, and these constraints disappear.

15.3.3 I–Xe chronology

Podosek (1970) used the slightly variable initial ^{129}I/^{127}I ratios of 0.7×10^{-4} to 1.3×10^{-4} measured in various meteorites to calculate the relative cooling times of those meteorites, by assuming that 'hot' and 'cold' iodine sources were homogenised in the solar nebula. It is not necessary to know the iodine isotope production ratio or the dilution factor of 'hot' by 'cold' iodine in the solar nebula for this calculation. However, to interpret the isotopic variations in terms of cooling times, it is necessary to assume initial homogeneity of the ^{129}I/^{127}I ratio in the solar nebula. Crabb *et al.* (1982) argued instead that the variations in initial ratio are due to imperfect mixing of iodine from different sources (variable dilution factors). More recently, Podosek's research group has at times felt the evidence to be equivocal (Bernatowicz *et al.*, 1988), and at other times argued that the 'dates' have genuine age significance (Swindle *et al.*, 1991).

To solve these uncertainties, it was necessary to test the accuracy of I–Xe ages by comparison with absolute dating methods. Until recently this was not possible because absolute dating methods (which measure ages back from the present) were not sufficiently precise to measure age differences of about 1 Myr in materials 4570 Myr old. However, the availability of new high-precision Pb–Pb ages (section 5.3.1) has allowed relative I–Xe ages to be anchored against absolute Pb–Pb ages and tested for their reliability.

Nichols *et al.* (1994) began this work by dating phosphate mineral separates (apatite) from the primitive achondrite Acapulco, whose Pb–Pb age is 4557 ± 2 Myr (Gopel *et al.*, 1994). Brazzle *et al.* (1999) continued this work by obtaining step-heating I–Xe ages on apatite separates from three other chondrites also dated by Pb–Pb. The results gave excellent concordance between I–Xe and Pb–Pb ages (Fig. 15.10), demonstrating that the relative I–Xe 'ages' date real events. Since iodine is a volatile element, Brazzle *et al.* inferred that it could not have been incorporated into the refractory minerals that were first crystallised from the nebula. Therefore, it must have been adsorbed onto

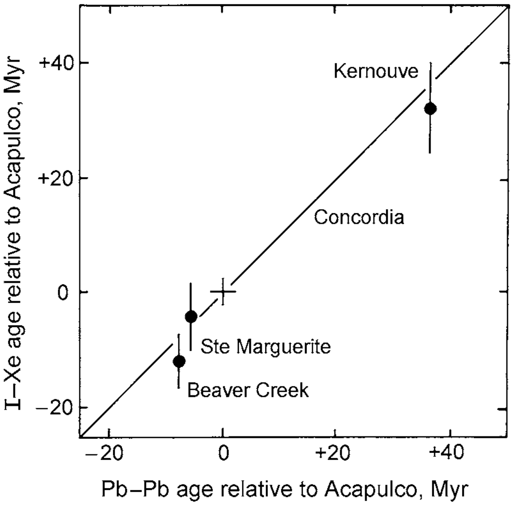

Fig. 15.10. Correlation diagram to test the concordancy of Xe/Xe and Pb/Pb ages on apatite separates from chondritic meteorites. Ages are given relative to Acapulco. After Brazzle *et al.* (1999).

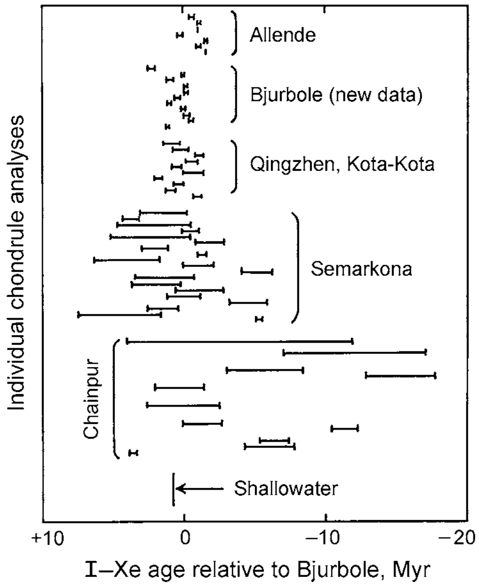

Fig. 15.11. Xe/Xe ages for individual chondrules for several meteorites relative to whole-rock samples of the standard Bjurbole. The achondrite Shallowater is shown for reference. Modified after Whitby *et al.* (2002).

cooling surfaces and subsequently re-distributed into secondary minerals (e.g. apatite) during very early post-formation metamorphism. It is this later event that the I–Xe and Pb–Pb analysis of apatite is thought to be dating.

In order to test the ability of the I–Xe method to date primary meteorite condensation, Gilmour *et al.* (2000) analysed individual chondrules and clasts from a variety of 'ordinary' (as opposed to carbonaceous) chondrites. Subsequently, Whitby *et al.* (2002) focussed in more detail on the enstatite chondrites Qingzhen and Kota Kota. Because the latter two chondrites are 'unequilibrated', they have a relatively simple history that should allow the most precise dating of their primary condensation. (The step-heating method used for all I–Xe analyses can exclude the effects of late low-temperature metamorphism and shock events that most meteorites have suffered.) On the other hand, the lack of equilibration of the enstatite chondrites means that there was less opportunity to homogenise any primordial iodine isotope variations between chondrules. The analysis of individual chondrules therefore provides more control on the degree of iodine isotope homogeneity in the early solar system than did the earlier data from whole-rock chondrites.

Results from this study are shown in Fig. 15.11, together with results from other studies on single chondrules, summarised by Swindle *et al.* (1996). Ages are quoted relative to whole-rock analyses of the chondrite Bjurbole, which has traditionally been used as an irradiation standard. The results show that the meteorites Chainpur and Semarkona yield scattered chondrule ages, which is attributed to shock disturbance or aqueous alteration (Swindle *et al.*, 1996). However, the analyses from Qingzhen, Kota Kota and Allende, together with most of the new Bjurbole analyses, gave more consistent results.

Gilmour *et al.* (2000) and Whitby *et al.* (2002) argued that the consensus of chondrule ages similar to Bjurbole was dating the primary cooling of chondrules shortly after their formation, and was not the result of later re-setting. However, they also noted that these ages overlap with the achondrite Shallowater. The latter object also gives consistent I–Xe results, leading to its recent adoption as a standard for I–Xe analysis (e.g. Brazzle *et al.*, 1999). Because whole-rock samples of Shallowater are only 0.6 Myr younger than Bjurbole, this would imply that the differentiation of small planetesimals (represented by the achondrites) was already occurring at the same time as primary chondrule formation. Comparison with other extinct nuclide geochronometers may be used to test this model (section 15.5.2).

More surprising recent results come from the I–Xe analysis of halite (sodium chloride) from the H (high-metal) chondrite 'Zag'. This material yields an I–Xe age 5 Myr *older* than Bjurbole and Shallowater, implying that aqueous fluids were present on Zag at an extremely early time. It also implies that the halite on Zag pre-dates calcium–aluminium inclusions (see below), which are usually regarded as the oldest solar-system objects. However, the I–Xe step-heating results for Zag indicate some disturbance, so the result may be unreliable as a true indication of age (e.g. Ott, 2000).

15.4 Very-short-lived species

15.4.1 Al–Mg

The nuclide ^{26}Al has a half-life of 0.72 Myr and decays to ^{26}Mg. The search for extinct ^{26}Al was a much more difficult task than the search for ^{129}I, and was only made possible by the fall of the Allende carbonaceous chondrite in February 1969. Allende is an agglomerate of fine-grained debris and chondrules, but also contains 'inclusions' with a refractory mineralogy, which appear to be very early condensation products from the solar nebula. These are normally referred to as calcium–aluminium inclusions or 'CAIs'.

Analysis of Mg isotope ratios in minerals separated from Allende inclusions reveals mass-fractionation-dependent variations in ^{25}Mg/^{24}Mg ratio. These are normally of the order of a few parts per mil (Fig. 15.12), but some inclusions (e.g. EK1-4-1 and C1) exhibit larger effects. These were termed FUN samples (showing Fractionation and Unknown Nuclear anomalies) by Wasserburg *et al.* (1977). Because ^{27}Al was always a nuclide of comparatively low abundance, it was at first very difficult to find radiogenic ^{26}Mg abundances outside error of mass-fractionation processes. The first such evidence for radiogenic ^{26}Mg was demonstrated by Lee *et al.* (1976). Subsequently, larger ^{26}Mg anomalies were found by very careful hand picking of inclusion- and alteration-free plagioclase grains from the WA Allende inclusion. Because these grains have very high Al/Mg ratios, they provide the best chance of finding ^{26}Mg anomalies. This search revealed an excess ^{26}Mg abundance of 97 parts per mil in one anorthite grain (Lee *et al.*, 1977).

It is most convenient to display Al–Mg data on an isotope ratio *versus* element ratio plot somewhat analogous to an isochron diagram (e.g. Fig. 15.13). Hence, the ^{26}Mg/^{24}Mg ratio is plotted against an Al/Mg ratio. In a conventional isochron diagram, the ratio plotted on the abscissa would be ^{26}Al/^{24}Mg. However, since every ^{26}Al atom has been converted into ^{26}Mg by radioactive decay at the present day, the ^{27}Al/^{24}Mg ratio is plotted instead. Therefore, the slope of any array of data points observed in this diagram has no direct age significance, but indicates the initial ^{26}Al/^{27}Al ratio in the sample suite at the time when sub-systems were isolated from a common reservoir. Hence, these arrays will be called pseudochrons.

The data shown in Fig. 15.13 for separated minerals from the Allende EGG-3 inclusion display a good ^{26}Mg/^{27}Al correlation, yielding a well-defined initial ^{26}Al/^{27}Al ratio of 4.9×10^{-5} (Armstrong *et al.*, 1984).

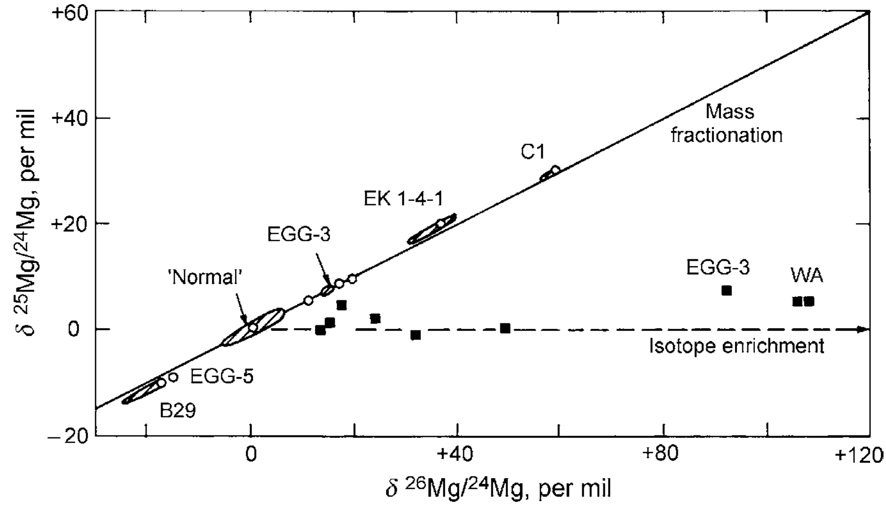

Fig. 15.12. ^{25}Mg/^{24}Mg *versus* ^{26}Mg/^{24}Mg isotope diagram, showing deviations of Allende inclusions from the normal solar-system value, in parts per mil (δ). These may be due to mass fractionation in the solar nebula (open symbols) or decay of extinct ^{26}Al (solid symbols). After Wasserburg and Papanastassiou (1982).

A similar array for the WA inclusion gave a $^{26}Al/^{27}Al$ ratio of $(5.1 \pm 0.6) \times 10^{-5}$ (Lee *et al.*, 1977). However, in the inclusion USNM 3529-26 (Armstrong *et al.*, 1984), minerals from different parts of the inclusion gave different initial ratios, with a higher value in the core (3.8×10^{-5}) than the rim (2.3×10^{-5}). This spatial variation is best explained by Mg loss, particularly from the margins of the inclusion, during a later metamorphic event. The event may have resulted from the heat output of ^{26}Al decay itself.

Subsequent studies of Mg isotope ratios in Allende inclusions have made use of the ion microprobe (SIMS) for direct analysis of material with very low common-Mg contents. Analysis of Allende melilites and spinels by Steele and Hutcheon (1979) gave an initial $^{26}Al/^{27}Al$ ratio of $(2 \pm 1) \times 10^{-5}$, although data on the refractory mineral hibonite (from the same inclusion) implied a ratio as high as 8×10^{-5}. Nevertheless, these results are broadly in line with the data on separated minerals.

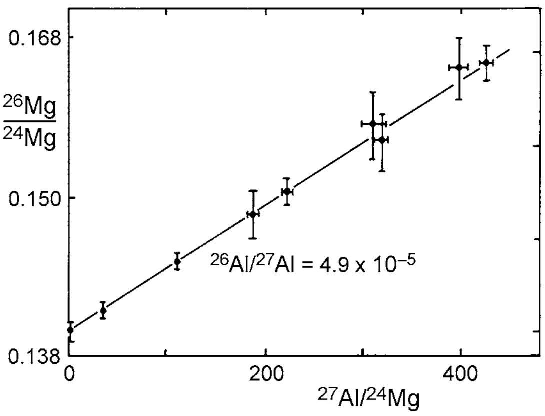

Fig. 15.13. Plot of δ Mg against Al/Mg ratio for the Allende EGG-3 inclusion, showing the best-fit line of constant initial $^{26}Al/^{27}Al$ ratio with a value of 4.9×10^{-5}. After Armstrong *et al.* (1984).

The great significance of ^{26}Al for cosmochemistry is its short half-life of 0.72 Myr. Because this is only 4% of the half-life of ^{129}I, its presence in the early solar system constrains a nucleosynthetic event to have occurred much more imminently before the coalescence of the solar system. Classical nucleosynthetic models (e.g. Arnett, 1969; Truran and Cameron, 1978) attribute ^{26}Al to explosive carbon burning in the envelope of a supernova, and predict a $^{26}Al/^{27}Al$ production ratio of about 10^{-3}. It would take only 3 Myr for this ratio to decay to the value of 5×10^{-5} found in several meteorite samples. Therefore, Lee *et al.* (1976) suggested that the observed anomalies were due to late addition to the solar nebula of freshly synthesised material from a nearby nova or supernova explosion. Cameron and Truran (1977) pointed out that such an explosion in the vicinity of a condensing solar nebula was a very unlikely coincidence unless the supernova itself triggered the collapse of an interstellar cloud to form the solar system. This model is illustrated in Fig. 15.14.

For a time, the 'supernova-trigger' model for solar-system coalescence was widely accepted. However, spectral data from the High Energy Astronomical Observatory satellite (HEAO 3) revealed a γ line (Fig. 15.15) due to decay of ^{26}Al from a diffuse galactic source (Mahoney *et al.*, 1984). An average galactic $^{26}Al/^{27}Al$ ratio of about 10^{-5} was determined, which is remarkably close to that deduced for the early solar system from Allende inclusions. This high abundance

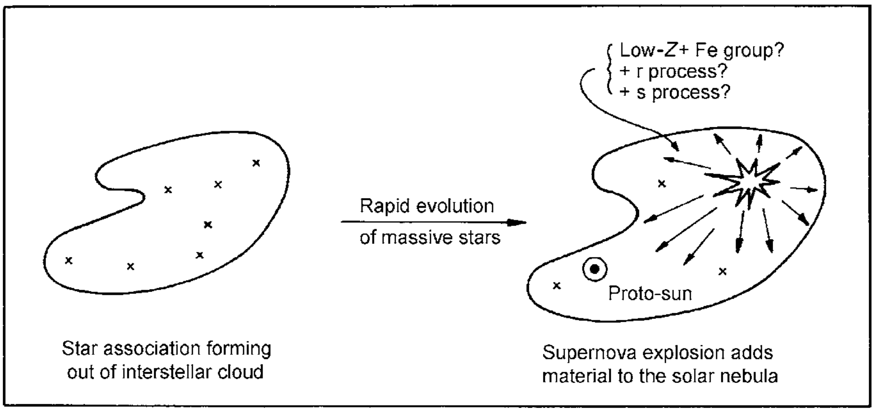

Fig. 15.14. Schematic illustration of a model in which solar-system collapse is promoted by a supernova, which also seeds it with short-lived nuclides. After Wasserburg (1985).

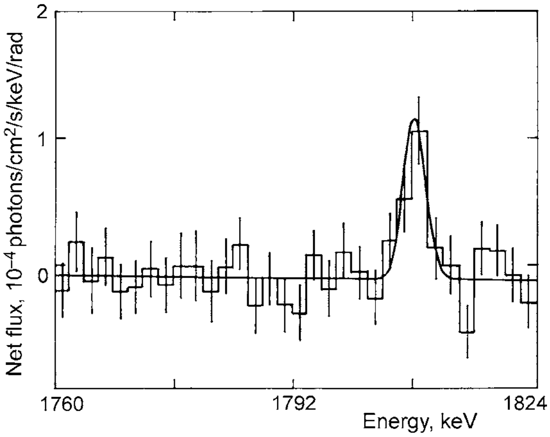

Fig. 15.15. Galactic γ-ray spectrum, showing a peak at 1808 keV that is attributed to decay of excited ^{26}Mg, itself produced by the decay of ^{26}Al in interstellar space. After Mahoney *et al.* (1984).

of ^{26}Al in the galaxy means that supernovae, which are rare, cannot be the principal sources. Indeed, recent experimental studies (Champagne *et al.*, 1983) suggest that red giants can generate Al with a 26/27 production ratio of unity. Nevertheless, the isotopic data on Allende inclusions still imply late injection of ^{26}Al into the pre-solar cloud. For example, Wasserburg (1985) suggested that this injection could be supplied by rapidly evolving stars within the interstellar cloud itself, followed by rapid condensation on a roughly 1-Myr timescale (Wasserburg, 1985).

A very different explanation was proposed by Clayton (1975; 1979), who argued that most isotopic anomalies observed in meteorites, including extinct radionuclide signatures, are inherited from pre-solar dust grains. If this model were true for ^{26}Al, then both Al isotope and Al/Mg ratios would have to be inherited intact from these pre-solar materials. This would in turn imply that many meteorite mineral phases (e.g. Ca–Al inclusions in Allende) are also pre-solar. Wasserburg (1985) contested this argument on mineralogical grounds, believing that most or all of the meteorite phases analysed had crystallised within the solar system. Evidence supporting Wasserburg was provided by the discovery of ^{26}Mg excesses in a clast from the chondrite Semarkona (Hutcheon and Hutchison, 1989). Hutcheon and Hutchison argued that the mineralogy and REE chemistry of the clast were the result of igneous processes, implying a planetary, rather than nebular, origin.

All of the samples described above (inclusions and clasts) are now generally thought to have formed during solar-system condensation. However, evidence for the preservation of pre-solar *grains* in the Murchison carbonaceous chondrite has recently been found. These grains are composed of silicon carbide, and have exotic rare-gas signatures that match the abundance patterns expected in carbon-burning red giants (Lewis *et al.*, 1990). This means that they have escaped significant heating during solar-system coalescence. Zinner *et al.* (1991) found large excesses of ^{26}Mg in some of these grains, equivalent to initial ^{26}Al/^{27}Al ratios from 10^{-5} up to nearly unity. These ratios probably date from the time of expulsion of the grains, in the solar wind of a red giant, into interstellar space. Therefore, one model suggests that the solar wind from such a star (rather than a supernova) triggered the collapse of a giant molecular cloud to form the solar system (Nuth, 1991).

A totally different explanation of ^{26}Al signatures that has been proposed at various times (e.g. Lee, 1978) is their generation by spallation reactions caused by intense solar radiation. For example, such irradiation may have occurred if the sun went through a ‘T Tauri’ stage early in its evolution. However, Shu *et al.* (1997) argued that the greatest radiation intensity was reached at an earlier stage in the Sun’s evolution, as a protostar still ‘embedded’ in the nebular disc. Lee *et al.* (1998) used this model to explain the presence of several of the very-short-lived species whose traces are observed in meteorites. This model is discussed further below, in an examination of the spallogenic nuclide ^{10}Be (section 15.4.3).

Returning to the question of the distribution of ^{26}Al, recent work by Russell *et al.* (1996) suggested that addition of ^{26}Al to the solar nebula was more widespread than previously thought, and therefore that this and other radionuclides may have been homogeneously distributed. Firstly, Mg isotope anomalies were found in two inclusions from the unmetamorphosed ordinary chondrites Semarkona and Moorabie. These gave initial ^{26}Al/^{27}Al ratios of 5×10^{-5}, exactly the same as those found in inclusions from carbonaceous chondrites. The observation of consistent ratios in inclusions from different chondrite groups suggests that these inclusions might have been fairly widely distributed in the nebula.

Russell *et al.* (1996) also detected the first evidence for extinct ^{26}Al in Al-rich *chondrules* (as opposed to inclusions) from Inman and Chainpur. The chondrules gave lower initial ^{26}Al/^{27}Al ratios than the inclusions, around 1×10^{-5}. If the decrease from a typical CAI value of 5×10^{-5} to a chondrule value of 1×10^{-5} is attributed to decay of ^{26}Al in a homogeneous reservoir, the data imply a period of about 2 Myr between CAI formation and chondrule formation. This time span is consistent with U–Pb ages on chondrules and inclusions (section 5.3.1), thus supporting the hypothesis of a homogeneous ^{26}Al distribution. Similar results were found by Kita *et al.* (2000) for two ferromagnesian chondrules from Semarkona. Al–Mg pseudochrons gave initial ^{26}Al/^{27}Al ratios in the narrow range (6–9) $\times$ 10^{-6}, again implying a period of about 2 Myr between CAI formation and chondrule formation.

The occurrence of ^{26}Al was finally extended to achondrites by Srinivasan *et al.* (1999). These workers found evidence for a small ^{26}Al signal (^{26}Al/^{27}Al = 7.5×10^{-7}) in the eucrite Piplia Kalan, showing that this nuclide survived into the period of differentiation of the Eucrite Parent Body, and could have provided a heat source for the melting of such bodies. The ^{26}Al signal was actually larger than expected, and suggests that planetary differentiation could have occurred as early as 5 Myr after the formation of CAIs, assuming that there was a homogeneous distribution of this nuclide.

15.4.2 Ca–K

^{41}Ca decays to ^{41}K with a half-life of only 0.1 Myr. Hence, if ^{41}K excesses were found in solar-system material, they would imply a very late addition of nucleosynthetically 'hot' material to the solar nebula. Such anomalies might be expected in Allende material displaying ^{26}Al signatures. Begemann and Stegmann (1976) sought ^{41}Ca signatures in Allende samples, and believed that they had found them. However, subsequent work by Hutcheon *et al.* (1984) attributed this signal to (^{40}Ca^{42}Ca)$^{2+}$ dimers, creating a peak that could not be resolved in mass from ^{41}K. Nevertheless, subsequent work by Srinivasan *et al.* (1994; 1996) finally moved ^{41}Ca from a species thought absent to a species known to have been present in the early solar system.

Srinivasan *et al.* looked for ^{41}K, the decay product of ^{41}Ca, in CAIs from the Efremovka CV3 carbonaceous chondrite. These inclusions were regarded as an ideal place to search for ^{41}K anomalies because of their unusually fresh petrography and the known presence of ^{26}Al anomalies. The pristine nature of the samples is very important, because ^{41}K anomalies are visible only at extreme Ca/K ratios, which would be compromised by re-mobilisation of common potassium.

Srinivasan *et al.* used the ion microprobe to measure K isotope ratios in pyroxenes and other high-Ca phases from four different inclusions. Special precautions were taken to resolve the ^{41}K signal from interfering molecular ions. ^{40}CaH^{+} was resolved by its excess mass at high spectral resolution. On the other hand, (^{40}Ca^{42}Ca)$^{2+}$ ions could not be resolved by mass, but were monitored and corrected via the related species (^{40}Ca^{43}Ca)$^{2+}$. The reliability of this correction is demonstrated by the constant ^{41}K/^{39}K ratios determined in terrestrial samples with Ca/K variations spanning nine orders of magnitude. In contrast, Efremovka inclusions exhibited a strong correlation between ^{41}K/^{39}K and ^{40}Ca/^{39}K ratios (Fig. 15.16). If this correlation results from *in situ* decay of ^{41}Ca after the inclusions were formed, its slope corresponds to an initial ^{41}Ca/^{40}Ca ratio of 1.4×10^{-8}. Minerals from the same suite of inclusions also gave initial ^{26}Al/^{27}Al ratios typical of other CAIs, around 5×10^{-5}.

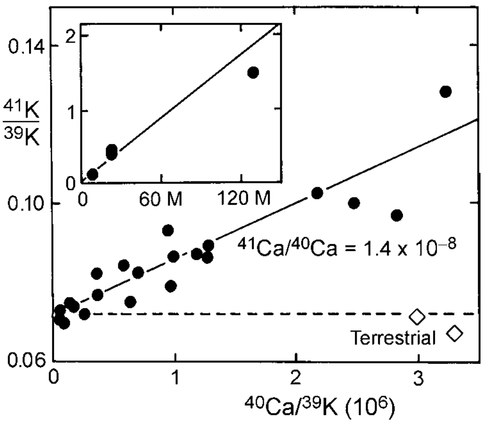

Fig. 15.16. K–Ca pseudochron diagram for pyroxenes in Efremovka inclusions, indicating a ^{41}Ca/^{40}Ca ratio of 1.4×10^{-8} in the solar nebula at the time of their crystallisation. Three radiogenic points (inset) also lie within error of the best-fit line: (◇) = terrestrial minerals. After Srinivasan *et al.* (1996).

In principle, the ^{41}K signal in Efremovka inclusions could be explained by recent cosmogenic production of ^{41}Ca by cosmic-ray neutrons. However, Srinivasan *et al.* cited rare-gas isotope evidence for Efremovka which indicated a low cosmogenic neutron flux during the fragment's 11-Myr exposure history in space. A second alternative is that ^{41}K was inherited as a 'fossil' component from decay of ^{41}Ca in pre-solar grains. However, this can be ruled out because the correlation between ^{41}K/^{39}K and Ca/K ratios is observed in grains which clearly crystallised from a liquid. Therefore, Srinivasan *et al.* concluded that the ^{41}K signal could best be explained by the presence of live ^{41}Ca in the early solar system.

Srinivasan *et al.* also considered the possibility that ^{41}Ca was manufactured in the solar nebula by bombardment of dust grains with energetic particles from an early 'active' Sun. However, they argued that this model cannot produce ^{41}Ca and ^{26}Al in their correct relative abundances. Therefore, the most attractive model attributes both nuclides to a common nucleosynthetic process immediately before solar-system condensation. This argument was supported by the discovery of correlated enrichments of ^{26}Mg and ^{41}K in several grains of hibonite in the three carbonaceous chondrites Murchison, Allende and Efremovka (Sahijpal *et al.*, 1998). The correlations were observed on a microscopic scale by ion-microprobe analysis, and therefore imply a common source for the extinct parents, ^{26}Al and ^{41}K.

If we assume simultaneous injection of ^{41}Ca and ^{26}Al, and we know the production ratios relative to stable calcium and aluminium, we can solve for both Δ and the dilution factor of 'hot', freshly injected material by 'cold' pre-existing material. This is the same approach as that attempted for the two longer-lived r-process nuclei ^{129}I and ^{244}Pu (section 15.3.2). Unfortunately, similar problems arise here, because the production ratios are poorly constrained. However, the half-life of ^{41}Ca is so short (0.1 Myr) that tight constraints on Δ arise from almost any model. In practice, both supernovae and red giants (asymptotic giant branch, or AGB, stars) can be made to fit the data, implying a Δ value of 1 Myr or less, and a dilution factor of 100 or more.

15.4.3 Be-10

The 'canonical' model involving late incorporation of 'hot' nucleosynthetic material into the solar nebula has recently been undermined by evidence for the production of ^{10}Be in the early solar system. ^{10}Be is one of the class of nuclides that cannot be produced by stellar nucleosynthesis because it is unstable in stars. Hence production of ^{10}Be is attributed to spallation reactions involving cosmic rays, termed the 'x-process' (section 1.2.2). Evidence for extinct ^{10}Be in the early solar system implies that other extinct nuclides might likewise have had spallogenic origins.

^{10}Be decays to ^{10}B with a half-life of 1.5 Myr. Evidence for the existence of extinct ^{10}Be in the early solar system was discovered by McKeegan *et al.* (2000) from the observation of ^{10}B/^{11}B variations that were positively correlated with Be/B ratios in melilite grains from an Allende CAI (Fig. 15.17). The slope of the array indicated an initial ^{10}Be/^{9}Be ratio of 9.5×10^{-4} at the time of CAI crystallisation, which was much too high to be explained by cosmogenic production by galactic cosmic rays. Therefore, McKeegan suggested that ^{10}Be resulted from very intense radiation in the solar nebula during its early history. This raises the possibility that the other very-short-lived species such as ^{26}Al, ^{41}K and ^{53}Mn could also have been produced in this way. Such models have been proposed before (e.g. Lee, 1978), but had largely been discarded due to the success of the 'late-addition' model. However, the observation of ^{10}Be in the solar nebula requires that this model be re-examined.

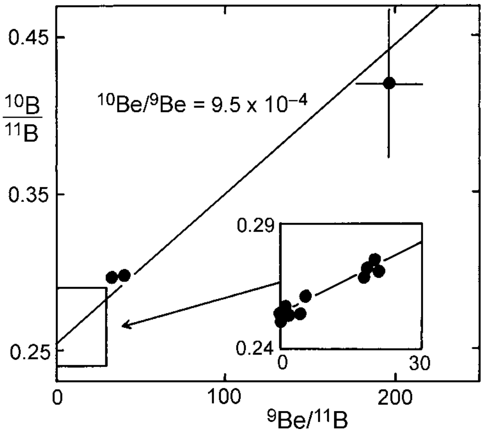

Fig. 15.17. Be–B correlation diagram, showing evidence for the existence of extinct ^{10}Be in an Allende CAI. After McKeegan *et al.* (2000).

One variant of the spallation production model recently proposed for extinct nuclides is the 'x-wind' model (Shu *et al.*, 1997; Lee *et al.*, 1998). In this model, protosolar rock debris in a 'reconnection ring' in the stellar accretion disc is irradiated by the protosun, during magnetic 'reconnection' events. These provoke impulsive flares, accelerating energetic particles to very high speeds so that they are capable of causing the production of extinct nuclides by spallation. After irradiation, most of this matter is funnelled back into the star. However, a sudden decrease in the solar magnetic field can cause the 'x region' to collapse into the zone of irradiated protosolar rock debris, flinging some of this material out to planetary distances (Fig. 15.18). This model can also explain the intense, but short-lived, heating episodes that are need to explain the high-temperature mineralogy of CAIs, and to a lesser extent, chondrules (Shu *et al.*, 1996).

There has been extensive debate about the ability of the x-wind model to explain the abundances of short-lived extinct nuclides in their correct proportions. For example, Sahijpal *et al.* (1998) argued that spallation cannot explain the observed abundances of ^{26}Al without over-production of ^{41}Ca. However, Lee

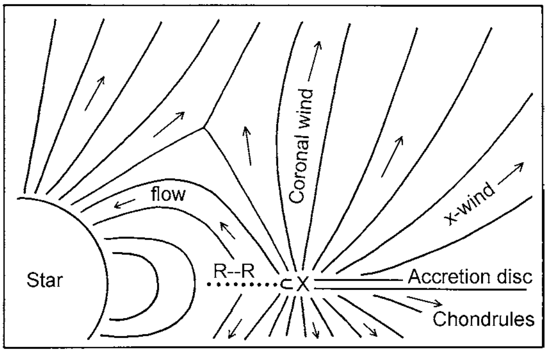

Fig. 15.18. Cartoon illustrating the 'x-wind' production of extinct nuclides by irradiation of the solar nebula. Dots = CAI precursors. R–R = reconnection ring; X = x-region. After Shu *et al.* (1997).

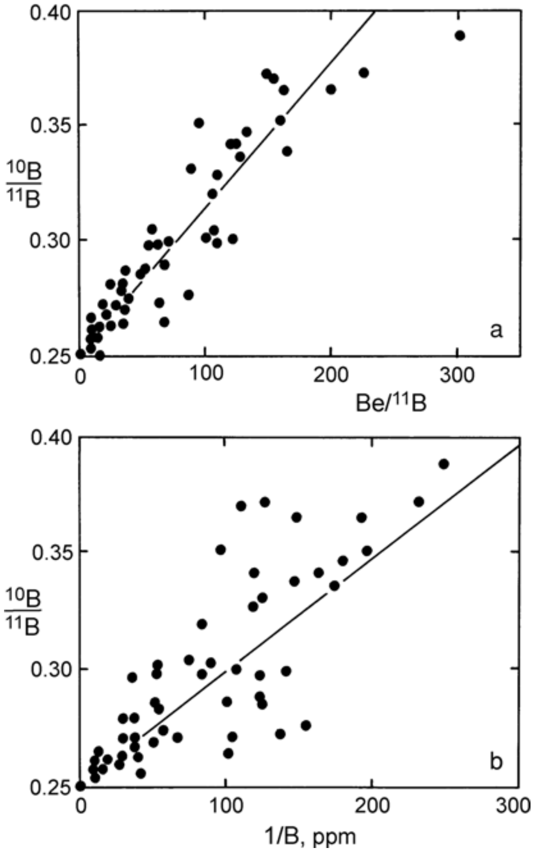

Fig. 15.19. Plots of boron isotope ratio against (a) Be/B ratio and (b) 1/B concentration to evaluate pseudochron *versus* mixing models for aggregate data from six CAI. Error bars are omitted for clarity. Modified after Sugiura *et al.* (2001).

et al. (1998) argued that mantling of CAIs with an Fe–Mg rich covering could enhance production of ^{26}Al relative to ^{41}Ca and therefore explain the abundances of all of the short-lived extinct nuclides except ^{60}Fe. On the other hand, Russell *et al.* (2001) predicted that spallation production would produce a heterogeneous distribution of the very-short-lived extinct species in meteorites. In theory this should allow the model to be tested; however, the actual degree of isotope heterogeneity is hard to assess.

Further evidence for the existence of extinct ^{10}Be in the early solar system was provided by Sugiura *et al.* (2001) from analysis of CAIs from Allende and Efremovka. Each of four inclusions from Efremovka and two from Allende exhibited positive correlations between ^{10}B/^{11}B and Be/B ratios in analysed melilite grains. The slopes of the arrays varied slightly, but all fell within error of the average ^{10}Be/^{9}Be ratio of 6.2×10^{-4} (Fig. 15.19a). Al–Mg measurements were made in coexisting anorthite from the same inclusions; however, these were much more scattered, and fell below the 'canonical' ^{26}Al/^{27}Al ratio of 5×10^{-5} which had previously been observed in many CAIs. This was attributed to re-equilibration during a later disturbance. Hence, it was suggested that diffusion of B in melilite must be slower than diffusion of Mg in anorthite. However, the strength of the Be–B pseudochron (Fig. 15.19a) raises the alternative possibility that it could be a mixing line.

To test the possibility of a mixing line, Sugiura *et al.* compared the data on the Be–B pseudochron diagram with a plot of ^{10}B/^{11}B ratio against the reciprocal of boron concentration (Fig. 15.19b). The good correlation in the latter diagram shows that the data are indeed primarily a mixing line between an exotic ^{10}B-enriched component and common boron. However, because the quality of the pseudochron correlation was better than the mixing line, Sugiura *et al.* suggested that the pseudochron really does represent a signature of extinct ^{10}Be from the early solar system, rather than cosmogenic isotope production over the subsequent 4.5 Byr.

Some doubts about the widespread importance of spallation production come from a recent study of hibonite grains in the carbonaceous chondrite Murchison (Marhas *et al.*, 2002). In this meteorite, two different types of hibonite grain are observed, one of which has large mass-fractionation anomalies, whereas the other has extinct-nuclide anomalies. Marhas *et al.* investigated the former type, to see whether they would nevertheless display ^{10}Be anomalies. This was indeed the case, since ^{10}Be/^{9}Be ratios near 5×10^{-4} were observed, but no evidence of extinct ^{26}Al or ^{41}Ca was observed. Marhas *et al.* attributed the ^{10}Be anomalies in these and other CAI minerals to energetic particles from an early active Sun. However, they attributed the absence of ^{26}Al and ^{41}Ca anomalies in the analysed hibonites to their crystallisation *before* the solar nebula was injected with 'hot' nucleosynthetic material by a nearby stellar source. In addition, ^{10}Be (accompanied by ^{26}Al and ^{41}Ca) can also be produced in the jets of heavily irradiated material that are expelled from a supernova after its explosion. Therefore, in view of these various possibilities, the present author believes that it would be premature to reject the 'late-hot-addition' model in favour of a purely spallogenic model for short-lived extinct nuclides.

15.5 Short-lived species in planetary differentiation

Although the very-short-lived species ^{26}Al and ^{41}Ca are suggestive of very late addition of nucleosynthetically 'hot' material to the nebula, they are too short-lived to demonstrate the survival of such material into the period of early differentiation into planetesimals and planets. However, a group of slightly longer-lived species fulfils this role, and also provides additional evidence for the type of late nucleosynthetic additions.

15.5.1 Pd–Ag

^{107}Pd decays by β emission to ^{107}Ag with a half-life of 6.5 Myr. The only objects with Pd/Ag ratios high enough to yield measurable variations in the abundance of ^{107}Ag are iron meteorites. The first successful discovery of radiogenic ^{107}Ag was made by Kelly and Wasserburg (1978) on the Santa Clara meteorite. They deduced that about 10 Myr might have elapsed between the last nucleosynthetic event and the coalescence and differentiation of iron-cored small planets. Subsequent work has revealed radiogenic ^{107}Ag in several meteorites (Chen and Wasserburg, 1984; 1990), of which the best data are from Gibeon. These results yield an initial ^{107}Pd/^{108}Pd ratio of 2.3×10^{-5} (Fig. 15.20). Very similar results were also seen in relatively low-Pd/Ag samples from Canyon Diablo, using high-precision MC-ICP-MS analysis (Carlson and Hauri, 2001). Since ^{107}Pd *versus* Ag correlations are observed in bodies that have clearly been melted since accretion of the solar system, the silver isotope signatures must reflect the presence of 'live' ^{107}Pd in the early solar system. They cannot have been inherited from pre-solar grains (as proposed for other systems by Clayton, 1975).

15.5.2 Mn–Cr

^{53}Mn decays to ^{53}Cr with a half-life of 3.7 Myr. For several reasons, this extinct nuclide reinforces the evidence from ^{107}Pd for the early history of planetary differentiation. Birck and Allègre (1985; 1988) found correlated variations in ^{53}Cr/^{52}Cr and Mn/Cr ratios in several meteorites, including Allende, Murchison, Indarch and the pallasite meteorite Eagle Station. Since the mixed silicate–iron mineralogy of

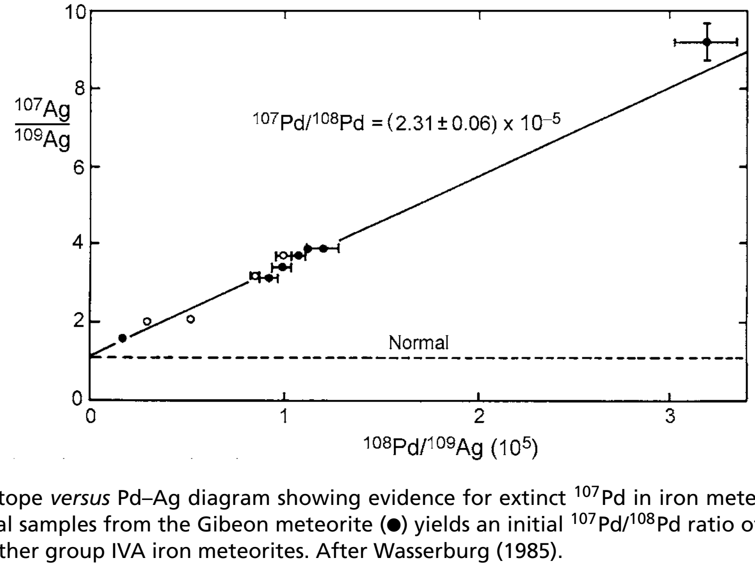

Fig. 15.20. Ag isotope *versus* Pd–Ag diagram showing evidence for extinct ^{107}Pd in iron meteorites. The best-fit line to seven metal samples from the Gibeon meteorite (●) yields an initial ^{107}Pd/^{108}Pd ratio of 2.3×10^{-5}. Open symbols denote other group IVA iron meteorites. After Wasserburg (1985).

the pallasites indicates a high-temperature origin, the Mn–Cr isotope systematics must result from *in situ* decay of ^{53}Mn in a differentiated planetary body. Hence ^{53}Mn provides additional evidence for nucleosynthetic processes immediately before coalescence of the solar system.

^{53}Mn is part of the iron group of elements (section 1.2), which are thought to be synthesised in large stars shortly before a supernova explosion. Hence it was argued (e.g. Rotaru *et al.*, 1992) that a supernova did indeed briefly pre-date solar-system condensation, as initially proposed on the basis of ^{26}Al. From the 3.7 Myr half-life of ^{53}Mn, it would follow that such an event occurred about 20 Myr before planetary differentiation. However, there are other possible routes for the synthesis of ^{53}Mn (Birck and Allègre, 1985). Furthermore, curium isotope evidence (or the lack of it; see below) argues against a late r-process addition to the solar nebula. Therefore, although there is good evidence for a late nucleosynthetic addition to the solar nebula, its source remains in doubt.

Although doubts remain about the source of ^{53}Mn, its half-life of 3.7 Myr gives it great potential as a chronometer of early solar-system evolution. To test this potential, Lugmair and Shukolyukov (1998) performed a Mn–Cr study of a large group of achondrites of various types. These are essentially all igneous rocks produced by the very early differentiation of one or more asteroids. Firstly, Lugmair and Shukolyukov analysed two ‘angrites’, Lewis Cliff (LEW) and Angra dos Reis (ADOR), which are thought to have rapid and simple cooling histories. Because of their well-defined Pb–Pb age of 4558 ± 0.5 Myr, these meteorites were used to anchor the Mn–Cr relative dating method in the same way that the I–Xe method was anchored. The method was then tested by analysing the primitive achondrite Acapulco, which gave a Mn–Cr age only 3 Myr younger than the angrites, consistent with its Pb–Pb age of 4557 ± 2 Myr. In addition, the Mn–Cr and I–Xe ages of Ste Marguerite and Richardton were also in excellent agreement (Gilmour and Saxton, 2001). Hence, the assumption of initial ^{53}Mn homogeneity, on which the Mn–Cr dating method is based, seems well justified for these materials.

Lugmair and Shukolyukov (1998) also analysed a suite of eight eucrites attributed to a single parent body that is tentatively identified with the asteroid Vesta 4. Two of these (Juvinas and Chervony Kut) gave good internal Mn–Cr pseudochrons, with inferred ages around 4563–4564 Myr, using the calibration against Pb–Pb described above. In addition, the complete suite gave an excellent whole-rock pseudochron with a ^{53}Mn/^{55}Mn ratio (Fig. 15.21) equivalent to an age of 4564.5 Myr using the same calibration. This was interpreted as the time of differentiation of the parent body, and is only 3 Myr younger than the Pb–Pb ages of CAIs (section 5.3.1). This supports I–Xe ages by indicating that formation and differentiation of planetesimals occurred extremely early.

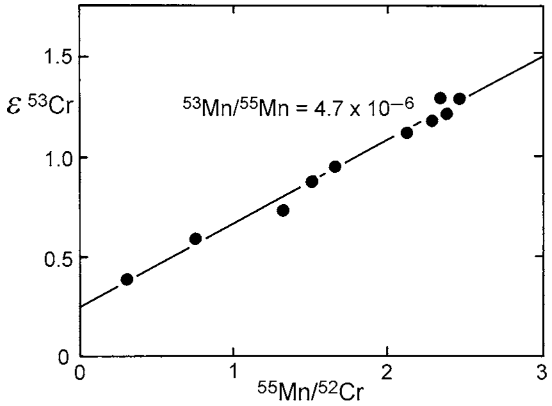

Fig. 15.21. Mn–Cr pseudochron diagram for whole-rock samples of achondrites, yielding an initial ^{53}Mn/^{55}Mn ratio of 4.7×10^{-6} at the time of differentiation of the eucrite parent body. After Lugmair and Shukolyukov (1998).

Three chondrites analysed by Lugmair and Shukolyukov (1998) were found to lie perfectly on the angrite pseudochron. However, a detailed study of individual chondrules from Chainpur and Bishunpur (Nyquist *et al.*, 2001) gave internal pseudochrons with slopes indicating an age 10 Myr older than the angrites. Nyquist *et al.* attributed this to a Mn/Cr fractionation event in the chondrite precursors of the early nebula (due to variations in volatility), rather than as the actual age of chondrule formation. Therefore the calculated age of 4568 Myr is reasonable, since it is nearly 4 Myr older than the Eucrite parent body and is within error of the Pb–Pb ages of CAIs.

All of these data are summarised on a plot of initial Cr isotope ratios against Mn isotope ratios determined from the Mn–Cr pseudochron diagrams (Fig. 15.22). Moving backwards in time from the top-left corner, the data suggest that all the achondrite samples (eucrites, angrites and primitive achondrites) can be derived by Mn–Cr fractionation from a source that is either the Eucrite Parent Body (Vesta) or a closely related one. Some whole-rock chondrites lie on the angrite evolution line, but Indarch lies below this with a lower initial Cr isotope ratio, which, however, is consistent with the Bulk Earth composition. Lugmair and Shukolyukov (1998) attributed this less radiogenic Cr isotope ratio

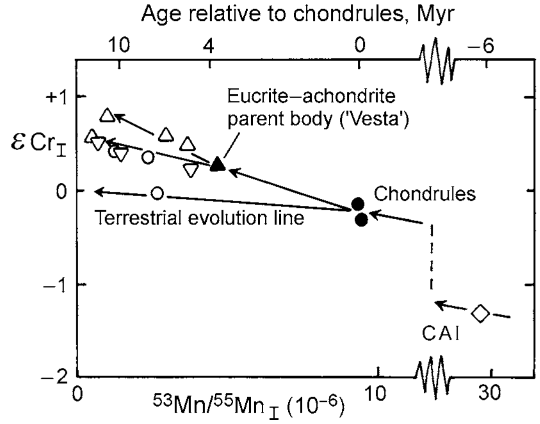

Fig. 15.22. Mn–Cr isotope evolution diagram for the early solar system. (△) = eucrites; (▽) = angrites and primitive achondrites; (○) = chondrite whole-rocks; (●) = chondrule initial ratios. After Nyquist *et al.* (2001).

to original Mn isotope heterogeneity in the nebula, but it is easier to explain it by invoking variable Mn/Cr fractionation in the nebula due to the different volatilities of these two elements (Birck *et al.*, 1999).

The latter model is supported by the new Chainpur and Bishunpur chondrule pseudochrons. However, whole-rock data for carbonaceous chondrites (Birck *et al.*, 1999, not shown here) are more scattered. In addition, the Allende inclusion (CAI) analysed by Birck and Allègre (1985) gives an apparent Mn–Cr age up to 10 Myr older than its Pb–Pb age. However, these inclusions contain many isotopic anomalies, and are the one clear example of inhomogeneous extinct-nuclide distribution, so we cannot assume that their Mn isotope systematics were homogenised with other solar-system materials. Therefore, more Mn–Cr data are needed from the very early bodies (carbonaceous chondrites and inclusions) in order to understand this primitive stage in the evolution of the solar nebula.

Mn–Cr data also provide evidence about the later cooling of chondrite parent bodies. This comes from the observation of ^{53}Mn excesses in carbonate fragments from two chondritic meteorites (Endress *et al.*, 1996). These poly-crystalline fragments, mostly of dolomitic composition, are uniformly spread through the carbonaceous chondrites Orgueil and Ivuna. They are interpreted as remnants of carbonate veins that formed during very early aqueous alteration of the meteorite parent body. Five dolomite fragments, analysed by ion microprobe, define a relatively linear array on the Mn–Cr pseudochron diagram. The slope of this array corresponds to a ^{53}Mn/^{55}Mn ratio of 2×10^{-6} at the time of carbonate crystallisation. The time required to achieve this ratio, starting from the value of 4.4×10^{-5} in 4567-Myr Allende inclusions, is less than 20 Myr. This indicates that the carbonaceous chondrite parent body cooled very rapidly after aggregation to temperatures at which liquid water could exist. Other ^{53}Mn evidence for very early hydrous alteration was found in the CV3 chondrite Mokoia (Hutcheon *et al.*, 1998).

15.5.3 Fe–Ni

^{60}Fe decays to ^{60}Ni (*via* ^{60}Co) with a half-life of 1.5 Myr. Shukolyukov and Lugmair (1993a) found ^{60}Ni excesses as high as 50 ε units in the achondrite Chervony Kut, facilitated by the extremely high Fe/Ni ratios in this meteorite (up to 350 000). These ratios are attributed to partition of nickel into the cores of differentiated planetesimals. Whole-rock samples of Chervony Kut displayed a correlation between ^{60}Ni/^{58}Ni and Fe/Ni ratios, indicating that ^{60}Fe was still alive at the time of differentiation, with a ^{60}Fe/^{56}Fe ratio of 3.9×10^{-9}. Whole-rock analysis of the achondrite Juvinas also generated a pseudochron relation, but with a lower ^{60}Fe/^{56}Fe ratio of about 4×10^{-10} (Shukolyukov and Lugmair, 1993b). The difference between these extinct-nuclide abundance ratios implies a difference in closure age of about 4.7 Myr between the two meteorites, if the parent body had a homogeneous ^{60}Fe/^{56}Fe ratio.

This evidence points to widespread distribution of ^{60}Fe in the solar nebula, and suggests that this nuclide was a major source of heat. Coupled with ^{26}Al, ^{60}Fe would be capable of causing planetary melting within a few million years of accretion. Furthermore, the existence of ^{60}Fe in the solar nebula requires a late supernova contribution, since there is no suitable target nuclide to produce this isotope by spallation. Lee *et al.* (1998) questioned the evidence for extinct ^{60}Fe in the early solar system, and suggested instead that it could have been produced by cosmogenic irradiation of the Eucrite Parent Body before its break-up. However, more recent work has confirmed the existence of 'live' ^{60}Fe in troilites from unmetamorphosed ordinary chondrites (Tachibana and Huss, 2003). Hence, it now seems fairly certain that ^{60}Fe was introduced into the early solar system by late injection from a supernova, thus reinstating the 'supernova-trigger hypothesis'.

15.5.4 Hf–W

^{182}Hf decays to ^{182}W (tungsten) by double β decay with a half-life of 9 Myr. Norman and Schramm (1983) proposed the Hf–W system as an r-process chronometer, but its application was delayed by the technical difficulties of tungsten isotope analysis (which are similar to those for osmium, section 8.1). Harper *et al.* (1991) and Harper and Jacobsen (1996) successfully compared W isotope compositions in the Earth and iron meteorites by N-TIMS analysis, and these results were verified and extended by Lee and Halliday (1995; 1996) using MC-ICP-MS (section 2.5.1).

Lee and Halliday presented the combined data set from the above studies in the form of ε^{182}W values, representing part-per-10 000 variations in ^{182}W/^{183}W (Harper and Jacobsen, 1996) or ^{182}W/^{184}W ratio (Lee and Halliday, 1995; 1996), relative to a terrestrial tungsten standard, NIST 3163. Their results gave that ε W values that were within error of zero in terrestrial lavas, a lunar mare basalt and bulk powders of the carbonaceous chondrites Allende and Murchison (Fig. 15.23). In contrast, sawn blocks from iron meteorites (as well as metal phases from ordinary chondrites) had ε values clustering around ε W of −4.

In principle, these variations could be explained by invoking cosmogenic production, pre-solar grains, or live ^{182}Hf in the early solar system. However, the negative ^{182}W anomaly in iron meteorites is unique because it represents an isotope deficiency rather than an enrichment. This makes both cosmogenic and pre-solar origins for the anomaly quite unlikely, whereas it can be readily explained by elemental Hf–W partitioning while ^{182}Hf was still alive in the early solar system. Since W is strongly siderophile, whereas Hf is lithophile, the iron cores of meteorite parent bodies developed very low Hf/W ratios. Furthermore, evidence from the Fe–Ni system (section 15.5.3) shows that these cores formed very early, within about 5 Myr of chondrite formation. Therefore, iron meteorites should preserve a nearly primordial ε^{182}W composition for the solar system. In contrast, ^{182}W growth would continue in other solar-system bodies until ^{182}Hf became extinct.

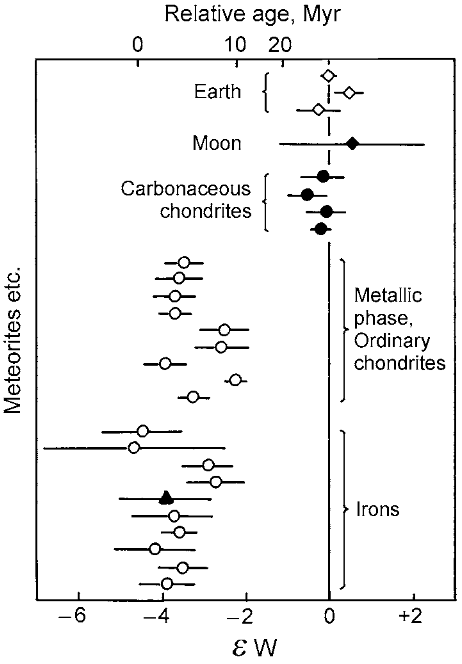

Fig. 15.23. Measured tungsten isotope values for various solar-system objects, relative to a terrestrial tungsten standard: (▲) = data of Harper and Jacobsen (1996). Data from Lee and Halliday (1996).

Harper and Jacobsen (1996) did not have ^{182}W data on chondrites to use as a benchmark for solar-system W isotope evolution. Instead, they estimated the initial solar-system ^{182}Hf/^{180}Hf ratio from a predicted supernova production ratio of 2×10^{-5}. This implied that the present-day chondritic tungsten composition, and hence that of the Bulk Earth, was essentially the same as that of iron meteorites. With this assumption, the measured excess of four epsilon units in the Bulk Silicate Earth implied that terrestrial Hf/W fractionation occurred while ^{182}Hf was still alive, due to very early core formation. In contrast, Lee and Halliday (1995; 1996) made direct measurements of W isotope ratios in two bulk chondrite samples, and found ε values of +4 relative to iron meteorites, essentially the same as the Bulk Silicate Earth. This led to the opposite conclusion from that of Harper and Jacobsen (1996); namely that the Earth's core segregated relatively *late*, after ^{182}Hf had become extinct.

The small amount of chondrite data analysed by Lee and Halliday (1995; 1996) implied an unexpectedly high ^{182}Hf/^{180}Hf ratio of 2.6×10^{-4} in the early solar system. Moreover, more detailed work by Lee and Halliday (2000) appeared to support this ratio. For example, separated metal and silicate phases from the H4 chondrites Forest Vale and Ste Marguerite gave Hf–W pseudochrons equivalent to initial ^{182}Hf/^{180}Hf ratios of 1.9×10^{-4} and 1.8×10^{-4}, respectively. The previously analysed whole-rock samples of Allende and Murchison also plotted near these pseudochrons.

Unfortunately, subsequent work by three different research groups did not confirm these results. First indications of this discrepancy were obtained by Schoenberg *et al.* (2002a) and confirmed in more detailed work by Yin *et al.* (2002) and Kleine *et al.* (2002). The latter groups obtained consistent metal-silicate pseudochrons for four different chondrites (Dalgety Downs, Dhurmsala, Forest Vale and Ste Marguerite), with a

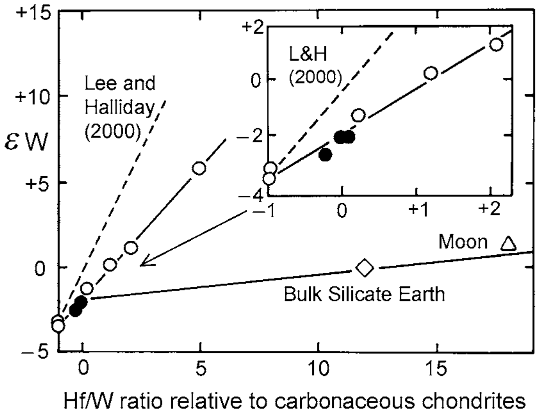

Fig. 15.24. Hf–W pseudochron for metal–silicate separates from two chondrites (○) and two carbonaceous chondrites (●). The inset shows the lower part of the chondrite pseudochron. Dashed line shows the carbonaceous chondrite array of Lee and Halliday (2000). After Yin *et al.* (2002).

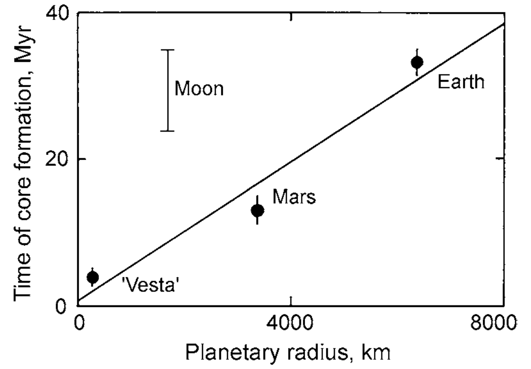

Fig. 15.25. Plot of estimated times of core formation for solar-system bodies, compared with their measured or estimated radii. After Kleine *et al.* (2002).

consistent initial ^{182}Hf/^{180}Hf ratio near 1×10^{-4}. Both groups also found that whole-rock carbonaceous chondrites plotted on the metal-silicate pseudochrons (e.g. Fig. 15.24) with ε W around −2. Finally, Yin *et al.* also measured a CAI composition lying on the same chondrite pseudochron, suggesting that a ^{182}Hf/^{180}Hf ratio near 1×10^{-4} is also the best estimate of the starting composition of the solar nebula. The steeper pseudochron obtained by Lee and Halliday (2000) remains unexplained, but new data obtained by Halliday (2002) were consistent with the results obtained by the three other research groups. The implications of this Hf isotope ratio for the Δ value since last r-process addition will be discussed further in section 15.7.

A two-point pseudochron between the average chondrite composition and the Bulk Silicate Earth (taken to be $\varepsilon = 0$) yields the ^{182}Hf/^{180}Hf isotope composition of the Bulk Silicate Earth at the average time of core formation. This has a value of 1.1×10^{-5}, which (when coupled with a starting composition in the solar nebula of 1×10^{-4}) leads to an average time of terrestrial core formation around 30 Myr. In contrast, the data of Lee and Halliday (1995; 2000) implied a minimum age of core formation around 60 Myr. However, no maximum age constraint was available, since their chondritic and Bulk Silicate Earth results were within error.

Similar calculations can be made for the time of core formation in the asteroid Vesta and for Mars, using tungsten isotope compositions of the silicate fractions of these bodies. These can be determined by analysing the compositions of basaltic achondrites or eucrites (both attributed to Vesta) and from SNC meteorites (attributed to fragments ejected from Mars during impact events). From these analyses, Kleine *et al.* (2002) argued that the times of core formation in Vesta, Mars and the Earth were consistent with their planetary radii (Fig. 15.25). The new data are also consistent with evidence from the Pd–Ag system for early core formation in the Earth and in meteorite parent bodies (Hauri *et al.*, 2000).

The estimated formation age of the Moon is also plotted in Fig. 15.25, but it can be seen that this is the same as that of the Earth's core, despite the Moon's small radius. This is because most researchers now agree that the Moon was formed in a giant impact between the proto-Earth and another planetary body about the size of Mars (e.g. Hartman, 1986). Therefore, when speaking of the age of the Moon, we are estimating the time between CAI formation and this giant impact.

Lee *et al.* (1997) carried out several analyses on the major groups of lunar rocks, including the lunar highlands (anorthosite, troctolite and norite), mare basalts, and so-called KREEP basalts (which are rich in incompatible elements). On a Hf–W pseudochron diagram, these samples display considerable scatter, which is attributed to Hf–W fractionation within each sub-group after the extinction of ^{182}Hf. For example, the age of the mare basalts (about 4.2 Byr) is much younger than the ages of formation of the Moon or the extinction of ^{182}Hf, but we can recover the approximate composition of the mare basalt source by averaging all of the mare data. This average falls close to a three-point pseudochron for lunar soil, which is expected to be a relic from very early lunar differentiation. Similarly, the averages of highland anorthosites, highland mafic

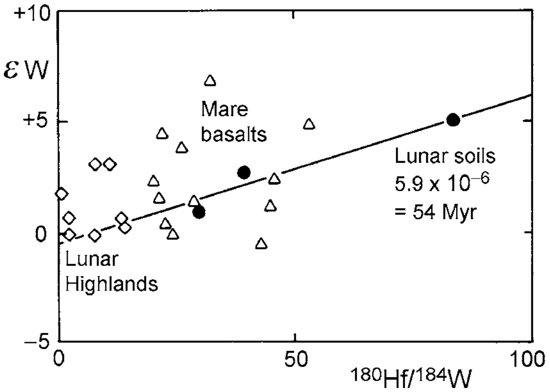

Fig. 15.26. Hf–W pseudochron diagram for lunar samples. The regression is based on three lunar soils (●). Other symbols: (◇) = highland rocks; (△) = KREEP and mare basalts. Data from Lee *et al.* (1997).

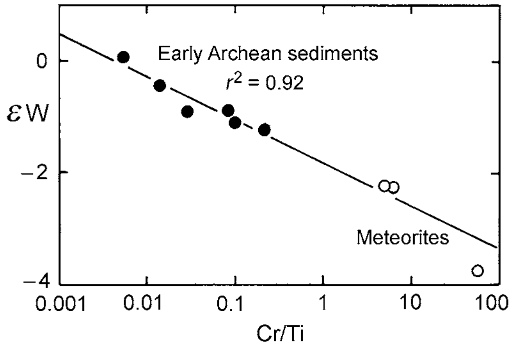

Fig. 15.27. Plot of ε W against Cr/Ti ratio (on a log scale), showing a possible mixing line between terrestrial sediment (●) and various types of meteorite (○). After Schoenberg *et al.* (2002).

rocks and KREEP basalts are also near to the soil pseudochron, whose slope indicates a ^{182}Hf/^{180}Hf ratio of 5.9×10^{-6}.

Lee *et al.* (1997) interpreted the Hf–W pseudochron as the age of massive lunar differentiation. This is thought to represent crystallisation from a lunar magma ocean formed when the Moon aggregated in Earth orbit after the giant impact between the proto-Earth and the impactor. Modelling of the collision suggests that the core of the impactor was added to the Earth's core, and much of the mantle of the impactor was added to the Earth's mantle, but a residue of the impactor's mantle was thrown into orbit to form the Moon. Using the new ^{182}Hf/^{180}Hf ratio of 1.0×10^{-4} for chondrites leads to an estimate for the Moon-forming giant impact (54 Myr) slightly younger than the average age of the Earth's core, which is the expected order of events.

A final application of the Hf–W method worth mentioning is in searching for evidence of the intense 'early meteorite bombardment' that the Earth was subjected to shortly after its accretion. This bombardment might be expected to leave traces in Early Archean terrestrial sediments. Therefore, Schoenberg *et al.* (2002b) searched for W isotope anomalies in the oldest (metamosphosed) sediments from Isua in western Greenland. They claimed to find negative ε W values in these sediments (relative to all other terrestrial materials analysed), which can be explained by contamination of the sediments by meteoritic debris, either from iron meteorites or from chondrites. In particular, they observed an inverse correlation between ε W and the logarithm of the Cr/Ti elemental ratio in these sediments, which is believed to be a good indicator of contamination by meteoritic material (Fig. 15.27).

15.5.5 ^{146}Sm–^{142}Nd

^{146}Sm is the longest-lived of the extinct nuclides, with a half-life of 103 Myr. Its extant lifetime of a few hundred million years would therefore have been long enough to extend into the period of early differentiation of the silicate Earth. Therefore, if strong Sm/Nd fractionation occurred during early crust formation, variations in the abundance of the daughter product, ^{142}Nd, might be detected in Early Archean rocks.

^{142}Nd isotope variations were detected during early studies of the achondrite Angra dos Reis (Lugmair and Marti, 1977) but their occurrence in terrestrial materials has been a subject of considerable debate. Because the variations are so small, they are quoted in ppm (μ) relative to standard terrestrial Nd. The first claim of a positive terrestrial ^{142}Nd anomaly was made by Harper and Jacobsen (1992), based on analysis of one sample from Isua, western Greenland. However, other workers (Galer and Goldstein, 1992; McCulloch and Bennett, 1993) observed only normal ^{142}Nd in other Early Archean rocks. Therefore, a much more detailed investigation was carried out by Sharma *et al.* (1996).

Sharma *et al.* analysed three types of sample: normal Nd, normal Nd spiked with 30 or 57 ppm ^{142}Nd, and 3.8-Byr-old rocks from Isua, West Greenland. The latter included one sample with a claimed 32-ppm excess of ^{142}Nd and one unknown sample. Samples were run in static mode on a Finnigan MAT 262 machine. Focus positions were shown to have some influence on the measured relative abundances of ^{142}Nd; nevertheless, results for the three types of sample were generally consistent with the predicted ^{142}Nd excesses (Fig. 15.28). Hence, the existence of ^{142}Nd anomalies

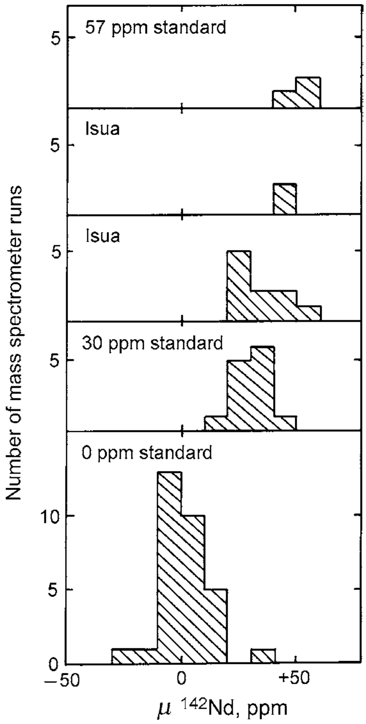

Fig. 15.28. Histograms of μ ^{142}Nd data for three artificial standards, compared with two rock samples from Isua. Data from Sharma *et al.* (1996).

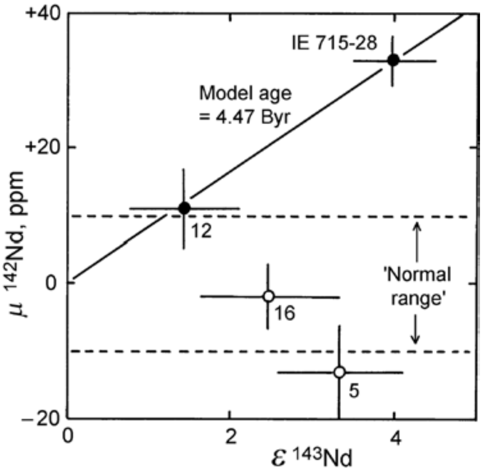

Fig. 15.29. Plot of ε ^{142}Nd against μ ^{143}Nd for four Isua samples, only one of which has a clear ^{142}Nd anomaly. This composition can be explained by a differentiation event 4.47 Byr ago. After Jacobsen and Harper (1996).

in the Earth was confirmed with a fairly high degree of confidence.

Jacobsen and Harper (1996) showed that the ^{142}Nd excess can be used with initial ε ^{143}Nd values to model early differentiation of the silicate Earth. A simple two-stage model assumes Bulk Earth evolution until time T, when Sm/Nd fractionation occurs in some part of the mantle. The fractionated mantle reservoir is subsequently sampled at the time of magmatism. For the 3.81-Byr-old Isua rocks, this model yields an age of 4.47 Byr for the fractionation event, 100 Myr after accretion of the Earth (Fig. 15.29). In contrast, 4-Byr-old samples of Acasta gneiss, with calculated initial ^{143}Nd values ($\varepsilon[t]$) of +3.5, gave no ^{142}Nd anomaly. However, high ε ^{143}Nd values in these samples may be metamorphic artefacts (section 4.4.4).

15.6 Absent species

15.6.1 Cm–U

^{247}Cm (curium) decays to ^{235}U with a half-life of 16 Myr. The significance of this species is that, like ^{244}Pu, it is formed by the r-process only, but, unlike ^{244}Pu, it has a comparatively short half-life. Hence the abundance of ^{247}Cm can theoretically indicate whether late additions of material to the nebula (called for above) were r-process products. Since the strongest evidence for late addition is represented by ^{26}Al and ^{41}Ca anomalies in CAIs, these samples have the best chance of being enriched in the daughter product of curium, which is ^{235}U. The search for ^{247}Cm therefore consists of looking for very small variations in uranium isotope composition. Unfortunately, ^{235}U is normally used as an enriched isotope in the determination of U abundances by isotope dilution, and hence most laboratories are susceptible to artificial perturbations in this ratio. Perhaps for this reason, numerous claims for excess ^{235}U have been made, but all are suspect.

In an attempt to resolve this problem, Chen and Wasserburg (1981) carried out a very careful investigation of U isotope compositions in samples for which large ^{26}Al signatures had been demonstrated, using a double ^{233}U/^{236}U spike to correct for mass fractionation during analysis (section 2.4.2). This study placed a maximum limit of ±0.4% on uranium isotope variation in these very favourable samples, from which Chen and Wasserburg calculated a maximum initial ^{247}Cm/^{238}U ratio of 1.5×10^{-3}.

This value can be compared with the analogous ^{244}Pu/^{238}U ratio, which sets an upper limit on the dilution factor for late r-process material (section 15.3.2).

Since inferred initial ^{247}Cm abundances are substantially lower than those of ^{244}Pu, it was deduced that the late ^{26}Al addition to the solar nebula was not r-process material. Wasserburg (1985) argued that the low ^{247}Cm abundance places a strong lower limit on Δ (100 Myr, Wasserburg and Papanastassiou, 1982) for the last r-process addition to the solar nebula. However, this argument excludes only late *heterogeneous* additions of ^{247}Cm to the solar nebula, because it rests on the observed homogeneity of ^{235}U/^{238}U isotope ratios rather than their absolute value. Since there is increasing evidence for the homogeneity of extinct nuclide signatures in different types of samples, this evidence is quite weak.

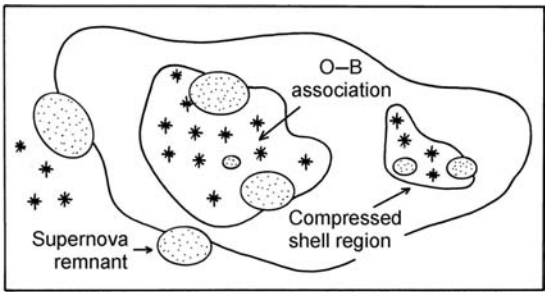

Fig. 15.30. Schematic illustration of a possible scenario for the formation of new star systems (including the solar system) in a giant molecular cloud containing supernova remnants (stippled). After Harper (1996).

15.7 Conclusions

In order to achieve a realistic model for the formation and early evolution of the solar nebula, it is necessary to use the results of several extinct-nuclide tracers. In an early review of the subject, Wasserburg and Papanastassiou (1982) drew attention to the relative similarity between the 'hot/cold' isotope ratios of roughly 1×10^{-4}, 0.5×10^{-4} and 0.2×10^{-4} for iodine, aluminium and palladium in chondrites. They pointed out that, if the additions of hot material occurred comparatively early (e.g. $\Delta \approx 200$ Myr), as suggested by Schramm and Wasserburg (1970), then their different half-lives would have attenuated the short-lived nuclides to very different degrees by the time of solar-system condensation. In contrast, the comparatively similar abundance ratios actually observed may imply a late addition with similar degrees of dilution by cold material.

More recent evidence should have narrowed the options for the origin of the solar system, but a unique model is still not available. The presence of very-short-lived species can be explained by the 'trigger hypothesis' (Cameron and Truran, 1977; Cameron *et al.*, 1995), by which a single event caused late injection of nuclides into a molecular cloud, and also triggered the collapse of the cloud. However, it is not clear whether this event involved a red giant or supernova. On the other hand, ^{129}I and ^{182}Hf are best explained by a supernova, and actinides must be produced in supernovae. However, more than one type of supernova may be required to fit all of the production ratios.

Wasserburg *et al.* (1996) argued that the effective frequency with which supernovae could contribute to galactic nuclide production could be much higher than the one per 100 Myr commonly assumed. In addition, they suggested that different types of supernovae could have contributed 'spikes' of different nuclides to the pre-solar nebula. For example, the low level of ^{129}I implies an early supernova source (Δ about 100 Myr). Wasserburg *et al.* then grouped ^{182}Hf with a late actinide addition from a second supernova (Δ about 10 Myr, but this can increase in the light of new Hf–W data). Finally, they attributed ^{41}Ca, ^{26}Al and ^{60}Fe to very late addition, either from a third supernova source or from a red giant. A model of multiple supernova sources was also proposed by Harper (1996), who envisaged star birth in a large molecular cloud with a complex series of injection and mixing events (Fig. 15.30).

According to the model of Shu *et al.* (1997) and Lee *et al.* (1998), some of the very-short-lived species (^{41}Ca, ^{26}Al and also ^{53}Mn) could also have been formed by spallation reactions when the sun was an embedded protostar. However, this mechanism cannot explain the presence of ^{60}Fe in the early solar system, so it seems likely that at least some of the ^{41}Ca, ^{26}Al and ^{53}Mn was introduced, along with ^{60}Fe, by a late supernova.

References

Armstrong, J. T., Hutcheon, I. D. and Wasserburg, G. J. (1984). Disturbed Mg isotopic systematics in Allende CAI. *Lunar Planet. Sci.* **15**, 15 (abstract).

Arnett, W. D. (1969). Explosive nucleosynthesis in stars. *Astrophys. J.* **157**, 1369–80.

Begemann, F., and Stegmann, W. (1976). Implications from the absence of ^{41}K anomaly in an Allende inclusion. *Nature* **259**, 549–50.

Bennett, C. L. (2003). NASA news release (11 February, 2003) on results from the Wilkinson Microwave Anisotropy Probe (WMAP). (From http://www.gsfc.nasa.gov.)

Bernatowicz, T. J., Podosek, F. A., Swindle, T. D. and Honda, M. (1988). I–Xe systematics in LL chondrites. *Geochim. Cosmochim. Acta* **52**, 1113–21.

Birck, J. L. and Allègre, C. J. (1985). Evidence for the presence of ^{53}Mn in the early solar-system. *Geophys. Res. Lett.* **12**, 745–8.

Birck, J. L. and Allègre, C. J. (1988). Manganese–chromium isotope systematics and the development of the early solar-system. *Nature* **331**, 579–84.

Birck, J. L., Rotaru, M. and Allègre, C. J. (1999). ^{53}Mn–^{53}Cr evolution of the early solar system. *Geochim. Cosmochim. Acta* **63**, 4111–17.

Brazzle, R. H., Pravdivtseva, O. V., Meshik, A. P. and Hohenberg, C. M. (1999). Verification and interpretation of the I–Xe chronometer. *Geochim. Cosmochim. Acta* **63**, 739–60.

Broecker, W. (1986). *How to Build a Habitable Planet*. Eldigio Press, Columbia University, 291 pp.

Cameron, A. G. W. (1962). The formation of the sun and the planets. *Icarus* **1**, 13–69.

Cameron, A. G. W., Hoflich, P., Myers, P. C. and Clayton, D. D. (1995). Massive supernovae, Orion gamma rays, and the formation of the Solar System. *Astrophys. J. (Lett.)* **447**, L53–7.

Cameron, A. G. W. and Truran, J. W. (1977). The supernova trigger for formation of the solar-system. *Icarus* **30**, 447–61.

Carlson, R. W. and Hauri, E. H. (2001). Extending the ^{107}Pd–^{107}Ag chronometer to low Pd/Ag meteorites with multicollector plasma-ionization mass spectrometry. *Geochim. Cosmochim. Acta* **65**, 1839–48.

Champagne, A. E., Howard, A. J. and Parker, P. D. (1983). Nucleosynthesis of ^{26}Al at low stellar temperatures. *Astrophys. J.* **269**, 686–8.

Chen, J. H. and Wasserburg, G. J. (1981). The isotopic composition of uranium and lead in Allende inclusions and meteorite phosphates. *Earth Planet. Sci. Lett.* **52**, 1–15.

Chen, J. H. and Wasserburg, G. J. (1984). The origin of excess ^{107}Ag in Gibeon (IVA) and other iron meteorites. *Lunar Planet. Sci.* **15**, 144 (abstract).

Chen, J. H. and Wasserburg, G. J. (1990). The isotopic composition of Ag in meteorites and the presence of ^{107}Pd in protoplanets. *Geochim. Cosmochim. Acta* **54**, 1729–43.

Clayton, D. D. (1975). Extinct radioactivities: trapped residuals of presolar grains. *Astrophys. J.* **199**, 765–9.

Clayton, D. D. (1979). Supernovae and the origin of the solar-system. *Space Sci. Rev.* **24**, 147–226.

Crabb, J., Lewis, R. S. and Anders, E. (1982). Extinct ^{129}I in C3 chondrites. *Geochim. Cosmochim. Acta* **46**, 2511–26.

Dicke, R. H. (1969). The age of the galaxy from the decay of uranium. *Astrophys. J.* **155**, 123–34.

Endress, M., Zinner, E. and Bischoff, A. (1996). Early aqueous activity on primitive meteorite parent bodies. *Nature* **379**, 701–3.

Galer, S. J. G. and Goldstein, S. L. (1992). Further ^{142}Nd studies of Archean rocks provide no evidence for early depletion. *EOS* **73**, 622 (abstract).

Gilmour, J. D. and Saxton, J. M. (2001). A time-scale of formation of the first solids. *Phil. Trans. Roy. Soc. Lond. A* **359**, 2037–48.

Gilmour, J. D., Whitby, J. A., Turner, G., Bridges, J. C. and Hutchison, R. (2000). The iodine–xenon system in clasts and chondrules from ordinary chondrites: implications for early solar system chronology. *Meteoritics Planet. Sci.* **35**, 445–55.

Göpel, C., Manhès, G. and Allègre, C. J. (1994). U–Pb systematics of phosphates from equilibrated ordinary chondrites. *Earth Planet. Sci. Lett.* **121**, 153–71.

Hagee, B., Bernatowicz, T. J., Podosek, F. A., Johnson, M. L., Burnett, D. S. and Tatsumoto, M. (1990). Actinide abundances in ordinary chondrites. *Geochim. Cosmochim. Acta* **54**, 2847–58.

Halliday, A. N. (2002). Cited by Fitzgerald, R. in: Isotope ratio measurements firm up knowledge of Earth's formation. *Phys. Today* **56 (1)**, 16–18.

Harper, C. L. (1996). Astrophysical site of the origin of the Solar System inferred from extinct radionuclide abundances. *Astrophys. J.* **466**, 1026–38.

Harper, C. L. and Jacobsen, S. B. (1992). Evidence from coupled ^{147}Sm–^{143}Nd and ^{146}Sm–^{142}Nd systematics for very early (4.5-Gyr) differentiation of the Earth's mantle. *Nature* **360**, 728–32.

Harper, C. L. and Jacobsen, S. B. (1996). Evidence for ^{182}Hf in the early Solar System and constraints on the timescale of terrestrial accretion and core formation. *Geochim. Cosmochim. Acta* **60**, 1131–53.

Harper, C. L., Volkening, J., Heumann, K. G., Shih, C.-Y. and Weismann, H. (1991). ^{182}Hf–^{182}W: new cosmochronometric constraints on terrestrial accretion, core formation, the astrophysical site of the r-process, and the origin of the Solar System. *Lunar Planet. Sci.* **22**, 515–16.

Hartman, W. K. (1986). Moon origin: the impact-trigger hypothesis. In: Hartman, W. K., Philips, R. J. and Taylor, G. J. (Eds.), *Origin of the Moon*. Lunar Planetary Institute, pp. 579–608.

Hauri, E. H., Carlson, R. W. and Bauer, J. (2000). The timing of core formation and volatile depletion in solar system objects from high-precision ^{107}Pd–^{107}Ag isotope systematics. *Lunar Planet. Sci.* **31**, 1812.

Hohenberg, C. M. (1969). Radioisotopes and the history of nucleosynthesis in the galaxy. *Science* **166**, 212–15.

Hohenberg, C. M., Podosek, F. A. and Reynolds, J. H. (1967). Xenon–iodine dating: sharp isochronism in chondrites. *Science* **156**, 233–6.

Hutcheon, I. D., Armstrong, J. T. and Wasserburg, G. J. (1984). Excess in ^{41}K in Allende CAZ: confirmation of a hint. *Lunar Planet. Sci.* **15**, 387–8 (abstract).

Hutcheon, I. D. and Hutchison, R. (1989). Evidence from the Semarkona ordinary chondrite for ^{26}Al heating of small planets. *Nature* **337**, 238–41.

Hutcheon, I. D., Krot, A. N., Keil, K., Phinney, D. L. and Scott, E. R. D. (1998). ^{53}Mn–^{53}Cr dating of fayalite formation in the CV3 chondrite Mokoia: evidence for asteroidal alteration. *Science* **282**, 1865–7.

Jacobsen, S. B. and Harper, C. L. (1996). Accretion and early differentiation history of the Earth based on extinct radionuclides. In: Basu, A. and Hart, S. R. (Eds.), *Earth Processes: Reading the Isotopic Code. Geophysics Monograph* **95**. American Geophysical Union, pp. 47–74.

Jeffrey, P. M., and Reynolds, J. H. (1961). Origin of excess ^{129}Xe in stone meteorites. *J. Geophys. Res.* **66**, 3582–3.

Kelly, W. R., and Wasserburg, G. J. (1978). Evidence for the existence of ^{107}Pd in the early solar-system. *Geophys. Res. Lett.* **5**, 1079–82.

Kita, N. T., Nagahara, H., Togashi, S. and Morshita, Y. (2000). A short duration of chondrule formation in the solar nebula: evidence from Al-26 in Semarkona ferromagnesian chondrules. *Geochim. Cosmochim. Acta* **64**, 3913–22.

Kleine, T., Munker, C., Mezger, K. and Palme, H. (2002). Rapid accretion and early core formation on asteroids and the terrestrial planets from Hf–W chronometry. *Nature* **418**, 952–5.

Lee, D.-C. and Halliday, A. N. (1995). Hafnium–tungsten chronometry and the timing of terrestrial core formation. *Nature* **378**, 771–4.

Lee, D.-C. and Halliday, A. N. (1996). Hf–W isotopic evidence for rapid accretion and differentiation in the early solar system. *Science* **274**, 1876–9.

Lee, D.-C. and Halliday, A. N. (2000). Hf–W internal isochrons for ordinary chondrites and the initial ^{182}Hf–^{180}Hf of the solar system. *Chem. Geol.* **169**, 35 43.

Lee, D.-C., Halliday, A. N., Snyder, G. A. and Taylor, L. A. (1997). Age and origin of the Moon. *Science* **278**, 1098–103.

Lee, T. (1978). A local proton irradiation model for isotopic anomalies in the solar system. *Astrophys. J.* **224**, 217–26.

Lee, T., Papanastassiou, D. A. and Wasserburg, G. J. (1976). Demonstration of ^{26}Mg excess in Allende and evidence for ^{26}Al. *Geophys. Res. Lett.* **3**, 109–13.

Lee, T., Papanastassiou, D. A. and Wasserburg, G. J. (1977). Aluminum-26 in the early solar-system: fossil or fuel? *Astrophys. J. (Lett.)* **211**, L107–10.

Lee, T., Shu, F. H., Shang, H., Glassgold, A. E. and Rehm, K. E. (1998). Protostellar cosmic rays and extinct radioactivities in meteorites. *Astrophys. J.* **506**, 898–912.

Lewis, R. S., Amari, S. and Anders, E. (1990). Meteoritic silicon carbide: pristine material from carbon stars. *Nature* **348**, 293–8.

Lineweaver, C. H. (1999). A younger age for the universe. *Science* **284**, 1503–7.

Lugmair, G. W. and Marti, K. (1977). Sm–Nd–Pu timepieces in the Angra dos Reis meteorite. *Earth Planet. Sci. Lett.* **35**, 273–84.

Lugmair, G. W. and Shukolyukov, A. (1998). Early solar system timescales according to ^{53}Mn–^{53}Cr systematics. *Geochim. Cosmochim. Acta* **62**, 2863–86.

Mahoney, W. A., Ling, J. C., Wheaton, W. A. and Jacobsen, A. S. (1984). HEAO-3 discovery of ^{26}Al in the interstellar medium. *Astrophys. J.* **286**, 578–85.

Marhas, K. K., Goswami, J. N. and Davis, A. M. (2002). Short-lived nuclides in hibonite grains from Murchison: evidence for Solar System evolution. *Science* **298**, 2182–5.

McCulloch, M. T. and Bennett, V. C. (1993). Evolution of the early Earth: constraints from ^{143}Nd–^{142}Nd isotopic systematics. *Lithos* **30**, 237–55.

McKeegan, K. D., Chaussidon, M. and Robert, F. (2000). Incorporation of short-lived ^{10}Be in a calcium–aluminum-rich inclusion from the Allende meteorite. *Science* **289**, 1334–7.

Nichols, R. H., Hohenberg, C. M., Kehm, K., Kim, Y. and Marti, K. (1994). I–Xe studies of the Acapulco meteorite: absolute I–Xe ages of individual phosphate grains and the Bjurbole standard. *Geochim. Cosmochim. Acta* **58**, 2553–61.

Niemeyer, S. (1979). I–Xe dating of silicate and troilite from IAB iron meteorites. *Geochim. Cosmochim. Acta* **43**, 843–60.

Norman, E. B. and Schramm, D. N. (1983). ^{182}Hf chronometer for the early Solar System. *Nature* **304**, 515–17.

Nuth, J. (1991). Small grains of truth. *Nature* **349**, 18–19.

Nyquist, L., Lindstrom, D., Mittlefehldt, D. *et al.* (2001). Manganese–chromium formation intervals for chondrules from Bishunpur and Chainpur meteorites. *Meteoritics Planet. Sci.* **36**, 911–38.

Ott, U. (2000). Salty old rocks. *Science* **288**, 1761–2.

Podosek, F. A. (1970). Dating of meteorites by the high-temperature release of iodine-correlated Xe^{129}. *Geochim. Cosmochim. Acta* **34**, 341–65.

Reynolds, J. H. (1960). Determination of the age of the elements. *Phys. Rev. Lett.* **4**, 8–9.

Rotaru, M., Birck, J. L. and Allègre, C. J. (1992). Clues to early solar-system history from chromium isotopes in carbonaceous chondrites. *Nature* **358**, 465–70.

Russell, S. S., Gounelle, M. and Hutchison, R. (2001). Origin of short-lived radionuclides. *Phil. Trans. Roy. Soc. Lond. A* **359**, 1991–2004.

Russell, S. S., Srinivasan, G., Huss, G. R., Wasserburg, G. J. and MacPherson, G. J. (1996). Evidence for widespread ^{26}Al in the Solar Nebula and constraints for nebular time scales. *Science* **273**, 757–62.

Sahijpal, S., Goswami, J. N., Davis, A. M., Grossman, L. and Lewis, R. S. (1998). A stellar origin for the short-lived nuclides in the early Solar System. *Nature* **391**, 559–61.

Schoenberg, R., Kamber, B. S., Collerson, K. D. and Eugster, O. (2002a). New W-isotope evidence for rapid terrestrial accretion and very early core formation. *Geochim. Cosmochim. Acta* **66**, 3151–60.

Schoenberg, R., Kamber, B. S., Collerson, K. D. and Moorbath, S. (2002b). Tungsten isotope evidence from ~3.8-Gyr metamorphosed sediments for early meteorite bombardment of the Earth. *Nature* **418**, 403–5.

Schonbachler, M., Rehkamper, M., Halliday, A. N. *et al.* (2002). Niobium–zirconium chronometry and early solar system development. *Science* **295**, 1705–8.

Schramm, D. N. and Wasserburg, G. J. (1970). Nucleochronologies and the mean age of the elements. *Astrophys. J.* **162**, 57–69.

Seeger, P. A., Fowler, W. A. and Clayton, D. D. (1965). Nucleosynthesis of heavy elements by neutron capture. *Astrophys. J. Suppl.* **11**, 121–66

Sharma, M., Papanastassiou, D. A., Wasserburg, G. J. and Dymek, R. F. (1996). The issue of the terrestrial record of ^{146}Sm. *Geochim. Cosmochim. Acta* **60**, 2037–47.

Shu, F. H., Shang, H., Glassgold, A. E. and Lee, T. (1997). X-rays and fluctuating X-winds from protostars. *Science* **277**, 1475–9.

Shu, F. H., Shang, H. and Lee, T. (1996). Toward an astrophysical theory of chondrites. *Science* **271**, 1545–51.

Shukolyukov, A. and Lugmair, G. W. (1993a). Live iron-60 in the early solar system. *Science* **259**, 1138–42.

Shukolyukov, A. and Lugmair, G. W. (1993b). ^{60}Fe in eucrites. *Earth Planet. Sci. Lett.* **119**, 159–66.

Srinivasan, G., Goswami, J. N. and Bhandari, N. (1999). ^{26}Al in eucrite Piplia Kalan: plausible heat source and formation chronology. *Science* **284**, 1348–50.

Srinivasan, G., Sahijpal, S., Ulyanov, A. A. and Goswami, J. N. (1996). Ion microprobe studies of Efremovka CAIs: II. Potassium isotope composition and ^{41}Ca in the early Solar System. *Geochim. Cosmochim. Acta* **60**, 1823–35.

Srinivasan, G., Ulyanov, A. A. and Goswami, J. N. (1994). ^{41}Ca in the early Solar System. *Astrophys. J. (Lett.)* **431**, L67–70.

Steele, I. M. and Hutcheon, I. D. (1979). Anatomy of Allende inclusions: mineralogy and Mg isotopes in two Ca–Al-rich inclusions. *Lunar Planet. Sci.* **10**, 1166–8 (abstract).

Sugiura, N., Shuzou, Y. and Ulyanov, A. (2001). Beryllium–boron and aluminium–magnesium chronology of calcium–aluminium-rich inclusions in CV chondrites. *Meteoritics Planet. Sci.* **36**, 1397–408.

Swindle, T. D., Caffee, M. W., Hohenberg, C. M., Lindstrom, M. M. and Taylor, G. J. (1991). Iodine–xenon studies of petrographically and chemically characterized Chainpur chondrules. *Geochim. Cosmochim. Acta* **55**, 861–80.

Swindle, T. D., Davis, A. M., Hohenberg, C. M., MacPherson, G. J. and Nyquist, L. E. (1996). Formation times of chondrules and Ca–Al-rich inclusions: constraints from short-lived radionuclides. In: Hewins, R. H., Jones, R. H. and Scott, E. R. D. (Eds.), *Chondrules and the Protoplanetary Nebula*. Cambridge University Press, pp. 77–86.

Tachibana, S. and Huss, G. R. (2003). Iron-60 in troilites from an unequilibrated ordinary chondrite and the initial Fe-60/Fe-56 in the early solar system. *Lunar Planet. Sci.* **34**, abstract 1737.

Trivedi, B. M. P. (1977). A new approach to nucleocosmochronology. *Astrophys. J.* **215**, 877–84.

Truran, J. W., and Cameron, A. G. W. (1978). ^{26}Al production in explosive carbon burning. *Astrophys. J.* **219**, 226–9.

Wasserburg, G. J. (1985). Short-lived nuclei in the early solar-system. In: Black, D. C. and Matthews, M. S. (Eds.), *Protostars and Planets II*. University of Arizona Press, pp. 703–37.

Wasserburg, G. J., Busso, M. and Gallino, R. (1996). Abundances of actinides and short-lived non-actinides in the interstellar medium: diverse supernova sources for the r-process. *Astrophys. J. (Lett.)* **466**, L109–13.

Wasserburg, G. J., Fowler, W. A. and Hoyle, F. (1960). Duration of nucleosynthesis. *Phys. Rev. Lett.* **4**, 112–14.

Wasserburg, G. J. and Hayden, R. J. (1955). Time interval between nucleogenesis and the formation of meteorites. *Nature* **176**, 130–1.

Wasserburg, G. J., Lee, T. and Papanastassiou, D. A. (1977). Correlated O and Mg isotopic anomalies in Allende inclusions: II magnesium. *Geophys. Res. Lett.* **4**, 299–302.

Wasserburg, G. J. and Papanastassiou, D. A. (1982). Some short-lived nuclides in the early solar-system – a connection with the placental ISM. In: Barnes, C. A., Clayton, D. D. and Schramm, D. N. (Eds.), *Essays in Nuclear Astrophysics*. Cambridge University Press, pp. 77–140.

Wasserburg, G. J., Schramm, D. N. and Huneke, J. C. (1969). Nuclear chronologies for the galaxy. *Astrophys. J. (Lett.)* **157**, L91–6.

Whitby, J. A., Gilmour, J. D., Turner, G., Prinz, M. and Ash, R. D. (2002). Iodine–xenon dating of chondrules from Qingzhen and Kota Kota enstatite chondrites. *Geochim. Cosmochim. Acta* **66**, 347–59.

Yin, Q., Jacobsen, S. B., Yamashita, K., Blichert-Toft, J., Telouk, P. and Albarede, F. (2002). A short timescale for terrestrial planet formation from Hf–W chronometry of meteorites. *Nature* **418**, 949–52.

Zinner, E., Amari, S., Anders, E. and Lewis, R. (1991). Large amounts of extinct ^{26}Al in interstellar grains from the Murchison meteorite. *Nature* **349**, 51–4.

16 Fission-track dating

'Fission tracks' are not, strictly speaking, radiogenic nuclides, but they are the damage tracks left by fission products, which represent a special kind of radiogenic nuclide. As such, the abundance of fission tracks in geological materials increases over time in the same way as the concentration of a radiogenic isotope. Fission-track dating was first developed simply as a dating tool for general application. However, the susceptibility of fission tracks to thermal re-setting, which was originally a disadvantage, has been put to very good use as a measure of cooling, uplift and burial processes.

16.1 Track formation

The spontaneous fission of ^{238}U releases about 200 MeV of energy, much of which is transferred to the two product nuclides as kinetic energy. They travel about 7 μm in opposite directions, leaving a single trail of damage through the medium which is about 15 μm long. Fission-fragment tracks were originally observed in cloud chambers and photographic emulsions. Subsequently, Silk and Barnes (1959) produced artificial tracks in muscovite by irradiating uranium-coated flakes in a reactor. The resulting fragment tracks were observed at high magnification under the electron microscope.

'Fission tracks' (Fleischer *et al.*, 1964) are found only in insulating materials. Fleischer *et al.* (1965a) proposed that the passage of the charged fission fragment causes ionisation of atoms along its path by stripping away electrons (Fig. 16.1a). The positively charged ions then repel each other, creating a cylindrical zone of disordered structure (Fig. 16.1b). This, in turn, causes relaxation stress in the surrounding matrix. It is the resulting 100-Å (10-nm)-wide zone of strain (Fig. 16.1c) which is actually seen under the electron microscope. Conductors do not display fission tracks because the free movement of electrons in their lattice structure neutralises the charged damage zone.

The ability to generate tracks depends on the mass of the ionising particle and the density of the medium. In muscovite, the lowest-mass particle which can generate tracks by irradiation is about 30 atomic mass units (a.m.u.). Fission fragments, with masses of about 90 and 135 a.m.u. respectively, are well above this threshold, so they always generate tracks. On the other hand, α particles, the major product of uranium decay, are so far below the critical mass that they cannot create tracks. Neither can they cause track erasure (Fleischer *et al.*, 1965b).

Price and Walker (1962a) showed that when irradiated material was abraded to expose fission tracks at the surface, the damage zone could be preferentially dissolved by mineral acids, leading initially to a very fine channel only 25 Å wide. However, this could be enlarged by further chemical etching to yield a wide pit that was observable under the optical microscope. Price and Walker (1962b) first discovered 'fossil' fission tracks in minerals, created by the spontaneous fission of dispersed uranium atoms. They went on to suggest (Price and Walker, 1963) that their density could be used as a dating tool for geological materials up to a billion years old. This was verified by Fleischer *et al.* (1965a), who obtained dates on artificial and natural glasses and minerals that were in agreement with ages obtained by other methods (Fig. 16.2).

Price and Walker (1963) demonstrated that spontaneous fission of ^{238}U was the only significant source of tracks in most natural materials. Induced fission of ^{235}U by natural thermal neutrons can be ignored, as can cosmic-ray-induced fission of uranium. Spallation recoils induced by cosmic rays could, in principle, generate tracks in geological material exposed at the surface for very long periods. This is the principal source of tracks in meteorites (e.g. Lal *et al.*, 1969), but atmospheric shielding reduces their abundance to negligible levels in terrestrial rocks (Fleischer *et al.*, 1975). Therefore the total production of spontaneous fission tracks (F_s) per unit volume of rock can be derived from the general decay equation [1.9]:

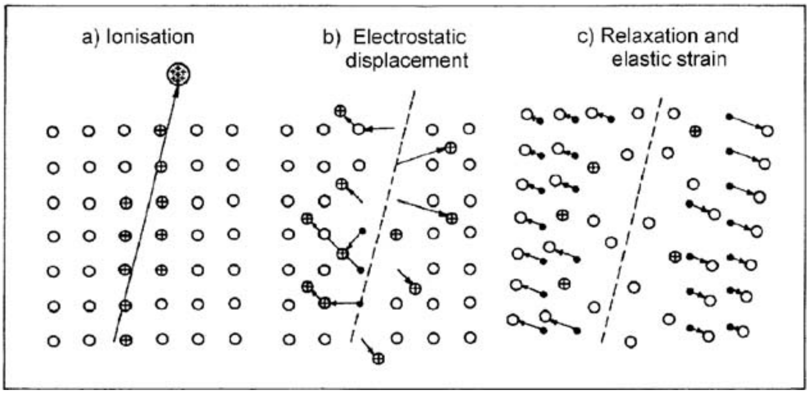

Fig. 16.1. Schematic illustration of the process of formation of a fission track in a crystalline insulating solid. After Fleischer *et al.* (1975).

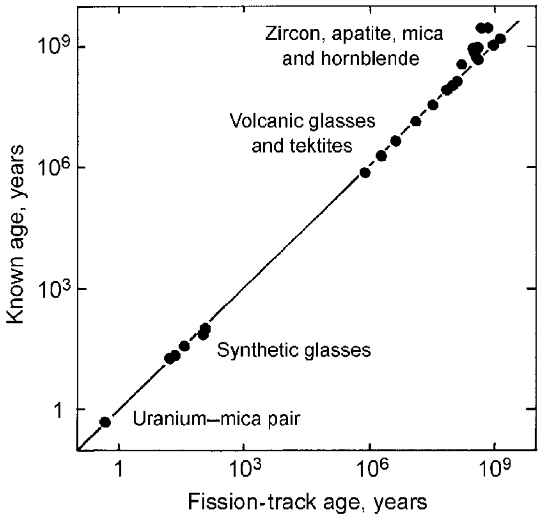

Fig. 16.2. A comparison of ages determined by fission-track analysis with those from historical or other radiometric sources. After Fleischer *et al.* (1965a).

$$F_s = \frac{\lambda_{\text{fission}}}{\lambda_\alpha}\,{}^{238}\text{U}(e^{\lambda_\alpha t} - 1) \qquad [16.1]$$

The ^{238}U fission decay constant is about $7 \times 10^{-17}\,\text{yr}^{-1}$ ($t_{1/2} = 9.9 \times 10^{15}$ yr; Naeser *et al.*, 1989). There is some disagreement as to its exact value, but it will be seen below that this uncertainty need not enter into geological age determinations. Fissiogenic decay is over a million times lower than the α-decay constant of ^{238}U, so it can be ignored in determining the isotopic abundance of uranium through time.

After polishing and etching a surface of the material to be dated, a fraction q of the total tracks will be visible at the surface. Therefore the measured spontaneous fission-track density, ρ_s, will be qF_s:

$$\rho_s = q\frac{\lambda_{\text{fission}}}{\lambda_\alpha}\,{}^{238}\text{U}(e^{\lambda_\alpha t} - 1) \qquad [16.2]$$

Price and Walker recognised that the most effective way of measuring the uranium concentration was to irradiate the sample with neutrons in a reactor, and thereby produce artificial tracks by the induced fission of ^{235}U. From [16.2], the induced track density will be

$$\rho_i = q\,{}^{235}\text{U}\varphi\sigma \qquad [16.3]$$

where φ is the thermal neutron flux per unit volume and σ is the cross-section of ^{235}U for induced fission by thermal neutrons. If the sample material, including uranium concentration and etching procedure, is identical for these two experiments, then the ratio of track densities can be used to solve for t, and then q drops out of the equation and the uranium concentrations are replaced by the ^{238}U/^{235}U isotope ratio of 137.88:

$$\frac{\rho_s}{\rho_i} = \frac{\lambda_{\text{fission}}}{\lambda_\alpha}\frac{137.88}{\varphi\sigma}(e^{\lambda_\alpha t} - 1) \qquad [16.4]$$

This can be rearranged to yield an equation in terms of t:

$$t = \frac{1}{\lambda_\alpha}\ln\left(1 + \frac{\rho_s}{\rho_i}\frac{\lambda_\alpha}{\lambda_{\text{fission}}}\frac{\varphi\sigma}{137.88}\right) \qquad [16.5]$$

It is possible to determine φ and σ directly by using flux monitors such as iron wire or copper foil. However, these types of flux monitors might not react to reactor conditions in exactly the same way as geological material. Therefore, a better procedure is to do a fission-track analysis of a standard material with known uranium concentration. Fleischer *et al.* (1965a) used fragments of glass microscope-slides to calibrate the Brookhaven graphite reactor in this way. However, this does not avoid the uncertainty of the ^{238}U fission decay constant.

To eliminate both the flux term and the decay-constant term, many workers started to use minerals dated by K–Ar analysis as internal standards for the irradiation. Fleischer and Hart (1972) formalised this system into the 'zeta calibration'. A sample of known age is used to calculate ζ by rearranging equation [16.4] and dividing both sides by the track density ρ_d in a given glass dosimeter:

$$\zeta = \frac{\varphi\sigma}{137.88\lambda_{\text{fission}}\rho_d} = \frac{e^{\lambda_\alpha t} - 1}{\lambda_\alpha(\rho_s/\rho_i)\rho_d} \qquad [16.6]$$

To date an unknown sample, the age equation [16.5] is now modified by substitution of ζ:

$$t = \frac{1}{\lambda_\alpha}\ln\left(1 + \frac{\zeta\lambda_\alpha\rho_s\rho_d}{\rho_i}\right) \qquad [16.7]$$

The failure to resolve the decay constant problem can perhaps be attributed to this method, which transfers the uncertainty into the age determination of the geological reference material. Use of such material was recommended for all fission-track dating studies by a working group of the IUGS Subcommission on Geochronology (Hurford, 1990). One of the most well-known of these standards is the 28-Myr-old Fish Canyon Tuff, Colorado (Naeser *et al.*, 1981; Hurford and Green, 1983).

16.2 Track etching

Several different types of geological material are suitable for the determination of fission-track ages. Fleischer and Price (1964a) tested them with various acid or alkali leaching solutions to determine the most effective etching treatment for track observation. The precise progress of the etching process depends on the composition of the matrix, and the nature, concentration and temperature of the acid. This can give rise to a surprising variation in the appearance of etched tracks in different materials (e.g. Fig. 16.3), and may affect the accuracy of track counting. These problems were discussed by Fleischer and Price (1964b) in an assessment of the fission-track dating of glass.

The geometry of an etched track depends on the rate of etching down the axis of the track (from its intersection with the surface), relative to the general rate of attack of the polished surface (Fig. 16.4a). One problem in accurate track counting is to distinguish etched tracks from other features. For example, track pits in glass are at first pointed, but with increasing etching time they round out. The optimal etching time is therefore a compromise between the need to make large enough pits to count quickly, and the tendency for large round-bottomed pits to be confused with etched porosity. However, this is not such a problem in mineral phases.

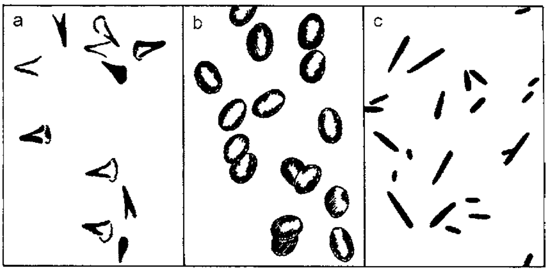

Fig. 16.3. Drawings of etched fission tracks induced by the same source (^{252}Cf) in various materials: (a) K-feldspar, (b) soda–lime glass and (c) Lexan polycarbonate. The width of each field is 40 μm. From photographs by Fleischer *et al.* (1968).

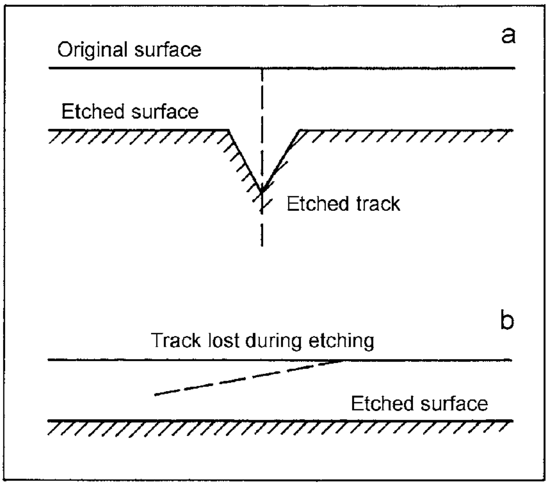

Fig. 16.4. Schematic illustration of the progress of track etching: (a) perpendicular and (b) tangential to the surface. After Fleischer and Price (1964b).

Another source of uncertainty, both for glass dating and for mineral dating, is caused by tracks that barely register in the etched surface. For example, tracks that are almost tangential to the surface may be completely erased by etching (Fig. 16.4b). Other tracks might not have intersected the original polished surface, but are exposed by the general attack of the surface during etching. These discrepancies will average out statistically if large numbers of tracks are counted with identical spatial geometry (see below), but may cause large

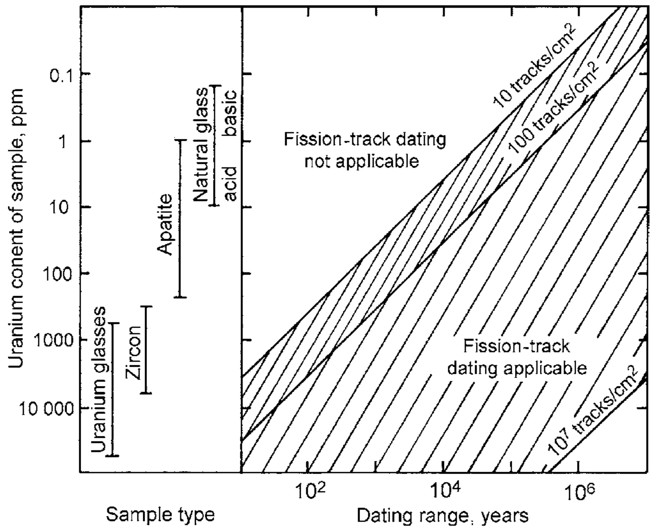

Fig. 16.5. Diagram to show the dating range for fission-track analysis of various kinds of geological material according to uranium content. After Wagner (1978).

errors when spatial geometry varies. A more detailed discussion of track formation and track etching is given by Fleischer *et al.* (1975).

Fleischer and Price (1964a) estimated the dating range of fission-track analysis with various types of material. Using the criterion that dates of reasonable precision can be determined only when the track density is at least 100 per cm^2, the lower end of the dating range can be estimated for various types of material according to uranium content (Fig. 16.5).

16.3 Counting techniques

Close examination must now be given to the assumptions involved in fission-track dating. The first of these, noted above, is that the induced track count is performed on identical material to that used for the spontaneous track count. Several different experimental methods that attempt to attain this ideal are available. Different approaches may be best for different types of sample material.

16.3.1 The population method

This expression was coined by Naeser (1979a), but was effectively the method adopted by the earliest workers (e.g. Price and Walker, 1963). The term refers to the fact that spontaneous and induced tracks are counted in different splits or sub-populations of material, which are nevertheless assumed to sample the same population. This depends on the material having a homogeneous distribution of uranium between the two splits. The method has proved particularly successful for dating glass and apatite, but unsuccessful for sphene and zircon, where uranium distribution is very variable both within and between grains.

To apply the population method, the sample is separated into two splits (Fig. 16.6). One is irradiated with, thermal neutrons, together with a standard (the flux monitor). Both spontaneous and induced tracks are to be registered under spherical (4π) spatial geometry. Therefore, after irradiation of the induced-track split, both splits are mounted in epoxy resin, ground, polished and etched under identical conditions. This reveals an internal surface of the material and also removes any extraneous superficial tracks generated by uranium-bearing dust particles. Track densities are counted in both splits. The induced-track density is calculated by subtracting the spontaneous-track density (un-irradiated sample) from the total track density (irradiated sample).

The population method should be statistically tested by counting track densities in numerous grains or glass shards in each split. Alternatively, if a large piece of glass or mineral is available, it can be cut or cleaved so that the two faces to be counted are nearly identical sections through the sample. The latter method was adopted by Price and Walker (1963) in their analyses of muscovite. Price and Walker took the extra precaution of irradiating the split for spontaneous-track counting in a cadmium box (which screens out thermal neutrons) so that both splits should be treated as nearly identically

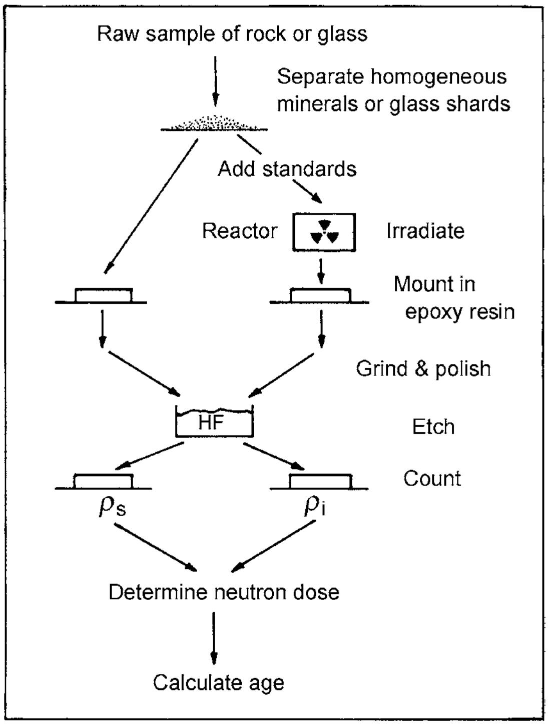

Fig. 16.6. Schematic illustration of the population method of fission-track analysis. After Naeser and Naeser (1984).

as possible prior to etching. However, this precaution has now been dispensed with.

In the analysis of apatite, pre-irradiation heating of the induced-track split to erase all spontaneous tracks by thermal annealing has been found advantageous (see below). This allows the induced-track density to be determined directly in the irradiated split. However, this procedure may be problematical in dating glass because it may affect the etching properties of the irradiated split, leading to systematic track-counting errors.

16.3.2 The external-detector method

In this technique (Fleischer *et al.*, 1965a) the uranium content of the material to be dated is determined by inducing counts in an external detector rather than in the sample material itself. The sample is ground, polished, etched and counted, after which a sheet of detector material is placed in intimate contact with the etched surface. This must be done with absolute cleanliness in order to exclude uranium-bearing dust grains (see above). The external detector is commonly a low-uranium mica or a plastic such as lexan. After irradiation, the external detector is removed from the sample, etched and counted (Fig. 16.7).

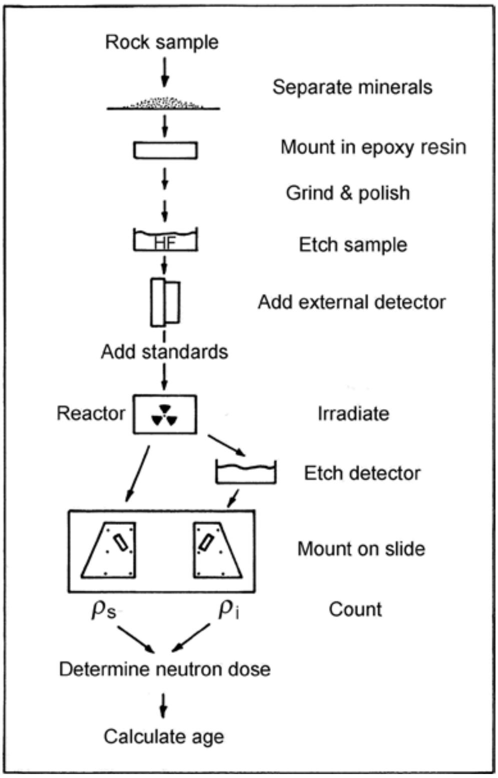

Fig. 16.7. Schematic illustration of the external-detector method of fission-track analysis, as described by Naeser (1979a). In this version the counting of spontaneous tracks is performed after irradiation, unlike the sequence described in the text. After Naeser and Naeser (1984).

The advantage of the external-detector method is that both spontaneous and induced tracks are generated by the same sample material. Hence, it is suited to the analysis of material with a very heterogeneous distribution of uranium. The main disadvantage of the method is that the spontaneous and induced tracks are recorded under different spatial-geometry conditions (Fig. 16.8). Spontaneous tracks are generated in the interior of the rock, and can therefore be formed by uranium atoms both above and below the etched plane (spherical or 4π geometry). In contrast, tracks induced in the external detector come out from the surface of the analysed material and are therefore generated with approximately one-half the frequency (hemispherical or 2π geometry). Reimer *et al.* (1970) questioned whether

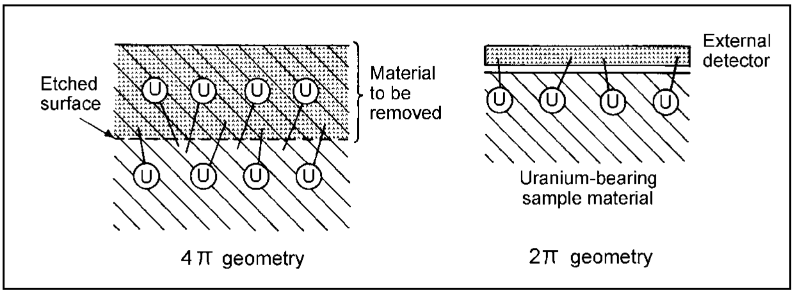

Fig. 16.8. Schematic illustration of the difference between 4π and 2π geometry in track formation.

the efficiency of induced-track formation is exactly 50%, or whether small biases are introduced. However, subsequent experiments (discussed by Hurford and Green, 1982) showed that the ideal efficiency of 50% is achieved in most cases.

16.3.3 Re-etching and re-polishing

The re-etching technique, described by Price and Walker (1963), is similar to the external-detector method in that a sample is irradiated *after* polishing, etching and counting of spontaneous tracks. However, the sample itself is now re-etched and re-counted to determine the induced-track density by subtraction. As for the external method, induced tracks are formed with only 50% efficiency (2π geometry). The disadvantage of this method is that spontaneous-track pits will be unduly enlarged after the second etch, and may obscure some induced tracks. It is consequently less popular than the external method.

The re-polishing technique (Naeser *et al.*, 1989) is an improvement on the re-etching method, and yields results similar to those obtained with the 'mirror-image' population method (Price and Walker, 1963). The sample is polished, etched and counted for spontaneous-track density. After irradiation, it is re-polished to a depth of at least 20 μm to reveal a new internal face with 4π track geometry. This is then etched and counted to determine the induced-track density by subtraction. The method has the advantage that both spontaneous and induced tracks are recorded under identical geometry, and spontaneous tracks are not over-enlarged by double etching. Also, surface contamination during irradiation is not a problem. The spontaneous and induced tracks are not generated by exactly the same sample material, but the two etched surfaces are so close together that uranium inhomogeneity in the grain as a whole is unlikely to bias the data significantly. A disadvantage compared with the normal population method is that the two etching steps are performed separately, and may therefore vary slightly in efficiency.

16.4 Detrital populations

An advantage of the external-detector method of fission-track counting is the ability to determine a separate age from each grain of the population (this also applies to the less widely used re-polishing method). This capability is useful if a heterogeneous age population is suspected, as in the case of sedimentary rocks with mixed provenance (e.g. Hurford and Carter, 1991). However, the scatter of analysis points generated by these kinds of sample can be a challenge when it comes to presentation of data.

Fission-track results for individual detrital grains may be presented in histogram form. However, a more quantitative age estimate is possible if errors are assigned to each individual grain determination, so that the data can be presented as a probability density function (Hurford *et al.*, 1984). This function is simply the summation of the Poisson age distributions for each of the individual grain determinations. Figure 16.9 shows such a plot for zircons from the reworked El Ocote tephra deposit in Mexico, which displays a bimodal age distribution (Kowallis *et al.*, 1986). The younger peak places a maximum age on the time of sedimentary reworking, and is in agreement with the estimated biostratigraphic age of associated fossil material. These results show that application of the population method to fission-track dating of this tephra would yield a meaningless average of the two age populations.

A problem with the probability density plot is that individual data points cannot be distinguished, so some important but small components in the data distribution can be buried under other data. To avoid this problem,

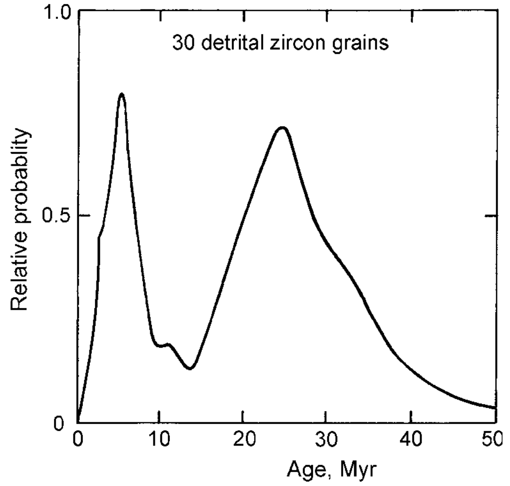

Fig. 16.9. Plot of probability density as a function of age for fission-track data on detrital zircons from the reworked El Ocote tephra from Mexico. After Kowallis *et al.* (1986).

Galbraith (1988) introduced a kind of isochron diagram for the presentation of fission-track data measured on individual grains of a heterogeneous sample. This 'radial' plot is designed for fission-track data sets with a high degree of scatter, due to either mixed detrital ages or variable cooling ages.

This diagram differs from other isochron plots used in geology because the two variables plotted are the apparent fission-track age of each grain and the standard error of each grain age (σ). These quantities are plotted in the form of age/σ against $1/\sigma$ (Fig. 16.10a). In this plot, the slope of an array indicates the average age of the suite of grains analysed, and this age can be indicated on a calibrated arc. In practice, Galbraith argued, it is more convenient to normalise the average slope to a horizontal, and plot the y axis on a log scale from $+2$ to -2 (Fig. 16.10b). The age of any individual point is then determined by projecting from the zero point on the y axis, through the data point, to the calibrated arc of ages (on a log scale).

An alternative data presentation of this type was proposed by Walter (1989). He suggested that additional assessments of the quality of detrital fission-track ages could be made if the raw data (spontaneous- *versus* induced-track densities) were plotted for each grain. This also yields an isochron diagram (Fig. 16.11) on which the slope of each correlation line is proportional to age. These lines should pass through the origin, corresponding to a grain with zero uranium content. The linearity of each correlation line can be used to assess the influence of systematic analytical errors or geological disturbance on the reliability of the best-fit ages. However, this presentation has not been as popular as the isochron diagram of Galbraith, which has found wide application to complex fission-track data sets, including partially annealed systems, as well as detrital systems.

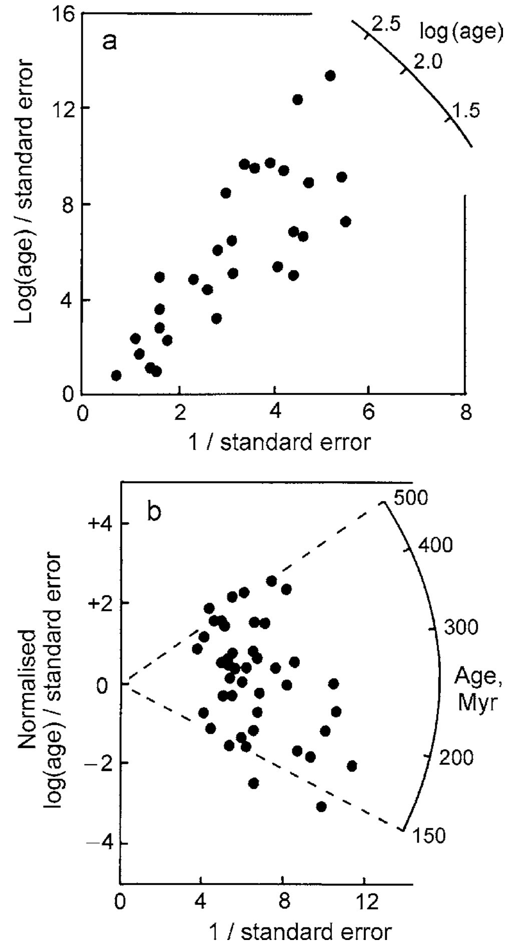

Fig. 16.10. Variations on the radial plot for presentation of single-grain fission-track data on heterogeneous samples: (a) raw data and (b) normalised. After Galbraith (1988).

16.5 Track annealing

From the very beginning of fission-track studies (Silk and Barnes, 1959) it has been known that fission-tracks can fade under certain conditions. This was first seen as

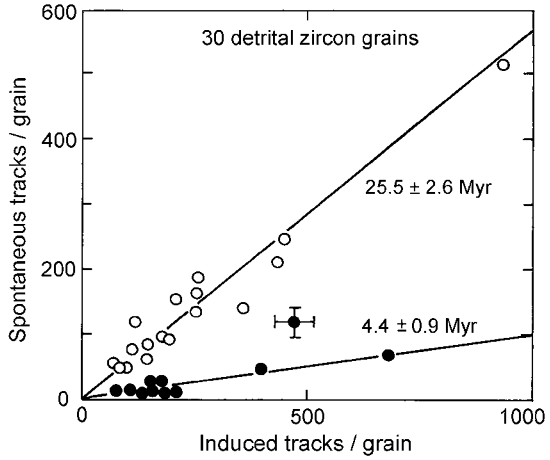

Fig. 16.11. Spontaneous- *versus* induced-track isochron diagram, showing data for individual zircon grains from the El Ocote tephra. After Walter (1989).

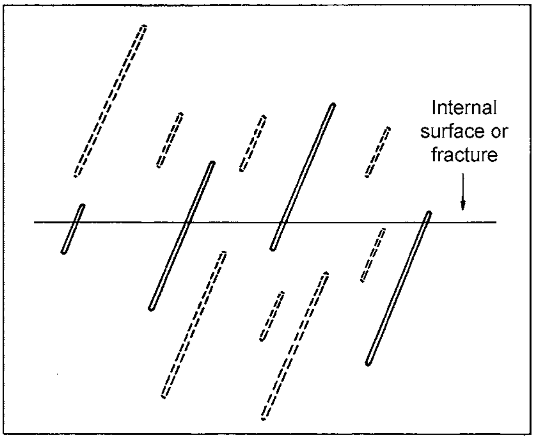

Fig. 16.12. Schematic illustration of the effect of track shortening on the observed density of etched tracks. Short and long tracks are of equal abundance, but the latter have a higher probability of becoming etched. After Laslett *et al.* (1982).

a result of electron bombardment during microscopy. However, elevated temperatures are the most important cause of track fading or 'annealing'. During this process the displaced ions within the damage track lose their charge and return to their normal lattice positions, after which the track is no longer susceptible to preferential acid attack.

Following experiments on track annealing in mica, Fleischer *et al.* (1964) claimed that track annealing progressed by the accumulated 'healing up' of short segments at random points along the length of tracks. However, subsequent work on other materials (e.g. on glass by Storzer and Wagner, 1969) has shown that the healing process occurs principally at the ends of each track, causing a regular and progressive shortening. As the length of tracks is diminished by healing, they have a smaller probability of intersecting the free surface during the etching treatment. Hence, fewer tracks become etched and the apparent track density decreases (Fig. 16.12). This correlation between track length and track density is termed the 'random-line-segment model' (Fleischer *et al.*, 1975).

Early studies showed that different materials have different degrees of resistance to fission-track annealing (Fleischer and Price, 1964a). In addition, a temperature–time relationship is found for the annealing process. The higher the temperature, the shorter the time required for complete annealing of tracks in any given material. To examine this behaviour, Fleischer and Price (1964b) performed laboratory annealing experiments on the mineral indochinite, and found that annealing obeyed a Boltzmann's law relation:

$$t = A\mathrm{e}^{E/(kT)} \qquad [16.8]$$

where t is the time for track fading, A is a constant, E is the activation energy, k is Boltzmann's constant and T is absolute temperature. Much of the work since this time has been devoted to determining accurate Boltzmann-relation annealing curves for various materials, both by laboratory work and in well-constrained geological studies.

Detailed laboratory experiments were performed on apatite and sphene by Naeser and Faul (1969) and on tektite glass by Storzer and Wagner (1969). The results showed that annealing is a progressive process. Different degrees of track annealing in different materials each define their own Boltzmann-relation lines on Arrhenius plots of time against reciprocal temperature (Fig. 16.13). The fan of annealing lines in Fig. 16.13 is evidence for the existence of a range of activation energies for track annealing within a single type of material. This implies that, as annealing progresses (measured in terms of the fraction of tracks lost), it also becomes progressively more difficult (Storzer and Wagner, 1969). Hence, when comparing the annealing properties of different minerals, it is necessary to compare samples with equal fractions of track loss, such as 50% (Fig. 16.13).

Following this line of investigation, Storzer and Poupeau (1973) compared laboratory annealing rates (in the same material) for freshly induced tracks and for spontaneous tracks that had been partially annealed in

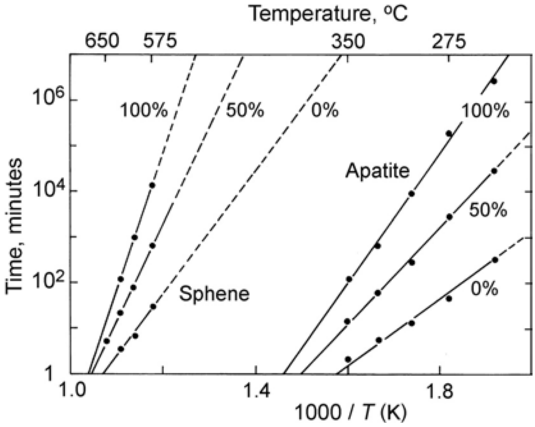

Fig. 16.13. Arrhenius plot to show the coherent progress of annealing in sphene (on the left) and apatite (on the right). After Naeser and Faul (1969).

nature. They found that as the temperature was raised the fresh tracks were initially lost at a much higher rate, but that at a certain 'plateau' temperature the rates of annealing became equal.

Storzer and Poupeau argued that if both spontaneous and induced tracks were subjected to a heat treatment before counting, then fission-track ages could be corrected for partial annealing in the environment. Track counting must be done by the population method; therefore the sample must have a uniform distribution of uranium. After irradiation of the induced-track sample, track-counting analysis is performed by stepwise annealing of both spontaneous- and induced-track samples in the laboratory. After each heating step, a new surface of both samples is polished, etched, and counted.

Results from this procedure are shown in Fig. 16.14 for a North American tektite. Above a certain threshold temperature (about 100 °C), induced tracks start to fade, but spontaneous tracks are resistant. Therefore the apparent fission-track age increases rapidly with temperature. However, as laboratory heating approaches the temperature at which annealing occurred in the environment, spontaneous tracks also start to fade, and the apparent age therefore reaches a plateau (Fig. 16.14). Storzer and Wagner (1982) argued that this 'plateau-annealing' technique can yield corrected fission-track ages in glasses with a precision of ±10% (2σ).

16.6 Uplift and subsidence rates

Wagner and Reimer (1972) demonstrated the usefulness of apatite fission-track ages for tectonic studies by applying them to Alpine uplift rates. Subsequently, Wagner *et al.* (1977) developed this technique by measuring apatite fission-track ages over a 3000-m range of vertical relief in the Central Alps. Fission-track ages on Alpine apatites do not conform to metamorphic isograds or terrane boundaries, but display a strong correlation with topographic relief (Fig. 16.15). They clearly represent cooling ages from Alpine metamorphism due to tectonic uplift, and can be used to calculate apparent uplift rates over the last few million years.

If a 'freezing-in' or 'blocking' temperature could be calculated for the Alpine apatites then the uplift rates in Fig. 16.15 could be converted into cooling rates. Two problems are faced in this task. The first is that the laboratory experiments show that blocking occurs over a range of temperatures. The second is that this range is itself dependent on the cooling rate. Hence, the argument is to some extent circular. Wagner *et al.* (1977) estimated a temperature for 50% track retention of 100–120 °C, half-way between 0% and 100% annealing temperatures of 60 and 180 °C, at a cooling

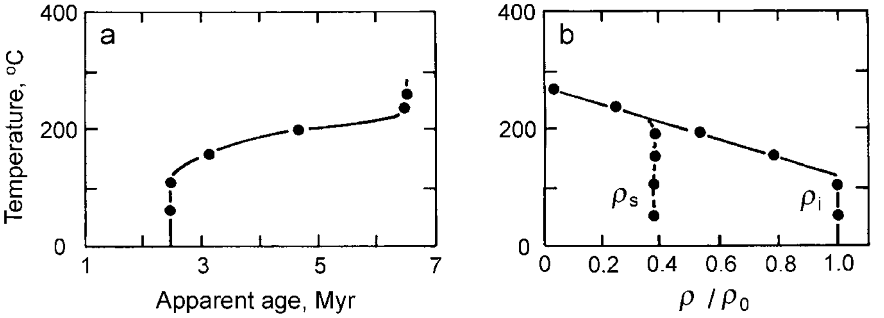

Fig. 16.14. Demonstration of the 'plateau-annealing' technique on a North American tektite: (a) apparent fission-track age as a function of temperature step; and (b) the fraction of induced and spontaneous tracks remaining at a given temperature (relative to the initial density ρ_0). After Storzer and Wagner (1982).

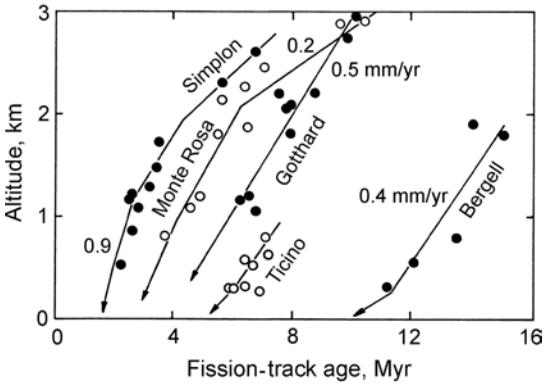

Fig. 16.15. Plot of fission-track ages against topographic altitude for Alpine apatites, and deduced apparent uplift rates. After Wagner *et al.* (1977).

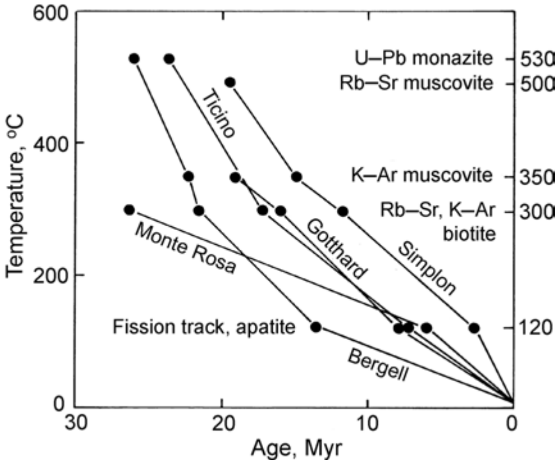

Fig. 16.16. Proposed cooling history for various regions of the Alps, based on time since closure of various radiogenic mineral systems (whose blocking temperatures are shown on the right-hand side). After Wagner *et al.* (1977).

rate of about 20 °C/Myr estimated from Rb–Sr biotite ages.

By combining apatite fission-track data with biotite K–Ar and Rb–Sr, muscovite K–Ar, muscovite Rb–Sr and monazite U–Pb data, Wagner *et al.* were able to calculate cooling rates for various regions of the Alps over the last 35 Myr (Fig. 16.16). These results suggest that cooling in the Central Alps (Ticino and Gotthard areas) has been relatively uniform, whereas that in the East (Bergell) has slowed and that in the West (Simplon and Monte Rosa) has speeded up during the last few million years. These conclusions are consistent with Fig. 16.15, and suggest that the Alps have undergone differential geographical uplift over time.

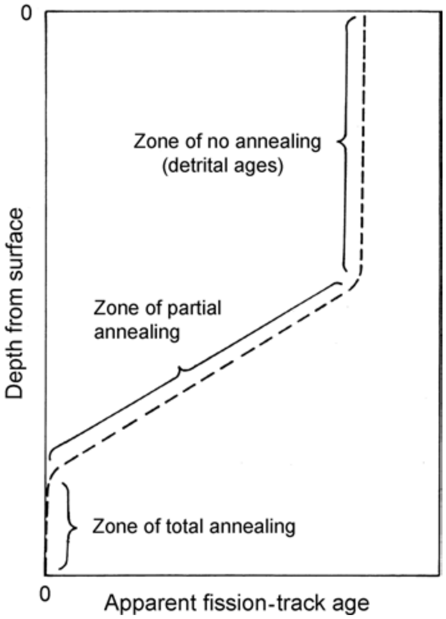

Fig. 16.17. Schematic illustration of the variation of apparent fission-track age with depth in borehole samples from a sedimentary basin. After Naeser (1979b) and Naeser *et al.* (1989).

The idea of using a vertical traverse of apatite fission-track ages to deduce tectonic histories was applied by Naeser (1979b) to borehole studies of sedimentary basins. Naeser proposed that, in sedimentary sequences that are at their maximum burial temperature, apparent fission-track ages would exhibit a relationship with burial depth similar to that shown in Fig. 16.17. At shallow depths, burial heating is insignificant and fission-track ages reflect the sediment source (detrital ages). As depth of burial increases, apatites undergo greater thermal annealing, and display decreasing apparent fission-track ages, until they finally reach a total annealing zone with zero apparent age. The interval between zero and total annealing is called the partial-annealing zone (PAZ).

The upper- and lower-temperature bounds of the PAZ will depend on the age of the sedimentary basin. Naeser (1981) collected fission-track age data from sedimentary basins with various burial rates. By making geological estimates of the effective burial (annealing) time in each basin, Naeser was able to make geological determinations of the Boltzmann lines for thermal annealing in apatite. These were confirmed by Gleadow and Duddy (1981) in a study of borehole

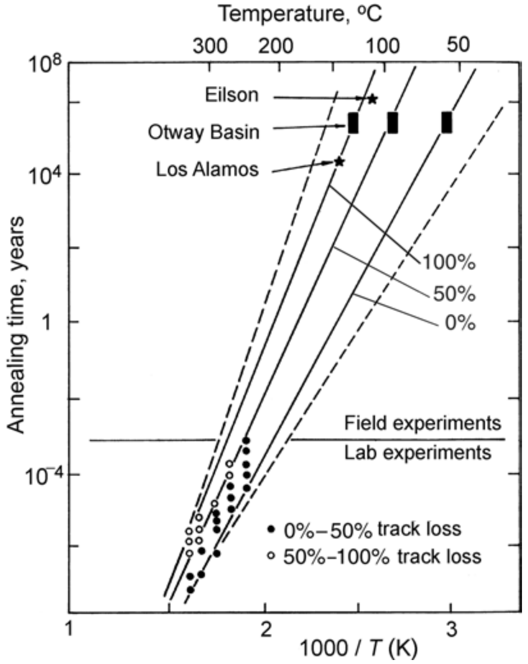

Fig. 16.18. Arrhenius plot for fission-track annealing in apatite from the Otway Basin boreholes (blocks), other boreholes (stars), and laboratory experiments (spots and dashed lines). After Gleadow and Duddy (1981).

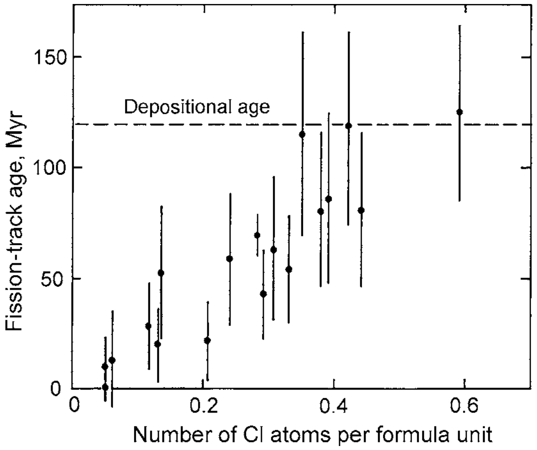

Fig. 16.19. Plot of measured fission-track ages in individual apatites from Otway Group sandstones, Australia, to show the compositional dependence of track annealing. After Green *et al.* (1985).

data from the Otway Basin of Victoria, SE Australia. This basin is particularly suitable for fission-track studies of burial rates because the basinal sediments were derived from an active volcanic province. Hence, the sediments entering the basin were essentially of zero age, with very little older provenance.

The effective annealing time at present-day downhole temperatures was estimated from the burial history of the basin, suggesting that peak temperatures have been maintained for about 30 Myr. Using these estimates, annealing properties were determined for the Otway Basin apatites (Fig. 16.18), which were consistent with other borehole data (Naeser, 1981). In addition, the Boltzmann line for 50% annealing was consistent with results of laboratory annealing experiments. However, the temperature *interval* between 0% and 100% annealing was narrower than that predicted by the divergence of Arrhenius-relation annealing lines from the laboratory data of Naeser and Faul (1969).

A complicating factor in the analysis of track fading in apatite is the discovery that annealing temperature is compositionally dependent (Green *et al.*, 1985). Fission-track analyses were performed on individual apatite grains from a single horizon in an Otway drill hole with a present-day temperature of 92 °C. These conditions result from progressive burial over the last 120 Myr. Chlor-apatite grains were found to give results near the depositional age, whereas fluor-apatites gave ages as low as zero (Fig. 16.19). Hence, when laboratory and geological annealing processes are compared, it is important that the material in the two types of experiment is as near compositionally identical as possible.

Bearing these findings in mind, Green *et al.* (1985) argued that Boltzmann lines for different percentages of track annealing did not have a fan-shaped distribution, but were parallel. This would imply that the activation energy for track fading was constant for all tracks in a given sample, and that track fading would *not* occur over a temperature interval, as assumed in the plateau method. However, close examination by Laslett *et al.* (1987) of the data set of Green *et al.* (1985) suggested that Boltzmann lines *are* divergent, although not to the extent suggested by early experiments (Fig. 16.20). This conclusion is also supported by more recent comparisons between laboratory data for apatite annealing and drill-hole data from the Otway basin (Green *et al.*, 1989). Hence, using more sophisticated models for the thermal and burial history of basin development, the laboratory and drill-hole data give coherent results.

In the above discussion, geologically well-known thermal-basin histories were used to calibrate the annealing behaviour of apatite tracks. Given this background, fission-track data can then be used to study geologically unknown basins. This evidence is especially

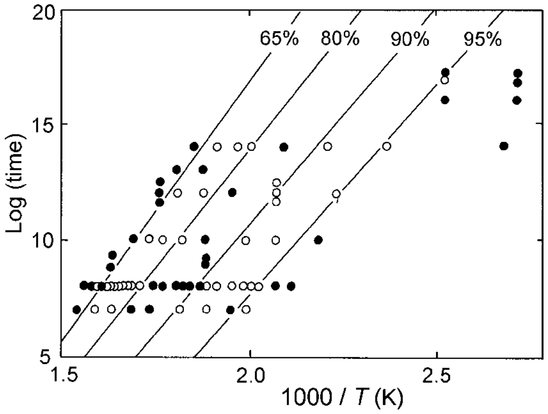

Fig. 16.20. Interpretation of laboratory annealing data, showing gently fanning Boltzmann lines that are consistent with field data from the Otway basin. Each line corresponds to a given percentage of track fading, fitted between each set of solid and open points. After Laslett *et al.* (1987).

pertinent to oil fields, because fission-track annealing occurs over the same temperature range as hydrocarbon maturation (Gleadow *et al.*, 1983). For example, Briggs *et al.* (1981) used this approach to compare the thermal histories of two sedimentary basins of the Tejon oil field, in the San Joaquin Valley of California. This oil field is divided into two parts by the seismically active White Wolf fault. One part, the Basin Block, was a Late Tertiary depocentre that underwent strong subsidence. The other, Tejon Block, was less depressed. Fission-track analysis of apatite from boreholes reveals the different geological histories of the two blocks (Fig. 16.21).

Naeser *et al.* (1989) used these data, together with Boltzmann-annealing lines from other geological locations, to calculate the thermal histories of the two blocks. Given geological evidence that the present-day down-hole temperatures are peak values, the temperatures necessary for total annealing can be used to calculate effective heating times of about 1 and 10 Myr for the Basin and Tejon blocks, respectively (Fig. 16.22). These results are consistent with geological evidence for much more rapid burial of the Basin Block, and do not require a perturbation in geothermal gradient.

16.7 Track-length measurements

Because annealing initially causes shortening of tracks rather than their complete erasure, the use of etched-track densities to chart the progress of annealing is

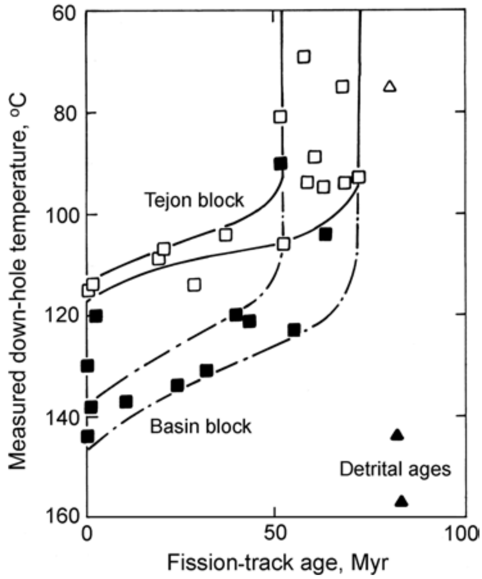

Fig. 16.21. A comparison between fission-track ages in boreholes from the Basin and Tejon blocks of the San Joaquin Valley, California. Apatite data (■, □) give thermal history information while zircon data (▲, △) yield provenance ages. After Naeser *et al.* (1989).

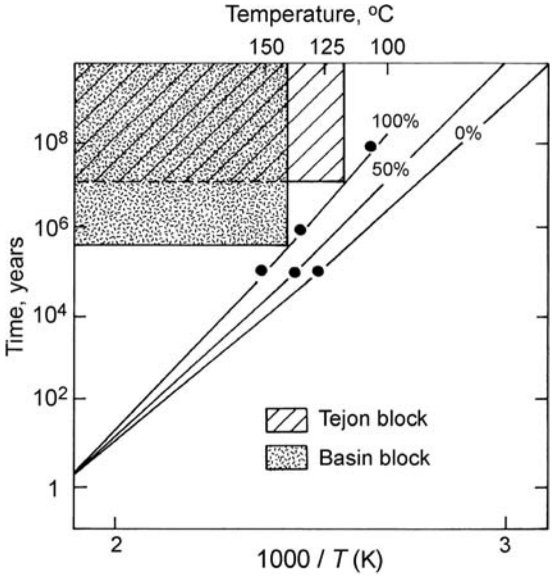

Fig. 16.22. Use of the Arrhenius plot to calculate effective heating times for the total annealing horizon in boreholes from the Tejon and Basin blocks, San Joaquin Valley, California. After Naeser *et al.* (1989).

an indirect approach. According to the 'random-line-segment model' of Fleischer *et al.* (1975) there should be a linear relationship between track density and average track length. However, when we only count track densities, we ignore information about the variation in track length on either side of the mean value. This *variation* in track length can yield additional information about the cooling history of a sample, because the longer the residence time of a sample in the partial annealing zone, the larger the variation in track length around the mean value. Therefore, fission-track data can be used more effectively to study the thermal history of a sample if the apparent age determined from track density is augmented by study of the length of etched tracks.

Track-length studies were first carried out in dating micas (Maurette *et al.*, 1964; Bigazzi, 1967), and were applied in detail to tektite glasses by Storzer and Wagner (1969). However, the etching of fission-tracks in glasses tends to yield circular pits because of the smaller difference in structure, and hence etching rate, between tracks and the free surface. Consequently, the progress of annealing in glasses is accompanied by a decrease in the diameter rather than length of etched tracks. Nevertheless, Storzer and Wagner showed that pit diameter was correlated with pit density in variably annealed tektite glasses, and were able to use the measurements of pit diameter to correct fission-track ages for the effects of annealing (Fig. 16.23).

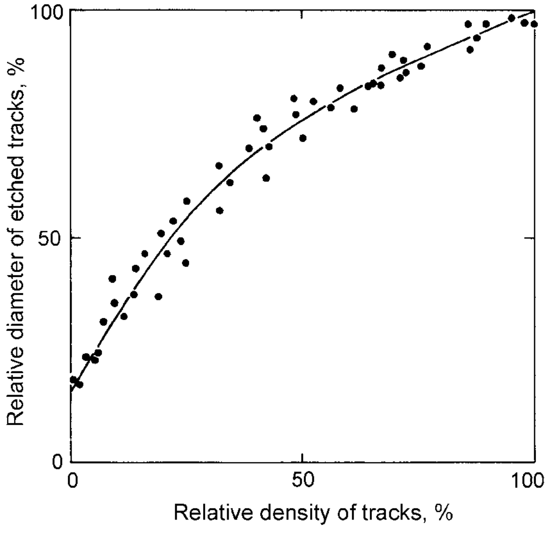

Fig. 16.23. Plot of mean pit diameter against pit density in variably annealed tektite glass samples, relative to the original pit size and density before annealing. After Storzer and Wagner (1969).

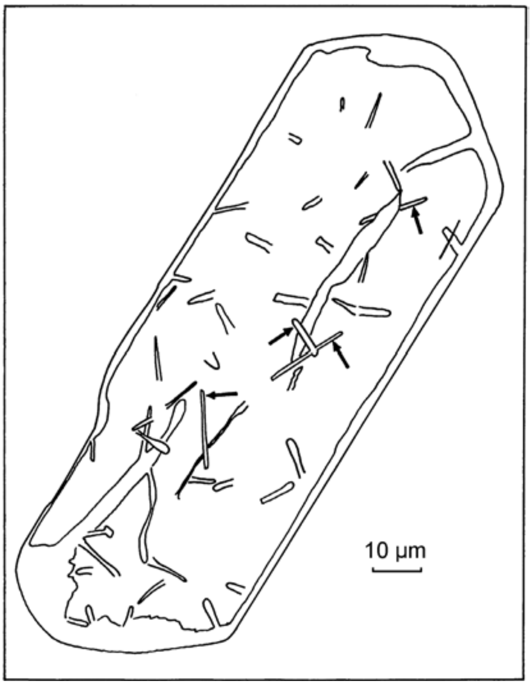

Fig. 16.24. Line drawing of high-contrast features in an etched apatite grain, viewed under dry (non-immersion) conditions. Four confined tracks are visible (arrowed). From a photograph by Gleadow *et al.* (1986).

For mineral samples, track-length data can be collected in two different ways. One is to measure the apparent lengths of tracks that intersect the etched surface. These are termed 'projected track lengths' (e.g. Dakowski, 1978). The alternative approach is to measure 'confined track length' (Bhandari *et al.*, 1971; Green, 1981; Laslett *et al.* 1982; 1984). These are tracks that do not break the general etched surface, but become etched by the penetration of acid down a channel inside the mineral that intersects the track (Fig. 16.24). The two most common types are termed 'Track-IN-Track' (TINT) and 'Track-IN-CLEavage' (TINCLE), respectively (Lal *et al.*, 1969; Fleischer *et al.*, 1975).

Measurement of confined tracks that are horizontal (parallel to the etched surface) leads to the minimum bias from the true track length. However, confined tracks must be counted using fixed selection criteria in order to exclude the possibility of subjective bias. Laslett *et al.* (1994) recommended the 'bright-reflection' criterion, which exploits the property that etched tracks at a low angle to the horizontal (less than about 15%) show a bright image in reflected light. In contrast, a criterion that requires tracks to be in

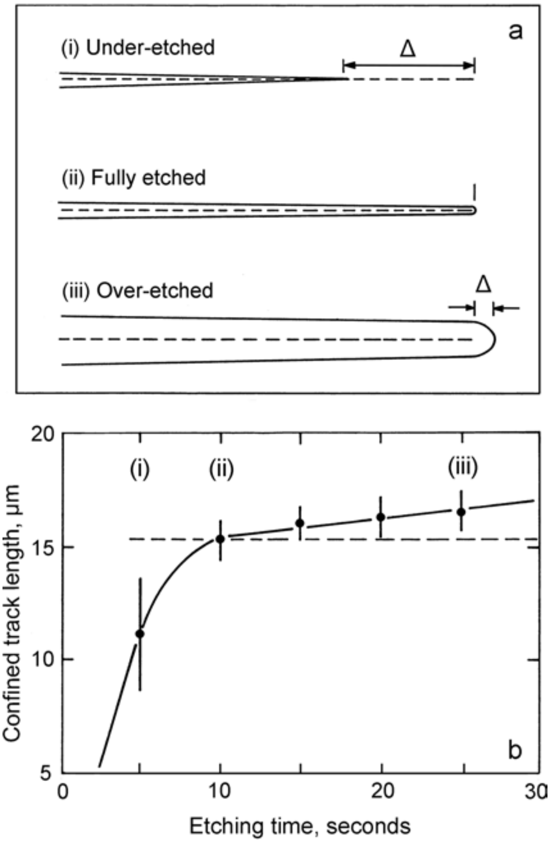

Fig. 16.25. Illustration of the progress of etching: (a) for a single track and (b) average track length in Durango apatite (Mexico) as a function of etching time in 5-M HNO_3 at 21 °C. After Laslett *et al.* (1984).

focus along their entire length is unsuitable because it causes a higher rejection rate for long tracks than for short tracks.

Another analytical variable that must be carefully controlled is the etching time. It is necessary that some tracks become over-etched to ensure that others are not under-etched. Since tracks have effectively zero width before etching, over-etched tracks can be recognised by their non-zero width, which is almost the same as the excess length (2Δ, Fig. 16.25a). The optimum etching time is determined by experiments on incremental etching (Fig. 16.25b). The standard etching time of 20 s used by Laslett *et al.* (1984) leads on average to 1 μm of over-etching.

Hejl (1995) identified an additional problem in recovering the true length distribution of annealed tracks from confined track lengths. This is due to the existence of unetchable gaps in the middle of tracks, a phenomenon that appears to be more widespread than previously realised. Hejl proposed that the true lengths of confined tracks could be recovered, despite the presence of unetchable gaps, by a double-etching procedure. This breaks through the 'unetchable gap' to produce a track with a wide middle (doubly etched) and a narrow extension (beyond the original gap). The total track length can then be measured (Fig. 16.26). This procedure would be more difficult on projected tracks.

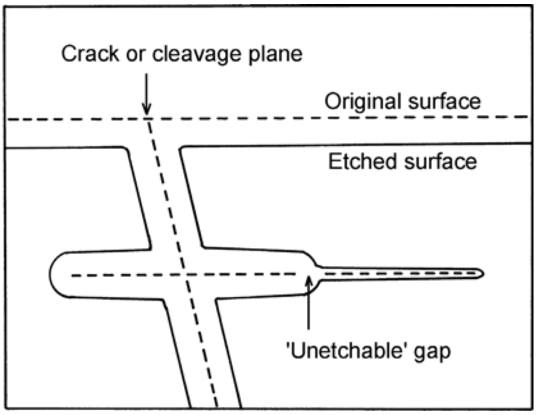

Fig. 16.26. Technique of double-etching to break though unetchable gaps in partially annealed tracks. After Hejl (1995).

A third cause of bias in confined track lengths is the effect of crystallographic orientation (Green and Durrani, 1977). Compared with un-annealed apatite grains, in which track length is effectively equal in all directions, annealed apatites exhibit less shortening of tracks parallel to the *c* axis than in other orientations. Therefore, in order to see the whole range of track lengths in an annealed apatite (and thus gain the maximum information), the prismatic section, containing tracks at all angles to the *c* axis, is observed (Gleadow *et al.*, 1986).

Laslett *et al.* (1982) and Gleadow *et al.* (1986) compared the results of projected and confined track lengths in samples with different thermal histories. They argued that, whereas projected track lengths yield only subtle indications of different thermal histories, confined tracks gave clear diagnostic indicators of thermal history. These can be divided into five types (Fig. 16.27).

Induced tracks (Fig. 16.27a) are the longest and most uniform type (16 ± 1 μm, based on several different types of sample). Tracks in undisturbed volcanics and rapidly cooled shallow intrusions are also uniform within a single sample (Fig. 16.27b), but there

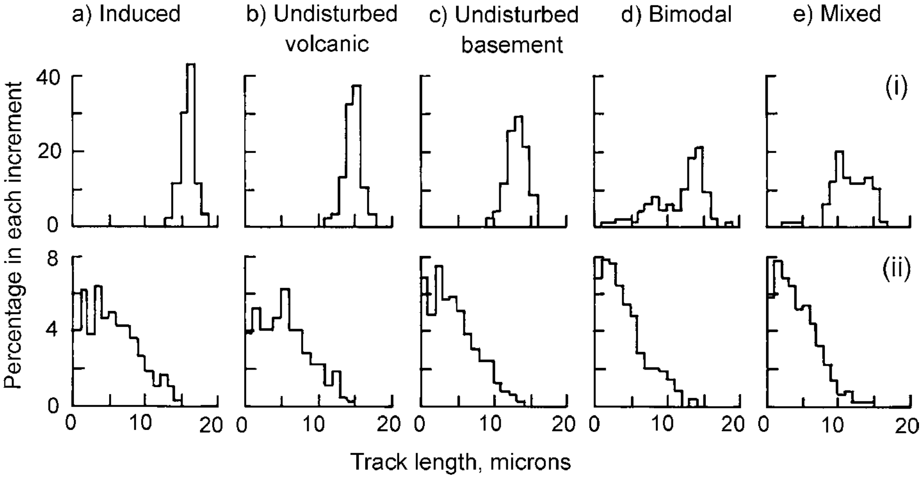

Fig. 16.27. Histograms of track length (as a percentage of total sample) for apatites with different types of thermal history (see the text). Top row: horizontal confined tracks; bottom row: projected tracks. After Gleadow *et al.* (1986).

is some variation between sample means (about 14–15.5 μm). This can be attributed to limited annealing at near-ambient temperatures over periods of tens of millions of years. Tracks in undisturbed basement apatite (Fig. 16.27c) are somewhat shorter (means of 12–14 μm), with a skewed distribution attributed to slow cooling from regional metamorphism. Finally, bimodal and mixed distributions (Figs. 16.27d and 16.27e) are attributed to various types of two-stage thermal history, in which pre-existing tracks were partially erased by a thermal event between initial cooling and the present.

16.7.1 Projected tracks

The apparent length of these tracks is biased from the true length distribution by three factors. Firstly, truncation by the surface reduces apparent length. Secondly, tracks undergo visual fore-shortening to an extent that depends on their angle to the surface. Thirdly, more frequent intersection of long tracks with the surface biases apparent length upwards. Together, these biases cause the projected track-length distributions in Fig. 16.27 to be severely obscured. However, useful information can be extracted from these distributions if projected lengths of spontaneous tracks are ratioed against the length of projected *induced* tracks (in a population experiment). In this case the biases are cancelled out.

Wagner (1988) performed this analysis by comparing the percentage of spontaneous tracks that exceeded a certain length, with the percentage of induced tracks over this length, to yield the ratio 'c_s/c_i'. A value of 10 μm was initially chosen as a convenient length cut-off for this analysis. However, Wagner and Hejl (1991) generalised the above approach by calculating an apparent fission-track age for all projected track lengths exceeding a series of cut-off lengths (x) from zero to 15 μm (at 1-μm intervals). Relative to the conventional fission-track age ($x = 0$), the normalised age (t) at various values of x is given as

$$t = \frac{c_s \rho_s}{c_i \rho_i} \qquad [16.9]$$

These apparent ages can then be plotted as an 'age-spectrum' diagram. The significant thing about this diagram is that the cut-off for preservation of fission-tracks of various lengths is related to temperature, although probably not as a linear function. Hence, the apparent-age diagram is itself a plot of temperature against time, if we can calibrate the cut-off length against temperature. As a preliminary calibration we can adopt the following points:

(1) A track length of zero should correspond to the conventional blocking temperature of about 120 °C, which marks the upper temperature limit of the PAZ.
(2) Wagner (1988) assigned a cut-off length of 10 μm to the blocking temperature of 60 °C at the lower temperature limit of the PAZ.
(3) A track length of 15 μm represents the case of zero annealing, which may be sustained at ambient temperatures of about 30 °C.

Wagner and Hejl presented fission-track age-spectrum diagrams for three rocks with different

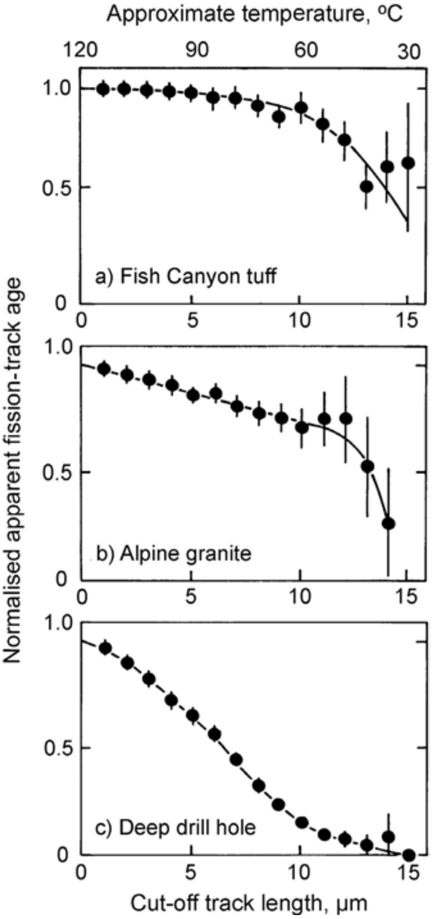

Fig. 16.28. Projected track-length age-spectrum diagrams for three geological examples: (a) Fish Canyon Tuff; (b) Alpine (Gotthard Pass) granite; and (c) paragneiss from 2353 m depth in the Continental Deep Drill hole, Bavaria. For discussion, see the text. Modified after Wagner and Hejl (1991).

thermal histories in order to assess the usefulness of this diagram (Fig. 16.28). The Fish Canyon Tuff from Colorado (Fig. 16.28a) shows the effects of rapid cooling through the PAZ, with minimal loss of short tracks, but some loss of long tracks. Therefore, it has either suffered a mild thermal pulse since eruption (for which there is little evidence), or else ambient temperatures are sufficient to cause some annealing. The Gotthard Pass granite from the Alps (Fig. 16.28b) shows the effect of slower cooling through the PAZ, due to a uniform but rapid uplift rate. Finally, a paragneiss from the Continental Deep Drill hole in Bavaria (Fig. 16.28c) shows the behaviour of a sample that is undergoing slow uplift, but is still buried. The sample came from 2353 m depth, with an ambient temperature of 70 °C, near the low-temperature limit (i.e. upper depth limit) of the PAZ.

16.7.2 Confined tracks

Although useful information can be extracted from projected track lengths, correction of the biases involved in this method has the effect of degrading the statistical quality of the data. This was demonstrated by Laslett *et al.* (1994) in a comparison of the usefulness of confined and projected track lengths for thermal-history analysis.

Confined track lengths bear a simpler relationship to the true track-length distribution, but projected tracks (also referred to as semi-tracks) are more numerous. Therefore, Laslett *et al.* performed simulations to test the ability of 2000 projected tracks and 100 confined tracks to recover the true track-length variation in a mixed population with lengths of 14.5 and 10 μm. The proportion of shorter tracks (p) was varied in different simulations from 20% to 80%. Results showed that when the shorter tracks made up 60%–80% of the population, both methods could recover the length of these tracks and the correct value of p with similar error bars (Fig. 16.29). However, when the proportion of short tracks fell below 50%, the projected track data were seriously compromised.

Laslett *et al.* concluded from this experiment that a relatively small number of confined-track measurements can more reliably recover the true track-length distribution than a large number of projected-track lengths. Hence, it is now generally agreed that confined tracks are superior to projected tracks for thermal-history analysis.

In order to use track-length analysis to make quantitative interpretations of thermal histories, Laslett *et al.* (1987) developed a model to predict the degree of track shortening after heating episodes of various intensities. This model was based on isothermal laboratory annealing experiments on large gem-quality apatite samples from Durango, Mexico (Green *et al.*, 1986). Arrhenius (temperature–time) relationships were observed for given fractions of track shortening. These are analogous to the Arrhenius relationships for track density (e.g. Fig. 16.18).

The isothermal model was extended to more complex thermal histories involving variable temperature conditions by Duddy *et al.* (1988), and applied to

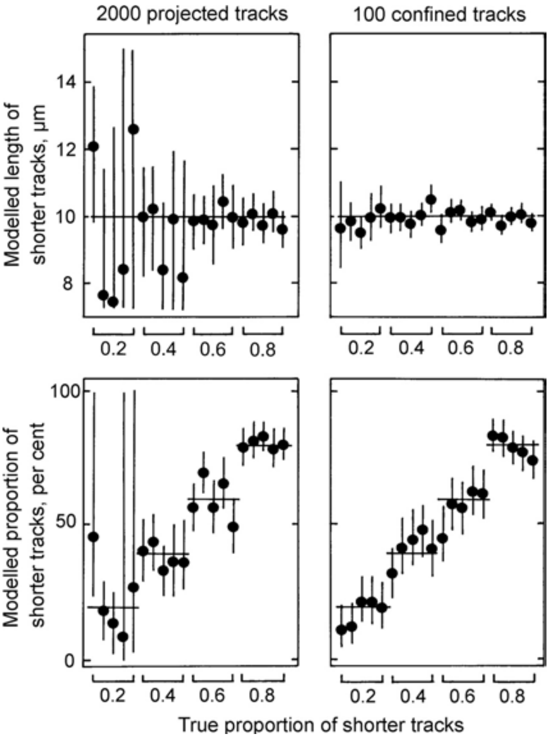

Fig. 16.29. Comparison of the success of projected and confined tracks to recover the length and the proportion of a population of short tracks amongst a population of longer tracks. Error bars indicate 95% confidence limits, except where they are truncated by the edge of the diagram. After Laslett *et al.* (1994).

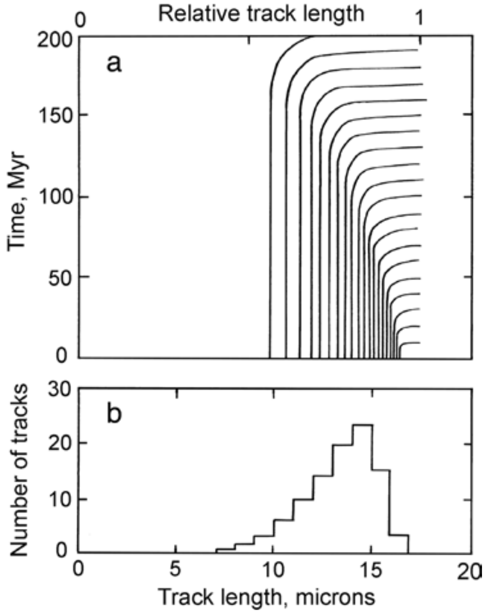

Fig. 16.30. Model for fission-track formation and annealing in a subsiding sedimentary basin: (a) progress of track formation and shortening; and (b) the resulting distribution of track-length data. Modified after Green *et al.* (1989).

geological timescales by Green *et al.* (1989). In their approach, a predicted temperature–time curve is divided into intervals (e.g. 1 Myr each), and after each interval the degree of shortening of existing tracks is calculated. At a constant elevated temperature, track shortening occurs rapidly at first, because the track ends are least energetically stable, but the rate subsequently slows considerably. In addition to the annealing of old tracks, new track formation is simulated at 10-Myr intervals. Tracks formed at each of these intervals define an evolution path of reduced track length against time (Fig. 16.30a). The sum of these evolution paths at the present day forms a histogram of track-length distribution (Fig. 16.30b).

Green *et al.* (1989) modelled the track-length distributions expected from several different types of thermal history. This process, of predicting track-length distributions from thermal-history data, is termed forward modelling. They tested the model results against data from the Otway Basin, SE Australia. In the Otway Basin case, the thermal-history problem is overconstrained because Green *et al.* had access to full track-length distributions for a suite of borehole samples from various depths. Therefore, they were able to simplify their analysis by discarding the information on track-length variation, and comparing only predicted and measured mean track lengths. This is really a waste of the track-length method, since it throws away the useful information about track-length variation. However, in this case it serves to verify the model. The result, compared with average measured track lengths from Otway Basin boreholes, is shown in Fig. 16.31.

A suite of samples at different depths is not always available from one locality, but by using the complete track-length distribution (rather than just the mean), it should be possible to test alternative thermal histories using a single sample. However, several different model thermal histories might generate track-length distributions that fit the observed data set. Therefore, it is desirable to test many different solutions in order to see what range of possible histories can generate the observed data. The final objective of this process,

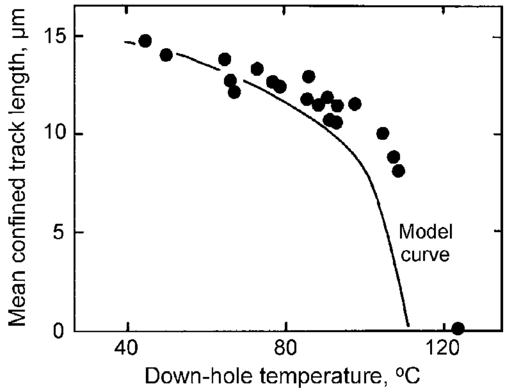

Fig. 16.31. Predicted curve for mean fission-track length against temperature in the Otway Basin, compared with measured data points from boreholes. After Green *et al.* (1989).

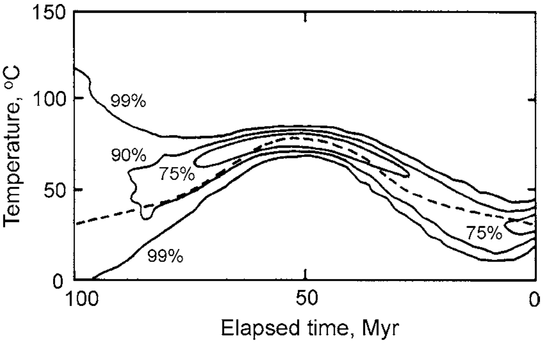

Fig. 16.32. Plot of probability density for modelled thermal histories of a sedimentary basin, based on fission-track data. In this test case the actual thermal history is known, and is shown for reference (dashed line). After Corrigan (1991).

to determine which thermal history best explains the observed track-length distribution, is termed inversion modelling (e.g. Corrigan, 1991; Gallagher, 1995).

Because initial track development and subsequent track shortening are processes subject to random noise, thermal histories cannot be uniquely determined, but must be based on probabilities. In practice, thermal histories chosen at random (the Monte Carlo method) are used to calculate track-length distributions by forward modelling. The results are then tested against the observed (or simulated) track-length data. After a few hundred iterations it is possible to map out a range of possible thermal histories that are consistent with the data set. Within this range of possibilities, the highest probability density defines an optimum, but not necessarily unique, thermal history (Fig. 16.32). Relatively well-constrained thermal histories can be projected back to the last temperature maximum, but beyond this time the thermal history is very poorly constrained (as indicated by the fanning out of the probability contours at ages over 60 Myr).

A continuing source of uncertainty in such modelling is the extrapolation of laboratory experiments to geological timescales. Gallagher (1995) compared three alternative annealing models that had been proposed during the preceding ten years. The first of these uses the laboratory data of Green *et al.* (1986), extrapolated by Laslett *et al.* (1987). The second model (Carlson, 1990) uses the same data set, coupled with an *ad hoc* geometrical model, but has been criticised as unrealistic in crystallographic terms (e.g. Green *et al.*, 1993). The third model is based on new laboratory data by Crowley *et al.* (1991). Since the models of Carlson and Crowley *et al.* diverge on opposite sides of the Laslett *et al.* model, the latter still appears to be the most useful for thermal-history modelling.

16.8 Pressure effects

Recently, Wendt *et al.* (2002) introduced a further twist to fission-track analysis by suggesting that the process of thermal track annealing in apatite is also pressure-dependent. They performed annealing experiments at 250 °C, for a variety of different times and pressures, on apatite from four geological occurrences. It was felt that experiments on spontaneous tracks in natural materials would be less likely to introduce artefacts into the experiments.

The results of these experiments for two of the samples used by Wendt *et al.* are presented in terms of track-length variations and track densities in Fig. 16.33 (a and b). These two samples were from Canada and Siberia, and both displayed evidence of slight prior annealing over their geological history. The results showed that pressures of 100 and 300 MPa had a dramatic effect on the extent of thermal annealing, compared with the behaviour at 0.1 MPa (ambient pressure). The effects were observed both on average track length (Fig. 16.33a) and on track density (Fig. 16.33b), and the effect was to *reduce* the extent of annealing at higher pressure.

The pressures of 100 and 300 MPa used in these experiments (corresponding to 1 and 3 kbar) are equivalent to depths of about 3.5 and 10 km in the crust. Comparison of these numbers with the 3.5-km depth of the Otway Basin, Australia, suggests that these pressure effects are occurring within the depth range where apatite fission-track data have been applied to geological problems. Hence, the evidence suggests that

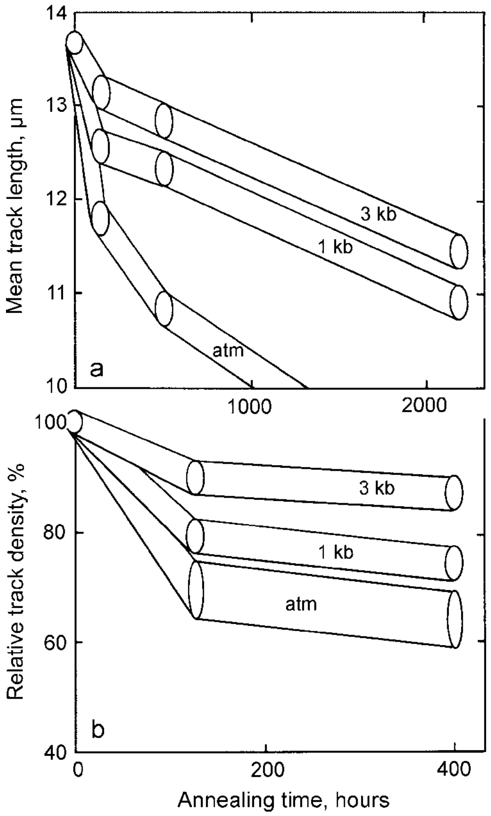

Fig. 16.33. Effects of pressure on the annealing of two natural apatites, expressed in terms of (a) track length and (b) track density. Each ellipse defines the range of properties of two different apatites. All experiments were carried out at 250 °C. Data from Wendt *et al.* (2002).

pressure effects could have a significant effect on calculated cooling histories. The controversial nature of this proposal is demonstrated by the scientific discussion that ensued (*Earth Planet. Sci. Lett.* **215**, pp. 299–316, 2003). Therefore, confirmatory experiments are clearly needed before wider conclusions are drawn.

References

Bhandari, N., Bhat, S. G., Rajogopalan, G., Tamhane, A. S. and Venkatavaradan, V. S. (1971). Fission fragment lengths in apatite: recordable track lengths. *Earth Planet. Sci. Lett.* **13**, 191–9.

Bigazzi, G. (1967). Length of fission-tracks and age of muscovite samples. *Earth Planet. Sci. Lett.* **3**, 434–8.

Briggs, N. D., Naeser, C. W. and McCulloh, T. H. (1981). Thermal history of sedimentary basins by fission-track dating. *Nucl. Tracks* **5**, 235–7 (abstract).

Carlson, W. D. (1990). Mechanisms and kinetics of apatite fission-track annealing. *Amer. Mineral.* **75**, 1120–39.

Corrigan, J. (1991). Inversion of apatite fission-track data for thermal history information. *J. Geophys. Res.* **96**, 10 347–60.

Crowley, K. D., Cameron, M. and Schaefer, R. L. (1991). Experimental studies of annealing of etched fission-tracks in fluorapatite. *Geochim. Cosmochim. Acta* **55**, 1449–65.

Dakowski, M. (1978). Length distributions of fission-tracks in thick crystals. *Nucl. Track Det.* **2**, 181–9.

Duddy, I. R., Green, P. F. and Laslett, G. M. (1988). Thermal annealing of fission-tracks in apatite 3. Variable temperature behaviour. *Chem. Geol. (Isot. Geosci. Section)* **73**, 25–38.

Fleischer, R. L. and Hart, H. R. (1972). Fission-track dating: techniques and problems. In: Bishop, W., Miller, J. and Cole, S. (Eds.), *Calibration of Hominoid Evolution*. Scottish Academic Press, pp. 135–70.

Fleischer, R. L. and Price, P. B. (1964a). Techniques for geological dating of minerals by chemical etching of fission fragment tracks. *Geochim. Cosmochim. Acta* **28**, 1705–14.

Fleischer, R. L. and Price, P. B. (1964b). Glass dating by fission fragment tracks. *J. Geophys. Res.* **69**, 331–9.

Fleischer, R. L., Price, P. B., Symes, E. M. and Miller, D. S. (1964). Fission-track ages and track-annealing behaviour of some micas. *Science* **143**, 349–51.

Fleischer, R. L., Price, P. B. and Walker, R. M. (1965a). Tracks of charged particles in solids. *Science* **149**, 383–93.

Fleischer, R. L., Price, P. B. and Walker, R. M. (1965b). Effects of temperature, pressure, and ionization on the formation and stability of fission tracks in minerals and glasses. *J. Geophys. Res.* **70**, 1497–502.

Fleischer, R. L., Price, P. B. and Walker, R. M. (1968). Charged particle tracks: tools for geochronology and meteor studies. In: Hamilton, E. and Farquhar, R. M. (Eds.), *Radiometric Dating for Geologists*. Wiley Interscience, pp. 417–35.

Fleischer, R. L., Price, P. B. and Walker, R. M. (1975). *Nuclear Tracks in Solids*. University of California Press, 605 pp.

Galbraith, R. F. (1988). Graphical display of estimates having differing standard errors. *Tectonometrics* **30**, 271–81.

Gallagher, K. (1995). Evolving temperature histories from apatite fission-track data. *Earth Planet. Sci. Lett.* **136**, 421–35.

Gleadow, A. J. W. and Duddy, I. R. (1981). A natural long-term track annealing experiment for apatite. *Nucl. Tracks* **5**, 169–74.

Gleadow, A. J. W., Duddy, I. R., Green, P. F. and Lovering, J. F. (1986). Confined fission track lengths in apatite: a diagnostic tool for thermal history analysis. *Contrib. Mineral. Petrol.* **94**, 405–15.

Gleadow, A. J. W., Duddy, I. R. and Lovering, J. F. (1983). Apatite fission-track analysis as a paleotemperature indicator for hydrocarbon exploration. *Australian Petrol. Explor. Soc. J.* **23**, 93–102.

Green, P. F. (1981). 'Track-in track' length measurements in annealed apatites. *Nucl. Tracks* **5**, 121–8.

Green, P. F., Duddy, I. R., Gleadow, A. J. W. and Tingate, P. R. (1985). Fission-track annealing in apatite: track length measurements and the form of the Arrhenius plot. *Nucl. Tracks* **10**, 323–8.

Green, P. F., Duddy, I. R., Gleadow, A. J. W., Tingate, P. R. and Laslett, G. M. (1986). Thermal annealing of fission tracks in apatite. 1. A qualitative description. *Chem. Geol. (Isot. Geosci. Section)* **59**, 237–53.

Green, P. F., Duddy, I. R., Laslett, G. M., Hegarty, K. A., Gleadow, A. J. W. and Lovering, J. F. (1989). Thermal annealing of fission-tracks in apatite 4. Quantitative modelling techniques and extension to geological timescales. *Chem. Geol. (Isot. Geosci. Section)* **79**, 155–82.

Green, P. F. and Durrani, S. A. (1977). Annealing studies of tracks in crystals. *Nucl. Track Det.* **1**, 33–9.

Green, P. F., Laslett, G. M. and Duddy, I. R. (1993). Mechanisms and kinetics of apatite fission-track annealing – discussion. *Amer. Mineral* **78**, 441–5.

Hejl, E. (1995). Evidence for unetchable gaps in apatite fission-tracks. *Chem. Geol. (Isot. Geosci. Section)* **122**, 259–69.

Hurford, A. J. (1990). Standardization of fission track dating calibration: recommendation by the Fission Track Working Group of the I.U.G.S. Subcommission on Geochronology. *Chem. Geol. (Isot. Geosci. Section)* **80**, 171–8.

Hurford, A. J. and Carter, A. (1991). The role of fission track dating in discrimination of provenance. In: Morton, A. C., Todd, S. P. and Haughton, P. D. W. (Eds.) *Developments in Sedimentary Provenance Studies. Geological Society Special Publication* **57**, 67–78.

Hurford, A. J., Fitch, F. J. and Clarke, A. (1984). Resolution of the age structure of the detrital zircon populations of two Lower Cretaceous sandstones from the Weald of England by fission-track dating. *Geol. Mag.* **121**, 269–77.

Hurford, A. J. and Green, P. F. (1982). A users' guide to fission-track dating calibration. *Earth Planet. Sci. Lett.* **59**, 343–54.

Hurford, A. J. and Green, P. F. (1983). The ζ age calibration of fission-track dating. *Isot. Geosci.* **1**, 285–317.

Kowallis, B. J., Heaton, J. S. and Bringhurst, K. (1986). Fission-track dating of volcanically derived sedimentary rocks. *Geology* **14**, 19–22.

Lal, D., Rajan, R. S. and Tamhane, A. S. (1969). Chemical composition of nuclei of $Z > 22$ in cosmic rays using meteoritic minerals as detectors. *Nature* **221**, 33–7.

Laslett, G. M., Galbraith, R. F. and Green, P. F. (1994). The analysis of projected fission track lengths. *Radiat. Meas.* **23**, 103–23.

Laslett, G. M., Gleadow, A. J. W. and Duddy, I. R. (1984). The relationship between fission track length and track density in apatite. *Nucl. Tracks* **9**, 29–38.

Laslett, G. M., Green, P. F., Duddy, I. R. and Gleadow, A. J. W. (1987). Thermal annealing of fission-tracks in apatite, 2. A quantitative analysis. *Chem. Geol. (Isot. Geosci. Section)* **65**, 1–13.

Laslett, G. M., Kendall, W. S., Gleadow, A. J. W. and Duddy, I. R. (1982). Bias in measurement of fission-track length distributions. *Nucl. Tracks* **6**, 79–85.

Maurette, M., Pellas, P. and Walker, R. M. (1964). Etude des traces fission fossiles dans le mica. *Bull. Soc. Franç. Minér. Cryst.* **87**, 6–17.

Naeser, C. W. (1979a). Fission-track dating and geological annealing of fission-tracks. In: Jäger, E. and Hunziker, J. C. (Eds.), *Lectures in Isotope Geology*. Springer-Verlag, pp. 154–69.

Naeser, C. W. (1979b). Thermal history of sedimentary basins: fission-track dating of subsurface rocks. In: Scholle, P. A., and Schluger, P. R. (Eds.), *Aspects of Diagenesis. Society of Economic and Paleontological Mineralogy Special Publication* **26**, pp. 109–12.

Naeser, C. W. (1981). The fading of fission-tracks in the geologic environment – data from deep drill holes. *Nucl. Tracks*. **5**, 248–50 (abstract).

Naeser, C. W. and Faul, H. (1969). Fission track annealing in apatite and sphene. *J. Geophys. Res.* **74**, 705–10.

Naeser, C. W., Zimmermann, R. A. and Cebula, G. T. (1981). Fission-track dating of apatite and zircon: an inter-laboratory comparison. *Nucl. Tracks* **5**, 65–72.

Naeser, N. D. and Naeser, C. W. (1984). Fission track dating. In: Mahaney, W. C. (Ed.), *Quaternary Dating Methods. Developments in Paleontology and Stratigraphy* **7**. Elsevier, pp. 87–100.

Naeser, N. D., Naeser, C. W. and McCulloh, T. H. (1989). The application of fission-track dating to the depositional and thermal history of rocks in sedimentary basins. In: Naeser, N. D. and McCulloh, T. H. (Eds.), *Thermal History of Sedimentary Basins*. Springer-Verlag, pp. 157–80.

Price, P. B. and Walker, R. M. (1962a). Chemical etching of charged particle tracks in solids. *J. Appl. Phys.* **33**, 3407–12.

Price, P. B. and Walker, R. M. (1962b). Observation of fossil particle tracks in natural micas. *Nature* **196**, 732–4.

Price, P. B. and Walker, R. M. (1963). Fossil tracks of charged particles in mica and the age of minerals. *J. Geophys. Res.* **68**, 4847–62.

Reimer, G. M., Storzer, D. and Wagner, G. A. (1970). Geometry factor in fission-track counting. *Earth Planet. Sci. Lett.* **9**, 401–4.

Silk, E. C. H. and Barnes, R. S. (1959). Examination of fission fragment tracks with an electron microscope. *Phil. Mag.* **4**, 970–2.

Storzer, D. and Poupeau, G. (1973). Ages plateaux de minéraux et verres par la méthode des traces de fission. *C. R. Acad. Sci. Paris* **276**, 137–9.

Storzer, D. and Wagner, G. A. (1969). Correction of thermally lowered fission track ages of tektites. *Earth Planet. Sci. Lett.* **5**, 463–8.

Storzer, D. and Wagner, G. A. (1982). The application of fission-track dating in stratigraphy: a critical review. In: Odin, G. S. (Ed.), *Numerical Dating in Stratigraphy*. Wiley, pp. 199–221.

Wagner, G. A. (1978). Archaeological applications of fission-track dating. *Nucl. Track Det.* **2**, 51–63.

Wagner, G. A. (1988). Apatite fission-track geochrono-thermometer to 60 °C: projected length studies. *Chem. Geol. (Isot. Geosci. Section)* **72**, 145–53.

Wagner, G. A. and Hejl, E. (1991). Apatite fission-track age-spectrum based on projected track-length analysis. *Chem. Geol. (Isot. Geosci. Section)* **87**, 1–9.

Wagner, G. A. and Reimer, G. M. (1972). Fission track tectonics: the tectonic interpretation of fission-track apatite ages. *Earth Planet. Sci. Lett.* **14**, 263–8.

Wagner, G. A., Reimer, G. M. and Jäger, E. (1977). Cooling ages derived by apatite fission-track, mica Rb–Sr and K–Ar dating: the uplift and cooling history of the Central Alps. *Mem. Ist. Geol. Min. Univ. Padova* **30**, 1–27.

Walter, R. C. (1989). Application and limitation of fission-track geochronology to Quaternary tephras. *Quaternary Int.* **1**, 35–46.

Wendt, A. S., Vidal, O. and Chadderton, L. T. (2002). Experimental evidence for the pressure dependence of fission-track annealing in apatite. *Earth Planet. Sci. Lett.* **201**, 593–607.

Index